Conference Proceedings of the Society for Experimental Mechanics Series

Bo Song · Dan Casem · Jamie Kimberley *Editors*

Dynamic Behavior of Materials, Volume 1

Proceedings of the 2013 Annual Conference on Experimental and Applied Mechanics

Springer

Conference Proceedings of the Society for Experimental Mechanics Series

Series Editor
Tom Proulx
Society for Experimental Mechanics, Inc.,
Bethel, CT, USA

For further volumes:
http://www.springer.com/series/8922

Bo Song • Dan Casem • Jamie Kimberley
Editors

Dynamic Behavior of Materials, Volume 1

Proceedings of the 2013 Annual Conference on Experimental and Applied Mechanics

Springer

Editors
Bo Song
Sandia National Laboratories
Department of Mechanics of Materials
Livermore, CA
USA

Dan Casem
US Army Research Laboratory
Aberdeen Proving Ground
Aberdeen, MD
USA

Jamie Kimberley
New Mexico Institute of Mining
and Technology
Socorro, NM
USA

ISSN 2191-5644 ISSN 2191-5652 (electronic)
ISBN 978-3-319-00770-0 ISBN 978-3-319-00771-7 (eBook)
DOI 10.1007/978-3-319-00771-7
Springer Cham Heidelberg New York Dordrecht London

Library of Congress Control Number: 2013947966

Printed on acid-free paper

Springer is part of Springer Science+Business Media (www.springer.com)

Preface

Dynamic Behavior of Materials, Volume 1: Proceedings of the 2013 Annual Conference on Experimental and Applied Mechanics represents one of eight volumes of technical papers presented at the SEM 2013 Annual Conference & Exposition on Experimental and Applied Mechanics organized by the Society for Experimental Mechanics and held in Lombard, IL, June 3–5, 2013. The complete Proceedings also includes volumes on: *Challenges in Mechanics of Time-Dependent Materials and Processes in Conventional and Multifunctional Materials; Advancement of Optical Methods in Experimental Mechanics; Mechanics of Biological Systems and Materials; MEMS and Nanotechnology; Experimental Mechanics of Composite, Hybrid, and Multifunctional Materials; Fracture and Fatigue; Residual Stress, Thermomechanics & Infrared Imaging, Hybrid Techniques and Inverse Problems.*

Each collection presents early findings from experimental and computational investigations on an important area within Experimental Mechanics, Dynamic Behavior of Materials being one of these areas.

The Dynamic Behavior of Materials track was initiated in 2005 and reflects our efforts to bring together researchers interested in the dynamic behavior of materials and structures and provide a forum to facilitate technical interaction and exchange. In the past years, this track has represented an ever-growing area of broad interest to the SEM community, as evidenced by the increased number of papers and attendance.

The contributed papers span numerous technical divisions within SEM, which may be of interest not only to the dynamic behavior of materials community but also to the traditional mechanics of materials community.

The track organizers thank the authors, presenters, organizers, and session chairs for their participation, support, and contribution to this track. We are grateful to the SEM Technical Division chairs who cosponsored and/or co-organized the sessions in this track. We would also like to acknowledge the SEM support staff for their devoted efforts in accommodating the large number of paper submissions this year, making the 2013 Dynamic Behavior of Materials track successful.

Livermore, CA, USA — Bo Song
Aberdeen, MD, USA — Dan Casem
Socorro, NM, USA — Jamie Kimberley

Contents

Chapter 1
Dynamic Deformation Behavior of AA2099-T8 Under Compression and Torsion Loads

Daniel O. Odoh, Gbadebo M. Owolabi, and Akindele G. Odeshi

Abstract The suitability of aluminum alloys in a vast majority of engineering applications forms the basis for the need to understand the mechanisms responsible for their deformation and failure under various loading conditions. Aluminum AA2099 alloy finds application in fuselage structures that are statically and dynamically loaded, stiffness dominated designs, and in lower wing structures. The fuselage structures and wings of aircraft experience huge damage due to foreign object impacts. AA2099 aluminum alloy has an advantage of high specific strength compared with other alloys in the AA2000, 6000, and 7000 series; this characteristic makes it the material of choice in high performance aerospace structures. In this paper, the dynamic high strain rate impact deformation of AA2099 aluminum alloy under compression and torsion loading conditions using the split Hopkinson pressure and Kolsky torsion bars was performed. Digital image photogrammetric evolution of localized strain in aluminum samples during deformation process using high speed digital camera is reported. Microstructural analysis of deformed aluminum samples was performed using high resolution electron microscopes in order to determine the influence of impact strain rate on localized strain along narrow adiabatic shear bands in the AA2099 aluminum alloys. Results obtained indicate that peak flow stress in the deformed aluminum sample depends on the strain rate at which the deformation test was performed. An increase in impact strain rate results into an increase in the peak flow stress observed in the impacted aluminum sample. The type of adiabatic shear band localized in the aluminum sample also depends on the strain rate at which material was impacted.

Keywords High strain rate impact • Digital image photogrammetric evolution • Microstructural analysis • Adiabatic shear bands • Dynamic deformation

1.1 Introduction

Aluminum alloys exhibit an attractive combination of mechanical and physical properties such as high stiffness, good fracture toughness, and a high strength to weight ratio making them materials of choice in the automobile [1] and defense industry [2]. The low density of aluminum makes it find greater application than steel in situations where fuel efficiency and economy are of great concern. Aluminum AA2099 alloy has a high specific strength when compared with other aluminum alloys and is usually used in structures that are dynamically or statically loaded such as fuselage structures of aircrafts and other low wing structural components[3].

The dynamic deformation of materials at strain rates in the region of 10^3 s^{-1} are characterized by intense strain localization [4]. The dynamic loading of materials results into a phenomenon referred to as an adiabatic shear band. Adiabatic shear bands (ASBs) are regions of narrow deformation with intense strain localization [5]. These narrow bands are planar or two dimensional microstructural features characterized by large shear [6]. Adiabatic shear bands are known to be characterized by intense strain localization, an elevated temperature, intense shearing and an elongation of micro-pores within the shear band preceding failure.

D.O. Odoh (✉) • G.M. Owolabi
Department of Mechanical Engineering, Howard University, 2300 Sixth Street NW, Washington, DC 20059, USA
e-mail: daniel.odoh@bison.howard.edu

A.G. Odeshi
Department of Mechanical Engineering, University of Saskatchewan, 57 Campus Drive, Saskatoon, SK S7N 5A9, Canada

B. Song et al. (eds.), *Dynamic Behavior of Materials, Volume 1: Proceedings of the 2013 Annual Conference on Experimental and Applied Mechanics*, Conference Proceedings of the Society for Experimental Mechanics Series,
DOI 10.1007/978-3-319-00771-7_1,

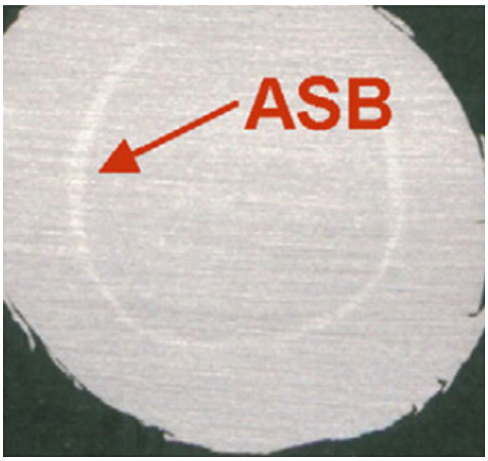

Fig. 1.1 Macroscopic view of transverse section of impacted monolithic aluminum showing adiabatic shear band region characterized by intense localization [7]

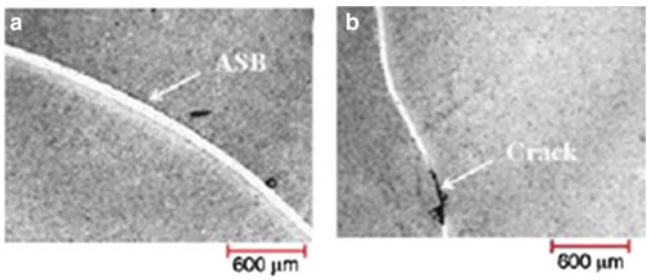

Fig. 1.2 (**a**) Adiabatic shear band in impacted steel sample. (**b**) Crack initiation and propagation within the adiabatic shear band [9]

Localized strain as a major characteristic of adiabatic shear band located in the transverse section of impacted monolithic aluminum sample is shown in Fig. 1.1.

During high strain rate loading of materials, three mechanisms are usually in place. These include work hardening, strain hardening and thermal softening [6]. Work hardening and strain hardening tend to increase the isothermal flow stress within the material while thermal softening tends to decrease it. This results into a 'war' of mechanisms, thermal softening tend to win over the other mechanisms during the deformation process and it is responsible for the continued deformation of the material under high strain rate loads instead of it experiencing fracture. Thermal (otherwise referred to as work) softening is an extremely important process that determines the onset of adiabatic shear band formation. As the plastic shearing of the sample occurs during the plastic deformation process, most of the kinetic energy of the hitting projectile is converted to heat. Based on the fact that the deformation process is so rapid, there is not enough time for the heat energy to be conducted away from the surface of the specimen and this results into tensile stresses been generated and concentrated in narrow bands referred to as adiabatic shear bands.

Adiabatic shear bands are microstructural defects that can trigger premature failure in materials under high strain rate loading. Once an ASB develops in a material under high strain rate loading, the performance of the material becomes compromised. The fragmentation of steel encasements after explosion has been observed to occur after strain localization which results into the formation of an adiabatic shear band [8].

Figure 1.2 shows the initiation and propagation of crack in impacted AISI 4340 steel samples, the adiabatic shear band formed serves as preferential site for the initiation of cracks; the material is to be changed or reprocessed since it will experience unexpected failure. Therefore, failure of materials under high strain rate loads are usually preceded by the formation of adiabatic shear bands. The tensile stresses generated inside an adiabatic shear band become sufficiently high enough to open up micro-pores inside these bands. Due to the coalescence of the micro-pores, voids are formed which elongate and rotate to elliptical shapes. These voids are finally connected, initiating micro cracks which propagate along the shear band leading ultimately to fracture. The need to explain failure of materials under high strain rate loading conditions has been the main reason for more research into the concept of adiabatic shear bands.

In this research work, the dynamic high strain rate loading of aluminum AA2099-T8 alloy is performed in compression and torsion using the split Hopkinson pressure and torsion Kolsky bars respectively in order to determine the influence of impact strain rate on the formation adiabatic shear band. Digital image photogrammetric evolution of localized strain in

aluminum samples during deformation process using high speed digital camera is determined. Microstructural analysis of deformed aluminum samples is performed using high resolution electron microscopes in order to determine the influence of impact strain rate on localized strain along narrow adiabatic shear bands in the AA2099 aluminum alloys.

1.2 Material and Experimental Procedure

The properties exhibited by AA2099-T8 aluminum alloy under various loading conditions can be traced to its elemental composition. Aluminum AA2099-T8 alloy can contain as high as 92 % of aluminum by weight and other elements in trace quantity. The chemical composition of the other elements in trace quantity in AA2099-T8 from ALCOA data sheet is given in Table 1.1.

The compression and torsion specimens with dimension are shown in Fig. 1.3a, b respectively.

The operation and working principle of the split Hopkinson pressure bar and torsion Kolsky bar that were used in this research work are described in details elsewhere [10]. The elastic waves obtained from the split Hopkinson and torsion Kolsky barsin voltage- time form are converted into stress–strain relationship by using a calibration factor obtained from the initial calibration of the bars. The processes involved in calibrating the bars and also converting the voltage-time data to stress–strain relationship are outlined elsewhere [11]. Figure 1.4 shows a typical voltage-time graph obtained during the compression of the cylindrical aluminum specimen.

The elastic wave technique is based on the assumption of a homogenous stress–strain relationship during material deformation. However, it has been observed that this usually does not hold true for all cases during high strain rate deformation of materials [4]. Therefore, there exists a need to determine localized strain in the aluminum sample by using a technique that is not based on a homogenous stress–strain assumption. The digital image correlation (DIC) technique used is a non-contact measuring technique used for determining the deformation which occurs on the surface of an object. It has several advantages among which include: Non-altering of the behavior of the specimen during testing, No recourse to analytical model, Measurement of large strain by correlation of series of images recorded during mechanical testing, Measurement of strain at local region of interest as well as a good strain accuracy. The 3D digital image correlation technique uses two high resolution photron cameras (shown in Fig. 1.5) that provide synchronized images of the deformation process in time steps.

The high resolution photron cameras make use of the principle of pattern matching on the specimen in the determination of localized strain. This is achieved by applying a random dot pattern on the surface of the AA2099-T8 specimen with black and white spray paints to provide a gray scale distribution. This ensures sufficient contrast between the un-deformed and the deformed images. Figure 1.6 shows a typical dot pattern made on the cylindrical compression specimen prior to testing.

Table 1.1 Chemical composition of AA2099-T8 aluminum alloy

Chemical composition (Wt. %)							
Cu	Li	Zn	Mg	Mn	Zr	Ti	Fe
2.4–3.0	1.6–2.0	0.4–1.0	0.10–0.50	0.10–0.50	0.05–0.12	≤0.10	≤0.07

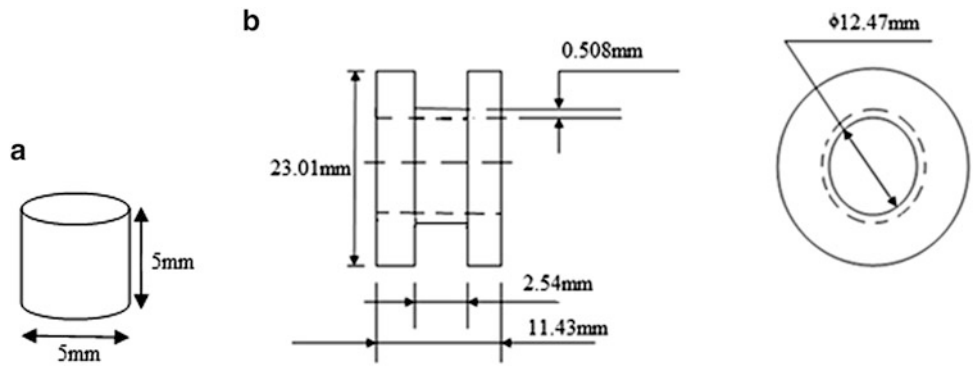

Fig. 1.3 (**a**) Compression specimen. (**b**) Torsion specimen

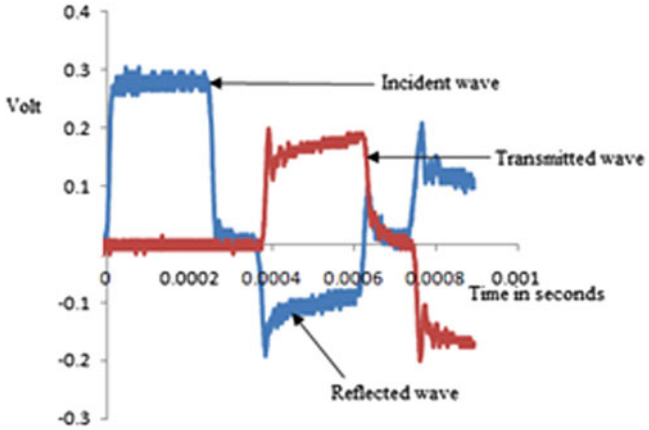

Fig. 1.4 Typical voltage-time graph obtained during compression test

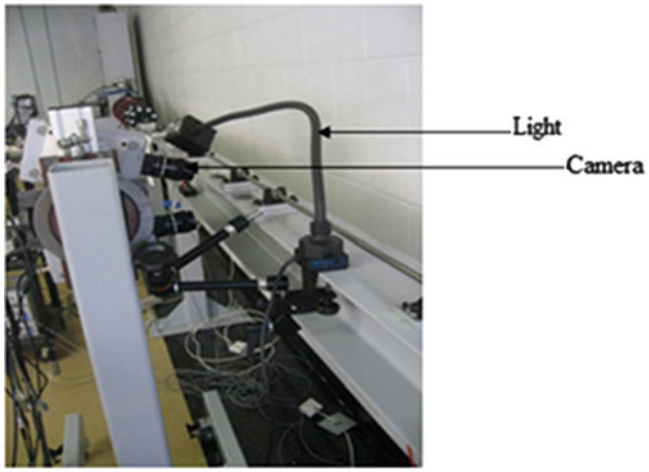

Fig. 1.5 Digital image correlation set-up showing high resolution digital cameras

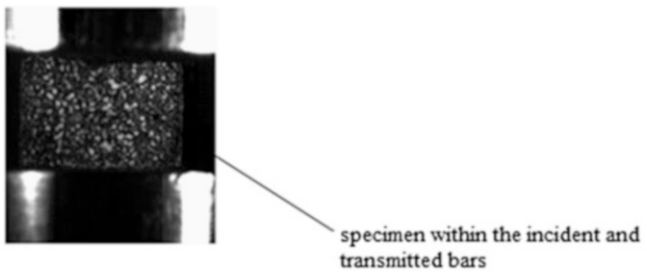

Fig. 1.6 Random dot pattern on cylindrical sample prior to torsion test

The compression experiment was captured by the digital cameras at an array of 192 × 216 pixels resolution and 124,000 frames per second (FPS) while the torsion test was performed at a pixel resolution of 320 × 128 and 140,000 FPS. Images of the deformation process captured by the high resolution camera are saved as tiff files and uploaded into a digital image software package for post processing to obtain full field strain versus time data. The software package referred to as Aramis is used to analyze the images captured during the deformation process. Strain calculation was performed in the correlation software using a 3 × 3 minimum facet point. This allows for a wide coverage of points on the deformed sample. The correlation technique used keeps track of the movement of the grayscale random pattern distribution within each facet relative to its centre point from image to image in order to obtain a displacement from which the strain is obtained.

The compression test was performed at strain rates ranging between 1,000 and 3,000 s^{-1} in order to determine the influence of strain rate on the deformation behavior of the aluminum sample as well as formation of adiabatic shear band within the specimen. The strain rate and corresponding impact velocity at which the compression tests were performed are reported in Table 1.2.

Table 1.2 Impact strain rate and corresponding velocity during compression test

Strain rate (/s)	Impact velocity (m/s)
1,000	9.60
1,500	12.10
2,000	18.64
3,000	19.80

Table 1.3 Impact strain rate and corresponding torque

Strain rate (/s)	Applied torque (Nm)
750	144.95
1,000	168.90
1,500	216.53

During the torsion test, a torque equivalent to the desired strain rate was applied resulting into torsion waves being generated on the incident bar of the torsion Kolsky bars. The impact strain rate at which test was performed and corresponding applied torque is recorded in Table 1.3.

1.3 Result and Discussion

The stress–strain results obtained from the compression and torsion loading of aluminum AA6061-T6 sample during dynamic impact test are reported. The effect of impact velocity and hence strain rate on the dynamic stress–strain relationship during impact of the compression specimen is discussed. Also the effect of applied torque (which is a function of strain rate) on the deformation of the torsion sample is also reported. The influence of strain rate on the adiabatic shear band behavior of the specimen is also outlined.

A typical stress–strain relationship obtained during the dynamic loading of the aluminum AA2099-T8 specimen is shown in Fig. 1.7.

As shown in Fig. 1.7, the deformation which occurs in the aluminum sample subjected to dynamic load is elastic up until the yield point. This means that the material will return to its initial condition if load was removed just before the yield point. However beyond the yield point, plastic deformation sets in and the material is permanently deformed from its initial condition. During the plastic deformation which occurs beyond the yield point, strain hardening and thermal softening are two mechanisms that occur simultaneously. These phenomena can be attributed to the heat generated inside the material due to the kinetic energy of the projectile being converted into heat energy. The strain hardening phenomenon dominates the deformation process up until a point when the material's maximum flow stress is reached. Once the maximum flow stress is reached, thermal softening dominates the deformation process and it is said to have 'won' the war over strain hardening. The domination of thermal softening is usually characterized by a stress collapse due to mechanical instability resulting from intense adiabatic heating along narrow paths leading to strain localization. During the thermal softening process, an increase in strain usually results into a decrease in the flow stress. The point when a drop in the material flow stress is observed is referred to as the critical strain and it is designated ε_{crit}.

Figure 1.8 shows the true stress versus true strain graph obtained at different impact velocities during the compression test. A peak flow stress of about 412 MPa was recorded for the test performed at 9.6 m/s; this increased to about 456 MPa for impact test performed at 19.8 m/s.

The critical strain and time during which thermo-mechanical instability occur increases as the impact velocity is increased. This can be attributed to an increase in the plastic strain and thermal softening in the specimen as the impact velocity increases. The increased thermal softening behavior of the specimen as impact velocity increases usually results into an increase in the plastic nature of the deformation process. An increase in the impact velocity has been observed to increase the temperature inside the shear band significantly, hence leading into significant effect in plasticity and material yielding. Beyond the critical strain, the peak stress recorded at each impact velocity experienced a drop due to stress collapse from mechanical instability as a consequence of intense adiabatic heating resulting in localization of strain.

The time history of the localization of strain along the compression specimen was determined via the digital image correlation technique and the conventional elastic wave techniques in order to compare both techniques. The strain-time history plot shows the path of strain localization in the specimen as a function of time in Fig. 1.9.

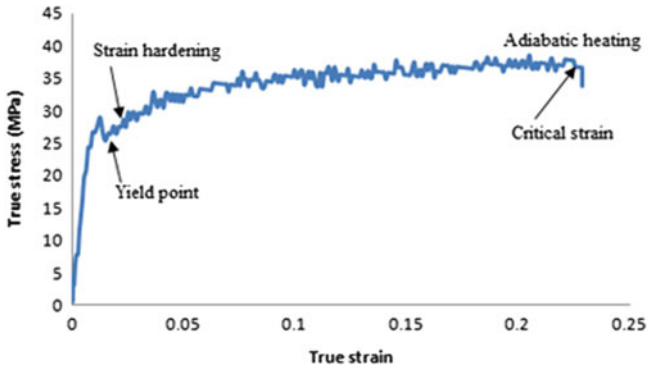

Fig. 1.7 Typical stress–strain curve for aluminum sample subjected to dynamic impact loading.

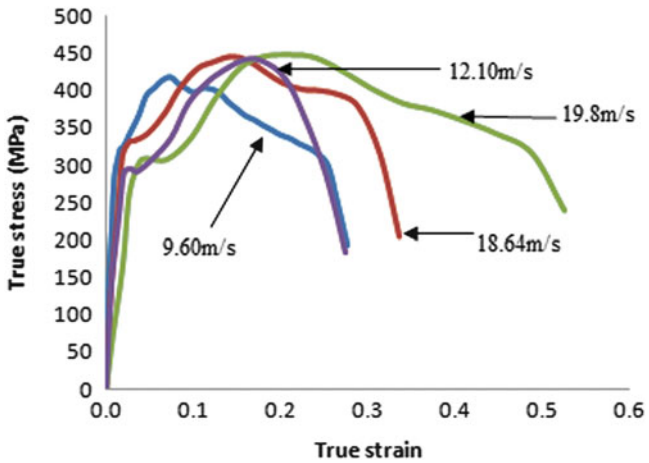

Fig. 1.8 Dynamic impact stress–strain relationship for AA2099-T8 aluminum alloy specimen as a function of impact velocity

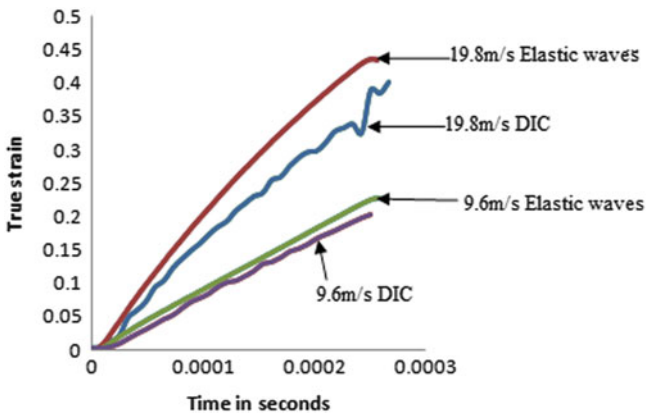

Fig. 1.9 Strain – time history obtained using 3D DIC system and elastic wave as a function of the impact velocity

It is observed from Fig. 1.9 that the elastic waves strain gauging technique gives a slightly higher result compared with the non-contact image correlation technique. During test conducted at 9.6 m/s, the strain determined via the digital image correlation system was 5.34 % lower than that recorded via the conventional strain gauging technique. Also, the strain obtained via the DIC method during tests conducted at 19.8 m/s was 7.8 % lower than that determined via the elastic wave technique. This decrease can be traced to the absence of an assumed homogenous stress- strain relationship in the digital image correlation technique. The homogenous stress- strain relationship is a situation which is assumed to hold true in the conventional elastic wave strain gauging technique; however, this assumption does not hold true in the DIC technique based on the fact that the DIC technique can be used to measure localized strain at region of interest. A linear relationship is

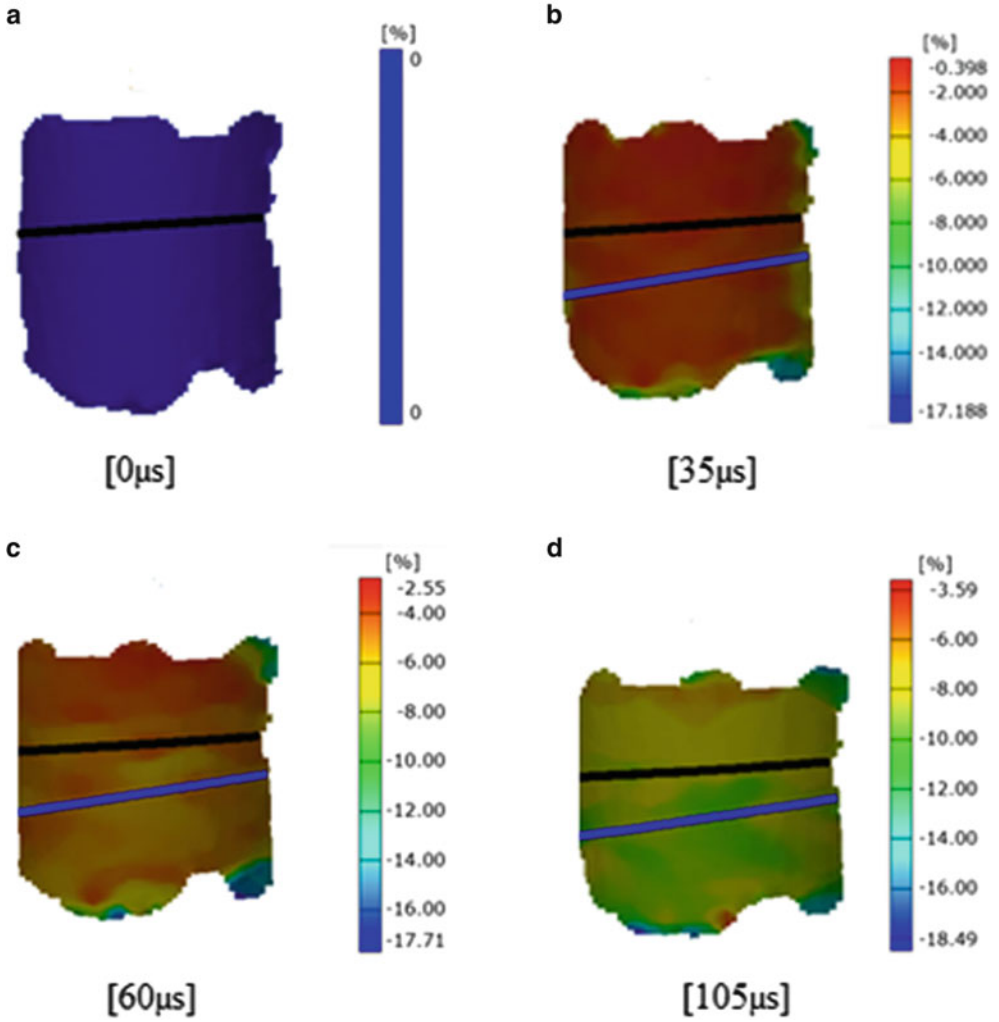

Fig. 1.10 Digital image correlation map of strain localization in compression specimen as a function of time at a velocity of 9.6 m/s (color figure in online)

observed between the time over which the deformation process occurs and the localization of strain. This signifies that the localized strain in the aluminum material increases linearly with time as the time of deformation increases, reaching a peak at the end of the deformation process. Figure 1.9 shows that the rate at which strain localization occurs increases as the impact velocity and hence strain rate increases. This is due to the fact that an increase in strain rate results into a higher possibility for occurrence of thermal softening and hence adiabatic heating. Therefore, at higher impact velocity, localized strain results from a quicker thermal softening process followed by adiabatic heating.

The pattern distribution of strain along compression samples deformed at different strain rates is obtained via the digital image correlation system. From this color map (shown in Fig. 1.10), the localized strain and average of strain at certain locations on the specimen can be determined. Figure 1.10 indicates the strain localization within the aluminum sample deformed at 9.6 m/s. Images A, B, C, and, D indicate the strain map distribution at time 0, 35, 60, and 105 μs respectively during the deformation process. Figure 1.10a indicates that no strain was localized in material at the start of the test corresponding to time 0 μs. As deformation progresses, the strain localized within material increases with time; At time $t = 35$ μs, the average localized strain within the material (region colored red in map) was about 2 %, this increased to about 6 % at deformation time corresponding to 60 μs. The average localized strain within the compression specimen at time $t = 105$ μs was about 12 %. From the image plot shown in Fig. 1.10, it is observed that the strain localized within the specimen increases with time. The strain prediction as time increases observed via the color map in Fig. 1.10 agrees with the trend observed using elastic wave technique.

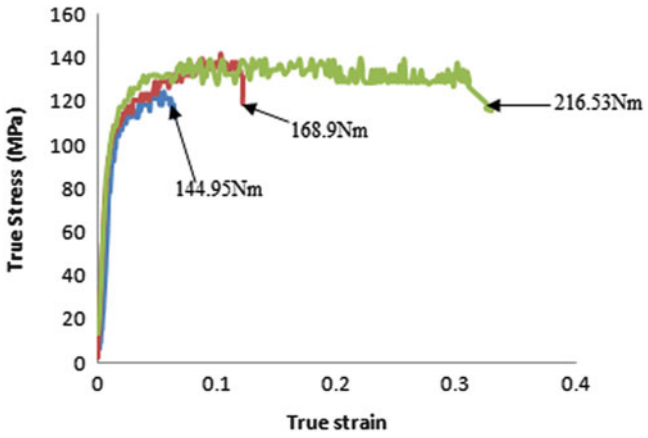

Fig. 1.11 Dynamic impact stress–strain relationship for AA2099-T8 aluminum alloy specimen as a function of impact velocity

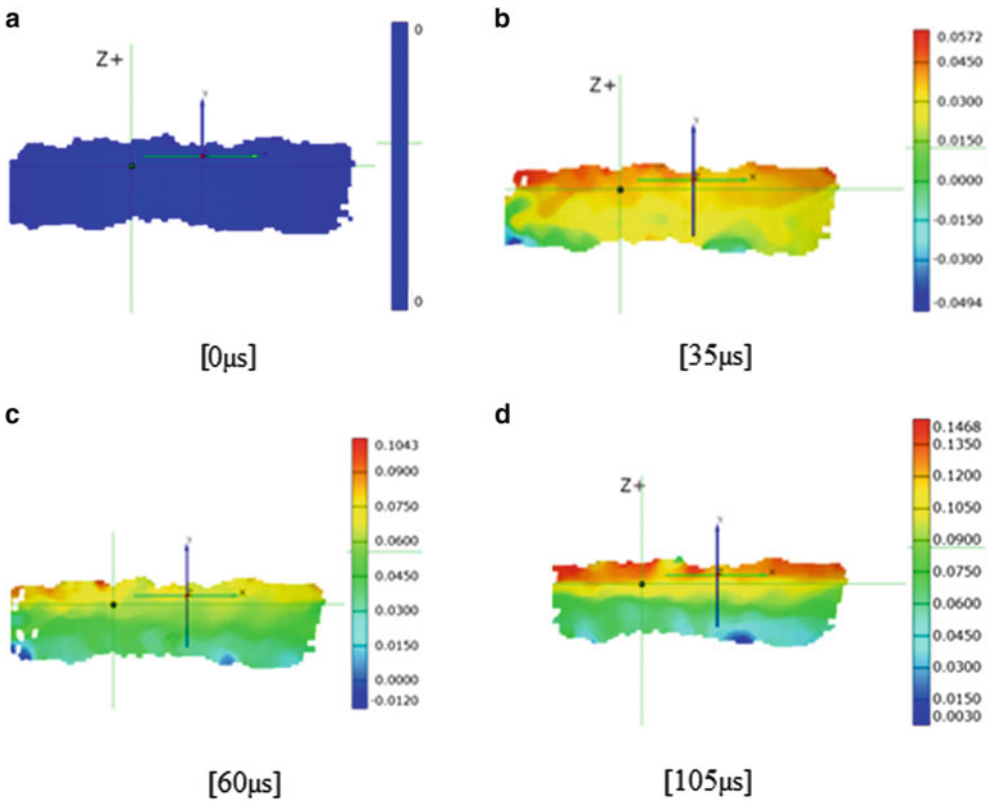

Fig. 1.12 Digital image correlation map of strain localization in compression specimen as a function of time at a velocity of 168.9 Nm

The torsion test of the aluminum sample was performed at strain rates ranging between 750 and 1,500 s^{-1} (see Table 1.3); Fig. 1.11 shows the dynamic stress- strain behavior of the aluminum alloy under torsional loads. The peak flow stress observed during test conducted at 210 Nm was 121 MPa and this increased to about 142 MPa at 168.9 Nm, the peak flow stress experienced at 216.53 Nm was 137 MPa. During the test conducted at 1,000 s^{-1}, the material became shattered into pieces and this indicates that the material cannot withstand torsional loading at strain rates beyond 1,000 s^{-1} and this explains why a lower peak flow stress is observed in the aluminum material loaded at 216.53 Nm compared with that loaded at 168.9 Nm.

Figure 1.12 shows the digital image correlation map of the aluminum sample when it is under a torsion load of 168.9 Nm. Figure 1.12a corresponds to the start of the test and indicates that no strain is localized within the aluminum material.

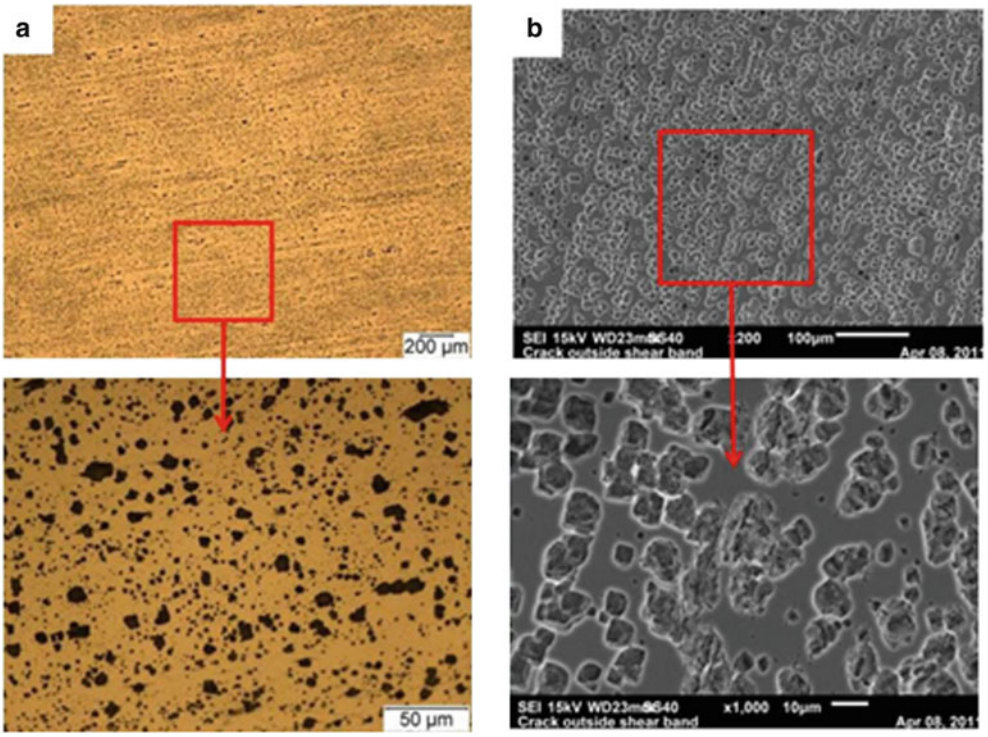

Fig. 1.13 Microstructural composition of the pre-impact aluminum alloy. (**a**) Optical. (**b**) SEM micrograph revealing elongated second phase structures

Figure 1.12b indicates that the average strain localized within the material was about 3 % at time t = 35 μs during the test, this value increased to about 6 % when the deformation time increased to 60 μs and 11 % at a deformation time of 105 μs. The increase in localized strain as deformation time increases during the torsion test is similar to that observed in the compression test and further confirms that as the deformation time progresses; the localized strain within the material also increases.

The microstructural examination of the deformed AA2099-T8 samples was performed in order to determine the effect impact velocity on formation of adiabatic shear bands within the aluminum sample. The pre-impact optical examination of AA6061-T6 aluminum alloy reveals very fine second phase particles. These second phase particles are usually irregular in shape and size and are uniformly dispersed within the material microstructure. Figure 1.13a, b show the optical and SEM images of the elongated second phase particles within the aluminum specimen before impact.

The examination of the aluminum samples impacted at 9.60 m/s indicate that no obvious adiabatic shear band was initiated during the deformation process. The micrograph of samples deformed at 12.10 m/s is shown in Fig. 1.14, this indicates a fairly deformed adiabatic shear band that has not fully developed.

During tests conducted at 18.64 m/s, very faint transformed adiabatic shear bands and cracks were observed to propagate at certain regions of the deformed aluminum specimen. Figure 1.15 shows optical micrographs of the aluminum sample impacted at 18.64 m/s, faint transformed shear bands are observed and crack can be visualized within the microstructure at higher microscope resolution

In samples impacted at 19.8 m/s, a fully formed transformed adiabatic shear band is observed within the aluminum material. These shear bands shown in Fig. 1.16 are heavily distorted grain structures with propagated crack along their path.

Table 1.4 shows the impact velocity, corresponding impact pressure, the strain rate, and the type of adiabatic shear band which initializes in the deformed aluminum alloy.

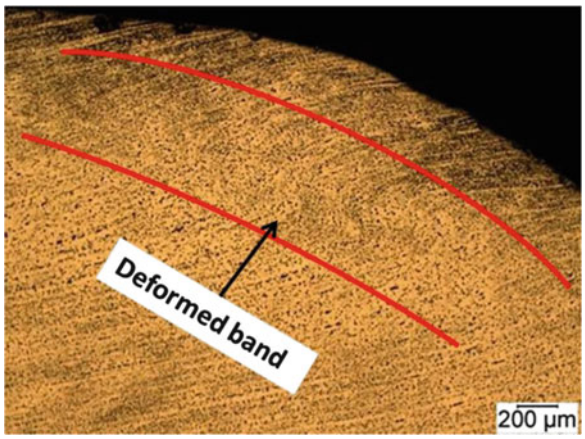

Fig. 1.14 Slightly deformed adiabatic shear band observed in AA2099-T8 alloy impacted at 12.10 m/s

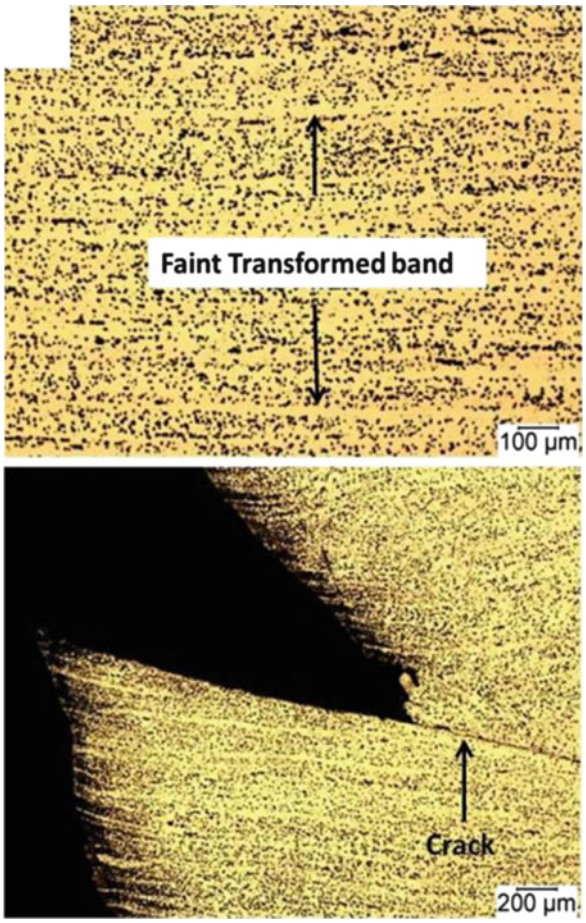

Fig. 1.15 Faint transformed adiabatic shear band in AA2099-T8 aluminum impacted at 18.64 m/s

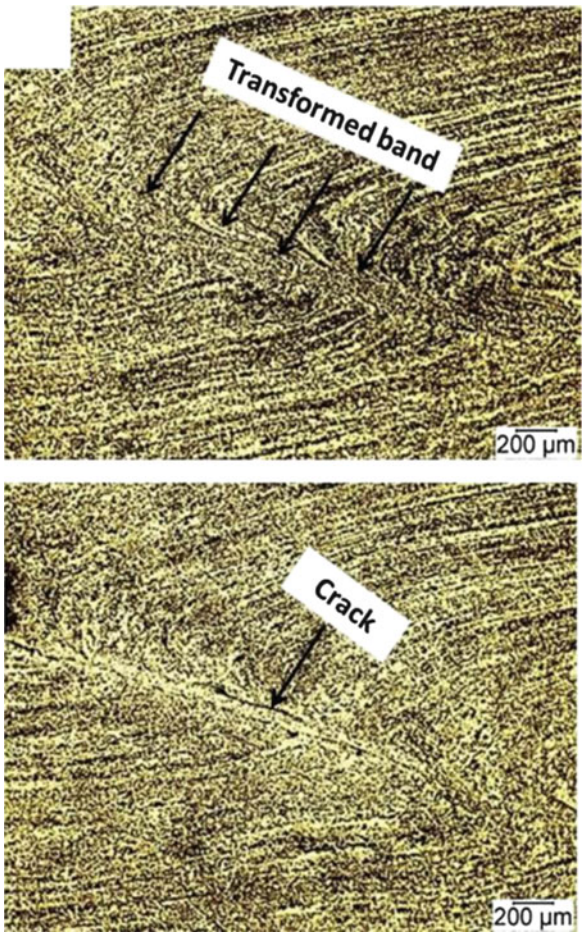

Fig. 1.16 Heavily distorted transformed shear bands observed in AA2099-T8 aluminum impacted at 19.8 m/s

Table 1.4 Data sheet for impact test performed on AA2099-T8 aluminum alloy

Impact velocity (m/s)	Impact pressure (kPa)	Strain rate (/s)	Type of adiabatic shear band
9.6	61.64	1,000	No obvious band
12.10	90.66	1,500	Slightly deformed band
18.64	126.72	2,000	Faint transformed band
19.80	215.67	3,000	Heavily distorted transformed band characterized by cracks

1.4 Conclusion

The high strain rate behavior of AA 2099-T8 aluminum alloy has been studied under compression and torsion load configurations. It is observed that the intensity of plastic deformation is a function of the strain rate at which the aluminum sample is impacted, intense strain localization is experienced as the impact velocity increases. During the compression test, an increase in impact velocity results into an increase in the peak flow stress within the material; no drop in peak flow stress was observed at the impact velocities at which test was performed. During the torsion test, the maximum stress observed in the hollow torsion specimen increased as the applied torque increased from 144.95 to 168.9 Nm; however a drop in peak stress was observed in the test performed at an applied torque of 216.53 Nm. The drop in peak flow stress can be attributed to the fact that heavily distorted transformed band already initiated in the aluminum sample and hence the internal strength of the material to resist impact had reduced. It is observed that during dynamic loading of the AA2099-T8 aluminum in compression and torsion, intense shear localization along narrow adiabatic shear bands initiates failure in the aluminum

sample. The type of shear band that initiates in the aluminum sample depends on the impact velocity or strain rate at which the impact is performed. The stress–strain behavior of the deformed aluminum sample determined via the conventional elastic wave strain gauging technique and the non-contact digital image correlation method are similar. The slight difference is due to the fact that non-homogenous stress–strain behavior is assumed in the DIC technique while a homogenous stress–strain relationship is assumed in conventional elastic wave technique. It is also observed that the localized strain within the impacted aluminum sample increases as the deformation time increases.

Acknowledgement The authors are grateful for the support provided by the Department of Defense (DoD) through the research and educational program for HBCU/MSI (contract # W911NF-12-1-061) monitored by Dr. Larry Russell (Program Manager, ARO)

References

1. Burger GB, Jeffrey PW, Lloyd DJ (1995) Microstructural control of aluminum sheet used in automotive applications. Mater Charact 35(1):23–39
2. Feng H, Bassim MN (1999) Finite element modeling of the formation of adiabatic shear bands in AISI 4340 steel. J Mater Sci Eng A266:255–260
3. Alloy 2099-T83 and 2099-T8E67 extrusion ALCOA aerospace technical fact sheet
4. Odoh DO (2012) Full-field measurement of AA-6061 T6 aluminum alloy under high strain rate compression and torsion loads. M.Sc. thesis, Howard University
5. Kuriyama S, Meyers MA (1985) Numerical analysis of adiabatic shear band in an early stage of its propagation. In: IUTAM symposium on MMMHVDF, Tokyo, 12–15 Aug 1985
6. Wright TW (2002) The physics and mathematics of adiabatic shear bands. Cambridge University Press, Cambridge
7. Owolabi GM, Odeshi AG, Singh MNK, Bassim MN (2007) Dynamic shear band formation in aluminum 6061-T6 and aluminum 6061-T6/Al_2O_3 composites. Mater Sci Eng A 457(1–2):114–119
8. Schoenfeld SE, Wright TW (2003) A failure criterion based on material instability. Int J Solids Struct 40(12):3021–3037
9. Odeshi AG, Al-ameeri S, Bassim MN (2005) Effect of high strain rate on plastic deformation of low alloy steel subjected to ballistic impact. J Mater Process Technol 162–163:385–391
10. Owolabi GM, Odoh DO, Odeshi AG, Whitworth H (2012) Full field measurements of the dynamic response of AA6061 T-6 aluminum alloy under high strain rate loads. In: Proceedings of the ASME 2012 International Mechanical Engineering Congress and Exposition (IMECE 2012), Houston, 9–15 Nov 2012
11. Gray GT (2000) Classic split-Hopkinson pressure bar testing. In: ASM handbook, vol 8, Mechanical testing and evaluation. ASM International, Materials Park, pp 462–476

Chapter 2
High Strain Rate Performance of Pressureless Sintered Boron Carbide

Tomoko Sano, Matthew Shaeffer, Lionel Vargas-Gonzalez, and Joshua Pomerantz

Abstract The processing technique used to consolidate ceramics powders can have a large effect on the microstructure, and hence the performance of the material. In this research, microstructure, mechanical properties, and the high strain rate compressive behavior of pressureless sintered boron carbide (B_4C) samples were examined and compared to those of conventional hot pressed B_4C. Penetration velocity tests were conducted on identical targets made with the pressureless sintered B_4C samples and hot pressed B_4C. Microstructural and post mortem characterization showed that test results of the pressureless sintered B_4C were affected by significant porosity in the samples. The effects of the processing technique on the microstructure, properties, and the high rate behavior of the pressureless sintered B_4C will be discussed.

Keywords Boron carbide • Pressureless sintering • Microstructure • High rate behavior

2.1 Introduction

Boron Carbide (B_4C) is used widely in abrasive, wear resistant components, and armor applications due to its high hardness and low density properties. Hot pressing B_4C powder is the typical commercial technique used to form personnel armor plates and components for various applications. B_4C components can reach nearly full theoretical density by the hot pressing technique, which requires vacuum or inert atmosphere, sintering temperatures near 2,300 K, and pressures up to 40 MPa [1]. The hot pressing technique using additives allows densification at lower temperatures, improves oxidation and thermal shock resistance, and increases mechanical properties by inhibiting grain growth. The limitation of the hot pressing technique is the high operation cost per batch and only plates or cylindrical shapes of a limited size can be produced. Also, in addition to a larger die, to achieve the same pressure applied to a smaller specimen, a much larger hot press equipment size is required for larger specimens. Another technique, pressureless sintering, is also used to consolidate and densify B_4C powders [2–4]. The pressureless sintering technique is a less expensive method, but requires fine grained starting power (<3 μm), higher temperatures (roughly 2,500 K) and amorphous carbon additions to achieve greater than 95 % theoretical density [5]. In both techniques, the additives could form precipitates or secondary phases at the grain boundaries that are detrimental to the mechanical performance.

In addition to quasi-static behavior, high rate compressive behavior is often tested using the Kolsky bar to evaluate the failure of structural ceramic materials [6, 7]. The high strain rate compressive behavior of B_4C has been studied by Paliwal and Ramesh [8]. In their experiment using the Kolsky bar, they determined at strain rates between 10^2 and 10^4/s, the peak compressive strength of a hot pressed B_4C sample reached 3.8 GPa. A similar study [9] on high strain rate compression testing also using the Kolsky bar comparing the baseline hot pressed B_4C results from Paliwal and Ramesh to two types of pressureless sintered B_4C, one hot isostatically pressed (HIPed) and the other sintered. All three B_4C types showed

T. Sano (✉) • L. Vargas-Gonzalez • J. Pomerantz
U.S. Army Research Laboratory, 4600 Deer Creek Loop, Aberdeen Proving Ground, MD 21005, USA
e-mail: tomoko.sano.civ@mail.mil

M. Shaeffer
Johns Hopkins University, Center for Advanced Metallic and Ceramic Systems, 028 Latrobe Hall, 3400 N. Charles St., Baltimore, MD 21218, USA

B. Song et al. (eds.), *Dynamic Behavior of Materials, Volume 1: Proceedings of the 2013 Annual Conference on Experimental and Applied Mechanics*, Conference Proceedings of the Society for Experimental Mechanics Series,
DOI 10.1007/978-3-319-00771-7_2,

comparable compressive strengths. The HIPed samples' compressive strength distribution ranged from 3.4 to 4.0 GPa, falling within the 3.1–4 GPa range of the hot pressed samples, and the sintered samples ranged from just over 3.0–3.7 GPa.

An often applied technique to evaluate the penetration resistance of armor materials is by the V_{50} test [10]. Several B_4C samples have been tested in the past, with various target assembly. One such impact test [11] which compared the V_{50} technique to depth of penetration measurements, tested 6 in. B_4C tiles (presumed to be hot pressed) with thicknesses of 1.0, 1.5, and 2.0 in. The B_4C was observed to have performed better compared to similarly tested silicon carbide (SiC) and 90 % alumina (Al_2O_3). A recent work by Dateraksa et al. [12] determined the V_{50} values of 100 × 100 mm^2 Al_2O_3, SiC and hot pressed B_4C tiles with S2 – glass composite backing plates. The V_{50} of the hot pressed B_4C was determined to be 829 m/s, or 2,720 ft/s and had the lowest V_{50} value of the materials tested.

2.2 Experimental

Pressureless sintered square B_4C tiles with the nominal dimensions of 50 × 50 × 8 mm, and hexagonal tiles with the nominal dimensions of 35 mm flat to flat and 20 mm thick were obtained. Density was measured by the Archimedes principle for both tile morphologies. For microstructural characterization and hardness measurements, samples from each tile morphology were cut, mounted with a Buehler cold mount epoxy, and polished on the Struers Rotopol-31 with decreasing diamond suspension sizes starting with 45 μm and ending with 0.25 μm. Microstructural and elemental characterizations were conducted on the FEI Nova NanoSEM600 (FEI Company, Hillsboro, OR) scanning electron microscope (SEM), and EDAX Pegasis XM4 (EDAX Inc. Mahwah, NJ) energy dispersive spectroscopy (EDS), respectively. X-ray diffraction spectra were obtained with the Siemens 05005 diffractometer for phase analysis. The polished samples were subjected to Knoop microindentation (Wilson Tukon 2100, Wilson Hardness, Norwood, MA) at 1.0, 2.9, 4.9, 9.8, and 24.5 Newton loads.

From the square tiles, flexural specimens according to the ASTM C1161 type B standard [13], and high strain rate compression samples with cuboidal dimensions 3.5 × 4.0 × 5.3 mm were machined by Bomas Machine Specialties Inc., Somerville, MA. Two sets of samples were machined such that for one set of samples, the loading surface (3.5 × 4.0 mm) was parallel to the square surface (referred to as "horizontal samples") and the other set of samples, the loading surface was perpendicular to the square surface (referred to as "vertical samples"). A set of horizontal and a set of vertical compression samples were also machined from the hexagonal tile with the same dimensions. Flexural strength experiments were conducted on the Instron 5500R load frame (Instron, Norwood, MA) with a lower support span of L = 40 mm and an upper support span of U = 20 mm. The width and thickness of the flexural specimens were recorded and loaded at 0.5 mm/min. Tests were conducted according to ASTM C1161.

High strain rate compression testing on the Kolsky bar with the same test setup as Paliwal and Ramesh [8] was conducted on five compression specimens from each sample set (square plate horizontal, vertical, hexagonal plate horizontal and vertical). Before testing, each specimen was measured for variance in the angle of the corners and the parallelism. A high speed camera was used to capture the specimen failure at 2.4 microsecond intervals with exposure times ranging from 230 nanoseconds to 1 microsecond, and the post mortem fragments were collected in a plexiglass box surrounding the specimen for SEM characterization.

To assess the penetration resistance of the pressureless sintered B_4C material, ceramic/ultra-high molecular weight polyethylene (UHMWPE) composite specimens were manufactured. Ten 50.8 × 50.8 × 07.4 mm samples were supplied for testing. A commercially available hot-pressed B_4C material (PAD – B_4C, CoorsTek, Inc. Vista, Vista, CA) was also procured at the same size to serve as the performance baseline. The composite backings were manufactured using Spectra Shield II® SR-3136 (Honeywell Specialty Materials, Morristown, NJ), a UHMWPE fiber and thermoplastic matrix sheet product. Each tile was bonded to the center of each composite backing using Sikaflex-252, a moisture-cure polyurethane-based sealant. Small strips of a 0.5 mm nylon line were used to control the adhesive thickness. The composite specimens were placed underneath a vacuum bag and cured under vacuum for 1 week at ambient room temperature.

The penetration resistance of the composite panels was evaluated through tests which are used to experimentally determine the probabilistic limit velocity (V_{50}) and derive a probabilistic curve. The probabilistic V_{50} value corresponds to the velocity at which the probability of the projectile being stopped or the projectile penetrating through the panel is at 50 %. The testing and the determination of the V_{50} value was conducted as specified in the MIL-STD-662F standard [10]. Each panel was impacted in the center of the ceramic strike face with a test projectile fired from a universal receiver. Impact velocities are varied until there are several partial and complete penetration values within a specified range of velocities. The values within the range of velocities are average to determine the V_{50} result. If a mixed mode of values within the specified range is obtained, then the entire range of tests can be input into a calculation algorithm to generate a logistic regression

curve. The mixed mode of results is a case in which the highest measured partial penetration velocities are slightly higher than the lowest complete penetration velocities. The logistic regression curve provides calculated probabilities of resistance to penetration of the composite panels throughout an entire V_0 to V_{100} range (V_0 being the velocity at which no projectiles will penetrate to V_{100} where all projectiles will penetrate).

2.3 Results and Discussion

For the square tiles, the density was measured to be 2.40 g/cm^3 or 95 % theoretical density, and 2.38 g/cm^3 or 94 % theoretical density for the hexagonal tiles. The porosity and graphite particles are believed to be the reason for less than full density. Microstructural and elemental characterization in the SEM was conducted on both square and hexagonal tiles samples. Numerous graphite particles (black areas) and some twinned grains were observed. Figure 2.1 shows the SEM micrograph of the hexagonal tile microstructure and that of PAD – B_4C. The EDS spectra collected showed 78 atomic % B, 22 atomic % C. XRD spectra were obtained for both the square plate and hexagonal plates. An example of the spectra from a hexagonal sample is shown in Fig. 2.2.

Ten Knoop indents were measured at each load for polished samples from the square and hexagonal tiles according to ASTM standard C1326 [14]. The average hardness (HK) at 24.5 N will be reported, as recommended by ASTM C1326 and by Swab [15]. At loads equal to or higher than 19.6 N, B_4C is load independent, and unaffected by the indentation size effect. For the square tile the HK was calculated to be 19.8 GPa with a standard deviation of 1.2 GPa. For the hexagonal tile, the HK was 20.1 GPa with a standard deviation of 1.6 GPa. These results are tabulated in Table 2.1, with the properties of the baseline hot pressed PAD – B_4C (from formerly BAE Systems, now CoorsTek). Although the HK values of the square and

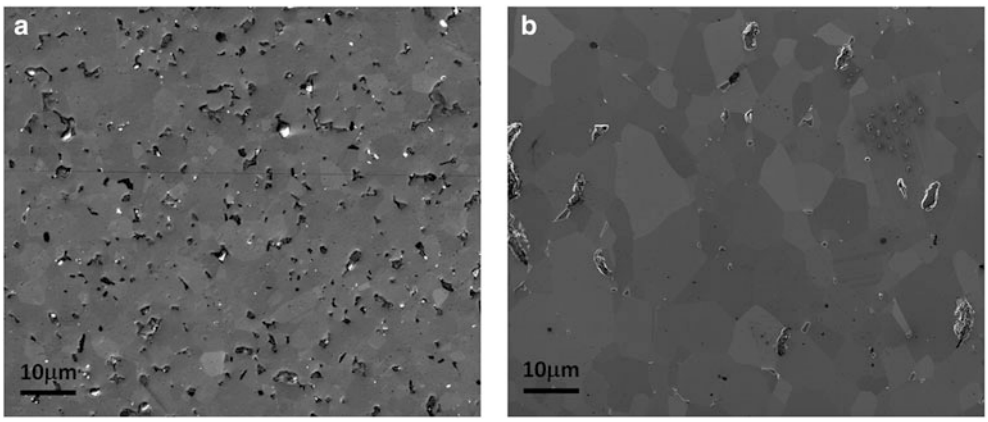

Fig. 2.1 SEM micrographs of the polished surface of (**a**) the hexagonal tile and (**b**) PAD – B_4C

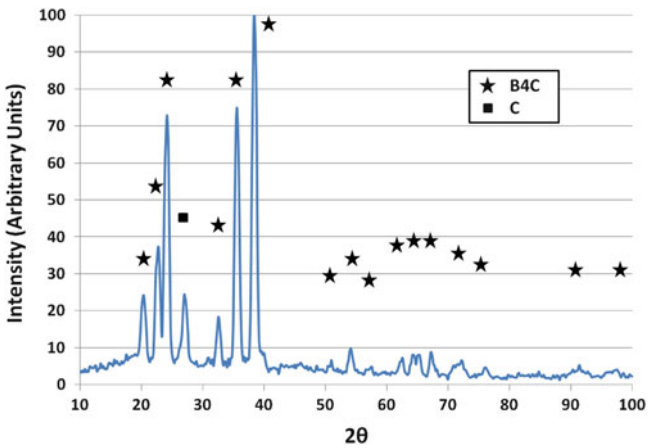

Fig. 2.2 XRD spectra of the hexagonal sample

Table 2.1 B_4C properties

	Density (g/cm^3)	HK (GPa)	Flexural strength (MPa)
Square plate	2.40	19.8	295 ± 38
Hexagonal plate	2.38	20.1	–
PAD [16]	2.50	19.9 (HK2)	398 ± 34

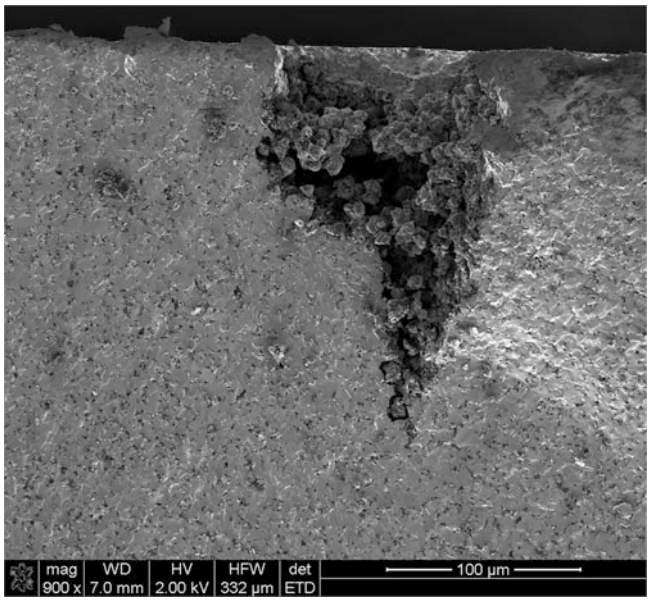

Fig. 2.3 A large pore observed in the fracture surface of the bar with the lowest flexural strength

hexagonal plates are comparable to the PAD – B_4C, several indents could not be measured due to the indents landing on a pore on the surface or just under the surface, causing severe cracking around the indent.

Four point flexure testing was conducted on 52 type B bars from the square tiles to determine the average flexural strength. The flexural strength was calculated using the following equation,

$$S = \frac{3PL}{4BD^2} \tag{2.1}$$

where S is the flexural strength, P is the break force, L is the outer support span, B is the width, and D is the thickness. The average flexural strength was 295 MPa with a standard deviation of 38 MPa at an average break force of 355 MPa. This value as well as that of PAD – B_4C are listed in Table 2.1. Fractography was conducted on the bar with the highest flexural strength of 366 MPa, and the bar with the lowest flexural strength of 212 MPa. Both bars failed by brittle transgranular fracture and revealed numerous porosities. Just like porosity was a factor in the hardness measurements, porosity significantly affected flexural strength. The bar with the lowest flexural strength had a significant pore, or a region of poor consolidation, shown in Fig. 2.3, where the fracture initiated.

High rate compression experiments were conducted on five samples from each of the plate types, and compared to the results of the baseline PAD – B_4C [8, 9]. The compressive strengths averages ranged from 2.9 to 3.7 GPa. A plot comparing the compressive strengths is shown in Fig. 2.4. Besides the hexagonal plate horizontal sample set showing a decreased compressive strength, the pressureless sintered plates preformed comparably to the PAD – B_4C. The outlier point at 1.3 GPa in the square plate, horizontal direction is believed to be a porous or sample with other significant flaws. Images captured by the high speed camera of this sample show a surface crack propagating across the length of the sample even before experiencing 0.5 GPa of stress. Images from tests on other samples also show surface cracks propagating across the samples, but at stresses much closer to the maximum observed stresses, as shown in Fig. 2.5. Figure 2.5 is the stress and strain versus time for a hexagonal sample in the horizontal direction that achieved 3.17 GPa compressive strength. The numbers along the stress curve indicate when the accompanying high speed camera images were captured. In Fig. 2.5b, image 5 captured at the maximum stress, the sample is still intact, showing only surface cracks at the strike face and the front corners. It is not until at image 6, after reaching the peak stress when the volumetric strain starts to increase, does the sample show significant failure

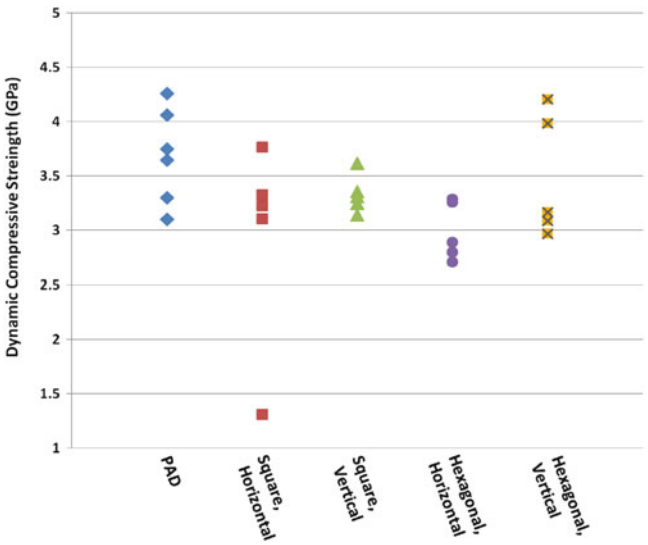

Fig. 2.4 Compressive strength of baseline PAD B4C, square, and hexagonal plates

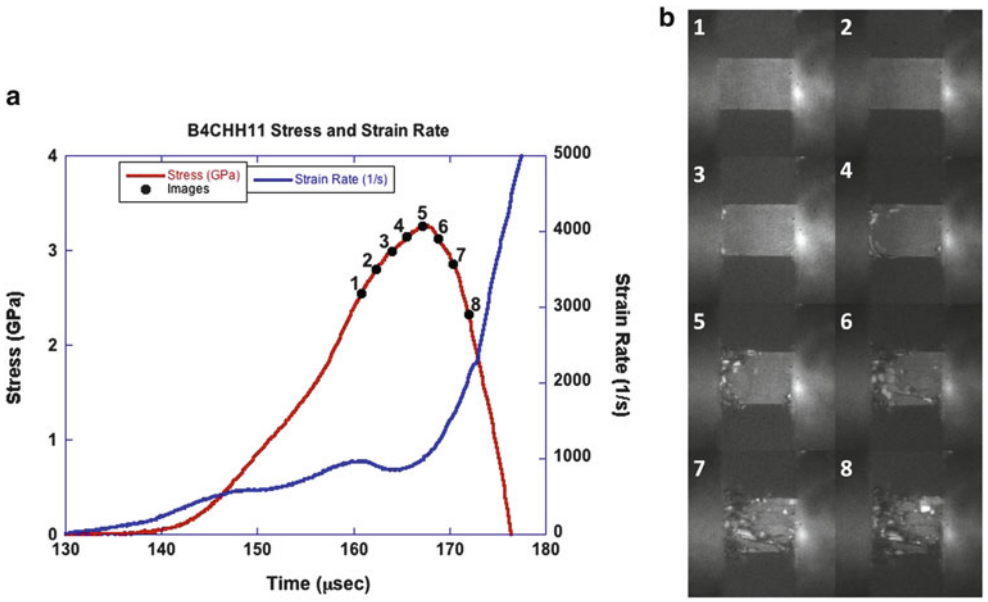

Fig. 2.5 (**a**) Plot of stress and strain versus time for the high strain rate compression testing of a hexagonal sample in the horizontal direction, and (**b**) high speed camera images of the sample during the experiment, captured at the numbered points along the stress curve

and surface cracks propagating across the length of the sample. This behavior has been observed in other ceramics [6] including SiC and Al_2O_3.

Fragments collected from the high strain rate compression experiments were evaluated in the SEM. No noticeable distinction was observed between the samples that performing better and those that performed poorly. All sample fragments showed evidence of transgranular fracture. Visual inspection of the collected fragments from all tests gave no quantitative indication whether the set of fragments were from a sample with higher or lower compressive strength. Several researchers [17–21] have correlated the average fragment size and size distribution to the defect density and strain rate at high loading rates. It has been observed that higher strain rate loading results in smaller fragment sizes and narrower fragment size distribution [20, 21] and that fracture stress scales with strain rate to the 1/3 power [18]. In this present study, the strain rates were comparable for all Kolsky bar experiments, so this observation cannot be confirmed. Although Keller and Zhou [22] found no correlation between fragments size distributions, average fragment size and material strength of TiB_2-Al_2O_3

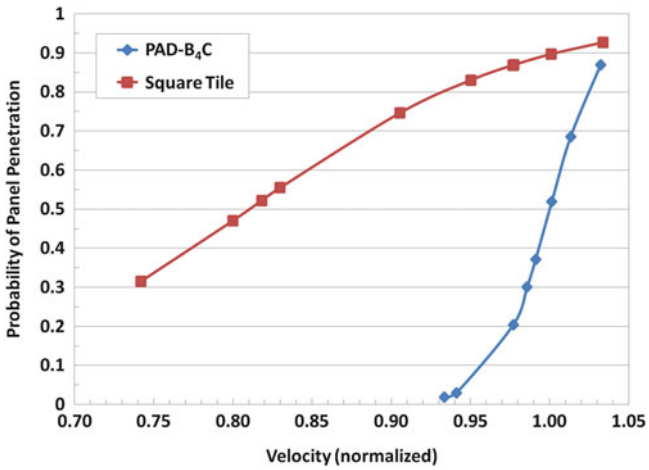

Fig. 2.6 Probability of panel penetration versus normalized impact velocity

ceramics, Moynihan et al. determined [23] that there is a link between fragmentation (and resulting fragment size distribution) to the failure mechanisms and the ballistic performance for B_4C. More samples of PAD, square, and hexagonal tiles need to be tested at a range of strain rates to correlate the fragment size and size distribution to the compressive strength.

The penetration tests were conducted at the same range in the same conditions for the PAD – B_4C and square plate B_4C samples. The V_{50} values for the PAD-B_4C and square tile B_4C panels were normalized with respect to the PAD-B_4C value (value of 1.00 with a standard deviation of 0.016). The square tile B_4C panels performed considerably worse than the PAD-B_4C panels, with a normalized V_{50} value of 0.810 with a large standard deviation of 0.082. Figure 2.6 shows the probability of panel penetration at various normalized impact velocities. The significance of the difference in performance is evident when you compare the panels near the normalized value of 0.94; PAD-B_4C has a 3 % probability while the square tile panel has over 80 % probability of panel penetration. If the probability curve is extrapolated based on the current data trend, the data would asymptotically curve toward a V_0 near the normalized penetration value of 0.60–0.65 (compared to the calculated V_0 value of PAD-B_4C near 0.92–0.93).

2.4 Conclusions

The microstructure, mechanical properties, and impact properties of pressureless sintered B_4C in two tile shapes were evaluated. The results were compared with baseline PAD – B_4C to determine the effects of the pressureless sintering on the various properties. It was determined that the porosity due to inadequate consolidation and sintering in the pressureless sintered tiles adversely affected the density, flexural strength, and the penetration values. However the pressureless sintered samples had no impurities, and showed comparable hardness and high strain rate compressive strength. It is believed that with reduced porosity, the mechanical properties and penetration properties of the pressureless sintered B_4C would be comparable to those of PAD–B_4C.

References

1. Thévenot F (1990) Boron carbide – a comprehensive review. J Eur Ceram Soc 6:205–225
2. Weaver GQ (1982) Sintered high density boron carbide, US Patent No. 4,320,204
3. Lee H, Speyer RF (2003) Pressureless sintering of boron carbide. J Am Ceram Soc 86(9):1468–1473
4. Roy TK, Subramanian C, Suri AK (2006) Pressureless sintering of boron carbide. Ceram Int 32:227–233
5. Cho N (2006) Processing of boron carbide. Thesis, Georgia Institute of Technology
6. Jiao T, Li Y, Ramesh KT, Wereszczak AA (2004) High rate response and dynamic failure of structural ceramics. Int J Appl Ceram Technol 1(3):243–253
7. Luo H, Chen WW, Rajendran AM (2006) Dynamic compressive response of damaged and interlocked SiC-N ceramics. J Am Ceram Soc 89 (1):266–273

8. Paliwal B, Ramesh KT (2007) Effect of crack growth dynamics on the rate-sensitive behavior of hot-pressed boron carbide. Scripta Mat 57:481–484
9. Sano T, Chin ESC, Paliwal B, Chen MW (2009) Comparison of slip cast and hot pressed boron carbide. In: Bansal NP, Singh JP (eds) Processing and properties of advanced ceramics and composites: ceramic transactions, vol 203. Wiley, New Jersey, p 107
10. U.S. Department of Defense (1997) V50 ballistic test for armor, MJL-STD662, 18 Dec 1997
11. Woolsey P, Kokidko D, Mariano SA (1989) Alternative test methodology for ballistic performance ranking of armor ceramics. MTL TR 89-43, DTIC 1989
12. Dateraksa K, Sujirote K, McCuiston R, Atong D (2012) Ballistic performance of ceramic/S_2-glass composite armor. J Magn Magn Mater 22 (2):33–39
13. ASTM C1161-02c (2002) Standard test method for flexural strength of advanced ceramics at ambient temperature. Annual book of ASTM standards, vol 15.01. ASTM, West Conshohocken
14. ASTM C1326-96 (2003) Standard test method for Knoop indentation hardness of advanced ceramics. Annual book of ASTM standards, vol 15.01. ASTM, West Conshohocken
15. Swab JJ (2004) Recommendations for determining the hardness of armor ceramics. Int J Appl Ceram Technol 1(3):219–225
16. Vargas-Gonzalez L, Speyer RF, Campbell J (2010) Flexural strength, fracture toughness, and hardness of silicon carbide and boron carbide armor ceramics. Int J Appl Ceram Technol 7(5):643–651
17. Grady DE (1982) Local inertial effects in dynamic fragmentation. J Appl Phys 53(1):322–325
18. Lankford J, Blanchard CR (1991) Fragmentation of brittle materials at high rates of loading. J Mater Sci 26:3067–3072
19. Grady DE (2008) Fragment size distributions from the dynamic fragmentation of brittle solids. Int J Imp Eng 35:1557–1562
20. Zhua F, Molinari J-F, Ramesh KT (2005) A cohesive model based fragmentation analysis: effects of strain rate and defects distribution. Int J Solids Struct 42:5181–5207
21. Levy S, Molinari JF (2010) Dynamic fragmentation of ceramics, signature of defects and scaling of fragment sizes. J Mech Phys Solids 58:12–26
22. Keller AR, Zhou M (2003) Effect of microstructure on dynamic failure resistance of titanium diboride/alumina ceramics. J Am Ceram Soc 86 (3):449–457
23. Moynihan TJ, LaSalvia JC, Burkins MS (2002) Analysis of shatter gap phenomenon in a boron carbide/composite laminate armor system. In: Proceedings of the 20th international symposium on ballistics, Orlando, 23–27 Sept 2002

Chapter 3
Interpretation of Strain Rate Effect of Metals

Kun Qin, L.M. Yang, and Shi-sheng Hu

Abstract Mesoscopic mechanism of strain rate effect of metals has been discussed based on dislocation theory. Strain rate effect and dislocation motion is bridged by using the decomposition of strain rate, Orowan's relationship and the stress dependence of dislocation velocity. The mechanism of strain rate effect has then been investigated qualitatively by using these three relationships. The process of strain rate effect has been well explained and some details of strain rate effect have been adequately discussed. These discussions are consistent with experiments.

Keywords Strain rate effect • Dislocation theory • Orowan's relationship • Dislocation velocity • Rate sensitivity

3.1 Introduction

It has been known that material behavior under impact differs from that under static loading. Typical characteristic of material behavior under impact is mechanical properties (yield strength, flow stress, strength, etc.) increase with strain rate, namely, strain rate sensitivity or strain rate dependence which is illustrated in Fig. 3.1. This is referred to as strain rate effect [1]. Up to present, the reason leads to strain rate effect is still not clear and needed to be identified.

Over the last six decades, research on strain rate effects mainly focused on material modeling based on experimental data. There are a number of empirical constitutive equations based on phenomenological methods that were proposed to depict the plastic behavior of materials exhibiting strain rate sensitivity. However, the mechanisms governing strain rate effects cannot be identified via phenomenological methods.

There were some researches on the use of dislocation theory to investigate mechanisms governing dynamic material properties. Lindholm (1964) examined strain rate effects in FCC metals experimentally using Hopkinson bar tests and tried to explain his results by dislocation theories [2]. He proposed that possible causes of strain rate effects are glide interaction and forest dislocations. This reason is similar to that for strain hardening. Ross (1997) stated that in ductile metals, the limiting velocity of dislocations might increase the flow stress associated with increases in strain or loading rate [3]. In recent experimental studies on metals, differences in microstructure arising from different strain rates have been reported [4]. There were also many researches at the dislocation level to study dynamic constitutive relations based on dislocation dynamics. Klepaczko proposed a constitutive model based on the kinetics of dislocation motion, in which dislocation density is the variable describing a microstructure [5, 6]. Based on microstructure, Zerilli and Amstrong proposed two constitutive relations that fitted well with experimental results [7–10]. Arising from Follansbee's work, a mechanical threshold stress constitutive relationship has been obtained, which describes strain rate effects mainly by a threshold stress and indicates that strong barriers to dislocation motion are created by high rate deformation [11]. Dislocation dynamics simulation is a direct approach to study the mechanisms governing strain rate effects. Zbib simulated dislocation motion under different strain rates using Micro3d and showed that the dislocation density increases with strain rate [12].

K. Qin (✉) • L.M. Yang
Faculty of Mechanical Engineering and Mechanics, Ningbo University, Ningbo 315211, People's Republic of China
e-mail: qinkun@nbu.edu.cn

S. Hu
School of Engineering, University of Science and Technology of China, Hefei 230027, People's Republic of China

B. Song et al. (eds.), *Dynamic Behavior of Materials, Volume 1: Proceedings of the 2013 Annual Conference on Experimental and Applied Mechanics*, Conference Proceedings of the Society for Experimental Mechanics Series,
DOI 10.1007/978-3-319-00771-7_3,

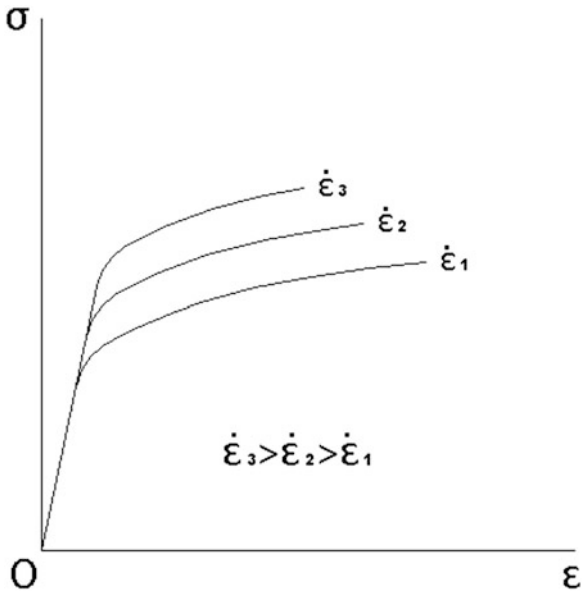

Fig. 3.1 Strain rate dependent of flow stress

Although some details of microstructure in strain rate effect have been observed via experiments, a reasonable theory that explains those experimental findings has not yet been built. To obtain a reasonable explanation of strain rate effects at mesoscopic level, more work is needed.

3.2 Analyses Based on Dislocation Dynamics

3.2.1 Kinematics Relationship of Strain Rate Effect

Orowan's relationship links directly strain rate and dislocation parameters in dislocation theory. Orowan's equation is kinematic and independent of materials. Straight dislocation models are described by [1]:

$$\dot{\varepsilon}_P = \alpha b \rho_m \bar{v} \tag{3.1}$$

where α is an orientation factor, b is the length of the Burgers vector, ρ_m is the density of movable dislocations and $\bar{v}$ is the average velocity of dislocations.

3.2.2 Kinetic Relationship of Strain Rate Effect

Experiments by Gilmand and Johnston (1957) demonstrated the relationship between dislocation velocity and resolved shear stress can be described by:

$$\bar{v} = A\tau^m \tag{3.2}$$

where A and m are material constants [13]. According to this relationship, the dislocation velocity is proportional to the resolved shear stress, which in turn is related to the applied stress. Although this relationship is empirical and can be presented in various formulas, it does describe the kinetic relationship of strain rate effect at mesoscopic scale. It indicates that dislocation velocity increases with stress.

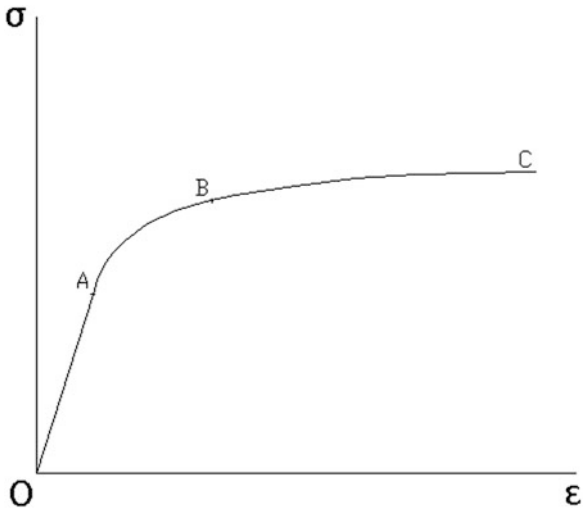

Fig. 3.2 A typical stress–strain curve for crystalline FCC materials

3.2.3 The Governing Relationships of Strain Rate Effect

Combining Eqs. 3.1 and 3.2, the relationship will be found between a plastic strain rate and a average dislocation velocity, and consequently a stress. For full yielding, the total strain rate corresponds to the plastic strain rate, which corresponds to an average dislocation velocity, and then a stress. Both Orowan's relationship and the stress dependence of dislocation velocity are governing relationship of strain rate effect. But the later is material-dependent, it might determine the rate sensitivity of materials.

Using Orowan's relationship and the stress dependence of dislocation velocity, experiments involving strain rate effect could be interpreted and analyzed in following sections.

3.2.4 Stress–Strain Curves at High Strain Rates

Figure 3.2 shows a typical stress–strain curve for FCC crystalline materials loaded at a high strain rate. The curve can be divided into three segments. *OA* corresponds to elastic deformation, *BC* corresponds to plastic hardening and *AB* corresponds to transition from elasticity to plasticity.

To simplify the discussion, perfect plasticity will first be considered; Fig. 3.3 shows a typical stress–strain curve for perfect plasticity. Segment *OA* defines the elastic response; the total strain rate is equal to the elastic strain rate, $\dot{\varepsilon} = \dot{\varepsilon}^e$. In segment BC, there is no elastic strain increase; hence the total strain rate is equal to the plastic strain rate, $\dot{\varepsilon} = \dot{\varepsilon}^p$. In segment AB, there are increases in both elastic and plastic strain; the total strain rate is therefore equal to the sum of the elastic and plastic strain rate, $\dot{\varepsilon} = \dot{\varepsilon}^e + \dot{\varepsilon}^p$. It can be seen that the elastic strain rate decreases while the plastic strain rate increases as deformation proceeds from yield to full plasticity – the elastic strain rate $\dot{\varepsilon}^e$ decreases from the total strain rate to zero, while the plastic strain rate $\dot{\varepsilon}^p$ increases from zero to the total strain rate $\dot{\varepsilon}$.

This phenomenon can be explained by using Orowan's relationship and stress dependence of dislocation velocity. Consider two points *a*, *b* on segment *AB*, as shown in Fig. 3.3, such that $\sigma_b > \sigma_a$. According to Eq. 3.2, the average dislocation velocity at *b* is larger than that at *a* $\bar{v}_b > \bar{v}_a$. As the dislocations move, the density of mobile dislocations increases, $\rho_a > \rho_b$. Based on Orowan's relationship, the plastic strain rate at b is larger than that at a, $\dot{\varepsilon}_b^p > \dot{\varepsilon}_a^p$. As the total strain rate is a constant, the elastic strain rate at *b* is therefore smaller than that at *a*, $\dot{\varepsilon}_b^e < \dot{\varepsilon}_a^e$. This also means that a high plastic strain rate corresponds to a high average dislocation velocity and a high flow (yield) stress.

For fully plastic deformation, the total strain rate is equal to the plastic strain rate, $\dot{\varepsilon} = \dot{\varepsilon}^p$. According to the preceding analysis, it can be deduced that a high total strain rate corresponds to a large plastic strain when the material is fully yielded, which in turn corresponds to a high dislocation velocity.

Based on above analysis, the process of high strain rate loading can be explained. When the applied stress exceeds that required to activate dislocation motion in segment *AB* of Fig. 3.3, the total strain rate $\dot{\varepsilon}$ comprises both elastic and plastic strain rate components. With a stress increase, the plastic strain rate increases while the elastic strain rate decreases, because the total strain rate is constant. Consider a given time interval Δt, for example the period *ab*. As the time increment Δt is

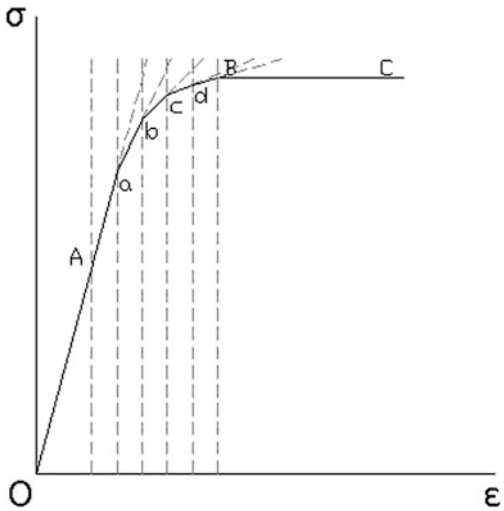

Fig. 3.3 A typical stress–strain curve for perfect plasticity

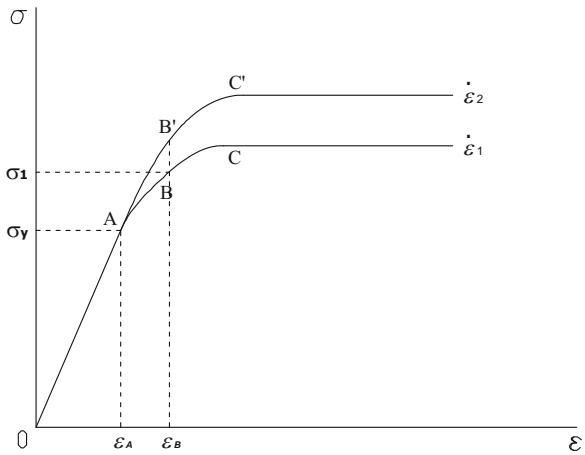

Fig. 3.4 Stress–strain curves of different strain rates

small, the stress, elastic strain rate and plastic strain rate are approximately their values corresponding to point a. In this time interval, there is an elastic strain increment given by $\dot{\varepsilon}^e \Delta t$. This elastic strain increment is accompanied by a stress increase. For next time interval *bc*, stress is then updated to the stress level at *b*. The plastic strain rate is also updated to the value corresponding to the stress at b. As the total strain rate is a constant, the elastic strain would be decreased. Consequently, in the time interval *bc*, the stress increase will be smaller than that in the preceding period *ab*. This incremental process will continue until complete plasticity is reached, whereby the elastic strain rate disappears.

The relative positions of two stress–strain curves of different strain rates $\dot{\varepsilon}_1 > \dot{\varepsilon}_2$ can also be figured out according to above analysis. Assuming the curve of $\dot{\varepsilon}_2$ is above the one of $\dot{\varepsilon}_1$, as shown in Fig. 3.4.

Combining $\dot{\varepsilon} = \dot{\varepsilon}^e + \dot{\varepsilon}^p$, Eqs. 3.1 and 3.2, using same above reasoning, it is deduced that $\dot{\varepsilon}^e_B > \dot{\varepsilon}^e_{B'}$ and $\dot{\varepsilon}^p_B < \dot{\varepsilon}^p_{B'}$. Consequently, $\dot{\varepsilon}^e_B / \dot{\varepsilon}^p_B > \dot{\varepsilon}^e_{B'} / \dot{\varepsilon}^p_{B'}$, namely, the slope of $\dot{\varepsilon}_1$ is larger than that of $\dot{\varepsilon}_2$. Obviously, this deduction contradicts with the assumption. Thereby, the assumption is invalid; the curve of $\dot{\varepsilon}_2$ should not be above the curve of $\dot{\varepsilon}_1$, or, the curve of a small strain rate should not be above the one of a large strain rate.

In the above analysis, it can be seen that a high total strain rate corresponds to a high plastic strain rate or a high average dislocation velocity when a crystalline material is fully yielded. However, on the transition segment before fully yielding, total strain rate is larger than plastic strain rate, to a given stress, there must be a non-zero elastic strain rate. Or, after the onset of yielding, there is an elastic strain rate corresponding to an elastic strain increase $\dot{\varepsilon}^e \Delta t$, which generates a stress increase according to Hooke's law. This stress increase causes the average dislocation velocity and the plastic strain rate to increase and in turn reduces the elastic strain rate until the plastic strain rate is equal to total strain rate. For fully yielding, a high strain rate corresponds to a high plastic strain rate, which implies a high dislocation velocity, and then a high stress. Therefore, in the process of strain rate effect, the increase in stress looks more like to respond to the elastic strain rate than to drive dislocations moving.

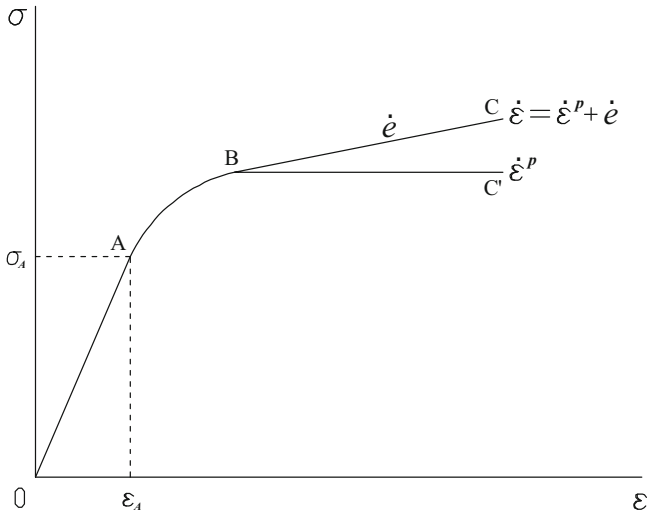

Fig. 3.5 A typical stress–strain curve of hardening plasticity

3.2.5 Uncoupling of Strain Hardening and Strain Rate Effects

The preceding discussions show that the effect of strain rate on yield stress is related to loading (or strain) rate while strain hardening depends more on material properties. It appears that strain rate effect has a significant influence on the segment AB in Fig. 3.2 and little influence after the material has fully yielded. It can be observed that strain hardening is related to strain while strain rate effect is not. The mechanism of strain hardening appears to be related to the threshold of dislocation motion while the mechanism of strain rate effect seems related to how fast dislocations move. These two effects can be examined separately.

For plastic hardening, a typical stress–strain curve is shown in Fig. 3.2 where the only difference with Fig. 3.3 is in the segment BC. In this segment, there is an increase in stress with strain for plastic hardening while there is no stress increase for perfect plasticity. This implies that there is an elastic strain rate for plastic hardening but none for perfect plasticity. As the slope of segment BC is relatively small compared to that of segment AB in Fig. 3.3, for simplification, the slope of segment BC is taken to be approximately constant, as shown in Fig. 3.5. As a stress increase corresponds to an increase in elastic strain, the linearity of the segment BC implies that the increase in elastic strain is constant which in turn implies a constant elastic strain rate. A strain rate $\dot{e}$ is used to represent this elastic strain rate corresponding to strain-hardening in segment BC. The total strain rate can be viewed as the sum of the plastic strain rate and this elastic strain rate, i.e., $\dot{\varepsilon} = \dot{\varepsilon}^p + \dot{e}$. Here, $\dot{\varepsilon}^p$ can be viewed as an actual plastic strain rate. With this actual plastic strain rate, the analysis for perfect plasticity in the preceding discussion can be applied to plastic hardening.

3.2.6 History Effect of Inconstant Strain-Rate Loading

History effect of inconstant strain-rate loading that can be observed in multi-step loading tests can also be understood by using the new interpretation of strain rate effect. Two strain rates are used in these tests, a high one and a low one. In the test, a sample is first loaded at the high strain rate and unloaded, then reloaded at the low strain rate and unloaded, and finally loaded again at the high strain rate. During first loading, a larger dislocation velocity is required that corresponds to a high flow stress. In first unloading, the dislocation density remains at that generated by the first high-rate loading. When the sample is subsequently reloaded at the low strain rate, only a lower dislocation velocity is required, the flow stress is correspondingly smaller, following the stress–strain curve of the low strain rate. In the third loading at the high strain rate, a high dislocation velocity is again required and hence a large flow stress is needed. Its stress–strain curve follows the extension of the one of the first loading due to the same strain rate, as shown in Fig. 3.6. These obtained stress–strain curves agree qualitatively with Lindholm's experiments [2].

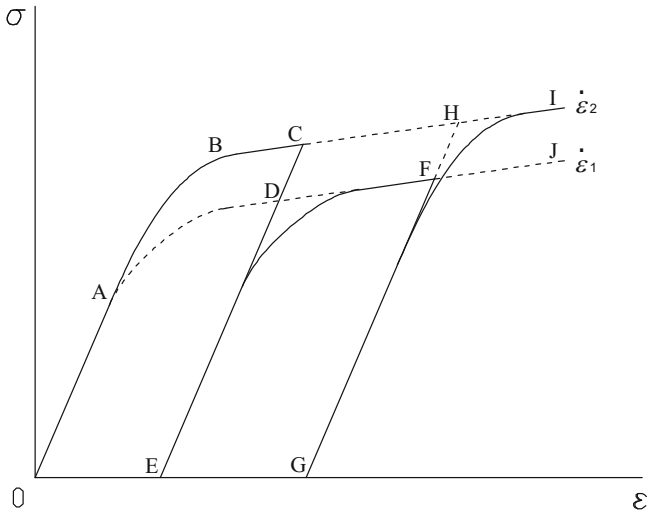

Fig. 3.6 Stress–strain curve under multi-path loading

3.2.7 Strain Rate Sensitivity of Metals

According to Orowan's relationship, an increase in strain rate is related to an increase in dislocation velocity. Considering the stress dependence of dislocation velocity, an increase in stress is then related to the increase in strain rate, which describes the strain rate sensitivity. Different strain rate sensitivities of metals have been examined through the molecular dynamics simulations of their stress dependence of dislocation velocity [14].

Experiments shows that the exponent m in Eq. 3.2 increases when temperature decreasing [15]. This indicates that for a given increase in dislocation velocity (i.e. a given increase in strain rate), the stress increase at low temperature is less than that at high temperature, namely, rate sensitivity reduces with decrease in temperature; vice versa. Thereby, this deduction well explains the experimental observation that rate sensitivity increases with temperature [1]. And the observation also validates the importance of the stress dependence of dislocation velocity in strain rate effects.

3.3 Conclusion

This study has focused primarily on strain rate effects at mesoscopic scale. A interpretation of strain rate effect has been proposed based on dislocation theory. It is proposed in this work that Orowan's relationship and the stress dependence of dislocation velocity make the mesoscopic mechanism of strain rate effect. The stress dependence of dislocation velocity is crucial to strain rate sensitivity. The elastic strain rate, the difference between the total strain rate and the plastic strain rate, directly contributes to the process of stress increasing. Several phenomena of strain rate effect have been discussed based on the interpretation and experiments agree with the discussion.

References

1. Meyers MA (1994) Dynamic behavior of materials. Wiley, New York
2. Lindholm US (1964) Some experiments with the split Hopkinson pressure bar. J Mech Phys Solids 12:317–335
3. Ross CA (1997) Review of strain rate effects in materials. Structures under extreme loading conditions, PVP-vol 351. ASME, New York, pp 255–262
4. Yasunaga K, Iseki M, Kiritani M (2003) Dislocation structures introduced by high-speed deformation in bcc metals. Mater Sci Eng A 350:76–80
5. Klepaczko JR (1988) Proceedings of international conference of DYMAT, Les Editions de Physique, Les Ulis, C3533
6. Klepaczko JR (1992) Short and long transients in dynamic plasticity of metals, modeling and experimental facts, in shock wave and high-strain-rate in materials. Marcel Dekker, New York
7. Zerilli FJ, Armstrong RW (1987) Dislocation-mechanics-based constitutive relations for material dynamics calculations. J Appl Phys 61:1816–1825

8. Zerilli FJ, Armstrong RW (1990) In shock compression of condensed matter-1989. Elsevier, Amsterdam
9. Zerilli FJ, Armstrong RW (1990) Description of tantalum deformation behavior by dislocation mechanics based constitutive equations. J Appl Phys 68:1580–1591
10. Zerilli FJ, Armstrong RW (1992) The effect of dislocation drag on the stress–strain behaviour of f.c.c. metals. Acta Met Mat 40:1803–1808
11. Follansbee PS (1986) Metallurgical application of shock-wave and high-strain-rate phenomena. Marcel Dekker, New York, p 451
12. Zbib HM, de la Rubia TD (2002) A multiscale model of plasticity. Int J Plasticity 18:1133–1163
13. Gilman JJ, Johnston WG (1957) Dislocations and mechanical properties of crystals. Wiley, New York
14. Qin Kun, Yang Li-Ming, Hu Shi-Sheng (2008) Strain rate sensitivities of face-centred-cubic metals using molecular dynamics simulation. Chin Phys Lett 25(7):2581–2584
15. Hull D, Bacon DJ (2001) Introduction to dislocations. Oxford: Butterworth Heinemann

Chapter 4
High Strain Rate Friction Response of Porcine Molar Teeth and Temporary Braces

S.J. Chen, Y.H. Chen, and Liren Tsai

Abstract Teeth replacement has been an important therapy for dental treatment, such as dental dentures and the filler materials. In order to obtain the mechanical properties of temporary braces and molar teeth, the Split Hopkinson Pressure Bar (SHPB) and Torsional Kolsky Bar (TKB) facility was adopted. The temporary braces were PMMA based materials manufactured by Tempron. The second large molar tooth from porcine mandible was chosen as the specimen in this research, because it is very similar to the human molar tooth.

In this study, low-speed diamond saw was utilized to prepare the tooth specimens, then, through the SHPB apparatus, the mechanical properties of porcine large molar tooth was measured and analyzed. The temporary braces were mixed using different percentages of PMMA compounds. SHPB and TKB facilities at Kaohsiung University of Applied Sciences were utilized to study the abrasion of temporary braces and its resistance to shock loadings. By comparing the results obtained from porcine tooth and PMMA braces, the characteristics of the dentine and durability of temporary braces would be studied. The results could be of great use for future dentures or filler materials developments.

Keywords Split Hopkinson pressure bar • Torsional Kolsky bar • Dentine • Enamel • Temporary braces

4.1 Introduction

Teeth are used to chew food, help pronunciation and maintain facial structure. A group of 32 permanent teeth accompany with us through our lives. Although the dental composition is similar to the bone, it is not connected with joint and does not produce red blood cells. It is composed of the middle dentine as the inner pulp and enamel as the outer layer. When teeth defects happened or teeth structure became incomplete because of teeth decay, use of the dental mouthpiece is a method to restore the original shape and strengthen its strength to ideal manner [1–3]. The integrity of tooth structure is shown in Fig. 4.1.

If you need to wear temporary brace, defected teeth will be trimmed to remove outermost layer, leaving a strong middle portion. It will help patients imprint corresponding teeth jaw bite and accurate record. And then compression molding will be prepared to do the denture teeth with corresponding teeth bite model. PMMA temporary braces had strength and appearance with near-real teeth, therefore most of braces use of such material [4]. The temporary braces with teeth model are show in Fig. 4.2.

Because of the way of eating, cleaning, cleaning appliances or other reasons, it is inevitable the teeth will be diseased or suffering from normal usage decay. People started to notice the importance of dental health, no matter a slight decay repair or replacement dentures; there are a number of related researches. Common dental diseases, including periodontal disease, dental calculus, dental caries, gingival inflammation and malocclusion, dental caries are the most common methods. In some dental caries, dentist used braces to treat serious defects so the patients would have better bite strength. Researches have been

S.J. Chen • Y.H. Chen • L. Tsai (✉)
Department of Mechanical Engineering, National Kaohsiung University of Applied Sciences, No.415, Jiangong Rd., Sanmin Dist., Kaohsiung City 807, Taiwan (R.O.C.)
e-mail: liren@cc.kuas.edu.tw; c1s2j3@gmail.com

B. Song et al. (eds.), *Dynamic Behavior of Materials, Volume 1: Proceedings of the 2013 Annual Conference on Experimental and Applied Mechanics*, Conference Proceedings of the Society for Experimental Mechanics Series,
DOI 10.1007/978-3-319-00771-7_4,

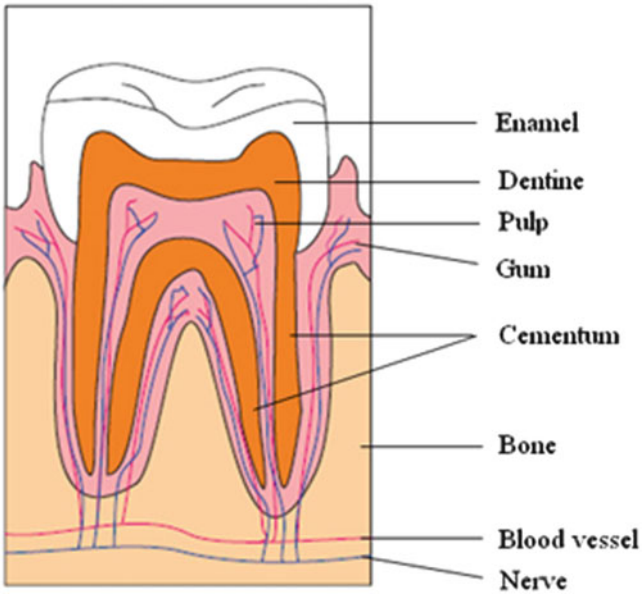

Fig. 4.1 Schematic diagram of tooth

Fig. 4.2 Temporary braces with teeth model

performed via SHPB device to testing dynamic response of human teeth [5], or the dental composites [6], but there very few researches were focused on the dynamic response of porcine dental. We select porcine teeth because of tooth structure is similar to human moreover porcine easier to research and achieved. In this study, both porcine molar teeth and temporary brace materials were studied using SHPB and TKB facilities.

4.2 Specimen Preparation

4.2.1 Teeth

Enamel is a hard dental tissue developed from ameloblast cells. Enamel is composed of 96 % inorganic hydroxyl-apatite crystal by weight or more than 86 % hydroxyl-apatite crystal by volume. It also contains organic matrix and a small amount of water; therefore, it is less hydrophilic compared to dentin which has higher water content. Dentin serves as an elastic support for enamel. Unlike enamel, dentin is composed of 70 % inorganic hydroxyl-apatite crystal by weight or 50 % hydroxyl-apatite crystal by volume. Dentin has a higher percentage of organic mineral (18 % by weight or 25 % by volume)

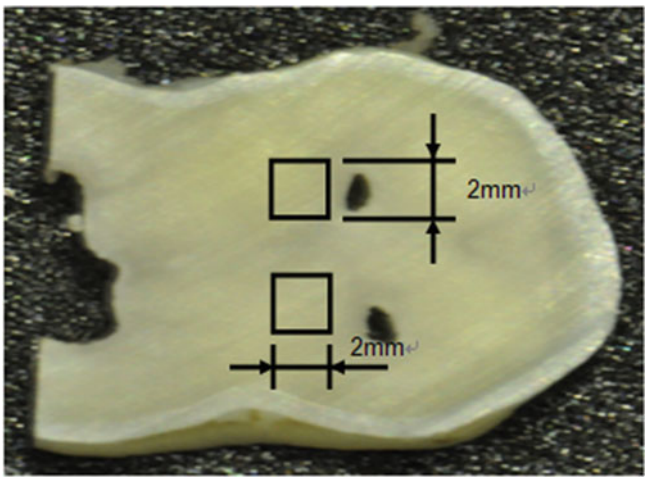

Fig. 4.3 The place for cut specimen

Fig. 4.4 The temporary braces specimen

and water (12 % by weight or 25 % by volume) compared to enamel. It is also considered more hydrophilic when compared to enamel [7, 8, 10]. In this research, second porcine molar teeth were examined using the Split Hopkinson pressure bar (SHPB). To prepare a proper specimen, the orientation and dimension of teeth samples were carefully chosen. The specimens were cut to 2 × 2 × 2 mm cubic shape from thin slice of teeth as shown in Fig. 4.3.

4.2.2 Temporary Braces

When the damage in the tooth was serious, denture must be used to replace the broken part of tooth. Before the dentures were molded to the proper shapes, temporary braces were used [9, 11]. Temporary braces specimens were prepared using TEMPRON temporary crown and bridge resin. We used different ratio of mixed stir and injected into the metal mold before it's solidify. The temperature was kept at 50 °C for 10 min before the specimens were removed from the metal mold. The specimens were stored in thermostat cabinets before each test. The Torsional Kolsky Bar (TKB) apply shear loading on specimens, so our specimen shape was designed as a dumbbell shape. The specimen is show in Fig. 4.4.

4.3 Experimental Setup

4.3.1 SHPB

Dynamic response was obtained using by a modified split Hopkinson pressure bar, which consist of the striker, incident, transmission bar and pulse shaper the lengths were 300, 1,000, 900 mm with same diameter 12.7 mm, respectively. The SHPB is based on the one dimension wave theory, when elastic wave propagation through incident bar, partly of the elastic wave propagated to the specimen and remained to reflect to the incident bar (Fig. 4.5).

The stress–strain formula is as following:

$$\dot{\varepsilon}(t) = \frac{C}{L}[\varepsilon_i(t) - \varepsilon_r(t) - \varepsilon_t(t)] \tag{4.1}$$

$$\varepsilon = \frac{2C}{L}\int_0^t \varepsilon_r(t)dt \tag{4.2}$$

$$\sigma = E\varepsilon_r(t) \tag{4.3}$$

In Eq. 4.1, where $\dot{\varepsilon}$ = strain rate, C = wave speed, L = length of Specimen, ε_i = strain of incident wave, ε_r = reflected wave and ε_t = transmitted wave. In Eq. 4.2, where ε = strain, the C, L, is the same as Eq. 4.1. In Eq. 4.3, σ = stress, E = elasticity modulus, ε_r is the same as Eq. 4.1.

4.3.2 TKB

The Torsional Kolsky Bar (TKB) [12], which includes pulley, clamp, 45° Strain Gage, Signal amplifiers and Digital Phosphor Oscilloscope, incident and transmitter bar, the lengths were, 2,000, 1,600 mm with same diameter 25.4 mm, respectively. It was illustrated in Fig. 4.6. All the elements were manufactured from Al-7075. By capturing the signals from shock waves, the shear stress versus strain signals during the dynamic friction process could be obtained. The Shear/Torque Pattern Strain Gages were utilized to measure the wave signal. In order to clamp clamping a pin and pulley rotation storage torque. It will produce a plastic wave when the torque release. While elastic wave propagated through incident bar, the elastic wave had two types. One was passed through to specimen, and the other was reflected back to incident bar, and by using one dimensional wave theory, the resultant stress versus strain curves were determined.

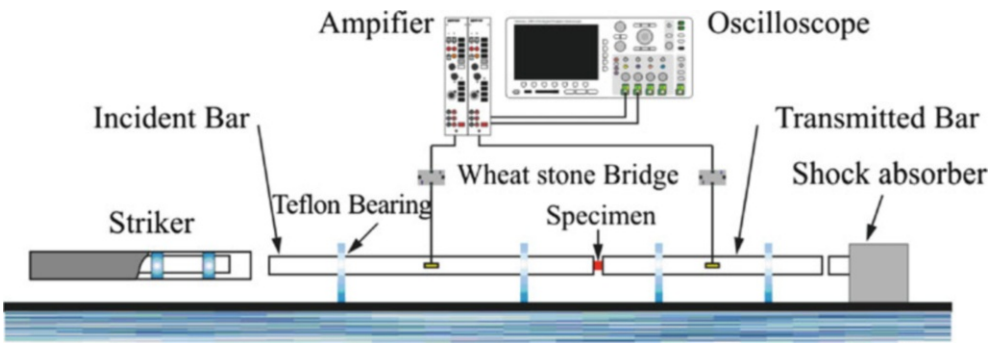

Fig. 4.5 SHPB system setup

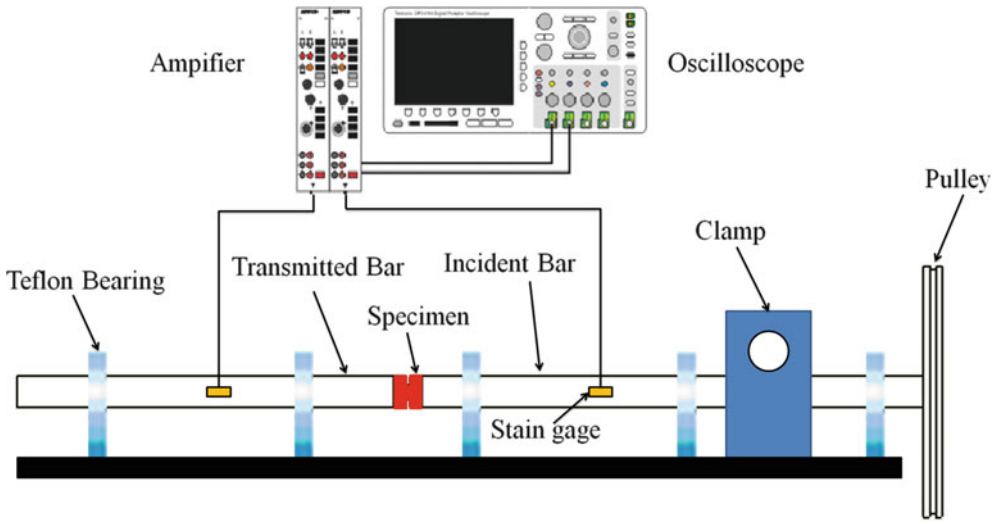

Fig. 4.6 TKB experiment setup

In this setup, a specimen is mounted between incident and transmitter bar. The shear stress–strain and strain rate is as follows:

$$\tau_s = G\frac{R_s * J_b}{R_b * J_s}\gamma_t \tag{4.4}$$

$$\gamma_s = -2\frac{R_s * C}{R_b * L_s}\int_0^t \gamma_r dt \tag{4.5}$$

$$\dot{\gamma}_s = -2\frac{R_s * C}{R_b * L_s} \tag{4.6}$$

In Eq. 4.4, where τ_s = shear stress, G = shear modulus, R_s = average radius of specimen, R_b = bar radius, J_s = polar moment of inertia of specimen, J_b = polar moment of inertia of bar and γ_t = transmitter wave. In Eq. 4.5, where C = torsion wave speed, L_s = gauge length and γ_r = reflected wave. In Eq. 4.6, $\dot{\gamma}_s$ = average shear strain.

4.4 Results and Discussion

4.4.1 Static and Dynamic Compression Test of Teeth

Several experiments were performed to exam the dynamic response of porcine molar tooth. It is shown that the dental specimen shattered to pieces when compressed under SHPB technique as the enamel and dentine structure were forced under dynamic loading. The stress–strain curve of selected dental specimen under dynamic and static compression was show in Fig. 4.7.

According to the result, the yield stress of dental specimen grows when the strain rate increased. The static test with strain rate 0.05 and we could find there had same trend in our static test. At about 20 MPa, yield started and after further compressed to 170 MPa, catastrophic failure happened. The dynamic yield stresses of dental specimen were 121 MPa at strain rate 1,450 s^{-1}, and 203 MPa at strain rate 2,900 s^{-1}, and 186 MPa at strain rate 3,700 s^{-1} and the Young's modulus showed 3, 6.67 and 7.25 GPa, respectively.

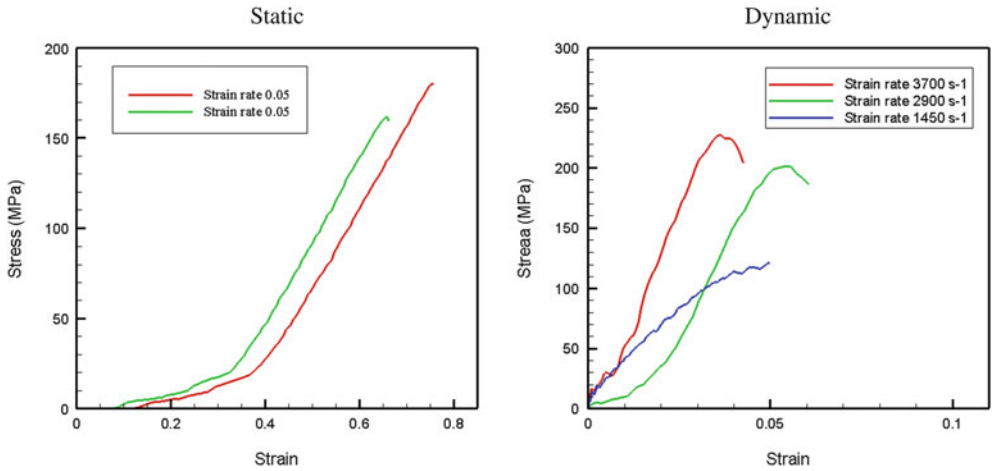

Fig. 4.7 Dynamic and static stress–strain responses

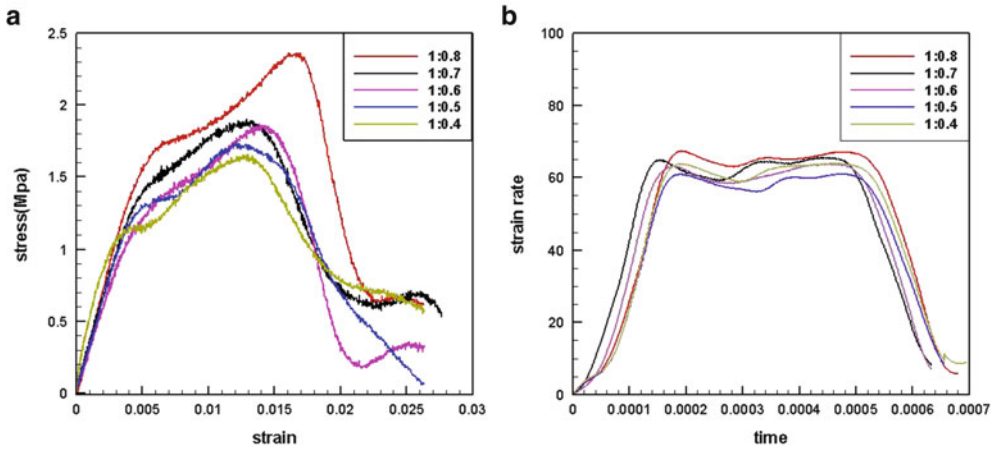

Fig. 4.8 Dynamic torsion test with same strain rate and different ratios for temporary braces (**a**) stress–strain curve (**b**) strain rate-time (μ_s) curve

4.4.2 Dynamic Torsion Test of Temporary Braces

In TKB experiments, we tested different mixing ratios temporary braces at varying strain rates. It is shown that the temporary braces subject to shear force of the impact when torsion TKB device produce shear failure. Therefore we could find there stress–strain curve and strain rate effect with different ratios for temporary braces. The stress–strain curve and strain rate-time curve was show in Fig. 4.8.

The mixing ratio 1 is mixture and 0.8–0.4 is temporary braces powder material. In this experiment the highest shear stress was 2.3 MPa of mixing ratio 1:0.8, the lowest was 1.6 MPa of mixing ratio 1:0.4. There were all about in 60 s^{-1}strain rate. So we could find when the strain rate at 60 s^{-1} temporary braces powder material proportion higher its stress higher. The stress higher strength is stronger.

4.5 Conclusion

When strain rate increased the yield stress and elastic modulus increases. In a structural point of view, due to the porous structure characteristics of the dentine, it has relative toughness to withstand the repetitive impact. Due to the porous structure of dentin it has limited deformation space. Under the protection of the outer layer of enamel, it can withstand a

larger compression load. When it reached its maximum pressure, it will lead to the slip deformation of inter-organizational. This also caused a fragmented specimen. By using the different force to test, the yield stresses of dental specimen were 121 MPa at strain rate 1,450 s^{-1}, and 203 MPa at strain rate 2,900 s^{-1}, and 186 MPa at strain rate 3,700 s^{-1} and the Young's modulus showed 3, 6.67 and 7.25 GPa respectively.

Dynamic shear tests of temporary braces were performed and the effective stress–strain curves. In our experiments that understand when temporary braces suffer friction shear stress, it will be deformation thus fracture. The specimen stress–strain curve could find it is a plastic material. Due to mixing ratio changes its stress–strain curve had been effect with the same strain rate 60 s^{-1}. The stress–strain with the ratio increases proportionately higher. Through the calculation of the above formula 1:0.8 at stress 2.3 MPa, 1:0.7 at stress 1.9 MPa, 1:0.6 at stress 1.8 MPa, 1:0.5 at stress 1.7 Mpa, 1:0.4 at stress 1.6 Mpa respectively.

References

1. Taha NA (2011) Fracture strength and fracture patterns of root filled teeth restored with direct resin restorations. J Dent 39:527–535
2. Meerbeek BV (2005) Micro-rotary fatigue of tooth biomaterial interfaces. Biomaterials 26:1145–1153
3. Marshall GW Jr, Marshall SJ (1997) The dentin substrate: structure and properties related to bonding. J Dent 25(6):441–458
4. Tanimoto Y, Hirayama S, Yamaguchi M, Nishiwaki T (2011) Static and dynamic moduli of posterior dental resin composites under compressive loading. Sci Dir 4:1531–1539
5. Vallee GE. Translating dental performance into engineering science within a senior capstone design project. Western New England College
6. Tanimoto Y (2006) Dynamic viscoelastic behavior of dental composites measured by split Hopkinson pressure bar. Dent Mater J 25(2):234–240
7. Tanimoto Y (2011) Static and dynamic moduli of posterior dental resin composites under compressive loading. J Mech Behav Biomed Mater 4:1531–1539
8. Vaseenon S (2011) Relationship between caries-affected dentin mineral density and microtensile bond strength. Master's thesis, University of Iowa
9. Honda MJ (2009) The induction of dentin bridge-like structures by constructs of sub cultured dental pulp-derived cells and porous HA/TCP in porcine teeth. Nagoya J Med Sci 71:51–62
10. Dwayne A (2012) Nanoscopic dynamic mechanical properties of intertubular and peritubular dentin. J Mech Behav Biomed Mater 7:3–16
11. Imbeni V (2005) The dentin–enamel junction and the fracture of human teeth. Nat Mater 4:229–232
12. Kobayashi T, Simons JW, Brown CS, Shockey DA (2008) Plastic flow behavior of Inconel 718 under dynamic shear loads. Sci Dir 35:389–396

Chapter 5
Dynamics of Interfaces with Static Initial Loading

Jacob C. Dodson, Ryan D. Lowe, Jason R. Foley, Christopher Mougeotte, David Geissler, and Jennifer Cordes

Abstract Accurately modeling the dynamic response of structural interfaces under high rate loading conditions is challenging due to lack of focused studies and validation data. In order to support the development and validation of accurate physics-based models of these interface dynamics, simulations and experiments using combined static torsional loads with dynamic compressive loading are performed. A ballistic impact generates dynamic compressive stress waves that propagate across the threaded interface of two coupled metallic bars with a known static torque. Strong phenomenological evidence of the release and conversion of static torsional energy due to the applied dynamic loads is seen in time-frequency analysis. The frequency band structure of the dynamic waves are also observed to vary under certain conditions. Applied torque is shown to relax almost completely during an experiment, with significant rotation of the transmission bar relative to the incident bar. The mechanism is believed to be release of the static torque and the generation of torsional waves.

Keywords Wave propagation • High strain-rate experimentation • Static loading • Dynamic loading • Interface dynamics • Structural dynamics

Nomenclature

ε	Strain
λ	Wavelength
μ_c	Interface friction coefficient of collar
μ_t	Interface friction coefficient of thread
r_t	Mean radius of thread
r_c	Mean radius of collar
T	Applied Torque
F	Equivalent Axial force
l	Thread lead
ρ	Density
ξ	Transmission efficiency
σ	Stress
τ	Transmission efficiency
ω	Angular frequency
ν	Poisson's ratio
c	Wave speed

J.C. Dodson (✉) • R.D. Lowe • J.R. Foley
Air Force Research Laboratory, AFRL/RWMF, 306 W. Eglin Blvd., Bldg. 432, Eglin AFB, FL 32542-5430, USA
e-mail: jacob.dodson@eglin.af.mil

C. Mougeotte • D. Geissler • J. Cordes
U.S. Army Armament Research, Development, and Engineering Command, Eglin AFB, FL 32542-5430, USA

B. Song et al. (eds.), *Dynamic Behavior of Materials, Volume 1: Proceedings of the 2013 Annual Conference on Experimental and Applied Mechanics*, Conference Proceedings of the Society for Experimental Mechanics Series,
DOI 10.1007/978-3-319-00771-7_5,

h Windowing function
r Reflection coefficient
t Transmission coefficient
v_s Striker velocity
E Elastic modulus
$\mathfrak{F}$ Fourier transform
$\mathfrak{S}$ Spectrogram amplitude

5.1 Introduction

Modeling and simulation is the preferred tool for rapid design and analysis of complex engineering structures in a variety of applications and corresponding loading conditions. However, the dynamics of mechanical wave propagation across interfaces is traditionally difficult to predict in simulations of impact events. The difficulty is compounded when static stresses, such as an applied static load or residual internal stresses from manufacturing, exist in a structure.

Interfaces themselves are also a rich area of experimental and theoretical mechanics research. Bolted interfaces and threaded connections [1] have been extensively studied for relevant structural design mechanisms such as fatigue and structural damping. Slip and frictional damping have been observed in bolted joints [2] and rotating cylindrical plates with intermittent contact [3]. Dynamic friction has also been considered in a number of studies [4]. A constitutive model for the dynamic response of interfaces including friction and microstructural considerations has been developed [5]. Additionally, the contribution of interfaces to nonlinear system response has been quantified for bolted interfaces [6]. The nonlinear effects of preload on the response curves of beams [7] and cohesive interfaces in beam bending [8] have been reported.

In a previous investigation [9], the Preload Interface Bar (shown below in Fig. 5.1) was introduced to quantify the effects of a static compressive load on the propagation of dynamic compression waves across a normal interface. This apparatus is based on the well-established and widely utilized split Hopkinson pressure bar (SHPB) apparatus for measuring elastic wave propagation [10, 11]. The unique feature of this apparatus is the designed capability of applying a normal static preload to the interface using a hydraulic ram prior to the dynamic loading from a striker.

The objective of this effort is to extend this earlier work to threaded interfaces and develop validation data to improve the state-of-the-art in interface simulation in impact dynamics. The storage of torsional mechanical energy in Kolsky bars has been reported [4, 12] as well as the use of hydrostatic compression for testing geomaterials, glass, and ceramics in a SHPB [13]. However, this is the first known example of combining static torsional preloads with dynamic compressive loading in a SHPB-like configuration.

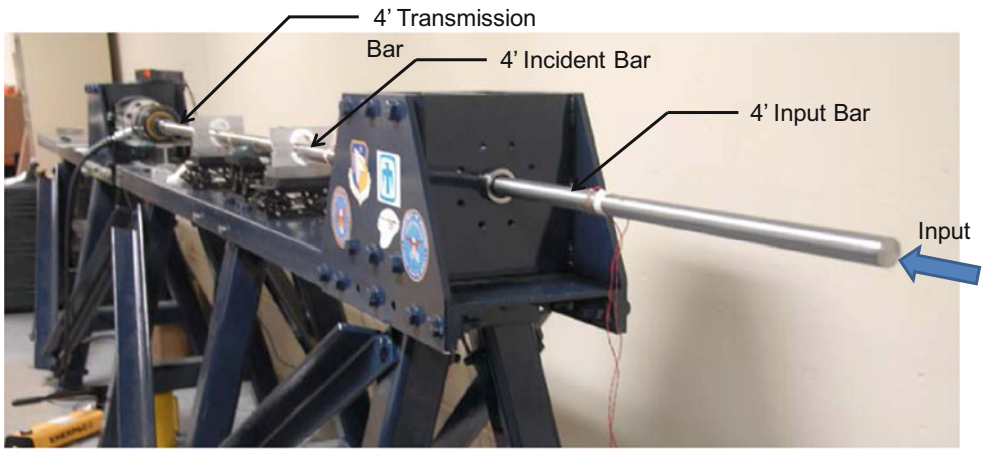

Fig. 5.1 The Preload Interface Bar was developed to study the propagation of stress waves through systems with combined static compressive and transient compressive loading

5.2 Test Apparatus

The incident and transmission bars are both 1.5 in (3.8 cm) diameter, 48 in (122 cm) long bars made from hardened AISI 1566 steel alloy ($\rho = 7.8$ g/cm^3, $E = 210$ GPa, $\nu = 0.29$). The corresponding wave speed (c), calculated using the well-known one-dimensional wave relation

$$c = \sqrt{E/\rho}\,, \tag{5.1}$$

is approximately 5,200 m/s. One end of each bar is machined with 1″-8 UNC threads (incident bar threads are male, the transmission bar threads are female). The ends were also marked with a rotational index to capture any relative rotation of the ends. An initial static torque preload was applied to the system prior to each test using DMC handle-less strap wrenches, model number BT-BS-618WT (the strength of the straps limited applied torque to less than 50 ft-lbf). A Multitorq digital torque transducer, model 2503-F-MT produced by CDI Torque Products, was used to monitor the applied torque (before the tests) and the breaking torque (after the tests) at 2″ from the interface. Dynamic excitation was provided by a 6 in. long steel striker propelled by an air gun with velocities ranging from 7 to 14 m/s. The impact generated transient stress waves that propagate down the incident bar and then reflect from and propagate through the interface. Figure 5.2 shows a schematic of the experimental apparatus as well as the location of the gages and sensors that were used to capture the dynamic response; Fig. 5.3 shows the as-built system and provides a pictorial reference of the experiment.

5.3 Simulation

Prior to testing, explicit finite element simulations were performed to predict the propagation of the waves across the interface. The full experiment geometry, including the impactor and both the incident and transmission bars, was modeled in Abaqus Explicit with one notable difference: the threads in the model were modeled as ribs (i.e., threads with no pitch) instead of fully featured threads. The friction coefficient at the interface was treated as an independent variable with frictionless ($\mu_t = \mu_c = 0$) and high friction ($\mu_t = \mu_c = 0.8$) as two representative cases. Equivalent static loads (F) were calculated from the applied torque (T) using the power screw equation [14, 15]

$$T = F\, r_t \left(\frac{l + 2\pi\mu_t r_c}{2\pi r_c - \mu_t l} + \frac{r_c}{r_t}\mu_c \right). \tag{5.2}$$

The equivalent axial preloads were calculated at the interface and applied to the model using an implicit solver. The applied torque and equivalent applied axial load are shown if Table 5.1.

The stress state due to the applied axial load became the initial condition for the system which was then dynamically simulated using the explicit solver. The initial stress distributions at the various preloads are shown in Fig. 5.4. Several configurations were run, spanning the planned experimental design space of striker impact velocities, applied static torque,

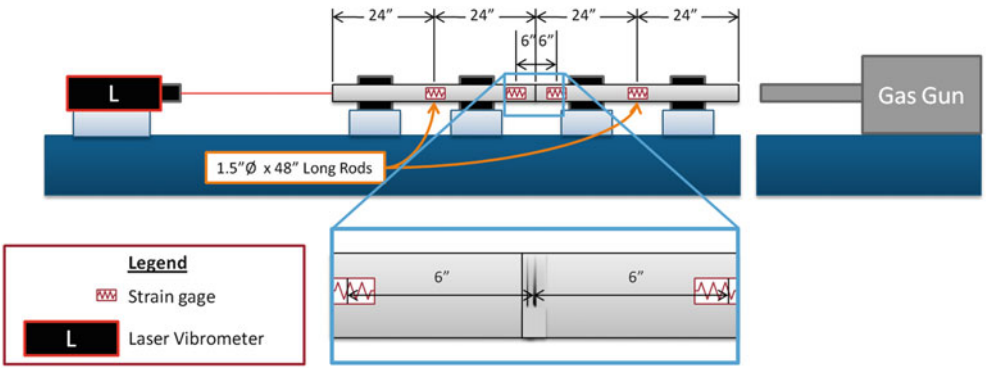

Fig. 5.2 Schematic of the threaded bar interface experiments showing the layout of the sensors. The system is supported by low-friction linear bearings

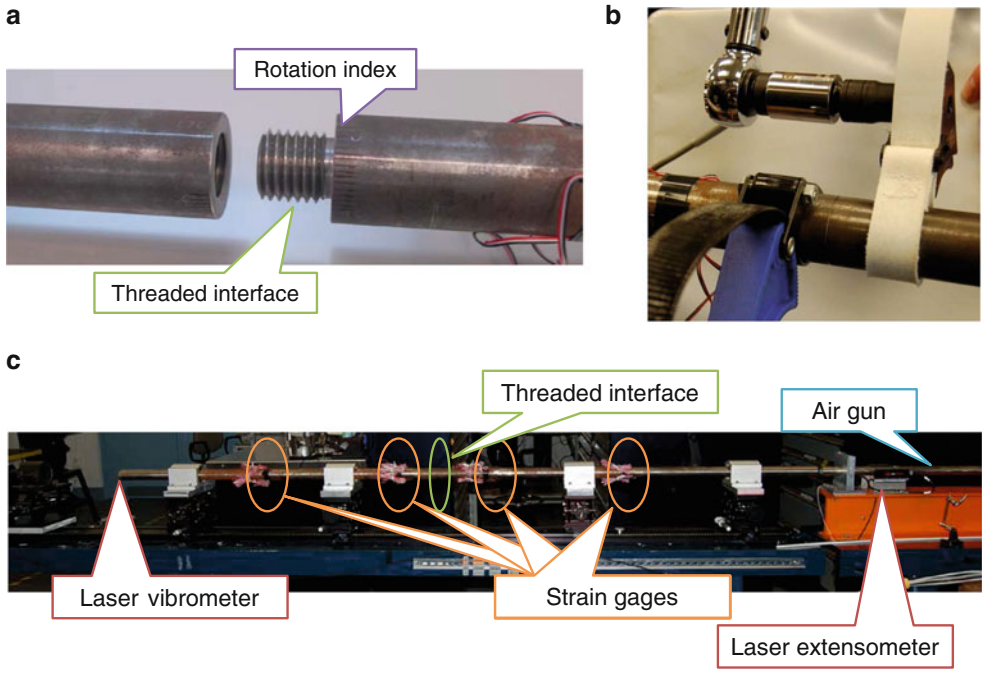

Fig. 5.3 Pictures of the threaded bar interface experiments showing (**a**) the details of the interface, (**b**) the method for applying the torque, and (**c**) the experiment layout and location of the sensors

Table 5.1 The equivalent static loads calculated with the power screw relation

Torque	Equivalent axial preload
Hand tight	Negligible
50 ft-lbf	3,075 lbf
100 ft-lbf	6,150 lbf
150 ft-lbf	9,225 lbf

and interface friction. Figure 5.5 shows the model predictions of dynamic strain across the threaded interfaces for varying torque and with different striker velocities. The predictions show a small but observable sensitivity to torque in the stress wave propagation in the incident bar. The sensitivity to striker velocity was much higher as expected, with the peak strain (and stress) varying linearly with the striker velocity. This follows from 1-D wave propagation expression for strain in a Hopkinson bar [16], i.e.,

$$\varepsilon_i = \frac{\sigma_i}{E_i} = \frac{\rho_i c_i}{E_i} v_s = \frac{1}{c_i} v_s, \tag{5.3}$$

where v_s is the striker velocity and ρ_i, c_i, and E_i are the density, wave speed, and elastic modulus of the incident bar, respectively.

The local stress state at the interface was also examined in these initial simulations to predict any plastic deformation and also to visualize the stress distribution. Three cases at varying torque levels are shown in Fig. 5.4. No plastic deformation was predicted, although significant local stresses developed at higher torque levels.

5.4 Experiment

The experiment test apparatus was set up at the AFRL Shock Dynamics Laboratory. Analog signal conditioning for the strain gages, (i.e., regulated constant-current excitation, analog filtering at 204 kHz, and amplification), is accomplished via a Precision Filter 28000 chassis with 28144A Quad-Channel Wideband Transducer Conditioner with Voltage and Current

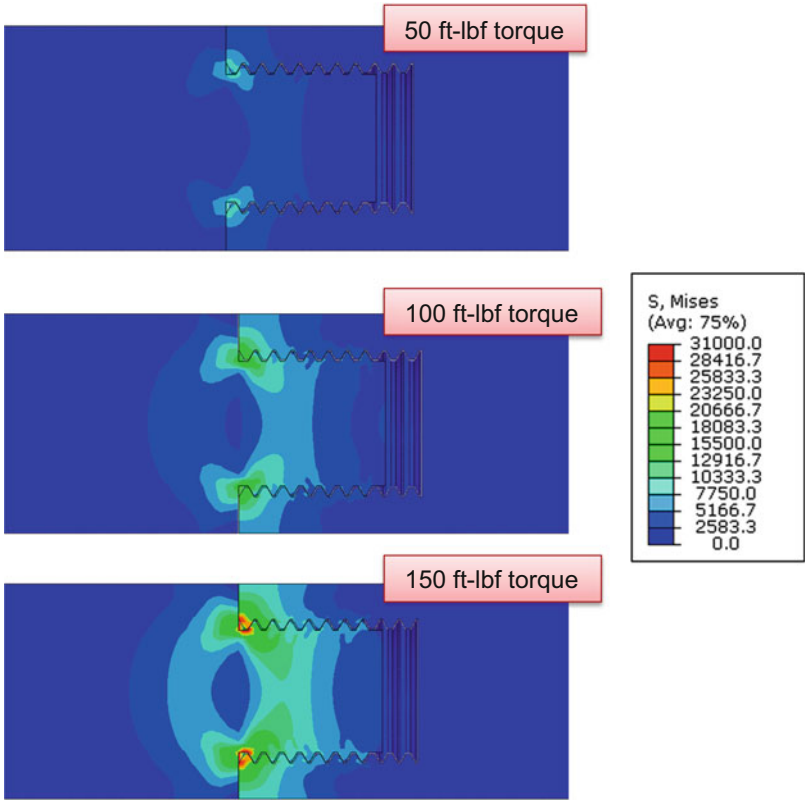

Fig. 5.4 Prediction of local static stress field (von Mises equivalent stress is shown in psi) in a threaded interface due to varying levels of applied static torque

Excitation cards [17]. A high rate instrumentation system using a National Instruments chassis paired with PXI-6133 multifunction input/output cards is used to digitize the analog data. The PXI-6133 samples at 2.5 MSa/s with 16 bits of vertical resolution [18].

A combination of direct mechanical (i.e., strain-based) and non-contact (laser vibrometer) measurements are performed on the bars. In the preliminary experimental effort discussed here, the primary measurements are the strain time history in the incident and the transmission bars on both sides of the interface. Uniaxial strain gages are mounted to the bar at multiple points on both the incident and transmission bars. The axial distribution allows tracking of the stress wave propagating through the system. The gages are oriented axially on the bar in diametrically opposed pairs to allow bending and/or extensional cancellation. This is feasible since the data acquisition system has sufficient number of phase-matched channels to independently capture the output from individual gages: the bending and extension are calculated from the axial strain in post-processing. Semiconductor strain gages are used; these have resistances of 120 or 350 Ω with a fast response time (~10 ns) and correspondingly higher bandwidth (~10 MHz) than foil gages (typically ~300 kHz [19]). The gage length is typically ~1 mm and the gage factor is about 150 [20], providing orders-of-magnitude improvement in sensitivity. The traditional disadvantage of semiconductor gages, a strong temperature dependence, is not a concern for these dynamic tests since the circuits can be balanced immediately prior to a test or run in an AC-coupled mode with minimal temperature excursions between data acquisition arming and trigger. The strain gages were wired with a floating shield/ground to avoid ground loops. Additionally, an OFV-332 Polytec laser vibrometer was used (paired with an OFV-3020 high speed (20 m/s) controller/demodulator) to perform a non-contact measurement of the surface velocity of the transmission bar with a bandwidth of up to 1.5 MHz [21].

5.4.1 Separation of Measured Strain

Using the strain gage pairs on the on the surfaces of the beam, we can decouple the strain due to bending and the strain due to axial extension or longitudinal motion. If we assume a coupled elementary rod and Timoshenko beam model, then our total axial displacement would be [22]

$$\bar{u}(x, y, t) = u(x, t) - y\varphi(x, t) \tag{5.4}$$

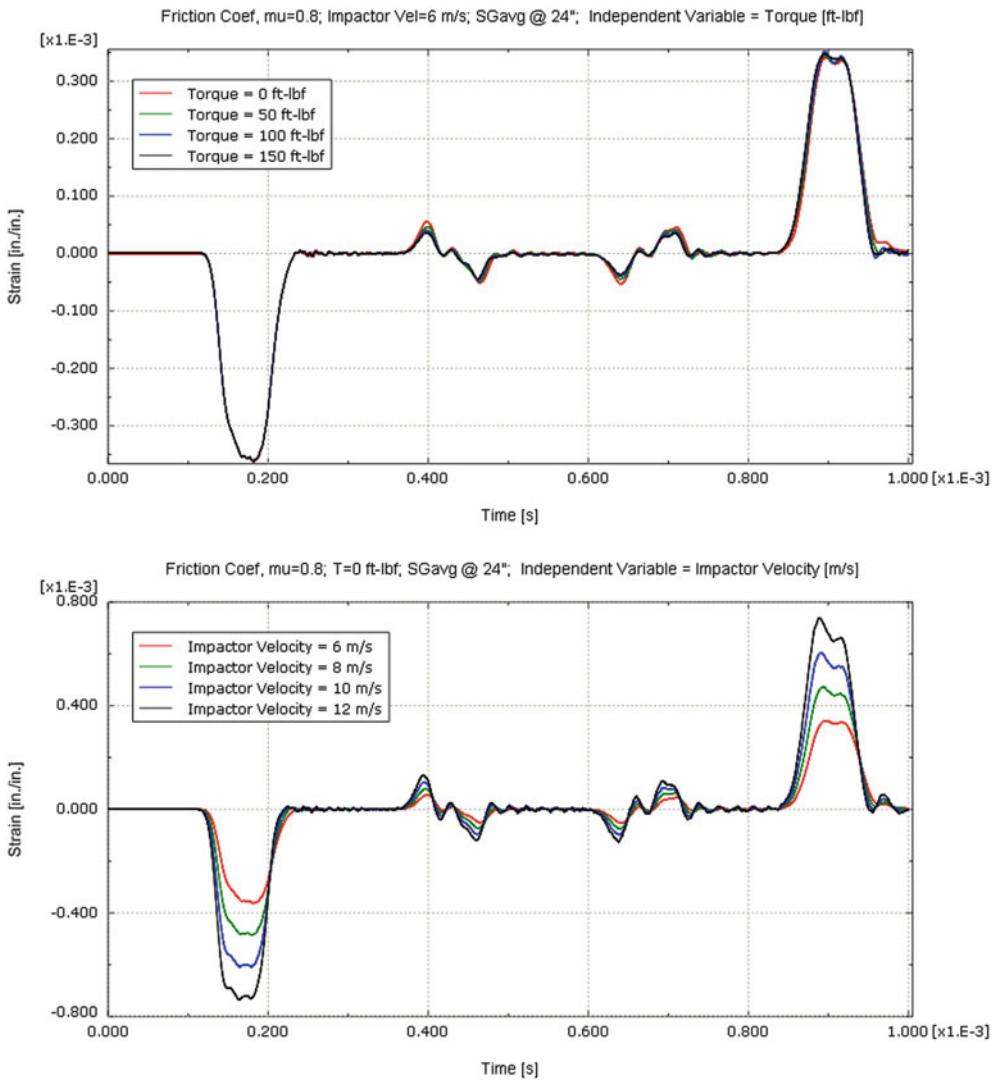

Fig. 5.5 Prediction of dynamic strain across the threaded interfaces for varying torque (*top*) and with different striker velocities (*bottom*)

where $\bar{u}(x,t)$ is longitudinal displacement and $y\varphi(x,t)$ is the axial displacement due to vertical/rotational motion. Now our axial strain on the top $\left(y=\frac{h}{2}\right)$ and the bottom $\left(y=-\frac{h}{2}\right)$ of the beam is

$$\varepsilon_x\left(x,\frac{h}{2},t\right)=\varepsilon_x^A(x,t)-\varepsilon_x^B(x,t) \tag{5.5}$$

$$\varepsilon_x\left(x,-\frac{h}{2},t\right)=\varepsilon_x^A(x,t)+\varepsilon_x^B(x,t) \tag{5.6}$$

Where $\varepsilon_x^A(x,t)$ is the axial strain component and $\varepsilon_x^B(x,t)$ is the bending strain component. Adding the measured strains on the top and bottom will cancel the bending strain, while subtraction of the measured strains will cancel the axial strain. From the experimental strain measurements we can decouple the strain due to axial motion and the strain due to flexural or bending motion. The decoupled strains can be written as

$$\varepsilon_x^A(x,t)=\frac{\varepsilon_x\left(x,\frac{h}{2},t\right)+\varepsilon_x\left(x,-\frac{h}{2},t\right)}{2} \tag{5.7}$$

$$\varepsilon_x^B(x,t) = \frac{\varepsilon_x\left(x,-\frac{h}{2},t\right) - \varepsilon_x\left(x,\frac{h}{2},t\right)}{2}. \tag{5.8}$$

5.5 Results and Analysis

The initial test matrix involved the bars being impacted at velocities ranging from 7 to 13 m/s, programming material (an index card) present or absent between the striker and incident bar, and under varying static torque of 0 (Hand tight), 25, and 40 ft-lbf. The data analysis focused on the strain time histories. A typical data set is shown in Fig. 5.6 (pre-torque of 40 ft-lbf); the longitudinal (axial) strain is shown in the top plot whereas the bending strain is shown in the bottom. The propagation of the wave through the bar and the subsequent partial reflection and transmission are seen in Fig. 5.6, but are further illustrated in highlights of the first pulse plotted in Fig. 5.7. Here the incident pulse is from SG-24-00 and the transmitted pulse is from SG 54-00.

5.5.1 Stress Transmission Coefficients

Stress transmission coefficients are used to quantify the performance of the interface. In this analysis of the threaded bar, we treat the interface as a black box and observe the signal energy into and out of the interface as shown in Fig. 5.8.

In a split Hopkinson bar with cross-sectional areas A_1 and A_2, the stress transmission coefficient t_{12} for the interface can be calculated using a uniaxial approximation [23]:

$$t_{12} = \frac{\sigma_1}{\sigma_2} = \frac{2\rho_1 c_1 A_1}{\rho_1 c_1 A_1 + \rho_2 c_2 A_2}. \tag{5.9}$$

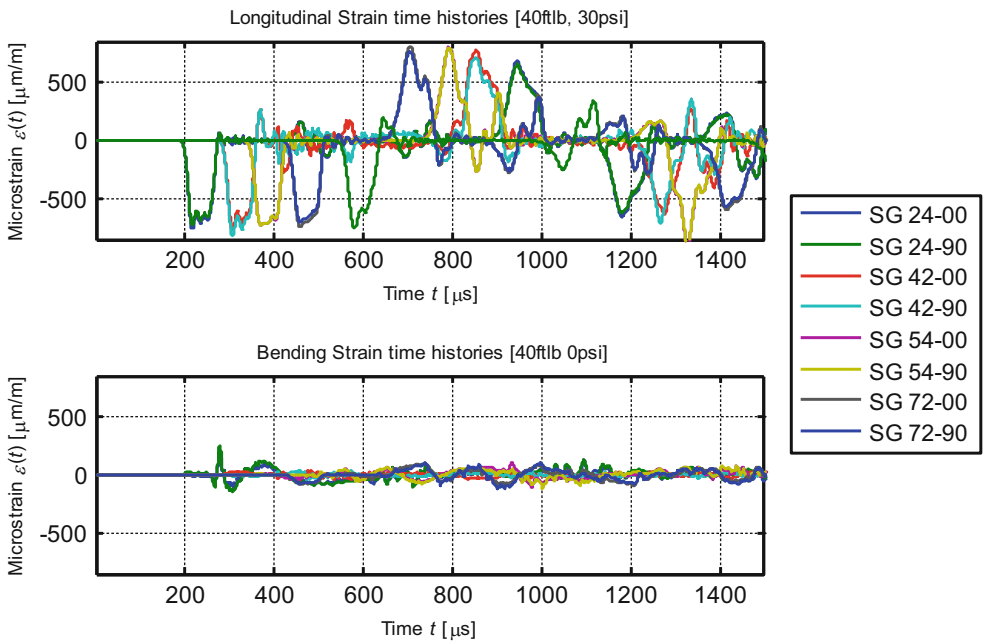

Fig. 5.6 Experimental data under 40 ft-lbf of static torque. The longitudinal (*top*) and bending strain (*bottom*) are shown for each of the gage sets, with results from both the 0° and 90° pairs shown

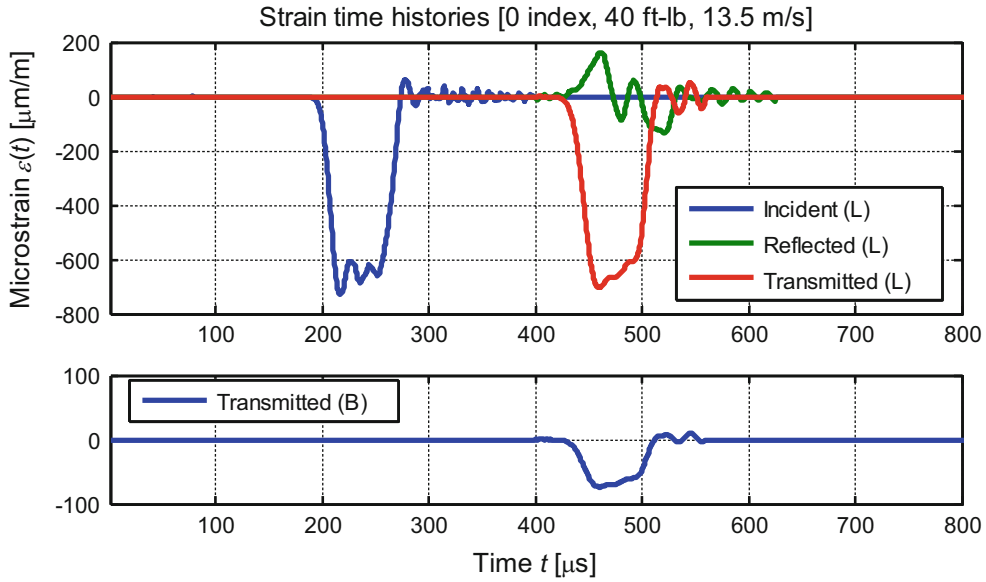

Fig. 5.7 The incident, reflected, and transmitted pulses across the threaded interface. The incident pulse is measured at 24 in. along the bar, while the transmitted pulse is measured at 54 in.

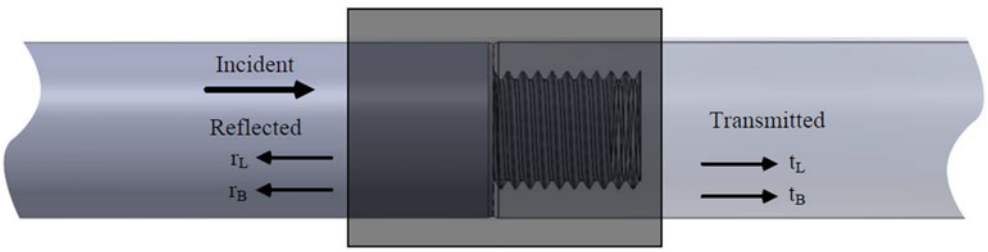

Fig. 5.8 The transmission and reflection of stress waves are analyzed by treating the threaded interface as a black box interface

For an ideal interface with perfect contact between bars with equal cross-section and identical material properties, t_{12} approaches unity. The corresponding reflection coefficient r_{12} for the interface is

$$r_{12} = 1 - t_{12} = \frac{\rho_2 c_2 A_2 - \rho_1 c_1 A_1}{\rho_1 c_1 A_1 + \rho_2 c_2 A_2}. \tag{5.10}$$

The transmission and reflection efficiency are related measures with respect to the averaged spectral power [24, 25]. The transmission efficiency τ_{12} and the reflection efficiency ρ_{12} are then

$$\tau_{12} = \frac{\text{transmitted vibrational power}}{\text{incident vibrational power}} \propto t_{12}^2, \tag{5.11}$$

$$\xi_{12} = \frac{\text{reflected vibrational power}}{\text{incident vibrational power}} \propto r_{12}^2. \tag{5.12}$$

A lossless ideal interface has $\tau_{12} \to 1$ with $\xi_{12} \to 0$. Conversely, a free surface has $\tau_{12} \to 0$ and $\xi_{12} \to 1$, respectively.

Experimentally, the longitudinal transmission and reflection efficiency of the interface in the frequency domain are given by

$$\tilde{\tau}_L(\omega) \propto \left(\frac{\tilde{\sigma}_{xx}^t(\omega)}{\tilde{\sigma}_{xx}^i(\omega)}\right)^2 = {t_L}^2. \tag{5.13}$$

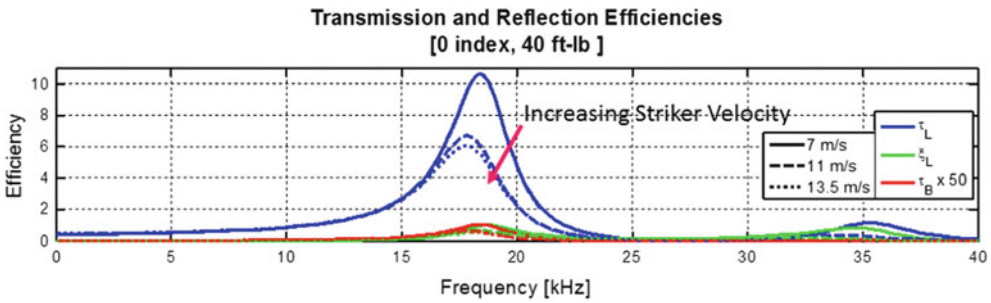

Fig. 5.9 Transmission and reflection efficiency for both bending and longitudinal waves under 40 ft-lbf initial static torque

and

$$\tilde{\xi}_L(\omega) \propto \left(\frac{\tilde{\sigma}^r_{xx}(\omega)}{\tilde{\sigma}^i_{xx}(\omega)}\right)^2 = {r_L}^2, \tag{5.14}$$

respectively, where the superscripts indicate incident (i), transmitted (t), and reflected (r), σ_{xx} is the axial principle stress, and $\tilde{\sigma}(\omega)$ indicates the Fourier transform of the stresses.

For a non-ideal interface where there is conversion between axial and bending motion then the bending efficiencies can be written as [26]

$$\tilde{\tau}_B(\omega) = 2\frac{k_L(\omega)}{k_B(\omega)}|t_B(\omega)|^2 \tag{5.15}$$

$$\tilde{\xi}_B(\omega) = 2\frac{k_L(\omega)}{k_B(\omega)}|r_B(\omega)|^2 \tag{5.16}$$

where $k_L(\omega)$ and $k_B(\omega)$ and the longitudinal and bending wavenumbers respectively. The wavenumber-velocity relation is

$$k(\omega) = \frac{\omega}{c(\omega)} \tag{5.17}$$

where ω is frequency (rad/sec) and $c(\omega)$ is the frequency dependent wavespeed. The Timoshenko beam theory was used to calculate the bending wave number, while the 1-D axial wave theory was used for the longitudinal wavenumber for this calculation. A perfect interface between two identical materials is expected to have a transmission of nearly unity value. Due to the conservation of energy, the sum of all the efficiencies is ideally unity. The efficiency of both the bending and longitudinal strain, as shown in Fig. 5.9, does not behave in an ideal fashion. In fact, the transmission alone greatly exceeds unity in the region of 18 kHz. The transmission being greater than unity implies that more dynamic energy is leaving the interface then entering the interface. We hypothesize that this amplification of the transmitted energy is due to the conversion of the statically loaded torque to dynamic energy.

5.5.2 *Time-Frequency Analysis*

In order to obtain more insight into the mechanisms participating in the frequency-dependent response of the system, joint time-frequency analysis is performed. The short-time Fourier transform (STFT) of a signal $x(t)$ is defined as

$$\mathfrak{F}^h_x(t,\omega) = \int_{-\infty}^{\infty} x(t')\, h^*(t-t')\, e^{-i\omega(t-t')}\, dt', \tag{5.18}$$

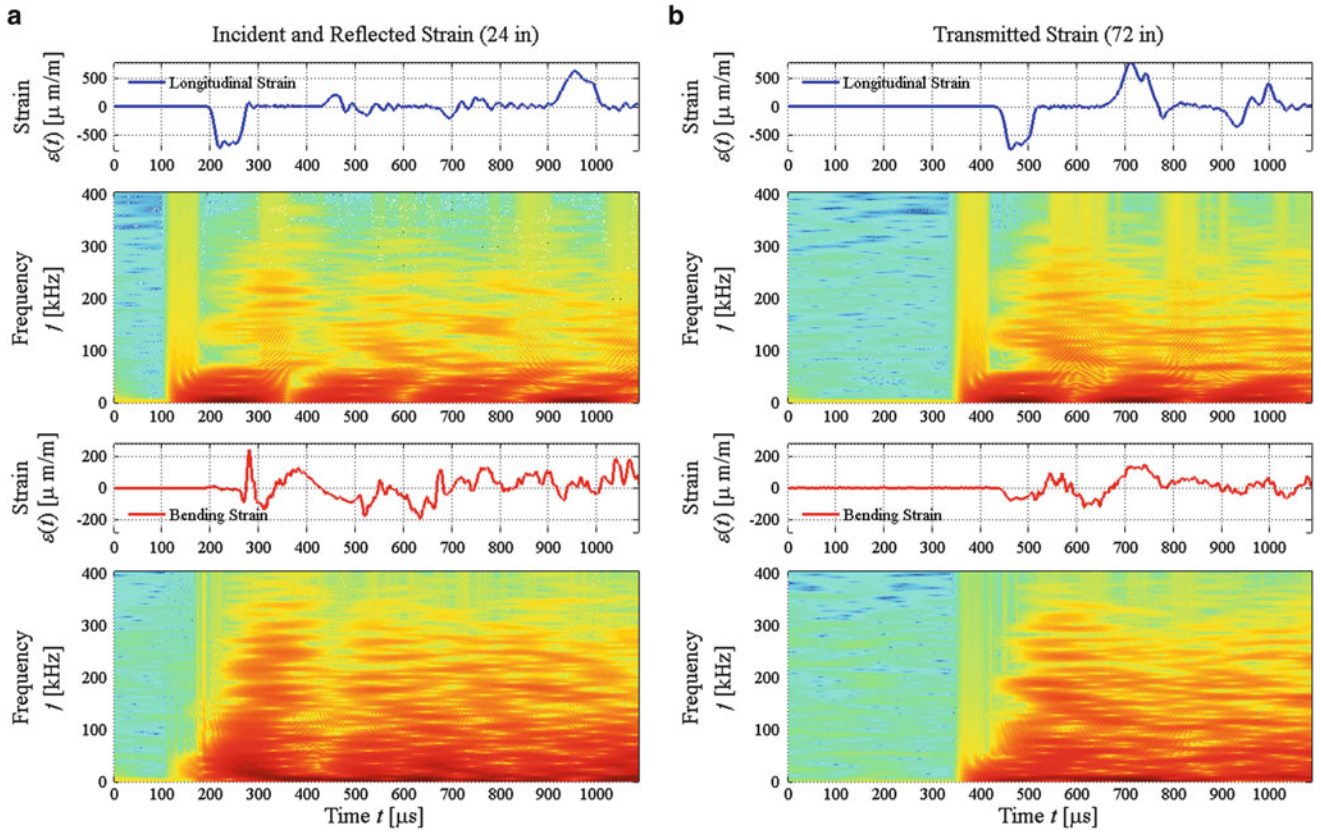

Fig. 5.10 Time-frequency data for hand tight (~0 ft-lbf) of static torque with $v_s = 13.5$ m/s and no index cards comparing (**a**) incident and reflected waves with (**b**) the transmitted waves (color figure in online)

where $h^*(t - t')$ is a time-domain window used to localize the transform about a particular time (t'). A spectrogram is a common tool for visualizing the STFT. A spectrogram is an amplitude plot of the STFT, i.e.,

$$\mathfrak{S}_x(t, \omega) = \left|\mathfrak{F}_x^h(t, \omega)\right|^2, \tag{5.19}$$

where $\mathfrak{S}_x^h(t, \omega)$ is plotted as a contour or colormap against time and frequency. Spectrograms for several cases are shown in Figs. 5.10, 5.11, 5.12, and 5.13a, b below.

Significant broadband mechanical excitation is evident for both longitudinal and bending strain seen in Figs. 5.10, 5.11, 5.12, and 5.13. Figure 5.11 provides evidence of frequency content in the transmitted stress wave that is not present in the incident wave (compare circled sections). This implies a nonlinear generation of high frequency content at the interface without excitation energy present. At higher torque levels (Figs. 5.12 and 5.13) where there is broadband excitation, the energy is localized into bands (again comparing circled sections). While the exact mechanism is still being investigated, the dispersive propagation of the energy follows the expected shape for longitudinal and bending waves (see dispersion curves overlaid Fig. 5.13a) which is evidence the energy release is physical in nature (i.e., not an electrical discharge or other artifact).

5.5.3 *Loss of Static Preloaded Torque*

The threaded interface was also observed to loosen significantly after the initial dynamic loading. To quantify this apparent hysteresis, the breaking torque was captured using an electronic torque wrench and documented as a function of impact velocity and programming material (i.e., number of index cards). The results, shown in Fig. 5.14, show the lost torque (relative to a pre-torqued interface without dynamic loading) is significant at hand tight but is almost complete even with higher preloads.

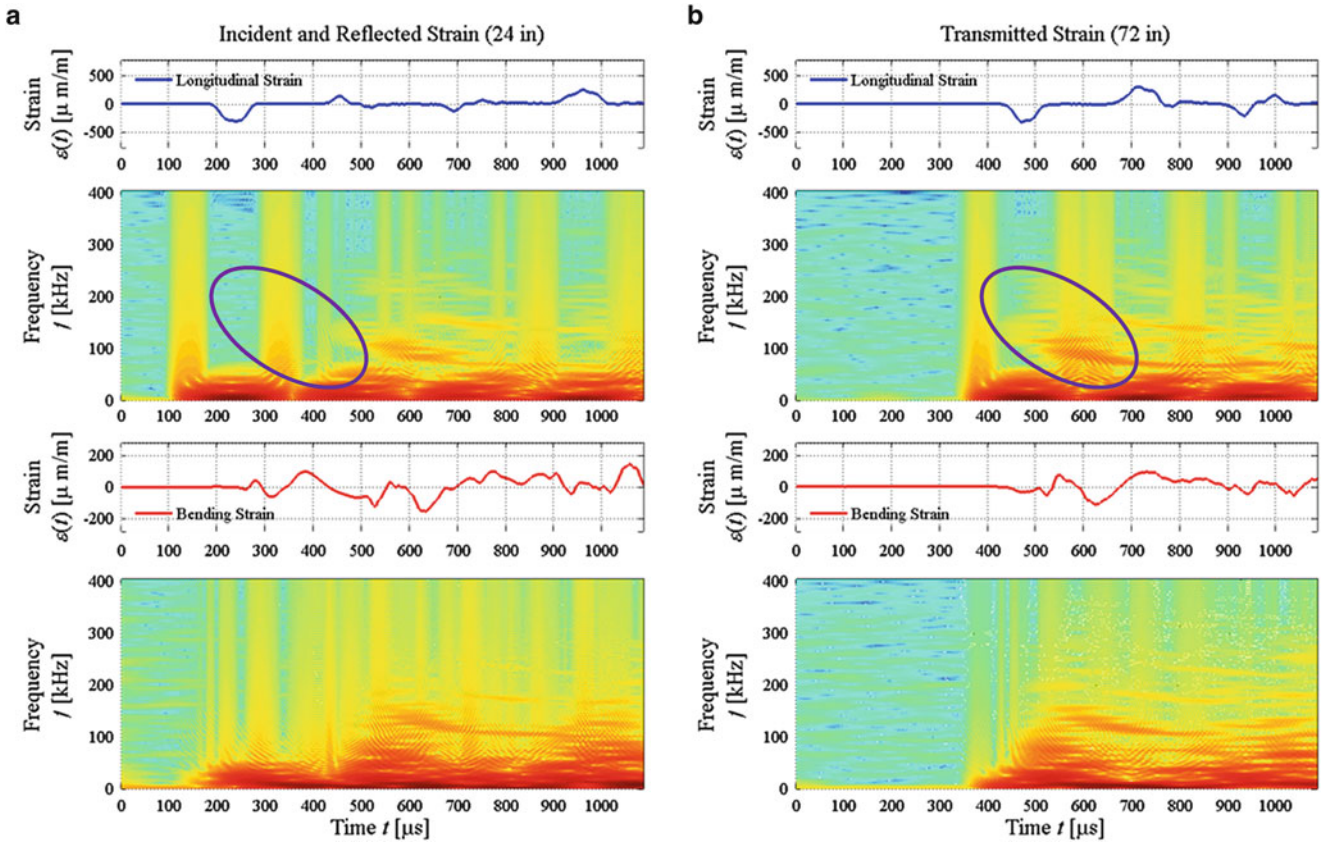

Fig. 5.11 Time-frequency data for hand tight (~0 ft-lbf) of static torque with $v_s = 7$ m/s and one index card comparing (**a**) incident and reflected waves with (**b**) the transmitted waves. The test is performed with mitigator to reduce input frequency content; the *circled* sections show the generation of high frequency in the transmitted signal that is not present in the incident wave (color figure in online)

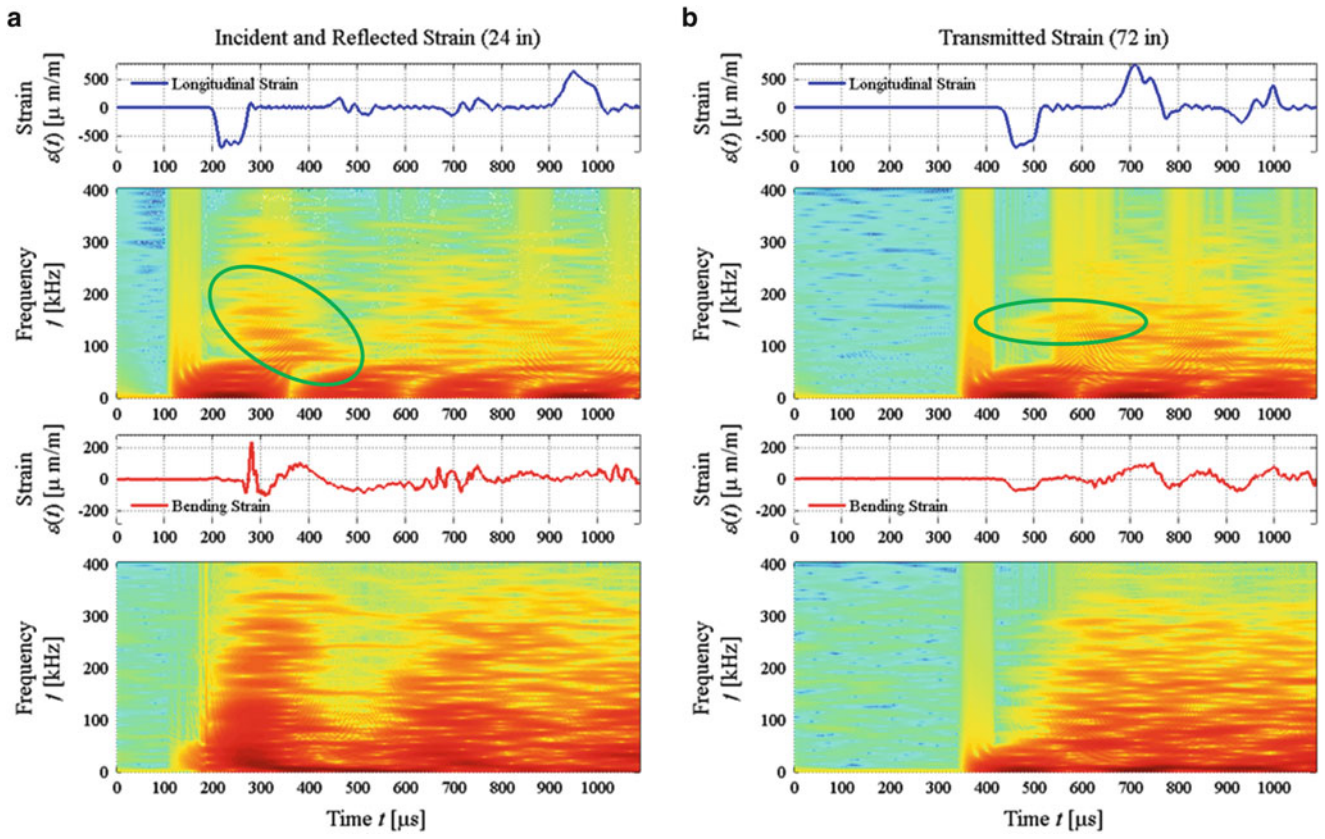

Fig. 5.12 Time-frequency data for 25 ft-lbf of static torque with $v_s = 13.5$ m/s and no index cards comparing (**a**) incident and reflected waves with (**b**) the transmitted waves (color figure in online)

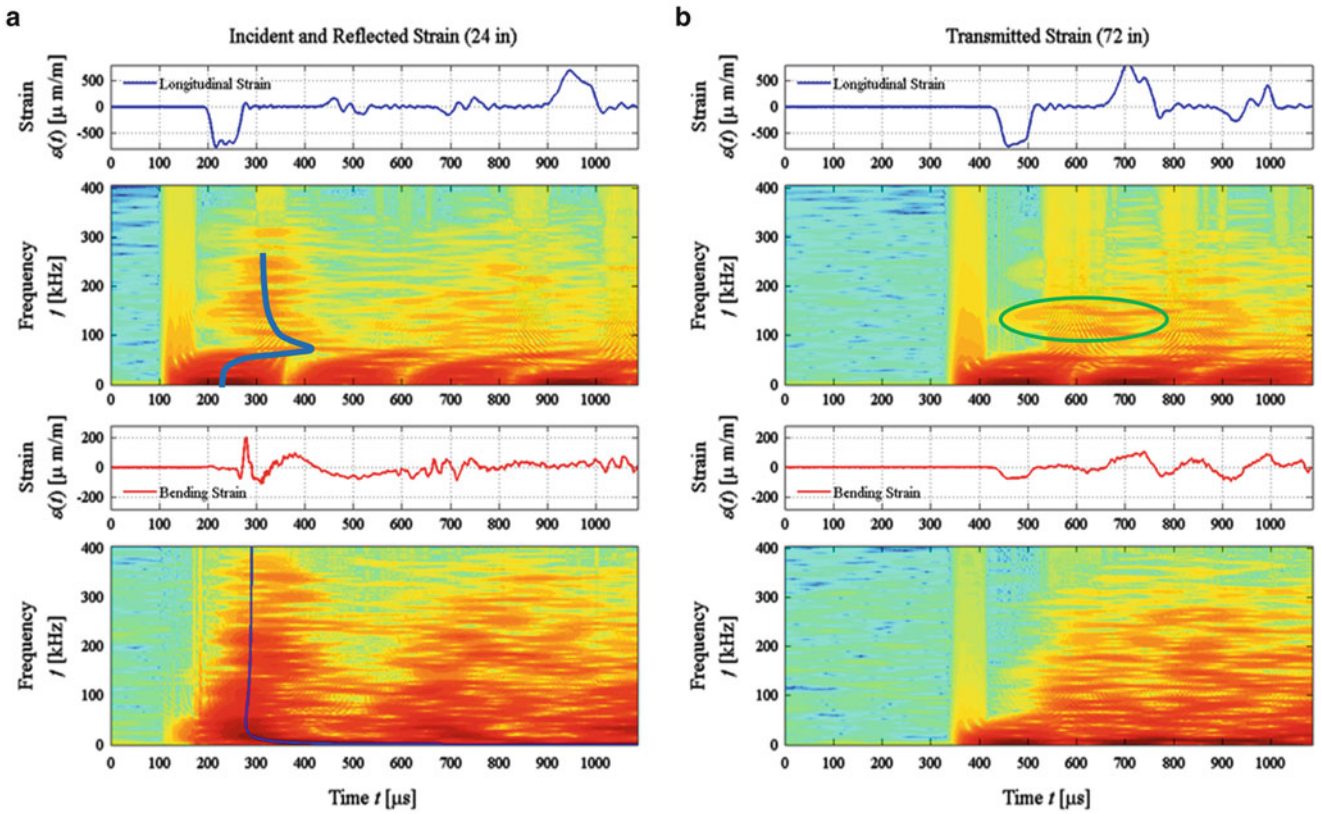

Fig. 5.13 Time-frequency data for 40 ft-lbf of static torque with $v_s = 13.5$ m/s and no index cards comparing (**a**) incident and reflected waves showing the dispersive time of arrival curves overlayed on the first incident pulse and (**b**) the transmitted waves (color figure in online)

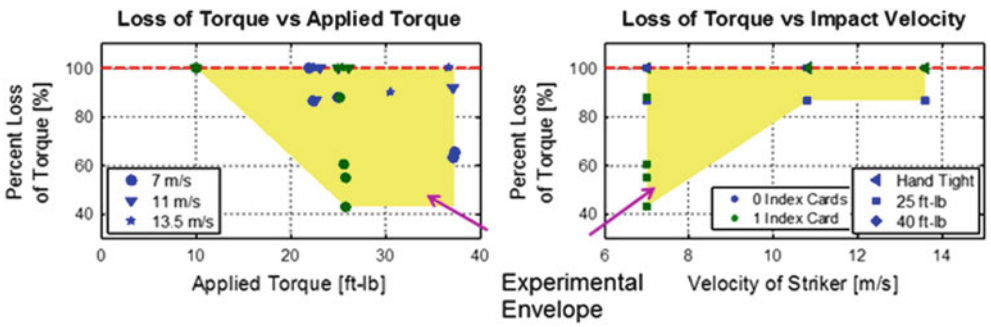

Fig. 5.14 Plot of loss of torque (relative to baseline) as a function of applied torque, impact velocity, and programming materials (# of index cards)

The rotation index was used to document significant rotation of the transmission bar relative to the incident bar in these experiments. Figure 5.15 shows images of the rotational index pre- and post-test. The rotational index has a spacing of 2 mm (0.07870 in.) which is approximately 3 degrees of rotation. In Fig. 5.15 for an initial pre-load of 25 ft-lb and striker velocity of 13.5 m/s, the index has a relative motion of about 10 mm (0.393 in.) which is approximately 15 degrees of rotation. It follows that the system is fully relaxing the applied static torque and generating dynamic waves during the impact event (as noted in the earlier discussion of Fig. 5.11). With the efficiency results, the evidence supports the conclusion that the interface is releasing all of the static torsional energy through some conversion mechanism. Due to the rotational motion of the bars during the dynamic event, we hypothesize that one mechanism of energy release is the generation of torsional waves.

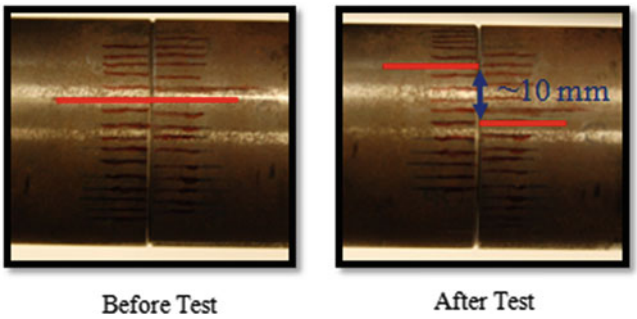

Fig. 5.15 Pictures of the rotational index at the interface before and after the dynamic event, this test was tightened to 25 ft-lbs and the striker had an impact velocity of 13.5 m/s. The index rotated approximately 15 degrees during the total dynamic event

5.6 Future Work

The next steps in this experimental study are to focus on direct observation of the release of static torque and conversion into dynamic torsional waves since the instrumentation in this initial study was sensitive only to longitudinal and bending waves. Specifically, strain gage rosettes will be used to simultaneously monitor and separate longitudinal, bending, and torsional waves. Wave propagation across normal interfaces will also be revisited using an updated Preload Interface Bar design.

5.7 Summary

Laboratory shock experiments on interfaces with static torque loads were performed, analyzed, compared with simulations, and shown to have strong phenomenological evidence of the release of static energy due to applied under dynamic loads. Time-frequency analysis shows evidence of both spontaneous generation of high frequency waves and the modification of the band structure under certain conditions. The applied torque was also shown to relax almost completely during an experiment, with significant rotation of the transmission bar relative to the incident bar. The mechanism is believed to be release of the static torque and the generation of torsional waves. This hypothesis will be tested in future work.

Acknowledgements Support from the Defense Threat Reduction Agency, the DoD/DOE Joint Munitions Program, the Air Force Office of Scientific Research (Program Manager: Dr. David Stargel), and the Joint Fuze Technology Program is gratefully acknowledged. Opinions, interpretations, conclusions and recommendations are those of the authors and are not necessarily endorsed by the United States Air Force.

References

1. Brennan FP, Kare RF (1994) Experimental analysis of preload in threaded connections. ASME, Houston
2. Groper M (1985) Microslip and macroslip in bolted joints. Exp Mech 25(2):171–174
3. Tangpong XW, Wickert JA, Akay A (2008) Finite element model for hysteretic friction damping of traveling wave vibration in axisymmetric structures. J Vib Acoust 130(1):011005–011007
4. Rajagopalan S, Prakash V (1999) A modified torsional Kolsky bay for investigating dynamic friction. Exp Mech 39(4):295–303
5. Anand L (1993) A constitutive model for interface friction. Comput Mech 12(4):197–213
6. Gaul L, Lenz J (1997) Nonlinear dynamics of structures assembled by bolted joints. Acta Mech 125(1):169–181
7. Chattopadhyay S (1993) Dynamic response of preloaded joints. J Sound Vib 163(3):527–534
8. Mendelsohn DA, Mokashi PS (2009) Frequency response of pre-stressed structures with nonlinear cohesive interfaces. Mech Mater 41 (10):1152–1161
9. Foley JR et al (2010) Split Hopkinson bar experiments of preloaded interfaces in IMPLAST '10. SEM, Providence
10. Davies RM (1948) A critical study of the Hopkinson pressure bar. Philos Trans R Soc Lond A Math Phys Sci 240(821):375–457
11. Parry DJ, Walker AG, Dixon PR (1995) Hopkinson bar pulse smoothing. Meas Sci Technol 6(5):443–446
12. Espinosa HD, Patanella A, Fischer M (2000) A novel dynamic friction experiment using a modified Kolsky bar apparatus. Exp Mech 40 (2):138–153
13. Purdue University (2010) Faculty webpage of Weinong Chen. [cited 2010 March 4]. Available from: https://engineering.purdue.edu/AAE/People/Faculty/showFaculty?resource_id=1261; https://engineering.purdue.edu/people/weinong.w.chen.1

14. National Council of Examiners for Engineering and Surveying (2005) Fundamentals of engineering supplied-reference handbook, 7th edn. National Council of Examiners for Engineering and Surveying, Clemson
15. Spotts MF (1985) Design of machine elements, 6th edn. Prentice-Hall, Englewood Cliffs
16. Gray GT III (2002) Classic split-Hopkinson pressure bar testing. In: Kuhn H, Medlin D (eds) ASM handbook, vol 8, Mechanical testing and evaluation. ASM International, Materials Park, pp 462–476
17. Precision Filters, Inc. (2009) Precision 28144 Quad-Channel Wideband transducer conditioner with voltage and current excitation (Datasheet). Precision Filters, Inc., Ithaca
18. National Instruments (2003) NI PXI-6133 specifications. (Available from ni.com). National Instruments, Austin
19. Ueda K, Umeda A (1998) Dynamic response of strain gages up to 300 kHz. Exp Mech 38(2):93–98
20. Kulite Semiconductor Products (2001) Kulite strain gage manual. Kulite Semiconductor Products
21. Polytec (2010) OFV-552 laser vibrometer. Polytec
22. Doyle JF (1997) Wave propagation in structures: spectral analysis using fast discrete Fourier transforms, 2nd edn. Springer, New York, xiv, 320 p
23. Siviour CR (2009) A measurement of wave propagation in the split Hopkinson pressure bar. Meas Sci Technol 20(6):065702
24. Leung RCN, Pinnington RJ (1990) Wave propagation through right-angled joints with compliance-flexural incident wave. J Sound Vib 142 (1):31–48
25. Leung RCN, Pinnington RJ (1992) Wave propagation through right-angled joints with compliance: longitudinal incidence wave. J Sound Vib 153(2):223–237
26. Cremer L, Heckl M, Petersson BAT (2005) Structure-borne sound. Springer, New York

Chapter 6
Loading Rate Effects on Mode I Delamination of Z-Pinned Composite Laminates

Andrew Schlueter, Niranjan D. Parab, and Weinong Chen

Abstract Fiber reinforced composites are susceptible to failure in interlaminar fracture mode called as delamination. Introduction of reinforcements in through the thickness direction (z-pins) suppresses the interlaminar fracture. Flying wedge test method was devised to examine the loading rate effects on dynamic delamination in the z-pinned composite laminates. The unpinned laminates were found to fracture in continuous stable crack propagation for the wedge velocities of 0–40 ms^{-1}. The z-pinned laminates were found to fracture in series of unstable crack propagations for the same range of wedge velocities. It was observed that the critical mode I strain energy release rate for unpinned laminates increases with increasing wedge velocity. The critical mode I strain energy release rate was observed to decrease with increasing wedge velocity for the z-pinned laminates.

Keywords Dynamic delamination • Z-pinned fiber reinforced composites • Flying wedge test method • Dynamic fracture • High speed impact

6.1 Introduction

Fiber reinforced composite laminates have become a standard material in weight critical applications in recent decades due to their high specific strength and specific stiffness. They are, however, subject to failure in a mode not typical of most engineering materials – delamination. In the last several years there has been much research into through-thickness reinforcement techniques that promise to reduce the susceptibility of fiber reinforced composite laminates to delamination damage. This research was first directed toward stitching, 3D weaving, and braiding techniques [1], but unfortunately these techniques cannot be used to provide through-thickness reinforcement of prepreg laminates. The only technique currently capable of providing through-thickness reinforcement of prepreg laminates in commercial quantities is z-pinning – the driving of small pins through the laminate prior to curing.

Z-pinning of the composite laminates was observed to improve the fracture performance of the laminates. Frietas et al. observed an increase of over 1,800 % in critical mode I strain energy release rate between the unpinned laminate and laminate with 0.5 % pin density using double cantilever beam (DCB) specimens [2]. Partridge and Cartié also used a standard DCB approach to test the effects of z-pinning on Mode I crack propagation and discovered an increase of approximately 600 % in critical mode I strain energy release rate in the steady-state with 0.5 % pins and a 2,500 % increase using 2 % pins over the pin-less control specimens [3].

Since most of the delamination damage in practice is due to the impact loading, the quasi-static fracture studies cannot capture the behavior of z-pinned laminates at high rate loading. The only rate-sensitive data on the delamination fracture of z-pinned composites was obtained by changing the crosshead speed in DCB test to 100 mm/min [4]. It was observed that the load required to propagate a crack of a given length increases with increasing loading rate. However, this study is not sufficient to capture the behavior of z-pinned composites under impact loading. Some analytical models were proposed to model the dynamic fracture in z-pinned composites [5–9]. These studies model the dynamic fracture using Euler-Bernoulli

A. Schlueter • N.D. Parab • W. Chen (✉)
Department of Aeronautics and Astronautics, Purdue University, West Lafayette, IN, USA
e-mail: wchen@purdue.edu

B. Song et al. (eds.), *Dynamic Behavior of Materials, Volume 1: Proceedings of the 2013 Annual Conference on Experimental and Applied Mechanics*, Conference Proceedings of the Society for Experimental Mechanics Series,
DOI 10.1007/978-3-319-00771-7_6,

and Timoshenko beam theories coupled with micromechanics based model for z-pin pullout. The main parameters in the model were the laminate elastic properties, z-pin pullout law used and the wedge velocity.

Despite the development of extensive theory about the rate effects on the mode I fracture behavior of z-pinned composites, there is no experimental work to validate the theory. In this study, flying wedge loading method was used to obtain the fracture parameters at various loading rates for z-pinned composites.

6.2 Experimental Procedure

6.2.1 Specimen Preparation

The composite plate was composed of 30 layers of Hexcel IM7/8852 unidirectional prepreg tape in 0° orientations. Between layer 15 and layer 16, a 0.0005 in. thick Kapton layer was inserted as the mid-layer to facilitate straight crack propagation. Z-pins were inserted in a diamond pattern using an ultrasonic horn (Branson series 200 handheld ultrasonic device) as described in [10] and the laminate was cured using an autoclave. The laminate plates with z-pins were cut using a water jet to the standard specimen size prescribed in ASTM D5528 for mode I double cantilever beam testing. One end of the specimen was machined with a notch design adapted from Klepaczko [11]. The notch design assists the initial penetration of the specimen by the wedge. The specimen end geometry is presented in Fig. 6.1.

Each specimen was painted white and lines were marked at one quarter of the thickness from top and bottom surfaces (corresponding to the neutral axes of the DCB specimen). Vertical lines were drawn perpendicular to these lines every 2.5 mm. This allows for several high-contrast points (the line intersections) to be visually tracked and measured during the fracture process. The final specimen can be seen in Fig. 6.2

6.2.2 Flying Wedge Test Method

In this experimental investigation, a wedge was driven into the specimen at a controlled, constant velocity while photographs of the process were recorded. To test the rate sensitivity of the fracture process, wedge velocities ranging from quasi-static (3 mm/min) to 50 m/s were used. For low velocities up to 3.3 m/s, a standard dynamic MTS servo-hydraulic load frame was used. For speeds from 25–50 m/s, a low-power gas gun setup was used.

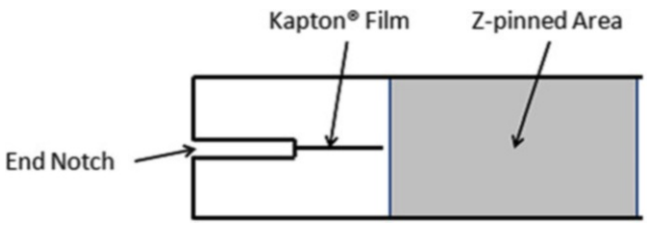

Fig. 6.1 Specimen geometry

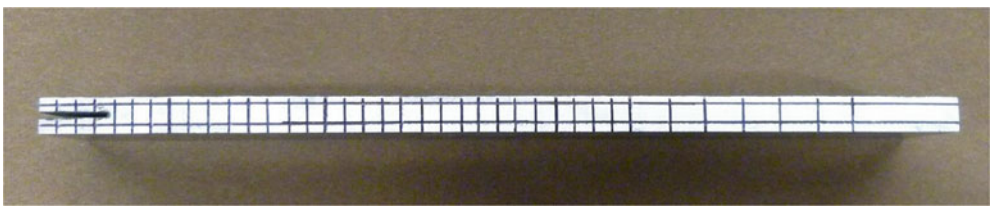

Fig. 6.2 Final specimen

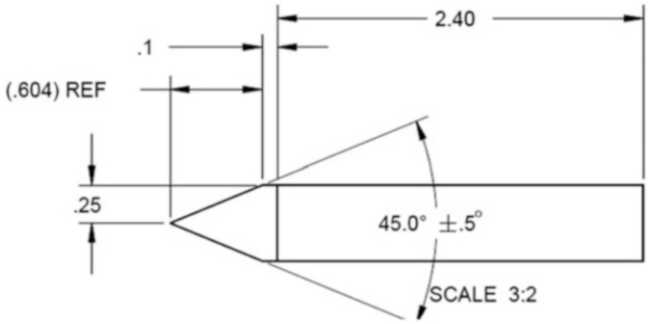

Fig. 6.3 Design specification for wedge

Fig. 6.4 Specimen installed in load frame

6.2.2.1 Low Velocity Testing

The quasi-static testing was performed using a MTS 810 load frame in closed loop control. The specimen and wedge were mounted on the load frame using custom fixtures. The flat end of the specimen was fitted in the upper fixture while half inch thick wedge was positioned in the notch. For quasi-static testing, 3 mm/min crosshead speed was used. The crack progress was filmed using a consumer-grade HD camcorder. The design specifications for the wedge are presented in Fig. 6.3

The specimen installation in the MTS load frame is presented in Fig. 6.4.

For low velocity testing, similar experimental setup was used with open loop control. The wedge velocities of 0.5, 1.0 and 3.3 m/s were used. The crack progress was recorded using Memrecam fx k3 high speed camera with frame rates of 3,000 frames per second and resolution of 1280 $\times$ 344 pixels.

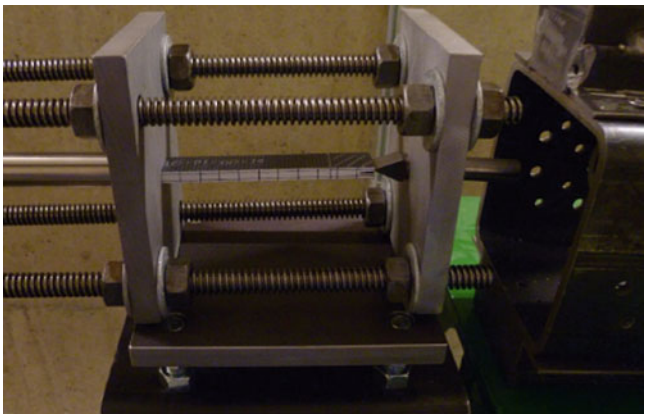

Fig. 6.5 High velocity testing apparatus

6.2.2.2 High Velocity Testing

A small-bore (3/4″ diameter) gas gun was used to perform the high velocity testing. The gun was capable of repeatably firing projectiles from 5 to 50 m/s. In the test, a protective cage was built around the specimen to protect the apparatus. The cage held the specimen and the wedge as shown in Fig. 6.5.

After installing and aligning the specimen, the striker was fired at the specimen. The velocity of the striker was detected by the laser velocity measurement system. The laser system also served as the trigger for the high speed camera. The striker drove the wedge at constant velocity into the specimen. The fracture process was recorded using Cordin 550 high speed camera at frame rates from 10,000 frames per second to 20,000 frames per second for different wedge velocities.

6.3 Analysis

The critical mode I strain energy release rate for the unpinned laminates was calculated using the model proposed by Freund [12]. The critical mode I strain energy release rate for the z-pinned laminates was calculated using the model proposed by Sridhar et al. [7]. The details are provided in following subsections

6.3.1 Image Processing

For the specimens whose fracture process was in the semi-unstable stick–slip regime, the image immediately prior to each crack propagation was assumed to characterize the critical Mode I characteristics (at the initiation of crack propagation). For those specimens whose fracture process was in the stable continuous-propagation regime, all images were equally valid, as the crack propagation was occurring continuously. For those specimens, eight images equally spaced across the time domain were chosen for processing. The first (un-fractured) image in each series was also processed in order to allow comparison with the un-cracked state.

The image files were then processed using ImageJ software [13]. The spacing between the two lines marked farthest apart on each specimen had been measured prior to testing. This allowed the setting of the scale in each image. Once the scale had been set, the location of each line intersection point, the crack tip, and the wedge tip were measured.

After obtaining the location of each line intersection point, a quintic spline was fitted to the beam profile obtained using the intersection points. The spline fit was used to obtain the boundary conditions for the beams as explained in following sections.

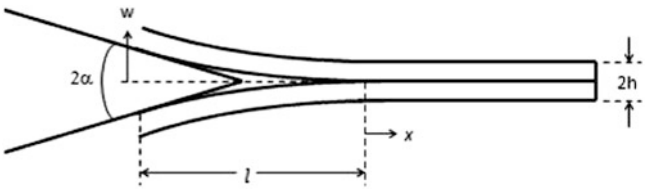

Fig. 6.6 Flying wedge loading of unpinned laminate

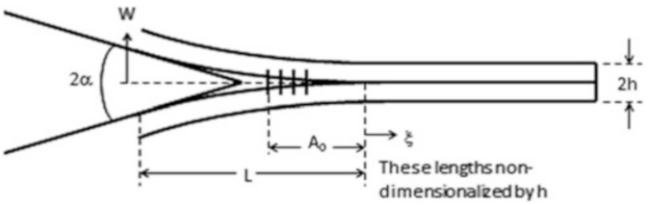

Fig. 6.7 Flying wedge loading in z-pinned specimen

6.3.2 *Unpinned Laminates (Fig. 6.6)*

The equation of motion for beam deflection is given by Freund model [12] as:

$$\frac{\partial^4 w}{\partial x^4} + K^2 \frac{\partial^2 w}{\partial x^2} = 0 \quad \text{where} \quad K^2 = \frac{12\rho v^2}{Eh^2} \tag{6.1}$$

Subject to boundary conditions

$$w(0) = 0, \quad \frac{\partial w}{\partial x}(0) = 0, \quad \frac{\partial w}{\partial x}(-l) = -\alpha, \quad \frac{\partial^2 w}{\partial x^2}(-l) = 0 \tag{6.2}$$

Where v is the wedge velocity, E is the young's modulus of the laminate and ρ is the density of the laminate
The solution for the boundary value problem described in Eqs. 6.1 and 6.2 is given by

$$w(x) = \frac{\alpha[kx\cos(kl) + \sin(kl) - \sin(k\{x+l\})]}{k[1-\cos(kl)]} \tag{6.3}$$

The spline fit for the beam profiles provides the parameter α. The strain energy release rate is calculated from the solution as

$$G = \frac{Eh^3}{12}\left(\frac{\partial^2 w}{\partial x^2}\right)^2_{x=0} \tag{6.4}$$

6.3.3 *Z-pinned Laminates*

The model to calculate the strain energy release rate for z-pinned laminates was developed by Sridhar et al. It assumes that the through-thickness reinforcement have a linear bridging relation of the form shown in Eq. 6.5.

$$p(w) = p_0\left(1 - \frac{2w}{h}\right) \tag{6.5}$$

The geometry and the coordinate system used in the problem are shown in Fig. 6.7.

The governing equation of motion for the z-pinned laminates is given by

$$\frac{\partial^4 w}{\partial \xi^4} + V^2 \frac{\partial^2 w}{\partial \xi^2} - \frac{{P_0}^2 w}{2} + P_0^2 = 0 \qquad \text{where} \quad V^2 = \frac{12v^2}{c_l^2}, \qquad P_0^2 = \frac{12P_0}{E} \tag{6.6}$$

The boundary conditions are given by

$$W(0) = 0, \quad W(-A_0) = \frac{1}{2}, \quad \frac{\partial W}{\partial \xi}(0) = 0, \quad \frac{\partial W}{\partial \xi}(-A_0) = Q_0 \tag{6.7}$$

Note that all the lengths are non-dimensionalized by half the thickness of the laminate (h). The beam profile is obtained by solving the governing equation and using the boundary conditions obtained from the fracture process images by fitting the spline solutions. The z-pin tractions are also obtained from the crack profile and material properties.

The critical mode I strain energy release rate at the crack tip for the z-pinned specimens consists of two separate terms. The energy is dissipated at the tip due to fracture (G_{tip}) along with the some part of energy dissipated directly by z-pin pullout (G_{pin}). The total critical mode I strain energy release rate G_{IC} for pinned laminates is given by

$$G_{IC} = G_{tip} + G_{pin} = \frac{Eh}{12}\left(\frac{\partial^2 W}{\partial x^2}\right)^2_{\xi=0} + \frac{1}{2}p_0 h \tag{6.8}$$

6.4 Results

The relationship of the critical strain energy release rate with the wedge velocity for the unpinned laminates is shown in Fig. 6.8.

It can be observed that the G_{Ic} values increase with increasing wedge velocity for unpinned laminates. The trend for z-pinned laminates with 0.5 % and 2.0 % pins by weight is presented in Figs. 6.9 and 6.10 respectively.

It should also be noted that addition of even small percentage (0.5 %) of z-pins increases the strain energy release rate almost seven fold. The trend in G_{Ic} is similar for z-pinned laminates with 0.5 % pins and 2.0 % pins however the critical strain energy release rate is almost thrice for the laminates with 2.0 % z-pins as compared to the laminates with 0.5 % z-pins. The G_{Ic} values decrease with increasing velocity till the wedge velocity of 40 m/s. The G_{Ic} values increase again for 50 m/s wedge velocity. This increase can possibly because of the fracture behavior entering a different behavior regime from arrested crack propagation to stable crack propagation.

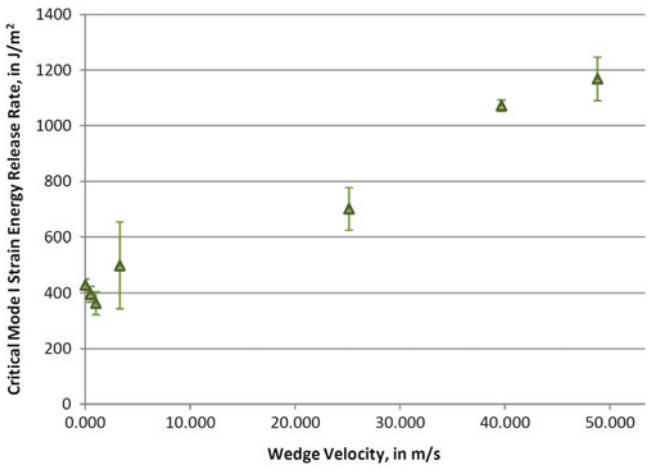

Fig. 6.8 Relationship between critical strain energy release rate and wedge velocity for unpinned specimens

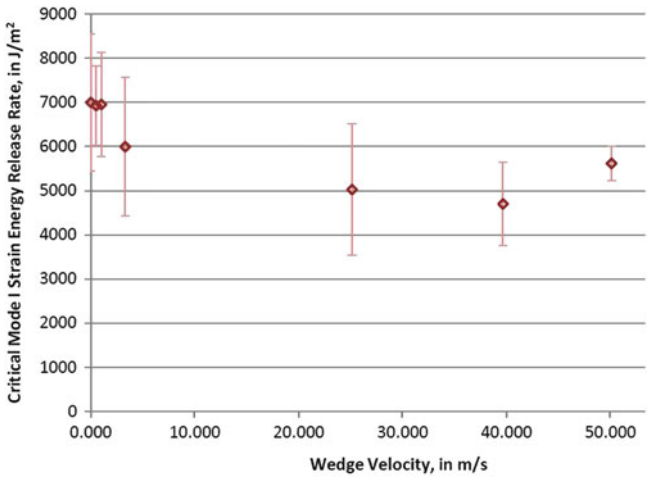

Fig. 6.9 Relationship between mode I critical strain energy release rate and wedge velocity for specimens with 0.5 % z-pins

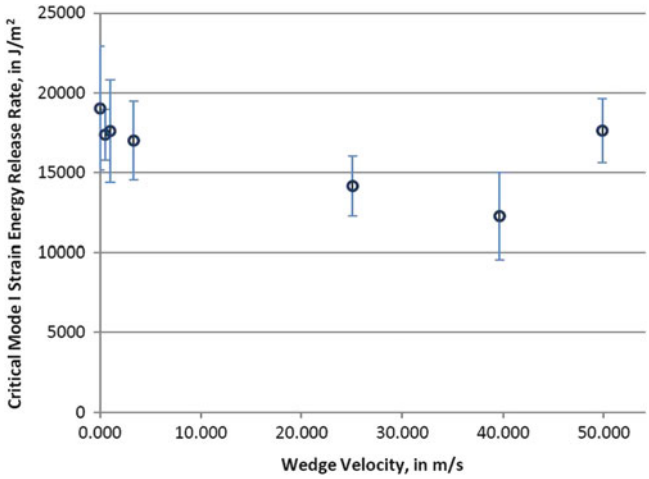

Fig. 6.10 Relationship between mode I critical strain energy release rate and wedge velocity for specimens with 2.0 % z-pins

6.5 Conclusions

Loading rate effects on z-pinned IM7/8552 carbon/epoxy composite laminates were investigated using a Flying Wedge test method. Two different types of crack propagation were observed for unpinned laminates and z-pinned laminates. The crack was observed to propagate in stable mode in unpinned laminates. The crack in z-pinned laminates was observed to propagate in start-stop mode in which the crack was arrested at certain points for some time followed by sudden propagation.

The critical mode I strain energy release rate was observed to increase with increasing wedge velocities for the unpinned laminates. The energy release rates were observed to decrease with increasing wedge velocities for z-pinned laminates for velocities ranging from quasi-static to 40 m/s. This trend was observed because of the dominance of the changes in the energy release rates of the pin pullout due to increasing wedge velocity. The energy release rate increases again from 40 to 50 m/s. This was probably because of the change in the fracture behavior from start-stop to stable crack propagation with increasing wedge velocity.

References

1. Dransfield KA, Baillie C, Yu-Wing Mai (1994) Improving the delamination resistance of CFRP by stitching – a review. Compos Sci Technol 50:305–317
2. Frietas G, Magee P, Dardzinski P, Fusco T (1994) Fiber insertion process for improved damage tolerance in aircraft laminates. Acta Mater 25:36–43

3. Partridge IK, Cartié DDR (2005) Delamination resistant laminates by Z-Fiber pinning: Part I. Manufacture and fracture performance. Compos Part A Appl Sci Manufactur 36(1):55–64
4. Liu H, Yan W, Yu X, Mai Y (2007) Experimental study on effect of loading rate on mode I delamination of z-pin reinforced laminates. Compos Sci Technol 67:1294–1301
5. Sridhar N, Beyerlein IJ, Cox BN, Massabo R (2001) Dynamic delamination in through-thickness reinforced DCB specimens. In: Proceedings of the 10th international conference on fracture, 2001
6. Sridhar N, Cox BN, Dunn CL, Beyerlein IJ (2001) Mechanics of crack bridging under dynamic loads. In: Materials Research Society symposium proceedings, vol 653
7. Sridhar N, Massabo R, Cox BN, Beyerlein IJ (2002) Delamination dynamics in through-thickness reinforced laminates with application to DCB specimen. Int J Fracture 118:119–144
8. Sridhar N, Yang QD, Cox BN (2003) Slip, stick, and reverse slip characteristics during dynamic fibre pullout. J Mech Phys Solids 51(7):1215–1241
9. Cox BN, Sridhar N, Beyerlein IJ (2001) Inertial effects in the pullout mechanism during dynamic loading of a bridged crack. Acta Mater 49:3863–3877
10. Partridge IK, Cartié DDR, Bonnington T (2003) Manufacture and performance of z-pinned composites. In: Shonaike G, Advani S (eds) Adv Polym compos. CRC Press, FL, 103–138
11. Klepaczko JR (1979) Application of the split Hopkinson pressure bar to fracture dynamics. In: Conference on mechanical properties of materials at high rates of strain, pp 201–214
12. Freund LB (1990) Dynamic fracture mechanics. Cambridge University Press, Cambridge
13. Rasband WS, Image J (1997–2012) U.S. National Institutes of Health, Bethesda, Maryland, USA, http://imagej.nih.gov/ij/

Chapter 7
Multi-scale Testing Techniques for Carbon Nanotube Augmented Kevlar

E.D. LaBarre, M.T. Shanaman, J.E. Tiffany, J.A. Thomas, X. Calderon-Colon, M. Morris, E.D. Wetzel, A.C. Merkle, and M.M. Trexler

Abstract We explore a method for improving the ballistic performance of Kevlar by augmentation with multi-walled carbon nanotubes (MWNTs). When developing new and improved soft armor, ballistic testing is expensive while the crude data obtained provide limited insight into those mechanisms which enable smart design. Therefore, we tested and modeled yarns and fabrics at various length scales to optimize our synthesis process and understand mechanisms contributing to ballistic performance, thus necessitating ballistic testing of only the potential best performers. Tensile testing of treated yarns was performed to measure the strength and modulus, both linked to ballistic performance, and to evaluate the relative success in infiltrating the Kevlar with MWNTs. Yarn friction and yarn pull-out tests were performed to measure the static and kinetic yarn-to-yarn interactions (friction), also critical to performance during a ballistic event. Example results from mechanical testing over multiple length scales, including ballistic testing, are reported. Finite element modeling was also used to study the effects of the fabric material properties and friction on ballistic performance. Simulation results were correlated with experimental data and used to guide materials optimization.

Keywords Kevlar • Carbon nanotubes • Friction • Modeling • Soft armor

7.1 Introduction and Motivation

Soft body armor is critical for personal protection against high speed projectiles. Soft armor is composed of ballistic fibers such as Kevlar, Twaron, or Spectra, which dissipate energy through fiber deformation and inter-fiber friction as yarns slide against each other. These high performance fabrics have an inherent hierarchical structure, spanning molecular to fibril to fiber to yarn to weave levels, with properties derived from many length scales contributing to the overall system ballistic performance [1]. For example, the mechanical properties of the fibers (e.g. strength, modulus), the number of fibers per yarn, the friction between fibers and yarns, and the specific weave pattern, among other factors, all contribute to the overall ballistic performance of the armor. The ultimate failure of the fabric is governed by a variety of mechanisms including yarn uncrimping, yarn pull-out, yarn translation, yarn stretching and ultimately breakage of fiber bonds [2, 3]. Which mechanisms dominate this energy absorption process is governed by not only fabric properties, but also projectile properties (e.g. projectile geometry, velocity). By increasing the energy dissipated via any of these mechanisms, the overall ballistic performance has the potential to improve.

Development of thinner, lighter-weight armor is critical to reduce the burden on warfighters and safety officers. The conventional approach to developing soft armor through iterative full-scale ballistic testing can be enormously expensive and time consuming. While certain chemical and/or structural changes to fibers or fabric architecture may yield improvements in ballistic performance, understanding the underlying associated mechanisms is essential for making targeted improvements in an efficient manner and ensuring that the optimal solution is realized. This understanding of the

E.D. LaBarre (✉) • M.T. Shanaman • J.E. Tiffany • J.A. Thomas • X. Calderon-Colon • M. Morris • A.C. Merkle • M.M. Trexler
Applied Physics Laboratory, Research and Exploratory Development Department, The Johns Hopkins University, 11100 Johns Hopkins RD, Laurel, MD 20723, USA
e-mail: Erin.LaBarre@jhuapl.edu

E.D. Wetzel
U.S. Army Research Laboratory, Weapons and Materials Research Directorate, Aberdeen Proving Ground, MD 21005, USA

B. Song et al. (eds.), *Dynamic Behavior of Materials, Volume 1: Proceedings of the 2013 Annual Conference on Experimental and Applied Mechanics*, Conference Proceedings of the Society for Experimental Mechanics Series,
DOI 10.1007/978-3-319-00771-7_7,

mechanisms can be accomplished by measuring properties key to ballistic performance at multiple length scales via lab scale testing, and then using these data to model the relationships between these properties and ultimate ballistic performance. Models can also be parametrically varied in order to determine the influence of various inputs to overall performance, thus guiding synthesis toward the optimal soft armor design. The constitutive/intrinsic properties of the fibers and yarns are, of course, important to ballistic performance [3, 4]. Of equal importance are the interactions and friction between the yarns and fibers in the weave [5]. Friction helps maintain the integrity of local fabric in the impact region by allowing more yarns to be involved in the impact, and it increases energy absorption by increasing yarn strain and kinetic energy [6].

Kevlar®, or poly(para-phenylene terephthalamide), is an aramid fiber exhibiting high tensile strength and high modulus [7]. The superior mechanical properties of Kevlar fibers arise primarily from (i) the strong intramolecular bonds between the constituent aromatic polyamides and (ii) the highly oriented fiber structure realized during the polymer spinning process [8]. Both the structure of the fabric (which allows the fibers to exchange energy via rubbing and friction) and the hierarchical mechanical properties of the fabric are important in dictating the ultimate ballistic performance of Kevlar-based materials [9]. We seek to improve the para-aramid fiber Kevlar through augmentation with carbon nanotubes (CNTs). With a modulus of 1 TPa and tensile strength of 60 GPa, CNTs are a factor of 5 less dense and a factor of 30 stronger than steel, and thus offer significant potential for strengthening materials [10]. It has been shown that swelling of Kevlar in a ($\leq$4 %) CNT suspension resulted in composites with improved mechanical properties due to interpenetration of CNTs into the fibers [11].

Although the increase in Kevlar mechanical properties when coupled with CNTs is compelling, this effect must be translated from the fiber scale to the yarn scale and ultimately, to the weave and fabric scale before it is practical as an armor material. Kevlar yarns and fabrics were reinforced with CNTs to maximize strength, modulus, and toughness as well as to enhance inter-yarn friction. Simultaneous increases in these properties should translate to increases in specific strain energy and sound velocity, and thus improved ballistic performance [3, 4]. Because of the use of nanoscale reinforcements, it is critical to understand mechanisms and properties at length scales ranging from nano to macro to understand how they ultimately contribute to the ballistic performance.

Without multi-scale experimental and modeling tools, it is difficult to predict how tuning various synthesis parameters will affect the ballistic performance. Rather than prepare fabrics of various treatment types and test at the full scale immediately, which yields limited information on underlying mechanisms influencing performance, a complete, multi-scale approach is proposed for testing and understanding the mechanics and interactions at appropriate length scales. In addition, by testing and measuring properties at smaller length scales, determination of which synthesis treatments have the greatest impact on properties can lead to down-selection and enable testing of only the best contenders. The combination of multi-scale experiments and modeling enables an understanding of the physical mechanisms governing the ballistic performance of the fabric, leading to a more efficient exploration and optimization of soft armor systems.

7.2 Experimental Methods

A variety of experimental methods was used to fully characterize the relevant intrinsic and extrinsic material properties of the CNT augmented Kevlar. Figure 7.1 below provides an overview of the length scales involved in testing and modeling of CNT-reinforced Kevlar. As can be seen in Fig. 7.1, testing is performed at the yarn, inter-yarn, weave and fabric length scales. These results provide inputs and validation data for computational models, which range in scales from molecular to continuum. The sum of this experimental and computational data leads to an increased understanding of the physical mechanisms characteristic of the Kevlar following each CNT treatment, thus enabling prediction of potential ballistic performance and lessening the requirement for full-scale ballistic testing.

7.2.1 Synthesis

Similar to the process used by O'Connor [11], CNT-Kevlar composites were prepared by soaking the Kevlar K129 yarns (spool, denier 1420, Composites One) and fabrics (Style 722/63, plain weave, JPS Composite Materials Corp) in a sonicated suspension of multi-walled carbon nanotubes (MWNT, 95 wt%, outer diameter 8 nm, length 10–30 nm) dispersed in N-methylpyrrolidone (NMP). Yarns were scoured with methanol prior to the MWNT treatment and dried at 60 °C. The K129 yarns and as-received fabrics were treated at multiple MWNT concentrations and for a range of times. After the treatment,

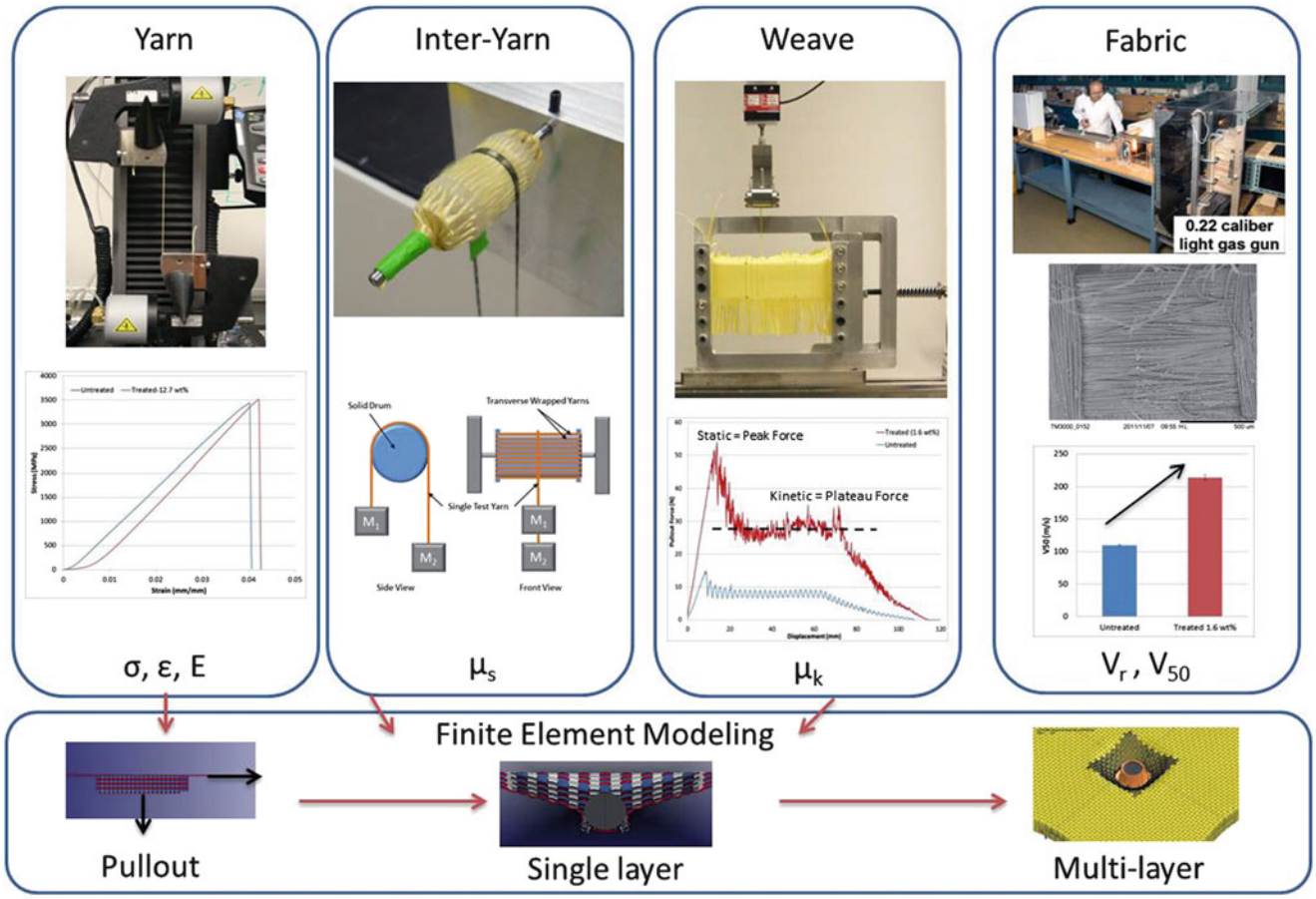

Fig. 7.1 Roadmap of multi-scale testing, and modeling. Nanoscale reinforcements augment Kevlar yarns and fabrics. Experiments are conducted on the yarn, inter-yarn, weave and fabric scale to measure relevant properties. Properties are fed into finite element models, which range in scale from molecular to continuum, and enable synthesis optimization

all the samples were rinsed with ethanol and dried at 60 °C in a vacuum oven. The uptake of nanotubes was recorded by weighing specimens before and after treatment. Percent uptake was approximately 10 % by mass for yarns, and up to 1.6 % for fabrics depending on the treatment conditions used.

7.2.2 Yarn Scale: Quasi-Static and High Rate Tensile Testing

Rate effects can influence the mechanical properties of polymeric materials, which is an important consideration since ballistic impact is a high rate event. Therefore, tensile tests of the ballistic yarns at both quasi-static and high-rates are required to determine how the constitutive properties change with strain rate. These properties feed into the finite element method (FEM) models and can help predict how changes in strength and modulus translate to behavior at larger length scales and in more complex systems. Yarn-level results for completed quasi-static tensile tests are discussed below while tensile testing of Kevlar yarns using a split-Hopkinson pressure bar (SHPB) is currently in progress.

Treated and untreated K129 1420 denier yarns were tested using a bollard type fixture with pneumatic grips on an Instron 5942 load frame as shown in Fig. 7.2a. ASTM D7269 Standard Method for Tensile Testing of Aramid Yarns was used as a guide. Load was applied by moving the crosshead at a rate of 127 mm/min while measuring the force with a 500 N load cell. The gauge length of the yarns, from grip to grip, was 254 mm. Tensile tests enable the measurement of the strength and modulus of the augmented Kevlar on the yarn scale. By examining the stress strain curves such as those in Fig. 7.2b, changes in the intrinsic material properties important for ballistic performance can be identified. Currently, no statistically significant improvements to strength or modulus have been measured as a result of MWNT treatment. However, modifications to the synthesis process are being pursued that are expected to increase the intrinsic strength and modulus.

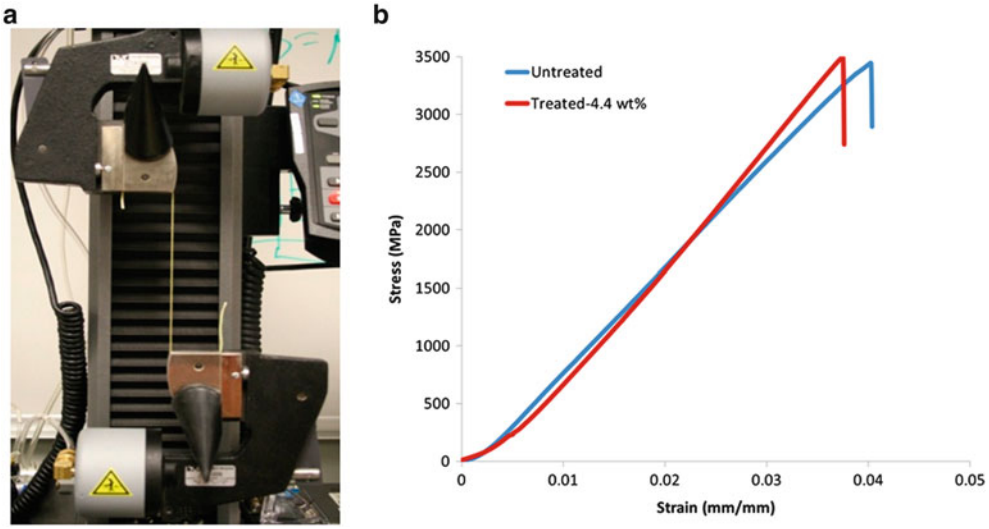

Fig. 7.2 Individual yarns were tested using bollard style pneumatic grips (**a**). Stress versus strain curve allows for comparison of strength and modulus between treated and untreated yarns (**b**)

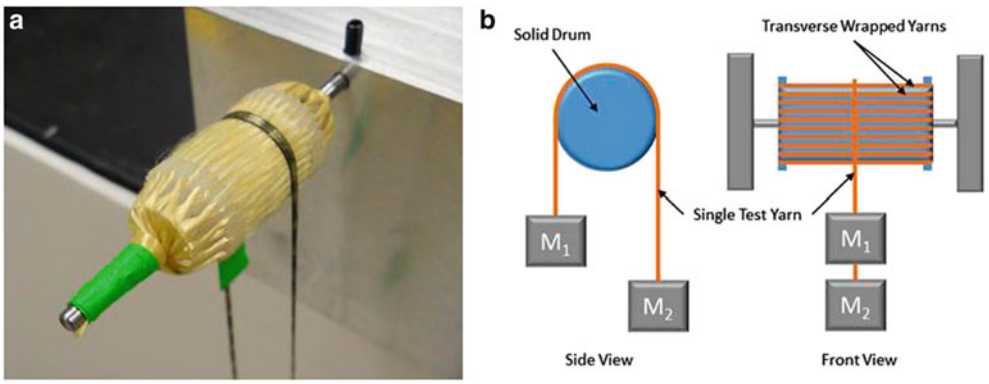

Fig. 7.3 Photograph of the wrapped drum used for static friction tests (**a**). Schematic of the static friction test (**b**)

7.2.3 Inter-yarn Scale: Static Friction Testing

The ability of the yarns to resist movement, or static friction, plays an important role in dissipating energy during ballistic impact. One way to understand the friction interplay between treated yarns is to measure these frictional interactions experimentally. The static friction coefficient was measured using a method similar to that employed by Dong [12] whereby a single yarn was pulled across a drum wrapped in a transverse fashion, which mimics the arrangement of yarns within a weave. The drum diameter was 16 mm and 32 yarns were distributed evenly along the circumference. A photograph of this setup is shown in Fig. 7.3a. A fixed mass (M1, 120 g) was suspended on one end of the yarn while another mass (M2) was increased slowly until motion was observed as pictured in the schematic in Fig. 7.3b. The static friction coefficient was calculated according to the Euler equation [13]:

$$\mu = \frac{1}{\pi} \ln\left(\frac{M_2}{M_1}\right) \tag{7.1}$$

Consistent with literature values [5], untreated K129 measured $\mu_s = 0.22 \pm 0.01$, whereas treated yarns experienced up to a 25 % increase in static friction with $\mu_s = 0.27 \pm 0.02$. These friction coefficients can be used as inputs into the FEM model to determine the impact of this friction increase on ballistic performance. In addition, the static friction test can be used in conjunction with the pull-out test to calculate the kinetic coefficient of friction, as described in the following section.

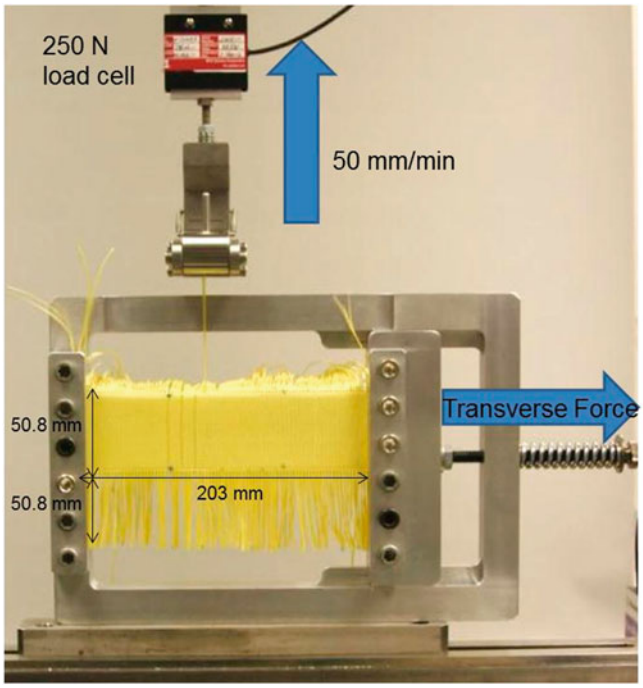

Fig. 7.4 Test setup for pull-out showing geometry of the pull-out specimen

7.2.4 Weave Scale: Pull-Out Testing

Since yarn translation is a valid physical mechanism that occurs during a ballistic event, it is important to understand the force that resists this motion: kinetic friction. The kinetic friction is governed by the geometry of the yarns and weave, as well as surface interaction between the yarns. In tandem with the static friction test, the yarn pull-out test can be used to derive the kinetic coefficient of friction experienced by a yarn in the weave.

A series of quasi-static pull-out tests was performed by varying the transverse force applied to the fabric similar to tests performed by Rao et al. [5, 14]. A 50 mm/min crosshead displacement rate was used for all tests, and a 250 N load cell was used to measure the yarn pull-out force. The transverse force was applied to the fabric using a spring with a known spring constant (33 N/mm). Yarns were pulled from the warp direction using every third warp yarn, as Shockey found that multiple yarns from a fabric sample can be pulled without changing the result if at least two yarns are between them [15]. Fabric samples were 229 mm tall by 203 mm wide. Before testing, fill yarns were removed from the top and bottom of the fabric as shown in Fig. 7.4. This provided a "lead" with ample room to grasp the yarn in the line grip and a 50.8 mm "tail." The intact fabric region was 50.8 mm tall (45–50 yarns). This height is especially important to keep constant because the number of yarn cross-over points in the fabric affects the magnitude of the frictional force.

An example of the pull-out test output is shown in Fig. 7.5a, where the peak force is the static force and the kinetic force is the average force in the plateau region. In the Figure, a treated (1.6 wt%) sample is compared to an untreated sample for a constant transverse force of approximately 100 N. The frictional forces measured are three to four times greater for the treated sample than the untreated sample. Differences in the amplitude and frequency of the oscillations in the plateau region were noted, with the treated sample exhibiting jagged stick-slip behavior, another indicator of the enhanced frictional forces.

In addition to comparing the relative magnitudes of the pull-out forces for a constant transverse force, the transverse force can be varied while the magnitudes of the pull-out forces are recorded. Pull-out force is linearly proportional to the transverse force as shown in Fig. 7.5b. As reported by Rao et al. [5], the slopes of the linear fits for both static and kinetic forces, m_s and m_k respectively, can then be used to predict the relationship between the static and kinetic friction coefficients:

$$\mu_k = \frac{m_k}{m_s}\mu_k \tag{7.2}$$

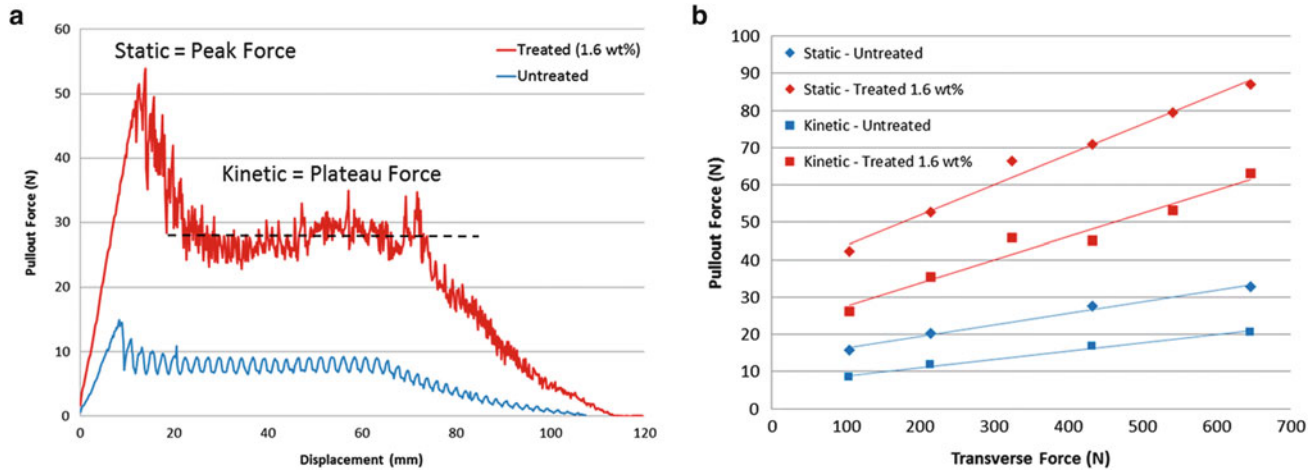

Fig. 7.5 The result of the pull-out test is static force (peak load) and kinetic force (plateau mean load). MWNT treated samples show higher static and kinetic force than untreated (**a**). As the transverse force is varied, the kinetic and static forces are plotted where the slope of this linear relationship can be used to determine friction coefficients (**b**)

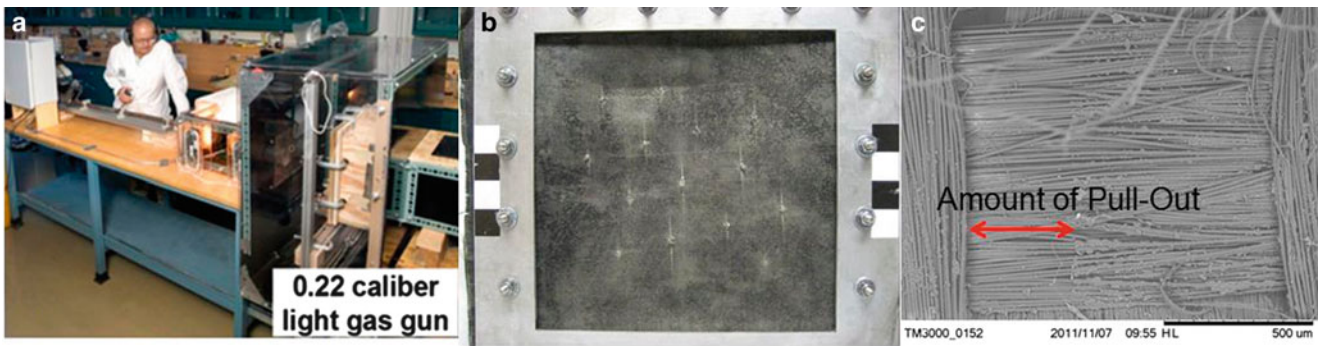

Fig. 7.6 Gas gun setup (**a**). Treated Kevlar fabric in holder post-test (**b**). SEM showing pull-out of fibers following impact (**c**)

By combining the slopes measured during the yarn pull-out tests and the static friction coefficients measured during the static friction tests, the kinetic friction coefficient can be calculated. Untreated K129 measured $\mu_k = 0.16$ while treated fabric measured $\mu_k = 0.21$. These experimentally determined friction coefficients can then be incorporated into FEM simulations for both untreated and treated Kevlar. Once the range of friction coefficients that can be fabricated is known, simulations can be used to evaluate the effect of friction on ballistic performance and guide synthesis toward the optimal friction level.

7.2.5 Fabric Scale: Modified Ballistic Testing

During a ballistic impact, kinetic energy is transferred to the fabric. As the stress wave spreads outward from the point of impact, energy is partially dissipated by fiber deformation and inter-fiber friction. In a low-velocity impact, the transverse wave has a longer time to propagate and more fabric area is involved, which leads to higher energy absorption and therefore the predominant failure mode becomes yarn pull-out. To study the specific mechanisms of friction and pull-out, modified ballistic testing was conducted by impacting 0.22 caliber steel spheres into a single ply of untreated and treated fabric. This type of test was conducted to quickly and inexpensively study the effects of MWNTs on the yarn pull-out mechanism during low velocity ballistic impact using statistical data without the need for a large sample quantity.

Lab-scale ballistic testing was performed using a smooth bore, He-pressurized gas gun to fire a 0.22 caliber steel sphere at a single ply of 381 mm by 381 mm Kevlar 129 fabric as shown in Fig. 7.6a. Holes were punched around the perimeter of the Kevlar fabric and it was secured in a frame using bolts, as shown in Fig. 7.6b. The inner frame dimension was approximately

279 mm by 279 mm. All specimens were aligned with the warp direction horizontal. For each single-ply specimen, 15 shots were taken. This pattern was designed such that none of the principal yarns for each of the 15 shots were shared, and the spacing between each impact, and between each impact and the inner edge of the target frame, was at least 50.8 mm. A pair of light chronographs measured the impact velocity and a light bar chronograph measured residual velocity, which helped to identify penetrating or perforations versus non-penetrating impacts ("stops") in cases when it was otherwise unclear solely from the damage to the fabric.

Perforation regions were examined using scanning electron microscopy (SEM) after testing. Failures occurred via fiber breakage as well as pull-out, as pictured in Fig. 7.6c. V_{50}, the velocity at which the probability of penetration is estimated to be 50 %, was estimated using velocities from 10 shots. For each calculation, half of the values were the highest non-penetrating shot velocities and half of the values were the lowest penetrating values. In each case, the correlating V_{50} span was calculated as the difference between the highest non-penetration and the lowest penetration. The V_{50} for treated (1.6 wt%) Kevlar was nearly double (214 m/s) that of the untreated Kevlar (110 m/s), suggesting that yarn pull-out resistance may be a critical factor under the ballistic conditions evaluated. This example illustrates the utility of the yarn pull-out tests for down-selecting to the best armor material synthesis conditions for full scale testing.

7.3 Modeling and Simulation

Models are being used to identify candidate mechanisms responsible for observed changes in material performance and to understand how desirable macroscopic properties can be realized by modifying the underlying molecular and fibril structures. These models are being employed from the molecular and fibril level (molecular dynamics simulations) to yarn and fabric level (FEM models) to elucidate how the hierarchical structure and properties at different length scales contribute to the system performance. Molecular Dynamics (MD) simulations help to show the relationship between the addition of carbon to the Kevlar fibrils and the mechanical properties of the fibers themselves [16]. Simulated and experimental tensile data can be compared, and by understanding how the material properties and structure interact at different length scales, we can begin to understand the mechanisms responsible for improved ballistic performance at the macroscale.

7.3.1 Pull-Out Model

Since yarn pull-out is an important mechanism that is active during ballistic impact, it must be accurately represented in the FEM ballistic model. A FEM pull-out model uses experimentally derived parameters such as strength and stiffness from tensile tests, and friction coefficients from the static friction test and yarn pull-out test. Simulations of the pull-out experiment, pictured in Fig. 7.7a, can be validated against experimental data (Fig. 7.7b), and enable verification that friction and yarn interaction are accurately represented in the ballistic model. A preliminary effort towards validation shows promising results out to 4 mm of displacement, and expansion of these simulations to greater length scales for improved comparison with experimental data is underway. Following completion and validation of these models, parametric studies can elucidate the relationship between friction and ballistic performance.

7.3.2 Single-ply Model

Analogous to the experimental case, a single-ply sheet of fabric modeled in quarter or half symmetry using LS-DYNA can enable simpler testing of material properties and performance. The single-ply system, impacted at a lower-range of velocities, allows for comparison of either the residual velocity of projectiles that penetrate the fabric, or the achievable ballistic limits of the fabric as the material properties are changed. An orthotropic elastic constitutive model was utilized, allowing for the fabric to be characterized as strong along the length of the yarn and comparatively weak in all other directions. Input material properties and failure characteristics for the orthotropic constitutive model were extracted from tensile tests, static friction and pull-out tests, pull-out models, and molecular models. The model was partitioned into three regions (Fig. 7.8a) as described in detail by Thomas et al. [16]: a high-resolution impact region, a medium-resolution shell region, and a low-resolution global membrane region. Figure 7.8b shows a simulation image of a single ply of Kevlar 129

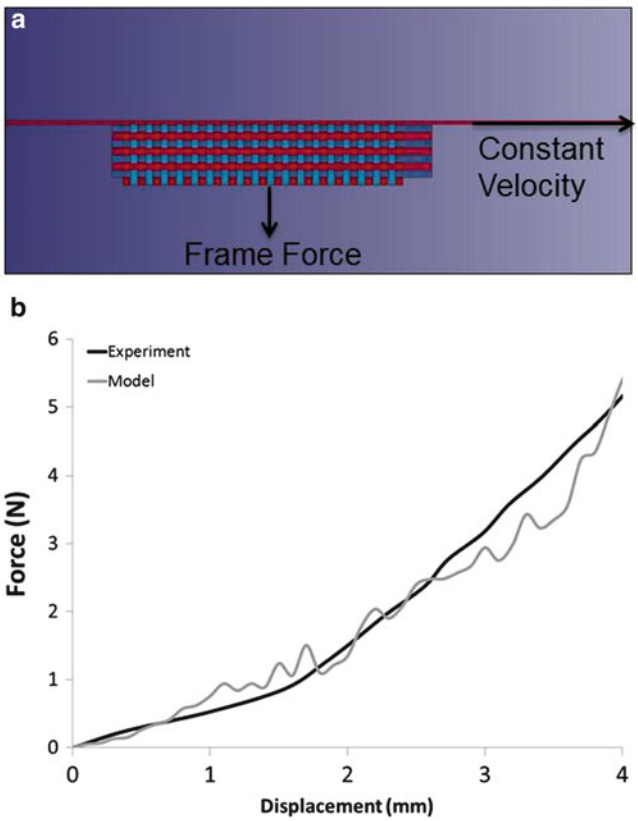

Fig. 7.7 Image of the FEM pull-out model showing a yarn being pulled at constant velocity while varying the frame force (**a**). Preliminary results showing pull-out model and experimental pull-out agreement up to 4 mm (**b**)

fabric being impacted with a 0.22 in.-diameter steel sphere at a velocity of 168 m/s. The fraying of the Kevlar yarn, which is divided into 24 fiber bundles, is observable.

Parametric studies enable variation of material properties within the synthesis parameter space to understand which properties have the most impact on ballistic performance. Model outputs can thus be used to design/tailor the best fabric treatment option. Parametric studies of fabric properties such as elastic modulus, breaking strength, friction coefficients, yarn geometry, denier, and weave pattern can be used to show trends and estimate the theoretical ballistic limit of the fabric to define the desired design space for the synthesis team. As an example of these parametric studies, a study has been performed to shed some light on the effects of both yarn strength and yarn-yarn friction on ballistic performance (measured as bullet velocity, where lower residual velocity correlates to better ballistic performance). The data in Fig. 7.8c indicate that yarn strength is a necessary, but not sufficient, indicator of fabric performance, and that friction, which enables energy exchange between yarns, must also be considered.

7.4 Future Work: Multi-layer Ballistic Testing and Modeling

The culmination of this multi-scale test methodology is the full-scale ballistic test and model. Soft armor is typically comprised of many (e.g. 22) layers of fabric. When performing a study with multiple synthesis variables, fabricating 22-layer samples for each processing variant would be prohibitively time consuming and costly. In addition to simple models, a full, multi-ply armor system can be simulated to test against real ballistic threats and predict the resulting theoretical ballistic limit (Fig. 7.9). Multi-ply armors can be simulated by stacking several iterations of the single-ply model atop one another until the desired armor thickness is achieved. As with the single-ply system, this model opens itself up to more parametric study possibilities, with possible variance in material directions, weave patterns, and even variance in material properties between layers. Through this form of modeling, the best possible armor system can be designed at a relatively lower cost compared to extensive iterative ballistic testing of the gamut of treatment options.

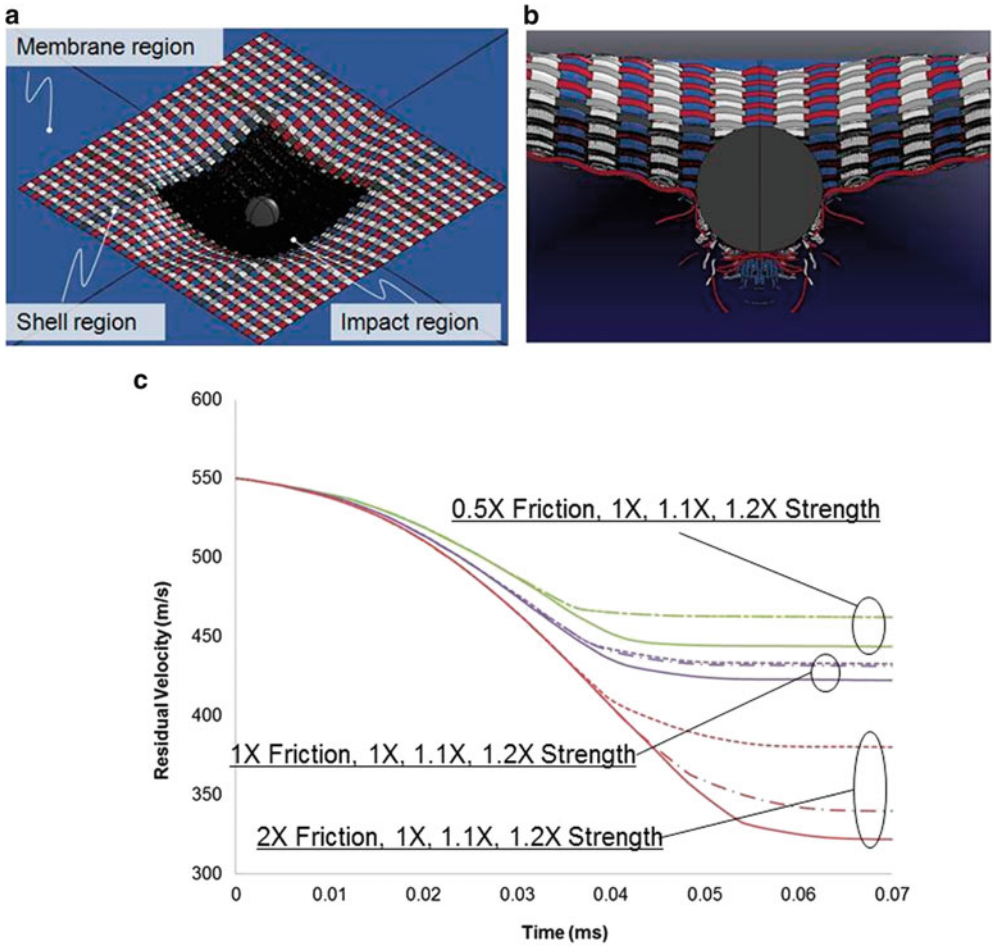

Fig. 7.8 Partitioned structure of the FEM single-ply Kevlar model. Quarter symmetry is evoked in all simulations (**a**). Penetration of steel sphere through a single Kevlar layer (**b**). Parametric study varying strength and friction shows that both strength and inter-yarn friction are critical to improving ballistic performance (reducing residual velocity) (**c**)

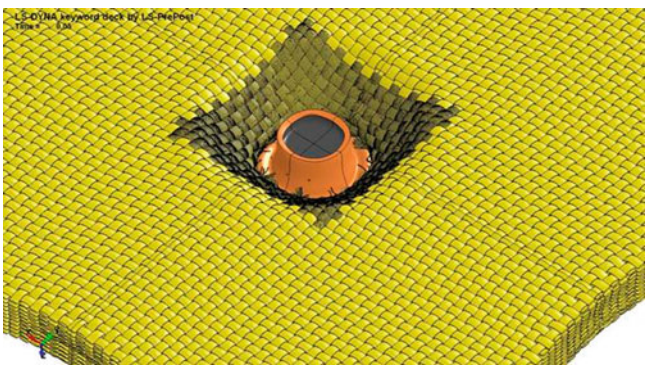

Fig. 7.9 Image from a FEM simulation of ten layers of untreated Kevlar impacted by a 9 mm projectile

By employing multi-scale testing and multi-scale modeling in parallel, as described herein, effort and cost can be minimized by testing only the most promising combinations of materials. Testing at length scales ranging from the yarn to the weave to single-ply fabric yields important information regarding choice of solvents, dispersants, and MWNT concentration, thus enabling down-selection of process variables and optimization of the nanotube reinforcement such

that the optimal material solution can be more quickly derived and tested at full scale. Simultaneously, parametric studies with FEM inform the synthesis process of limitations to friction benefits while MD simulations elucidate mechanisms responsible for increased yarn strength. This comprehensive multi-scale approach is presented as an alternative to full scale ballistic testing as quintessential for development of new ballistic materials.

7.5 Summary and Conclusions

We have presented a multi-scale approach for design and tailoring of soft armor with nanomaterials to improve ballistic performance. Intrinsic and extrinsic material properties were measured experimentally over multiple length scales. These properties can be utilized in FEMs, also at multiple length scales, with validation steps along the way, to understand mechanisms and perform parametric studies to aid identification of material treatments that optimize ballistic performance. Once refined, this method can be used to predict the ballistic limit for treated fabrics.

A preliminary demonstration of the utility of this approach was performed on untreated versus MWNT-augmented Kevlar materials. While tensile testing did not show statistically significant changes in strength or modulus, MWNT treatment did affect yarn interaction forces with static friction and pull-out tests revealing a 25% increase in friction coefficient. Single-ply, low velocity impact testing showed that the V_{50} nearly doubled following treatment with MWNTs. This result illustrates the importance of performing small scale experiments to understand the mechanisms responsible for improved ballistic performance.

Acknowledgements This work was funded in part by the Office of Naval Research Award Number N00014-12-1-0402. The authors also acknowledge support from the Johns Hopkins University Applied Physics Laboratory Research and Exploratory Development Business Area under internal research and development funds. We would also like to thank Larry Long at the Army Research Laboratory for assistance in performing ballistic experiments.

References

1. Grujicic M et al (2011) Multi-length scale computational derivation of Kevlar((R)) yarn-level material model. J Mater Sci 46(14):4787–4802
2. Carr DJ (1999) Failure mechanisms of yarns subjected to ballistic impact. J Mater Sci Lett 18(7):585–588
3. Jacobs MJN, Van Dingenen JLJ (2001) Ballistic protection mechanisms in personal armour. J Mater Sci 36(13):3137–3142
4. Cunniff PM, Auerbach MA, Vetter E, Sikkema DJ (2002) High performance "M5" fiber for ballistics/structural composites. In: 23rd army science conference. Assistant Secretary of the Army (Acquisition, Logistics and Technology), Orlando
5. Rao MP et al (2009) Modeling the effects of yarn material properties and friction on the ballistic impact of a plain-weave fabric. Compos Struct 89(4):556–566
6. Bazhenov S (1997) Dissipation of energy by bulletproof aramid fabric. J Mater Sci 32(15):4167–4173
7. Adanur S (1995) Wellington Sears handbook of industrial textiles. Technomic Pub., Lancaster
8. Yang HH (1993) Kevlar aramid fiber. Wiley, Chichester
9. Martinez MA et al (1993) Friction and wear behavior of Kevlar fabrics. J Mater Sci 28(5):1305–1311
10. Yu MF et al (2000) Strength and breaking mechanism of multiwalled carbon nanotubes under tensile load. Science 287(5453):637–640
11. O'Connor I et al (2009) High-strength, high-toughness composite fibers by swelling Kevlar in nanotube suspensions. Small 5(4):466–469
12. Dong Z, Sun CT (2009) Testing and modeling of yarn pull-out in plain woven Kevlar fabrics. Compos Part A Appl Sci Manuf 40(12):1863–1869
13. Nikonova EA, Pakshver AB (1973) The friction properties of textile yarns. Fibre Chem 4(6):657–660
14. Kalman DP et al (2009) Effect of particle hardness on the penetration behavior of fabrics intercalated with dry particles and concentrated particle-fluid suspensions. ACS Appl Mater Interfaces 1(11):2602–2612
15. Shockey DA, U.S.F.A.A.O.o.A. Research, and S. International (2002) Improved barriers to turbine engine fragments: final annual report. Office of Aviation Research, U.S. Federal Aviation Administration
16. Thomas JA et al (2012) Multiscale modeling of high-strength fibers and fabrics. In Proceedings of SPIE 8373, Micro- and Nanotechnology Sensors, Systems, and Applications IV, 83731S. doi:10.1117/12.919395

Chapter 8
Single Fiber Tensile Properties Measured by the Kolsky Bar Using a Direct Fiber Clamping Method

J.H. Kim, N.A. Heckert, W.G. McDonough, K.D. Rice, and G.A. Holmes

Abstract The Kolsky bar test has been widely used in measuring material behavior under high strain rate conditions. In particular, polymers used in ballistic applications have been characterized by this method to investigate high strain rate behavior during ballistic impact. Research conducted by Cheng et al. (J Eng Mater Technol-Trans ASME 127(2):197–203, 2005) and Lim et al. (J Mater Sci 45(3):652–661, 2010) measured high strain rate properties of single PPTA [Poly (*p*-phenylene terephthalamide)] fibers and aramid co-polymer fibers by gluing the fiber directly to the Kolsky bar, which is time consuming work and can be affected by wicking of the glue into the fiber gauge length area. Kim et al. (J Mater Sci. doi:10.1007/s10853-013-7142-y, 2013) investigated clamping effects of the glue-tab and direct gripping methods on the single PPTA fiber tensile properties under the quasi-static loading condition and applied the direct grip method for the Kolsky bar test to measure the tensile strengths at a high strain rate (Kim et al., Compos Sci Technol. doi:10.1016/j.compscitech.2012.03.021, 2012). This study extends the measurement capability for the tensile strength, failure strain and modulus that are important parameters that influence performance of soft body armor.

Keywords Single fiber tensile test • High strain rate • PPTA • Soft body armor • Direct fiber grip

8.1 Introduction

Important parameters influencing the ballistic performance of soft body armors are the mechanical properties of high strength fibers used in the armors. Although fibers deform at high rates during ballistic impact, the mechanical properties of these fibers are often characterized under quasi-static test conditions. To measure fiber properties under high strain rate (HSR) conditions, Kolsky bar tests [1, 2] have been utilized. However, testing at these rates requires relatively short fiber lengths compared to quasi-static testing. The gripping method in these studies consisted of gluing a fiber on the Kolsky bar. However, as emphasized by a study on clamp effects [3] and experimental results with sub-millimeter long fibers [4], tensile tests with short fibers were shown to be highly influenced by the gripping condition. Therefore, a direct clamp method for measuring tensile strengths [5] is recommended when using the Kolsky bar test to minimize the complexity inherent in the gluing method and to increase the test throughput. A recent study comparing fiber strengths, moduli, and failure strains from tests that used the glue-tab method and the direct grip method found that the direct grip method to be more reliable for short fiber lengths ($\leq$10 mm) [6].

One important aspect to understanding soft body armor performance is determining the mechanism of impact energy transfer and dissipation during impact. Strain energy dissipation in fibers of soft body armor subjected to ballistic impact

J.H. Kim • W.G. McDonough • G.A. Holmes (✉)
Materials Science and Engineering Division (M/S 8541), National Institute of Standards and Technology, Gaithersburg, MD 20899, USA
e-mail: gale.holmes@nist.gov

N.A. Heckert
Statistical Engineering Division (M/S 8980), National Institute of Standards and Technology, Gaithersburg, MD 20899, USA

K.D. Rice
Materials Measurement Science Division (M/S 8102), National Institute of Standards and Technology, Gaithersburg, MD 20899, USA

B. Song et al. (eds.), *Dynamic Behavior of Materials, Volume 1: Proceedings of the 2013 Annual Conference on Experimental and Applied Mechanics*, Conference Proceedings of the Society for Experimental Mechanics Series,
DOI 10.1007/978-3-319-00771-7_8, © The Society for Experimental Mechanics, Inc. 2014

depends on the dynamic stress–strain behaviors of the fibers. Therefore strain measurement provides essential information to understand the response of soft body armor under ballistic impact conditions. Typically, failure strain can be determined from a Kolsky bar test by reducing data using the classical wave method, but this method is less accurate for measuring failure strains of high strength fibers due to their small strains approximately 3 % to 4 % [7]. To measure small strains on the Kolsky bar test without relying on the wave method, several direct strain measurement methods have been used. One method involves attaching a strain gauge directly on the specimen; another uses digital image correlation by acquiring high speed images for a speckle painted specimen. Since fiber diameters are typically 10 μm to 20 μm, attaching a strain gauge or spray painting a speckle pattern on the fiber for the digital image correlation is a challenge. Therefore, a modified laser technique to measure the displacement of the Kolsky bar has been proposed as an alternative noncontact method [7].

In this study, we utilize a newly developed direct fiber clamping method and adapt a laser strain measurement technique to obtain fiber strengths and failure strains in a high throughput and repeatable manner. This enables the establishment of larger data sets of tensile properties, which are beneficial for statistical analyses and designing and modeling the performance of soft body armor systems.

8.2 Experimental Procedure

8.2.1 HSR Loading with PMMA Grip

For the tensile test under HSR loading, single PPTA [Poly (*p*-phenylene terephthalamide)] fibers were directly gripped by PMMA (polymethyl methacrylate) clamping blocks on the Kolsky bar as shown in Fig. 8.1. To aid in aligning and positioning the single fiber in the PMMA clamping blocks, a fiber specimen was first prepared by adhering it to a plastic template, with the adhesive placed outside of the clamping zone. The plastic template was then used to precisely locate the fiber only across the PMMA clamping blocks, whose clamping forces were controlled by screws that were tightened to a consistent torque value. After clamping the fiber, the template was cut before beginning the dynamic loading procedure. To measure single fiber failure strains at high rates, a non-contact laser technique [7] was utilized. A 100 mW laser with a wavelength of 658 nm was the laser source. A thin laser line generated by a Powell[1] lens illuminated the target on the Kolsky bar. The laser intensity increases as the displacement of the Kolsky bar increases. The gauge lengths of the fiber specimens for the HSR tests were chosen to be 5 mm and 8 mm. The preliminary tensile tests were performed under a strain rate of approximately 800 s^{-1}. The estimated uncertainty of the load cell obtained from the manufacturer was ±1 %.

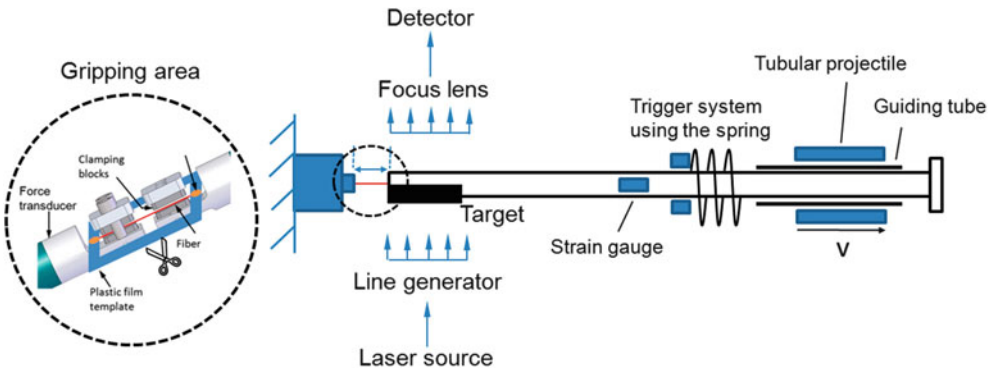

Fig. 8.1 Schematic close up of the Kolsky bar test setup and the direct grip

[1] Certain commercial materials and equipment are identified in this paper to specify adequately the experimental procedure. In no case does such identification imply recommendation or endorsement by the National Institute of Standards and Technology, nor does it necessarily imply that the product is the best available for the purpose.

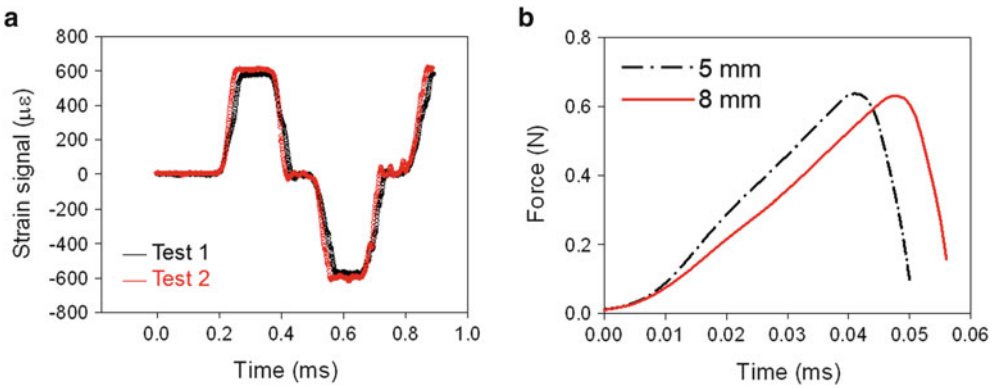

Fig. 8.2 Strain signals (**a**) and force signals (**b**) of the single fiber tensile tests under HSR loading conditions

8.3 Results and Discussion

For the single fiber test with fiber lengths less than 10 mm, a reliable gripping method is needed to grip a fiber reproducibly due to higher influence of gripping effects [6]. Stress–strain behaviors for the direct grip method with 2 mm gauge length were relatively variable compared to gauge lengths of 5 mm and longer. Therefore, 5 mm and 8 mm fibers were used in this study. In preliminarily tests under HSR loading condition, strain signals obtained by the strain gauge on the Kolsky bar for 8mm fiber tests show a nearly overlapped pattern in incident and reflected strain signals (see Fig. 8.2a). This represents repeatability of the loading system. Force signals of the single PPTA fibers were measured for 5 mm and 8 mm gauge lengths to investigate the force response of different fiber lengths as a function of time. Force-time curves for the 5 mm and 8 mm tests showing similar failure forces are chosen and shown in Fig. 8.2b. Since both fibers rupture at similar forces, it is not surprising that the 8 mm length test shows a longer time to failure than the 5 mm length test. The study presented here reports on finding to date with the single fiber tensile tests under two different loading conditions.

8.4 Concluding Comments

Single fiber tensile tests under HSR loading conditions using a PMMA fiber grip were carried out to investigate gripping effects for 5 mm and 8 mm gauge lengths. Using the test results showing similar failure forces, force-time responses of single fibers for the 8 mm fiber test was measured and showed a similar response up to fiber rupture with longer failure time compared to the 5 mm test. We will present preliminary results that will show that the direct gripping method is a reliable and applicable method to the HSR test with a range of fiber lengths.

References

1. Cheng M, Chen WN, Weerasooriya T (2005) Mechanical properties of Kevlar KM2 single fiber. J Eng Mater Technol-Trans ASME 127(2):197–203
2. Lim J, Zheng JQ, Masters K, Chen WNW (2010) Mechanical behavior of A265 single fibers. J Mater Sci 45(3):652–661
3. Phoenix SL, Sexsmith RG (1972) Clamp effects in fiber testing. J Compos Mater 6(3):322–337
4. Thomason JL, Kalinka G (2001) A technique for the measurement of reinforcement fibre tensile strength at sub-millimetre gauge lengths. Compos Part A-Appl Sci Manufactur 32(1):85–90
5. Kim JH, Heckert NA, Leigh SD, Rhorer RL, Kobayashi H, McDonough WG, Rice KD, Holmes GA (2012) Statistical analysis of PPTA fiber strengths measured under high strain rate condition. Compos Sci Technol. doi:10.1016/j.compscitech.2012.03.021
6. Kim JH, Holmes GA, Leigh SD, Kobayashi H, McDonough WG, Rice KD, Holmes GA (2013) Effects of fiber gripping methods on the single fiber tensile test: I. Non parametric statistical analysis. J Mater Sci. doi:10.1007/s10853-013-7142-y
7. Lim J, Chen WNW, Zheng JQ (2010) Dynamic small strain measurements of Kevlar 129 single fibers with a miniaturized tension Kolsky bar. Polym Test 29(6):701–705

Chapter 9
A Testing Technique for Characterizing Composite at Strain Rates up to 100/s

Guojing Li and Dahsin Liu

Abstract As the use of fiber composites extends to automotive applications, there is a need to characterize the composite properties at low strain rates, such as below 100/s. In performing such low strain rate tests, the commonly used split Hopkinson's pressure bar for high strain rate investigations should become inadequate. A high-speed hydraulic testing machine may be suitable for the low strain rate testing, however, it is not necessary within the reach of general engineers due to its high cost. Based on a drop weight impact tester, this study presents an affordable testing technique for characterizing a carbon composite at low strain rates up to 125/s. Experimental results from static testing and slip Hopkinson's bar testing were also performed for comparisons.

Keywords Fiber composite • Strain rate • Drop weight impact • Slip Hopkinson's pressure bar

9.1 Introduction

Owing to their high stiffness and high strength with low density, fiber-reinforced polymer matrix composites are excellent materials for high-performance structures which are commonly exposed to dynamic environments. The behavior of composite materials under high strain rates, however, can be quite different from that under low strain rates. Taking the automotive application as an example, the composite materials and structures may be subject to vibration and dynamic loading with a strain rate up to 100/s. Hence, there is a need to characterize the properties of automotive composites from static to low strain rate of that level.

Among the dynamic testing techniques available, split Hopkinson's pressure bar (SHPB) [1] is the most commonly used method for high strain rate characterizations, such as from 10^2/s to 10^4/s. Its usefulness for strain rates lower than 100/s, however, should become very challenging, if not impossible. In order to fill the gap between static loading and high strain rate testing, high-speed hydraulic testing machines, such as Instron's VHS 8800 [2], should prove to be useful. However, in order to achieve high-speed loading rates, large pneumatic capacity is required for fast response. An efficient feed-back system is also needed to achieve constant loading rates. Accordingly, the high-speed hydraulic testing machine may become very costly and not necessarily reachable to general engineers. Based on a conventional drop weight impact tester (DWIT), this study presents an affordable testing technique for performing dynamic characterizations of fiber composites up to a strain rate of 125/s.

G. Li • D. Liu (✉)
Department of Mechanical Engineering, Michigan State University, East Lansing, MI 48824, USA
e-mail: liu@msu.edu

B. Song et al. (eds.), *Dynamic Behavior of Materials, Volume 1: Proceedings of the 2013 Annual Conference on Experimental and Applied Mechanics,* Conference Proceedings of the Society for Experimental Mechanics Series,
DOI 10.1007/978-3-319-00771-7_9,

9.2 Drop Weight Impact Tester

9.2.1 Force Equilibrium

In order to achieve constant strain rates in drop weight impact testing, an existing DWIT was modified to be equipped with a large impacting mass so the specimen being tested can deform with a strain rate as constant as possible. Shown in Fig. 9.1 is a DWIT attached with an impacting mass of 150 kg. As the large mass and impact head drop onto the specimen, a relatively constant speed of deformation can be achieved in the specimen due to the significantly large weight induced by the large impacting mass against the resistance of the specimen.

Besides constant strain rates, or at least nearly constant strain rates, a constant force through the specimen is also required for validating the dynamic testing. As the impact occurs, the impact head will contact the top surface of the specimen. The impact-induced force will subsequently propagate to the bottom surface of the specimen. Although very short, a period of time is required for the specimen to achieve constant force through the length. Once the force in the specimen reach equilibrium during the impact testing, the testing result can be used for further analysis, otherwise the test is deemed invalid and the testing result should be nullified.

Right after the contact-impact takes place, the top surface of the specimen may experience damage while the remaining of the specimen remains intact. This is likely to occur in brittle specimens such as polymer composites. If the premature damage does occur, the impact test should be claimed invalid because the specimen does not reach the equilibrium condition.

9.2.2 Shaper

In order to achieve uniform force through the specimen and to avoid any premature damage to the specimen, a material softer than the specimen, so-called shaper, may be added between the impact head and the top load cell as shown in Fig. 9.1. Identifying the right type of material and the associated thickness as the shaper involves many trial-and-errors. Soft materials such as copper and rubbers are often used by composite engineers as shaper materials. It should also be pointed out that the strain rate is usually reduced when softer shaper is added to the impact system. Hence, it is a challenging task to achieve force equilibrium in the specimen by introducing a shaper without significantly reducing the strain rate.

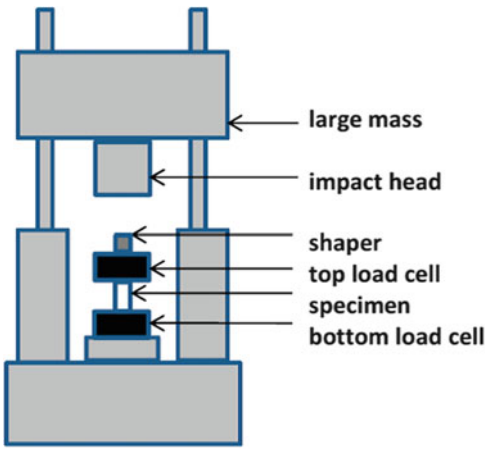

Fig. 9.1 DWIT setup for compressive strain rate testing

9.3 Testing Procedures and Data Analysis

9.3.1 Testing Specimens

9.3.1.1 Thin Specimen

As an example, a laminated carbon composite with a thickness of 1.6 mm was investigated in this study. All composite specimens were machined to have dimensions of 63 × 19 mm. Each of them was then bolted with steel angles from both sides and at both ends as shown in Fig. 9.2, resulting in a 19 × 19 × 1.6 mm testing zone. Each specimen-angle set was then bolted to the top and the bottom load cells, shown in Fig. 9.1, for impact testing.

9.3.1.2 Thick Specimen

Due to the concern of specimen buckling and premature damage, thick specimens with dimensions of 12.7 × 12.7 × 6.4 mm without the clamping angles were also used for studying the composite response. The thick specimens were obtained by bonding four 1.6 mm specimens together with an adhesive. Because of the high bonding strength of the adhesive, a specimen may split between individual composite plies rather than along the bonding interfaces when subjected to compressive loading. Besides, a thick layer of grease was applied to the surfaces between the specimen and the load cells to warrant free transverse expansion during compression. The thick specimen should work better than the thin specimen in terms of simplicity (without the supporting angles) and higher resistance to buckling. However, cautions must be exercised in selecting the dropping height so no hard-to-hard impact, such as between the impact head and the top load cell and between the two load cells, would occur.

9.3.2 Effect of Shaper

9.3.2.1 Shaper Material

The task to identify a suitable shaper material with an adequate thickness for the carbon composite material under investigation was essentially based on trial-and-errors. Four tests based on different shapers, from hard to soft, are given in Fig. 9.3. The force measured by the top load cell is much more significantly affected by the hardness/softness of the shaper than that measured by the bottom load cell. Figure 9.3a shows a large difference of measurements from the two load cells when a hard material was used as the shaper. Both Fig. 9.3b, c show significant improvements in the equilibrium of the two forces measured by the top and the bottom load cells when a hard rubber and a medium soft rubber were used as shapers, respectively. Using a soft rubber as a shaper, a good agreement up to 2.5 ms between the two measurements was obtained and is shown in Fig. 9.3d. It demonstrates the equilibrium of the dynamic force through the length of the specimen. The result from Fig. 9.3d can then be used for further analysis.

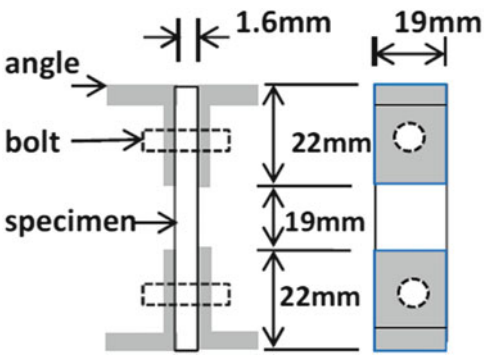

Fig. 9.2 Thin specimen with bolted angles

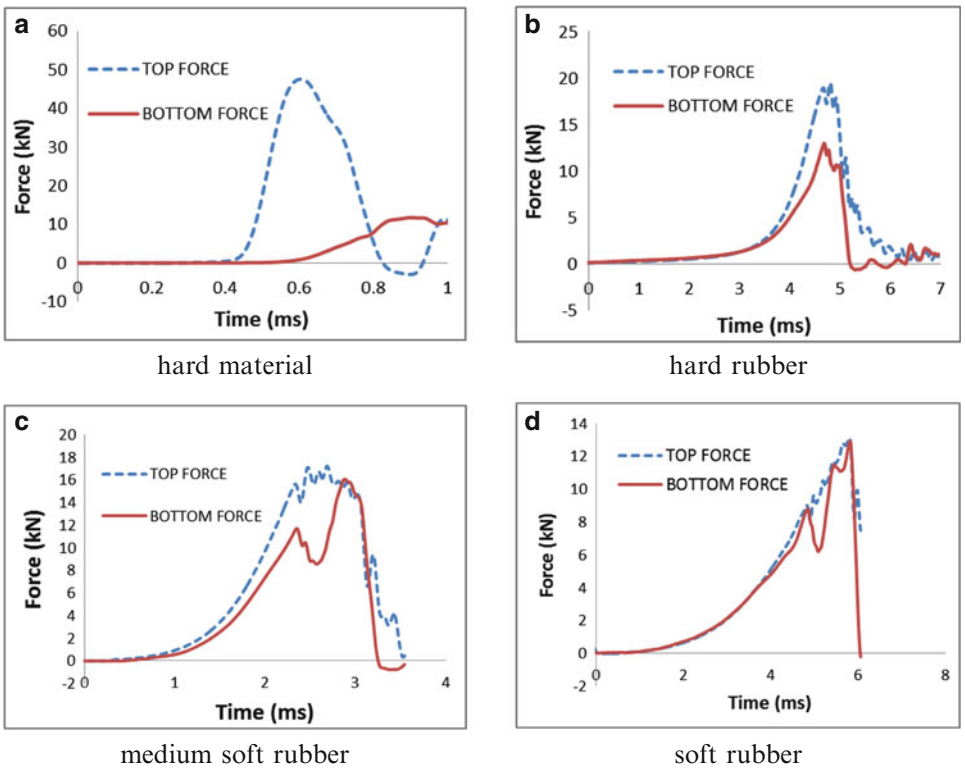

Fig. 9.3 Effect of shaper softness on the balance of top and bottom forces

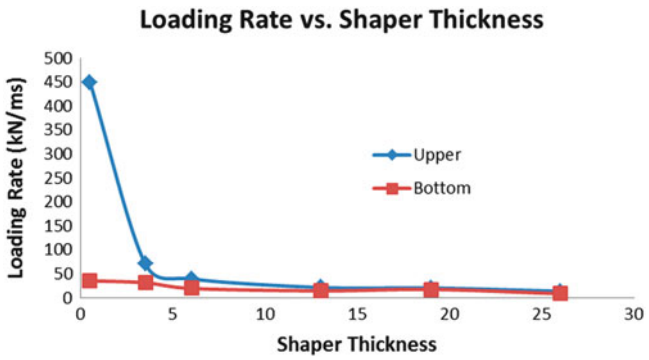

Fig. 9.4 Decrease of loading rate due to the increase of shaper thickness

9.3.2.2 Shaper Thickness

From Fig. 9.3, it clearly shows that the peak force measured by the top load cell decreases as the two forces measured from the two load cells become closer. The peak force measured by the bottom load cell, however, remains relatively constant. This clearly indicates the function of the shaper in reducing the top force and achieving the balance of the two forces. Figure 9.4 shows that the loading rate (and the strain rate) decreases as the thickness of the shaper increases (becomes softer). This is especially significant in the top load cell although the bottom load cell also experiences reduction of loading rate.

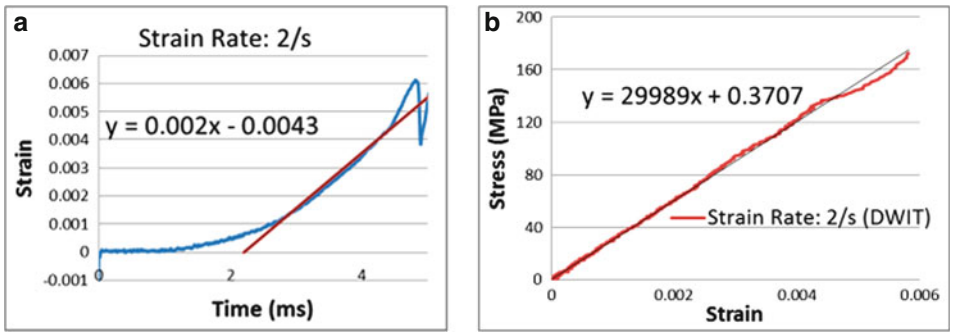

Fig. 9.5 DWIT based compressive testing results

Table 9.1 Young's modulus and yielding stress at various strain rates

Strain rate (1/s)	0	2	3	8	18	30	63	125	200	250
Young's modulus (GPa)	28	30	30	34	31	29	30	31	26.5	23.4
Yielding stress (MPa)	160	165	185	250	275	160	270	150	160	265

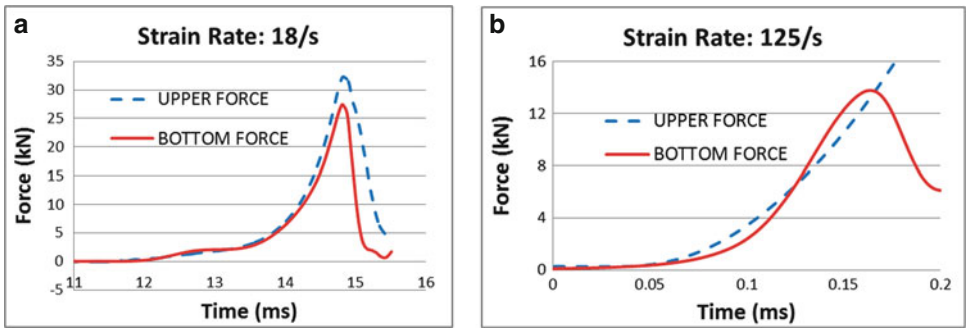

Fig. 9.6 Force histories measured by load cells at different compressive strain rates

9.3.2.3 Identification of Strain Rates

The strain history of Fig. 9.3d is given in Fig. 9.5a. It was obtained from a strain gauge mounted on the specimen. The nearly constant strain rate can be identified as 2/s by taking the derivative of the largely linear portion of the strain history as shown in Fig. 9.5a. The corresponding stress–strain relation for the nearly constant strain rate of 2/s is given in Fig. 9.5b. The Young's modulus and the yielding stress can then be identified as 30 GPa and 165 MPa, respectively. Tests for higher strain rates of up to 63/s were also performed and the resulting Young's moduli and yielding stresses at several strain rates are summarized in Table 9.1.

9.3.2.4 Higher Strain Rates

As far as the concern of force balance, thin specimens held with metallic angles were useful for strain rate testing up to 8/s. For higher strain rates, thick specimens that are constructed by bonding four thin specimens together are required. Figure 9.6a shows the result obtained from a thick specimen at a strain rate of 18/s. It was also found that thick specimen was useful for strain rates up to 63/s. As shown in Fig. 9.6b, however, the top force and the bottom force deviate when the strain rate reaches 125/s. A softer shaper will be required to achieve the balance of the forces between the two load cells although it is also recognized that the strain rate will decrease as the softer shaper is employed. Possible Young's modulus and yielding stress based on Fig. 9.6b also presented in Table 9.1.

9.4 Split Hopkinson's Pressure Bar

In order to identify the behavior of the carbon composite at even higher strain rates, such as higher than 100/s, a conventional split Hopkinson's pressure bar (SHPB) was used along with thick specimens. Figure 9.7 shows the experimental result. The forces in the incident bar and transmission bar were measured with the strain gauges attached to the bars while the strain in the specimen was measured from a strain gauge attached to it. Figure 9.7a shows the forces at the two ends of the specimen. Although they are not identical, they are relatively similar from an overall sense. The experimental results were used for further analyses.

The corresponding strain history and strain rate history for Fig. 9.7a are given in Fig. 9.7b, c, respectively. Based on the near linearity between 0.03 and 0.1 ms in Fig. 9.7b and the plateau in Fig. 9.7c between 0.03 and 0.06 ms, there seems to exist a nearly constant strain rate of approximately 250/s between 0.03 and 0.06 ms. The corresponding stress–strain curve is given in Fig. 9.7d. The 250/s corresponds to a strain range between 0.004 and 0.006 and a modulus around 26.5 GPa. This result is also presented in Table 9.1 along with the results from the drop weight impact tests. The zero strain rate given in Table 9.1 represents static testing based on a hydraulic testing machine.

Figure 9.8 shows all the stress–strain curves for comparison. Both the curves associated with strain rates of 200 and 250/s are presented by dash-dot lines. The valid range based on the nearly constant strain rates between 0.03 and 0.06 ms, however, are shown with solid lines.

9.5 Discussions

1. The microstructure of the fiber composite, if there is any, must be considered in the selection of specimen dimensions.
2. The thick specimens work better than the thin specimens for compressive testing as well as higher strain rate testing.
3. The large impacting mass is adequate for achieving nearly constant strain rates up to 125/s.
4. Trial-and-errors are required for identifying a suitable shaper material with an associated thickness for achieving force balancing. As the shaper becomes softer, the loading rate (strain rate) due to the same impacting force decreases.
5. Multiple tests are required for obtaining a reliable testing result.
6. It is a challenging task to achieve force equilibrium in the specimen by introducing a shaper without significantly reducing the strain rate.

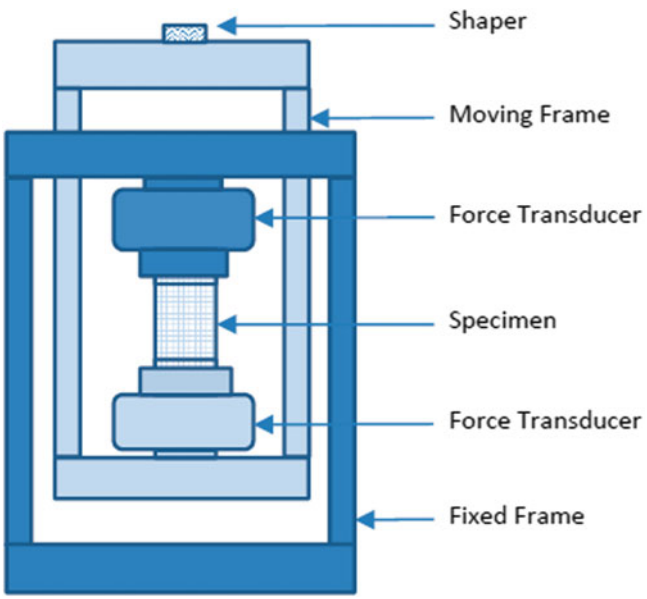

Fig. 9.7 Loading fixture for DWIT based tensile strain rate testing

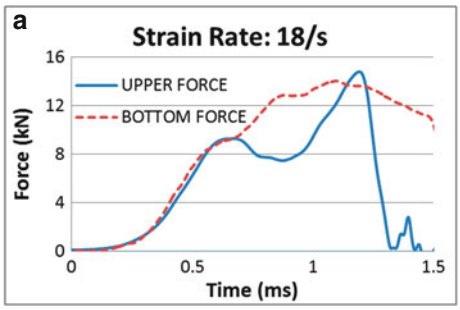

forces recorded in both force transducers

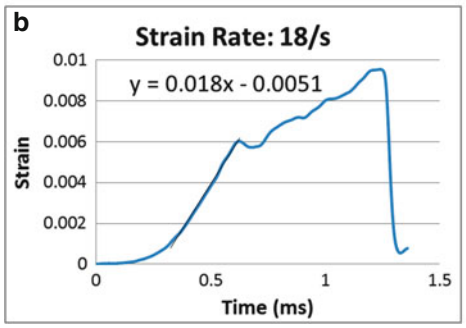

strain history and strain rate

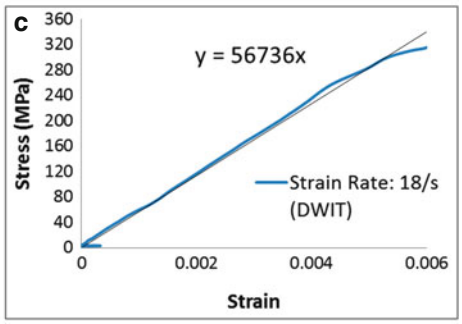

stress-strain relation

Fig. 9.8 DWIT based tensile testing results

9.6 Summary

Based on the preliminary investigations in this study, the Young's modulus and yielding stress of the carbon composite were obtained for strain rates ranging from 0 to 250/s. The investigations included static loading (zero stain rate), drop weight impact testing (up to 125/s) and split Hopkinson's pressure bar testing (200 and 250/s). The Young's moduli fluctuate between 23.4 and 34 GPa while the yielding stresses fluctuates between 160 and 275 MPa within the range of strain rates from 0 to 250/s. This study demonstrates the usefulness of the modified drop weight impact tester for low strain rate (up to 125/s) testing. For reliable testing results, multiple tests are highly suggested.

Acknowledgements This research was sponsored by the Army Research Laboratory and was accomplished under Cooperative Agreement Number W911NF-11-2-0017. The authors wish to express their sincere appreciation for the financial support.

References

1. Chen W, Bo Song (2011) Split Hopkinson (Kolsky) bar, design, testing and applications, Springer, New York, USA
2. http://www.instron.us/wa/product/VHS-8800-High-Strain-Rate-Systems.aspx

Chapter 10
A New Technique of Dynamic Spherical Indentation Based on SHPB

Song Li and Liang Haozhe

Abstract A new technique for testing dynamic spherical indentation of materials was proposed. It is implement by putting a WC alloy ball between two specimens. One of the specimens was bonded with input bar and the other was bonded with the output bar. Two specimens then was pressed in the process of indentation. This simple arrangement can accomplish a very accurate measurement of force and displacement during the indentation. A FEA simulation has been carried out using ABAQUS/explicit to evaluation this new technique. The dynamic indentation test of 7075-T4 aluminum alloy was conducted. The simulation and experiment result show the new method gives a more accurate results compare to other dynamic indent experimental method.

Keywords Dynamic • Indentation • SHPB • Mechanical property • Test

10.1 Introduction

Instrumented indentation has become an indispensable tool for probing the quasi-static mechanical properties at small length scales nowadays. It also has been used to test the dynamic properties at high strain-rate. Most apparatus for dynamic indentation experiment are based on Hopkinson Bar [1, 2]. Subhash et al. used the Hopkinson bar as the dynamic load unit. Nilsson used the SHPB as a complete loading and testing device to obtain the indentation load and depth history. Subhash and Nilsson both used conical or pyramidal indenters in there research work. In this paper, we use a spherical indenter for the dynamic indentation test since more fundamental mechanical behavior may be obtained from a spherical indentation experiment [3].

10.2 Spherical Dynamic Indentation Test Using SHPB

10.2.1 The Apparatus

The suggested double specimen dynamic indentation experimental device is shown in Fig. 10.1. It simply replaces the specimen of a traditional Hopkinson pressure bar system with two specimens and a tungsten carbide ball. Ignoring the inertia of the ball, the two specimens will be press-in with the same load during the experiment. With this modification on SHPB, the dynamic indentation load and indentation depth can be obtained very conveniently by using the conventional SHPB measurement and data processing method.

S. Li (✉) • L. Haozhe
Mechanics and Materials Science Research Center, Ningbo University, Ningbo 315211, China
e-mail: songli@nbu.edu.cn; lhz19890407@126.com

B. Song et al. (eds.), *Dynamic Behavior of Materials, Volume 1: Proceedings of the 2013 Annual Conference on Experimental and Applied Mechanics*, Conference Proceedings of the Society for Experimental Mechanics Series,
DOI 10.1007/978-3-319-00771-7_10,

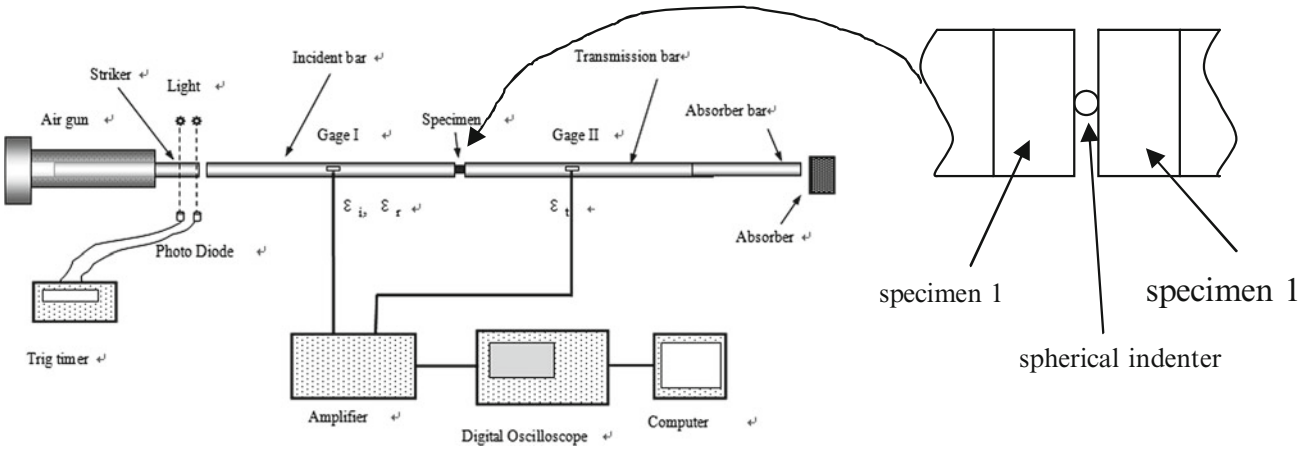

Fig. 10.1 Dynamic spherical indentation device

10.2.2 The Data Processing Method

With The measured data of the incident wave, reflected wave and transmission wave, the indentation load and indentation depth can be calculated using the following equations:

$$\begin{cases} \varepsilon_i(x_{\mathrm{I}}, t) = \varepsilon_i(t - x_1/C_0) \\ \varepsilon_r(x_{\mathrm{I}}, t) = \varepsilon_r(t + x_1/C_0) \\ \varepsilon_t(x_{\mathrm{II}}, t) = \varepsilon_t(t + x_2/C_0) \end{cases} \tag{10.1}$$

$$\begin{cases} \dot{u}(t) = \dfrac{1}{2}C_0(\varepsilon_i(x_{\mathrm{I}}, t) - \varepsilon_r(x_{\mathrm{I}}, t) - \varepsilon_t(x_{\mathrm{II}}, t)) \\ u(t) = \dfrac{1}{2}C_0 \displaystyle\int_0^t (\varepsilon_i(x_{\mathrm{I}}, t) - \varepsilon_r(x_{\mathrm{I}}, t) - \varepsilon_t(x_{\mathrm{II}}, t))dt \\ P(t) = A_0E_0\varepsilon_t(x_{\mathrm{II}}, t) \end{cases} \tag{10.2}$$

Where, C_0 is the bar stress wave speed, E_0 is the Young's modulus of bar material, A_0 is the area of the cross section of the bar, x_1 is the distance between the gage I on incident bar and the bar-specimen face, x_2 is the distance between the gage II on transmission bar and the bar-specimen face, $u(t)$, $\dot{u}(t)$ are the indentation depth and indentation velocity and P is the indentation load.

10.2.3 Evaluating the Experiment

The FEA code ABAQUS is used to simulate the experiment, test and data processing. Figure 10.2 is the Model for simulation. The indentation load and indentation depth can be measured on the model and a virtual experiment can be carried out. For simplicity, the ball is considered as a rigid body. The Johnson cook constitutive model is used for the specimen and the material parameters is show in Tables 10.1 and 10.2. In general, the simulations gives some mixed information and the performance of the device is sensitive to specimen material, geometry and the shape of the loading pulse. Here we only present the better result.

An ideal dynamic spherical indentation model (Fig. 10.3) is built to evaluated the effectivity of the new device. In simulation, the indentation load is calculate from the stress signal at the gage position on the model shown in Fig.10.2 using the Eq. 10.2.

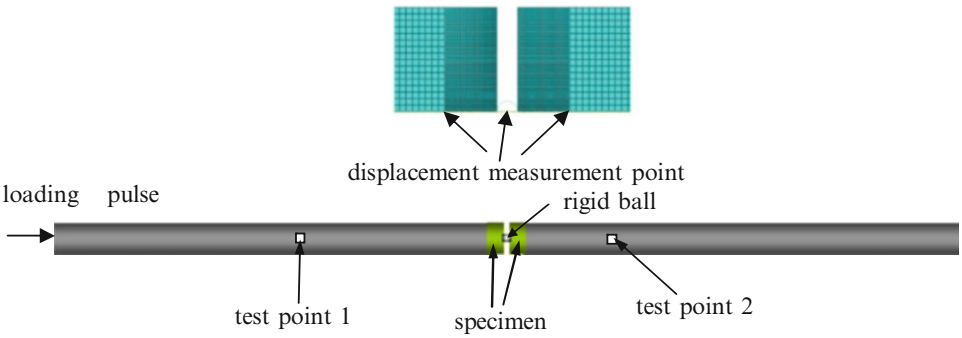

Fig. 10.2 Model for FEA simulation

Table 10.1 Parameters of the bar and specimen

材料	E/GPa	μ	$\rho/g/cm^3$
#45 Steel	210	0.29	7.80
7075T4	70	0.28	2.70

Table 10.2 Parameters of the Johnson-cook constitutive model

Material	A/MPa	B/MPa	C	n	m
45# Steel	1150	739	0.014	0.26	1.03
7075T4	369	684	0.0083	0.73	1.7

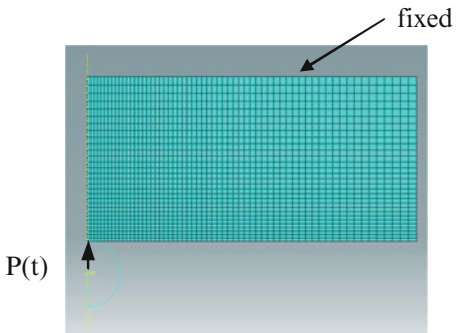

Fig. 10.3 The ideal dynamic indentation experiment arrangement

10.2.4 Some Results of Simulation

For a steel bar SHPB device and aluminum specimen, Fig. 10.4 gives the dynamic indentation pattern (Von Mises Stress Contour). It can be seen, the deformation of the two specimen is approximately symmetric.

The indentation depth of two specimen can be measured on the FEA model (Fig. 10.5). For this situation, the indentation depths are only slightly different.

A virtual dynamic indentation experiment can also be carried out on the FEA model. By measuring the Stress(or Strain) signal at the gage's position and utilizing the Eqs. 10.1, 10.2, and 10.3, the indentation depth and load can be calculated (Figs. 10.6, 10.7, and 10.8) and also the calculated result can be evaluated by comparing the result with the model in Fig. 10.3.

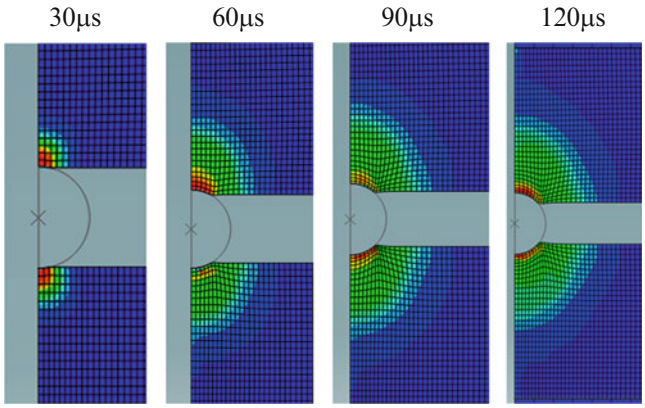

Fig. 10.4 The Von Mises Stress Contour during the indentation

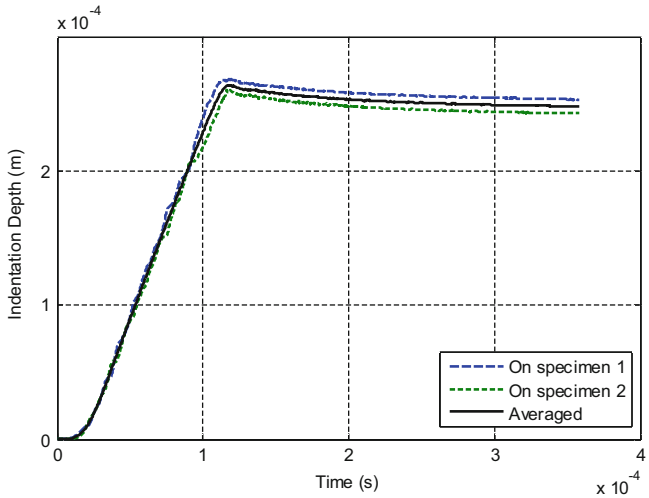

Fig. 10.5 The indentation depth measured on the FEA model

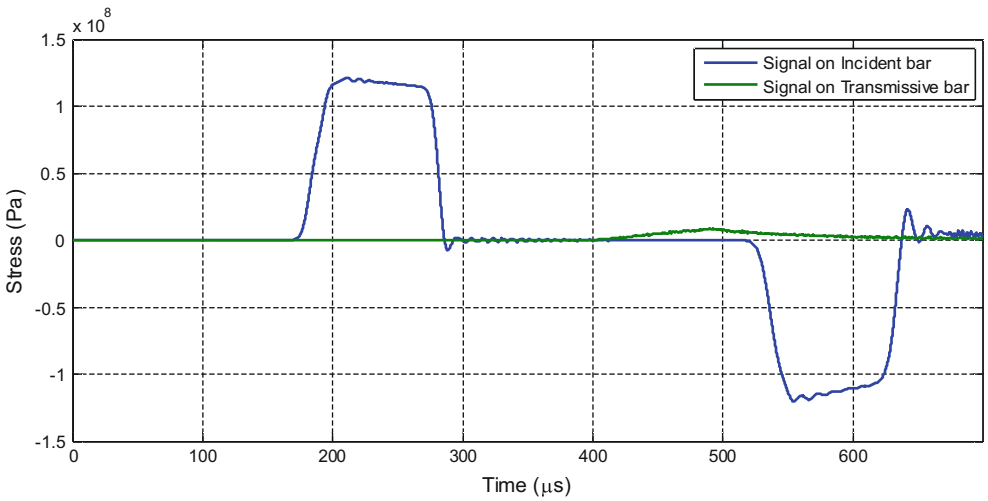

Fig. 10.6 The tested signal waveforms in the virtual dynamic indentation experiment

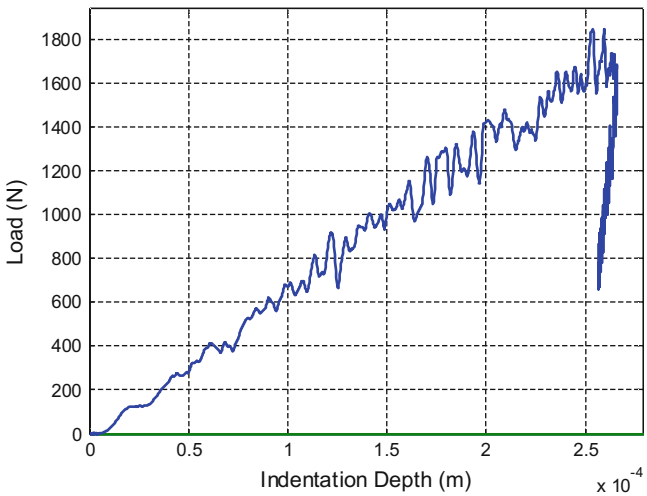

Fig. 10.7 The calculated indentation Depth-Load curve

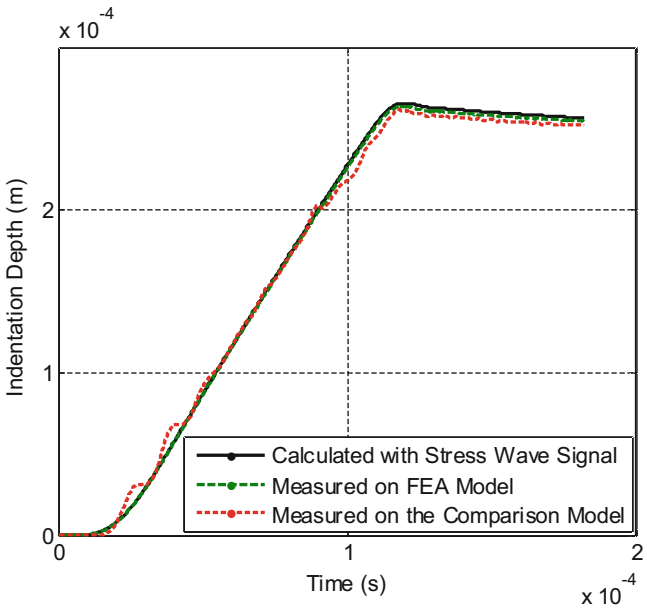

Fig. 10.8 The comparison of indentation depth

The indentation load history can be calculated using Eq. 10.2 with the transmission wave signal (Fig. 10.6) and then this load was applied on the comparison model (ideal dynamic indentation model). By this way, a 'accurate' indentation depth can be obtained on this model. Figure 10.8 shows the depth history obtain in different way. This comparison shows the new experiment method is effective.

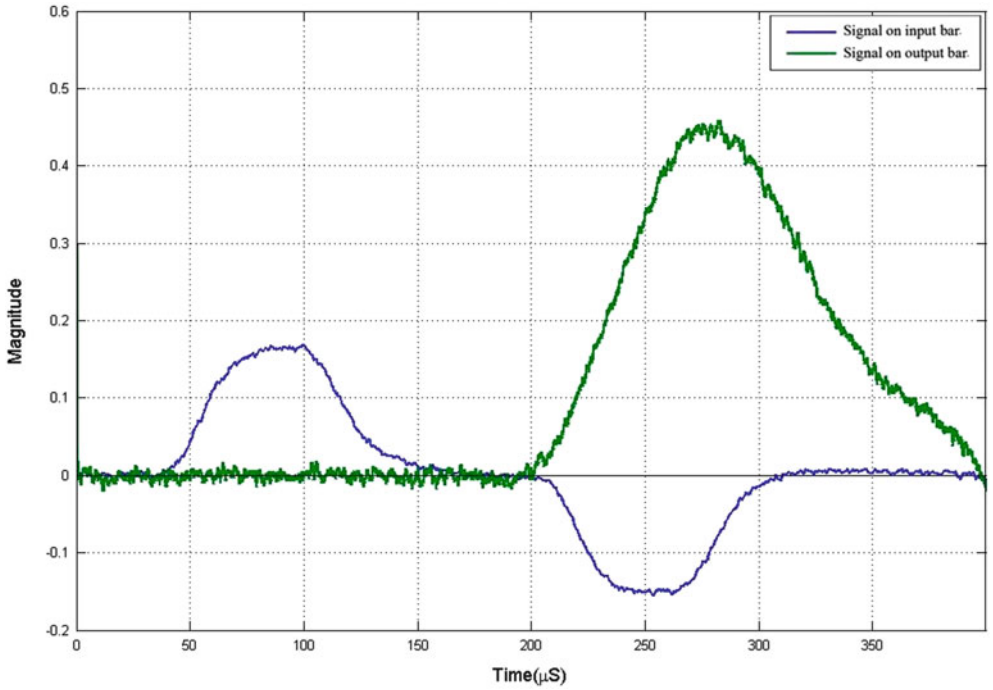

Fig. 10.9 Original experimental waveforms

10.3 Experiment on 7075-T4 Aluminum Alloy

The 7075 T4 aluminum alloy specimens were tested. The aluminum alloy Φ14.5 Hopkinson pressure bar system in Ningbao University and a Φ1.59 tungsten carbide ball are used. The specimen size is Φ12*6. Semiconductor strain gages were used for output bar signal measurement. Figure 10.9 shows a typical experimental waveforms.

With the signal data, the dynamic indentation curve can be obtained. Figure 10.10 give some experimental result.

For a dynamic test, the estimation of experimental strain rate usually is concerned, it can be seen in Fig. 10.4 the deformation distribution is complicated for the indentation test. It is difficult to give the accurate strain rate values. Subhash [1] defined the mean strain rate as the ratio of the indentation velocity and the indentation size. Following him, we can estimate the mean strain rate in the three experiments is above $1 \times 10^4 s^{-1}$.

10.4 Conclusion

A new method for dynamic spherical indentation test is presented. This device is very convenient to build. The data processing is simple also. The effectivity is partially verified by FEA simulation.

Though there are some uncertainties and more detail evaluating needed, it may provide a simple, low cost and accurate experiment method for studying the dynamic mechanical behavior of material at high strain rate.

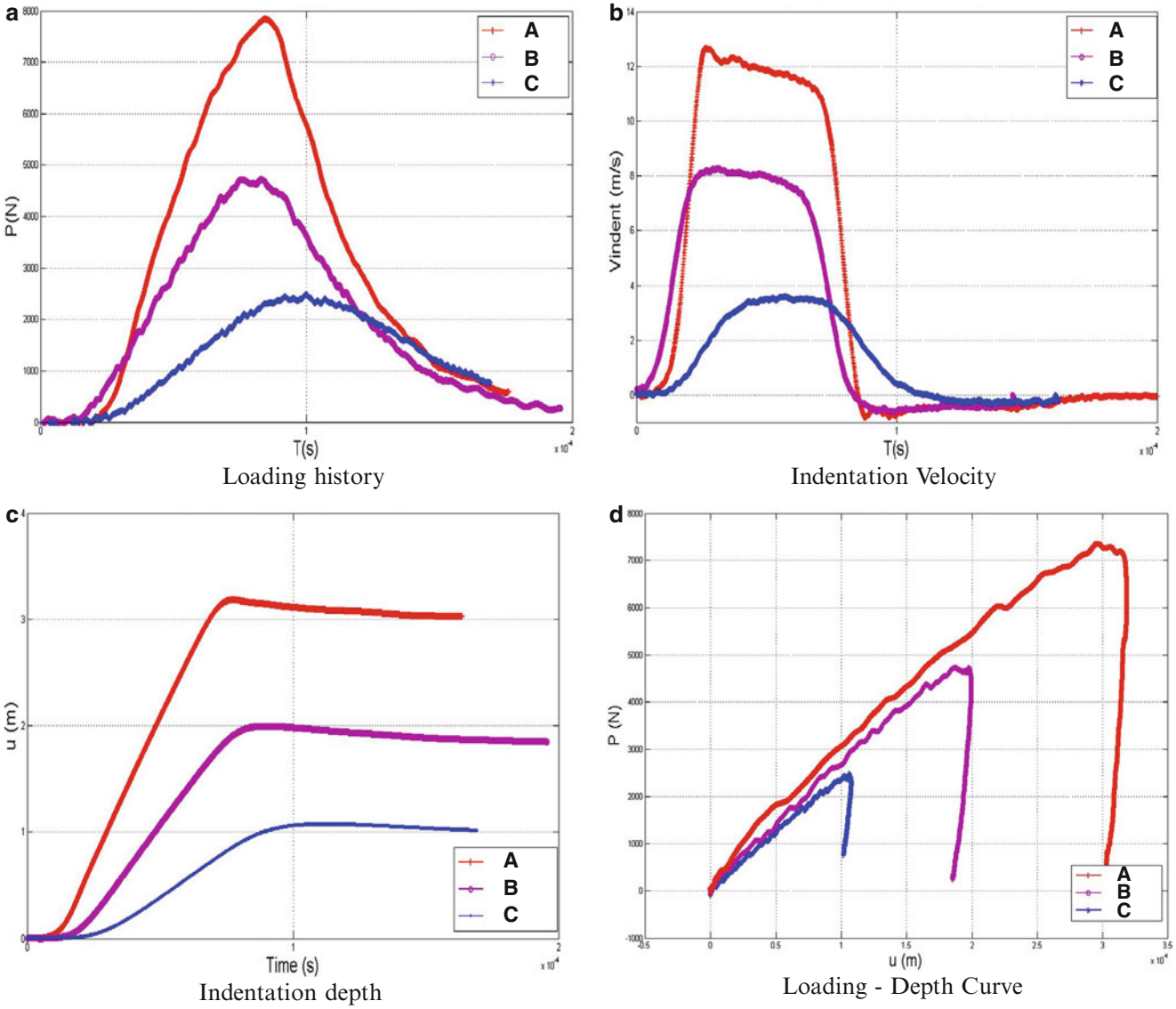

Fig. 10.10 Test result of dynamic spherical indentation experiment

Acknowledgement The authors would like to acknowledge the support from NSF of China, Project No. 11272162.

References

1. Subhash G, Koeppel BJ, Chandra A (1999) Dynamic indentation hardness and rate sensitivity in metals. J Eng Mater Technol 121(3):257–263
2. Nilsson M (2002) Dynamic hardness testing using a split-Hopkinson pressure bar apparatus, methodology report, Swedish deference Research Agency, FOI-R—0447—SE, March 2002
3. Cheng YT, Cheng ZM (2004) Scaling, dimensional analysis, and indentation measurements. Mate Sci Eng R44:91–149

Chapter 11
Analysis and Simulations of Quasi-static Torsion Tests on Nearly Incompressible Soft Materials

Adam Sokolow and Mike Scheidler

Abstract A new torsional Kolsky bar test has been developed at Purdue University in an effort to eliminate the effects of radial inertia that complicate the analysis of compression Kolsky bar tests on soft materials such as brain tissue (Nie X, Prabhu R, Chen W, Caruthers JM, Weerasooriya T (Exp Mech 51(9):1527–1534, 2011); Sanborn B, Nie X, Chen W, Weerasooriya T (J Biomech 45:434–439, 2012); Nie X, Sanborn B, Weerasooriya T, Chen W (Int J Impact Eng 53:56–61, 2013). In an effort to quantify the complete stress and strain states in this torsion test as well as to determine the influence of any inertial effects on the test data, we have undertaken numerical simulations of both dynamic and quasi-static torsion tests on very soft and nearly incompressible materials. Here we present the results of our quasi-static torsion simulations on nonlinear elastic specimens. Results are presented for thin solid (disc-shaped) specimens and thin annular (washer-shaped) specimens, although only the latter are used in the Purdue Kolsky bar tests. On the other hand, a pure torsional deformation is possible only for incompressible solid specimens. The differences between the stress states in solid and annular specimens provides insight into axially nonuniform stresses that develop in annular specimens. In addition, explicit closed-form solutions for the full stress state for pure torsion of an incompressible solid specimen have been used to verify the numerical simulations.

Keywords Torsion • Kolsky bar • Soft materials • Incompressible • Mooney-Rivlin

11.1 Introduction

Fully nonlinear, viscoelastic constitutive models are required to capture the strain-rate sensitivity of soft tissues, and parametrization of these models requires well-controlled, high-rate material characterization tests. Kolsky bar tests have traditionally been used to study the strain-rate effects in inelastic solids (cf. Gray [1], Chen and Song [2]). In a compression Kolsky bar test, a compressive wave is generated in an incident bar and travels through the specimen into a transmission bar, subjecting the specimen to a state of uniaxial stress. Assuming the specimen is in dynamic equilibrium with the bars, the strain measured in the elastic bars is used to deduce the axial stress, strain and strain-rate in the specimen by considering the incident, transmitted, and reflected waves. A similar approach utilizes a torsional wave in the Kolsky bar instead of a compressive wave [3, 4].

The standard Kolsky bar techniques work very well on metals, composites and stiff polymers, but considerable difficulties are encountered for gelatins and soft biological specimens that are nearly incompressible. In the latter cases, the impedance mismatch between the bars and the specimen results in most of the incident wave being reflected, in which case the strain gages on the bars do not register useful signals. Axial inertial effects also become important as the slower specimen wave speeds require longer times to reach dynamic equilibrium. Furthermore, radial inertia effects in compression tests result in stress states that are not uniaxial, i.e., significant radial and hoop stresses that cannot be measured [5–7]. Studies utilizing compression Kolsky bar techniques purportedly removed radial inertia effects by switching from solid to annular specimens [2]. It was later shown that annular specimens are also plagued by radial inertia effects and that the observed increases in axial stress at high strain-rates were falsely attributed to viscoelastic properties of the specimen [6, 8, 9].

A. Sokolow • M. Scheidler (✉)
Soldier Protection Sciences Branch, US Army Research Laboratory, Aberdeen Proving Ground, Aberdeen, MD 21005, USA
e-mail: michael.j.scheidler2.civ@mail.mil

B. Song et al. (eds.), *Dynamic Behavior of Materials, Volume 1: Proceedings of the 2013 Annual Conference on Experimental and Applied Mechanics*, Conference Proceedings of the Society for Experimental Mechanics Series,
DOI 10.1007/978-3-319-00771-7_11,

Recently, a variation of the torsional Kolsky bar test has been used to study the strain-rate sensitivity of nearly incompressible, soft materials such as brain tissue [8, 10, 11]. In this modified torsion test, the transmission bar is replaced with a torque load cell and the faces of the relatively thin annular specimens are glued to the bar and the load cell. A shear stress vs. shear strain curve is deduced from the strain measured in the incident bar and the torque measured at the load cell. Comparison of stress-strain curves at different rates yields information on the rate-sensitivity of the shear stress. The effects radial inertia in this torsional Kolsky bar test are expected to be much lower than in a compression test at the same strain-rate. However, a preliminary theoretical analysis (not included here) indicates that for specimens as soft as brain tissue and for strain-rates on the order of $500/\mathrm{s}$ or higher, angular inertia effects may be significant.

The torsion and compression tests on soft materials differ in another significant way. As noted above, for compression tests the desired uniaxial stress state may be impossible to achieve dynamically, but uniaxial stress can always be achieved quasi-statically if frictional effects at the specimen faces are negligible. However, even in a quasi-static torsion test the desired state of pure shear stress is impossible to achieve except for infinitesimal deformations. Significant axial and hoop stresses develop in solid and annular torsion specimens, and significant radial stresses also develop in solid specimens. Furthermore, the boundary conditions for annular specimens result in axial variations in the hoop and axial stresses even in a quasi-static test. Thus, unlike quasi-static compression tests, the stress state in quasi-static torsion tests on soft materials is already quite complicated, and inertial effects in the corresponding dynamic test will further complicate these stress states. Even if the full stress state could be measured in a dynamic torsion test, it would be difficult to sort out the role of inertial effects from nonlinear elastic (or viscoelastic) effects without results for the corresponding quasi-static case for comparison. This problem is compounded by the fact that in the Kolsky bar test only the torque on one face of the specimen can be measured; hence, only the torsional (θz) stress component can be inferred, and this is known only on the face of the specimen in contact with the load cell.

In view of these issues, we have undertaken numerical simulations of both dynamic and quasi-static torsion tests on soft and nearly incompressible materials. Unlike a real torsion test, the simulations provide the complete stress and strain states at each point in the specimen, although a constitutive model must necessarily be assumed. The nonlinear elastic constitutive model used for the specimen in our simulations is a compressible version of the well-known Mooney-Rivlin model for incompressible materials, with bulk and shear moduli chosen to yield a nearly incompressible material. Although soft tissues are viscoelastic, and the goal of Kolsky bar tests is to quantify their strain-rate sensitivity, elastic constitutive models are particularly useful for studying inertial effects. The stress in an elastic material is rate-independent, thus any differences between the quasi-static and dynamic simulations of the torsion test must necessarily be due to inertial effects.

In this paper we present the results of our quasi-static simulations, which serve as a baseline for understanding the dynamic torsion simulations that are in progress. We have performed a parametric study of the two parameters (the shear modulus and a non-dimensional parameter) that characterize the deviatoric stress in the Mooney-Rivlin model. We also consider both thin solid (disc-shaped) specimens and thin annular (washer-shaped) specimens, although only the latter have been used in the Purdue Kolsky bar tests. However, explicit closed-form solutions for the full stress state are available only for the solid specimen. These solutions have been used to verify the numerical simulations. In addition, the differences between the stress states in solid and annular specimens provide insight into axially nonuniform stresses that develop in annular specimens.

The paper is organized as follows. Section 11.2 contains an analysis of pure torsion of a general incompressible isotropic elastic specimen which may be solid or annular. At the end of that section we discuss the departures from pure torsion that are expected for annular specimens. In Sect. 11.3, the results of Sect. 11.2 are applied to the special case of an incompressible Mooney-Rivlin material. Explicit expressions are available for the normal stress components and the pressure in this case. In Sect. 11.4 we compare the results of our numerical simulations of quasi-static torsion on solid and annular specimens of a nearly incompressible Mooney-Rivlin material. We also compare these results with the theoretical predictions in the previous sections. Section 11.5 contains some concluding remarks. Additional details regarding the simulations are given in the Appendix.

11.2 Torsion of an Incompressible Isotropic Elastic Material

Our theoretical analysis of torsion of incompressible isotropic elastic materials is divided into four sections. In Sect. 11.2.1 we discuss a particular representation for the general class of incompressible isotropic elastic materials.[1] Section 11.2.2 contains an analysis of pure torsional deformation and a derivation of those relations for the stress components that are

[1] The linear theory of elasticity is valid only for infinitesimal deformations. Here an *elastic material* refers to the general *nonlinear*, properly invariant theory of elasticity, unless specified otherwise. The special case of the Mooney-Rivlin model will be discussed later in this section.

independent of the boundary conditions on the lateral surface(s). In Sect. 11.2.3 we impose the condition that the outer lateral surface be stress-free and use the radial equilibrium equation to complete the determination of the full stress state. Section 11.2.4 contains a brief discussion of more general classes of torsional deformations that may be more appropriate for annular specimens. General background for the material in this section can be found in the books by Truesdell and Noll [12], Gurtin [13], and Batra [14].

11.2.1 Incompressible Isotropic Elastic Materials

The Cauchy stress tensor $\boldsymbol{T}$ can decomposed into a pressure (or hydrostatic stress) p and a deviatoric stress tensor $\boldsymbol{S}$ (i.e., tr $\boldsymbol{S} = 0$):

$$T = -p\,I + S\,, \qquad p \equiv -\frac{1}{3}\,\mathrm{tr}\,T\,, \qquad S = \mathrm{dev}\,T \equiv T - \frac{1}{3}\,(\mathrm{tr}\,T)I\,, \tag{11.1}$$

where $\boldsymbol{I}$ denotes the identity tensor. The standard sign convention for the Cauchy stress tensor is used in this paper: normal stress components are taken positive in tension. For a compressible (i.e., unconstrained) material, constitutive relations must be provided for p and $\boldsymbol{S}$. However, for an incompressible material the Cauchy stress tensor $\boldsymbol{T}$ is given by:

$$T = -\hat{p}\,I + \hat{S}\,, \tag{11.2}$$

where $\hat{p}$ is an indeterminate scalar and $\hat{S}$ is the determinate part of the stress, which need not be deviatoric. The indeterminacy of $\hat{p}$ means that it is not subject to any constitutive relation. However, the value of $\hat{p}$ at each point must be such that the boundary conditions and momentum balance (or in the quasi-static case, the equilibrium equations) are satisfied. Equations (11.1) and (11.2) imply that

$$p = \hat{p} - \tfrac{1}{3}\,\mathrm{tr}\,\hat{S}\,, \qquad S = \mathrm{dev}\,\hat{S}\,. \tag{11.3}$$

For an incompressible material the pressure p is also indeterminate, but $\hat{p}$ and p are generally not equal; nevertheless, some authors refer to $\hat{p}$ as the "pressure".

For an incompressible elastic material the determinate stress $\hat{S}$ is, by definition, a function of the deformation gradient $\boldsymbol{F}$. If the material is also isotropic, then $\hat{S}$ is an isotropic function of the left Cauchy-Green deformation tensor $\boldsymbol{B} = \boldsymbol{F}\boldsymbol{F}^T$. A general representation for such functions is given by:

$$\hat{S} = \mu\,\left[\,\omega B - (1-\omega)B^{-1}\right] = 2\,C_{10}B - 2\,C_{01}B^{-1}, \tag{11.4}$$

where the elastic moduli C_{10}, C_{01} and μ and the dimensionless parameter ω are scalar-valued functions of tr$\boldsymbol{B}$ and tr($\boldsymbol{B}^{-1}$). Note that $C_{10} = \frac{1}{2}\mu\,\omega$ and $C_{01} = \frac{1}{2}\mu(1-\omega)$. It has been found that the inequalities $C_{10} > 0$ and $C_{01} \geq 0$ imply physically reasonable response and are consistent with experimental data on nearly incompressible isotropic elastic solids; equivalently, $\mu > 0$ and $0 < \omega \leq 1$. These inequalities are assumed throughout the paper.

11.2.2 Pure Torsion

Torsion of a solid cylinder or cylindrical tube of an incompressible isotropic elastic material is commonly covered in text books on continuum mechanics (cf. [12, 14, 15]). Let (r, θ, z) and (R, Θ, Z) denote the deformed and reference coordinates of a material point relative to a cylindrical coordinate system. In the undeformed reference configuration, the cylinder has length L (along the Z-axis) and (outer) radius R_o; for an annular specimen the inner radius is R_i. The end of the cylinder at $Z = 0$ is fixed while the other end ($Z = L$) is rotated by an angle $\Psi(t)$, where t denotes time. This results in an angle of twist per unit length $\psi(t) = \Psi(t)/L$. A *pure torsional deformation* is given by:

$$r = R\,, \qquad \theta = \Theta + \psi(t)Z\,, \qquad z = Z\,, \tag{11.5}$$

Note that there is no change in the length or the radius of the specimen. For the pure torsional deformation (11.5), the physical components of $\boldsymbol{F}$, $\boldsymbol{B}$ and $\boldsymbol{B}^{-1}$ (i.e., their components relative to the unit basis vectors along the cylindrical coordinate directions) are given by:

$$[F] = \begin{bmatrix} 1 & 0 & 0 \\ 0 & 1 & \psi r \\ 0 & 0 & 1 \end{bmatrix}, \qquad [B] = \begin{bmatrix} 1 & 0 & 0 \\ 0 & 1+\psi^2 r^2 & \psi r \\ 0 & \psi r & 1 \end{bmatrix}, \qquad [B^{-1}] = \begin{bmatrix} 1 & 0 & 0 \\ 0 & 1 & -\psi r \\ 0 & -\psi r & 1+\psi^2 r^2 \end{bmatrix}. \tag{11.6}$$

Thus pure torsion is radially inhomogeneous. Since $\mathrm{tr}B = \mathrm{tr}(B^{-1}) = 3+\psi^2 r^2$, the functions C_{10}, C_{01}, μ and ω in Eq. (11.4) depend only on $\psi^2 r^2$ in this case. The Eulerian finite strain tensors corresponding to $\boldsymbol{B}$ and $\boldsymbol{B}^{-1}$ are $E = \frac{1}{2}(B - I)$ and $\mathcal{E} = \frac{1}{2}(I - B^{-1})$; the latter is known as the Almansi strain tensor. Both $\boldsymbol{E}$ and $\mathcal{E}$ reduce to the infinitesimal strain tensor $\boldsymbol{\varepsilon}$ in the small strain limit. For pure torsion the only nonzero off-diagonal component of $\boldsymbol{E}$ and $\mathcal{E}$ is

$$E_{\theta z} = \mathcal{E}_{\theta z} = \frac{1}{2}\psi r\,, \tag{11.7}$$

which we take as our measure of shear strain in pure torsion.

For pure torsion of an incompressible isotropic elastic material, Eqs. (11.2), (11.4), (11.6) and (11.7) imply that the shear stress components are given by:

$$T_{\theta z} = \mu\psi r = 2\mu E_{\theta z}\,, \qquad T_{rz} = T_{r\theta} = 0\,; \tag{11.8a}$$

and the differences in the normal stress components are given by:

$$T_{\theta\theta} - T_{zz} = \mu\psi^2 r^2\,, \qquad T_{\theta\theta} - T_{rr} = \mu\omega\psi^2 r^2\,, \qquad T_{rr} - T_{zz} = \mu(1-\omega)\psi^2 r^2\,. \tag{11.8b}$$

We refer to the shear stress component $T_{\theta z}$ as the *torsional stress*. It is clear from Eq. (11.8a) that μ can be interpreted as a (generally strain-dependent) shear modulus.

From the relations in (11.8) we see that the normal stress differences are proportional to the torsional stress:

$$T_{\theta\theta} - T_{zz} = \psi r \cdot T_{\theta z}\,, \qquad T_{\theta\theta} - T_{rr} = \omega\psi r \cdot T_{\theta z}\,, \qquad T_{rr} - T_{zz} = (1-\omega)\psi r \cdot T_{\theta z}. \tag{11.9}$$

Note that relations identical to (11.8) and (11.9) hold for the deviatoric stress tensor $\boldsymbol{S}$, since the pressure term in $(11.1)_1$ does not contribute to the off-diagonal components and the pressure cancels from the normal stress differences. The relation on the left in (11.9) is the well-known *universal relation* between the hoop, axial and torsional stress. The term "universal" refers to the fact that this relation does not explicitly involve the constitutive functions (e.g., μ or ω in the representation (11.4)).

11.2.3 Pure Torsion with Stress-Free Outer Boundary

If we proceed as above and use the relations (11.2), (11.4) and (11.6) to evaluate the normal stress components (as opposed to their differences) we find that they are indeterminate. For example, $T_{rr} = -\hat{p} + \mu(2\omega - 1)$, where the indeterminacy in $\hat{p}$ results in an indeterminacy in T_{rr}. In order to solve for the normal stress components for a quasi-static pure torsion, we need to invoke the equation for radial equilibrium and the stress-free boundary condition on the outer lateral surface. Since $T_{r\theta}$ and T_{rz} are zero, the radial equilibrium equation reduces to

$$\frac{\partial T_{rr}}{\partial r} + \frac{T_{rr} - T_{\theta\theta}}{r} = 0\,. \tag{11.10}$$

Rather than first solving for $\hat{p}$ and using this in the relation above for T_{rr}, it is simpler to solve for T_{rr} directly. Indeed, on using (11.8b) to evaluate the $T_{rr} - T_{\theta\theta}$ term above, integrating from r to R_o, and then using the fact that $T_{rr} = 0$ at $r = R_o$, we obtain the following relation for the radial stress:

$$T_{rr} = -\psi^2 \int_r^{R_o} \mu\omega r \, dr \, . \tag{11.11}$$

Then from (11.8b) we see that the hoop and axial stresses are given by:

$$T_{\theta\theta} = T_{rr} + \mu\omega\psi^2 r^2 \, , \qquad T_{zz} = T_{rr} - \mu(1-\omega)\psi^2 r^2 \, . \tag{11.12}$$

Since μ and ω are functions of $\psi^2 r^2$, and these functions are essentially arbitrary, the integral in (11.11) cannot be evaluated in closed form except in special cases. However, since μ and ω are positive, important qualitative conclusions may be inferred directly from (11.11) and (11.12), as summarized below.[2] In the following we assume that the angle of twist Ψ and hence the angle of twist per unit length, ψ, is nonzero.

For pure torsion of an incompressible *solid or annular specimen* with a stress-free outer surface:

Conclusion 1. T_{rr} is negative for $r < R_o$. Thus the radial stress is compressive except at the outer surface where it is zero.

Conclusion 2. Since $T_{rr} < 0$ for $r < R_o$, it follows that $T_{zz} < 0$ for $r < R_o$; furthermore, T_{zz} is also negative for $r = R_o$ unless $\omega = 1$, in which case $T_{zz}|_{r=R_o} = 0$. Thus the axial stress is compressive everywhere except possibly at the outer surface $r = R_o$, where it is either compressive or zero.

Conclusion 3. Since $T_{rr}|_{r=R_o} = 0$, it follows that the hoop stress $T_{\theta\theta}$ is positive (i.e., tensile) at the outer lateral surface.

Conclusion 4. The radial, hoop, and axial stresses depend on both constitutive functions μ and ω, while the torsional stress is independent of ω. It follows that *no information on the dimensionless constitutive function ω can be inferred from measurements of the torsional stress $T_{\theta z}$ alone*.

For a solid specimen, the relations (11.11) and (11.12) imply that $-T_{rr} = -T_{\theta\theta} = -T_{zz} = p > 0 \quad at \quad r = 0$. Also, recall that $T_{\theta\theta} > 0$ at $r = R_o$ (Conclusion 3).

Thus for pure torsion of an incompressible *solid specimen* with a stress-free outer surface:

Conclusion 5. The material is in a state of hydrostatic compression on the axis of the specimen ($r = 0$).

Conclusion 6. The hoop stress changes sign from compressive to tensile at some radial location in the interior.

Since Conclusion 1 applies to solid or annular specimens, for annular specimens we see that $T_{rr}|_{r=R_i} < 0$:

Conclusion 7. For pure torsion of an incompressible *annular specimen* with a stress-free outer surface, a non-zero, compressive normal stress must be applied on the inner surface in order that radial equilibrium be satisfied.

11.2.4 Radially Non-uniform Torsional Deformations for Annular Specimens

Conclusion 7 implies that for incompressible annular specimens, a class of torsional deformations more general than pure torsion must be considered if both the outer and inner lateral surfaces are stress-free. Recall that a pure torsional deformation, by definition, does not involve any radial displacement. If on the other hand, we consider torsional deformations for which the specimen may deform radially (i.e., $r = \hat{r}(R, t)$), then it is possible to satisfy radial equilibrium as well as the stress-free boundary condition on the inner and outer surfaces. In this case it can be shown that the only volume preserving deformations consistent with Eqs. $(11.5)_{2,\,3}$ are of the general form:

$$r = \sqrt{R^2 + \beta(t)} \, , \qquad \theta = \Theta + \psi(t) Z \, , \qquad z = Z \, . \tag{11.13}$$

Note that Eq. $(11.13)_1$ reduces to $r = R$ iff $\beta(t) \equiv 0$. The value of $\beta(t)$ necessary for the satisfaction of radial equilibrium and both stress-free boundary conditions depends on the angle of twist and the particular constitutive equation for the material (within the class of incompressible isotropic elastic materials); only an implicit relation for β can be derived.

[2] Some of these conclusions can be found in Truesdell and Noll [12]; others appear to be new.

Although the torsional deformation (11.13) is of some theoretical interest, it would be difficult to apply a torque on the face of a specimen while admitting a radial deformation. In particular, this class of torsional deformations is not relevant to the quasi-static version of torsional Kolsky bar test, since the faces of the specimen are glued to the bar and the load cell and hence are not free to deform radially. Nevertheless, it is clear from the discussion above that at axial locations between the two faces, an annular specimen will have a tendency to deform radially in order to satisfy the stress-free boundary conditions on the inner and outer surfaces. Since relatively short annular specimens are used, the constraints at either end of the specimen can be expected to severely restrict (though not completely eliminate) the radial deformation in the interior. It is not clear whether any of the four conclusions on the previous page continue to hold in this case. We rely on numerical simulations for quantitative estimates since a theoretical analysis of this problem is intractable.

11.3 Pure Torsion of an Incompressible Mooney-Rivlin Material

In our torsion simulations we used a compressible version of the Mooney-Rivlin for the specimen. The classical Mooney-Rivlin constitutive model is an incompressible isotropic elastic model originally proposed for elastomers (cf. [12, 14]). It is also commonly used for softer nearly incompressible materials since it exhibits many of the qualitative features observed experimentally in large strain deformations of such materials. The determinate stress $\hat{S}$ for the incompressible Mooney-Rivlin model is given by (11.4) with the functions C_{10}, C_{01}, μ and ω taken to be constants. For infinitesimal deformations this leads to $\boldsymbol{S} = 2\mu \operatorname{dev} \boldsymbol{\varepsilon}$, where $\boldsymbol{\varepsilon}$ is the infinitesimal strain tensor. Thus μ agrees with the shear modulus in the linear theory of elasticity. The special case $\omega = 1$ (equivalently, $C_{01} = 0$) is known as a neo-Hookean material.

For the incompressible Mooney-Rivlin model the relations (11.8) and (11.9) do not simplify further (aside from the fact that μ and ω are now constants), but the relations (11.11) and (11.12) reduce to:

$$T_{rr} = -\frac{1}{2}\,\mu\psi^2 \cdot \omega\big(R_o^2 - r^2\big), \tag{11.14a}$$

$$T_{\theta\theta} = \frac{1}{2}\,\mu\psi^2 \cdot \omega\big(3r^2 - R_o^2\big), \tag{11.14b}$$

$$T_{zz} = -\frac{1}{2}\,\mu\psi^2 \cdot \big[\omega R_o^2 + (2 - 3\omega)r^2\big]. \tag{11.14c}$$

These relations, together with $p = -\frac{1}{3}(T_{rr} + T_{\theta\theta} + T_{zz})$, imply that the pressure is given by:

$$p = \frac{1}{2}\,\mu\psi^2 \cdot \left[\omega R_o^2 + \frac{1}{3}(2 - 7\omega)r^2\right]. \tag{11.15}$$

The relations (11.14) and (11.15) are valid for both solid and annular specimens. All of the qualitative results discussed in the previous section still apply, of course. In particular, for an annular specimen of an incompressible Mooney-Rivlin material, a compressive normal (i.e., radial) stress must be applied to the inner lateral surface $r = R_i$ to maintain a quasi-static pure torsion. As noted in the previous section, the more general class of torsional deformations (11.13) permits a stress-free inner surface for an appropriate choice of $\beta(t)$, but even for a Mooney-Rivlin material β can only be given implicitly. The relation is given in §95 of Truesdell and Noll [12]: β depends on ω, ψ, R_i and R_o, but is independent of μ.

For pure torsion of a solid specimen, the relations (11.14) and (11.15) now yield an explicit relation for the hydrostatic stress state on the axis of the specimen:

$$-T_{rr} = -T_{\theta\theta} = -T_{zz} = p = \frac{1}{2}\,\omega\mu\psi^2 R_o^2 > 0 \quad \textit{at} \quad r = 0\,. \tag{11.16}$$

From (11.15) it follows that p decreases with r if $\frac{2}{7} < \omega \le 1$; p is constant if $\omega = \frac{2}{7}$; and p increases with r if $0 < \omega < \frac{2}{7}$. While the pressure is compressive at the center, as shown by (11.16), at the outer surface it is tensile for $0 < \omega < \frac{1}{2}$, zero for $\omega = \frac{1}{2}$, and compressive for $\frac{1}{2} < \omega \le 1$. Thus for $0 < \omega < \frac{1}{2}$, the pressure changes sign in the interior of the specimen.

11.4 Numerical Simulations of Quasi-static Torsion

In this section we supplement our theoretical results on pure torsion with numerical simulations for both solid and annular specimens. Dimensions of the specimen were chosen for comparison to previous experiments [8, 10, 11]. The solid specimen was defined as a cylinder of radius $R_o = 9.5$ mm and length $L = 1.7$ mm, giving a length-to-diameter ratio of 0.09. The annular specimen was similar in size except for the removal of a core of radius $R_i = 7.35$ mm. One face of the specimen was subjected to a rigid rotation while the other face was fixed, so that material points on either face could not undergo axial or radial displacements.[3] Stress-free boundary conditions were used on the outer surface $r = R_o$ and, for the annular specimen, on the inner surface $r = R_i$.

In our torsion simulations we used a compressible version of the Mooney-Rivlin for the specimen. The equation of state for the pressure in this model is

$$p = -\kappa \ln J \approx \kappa(1 - J)\,, \qquad J = \det F\,, \tag{11.17}$$

where κ is the bulk modulus. We used $\kappa = 2.3$ GPa for all simulations; this is the bulk modulus of water and approximates the bulk modulus of many gelatins and soft tissues (such as brain tissue). The shear modulus was varied by almost three orders of magnitude: $\mu = 800, 80, 8$ and 2 kPa; the lowest value is commonly used for brain tissue. The corresponding ratios of bulk to shear modulus varied from 2,875 to 1.15×10^6, so that in all cases the material was nearly incompressible. For each value of the shear modulus, simulations were performed for three values of the non-dimensional parameter ω: 0.3, 0.6, and 1 (neo-Hookean model). This resulted in 12 simulations each for the solid and annular specimens.

In order to condense the information from all of these simulations and also to more clearly display the relative magnitude of the stresses in each case, in Figs. 11.1 and 11.2 all stress components have been normalized by an appropriate "maximum" torsional stress, and the same non-dimensional vertical scale is used for all plots. The normalization is different for the two figures (as discussed below), but in each case the base symbol T^* is used for the normalized stress components.

In Fig. 11.1 we examine the radial variation in the torsional and normal stress components at an axial location in the middle of the specimen ($Z = L/2$). The angle of twist is $\Psi = 0.1$ radians; the angle of twist per unit length is $\psi = 0.059$ radians/mm. The corresponding shear strain $E_{\theta z} = \frac{1}{2}\psi r$ varies from 0 to 0.28 for the solid specimen and from 0.22 to 0.28 for the annular specimen. All stress components have been normalized by $\mu\psi R_o$, which is the maximum torsional stress that would occur in a pure torsional deformation. Results for the solid and annular specimens are given in the left and right columns, respectively. Each of the 8 plots in the figure contain 12 curves – one for each of the 12 simulations, as discussed above.

For the normalized torsional stress $T^*_{\theta z}$, the 12 curves are indistinguishable for both the solid and annular specimen. This is consistent with the theoretical relation (11.8a) for $T_{\theta z}$ for the case of pure torsion of an incompressible Mooney-Rivlin material, which implies that $T^*_{\theta z} = \mu\psi r/\mu\psi R_o = r/R_o$, independent of μ or ω. For both specimen geometries, the line r/R_o (not plotted) would be indistinguishable from the curves in the top plots, the maximum error in each case being less than 1 %.

The theoretical relations (11.14) predict that each of the normal stress components are also proportional to the shear modulus μ for pure torsion of an incompressible Mooney-Rivlin material. In this case the normalized stress components T^*_{rr}, $T^*_{\theta\theta}$ and T^*_{zz} would be independent of μ, resulting in at most three distinguishable curves – one for each of the three values of ω. This feature is observed in Fig. 11.1 for both specimen geometries. In fact, for the annular specimen the normalized radial stresses are so small that all the curves are indistinguishable from the horizontal axis $T^*_{rr} = 0$.

For the solid specimen the normal stresses in the simulations agree very well with the theoretical predictions (11.14) for pure torsion of an incompressible Mooney-Rivlin material; the maximum differences were a few percent and would not be distinguishable on the plots. Since it is clear from Fig. 11.1 that the normal stresses in the annular specimen simulations do not agree (even qualitatively) with those for the solid specimen, it follows that they do not agree with the theoretical predictions for pure torsion of an incompressible Mooney-Rivlin material. Of course, the fact that the radial stress is essentially zero throughout the annular specimen is not unexpected in view of the fact that it is zero on the inner and outer lateral surfaces.

The primary motivation for using annular specimens in torsion tests is that the shear or torsional stress $T_{\theta z}$ and the shear strain $E_{\theta z}$ are radially nonuniform, and smaller variations in these quantities are expected for annular specimens. For the torsional stress this is verified in the top plots in Fig. 11.1. Data from torsion tests is typically plotted as volume-averaged shear stress vs. volume-averaged shear strain, with the averages inferred from the measured torque and angle of twist.

[3] Actually, for the solid specimen this statement requires some qualification. Refer to the Appendix for additional details.

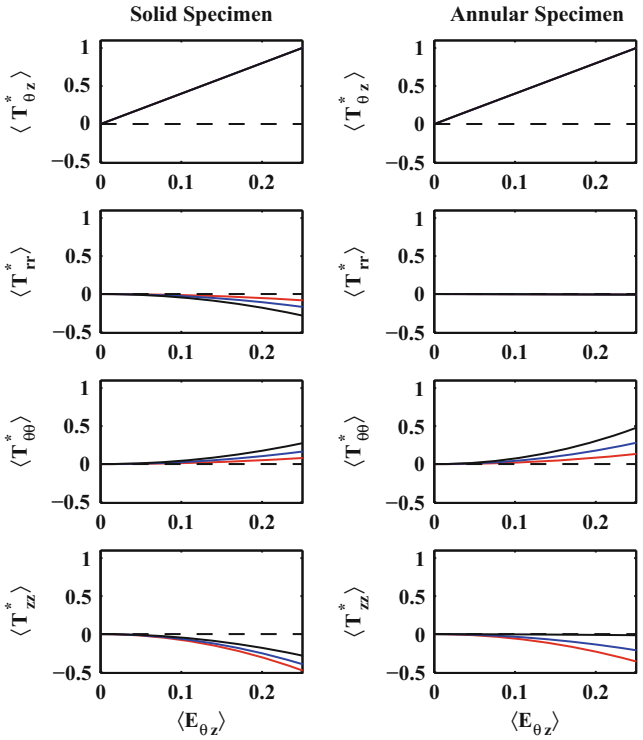

Fig. 11.1 A family of curves of the stress state as it depends on the referential radius for both the solid and annular specimen, shown are three decades of shear modulus ($\mu = 800$, 80, 8, and 2 kPa). Here a T^* denotes that the stress has been normalized to the maximal shear stress, i.e., divided by $\mu\psi R_o$. For each shear modulus, $\omega = 0.3$ (*red*), $\omega = 0.6$ (*blue*), and $\omega = 1.0$ (*black*) are shown. Note, due to the normalization, decades of shear moduli can be plotted on the same scale and collapse to a single *color line* depending on ω. Radial values taken along $Z = L/2$ (color figure in online)

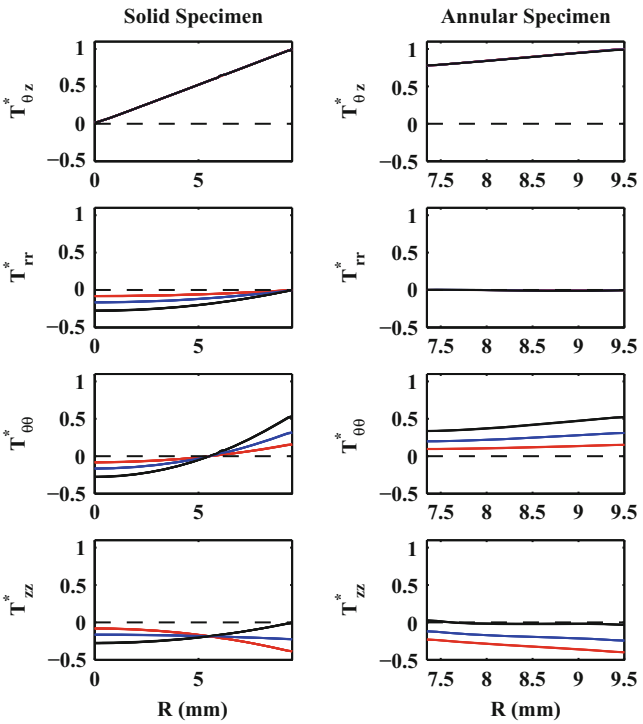

Fig. 11.2 Volume-averaged stress vs. volume-averaged strain for a shear modulus $\mu = 80$ kPa and $\omega = 0.3$ (*red*), $\omega = 0.6$ (*blue*), and $\omega = 1.0$ (*black*). Here a $\langle T^* \rangle$ denotes that the average stress has been normalized by the average shear stress for the solid specimen at the final average Eulerian shear strain of 0.25 (color figure in online)

Figure 11.2 reports the volume-averaged stress-strain curves obtained from the numerical simulations discussed above, but only the results for the $\mu = 80$kPa case are considered here. As in the previous figure, normal stress components are also included. Volume-averaged quantities are inclosed in angle brackets. All stresses have be normalized by the average torsional stress for the solid specimen at the final average shear strain of 0.25.

The top two panels in Fig. 11.1 show that the average shear stress is virtually unaffected by hollowing out the solid specimen. The ratio of normal to shear stress increases with strain. Consideration of Eqs. (11.14) in conjunction with Figs. 11.1 and 11.2 show that the shear stress depends linearly on ψ, while the remaining diagonal components depend quadratically on ψ. Thus for larger angles of twist or for thin specimens the normal stresses will become larger than the shear stress. Note that the figures have been normalized so that the shear stress at shear strain of 0.25 is of order unity (total angle of twist of roughly 8°). A smaller shear strain of 0.1 in the annular specimen gives an average hoop stress that is 5–20 % of the shear stress depending on ω, and an average axial stress 1–15 % of the shear stress.

For the normal stress components, the differences in results for the two specimen geometries are more subtle. Symmetry and momentum balance require that the volume average of the radial stresses to equal the negative of the volume average of the hoop stresses: $\langle T_{\theta\theta}\rangle = -\langle T_{rr}\rangle$, provided that T_{rz} is negligible. This is clearly the case for the solid specimen in Fig. 11.2 (left column, middle two panels). However, the case of the annular specimen is more complicated. The simulations produce radial stresses that are negligibly small when compared to the hoop stresses. Taking the relation $\langle T_{\theta\theta}\rangle = -\langle T_{rr}\rangle$ and setting $\langle T_{rr}\rangle$ to 0 implies that either $T_{\theta\theta}$ changes sign, or that it is identically zero. Both of these cases are ruled out for the hoop stress from Fig. 11.1. We now consider a more general deformation for which T_{rz} is no longer zero. Starting with momentum balance, and assuming a rotationally symmetric answer yields the following result:

$$-\iint \frac{1}{r} T_{\theta\theta}\, \mathrm{d}r\mathrm{d}z + \left[\int T_{zr}\mathrm{d}r\right]_{z=L} - \left[\int T_{zr}\mathrm{d}r\right]_{z=0} = 0 \tag{11.18}$$

Simulation results of the annular specimen support Eq. (11.18). Although the magnitude of T_{zr} is small, its axial gradient accounts for the deviation from the relation $\langle T_{\theta\theta}\rangle = -\langle T_{rr}\rangle$.

The boundary conditions for annular specimens result in axial variations in the stress components, although these results are not plotted here. For the normal stresses, these axial variations were concentrated within ~0.25 mm of R_i and R_o and essentially vanished away from the specimen edges. Both hoop and axial stresses varied as much as 30 % in this region. In contrast, the variations in this region for the shear stress $T_{\theta z}$ were typically less than 5 %. The shear components T_{rz} and $T_{r\theta}$ that develop, although smaller in magnitude (typically less than 10 % of the shear stress), varied considerably from one end of the specimen regardless of the radial coordinate.

Finally, in view of the fact that the normal stress components in the annular specimen simulations do not agree with the stresses predicted for a pure torsional deformation, it is reasonable to expect that the strains in the annular specimen simulations would be substantially different from the strains in pure torsion. We were surprised to find that this was not the case. For both the solid and annular specimens, the strain state was very close to that for a pure torsional deformation, with the annular specimens showing slightly better agreement.

11.5 Discussion and Conclusions

The specimen geometry strongly influences the stress state in quasi-static torsion tests on soft and nearly incompressible elastic materials. For both solid and annular specimens, the hoop and axial stresses in the numerical simulations were a substantial fraction of the torsional stress, although the radial variation and the magnitude of these normal stresses differed for the two geometries. For annular specimens the radial stress was negligible, while for solid specimens it was also a substantial fraction of the torsional stress. For solid specimens the stress state in the simulations closely approximates the theoretical predictions for pure torsional deformation of an incompressible material. This was not the case for the annular specimens, even though the strain state was close to that for a pure torsional deformation. Further analysis is underway to understand this result.

Both theory and simulations show that the radial, hoop, and axial stresses depend strongly on both the shear modulus μ and the dimensionless parameter ω in the elastic constitutive model, while the torsional stress is independent of ω. It follows that no information on ω can be inferred from measurements of the torsional stress $T_{\theta z}$ alone. This has implications for the use of numerical inverse methods for determining best fits of the material parameters to experimental data. Any such method applied to torsion data alone would generate some "best fit" for ω, which in turn would lead to estimates for the normal stress

components that cannot be measured in the torsion test, but such results would have no merit. Material characterization tests that generate other stress-strain states would be necessary to determine this parameter.

Simulations and analysis are underway to probe the inertial effects in high-rate dynamic torsion tests on these soft materials. The shear wave speed mismatch between the bar and the specimen will load the specimen faster than it can reach dynamic equilibrium. During this "ring up period" there will be axial variations in the stresses. Loading will begin at the bar-specimen interface and then propagate to the torque sensor. This dwell will violate the dynamic equilibrium assumption. The quadratic dependence of the normal stress components on the shear strain in Eqs. (11.14) will exacerbate this effect, producing non-uniform radial, axial, and hoop accelerations.

Appendix: Details of the Numerical Simulations and Methods

The numerical modeling of was divided into two parts: meshing and the solver followed by post processing and analysis. Meshes were generated in Cubit (V12.1; Sandia National Laboratory) and in TrueGrid (V2.3.4; XYZ Scientific Applications, Inc.). Simulations were performed using Sierra SolidMechanics (Adagio 4.24; Sandia National Laboratory). Adagio is an implicit, nonlinear preconditioned conjugant gradient solver. Reduced integration on HEX8 element meshes was performed to avoid volumetric locking. Due to the highly constrained nature of the problem, extreme care had to be taken to ensure the mesh was structured and symmetric to prevent mesh artifacts. Postprocessing of simulation results was carried out in ParaView (V3.14.0; Kitware) and MATLAB (The MathWorks, Natick, MA).

Utilizing the symmetry of the problem, the state of the material was reduced to five, 1-D radial slices in the reference configuration in ParaView for further analysis in Matlab. Averages taken over the five circular faces assumed rotational symmetry and were implemented using a composite Simpson's integration. Similarly, volumetric averages were calculated from the five circular slices utilizing 5-point Simpson integration. Continuous plots over the radius of the specimens have been linearly interpolated between elements.

In practice, enforcing the glued boundary conditions in the simulations for the solid specimens resulted in erroneously large pressures. These pressures were concentrated in a small region containing the axis of the specimen ($r = 0$). These pressures were alleviated by relaxing the glued boundary conditions on the specimen faces to allow for a radial expansion. This resulted in extremely small radial displacements ($\sim$ microns), keeping the deformation close to pure torsion (Figs. 11.1 and 11.2). We suspect the large pressures resulted from highly constrained hex elements at the center. These elements undergo what can be approximated as a shear and a rotation. Outer elements, however, are closer to a pure shear strain. Due to the compressible Mooney-Rivlin model implemented in the code, the elements underwent volume changes producing pressures larger than in the incompressible case. Similar simulations were conducted on the annular specimen that relaxed the glued boundary condition. These, in contrast, resulted in deformations consistent with Eq. (11.13) where radial strains were on the order of 10 % and neither the deformation nor the stress state resembled that of pure torsion.

References

1. Gray GT (2000) Classic split-Hopkinson pressure bar testing. ASM Handb 8:462–476
2. Chen W, Song B (2011) Split Hopkinson (Kolsky) bar: design, testing and applications. Springer, New York
3. Gilat A (2000) Torsional Kolsky bar testing. ASM Handb 8:505–515
4. Hartley KA, Duffy J, Hawley RH (1985) The torsional Kolsky (split Hopkinson) bar. Met Handb 8:218–228
5. Warren TL, Forrestal MJ (2010) Comments on the effect of radial inertia in the Kolsky bar test for an incompressible material. Exp Mec 50(8):1253–1255
6. Scheidler M, Kraft R (2010) Inertial effects in compression Hopkinson bar tests on soft materials. In: Proceedings of the army research lab ballistic protection technologies workshop, Aberdeen, MD, USA
7. Scheidler M, Fitzpatrick J, Kraft R (2011) Optimal pulse shapes for SHPB tests on soft materials. Dyn Behav Mater 1:259–268
8. Sanborn B, Nie X, Chen W, Weerasooriya T (2012) Inertia effects on characterization of dynamic response of brain tissue. J Biomech 45:434–439
9. Sanborn B (2011) An experimental investigation of radial deformation of soft materials in Kolsky bar experiments. Master's thesis, Purdue University
10. Nie X, Prabhu R, Chen W, Caruthers JM, Weerasooriya T (2011) A Kolsky torsion bar technique for characterization of dynamic shear response of soft materials. Exp Mech 51(9):1527–1534

11. Nie X, Sanborn B, Weerasooriya T, Chen W (2013) High-rate bulk and shear responses of bovine brain tissue. Int J Impact Eng 53:56–61
12. Truesdell C, Noll W (1965) The non-linear field theories of mechanics. Springer, Berlin/New York
13. Gurtin M (1981) An introduction to continuum mechanics. Academic, New York
14. Batra RC (2006) Elements of continuum mechanics. American Institute of Aeronautics and Astronautics, Reston
15. Batra RC (2002) Universal relations for transversely isotropic elastic materials. Math Mech Solids 7(4):421–437

Chapter 12
Damage of Rubber Foams During Large Cyclic Compression

Jevan Furmanski, Carl M. Cady, Andrea Labouriau, Brian M. Patterson, Kevin Henderson, and Eric N. Brown

Abstract Polymeric foams are employed as cushions in many applications to prevent components from experiencing large dynamic stresses in service. While the performance of foam cushions may be quantified through certain mechanical variables, the strength and damage behavior of these materials remains poorly understood. The present work examined the deformation response of a rubbery Room Temperature Vulcanizing (RTV) foam under large cyclic compressions, subjected to a large dose of gamma radiation. Reduction in load carrying capacity occurred for all cases, attributable to some combination of material changes (Mullins effect) and permanent plasticity and damage to the microscopic ligaments surrounding pores in the material. Irradiation dose correlated to changes in the rate of nonlinear cyclic degradation, potentially pointing to a radiation aging effect.

Keywords Damage • Large strain • Cyclic loading • RTV • Foam

12.1 Introduction

The mechanical requirements for foam performance may not be extensively defined, particularly when it comes to long-term dynamic performance. That is to say, if a foam may sustain damage during service from load or strain excursions, the damage tolerance of that foam is not necessarily understood to be critical to overall its function. Indeed, it may be that due to any number of effects that one foam may outperform another under extreme (but credible) loading scenarios. This is an important dimension of foam mechanical performance, which is sensitive to aging and radiation effects, chemistry, and the microarchitecture derived from the manufacturing process.

Cyclic loading can be employed to elucidate damage caused to the microarchitecture of the foam during service, as only upon unloading and reloading are permanent changes to the structure manifest. These changes also reflect damage caused by monotonic or rare events, and do not only inform the material response under cyclic loading. The qualitative nature of the degradation of the foam upon load cycling implies the mechanisms underlying the phenomena, be they plastic flow, buckling and kinking, or microligament fracture. The apparent active damage mechanisms, inferred from the cyclic degradation behavior observed in the experiments, and their implications can be compared to X-ray micro CT (microtomoraphy or computed tomography) observation and numerical simulation of the microarchitecture during severe cyclic compressions to more precisely clarify the local events related to mechanical degradation. This path not only clarifies mechanisms of degradation, but will enable a design-based predictive approach to foam mechanical performance.

J. Furmanski (✉) • C.M. Cady
MST-8, Mail Stop G755, Los Alamos National Laboratory, Los Alamos, NM 87545, USA
e-mail: jevanf@gmail.com

A. Labouriau • B.M. Patterson •
K. Henderson
MST-7, Mail Stop E549, Los Alamos National Laboratory, Los Alamos, NM 87545, USA

E.N. Brown
P-23, Mail Stop H803, Los Alamos National Laboratory, Los Alamos, NM 87545, USA

B. Song et al. (eds.), *Dynamic Behavior of Materials, Volume 1: Proceedings of the 2013 Annual Conference on Experimental and Applied Mechanics*, Conference Proceedings of the Society for Experimental Mechanics Series,
DOI 10.1007/978-3-319-00771-7_12,

This work investigates cyclic damage to an Room Temperature Vulcanizing (RTV) foam, either as-received, or subjected to a substantial, 20 Mrad, radiation dose. Furthermore, data are given on degradation rates for a range of cyclic compressions, and interpretations are given of the measured outcomes.

12.2 Material and Methods

RTV foam, designated SX358, was obtained in a 1.0 mm thick sheet. The sheet had been previously aged at 70 °C under 25 % compression for 120 days to simulate long term nominal service. Smaller samples were cut from the sheet and exposed to 0–30 Mrad of gamma radiation at the Sandia National Laboratories Gamma Irradiation Facility (GIF), while simultaneously under static compression of 0–50 %. Compression fixtures were manufactured for the purpose of holding a compression during irradiation, using brass shims to set the gap between two aluminum platens. Disc samples ½″ diameter were punched from these subsheets for compression testing. Generally speaking, the specimens must be fixed to the lower platen using 2-sided tape, to prevent the movement of the specimen during load cycling, and later, the migration of damaged foam fragments.

Large strain cyclic compression waveforms were imposed on the disc specimens, and the loading fixture is shown in Fig. 12.1. The platens interface with gap-setting shims (e.g., 1.00 mm initial gap) to determine the zero-strain condition, which are then removed before testing. A repeatable initial gap is critical to the precision of the test at large strains, where the hardening rate becomes nearly asymptotic, and 10 microns of position error can be significant. The lower platen fixes to the machine snugly onto a grip platen, while the upper platen is loaded through a ball that contacts a cone in the platen to allow small misalignments in the system during testing, and also to run the test effectively in a constant-pressure boundary condition, instead of a constant-displacement boundary condition, which may give less consistent results due to possible partial sampling of the foam volume. The fixtures can also be loaded in constant-displacement mode using snug-fitting cylindrical inserts instead of the ball.

The loading program cycles the specimen at 50 % strain for 20 cycles, then moving on to 62 %, 67 %, 75 %, and 87 % strain, each for 20–50 cycles, all imposed on the same specimen (though individual tests of interest can be run separately to reject the effects of prior loading history). All tests were run at 0.01 mm/s to avoid both creep (occurring at lower rates) and hysteretic heating effects (occurring at higher rates). Strain in this case is determined from the initial 1 mm sheet thickness and not from the post-irradiation/compression dimensions. Characteristic load–displacement curves for a 3 mm thick specimen are shown in Fig. 12.2. The observable to look for here is first whether the peak load drops under repeated loading, and then whether the load drop stabilizes (shakes down) to a new state. Initial drops in peak load are attributable to a Mullins Effect (in the first 1–2 cycles) or perhaps progressive plasticity. Sudden changes to the shakedown state, or constant linear reduction in peak loading, both point to cyclic degradation and damage mechanisms. There is also a qualitative change in the test around 65 % strain, where the material clearly goes through a yield transition. This nonlinear load drop only occurs once in the entire sequential loading program, and is associated with a large single-cycle load drop.

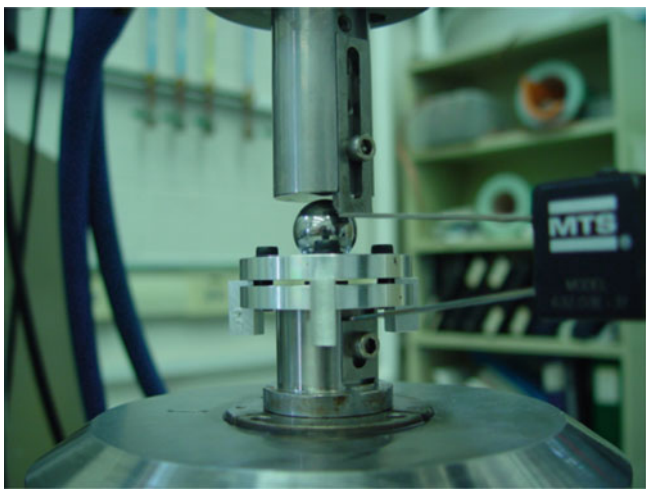

Fig. 12.1 Loading compression platens with ball bearing, gap-setting shims, and extensometer

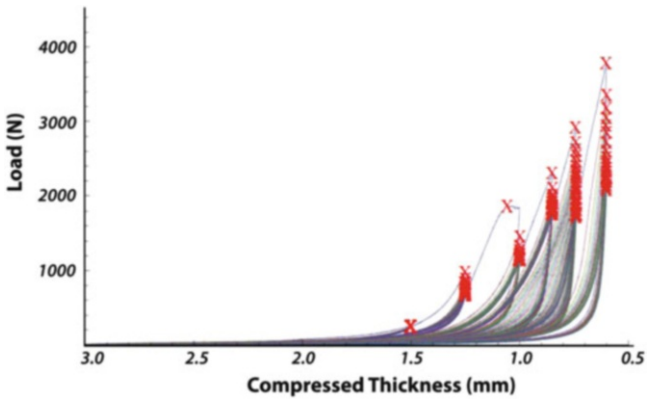

Fig. 12.2 Cyclic compression to six different compressive strain (displacement) states for a 3 mm thick RTV foam. The peak conditions are shown with a red X

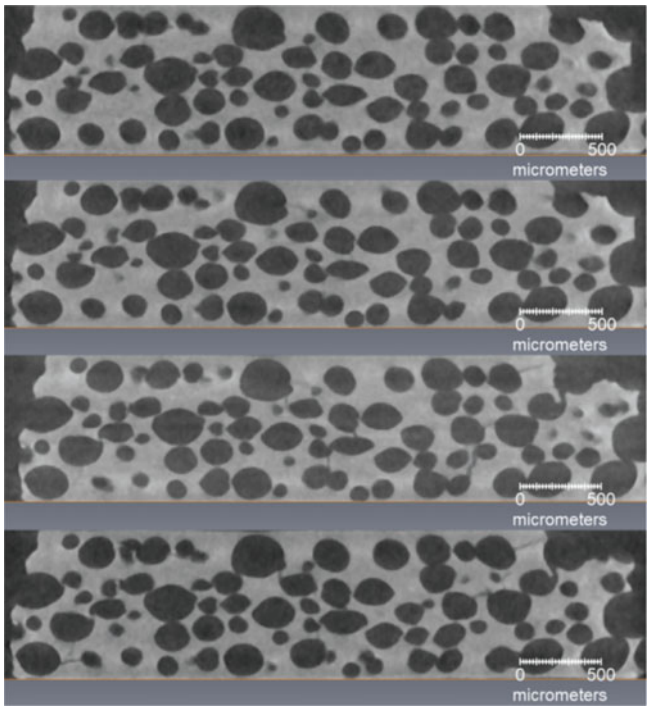

Fig. 12.3 X-ray micro CT reconstructed slices through 20 Mrad dosed SX358 (*top to bottom*); pre-compression, relaxed after one 75 % compression, relaxed after 11 compression cycles, and relaxed after 21 cycles. Damage progression continues with further cycles

X-ray micro CT images were collected on 4-mm wide, 1-mm thick punched pieces of the RTV foam. The samples were each imaged under no load, single cycled in a CT-compatible compression cell to 75 % compression, allowed to relax back to 1-mm and re-imaged. The cycling/relaxation/imaging was repeated with 10 compression cycles up to 51 total. Figure 12.3 shows the damage progression with repeated cyclic loading. The metrics (number and size) of the cracks increases with loading cycles, the initial compression loading does not create all of the damage.

12.3 Results

Control (as received) and 10 Mrad irradiated (uncompressed) materials were first compared to examine the extent of a radiation effect even at this somewhat modest dose, up to 75 % compression. While only four control and two irradiated tests were run, there were substantial differences observed over 50 loading cycles.

It can be seen from Fig. 12.4a that the irradiated group (orange fit lines) reduce their load capacity more than the control (as a percentage of the first cycle value). In Fig. 12.3b, it is less obvious that the degradation of the irradiated groups is more

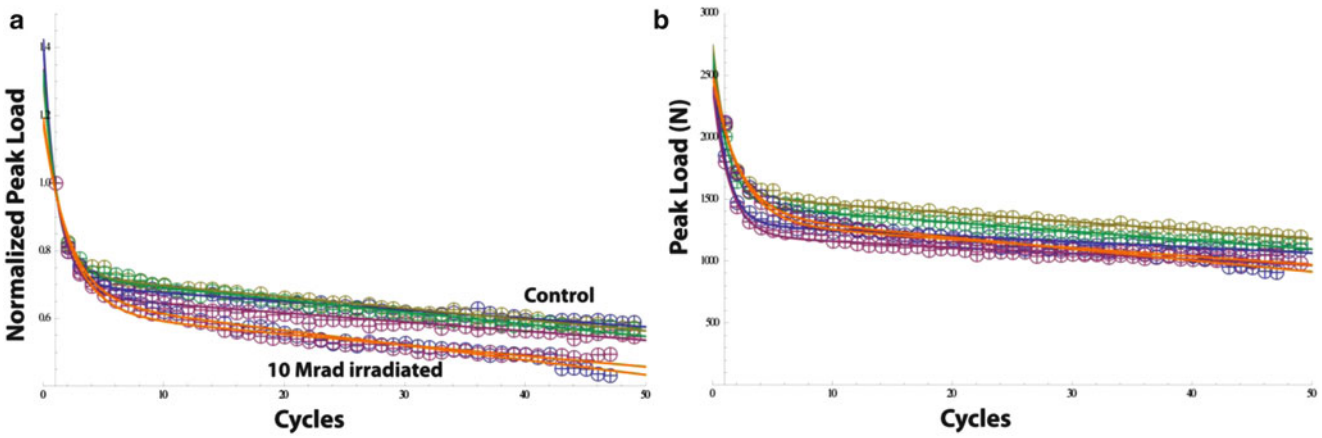

Fig. 12.4 As-received (control) and 10 Mrad irradiated SX 358 RTV foam peak load degradation for up to 50 displacement cycles up to 75 % strain. The normalized data (**a**) show the irradiated material to degrade more than the control, though the absolute data (**b**) obscure this somewhat. See Table 12.1 for a breakdown on the relative degradation rates of the two materials (color figure in online)

Table 12.1 Coefficient for normalized cyclic degradation fit

	A	B	C	D
Control 1	0.701	1.03	−0.892	−0.00359
Control 2	0.67	0.991	−0.721	−0.00401
Control 3	0.73	0.793	−0.772	−0.00455
Control 4	0.727	0.83	−0.8	−0.00494
10 Mrad 1	0.652	0.809	−0.468	−0.00671
10 Mrad 2	0.618	0.931	−0.457	−0.0052

severe, as the absolute data for all groups somewhat overlap. However, given the agreement in the normalized plot, it is believed that the variation in the absolute load values inside each group are actual material variability effects. These are reasons to always plot both normalized and absolute peak load degradation – different interpretations can be drawn from each.

Figure 12.4a employs a nonlinear fit to the peak load degradation, following the equation $P_{peak\_norm} = A(1 + B\,Exp(C\,N) + D\,N)$, where N is the number of cycles, and this fit works quite well for all the data. For absolute data, only A changes. Investigating this equation a bit, one can interpret A as the infinite cycle peak load, B as the strength of the nonlinear degradation, C as the rate of nonlinear degradation, and D as the strength of the linear degradation term. Quantifying these coefficients yields significant insight into the relative degradation rates according to each term, which in turn is thought to represent the activity of distinct inelastic mechanisms.

There are two effects that jump out of Table 12.1, which then makes Fig. 12.4a easier to interpret. The irradiated group experiences pronounced linear degradation (greater negative D), and a slower "time constant" C for the nonlinear degradation. Together, what these imply is that radiation exposure slows down nonlinear degradation, almost by two times, and accelerates linear cyclic degradation.

With such low numbers of test, it is difficult to definitively state that radiation has damaged the material's resistance to cyclic compression, but the data in Fig. 12.4a and Table 12.1 do seem to imply the two materials are distinct. It is also notable that the data in Fig. 12.4b show substantial scatter, even after only one cycle. Using the curve fit, however, the theoretical initial "cycle zero" peak load capacity of the specimen can be inferred, and this appears to converge quite well for the materials, even though they differ in their cyclic response. It is important to note that the first cycle has indeed damaged the material, and that this value does not set the safety peak load for the undamaged material, but rather the "cycle zero" load capacity value is best considered when determining safe loads and strains. This is also a crucial difference between using an exponential nonlinear fit term and a power-law fit term, as a power-law fit cannot be extrapolated back to cycle zero. It may also be useful to normalize to the cycle zero response rather than the first cycle response, for this reason, and because it does appear that there is a relatively close agreement in this extrapolated value between specimens.

Initial results have also been obtained for three other irradiated SX358 materials: 20 Mrad under 37 % compression, 10 Mrad under 0 % compression, and 5 Mrad under 0 % compression; all of these came from the same material batch as above. These were subjected to a program of increasing cyclic compression, as seen above in Fig. 12.2, which helps to clarify the strains at which inelastic deformations become first evident, then severe. There were differences in the

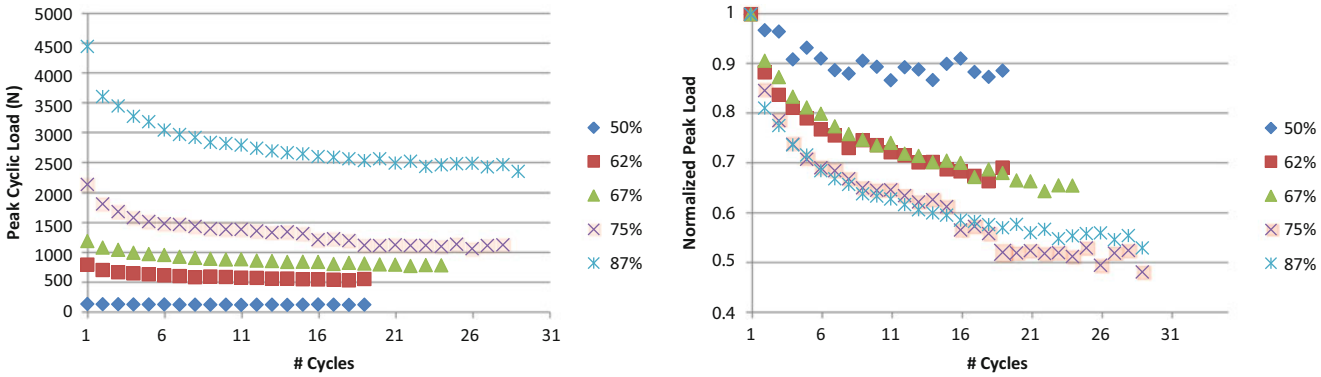

Fig. 12.5 20 Mrad, 37 % strain irradiation/precompression. Note the discontinuous degradation of the peak load at 75 % cyclic strain at cycle 15. The lowest strain test that experienced sudden degradation (75 %) is highlighted

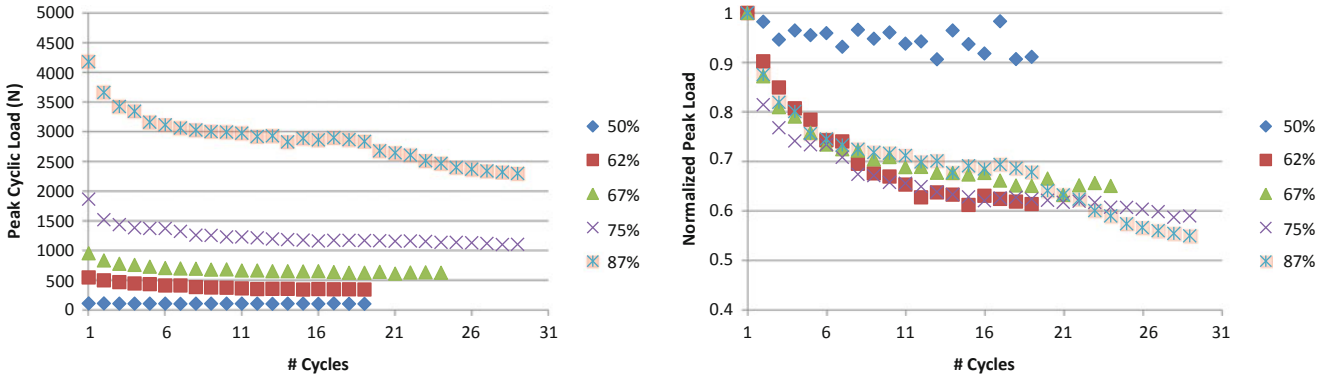

Fig. 12.6 5 Mrad, 0 % strain irradiation/precompression. Here the response at 75 % is stable and may start to degrade slightly at cycle 20, but severe degradation does not set in until 20 cycles at 87 % strain. The lowest strain test that experienced sudden degradation (87 %) is highlighted

performance between the 20 Mrad-37 % material (Fig. 12.4) and the 5 Mrad-0 % material (Fig. 12.6). Figures 12.5 and 12.6 show the absolute peak load degradation with load cycling, and also the normalized drop from the first cycle at each condition. Both materials appear to effectively shake down up to 67 % strain, though longer tests are really required to clarify the extent to which a stable state really is reached (see Fig. 12.4).

However, there are clear differences in the responses. There is apparently less plastic degradation at intermediate cyclic strains in the 20 Mrad-37 % material, which could be an effect of irradiation or precompression set. Note that, at 75 % strain, the 20 Mrad-37 % strain material undergoes a sudden, discontinuous degradation at cycle 15, while at the same conditions the 5 Mrad 0 % are either stable or may start to degrade weakly around cycle 20. At 87 % strain the 5 Mrad-0 % material appears to undergo a similar sudden degradation, while the response for the 20 Mrad-37 % material is likely progressive damage (decreasing slope) with some small-step discontinuous effects past 20 cycles. The interpretation from this data is that the 20 Mrad-37 % strain precompressed material undergoes apparently severe damage at a less severe cyclic compression than the 5 Mrad-0 % material. Deleterious changes to the onset conditions for damage and failure of foams due to environment and storage strain history are the target observable of this work, and maybe be framed here sufficiently well to motivate their further study.

It is interesting to observe that the normalized degradation plots show that, above 50 %, the nonlinear degradation appears to behave very similarly with little sensitivity to increasing compressions. To be sure, there are differences between 50–70 % and 75–87 %, but these appear be relatively constant within those groupings, and less different outside of them than one might expect. This apparent normalized insensitivity may be due to the process being essentially driven by viscoplasticity, in which plastic strain accumulation will increase with increasing applied load. Thus, in absolute terms the nonlinear degradation is indeed quite different between groups, but when normalized this difference largely disappears. Future work on the viscoplastic deformation of both solid RTV and these foams will likely reveal a flow law that matches these observations.

12.4 Conclusions

This methodology of subjecting foams to increasingly severe cyclic compressions appears to be effective in extracting both the nonlinear inelastic response of foams under these conditions, but also discriminates their relative effects such that they can be evaluated for performance. This method can and should be used on a range of foam materials to determine the strains at which each begins to display substantial inelastic behavior, and the rate at which these inelastic mechanisms evolve. It is also worth noting that at 50 % compression there appears in most groups to be changes to the peak load capacity beyond the four cycles often employed when evaluating Mullins-type degradation behavior. It is the overall hypothesis of this work that the distinction between blown RTV foams and cast cellular silicone foams will differ substantially in how they evolve their inelastic degradation responses, and though this work did not achieve a direct comparison of these materials, it did establish the method as able to complete the comparison. Further, direct observation of the mechanisms governing compressive degradation have yet to be completed, and the path to this is described in the Future work section.

Acknowledgements Los Alamos National Laboratory is operated by LANS, LLC, for the NNSA of the US Department of Energy under contract DE-AC52-06NA25396.

Chapter 13
Extreme Tensile Damage and Failure in Glassy Polymers via Dynamic-Tensile-Extrusion

Jevan Furmanski, Eric N. Brown, George T. Gray III, Carl Trujillo, Daniel T. Martinez, Stephan Bilyk, and Richard Becker

Abstract Dynamic-tensile-extrusion (DTE) is an integrated test technique that allows the study of material deformation at high strain-rates (>10,000 s^{-1}) and large strains (>1), under hydrostatic tension. This is an important compliment to the more traditional Taylor cylinder impact test, which achieves large strain and high strain-rate deformation, but under hydrostatic compression. Hydrostatic compression is known to suppress many forms of damage in materials. DTE has been previously employed on a number of metal and polymer systems that manifested tensile instabilities. More recently, this technique has explored stable tensile damage in high-density polyethylene (HDPE), which pointed to a pressure-mediated shear damage phenomenon. The current work extends the technique to the behavior of the glassy polymers polymethylmethacrylate (PMMA) and polycarbonate (PC). PMMA was found to undergo unstable brittle fracture at nearly all conditions, and therefore did not yield interpretable experimental results. PC (discussed herein) necked and either failed in a brittle fashion or the neck was arrested prior to failure. In the arrested condition, the neck was seen to become opaque from an apparent accumulation of small-scale damage, and a void nucleated at the centerline. A corkscrew fracture process was observed in PC, though its mechanics are not yet understood. It is worth noting that simulations of pressure-hardening PC indicate that it will not extrude or even neck during DTE without the action of a damage process reducing the flow strength of the material.

Keywords Dynamic-tensile-extrusion • DTE • Large strain • Polycarbonate • Extreme loading

13.1 Introduction

Few experimental approaches are available for unambiguously assessing the deformation response of materials under extreme mechanical loading conditions, i.e., simultaneous large strains ($\varepsilon > 1$) and high strain-rates ($d\varepsilon/dt > 10{,}000\ s^{-1}$) [1]. The Dynamic-Tensile-Extrusion (Dyn-Ten-Ext) test was developed by G.T. Gray and co-workers at Los Alamos National Laboratory (LANL) to examine extreme tensile conditions in materials [2, 3]. It has since been extended to the investigation of a number of polymers including polytetrafluoroethylene (PTFE) and polychlorotrifluoroethylene PCTFE [4–6], polyurea [4, 7], and polyethylene [4, 8]. The technique utilizes the same hardware as a Taylor cylinder impact test [9], except that a conical extrusion die is fixed to the end of the gun barrel, forcing the specimen to extrude through it at a high velocity and the anvil is not employed. Like the Taylor cylinder impact test that accessed unique high strain and strain-rate phenomena in polymers under compression (see for examples [10–16]), Dyn-Ten-Ext accesses these effects in polymers that exhibit a strong stress asymmetry. The leading edge of the specimen is relatively unaffected by the extrusion process, but the trailing portion rapidly decelerates inside the die, and thus the extruded ligament between the two ends is pulled in high strain-rate tension, typically to large strains and, ultimately, to failure. As shown in Fig. 13.1, a finite element simulation of high-density

J. Furmanski (✉) • G.T. Gray III • C. Trujillo • D.T. Martinez
MST-8, Mail Stop G755, Los Alamos National Laboratory, Los Alamos, NM 87545, USA
e-mail: jevanf@gmail.com

E.N. Brown
P-23, Mail Stop H803, Los Alamos National Laboratory, Los Alamos, NM 87545, USA

S. Bilyk • R. Becker
Army Research Laboratory, RDRL-WMP-C, Aberdeen Proving Ground, Aberdeen, MD 21005, USA

B. Song et al. (eds.), *Dynamic Behavior of Materials, Volume 1: Proceedings of the 2013 Annual Conference on Experimental and Applied Mechanics*, Conference Proceedings of the Society for Experimental Mechanics Series,
DOI 10.1007/978-3-319-00771-7_13,

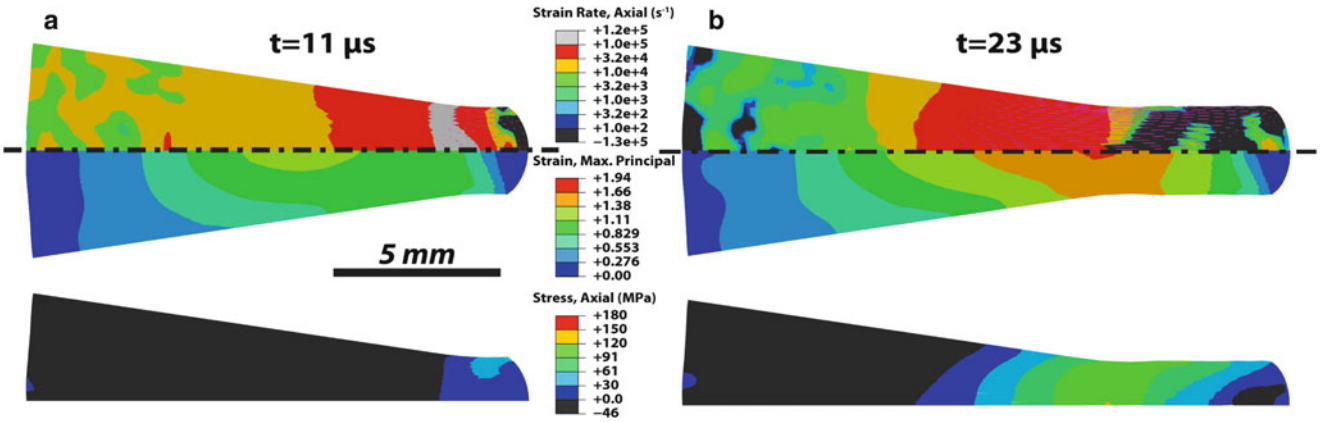

Fig. 13.1 Dyn-Ten-Ext simulation for HDPE at an initial velocity of 447 ms^{-1} and exit diameter 2.8 mm, showing axial logarithmic strain, strain rate (s^{-1}) and axial tensile stress (MPa) at two time points after specimen-die contact. The axial strain exceeds 1 in the critical section during extrusion, and the strain-rate likewise exceeds 10^4 s^{-1} in this region. The critical section is under tension, while the tip and tail in the die remain in compression. The strain-rate diminishes rapidly a short distance past the die exit, after which point plastic deformation has effectively ceased

polyethylene (HDPE) undergoing Dyn-Ten-Ext, through a die of exit diameter 3.60 mm with an initial velocity of 447 s^{-1}, predicts that the ligament achieves a strain of 1–1.9 at a strain-rate of 10^4–10^5 s^{-1} in the critical tensile section during extrusion, thus achieving extreme tensile test conditions.

Thus, as an integrated test that generates extreme tensile deformation, Dyn-Ten-Ext provides a means to challenge the quantitative accuracy of constitutive models parameterized under less extreme conditions. Additionally, it provides a direct qualitative assessment of the mechanisms of deformation and damage under extreme conditions, which may or may not differ from those observed at lower strain-rates. For example, recent work has shown that the failure phenomena observed in Dyn-Ten-Ext qualitatively matched expectations derived from the microstructure and low strain-rate response in PTFE and PCTFE [5, 6], and Polyurea [7].

The primary aim of this work is to identify the (potentially distinct) mechanisms of damage inception and progression in polymethylmethacrylate (PMMA) and polycarbonate (PC) – two transparent glassy polymers employed widely for structural and ballistic applications. The extreme tensile response of these polymers is of substantial interest to their ballistic suitability, as the dynamic mechanics of tensile damage and failure in them is unclear and likely dominates their performance.

13.2 Materials and Methods

Large sheets (2.44 × 1.22 m) of PC were obtained from Bayer Sheffield Plastics Makrolon. As previously mentioned, the Dyn-Ten-Ext apparatus in use at LANL is a slight modification to the Taylor cylinder impact Facility [9]. The barrel has a smooth 7.62 mm (0.300 in.) bore. The barrel discharges into a target chamber that is evacuated with a roughing pump for testing to prevent interaction of the projectile with an atmosphere. While the chamber contains a polished hardened steel anvil during Taylor cylinder impact testing, for Dyn-Ten-Ext this is replaced with a catch tank loosely filled with cloth for soft recovery of any specimen fragments. The main data collected during Dyn-Ten-Ext testing consist of initial velocity from the bore prior to interaction with the die and high-speed multiframe photography of the extruded material for obtaining deformed shape and speed, which is then compared to FEA simulations to understand the material behavior during the test. The specimen initial velocity is measured via two pressure transducers on the barrel near the target chamber and captured with an oscilloscope. The images of the extruded material are captured with an Imacon 200 or Shimadzu HPV2 framing camera (Hadland, Santa Cruz CA), typically with a 3–5 µs interframe time, and illumination is provided opposite the camera by a Powerlight 2599 flash lamp (Photogenic, Bartlett IL). The velocity of extruded material is collected from the captured images and is calibrated with a transparent scale near the die exit.

The Dyn-Ten-Ext specimen geometry can be a sphere or a hemisphere-ended cylinder, both of which use a diameter and length of 7.60 mm. The die uses a conical reducing section inclined 9° (half-angle) to the extrusion axis. The die exit diameter is specified depending on the desired draw ratio to be imposed prior to the onset of dynamic self-extrusion after the

die exit. The nominal design of the die uses an exit diameter of 2.80 mm (0.110 in.), which imposes an axial true strain $\varepsilon \sim 2$ at the die exit.

Numerical modeling was performed on a 12-processor Linux computer using the hydrocode ALE3D [17]. An ALE3D input file was created describing the geometry, initial conditions, boundary conditions, and material response models. Analyses were conducted using a two-dimensional axisymmetric geometry in a quadrilateral element computational domain with explicit time integration in an Eulerian framework. The boundary of the extruding die was described using a rigid slide surface. The Mulliken-Boyce (M-B) constitutive relation [18, 19] was used to describe thermo-mechanical deformations of PC subjected to Dyn-Ten-Ext loading rates. Mulliken-Boyce is a physically based constitutive model with pressure and rate-dependent elastic–plastic response and also accounts for dominant mechanisms (molecular motions) as related to yield behavior over a wide range of temperatures and strain rates. The Mie-Gruneisen equation of state was used for volumetric response and material failure was described using the Johnson-Cook fracture model with failure strain dependence on triaxiality.

13.3 Results

A range of results were obtained as the input velocity of the test was increased, progressing from intact arrest with incipient cracking and void nucleation, to terminal damage progression though a circumferential tearing and central void progression process. This is a useful set of results because it captures the evolution of damage under extreme tensile conditions, and also reveals that two separate mechanisms (or at least pathways) of damage are active during the deformation.

At lower velocities, the specimen did not extrude, but was observed to form a neck (Fig. 13.2, left). Behind this neck a spherical void was seen to nucleate in a number of cases. Further behind the neck, a circumferential fracture was seen to initiate. These arrested damage features are believed to dominate failure, and result in the rupture and failure of the specimen under more extreme conditions (Fig. 13.2, right).

Video of the failure process during extrusion elucidates the dynamics, though they appear potentially quite complicated. In a test at an intermediate velocity (523 m s^{-1}, Fig. 13.3) the extruded ligament is tearing while extending, and ultimately the fracture is in a helical or corkscrew geometry. Much of the behavior during extrusion appears fluid-like, which may be difficult to model. However, recovered failed specimens (Fig. 13.4) show that the torn ligament recovers to something approximating its original configuration. This indicates that the behavior is in fact solid-like, though at high rates it may appear to be fluid-like.

The simultaneous activity of a void nucleation and coalescence process combined with circumferential fracture is and intriguing result that deserves further study. Indeed, for ballistic applications, if two such mechanisms interact cooperatively during failure, then the mechanics need to be systematically investigated in a controlled manner like that provided by Dynamic Tensile Extrusion. Using this integrated testing system to improve the understanding of the damage physics in PC will enable more advanced damage models to be developed, that will then allow for improved performance of transparent ballistic systems.

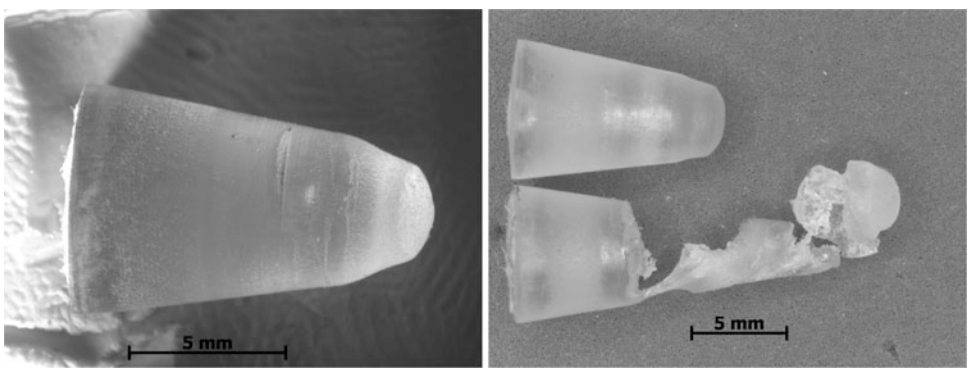

Fig. 13.2 Dynamic-Tensile-Extrusion of polycarbonate (PC). *Left*: Arrested intact specimen, showing necking, void nucleation behind the neck, and circumferential fracture behind the void. *Right*: Comparison of arrested intact specimen and failed specimen, where central voiding and peripheral fracture have proceed nearly to complete failure. There is a small ligament of unfractured material remaining in the failed part

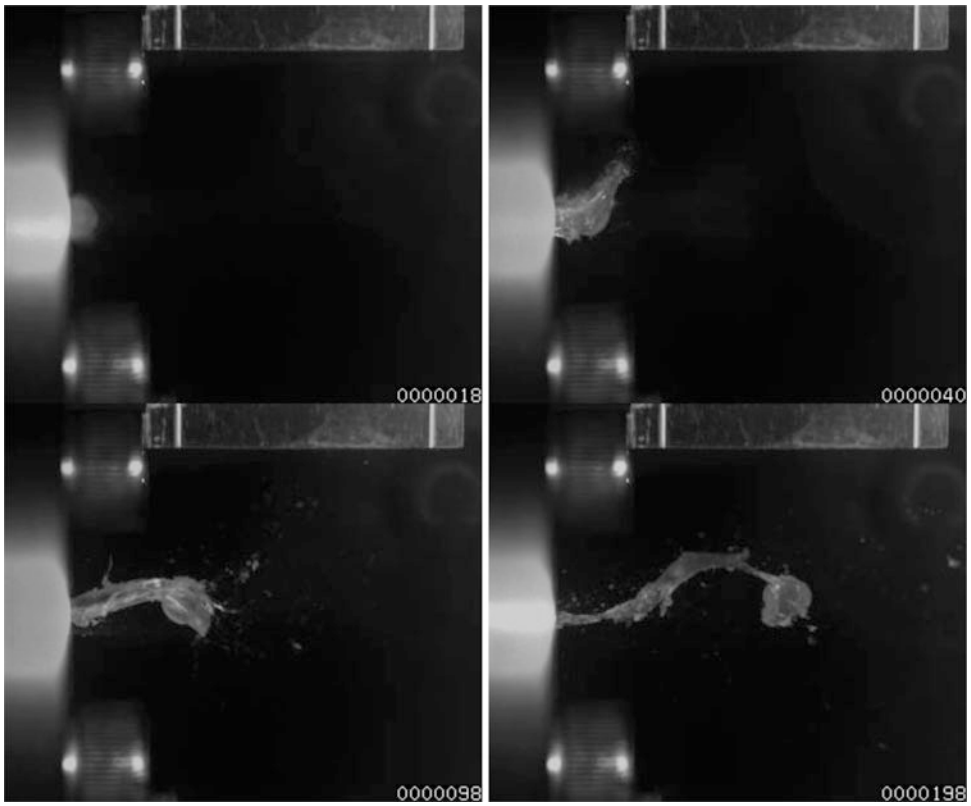

Fig. 13.3 Dynamic-Tensile-Extrusion of polycarbonate (PC) as captured at the die exit by a Shimadzu high speed framing camera. The time in microseconds from camera trigger is noted in the *lower-right* of the images. The test conditions were initial velocity 523 m s^{-1}, with a die exit of 0.142 in. The failure is in the corkscrew fracture/tearing mode. While it appears to behave in a molten fashion, the recovered pieces were found to have retracted almost to their original shape, indicating solid behavior (see below)

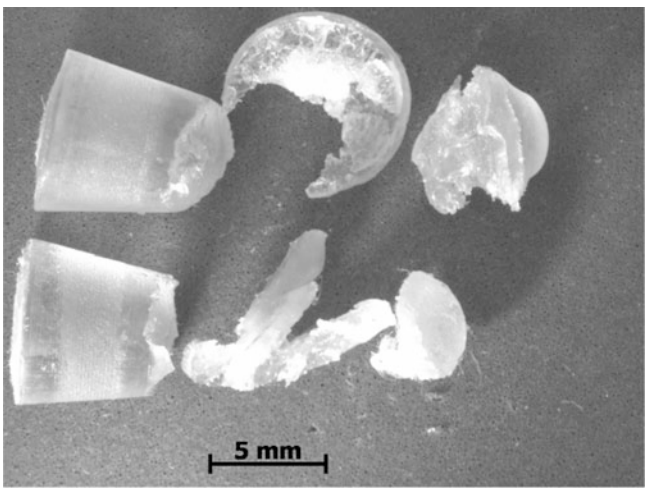

Fig. 13.4 Soft-recovered PC specimens after Dyn-Ten-Ext. Note the circumferential fracture (*top*) and helical corkscrew fracture (*bottom*) of the extruded ligament. The center of the specimen appears pulverized, which may match expectations of a voiding mechanism implied by the unbroken necked specimen (Fig. 13.2)

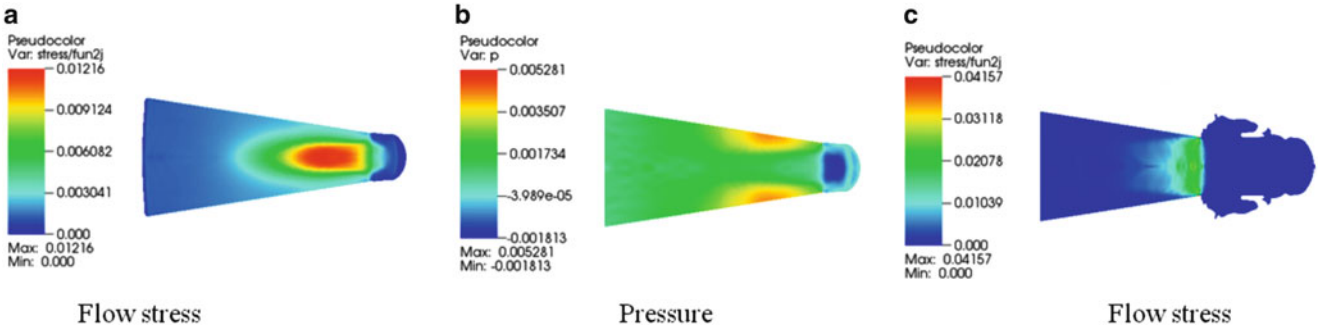

Fig. 13.5 Numerical results of PC specimens after Dyn-Ten-Ext. All contours shown are 28 μs after the specimen has contacted the extruding die, with (**a**) and (**b**) show stress evolution for an impact velocity of 451 m s^{-1}. (**c**) Shows fracture and von Mises stress for an impact velocity of 523 m s^{-1}

Numerical results of Dyn-Ten-Ext tests predicted the observed arrested damage features for PC at low impact velocities (Fig.13.5a, b). There was no fracture for impact velocities below 450 m s^{-1} and flow stresses within the material approached 1200 MPa with pressure on order of 350 MPa. At higher impact velocities, the specimen exhibited regions of fracture using M-B strength and J-C fracture showing reasonable agreement with observed. Ahead of the high stress region shown in green (Fig. 13.5c), the material has failed as it exits the die. Ahead of this failed region is a stress free nose of PC that broke off the specimen.

Additional analysis was completed using modified pressure dependence in the M-B model. PC exhibited greater deformation when pressure dependence was reduced. While the results are in qualitative agreement, the models need further validation and additional fracture data is required.

Acknowledgements Los Alamos National Laboratory is operated by LANS, LLC, for the NNSA of the US Department of Energy under contract DE-AC52-06NA25396. This research was supported by Campaign 2: Dynamic Behavior of Materials and the Joint DoD/DOE Munitions Program and the US Army Research Laboratory.

References

1. Funk DJ et al (2009) A summary report on the 21st century needs and challenges of compression science workshop. Los Alamos National Laboratory Report LA-UR-09-07771
2. Cao F et al (2008) Dynamic tensile extrusion response of tantalum. Acta Mater 56(19):5804
3. Gray GT et al (2006) Influence of shock prestraining and grain size on the dynamic-tensile-extrusion response of copper: experiments and simulation. Shock Compression of Condensed Matter – 2005 845:725
4. Furmanski J, Trujillo CP, Martinez DT, Gray GT III, Brown EN (2012) Dynamic-tensile-extrusion for investigating large strain and high strain-rate behavior of polymers. Polym Test 31:1031
5. Brown EN, Trujillo CP, Gray GT (2009) Dynamic-tensile-extrusion response of fluoropolymers. Shock Compression of Condensed Matter – 2009 1195:1233
6. Brown EN, Gray GT III, Trujillo CP (2009) Influence of necking propensity on the dynamic-tensile-extrusion response of fluoropolymers. DYMAT 2009 vol 1, 2009, DYMAT 2009 – 9th international conference on the mechanical and physical behaviour of materials under dynamic loading 1:171
7. Furmanski J, Cady C, Rae P, Trujillo CP, Gray GT III, Brown EN (2012) Dynamic-tensile-extrusion of polyuria. Shock Compression of Condensed Matter – 2011 1426:1085
8. Furmanski J, Brown EN, Clements B, Cady CM, Gray GT III (2012) Large-strain time-temperature equivalence in polymers for prediction of extreme deformation and damage. European Physical Journal: DYMAT 2012 – 10th international conference on the mechanical and physical behaviour of materials under dynamic loading 26:01057
9. Maudlin PJ, Gray GT III, Cady CM, Kaschner GC (1999) High-rate material modeling and validation using the Taylor cylinder impact test. Phil Trans R Soc Lond A 357:1707
10. Rae PJ, Brown EN, Clements BE, Dattelbaum DM (2005) Pressure induced phase change in poly(tetrafluoroethylene) at modest impact velocities. J Appl Phys 98(6):063521
11. Brown EN, Rae PJ, Orler EB (2006) The influence of temperature and strain rate on the constitutive and damage responses of polychlorotrifluoroethylene (PCTFE, Kel-F 81). Polymer 47(21):7506
12. Rae PJ, Brown EN (2006) The Taylor impact and large strain response of poly(ether-etherketone) (PEEK). In: Furnish MD, Elert M, Russell TP, White CT (eds) Shock compression of condensed matter 2005: proceedings of the conference of the American Physical Society Topical Group on shock compression of condensed matter, AIP conference proceedings, vol 845, p 1399

13. Rae PJ, Brown EN, Orler EB (2007) On the mechanical properties of poly(ether-ether-ketone) (PEEK) with emphasis on the large compressive strain response. Polymer 48(2):598
14. Brown EN, Trujillo CP, Gray GT III (2007) Influence of polyethylene molecular conformation on Taylor impact measurements: a comparison of HDPE, UHMWPE, and PEX. In: Elert M, Furnish MD, Chau R, Holmes N, Nguyen J (eds) Shock compression of condensed matter 2007: proceedings of the conference of the American Physical Society Topical Group on shock compression of condensed matter, AIP Conference Proceedings, vol 955, p 691
15. Sarva S, Mulliken AD, Boyce MC (2007) Mechanics of Taylor impact testing of polycarbonate. Int J Solid Struct 44:2381
16. Bourne NK, Brown EN, Millett JCF, Gray GT III (2008) Shock, release and Taylor impact of the semicrystalline thermoplastic polytetrafluoroethylene. J Appl Phys 103(074902)
17. Nichols AL (ed) (2009) Users manual for ALE3D: an arbitrary Lagrange/Eulerian 2D and 3D code system. Lawrence Livermore National Laboratory, Livermore
18. Mulliken AD, Boyce MC (2006) Mechanics of the rate-dependent elastic–plastic deformation of glassy polymers from low to high strain rates. Int J Solid Struct 43:1331
19. Mulliken AD (2006) Mechanics of amorphous polymers and polymer nanocomposites during high-rate deformation. Doctoral thesis, Massachusetts Institute of Technology

Chapter 14
Strain Rate and Temperature Dependence in PVC

M.J. Kendall and C.R. Siviour

Abstract Polymers are frequently used in applications in which they may be exposed to high rate or impact loading and there is growing industrial importance in understanding their mechanical behaviour at different strain rates. This paper describes research that has been performed to better understand and predict the dependence on strain rate of mechanical properties such as yield stress. In particular, the processes that govern the high rate response within polymers are better understood by investigating the relationship between rate dependence and temperature dependence. In particular, the mechanical behaviour of poly(vinyl chloride) with different amounts of plasticizer has been studied at strain rates from 0.001 to 5,000 s^{-1} and temperatures from −115 °C to +80 °C. Time-temperature superposition and a novel experimental method are used to understand the effects of strain rate in terms of relevant transitions and adiabatic heating in the material. The experimental work presented is supported by constitutive modeling and careful consideration of the processes involved in the high rate loading.

Keywords Strain • Rate • Adiabatic • Temperature • Polymer

14.1 Introduction

The mechanical properties of polymers are studied because of their widespread scientific and industrial importance, as seen in the automotive, aerospace, military, and medical industries. A considerable amount of research has been completed in both the impact behavior of polymers, and the sensitivity of polymers to variables such as temperature and strain rate. As high performance materials continue to be developed, there has been increased demand for test methods capable of analyzing and comparing materials over a wide range of strain rates. The demand is particularly apparent in testing low-impedance materials at high rates, for which there can be difficulties in obtaining dynamic stress equilibrium.

Polymers are very sensitive to both temperature and strain rate. In several polymers, the sensitivity is understood to increase at lower temperatures and/or higher rates of strain because of a lack of secondary mobility (β-motions), which causes increased strength and stiffness. Alternatively, the increased strength in more rubbery or elastomeric polymers is accounted for by the change in molecular mobility during the glass transition (or α-transition). In many cases, these transitions are observed in polymers at low temperatures, but can be shifted in temperature by changes in strain rate: the transition temperature increases with increasing rate. This phenomenon was observed in PVC by Bauwens in 1969, where the effect was captured via the Ree-Eyring theory of non-Newtonian flow [1]. Similarly, attempts to connect the effects of temperature and strain rate via time-temperature superposition have been investigated using the well-known WLF equation [2], or a linear time-temperature equivalence mapping [3–5]. In experimentally unifying these phenomena, Cady et al. mentioned the possibility of simulating high rate response of polymers by low rate/low temperature tests [6], and more recently, Furmanski et al. [7, 8] found a linear empirical formulation of time-temperature equivalence in HDPE, while using jump-rate compression tests to investigate isothermal high rate response with the absence of adiabatic heating.

The change from isothermal to adiabatic conditions as the strain rate increases is an important consideration, which must be considered alongside the temperature dependence of yield stress when considering changes in material behavior as a

M.J. Kendall (✉) • C.R. Siviour
Department of Engineering Science, University of Oxford, Parks Road, Oxford OX1 3PJ, UK
e-mail: michael.kendall@eng.ox.ac.uk

B. Song et al. (eds.), *Dynamic Behavior of Materials, Volume 1: Proceedings of the 2013 Annual Conference on Experimental and Applied Mechanics*, Conference Proceedings of the Society for Experimental Mechanics Series,
DOI 10.1007/978-3-319-00771-7_14,

function of strain rate. Important studies involving the measurement of temperature rise in specimens during high rate deformation have been conducted by a number of authors. A notable achievement was by Chou et al., who showed that the temperature rise in specimens increases significantly after yield [9]. Furthermore, Arruda et al. presented visible increases in strain softening with increases in strain rate, coupled with corresponding temperature measurements using infrared detectors [10]. Rittel used thermocouples to measure the temperature rise in specimens undergoing high rate deformation and later confirmed the accuracy of this method via infrared techniques [11, 12]. Additionally, Garg et al. used infrared techniques to measure the temperature rise of PC undergoing high rate deformation [13]. Good agreement was observed between the experimentally measured temperature rise and the 'theoretical' rise obtained by assuming that 100 % of the mechanical work is converted to heat, and adiabatic conditions prevail.

By combining an understanding of temperature dependence with an appreciation of adiabatic conditions, there is an opportunity to better understand and capitalize on the analogous effects of temperature and strain rate in polymers. This paper presents a large amount of uniaxial compression data on three different PVCs, which also includes data obtained using a novel experimental method that aims to predict and experimentally simulate the stress–strain response expected in a polymer, by performing a low rate experiment at reduced temperatures. A key development is to simulate not only the increase in modulus and yield stress, by reducing the temperature at the start of the experiment, but also the effects of adiabatic heating by increasing appropriately the temperature as the experiment progresses. The opportunity to predict or simulate high rate loading not only avoids several obstacles of high rate testing, such as dynamic equilibrium, but also allows for microscopic investigation on much smaller length scales through the use of electron and optical microscopy, especially in composite materials in which one component exhibits rate and temperature dependence whilst the other does not. In addition, future development of the technique to increase its fidelity beyond that presented in this paper may provide an opportunity to better understand the mechanisms of high rate deformation, especially the conversion of work to either heat or to structural changes in the material.

14.2 Experimental Method

14.2.1 Materials

Low, medium, and high rate compression tests were conducted with three kinds of PVC. One (un-plasticized) manufactured by Solvin using the resin Solvin DGA166-09 (will be referred to as 'PVC'), and two PVCs with differing amounts of plasticizer: one plasticized PVC (referred to as 'PPVC') Solvin 264-01PC, with a low plasticizer level of 20 parts per hundred resin (phr), and one plasticized PVC (referred to as 'sPPVC') Solvin 264-05PC, with a high plasticizer level of 60 phr. Diisononyl phthalate (DINP) was used as the plasticizing agent. The PVC came as pressed plates with dimensions of 11.5 $\times$ 20 cm and a thickness of 2.5 mm. These plates were machined to the specified specimen geometry, such that the axis of the specimen in the loading direction was perpendicular to the plane of the plate. All specimens were lubricated with a thin layer of petroleum jelly [14], and little to no barreling was observed.

14.2.2 Compression Testing

Uniaxial compression tests were performed over rates ranging from 10^{-3} s^{-1} to 4,700 s^{-1}. Quasi-static tests at 10^{-3}, 10^{-2} and 10^{-1} s^{-1} were performed using an Instron testing machine. Force measurements were taken from the load cell and displacement measurements from a clip gage extensometer attached to the loading platens. Quasi-static experiments were conducted over the temperature range -115 °C to 100 °C using a standard Instron environmental chamber. Here temperature readings from the environmental chamber were confirmed by the use of thermocouples attached to the platens adjacent to the specimen-platen interface. Temperatures were recorded with a National Instruments USB thermocouple reader. The colder temperatures were obtained using liquid nitrogen, with a standard tank attachment to the environmental chamber.

Experiments at rates ranging from 1 to 100 s^{-1} were conducted on a custom-built hydraulic load frame. Linear variable differential transformers (LVDTs) were used to measure the displacements of the anvils, and a strain gauge based load cell measured the force supported by the specimen. These data were used to calculate the stress–strain relationship in the sample.

High rate testing was performed at 1,770–4,700 s^{-1} on a split-Hopkinson pressure bar (SHPB) apparatus using magnesium alloy (AZM) bars for both PPVC and sPPVC, and using steel bars for PVC. The striker bar, incident bar, and

transmitted bars all had diameters 12.6 mm, with lengths of 0.5, 1.0, and 0.5m, respectively. The strain gauges were placed 0.5 m from the specimen-bar interface on the incident bar and 50 mm from the specimen-bar interface on the transmitted bar. Dynamic equilibrium was confirmed after each test by calculating force-time profiles for both specimen-bar interfaces.

Dynamic Mechanical and Thermal Analysis (DMTA) testing was conducted in order to understand the rate and temperature dependence of the molecular mobility transitions. These experiments were carried out on a TA Instruments DMTA Q800. The rectangular specimens had dimensions of 2.5 mm height, 10 mm width, and 35 mm length, and were used in the dual-cantilever mode of the DMTA machine with a set amplitude of 20 μm. Tests were performed at temperatures ranging from −100 °C to 100 °C, and frequencies of 0.1, 10, and 10 Hz.

14.2.3 Simulating Adiabatic Conditions

In order to simulate a given strain rate, $\dot{\varepsilon}$, an initial temperature T was calculated using a mapping technique that compared the dependence of yield stress on temperature at a fixed rate to the dependence on strain rate at room temperature. The mapping is based on the same linear time-temperature equivalence method (Eq. 14.2 in Sect. 3.1) which has been successfully applied in previous papers [3–5, 15].

In order to complete the simulation process, the effects of adiabatic heating were then included. The rate at which the system is expected to behave adiabatically can be calculated from the size of the specimen and the thermal diffusivity of the specimen material, as seen later in Sect. 3.1 when discussing the rate dependence of PPVC (Fig. 14.1b). Specimen heating is understood to start at the onset of plastic deformation, which in practice can be taken to be the either the start of yielding, or the point of peak stress during yield. Experimental data by other authors support this assumption and the assumption that that 100 % of the post-yield work put into deforming the specimen is converted to heat [9, 12, 13].

The stress–strain response was integrated via the trapezium rule and then converted into the theoretical temperature rise of a specimen under deformation using the equation:

$$\Delta T(\varepsilon) = \frac{\eta}{\rho C} \int_0^{\varepsilon} \sigma d\varepsilon \tag{14.1}$$

which allowed for the calculation of theoretical temperature rises due to adiabatic heating. The adiabatic temperature rise was simulated in the low rate experiments using the environmental chamber, with the temperature rise being regulated manually in increments of 0.01 % strain. Each simulation test was conducted at a strain rate of 10^{-3} s^{-1}.

14.3 Experimental Results and Discussion

14.3.1 Compression Testing and DMTA

The stress–strain behaviours of PVC, PPVC, and sPPVC under uniaxial compression are presented in Figs. 14.1 and 14.2. It should be noted that in all the data presented, the end of the stress–strain curve represents the end of the loading, and are not a feature of the specimen response. The results in Fig. 14.1 describe the behaviour of each material at 12 different strain rates at room temperature. PVC exhibits glassy polymer behaviour for all of the tested strain rates. The adiabatic heating effect of the polymer is seen in the large amount of strain softening after yield during the high rate tests. When comparing the curves of PPVC at different strain rates (Fig. 14.1b), there appears to be a clear transition between those experiments (at rates of 0.1 s^{-1} and below) in which post-yields strain hardening is significant, and those (at rates of 1 s^{-1} and above) in which this hardening is not observed. Using a thermal diffusivity value of 0.11 mm^2 s^{-1} the strain rate at which the adiabatic heating would become significant is of the order 0.28 s^{-1}. The data presented, therefore, are consistent with adiabatic heating playing a role in the reduction of strain hardening at higher rates of strain. For sPPVC, the effect of the glass transition is seen in Fig. 14.1c by the change in its response going from a rubbery response to a more glassy response at higher rates. This is an effect of the glass transition, or α transition shifting to a higher temperature. The behaviour of each material depends strongly on strain rate, as seen by the change in yield stress, here defined as the peak stress, with increasing strain rate.

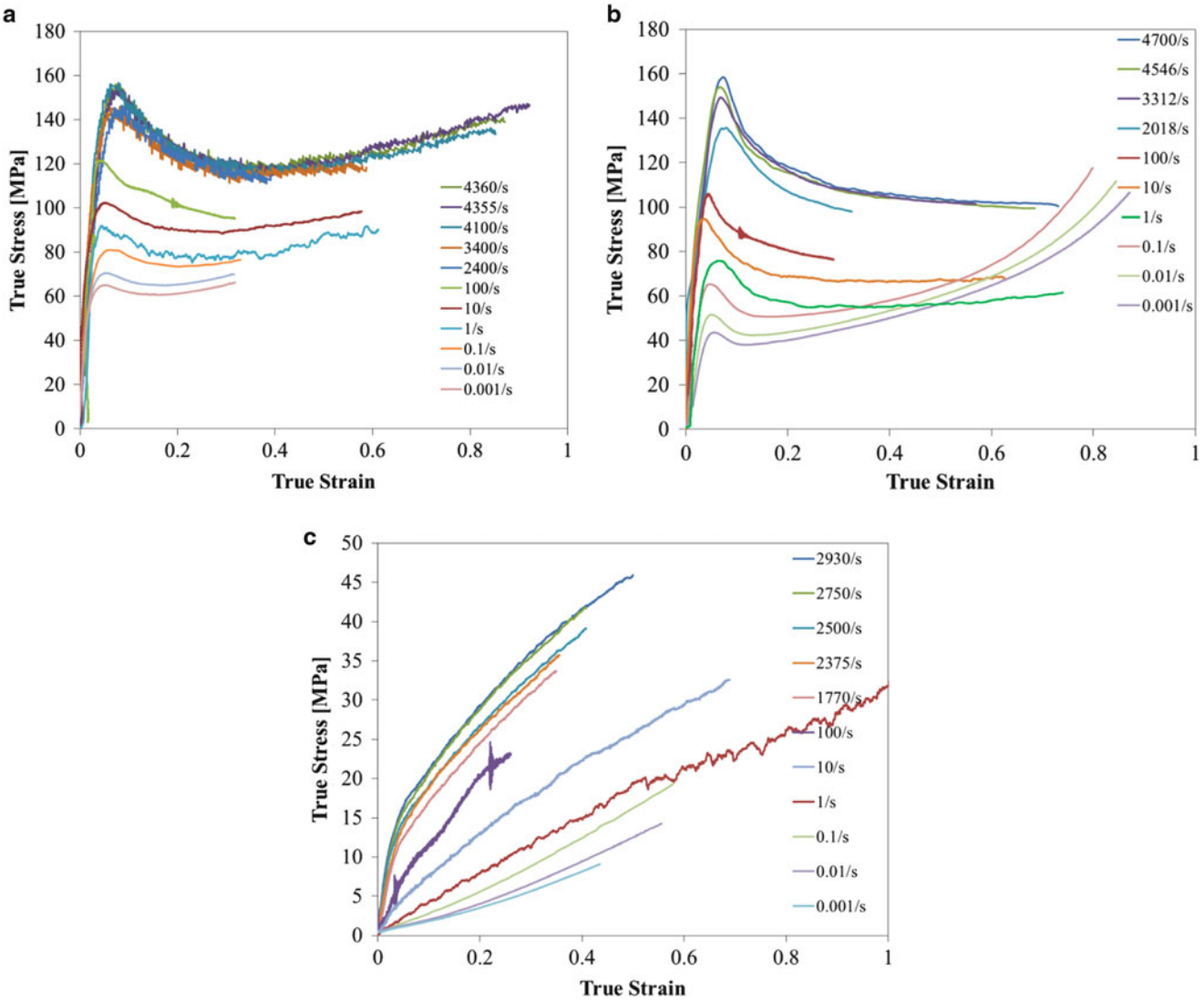

Fig. 14.1 (**a**) PVC, (**b**) PPVC, and sPPVC (**c**) stress–strain behavior in uniaxial compression at room temperature over a range of strain rates

The temperature dependence of each material under quasi-static loading is seen in Fig. 14.2. In PVC's response, the effect of the glass transition is seen at approximately 80 °C, which is consistent with the DMTA data. At 100 °C the polymer exhibits a more rubbery response, similar to that of sPPVC. The response of PPVC is characterized by increasing gradients of strain hardening with decreasing temperature. In addition, the effect of the glass transition is seen at approximately 50 °C, which is consistent with the DMTA data for PPVC. The temperature dependence of sPPVC illustrates the material transitioning through the glass transition temperature, offering an array of responses throughout the range of temperatures. sPPVC's sub-room temperature glass transition is seen at approximately −40 °C, after transitioning from a more leathery response to a response much like PVC or that of a glassy polymer. It is worth noting the distinctive similarity between sPPVC's response at −20 °C and strain rates centred at 2,500 s^{-1}. These similarities highlight the interplay between temperature and strain rate in a materials response and offers opportunities in analysis, which will be discussed in greater detail below.

A comparison of the dependence of PVC, PPVC, and sPPVC's yield strength upon temperature and strain rate data, and DMTA data, is useful in predicting the material transitions, which occur at high strain rate/low temperature, and the rate at which they occur. PVC's yield stress dependence upon temperature has been seen to be very similar to the shape of the curve produced in DMTA when measuring the dependence of the storage modulus with respect to temperature, presented in Fig. 14.3. This similarity illustrates the consistency of and confirms α and β transitions in the uniaxial compression data and the DMTA data [16].

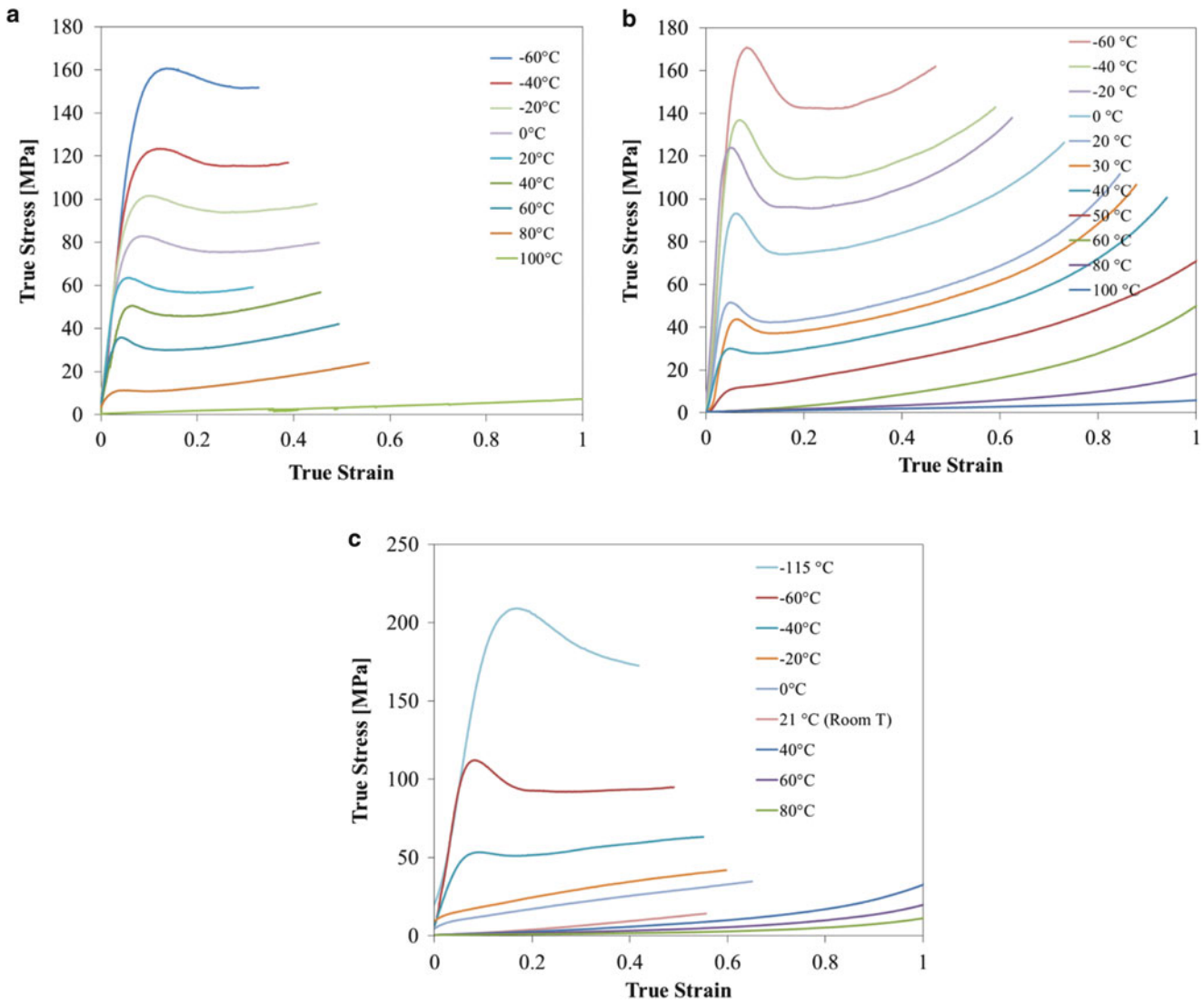

Fig. 14.2 (**a**) PVC, (**b**) PPVC, and sPPVC (**c**) stress–strain behavior in uniaxial compression over a range temperatures. All tests were conducted at a strain rate of 10^{-2} s^{-1}

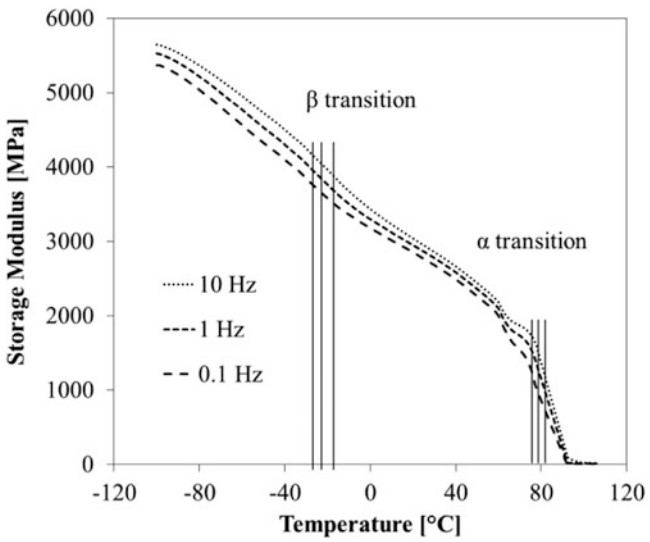

Fig. 14.3 DMTA data for PVC: temperature dependence of the storage modulus at 10, 1, and 0.1 Hz

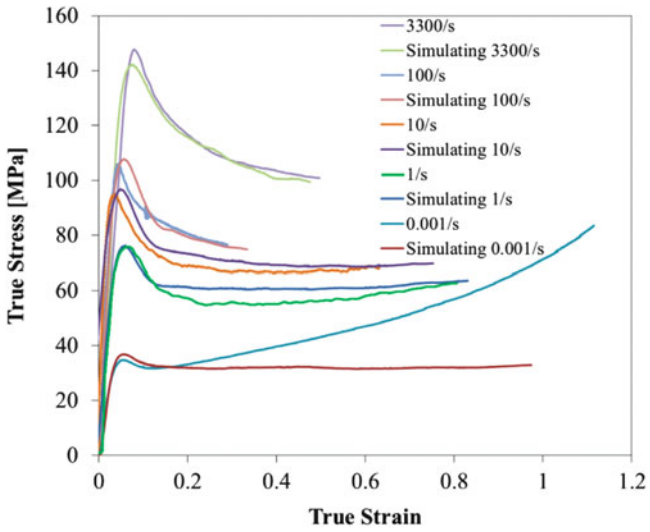

Fig. 14.4 PPVC's response to 0.001–3,300 s^{-1} strain rates and these same strain rates simulated via the simulating adiabatic conditions (*SAC*) method. The 0.001 s^{-1} response is shown to highlight the shift in material response from an isothermal to an adiabatic response

From time-temperature equivalence we are able to predict the strain rate at which the β transition begins to affect the results from room temperature testing on PVC – seen as the point at which the polymer's strength has an increase in sensitivity to strain rate. By assuming the β transition temperature increases linearly with the logarithm of strain rate, a line fitted to the locations of the beta transition temperatures in DMTA testing is extrapolated to predict the location of the strain rate (at room temperature) at which the transition occurs. The beta transition temperatures obtained from the DMTA data are indicated in Fig. 14.3. Using Eq. 14.2, the beta transition seen on the DMTA results is shifted up to room temperature by increments of the change in temperature of the beta transition (5 °C for PVC, or D in Eq. 14.2) per decade of strain rate (found from the comparison of test frequencies).

$$T - T_0 = D[\log \dot{\varepsilon}_0 - \log \dot{\varepsilon}] \tag{14.2}$$

Where D is a mapping parameter that quantifies the interaction between rate and temperature and maps from a temperature T to a new temperature T_o and mapping the strain rate $\dot{\varepsilon}_0$ to a new strain rate $\dot{\varepsilon}$ (i.e. a set of data would be comprised of experiments at a reference temperature T_o while varying strain rate, and a set of data would consist of experiments at a reference strain rate of $\dot{\varepsilon}_0$ with varying temperature).

By calculating this shift, the strain rate at which the beta transition is expected to occur at room temperature was found. This was compared with the value of strain rate that would be found from a bilinear fit to the yield stress versus log strain rate curve and calculating where the two lines intersect. The DMTA shifting method produced a value of 2.9 for the logarithm of strain rate, or roughly 800 s^{-1}. A bilinear fit to the yield stress data on the same material is 2.8. A clear connection between the interplay of temperature and rate dependence is seen by the very close agreement between the values from the two methods.

14.3.2 Simulating Adiabatic Conditions

Initial experiments were performed to evaluate the response of the PPVC to loading over a range of strain rates and temperatures (Figs. 14.1b and 14.2b). When comparing the curves at different strain rates (Fig. 14.1b), there appeared to be a clear transition between those experiments (at rates of 0.1 s^{-1} and below) in which post-yields strain hardening is significant, and those (at rates of 1 s^{-1} and above) in which this hardening is not observed. As mentioned in Sect. 3.1, the strain rate in which the transition from isothermal to adiabatic heating takes place in PPVC was calculated of the order 0.28 s^{-1}. This calculation confirms that adiabatic heating plays a role in the reduction of strain hardening at higher rates of strain.

The data in Figs. 14.1b and 14.2b were used to obtain the required information to implement the simulation technique. As described above, initial temperatures were chosen to match the yield stress of the rate to be simulated, whilst temperature profiles were obtained by integrating the stress–strain curve. The experimental data thus obtained are shown in Fig. 14.4. Here each set of room temperature data is accompanied by the Simulating Adiabatic Conditions curve (SAC), which was obtained by performing an experiment at 0.001 s^{-1} with the appropriate temperature profiling – note that for completeness

an additional SAC curve was obtained at 0.001 s^{-1} even though this does not represent a physically plausible loading condition. The good agreement between the SAC stress–strain curves and the curves they were simulating indicates that this is a promising technique for predicting, simulating and understanding high rate behavior. In particular, not only has the apparent modulus and yield stress at each strain rate has been successfully simulated but also the more rapid increase in modulus and yield stress (caused by the β transition) at higher rates.

The post-yield behavior in the high rate experiments has also been simulated with good agreement. There are a number of possible causes for the discrepancies observed in both the yield and post-yield behavior. Experimentally, it is difficult to achieve a well-controlled temperature profile in the specimens, due to the thermal inertia in the temperature chamber. In addition, although care was taken to measure the temperature in a number of locations close to the specimen, the specimen may not be in thermal equilibrium with the platens or the surrounding air in the chamber. More positively, the differences may be the result of mechanical behavior of the polymer that has not been accounted for in the simplistic assumptions used in this paper. As the strain rate changes the mechanical processes that govern the observed response are likely to change, especially as the influence of the beta transition changes. In addition, the processes that govern post-yield behavior may not have the same temperature dependence as those that govern yield. Finally, the discrepancies might result from inadequacy in the assumption that all of the work done on the specimen is converted to heat: the beta factor, η, may not be 1. It is hoped that in future work, with suitable technical improvements to the heating control, experiments with suitable fidelity will allow the behavior to be explored in more detail, giving better understanding of the mechanisms that govern high strain rate response.

14.4 Conclusion

Three PVCs with different plasticizer levels have been characterized through uniaxial compression experiments over a broad range of strain rates and temperatures. DMTA characterization has also been performed on one of these materials. In both materials, the effects of polymer transitions on the rate dependence are clear, the glass transition in each of the materials, and the β transition in the unplasticized. Moreover, in the unplasticized PVC, DMTA data have been successfully extrapolated to predict the strain rate at which the β transition begins to affect the rate dependence of the material.

Additional data presented in this paper show that it is possible to experimentally simulate the high strain rate response of a polymer by performing low strain rate experiments with suitable temperature profiles. The key development was not only to modify the initial temperature in order to simulate the change in yield stress, but also to capture the post-yield behavior by simulating adiabatic heating in the specimen. The straightforward, yet effective approach, offers significant opportunities in better understanding the high rate behavior in a large number of materials. In particular, this technique offers the possibility of better characterizing the behavior of composite materials in which one component is rate sensitive, and to perform experiments on these materials using in-situ diagnostics that cannot be applied to high rate experiments. As well as these immediate opportunities, the simulation of adiabatic conditions as a function of strain offers the potential to develop further insights into the effects of temperature rises in high rate deformation, and highlights the connection between a polymer's temperature-dependent and rate-dependent behavior. Future experiments will allow us to develop a stronger understanding of the mechanisms that underlie the constitutive behavior of several polymers, allowing for improved prediction methods and constitutive model developments.

Acknowledgements The authors would like to thank Dr. J.L. Jordan and Dr. J.R. Foley for their support of the research, R. Duffin and R. Froud for ongoing technical support, and H. Schiffter and T. Healey for help in conducting DMA testing. M.J. Kendall would also like to acknowledge Dr. I. Dyson for help with low rate testing, and Dr. D.R. Drodge and Dr. E.J. Wielewski for helpful discussions and suggestions. Effort sponsored by the Air Force Office of Scientific Research, Air Force Material Command, USAF, under grant number FA8655-09-1-3088. The US Government is authorized to reproduce and distribute reprints for Governmental purpose notwithstanding any copyright notation thereon. The authors thank Dr. R. Pollak for his ongoing support.

References

1. Bauwens JC, Bauwens-Crowet C, Homès G (1969) Tensile yield-stress behavior of poly (vinyl chloride) and polycarbonate in the glass transition region. J Polym Sci Part A-2 7:1745–1754
2. Williams ML, Landel RF, Ferry JD (1955) The temperature dependence of relaxation mechanisms in amorphous polymers and other glass-forming liquids. J Am Chem Soc 77(14):3701–3707

3. Siviour CR, Walley SM, Proud WG, Field JE (2005) The high strain rate compressive behaviour of polycarbonate and polyvinylidene difluoride. Polymer 46(26):12546–12555
4. Brown EN, Willms RB, Gray GT, Rae PJ, Cady CM, Vecchio KS, Flowers J, Martinez MY (2007) Influence of molecular conformation on the constitutive response of polyethylene: a comparison of HDPE, UHMWPE, and PEX. Exp Mech 47(3):381–393
5. Williamson DM, Siviour CR, Proud WG, Palmer SJP, Govier RK, Ellis K, Blackwell P, Leppard C (2008) Temperature–time response of a polymer bonded explosive in compression (EDC37). J Phys D Appl Phys 41(8):085404
6. Cady CM, Blumenthal W, Gray G III, Idar D (2003) Determining the constitutive response of polymeric materials as a function of temperature and strain rate. In: Journal de Physique IV (Proceedings), vol 110, pp 27–32
7. Furmanski J, Trujillo CP, Martinez DT, Gray GT, Brown EN (2012) Dynamic-Tensile-Extrusion for investigating large strain and high strain rate behavior of polymers. Polym Test 31(8):1031–1037
8. Furmanski J, Brown EN, Clements B, Cady CM, Gray GT (2012) Large-strain time-temperature equivalence in high density polyethylene for prediction of extreme deformation and damage. EPJ Web Conf 26:01057
9. Chou S, Roberston K, Rainey J (1973) The effect of strain rate and heat developed during deformation on the stress–strain curve of plastics. Exp Mech 13:422–432
10. Arruda EM, Boyce MC, Jayachandran R (1995) Effects of strain rate, temperature and thermomechanical coupling on the finite strain deformation of glassy polymers. Mech Mater 19(2–3):193–212
11. Rittel D (1999) On the conversion of plastic work to heat during high strain rate deformation of glassy polymers. Mech Mater 31(2):131–139
12. Regev A, Rittel D (2007) Simultaneous transient temperature sensing of impacted polymers using infrared detectors and thermocouples. Exp Mech 48(5):675–682
13. Garg M, Mulliken AD, Boyce MC (2008) Temperature rise in polymeric materials during high rate deformation. J Appl Mech 75(1):011009
14. Trautmann A, Siviour CR, Walley SM, Field JE (2005) Lubrication of polycarbonate at cryogenic temperatures in the split Hopkinson pressure bar. Int J Impact Eng 31:523–544
15. Jordan JL, Foley JR, Siviour CR (2008) Mechanical properties of Epon 826/DEA epoxy. Mech Time-Dep Mater 12(3):249–272
16. Kendall MJ, Siviour CR (2012) Strain rate dependence in plasticized and un-plasticized PVC. EPJ Web Conf 26:02009

Chapter 15
Strain Rate Dependence of Yield Condition of Polyamide 11

Masahiro Nishida, Rie Natsume, and Masayuki Hayashi

Abstract Polyamide 11 (PA11) is one of bioplastics (plant-derived plastics or recyclable-resource-based plastics). It is produced from renewable castor seeds. The castor seeds are inedible. This point is important in the future potential because of the food insecurity in the future. In general, because yield condition of plastics depends on the hydrostatic pressure, the yield stress of compression is larger than that of tension. The yield stresses of PA11 were measured at high and low strain rates by using a split Hopkinson pressure bar (Kolsky bar) method and a universal testing machine. We determined constants of Druker-Prager yield criterion (a pressure-dependent model) for PA11, and drew the yield curves in the plane of the equivalent stress (the second deviatoric stress) and the hydrodynamic pressure (invariant-first invariant of stress) and in the plane of principle stresses (the plane stress space). The strain rate dependence of the yield condition of PA11 was examined.

Keywords Bioplastics • Strain rate sensitivity • Yield criterion • Split Hopkinson pressure bar method • Dynamic properties

15.1 Introduction

The increasing use of plastics products worldwide is causing considerable damage to the environment; biodegradable plastics (plastics that can decompose in the natural environment) and bioplastics (plant-derived or recyclable-resource-based plastics) are therefore being extensively investigated, and new biodegradable plastics and bioplastics continue to be developed. In Japan, such polymers are already used in many industrial products, such as the interior parts of cars, parts of computer cases, cell-phone cases, and Styrofoam peanuts (extruded foam). However, such applications are currently limited to machine parts that are subjected to low loading forces. Many studies have been conducted to develop various industrial products that can be manufactured using biodegradable plastics and bioplastics.

In most cases, the impact resistances of biodegradable plastics and bioplastics are based only on the experimental results of Izod/Charpy impact strength tests and Dynatup impact tests. However, the basic mechanical properties of such plastics, including their impact resistances, remain unknown. High-accuracy simulation needs high-accuracy material parameters, such as yield stress, strain rate dependence and pressure dependence, elongation, and ultimate stress.

Polyamide 11 (PA11) is one of bioplastics. It is produced from renewable castor seeds. The castor seeds are inedible. This point is important in the future potential because of the food insecurity in the future. In the present study, the stress–strain curves of polyamide 11 were measured using a universal testing machine and a split Hopkinson pressure bar system (the Kolsky bar system). The material constants of the Druker-Prager yield criterion for the bioplastic polyamide 11 were determined. The strain rate dependence of the Druker-Prager yield condition of PA11 was examined.

M. Nishida (✉) • R. Natsume • M. Hayashi
Department of Mechanical Engineering, Nagoya Institute of Technology, Gokiso-cho, Showa-ku, Nagoya, Aichi 466-8555, Japan
e-mail: nishida.masahiro@nitech.ac.jp

B. Song et al. (eds.), *Dynamic Behavior of Materials, Volume 1: Proceedings of the 2013 Annual Conference on Experimental and Applied Mechanics*, Conference Proceedings of the Society for Experimental Mechanics Series,
DOI 10.1007/978-3-319-00771-7_15,

15.2 Experimental Methods

15.2.1 Materials and Specimens

We used polyamide 11 (Arkema; Rilsan PA11, BMN O TLD). Figure 15.1 shows the chemical structural formula of polyamide 11. The properties taken from the manufacturer's data are shown in Table 15.1. Molded plates of 10 mm in thickness were made from polyamide 11 pellets using a conventional hot press at 30 MPa for 30 min. Compressive test specimens were made from the molded plates using the lathe, and then their end faces were polished. In the quasi-static compressive tests, the diameter was 10 mm and the thickness was 15 mm based on ASTM D695-02a. In the dynamic compressive tests, the diameter was 15 mm and the thickness was 5 mm (slender ratio 0.33).

Because they are easy to make, plate-type specimens were employed as tensile test specimens. Based on the results of compressive tests, we decided that for static tensile tests, the gage length of specimens was 10 mm and the gage length region was 5 mm by 2 mm, as shown in Fig. 15.2, and for dynamic tensile tests, the gage length of specimens was 4 mm and the gage length region was 3 mm by 3 mm. In the case of dynamic tensile tests, the specimens were connected with the input and output bars using support jigs, fixing pins of 3 mm in diameter, and glue, as shown in Fig. 15.3.

15.2.2 Compressive Tests

In the quasi-static compressive tests, we used a universal testing machine (RTM-500, A&D Company, Ltd., Tokyo, Japan). At high strain rates, the compressive properties were examined by the split Hopkinson pressure bar system shown in Fig. 15.4. The input and output bars were made of an aluminum alloy (6065-T6), and their diameters and lengths were

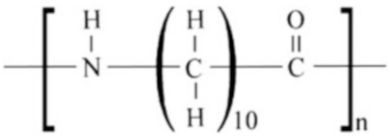

Fig. 15.1 Chemical structural formula of PA11

Table 15.1 Properties of polyamide 11 [1]

Density		1.03 g/cm^3
Heat deflection temperature	Under 0.45 MPa	138 °C
	Under 1.80 MPa	42 °C
Melting point		187–191 °C
Tensile yield stress		41 MPa
Charpy impact 23 °C	Unnotched	No break
	Notched	9 kJ/m^2

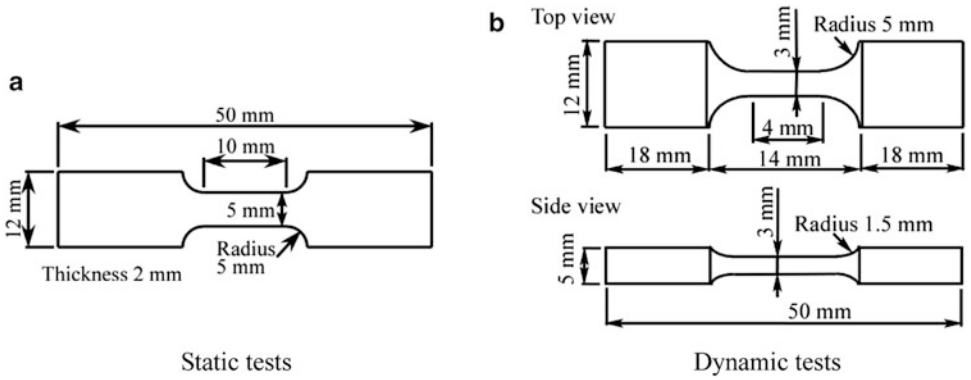

Fig. 15.2 Tensile test specimens

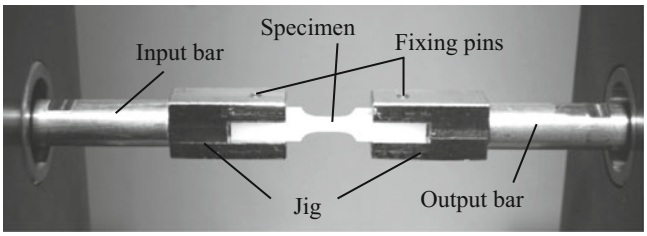

Fig. 15.3 Connection of dynamic tensile test specimens with input and output bars

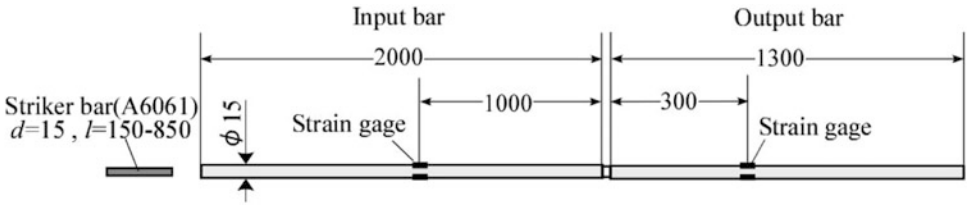

Fig. 15.4 Experimental setup for split Hopkinson pressure bar method (Kolsky bar)

Table 15.2 Material constants of input and output bars used in calculations

	Density [kg/m^3]	Elastic wave velocity in bar, c_3 [m/s]	Young's modulus E [GPa]
Aluminum alloy, A6065-T6	2.77×10^3	5,170	73
Stainless steel, SUS304	8.0×10^3	4,970	200

15 mm and 2,000 mm/1,300 mm. Strain gages were placed on the side of an input bar, 1,000 mm away from the specimen, and on an output bar, 300 mm away from the specimen. The stresses and strains of the specimens [2, 3] were calculated from the strains of the bars, measured by strain gages, based on the following equations:

$$\sigma(t) = \frac{AE}{A_S}\varepsilon_T(t) \tag{15.1}$$

$$\varepsilon(t) = \frac{2c_3}{L}\int_0^t [\varepsilon_I(t) - \varepsilon_T(t)]\, dt \tag{15.2}$$

where ε_I and ε_T are the axial strain in the input bar induced by the incident wave and the axial strain in the output bar induced by the transmitted wave, respectively. E and c_3 are the Young's modulus and elastic wave velocity of the input and output bars, respectively. L is the specimen thickness. A and A_s are the cross-sectional areas of the input/output bars and the specimens. The material constants of the aluminum alloy (A6065) bars used in the calculations are shown in Table 15.2. We used brass strikers 15 mm in diameter and 615 mm in length. We preserved the specimens in a desiccator at a humidity of 30–40 % until just before use in order to avoid the effects of moisture absorption on the specimens. During the experiments, our laboratory was maintained at a temperature of 18–25 °C and a humidity of 30–65 %.

15.2.3 Tensile Tests

In the quasi-static tensile tests as well as compressive tests, we used a universal testing machine (RTM-500, A&D Company, Ltd., Tokyo, Japan). At high strain rates, the dynamic properties of the specimens were examined by the tensile split Hopkinson bar test, as shown in Fig. 15.5. The strain on the specimens was calculated from the strain of the bars, as measured by the strain gages, using Eq. 15.2. The stress history of tensile tests was calculated from Eq. 15.1. The input and output bars were made of stainless steel (SUS304), and their material constants used in the calculations are listed in Table 15.2.

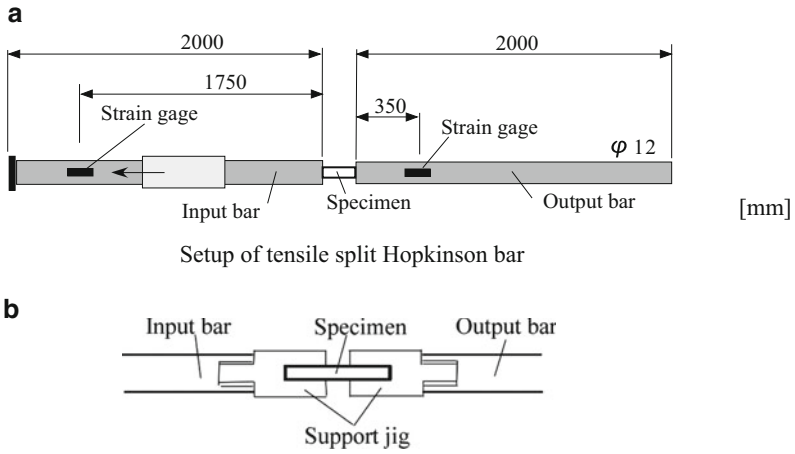

Fig. 15.5 Experimental setup for dynamic tensile tests method (Kolsky bar)

15.3 Results and Discussion

Figures 15.6a, b show the true stress–strain curves of the static compressive and tensile tests. Instantaneous cross-sectional areas of specimens were calculated using camera images of specimens during experiments. The true stresses in tensile tests and compressive tests increased with increasing strain rate. Results of Young's modulus, yields yield stress, and yield strain are shown in Tables 15.3 and 15.4. For each strain rate, the yield stress of the compressive tests was 6–8 % larger than that of the tensile tests. In general, the yield stress of plastics depends on hydrostatic pressure and the yield stress of compressive tests was larger than that of the tensile tests. The yield stresses of polyamide 11 also depended on hydrostatic pressure. A smaller pressure dependence of the yield stress was observed compared with the values of 1.33 for polyvinyl chloride and 1.20 for polycarbonate [4].

As shown in Fig. 15.7a, the yield stresses from the tensile test and the compressive test were plotted in the plane of the equivalent stress (the second deviatoric stress) and the hydrostatic pressure (the first invariant of stress). Among the pressure-dependent models of yield stress, such as the Mohr–Coulomb yield criterion, the Drucker-Prager yield criterion [5], the Raghava yield criterion [4], and the semi-analytical model [6] proposed by the Daimler group, used, for example, as material model #187 in LS-DYNA, the Drucker-Prager yield criterion is the simplest model. In the space of principle stresses, the Drucker-Prager yield surface represents a cone whose axis matches the space diagonal of the coordinate system of the principal stresses σ_1, σ_2, and σ_3. In terms of the equivalent stress and the hydrostatic stress, the Drucker-Prager criterion can be expressed as

$$f(\sigma_{vm},\ p) = \sigma_{vm} - A_0 - A_1 p \tag{15.3}$$

where σ_{vm} is the equivalent stress (or von Mises stress), p is the hydrostatic pressure (or mean stress), and A_0 and A_1 are material constants. By fitting Eq. 15.3 to the results at strain rates of order 10^{-3} s^{-1} to 10^{-4} s^{-1} in Fig. 15.7a, the material constants were determined.

$$f(\sigma_{vm},\ p) = \sigma_{vm} - 43.6 - 0.113p \quad \text{for } 2.0 \times 10^{-3}(\text{tension}) \text{ and } 1.9 \times 10^{-3}(\text{compression}) \tag{15.4}$$

$$f(\sigma_{vm},\ p) = \sigma_{vm} - 42.8 - 0.123p \quad \text{for } 1.0 \times 10^{-3}(\text{tension}) \text{ and } 0.91 \times 10^{-3}(\text{compression}) \tag{15.5}$$

$$f(\sigma_{vm},\ p) = \sigma_{vm} - 39.9 - 0.079p \quad \text{for } 7.9 \times 10^{-4}(\text{tension}) \text{ and } 5.1 \times 10^{-4}(\text{compression}) \tag{15.6}$$

Equations 15.4, 15.5, and 15.6 are represented by the solid line in Fig. 15.7a. Figure 15.7b shows yield loci in the plane of principle stresses, σ_1 and σ_2, (plane stress space) for strain rates of order 10^{-3} s^{-1} to 10^{-4} s^{-1}. The yield loci expanded with increasing strain rate, which is explained by the strain rate sensitivity of the material, as observed in most engineering plastics.

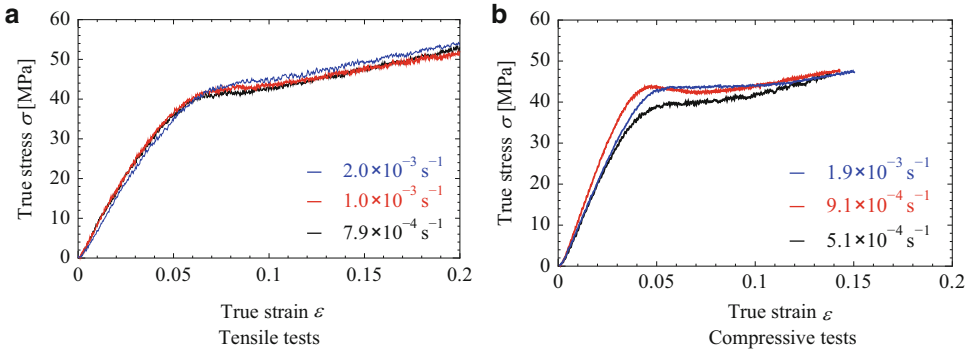

Fig. 15.6 Stress–strain curves of static tests

Table 15.3 Young's modulus, yields stress, and yield strain of static tensile tests

Strain rate [s^{-1}]	Young's modulus [GPa]	Yield stress [MPa]	Yield strain [%]
7.9×10^{-4}	0.85	38.9	4.6
1.0×10^{-3}	0.89	41.3	4.8
2.0×10^{-3}	0.84	42.0	5.2

Table 15.4 Young's modulus, yields stress, and yield strain of static compressive tests

Strain rate [s^{-1}]	Young's modulus [GPa]	Yield stress [MPa]	Yield strain [%]
5.1×10^{-4}	1.10	41.2	4.2
0.91×10^{-3}	1.32	44.6	3.7
1.9×10^{-3}	1.14	45.2	4.3

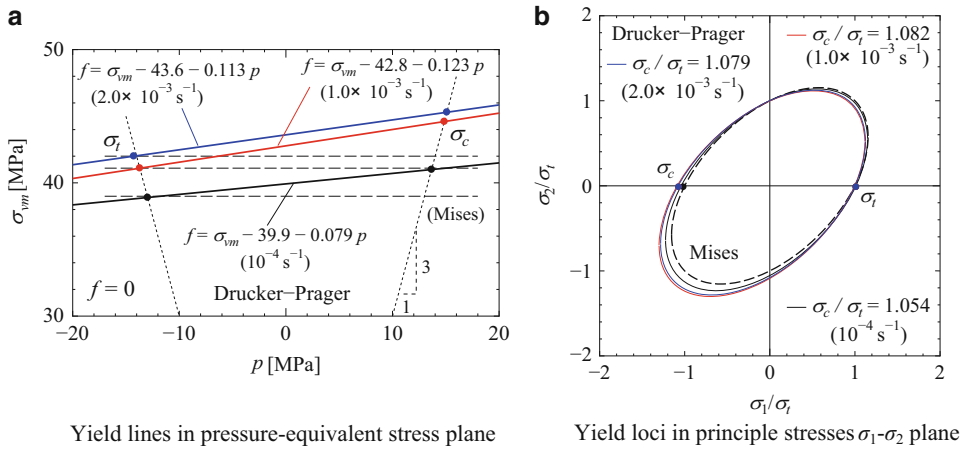

Yield lines in pressure-equivalent stress plane

Yield loci in principle stresses σ_1-σ_2 plane

Fig. 15.7 Hydrostatic pressure dependence of yield stress for polyamide 11 at low strain rates

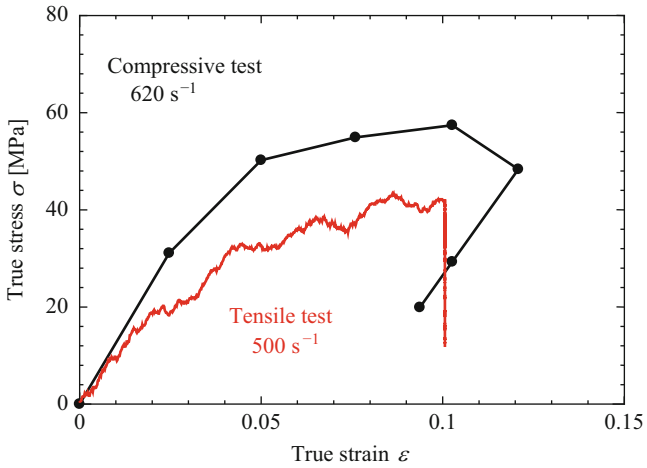

Fig. 15.8 Stress–strain curves of dynamic tests

Table 15.5 Young's modulus, yields stress, and yield strain of dynamic tensile tests

	Yield stress [MPa]
Tensile test (600 s^{-1})	40.2
Compressive test (660 s^{-1})	52.5

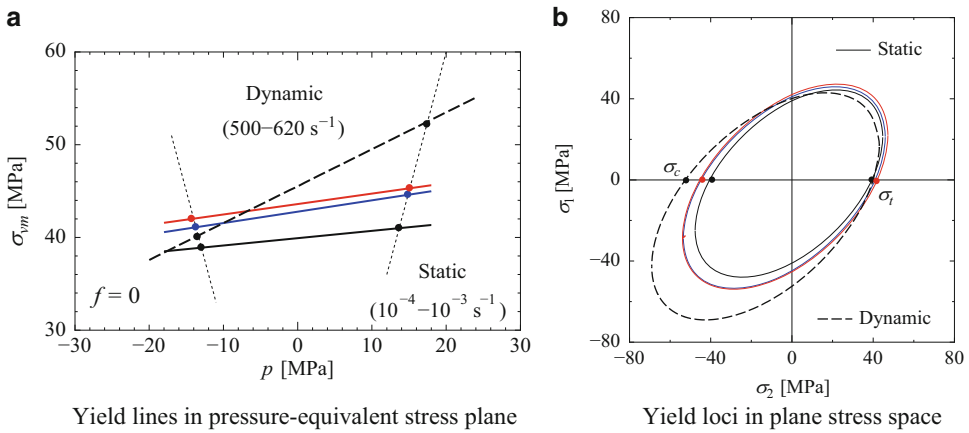

Yield lines in pressure-equivalent stress plane

Yield loci in plane stress space

Fig. 15.9 Hydrostatic pressure dependence of yield stress for polyamide 11 at high strain rates

Figures 15.8 shows true stress–strain curves of dynamic compressive and tensile tests, and Table 15.5 shows the results of Young's modulus and yields stress of dynamic tests. Instantaneous cross-sectional areas of specimens were calculated using high-speed video camera images of specimens during experiments. The yield stress in the compressive tests was twice as large as that of the tensile tests. Figure 15.9a shows the Drucker-Prager yield criterion and the yield stresses from the tensile test and the compressive test in the plane of the equivalent stress (the second deviatoric stress) and the hydrostatic pressure (the first invariant of stress), and Fig. 15.9b shows yield loci in the plane of principle stresses, σ_1 and σ_2, for strain rates of order 10^2 s^{-1}. They are an unnatural shape in Fig. 15.9a and large yield loci in Fig. 15.9b. It is highly possible that the main reason for this is a higher viscosity of polyamide 11. Further experiments are required.

15.4 Conclusions

Strain rate dependence of yield behavior in a bioplastic, polyamide 11, was investigated experimentally using a universal testing machine, a split Hopkinson pressure bar, and a tensile split Hopkinson bar. It was observed that the hydrostatic pressure dependence of the yield behavior in this plastic was not significantly influenced at low strain rates. At a high strain rate, the yield stress of compressive tests was twice as large as that of the tensile tests.

Acknowledgment The authors are greatly indebted to Professor K. Ogawa of Osaka University for his valuable advice with respect to the tensile split Hopkinson bar. The authors are greatly indebted to ARKEMA Japan, Dr. Atsushi Miyabo and Mr. Shinya Matsuno, for the help with making specimens.

References

1. Arkema, manufacturer report
2. Gray GT III (2000) Classic split Hopkinson pressure bar testing. In: ASM handbook. Mechanical testing and evaluation, vol 8. ASM, pp 462–476
3. Chen W, Song B (2010) Split Hopkinson (Kolsky) bar: design, testing and applications. Springer, New York
4. Raghava RS, Caddell RM, Yeh GSY (1973) The macroscopic yield behavior of polymers. J Mater Sci 8:225–232
5. Drucker DC, Prager W (1952) Soil mechanics and plastic analysis or limit design. Q Appl Math 10(2):157–165
6. Du Bois PA, Kolling S, Feucht M, Haufe A (2008) The influence of permanent volumetric deformation on the reduction of the load bearing capability of plastic components. In: Proceedings of the 10th international LS-DYNA conference, pp 19-35–19-42

Chapter 16
Effect of Strain Rate on Mechanical Response of PBX Simulants

Chunghee Park, Hoon Huh, and Jungsu Park

Abstract This paper is concerned with the effect of the strain rate on the mechanical response of polymer-bonded explosive (PBX) simulants at various strain rates ranging from 0.0001 to 3,710 s^{-1}. The mechanical response of PBXs at intermediate and high strain rates is important in the prediction of deformation modes of PBXs in a warhead system which undergoes severe dynamic loads. Inert PBX stimulants, which have analogous mechanical response to PBXs, were utilized for all material tests due to safety reasons. The uniaxial compressive tests at quasi-static and intermediate strain rates ranging from 0.0001 to 100 s^{-1} were conducted with cylindrical specimens using a dynamic material testing machine (INSTRON 8801) and a developed high-speed material testing machine (HSMTM). A novel experimental method is developed for the uniaxial compressive tests at intermediate strain rates ranging from 10 to 100 s^{-1}. The split Hopkinson pressure bar (SHPB) was used for the uniaxial compressive tests at high strain rates ranging from 1,200 to 3,710 s^{-1}. The pulse shaping technique was adopted for the SHPB tests to minimize wave dispersion and to facilitate stress equilibrium and constant-strain-rate deformation in the specimen. Deformation behavior was investigated using captured images obtained from a high-speed camera. The effect of the strain rate on the mechanical response during the uniaxial compressive deformation is quantitatively investigated from the experimental data at the various strain rates.

Keywords PBX simulant • Mechanical response • Effect of strain rate • High-speed material testing machine • Split Hopkinson pressure bar

16.1 Introduction

Polymer-bonded explosives (PBXs) are specialized particulate composites that mainly consist of explosive crystals held together by a polymer binder. The use of PBXs has increased due to its precise manufacturing process and ease of handling. When the warhead system including polymer-bonded explosives (PBXs) infiltrates or penetrates into a target, severe dynamic loads are applied to PBXs in the warhead within a few milliseconds during the infiltration or penetration. The dynamic loads induce not only localized large deformation of PBXs with high strain rates but also small deformation with low and intermediate strain rates. Thus, PBXs undergo deformation with a wide range of strain rates irregularly distributed from the quasi-static level to the high level. The effect of the strain rate on the mechanical response of PBXs should be thoroughly investigated to perform the numerical simulation accurately.

The effect of the strain rate on the mechanical properties of PBXs has been widely investigated. Peeters et al. [1] investigated the development of an equation-of-state creep model and a linear viscoelastic model for the analysis of polymer-bonded explosive material systems. They showed comparisons between the experimental results of uniaxial creep tests, uniaxial tensile and compressive tests as a function of the strain rate, cyclic loading tests, stress relaxation tests and analytical model predictions. Gray III et al. [2] analyzed compressive test data at high and low strain rates obtained

C. Park • H. Huh (✉)
KAIST, School of Mechanical, Aerospace and Systems Engineering, 291 Daehak-ro, Yuseong-gu, Daejeon 305-701, Republic of Korea
e-mail: hhuh@kaist.ac.kr

J. Park
The 4th R&D Institute-2, Agency for Defense Development, Bugyuseong daero 488 beon gil, Yuseong-gu, Daejeon 305-152, Republic of Korea

B. Song et al. (eds.), *Dynamic Behavior of Materials, Volume 1: Proceedings of the 2013 Annual Conference on Experimental and Applied Mechanics*, Conference Proceedings of the Society for Experimental Mechanics Series,
DOI 10.1007/978-3-319-00771-7_16,

on several different energetic composites such as PBX 9501, XO242-92-4-4, PBXN-9 and the polymeric binder used in PBX 9501 and XO242-92-4-4 composites. They investigated the effects of energetic-to-binder ratios, different binder systems and different energetic formulations. All the energetic composites exhibited increasing elastic modulus, maximum flow stress and strain at maximum stress as the strain rate increased at ambient temperature. In addition, they reported that the ratio of the crystal fracture of particles increases in the compressive tests at high strain rates, while the debonding is the dominant failure mechanism in the compressive tests at low strain rates. Foster Jr. et al. [3] conducted high-strain-rate compressive tests of PBXN-109 at a speed of 69 m/s, and investigated the mechanical properties and microstructures using scanning electron microscopy (SEM) images. Millett et al. [4] performed plate impact experiments of polychloroprene, widely used in PBXs as a bonding agent, using 75 mm and 50 mm bore gas guns and studied the shock response at high strain rates. Idar et al. [5] reported the mechanical properties of PBX 9501 as a function of the strain rate and temperature. They conducted uniaxial tensile and compressive tests at quasi-static strain rates and uniaxial compressive tests at high strain rates using a split Hopkinson pressure bar (SHPB). Grantham et al. [6] conducted high-strain-rate Brazilian tests of PBS 9501, which is the simulant material of PBX 9501, using the SHPB at the strain rate of 2,300 s^{-1} to observe the deformation behavior of PBS 9501. Cady et al. [7] investigated the mechanical properties of PBX binder materials such as extruded Estane, plasticized Estane and plasticized hydroxyl-terminated polybutadiene (HTPB) as a function of temperatures ranging from −75 °C to 23 °C and strain rates ranging from 0.001 to 2,800 s^{-1}. Siviour et al. [8] studied the mechanical properties of polymer-bonded sugar (PBS) at high strain rates. By introducing the mechanical properties of PBS at the strain rate of 2,000 s^{-1}, they emphasized the mechanical properties at intermediate strain rates. The above-mentioned studies focused on qualitative observations of the changes of the mechanical response of PBXs as a function of the strain rate. Although various kinds of material tests with PBXs were performed so far, there is no experimental method for uniaxial compressive tests at intermediate strain rates of approximately 100 s^{-1}.

In this study, a novel compressive test method was developed and performed to acquire the mechanical response of two kinds of PBX simulants at intermediate strain rates ranging from 10 to 100 s^{-1}. At the same time, the uniaxial compressive tests at quasi-static and low strain rates ranging from 0.0001 to 1 s^{-1} and the SHPB tests at high strain rates above 1,000 s^{-1} were conducted to investigate the effect of the strain rate of the mechanical response of PBX simulants. The effect of the strain rate on the mechanical response during the uniaxial compressive deformation is quantitatively investigated from the experimental data at the various strain rates.

16.2 Specimen Preparation

PBXs are specialized particulate composites that mainly consist of explosive crystals held together by a polymer binder. In this study, inert PBX simulants, which have analogous mechanical response to PBXs, were utilized for all material tests for safety reasons. Particle-shaped explosive ingredients were substituted with ammonium sulfate and calcium carbonate to make the inert PBX simulants [9]. Hydroxyl-terminated polybutadiene (HTPB), which is used in PBXN-110 series of PBXs, was utilized as a binder material. PBX simulants also included an anti-oxidant, a curing catalyst, a plasticizer and a reactant. Two kinds of PBX simulants were produced with the different particle sizes and chemical compositions. These PBX simulants were named PBX-S-2 and PBX-S-3, respectively, according to the order of development.

The specimens for the uniaxial compressive tests at quasi-static and intermediate strain rates were designed based on the ASTM standard. ASTM D695 specifies that cylindrical specimens should be 12.7 mm in diameter and 25.4 mm long. The slenderness ratio was equal to 2. However, this standard is valid only for the quasi-static test, and does not include the high-speed test method and the corresponding specimens. For structural stability during the dynamic tests, it might be better to make the compressive test specimen with a smaller slenderness ratio. Considering the difficulty of production and the size of the particles, the dimensions of the cylindrical compressive test specimen were determined to be 18 mm in diameter and 18 mm long with the slenderness ratio equal to 1. The prepared uniaxial compressive test specimen is shown in Fig. 16.1a. Dynamic stress equilibrium is one of the most important issues in the SHPB tests for soft materials. It is reported that thinner specimens are helpful for reaching the stress equilibrium in soft materials [10, 11]. Considering the diameter of the incident and transmission bar (20 mm), the dimensions of the SHPB test specimen were determined to be 10 mm in diameter and 5 mm long with the slenderness ratio equal to 0.5, as shown in Fig. 16.1b. In addition, SHPB tests with specimens with the same diameter and a length of 10 mm were conducted to supplement the relatively low strain rates in the high-strain-rate conditions.

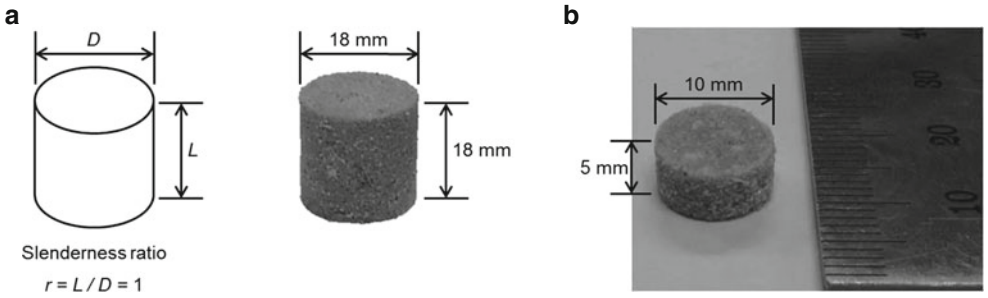

Fig. 16.1 (**a**) Uniaxial compressive test specimen and (**b**) SHPB test specimen

16.3 Experimental Setup

A dynamic material testing machine, the INSTRON 8801 shown in Fig. 16.2a was utilized for the uniaxial compressive tests at quasi-static and low strain rates ranging from 0.0001 to 1 s^{-1}. A servo-hydraulic-type high-speed material testing machine (HSMTM) developed as shown in Fig. 16.2b was used for the uniaxial compressive tests at intermediate strain rates from 10 to 100 s^{-1}. The maximum speed of the moving cylinder was 7,800 mm/s, and the maximum allowable load was 30 kN. The compressive load was acquired from a piezoelectric-type load cell, Kistler 9051A, and the displacement was measured with a linear displacement transducer (LDT) from SENTECH and a high-speed camera, PHOTRON FASTCAM SA4. A digital image correlation (DIC) method was applied with images captured by the high-speed camera to verify the strain measurement by the LDT. Two electric compressors were used to compress the operating hydraulic oil up to a pressure of 300 bars, and two accumulators with a capacity of 5 L were used to make the response time faster. The servo-hydraulic valve, MOOG D792, has a maximum flow rate of 240 L/min. A compressive jig system shown in Fig. 16.3a was employed for the uniaxial compressive tests with the HSMTM because the HSMTM was originally developed for tensile tests at intermediate strain rates [12, 13]. This jig system converts a tensile load to a compressive load. The sequential movement of the compressive jig system is shown in Fig. 16.3b. A compressive test must be conducted at a constant speed. Therefore, the lower jig of the HSMTM grasped the grip section of the compressive jig system after the designated speed was achieved. A stopper prevented further deformation of the specimen so that only the designated strain was applied to the specimen. The designated strain could be controlled by replacing the stopper. The grip section should be broken after achieving the designated strain. The grip section has a region with a reduced cross-sectional area, so fracture takes place in this region after the designated strain is achieved. Teflon tape and petroleum jelly were used for lubrication to avoid barreling of the specimen. Figure 16.4 shows the installation of the compressive jig system and a specimen to the HSMTM. The experimental conditions at quasi-static to intermediate strain rates are tabulated in Table 16.1.

The SHPB is widely utilized for material tests at high strain rates above 1,000 s^{-1}. Kolsky designed the SHPB test based on one-dimensional elastic wave theory to acquire stress–strain relationships at high strain rates [14]. A schematic diagram of the SHPB test system is shown in Fig. 16.5. The SHPB consists of incident and transmitted bars. A specimen is located between those two bars. A stress wave is generated by the impact of a striker bar, and a stress–strain relationship at the high strain rate is obtained by propagation of the generated stress wave. The stress and strain can be calculated from the transmitted and reflected pulses measured from strain gages attached to the incident and transmitted bars. The SHPB system was constructed using 20 mm diameter polycarbonate bars, as shown in Fig. 16.6. Polycarbonate was utilized as the bar material in the SHPB system after considering the mechanical impedance ratio between the specimen and the bars. The length of the striker, incident and transmitted bars are 200 mm, 1,500 mm and 1,500 mm, respectively. Strain gages were attached to 500 mm from the specimen location. A pulse shaper can help to induce constant-strain-rate deformation. Polyvinyl chloride (PVC) tapes with 6 mm in diameter and 0.5 mm thick were determined as the pulse shaper via a parametric study on the size effect of the pulse shaper. Various dimensions of PVC pulse shapers and attachment of a pulse shaper are shown in Fig. 16.7. In addition, petroleum jelly was used to minimize the interfacial friction between the specimen and the bars.

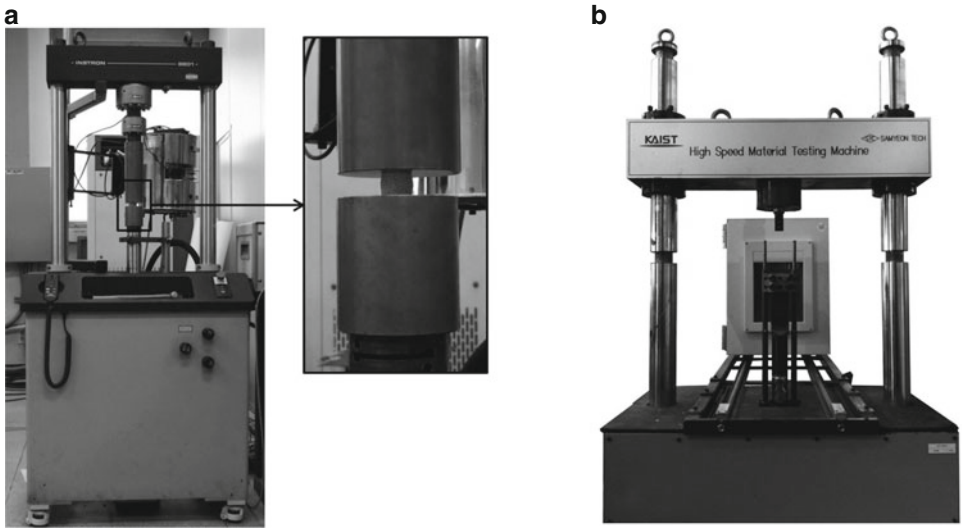

Fig. 16.2 (**a**) Dynamic material testing machine, INSTRON 8801 and (**b**) high-speed material testing machine (HSMTM)

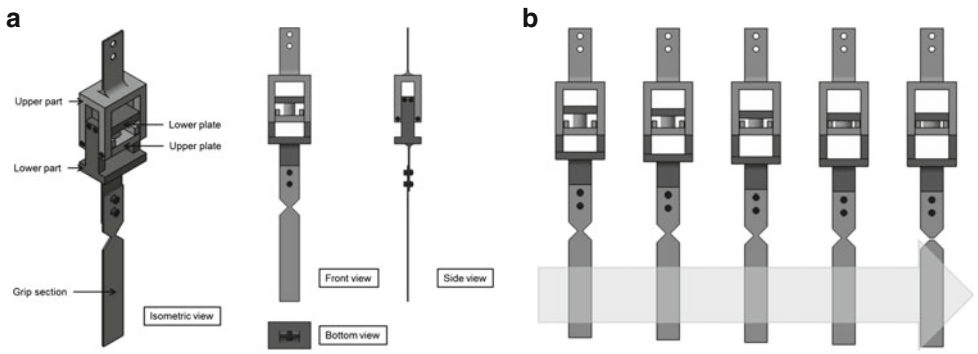

Fig. 16.3 (**a**) Compressive jig system for the HSMTM and (**b**) Sequential movement of the compressive jig system

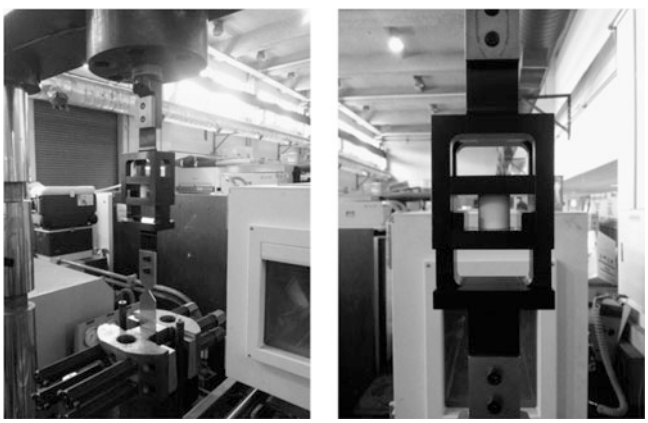

Fig. 16.4 Installation of the compressive jig system and a specimen to the HSMTM

Table 16.1 Experimental conditions of the uniaxial compressive tests at quasi-static and intermediate strain rates

Apparatus	Desired strain rate [s^{-1}]	Crosshead speed [mm/s]
INSTRON 8801	0.0001	0.0018
	0.001	0.018
	0.01	0.18
	0.1	1.8
	1	18
HSMTM	10	180
	100	1,800

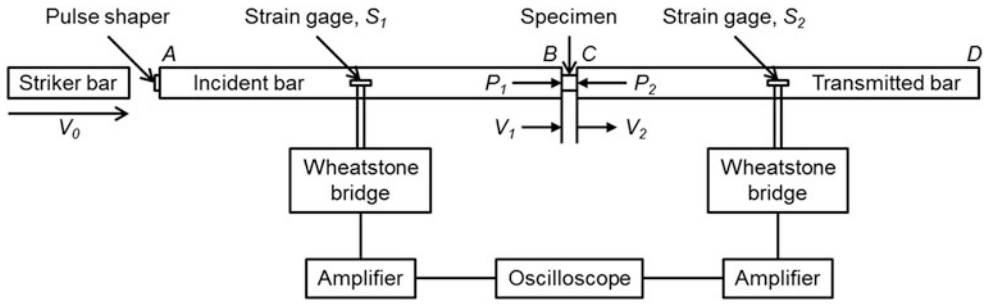

Fig. 16.5 Schematic diagram of the SHPB system

Fig. 16.6 SHPB system with polycarbonate bars

16.4 Experimental Results

Sequential deformed shapes from a compressive test at an intermediate strain rate of 100 s^{-1} and an SHPB test at an high strain rate of 2,240 s^{-1} are shown in Fig. 16.8. Each figure is captured with the same period of 1 ms and 50 μs, respectively. The lubricant between the bars and the specimen worked appropriately, so no barreling was observed on the specimen. The engineering stress, engineering strain and engineering strain rate can be calculated from the pulses using the following equations [15]:

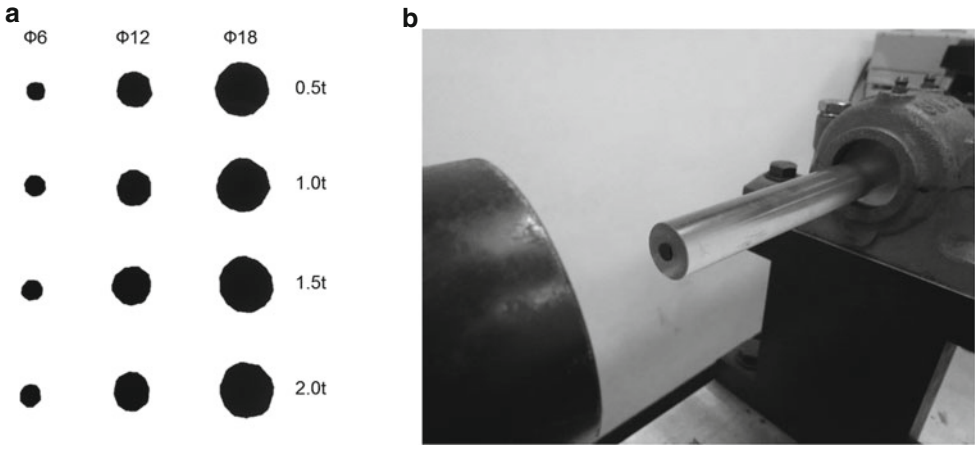

Fig. 16.7 (**a**) Various dimensions of pulse shapers and (**b**) attachment of a pulse shaper to the end tip of the incident bar

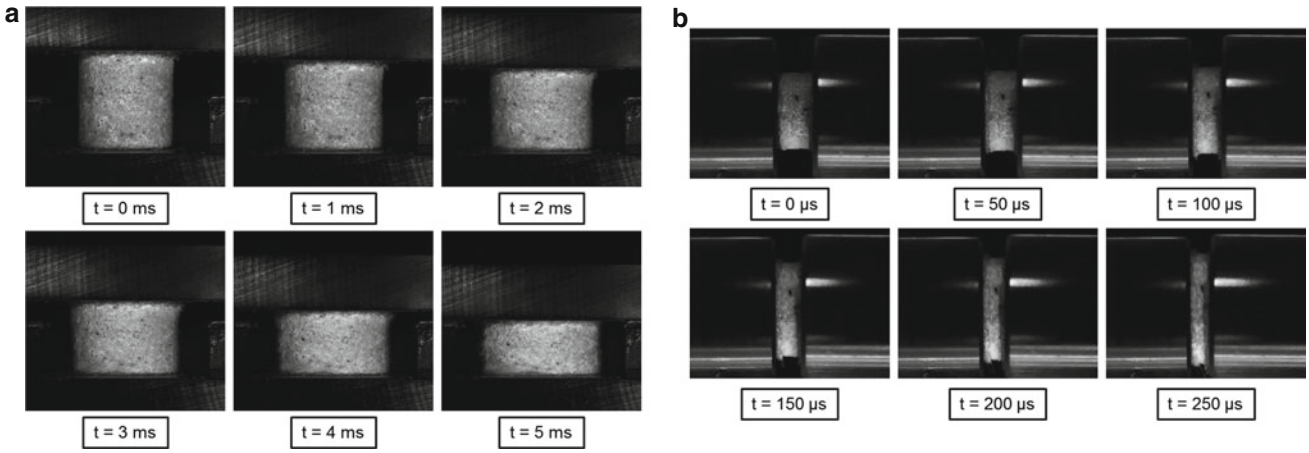

Fig. 16.8 Sequential deformed shapes: (**a**) during a compressive test at 100 s^{-1} and (**b**) during an SHPB test at 2,240 s^{-1}

$$\sigma = \frac{A_b}{A_s} E_b \varepsilon_t \tag{16.1}$$

$$\dot{\varepsilon} = -2\frac{C_b}{L_s}\varepsilon_r \tag{16.2}$$

$$\varepsilon = -2\frac{C_b}{L_s}\int_0^t \varepsilon_r dt \tag{16.3}$$

where A_b and A_s are the cross-sectional areas of the bars and the specimen, respectively; E_b is the elastic modulus of the bar material; C_b is the elastic bar wave speed of the bar material; L_s is the initial length of the specimen; and ε_t and ε_r are the measured strain from the transmitted and reflected pulses, respectively. The engineering strain and engineering stress can be converted to true strain and true stress with the following equations:

$$\varepsilon_{\text{true}} = \ln\left(1 + \varepsilon_{\text{eng.}}\right) \tag{16.4}$$

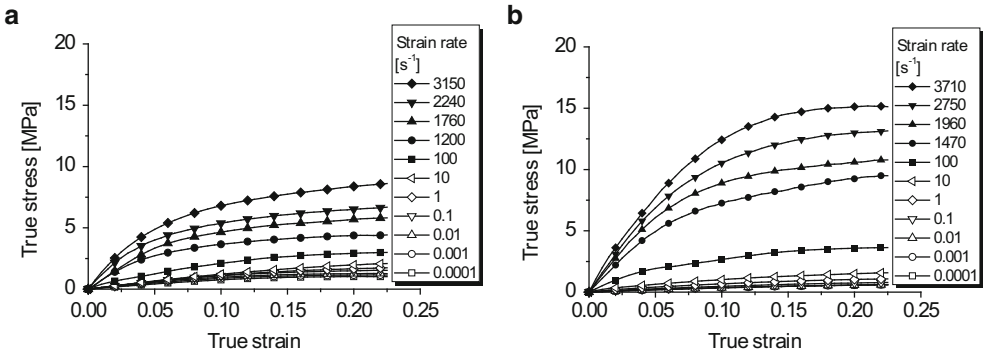

Fig. 16.9 True stress–true strain curves of PBX simulants as a function of the strain rate: (**a**) PBX–S–2 and (**b**) PBX–S–3

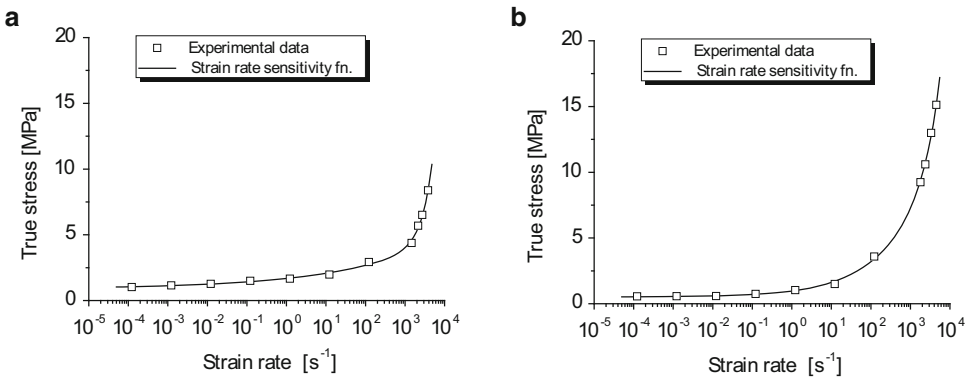

Fig. 16.10 Strain rate sensitivities of PBX simulants: (**a**) PBX–S–2 and (**b**) PBX–S–3

$$\sigma_{\text{true}} = \sigma_{\text{eng.}} \cdot \left(1 + \varepsilon_{\text{eng.}}\right) \tag{16.5}$$

True stress–true strain curves of PBX–S–2 and PBX–S–3 as a function of the strain rate are shown in Fig. 16.9. The true stress–true strain curves are plotted with the same scale of Y-axis to compare the magnitude of the flow stress. The curves are obtained from the uniaxial compressive tests at quasi-static and intermediate strain rates and from the SHPB tests at high strain rates. The flow stresses increase as the strain rate increases for both PBX–S–2 and PBX–S–3. The increase is considerably large, especially at higher strain rates. It can also be seen in the strain rate sensitivities of PBX simulants at the true strain of 0.2 as shown in Fig. 16.10. The strain rate sensitivities of PBX–S–2 and PBX–S–3 were formulated with a 2nd-order exponential growth function as follows:

$$\sigma(\dot{\varepsilon}) = h_1 + A_1 \cdot e^{\{\ln(\dot{\varepsilon}/\dot{\varepsilon}_0) - h_2\}/t_1} + A_2 \cdot e^{\{\ln(\dot{\varepsilon}/\dot{\varepsilon}_0) - h_2\}/t_2} \tag{16.6}$$

16.5 Discussion

The flow stresses of PBX simulants increase as the strain rate increases as shown in Figs. 16.9 and 16.10. This effect of the strain rate can be explained by the intrinsic characteristics of the polymer binder. It is noticed that the elastic modulus and flow stresses of polymers increase significantly as the strain rate increases. Moreover, the effect of the strain rate on the mechanical response of PBX simulants is highly influenced by the mechanism of failure in accordance with the strain rate as

well as the intrinsic characteristics of the polymer binder. It was reported that the debonding stresses between the particles and the polymer binder increase as the elastic modulus of the polymer binder increases [16]. The debonding stresses between the particles and the polymer binder increase as the strain rate increases since the elastic modulus of the polymer binder increases with increasing strain rates. It corresponds with the previous research work by Gray III et al. [2] reported that the ratio of the crystal fracture of particles increases in the compressive tests at high strain rates, while the debonding, which can also be expressed as the interfacial failure, is the dominant failure mechanism in the compressive tests at low strain rates.

A 2nd-order exponential growth function is used to describe the complicated strain rate sensitivities as shown in Fig. 16.10. The function is constructed from two increasing regions. The first increasing region is from quasi-static to low strain rates ranging from 0.0001 to 10 s^{-1}, and the second increasing region is a higher strain rate region above 1,000 s^{-1}. The mechanical response of PBX simulants is significantly changed for a boundary strain rate between 10 and 1,000 s^{-1}. The change of the dominant failure mechanism from the interfacial failure to the crystal fracture takes place in this region. This type of trend can be observed when material tests of polymers are performed as a function of the temperature. The mechanical response of polymers changes significantly around the glass transition temperature. Thus, this boundary strain rate might be called the glass transition strain rate. The exact value of the glass transition strain rate can be determined with further experimental investigation around the strain rate of 100 s^{-1}.

16.6 Conclusions

This article is concerned with the effect of the strain rate on the mechanical response of PBX simulants at the various strain rates ranging from 0.0001 to 3,710 s^{-1}. The uniaxial compressive tests at from quasi-static to intermediate strain rates and the SHPB tests at high strain rates were conducted to acquire the mechanical response of PBX simulants as a function of the strain rate. The contributions made by this article are summarized below:

1. The uniaxial compressive tests at quasi-static and intermediate strain rates ranging from 0.0001 to 100 s^{-1} were conducted with cylindrical specimens modified from the ASTM D695 standard. A new compressive jig system is designed to perform the uniaxial compressive tests at intermediate strain rates of approximately 100 s^{-1}. Teflon tape and petroleum jelly were utilized to avoid barreling of the specimen.
2. The SHPB tests were conducted at high strain rates ranging from 1,200 to 3,710 s^{-1}.. Polycarbonate was employed as the bar material due to the low mechanical impedance of the specimen. Pulse shapers that have similar mechanical properties to the specimen were used to facilitate stress equilibrium, and to induce constant-strain-rate deformation in the specimen.
3. The strain rate sensitivity was formulated with a 2nd-order exponential growth function. The proposed strain rate sensitivity function succeeds in correctly describing the various complicated strain rate sensitivities of PBX simulants.
4. When the crosshead speed is constant during the compressive test, the true strain rate increases as the length of the specimen decreases. Therefore, it is necessary that the change in the true strain rate of the specimen should be considered.

References

1. Peeters RL, Hackett RM (1981) Constitutive modeling of plastic-bonded explosives. Exp Mech 21(3):111–116
2. Gray GT III, Idar DJ, Blumenthal WR, Cady CM, Peterson PD (1998) High- and low-strain rate compression properties of several energetic material composites as a function of strain rate and temperature. In: 11th international detonation symposium
3. Foster JC Jr, Glenn JG, Gunger M (2000) Meso-scale origins of the low-pressure equation of state and high rate mechanical properties of plastic bonded explosives. Shock Compression of Condensed Matter – 1999
4. Millett JCF, Bourne NK (2001) Shock response of the elastomer, polychloroprene. J Appl Phys 89(5):2576–2579
5. Idar DJ, Thompson DG, Gray GT III, Blumenthal WR, Cady CM, Peterson PD, Roemer EL, Wright WJ, Jacquez BJ (2002) Influence of polymer molecular weight, temperature, and strain rate on the mechanical properties of PBX 9501. Shock Compression of Condensed Matter – 2001
6. Grantham SG, Siviour CR, Proud WG, Field JE (2004) High-strain rate Brazilian testing of an explosive simulant using speckle metrology. Meas Sci Technol 15(9):1867–1870
7. Cady CM, Blumenthal WR, Gray GT III, Idar DJ (2006) Mechanical properties of plastic-bonded explosive binder materials as a function of strain-rate and temperature. Polym Eng Sci 46(6):812–819
8. Siviour CR, Laity PR, Proud WG, Field JE, Porter D, Church PD, Gould P, Huntingdon-Thresher W (2008) High strain rate properties of a polymer-bonded sugar: their dependence on applied and internal constraints. Proc R Soc A 464(2093):1229–1255
9. Park C, Jeong S, Huh H, Park J (2013) Material behaviors of PBX simulant with various strain rates. Key Eng Mater 535–536:117–120

10. Song B, Chen W, Frew DJ (2004) Dynamic compressive response and failure behavior of an epoxy syntactic foam. J Compos Mater 38 (11):915–936
11. Song B, Chen W (2004) Dynamic stress equilibrium on a rubber specimen during a split Hopkinson pressure bar experiment. Exp Mech 44 (3):300–312
12. Kim JS, Huh H, Lee KW (2009) Evaluation of dynamic tensile characteristics of polypropylene composites with temperature variation. J Compos Mater 43(23):2831–2853
13. Park C, Huh H, Kim J, Ahn C (2012) Determination of true stress–true strain curves of polymers at various strain rates using force equilibrium grid method. J Compos Mater 46(17):2065–2077
14. Kolsky H (1949) An investigation of the mechanical properties of materials at very high rates of loading. Proc Phys Soc Section B 62(11):676–700
15. Chen WW, Song B (2011) Chapter 4. Kolsky compression bar experiments on soft materials, Split Hopkinson (Kolsky) bar – design, testing and applications, Springer, New York, pp 119–175
16. Palmer SJP, Field JE, Huntley JM (1993) Deformation, strengths and strains to failure of polymer bonded explosives. Proc R Soc A 440 (1909):399–419

Chapter 17
Effect of Loading Rate on Dynamic Fracture Toughness of Polycarbonate

Anshul Faye, Sumit Basu, and Venkitanarayanan Parameswaran

Abstract Accurate estimation of dynamic fracture properties of materials is important for component design under impact conditions. Amorphous glassy polymers have wide engineering applications. For Polymethyl methacrylate (PMMA), which is a brittle amorphous polymer, literature indicates that the fracture toughness increases at higher loading rates compared to that under static loading conditions. Motivated by this observation, in the present work, another amorphous polymer named Polycarbonate (PC), which is ductile in nature, is considered and effect of loading rate on fracture toughness of PC is investigated. Experiments using the single edge notched (SEN) specimen subjected to 3-point bending are performed at various loading rates. A UTM is used for low loading rate experiments. High loading rate experiments are conducted using Hopkinson pressure bar. Ultra high speed imaging (100,000 fps) is used to make accurate measurement of fracture initiation time in these experiments. Attempts are being made to investigate the near notch deformation in detail. A hybrid experimental and numerical approach is pursued in which finite element simulations are performed using the boundary conditions obtained from experiments. A rate and temperature dependant constitutive model is used for PC. Stress intensity factor (SIF), evaluated from simulation is correlated with experimentally measured SIF. Results show that that dynamic fracture initiation toughness of PC does not vary significantly at higher loading rates; values remain close to that obtained under quasi-static loading conditions.

Keywords Polycarbonate • Dynamic fracture toughness • Hopkinson bar • High speed imaging • Amorphous polymers

17.1 Introduction

Polycarbonate is an amorphous glassy polymer and is ductile in nature. Compared to other amorphous polymers, PC is known to be tougher and hence used in majority of applications requiring impact resistance. Accurate estimation of dynamic fracture properties thus becomes important for effective use of PC. Objective of present work is to study of dynamic fracture behavior of PC at higher rate of loading. Another polymer of the same class but brittle in nature, named Polymethylmetrhacrylate (PMMA) is studied in literature and it has been shown to have very high fracture toughness compared to its static value at very high rate of loading as shown in Fig. 17.1 [1–5]. These studies motivate us to investigate the behavior of PC at higher loading rates with the aim of establishing whether the behavior observed for PMMA is typical of all amorphous glass polymers or not.

Present work follows a hybrid experimental and numerical approach. Single edge Notched (SEN) specimen, shown in Fig. 17.2a, was used for the experiments. Dynamic experiments were performed using Hopkinson bar test setup and the load-point displacement and crack initiation time from the experiments were used as input for the numerical simulations. Dynamic numerical simulations were performed using an elastic-viscoplastic, rate dependent constitutive model for PC. This approach offers a more accurate way of determining the dynamic fracture toughness. In addition, it also facilitates detailed study of notch tip field, which will help in understanding the micromechanics of dynamic failure in PC.

A. Faye (✉) • S. Basu • V. Parameswaran
Indian Institute of Technology Kanpur, Kanpur, UP, India 208016
e-mail: anshulfy@iitk.ac.in

B. Song et al. (eds.), *Dynamic Behavior of Materials, Volume 1: Proceedings of the 2013 Annual Conference on Experimental and Applied Mechanics*, Conference Proceedings of the Society for Experimental Mechanics Series,
DOI 10.1007/978-3-319-00771-7_17,

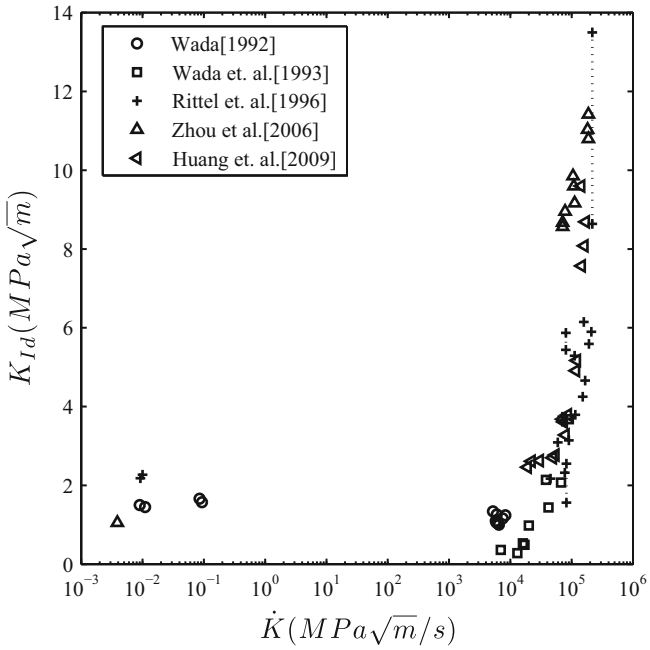

Fig. 17.1 Effect of loading rate on dynamic fracture toughness of PMMA [1–5]

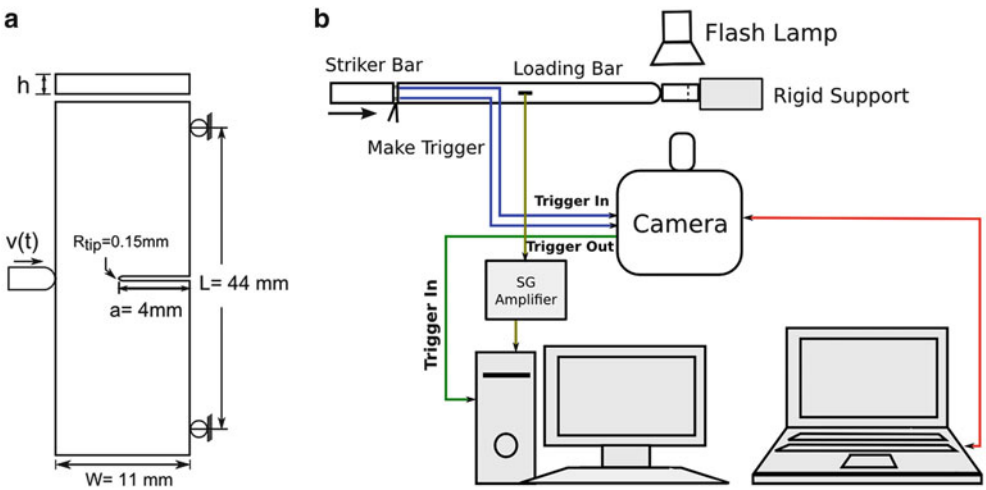

Fig. 17.2 (**a**) SEN specimen geometry, (**b**) Dynamic experimental setup

17.2 Experiment

Fracture experiments were conducted on PC at various loading rates. It has been shown that fracture toughness of PC varies with thickness as well as notch tip radius [6, 7]. Hence to explicitly identify the effect of loading rate on fracture toughness of PC, dimensions of the SEN specimen were kept constant for all experiments. Semicircular notch with a radius of 150 μm was used in all experiments. SEN specimens were tested in 3-point bend loading configuration at a range of loading rates. Low loading rate quasi-static tests were performed on a screw driven UTM to determine the static values of initiation toughness of PC and high loading rate dynamic fracture tests performed using Hopkinson bar test setup. Hopkinson bar test setup used consisted of a 2 m long and 12.5 mm diameter aluminum loading bar and a striker bar of 300 mm. The loading bar was appropriately instrumented to record the incident and reflected waves during the experiments. Ultra high speed imaging was used to capture the initiation of crack during dynamic fracture. Experimental setup for the dynamic experiments is shown in Fig. 17.2b.

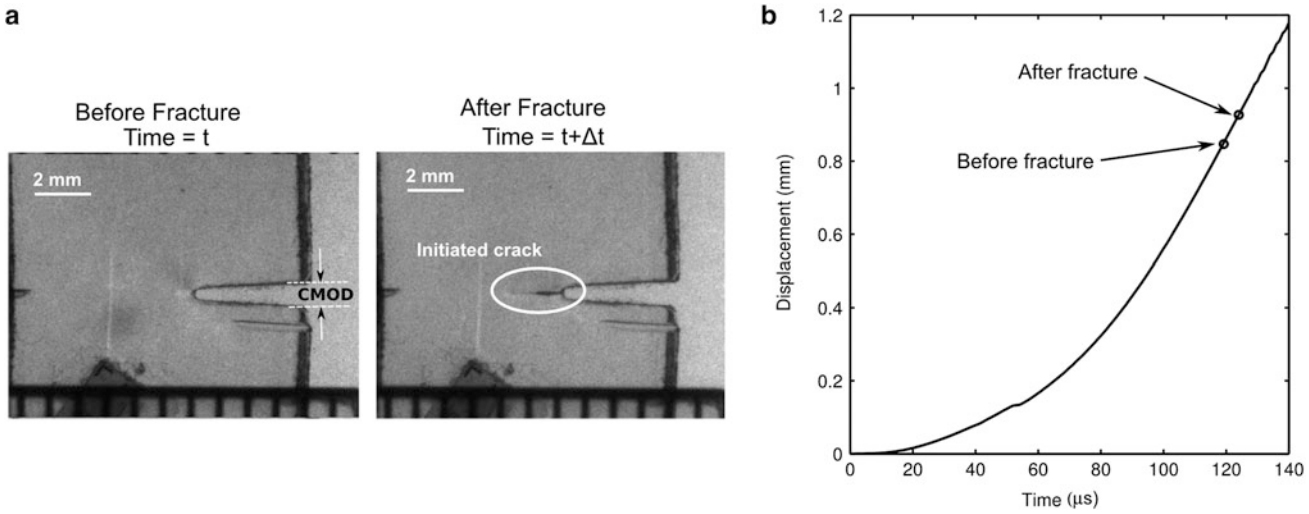

Fig. 17.3 (**a**) Images just before and after the crack initiation, (**b**) Load-point displacement history

Using the conventional one-dimensional wave calculation, load-point displacement and the load at the bar end was calculated from incident and reflected waves recorded during the experiment. Synchronization of high speed images with Hopkinson bar data provides us the crack initiation time within an accuracy of interframe time used to capture images, which is 5–10 μs in the present case. From a typical experiment the images just before and after the crack initiation are shown in Fig. 17.3a. For the same experiment load-point displacement history is also shown in Fig. 17.3b.

Contact loss between loading bar and specimen was noticed in some experiments. In such a situation, it has been suggested that crack mouth opening displacement (CMOD) remain least unaffected by the loss of contact and hence SIF calculation using CMOD will give accurate estimation of SIF [8]. CMOD was measured from the recorded images, as shown in Fig. 17.3a. SIF from CMOD can be obtained using Eq. 17.1,

$$K_I(t) = \frac{E'}{4\sqrt{a}} \frac{f(a/w)}{v(a/w)} \cdot CMOD(t) \tag{17.1}$$

where $f(a/w)$ and $v(a/w)$ given below, are function of crack length 'a' and specimen width 'w' and $E' = E/(1-\nu^2)$. [11]

$$f(a/w) = \frac{1.99 - (a/w)(1-a/w)\left[2.15 - 3.93(a/w) + 2.7(a/w)^2\right]}{(1+2a/w)(1-a/w)^{1.5}} \text{ and } v(a/w) = \left(0.76 - 2.28(a/w) + 3.87(a/w)^2 - 2.04(a/w)^3 + \frac{0.66}{(1-a/w)^2}\right)$$

17.3 Constitutive Model

To simulate the behavior of PC, the rate dependent elastic-viscoplastic constitutive model given by Boyce et al. is used [9]. In the general 3-dimensional version of the model, under the assumption of isotropic thermoelasticity, small elastic strains and small deviation from the reference temperature T_0, the elastic free energy function (f_e) is given as,

$$\rho f_e = -\frac{\rho c_v}{2T_0}(T - T_0)^2 - C\alpha_c(T - T_0)I_1 + \frac{1}{2}CI_1^2 + 2GI_2 \tag{17.2}$$

where ρ is the density, C is the modulus of rigidity, G is the shear modulus, c_v is the specific heat at constant volume for the material and T denotes the temperature. In Eq. 17.2 $I_1 = tr(\mathbf{E}_e)$ and $I_2 = tr(\mathbf{E}_e'^2)$, $\mathbf{E}_e'$ being the deviator of elastic strain $\mathbf{E}_e$. Using the elastic free energy function given by Eq. 17.2, the Jaumann rate of stress $(\overset{\nabla}{\sigma})$ is derived as,

$$\overset{\nabla}{\sigma} = \mathbf{L}^e : \mathbf{D}^e - C\alpha_c\dot{T}\mathbf{I} \tag{17.3}$$

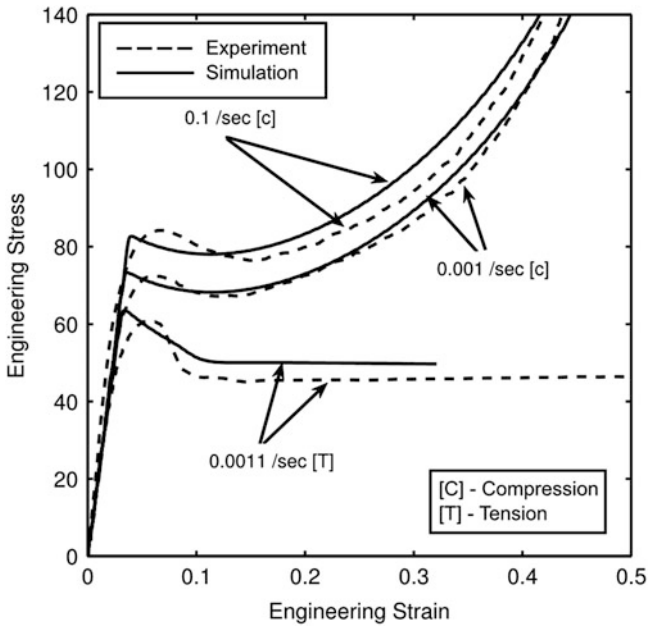

Fig. 17.4 Uni-axial tension and compression curves for PC

where $\mathbf{L}^e$ is the elastic modulus tensor, $\mathbf{D}^e$ is the elastic rate of strain tensor and α_c is the thermal expansion coefficient for material. $\mathbf{I}$ is the unit tensor.

Energy dissipative plastic flow in the material is driven by the effective stress $\bar{\sigma} = \sigma - \mathbf{b}$, where $\mathbf{b}$ is the back stress tensor. Then the plastic strain rate tensor $\mathbf{D}^p$ is defined as,

$$\mathbf{D}^p = \frac{\dot{\gamma}_p}{\sqrt{2}\tau}\bar{\sigma} \tag{17.4}$$

In Eq. 17.4, $\dot{\gamma}_p$ is the equivalent plastic strain rate and τ is the equivalent shear stress. At very high rate of loading the heat generated by plastic dissipation does not get enough time to diffuse and causes local self heating of material. In such cases adiabatic assumption is valid and the rate of temperature increase can be found from energy dissipation as,

$$\rho c_v \dot{T} = \bar{\sigma} : \mathbf{D}^p \tag{17.5}$$

Parameters of the constitutive model were obtained from the quasi-static uni-axial tensile and uni-axial compressive response (strain rate range of 10^{-3}/s to 1/s) of PC. Experimental stress–strain curves are compared with those obtained from simulation in Fig. 17.4 for the final set of parameters determined. The two are in good agreement as can be seen from Fig. 17.4.

17.4 Simulation

Following the hybrid approach, dynamic simulations were performed using Abaqus/Explicit 6.10. The material model for PC is implemented in Abaqus using VUMAT. Only half of the specimen is modeled due to symmetric loading and geometry of specimen. FE model is in shown in Fig. 17.5a. Plane strain isoparametric elements with reduced integration (CPE4R) were used for meshing the FE model. Loading bar end and the supports were modeled as analytic rigid surfaces because of their higher stiffness compared to specimen material. Surface to surface contact was applied between all contact surfaces. Mesh was sufficiently refined near the notch tip as shown in Fig. 17.5a. Elastic modulus of 2,100 MPa and Poisson's ratio 0.38, obtained from quasi-static experiments were used in the simulations.

Load-point displacement history obtained from experiment was applied as boundary condition to the loading bar end and the simulation was run till the time of fracture recorded during experiment. After the simulation dynamic J-Integral was

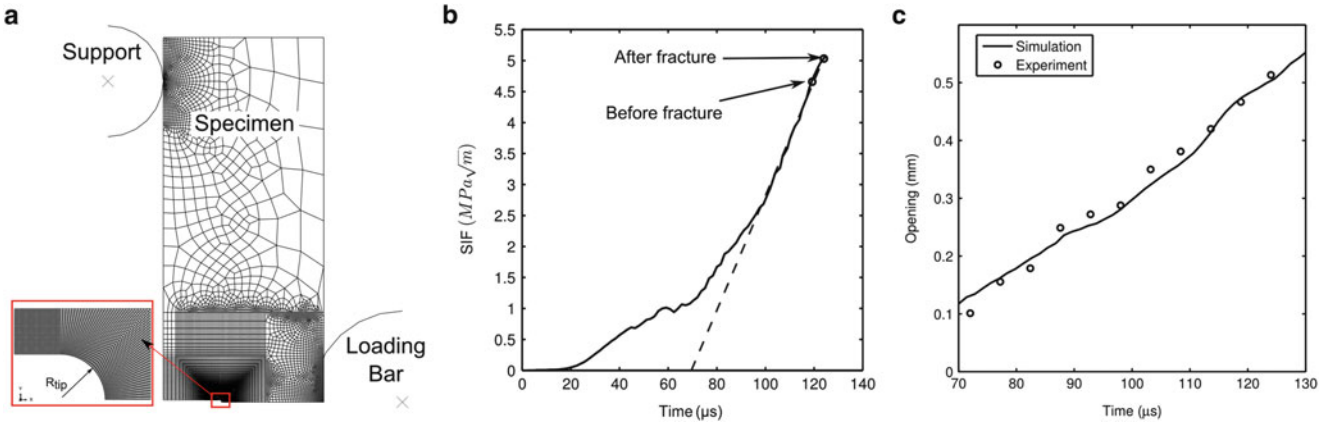

Fig. 17.5 (**a**) FE model (**b**) Dynamic SIF history from simulation, (**c**) CMOD from simulation compared with experiment

Table 17.1 Dynamic SIF values at different rates

		SIF (MPa$\sqrt{\text{m}}$)		
Specimen	K – Rate (MPa$\sqrt{\text{m}}$/ sec)	From CMOD (experiment)	From CMOD (simulation)	From J-integral (simulation)
1	3.81×10^4	5.05 ± 0.05	5.35 ± 0.25	5.40 ± 0.16
2	9.02×10^4	5.60 ± 0.10	5.00 ± 0.05	4.87 ± 0.21
3	9.05×10^4	5.40 ± 0.15	5.05 ± 0.15	4.80 ± 0.13
4	9.22×10^4	–	5.40	5.46
5	1.32×10^5	4.75 ± 0.25	4.65 ± 0.15	4.68 ± 0.07

calculated using the domain integral method [10] and then dynamic SIF was calculated from J-Integral using the following relation between J and K_d.

$$K_d = \sqrt{JE'} \tag{17.6}$$

where E' is the Young's modulus of material in plane strain condition.

SIF history for a particular simulation is shown in Fig. 17.5b. Rate of loading is defined in terms of slope of K_d -time curve. CMOD from simulations is also compared with that measured from recorded images. As shown in Fig. 17.5c, the two are in agreement within 3 %, validating the FE model.

17.5 Results and Discussion

Dynamic fracture initiation toughness of PC at different SIF rates obtained from experiments and simulations are reported in Table 17.1. These values and quasi-static fracture toughness values are plotted as a function of loading rate in Fig. 17.6. Quasi- static values of initiation toughness are calculated using the standard formula for SEN specimen [11]. In Fig. 17.6, experimental toughness values are scattered without any indication of a clear trend against loading rate. In an average sense dynamic fracture toughness values remains almost same as static fracture toughness, as evident from the linear fit through data in Fig. 17.6. In simulations, SIF values calculated from CMOD are close to that calculated from J-Integral and therefore validate the use of CMOD obtained from experiments to determine SIF.

PC is a ductile material and hence plastic deformation near the notch tip is expected to affect the initiation toughness values of PC. Figure 17.7a, b shows the equivalent plastic strain contours for Specimen1 loaded at SIF rate 3.81×10^4 MPa$\sqrt{\text{m}}$/ sec and for Specimen5 loaded at SIF rate 1.32×10^5 MPa$\sqrt{\text{m}}$/ sec , respectively. Fracture initiation time for specimen1 is 87 μs and that for specimen5 is 90 μs. Locations of maximum plastic strain regions are indicated in Fig. 17.7. For both the specimen shape of plastic zone looks similar and it extends up to about 0.3 mm in front of the tip. It is observed that the height of the plastic zone in slightly larger for the specimen1 than that for the specimen5. It gives an indication about the suppression of notch tip plasticity at higher rates of loading.

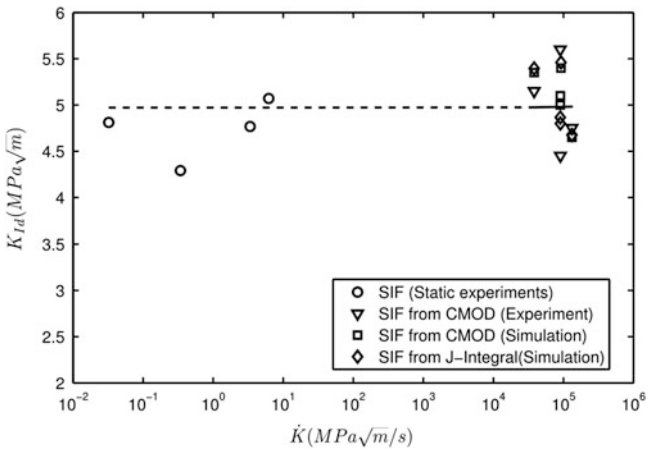

Fig. 17.6 Variation of dynamic fracture toughness of PC w.r.t. loading rate

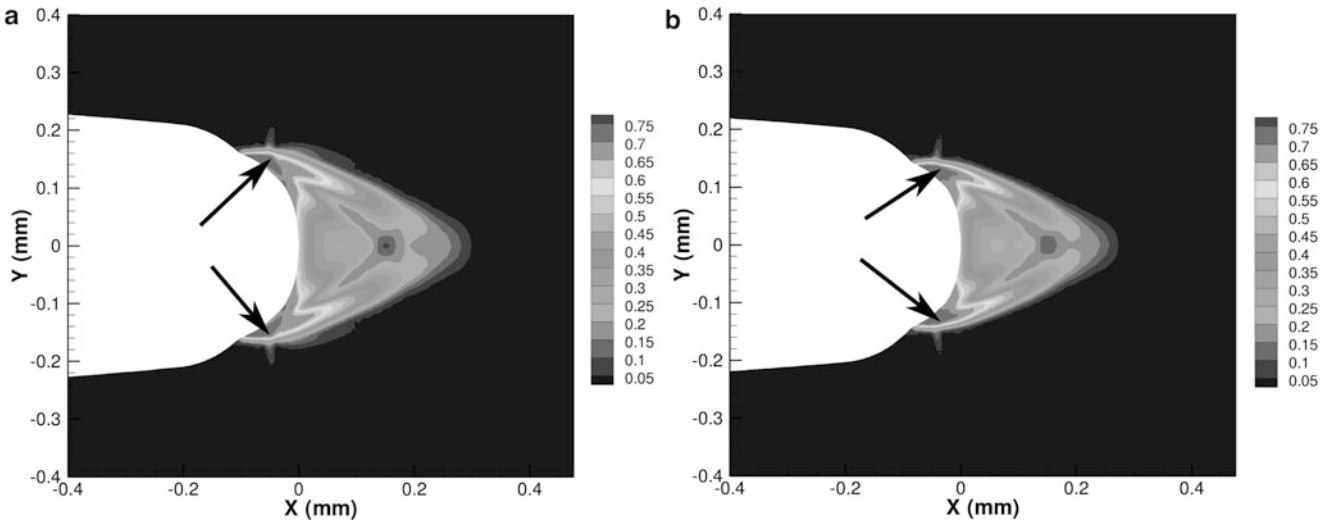

Fig. 17.7 Equivalent plastic strain distribution near notch tip at the time of fracture initiation for (**a**) Specimen 1, (**b**) Specimen 5

17.6 Conclusion

Present work addresses the variation of dynamic fracture initiation toughness of PC with the loading rate. Towards this end dynamic SIF of PC is determined by adopting a combined experimental and numerical approach. Results show that dynamic initiation toughness of PC does not vary significantly than its quasi-static values and remain almost same. This trend is opposite of that is reported for PMMA (shown in Fig. 17.1) which shows a significant increase in fracture toughness at higher rates. Further efforts are in progress to investigate these effects in details by studying the near notch tip fields in experiments as well as in simulations.

Acknowledgements The financial support through grant number SR/FST/ETII-003/2006 under the FIST program by Department of Science and Technology, Government of India for the Ultra-high speed camera used in this study is acknowledged.

References

1. Wada H (1992) Determination of dynamic fracture toughness for PMMA. Eng Fract Mech 41(6):821–831
2. Wada H, Seika M, Calder CA, Kennedy TC (1993) Measurement of impact fracture toughness for PMMA with single-point bending test using an air gun, Engg. Fract Mech 46(4):715–719

3. Rittel D, Maigre H (1996) An investigation of dynamic crack initiation in PMMA. Mech Mater 23:229–239
4. Zhou J, Wang Y, Xia Y (2006) Mode-I fracture toughness of PMMA at high loading rate. J Mater Sci 41:8363–8366
5. Huang S, Luo S, Xia K (2009) Dynamic fracture initiation toughness and propagation toughness of PMMA. In: Proceedings of the SEM annual conference, Albuquerque, 1-4 June 2009
6. Inberg JPF, Gaymens RJ (2002) Polycarbonate and co-continuous polycarbonate/ABS blends: influence of specimen thickness. Polymers 43:3767–3777
7. Inberg JPF, Gaymens RJ (2002) Polycarbonate and co-continuous polycarbonate/ABS blends: influence of notch radius. Polymers 43:4197–4205
8. Jiang F, Vecchio KS (2009) Hopkinson bar loaded fracture experimental technique: a critical review of dynamic fracture toughness tests. Appl Mech Rev 62
9. Boyce MC, Parks DM, Argon AS (1988) Large inelastic deformation of glassy polymers, part I: rate dependent constitutive model. Mech Mater 7:15–33
10. Shih CF, Moran B, Nakamura T (1985) Energy release rate along a three-dimensional crack front in a thermally stressed body. Int J Fract 30:79–102
11. Tada H, Paris PC, Irwin GR (2000) The stress analysis of cracks handbook, 3rd edn. ASME, New York

Chapter 18
Mixed Mode Fracture Behavior of Layered Plates

Arun Jose Jacob, Servesh Kumar Agnihotri, and Venkitanarayanan Parameswaran

Abstract Layered architecture is used in applications such as thermal protection systems, body and vehicle armor etc. Layered materials are non homogeneous solids in which material properties vary in steps, leading to property jumps across the interface. The present study focuses on understating the mixed mode fracture behavior of layered plates in which elastic and fracture properties vary along the crack front. Single edge notched specimens, fabricated by joining Polymethyl-methacrylate (PMMA) and Epoxy sheets using an Epoxy based adhesive (Araldite), were subjected to mixed mode loading. The thickness averaged stress intensity factor was determined through photoelasticity. A progressive mode of cracking was observed in which the crack initiated first in the Epoxy layer followed by crack initiation in the PMMA layer. The crack initiation angles were similar in both layers during the initial stages of crack growth. However, during the later stages the cracks in the two layers followed different paths with some amount of crack twisting. Similar experiments were also conducted under dynamic loading using a Hopkinson bar setup. High speed imaging was used to capture the dynamic phenomena. The effect of layering on the crack initiation toughness, crack speed and crack path were investigated.

Keywords Layered plates • Photoelasticity • Fracture • Crack twisting • Mixed-mode

18.1 Introduction

Layered structures have a wide range of applications such as wind shields, heavy armors, thermal protection systems etc. They offer the scope for selection of individual layer properties and overall layered architecture to accommodate the required property in the material and thereby optimizing the overall performance of the material. This advantage comes with the additional complexities in terms of material characterization and failure analysis. Fracture of layered structures is sensitive to the layer architecture, change of elastic and fracture properties from one layer to the other, type of loading experienced and the orientation of the crack.

Fracture behavior of layered materials has received considerable attention. Layered materials are made by joining two or more materials together. The behavior of stationary as well as propagating crack in layered materials has been reported by several researchers in which cracks are oriented along the interface [1–9]. Crack propagation cross the interface has also been studied [10–12]. In most of the existing studies cracks are oriented in such a way that the material properties vary in the plane of the crack. Therefore there is no property variation across the crack front and hence a two dimensional approach is applicable.

In the recent years, behavior of through thickness edge cracks in a layered plate having property (both elastic and fracture) jumps along the crack front has also received attention. In this situation, the two dimensional approach is not applicable and stress intensity factor (SIF) can vary along the crack front. Recent studies [13, 14] indicate that for an edge cracked plate with gradation along the crack front subjected to in plane bending, the SIF scales with elastic modulus. This implies that layer having higher elastic modulus will have higher SIF. Therefore, the critical condition at which the crack becomes unstable will depend on the relative variation of SIF and fracture toughness across the plate thickness. Recently [15], a set of

A.J. Jacob • S.K. Agnihotri (✉) • V. Parameswaran
Department of Mechanical Engineering, Indian Institute of Technology Kanpur, Kanpur 208016, India
e-mail: servesh@iitk.ac.in

B. Song et al. (eds.), *Dynamic Behavior of Materials, Volume 1: Proceedings of the 2013 Annual Conference on Experimental and Applied Mechanics*, Conference Proceedings of the Society for Experimental Mechanics Series,
DOI 10.1007/978-3-319-00771-7_18,

experiments was performed to investigate the crack initiation and growth in layered plates subjected to plane bending. In this study pure mode I loading was considered. Present study focuses on mixed-mode crack propagation in layered plates subject to in-plane bending. The same two layer system used in [15], comprising of two different polymers, Epoxy (LY556) and Poly methyl methacrylate (PMMA) is considered. The experimental technique of photoelasticity is used to record the stress-field from which the SIF is determined. Cracks subjected to quasi-static and dynamic loads are investigated.

18.2 Experimental Details

18.2.1 Specimen Preparation and Characterization

The specimens were prepared by bonding Epoxy and PMMA sheets using an Epoxy based adhesive (Araldite). Epoxy and PMMA have different elastic modulus and fracture properties which would provide the necessary mismatch at the interface to study the fracture behavior. The PMMA sheets of nominal thickness 5.5 mm were commercially procured. Epoxy sheet of nominal thickness 5.7 mm were cast in-house. The details of the casting procedure and bonding of Epoxy and PMMA sheets are reported in [13] and [15]. The specimen was sized to final dimension of 210 $\times$ 50 mm. A notch of required dimension was introduced using a saw and a natural crack was extended by forcing a sharp razor blade into the root of the notch. Elastic, fracture and optical properties of Epoxy and PMMA, obtained from previous study [15], are shown in Table 18.1.

18.2.2 Static Testing

Single edged notched (SEN) specimens were subjected to asymmetric four-point bending in a UTM. Figure 18.1 show the asymmetric four-point bend (AFPB) configuration used to study the mixed mode crack propagation behavior in layered plate. Different crack tip mode mixities were introduced by varying the eccentricity (s) between loading axis and crack plane. For AFPB configuration we have chosen the parameters $\frac{C}{W} = 1.27$ and $\frac{D}{W} = 0.63$ where C and D are indicated in Fig. 18.1. The specimen was placed in a light field circular polariscope during loading and isochromatic fringes were recorded using a CCD camera for further analysis.

Table 18.1 Properties of materials used [15]

Material	Elastic modulus (GPa)	Poisson's ratio	Fringe constant (MPa-m/fringe)	Fracture toughness (MPa-$\sqrt{m}$)
PMMA	2.67	0.344	0.239	0.95 $\pm$ 0.11
Epoxy	3.44	0.345	0.018	0.53 $\pm$ 0.04

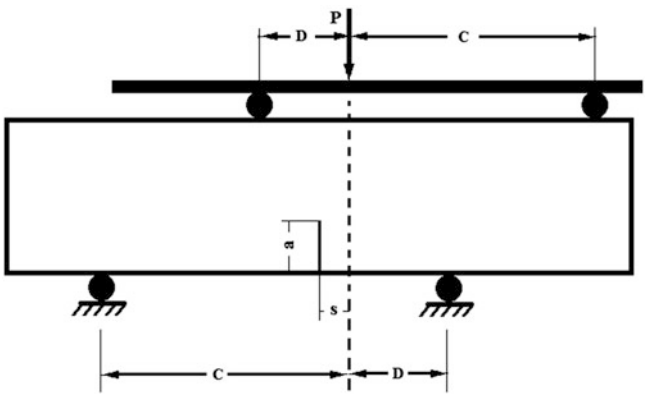

Fig. 18.1 Asymmetric four-point bend configuration

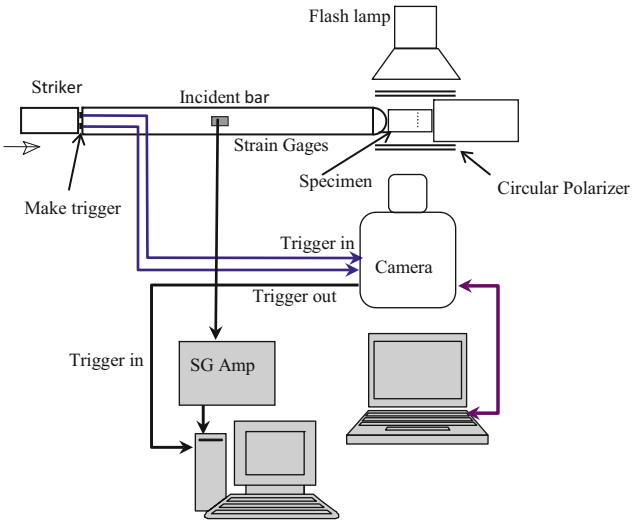

Fig. 18.2 Schematic of the experimental setup for dynamic loading

18.2.3 Dynamic Testing

As it is difficult to ensure proper loading in the AFPB configuration in a dynamic test, eccentric three-point loading is used in the dynamic experiments. SEN specimens were subjected to dynamic three-point bending as shown in Fig. 18.2. An Aluminum bar of 2 m length and 12.5 mm diameter was used for this purpose. Experiments were performed on individual Epoxy and PMMA sheets as well as layered PMMA-Epoxy specimens. A SIM02-16 ultra high speed camera coupled with circular polarizer was used to capture the isochromatics during fracture process. Sixteen images were captured at an interval of 15 microseconds. Figure 18.2 shows the schematic of the experimental set up. A make trigger circuit attached on the impact face of the bar was used to trigger the camera. The flash lamps and the strain gauge data acquisition system was triggered by the camera itself. The captured images were analyzed to determine the SIF as explained in the next section.

18.3 Analysis of Isochromatics

Analysis of crack tip isochromatics to extract the fracture parameters (SIF) is a well established procedure for a homogeneous plate. The procedure involves which fitting the asymptotic crack tip stress fields to the fringe data using a non linear least square algorithm [16]. It has been shown that cracks in layered plates subjected to mode-I loading, the strain fields are invariant through the thickness [15]. In this case an equivalent plate approach is applicable. This approach enables us to consider the layered plate as a homogenous plate of equivalent elastic modulus E_{eq}, and equivalent fringe constant $f_{\sigma \mathrm{eq}}$ for the purpose of analyzing the fringes. To establish the validity of this assumption for mixed mode loading, a three dimensional finite element analysis of a cracked layered plate was carried out. The contours plots of various strain components are shown in Fig. 18.3 for two locations across the thickness, one at mid thickness of Epoxy layer and other at mid thickness of the PMMA layer. It can be observed that near to the crack tip strain contours match well in two layers indicating that a state of iso-strain situation can be assumed in the case of mixed mode loading as well. The isochromatics were analyzed using an equivalent fringe constant ($f_{\sigma eq}$) calculated using the following equation [15].

$$\frac{1}{f_{\sigma eq}} = \frac{1}{E_{eq} h_t} \left(\frac{E_p h_p}{f_{\sigma p}} + \frac{E_e h_e}{f_{\sigma e}} \right) \tag{18.1}$$

Where, $f_{\sigma p}$ and $f_{\sigma e}$ denote the optical fringe constant of PMMA and Epoxy respectively, E_p and E_e respective elastic modulus, h_p and h_e respective thickness. In Eq. 18.1, $h_t = h_1 + h_2$ is the total thickness of the plate, having an equivalent elastic modulus E_{eq}, given by

$$E_{eq} = \frac{1}{h_t} \int_0^{h_t} E(z) dz = \frac{1}{h_t} \sum_{i=1}^{n} E_i h_i \tag{18.2}$$

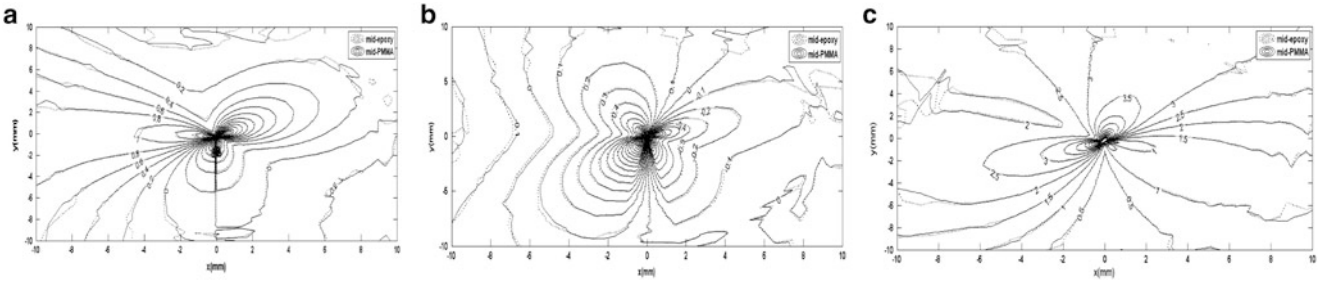

Fig. 18.3 Contour plots of in Epoxy and PMMA layers for AFPB with s = 6 mm (**a**) opening strain (ε_{11}) (**b**) normal strain (ε_{22}) (**c**) shear strain (ε_{12})

The near tip stress field in the equivalent plate will have a structure given by Eq. 18.3 [16].

$$\sigma_{ij} = \sum_{n=0}^{N} A_n r^{(n-1/2)} f_n(\theta) + \sum_{m=0}^{M} B_m r^m g_m(\theta) - \sum_{n=0}^{N} C_n r^{(n-1/2)} h_n(\theta) - \sum_{m=0}^{M} D_m r^m k_m(\theta) \tag{18.3}$$

Where r and θ denote the polar coordinate of a point with respect to the crack tip and $f_n(\theta)$, $g_m(\theta)$, $h_n(\theta)$, and $k_m(\theta)$ are trigonometric functions, explicit form of which are available in [16]. In Eq. 18.3, constants A_n, B_m, C_n and D_m can be evaluated from isochromatic fringe data using the least square over deterministic method described in [16]. The opening mode SIF K_I and sliding mode SIF K_{II} are related to the coefficients, A_0 and C_0 as shown in Eq. 18.4.

$$K_I = \sqrt{2\pi} A_0, K_{II} = \sqrt{2\pi} C_0 \tag{18.4}$$

Mode mixity (Θ), which shows the strength of mode-II stress field relative to mode I field, is defined as

$$\Theta = \tan^{-1}\left(\frac{K_{II}}{K_I}\right) \tag{18.5}$$

The SIF thus obtained is the thickness averaged SIF or equivalent SIF (K_{eq}) for the equivalent homogenous plate. The SIF in each individual layer is given by

$$K_e = \frac{E_e}{E_{eq}} K_{eq}, K_p = \frac{E_p}{E_{eq}} K_{eq} \tag{18.6}$$

where, subscripts e and p refer to Epoxy and PMMA respectively.

To extract the SIF and other constants (Eq. 18.3) from isochromatics, the fringe order at a select set of points around the crack-tip was sampled. To check the accuracy of solution, fringes are regenerated using the extracted coefficients and compared with the fringes obtained experimentally.

Crack propagation angle is calculated using the experimentally determined SIFs in maximum tangential stress (MTS) criterion and in the minimum strain energy density (SED) criterion [17]. The actual crack propagation angle has been compared with those predicted by MTS and minimum SED criteria. The criticality condition for crack initiation is also calculated using the MTS and SED criteria for the Epoxy layer.

18.4 Results

18.4.1 Static Test

The results of the AFPB test will be discussed in this section. The load–displacement record of the layered plate subjected to AFPB loading (s = 6 mm) is shown in Fig. 18.4. The isochromatics corresponding to the selected loads (a, b, c in Fig. 18.4) are shown in Fig. 18.5. As Epoxy is less tough compared to PMMA, the initiation of the crack growth was first observed in

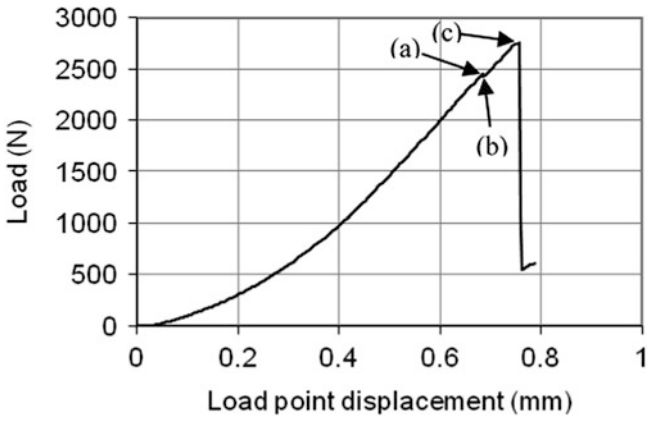

Fig. 18.4 Load displacement record for AFPB with s = 6 mm

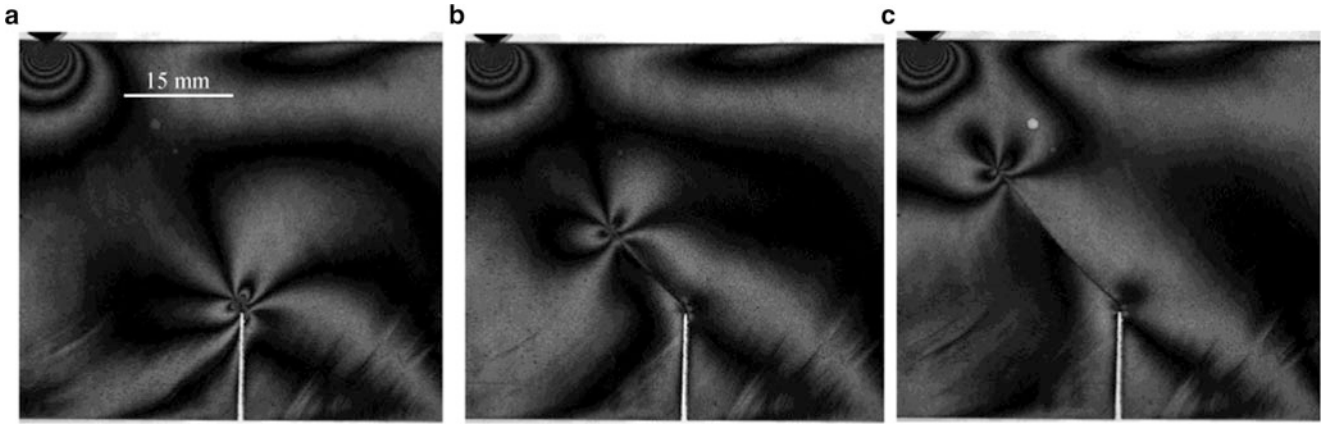

Fig. 18.5 Stable crack growth in PMMA-Epoxy plate in asymmetric four-point bending (**a**) just before crack jump (load 2440 N) (**b**) after first crack jump (load 2405 N) (**c**) just before final unstable failure (load 2604 N)

Epoxy layer with an associated drop in load, point (b) in Fig. 18.4. With the increase in load, crack extended stably in the Epoxy layer to some distance, followed by crack extension in PMMA. Close to the maximum load, the PMMA crack initiated causing the load to drop suddenly along with failure of the specimen. As can be seen in Fig. 18.5a, before initiation of the Epoxy crack, the state of stress is mixed-mode. Once the Epoxy crack starts extending, the state of stress at the Epoxy crack-tip is predominantly opening mode as can be seen from Fig. 18.5b, c. It can be noticed that the crack in Epoxy layer moves towards the closest loading point.

The isochromatics, up to load at which Epoxy crack initiates, were analyzed to determine the thickness averaged mixed mode SIF, as explained in Sect. 18.3. Once the Epoxy crack has extended, it is assumed that the fringes observed are primarily due to the stress fields at the Epoxy crack tip and these fringes were analyzed using the optical constant of Epoxy layer. Figure 18.6 shows the SIF as a function of applied load. In Fig. 18.6, solid symbols represent the equivalent SIF, before the crack extension in Epoxy layer and open symbols are the SIF calculated from the fringes at the Epoxy crack tip after it has extended. During the crack growth, K_I remains almost constant and close to the fracture toughness of the Epoxy and K_{II} drops to very low value. It can be noticed that as the crack in Epoxy layer moves towards the loading point, mixed mode conditions are prevail at the crack tip.

The crack surfaces, shown in Fig. 18.7 indicates that initially the cracks in both layers extend along the same direction, however, the direction of extension become slightly different in the two layers towards the later part of the crack propagation. Coordinates of the points on the crack surface were measured using a coordinate measuring machine. Figure 18.8 shows the profile of the crack surface in both layers at two different y-planes indicated by two arrows labeled as ‘a’ and ‘b’ in Fig. 18.7. It can be noticed that the cracks in both Epoxy and PMMA layers initially start off at the same angle which confirms that the mode mixity at PMMA and Epoxy crack tips are the same before their initiation, despite the fact that the two crack tips initiated at two different instants. Once the crack initiates in Epoxy layer, PMMA layer restricts the propagation of Epoxy crack at the interface. At location ‘a’, the Epoxy crack profile indicates crack twisting whereas the PMMA crack profile does not. Considerable crack twisting is observed for crack surfaces in both layers at location ‘b’.

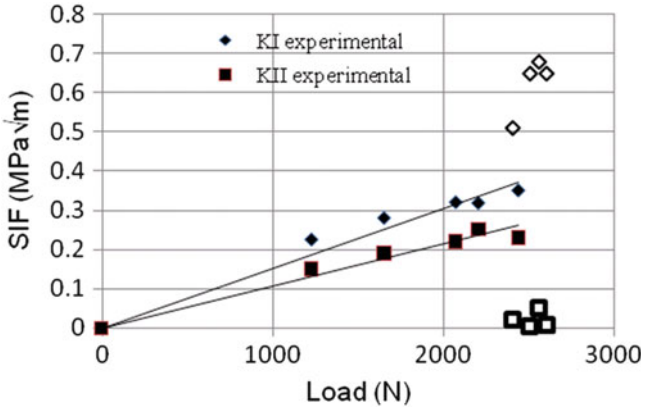

Fig. 18.6 Stress intensity factor as a function of load in AFPB

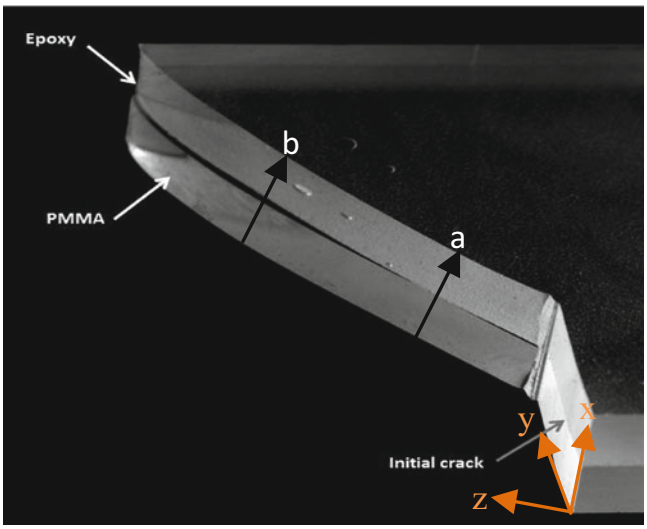

Fig. 18.7 Fracture surface of failed specimen (s = 6 mm)

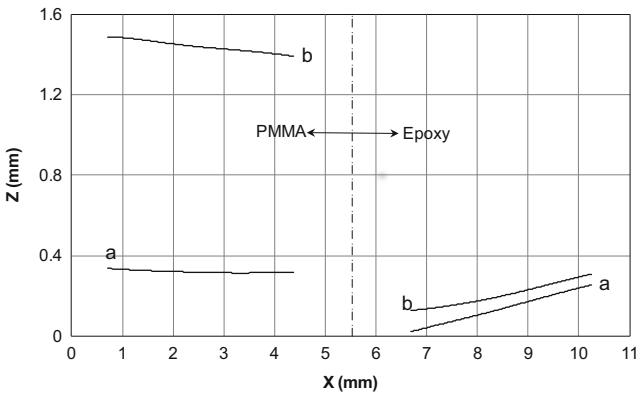

Fig. 18.8 Profile of the crack surface

The initial crack propagation angle was calculated using MTS and minimum SED criterion and compared with the angle measured from the specimen. A good match was observed between the calculated crack propagation directions (45.8°) and the measured crack propagation direction (45°). A mode mixity of 0.58 was obtained using Eq. 18.5. Using the SIF obtained experimentally just prior to initiation of Epoxy crack, the criticality of crack tip stress state was checked for crack initiation in the Epoxy layer by using MTS and minimum SED criteria. It was observed that the equivalent mode I SIF, calculated using MTS and SED criterion (0.54 ± 0.03 MPa√m), is close to the mode-I fracture toughness of Epoxy. Similar results were also obtained for s = 8 mm.

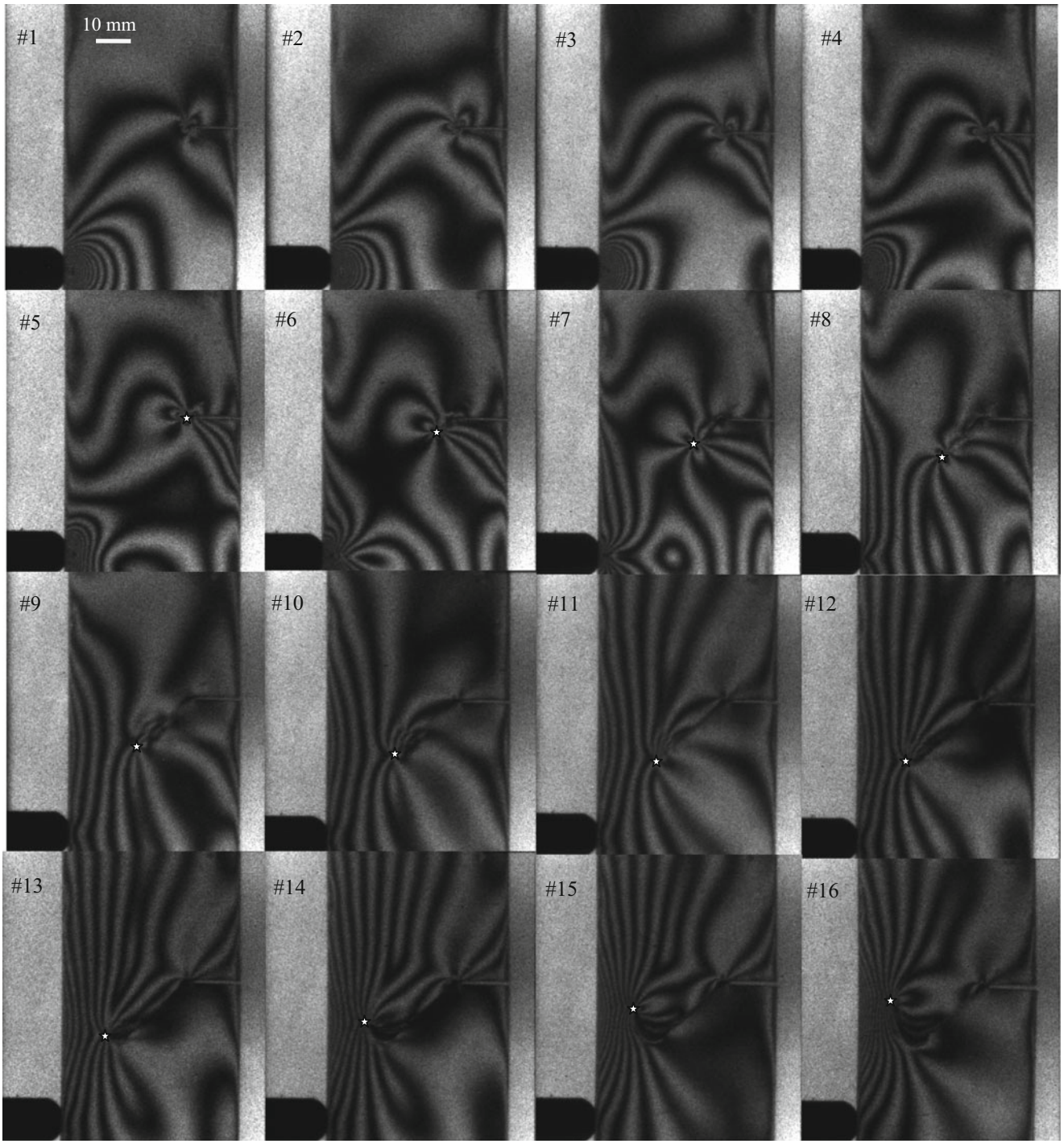

Fig. 18.9 Crack propagation in PMMA-Epoxy layered subjected to asymmetric three-point dynamic loading. The star indicates the crack tip in Epoxy layer. The time interval between two pictures is 15 microseconds

18.4.2 Dynamic Loading

SEN specimens were subjected to dynamic three-point bending such that the loading point is offset by 40 mm with respect to the crack. Figure 18.9 shows the isochromatics for a PMMA-Epoxy specimen during the fracture of the specimen. White star indicates the crack tip location at different times along the crack path. First five pictures show the development of the mixed mode stress field around the crack tip. In the sixth picture the crack has already started moving. After initiation, the Epoxy

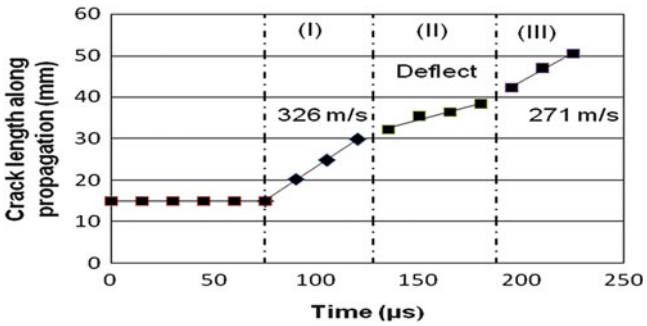

Fig. 18.10 Crack length along propagation for dynamic fracture of PMMA-Epoxy layered plates

crack tip moves predominantly under opening mode condition as can be seen from sixth picture onwards. It can be observed from Fig. 18.8 that initially, the crack starts moving towards the loading point (picture #5 to #9) then it deflects from its original path and moves away from the loading point (picture #10 to #16).

Figure 18.10 shows the crack length along the crack propagation path. Three distinct regions having difference in slope can be seen in Fig. 18.10. It is observed that the crack starts propagating towards the loading point after 75 microseconds with a constant velocity of 326 m/s (regime 1). During deflection, the crack tip moves with a reduced velocity (regime 2) and then it changes direction and moves away from the loading point with a constant velocity of 271 m/s (regime 3).

The thickness averaged mode-I and mode-II SIF obtained from the fringe analysis are 0.4($\pm$0.03) MPa$\sqrt{}$m and 0.46 ($\pm$0.02) MPa$\sqrt{}$m respectively. From these values of SIFs and using Eq. 18.6, the SIFs in the Epoxy layer was evaluated. Using these values of SIFs in the MTS and minimum SED criteria, the crack propagation angle was calculated. A reasonable match was obtained between the calculated crack propagation angle (55° $\pm$ 2°) and the angle measured from the specimen (50°). Using the measured crack propagation angle, criticality of the crack tip stress field has also been checked prior to the crack initiation in Epoxy layer and it is found that the equivalent mode-I SIF (0.86 MPa$\sqrt{}$m) is about 60 % higher than the fracture toughness of the Epoxy (see Table 18.1).

18.5 Conclusions

In this study, fracture behavior of layered plate having an edge crack subjected to mixed mode quasi-static and dynamic three-point loading was investigated. Experiments were performed to obtain the thickness averaged SIF (K_I and K_{II}) in the two layer plate. For the particular combination used in this study, crack growth started in Epoxy layer due to its lower fracture toughness. Criticality of the state of stress field at Epoxy crack tip just before initiation was checked using MTS and minimum SED criteria. Results also showed that once crack growth initiates in the Epoxy layer, the Epoxy crack grew stably till some distance before crack initiated in PMMA layer. When crack started to propagate in PMMA layer it initially follows the same path as the crack in the Epoxy layer thus confirming the same mode mixity as that of the Epoxy crack prior to propagation. Fracture surface examination of failed specimen showed that though cracks in the two layers started propagating in the same direction initially, in the course of propagation the cracks followed slightly different paths. When subjected to dynamic loading, the crack tip in Epoxy and PMMA initiates at different instants of time. As Epoxy is relatively brittle than PMMA, crack propagates in Epoxy earlier than PMMA.

Acknowledgements The authors would like to acknowledge the financial support under the FIST program by Department of Science and Technology, Government of India for the Ultra-high speed camera used in this study through grant number SR/FST/ETII-003/2006.

References

1. Rice JR, Sih GC (1965) Plane problems of cracks in dissimilar media. J Appl Mech 32:418–423
2. Xu L, Tippur HV (1995) Fracture parameters for interfacial cracks: an experimental-finite element study of crack tip fields and crack initiation toughness. Int J Fract 71:345–363
3. Ricci V, Shukla A, Singh RP (1997) Evaluation of fracture mechanics parameters in bimaterial systems using strain gauges. Eng Fract Mech 58:273–283

4. Tippur HV, Rosakis AJ (1991) Quasi-static and dynamic crack growth along bimaterial interfaces: a note on crack-tip field measurements using coherent gradient sensing. Exp Mech 31:243–251
5. Yang W, Suo Z, Shih CH (1991) Mechanics of dynamic debonding. Proc R Soc (London) A433:679–697
6. Liu C, Lambros J, Rosakis AJ (1993) Highly transient elastodynamic crack growth in a bimaterial interface: higher order asymptotic analysis and optical experiments. J Mech Phys Solid 41(12):1857–1954
7. Singh RP, Shukla A (1996) Subsonic and intersonic crack growth along a bimaterial interface. J Appl Mech 63:919–924
8. Singh RP, Kavaturu M, Shukla A (1997) Initiation, propagation and arrest of an interface crack subjected to controlled stress wave loading. Int J Fract 83:291–304
9. Shukla A, Kavaturu M (1998) Opening-mode dominated crack growth along inclined interfaces: experimental observations. Int J Solid Struct 35(30):3961–3975
10. Erdogan F, Biricikoglu V (1973) Two bonded half planes with a crack going through the interface. Int J Eng Sci 11:745–766
11. Singh RP, Parameswaran V (2003) An experimental investigation of dynamic crack propagation in a brittle material reinforced with a ductile layer. Opt Lasers Eng 40(4):289–306
12. Parameswaran V, Shukla A (1998) Dynamic fracture of a functionally gradient material having discrete property variation. J Mater Sci 33(13):3303–3311
13. Wadgaonkar SC, Parameswaran V (2009) Structure of near tip stress field and variation of stress intensity factor for a crack in a transversely graded material. J Appl Mech 76(1):011014
14. Kommana R, Parameswaran V (2009) Experimental and numerical investigation of a cracked transversely graded plate subjected to in plane bending. Int J Solid Struct 46(11–12):2420–2428
15. Bankar UH, Parameswaran V (2013) Fracture of edge cracked layered plates subjected to in-plane bending. Exp Mech 53(2):287–298
16. Dally JW, Riley WF (2001) Experimental stress analysis, 3erth edn. College House Enterprise, Knoxville
17. Anderson TL (1995) Fracture mechanics: fundamentals and applications, 2nd edn. CRC Press, Boca Raton

Chapter 19
Failure Analysis of Micron Scaled Silicon Under High Rate Tensile Loading

Steven Dubelman, Nithin Raghunathan, Dimitrios Peroulis, and Weinong Chen

Abstract Structures have been built at micro scales with unique failure mechanism not yet well understood, in particular, under high-rate loading conditions. Consequently, MEMS devices suffer from inconsistent performance and insufficient reliability. This research aims to understanding the failure mechanisms in micro-scaled specimens deforming at high rates. Single crystal silicon micro beams that are 4 μm thick are subjected to tensile loading at average strain rates of 100 s^{-1} using a miniature modified Kolsky tension bar. A capacitance displacement system and piezoelectric load cell are incorporated to measure the strain and stress of the silicon micro beams directly to ensure precision. Extreme fragmentation of the beams occurs during failure and this phenomenon is observed using a high speed camera. A debris retention system is used to capture the silicon fragments for direct inspection using a Scanning Electron Microscope. The failure mechanism of the micro beams is attributed the presence of sub micron scaled surface defects rather than any one large critical flaw.

Keywords Silicon • Dynamic • MEMS • Micro • Impact test • Kolsky bar

19.1 Extended Abstract

A modified mini Kolsky bar setup was used to subject single crystal silicon micro-specimens to impact tensile loading conditions. The specimens contain a frame that holds a fixed-fixed silicon cantilever that is 4 μm thick and has a width of 0.6 mm and a gage length of 4 mm. The specimens were produced using deep reactive ion etching of a <100> silicon-on-insulator wafer and a shown schematically and physically in Fig. 19.1. Support strips are in place so that the specimen can be handled and are removed once the specimen is fixed in the Kolsky bar apparatus.

The modified Kolsky bar uses of a tubular striker, which is fired via a spring loaded trigger system at a flange. This transmits a wave through the 7075-T651 aluminum incident bar, whose length and diameter are 1.65 m and 0.65 cm respectively. The wave triggers the strain gage that is located 0.86 m from the end of the incident bar where one end of the silicon specimen is fixed. The other end of the specimen is fixed to a rigid body with a 22.24 N capacity load cell which will directly measure the tensile load of the micro specimens. Using a capacitor displacement system that is placed directly at the end of the incident bar, a displacement history is obtained. The capacitor is designed to measure between 1 and 100 μm of displacement and is attached to a precision slide for regular calibration verifications.

Once data has been acquired the stress strain histories of the specimens can be determined using Eqs. 19.1, 19.2, and 19.3, where σ is engineering stress, f is force, A is the cross sectional area, t is time, ε is strain, $\dot{\varepsilon}$ is strain rate, Δl is displacement, $l_\circ$ is initial gage length, and v is velocity.

$$\sigma = \frac{1}{A} f(t) \tag{19.1}$$

$$\varepsilon = \frac{\Delta l}{l_\circ} \tag{19.2}$$

S. Dubelman (✉) • N. Raghunathan • D. Peroulis • W. Chen
School of Material Science and Engineering, Purdue University, 701 West Stadium Avenue, West Lafayette, IN 47907, USA
e-mail: sdubelma@purdue.edu

B. Song et al. (eds.), *Dynamic Behavior of Materials, Volume 1: Proceedings of the 2013 Annual Conference on Experimental and Applied Mechanics*, Conference Proceedings of the Society for Experimental Mechanics Series,
DOI 10.1007/978-3-319-00771-7_19,

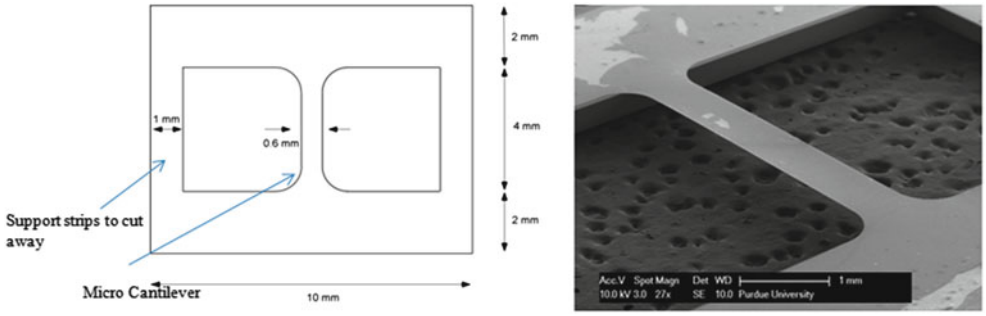

Fig. 19.1 A schematic and SEM image of the single crystal silicon micro cantilever

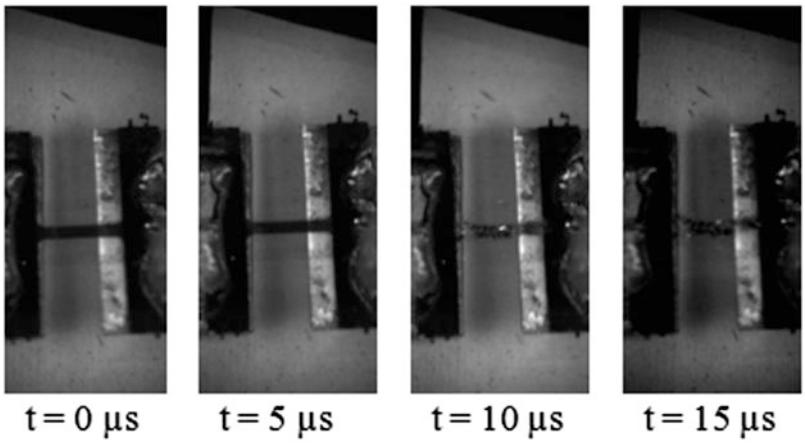

Fig. 19.2 High speed images taken at 200,000 frames per second capturing the failure event

$$\dot{\varepsilon} = \frac{v}{l_\circ} \tag{19.3}$$

The single crystal silicon micro-beams have an average dynamic tensile strength of 1.26 GPa with a standard deviation of 0.310 GPa. The average failure strain of the beams is 0.60 % with a standard deviation of 0.148 %. The dynamic average elastic modulus of the beams is 226.8 GPa with a standard deviation of 18.50 GPa. The average strain rate of the experiments was 92 s^{-1}.

A high speed camera was used to capture the failure event as it occurred. The images were taken at 200,000 frames per second, so the time step interval between images is 5 µs. These high speed images can be seen in Fig. 19.2. The silicon specimen shattered into many pieces rather than failing into two separate pieces at the largest flaw.

Do the size scale and high aspect ratio of the silicon specimens, the current hypothesis to explain the observed failure is that instead of one critical large flaw dominating the failure process, many smaller flaws will run simultaneously, causing multiple fracture pieces.

Chapter 20
Dynamic Fracture Analysis of Semi-circular Bending (SCB) Specimen by the Optical Method of Caustics

Guiyun Gao, Jie Zhou, and Zheng Li

Abstract Semi-Circular Bending (SCB) specimens are widely used in fracture analysis of geo materials due to their simple geometry and loading condition, and also the ability of introducing complete combinations of mode I and mode II fracture. Here SCB specimens of Poly (methyl methacrylate) (PMMA) with different pre-crack angles and positions were employed. An optical method of caustics was applied to calculate the crack initiation, crack propagation, stress intensity factor and fracture toughness, etc. Considering the dynamic crack propagation, the initial curve and caustic pattern in mixed mode fracture were deduced. Then the dynamic fracture parameters could be determined by measuring the caustic patterns obtained by a high speed camera and the specimen geometry. Moreover, we also compared the fracture mode of different pre-crack angles and positions. Finally, the interaction between cracks was also investigated by using this optical method. Results showed that the fracture mode of SCB specimen can be adjusted by pre-crack position and angle.

Keywords Semi-Circular Bending (SCB) • Mixed mode fracture • Stress intensity factor (SIF) • Crack interaction • Caustics

20.1 Introduction

Dynamic fracture plays a vital important role in engineering applications (e.g. explosion, earthquake, and landslide.). The process of brittle fracture under mixed mode loading is more complicated than the traditional fracture in pure mode I especially under dynamic loading. Thus, extensive studies including theoretical and experimental research work have been conducted to investigate the mixed mode brittle fracture in different engineering materials and configurations [1, 2]. Semi-Circular Bending (SCB) specimens are widely used for fracture analysis of geo materials due to their simple geometry and loading condition, and also the ability of introducing pure mode I and pure mode II fracture and the combinations of mode I and mode II fracture [3–6]. Previous work showed that the mixed mode I/II could be introduced in this specimen by changing the crack line relative to the direction of tensile load [7]. However, limited effort was done to investigate the dynamic fracture behavior of this kind of specimens.

Recently the method of caustics has been extended to investigate static as well as dynamic fracture problems of various materials [8–10]. Yao et al. [11] and Gong et al. [12] recently studied the dynamic fracture of orthotropic materials by the method of caustics. Therefore, this method is suitable for dynamic fracture and obtains the fracture parameters directly.

Here, we utilized the SCB specimens of Poly (methyl methacrylate) (PMMA) with different pre-crack angles and positions thoroughly. Combined with a high speed camera system, the dynamic process of crack initiation and propagation can be obtained.

G. Gao • J. Zhou • Z. Li (✉)
State Key Laboratory of Turbulence and Complex System and College of Engineering, Peking University, Beijing 100871, China
e-mail: lizheng@pku.edu.cn

B. Song et al. (eds.), *Dynamic Behavior of Materials, Volume 1: Proceedings of the 2013 Annual Conference on Experimental and Applied Mechanics*, Conference Proceedings of the Society for Experimental Mechanics Series,
DOI 10.1007/978-3-319-00771-7_20,

20.2 Dynamic Mixed Mode Caustic Method

20.2.1 Principle of Caustic Method

When a beam of parallel light rays is incident on a specimen under loading, the light beam will be deflected from the near crack tip region of the specimen due to change of thickness and refractive index. The refracted rays deviate from parallelism and, under suitable conditions, generate a three dimensional surface in space which separates an illuminated region from a dark region (see Fig. 20.1). This surface, composed of points of maximum luminosity, is the so called the "caustic" surface. The rays are tangent to the caustic surface, and the cross-sections of the surface can be observed as bright curves (caustic curve) on a screen parallel to the specimen.

The position of one light beam at point $P'(x',y')$ on the reference plane, at a distance z_0 behind the specimen, is described by the equation

$$r' = \lambda_m r + w = \lambda_m r - z_0 \text{grad}\Delta s \tag{20.1}$$

where λ_m is a scale factor ($\lambda_m = 1$ for parallel light beams, $\lambda_m < 1$ for convergent light, and $\lambda_m > 1$ for divergent light), w is the deflection factor which could be determined by the difference in optical path length Δs (Fig. 20.2). Consider the relation between Δs and stress in plane stress state for optical isotropic materials, the mapping relation can be expressed as

$$r' = \lambda_m r - z_0 dc\text{grad}(\sigma_{11} + \sigma_{22}) \tag{20.2}$$

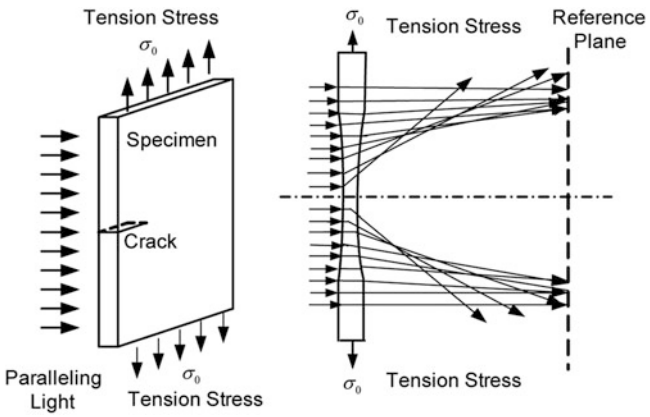

Fig. 20.1 Principle of caustic method in transmission mode

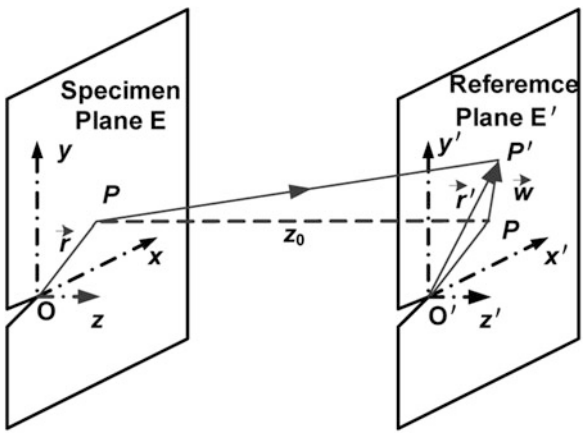

Fig. 20.2 Light beam deflection

20.2.2 Method of Caustics in Mixed Mode Dynamic Fracture

The singular (n = 1 terms) stress fields are given by Nishioka T. [13] and Rosakis A.J. [14] as

$$\begin{aligned}\sigma_{11} &= \frac{K_I^d(t)}{\sqrt{2\pi}} B_I(v)\left\{(2\alpha_l^2-\alpha_s^2+1)\frac{\cos\frac{\theta_l}{2}}{r_l^{1/2}} - \frac{4\alpha_l\alpha_s}{(1+\alpha_s^2)}\frac{\cos\frac{\theta_s}{2}}{r_s^{1/2}}\right\} \\ &\quad -\frac{K_{II}^d(t)}{\sqrt{2\pi}} B_{II}(v)\left\{(2\alpha_l-\alpha_s^2+1)\frac{\sin\frac{\theta_l}{2}}{r_l^{1/2}} - (1+\alpha_s^2)\frac{\sin\frac{\theta_s}{2}}{r_s^{1/2}}\right\} \\ \sigma_{22} &= \frac{K_I^d(t)}{\sqrt{2\pi}} B_I(v)\left\{-(\alpha_s^2+1)\frac{\cos\frac{\theta_l}{2}}{r_l^{1/2}} + \frac{4\alpha_l\alpha_s}{(1+\alpha_s^2)}\frac{\cos\frac{\theta_s}{2}}{r_s^{1/2}}\right\} \\ &\quad -\frac{K_{II}^d(t)}{\sqrt{2\pi}} B_{II}(v)\left\{-(\alpha_s^2+1)\frac{\sin\frac{\theta_l}{2}}{r_l^{1/2}} + (1+\alpha_s^2)\frac{\sin\frac{\theta_s}{2}}{r_s^{1/2}}\right\}\end{aligned} \tag{20.3}$$

where

$$r_l e^{i\theta_l} = z_l = x_l + i\alpha_l x_2,\ r_s e^{i\theta_s} = z_s = x_s + i\alpha_s x_2, \alpha_l = \left(1-\frac{v^2}{c_l^2}\right)^{1/2},\ \alpha_s = \left(1-\frac{v^2}{c_s^2}\right)^{1/2},$$
$$B_I = (1+\alpha_s^2)/\left\{4\alpha_l\alpha_s - (1+\alpha_s^2)^2\right\},\ B_{II} = 2\alpha_s/\left\{4\alpha_l\alpha_s - (1+\alpha_s^2)^2\right\},$$

v is crack speed, and cl, cs are the longitudinal and shear wave velocity.

By substituting Eq. 20.3 into Eq. 20.2, we could get the corresponding displacement fields:

$$\left.\begin{aligned}x' &= r_l\cos\theta_l + \frac{2}{3}\lambda Q(v)\, r_l^{-\frac{3}{2}}\left\{\beta_I\cos\frac{3}{2}\theta_l - \beta_{II}R(v)\sin\frac{3}{2}\theta_l\right\} \\ y' &= \frac{r_l}{\alpha_l}\sin\theta_l + \frac{2}{3}\alpha_l\lambda Q(v)\, r_l^{-\frac{3}{2}}\left\{\beta_I\sin\frac{3}{2}\theta_l + \beta_{II}R(v)\cos\frac{3}{2}\theta_l\right\}\end{aligned}\right\} \tag{20.4}$$

where

$$Q(v) = B_I(v)(\alpha_l^2-\alpha_s^2), R(v) = B_{II}(v)/B_I(v), \lambda = -\frac{3}{2\sqrt{2\pi}}cdz_0\left\{(K_I^d)^2 + (K_{II}^d)^2\right\}, \beta_I = \frac{K_I^d}{\sqrt{(K_I^d)^2+(K_{II}^d)^2}},$$
$$\beta_{II} = \frac{K_{II}^d}{\sqrt{(K_I^d)^2+(K_{II}^d)^2}}$$

The condition for the existence of a caustic curve is the vanishing of the Jacobian of the transformation Eq. 20.4. For the case of a mixed mode crack we get a curve with respect to the (r_l, θ_l,) parameters, which is the image of the "initial curve" in the (r_l, θ_l,) plane. This curve is obtained by setting

$$J = \frac{\partial(x',y')}{\partial(x,y)} = \begin{vmatrix}\frac{\partial x'}{\partial r} & \frac{\partial x'}{\partial\theta} \\ \frac{\partial y'}{\partial r} & \frac{\partial y'}{\partial\theta}\end{vmatrix} = 0, \tag{20.5}$$

and it can be derived as

$$r_0^d = Q^{\frac{2}{5}}(v)H \tag{20.6}$$

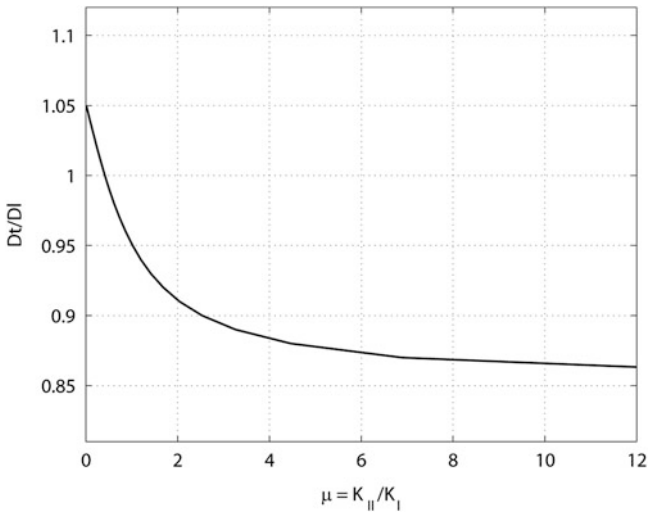

Fig. 20.3 The relation between typical diameters of the caustic curve D_t/D_l and $\mu = K_{II}/K_I$

where

$$A = \lambda^2\alpha_l^2\left(\beta_I^2 + \beta_{II}^2R^2(v)\right), B = \lambda\left(1-\alpha_l^2\right)\left(\beta_I\cos\frac{5}{2}\theta_l - \beta_{II}R(v)\cos\frac{5}{2}\theta_l\right), H = \left(\frac{-B+\sqrt{B^2+4A}}{2}\right)^{\frac{2}{5}}.$$

In static case, the stress intensity factor and the relation between mode I and mode II stress intensity factor could be determined as [15]:

$$K_I = \frac{2\sqrt{2\pi}}{3d|c|z_0(1+\tan^2\alpha)^{\frac{1}{2}}}\left(\frac{D_t}{\frac{10}{3}\sin\frac{2}{5}\pi\cos\frac{2}{5}\alpha}\right)^{\frac{5}{2}}, K_{II} = \mu K_I \tag{20.7}$$

where

$\mu = \tan\alpha$, $|\alpha| = \frac{5}{2}\arctan\left\{[2\sin\frac{2}{5}\pi - \eta(1+\cos\frac{\pi}{5})]/(\eta\sin\frac{\pi}{5})\right\}$, $\eta = D_t/D_l$, and D_t and D_l are the typical diameters.

Hence, if we define $H = \left(\frac{-B+\sqrt{B^2+4A}}{2}\right)^{\frac{2}{5}} = \lambda^{\frac{2}{5}}H'$, the initial curve function could by denoted as

$$r_l = Q^{\frac{2}{5}}(v)\lambda^{\frac{2}{5}}H' = Q^{\frac{2}{5}}(v)\left\{\frac{3}{2\sqrt{2\pi}}|c|dz_0(1+\tan^2\alpha)^{\frac{1}{2}}K_I\right\}^{\frac{2}{5}}H' \tag{20.8}$$

And the caustic curve corresponding to the initial curve around crack tip for mixed-mode fracture can be deduced

$$\left.\begin{aligned} x_c^{'} &= \lambda^{\frac{2}{5}}Q(v)^{\frac{2}{5}}\left\{H'\cos\theta_l + \frac{2}{3}H'^{-\frac{3}{2}}\left[\beta_I\cos\frac{3}{2}\theta_l - \beta_{II}R(v)\sin\frac{3}{2}\theta_l\right]\right\} \\ y_c^{'} &= \lambda^{\frac{2}{5}}Q(v)^{\frac{2}{5}}\left\{H'\frac{1}{\alpha_l}\sin\theta_l + \frac{2}{3}\alpha_lH'^{-\frac{3}{2}}\left[\beta_I\sin\frac{3}{2}\theta_l + \beta_{II}R(v)\cos\frac{3}{2}\theta_l\right]\right\} \end{aligned}\right\} \tag{20.9}$$

For mixed mode crack, the sketch of caustic curve from Eq. 20.9 is given in Fig. 20.3, and the typical diameters of the caustic curve D_t and D_l can be expressed as follows:

$$\left.\begin{aligned} D_t(t) &= [\lambda Q(v)]^{\frac{2}{5}}\delta_y = \left[\frac{3}{2\sqrt{2\pi}}|c|dz_0(1+\tan^2\alpha)^{\frac{1}{2}}K_IQ(v)\right]^{\frac{2}{5}}\delta_y \\ D_l(t) &= [\lambda Q(v)]^{\frac{2}{5}}\delta_x = \left[\frac{3}{2\sqrt{2\pi}}|c|dz_0(1+\tan^2\alpha)^{\frac{1}{2}}K_IQ(v)\right]^{\frac{2}{5}}\delta_x \end{aligned}\right\} \tag{20.10}$$

where

$$\delta_x = \delta_x(\theta_{x1}) - \delta_x(\theta_{x2}), \delta_y = \delta_y(\theta_{y1}) - \delta_y(\theta_{y2})$$

$$\delta_x(\theta_l) = H' \cos\theta_l + \frac{2}{3} H'^{-\frac{3}{2}} \left[\beta_I \cos\frac{3}{2}\theta_l - \beta_{II} R(v) \sin\frac{3}{2}\theta_l \right],$$

$$\delta_y(\theta_l) = H' \frac{1}{\alpha_l} \sin\theta_l + \frac{2}{3} \alpha_l H'^{-\frac{3}{2}} \left[\beta_I \sin\frac{3}{2}\theta_l + \beta_{II} R(v) \cos\frac{3}{2}\theta_l \right];$$

θ_{x1}, θ_{x2} and θ_{y1}, θ_{y2} can be obtained through the solution of $\frac{dx'_c}{d\theta} = 0$ and $\frac{dy'_c}{d\theta} = 0$, respectively. Thus the mixed-mode stress intensity factor can be obtained by measuring the characterization geometry of caustic patterns of the dynamic process.

20.2.3 Mixed Mode Fracture with Different K_{II}/K_I Ratios

The relation between typical diameters of the caustic curve D_t/D_l and $\mu = K_{II}/K_I$ is depicted as Fig. 20.3, which is consistent with Nishika [16]. Here the elastic stress wave velocities of Polymethyl methacrylate (PMMA) are $C_l = 2{,}700$ m/s and $C_s = 1{,}300$ m/s.

The initial curves and caustic curves with different μ and crack propagation velocities are shown in Fig. 20.4. These figures indicate that the initial curves are circles at lower speed (e.g. $v = 250$ m/s, $v/C_s = 0.19$), while with the speed increases the initial curve becomes elliptical and larger than static case.

For open mode crack ($\mu = 0$), the initial curve is continuous for different crack velocity. But in mixed mode cases, the initial curve becomes more noticeable asymmetry and discontinuous at the crack flanks.

However, in low crack propagation velocity ($v/C_s < 0.2$), the dynamic initial curves and the caustic curves are very close to the static ones, which are consist with those of Nishika [16]. Even the velocity increases to 500 m/s ($v/C_s = 0.4$), the difference is only about 3 % from static cases. Therefore, the precise evaluation of mixed-mode dynamic stress intensity factor is strongly dependent on the crack velocity.

20.3 Experimental Procedure

Semicircular bending specimens with different types of pre-cracks are chose to study the mixed-mode fracture. Straight and oblique cracks are fabricated individually to optimize the specimen type. The radius of specimens is 80 mm and the value of 2S/2R equals to 0.75. Two types of specimens as shown in Fig. 20.5 were chosen and their parameters are listed in Table 20.1. For Type I specimen, different inclination angles were studied while the crack length a remains the same. The other type of specimens was designed to have the same initial crack tip position. The interactions of two cracks were also experimentally studied by using the specimens of Type II and the relative position of the two cracks are shown in Fig. 20.5.

The dynamic impact is applied by a drop weight which is about 0.68 kg weight and 374 mm high (loading velocity is 2.71 m/s). The setup of dynamic transmitted caustic method is schematically shown in Fig. 20.6. The dynamic caustic patterns are recorded by the DDGS-II multi-sparks high speed photographic system (modified Cranz-Shardin high speed photographic system). This system consists of 16 point lights and 16 cameras, which could record the 16 frames of caustic patterns in the dynamic fracture process. The distance between the reference plane and the specimen z_0 is set to 440 mm.

20.4 Results and Discussion

20.4.1 Caustic Patterns

The dynamic fracture process is recorded by the high speed photographic system, and the shadow spot patterns are shown in Fig. 20.7. It is indicated that in the beginning the size of the caustic pattern increases with time in the range less than 256 microseconds, while the position does not change. Then the pattern becomes unstable and the crack grows rapidly till the specimen breaks. Similar variation can be observed in the dynamic fracture process of other specimens with different crack positions and angles.

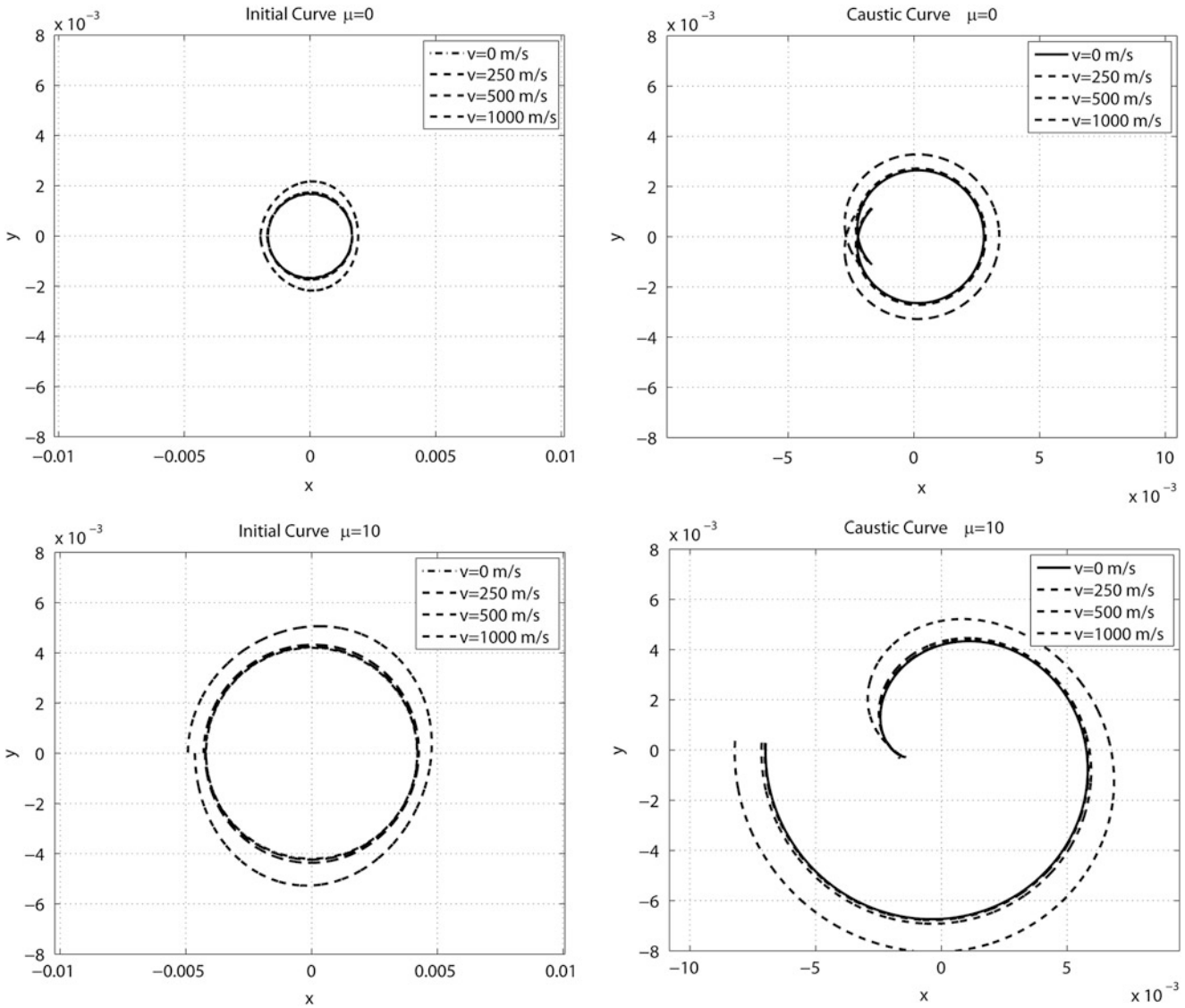

Fig. 20.4 Typical initial and caustic curves of mixed mode crack for propagating cracks: (**a**) mode I ($\mu = 0$)and (**b**) mixed mode ($\mu = 10$)

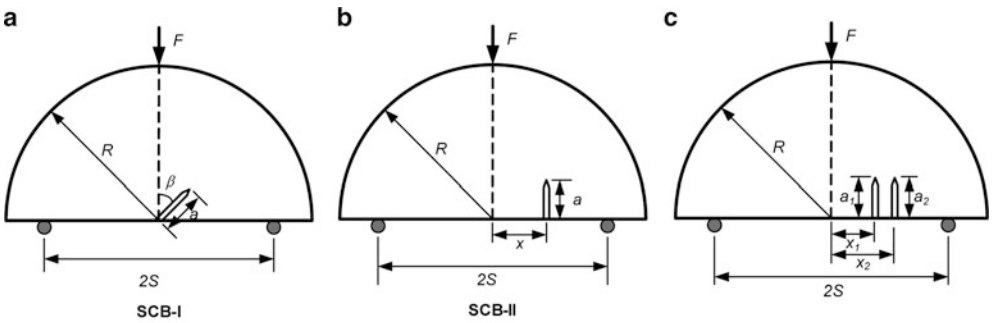

Fig. 20.5 Two types of SCB specimens and crack interaction

Table 20.1 Specimen design

Type	No.	a(mm)	Angle	x_0
I	SCB-I-3	32	45°	22.63
	SCB-I-1	32	60°	27.71
	SCB-I-2	32	70°	29.96
II	SCB-II-3	22.63	0°	22.63
	SCB-II-1	16	0°	27.71
	SCB-II-2	11.24	0°	29.96
No.	a1(mm)	x1(mm)	a2(mm)	x2(mm)
SCB-II-9	22.6	22.6	16	27.71
SCB-II-11	16	22.6	16	22.6

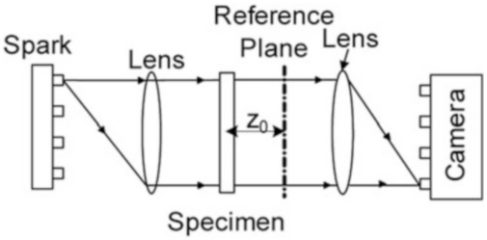

Fig. 20.6 Experimental setups

Fig. 20.7 Typical caustic patterns of SCB specimen

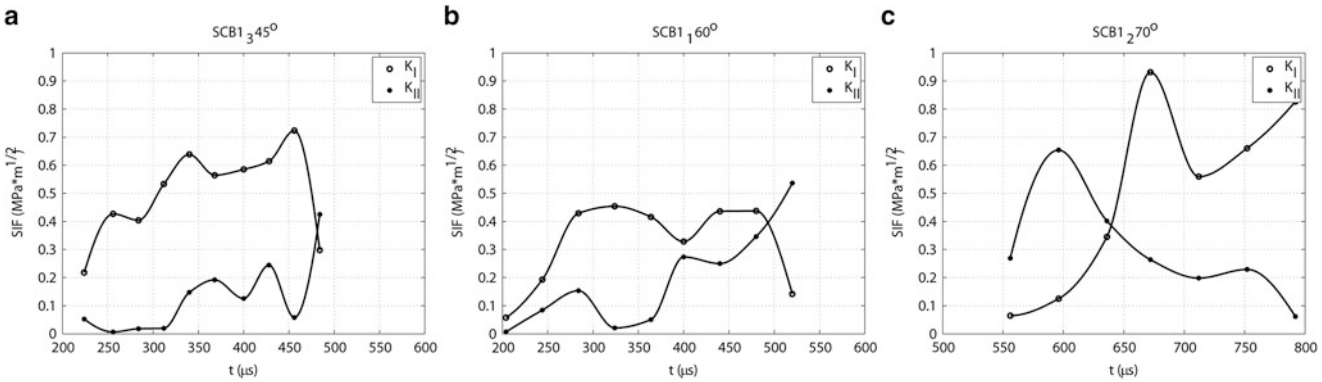

Fig. 20.8 Stress intensity factor of type I specimens with different angles

20.4.2 Comparison of Different Types of Specimens

By fitting the crack length versus time curves, we can obtain the crack propagation velocity. And the velocities are ranged from 200 to 260 m/s, which are lower than 0.2 times of shear wave velocity. Therefore, the dynamic caustic and initial curves are very similar to static ones, and can be evaluated using static equations (Figs. 20.8 and 20.9).

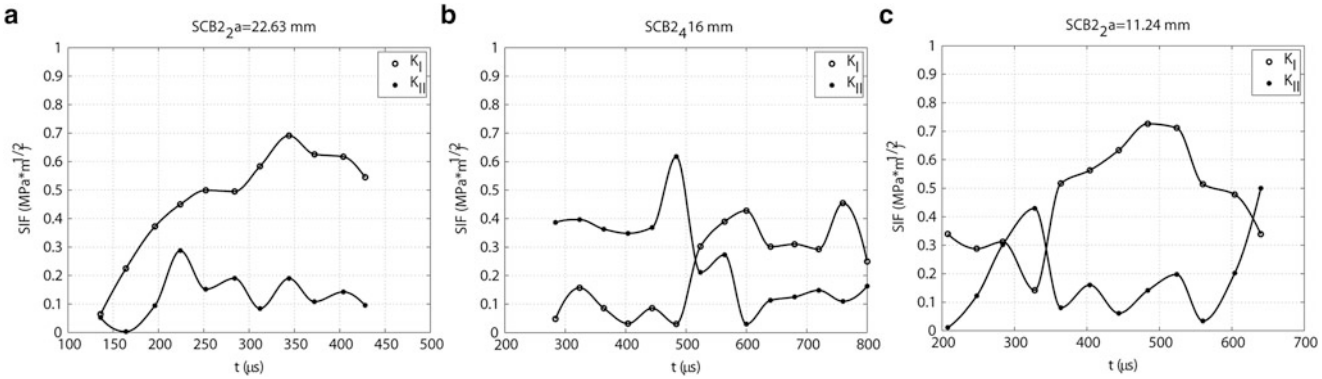

Fig. 20.9 Stress intensity factor of type II specimens with different angles

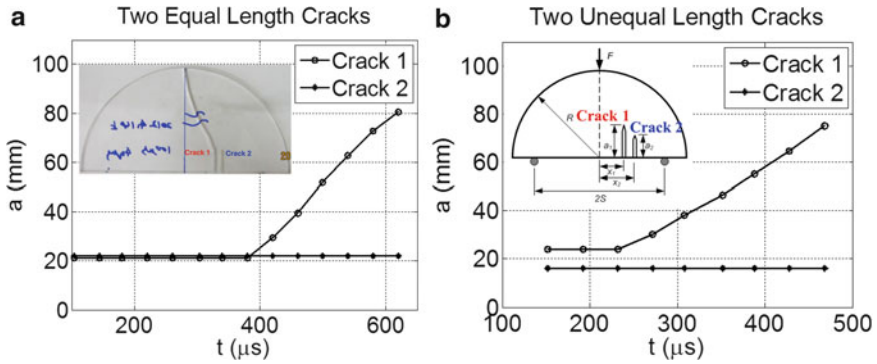

Fig. 20.10 The length of the two parallel cracks (**a**) equal length cracks (**b**) unequal length cracks

The stress intensity factor varies with time. For smaller angle, the mode I fracture dominates and the specimen fractures in mode I. With angle increasing, the ratio of mode II crack increases and when the angle reaches certain value, the crack will initiate in mode II [17]. When the angle reaches 60°, the mode I and mode II stress intensity factors are comparable, and specimens fracture in mixed mode. And fracture is induced by mode II fracture at angle 70°.

For Type II specimen, the deviation of crack position from center position can lead to the increase of mode II ratio. From the stress intensity factors results obtained above, we could find that the deviation of pre crack from central axis leads to similar effect as that increase of angle β. However, the fabrication of Type II specimen is much easier than the Type I specimen.

20.4.3 Crack Interaction

The SCB specimen with two equal cracks broken into several pieces, which indicates that these two cracks interacts with each other. The crack growth can be clearly observed from the evolution of caustic patterns. The crack length and the stress intensity factor could be obtained as shown in Figs. 20.10 and 20.11. We could find that these two cracks influence each other, and compete in the fracture process. For equal cracks, the crack a1 which is near to the middle of the specimen initiated more quickly than the far one. In unequal case, however, the shorter and deviated crack initiated first and then reached the other end of the specimen, while the other crack do not initiate finally.

The existence of the two equal cracks with length of 22.63 mm changed the fracture mode in a competing manner. As shown in Fig. 20.11, the mode I stress intensity factor of these two cracks were first equals to mode II stress intensity factor. Then due to the competing effect, the crack a1 was dominated by mode I fracture while the stress concentration of the crack

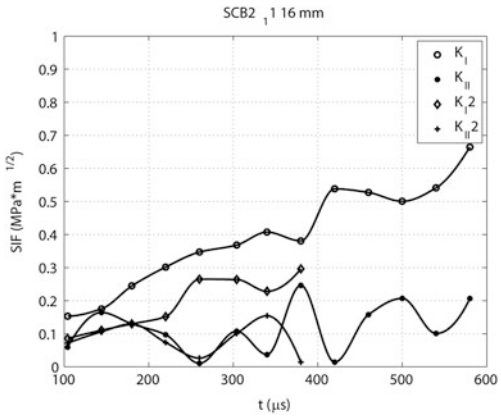

Fig. 20.11 The evolution of stress intensity factors of specimen with two equal length cracks

a2 still increased until a1 crack initiated. We should also notice that the stress intensity factors and their critical value are all small than that in the single crack case. Therefore, the fracture toughness of this multi-cracks condition should include the effect of crack interaction that decreases the stress concentration.

20.5 Conclusions

This article experimentally studies the dynamic fracture of SCB specimens with different pre-crack angles and positions using optical method of caustics. By considering the dynamic crack propagation, mixed-mode initial curve and caustic pattern were derived. The dynamic fracture parameters could be determined by measuring the caustic patterns obtained from a high speed camera. Two types of specimens were used and compared. Different inclination angles lead to different fracture mode, while the change of crack position in Type II specimen reveals similar results which indicate that crack mode is affected by the crack tip position. The interaction between cracks could also be observed clearly in dynamic process where the competition of cracks and fracture mode exists. The optical method of caustics could be extended to investigate the dynamic fracture of other brittle materials like rocks.

Acknowledgments This research work was supported by National Basic Research Program of China (973 Program) under Grant No. 2010CB731503.

References

1. Ayatollahi MR, Aliha MRM (2007) Fracture toughness study for a brittle rock subjected to mixed mode I/II loading. Int J Rock Mech Min Sci 44(4):617–624
2. Khan K, Al-Shayea NA (2000) Effect of specimen geometry and testing method on mixed mode I–II fracture toughness of a limestone rock from Saudi Arabia. Rock Mech Rock Eng 33(3):179–206, 2000/07/01
3. Adamson RM, Dempsey JP, Mulmule SV (1996) Fracture analysis of semi-circular and semi-circular-bend geometries. Int J Fract 77(3):213–222
4. Dai F, Chen R, Xia K (2010) A semi-circular bend technique for determining dynamic fracture toughness. Exp Mech 50(6):783–791, 2010/07/01
5. Dai F, Xia K (2009) Determination of dynamic fracture parameters using a semi-circular bend technique in split Hopkinson pressure bar testing. In: Proceedings of the SEM annual conference, Albuquerque
6. Lim IL, Johnston IW, Choi SK, Boland JN (1994) Fracture testing of a soft rock with semicircular specimens under 3-point bending. 2. Mixed-mode. Int J Rock Mech Min 31(3):199–212
7. Ayatollahi MR, Aliha MRM, Hassani MM (2006) Mixed mode brittle fracture in PMMA – An experimental study using SCB specimens. Mat Sci Eng A-Struct 417(1–2):348–356
8. Papadopoulos GA (2011) New formula of experimental stress intensity factor evaluation by caustics. Int J Fract 171(1):79–84
9. Gao GY, Li Z, Xu J (2011) Optical method of caustics applied in viscoelastic fracture analysis. Opt Lasers Eng 49(5):632–639
10. Pazis DN, Agioutantis Z, Kourkoulis SK (2011) The optical method of reflected caustics applied for a plate with a central hole: critical points and limitations. Strain 47(6):489–498

11. Yao XF, Xu W, Arakawa K, Takahashi K, Mada T (2005) Dynamic optical visualization on the interaction between propagating crack and stationary crack. Opt Lasers Eng 43:195–207
12. Gong K, Li Z (2008) Caustics method in dynamic fracture problem of orthotropic materials. Opt Lasers Eng 46:614–619
13. Nishioka T, Atluri SN (1983) Path-independent integrals, energy release rates, and general solutions of near-tip fields in mixed-mode dynamic fracture mechanics. Eng Fract Mech 18(1):1–22
14. Rosakis AJ (1980) Analysis of the optical method of caustics for dynamic crack propagation. Eng Fract Mech 13(2):331–347
15. Cheng L (1989) Determination of the dynamic stress intensity factors K. Acta Mechanica Sinica 5(3):244–252
16. Nishioka T, Kittaka H (1990) A theory of caustics for mixed-mode fast running cracks. Eng Fract Mech 36(6):987–998
17. Ayatollahi MR, Aliha MRM (2006) On determination of mode II fracture toughness using semi-circular bend specimen. Int J Solid Struct 43 (17):5217–5227

Chapter 21
Effect of Loading Rate on Dynamic Fracture Behavior of Glass and Carbon Fiber Modified Epoxy

Vinod Kushvaha, Austin Branch, and Hareesh Tippur

Abstract The effect of loading rate on dynamic fracture behavior of particulate epoxy composites filled with milled micron size glass and carbon fibers (rod shaped filler) polymer composite is studied. The dynamic fracture experiments are carried out on pre-notched specimens. Three different dynamic strain-rates are achieved using different pulse shapers. An experimental setup comprising of a long-bar apparatus is used to deliver one-point edge impact loading to an unconstrained specimen. A controlled stress pulse is delivered to the specimen by launching a striker towards a long incident bar. Inertially driven crack propagation is seen in all cases. Using 2D Digital Image Correlation (DIC) method used in conjunction with high-speed photography (~300,000 frames per second), in-plane displacement fields around the propagating crack tip are determined during the facture event. The stress intensity factor histories are extracted using the optical measurements.

Keywords Dynamic fracture • Loading rate • Particulate composite • Glass fiber • Carbon fiber

21.1 Introduction

The particle-filled polymer composites (PPC) have been widely used in various engineering fields due to their excellent mechanical characteristics, chemical resistance, electric insulation, and adhesion properties. They are also relatively easy to process at a relatively low cost. Their structural simplicity in terms of macroscopic isotropy, unlike fiber reinforced composites, is another aspect desirable for mechanical design. In particulate composites, the fillers modify their mechanical performance by reinforcing the polymer matrix. Therefore, the filler concentration, filler size and shape, and filler interfacial strength with the polymer matrix have a significant impact on the mechanical properties of PPC. Among the various modifications of mechanical properties, the stiffening, strengthening and toughening of the polymer matrix are the most useful for structural applications.

The prior works in this area suggest that the particle shape effect on fracture toughness for particulate composites under dynamic loading remain largely unexplored [1–5]. Therefore, the focus of the previous study was to understand the effect of two basic parameters, filler shape (flake, rod and sphere) and their volume fraction (5 %, 10 %, and 15 %) on fracture behavior of glass filled epoxy composite under the same dynamic loading rate [6]. However, this gap needs to be bridged because failure of the PPC could initiate differently under different loading rates. Hence, the present study focuses on the loading rate effects of rod-shaped glass (showed maximum improvement in fracture toughness compared to neat epoxy in the previous study) and rod-shaped carbon filled epoxy composites.

V. Kushvaha • A. Branch • H. Tippur (✉)
Department of Mechanical Engineering, Auburn University, Auburn, AL 36849, USA
e-mail: htippur@eng.auburn.edu

B. Song et al. (eds.), *Dynamic Behavior of Materials, Volume 1: Proceedings of the 2013 Annual Conference on Experimental and Applied Mechanics*, Conference Proceedings of the Society for Experimental Mechanics Series,
DOI 10.1007/978-3-319-00771-7_21,

21.2 Material Preparation

Rod shaped glass fillers (average length 800 μm and average diameter 10 μm; aspect ratio 80) and carbon fillers (average length 60 μm and average diameter 8 μm; aspect ratio 7.5) were chosen (Fig. 21.1) to study their relative loading rate effects on dynamic fracture toughness of PPC. The fillers were dispersed into a low-viscosity epoxy (Bisphenol-A resin and Amine based hardener; densities 1,130 kg/m^3 and 961 kg/m^3, respectively). To carry out the comparative dynamic fracture study, 10 % glass-filled and 5 % carbon-filled epoxy by volume sheets were cast separately. The sheets were machined into specimens having dimensions of 60 × 30 × 9 mm (Fig. 21.2). An edge notch of 6 mm length was introduced at the mid-span of each specimen using diamond impregnated circular saw and the notch tip sharpened using a razor blade.

21.3 Material Property Measurement

Physical and elastic properties were measured and are tabulated in Table 21.1. The stress wave transducers were used to perform pulse-echo measurements to determine longitudinal (C_l) and shear wave (C_s) speeds at discrete locations. Dynamic elastic modulus and Poisson's ratio were calculated using,

$$C_l = \sqrt{\frac{E_d(1-v_d)}{\rho(1+v_d)(1-2v_d)}},\ C_s = \sqrt{\frac{E_d}{2\rho(1+v_d)}}.$$

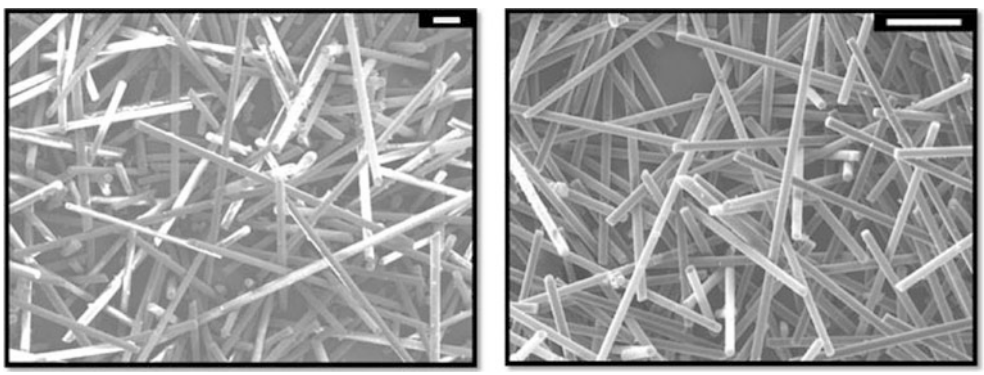

Fig. 21.1 SEM micrographs of rod shaped glass (*left*) and carbon (*right*) fillers used in present study (scale bar: 50 μm)

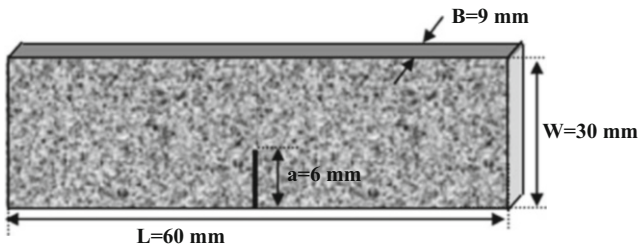

Fig. 21.2 Schematic of test specimen

Table 21.1 Material properties of glass or carbon-filled epoxy composites

Particle type	Density ρ (kg/m^3)	Longitudinal wave speed C_l (m/s)	Shear wave speed C_s (m/s)	Elastic modulus E_d (GPa)	Poisson's ratio v_d
Rod (carbon, $V_f = 5$ %)	1,186	2,545	1,212	4.72	0.35
Rod (glass, $V_f = 10$ %)	1,285	2,534	1,243	5.33	0.34
Neat epoxy	1,146	2,481	1,128	3.99	0.37

21.4 Experimental Details

A schematic of the experimental setup used for dynamic fracture tests is shown in Fig. 21.3. The setup included a 6 ft long, 1 in. diameter long-bar with 1/4 in. diameter bull-nose tip against the unconstrained specimen and a 12 in. long, 1 in. diameter striker held inside the barrel of a gas gun. Both the long-bar and the striker were of the same diameter and made of aluminum 7,075 to eliminate the impedance mismatch between them. The striker is launched towards the long-bar using the gas-gun at a velocity of 16 m/s. When the striker contacts the long-bar, a compressive stress wave propagates through the bar and gets transmitted into the specimen. Three different dynamic loading rates were achieved through the usage of different pulse shapers between striker and long-bar shown in Fig. 21.3. A soft Aluminum 1,100 disc (designated as 'Al-PS') of diameter 8 mm and thickness 0.9 mm produced a *strain-rate* of 10.7/s, *measured on the long-bar*. A combined polycarbonate washer (outer diameter 6.3 mm, inner diameter 2.2 mm and thickness 0.7 mm) and Al 1,100 sandwich pulse shaper (designated as 'PC-PS') produced a slightly lower strain rate of 3.7/s. The highest strain rate was 42.0/s when no pulse shaper (designated as 'No-PS') was used.

A stochastic black and white speckle pattern was sprayed on to the specimen for deformation measurements using DIC. The pattern is photographed using a Cordin-550 ultrahigh-speed digital camera. It has 32 independent CCD image sensors positioned radially around a rotating mirror which sweeps light over these sensors. Prior to loading, a set of 32 undeformed images were recorded at a rate of ~300,000 frames per second at a resolution of 1,000 × 1,000 pixels per image. When the striker contacts the long-bar and completes the circuit, a signal is sent to the delay generator which in turn triggers the camera. The camera triggers a high energy flash lamp control unit and initiates image capture. Thus, a second set of 32 deformed images were captured at the same framing rate. Therefore each image in the undeformed set had a corresponding image in the deformed set. The recorded sets of deformed and undeformed images are then correlated to obtain in-plane displacements.

21.5 Optical Data Analysis

The recorded undeformed set and deformed set of images were correlated using a digital image correlation tool ARAMIS™ and the in-plane crack-opening (u_y) and crack-sliding (u_x) displacement fields were estimated near the crack tip (Fig. 21.4). In order to extract stress intensity factor (SIF) history, (u_y, u_x) displacement fields were digitized by identifying the current crack-tip location and subsequently establishing the Cartesian and polar coordinates. A number of data points were collected in the vicinity of the current crack- tip $0.5 < r/B < 1.5$ (where B is sample thickness) and [$(-150^\circ < \theta < -90^\circ)$ and

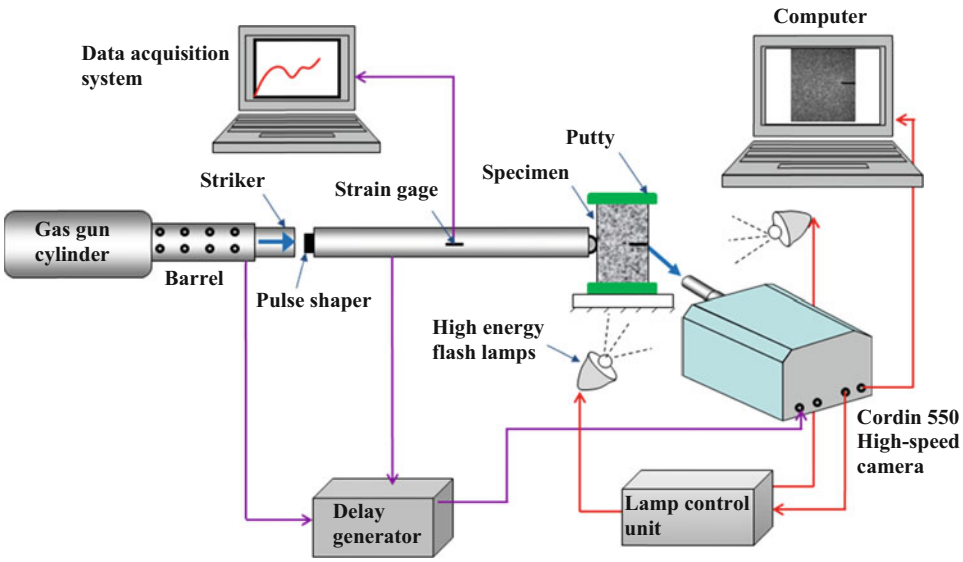

Fig. 21.3 Schematic of experimental setup

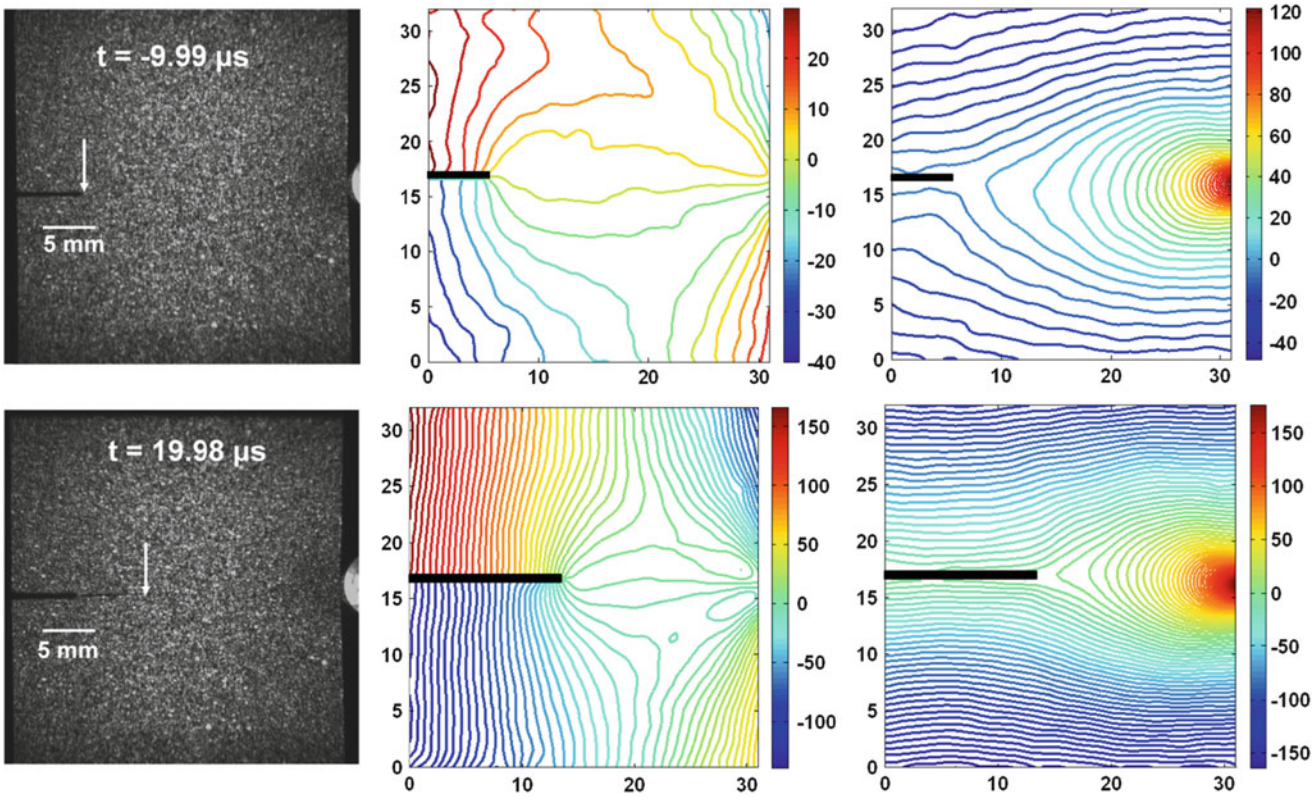

Fig. 21.4 Sample acquired speckle images for pre ($t = -9.99$ μs) and post-crack initiation ($t = 19.98$ μs) time instants with crack opening (u_y) and crack sliding (u_x) displacement contours (contour interval 5 μm) for 10 % glass-filled epoxy specimen tested using 'Al-PS'

$(90° < \theta < 150°)$] as it has been shown that 3D deformations and far field effects are minimum in this region [7]. At each data point, (u_y, u_x) displacement values as well as the location of these points were stored. The asymptotic expressions for a dynamically loaded stationary crack given in Ref. [8] were used to extract mode-I and –II SIFs using an over-deterministic least-squares analysis of the optical data. In doing so, the rigid body translation and rotation terms were taken into account. Once the crack starts propagating, the asymptotic expressions for sliding and opening displacements for a steadily growing crack (assuming transient effects to be negligible) are evaluated using expressions in Ref. [9]. For mode I problem, the crack-opening displacements (u_y) can be viewed as with mode I-rich information whereas crack sliding displacements (u_x) with mode II-rich information. Thus, u_y and u_x were used to extract mode-I and –II stress intensity factors K_I and K_{II}, respectively.

21.6 Effect of Loading Rate

The loading rate effect on dynamic fracture toughness was studied by comparing the stress intensity factor histories for rod shaped 10 % V_f glass-filled and 5 % V_f carbon-filled epoxy (Table 21.2). Plot of K_I histories are shown in Fig. 21.5. In each plot, histories for K_{II} are also provided for completeness. Being a symmetric loading experiment, as expected, K_{II} histories are essentially negligible within the measurement errors. The data from both pre- and post-crack initiation periods are shown. It should be noted that the measured histories of each samples have been shifted relative to each other along the time axis to make crack initiation time (identified as $t = 0$) of each experiment coincide. For 10 % V_f glass-filled PPC, the K_I histories show a monotonic increase until and after crack initiation in all the three cases. As the loading rate is increased for the 'Al-PS' and 'No-PS' cases, K_I histories show higher slope for the 'No-PS' ($dK_I/dt = 182 \times 10^3$ MPa$\sqrt{}$m/s) case followed by the 'Al-PS' ($dK_I/dt = 86 \times 10^3$ MPa$\sqrt{}$m/s) and 'PC-PS' ($dK_I/dt = 53 \times 10^3$ MPa$\sqrt{}$m/s) cases, respectively, before crack initiation as expected. In 'No-PS' and 'Al-PS' cases, a modest kink in the history are noticeable based on when the crack initiated during the interframe period. The 'No-PS' case produces the highest crack initiation toughness as well as post-initiation K_I values. The 'Al-PS' and 'PC-PS' cases, respectively, follow. The rate of increase of K_I was approximately constant for the 'No-PS' and 'Al-PS' cases but greater than the 'PC-PS' case, once the crack initiates. For 10 % V_f

Table 21.2 Crack initiation toughness (in MPa$\sqrt{m}$) comparison (% increase is relative to the 'PC-PS' case)

Pulse shaper type	Crack initiation toughness	Glass (10 % V_f)	Carbon (5 % V_f)
'PC-PS'	K_I	2.60	1.63
'Al-PS'	K_I	3.10	1.90
	% increase in K_I	19	17
'No-PS'	K_I	3.42	2.83
	% increase in K_I	32	74

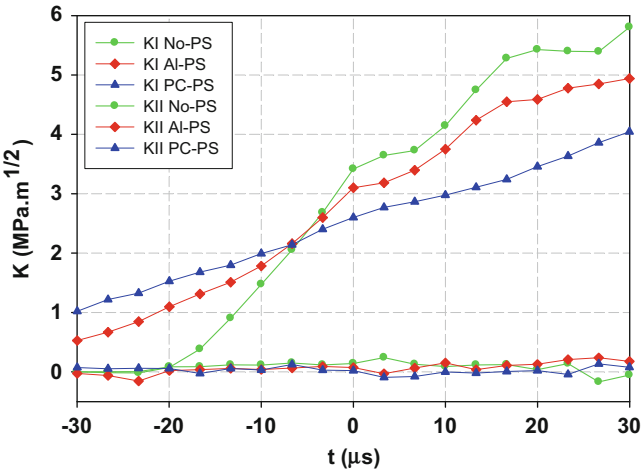

Fig. 21.5 K_I and K_{II} histories for 10 % V_f glass-filled epoxy with different loading rate. Before crack initiation, dK_I/dt were ~182 × 10^3, 86 × 10^3 and 53 × 10^3 MPa$\sqrt{m}$/s for 'No-PS', 'Al-PS' and 'PC-PS' cases, respectively, compared to dK_I/dt of 1 × 10^{-4} MPa$\sqrt{m}$/s in quasi static loading case. (Histories for K_{II} are also provided for completeness. Being a symmetric loading experiment, K_{II} histories are essentially negligible within the measurement errors.)

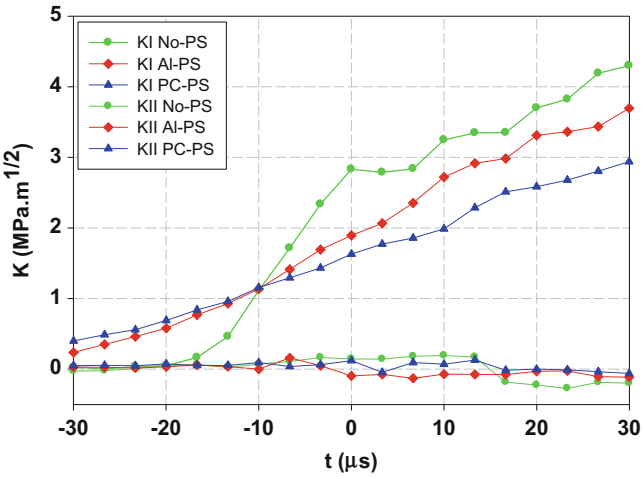

Fig. 21.6 K_I and K_{II} histories for 5 % V_f carbon-filled epoxy with different loading rate. Before crack initiation, dK_I/dt were ~178 × 10^3, 55 × 10^3 and 41 × 10^3 MPa$\sqrt{m}$/s for 'No-PS', 'Al-PS' and 'PC-PS' cases, respectively

(Fig. 21.5); glass-filled epoxy show 19 % and 32 % increase in crack initiation toughness for the 'Al-PS' and 'No-PS' cases, respectively, compared to the 'PC-PS' case.

Similar trend in loading rate behavior is observed in case of carbon fiber-filled epoxy before and after crack initiation. For 5 % V_f (Fig. 21.6), carbon-filled epoxy shows 17 % and 74 % increase in crack initiation toughness for the 'Al-PS' and 'No-PS' cases, respectively, compared to the 'PC-PS' case.

21.7 Fractographic Evaluation

The fractographic study was carried out to understand the toughening mechanisms behind the increase in crack initiation toughness due to loading rate differences. As the stress wave propagates through the specimen, the crack front is driven forward. When the crack front encounters filler particles during propagation, the crack path is influenced. A careful observation of fractographs suggests that the interaction of the crack front with the filler leads to the following primary failure modes: (a) Matrix cracking; (b) Filler-matrix interface separation; (c) Filler pullout; (d) Filler breakage. Hence, during crack growth each of these failure modes contribute to energy dissipation adding to an overall increase in the crack initiation and propagation SIF values. In case of glass-filled epoxy, it is evident from the micrographs that matrix cracking is higher for the 'No-PS' case followed by the 'Al-PS' and 'PC-PS' cases, respectively. Also, due to the higher loading rate the filler-matrix interface separation for the fibers oriented along the crack front is maximum for the 'No-PS' case followed by the 'Al-PS' and 'PC-PS' cases, respectively. The fibers bridging the crack front resist the crack growth due to their relatively longer length, ~800 μm, and likely break before pulled out of the matrix as the crack continues to open. The reported tensile strength of the fibers being of the order of 3 GPa, the process seems to contribute to a rather high apparent crack initiation and propagation toughness values of the PPC. The higher loading rate makes the material behave stiffer and more fibers break than pullout. Hence the fiber pullout was found to be more for the 'PC-PS' case followed by the 'Al-PS' and 'No-PS' cases, respectively, resulting in the lowest crack initiation toughness for the 'PC-PS' case among all the three cases (Fig. 21.7).

For carbon-filled epoxy, the dominant failure modes were matrix cracking, fiber-matrix separation and fiber pullout with evidence of relatively few fractured fibers. As in the glass-filled epoxy, carbon-fiber filled epoxy also showed significantly higher matrix cracking for the 'No-PS' case followed by the 'Al-PS' and 'PC-PS' cases, respectively. On the fracture surface, foot prints due to fiber pull out (seen as cavities in Fig. 21.8) can be identified. It is likely that the fibers bridging the crack front do not resist crack growth as well as the glass fibers due to a relatively short average length (~60 μm) resulting in pull out more readily as the crack continues to open. Hence due to the dominance of fiber pull out, the SIF values in the 'No-PS' case show a dramatic decrease once the crack initiates.

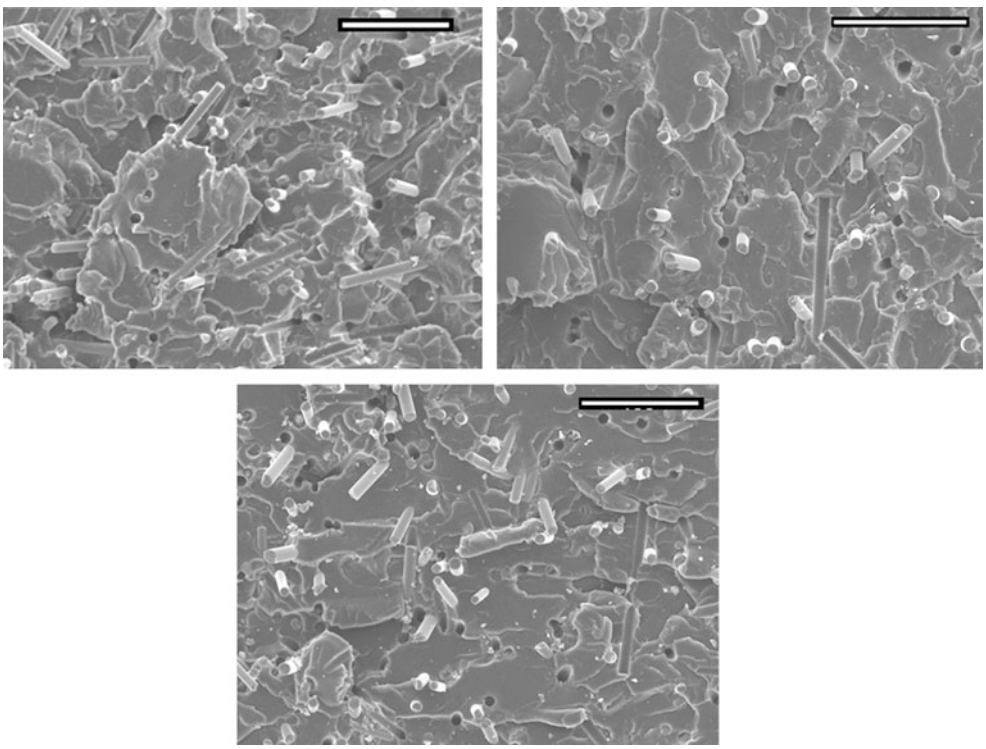

Fig. 21.7 Fractographs of 10 % V_f glass-filled epoxy for the 'No-PS' case (*top left*), 'Al-PS' case (*top right*) and 'PC-PS' case (*bottom*) respectively; scale bar = 100 μm

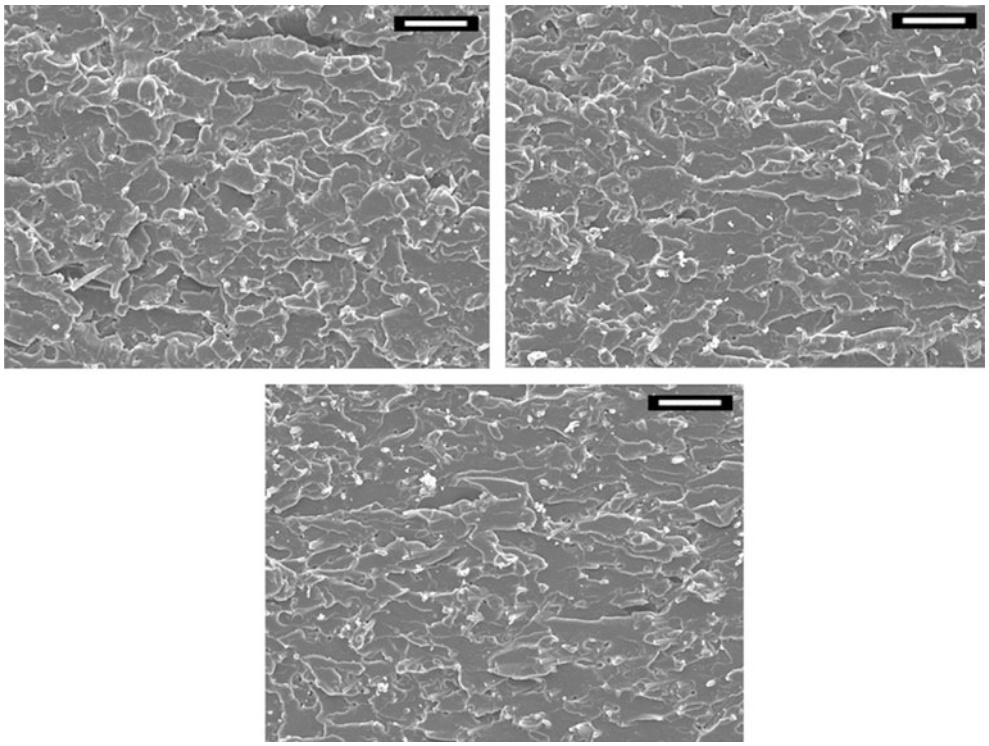

Fig. 21.8 Fractographs of 5 % V_f carbon-filled epoxy for the 'No-PS' case (*top left*), 'Al-PS' case (*top right*) and 'PC-PS' case (*bottom*) respectively; scale bar = 100 μm

21.8 Conclusion

In this study, the effect of loading rate on dynamic fracture behavior of discrete glass- and carbon-fiber filled epoxy composites were investigated experimentally using Digital Image Correlation in conjunction with high speed photography.

For both glass- and carbon-filled epoxy composites, the 'No-PS' case produced the highest crack initiation toughness as well as post-initiation K_I values followed by the 'Al-PS' and 'PC-PS' cases, respectively. The 10 % V_f; glass-fiber filled epoxy show 19 % and 32 % increase in crack initiation toughness for the 'Al-PS' and 'No-PS' cases, respectively, compared to the 'PC-PS' case. For 5 % V_f; carbon-fiber filled epoxy shows 17 % and 74 % increase in crack initiation toughness for the 'Al-PS' and 'No-PS' cases, respectively, when compared to the 'PC-PS' case. The fractographic evaluation is used to explain the plausible mechanisms associated with the different loading rates during dynamic fracture and their potential contribution to the differences in their macroscale fracture parameters.

Acknowledgement The authors would like to thank the National Science Foundation for supporting this research through a grant NSF-CMMI-1100700.

References

1. Song SG et al (1996) Reinforcement shape effects on the fracture behavior and ductility of particulate-reinforced 6061-Al matrix composites. Metall Mater Trans A 27(11):3739–3746
2. Nakamura Y et al (1992) Effect of particle-size on the fracture toughness of epoxy-resin filled with spherical silica. Polymer 33(16):3415–3426
3. Nakamura Y et al (1992) Effect of particle-size on mechanical properties of epoxy-resin filled with angular-shaped silica. J Appl Polym Sci 44 (1):151–158
4. Spanoudakis J, Young RJ (1984) Crack-propagation in a glass particle-filled epoxy-resin. 1. Effect of particle-volume fraction and size. J Mater Sci 19(2):473–486

5. Kitey R, Tippur HV (2005) Role of particle size and filler-matrix adhesion on dynamic fracture of glass-filled epoxy. I. Macromeasurements. Acta Materialia 53(4):1153–1165
6. Kushvaha V, Tippur H (2012) Effect of filler particle shape on dynamic fracture behavior of glass-filled epoxy. Conf Proc Soc Exp Mech Series 1 (Dynamic Behavior of Materials):513–522
7. Tippur HV, Krishnaswamy S, Rosakis AJ (1991) Optical mapping of crack tip deformations using the methods of transmission and reflection coherent gradient sensing-A study of crack-tip K-dominance. Int J Fract 52(2):91–117
8. Westergaard HM (1939) Bearing pressure and cracks. ASME Appl Mech 6:49–53
9. Nishioka T, Atluri SN (1983) Path-independent integrals, energy-release rates, and general-solutions of near-tip fields in mixed-mode dynamic fracture-mechanics. Eng Fract Mech 18(1):1–22

Chapter 22
Application of Element Free Galerkin Method to high Speed crack Propagation Analysis

A. Agarwal, N.N. Kishore, and V. Parameswaran

Abstract The Element Free Galerkin method is used to find numerical solutions of dynamic fracture problems. Moving Least Square(MLS) approximation is used for interpolation of test and trial functions. Galerkin weak form is employed for discretizing governing equations. Lagrange multipliers are applied in constrained Galerkin weak form to enforce essential boundary conditions. For dynamic case, separate weak forms are generated for the governing equation and the essential boundary conditions. Visibility criterion is used for the construction of influence domain for the bodies having discontinuities. For different problems, fracture parameters like J-integral, dynamic stress intensity factor are calculated. A mixed mode problem – a plate having an oblique crack is also analyzed under both dynamic and static loading conditions. Some crack propagation experiments are conducted on a split Hopkins set up and from the experimental data for applied force, crack path and crack speed, crack propagation is simulated using EFGM for all cases.

Keywords Meshless method • Dynamic fracture • Numerical simulation • Experimental varification • High speed imaging

22.1 Introduction

The analysis of high speed crack propagation is significantly critical in several practical applications like fracture control in construction blasting and crack arresting in engineering structures. In the last two decades, several mesh free methods have been developed. These methods have an advantage over FEM in modeling crack propagation along a complex path because of the absence of any rigid connectivity among nodes. Element free Galerkin method (EFGM) [3] is one of the efficient mesh free methods. It is based on moving least squares (MLS) interpolants. The essential idea of EFG methods is the use of moving least square interpolants. Such interpolants were described in a limited form by Shepard [1]. Belytschko [2] provided a comprehensive review of the state-of-the-art in meshless methods. Tabbara [4] used EFGM to model dynamic fracture problems. But this method lacked the versatility of constantly adjusting crack path direction and crack speed to model real life problems.

In the present work, an enriched mesh is used around the crack tip to capture the steep variation of stresses near it. First, EFGM is applied to plates having stationary cracks in Mode-I and mixed mode loading cases. Then, crack propagation experiments are conducted on epoxy plates in a split Hopkins setup under 3-point bending conditions. Images of the specimen with photographic fringes are taken using a high speed camera. Simulations are made using EFGM and dynamic stress intensity factor is evaluated by computing J-integral around the crack tip and variation of dynamic SIF with time is plotted for all cases.

A. Agarwal • N.N. Kishore (✉) • V. Parameswaran
Indian Institute of Technology, Kanpur, India
e-mail: nnk@iitk.ac.in

B. Song et al. (eds.), *Dynamic Behavior of Materials, Volume 1: Proceedings of the 2013 Annual Conference on Experimental and Applied Mechanics*, Conference Proceedings of the Society for Experimental Mechanics Series,
DOI 10.1007/978-3-319-00771-7_22,

22.2 Element-Free Galerkin Method

The EFGM employs Moving Least Squares (MLS) approximants for the construction of test and trial functions [5]. Galerkin weak form is used for the development of discretized governing equations. Numerical integration is done via background mesh in order to calculate nodal stiffness and mass matrices.

22.2.1 MLS Approximation

Let $u(x)$ be the function of field variable defined in the domain. The approximation of $u(x)$ at any point x in the domain is denoted by $u^h(x)$ and is expressed [6] as the inner product of a vector of basis functions $\boldsymbol{p}(x)$ and a vector of the coefficients $\boldsymbol{a}(x)$ i.e.

$$u^h(x) = \sum_{j=1}^{m} p_j(x)a_j(x) = \boldsymbol{p}^T(x)\boldsymbol{a}(x) \tag{22.1}$$

where,

$$\boldsymbol{p}^T = [\ 1 \ \ x \ \ x^2 \ldots\ldots x^m\ ] \tag{22.2}$$

and $\boldsymbol{a}(x)$ is given by

$$\boldsymbol{a}^T(x) = [\ a_1(x) \ \ a_2(x) \ldots\ldots a_m(x)\ ] \tag{22.3}$$

The unknown coefficients $a(x)$ at any given point are determined by minimizing the weighted discrete $\mathcal{L}_2$ norm w.r.t. $\boldsymbol{a}(x)$. The weighted discrete $\mathcal{L}_2$ norm is defined as,

$$J(x) = \sum_{I=1}^{n} w(x - x_I)[u_L^h(x_I, x) - u_I]^2 \tag{22.4}$$

where n is the number of nodes in the support domain for which weight function $w(x - x_I) \neq 0$ and u_I is the nodal parameter at node I.

The minimization of norm in Eq. (22.4) leads to the following set of linear equations:

$$\frac{\partial J(x)}{\partial a(x)} = \mathbf{A}a(x) - \mathbf{B}u = 0 \tag{22.5}$$

Substituting Eq. (22.5) into Eq. (22.1),

$$u^h(x) = \sum_{I=1}^{n} \phi_I(x)u_I = \phi(x)u \tag{22.6}$$

Here, shape functions $\phi_I(x)$ can be written as:

$$\phi_I(x) = \sum_{j=1}^{m} p_j(x)(\mathbf{A}^{-1}(x)\mathbf{B}(x))_{jI} = \mathbf{p}^T\mathbf{A}^{-1}\mathbf{B}_I \tag{22.7}$$

and

$$u^T = [u_1 \quad u_2 \quad \ldots \quad u_n]$$

Here m is the order of polynomial basis $p(x)$. To prevent the singularity of moment matrix $\mathbf{A}$, m should be kept much smaller than n, the number of nodes in the support domain of that point.

To obtain strains and stresses from displacement data, the partial derivatives of the shape functions are required, which can be written as follows:

$$\phi_{I,x} = \mathbf{p}_{,x}^T \mathbf{A}^{-1} \mathbf{B}_I + \mathbf{p}^T \mathbf{A}_{,x}^{-1} \mathbf{B}_I + \mathbf{p}^T \mathbf{A}^{-1} \mathbf{B}_{I,x} \tag{22.8}$$

where,

$$\mathbf{B}_{I,x}(x) = \frac{dw(x - x_I)}{dx} \mathbf{P}(x_I) \tag{22.9}$$

and

$$\mathbf{A}_{,x}^{-1} = -\mathbf{A}^{-1} \mathbf{A}_{,x} \mathbf{A}^{-1} \tag{22.10}$$

In the above expression $\mathbf{A}_{,x}$ is computed by

$$\mathbf{A}_{,x} = \sum_{I=1}^{n} w(x - x_I)_{,x} \mathbf{p}(x_I) \mathbf{p}^T(x_I) \tag{22.11}$$

In EFGM, weight functions have a compact support, which means that the weight function $w(x - x_I)$ should be non-zero only for a small neighbourhood of node I, known as the domain of influence of node I.

The weight functions depend on $\bar{r}$, where $\bar{r} = r/\rho$
where r is the distance between point of interest x and node x_I i.e. $r = |x - x_I|$ and ρ is the radius of the compact support of node I.

In the present work, cubic spline weight function has been used, which is represented as:

$$w(\bar{r}) = \begin{cases} \frac{2}{3} - 4\bar{r}^2 + 4\bar{r}^3 & \text{for } \bar{r} \le \frac{1}{2} \\ \frac{4}{3} - 4\bar{r} + 4\bar{r}^2 - \frac{4}{3}\bar{r}^3 & \text{for } \frac{1}{2} < \bar{r} \le 1 \end{cases} \tag{22.12}$$

In two-dimensional case, the weights w_x and w_y in x and y directions respectively are found out with x and y distances, r_x and r_y respectively. Then weight function at any given point is given by $w_x w_y$.

The derivatives of w_I can be computed by

$$\frac{\partial w_I}{\partial x} = \frac{\partial w_I}{\partial r} \frac{\partial r}{\partial x}, \quad \frac{\partial w_I}{\partial y} = \frac{\partial w_I}{\partial r} \frac{\partial r}{\partial y} \tag{22.13}$$

where,

$$\frac{\partial w_I}{\partial r} = \begin{cases} -8 & \bar{r} \le \frac{1}{2} \\ -4 & \frac{1}{2} < \bar{r} \le 1 \\ 0 & r > 1 \end{cases}$$

After discretization, the following set of equations is obtained,

$$\mathbf{M}\ddot{\mathbf{U}} + \mathbf{K}\mathbf{U} + G\lambda - \mathbf{F} = 0 \tag{22.14}$$

$$G^T \mathbf{U} - q = 0$$

where,

$$M_{IJ} = \int_{\Omega} \rho \Phi_I \Phi_J \ddot{\mathbf{u}}_J$$

$$K_{IJ} = \int_{\Omega} B_I^T D B_J d\Omega$$

$$G_{IJ} = -\int_{\Gamma_u} \Phi_I^T \mathbf{N}_J d\Gamma$$

$$\lambda = \sum_{I=1}^{n_\lambda} \begin{pmatrix} N_I & 0 \\ 0 & N_I \end{pmatrix} \begin{pmatrix} \lambda_{uI} \\ \lambda_{vI} \end{pmatrix}$$

$$F_I = \int_{\Omega} \Phi_I^T \mathbf{b} d\Omega + \int_{\Gamma_t} \Phi_I^T \bar{\mathbf{t}} d\Gamma = \begin{Bmatrix} F_{xI} \\ F_{yI} \end{Bmatrix}$$

$$q_I = -\int_{\Gamma_u} \mathbf{N}_I^T \bar{\mathbf{u}} d\Gamma$$

$$B_I = \begin{pmatrix} \phi_{I,x} & 0 \\ 0 & \phi_{I,y} \\ \phi_{I,y} & \phi_{I,x} \end{pmatrix}$$

Here λ is a vector of Lagrangian multipliers with N_I as the Lagrange interpolant at node I.

For dynamic problems, Liu[7] proposed a method in which the above set of weak forms is discretized and decomposed to get a set of orthogonal vectors. These orthogonal vectors are used to produce a condensed system of equations. So, for dynamic problem having homogeneous essential boundary conditions,

$$\underbrace{V^T \mathbf{K} V}_{\tilde{\mathbf{K}}} \tilde{\mathbf{U}} + \underbrace{V^T \mathbf{M} V}_{\tilde{\mathbf{M}}} \ddot{\tilde{\mathbf{U}}} - \underbrace{V^T \mathbf{F}}_{\tilde{\mathbf{F}}} = 0$$

22.2.2 Visibility Criterion

It is a way of introducing discontinuities into meshless approximation. In this method, the difference comes only in defining the domain of influence of each node. The domain of influence of a node is defined as the field of vision at that node. All internal and external boundaries are considered to be opaque so that the field of vision is interrupted whenever a boundary is encountered.

As shown in Fig. 22.1, for determining domain of influence of marked node, the lines joining this node and crack tips are drawn. The dotted region is the part of domain where a straight ray from the node cannot reach. So this dotted region is removed from the domain of influence of marked node.

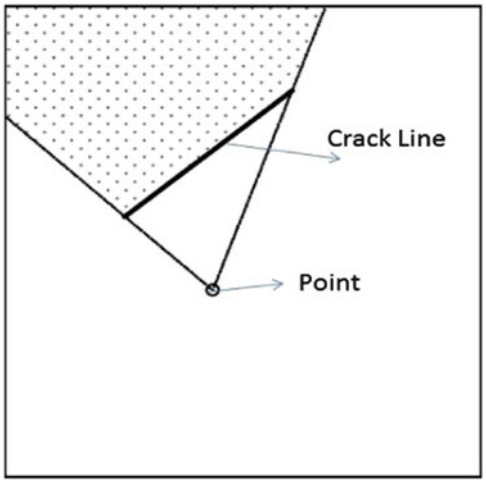

Fig. 22.1 Domain of influence of a node adjacent to a line of discontinuity

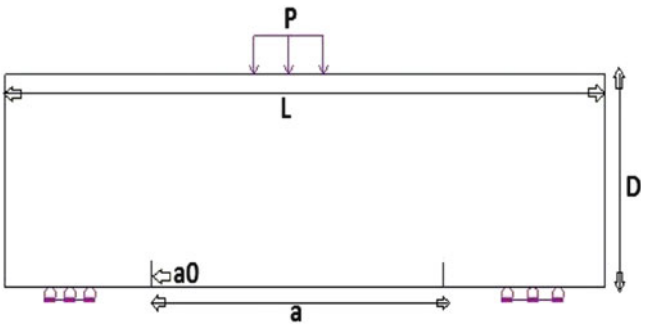

Fig. 22.2 Geometry of the plate

22.2.3 Crack Propagation in Epoxy Plate Under Dynamic Loading: Numerical and Experimental Analysis

22.2.3.1 Double Cracks

In this problem, three point flexural load is applied on a rectangular plate made of epoxy, having two symmetric cracks as shown in Fig. 22.2. The material properties and dimensions of the plate are as follows: Length, $L = 0.12$ m; Height, $D = 0.028$ m; Initial Crack Lengths, $a_0 = 0.005$ m; Distance between initial cracks, $a = 0.06$ m.

Young's modulus, $E = 3.4$ GPa , Poisson's ratio, $\nu = 0.34$, Density, $\rho = 1{,}900\,\mathrm{kg/m^3}$

In the experiment, this plate is subjected to a bending load in a Split-Hopkinson set-up. The variation of applied force with time is shown in Fig. 22.3. Photographs of the specimen are taken at different instants of time using a high speed camera. Each of these photographs contains fringes corresponding to maximum shear stresses.

As the plate is loaded from the top, it bends upwards and crack tips start experiencing opening stresses. When the stress intensity factor around the crack tip reaches its critical value (fracture toughness), cracks start propagating at a very high speed along a curved path and finally coalesce at the loading point, leading to the breakage of the specimen. The path taken by the cracks and the final state of the specimen can be seen in Fig. 22.4. Variations of crack length and crack tip velocity are shown in Figs. 22.5 and 22.6 respectively.

In the numerical analysis, the crack is propagated along the path obtained from the experimental data. Also the crack velocity is known from the experiment (Fig. 22.6). The simulated crack path is shown in Fig. 22.7. A uniform mesh is taken with a 31 $\times$16 nodal grid. Cubic spline is chosen as the weight function and 4 $\times$4 quadrature is taken for the shape function construction. The time step chosen for the time integration is 0.5 μs. The wave velocity in the material is around 1,350 m/s and the average nodal spacing is 0.003 m, so the average time taken by the stress wave to move between two consecutive nodes is 2.2 μs. So the time step chosen is small as compared to time taken by the stress wave to move between two consecutive nodes.

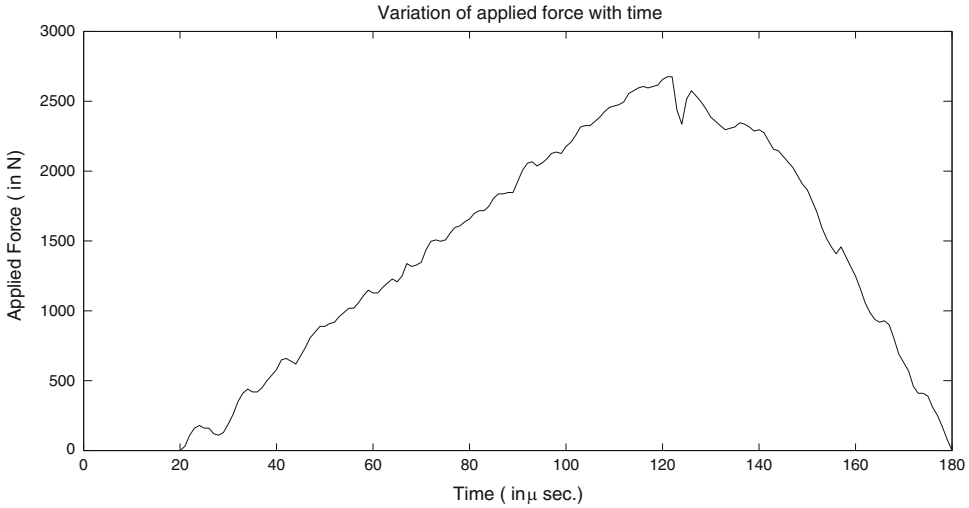

Fig. 22.3 Variation of applied force with time

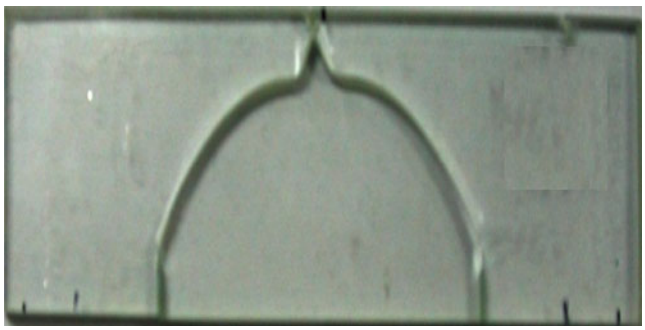

Fig. 22.4 Final state of the specimen

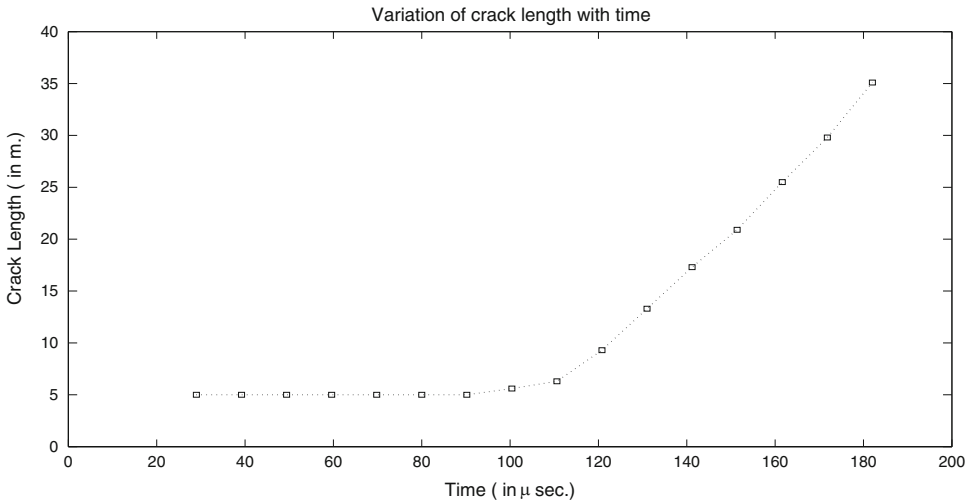

Fig. 22.5 Variation of crack length with time

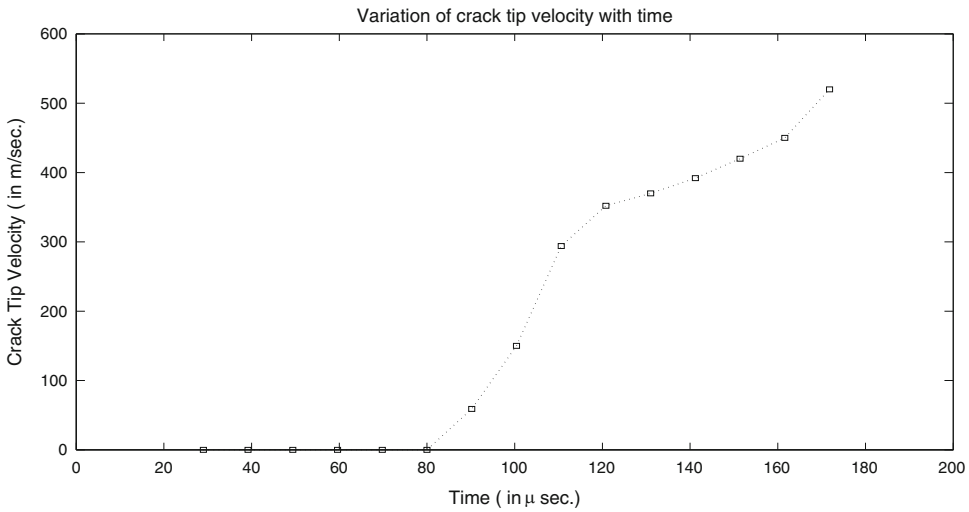

Fig. 22.6 Variation of crack speed with time

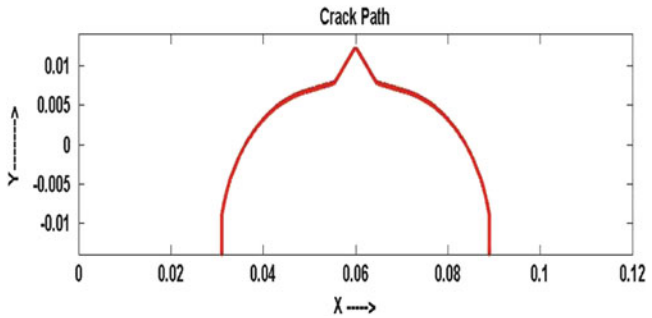

Fig. 22.7 Simulated crack path

The stress contours corresponding to maximum shear stress are shown in Fig. 22.8. The location of the crack tip can be easily seen in these contours, the stress concentration near the crack tip, as more number of fringes develop around it. Comparing these contours with the images, it can be seen that the stress distribution in the plate as obtained by EFGM is similar to the one obtained from photographic fringes. The dynamic effective stress intensity factor is evaluated by computing J-integral along a path around the instantaneous crack tip location. The variation of dynamic effective stress intensity factor K_{eff} with time is shown in Fig. 22.9. It can be seen from this plot that K_{eff} initially increases with time and as the crack starts propagating, it initially decreases before finally increasing steeply.

22.3 Conclusions

A meshless element-free Galerkin method (EFGM) is used to solve dynamic fracture problems. For handling discontinuities associated with fracture problems, a visibility criterion is used for influence domain construction. An enriched nodal arrangement is used around the crack tip to visualize steep variation of stresses around the tip. For crack propagation problems, these enriched nodes are moved along the crack path to redistribute them around the new crack tip position. A mixed mode problem – a plate having an oblique crack is also solved. Some experiments are performed on epoxy plate having crack in a split hopkinson set-up. Under three point bending loads, the cracks propagate leading to the failure of the material. Simulations are developed to show variation of maximum shear stress in the plates. These results are in close conformity with the photographic fringes in the specimen, obtained using a high speed camera.

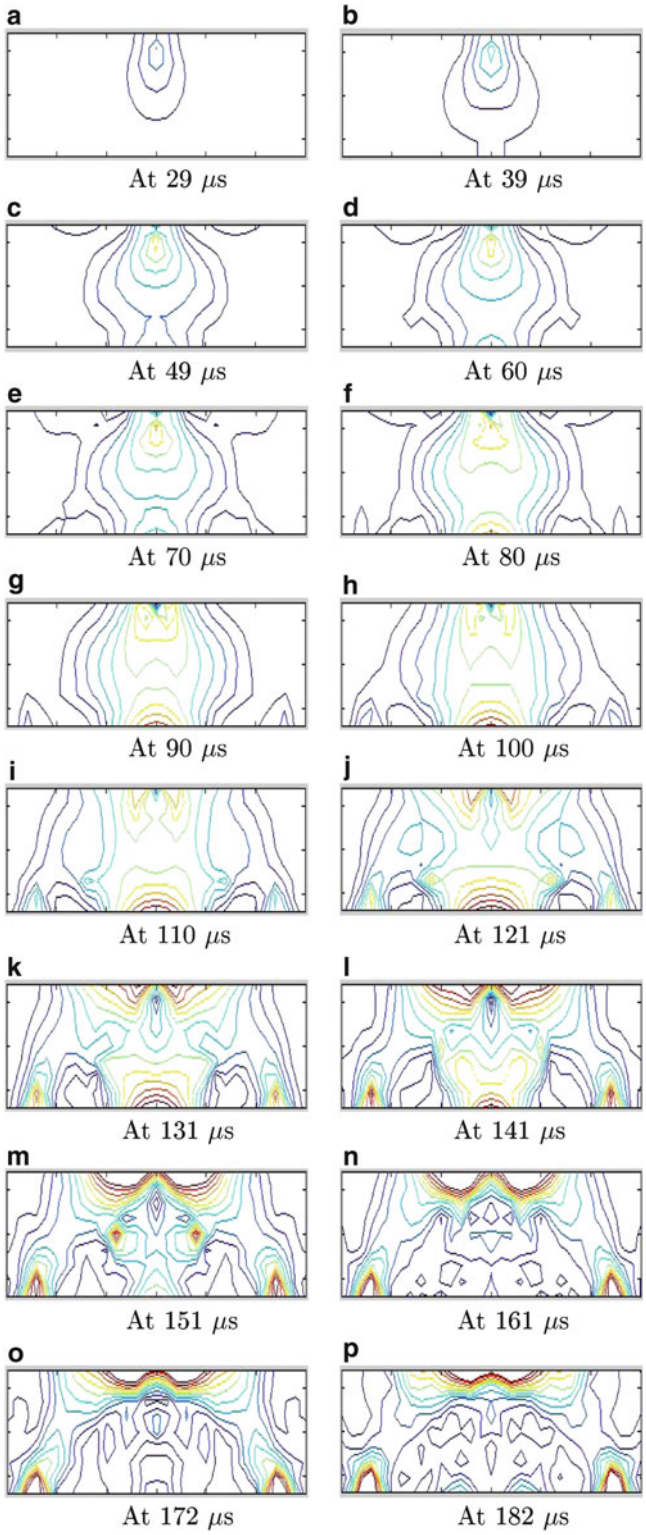

Fig. 22.8 Maximum shear stress contours at various instants of time. (**a**) At 29 μs. (**b**) At 39 μs. (**c**) At 49 μs. (**d**) At 60 μs. (**e**) At 70 μs . (**f**) At 80 μs. (**g**) At 90 μs. (**h**) At 100 μs. (**i**) At 110 μs. (**j**) At 121 μs. (**k**) At 131 μs. (**l**) At 141 μs. (**m**) At 151 μs. (**n**) At 161 μs. (**o**) At 172 μs. (**p**) At 182 μs

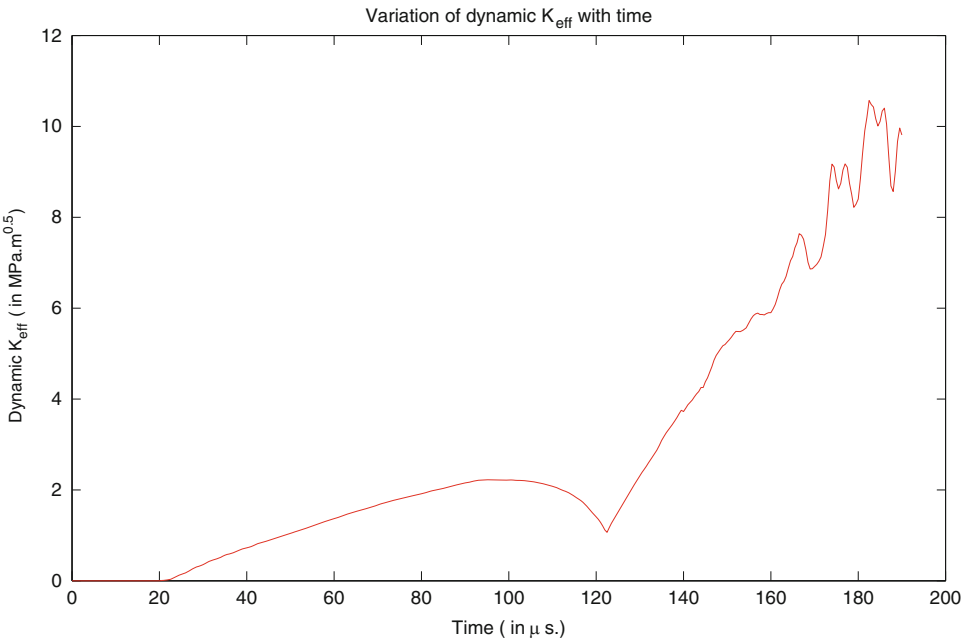

Fig. 22.9 Variation of dynamic K_{eff} with time

Acknowledgements The Authors acknowledge the financial support through grant no. SR/FST/ET11-003/2006 under FIST program by Department of Science and Technology, Govt. of India for the ultra high speed camera used in this study.

References

1. Shepard D (1968) A two-dimensional interpolation function for irregularly spaced points. In: ACM national conference, New York, NY, pp 517–524
2. Belytschko T, Krongauz Y, Organ D, Fleming M, Krysl P (1996) Meshless methods: an overview and recent developments
3. Belytschko T, Organ D, Krongauz Y (1995) A coupled finite element – element-free Galerkin method. Comput Mech 17:186–195
4. Belytschko T, Lu YY, Gu L, Tabbara M (1995) Element free Galerkin methods for static and dynamic fracture. Int J Solid Struct 32:2547–2570
5. Li S, Liu WK (1996) Moving least-square reproducing kernel method (II) Fourier analysis. Comput Methods Appl Mech Eng 139:159–193
6. Lancaster P, Salkauskas K (1981) Surfaces generated by moving least squares methods. Math Comput 37:141–158
7. Liu GR (2003) Mesh free methods-moving beyond finite element methods. CRC, Boca Raton

Chapter 23
Improving Ballistic Fiber Strength: Insights from Experiment and Simulation

C.W. Lomicka, J.A. Thomas, E.D. LaBarre, M.M. Trexler, and A.C. Merkle

Abstract The ability to understand and predict failure mechanisms of ballistic fibers through molecular modeling will aid the development of improved next generation fiber material for soft armor systems. By hybridizing tensile test data performed over a range of strain rates with predictions from molecular simulation, the molecular failure mechanisms of neat and carbon-infused para-aramid polymer fibrils (i.e. Kevlar ®) are elucidated and analyzed. To begin, electronic structure calculations are used to generate intermolecular potential functions for polymer monomers and carbon fragments. The carbon/polymer interactions are found to be stronger than the polymer/polymer interactions, indicating that carbon fragments can enhance the internal binding energy of a polymer fibril. Next, using molecular dynamics simulation, the effects of this enhanced interaction energy on the elastic modulus of polymer fibrils is predicted. The predicted elastic modulus of the neat polymer fibril modulus is order-of-magnitude consistent with that measured for fibers during tensile testing. Within the context of the molecular dynamics simulations, carbon/polymer composite fibrils exhibit higher failure stresses than the neat samples. By systematically varying the carbon concentration within the simulations, an optimal carbon concentration that maximizes fibril strength is identified. The competing mechanisms responsible for this optimization process are identified, and a suggested carbon treatment process is proposed. These insights from models can enable exploitation of mechanisms governing each length scale by guiding design and fabrication of an improved ballistic soft armor.

Keywords Kevlar • High-strength fiber • Electronic structure • Molecular dynamics • Multi-scale modeling

23.1 Introduction and Motivation

Kevlar aramid fibers are widely recognized for their superior mechanical properties. Specifically, the combination of low weight and high strength (it is five times stronger than steel on an equal-weight basis [1]) make Kevlar an industry standard for personnel armor [2]. In response to emerging threats, however, new techniques for further improving the strength of these products are needed. Additionally, reduction in the warfighter's load remains a critical challenge. To assist in these efforts, this work focuses on (i) understanding the failure mechanisms associated with ballistic impact of Kevlar and (ii) understanding how the fiber nanostructure can be modified to increase its mechanical strength without significantly affecting the specific weight.

The superior mechanical properties of Kevlar fibers arise primarily from the strong non-bonded interactions between polymer monomers. At the molecular level, Kevlar is a polymer consisting of a repeating set of para-oriented aromatic amide groups. Owing to π-π stacking between polymer chains, the binding energy between two adjacent Kevlar polymers is stronger than that between other types of polymers. This stacking mechanism also contributes to the long-range, highly-ordered polymer structure observed in Kevlar fibers.

Recent experiments have indicated that treating Kevlar fabric with multi-walled carbon nanotubes (CNTs) can improve the ballistic performance of Kevlar [3]. The underlying mechanisms responsible for these improvements remain unclear. Within the context of our multi-scale model, however, we can systematically predict the effect of such treatments on the

C.W. Lomicka (✉) • J.A. Thomas • E.D. LaBarre • M.M. Trexler • A.C. Merkle
Research and Exploratory Development Department, The Johns Hopkins University Applied Physics Laboratory, 11100 Johns Hopkins Road, Laurel, MD 20723, USA
e-mail: christian.lomicka@jhuapl.edu

B. Song et al. (eds.), *Dynamic Behavior of Materials, Volume 1: Proceedings of the 2013 Annual Conference on Experimental and Applied Mechanics*, Conference Proceedings of the Society for Experimental Mechanics Series,
DOI 10.1007/978-3-319-00771-7_23,

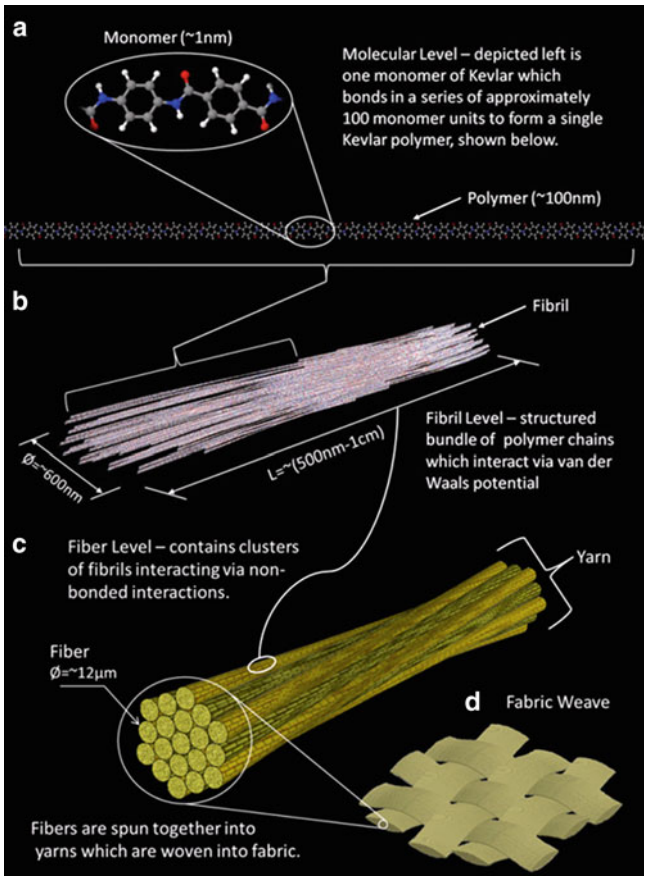

Fig. 23.1 Hierarchical description of Kevlar, adapted from Refs. [4, 5]

mechanical properties of Kevlar fibrils and identify the physical mechanisms responsible for such changes. Thus, motivated by these experimental findings, the objective of this investigation is to identify the effects of CNT strength and binding energy on the stiffness and strength of Kevlar fibrils.

In a previous work, we proposed a multiscale mathematical model for understanding the relationship between polymer chemistry, nanostructure, and the macroscopic mechanical behavior of Kevlar [4]. This model, which is summarized in Fig. 23.1, seeks to describe Kevlar at four fundamental levels: molecular, fibril, fiber, and fabric. This approach is intrinsically hierarchical, as the results of each lower level (smaller length/time scale) provide physical and mathematical input to the next level of modeling. Using this approach, we can elucidate the fundamental physical mechanisms which affect the overall ballistic performance of the material and, specific to this work, identify how the polymer nanostructure can be tuned to maximize ballistic performance of a Kevlar fabric.

In this effort, we specifically examine the molecular and fibril levels of the hierarchical model. At these length scales, Kevlar cannot be described using traditional continuum-level modeling approaches (e.g. Finite Element Method). Instead, to predict and understand the mechanical properties of these polymers at these length scales, we must use a combination of electronic structure calculations and molecular dynamics simulations. Electronic structure calculations are first-principle in nature and provide numerical solutions of Schrödinger's equation in order to determine potential energy landscapes between Kevlar monomers. Molecular dynamics, which are classical in nature, use the potential energy landscapes derived from electronic structure calculations to predict the mechanical properties of polymer chains and bundles. Combined, these two modeling approaches allow us to computationally predict the changes in the mechanical properties of the Kevlar fibers due to changes in polymer chemistry and nanostructure.

23.2 Molecular Level and Electronic Structure Calculations

At the molecular level, as illustrated in Fig. 23.1a, Kevlar polymers consist of a repeating set of para-oriented aromatic amide groups with an average monomer length of 1.2 nm. The molecular weight of the monomer is 236 g/mol, with the majority (71 %) of this weight coming from the carbon atoms. Although these molecular blocks are common among

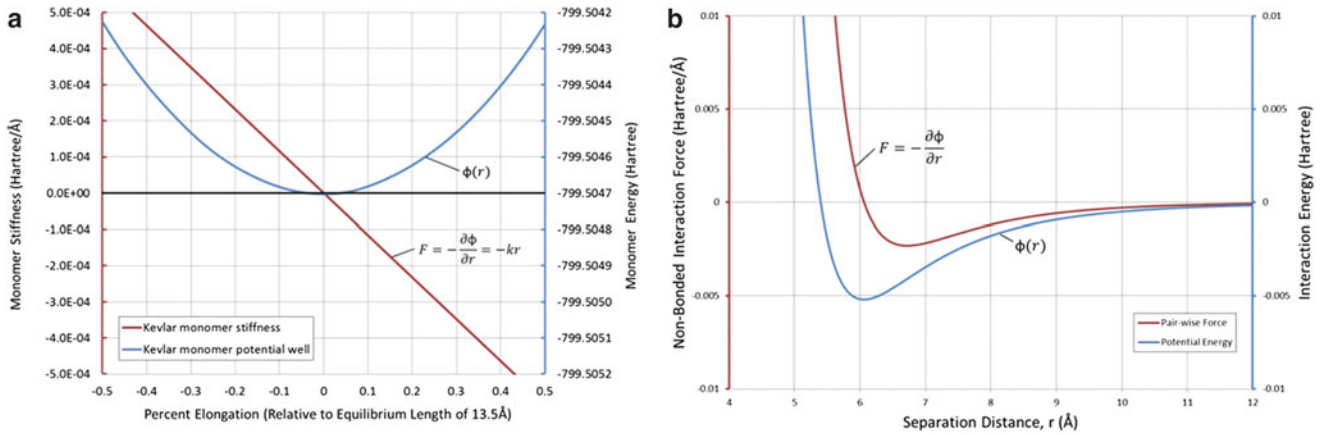

Fig. 23.2 Potential Energy landscape [φ(r)] from electronic structure calculation data. (**a**) *Left* – describes the intramolecular bond stiffness of pristine Kevlar. (**b**) *Right* – describes the non-bonded intramolecular effect between Kevlar polymers; adapted from Ref. [4]

high-strength polymers, the higher-ordered alignment between the direction of the inter-monomer bonds and the direction of the repeating polymer chain make the Kevlar monomer and polymer uniquely stiff. At this level, the mechanical properties of the Kevlar polymer are governed the intramolecular and intermolecular interactions. The effect of such interactions on the stiffness of the chain can be predicted using *ab initio* electronic structure methods.

Electronic structure calculations are a computational method to solve Schrödinger's wave equation to predict the distribution of electrons about a molecule. These *ab initio* calculations are first principle in nature. The only inputs required to solve the electronic structure are the atomic positions and a basis set of liner independent functions to solve for the orbital occupation. From these calculations, the potential energy landscape between molecules can be calculated.

Electronic structure calculations for pristine Kevlar polymers and Kevlar-CNT composites were completed as previously described [4], and the results can be seen in Fig. 23.2. For the small displacements realized in this system, as presented in Fig. 23.2a, bonded interactions can be approximated as linear springs with a spring constant calculated from the curvature of the potential well [6]. Non-bonded interactions, which realize larger separation distance in the simulation, mimic the behavior of other non-bonded systems [6]: shorter range repulsion due to electron exchange and longer range attraction arising from dispersion. No long-range electrostatic interactions were identified in the electronic structure calculations, which is expected since the monomers have no net charge. The absence of such long range interactions, combined with the shape of the potential energy surface, suggest that non-bonded interactions can be fit to a Lennard-Jones potential [4]. The resultant potential used in this work is presented in Fig. 23.2b.

The potential energy landscape provided by these calculations allows us to predict the magnitude of the bonded and non-bonded interactions within and between polymer chains. The potential energy functions in Fig. 23.2 provide the key input to the molecular dynamics simulation, which we used to predict how these governing interactions and crystalline structure influence the response of the fibril to an applied load. The forces acting on each monomer are calculated from the opposite of the spatial gradient of the potential energy functions. These potential energy landscapes provide the information required to determine the intramolecular and intermolecular forces acting on all of the monomers within the molecular dynamics simulations.

23.3 Fibril Level and Molecular Dynamic Simulations

The fibril level consists of highly ordered Kevlar polymer bundles. Archetypal Kevlar fibrils are 600 nm in diameter and 500 nm to several thousand nanometers in length [7]; a typical fibril is illustrated in Fig. 23.1b. Kevlar fibrils have a highly ordered structure because of π-π stacking; as previously discussed at the molecular level, monomers of different chains have a higher binding energy when stacked vertically than in plane. The mechanical properties of these fibril bundles are governed by the non-bonded interactions between Kevlar polymer chains, as well as the crystalline defect concentration and associated long-range structure of the fibril. Molecular dynamics simulations model the aggregate effect of the Kevlar polymers interacting together, within the fibril structure; as such, the mechanical properties of the simulated Kevlar can be computed.

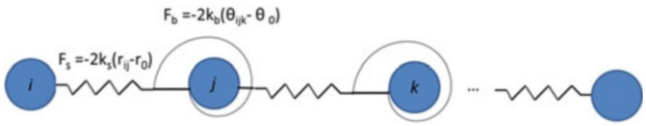

Fig. 23.3 Polymer bead-spring model of intramolecular interactions

Molecular dynamics is a numerical time integration algorithm based on classical Newtonian physics. It tracks the position and momentum of every particle through time, and updates these properties each time-step based on calculated forces acting upon each molecule within the system. Forces acting on each molecule come from bonds, pair wise interactions, and applied loads. Essentially, molecular dynamics can be considered a computational experiment; given a set of input conditions such as particle mass, positions and velocities, as well as a description of the intramolecular, intermolecular, and applied forces, it will deterministically solve the time evolution of the system, yielding information about mechanical properties.

Specifically, in this analysis, initial positions and velocities were created and every monomer in the fibril system was integrated through time using the Verlet algorithm with a time step of 1 fs. All simulation initial configurations were quenched with a thermostat via a canonical ensemble for 50 ps to equilibrate the system temperature to 300 K. Once the fibrils were equilibrated at 300 K, and the thermostat no longer had a significant effect, the simulation was returned to a microcanonical ensemble. The final step of the molecular dynamics simulation was to add axial loading to the fibril in order to predict the engineering stress–strain relationship of individual Kevlar fibrils, and understand how this response is affected by the addition of long fragments of carbon (e.g., CNTs) to the fibrils.

To model the intramolecular forces, each Kevlar polymer is modeled as a bead-spring chain as shown in Fig. 23.3. This is motivated by the intramolecular potential energy well of Fig. 23.2a; the relationship between force and strain for small displacements is linear about the equilibrium configuration where, the potential-energy-well can be molded as a harmonic oscillator. As the monomer bond strength is an order-of-magnitude greater than the non-bonded strength, the assumption of small bond displacements is valid. Therefore, each monomer is represented as a point mass equal to the weight of all 28 constitutive atoms and bonded to neighbors by a linear stretch spring constant and an angular bending (torsional) spring constant. These two spring constants characterize the intramolecular forces acting on monomers within each polymer. The stretch spring constant is indicative of the monomer bond tensile stiffness. The stretch energy, U_s, between neighboring monomers is defined as:

$$U_s = k_s(r_{ij} - r_0)^2$$

where k_s is the stretch spring constant (including a ½ factor from typical liner spring definition), r_{ij} is the distance between monomers i and j, and r_0 is the equilibrium distance between monomers. From electronic structure calculations, k_s and r_0 were set to 304.69 kJ/mol and 13.15 Å, respectively [4]. The bending energy, U_b, between two neighboring monomers is defined as:

$$U_b = k_b(\theta_{ijk} - \theta_0)^2$$

where k_b is the torsional spring constant, θ_{ijk} is the angle formed by monomers i, j, and k, and θ_0 is the equilibrium angle. Kevlar is a stiff linear polymer and it was assumed that the angular rigidity was order of magnitude consistent with the linear stiffness; therefore, the assumption was made that $k_b = k_s$, and the equilibrium angle was set to π radians (180°).

Intermolecular forces act between neighboring monomers of different polymer chains. These pair-wise forces represent the total effect of non-bonded interactions which are comprised of exchange, dispersion, electrostatic and induction forces, which are again, determined via electronic structure calculations. Within the context of these molecular dynamic simulations, the non-bonded interaction energy, U_{LJ}, is modeled via the Lennard-Jones potential:

$$U_{LJ} = 4\varepsilon\left[\left(\frac{\sigma}{r}\right)^{12} - \left(\frac{\sigma}{r}\right)^{6}\right]$$

where ε is the energy value at the depth of the potential-well which correlates to the strength of the intermolecular interaction, σ is the distance where the intermolecular potential is zero, and r is the separation distance between monomers. The Lennard-Jones potential function is an empirical fit to the intermolecular electronic structure calculation data of Fig. 23.2b; the first term, $(\sigma/r)^{12}$, yields a stiff repulsive interaction for short distances of r and the second term, $-(\sigma/r)^6$, provides the long range attractive interaction. Recognize that the pair-wise force between monomers, as a function of separation distance, is equal to the opposite of the spatial gradient of the potential energy function $U_{LJ}(r)$. Accordingly, ε was set to $-5.2{\cdot}10^{-3}$ Hartrees (13.65 kJ/mol) and σ was set to 5.4 Å [4].

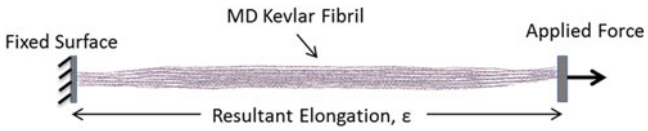

Fig. 23.4 MD Tensile loading of fibrils

In addition to pristine Kevlar fibrils, we investigate the behavior of carbon/Kevlar composite structures. To accomplish this, CNTs were simulated by adding additional bead-spring polymers to the simulations with the molecular characteristics of carbon. The intramolecular bonds for CNTs were set as rigid in recognition of their ultra-high elastic modulus (~1 TPa) [8]. The intermolecular interactions between carbon and Kevlar were also modeled via the Lennard-Jones Potential with, ε set to $-5.71{\cdot}10^{-3}$ Hartrees (15.0 kJ/mol) and σ was set to 3.4 Å, in accordance with pervious electronic structure calculations [4].

To predict the engineering stress–strain relationship of Kevlar and carbon/Kevlar composite fibrils, an axial load was applied and the resulting displacement was recorded. This was implemented in the model by fixing one end of the fibril and adding a linearly time varying tensile force to the other end. The applied tensile force is described by:

$$F_{applied\_tension}(t - \tau_0) = \alpha \cdot (t - \tau_0)$$

where α is the rate of force applied and τ_0 is the start time of the tensile test; for these simulations, α and τ_0 were set to 8.0 N/s and 50 ps, respectively. This fibril loading is illustrated in Fig. 23.4.

23.4 Results

Typical stress strain elastic responses of a Kevlar and a carbon/Kevlar composite fibril are illustrated in Fig. 23.5. The fibril cross section was calculated at the fibril midpoint, immediately before the first time step of axial loading. For the cases shown in Fig. 23.5, the cross section is $2.6{\cdot}10^{-19}$ m^2. The plot shows that the modulus is nearly the same for the two scenarios; however, the presence of carbon increased the failure stress of the composite. The elastic stress strain response was best fit to a line to determine the modulus of elasticity. A suite of ten baseline runs established an average elastic modulus of 187 GPa. This is higher than experimentally measured values for Kevlar thread which found the modulus to be between 70 GPa for Kevlar-29 and 143 GPa for Kevlar-149. However, the MD simulations provided order-of-magnitude consistent results to experiment, which is promising. The over-prediction is to be expected as the ordered fibrils in the simulation do not account for defects. As discussed by Panar et al. [9], defects in the ordered structure of the fibril exist at regular intervals of 500 nm. These defects reduce the overall stiffness of the fiber relative to that of the constituent (and ordered) fibrils. Also note that the undulations in this plot are an artifact of the thermal velocity of the monomers resonating in the system and the shape of the potential energy surface.

The data presented in Fig. 23.5 for the carbon/Kevlar composite were predicted using the nominal carbon/Kevlar interaction potential extracted from the electronic structure calculations and a nominal carbon weight percent of 0.2 %. In practice, however, these parameters can be tuned by functionalizing the ends of the CNT to increase carbon/Kevlar bond strength and/or increase the quantity of carbon included to the composite material. Using the methodology presented here, we can explore this design space and predict which combinations of binding strength and weight percent will generate the greatest improvements in performance.

In Fig. 23.6, we present the variation in fiber failure stress as a function of carbon fraction (wt%) for three different carbon/Kevlar interaction strengths. The three interaction strengths considered are nominal, which is characteristic of the actual carbon/Kevlar physical system, as well as two times (2×) and three times (3×) nominal, which explore how possibly increasing the binding energy could affect the system, but are not physically representative of the carbon/Kevlar behavior. Note that the fiber failure strain reported in this chart is normalized by the value we predicted for the neat sample. The data presented in this plot depict several interesting trends. First, for each interaction strength, observe that the failure stress does not increase monotonically with carbon fraction. Instead, for the nominal and 2× nominal Kevlar/carbon systems, the failure stress is maximized at a weight percent of 0.5 %. For the 3× nominal interaction strength, the failure stress decreases with increasing carbon content. These predictions indicated that, while small quantities of carbon can increase the fibril failure strain, too much carbon will deteriorate the performance of the system. Similar trends exist with respect to interaction energy. While increasing the Kevlar/Carbon interaction energy up to a factor of two tends to increase the failure strain of the fibril at each carbon weight percent, increasing the strength by a factor of 3 reduces the performance at each carbon weight

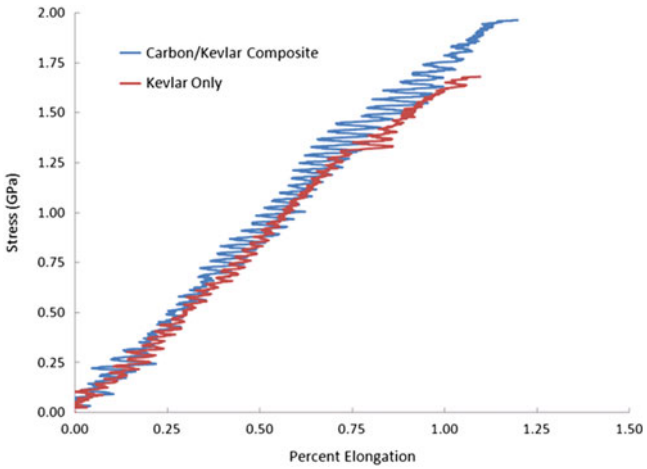

Fig. 23.5 Typical stress strain responses of a Kevlar and a composite fibril

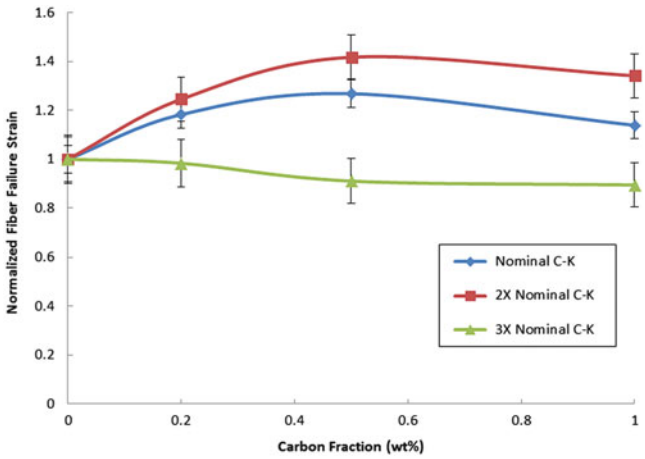

Fig. 23.6 MD results depicting fiber failure strain as a function of carbon fraction. Results indicate that a carbon wt% of 0.5 % may lead to the maximum failure strain possible, with decreasing strains realized upon further carbon addition. The different series depict differences realized as a result of increasing the non-bonded interactions between Kevlar and carbon

percent. Although we are still exploring the mechanism responsible for these non-monotonic trends, the results indicate that there exists an optimum combination of carbon concentration and corresponding interaction strength to maximize ballistic performance.

23.5 Next Steps

Currently, we are working to expand our computational capabilities in order to simulate larger fibrils. This will allow us to extend our research to include (i) CNT location effects within the fibril and (ii) the effect of defects in the intra-fibril structure. Existing CNT treatment of Kevlar delivers surface coating to the fibril; the high strength non-bonded interaction of Kevlar makes the structure difficult to penetrate. We intend to use molecular dynamics to investigate if there is value in exploring synthesizing techniques that would allow deeper impregnation and more uniform distribution of carbon within the fibril. Additionally, we intend to expand our model to include carbon nanostructure morphology effects. This will allow us to model various carbon allotropes such as graphene and other fullerene structures.

Acknowledgments The authors gratefully acknowledge support from the Johns Hopkins University Applied Physics Laboratory Research and Exploratory Development Business Area. This work was funded in part by the Office of Naval Research Award Number N00014-12-1-0402 under the direction of Lee Mastroianni and Jim MacKiewicz.

References

1. DuPont (2013) Better, stronger, and Safer with Kevlar ® Fiber. DuPont ™ Kevalar ®. http://www2.dupont.com/personal-protection/en-us/dpt/kevlar.html, Feb 2013
2. Lubin G (1998) Handbook of composites, 2nd edn. Chapman and Hall, London
3. O'Connor I, Hayden H, Coleman JN, Gun'ko YK (2009) High-strength, high-toughness composite fibers by swelling Kevlar in nanotube suspensions. Small 5(4):466–469
4. Thomas JA et al (2012) Multiscale modeling of high-strength fibers and fabrics. In Proceeding of SPIE 8373, Micro- and Nanotechnology Sensors, Systems, and Applications IV, 83731S (May 1, 2012); doi:10.1117/12.919395
5. Grujicic M, Glomski P, Pandurangan B, Bell W, Yen C-F, Cheeseman B (2011) Multi-length scale computational derivation of Kevlar yarn-level material model. J Mater Sci 46(14):4787–4802
6. Kittel C (2005) Introduction to solid state physics, 8th edn. Wiley, New Jersey
7. Hagege R, Jarris M, Sutton M (1979) Direct evidence of radial and tangential morphology of high-modulus aromatic polyamide fibres. J Microsc 115(1):65–72
8. Ashby M, Ferreira P, Schodek D (2009) Nanomaterials, nanotechnologies, and design. Elsevier, New York
9. Panar M, Avakian P, Blume RC, Gardner KH, Gierke TD, Yang HH (1983) Morphology of poly (p-phenylene terephthalamide) fibers. J Polym Sci Polym Phys 21:1955–1969

Chapter 24
Simulating Wave Propagation in SHPB with Peridynamics

Tao Jia and Dahsin Liu

Abstract Split Hopkinson's pressure bar (SHPB) is commonly used for characterizing materials at high strain rates. In obtaining an admissible stress–strain curve at a specific strain rate, force equilibrium through the specimen is required. Due to the blunt collision between the striker bar and the incidence bar in SHPB, a strain wave with a blunt wave front is usually obtained in SHPB test. Unfortunately, the blunt wave front can damage the specimen prematurely, resulting in an inconclusive test. Hence, a gradual loading ramp, such as that commonly practiced in quasi-static characterizations is preferred. In order to achieve a gradual loading fashion, a shaper made of a softer material should be placed in between the striker bar and the incidence bar. The selection of the shaper material and its dimension and thickness, however, is not trivial. Numerous trial-and-errors are usually required. This study presents the simulation of wave propagation in SHPB based on peridynamics. In addition to striker bar, incidence bar and transmission bar, the one-dimensional peridynamic simulation can also accommodate a shaper. Hence, it can be used for shaper design.

Keywords Peridynamic • Slip Hopkinson's pressure bar • Strain rate • Impact • Wave propagation

24.1 Introduction

Continuum mechanics is based on the following partial differential equation:

$$\rho \ddot{u} = \nabla \sigma + b \tag{24.1}$$

All solid mechanics studies based on continuum mechanics, analytical as well as numerical, are based on the differential governing equation which requires the displacement field of concern to be continuous. This requirement does not hold wherever there is a crack. When a crack takes place, new boundaries and boundary conditions are required to process the partial differential equation. Hence, in investigating a dynamic crack propagation problem, knowledge of crack propagation position and direction, and often time fracture mechanics, are required. This requirement may become very demanding and impossible especially in studying fiber-reinforced composite materials.

Instead of differential equation, Silling and associates [1–18] have investigated an alternative formulation for continuum mechanic, so-called peridynamics. Its equation of motion can be expressed as follows

$$\rho \ddot{u} = \int f \, dV + b \tag{24.2}$$

where ρ is mass density, $\ddot{u}$ is acceleration, f is bond force and b is body force. The bond force f is a function of displacements. Integrations exist everywhere whether the functions are continuous or not. Equation 24.2 can be applied directly to

T. Jia • D. Liu (✉)
Dept. of Mechanical Engineering, Michigan State University, East Lansing, MI 48824, USA
e-mail: liu@msu.edu

B. Song et al. (eds.), *Dynamic Behavior of Materials, Volume 1: Proceedings of the 2013 Annual Conference on Experimental and Applied Mechanics*, Conference Proceedings of the Society for Experimental Mechanics Series,
DOI 10.1007/978-3-319-00771-7_24,

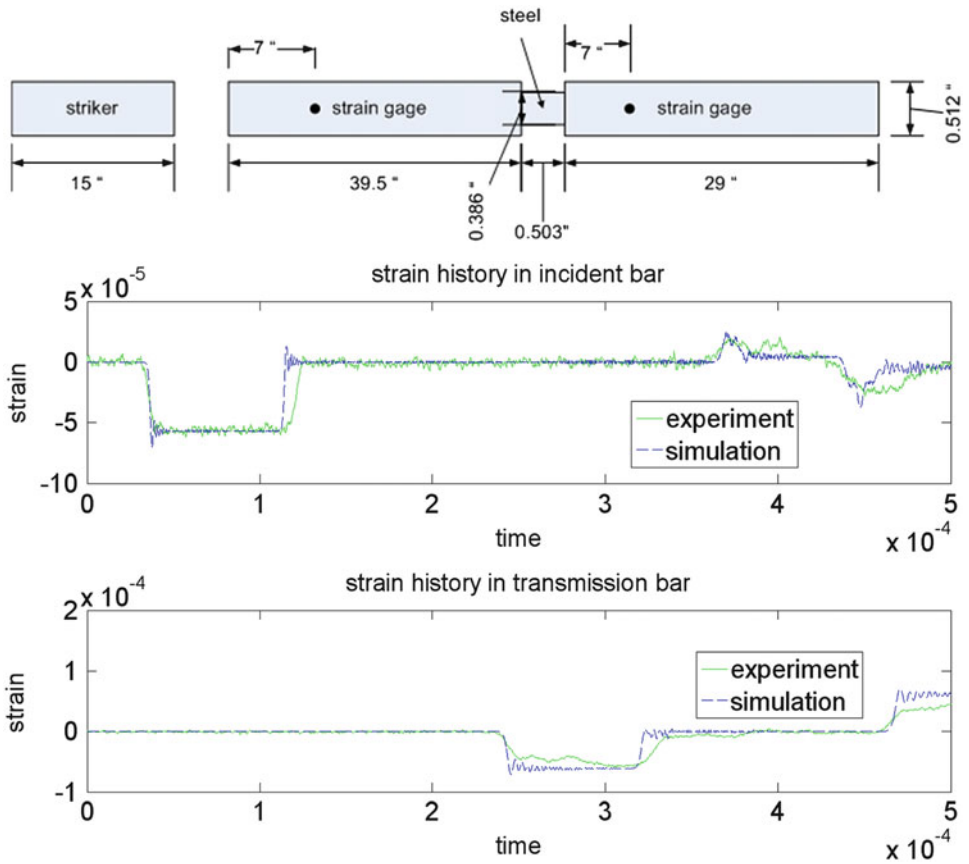

Fig. 24.1 Experimental and peridynamic result of SHPB simulation

continuous points as well as discontinuous points, such as a crack. The ability to apply this equation to all points renders peridynamics more useful for fracture analysis than the conventional continuum mechanics, which requires knowledge of fracture mechanics. For example, there is no need for a separate crack growth law based on stress intensity factors in peridynamic analysis.

In this study, a peridynamic numerical scheme based on Eq. 24.2 is formulated and applied to split Hopkinson's pressure bar (SHPB). Figure 24.1 shows a schematic diagram of an SHPB. It includes a striker bar, an incident bar, a specimen and a transmission bar. All the bars are made of 347 stainless steel with a Young's modulus E = 193 GPa and a mass density $\rho = 8{,}027\ kg/m^3$. The incident bar and the transmission bar are instrumented with strain gages.

In the SHPB test, the striker bar is fired into the left end of the incident bar. This creates a constant pressure input with a period of time. The striker bar is 0.191 m in length. The wave velocity in the striker can be calculated as

$$c = \sqrt{\frac{E}{\rho}} = 4903\ m/s \tag{24.3}$$

The duration of the constant pressure input is equal to the time the wave takes to travel through the striker twice, i.e.

$$t_0 = 2 \times \frac{0.191}{4903} = 7.79 \times 10^{-5} s \tag{24.4}$$

It is also equal to the time when the striker bar separates from the incident bar. Figure 24.2 shows the incidence bar and the strain wave generated based on a pressure of 10 MPa in firing the striker bar. For comparison purpose, experimental results are scaled to numerical result.

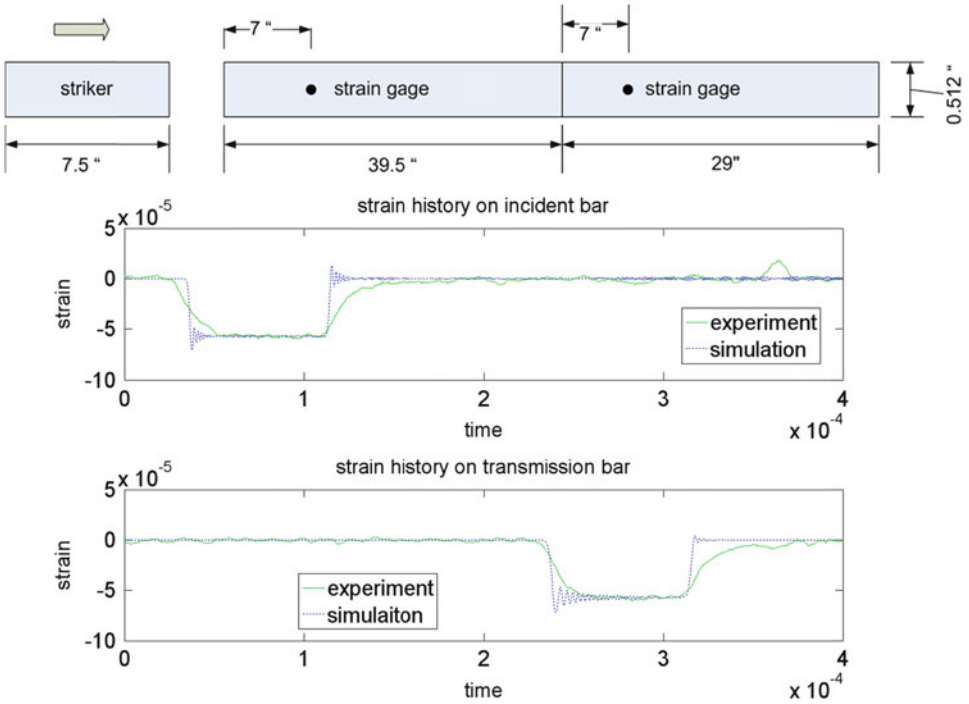

Fig. 24.2 Experimental and peridynamic results of SHPB without a specimen

24.2 Comparison Between Simulation and Testing

24.2.1 Wave Propagation in a Single Bar

In peridynamic simulation, parameters such as size of horizon, time step and grid density are important factors for numerical accuracy. In order to determine the optimal parameters, numerical analysis based on different size, step and density are performed. Figure 24.3 shows the results based on grid density. As expected, high grid density, i.e. small distance between points dx gives better results when compared with analytical solution.

24.2.2 Two Bars in Contact

As a beginning study, the incidence bar and transmission bar are placed in contact with each other, as shown in Fig. 24.2. The two bars are made of the same material and have an identical cross-sectional area. This study is performed to examine the effect due to the interface between the two bars. The experimental results are obtained by the strain gages installed in the incidence bar and transmission bar. The study shows that approximately 12 % of the wave reflects back to the incidence bar. After that, the two bars separate and the strain wave traveling to the transmission bar does not propagate to the incidence bar.

From the strain history of the transmission bar, the average period is $2.95 \times 10^{-4} s$. Theoretical value of the period is

$$\frac{L2}{c} = 3 \times 10^{-4} s \tag{24.5}$$

where L2 is the length of transmission bar. The error between the measurement and the theory is 1.67 %. In addition, the strain wave periods match very well even after several periods. A good comparison can then be concluded for the transmission bar. The simulation for the incidence bar, however, is not as good as that for the transmission bar. Oscillations in the incidence bar do not look like reflection wave. They are smaller than reflection wave.

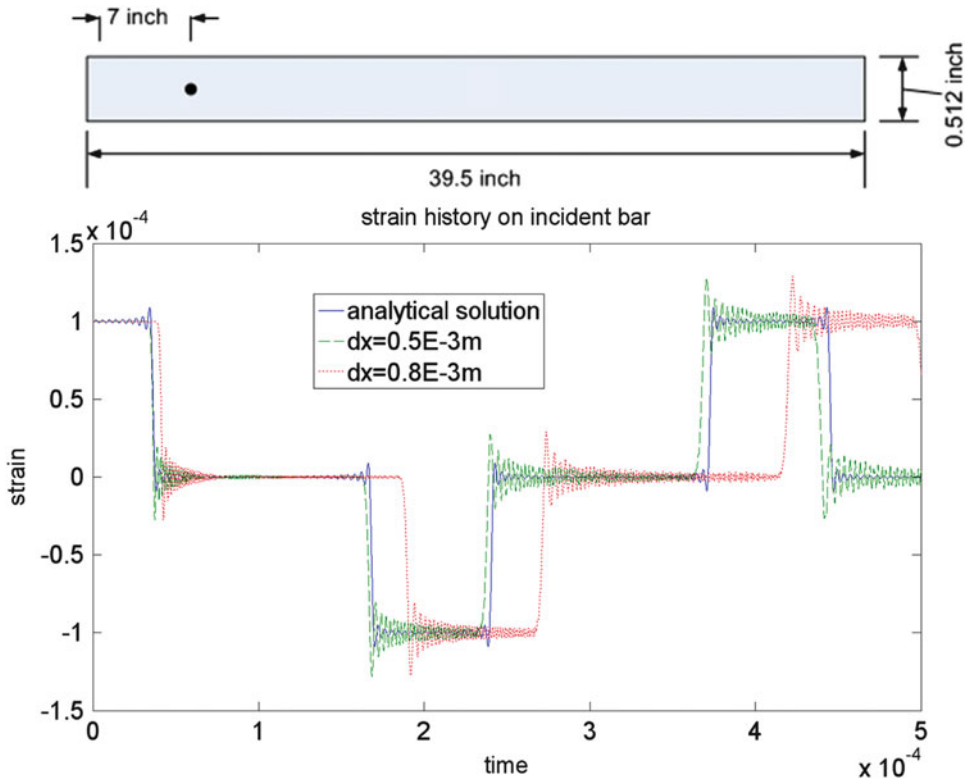

Fig. 24.3 Peridynamic simulation of wave propagation in a simple bar

24.2.3 Different Cross-Section Areas Across an Interface

This study is focused on the interface in the transmission bar. There are two kinds of change in the interface; one is the change of cross-sectional area and the other is the change of material. Both of them can produce reflection. To identify the cross-interface bond force, a composite coefficient c should be identified. Shown below is the calculation of the coefficient. It begins with finding the bond force c_1 between the two cross-sectional areas or the two materials. Similarly, the bond force c_2 can be identified. Since they should be equal to each other, the composite coefficient can then be identified.

The bond force on c_1 is

$$f_1 = c_1 \frac{u_3 - u_1}{x_3 - x_1}$$

The bond force on c_2 is

$$f_2 = c_2 \frac{u_2 - u_3}{x_2 - x_3}$$

Since

$$f = f_1 = f_2 = c \frac{u_2 - u_1}{x_2 - x_1}$$

$$c = \frac{1}{\frac{1}{c_1}\frac{x_3 - x_1}{x_2 - x_1} + \frac{1}{c_2}\frac{x_2 - x_3}{x_2 - x_1}} \tag{24.6}$$

The effect due to different materials can also be identified accordingly. Simulation results match well with experiment results. Hence, the technique in finding the interface bond is validated.

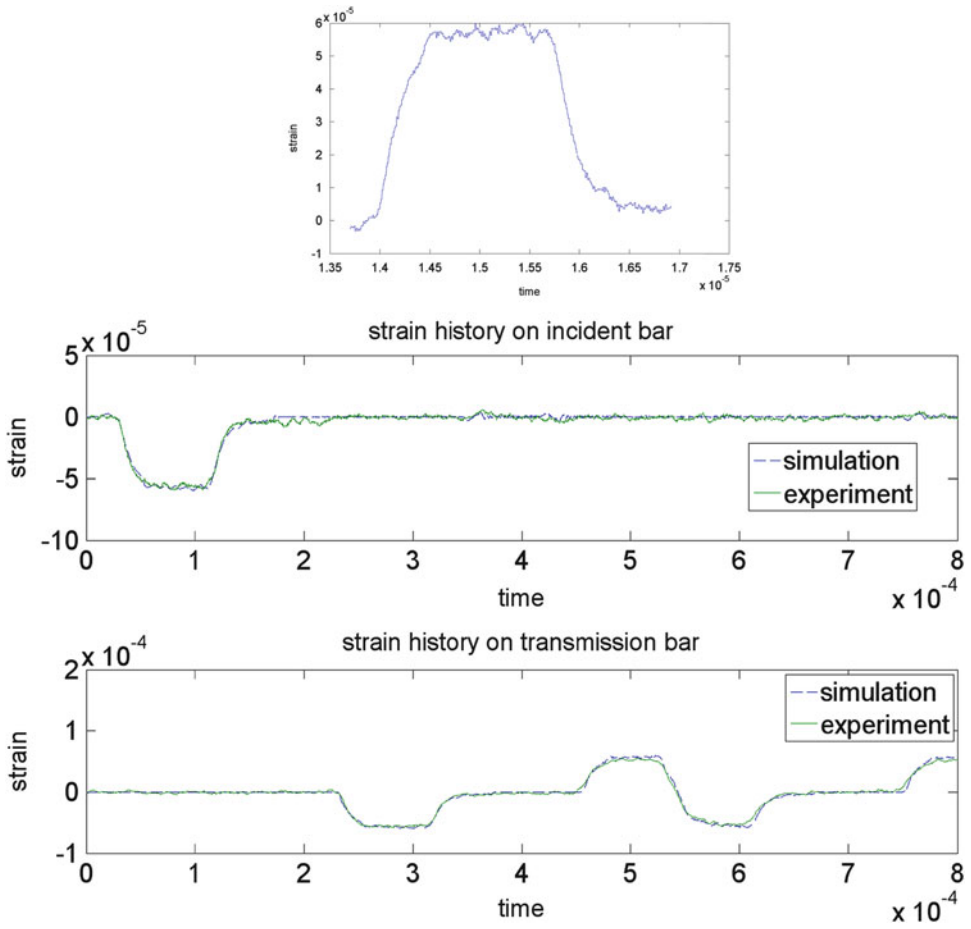

Fig. 24.4 Experimental result as an input for peridynamic simulation

In simulation, a perfect bonding may be assumed for simplicity. This is equivalent to claim that the two bars are in contact with each other and under compression and they act like one bar. This claim may not be the case in the real experiment. In fact, no matter how well the two bars are aligned, the bonding condition is not perfect. That is, part of the wave will be reflected even if the two bars have identical material properties and cross-sectional area. Hence, the numerical simulation program should be modified to capture this phenomenon. In the simulations, various cross-interface bonds are assumed and numerical results show better agreement with the experiments.

24.2.4 Using Experimental Result as an Input

Theoretically, the input pressure on the incident bar should resemble a square wave. However, due to imperfect impact between the striker bar and the incidence bar, the impact-induced strain wave may not be a perfect rectangular wave. This is one of the reasons that the strain wave observed in the incidence bar is different from simulation. It then is possible to use the strain wave measured from the incidence bar as an input to the peridynamic simulation. Figure 24.4 shows the experimental result from the incident wave and the wave propagation through the transmission bar. The peridynamic simulation matches perfectly with the experimental measurement.

24.3 Summary

This study lays the foundation for using peridynamic analysis in simulating the wave propagation in slip Hopkinson's pressure. The numerical results indicate that the closer the simulation the better match with experimental results.

Acknowledgements The authors wish to express their sincere thanks to Army Research Office for financial support, Dr. Larry Russell as program manager and Dr. Chianfong Yen of Army Research Laboratory for technical critique.

References

1. Silling SA (2000) Reformulation of elasticity theory for discontinuities and long-range forces. J Mech Phys Solid 48:175–209
2. Gerstle WH, Sau N, Silling SA (2007) Peridynamic modeling of concrete structures. Nucl Eng Des 237:1250–1258
3. Silling SA, Simmermann M, Abeyaratne R (2003) Deformation of a peridynamic bar. J Elast 73:173–190
4. Silling SA (2003) Dynamic fracture modeling with a meshfree peridynamic code. In: Bathe KJ (ed) Computational fluid and solid mechanics. Elsevier, Amsterdam, pp 641–644
5. Silling SA, Askari E (2005) A meshfree method based on the peridynamic model of solid mechanics. Comput Struct 83:1526–1535
6. Silling SA, Bobaru F (2005) Peridynamic modeling of membranes and fibers. Int J Non-linear Mech 40:395–409
7. Gerstle WH, Sau N, Silling SA (2005) Peridynamic modeling of plain and reinforced concrete structures. In: 18th international conference on structural mechanics and reactor technology (SMiRT 18), Beijing, SMiRT18-B01-2
8. Weckner O, Askari A, Xu J, Razi H, Silling SA (2007) Damage and failure analysis based on peridynamics – theory and applications. In: 48th AIAA/ASME/ASCE/AHA/ASC structures, structural dynamics, and materials conference, Honolulu, 23–26 Apr 2007
9. Bobaru F, Alves LA, Silling SA, Askari A (2008) Dynamic crack branching and adaptive refinement in peridynamics. In: 8th world congress on computational mechanics, Venice, 30 June-5 July 2008
10. Silling SA, Askari E (2004) Peridynamic modeling of impact damage. In: Moody FJ (ed) Problems involving thermal-hydraulics, liquid sloshing, and extreme loads on structures, PVP, vol 489. American Society of Mechanical Engineers, New York, pp 197–205
11. Bobaru F, Silling SA (2004) Peridynamic 3D models of nanofiber networks and carbon nanotube-reinforced composites, materials processing and design: modeling, simulation, and applications, NUMIFORM 2004. Am Inst Phys Conf Proc 712:1565–1570
12. Askari A, Xu J, Silling SA (2006) Peridynamic analysis of damage and failure in composite. In: 44th AIAA aerospace sciences meeting and exhibit, Reno, Nevada, AIAA-2006-88
13. Xu J, Askari A, Weckner O, Razi H, Silling SA (2007) Damage and failure analysis of composite laminates under biaxial loads. In: 48th AIAA/ASME/ASCE/AHA/ASC structures, structural dynamics, and materials conference, Honolulu, 23–26 Apr 2007
14. Warren TL, Silling SA, Askari A, Weckner O, Epton MA, Xu J (2009) A non-ordinary state-based peridynamic method to model solid material deformation and fracture. Int J Solid Struct 46:1186–1195
15. Demmie PN, Silling SA (2007) An approach to modeling extreme loading of structures using peridynamics. J Mech Mater Struct 2(10):1921–1945
16. Silling SA, Lehoucq RB (2008) Convergence of peridynamics to classical elasticity. J Elast 93:13–37
17. Lehoucq RB, Silling SA (2008) Force flux and the peridynamic stress tensor. J Mech Phys Solid 56:1566–1577
18. Silling SA, Epton M, Weckner O, Xu J, Askari E (2007) Peridynamic states and constitutive modeling. J Elast 88:151–184

Chapter 25
Investigation of Dynamic Failure of Metallic Adhesion: A Space-Technology Related Case of Study

D. Bortoluzzi, M. Benedetti, C. Zanoni, J.W. Conklin, and S. Vitale

Abstract Mechanisms for space applications often present criticalities, mainly because of tribological issues. Contacts between metallic surfaces easily develop adhesive bonds, thanks to the inhibition of the formation of oxides due to the vacuum environment. If anti-adhesive coatings and/or lubricants are not allowed, adhesion issues are further enhanced and may require a specific investigation to be characterized.

In the LISA Pathfinder space mission, a mechanism is designed to constrain a 2 kg Au-Pt cubic test mass during the spacecraft launch phase, and subsequently release it to free-fall for the mission scientific phase, when the final orbit is commissioned. The release of the test mass to free-fall must be performed such that its residual velocity with respect to the spacecraft is less than 5 μm/s. This requirement sets an upper limit to the impulse which can be developed by adhesion forces arising at the contact between the test mass and the constraining mechanism, upon the separation of the two metallic surfaces.

A novel and specific ground-based test activity is developed to qualify the mechanism, and the behaviour of metallic adhesion is studied in the conditions of dynamic failure. The results are here presented and discussed.

Keywords Adhesion force to elongation profile • Dynamic failure of adhesion • Impulse measurement • Space mechanism qualification

25.1 Introduction

The eLISA/NGO [1] is an ESA candidate large class space mission. Its main goal is the measurement of gravitational waves in space, where the emission of the most predictable and powerful sources may be identified. Several technologies required in the scope of this project are under development and need a flight test. For this reason, a space mission called LISA-Pathfinder [2] will be launched in late 2014. The core of both these missions is a set of free-falling 2 kg Au/Pt cubic test masses (TM), hosted inside the spacecraft, which constitute the wave sensing elements. An object is free falling or drag free when it is freed of all but planetary gravitational force. A mission critical phase is the transition of the TM between the launch condition and the science mode. In the first, the test mass has to be firmly constrained inside its housing, while in the second it must be set into free fall minimizing any electrical, magnetic or thermal effect to the level of 10 f in the

D. Bortoluzzi (✉) • M. Benedetti • C. Zanoni
Department of Industrial Engineering, University of Trento, Via Mesiano 77, Trento 38123, Italy

Italian Institute of Nuclear Physics, Gruppo collegato di Trento, Via Sommarive 14, Trento 38123, Italy
e-mail: daniele.bortoluzzi@ing.unitn.it; matteo.benedetti@ing.unitn.it; carlo.zanoni@ing.unitn.it

J.W. Conklin
Mechanical and Aerospace Engineering, University of Florida, Gainesville, FL, USA
e-mail: jwconklin@ufl.edu

S. Vitale
Department of Physics, University of Trento, Via Sommarive 14, Trento 38123, Italy

Italian Institute of Nuclear Physics, Gruppo collegato di Trento, Via Sommarive 14, Trento 38123, Italy
e-mail: vitale@science.unitn.it

B. Song et al. (eds.), *Dynamic Behavior of Materials, Volume 1: Proceedings of the 2013 Annual Conference on Experimental and Applied Mechanics*, Conference Proceedings of the Society for Experimental Mechanics Series,
DOI 10.1007/978-3-319-00771-7_25,

measurement bandwidth (1–30 mHz). A capacitive control system (Drag-Free and Attitude Control System) is designed to precisely centre the TM in the housing by applying electric fields. Unfortunately, its authority is very low (on the order of 10^{-6} N) and makes available a very limited capability to control the TM once it is set into free-fall.

Two mechanisms are designed to operate on the TM: the CVM (Caging and Venting Mechanism), which secures the TM during launch, and the GPRM (Grabbing Positioning and Release Mechanism), which grabs, centres and releases it in orbit. In order to release the TM to free fall, the GPRM holds the TM while the CVM retracts its fingers, then the grabbing sub-mechanism hands the TM over the release-dedicated tips and finally the TM is released by their quick retraction. Unfortunately, due to the adhesion phenomenon it is possible the TM is pulled by the retracting tips of the GPRM and acquires a momentum. This phenomenon is enhanced by the fact that all the surfaces are gold coated in order to minimize electrodynamic disturbances. As mentioned, the TM control authority is very low: for this reason the maximum release velocity which can be controlled is 5 μm/s (equivalently, the maximum momentum is 10^{-5} kgm/s).

Due to the criticality of this phase for the success of the mission a specific testing campaign is put in place at the University of Trento (Italy). The experiment is performed with the Transferred Momentum Measurement Facility (TMMF) which reproduces the release of the TM in LISA-Pathfinder. As mentioned, the key element in the transfer of momentum to the released TM is adhesion arising at the contact between the TM and a release-dedicated tip. As a consequence, the TM injection experiment is focused on a deeper understanding of the behaviour of adhesive bonds under quick separation. Recent updates of the facility, aimed at improving the representativeness of the in-flight conditions, enhance a systematic effect on the measurements. This paper presents the main challenges of the test set-up, the test results achieved, and the data analysis procedure developed to disentangle the effect of adhesion from other disturbances.

25.2 Experimental Apparatus and Procedure

An experimental setup, the Transferred Momentum Measurement Facility (TMMF), has been designed and realized at the University of Trento (Italy) to characterize metallic adhesion in an environment similar to the in-flight one [3–5]. The novelty of this approach is the study of the adhesion bond in dynamic conditions. The main idea under this setup is to suspend inside a vacuum chamber a TM mock-up realizing a simple pendulum, which provides a free-fall like condition on the horizontal plane. The TM mock-up hosts a cylindrical Au/Pt gold coated insert representative of the flight TM geometry, surface and bulk material. A release tip mock-up (Au/Pt lenticular disk, 2 mm diameter, 1 mm thickness, 10 mm radius of curvature) is connected to a piezo linear stage and can be commanded to engage the TM on the insert and then perform a quick retraction, similarly to the in-flight TM release procedure. The TM swing motion produced by the adhesion pull during the tip retraction is measured by means of a laser interferometer, whose beam is reflected by the mirror finished rear surface of the insert. The TM yaw (φ) and pitch (ψ) angles are also measured by means of an optical lever, composed of another laser beam reflected by the insert on a Position Sensing Device.

The facility is depicted in Fig. 25.1 and can be schematically subdivided into six subsystems described in [5]. A vacuum system provides the required vacuum environment (10^{-7} mbar). A 6 dof antivibration table guarantees that the seismic activity does not influence the system. A plasma source, able to perform ion etching (Ar^+ or O^-), allows the cleaning of the mock-ups surfaces. Several positioning stages are used to actuate the displacement (x, y and z) and the rotation about the vertical axis (φ) of the suspension point of the TM, in order to control its position and yaw angle.

The tip mock-up direction of actuation can be adjusted by varying both yaw and pitch angular positions of the actuation systems through a rotational stage and a tilting platform, respectively. Several yaw and pitch configurations are explored and analysed. The yaw-pitch matrix is then enlarged in order to search the direction of maximum impulse, if it lies on the border. In this way the angles that maximize the transferred momentum are find. In fact, the optimal yaw-pitch configuration may differ from that of nominal alignment due to deviation from the ideal spherical tip shape, non-uniform surface roughness, and small ground tilting.

The TM mock-up is approached and kept still by a blocking system, composed of three screws with a needle edge, carrying an anti-adhesive coating. The x-position as well as the attitude in terms of pitch and yaw of the blocking system is adjusted through a linear position and a double-tilting platform. To apply the preload, the release tip is actuated against the TM. The measurement of the preload force is performed indirectly from the commanded forward stroke of the retraction system, assuming that the stiffness of the blocking system is much higher than the release tip one. The attitude of the blocking system is adjusted so as to keep the TM aligned with respect to both gravity and torsional equilibrium position of the suspending wire during the loading and unloading phase. This is performed to reduce as much as possible spurious forces and torques, acting on the contact patch, which can weaken the strength of the adhesive bond.

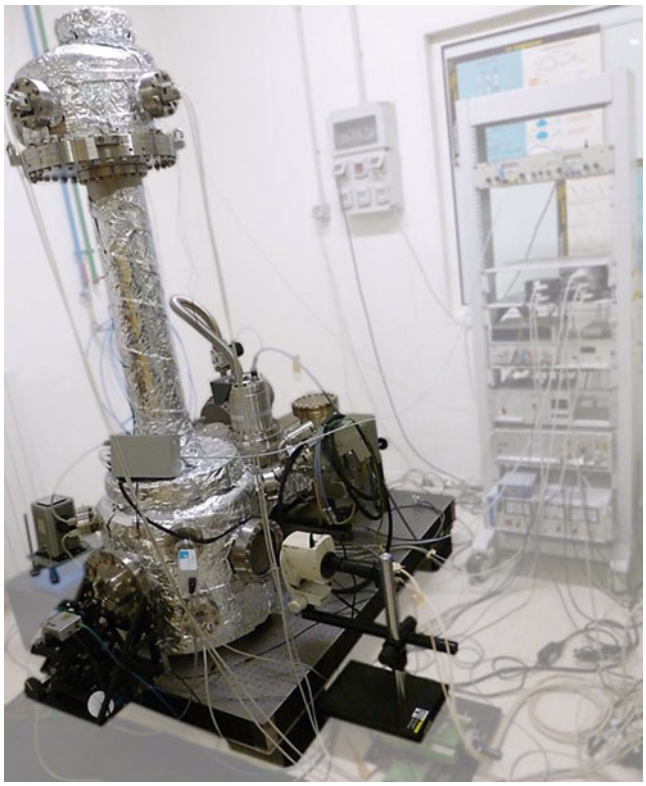

Fig. 25.1 The transferred momentum measurement facility

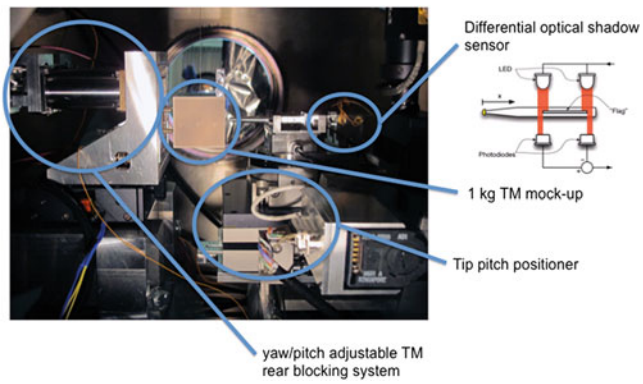

Fig. 25.2 Detail of the release experiment in the TMMF

The main goal of the experiment is the prediction of the residual velocity of the LISA Pathfinder TM after the in-flight injection into geodesic. However, the results of the TMMF cannot be directly transposed to the in-flight conditions because the actuator adopted in the TMMF to perform the retraction of the release tip is based on an ultra-sonic piezo while the Grabbing Positioning and Release Mechanism (GPRM) actuates the release tip by means of a piezo stack. This difference results in a reduced quickness of the TMMF piezo, which is assumed to enhance the momentum transfer to the TM.

In order to extrapolate the ground test results to the in-flight condition, the TM release may be simulated by including the effect of adhesion and the TM dynamics in the GPRM electro-mechanical model previously identified [6, 7]. Adhesion is assumed to produce a force as a function of the elongation at the contact, independently of the tip retraction velocity. This means that the relevant information of the ground testing campaign consist in the adhesion force-to-elongation curve produced during the different release experiments realized in representative conditions.

Adhesion force acts on the TM for few milliseconds, producing an acceleration which can be identified by the measurement of the TM motion. Elongation of adhesion was previously indirectly estimated through the dynamic characterization of the tip actuation system [8]. This approach however resulted in a limited accuracy of the estimation of the force to elongation profile. The last version of the tip actuation subsystem has been equipped with a differential optical shadow sensor [9] (DOSS), illustrated in Fig. 25.2, which directly measures the position of the release tip. This sensor

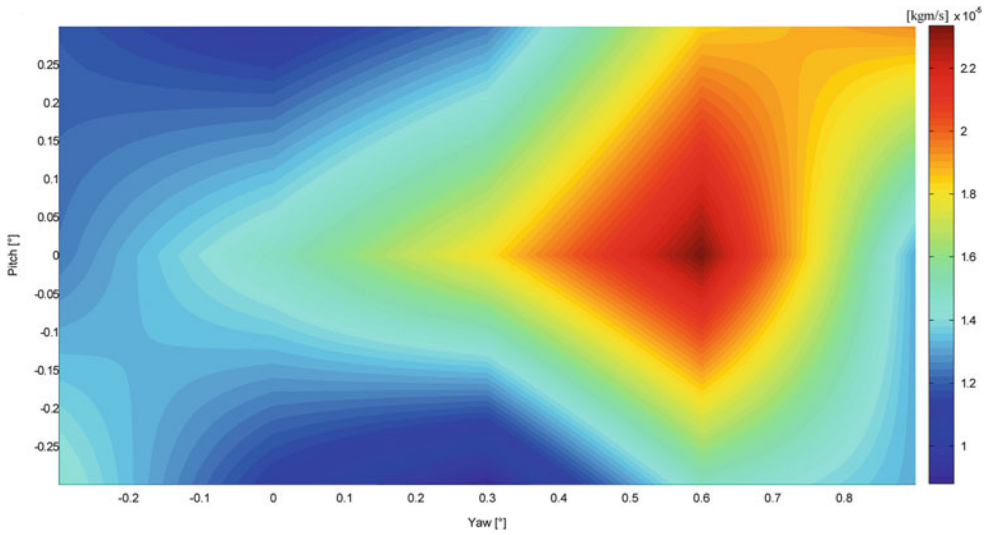

Fig. 25.3 Example of test matrix in terms of mean impulse

measures the incident light emitted by a pair of LED with a pair of photodiodes. The lights are partially shadowed by a flag connected to the release tip: its displacement is measured by the difference of the signals of the two photodiodes. The DOSS is calibrated by measuring the displacement of the release tip with the interferometer and with the DOSS, at the same time.

The experimental procedure can be summarized as follows:

1. After the stabilization of the pendulum, the TM is approached on its opposite sides by the blocking needles and the tip until a stable and *nominally* unloaded configuration is found.
2. The contact preload is gradually increased up to the maximum value (400 mN).
3. The preload is kept constant for roughly 10 s.
4. The preload is gradually reduced to a minimum value. A small residual preload is unavoidable in order to guarantee a stable contact between the surfaces.
5. At t = 0 s the release tip is retracted 200 μm away from the TM mock-up by commanding the linear stage at the maximum acceleration.
6. During the first 0.5 s preceding and following the release, the TM position and attitude are measured. The pendulum is designed to provide large and easily measurable swing oscillation with a resonant frequency of about 0.47 Hz, therefore the TM is nearly free-falling when subjected to a pull event of few milliseconds. More details on the measurement performance of the TMMF are in [10–12].
7. At t = 0.5 s the blocking needles are retracted to avoid collisions with the oscillating TM.

The release tests are performed in the same conditions in terms of maximum preload before release and maximum commanded acceleration of the tip. Five of these tests have been carried out per each pair of pitch and yaw angles. An example of test matrix in terms of mean impulse is illustrated in Fig. 25.3. Notably, the maximum impulse is about twice over the requirement (10^{-5} kgm/s), showing the criticality of adhesion in the TM release to free-fall. Figure 25.5 illustrates the displacement and attitude signals of the TM during its incipient motion, when the adhesion pull and failure occurs. Point 4 of the procedure determines a systematic addictive effect that may lead to overestimate the transferred momentum. As a matter of facts, the residual preload between the tip, the TM and the needles converts itself into TM impulse once the tip is retracted. This effect is determined by:

$$I = \sqrt{m\frac{F_{pl}^2}{k}} \tag{25.1}$$

where I is the transferred momentum, F_{pl} is the preload force, k is the stiffness of the needles and m is the TM mass. Unfortunately the repeatability of this effect is low and it must be taken into account in the estimation of the adhesion pull because their contribution may be comparable.

It is worth noting how this contribution to the momentum depends on the TM mass. In the earlier version of this testing campaign the TM mass was light (roughly 10 and 100 g). In order to be more representative of in-flight conditions, the mass used is now 844 g. This enhances the momentum imparted by the needles. A specific data analysis procedure is presented in the following section for decoupling the force-to-elongation law from this preload effect.

25.3 Data Analysis and Identification of Adhesion

The mathematical model of the dynamics of the TM under the action of the blocking system and the adhesion pull is written and is fitted to the measured TM swing displacement data. Thanks to the availability of the release tip displacement signal (x_{tip}), the dynamics of the release tip actuation system is no more modelled (Fig. 25.4).

The adhesion force (F_{ad}) to elongation (Δx) profile is assumed to be described by an exponential function, parametrically defined by three constants (X_1, X_2, and X_3) [7]:

$$F_{ad} = X_1 e^{-\left(\frac{\Delta x}{X_2}\right)^{X_3}} \Delta x \tag{25.2}$$

where Δx is the difference between the TM and the release tip displacements ($x_{tip} - x_{TM}$).

The push of the blocking needles F_{nd} on the TM is given by:

$$F_{nd} = \begin{cases} 0 & x_{TM} \geq x_0 \\ k(x_0 - x_{TM}) & x_{TM} < x_0 \end{cases} \tag{25.3}$$

where x_0 is the initial compression of the needles under the action of the preload force (F_{pl}/k).

The mathematical model describing the TM motion is then:

$$m\ddot{x}_{TM} = F_{nd} + F_{ad} \tag{25.4}$$

Equation 25.3 is solved numerically by substituting to x_{tip} the measured tip displacement signal and by assuming a guess for the three unknown parameters X_1, X_2, and X_3. Such a model is fit to the measured TM displacement profile minimizing the deviation of the predicted motion from the measured one.

An example of the tip and TM displacement signals is shown in Fig. 25.5. The plots show that the motion of the tip is much quicker than that of the TM and the latter is accelerated for less than 3 ms.

The result of the fitting procedure is shown in Fig. 25.6, where the measured and the theoretical motion profiles of the TM are plotted. The standard deviation of the residuals (defined as the difference between the measured and predicted TM positions) is about 0.11 nm, which is in the range of the measurement noise of the laser interferometer.

In Fig. 25.7 the force exerted by the preloaded blocking needles (F_{nd}) and adhesion (F_{ad}) are plotted as functions of time, showing that, as expected, for this test the contribution of the preloaded blocking system is relevant in the overall momentum transfer to the TM.

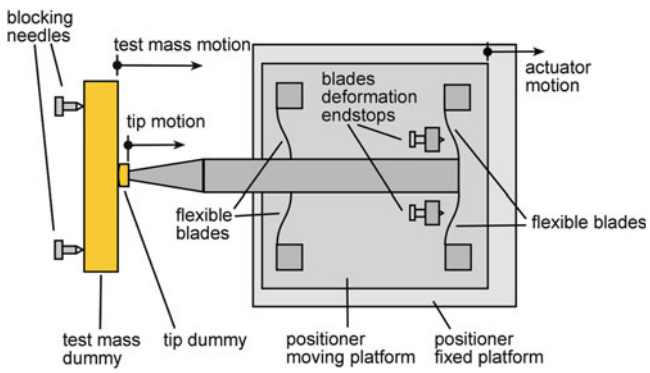

Fig. 25.4 Sketch of the test mass release experiment

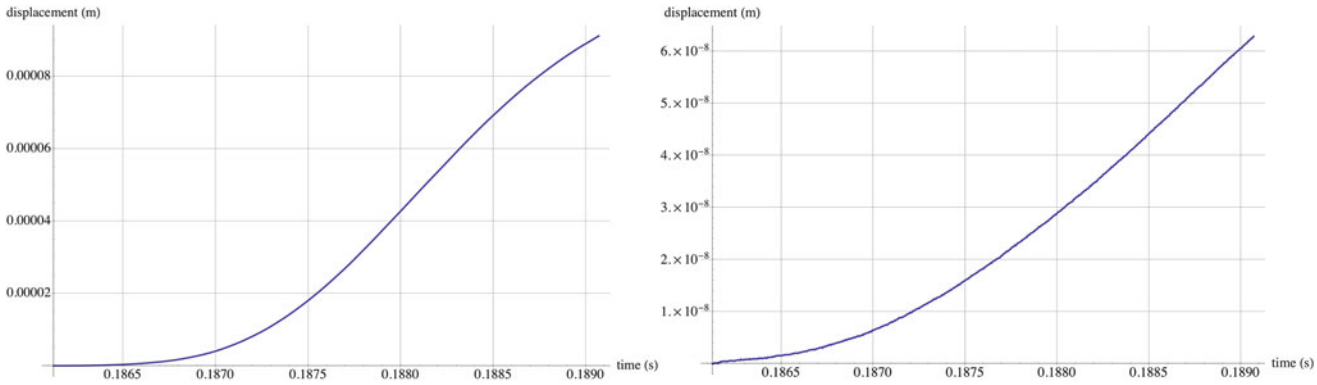

Fig. 25.5 Release tip and test mass displacement signals

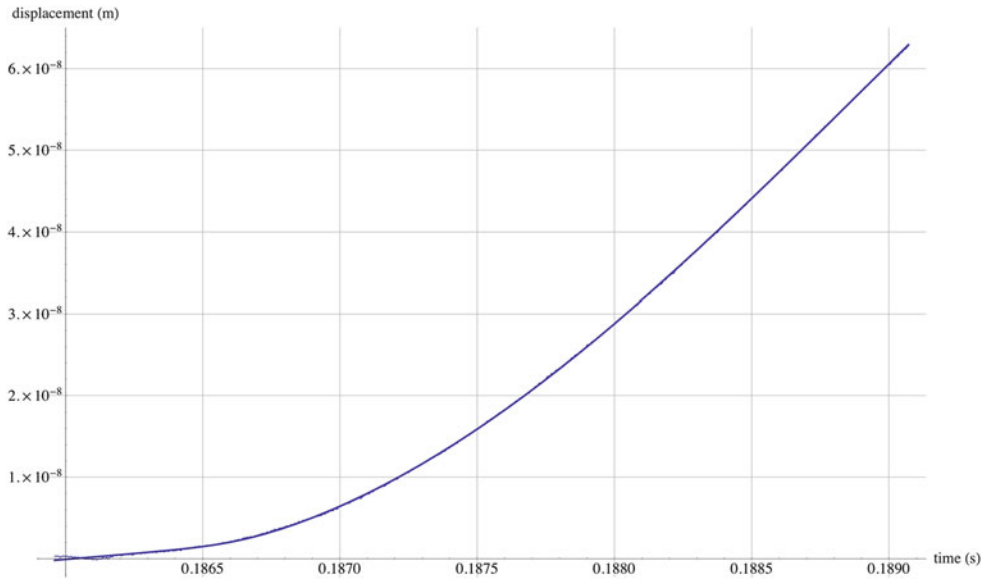

Fig. 25.6 Measured and fitted test mass displacement signal

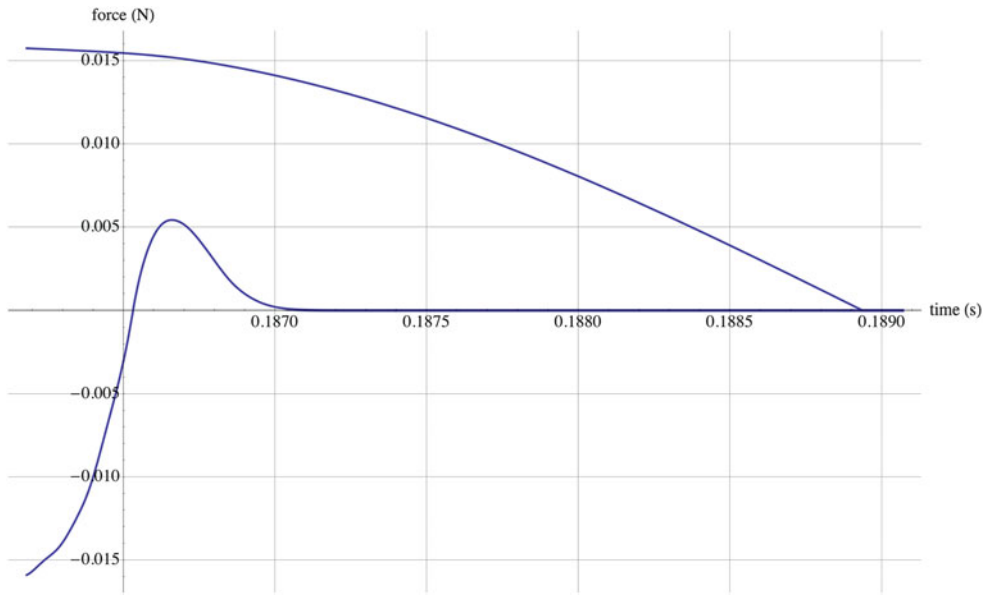

Fig. 25.7 Blocking needles and adhesion forces time profiles

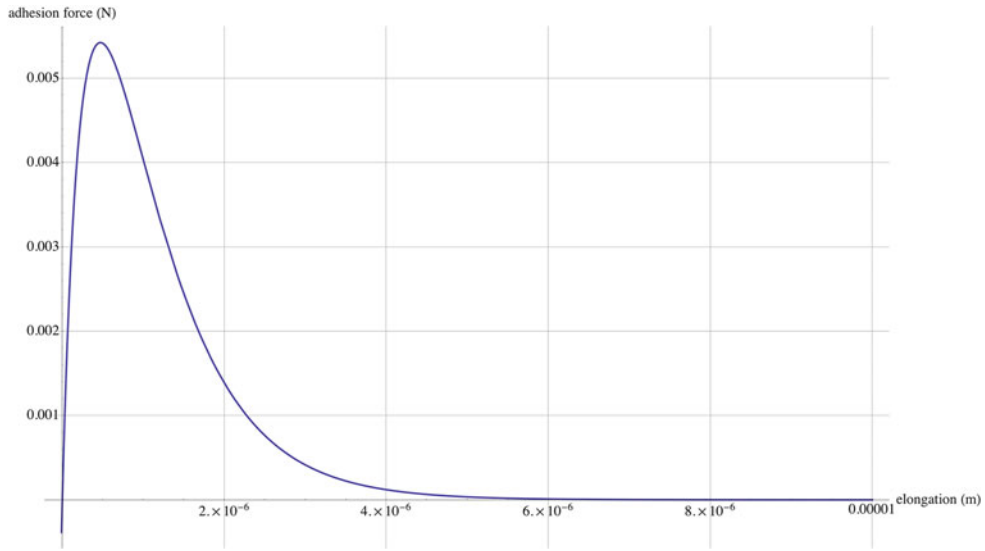

Fig. 25.8 Adhesion force as a function of elongation

Fig. 25.9 Elongation velocity of the adhesive bond

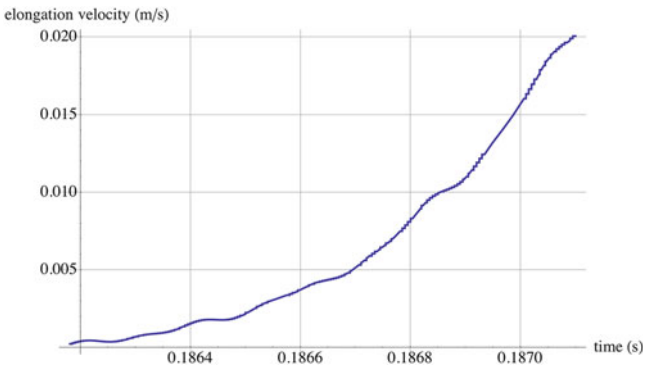

In Fig. 25.8 the adhesion force to elongation function is plotted. In this test adhesion resulted limited: a pull-off force (the curve peak) of about 5 mN and elongations of about 5 μm are produced. This is consistent with the thickness and the ductility the gold coating (about 1 μm).

It can be noted that the combination of pull-off force and elongation is associated with the bonding energy, which is the physical parameter which mainly promotes transfer of momentum from the release tip to the TM [13].

Finally, from Fig. 25.9 it can be underlined that in this test adhesion is subjected to high velocities of elongation (at the pull-off, about 5 mm/s).

25.4 Conclusions

In the framework of the ground testing of the LISA Pathfinder mission, a facility is developed for the qualification of a mechanism designed to perform a mission critical phase, that is the release of a cubic test mass to free-fall inside the spacecraft. The criticality of such a phase consists in the possible development of adhesive bonds between the test mass to be released and the mechanism designed for such a task. In particular, the release of the test mass must be performed by giving a maximum residual velocity of 5 μm/s, that is developing a maximum impulse of 10^{-5} kgm/s during the dynamic rupture of adhesion. The measured impulses are larger than the requirement, however they need to be extrapolated to the in-flight conditions where a quicker actuator will be adopted to perform the retraction of the release-dedicated test mass holding tips. In order to estimate the in-flight release velocity, the adhesion force to elongation profile is required. Such behaviour is

estimated by fitting a mathematical model of the ground-based release experiment to the measured data. The results show that adhesion is present and produces measurable force and elongation at the contact between the release tip and test mass. The bonds are subjected to high elongation velocities and adhesion is therefore characterized under dynamic conditions.

References

1. Bell TE (2008) Hearing the heavens. Nature 452:18–21
2. Antonucci F et al (2012) The LISA pathfinder mission. Class Quantum Grav 29:124014
3. Bortoluzzi D, De Cecco M, Vitale S, Benedetti M (2008) Dynamic measurements of impulses generated by the separation of adhered bodies under near-zero gravity conditions. Exp Mech 48:777–787
4. Bortoluzzi D, Benedetti M, Baglivo L, Vitale S (2010) A new perspective in adhesion science and technology: testing dynamic failure of adhesive junctions for space applications. Exp Mech 50:1213–1223
5. Bortoluzzi D, Benedetti M, Baglivo L, De Cecco D (2011) Measurement of momentum transfer due to adhesive forces: on-ground testing of in-space body injection in geodesic motion. Rev Sci Instrum 82(125107)
6. Bortoluzzi D, Mausli PA, Antonello R, Nellen PM (2011) Modeling and identification of an electro-mechanical system: the LISA grabbing positioning and release mechanism case. Adv Space Res 47(3):453–465
7. Bortoluzzi D, Conklin JW, Zanoni C (2013) Prediction of the LISA-pathfinder release mechanism in-flight performance. JAdv Space Res 51 (7):1145–1156
8. Bortoluzzi D, Benedetti M, Conklin JW, Zanoni C (2012) Measurement of metallic adhesion force-to-elongation profile under high separation-rate conditions. In: SEM international conference and exposition on experimental and applied mechanics, Bethel, 11–12 June 2012
9. Remo JL (1997) High-resolution optic displacement measurement using a dual- photodiode sensor. Opt Eng 36:2279–2286
10. Benedetti M, Bortoluzzi D, Vitale S (2008) A momentum transfer measurement technique between contacting free-falling bodies in the presence of adhesion. J Appl Mech 75:011016
11. Benedetti M, Bortoluzzi D, Baglivo L, Vitale S (2011) An optimal two-input approach for impulse measurements in the nanoNs range produced by contact forces. Mech Syst Sign Proc 25:1646–1660
12. De Cecco M, Bortoluzzi D, Baglivo L, Benedetti M, Da Lio M (2009) Measurement of the momentum transferred between contacting bodies during the LISA test mass release phase – uncertainty estimation. Meas Sci Technol 20–5:1–15
13. Benedetti M, Bortoluzzi D, Vitale S (2008) A momentum transfer measurement technique between contacting free-falling bodies in the presence of adhesion. J Appl Mech Trans ASME 75:011016

Chapter 26
Shock Wave Profile Effects on Dynamic Failure of Tungsten Heavy Alloy

E.N. Brown, J.P. Escobedo, C.P. Trujillo, E.K. Cerreta, and G.T. Gray III

Abstract It is well established that dynamic fracture or spall is a complex process strongly influenced by both the microstructure and the loading profile – the shape of the shock wave as a function of time – imparted to the specimen. For ductile metals it has been observed that the spall response is highly dependent on the pulse shape in addition to the peak stress. Here tungsten heavy alloy (WHA) specimens have been subjected to a shock wave loading profiles with a similar peak stress of 15.4 GPa but varying duration. Contrary to the strong dependence of strength on wave profile observed in ductile metals, for WHA, specimens subjected to significantly different wave profiles exhibited similar spall strength. Post mortem examination of recovered samples revealed that dynamic failure is dominated by brittle cleavage fracture, with additional energy dissipation through crack branching in the more brittle tungsten particles. Overall, in this brittle material all relevant damage kinetics are equally supported by both loading profiles considered, and the spall strength is shown to be dominated by the shock peak stress, independent of loading profile.

Keywords Dynamic fracture • Dynamic failure • Spall • Tungsten heavy alloy • WHA

26.1 Introduction

The influence of shock-wave-loading profile on the failure processes in a brittle material has been investigated. Tungsten heavy alloy (WHA) specimens have been subjected to two shock-wave loading profiles with a similar peak stress of 15.4 GPa but different pulse durations. Contrary to the strong dependence of strength on wave profile observed in ductile metals, for WHA, specimens subjected to different loading profiles exhibited similar spall strength and damage evolution morphology. Post-mortem examination of recovered samples revealed that dynamic failure for both loading profiles is dominated by brittle cleavage fracture, with additional energy dissipation through crack branching in the more brittle tungsten particles. Overall, in this brittle material all relevant damage kinetics and the spall strength are shown to be dominated by the shock peak stress, independent of pulse duration. More complete presentations of this work have recently been presented by Escobedo et al. [1] and Brown et al. [2].

26.2 Material Characterization

All target materials were prepared from a tungsten heavy alloy (WHA) plate with a composition of ~92.5 % W and the remainder of Ni and Fe. The alloy possesses a composite microstructure of tungsten particles in an austenitic matrix comprised of tungsten, nickel and iron. Representative results of the initial characterization, performed by means of electron backscatter diffraction (EBSD) measurements, are given in Fig. 26.1. A phase map of the metallic composite is given in Fig. 26.1a. The dark regions

E.N. Brown (✉)
P-23, MS H-803, Los Alamos National Laboratory, Los Alamos, NM 87545, USA
e-mail: en_brown@lanl.gov

J.P. Escobedo • C.P. Trujillo • E.K. Cerreta • G.T. Gray III
MST-8, MS G-755, Los Alamos National Laboratory, Los Alamos, NM 87545, USA

B. Song et al. (eds.), *Dynamic Behavior of Materials, Volume 1: Proceedings of the 2013 Annual Conference on Experimental and Applied Mechanics*, Conference Proceedings of the Society for Experimental Mechanics Series,
DOI 10.1007/978-3-319-00771-7_26,

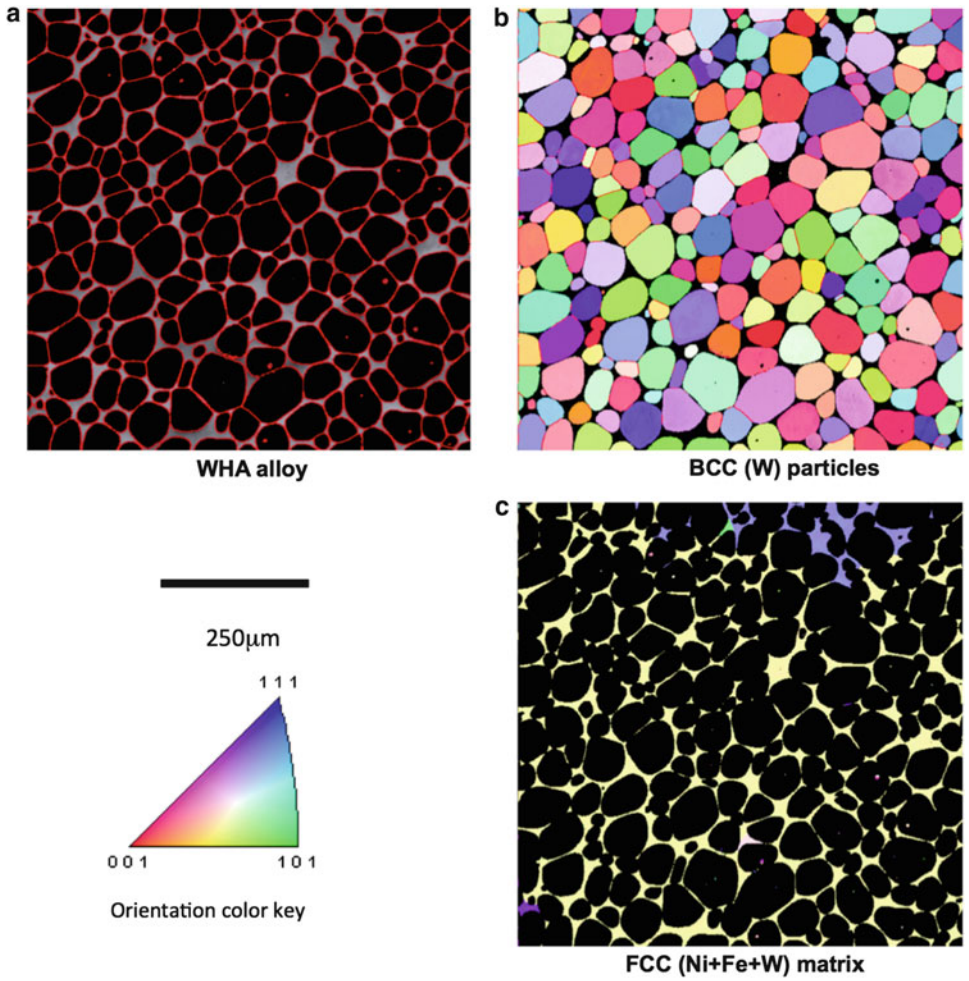

Fig. 26.1 EBSD results of initial characterization. (**a**) Phase map of the WHA alloy. *Dark phase* correspond to the W particles, the *light-colored phase* is the matrix, and the *red lines* demarcate particle – matrix interfaces. (**b**) Orientation map showing only the W-particles. No texture is observed. (**c**) Orientation map showing only the large crystalline domains of the FCC matrix. For the last two maps, the crystalline orientation color is according to the color key (color figure in online)

correspond to the W particles, identified as a phase with a body centered cubic (BCC) structure. The red lines demarcate the boundary between the W particles and the matrix. The matrix is shown as the light-colored phase, identified as a phase with a face centered cubic (FCC) structure. An orientation map showing only the W particles is given in Fig. 26.1b. The color of each particle is assigned based on its specific crystallographic orientation, as given by the accompanying color key. No preferred orientation, i.e. texture, is observed in the W particles. The orientation map showing the FCC matrix is shown in Fig. 26.1c. Large FCC crystalline domains are observed to dominate the microstructure in the matrix. To obtain a statistical representation of the distribution of the W particles, additional maps like those shown in Fig. 26.1 were generated at different areas of the as-received WHA plate. These measurements yielded values for the area fraction (i.e. volume fraction) of W particles of 0.859 ± 0.003 and a particle size of ~50 ± 19 μm. In addition, the particle-matrix boundary density was measured to be 86.2 ± 1.9 mm/mm^2, while the particle-particle boundary density was 10.3 ± 0.3 mm/mm^2.

26.3 Plate Impact Experiments

Plate impact experiments were conducted using the 80 mm bore gas launcher previously presented by Gray [3]. Two identical WHA targets, 20 mm in diameter and 4 mm-thick, were prepared with press fit momentum trapping rings to mitigate perturbations from edge release waves. The experimental parameters are listed in Table 26.1 and the schematics for

Table 26.1 Parameters for the plate impact experiments

Exp. ID	Impactor			Peak free surface velocity (mm/μs)	Pulse duration (μs)	Compressive stress (GPa)
	Material	Thickness (mm)	Velocity (mm/μs)			
L (long pulse)	W	2.0	0.383	0.375	0.5	15.37
S (short pulse)	W/ldm	0.5/5	0.391	0.377	0.05	15.46

Notes: (a) *ldm,* low density material, microballoons

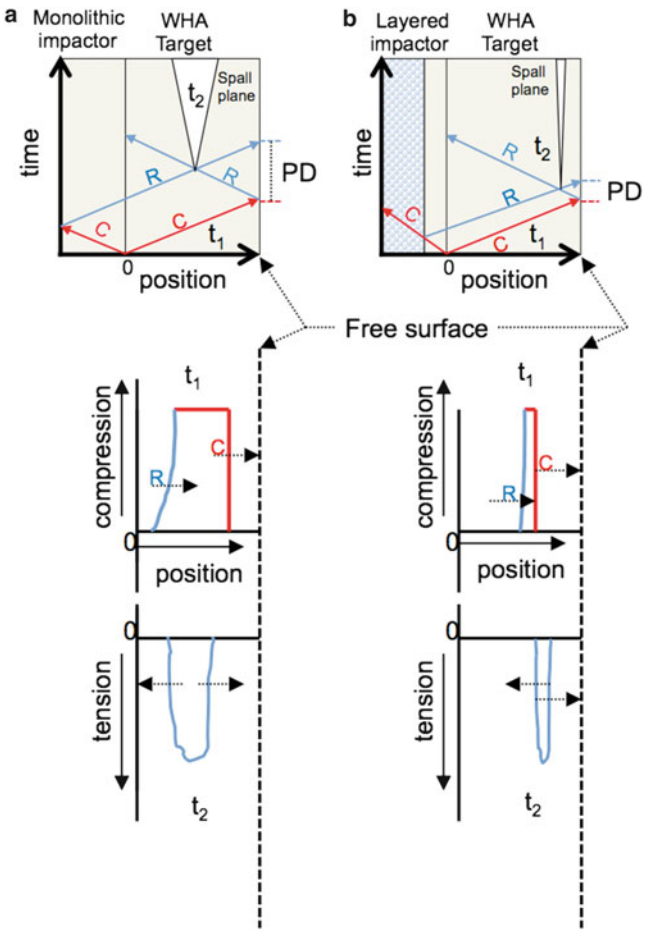

Fig. 26.2 Schematics showing the x-t diagrams of the trajectory and interaction of compressive (*C, colored as red*) and release (*R, colored as blue*) waves, as well as the development of compressive and tensile pulses for: (**a**) the monolithic WHA impactor imposing a loading profile with long pulse duration in compression and wide tensile pulse; and the (**b**) the layered impactor imposing a loading profile with shorter pulse duration in compression and a narrow tensile pulse (color figure in online)

the two experiments are shown in Fig. 26.2. A loading profile with a long-pulse duration was achieved by using a 2 mm-thick W monolithic impactor. The relative thickness of the target and impactor was chosen to locate the spall plane at the midline of the target (Fig. 26.2a). Furthermore, this geometry causes a relatively slow interaction of release waves that generates a wide tensile pulse within the WHA. Alternatively, a profile with a significantly shorter pulse duration was achieved with a layered impactor consisting of a 0.5 mm-thick W backed with a low-density microballoon composite ($\rho = \sim 400$ kg/m^3, almost 50 times lower density than WHA). From here on, this second short-pulse profile is referred to as profile S. For this geometry, the release waves interact relatively faster than the previous case which results in a narrower tensile pulse (Fig. 26.2b). Impact velocity was measured to an accuracy of 1 % using a sequential pressure transducer method and sample tilt was fixed to ~1 mrad by means of an adjustable specimen mount. Both experiments were executed to achieve a peak

compressive stress of ~15.4 GPa, which is significantly higher than the reported range for the spall strength of WHA. The free surface velocity (FSV) profiles were measured using Photon Doppler Velocimetry (PDV) [4] single-point probes. Following impact, all samples were soft recovered by decelerating them into low-density foam.

26.4 Free Surface Velocity Profiles

The free surface velocity (FSV) profiles for the experiments reported herein are shown in Fig. 26.3a. These measurements were performed at the sample back free surface. Key parameters and calculated values are listed in Table 26.1. The peak free surface velocities are 0.375 and 0.377 mm/μs, corresponding to peak compressive stresses of ~15.4 GPa (calculated using the Hugoniot parameters for tungsten: $C_o = 4.022$ mm/μs and $s = 1.26$). Both loading profiles exhibit a slight inflection in the shock front at ~0.1 mm/μs, potentially indicative of the Hugoniot elastic limit (HEL). Although the long pulse profile exhibits some rounding and increases slightly with time, the stress pulse remains within 95 % of the peak stress for ~0.5 μs, before starting to release. In contrast, the short pulse profile exhibits a sharp transition at peak stress and remains within 95 % of the peak stress for less than 0.05 μs. Upon release both profiles exhibit a classic pull-back signal and ringing, generally indicative of spall or dynamic fracture occurring within the sample [5, 6].

A more detailed view of the pull-back regions are shown in Fig. 26.3b. The drops in the free surface velocity (ΔFSV) from the peak states to the minima are 0.056 and 0.067 mm/μs for the long and short pulse profiles respectively. From these results, the spall strengths (σ_{spall}) for the two experiments can be determined using the relationships proposed by Novikov [7] and the correction proposed by Kanel [8]:

$$\sigma_{spall} = \frac{1}{2}\rho_0 c_B(\Delta FSV + \delta), \tag{26.1}$$

where ρ_o is the ambient density (19,260 kg/m^3), c_B is the bulk sound speed (4.022 mm/μs), and ΔFSV is the observed pull-back signal (as shown in Fig. 26.3b). The accuracy of the spall strength is improved by correcting for the ΔFSV in Eq. 26.1 [8]

$$\delta = h\left(\frac{1}{C_B} - \frac{1}{C_L}\right) * \frac{|\dot{u}_1 * \dot{u}_2|}{|\dot{u}_1| + \dot{u}_2}, \tag{26.2}$$

where h is the thickness of the spalled region (measured in optical micrographs as ~1.75 mm for profile L and 0.4 mm for profile S), C_L is the longitudinal sound speed (5.22 mm/μs), and are the unloading and re-compression rates calculated as

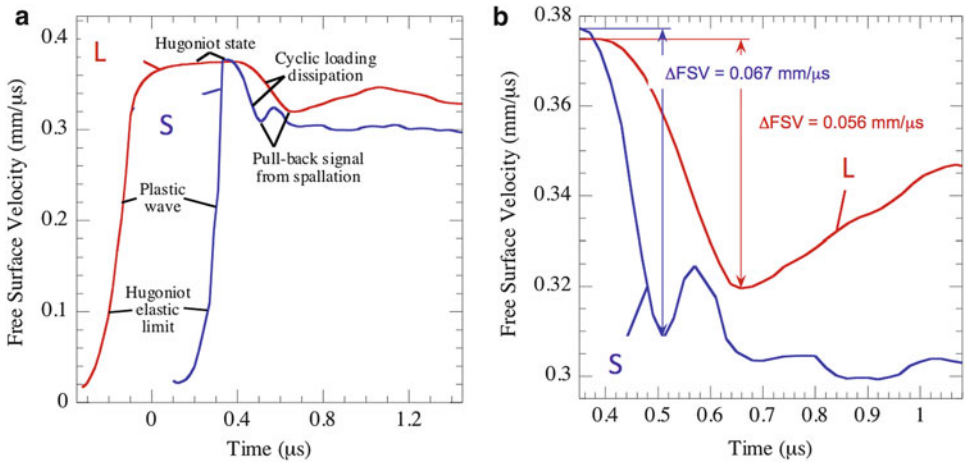

Fig. 26.3 (**a**) Traces of the free surface velocity showing shock loading with long (*L*) and short (*S*) pulse durations. The *curves* are plotted such that the drop from the peak state starts at similar times for both experiments. (**b**) Region of the free surface velocity highlighting the pull-back signal, indicative of spall plane formation

Table 26.2 Calculated and measured parameters from FSV data

	Pull-back characteristics					
Exp. ID.	ΔFSV (mm/μs)	$\dot{u}_1$ (mm/μs^2)	$\dot{u}_2$ (mm/μs^2)	δ (mm/μs)	Spall strength (GPa)	Corrected spall strength (GPa)
L	0.056	0.144	0.036	0.0029	2.16	2.28
S	0.067	0.295	0.114	0.0020	2.59	2.66

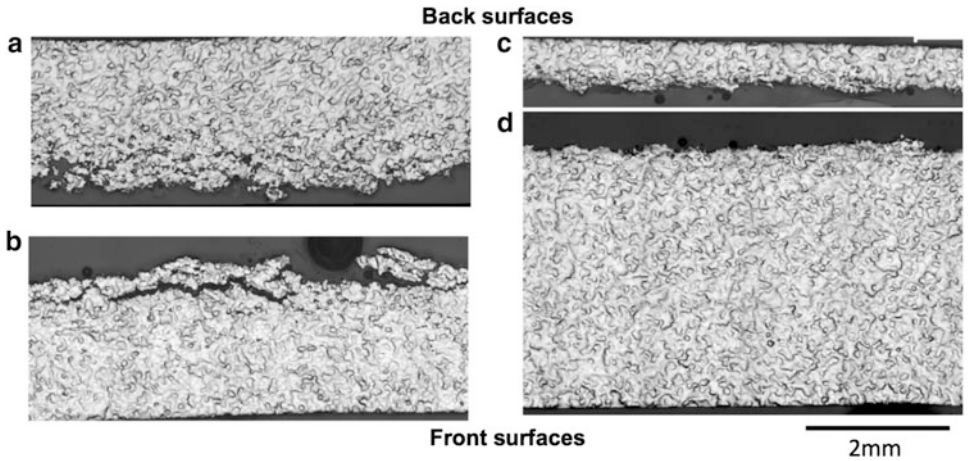

Fig. 26.4 Optical micrographs of the spalled samples loaded with the longer pulse (**a**–**b**); and (**c**–**d**) profile S. The shock direction is from *bottom to top*. The spall plane is significantly rougher for the longer pulse, while it is more localized with less bifurcation of cracks for the shorter pulse

$$|\dot{u}_1| = -\frac{1}{2}\frac{dFSV}{dt} \text{ and } \dot{u}_2 = -\frac{1}{2}\frac{dFSV}{dt}, \tag{26.3}$$

where $dFSV/dt$ is measured from the pull-back signal and listed in Table 26.2. The unloading rates are normally interpreted as indicators of the kinetics of the tensile pulse imposed on the target [9, 10]. As such, these values indicate that the sample subjected to the shorter pulse profile experienced a faster tensile stress rate as compared with the sample subjected to the longer pulse profile.

The corrected spall strength values calculated using Eqs. 26.1, 26.2, and 26.3 are listed in Table 26.2, they differ by only ~14 %, being slightly higher in profile S as compared to the profile L. These spall strength values are consistent with those reported in the literature [11–13]. It is worth noting that the difference between the two specimens is less than the sample-to-sample scatter generally reported for WHA and is consistent with the statistical variation within a given sample reported by Vogler and Clayton [13], therefore being statistically insignificant for this brittle material. Moreover, this difference is an order of magnitude less than reported for the spall strength dependence on wave profile observed in ductile metals [14–16]. For these two reasons the difference between the two samples reported in this article can be considered negligible.

26.5 Optical Microscopy

Several differences are observed in the optical micrographs of the cross sections of the recovered samples presented in Fig. 26.4. The location of the spall plane within the thickness of the target is as expected, centered for the profile L but near the rear of the target for the shorter pulse profile. This results from the difference in timing for the interaction of the release waves off the back of the impactor and target because of the different impactor designs, as shown previously in Fig. 26.2. Of greater interest is that the spall plane in both samples is very localized in the form of cracks consistent with brittle fracture in contrast to the diffuse damage zones seen in ductile metals failing via void nucleation and growth [16]. Minimal plastic deformation is observed in the microstructure adjacent to the spall plane and no voids are seen to occur, as is associated with incipient spall in ductile materials. In neither case are the cracks perfectly flat, but rather follow a path with fracture roughness and crack-path tortuosity consistent with the length-scale of the tungsten particles.

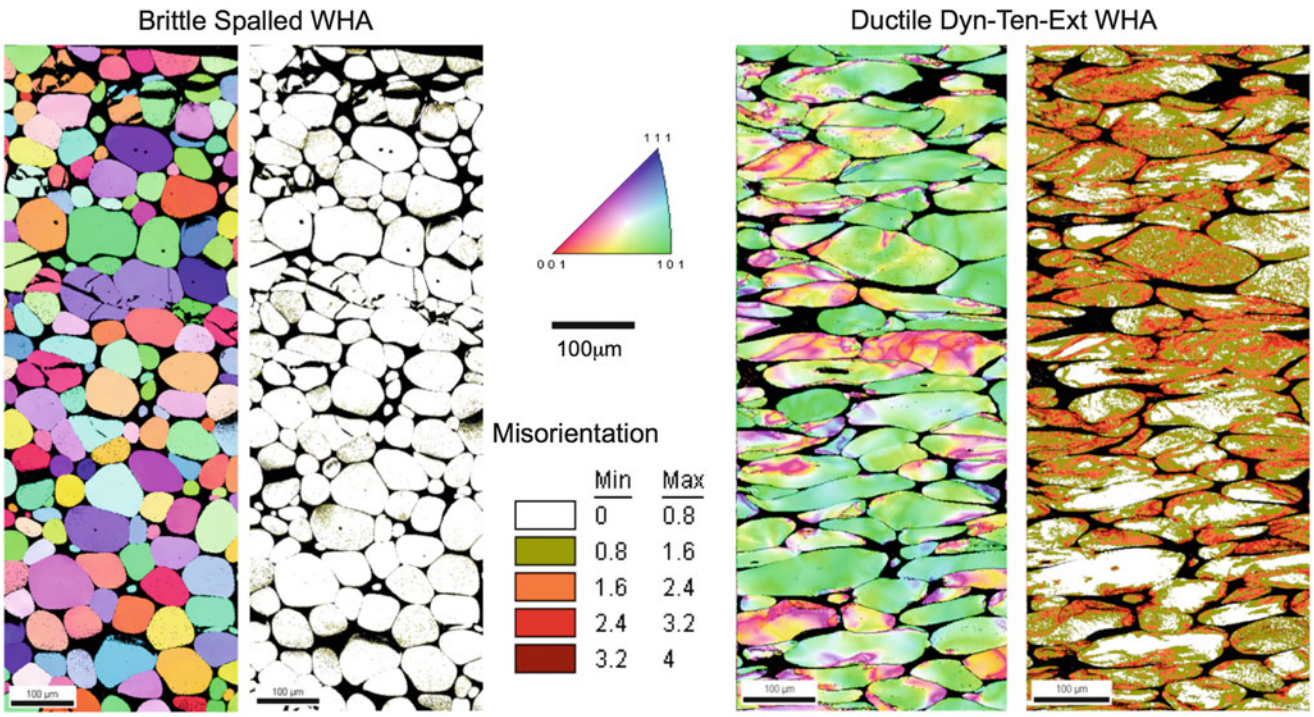

Fig. 26.5 EBSD orientation maps near the spall plane of the spalled specimens loaded with the long pulse on the *left*. The shock direction is from *bottom to top* and the color indicates the particle's crystalline orientation with respect to the shock direction according to the color key. EBSD orientation maps of a WHA Dynamic Tensile Extrusion sample on the *right*. The Dyn-Ten-Ext sample has been extruded from *left to right* (color figure in online)

26.6 Electron Backscatter Diffraction Microscopy

Electron backscatter diffraction (EBSD) images in Fig. 26.5 further highlight secondary cracks formed underneath the primary crack (i.e. spall plane). There is a set of cracks that have linked up across multiple particles and significant fracturing of individual W particles is seen where the crack does not appear to propagate into the matrix or surrounding particles. This type of sub-surface damage of the brittle phase is often observed when mechanical toughening is achieved through a multi-phase composite microstructure. Interestingly, when the same WHA is load under Dynamic Tensile Extrusion where very large tensile strains and strain rates are achieved, this more constrained loading allows for substantial plasticity within tungsten particles. Almost no cracking is observed. Rather the tungsten particles rotate to align with the extrusion direction and undergo substantial deformation.

26.7 Conclusions

Although the imposed wave profiles do not significantly affect the value of the spall strength of WHA, the difference in wave-form does significantly change the area of the sample put into tension. A wide damage zone in the form of cracks is observed in the sample loaded with the longer pulse. It is noteworthy that this difference in the amount of additional cracking is captured as the acceleration measured in the free surface velocity trace after the pull-back minima. The acceleration rates appear to be indicative of the ability to form a complete spall plane. In this regard, the higher rate measured with the shorter pulse correlates with a single, flatter, less tortuous, spall plane observed in the spalled sample.

Acknowledgements Los Alamos National Laboratory is operated by LANS, LLC, for the NNSA of the US Department of Energy under contract DE-AC52-06NA25396.

References

1. Escobedo JP, Brown EN, Trujillo CP, Cerreta EK, Gray GT III (2013) The effect of shock-wave profile on dynamic brittle failure. J Appl Phys 113:103506, http://dx.doi.org/10.1063/1.4794002
2. Brown EN, Escobedo JP, Trujillo CP, Gray GT III (2012) The effect of shockwave profile shape on dynamic brittle failure. EPJ Web Conf 26:02010, http://dx.doi.org/10.1051/epjconf/20122602010
3. Gray GT III (2000) Shock wave testing of ductile materials. In: Kuhn H, Medlin D (eds) ASM handbook, vol 8. ASM International, Metals Park, p 530
4. Strand OT, Goosman DR, Martinez C, Whitworth TL, Kuhlow WW (2006) Compact system for high-speed velocimetry using heterodyne techniques. Rev Sci Instrum 77(8):083108
5. Seaman L, Curran DR, Shockey DA (1976) Computational models for ductile and brittle fracture. J Appl Phys 47(11):4814
6. Antoun LST, Curran D, Kanel G, Razonerov S, Utkin A (2002) Spall fracture. Springer, New York
7. Novikov SA, Divnov II, Ivanov AG (1966) Investigation of the fracture of steel, aluminum and copper during explosive loading. Fiz Metallov Metalloved 21(44):608
8. Kanel GI (2001) Distortion of the wave profiles in an elastoplastic body upon spalling. J Appl Mech Tech Phys 42(2):358
9. Johnson JN, Gray GT, Bourne NK (1999) Effect of pulse duration and strain rate on incipient spall fracture in copper. J Appl Phys 86(9):4892
10. Gray GT (1993) High pressure compression of solids. Springer, New York
11. Dandekar DP, Weisgerber WJ (1999) Shock response of a heavy tungsten alloy. Int J Plast 15(12):1291
12. Bless SJ, Tarcza K, Chau R, Taleff E, Persad C (2006) Dynamic fracture of tungsten heavy alloys. Int J Impact Eng 33:100
13. Vogler TJ, Clayton JD (2008) Heterogeneous deformation and spall of an extruded tungsten alloy: plate impact experiments and crystal plasticity modeling. J Mech Phys Solids 56(2):297
14. Gray GT, Bourne NK, Henrie BL, Millett JCF (2003) Influence of shock-wave profile shape (triangular “Taylor-wave” versus square-topped) on the spallation response of 316L stainless steel. J de Phys IV 110:773
15. Gray GT, Bourne NK, Henrie BL (2007) On the influence of loading profile upon the tensile failure of stainless steel. J Appl Phys 101 (9):093507
16. Koller DD, Hixson RS, Gray GT, Rigg PA, Addessio LB, Cerreta EK, Maestas JD, Yablinsky CA (2005) Influence of shock-wave profile shape on dynamically induced damage in high-purity copper. J Appl Phys 98(10):103518

Chapter 27
Adhesively Joined Crush Tube Structures Subjected to Impact Loading

Luis F. Trimiño and Duane S. Cronin

Abstract The use of lighter structural and energy absorbing materials to increase fuel efficiency in transportation systems has provided a motivation to investigate the use of new joining techniques based on the use of high strength and high tenacity adhesives. Current joining techniques, such as spot-welding, limit the possible weight reduction that can be achieved if lighter sections, dissimilar materials and/or novel geometries were to be used.

To address this need, a parallel program on adhesive material characterization, numerical modeling and experimental testing has been undertaken using representative thin-walled steel crush tubes. Adhesive characterization was undertaken at quasi-static and high strain rates to determine the material properties, and this data was used to define a constitutive model for the adhesive. The adhesive model was then implemented in numerical simulations of representative crush tubes for comparison to experimental testing. Although the model predictions in terms of peak and average crush loads as well as final deformations and fracture pattern in the adhesive were in good agreement with the experimental tests conducted at dynamic loading rates, further research is required to develop constitutive models that can better describe local aspects of the fracture process in adhesive materials.

Keywords Dynamic axial crushing • Thin-walled bonded sections and numerical simulations

27.1 Introduction

Lighter structures are essential to increase fuel efficiency in transportation systems [1] and have provided a motivation to investigate the use of new joining techniques based on the use of high strength and high tenacity adhesives. Conventional joining techniques, such as resistance spot-welding, limit the possible weight reduction that can be achieved through the use of thinner sections, dissimilar materials and/or novel geometries; to elaborate, welding operations require a minimum thickness in the parts to be joined, otherwise, the electrode just burns trough the material. Because of this manufacturing limitation, the thickness of the component may not be the optimal one; precluding then, potential weight savings. Other limitations could be imposed, by example the use of a novel geometry like a tapered crush tube [2]; again this may not be possible because of the limitations of the welding machines. Adhesive bonding can address many of these limitations in structures, especially the ones used for transportation systems and the automotive industry.

In this work, attention was focused on axial crush tubes made out of steel hats sections bonded together with a structural adhesive, since this represents a challenging impact scenario to address with adhesively bonded structures. Some authors [3–6] have investigated bonded structures, such as closed sections made out of channels and hats, under quasi-static load and dynamic impact conditions. However, the testing of these structures in the expected range of strain rates for automotive crash scenarios is challenging in terms of cost and equipment requirements. Computer simulation is a valuable tool to further investigate these scenarios. The accuracy of computer models may be limited by the material constitutive models, the type of element selected for representation of the geometry and algorithm implementations for the solution. In this study a computer

L.F. Trimiño (✉) • D.S. Cronin
Department of Mechanical and Mechatronics Engineering, University of Waterloo, 200 University Avenue West, Waterloo, ON N2L 3G1, Canada
e-mail: ltrimino@uwaterloo.ca; dscronin@uwaterloo.ca

B. Song et al. (eds.), *Dynamic Behavior of Materials, Volume 1: Proceedings of the 2013 Annual Conference on Experimental and Applied Mechanics*, Conference Proceedings of the Society for Experimental Mechanics Series,
DOI 10.1007/978-3-319-00771-7_27,

model of a crush tube subjected to an axial impact is analyzed using different methods to represent the adhesive layer. The performance of the simulation was compared to experimental testing of the same event.

27.2 Methods

Dynamic testing of crush tubes using an Instrumented Falling Weight Impactor (IFWI), or drop tower, was performed in this study to evaluate the structure response during crash scenarios were strain rates may be significant. Dynamic compression testing has been used by a number of research groups for a broad range of applications. For example, Abramowicz and Jones [7] used an IFWI to determine the changes in buckling modes for steel tubing subjected to different impact velocities. Belingardi [6] used an instrumented drop tower to determine the structural response of built up closed sections to axial impact.

A Rosand drop tower (Model IFWI5HV), in conjunction with high speed video imaging; were used to obtain force-displacement diagrams of crush tube structures subjected to axial dynamic impact. The drop tower (Fig. 27.1) consists of a falling weight guided by rails, which ensures that the striker falls completely vertical, and a piezoelectric load cell located below the specimen to measure the loads during the event (Kitstler model# 9071A). In this study, axial crush tubes were impacted with a fixed mass of 56.18 kg that was dropped from a height of 2.73 m. By conservation of energy an impact velocity of 7.31 m/s should be achieved, and the IFWI system consistently measured an impact speed of 7.24 m/s (i.e. within 1 %) for the experimental tests. The IFWI system measured the impact velocity using an optical technique with two lasers a known distance apart and a timer to measure the length of time required to traverse the known distance. Specimen deformation can be measured in a number of ways. In this study, the displacement was obtained by double integrating the acceleration curve of the dropped weight; this acceleration curve was determined by dividing the measured force data by the mass of the impactor. Analysis of the high speed video footage was used to verify that the displacement data generated by the drop tower and the measured impact velocity prior to impact were accurate.

Commercial roll formed mild steel sections 1.2 mm in thickness were used to build crush tube structures by bonding two hat sections back to back using an epoxy adhesive (DP-460NS, 3M), representative of an actual geometry intended for field use in automotive energy absorbing structures (Fig. 27.2). To define the material properties of the steel alloy, a series of quasi-static and dynamic tensile test were perform using steel samples cut off from the roll form.

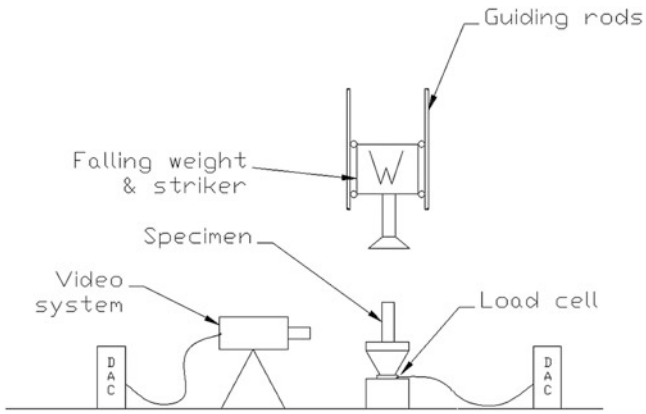

Fig. 27.1 IFIW schematic

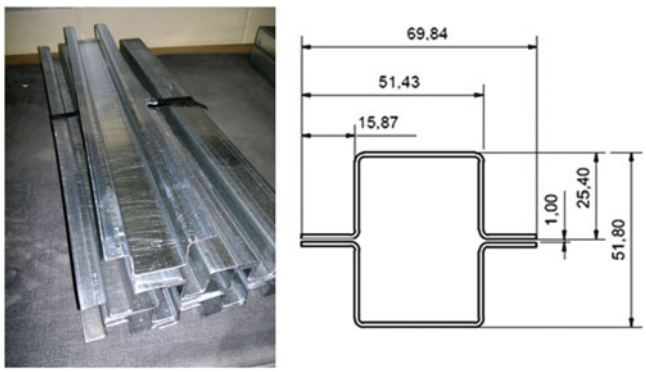

Fig. 27.2 Steel sections, as received (*left*). Assembled tube dimensions (right)

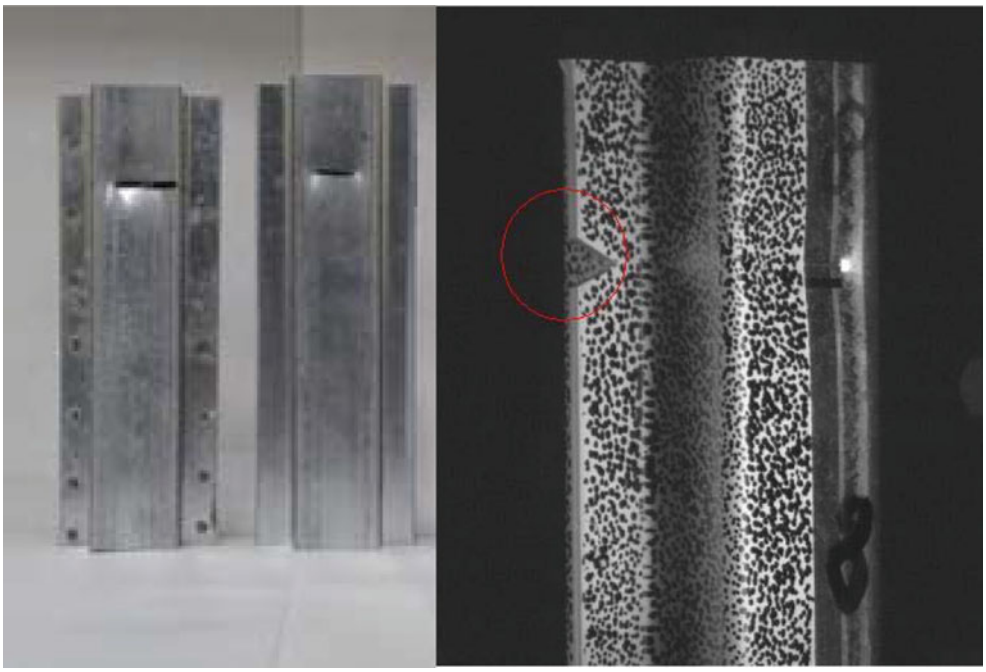

Fig. 27.3 Assembled crush tubes, from *left to right*: welded, bonded, notch detail

The sections were assembled into crush tubes maintaining a 1 mm bond thickness at the joining surface by means of spacers and then cured in a convection oven for 1 h at 75 °C. The assembled sections were then cut to 200 mm lengths and later indented with a buckle initiator using a manual press. The buckle initiator reduced the peak load required to initiate the folding process during axial loading.

The tubes included an additional notch (Fig. 27.3); simulations early in the test program demonstrated the need for this notch to enable consistent initiation of folding.

27.3 Simulation of Axially Impacted Crush Tubes

Numerical models were developed to represent dynamic impact events in the IFWI apparatus by mimicking the boundary and impact conditions of the experiment. The simulations were undertaken using a commercial finite element program (LS-Dyna LSTC version ls971_d_R4.2.1). A rigid plane was used to represent the impactor, with the provision that the plane's mass and velocity match the impact cart in the IFWI machine at the time of impact. Energy losses during the actual event, such as friction between the rails and the impactor cart, energy lost to the sound of the impact, deformation and rebound in the impactor and/or the small amount of heat generated in the crush tube during the deformation process, were considered to be small and were not replicated by the simulation.

The crush tube was represented by constructing an exact copy of the geometry using 3 mm shell elements for the commercial roll form sections. Cohesive or tie break elements were used to represent the adhesive layer joining the sections.

The steel material was described in the code, by defining a table of strain rates and for each specified strain rate in the table a curve of true stress versus plastic strain was provided. Data from uniaxial tensile testing of the material at strain rates of 1.6×10^{-3}, 10 and 100 1/s was used to obtain the plastic curves. Although the nominal strain rate value for this particular experiment is around 40 1/s, obtained by dividing the impact speed of the event (7.24 m/s) by a characteristic length (200 mm of axial length), is in the range of the provided data for the steel material; measurements in simulation have shown that the local strain rates can be as high as 400 1/s in the folding areas [8]. Data for 1,000 1/s was included by extrapolating the experimental data using a curve fit that considered all the information that describes the stress–strain curve at the different strain rates but disregarded the yield peaks.

The adhesive material was represented in the numerical simulations using a cohesive element formulation (MAT_COHESIVE_GENERAL [9]), with a single layer of solid elements between the two steel sections; and also by using a simple numerical tie-break.

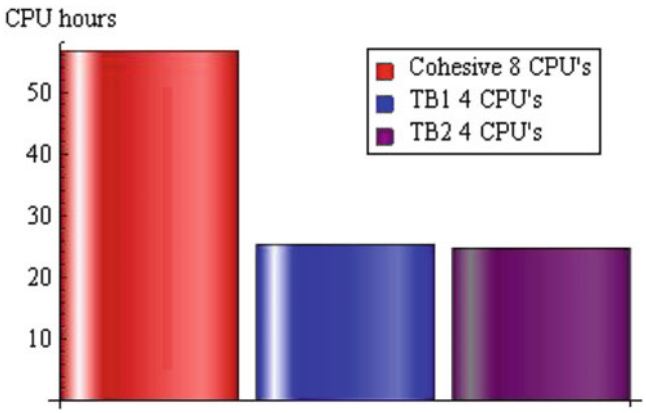

Fig. 27.4 CPU time to completion for simulations using different material implementations in the bonded joint of a double cantilever beam test

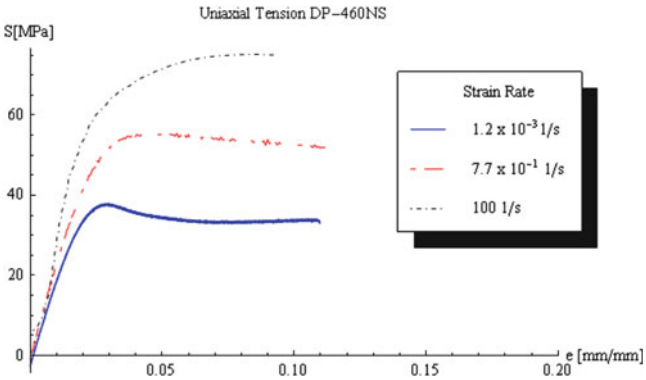

Fig. 27.5 Tensile testing of adhesive materials DP-460NS

Although cohesive elements are widely used to predict adhesive response under mixed-mode loading, this approach is limited in that it does not incorporate strain rate effects for the adhesive. This limitation could be addressed using solid elements with a material formulation allowing for the inclusion of strain rate effects; however, this would require multiple elements through the thickness of the adhesive and result in a dramatic increase in computational time. Tie-break approaches potentially offer major savings in computational time (Fig. 27.4) and two different formulations were explored.

The first implementation (TB1) defined a tie-break between surfaces in contact with the hats. For this formulation, the tie-break is active for nodes initially in contact, and failure is defined by stress values in both the normal and shear directions. In this implementation, failure stress values in the normal direction, for the particular adhesive material used are the only data required.

This element also requires a critical opening for failure. This opening can be defined as the distance at which first yield occurs; in this case 0.1 mm was used. Predicting the critical distance accurately may be essential to achieving meaningful results since it can affect the amount of energy the joint dissipates once the tie fails, and hence change the response of the model.

The second implementation (TB2) used the discrete crack model. This type of contact aims to provide a better representation of the material by incorporating energy considerations in the failure criteria, while eliminating the numerical burden imposed by cohesive elements. In this case, failure also accounts for energy release rates, which determine when the failure occurs. The epoxy adhesive material used to build the crush tubes in this study was a toughened epoxy (DP-460NS, 3M); this adhesive is a two-part epoxy material with high tenacity and high deformation at failure. Due to the nature of the elements selected to represent the adhesive in the numerical code results from a series of different mechanical tests, uniaxial universal tension and lap shear test using thick steel adherents performed at different strain rates were used to define the mechanical properties of the material (Figs. 27.5 and 27.6). It is evident that the mechanical properties are sensitive to strain rate and the measured properties in the lap shear test can vary depending on the nature of the adherents, a good example of this behavior and experimental data is provided by Rahman, for magnesium with steel lap joints [10]. Results presented in Fig. 27.6. are only valid for steel on steel joints.

The mechanical properties of the adhesive used in the tube assembly as well as the curve for the opening displacement required to build the cohesive model and the tie-breaks are provided in Tables 27.1 and 27.2 respectively.

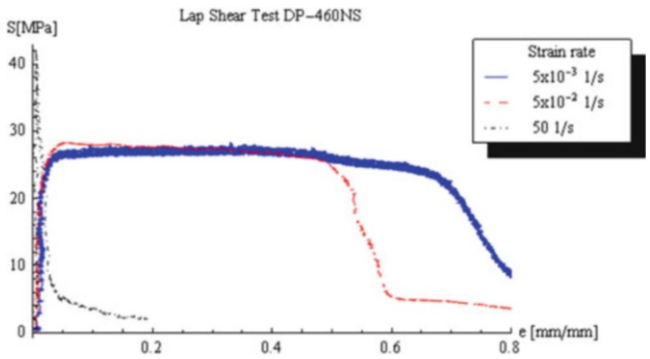

Fig. 27.6 Lap shear test of steel on steel specimens bonded with DP-460NS

Table 27.1 Adhesive mechanical properties of DP-460NS

Mechanical property	DP-460NS
E [GPa]	2.2
Poisson Ratio ν	0.41
Yield Stress [MPa]	36
Ultimate Stress [MPa]	37.7
Strain to failure	0.108
Density [kg/m^3]	1200
K_{IC} [MPa mm]	2.82
K_{IIC} [MPa mm]	3.13

Table 27.2 Traction-separation (T vs. δ) curve for adhesive model

d	0	0.03	0.07	0.09	0.11	0.22	0.35	0.47	0.58	0.61	0.66	1.00
T	0	0.73	0.93	0.97	0.98	1.00	1.00	0.98	0.92	0.85	0.62	0

27.4 Results

Figure 27.7 shows the axial deformation behavior of one of the adhesively bonded hat sections tested under dynamic loads, as well as the simulations using different type of elements to represent the adhesive joint. The load–displacement histories predicted by the numerical model are in good agreement with the dynamic impact test. However, the model predicts a higher plateau force after the first yield and lower final deformation, measured by the stroke of the striker. In the case of the experimental hats, the geometry of the cross section was highly sensitive to deformation during the indentation process. This introduced changes in the material and geometry that were not fully captured in the model; hence the model prediction was slightly different than the one by the experiments. From the figure it is clear that there is a good agreement between the experiment and the simulations. There is a consistent rise at the end of the force-displacement diagram, starting at around 38 mm of compression, in all of the bonded hat sections. This end rise corresponds to the consolidation of the deformed top and the subsequent increase in load to start forming a new fold, which was also accurately captured by the simulation.

From Fig. 27.8 it can be seen that the hats did not develop the typical folding pattern that is expected during this type of event [6, 11–15]. As a consequence there must be additional stresses in the bond that impinges the adhesive layer to carry the load causing debonding which in term prevents the development of a traditional folding pattern. There was an incipient fold under the deformed area but the impact event runs out of energy before the formation of this second fold can progress.

The deformation of the structure was also captured reasonably well by the simulations (Fig. 27.9) considering that it is quite difficult to introduce the exact same deformations present in the tubes after the manufacturing, since this was a manual process. Typical quantitative values that are used to characterize axial crushing experiments such as absorbed energy, specific energy, mean force and peak forces (Table 27.3) are also in good agreement between simulation and experiment.

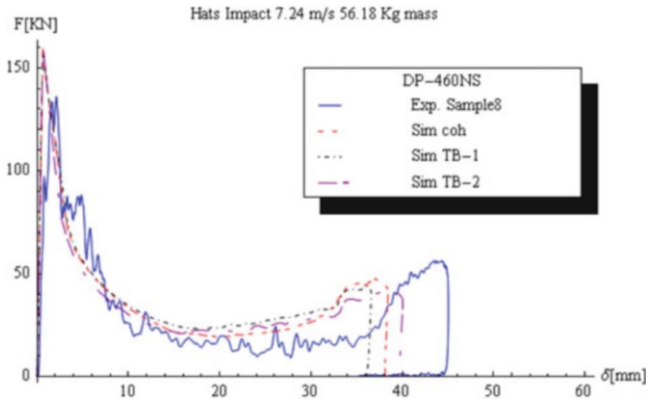

Fig. 27.7 Tube sections bonded using DP-460NS, dynamic load

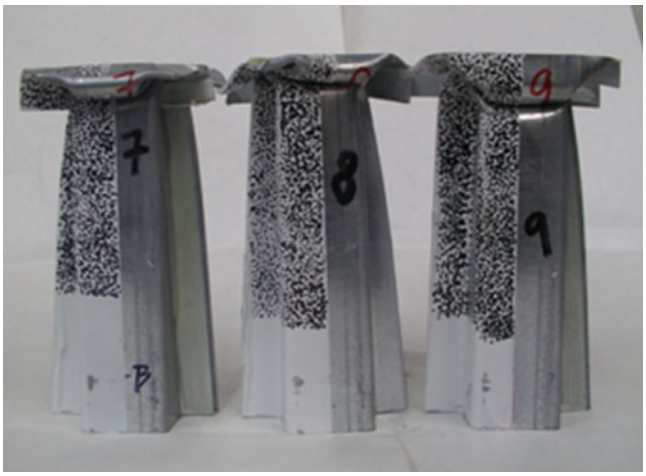

Fig. 27.8 Impacted tubes, experiments

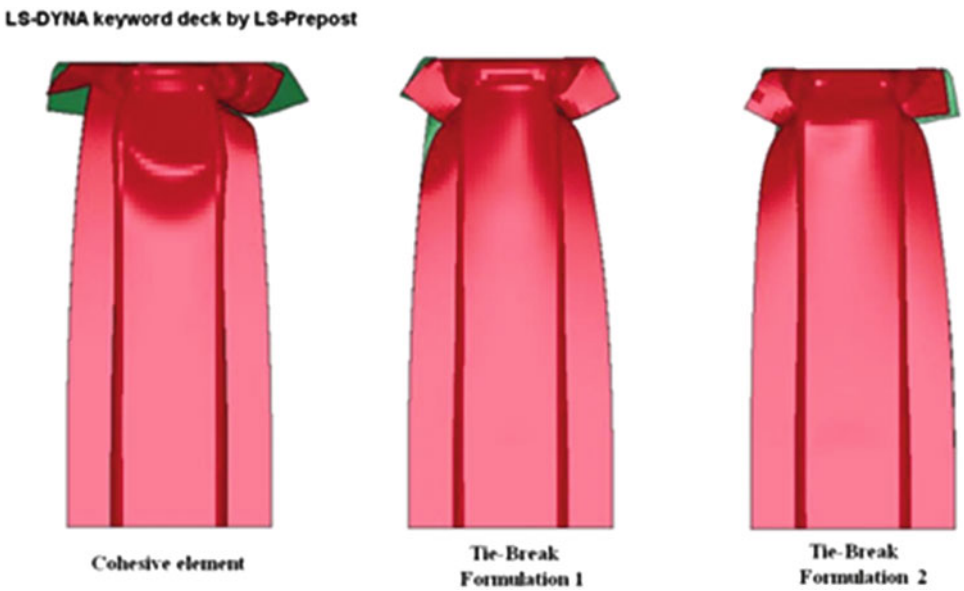

Fig. 27.9 Impacted tubes, simulations. From *left to right*: cohesive element, TB1 and TB2

Table 27.3 Summary dynamic impact for structures bonded with DP-460NS; simulation versus experiment results

	Hats			
Measurement	Exp	Coh	TB1	TB2
Energy absorb [kJ]	1.480	1.450	1.460	1.460
Specific energy abs [kJ/kg]	3.370	3.300	3.320	3.320
Mean force [kN]	33.10	37.96	39.92	36.54
Peak force [kN]	136.2	159.8	156.6	160.1

27.5 Discussion

It has been shown that the use of numerical models to accurately represent a structure subjected to impact loads is certainly within the capability of current software codes. Numerical codes provide designers with a high level of flexibility, allowing them to explore many different aspects of an impact event without the need for expensive experimental set ups.

During this study the results between simulation and experiment were in good agreement, although a few differences were noticed. It is important that the selected material model can accurately capture the behavior of the materials in the structure and that the geometries and loads depicted by the model are as close as possible to the actual experiment. In some cases, high sensitivity to small geometric differences was noted.

Many different numerical representations are available for adhesive materials including cohesive elements and different tie-break options. The implementations investigated provided accurate prediction for structural performance at the macro level. By this, it should be understood that the load–displacement diagram generated by the model and the predicted deformations were in good agreement with the actual structure under the same loading conditions as in the actual experiment.

The numerical implementations investigated did not consider strain rate effects. While this is not important for quasi-static events, strain rate effects can be important for dynamic conditions. Although the model did not account for strain rates in the adhesive material, strain rates generated in the dynamic test were low enough that it made no significant difference between the experiments and the simulations. At higher velocities, or for different joint designs, strain rates could have a more significant impact. As was previously shown, the mechanical properties of this particular adhesive are sensitive to strain rate, which suggests that models must include provisions for strain rate effects.

To obtain a better insight into joint stresses, crack propagation and bond failure, a more complex model is required, ideally a series of solid elements with the proper material model. At this level of detail, the material description will require properties that are join dependent, such as the appropriate traction separation curve, besides the intrinsic properties of the material itself such as yield stress and energy release rate in the required range of expected strain rates.

In global terms, either cohesive elements or tie-breaks can accurately predict crush tube structure responses, and capture the behavior of the adhesive joint, but cannot provide a more detailed description of the failure process inside the material. Material damage mechanisms such as crazing and shear bands which are typical of epoxy materials during loading need to be characterized and understood before more detailed modeling can be implemented. Unfortunately, models assembled in the manner described in this work do not produce any insights regarding the damage mechanism that triggers ultimate failure. At this point, further research is required to characterize damage in epoxy materials and to understand how these failure modes would be affected by changes in dynamic load rates and by the interaction of different materials in the joint.

Acknowledgement The authors gratefully acknowledge the use of SHARCNET computing facilities, material testing undertaken by Jeff Wemp and Christopher Thom, and support from the Ontario Centre's of Excellence (OCE) and 3M Company.

References

1. Cui X, Zhang H, Wang S, Zhang L, Ko J (2011) Design of lightweight multi-material automotive bodies using new material performance indices of thin-walled beams for the material selection with crashworthiness consideration. Mater Des 32:815–821
2. Shariatpanahi M, Masoumi A, Ataei A (2008) Optimum design of partially tapered rectangular thin-walled tubes in axial crushing. Proc Inst Mech Eng Part B J Eng Manuf 222:285–291
3. Peroni L, Avalle M (2006) Experimental investigation of the energy absorption capability of bonded crash boxes. Trans Built Environ 87:445–454
4. Avalle M, Peroni L, Peroni M, Scattina A (2010) Bi-material joining for car body structures: experimental and numerical analysis. J Adhes 86:539–560

5. Peroni L, Avalle M, Belingardi G (2009) Comparison of the energy absorption capability of crash boxes assembled by spot-weld and continuous joining techniques. Int J Impact Eng 36:498–511
6. Belingardi G, Goglio L, Rossetto M (2005) Impact behaviour of bonded built-up beams: experimental results. Int J Adhes Adhes 25:173–180
7. Abramowicz W, Jones N (1997) Transition from initial global bending to progressive buckling of tubes loaded statically and dynamically. Int J Impact Eng 19:415–437
8. Trimiño L (2012) Analysis and performance of adhesively bonded crush tube structures. University of Waterloo, Waterloo
9. Livermore software technology corporation (LSTC) (2007) LS-DYNA Keyword user manual material models version 971. Livermore software technology corporation (LSTC)
10. Rahman NM, Mian A, Newaz GM (2004) Analysis and characterization of adhesively bonded Mg-steel lap joints. In: Proceedings of the ASME international mechanical engineering congress, vol 117, Anaheim, 13–19 Nov 2004, pp 129–35
11. Jones N (1989) Structural impact. Cambridge University Press, Cambridge
12. Abramowicz W, Jones N (1984) Dynamic axial crushing of square tubes. Int J Impact Eng 2:179–208
13. White MD, Jones N (1999) Experimental quasi-static axial crushing of top-hat and double-hat thin-walled sections. Int J Mech Sci 41:179–208
14. White MD, Jones N (1999) A theoretical analysis for the dynamic axial crushing of top-hat and double-hat thin-walled sections. Proc Inst Mech Eng Part D J Automob Eng 213:307–325
15. Tarigopula V, Langseth M, Hopperstad OS, Clausen AH (2006) Axial crushing of thin-walled high-strength steel sections. Int J Impact Eng 32:847–882

Chapter 28
Dynamic Buckling of Submerged Tubes due to Impulsive External Pressure

Neal P. Bitter and Joseph E. Shepherd

Abstract An annular geometry is used to experimentally study fluid-structure interaction and dynamic buckling of tubes submerged in water and subjected to axially-propagating pressure waves. Wave propagation, vibration, and buckling of the specimen tubes are characterized using pressure and strain measurements. Emphasis is placed on pressures near or slightly exceeding the buckling threshold, where buckling deformation is excited but remains elastic or only slightly plastic due to the short duration of the pressure pulse. Measured wave speeds and non-axisymmetric vibration frequencies are in good agreement with predictions from simple fluid-structure interaction models. Near the buckling threshold, the amplitude of non-axisymmetric deformation is observed to grow rapidly with small increases in pressure until plastic deformation occurs, which results in a substantial loss of strength of the tube. Systematic mode 2 variations in wall thickness are found to control the buckle orientation, since the major axis of mode 2 buckles is always aligned with the location where the tube wall is thinnest.

Keywords Dynamic buckling • Fluid-structure interaction • Buckling threshold • Imperfect structures • Impulsive loads

28.1 Introduction

Submerged cylindrical tubes and pipes are routinely used in a variety of marine applications, such as submersible vehicles, drilling and mining equipment, and trans-ocean pipelines and communication networks. In addition to withstanding the hydrostatic pressure of the target environment, many of these submerged structures must also survive dynamic loads, such as those due to underwater blasts. In this paper, a unique annular geometry and projectile impact facility is used to study the buckling of cylindrical tubes under these types of load conditions.

Dynamic buckling of tubes subjected to external blast waves has been studied by a number of researchers. Lindberg investigated buckling of very thin shells with ratios of radius to thickness of about $a/h = 480$ and found that the response was governed by elastic effects alone [1]. For much thicker tubes with $a/h = 10{-}30$, Abrahamson et al. found that the buckle development is dominated by the effects of plasticity [2]. For intermediate cases, the behavior is more complex since both elastic and plastic effects are important [3]. In addition to studying various tube geometries, experiments have also been conducted under a wide range of load conditions, ranging from impulsive to quasi-static [4–7].

A significant challenge in the experiments cited above was making comparisons between experimental measurements and theoretical predictions. In most of the experiments, the response of the tube was analyzed only by post-collapse examination, so the behavior during the initial stages of buckling could not be evaluated. In a few cases [4, 8], strain measurements were taken as the tube buckled, but only limited data was reported. In the present experiments, tubes are loaded using shock waves in water rather than blast waves in air, which facilitates dynamic strain measurement during the buckling of the tube. These experiments also explore the effects of fluid-structure interaction that are introduced by the presence of a dense fluid surrounding the tube.

N.P. Bitter (✉) • J.E. Shepherd
California Institute of Technology, 1200 E. California Blvd, Pasadena, CA 91125, USA
e-mail: nbitter@caltech.edu; joseph.e.shepherd@caltech.edu

B. Song et al. (eds.), *Dynamic Behavior of Materials, Volume 1: Proceedings of the 2013 Annual Conference on Experimental and Applied Mechanics*, Conference Proceedings of the Society for Experimental Mechanics Series,
DOI 10.1007/978-3-319-00771-7_28,

28.2 Experimental Setup

In this paper, buckling of tubes is studied using shock waves in an annulus of water surrounding a specimen tube. The apparatus, shown in Fig. 28.1, consists of a thin-walled specimen tube mounted concentrically inside of a larger, thick-walled cylindrical vessel. The outer vessel is made from 4140 high strength steel and has an inner radius of 38.1 mm, wall thickness of 25.4 mm, and length 0.97 m. Specimen tubes are mounted concentrically inside of this vessel, and the ends of the specimen are supported and sealed using internal plugs with gland seals. These plugs restrict inward radial motion of the specimen tube at its ends, but they do not constrain axial motion. However when the tube compresses under external pressure, friction between the inside of the specimen tube and these plugs may constrain axial motion as well. The upper plug, located on the left side of Fig. 28.1, is mounted to a support plate which prevents axial loads on the specimen tube. As shown in the inset photograph, this support plate features four holes which allow pressure waves to pass through with minimal obstruction.

The annular gap between the specimen tube and the outer cylinder is filled with distilled water, and a buffer is inserted into the top of the fixture. A vertically oriented gas gun then fires a projectile into the buffer, which produces a stress wave in the buffer that is then transmitted into the water. The gas gun, described in more detail in Ref. [9], consists of a vertically oriented barrel (50 mm inner diameter) connected to a compressed air reservoir. A 1.5 kg, 120 mm long steel projectile with a flat front is used and is sealed against the gas gun barrel by a pair of o-rings. Prior to the shot, the gas gun's chamber behind the projectile is evacuated so that the projectile is held in place by the vacuum. The compressed air reservoir is then charged to the desired initial pressure, typically between 140 and 350 kPa. Finally, remotely operated valves close the vacuum line and connect the air reservoir to the chamber, launching the projectile down the tube. Typical projectile speeds are between 6 and 30 m/s.

As the projectile emerges from the gas gun barrel, it impacts the buffer shown in Fig. 28.1. The buffer is 76 mm in diameter and 127 mm long, made from either 6061-T6 aluminum or 304 stainless steel, and capped with a steel striker plate to prevent damage during the projectile impact. During impact, a compressive stress wave is produced in the buffer which is then transmitted into the water. This shock wave then passes through the holes in the support plate and travels axially along the outside of the specimen tube. The pressure pulse consists of sharp shock wave followed by an approximately exponential decay of pressure, and the time constant of this decay is governed by the wave mechanics in the projectile and buffer. Thus by changing the lengths and materials of these two components, the duration of the pressure pulse can be adjusted. Unless stated otherwise, the results in this paper were obtained using a 6061-T6 aluminum buffer.

The pressure load applied to the specimen tube is measured using a row of six pressure transducers (PCB model 113A23) which have a response time less than 1 μs and a resonant frequency greater than 500 kHz. These transducers are positioned in increments of 150 mm along the thick-walled outer tube and are mounted flush with the inner surface of that tube. Since the annulus of water between the specimen tube and the outer cylinder is only 15–20 mm in width, the radial transit time of pressure waves is 10–15 μs, which is much shorter than the other timescales involved in the response of the tube and the motion of the pressure wave. As a result, the pressure measured by the transducers is expected to be very close to the actual pressure at the surface of the specimen tube.

The response of the specimen tube is measured using bonded strain gauges which are coated with a compliant sealant (Vishay PG, M-Coat D) to prevent degradation of the adhesive and electrical interference due to the surrounding water. Strain measurements are amplified using a Vishay 2310B signal conditioner operated in wide-band mode, which corresponds to a − 3 dB cutoff frequency of 250 kHz. All pressure and strain signals are simultaneously digitized at 1 MHz.

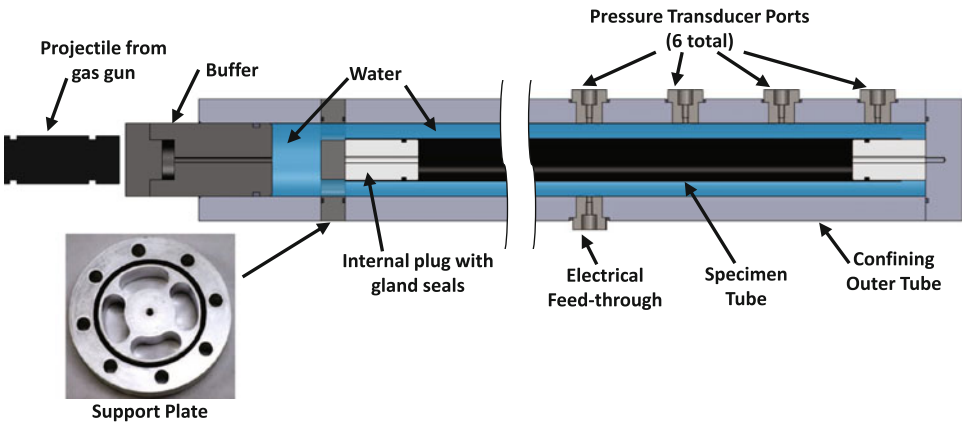

Fig. 28.1 Diagram of experimental apparatus. *Inset* photograph shows a support plate used to prevent axial loading of the specimen tube

Table 28.1 Properties of specimen tubes. Static buckling threshold p_{static} calculated using Eq. 28.1

Tube number	Material	Mean radius a [mm]	Wall thickness h [mm]	a/h	p_{static} [MPa]
30	6061-T6 Alum.	15.4	0.89	17.4	3.67
32	6061-T6 Alum.	21.8	0.89	24.5	1.31
34	6061-T6 Alum.	21.8	0.89	24.5	1.31
36	304 Stainless	15.4	0.89	17.4	10.0
42	6061-T6 Alum.	15.4	0.89	17.4	3.67
43	6061-T6 Alum.	15.4	0.89	17.4	3.67
46	6061-T6 Alum.	21.8	1.24	17.5	3.61
47	6061-T6 Alum.	21.8	0.89	24.5	1.31
50	6061-T6 Alum.	21.8	0.89	24.5	1.31
52	6061-T6 Alum.	21.8	0.89	24.5	1.31
54	304 Stainless	21.6	1.17	18.5	8.16

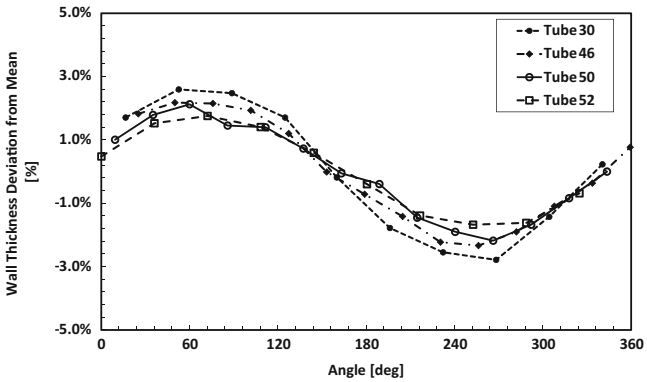

Fig. 28.2 Variations in wall thickness around the circumference of four specimen tubes. Variations are reported as percentages of the mean wall thickness

28.2.1 Specimen Tubes

Specimen tubes were made from either 6061-T6 aluminum or 304 stainless steel and were 0.91 m long. The dimensions of the tubes discussed in this paper are listed in Table 28.1. A key parameter affecting the buckling behavior is the ratio a/h, which falls in the range of 17–25 in these experiments.

28.2.2 Wall Thickness Variations

It is well-known that tube imperfections play a critical role in determining the static buckling limit [10, 11] and are expected to play a similarly important role in dynamic buckling. One important type of imperfection is the shape imperfection, which consists of an initial non-circularity of the tube in the absence of applied loads. A second type of imperfection is wall thickness variation, in which the wall thickness varies around the circumference of the tube.

In an effort quantify these imperfections, the wall thickness of each tube was measured at various points around the circumference using a round-tipped micrometer. Aluminum tubes, which were manufactured seamlessly by extrusion, featured systematic variations in wall thickness around the circumference. The size of these variations was typically 2–4 % of the mean wall thickness for 6061-T6 aluminum, though for other alloys variations as high as 10 % were observed. A sampling of these measurements demonstrating the sinusoidal variation of wall thickness is provided in Fig. 28.2. These systematic variations appear to be uniform, or at least slowly varying, along the axis of the tube since the wall thickness profile is similar at both ends. No attempt was made to measure the shape imperfection of the tubes, i.e., the deviation from

circularity. However, the wall thickness variation appears to the most important imperfection since, without exception, tubes that buckled in a mode 2 shape formed buckles that were aligned with the points of minimum and maximum wall thickness.

The steel tubes selected for this experiment were of welded construction, and systematic wall thickness variations were not observed. Instead, the wall thickness was close to uniform around the circumference except in the vicinity of the weld, where a localized region of lesser wall thickness was measured. Although for some tubes the buckles were exactly aligned with the welds, this was not exclusively the case.

28.3 Results

Depending on the amplitude and impulse of the pressure wave, the response of the specimen tubes can be divided into several regimes. For low enough pressures, the tube remains axisymmetric during the entire response. At moderate pressures, elastic buckles begin to develop, but if the impulse of the load is small these buckles do not grow large enough to induce plastic deformation. As the pressure or impulse is increased further, however, plastic deformation will eventually occur. Finally, for very large pressures the tube collapses catastrophically during a single load event.

28.3.1 Linear Elastic Regime

For pressure waves of small amplitude or low impulse, the tube's response is elastic and primarily axisymmetric. Examples of pressure and strain traces in this regime are plotted in Fig. 28.3. Figure 28.3a shows that the pressure wave has the form of an exponential that travels along the tube with approximately fixed speed and shape. The pressure wave then reflects off of the bottom end of the test fixture and traverses the specimen tube once more.

The classical static buckling pressure for a long tube is given by [12]:

$$p_{static} = \frac{Eh^3}{4a^3(1-\nu^2)} \tag{28.1}$$

For the tube corresponding to Fig. 28.3, the static buckling pressure is only about 3.7 MPa while the peak measured pressure is about 5 MPa. As will be demonstrated in subsequent sections, buckling does not occur because non-axisymmetric deformation grows too slowly to become significant during the short duration of the pressure load.

Figure 28.3b shows the corresponding hoop strain traces at seven locations along the tube. The strain traces appear to mirror the pressure traces, with the exception of high frequency vibrations that are more prominent in the strain measurements than in the pressure traces. For these low pressures, the response is analogous to that of a waterhammer

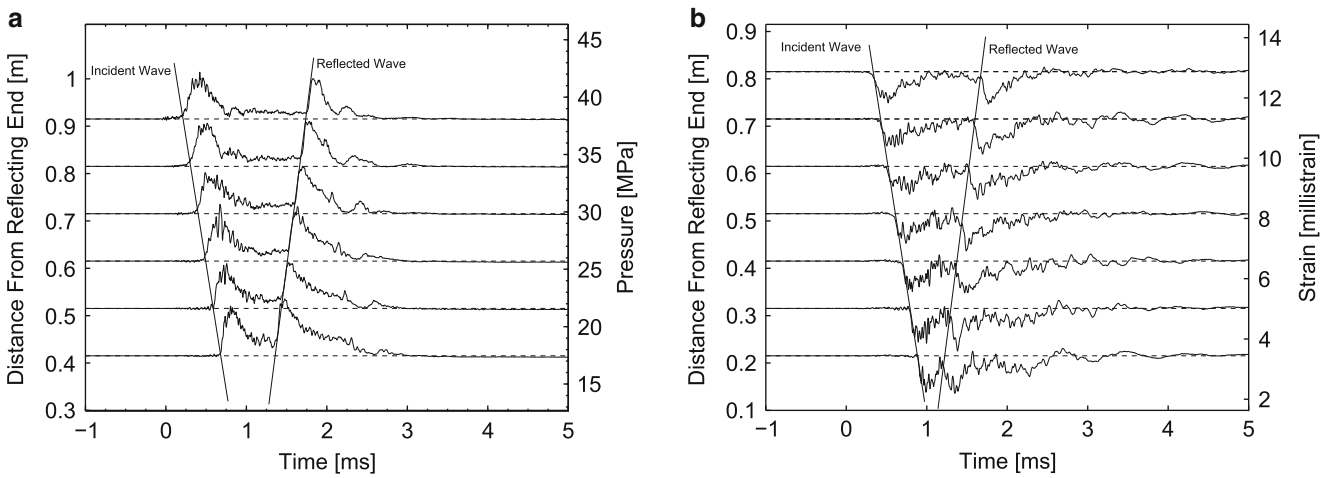

Fig. 28.3 Pressure (**a**) and strain (**b**) histories for Tube 42. The peak pressure is 5.0 MPa and the static buckling pressure is 3.67 MPa

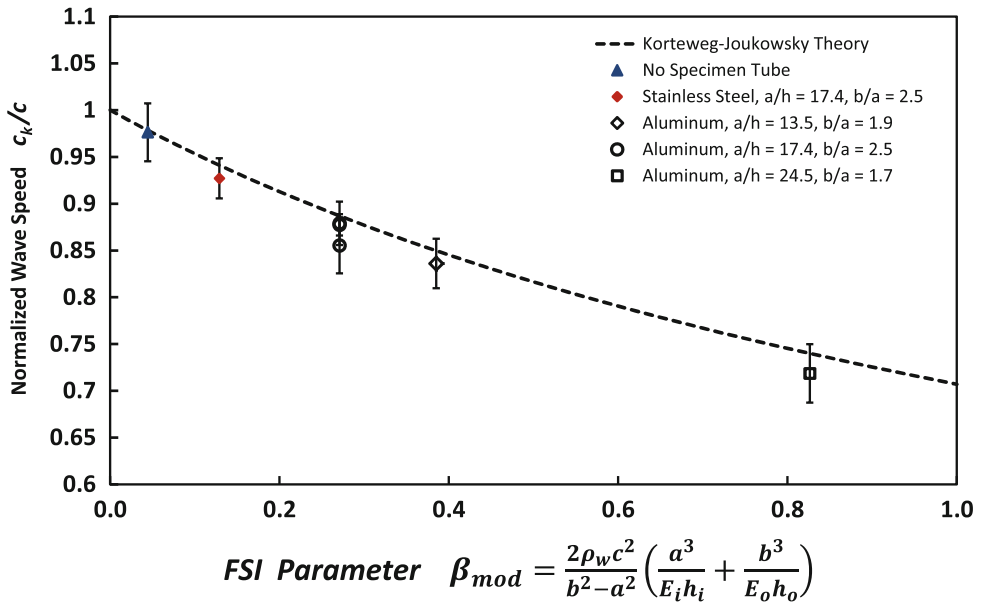

Fig. 28.4 Comparison of measured wave speeds with the predictions of the modified Korteweg-Joukowsky theory for several tube materials and sizes

event occurring on the inside of a tube. Inaba and Shepherd studied this scenario using a very similar projectile impact facility [9] and recorded pressure and strain traces that look very similar to those of Fig. 28.3.

The similarity between the present results and the response of a tube during a waterhammer-type event suggests that for low pressures in which buckling does not occur, the response may be predicted using suitably adapted waterhammer models. One of the simplest waterhammer models was first proposed by Korteweg [13] and later applied to waterhammer experiments by Joukowsky [14]. Commonly termed the Korteweg-Joukowsky model, this theory is based on the assumptions that radial inertia of the tube and fluid as well as axial bending of the tube are small [15]. Under these approximations, the speed c_{KJ} of the coupled fluid-solid wave is given by:

$$c_{KJ} = \frac{c}{\sqrt{1+\beta}} \tag{28.2}$$

where

$$\beta = \rho_w c^2 \frac{2a}{Eh} \tag{28.3}$$

Here c and ρ_w are the acoustic speed and density of the water, E is the elastic modulus of the tube, and a and h are the mean radius and wall thickness. The parameter β describes the extent of the fluid-solid coupling, which increases as β increases and hence reduces the velocity of the wave motion. This model can be adapted for the current experimental setup in which pressure waves propagate in the annular space between two flexible tubes. The speed of these pressure waves is still in the form of (28.2), but the fluid-structure interaction parameter β must be replaced with a modified parameter given by:

$$\beta_{mod} = \frac{2\rho_w c^2}{b^2 - a^2}\left(\frac{a^3}{E_i h_i} + \frac{b^3}{E_o h_o}\right) \tag{28.4}$$

where a and b are the mean radii of the inner and outer tubes, and the properties of these tubes are designated by subscripts i and o. Note that if the inner tube is made very small ($a \to 0$), then the original Korteweg-Joukowsky theory of (28.3) is recovered.

The predictions of this model are compared with experimental measurements in Fig. 28.4 and agree quite favorably, with errors less than 1–4 %. The fact that the measured wave speeds are consistently lower than the predictions is due to small air bubbles in the water, which accumulate as the vessel is filled. These bubbles are difficult to eliminate since even a very small void fraction can significantly reduce wave speeds [16], though this effect is somewhat less significant for shock waves of finite strength [17].

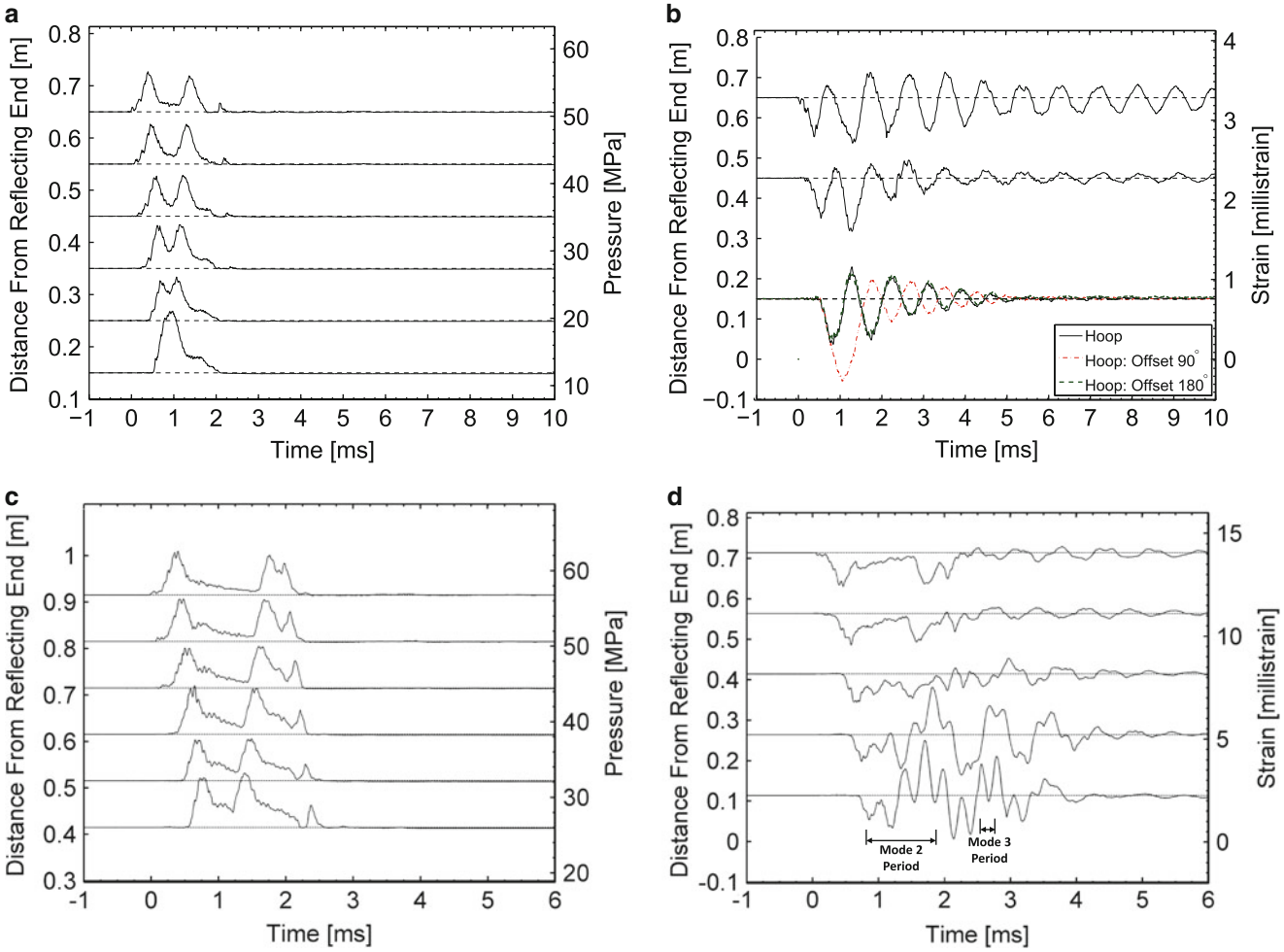

Fig. 28.5 (**a**) and (**b**): Pressure and hoop strain traces for Tube 54 showing mode 2 elastic vibrations. (**c**) and (**d**): Pressure and hoop strain traces for Tube 30 showing superposition of buckles in modes 2 and 3

28.3.2 Nonlinear Elastic Regime

Increasing the amplitude or duration of the pressure wave further results in excitation of elastic buckles. Pressure and strain measurements in this regime are shown in Fig. 28.5. In Fig. 28.5a, b, the response of a welded stainless steel tube (Tube 54) is shown. The tube develops a mode 2 buckle which remains elastic throughout the response, and when the pressure wave dies away the tube continues to vibrate in this mode 2 shape. The fact that the buckle consists of two lobes is confirmed by examining the three strain traces located 150 mm from the reflecting end of the tube. At this location, three hoop strain gauges were attached at three positions around the tube circumference: the first guage was located at the weld where a local minimum in wall thickness was measured, and the other two gauges were spaced in increments of 90°. For this tube, the buckle was aligned exactly with the weld (though this was not always the case for welded tubes) and the strain traces measured at the weld and 180° away are exactly in phase, while the strain trace between them is exactly out of phase. This indicates that the buckle is in a mode 2 shape.

In Fig. 28.5c, d, pressure and strain traces are shown for an aluminum tube (Tube 30) in which the peak pressure was about twice the static buckling pressure (3.7 MPa). In this case, elastic buckles of both modes 2 and 3 were simultaneously excited near the bottom end of the tube.

The frequencies of elastic vibration in modes 2 and 3 were extracted from the experimental strain traces using either a fast Fourier transform or by counting periods, depending on the number of cycles that were present in the data. To compare these measured frequencies with theoretical predictions, the tube was modeled using the shell equations of Sanders [18] which are

appropriate for low circumferential wavenumbers n. The circumferential displacement v, radial displacement w, and pressure p are taken to be harmonic vibrations of the following form:

$$\begin{aligned} v &= V \sin(n\theta)\cos(\omega t) \\ w &= W \cos(n\theta)\cos(\omega t) \\ p &= P \cos(n\theta)\cos(\omega)t \end{aligned} \tag{28.5}$$

in which case the equations of Sanders can be expressed as:

$$\begin{bmatrix} \Omega^2 - n^2(1+\alpha^2) & -n(1+\alpha^2 n^2) \\ n(1+\alpha^2 n^2) & 1+\alpha^2 n^4 - \Omega^2 \end{bmatrix} \begin{bmatrix} V \\ W \end{bmatrix} = -\frac{Pa^2(1-\nu^2)}{Eh} \begin{bmatrix} 0 \\ 1 \end{bmatrix} \tag{28.6}$$

where $\alpha^2 = h^2/12a^2$ is the shell parameter and Ω is the ratio of the frequency ω to the natural frequency of axisymmetric vibration:

$$\Omega \equiv \omega \sqrt{\frac{\rho a^2(1-\nu^2)}{E}} \tag{28.7}$$

The annulus of fluid was modeled using the linear wave equation for the velocity potential ϕ:

$$\frac{1}{c^2}\frac{\partial^2 \phi}{\partial t^2} = \frac{\partial^2 \phi}{\partial r^2} + \frac{1}{r}\frac{\partial \phi}{\partial r} + \frac{1}{r^2}\frac{\partial^2 \phi}{\partial \theta^2} \tag{28.8}$$

which is subject to velocity boundary conditions at the inner ($r = a$) and outer ($r = b$) surfaces of the fluid annulus:

$$\left.\frac{\partial \phi}{\partial r}\right|_{r=a} = \left.\frac{\partial w}{\partial t}\frac{\partial \phi}{\partial r}\right|_{r=b} = 0 \tag{28.9}$$

The velocity potential ϕ is assumed to be of the form:

$$\phi(r, \theta, t) = \Phi(r)\cos(n\theta)\cos(\omega t) \tag{28.10}$$

Using using standard techniques from the theory of acoustics [19], the pressure at the surface of the specimen tube ($r = a$) is found to be:

$$P = \rho_w \omega^2 W \left[\frac{J_n(\gamma a)Y_n'(\gamma b) - J_n'(\gamma b)Y_n(\gamma a)}{J_n'(\gamma a)Y_n'(\gamma b) - J_n'(\gamma b)Y_n'(\gamma a)}\right] \tag{28.11}$$

where J_n and Y_n are nth order Bessel functions of the first and second kind and $\gamma = \omega/c$ is the radial wavenumber. Equations (28.6) and (28.11) constitute an eigenvalue problem for the frequency ω of vibration which can be solved numerically. The procedure used to derive Eqs. (28.6) and (28.11) and solve for the eigenvalues follows closely that of Warburton [20], who studied the vibration of tubes either containing a liquid or submerged in an infinite medium. The present analysis extends that method by considering an annulus of fluid and using shell equations which are better suited for low circumferential wavenumbers. Table 28.2 compares the experimentally measured frequencies of vibration in modes 2 and 3 with the lowest eigen-frequency from this model, and good agreement is found.

28.3.3 Slightly Plastic Regime

To investigate the behavior very close to the onset of plastic deformation, a single tube was subjected to successive shots of gradually increasing pressure until plastic deformation first occurred. Pressure and strain traces from this shot sequence are shown in Fig. 28.6.

Table 28.2 Comparison of predicted and measured vibration frequencies in modes 2 and 3. The corresponding dimensions and materials are available in Table 28.1

Tube number	Mode number n	Predicted frequency [kHz]	Measured frequency [kHz]	Error [%]
30	2	1.28	1.24	3.0
30	3	4.05	3.97	2.0
34	2	0.53	0.54	2.4
34	3	1.76	1.85	4.7
36	2	1.75	1.82	3.8
43	2	1.28	1.20	6.4
46	2	0.86	0.85	1.2
46	3	2.84	2.82	0.7

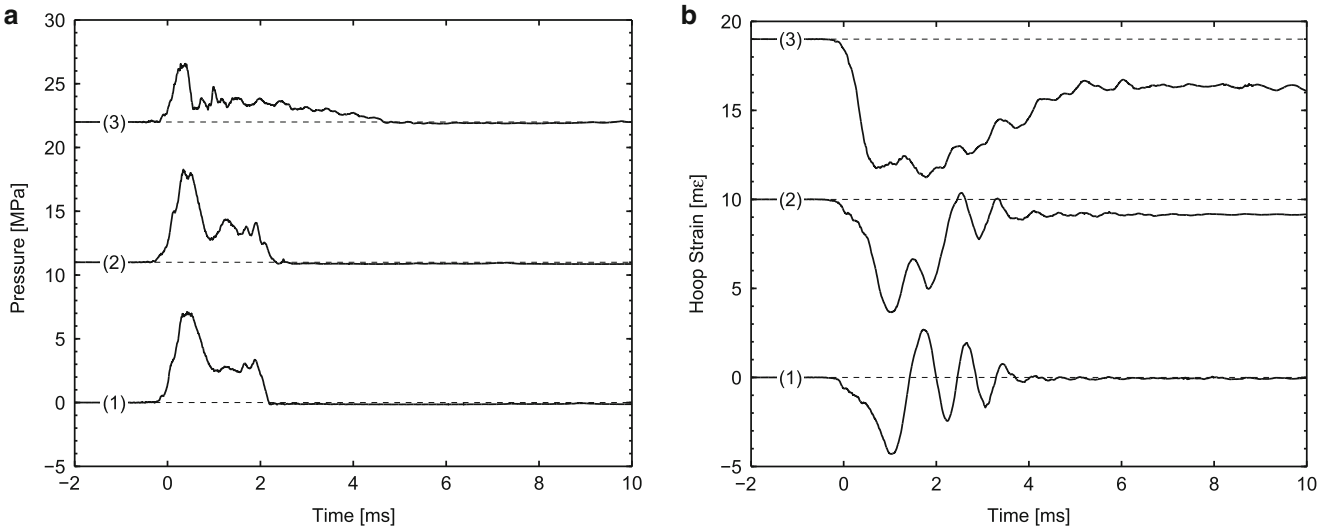

Fig. 28.6 Pressure (**a**) and strain (**b**) traces for three consecutive shots using Tube 52 in which the pressure was gradually increased from shot to shot. Strain data was recorded 0.25 mm from the reflecting end of the tube, while pressure data was recorded at 0.15 m. Pressure and strain traces have been offset vertically for clarity

In the first shot, marked (1), mode 2 vibrations were excited but remained purely elastic with a peak measured strain of 4.3 millistrain, which is slightly below the yield value of about 4.5 millistrain for 6061-T6 aluminum. In the second shot (2), the peak measured strain was 6.3 millistrain and slight plastic deformation occurred, as evidenced by the final strain offset at the end of the trace. This offset is the result of residual stresses that are produced when the tube returns to its unloaded configuration after experiencing plastic deformation. It is worth noting that the pressure wave remains unchanged despite the occurrence of plastic deformation; however, the buckle grew slowly enough that plastic deformation did not occur until long after the arrival of the incident shock wave.

In the third shot (3), the peak strain was about 7.7 millistrain and further plastic deformation occurred. In this case, the peak measured pressure dropped by about 40 % relative to shot (2), despite a 5 % increase in the velocity of the projectile from the gas gun. Furthermore, the pressure wave dispersed considerably and decayed more slowly over time than in previous shots, indicating a strong interaction between the shock wave and the buckle. In spite of the considerable reduction in peak pressure, substantial plastic deformation was produced which demonstrates the reduction in the strength of the tube upon incidence of plastic deformation.

The progression of peak strains across the elastic and plastic regimes described above can be illustrated by plotting the peak measured strain against the peak measured pressure, as shown in Fig. 28.7. For low pressures, the peak strain is close to the static value given by:

$$\epsilon_{static} = \frac{pa(1-\nu^2)}{Eh} \tag{28.12}$$

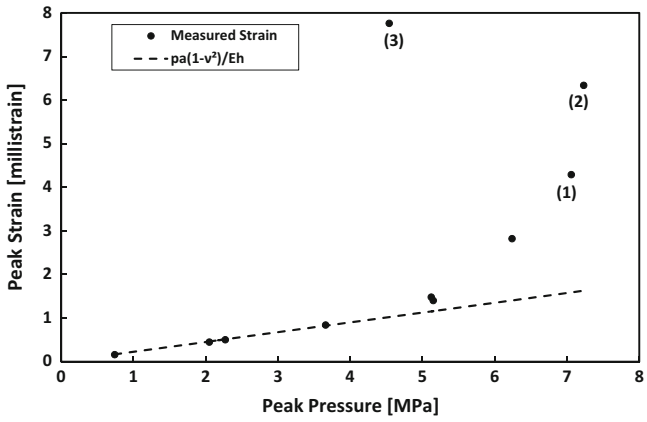

Fig. 28.7 Progression of peak strains as peak pressure is increased for Tube 52. Static buckling pressure is 3.67 MPa. Numbers in parenthesis correspond to the strain traces shown in Fig. 28.6

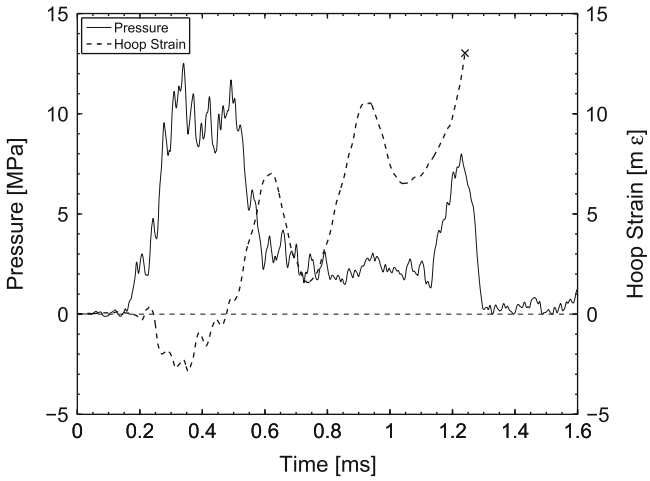

Fig. 28.8 Pressure and strain traces for a collapsing tube (Tube 43) with a static buckling pressure of 3.7 MPa. Pressure and strain were measured 150 mm from the top end of the specimen tube. The strain gauge de-bonded from the surface of the tube at the point marked by an **x**

At about the static buckling threshold (in this case, 3.67 MPa) the strain begins to deviate from the linear trend, but this deviation initially remains small since the buckles do not grow rapidly enough to become significant during the short load duration. However, the peak strain appears to grow exponentially with pressure, so eventually large increases in strain are observed which bring the tube into the plastic range. In Fig. 28.7, the numbered points correspond to the strain traces shown in Fig. 28.6, where the onset of plastic deformation was examined. As shown at point (3), plastic deformation of the tube results in a considerable reduction of the peak pressure. However, the reduction in pressure and dispersion of the pressure wave may not be entirely due to deformation generated during shot (3), but may also involve the plastic deformation that remains from the preceding shot (2).

28.3.4 Collapse

The final regime of motion considered is that of pressures much greater than the buckling threshold. Examples of pressure and strain traces are shown in Fig. 28.8. The strain trace exhibits a sequence of vibrations superimposed over an offset that increases with time. Based on the frequency of these vibrations and the 3-lobed shape of the tube after collapse (shown in Fig. 28.9), these are interpreted as mode 3 vibrations. Even at this high pressure, the buckle appears to grow on a time-scale that is slow compared to motion of the pressure wave. For instance, the leading edge of the pressure wave has traveled nearly 0.5 m away from this location by the time the yield strain (about 4.5 millistrain) is first reached. This suggests that the incident pressure wave is not strongly affected by the development of buckles. However the reflected pressure wave, which arrives at about 1.2 ms, interacts with the buckle and its amplitude is reduced considerably.

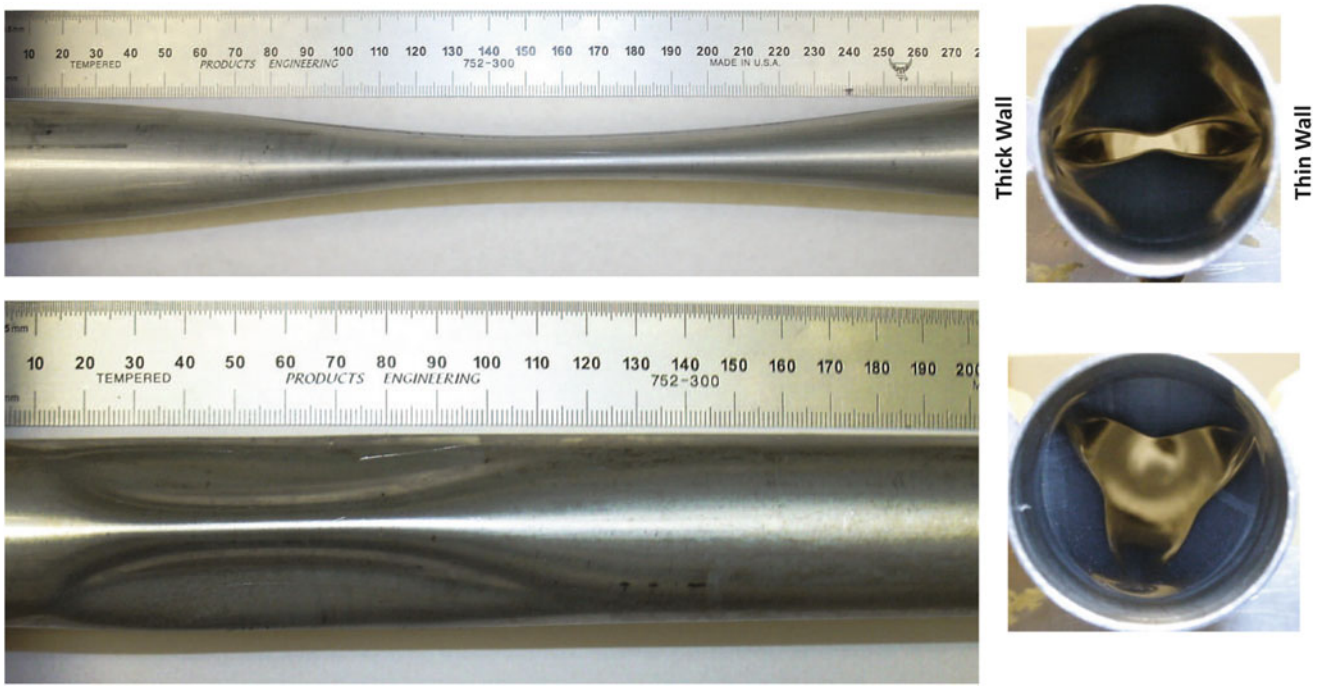

Fig. 28.9 Post-collapse photographs of Tube 37 (*top*) and Tube 43 (*bottom*) buckled in modes 2 and 3. The *bottom* photographs were taken following the test which generated the data plotted in Fig. 28.8. The thickest and thinnest points on the tube wall of the *top* photograph are indicated, demonstrating the alignment of the buckle with these points

Post-collapse photographs of tubes buckled in modes 2 and 3 are shown in Fig. 28.9. In the top pair of photographs, the thickest and thinnest points along the tube wall are indicated and the buckle is seen to align with these points. For extruded tubes, which featured sinusoidal wall-thickness variations around the circumference, alignment of the buckle with the points of maximum and minimum wall thickness was always observed for mode 2 buckles, indicating that this type of imperfection plays the dominant role in determining the orientation of the buckle. For mode 3 buckles, no clear trend was observed regarding the orientation of the buckle relative to the tube's wall thickness variations.

As shown in Fig. 28.9, the length of mode 2 buckles (about 8–10 tube diameters) is much longer than the length of mode 3 buckles (3–4 tube diameters). For a given mode number, these ratios of buckle length to tube diameter did not change significantly as the pressure was increased or the tube diameter changed.

28.3.5 Measurements of the Buckling Threshold

To make measurements of the buckling threshold, multiple shots were conducted on a single tube while gradually raising the peak pressure by increasing the projectile velocity from the gas gun. This was done until plastic deformation was first reached, at which point the tube was considered to be buckled. Each shot was characterized by its peak pressure and impulse, where the impulse was computed by integrating the pressure trace over the first 15 ms of data. The point at which buckling occurred can then be represented on a plot of pressure vs. impulse.

The results of this approach are shown in Fig. 28.10 for tubes with $a/h = 24.5$. Each line of data points represents a sequence of consecutive shots in which the projectile velocity from the gas gun was gradually increased, and the points marked by a black **x** mark the onset of plastic deformation, and hence represent points on the buckling threshold. As shown in the figure, the peak pressure and impulse increase in proportion to one another, which is expected since the apparatus operates at an approximately fixed load duration which is governed by the wave mechanics in the projectile and buffer.

One way to control ratio of peak pressure to peak impulse (i.e., the slope on the pressure-impulse diagram) is to change the lengths or materials of the buffer and projectile (see Fig. 28.1). For Tube 47 in Fig. 28.10 the usual aluminum buffer was used which was employed in all prior results presented in this paper. However, to obtain the data for Tube 50, a steel buffer was used instead, which reduced the slope on the pressure-impulse diagram and allowed a second point on the buckling

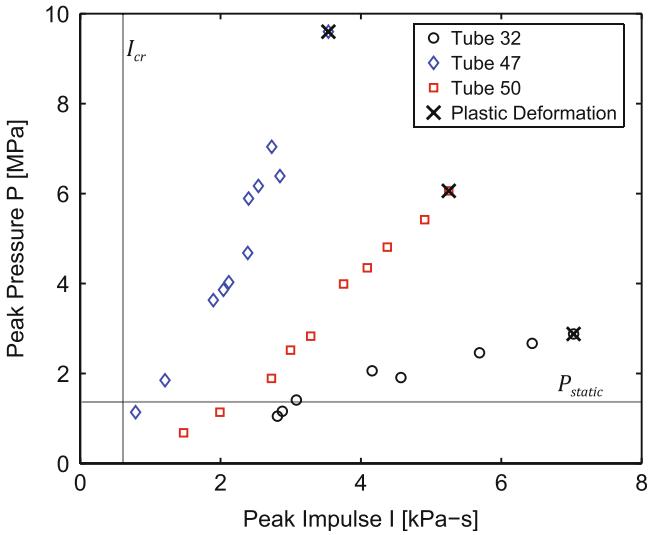

Fig. 28.10 Pressure vs. impulse curves for three identical aluminum tubes with radius $a = 22$ mm and $a/h = 24.5$. The static buckling threshold for these tubes is 1.3 MPa. Tube 47 was tested with an aluminum buffer, Tube 50 with a steel buffer, and Tube 32 in an alternate apparatus, allowing various regions of the pressure-impulse space to be reached. *Black* **x** marks points at which plastic deformation first occurred

threshold to be found. A third point on the buckling threshold was found using Tube 32 and an even smaller slope was achieved by making measurements in an alternate test apparatus which is very similar to that shown in Fig. 28.1, but features windows for visualizing the buckling process. The compliance of these windows reduces the speed of the pressure waves and increases the impulse for a given peak pressure.

The three tubes tested in Fig. 28.10 were identical, so differences in the peak pressure at which buckling occurred are caused only by the change in impulse of the pressure wave. For the shortest impulse tested, the peak pressure required to buckle the tube was about seven times the static buckling threshold, which highlights the importance of inertial effects. The trend observed in these results agrees with the theoretical predictions of [7], which show that for large impulses the dynamic buckling threshold tends towards the static buckling pressure (1.3 MPa in this case), while for small impulses the threshold approaches a vertical asymptote at a particular critical impulse. In Ref. [7], the following semi-empirical estimate of the critical impulse is suggested:

$$I_{cr} = 1.15\sqrt{\rho E}\frac{h^2}{a} \tag{28.13}$$

This formula predicts a critical impulse of about 0.57 kPa-s for the tubes in Fig. 28.10, though the effects of plasticity will become important as this limit is approached. This prediction is not inconsistent with the measurements shown in Fig. 28.10, but additional data points at lower impulses are needed to confirm that the buckling threshold approaches this asymptote.

28.4 Conclusions

Dynamic buckling of cylindrical tubes has been studied by submerging them in a thin annulus of water and generating axially-propagating shock waves in the water using a projectile impact facility. Measurements reveal that for low pressures, the response is similar to that of a waterhammer event occurring inside of a pipe, and suitably adapted waterhammer models are capable of adequately predicting the speed of the coupled fluid-solid waves. Elastic buckles are observed at higher pressures, but due to inertial effects these buckles do not fail the tube until the peak pressure is several times greater than the static buckling pressure. At that point, the onset of plastic deformation is found to substantially reduce the tubes' load-carrying capacity; however, it appears that plastic deformation does not significantly affect the motion of pressure waves since the leading edge of the pressure wave travels far from the buckle by the time plastic deformation is reached. Finally, these experiments have demonstrated that extruded tubes often feature sinusoidal wall thickness variations around the circumference, and these variations play a critical role in determining the orientation of mode 2 buckles.

Acknowledgements This research was supported by the Office of Naval Research DOD MURI on Mechanics and Mechanisms of Impulse Loading, Damage and Failure of Marine Structures and Materials (ONR Grant No. N00014-06-1-0730), program manager Dr. Y. D. S. Rajapakse. Tomohiro Nishiyama of the Japan Patent Office and Prof. Kazuaki Inaba, currently at the Tokyo Institute of Technology, executed the initial

design of the annular tube implosion fixture and supervised its fabrication while working at Caltech. Preliminary experiments on buckling using this facility were conducted by Mr. Jason Damazo and Dr. Rafal Porowski, currently at the research Center for Fire Protection in Poland. We are also grateful to Prof. Ravichandran of Caltech, who provided technical advice and leadership of the Caltech MURI.

References

1. Lindberg HE (1964) Buckling of a very thin cylindrical shell due to an impulsive pressure. J Appl Mech 31:267–272
2. Abrahamson G, Florence A, Lindberg H (1966) Investigation of response of simplified ICBM-type structures to impulsive loading. Technical report AFWL-TR-65-136, Stanford Research Institute
3. Anderson D, Lindberg H (1968) Dynamic pulse buckling of cylindrical shells under transient lateral pressures. AIAA J 6(4):589–598
4. Lindberg H, Anderson D, Firth R, Parker L (1965) Response of reentry vehicle-type shells to blast loads. Technical report LMSC-B130200-VOL-4-C, Stanford Research Institute
5. Lindberg HE, Firth RD (1967) Structural response of spine vehicles, volume II: Simulation of transient surface loads by explosive blast waves. Technical report AFWL-TR-66-163, vol II, Stanford Research Institute
6. Lindberg HE, Sliter GE (1969) Response of reentry-vehicle-type shells to transient surface pressures. Technical report AFWL-TR-68-56, Stanford Research Institute
7. Lindberg H, Florence A (1987) Dynamic pulse buckling. Martinus Nijhoff, Boston
8. Lindberg HE (1974) Stress amplification in a ring caused by dynamic instability. J Appl Mech 41:392–400
9. Inaba K, Shepherd JE (2010) Flexural waves in fluid-filled tubes subject to axial impact. J Press Vessel Technol 132:021302
10. Hutchinson J, Koiter W (1970) Postbuckling theory. Appl Mech Rev 23(12):1353–1366
11. Kempner J, Pandalai K, Patel S, Crouzet-Pascal J (1957) Postbuckling behavior of circular cylindrical shells under hydrostatic pressure. J Aeronaut Sci 24:253–264
12. Timoshenko SP, Gere JM (1961) Theory of elastic stability, 2nd edn. McGraw-Hill, New York
13. Korteweg D (1878) Über die fortphlanzungsgeschwindigkeit des schalles in elastisches röhren (on the velocity of propagation of sound in elastic pipes). Annalen der Physik und Chemie 9(5):525–542
14. Joukowsky N (1900) Über den hydraulishen stoss in wasserleitungsröhren (on the hydraulic hammer in water supply pipes). Mémoires de l'Académie Impériale des Sciences de St. Péterbourg 9(5), Series 8
15. Shepherd JE, Inaba K (2010) Shock loading and failure of fluid-filled tubular structures. In: Shukla A, Ravichandran G, Rajapakse Y (eds) Dynamic failure of materials and structures. Springer, New York, pp 153–190
16. Wood AB (1955) A textbook of sound, 3rd edn. G Bell, London
17. Ando K, Sandada T, Inaba K, Damazo J, Shepherd JE, Colonius T, Brennen CE (2011) Shock propagation through a bubbly liquid in a deformable tube. J Fluid Mech 671:339–363
18. Leissa AW (1973) Vibration of shells. Technical report NASA SP-288, National Aeronautics and Space Administration
19. Junger MC, Feit D (1972) Sound, structures, and their interaction, 2nd edn. MIT, Cambridge
20. Warburton G (1961) Vibration of a cylindrical shell in an acoustic medium. J Mech Eng Sci 3(1):69–79

Chapter 29
High Strain Rate Response of Layered Micro Balloon Filled Aluminum

Venkitanarayanan Parameswaran, Jim Sorensen, and Manish Bajpai

Abstract Recent interest in blast mitigation has given rise to the development of many novel materials and systems. Sandwich materials composed of a soft deformable core sandwiched between two strong face sheets and multilayer structures with alternating deformable and stiff layers have been actively explored for blast mitigation. Understanding the deformation, failure and energy absorption characteristics of such systems is critical for their successful design and application. The present work focuses on understanding the high strain rate response of multilayer structures in which the soft deformable layer is made of micro-balloon filled aluminum. High strain rate experiments are performed using a split Hopkinson pressure bar (SHPB). An ultra high speed camera is used simultaneously to resolve the deformation and failure process in real-time. Experiments are conducted on micro-balloon filled aluminum with different density to understand the effect of the density on the stress–strain characteristics.

Keywords Sandwich materials • Aluminum foam • Blast loading • High strain rate • High speed imaging

29.1 Introduction

Sandwich construction has gained a lot of attention in recent years particularly in the context of blast mitigation. A sandwich construction essentially consists of a light and soft core material placed in between two strong, thin face sheets. The construction offers good flexural rigidity at relatively lower weight compared to an equivalent monolith. Such materials are being extensively used in naval and aerospace applications. The response of these materials, when subjected to rapid loading, as encountered in an impact or explosive blast, has become an active area of research in recent years [1–5]. When subjected to blast or shock loading, the face sheets will deform somewhat but, being relatively rigid will transmit most of the force to the softer core. Therefore understanding the dynamic deformation of the core is important in evaluating the performance of such sandwich materials.

The high strain rate response of polymeric and metallic foams has been investigated by many researchers [6–9]. Foams made by embedding hollow micro-spheres (micro balloons) in polymers and metals have also been investigated. Dynamic response of syntactic foams prepared by embedding hollow glass spheres has been reported in [10]. High strain rate response of Aluminum embedded with cenospheres [11] and also silicon carbide hollow [12] spheres has also been reported. The present study focuses on understanding the high strain rate response in compression of Aluminum embedded with micro balloons and sandwich materials with micro balloon embedded Aluminum as the core.

V. Parameswaran (✉) • M. Bajpai
Department of Mechanical Engineering, Indian Institute of Technology Kanpur, Kanpur 208016, India
e-mail: venkit@iitk.ac.in

J. Sorensen
CPS Technologies Corporation, 111 S. Worcester Street, Norton, MA 02766, USA

B. Song et al. (eds.), *Dynamic Behavior of Materials, Volume 1: Proceedings of the 2013 Annual Conference on Experimental and Applied Mechanics*, Conference Proceedings of the Society for Experimental Mechanics Series,
DOI 10.1007/978-3-319-00771-7_29,

29.2 Experimental Details

29.2.1 Materials

The core and sandwich materials investigated in this study were prepared at CPS Technologies Corporation, MA, USA. Three different core types are considered in this study. These are (i) core prepared by infiltrating aluminum through a preform of ceramic bubbles having diameters in the range of 60–100 μm, referenced henceforth as C1, (ii) core prepared by infiltrating aluminum through a preform consisting of ceramic bubbles plus 1 mm diameter silicon-carbide (SiC) spheres, referred as C2 and (iii) core prepared by infiltrating aluminum through a preform consisting of ceramic bubbles plus 3 mm diameter silicon-carbide spheres, referred as C3. The sandwich materials considered in this study include (i) sandwich having two 1 mm thick Nextel face sheets with 4.2 mm thick C1 type core (total thickness of 6.2 mm), henceforth referred to as S1, (ii) sandwich having Saffil face sheets (very low volume fraction of Saffil Fibers) with C1 type core for a total thickness of 3 mm, referred to as S2 and (iii) sandwich having two 1 mm thick Nextel face sheets with C3 type core of thickness 4.7 mm (total thickness of 6.7 mm), referred to as S3. X-ray-CT scan (Procon Mini CT- Micro CT scanner) images of some of the samples are shown in Fig. 29.1. The micro-balloons are very uniformly distributed in C1 and the micro-balloons as well as the SiC spheres are evenly distributed in C2 and C3.

29.2.2 Experimental Setup

The high strain rate tests were performed using a split-Hopkinson pressure bar (SHPB) set up. Depending on the required strain rate level either steel bars or Aluminum bars were used in the SHPB setup. Cubical samples were used for testing. In the case of samples C1, C2, S1 and S3, the typical sample size was 7 × 7 mm in cross section and of length in the range of 2–9 mm. A 12.7 mm diameter SHPB (with either Steel or Aluminum bars) was used for these tests. In the case of samples C3 and S2, the sample size was 10 × 10 mm in cross section and the length of the samples was 7–9 mm. A 20 mm diameter SHPB set up was used in these tests. An ultra-high speed camera (SIM02-16) was used in selected experiments to record the deformation of the samples in real time. A schematic of the experimental arrangement is shown in Fig. 29.2. A make trigger at the impact face of the incident bar was used to trigger the camera upon impact of the striker on to the incident bar. The data acquisition system was then triggered by the camera. This allowed time-synchronization between the strain signals and the recorded images. The strain and stress history in the specimen was calculated from the incident, reflected and transmitted strain signals recorded using strain gages installed at mid length of the incident and transmitter bars.

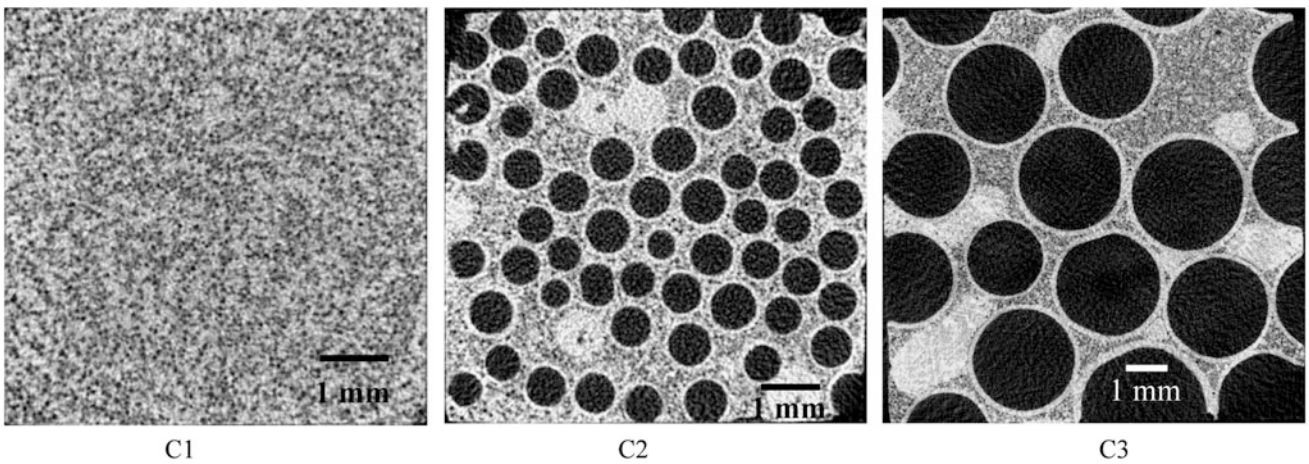

Fig. 29.1 Internal structure of the three cores considered in this study

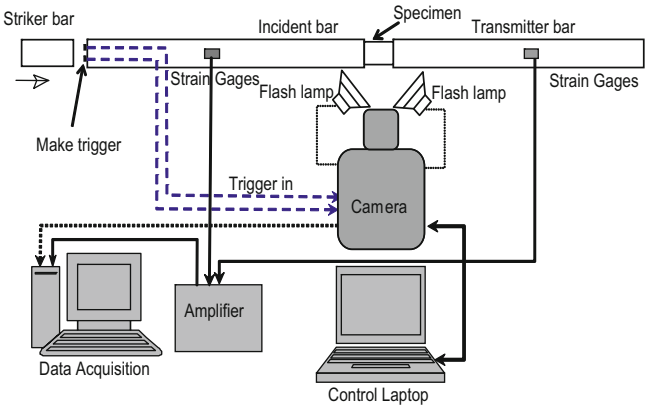

Fig. 29.2 Schematic of experimental setup

29.3 Results

29.3.1 High Strain Rate Response of Core Material

Figure 29.3 shows the stress–strain response of C1 type core material at three different strain rates. Figure 29.3a shows that the stress increases linearly up to a maximum value of about 200 MPa, following which there is a sudden drop in the stress to 160 MPa at around 9 % strain. Then the stress remains constant (plateau) at 160 MPa till a strain of 20 %. The strain rate, also shown in Fig. 29.3a, remains constant at a value of 4,000/s till a strain of 20 %. The sample thickness was 2.8 mm in this case. Beyond 20 % strain the stress starts increasing with a concomitant decrease in the strain rate. This behavior is typical of foams. After reaching a maximum stress, the pore walls start collapsing progressively resulting in a constant stress region. Once the collapse is complete, the foam compacts with an increase of stress for further deformation. Stresses in excess of 400 MPa can be observed in Fig. 29.3a.

Figure 29.4a shows images of the specimen taken during the dynamic deformation. The strain at which each of these images are captured is also given in this figure. In the first image corresponding to a strain of 2 %, no visible damage can be observed in the specimen. Careful observation indicates formation of cracks at nearly 45° to the loading direction in the second image corresponding to a strain of 9 %. These are indicted by white arrows. More cracks are seen in subsequent images. A photograph of the specimen recovered after the test is shown in Fig. 29.5. The specimen did not fragment into pieces though many cracks can be seen along the edges of the specimen. This is an indication that the foam has considerable ductility and despite the ceramic micro-balloons collapsing, the metallic matrix is able to compact without fragmenting into pieces.

The stress–strain response of the same core (C1) at lower strain rates is shown in Fig. 29.3b. The behavior in these cases is similar to that shown in Fig. 29.3a, however, in these tests the foam could not be loaded to complete compaction. The plateau stress is around 160 MPa. Beginning of compaction can be seen at around 25 % strain for the strain rate of 2,270/s. This indicates that the plateau stress is not affected by the strain rate in the strain rate range of 1,000/s–4,000/s. Real-time images of deformation of the foam for 1,300/s strain rate are shown in Fig. 29.4b. Once again, cracks oriented nearly 45° to the loading can be seen in the third picture (strain of 8 %). As the deformation progresses (within the constant stress region), more cracks appear and the specimen appears to be fragmenting as shown in picture #6. The image of the specimen recovered after the test is shown in Fig. 29.5. It can be observed that the specimen deformed without fragmenting into pieces though there is some fragmentation along the edges in case of 2,270/s strain rate.

Figure 29.6a shows the dynamic stress–strain response of the C2 type core at a strain rate of 2,000/s. It can be observed that the peak stress is little over 160 MPa and the plateau stress is around 100 MPa, both being less than that for C1 type core. The plateau stress is reached at around 10 % strain. In this test, the foam could not be taken to the consolidation stage. The real time images of deformation of the specimen are shown in Fig. 29.6b. Cracking at nearly 45° to the loading can be seen in picture number 3. These cracks are passing along the SiC bubbles as can be observed from picture 3 and 4. There are several un-collapsed SiC spheres even in pictures 5 and 6.

The dynamic stress–strain response of core type C3 at a stain rate of 3,000/s is shown in Fig. 29.7a. Even though the overall behavior is similar to that for core type C1, both the peak stress (before collapse) and the plateau stress are lower than C1 and C2 type cores. In this case the plateau stress is lower at around 50 MPa. The real-time images of deformation, shown in Fig. 29.7b, indicate initiation of cracks in the second image corresponding to a strain of 7 %. Collapse of a SiC bubble is clearly seen in the second and third images. As the specimen fails, it still transmits load till the strain reached 60 %. As can be seen in Fig. 29.7c, the specimen did not completely fragment.

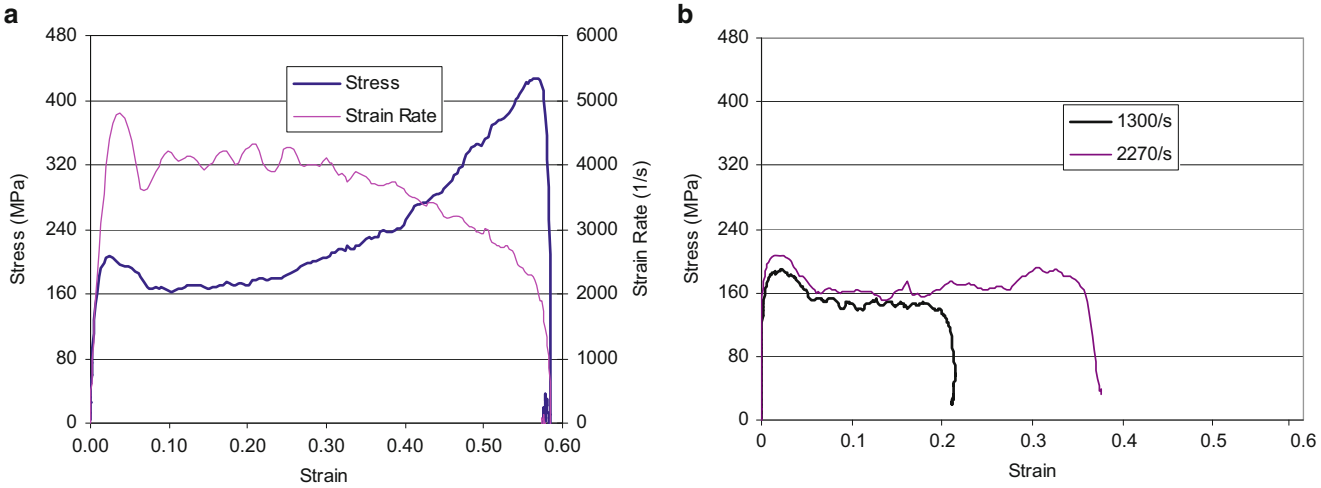

Fig. 29.3 Stress–strain response of C1 core at different strain rates

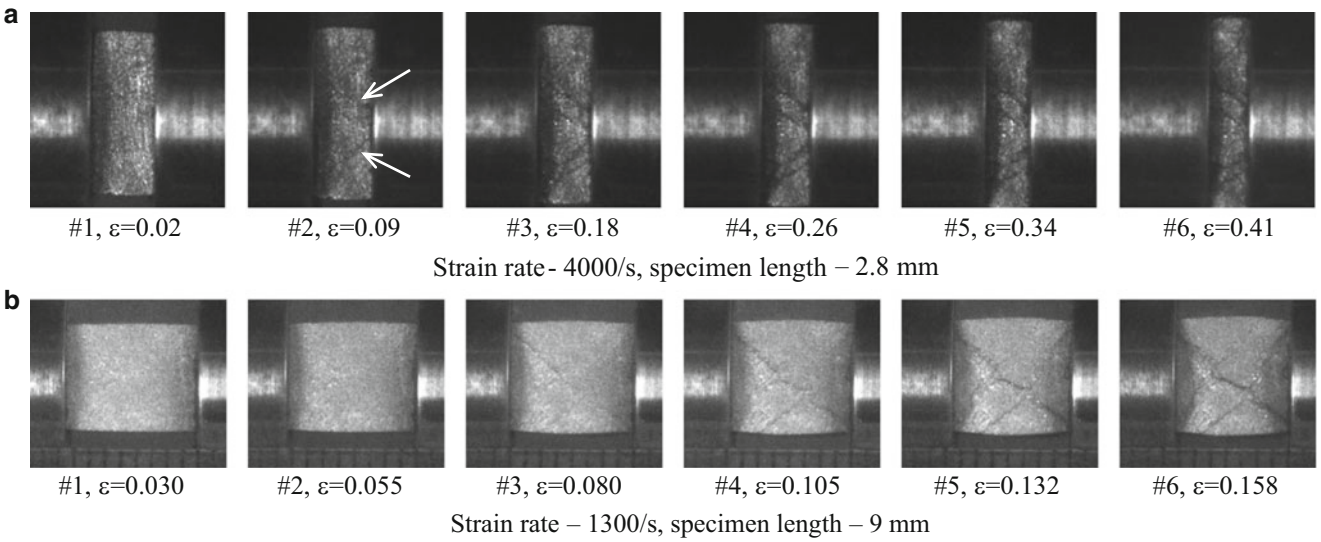

Fig. 29.4 Real time deformation of C1 core at two different strain rates

29.3.2 High Strain Rate Response of Sandwiches

The behavior of sandwich types S1 and S2 will be discussed first. Both these materials have the same type of core, however, different type of face sheets and thicknesses. The stress–strain response of the three sandwiches is shown in Fig. 29.8. Overall the behavior of S1 and S2 is similar to that obtained for the core C1, shown in Fig. 29.3. However, the peak and plateau stress for the sandwich S2, which has a very thin core is higher than that shown in Fig. 29.3 for the C1 core. We believe that the lateral constraint exerted by the face sheets allows the sandwich to withstand more stress before the bubbles collapse. However this effect is not evident in the sandwich S1 for which the core thickness is larger compared to that for S2. The constraint by the face sheets is not uniformly felt in the entire thickness of the core and therefore the behavior is similar to that for the core without face sheets. The stress–strain response of sandwich S3 having core type C3, shown in Fig. 29.8, is markedly different from that of the behavior of C3 type core shown in Fig. 29.7a. The peak stress (before collapse) is around 160 MPa which is higher than that observed in Fig 29.7a. After reaching the peak stress, there is a steep drop in the stress till a strain of about 5 %. Thereafter, there is a small constant stress region followed by increase in stress as a result of compaction. Contrary to this, the stress strain curve given in Fig. 29.7a for the C3 type core shows a gradual drop in stress

Fig. 29.5 Tested specimens

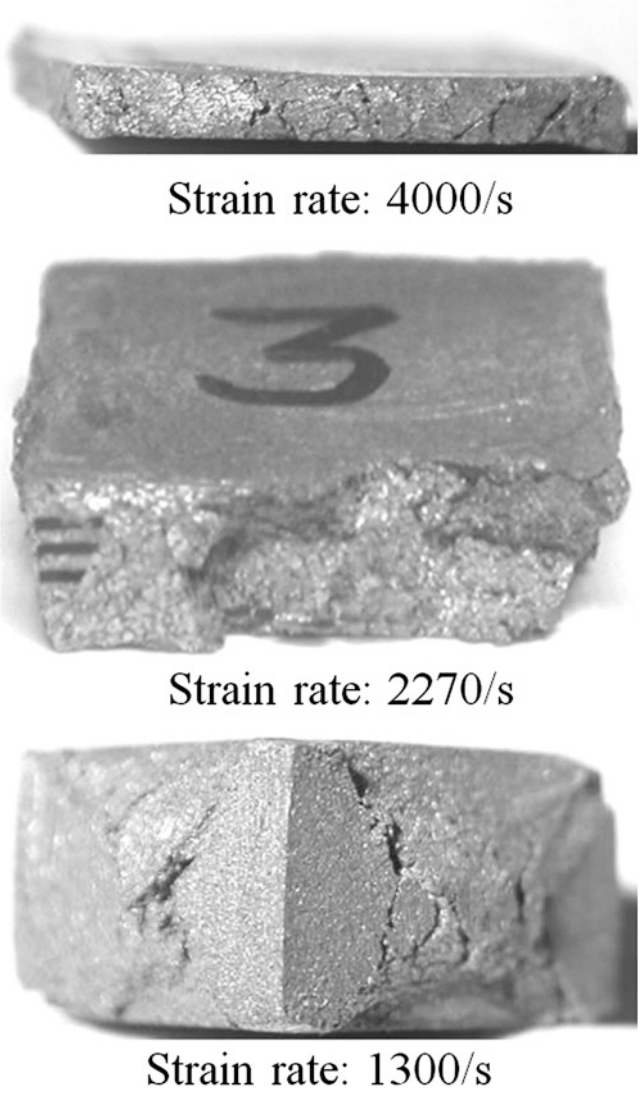

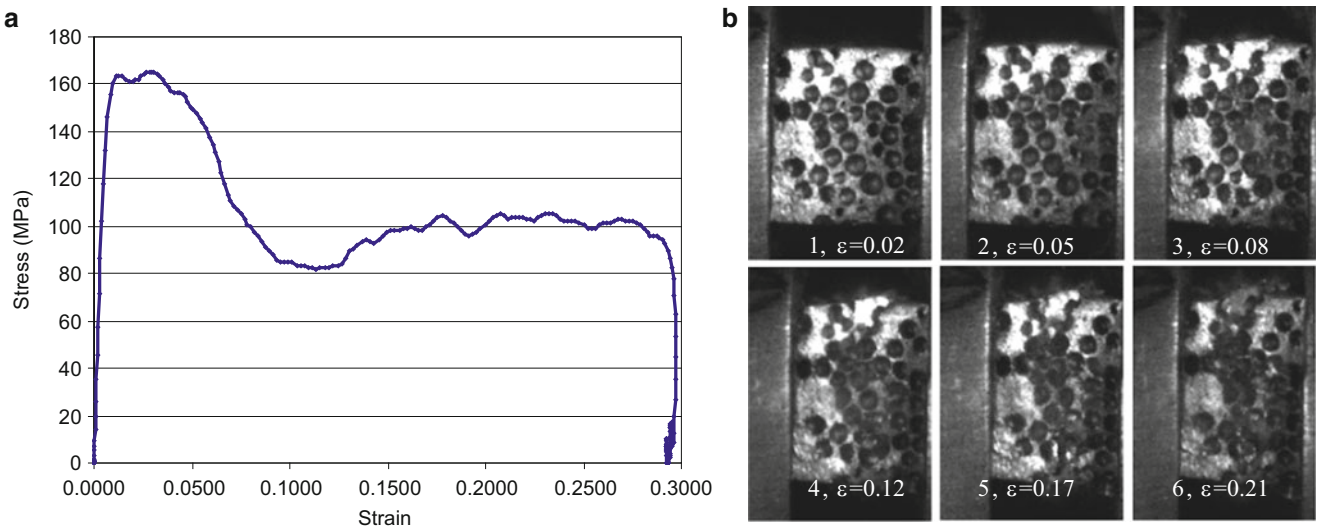

Fig. 29.6 (**a**) Stress–strain response of C2 core at 2,000/s strain rate (**b**) real-time images of deformation and failure

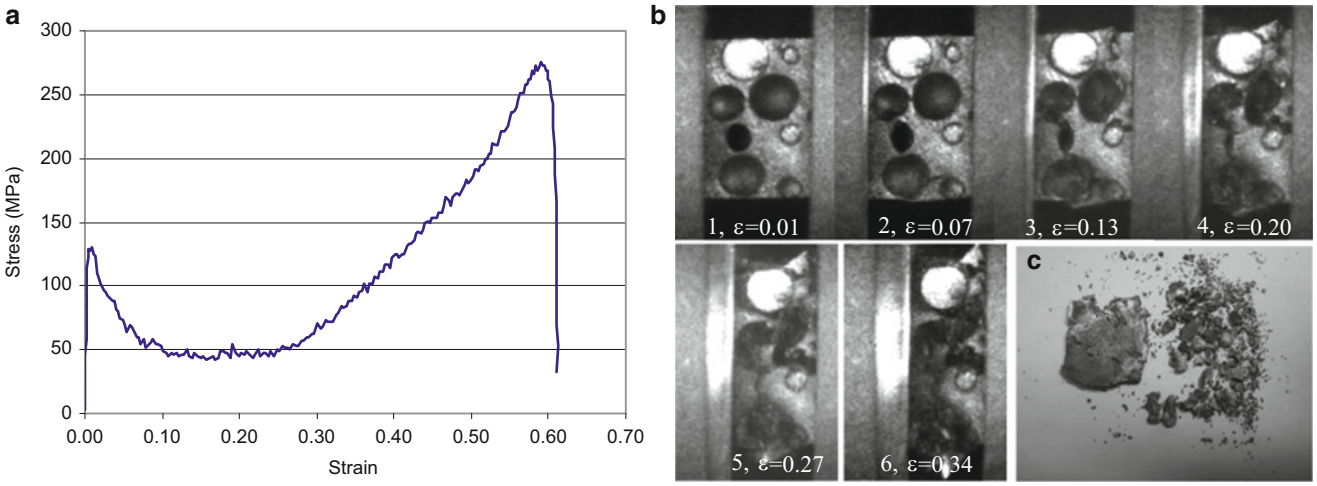

Fig. 29.7 (**a**) Dynamic stress–strain response of C3 (**b**) real-time images of deformation (**c**) image of specimen after test

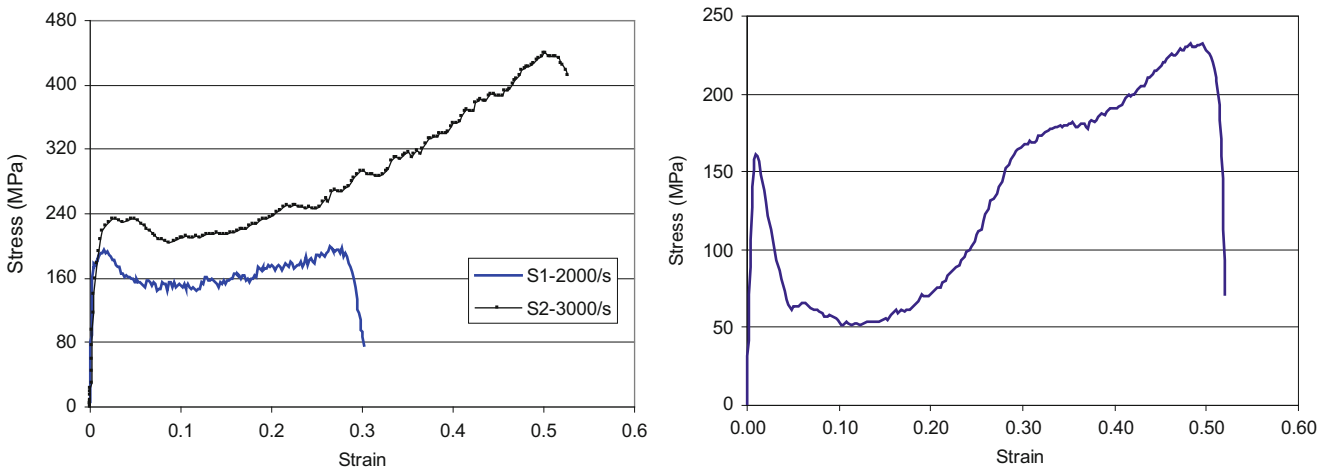

Fig. 29.8 Dynamic stress–strain response of sandwich S1 (2,000/s) & S2 (3,000/s) and S3 (3,000/s)

after reaching the initial peak stress of 125 MPa. Once again the higher value of the initial peak stress could be due to the constraint effect of the face sheets. This larger peak stress causes more rapid collapse of the spheres and matrix in the case of the sandwich S3 resulting in the sudden drop in stress.

29.4 Conclusions

The high strain rate response in compression of three different types of cores and three different sandwich materials has been investigated. The loading in the strain rate range of 1,300/s–4,000/s was achieved using a SHPB. An ultra-high speed camera was used to record the deformation and damage evolution in the specimen. The results of the study indicated the following. The stress–strain response of the three cores (C1, C2 & C3) and the three sandwiches (S1, S2 & S3) exhibited three distinct regions. An initial region where the stress increases linearly with strain till a maximum stress is reached; denoted as the initial peak stress. Thereafter with increasing strain the stress drops and remains nearly constant until some value of strain (plateau region); the constant stress will be denoted as the plateau stress and the strain up to which the stress remains constant will be denoted as the strain to compaction. Beyond this region, the stress continuously increases with strain.

Among the three cores, the core with the smallest size micro-balloons (C1) has the highest initial peak stress and plateau stress. This is followed by core type C2, having micro-balloons and 1 mm SiC hollow spheres. The lowest initial peak stress and plateau stress was observed for core type C3 which has micro-balloons and 3 mm SiC hollow spheres. The strain to compaction was highest for C1 type core and lowest for C3 type core. The stress drop (difference between the initial peak stress and the plateau stress) increases as the size of the SiC spheres increases. This is an indication that the collapse is more rapid. These observations indicate that the size of the micro-balloons/hollow spheres has a direct effect on the dynamic response of the core material. The results of the study also indicate that addition of face sheets has significant effect on the behavior of the core. The addition of the face sheets leads to an increase in the initial peak stress. In the case of sandwiches with a core, comparable in thickness to the face sheets, (S2 in this case), the constraint effect of the relatively stiffer face sheet can lead to higher initial peak stress as well as plateau stress. From an energy absorption perspective, foams having larger strain to compaction (extended plateau region) are beneficial. Though a higher plateau stress would increase the energy absorbed, it will also lead to transfer of larger forces and can cause damage to the main structure on which the energy absorbing layer is attached. The study reveals that proper selection of the core type and its thickness relative to the face sheets is important in obtaining best energy absorption characteristics.

Acknowledgements The first author acknowledges the financial support through grant number SR/FST/ETII-003/2006 under the FIST program by Department of Science and Technology, Government of India for the Ultra-high speed camera used in this study.

References

1. Tekalur SA, Bogdanovich AE, Shukla A (2009) Shock loading response of sandwich panels with 3-D woven E-glass composite skins and stitched foam core. Compos Sci Technol 69:736–753
2. Wang EH, Gardner N, Shukla A (2009) The blast resistance of sandwich composites with stepwise graded cores. Int J Solid Struct 46:18–19, 3492–3502
3. Jackson M, Shukla A (2011) Performance of sandwich composites subjected to sequential impact and air blast loading. Compos Part B Eng 42 (2):155–166
4. Gardner N, Wang E, Kumar P, Shukla A (2012) Blast mitigation in a sandwich composite using graded core and polyurea interlayer. Exp Mech 52(2):119–133
5. Gupta S, Shukla A (2012) Blast performance of marine foam core sandwich composites at extreme temperatures. Exp Mech 52(9):1521–1534
6. Chen W, Lu F, Winfree N (2002) High-strain-rate compressive behavior of a rigid polyurethane foam with various densities. Exp Mech 42 (1):65–73
7. Subhash G, Liu QL, Gao XL (2006) Quasistatic and high strain rate uniaxial compressive response of polymeric structural foams. Int J Impact Eng 32(7):1113–1126
8. Raj RE, Parameswaran V, Daniel BSS (2009) Comparison of quasi-static and dynamic compression behavior of closed-cell aluminum foam. Mater Sci Eng A256:11–15
9. Chakravarty UK (2010) An investigation on the dynamic response of polymeric, metallic, and biomaterial foams. Compos Struct 92 (10):2339–2344
10. Periasamy C, Tippur HV (2012) Experimental measurements and numerical modeling of dynamic compression response of an interpenetrating phase composite foam. Mech Res Commun 43:57–65
11. Luong DD, Gupta N, Daoud A, Rohatgi PK (2011) High strain rate compressive characterization of aluminum alloy/fly ash cenosphere composites. J Mater 63(2):53–56
12. Luong DD, Strbik OM III, Hammond VH, Gupta N, Cho K (2013) Development of high performance lightweight aluminum alloy/SiC hollow sphere syntactic foams and compressive characterization at quasi-static and high strain rates. J Alloy Compd 550:412–422

Chapter 30
Dynamic Triaxial Compression Experiments on Cor-Tuf Specimens

Alex B. Mondal, Wayne Chen, Brad Martin, and William Heard

Abstract A set of dynamic triaxial compression experiments at 50, 100, and 200 MPa confinement have been conducted with a modified Kolsky bar on cylindrical ultra-high strength concrete Cor-Tuf specimens of diameter 19 mm and length of 12.7 mm. The modified Kolsky bar utilized is capable of performing a triaxial compression test with a dynamic loading for a confining pressure of up to 400 MPa on specimens with 19.05 mm diameters. The experiment is composed of a hydrostatic phase which occurs at a quasi-static strain rate followed by a dynamic shear phase which occurs at a high strain rate. A set of 28 experiments were conducted at strain rates of 100 and 200 s^{-1}. The experiments show that the fracture strength of the material increases under increasing pressure. The specimens showed higher strength in the dynamic confined experiments than both the quasi-static TXC experiments and the unconfined-uniaxial dynamic tests. The strength increase was in part caused by specimen size difference. Although the trend towards brittle ductile transition is observed the specimens were not loaded in a high enough confinement for the phase change to occur.

Keywords Dynamic confined • Modified Kolsky bar • Split-Hopkinson pressure bar • Triaxial compression • Cor-Tuf

30.1 Introduction

The dynamic response of materials can be drastically different than its response under quasi-static and intermediate strain rates. Modeling events like: earthquakes, explosions, drilling, and structural impact require an understanding of material response at high rates of loading [1]. Moreover, for events like earthquakes and explosions, the loading conditions are not uni-axial but multi-axial [2].

The dynamic triaxial compression experiment is a combination of two experiments: Kolsky bar experiments and triaxial compression tests. Conventional Kolsky bar tests, also known as split-Hopkinson bar (SHPB) tests, are experiments used to determine the dynamic properties of materials under uni-axial load. Conventional triaxial compression (TXC) tests on the other hand are quasi-static tests used to test pressure sensitive materials under a multi-axial stress state.

Frew et al. [2], Lindholm et al. [3], Forquin et al. [4], Gary et al.[5], and Nemat-Nasser et al.[6] developed modified split Hopkinson bar techniques to allow for confinement following the first apparatus developed by Christensen et al. [7]. Christensen et al. [7] in 1972 were one of the first experimenters to modify a split Hopkinson pressure bar with confining pressure vessel capable of pneumatic pressures up to 206 MPa to test 19.05 mm diameter sand stone specimens. Nemat-Nasser et al. developed a 19 mm diameter Hopkinson bar that was capable of confining a specimen to 7 MPa with pneumatic pressure. Lindholm et al. [3] tested Dresser Basalt specimens under triaxial stress states from 0 to 690 MPa with dynamic loading along with formulating a fracture criterion.

A.B. Mondal (✉) • W. Chen
Purdue University, West Lafayette, IN 47907, USA
e-mail: amondal@purdue.edu

B. Martin
Air Force Research Laboratory, Eglin AFB, FL, USA

W. Heard
Engineer Research and Development Center, Vicksburg, MS, USA

B. Song et al. (eds.), *Dynamic Behavior of Materials, Volume 1: Proceedings of the 2013 Annual Conference on Experimental and Applied Mechanics*, Conference Proceedings of the Society for Experimental Mechanics Series,
DOI 10.1007/978-3-319-00771-7_30,

The dynamic TXC bar developed by Frew et al. [2] had the capacity to apply confining pressures up to 400 MPa hydraulically. This unique test platform included two pressure vessels instead of the previous methods which only used one pressure vessel. Implementing two pressure vessels allows one cell to load the specimen radially while the other loads the specimen axially.

The most recent development of a TXC Kolsky bar comes from Kabir [8], Kabir and Chen [9], and Martin et al. [10]. A dynamic TXC Kolsky bar, similar to the design developed by Frew et al. [2] except with larger pressure cells, was employed to study granular materials and sand by Kabir and Chen.

30.2 Methods and Materials

Cor-Tuf concretes are known in the family of ultra high performance concretes ranging from 190 to 244 MPa [11]. These ultra high strength concretes contain fine aggregates and powders unlike the coarse aggregates found in common concretes. In fact, the Cor-Tuf prepared included powder grains no bigger than 600 μm. The specimens utilized were fabricated by the Geotechnical Structures Laboratory (GSL) in the Engineering Research and Development Center (ERDC) of Army Engineers in Vicksburg, MS. The Cor-Tuf samples tested by GSL were 50 mm in diameter by 110 mm in length whereas the specimens studied under dynamic load were 19.05 mm diameter and 12.5 mm length.

The apparatus used for these experiments is a modified Kolsky bar capable of triaxially confining a specimen to a desired pressure of 400 MPa and is shown in Fig. 30.1. A similar apparatus was developed by Frew et al. [2]. The current apparatus was developed with the help of Frew [2] and initially assembled by Kabir et al. [9] who used to study dynamic behavior of granular materials under dynamic triaxial loading [8]. The axial stress and strain along are collected during both phases of the experiment and while internal measurements of radial stress and strain were attempted, they were ignored for inconsistencies. The line pressure in the chamber were measured by two Honeywell high pressure transducers with a capacity of up to 517 MPa. The linear variable displacement transducer or linear variable differential transformer (LVDT) is used to collect the axial strain on the specimen during the hydrostatic phase. The dynamic axial stress and strain of the Cor-Tuf, captured by Vishay Micro-Measurements strain gages located on the incident and transmission bars, were calculated through Kolsky bar methods.

It was necessary to shape the input pulse so that the specimen deformed at a desired constant rate and achieved dynamic stress equilibrium. Copper 110 alloy dampeners, with a measured tensile strength of 310 MPa, were used to pulse shape for all the experiments conducted. There are several variables that dictate the shape of a input pulse: projectile impact velocity, length of projectile, dampening cushion dimensions (diameter, thickness), and the cushion material. Experimenting with the settings allowed us to achieve the desired strain rates in the Cor-Tuf specimens. Due to the gas gun barrel length, a projectile of 30.4 cm length was utilized such that it reached a velocity capable of fracturing the specimen.

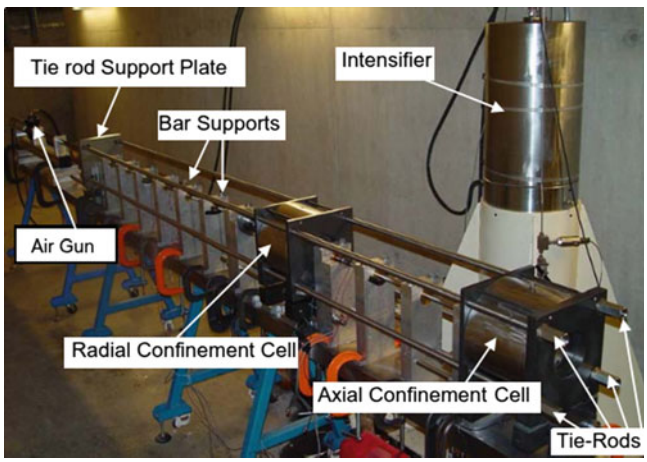

Fig. 30.1 Modified Kolsky bar with triaxial confinement [8]

30.3 Results

This research project was to supplement the work that had been conducted on Cor-Tuf at GSL in the quasi-static strain rate domain and to provide an understanding of the material behavior in the dynamic domain. A series of experiments were performed in the quasi-static domain by the GSL including: compression, unconfined compression, and triaxial compression on specimens with and without steel fibers. The mean unconfined strength of Cor-Tuf concrete without steel fibers was determined to be 210 MPa. The bulk modulus from hydrostatic compression was determined to be 22.7 GPa. The GSL conducted triaxial compression tests at confining pressures of: 10, 20, 50, 100, 200, and 300 MPa and found that the failure stresses did not vary for confining pressures under 50 MPa. Figure 30.2 is the failure surface determined through GSL data for plain Cor-Tuf without steel fibers (Cor-Tuf2).

This research has been focused on understanding the effects of confinement and high rate of deformation on the behavior on Cor-Tuf. A set of 28 dynamic triaxial compression Kolsky bar experiments were performed on Cor-Tuf specimens with diameters 19 mm and lengths of 12.7 mm. The plain Cor-Tuf experiments were conducted at four confinement levels and at two different strain rates. Specifically, compression experiments at 50, 100, 150, and 200 MPa were performed at strain rates of 100 and 200 s^{-1}.

A conventional uni-axial Kolsky bar analysis was performed to determine the specimen dynamic equilibrium, strain-rate of deformation, and axial stress – axial strain relationships. Figure 30.3 is the combination of results from GSL in Fig. 30.2 and the dynamic TXC experiments. The results plotted are the average principal stress differences versus the mean normal stress. Along with dynamic-confined results, average dynamic-unconfined and mean confined data is also provided.

30.4 Discussions

Figure 30.3 shows that the average failure strength of Cor-Tuf collected with the 19.05 mm diameter specimens have a failure envelope that is higher than the failure envelope found by the GSL. Figure 30.3 includes results from strain rates of 100 and 200 s^{-1} however they are not distinguishable. As mentioned previously, the specimens tested by GSL were much larger in comparison to the specimens tested with the modified Kolsky bar. Figure 30.4 shows that 19.05 mm diameter specimens tested under quasi-static load in the modified Kolsky bar has a higher fracture strength than specimens tested at the GSL under the same conditions. It was concluded that the higher failure envelope of the Cor-Tuf specimens tested under dynamic triaxial compression conditions was partly due to the specimen size and partly from dynamic effects.

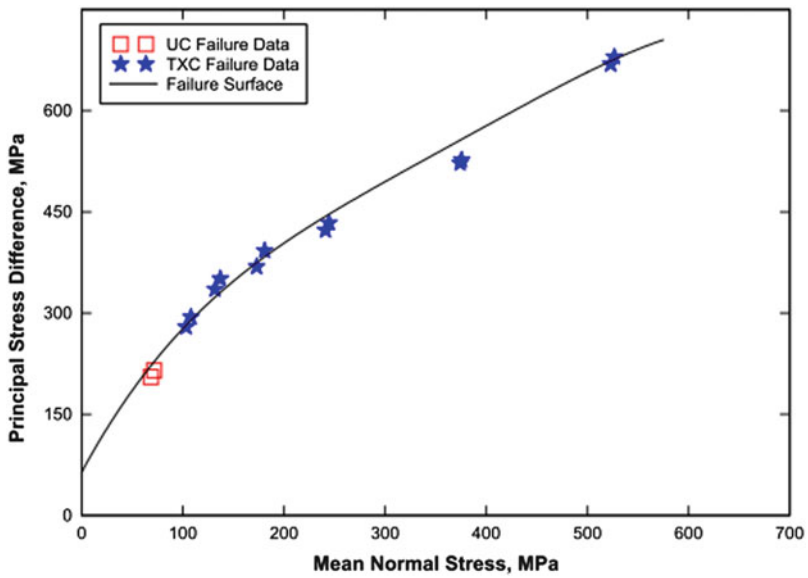

Fig. 30.2 Failure plane for Cor-Tuf2 tested on TXC

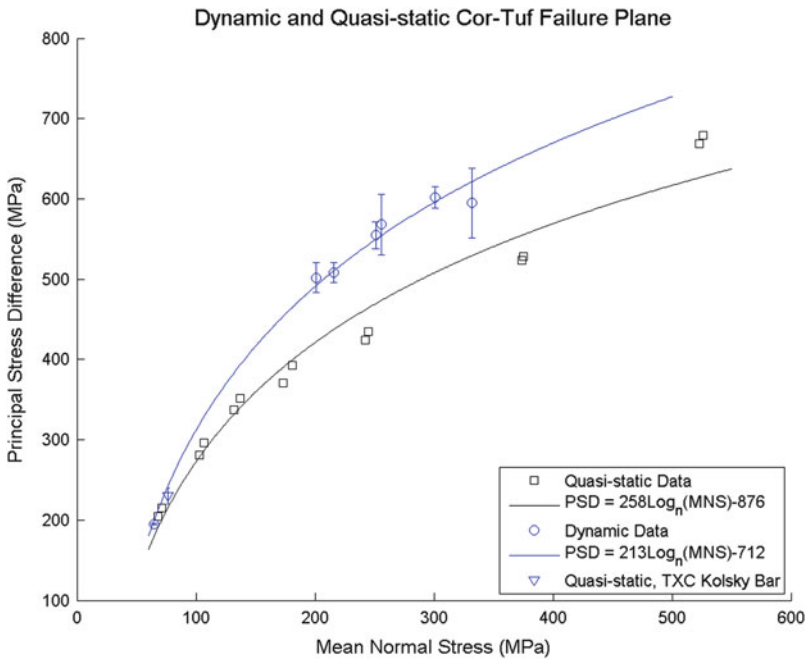

Fig. 30.3 Dynamic and quasi-static failure surface for Cor-Tuf

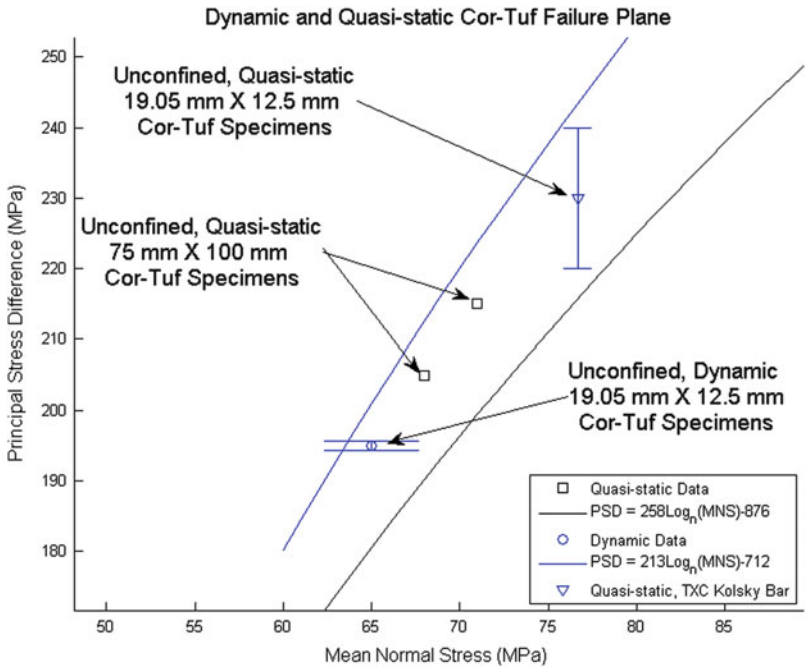

Fig. 30.4 Unconfined data for different Cor-Tuf specimen sizes

All the experiments shown were pulse shaped so that the strain rate of deformation was nearly constant. From the current experiments, no relationship could be determined between the strain rate and the material's dynamic fracture strength. Longer striker bars require higher gas pressure and a longer barrel to launch; the amplitude of the input stress wave required to fail the specimen could not be generated with a longer projectile and so the 30.4 cm striker bar was used. With a longer striker bar, a stress wave with a longer period would be possible and allow greater control of the strain rate of the specimen.

Acknowledgment This research was supported by a contract from ERDC to Purdue University. Boon-Him Lim provided the unconfied dynamic Cor-Tuf results included in this paper.

References

1. Kuhn H, Medlin D (2000) High strain rate tension and compression tests. ASM International, Member/Customer Service Center, Materials Park
2. Frew D, Akers S et al (2010) Development of a dynamic triaxial Kolsky bar, vol 21. Measurement Science and Technology, Institute of Physics Publishing Inc, Philadelphia, pp 105704–105704
3. Lindholm US, Yeakley LM et al (1974) The dynamic strength and fracture properties of Dresser Basalt. Int J Rock Mech Mining Sci 11(5): 181–191
4. Forquin P, Gary G et al (2008) A testing technique for concrete under confinement at high rates of strain. Int J Impact Eng 35(6):425–446
5. Gary G, Bailly P (1998) Behaviour of quasi-brittle material at high strain rate. Experiment and modelling. European J Mech-A/Solids 17(3): 403–420
6. Nemat-Nasser S, Isaacs J et al (2000) Triaxial Hopkinson techniques. ASM International, Member/Customer Service Center, Materials Park
7. Christensen R, Swanson S et al (1972) Split-Hopkinson-bar tests on rock under confining pres-sure. Exp Mech 12(11):508–513
8. Kabir ME (2010) Dynamic behavior of granular materials, vol 128. School of Aeronautics & Astronautics. Purdue University, West Lafayette. Doctor of Philosophy
9. Kabir ME, Chen WW (2009) Measurement of specimen dimensions and dynamic pressure in dynamic triaxial experiments. Rev Sci Instrum 80(12):125111–125117
10. Martin BE, Chen W et al (2009) Moisture effects on the high strain-rate behavior of sand. Mech Mater 41(6):786–798
11. Williams EG, Graham SS, Reed PA, Rushing TS (2009) Laboratory characterization of Cor-Tuf concrete with and without steel fibers, vol 86. US Army Corps of Engineers, Engineering Research Development Center – Geotechnical Structures Laboratory

Chapter 31
Deceleration-Displacement Response for Projectiles That Penetrate Concrete Targets

M.J. Forrestal, T.L. Warren, and P.W. Randles

Abstract We examined data from two sets of penetration experiments that recorded deceleration during penetration into concrete targets with compressive strengths of 23 and 39 MPa. The 76.2-mm-diameter, 13 kg projectiles contained a single-channel acceleration data recorder. We plotted deceleration versus displacement data and showed that this response could be closely approximated by a linear rise region with a depth of two projectile diameters followed by a tunnel region with constant deceleration until the projectile came to rest. A new empirical model predicts accurately the deceleration-displacement responses.

Keywords Concrete penetration • Deceleration-displacement • Empirical models • Deceleration measurements • Data modifications

31.1 Introduction

Our penetration technology studies attempt to provide a fundamental understanding of the penetration process for concrete and rock targets. For this study and recent publications [1, 2] we focus on projectiles that are large enough to contain an acceleration data recorder. In [1], the 76.2-mm-diameter, 13 kg projectiles are limited to striking velocities of 460 m/s. The projectiles lost small amounts of mass through abrasion and experienced very small deformations. Therefore, rigid-body deceleration data provide a measure for the net force acting on the projectile nose. For this study, we use the previously published deceleration-time data [1] and provide plots of deceleration-displacement data and show that this response could be closely approximated by a linear rise entry region with a depth of two projectile diameters followed by a tunnel region with constant deceleration until the projectile comes to rest. With these observations and a new empirical model, we predict accurately the deceleration-displacement response. In addition, we plotted specific kinetic energy (kinetic energy divided by projectile mass) versus displacement and show a nearly constant slope in the tunnel region. This slope corresponds to the magnitude of the nearly constant deceleration in the tunnel region. Our new empirical model predicts accurately this constant deceleration. Thus, we predict the maximum, constant deceleration in the tunnel region with two different methods. Predictions from both methods closely agree with each other and the deceleration data.

Other authors have published work on concrete penetration, and Li et al. [3] present an extensive review article. However, most experimental studies only provide penetration depth versus striking velocity data as discussed in [1, 4, 5]; whereas, this study focuses on deceleration data. In addition, the readers may wish to review the concrete penetration models published by Li and Chen [4], Rosenberg and Dekel [5], and Chen et al. [6].

M.J. Forrestal (✉)
Forrestal Consulting, 3029 Tanglewood Park W, Fort Worth, TX 76109, USA
e-mail: mjforrestal@gmail.com

T.L. Warren
Warren Consulting, 3804 Shenandoah Pl, NE, Albuquerque, NM 87111, USA
e-mail: tlwarre@msn.com

P.W. Randles
DTRA-CXTT, Kirtkland AFB, NM 87117-5669, USA
e-mail: philip.randles@abq.dtra.mil

B. Song et al. (eds.), *Dynamic Behavior of Materials, Volume 1: Proceedings of the 2013 Annual Conference on Experimental and Applied Mechanics*, Conference Proceedings of the Society for Experimental Mechanics Series
DOI 10.1007/978-3-319-00771-7_31,

31.2 Empirical Penetration Models

In [1, 2], we present empirical penetration equations and compare predictions with deceleration-time measurements. Guided by cavity-expansion, penetration equations for aluminum targets [7], force on the projectile nose was taken as the sum of a target strength term and a target inertial term. However, for striking velocities limited to 460 m/s, the strength term dominated the penetration process and the inertial term could be neglected. In this study, we use the penetration equations in [1] that neglect target inertia to predict deceleration-time responses. We now develop new empirical penetration equations that predict deceleration-displacement and velocity-displacement. The deceleration data in [1, 2] show an entry crater region followed by a tunnel region with nearly constant deceleration over most of the deceleration-time responses. Guided by these observations, we take force on the projectile nose to be of the form

$$F = \begin{cases} -cz, & 0 \le z \le 4a \\ -\pi a^2 R, & 4a \le z \le P \end{cases}, \tag{31.1a,b}$$

where Eq. (31.1a) describes the force acting on the nose of the projectile in the crater region, and Eq. (31.1b) describes the force acting on the nose of the projectile in the tunnel region. In Eqs. (31.1a, b), z is the current penetration displacement of the projectile nose tip, P is the final depth of penetration, $2a$ and m are the projectile diameter and mass, respectively, R is the target resistance parameter that is determined from penetration depth data, and c is a constant determined from the analysis.

From Newton's law for a rigid-body, deceleration-displacement is

$$a(z) = \frac{dV}{dt} = V\frac{dV}{dz} = \begin{cases} -\dfrac{cz}{m}, & 0 \le z \le 4a \\ -\dfrac{\pi a^2 R}{m}, & 4a \le z \le P \end{cases}, \tag{31.2a,b}$$

where V is the rigid-body velocity of the projectile. An integration of Eqs. 31.2a,b gives

$$V^2 = \begin{cases} V_s^2 - \dfrac{cz^2}{m}, & 0 \le z \le 4a \\ V_1^2 - \dfrac{2\pi a^2 R}{m}(z - 4a), & 4a \le z \le P \end{cases}, \tag{31.3a,b}$$

where V_s is the striking velocity, and V_1 is the velocity when the tip of the projectile is at $z = 4a$. From force continuity at $z = 4a$

$$c = \frac{\pi a R}{4}, \tag{31.4}$$

and from Eqs. 31.3a and 31.4 at $z = 4a$

$$V_1^2 = V_s^2 - \frac{4\pi a^3 R}{m}. \tag{31.5}$$

With Eqs. 31.3a,b, 31.4, and 31.5

$$V^2 = \begin{cases} V_s^2 - \dfrac{\pi a R}{4m} z^2, & 0 \le z \le 4a \\ V_s^2 - \dfrac{2\pi a^2 R}{m}(z - 2a), & 4a \le z \le P \end{cases}. \tag{31.6a,b}$$

Final penetration depth is obtained from Eq. 31.3b when $V = 0$ and $z = P$ which gives

$$P = \frac{mV_s^2}{2\pi a^2 R} + 2a, \quad 4a \le z \le P. \tag{31.7}$$

We determine the target resistance parameter R from striking velocity-penetration depth data. Therefore, from Eq. 31.7

$$R = \frac{mV_s^2}{2\pi a^2 (P - 2a)} \quad . \tag{31.8}$$

The projectile kinetic energy is $mV^2/2$, and we define the specific kinetic energy as $V^2/2$. We take the derivative of the specific kinetic energy with respect to z which gives

$$\frac{d}{dz}\left(\frac{V^2}{2}\right) = V\frac{dV}{dz} = \frac{dV}{dt}, \tag{31.9}$$

where the term on the right is rigid-body acceleration. We later plot $V^2/2$ versus z and note that the slope of the curve is the acceleration. For the tunnel region, the acceleration is constant and is given by

$$\frac{d}{dz}\left(\frac{V^2}{2}\right) = -\frac{\pi a^2 R}{m}, \quad 4a \le z \le P. \tag{31.10}$$

Later, we compare deceleration-time and deceleration-displacement responses. From [1], deceleration-time is given by

$$a(t) = \frac{dV}{dt} = \begin{cases} -\omega V_s \sin \omega t, & 0 \le z \le 4a \\ -\dfrac{\pi a^2 R}{m}, & 4a \le z \le P \end{cases}, \tag{31.11a,b}$$

where $\omega^2 = \pi a R/4m$. P and R are given by Eqs. 31.7 and 31.8.

31.2.1 Concrete Materials

In [1], we reported results from two sets of penetration experiments with concrete targets that had average compressive strengths of $\sigma_{cf} = 23$ and 39 MPa (3.3 and 5.7 ksi). The 23 MPa concrete used a granite aggregate, and the 39 MPa concrete used a limestone aggregate. Both aggregates had a maximum diameter of 9.5 mm. Details of the concrete mix design are given in [1].

As explained in [1], the unconfined compressive strength of concrete and rock materials depends on the sample geometry. For these material tests, the samples had a diameter of 50.8 mm and a length of 114 mm. Therefore, the values of σ_{cf} reported in [1] and used in this study are for these sample geometries.

31.2.2 Penetration Experiments

In this study, we use the data from our previously published paper. In [1], we conducted sets of penetration experiments into concrete targets with $\sigma_{cf} = 23$ and 39 MPa. Targets were cast in corrugated steel culverts with 1.83 m diameters. The projectiles dimensioned in Fig. 31.1 were machined from 4340 Rc45 steel and had a nominal mass of 13 kg, a 3.0 caliber-radius-head (CRH) nose shape, and contained an acceleration data recorder [8].

A 83-mm-diameter powder gun launched the 13 kg projectiles to striking velocities V_s between 140 and 460 m/s. Photographs from a high-speed, framing camera showed the launch packages were stripped from the projectiles prior to impact and also were used to measure the pitch and yaw. A streak camera was employed to measure projectile striking velocities. These measurements are given in Tables 31.1 and 31.2.

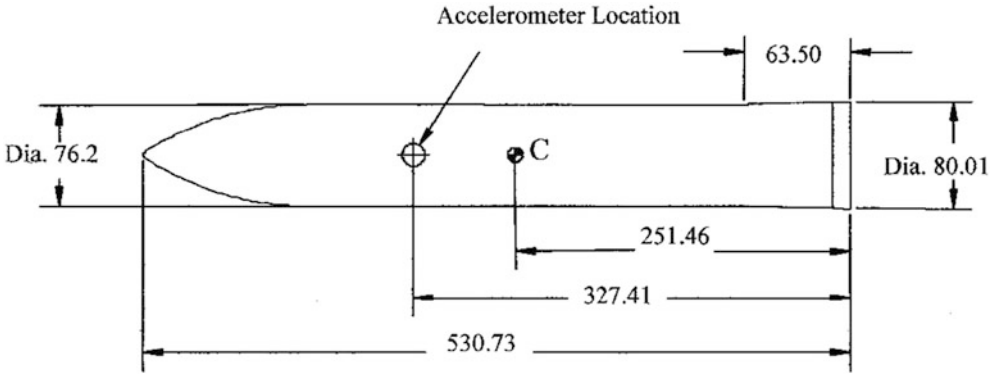

Fig. 31.1 Projectile geometry. Dimensions in mm

Table 31.1 Penetration data for the 1.83-m-diameter targets with average compressive strength $\sigma_{cf} = 23$ MPa (3.3 ksi)

Shot and projectile number	Projectile mass (kg)	Target length (m)	Striking velocity (m/s)	Pitch-yaw (degrees)	Penetration depth (m)	R (MPa)
SNL-00-06/2	13.0	1.83	139	0.3D, 0.2L	0.24	169
SNL-00-03/1	13.0	1.83	200	0.0, 0.4L	0.42	166
SNL-00-02/2	13.1	1.22	250	0.4D, 0.3R	0.62	166
SNL-00-05/3	13.1	1.83	337	0.2D, 0.1R	0.93	190
SNL-00-04/4	13.1	1.83	379	0.3U, 0.2R	1.18	187

Table 31.2 Penetration data for the 1.83-m-diameter targets with average compressive strength $\sigma_{cf} = 39$ MPa (5.7 ksi)

Shot and projectile number	Projectile mass (kg)	Target length (m)	Striking velocity (m/s)	Pitch-yaw (degrees)	Penetration depth (m)	R (MPa)
SNL-00-11/3	12.9	1.22	238	0.1D, 0.0	0.30	359
SNL-00-12/4	12.9	1.83	276	0.1D, 0.4L	0.38	354
SNL-00-09/1	12.9	1.22	314	0.2D, 0.2R	0.45	373
SNL-00-14/5	13.0	1.83	456	0.2U, 0.2R	0.94	343

31.3 Target Resistance Parameter *R*

We calculate R from Eq. 31.8. The average projectile mass is $m = 13$ kg, and the projectile radius is $a = 38.1$ mm. Tables 31.1 and 31.2 list the measured values of V_s and P, and the calculated values of R. The average values of R for the $\sigma_{cf} = 23$ and 39 MPa concretes are $R = 176$ and 357 MPa. Figures 31.2 and 31.3 show data and empirical model predictions for P versus V_s that use the average values of R.

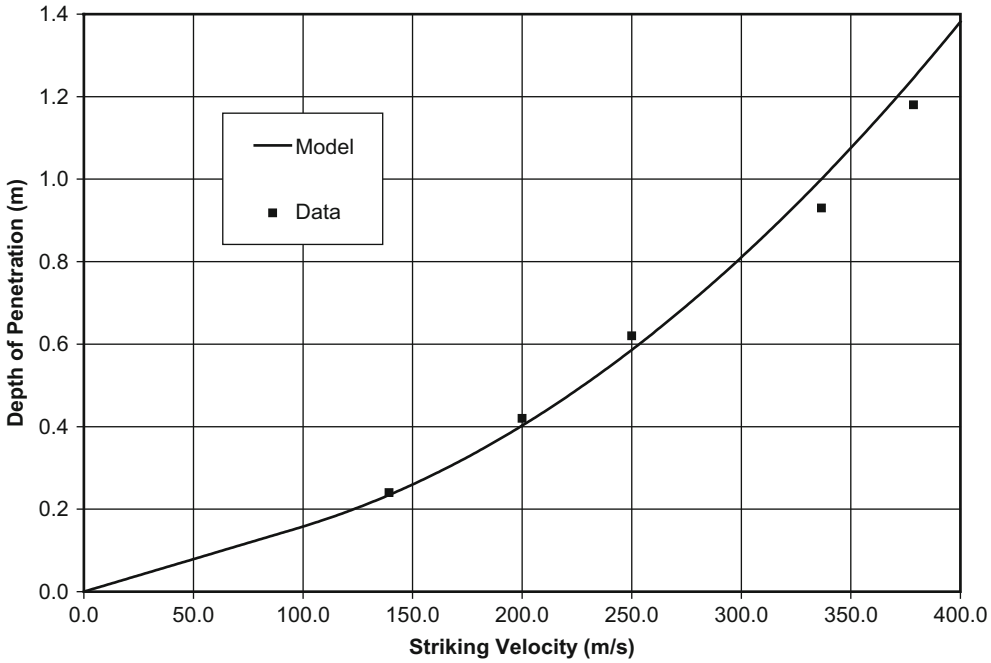

Fig. 31.2 Penetration depth versus striking velocity for $\sigma_{cf} = 23$ MPa and average $R = 176$ MPa

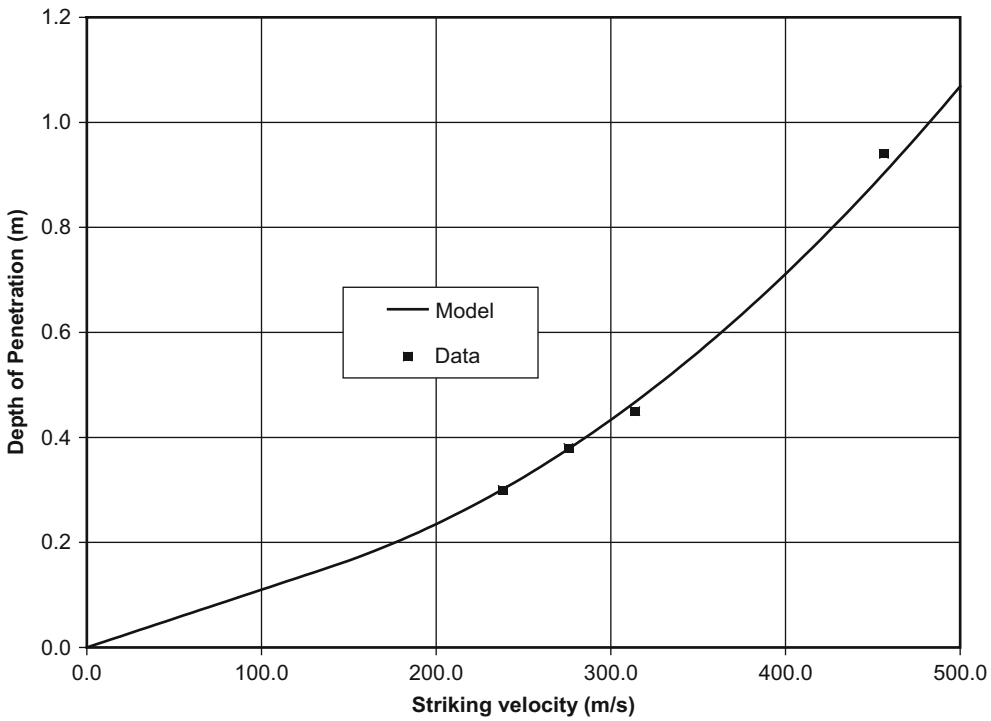

Fig. 31.3 Penetration depth versus striking velocity for $\sigma_{cf} = 39$ MPa and average $R = 357$ MPa

Table 31.3 Deceleration correction results for $\sigma_{cf} = 23$ MPa (3.3 ksi)

Shot and projectile number	V_s (m/s)	V_{sm} (m/s)	P (m)	P_c (m)
SNL-00-06/2	139	150	0.24	0.24
SNL-00-03/1	200	214	0.42	0.43
SNL-00-02/2	250	263	0.62	0.60
SNL-00-05/3	337	340	0.93	0.95
SNL-00-04/4	379	390	1.18	1.18

31.3.1 Deceleration Measurements

As shown in Fig. 31.1, the projectile was designed to contain a single-channel, acceleration data recorder. Thus, the experiments in [1, 2] recorded launch acceleration and deceleration during penetration. Rohwer [8] describes the development and operation of this 15 kHz data recorder.

Tables 31.1 and 31.2 record the striking velocities V_s measured with the streak camera. We can also perform an integration of the deceleration-time data to calculate the corresponding striking velocity. However, the measured deceleration data contain the structural and component responses of the mounted accelerometer as well as the rigid-body deceleration. The deceleration data are limited to 15 kHz from the data recorder [8], so higher frequency responses are eliminated. In addition, there are no available calibration experimental procedures that determine the transducer sensitivity with an internationally accepted input calibration standard [9, 10]. Currently, the accuracy of acceleration measurements are examined by performance evaluation tests that compare measured accelerations with measurements from other transducers such as strain gages and quartz gages [9]. Because of these limitations, we now compare striking velocities measured with the streak camera and those calculated from the deceleration data. Then, we correct the deceleration data such that the integrated deceleration data are in agreement with the streak camera data.

The striking velocity calculated from the measured deceleration data is

$$V_{sm} = -\int_0^{t_f} a_m(t')dt', \tag{31.12a}$$

where $a_m(t)$ is the measured deceleration and t_f is the time at which the projectile comes to rest. To be consistent with the models, velocities are taken positive in the direction of penetration and deceleration is taken as negative. The rigid–body velocity calculated from the measured deceleration data is

$$V_m(t) = V_{sm} + \int_0^t a_m(t')dt'. \tag{31.12b}$$

We now correct $V_m(t)$ with

$$V(t) = \left(\frac{V_s}{V_{sm}}\right) V_m(t), \tag{31.13a}$$

where $V(t)$ is the corrected value such that $V(0)$ is in agreement with the striking velocity V_s measured with the streak camera. The corrected value of acceleration is given by

$$a(t) = \left(\frac{V_s}{V_{sm}}\right) a_m(t). \tag{31.13b}$$

Tables 31.3 and 31.4 give the striking velocities measured by the streak camera V_s and those calculated from the deceleration data V_{sm}. In addition, final measured penetration depths P and those calculated from the corrected deceleration data P_c are also recorded in Tables 31.3 and 31.4. In summary, we corrected the deceleration data such that the striking velocities from the integrated acceleration data are in agreement with the streak camera data. We also note that measured penetration depths are in close agreement with those final depths calculated from a double integration of the corrected deceleration data.

Table 31.4 Deceleration correction results for $\sigma_{cf} = 39$ MPa (5.7 ksi)

Shot and projectile number	V_s (m/s)	V_{sm} (m/s)	P (m)	P_c (m)
SNL-00-11/3	238	259	0.30	0.32
SNL-00-12/4	276	294	0.38	0.37
SNL-00-09/1	314	334	0.45	0.46
SNL-00-14/5	456	478	0.94	0.93

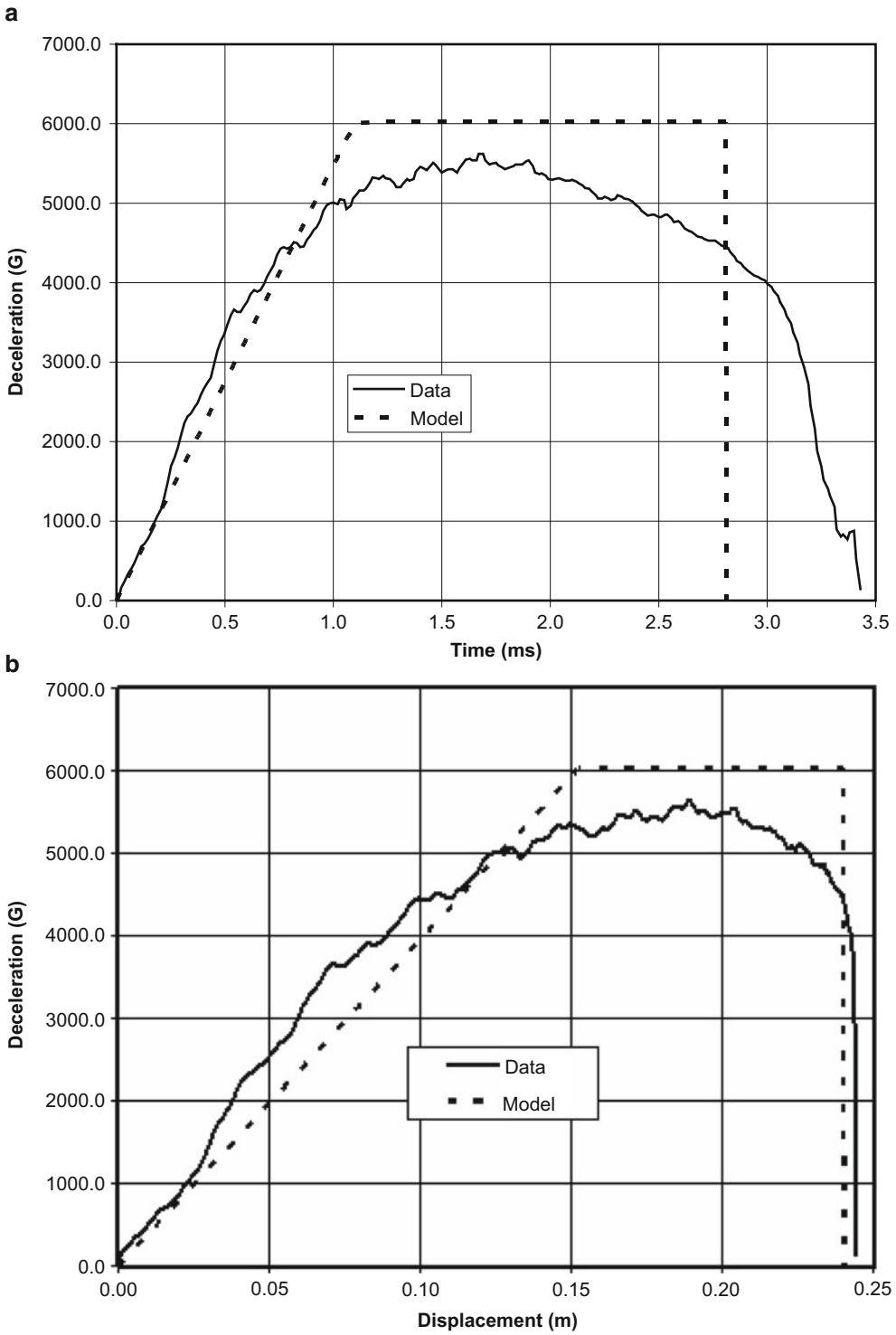

Fig. 31.4 Data and model comparisons for SNL-00-06/2 with $\sigma_{cf} = 23$ MPa and $V_s = 139$ m/s. (**a**) Deceleration-time, (**b**) deceleration-displacement, (**c**) specific kinetic energy-displacement, and (**d**) linear fit to specific kinetic energy-displacement in tunnel region

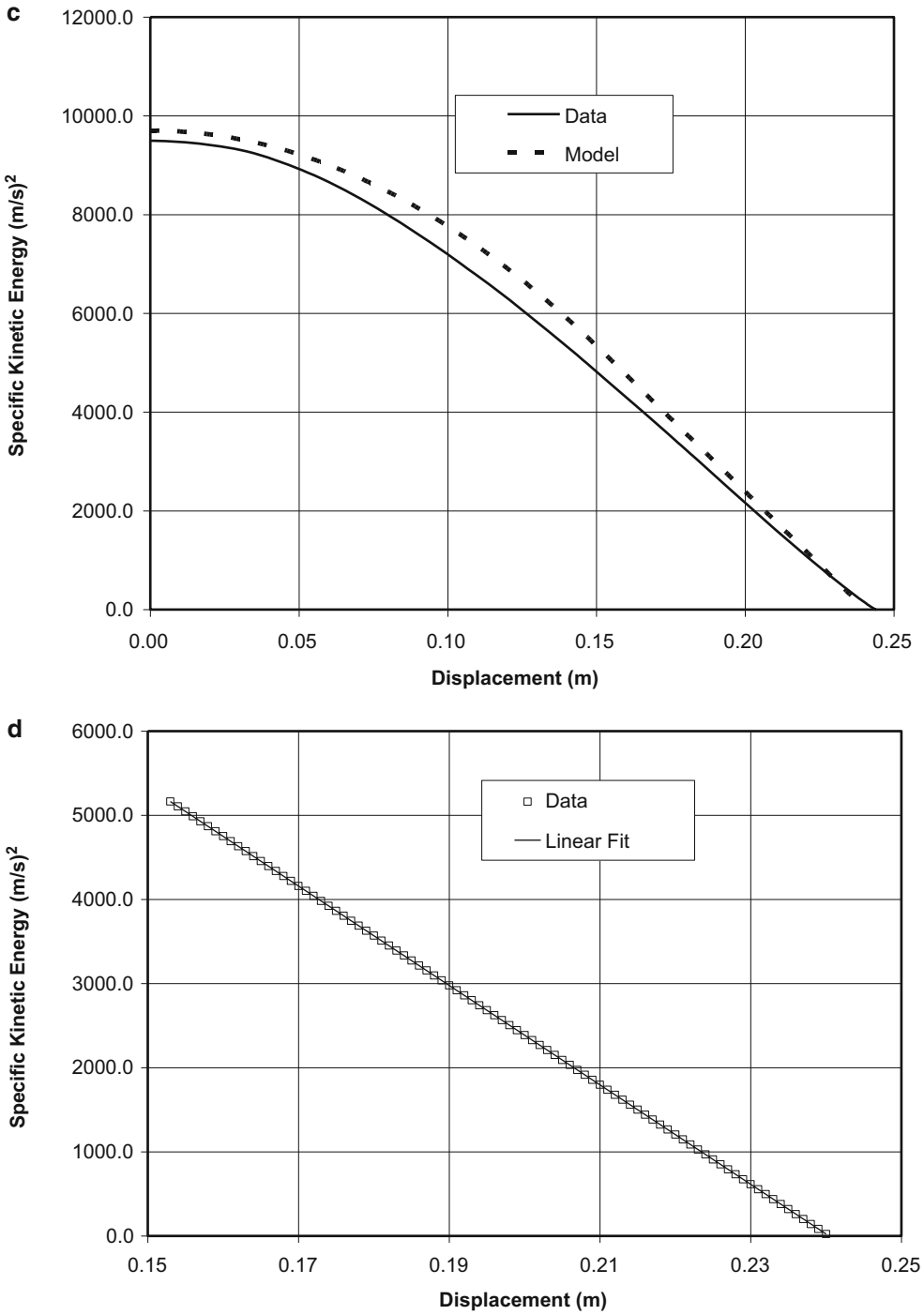

Fig. 31.4 (continued)

31.4 Data and Model Comparisons for $\sigma_{cf} = 23$ Mpa

Figures 31.4a–c, 31.5a–c, 31.6a–c, 31.7a–c, and 31.8a–c show deceleration-time, deceleration-displacement, and specific kinetic energy-displacement for $V_s = 139$, 200, 250, 337, and 379 m/s. In these figures, the model predictions input the target resistance parameter R (Eq. 31.8) determined from striking velocity versus penetration depth data. The deceleration data contains the structural and component responses of the mounted accelerometer as well as the rigid-body deceleration;

whereas, the models only predict the rigid-body responses. For such a complex problem the models are in reasonably good agreement with the data. The deceleration-time data and model predictions agree well until the end of the event. By contrast, the deceleration-displacement model predictions are in good agreement for the entire event. Equation 31.9 predicts that the derivative of the specific kinetic energy is proportional to the projectile acceleration. Figures 31.4c, 31.5c, 31.6c, 31.7c, and 31.8c show that the predicted slopes are in good agreement with the data.

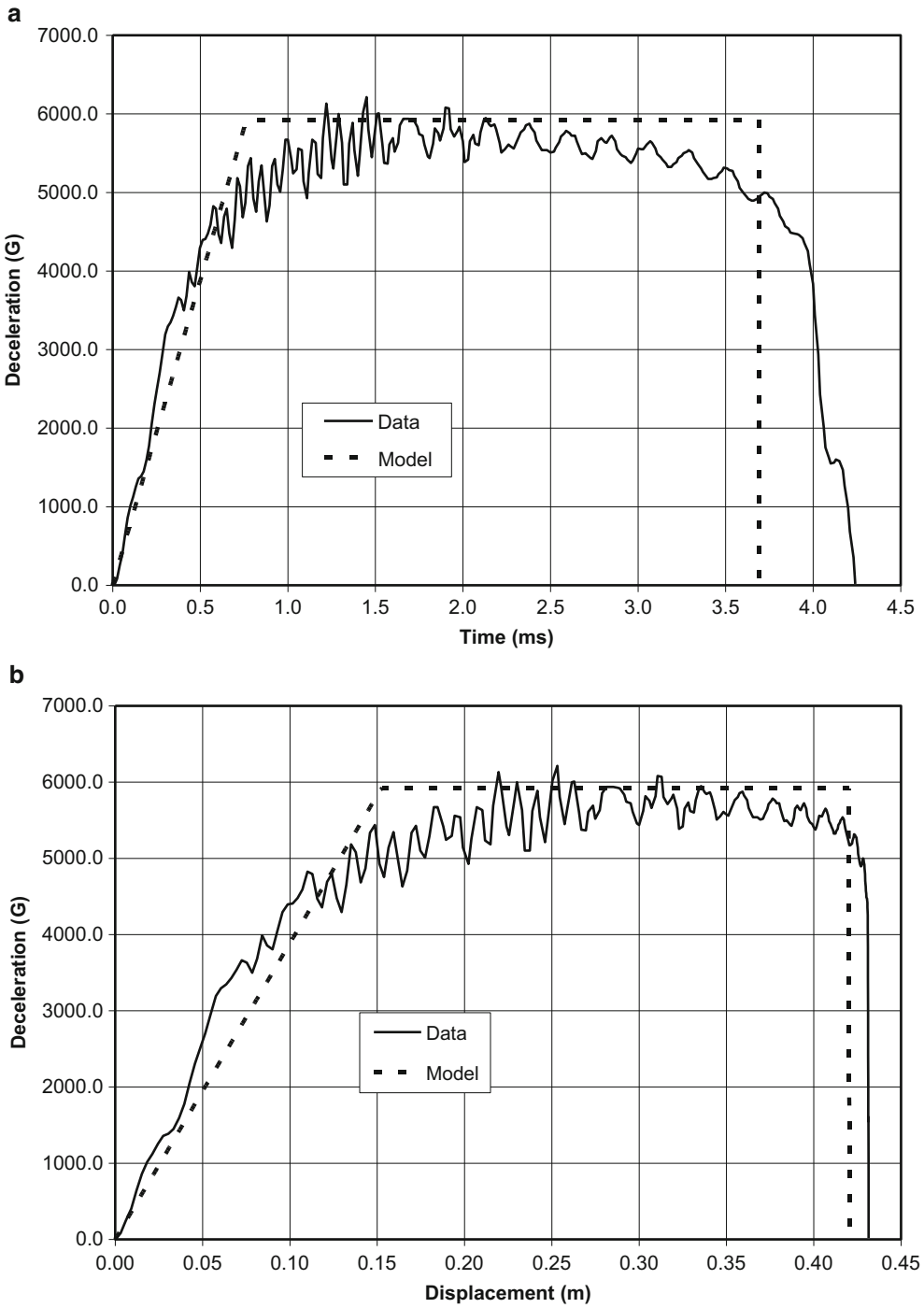

Fig. 31.5 Data and model comparisons for SNL-00-03/1 with $\sigma_{cf} = 23$ MPa and $V_s = 200$ m/s. (**a**) Deceleration-time, (**b**) deceleration-displacement, (**c**) specific kinetic energy-displacement, and (**d**) linear fit to specific kinetic energy-displacement in tunnel region

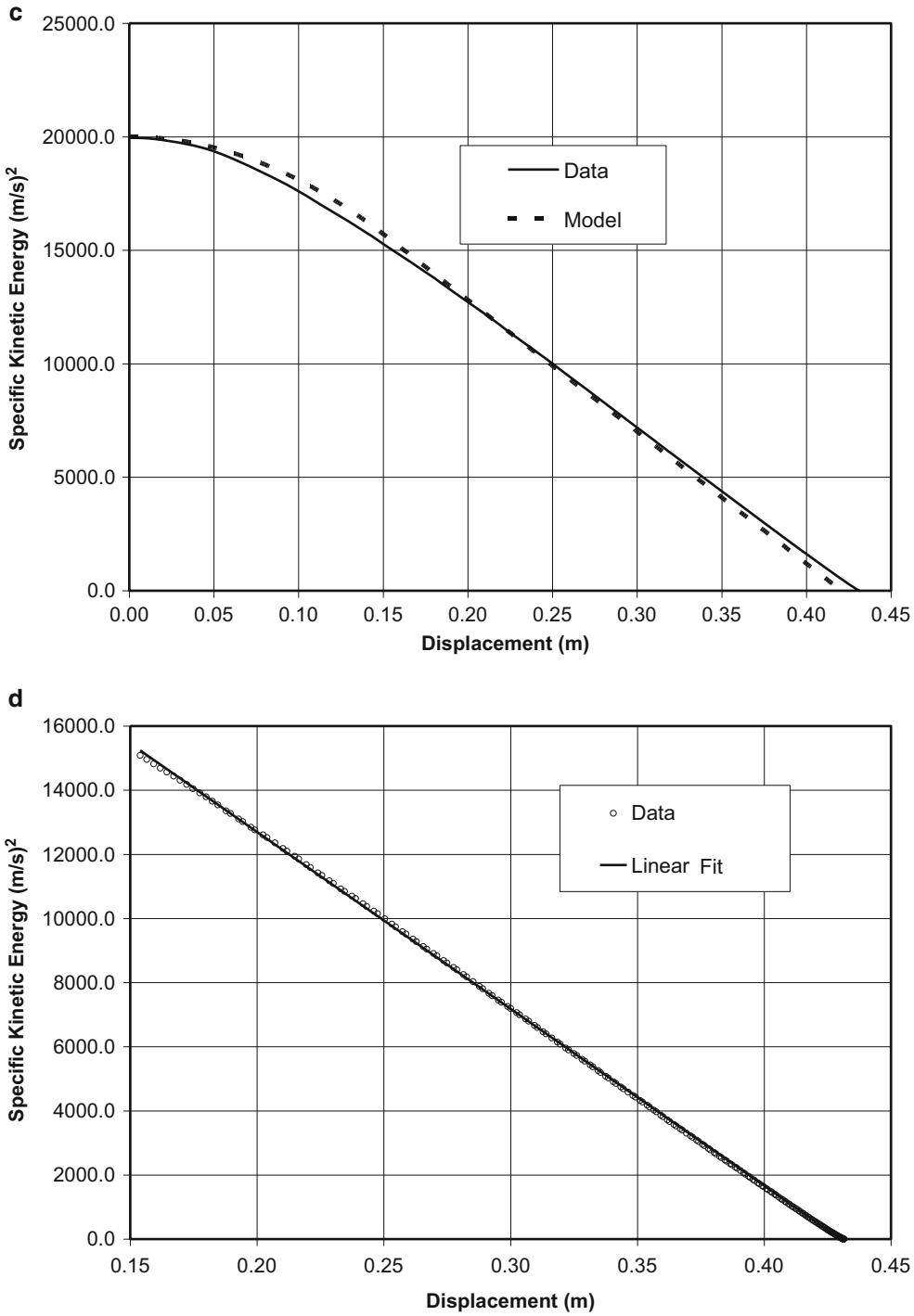

Fig. 31.5 (continued)

As previously discussed, the slopes of the curves in Figs. 31.4c, 31.5c, 31.6c, 31.7c, and 31.8c are rigid-body, projectile accelerations. In Figs. 31.4d, 31.5d, 31.6d, 31.7d, and 31.8d, we plot specific kinetic energy versus displacement data for the tunnel region $4a \leq z \leq P$ and show a least squares, linear fit. Since the data and linear fits are in excellent agreement, we take the slope of the linear fit as a measure of acceleration. This method calculates acceleration in the tunnel region from velocity-displacement data; whereas, the predictions in Figs. 31.4c, 31.5c, 31.6c, 31.7c, and 31.8c calculate the tunnel acceleration

from striking velocity versus penetration depth data. Table 31.5 presents values of the target resistance parameters R and the constant decelerations in the tunnel region ($1G = 9.81$ m/s^2) calculated from the two methods. In Table 31.5, Method 1 uses the penetration depth data, and Method 2 uses the slope of the specific kinetic energy versus displacement data. Results from both methods are in close agreement.

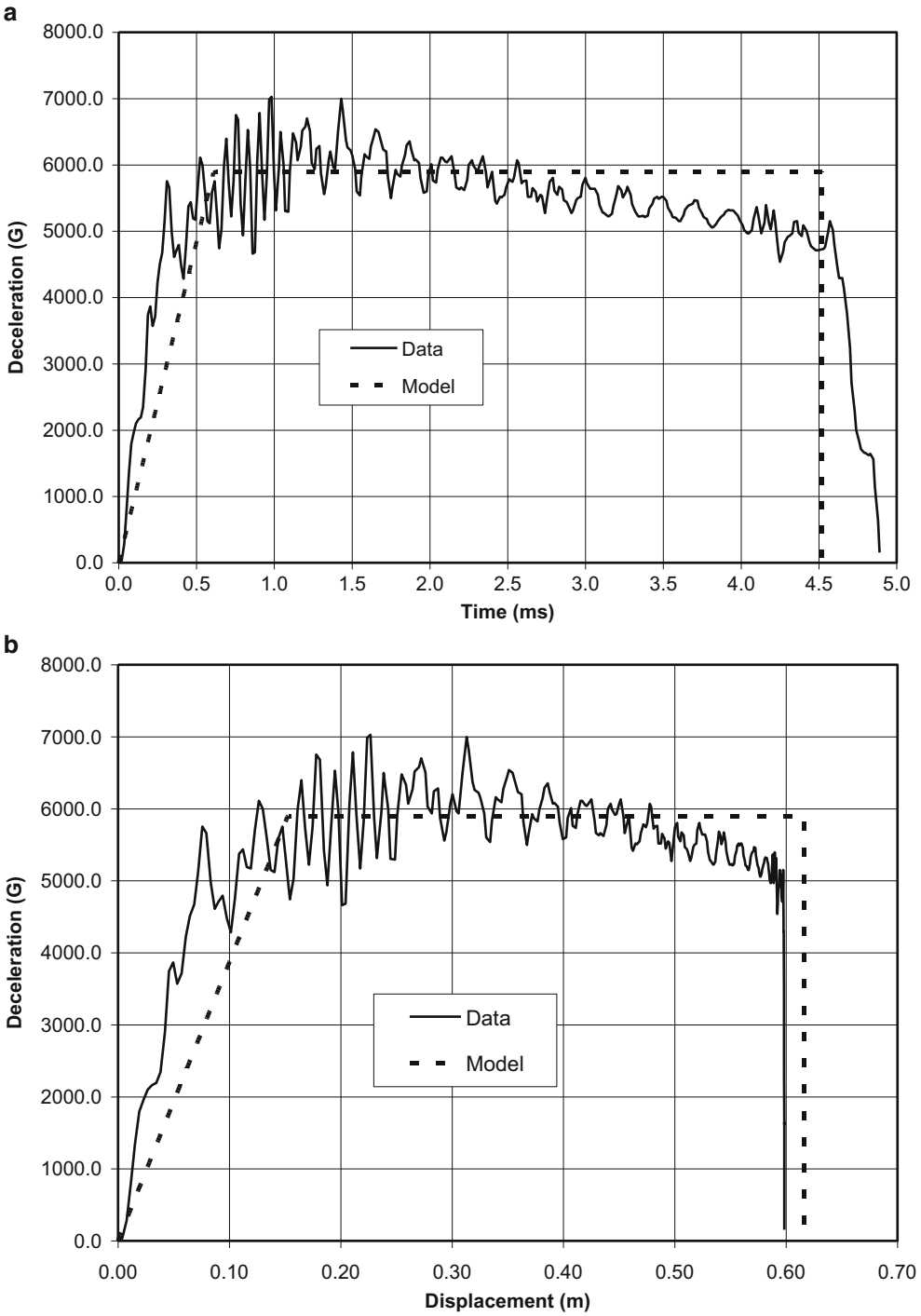

Fig. 31.6 Data and model comparisons for SNL-00-02/2 with $\sigma_{cf} = 23$ MPa and $V_s = 250$ m/s. (**a**) Deceleration-time, (**b**) deceleration-displacement, (**c**) specific kinetic energy-displacement, and (**d**) linear fit to specific kinetic energy-displacement in tunnel region

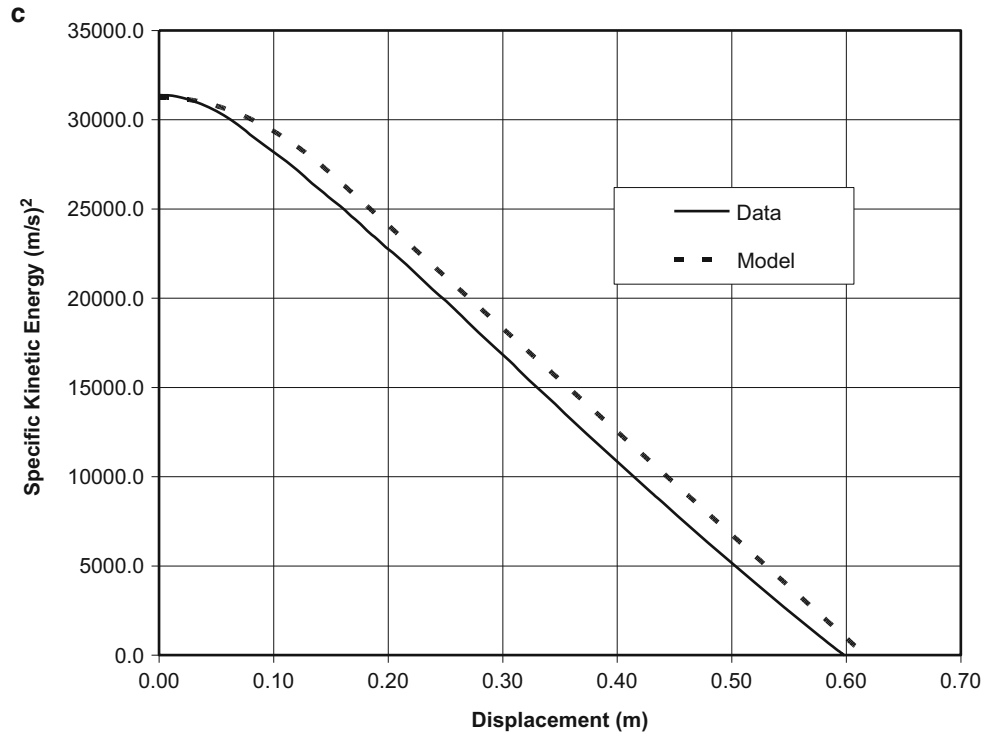

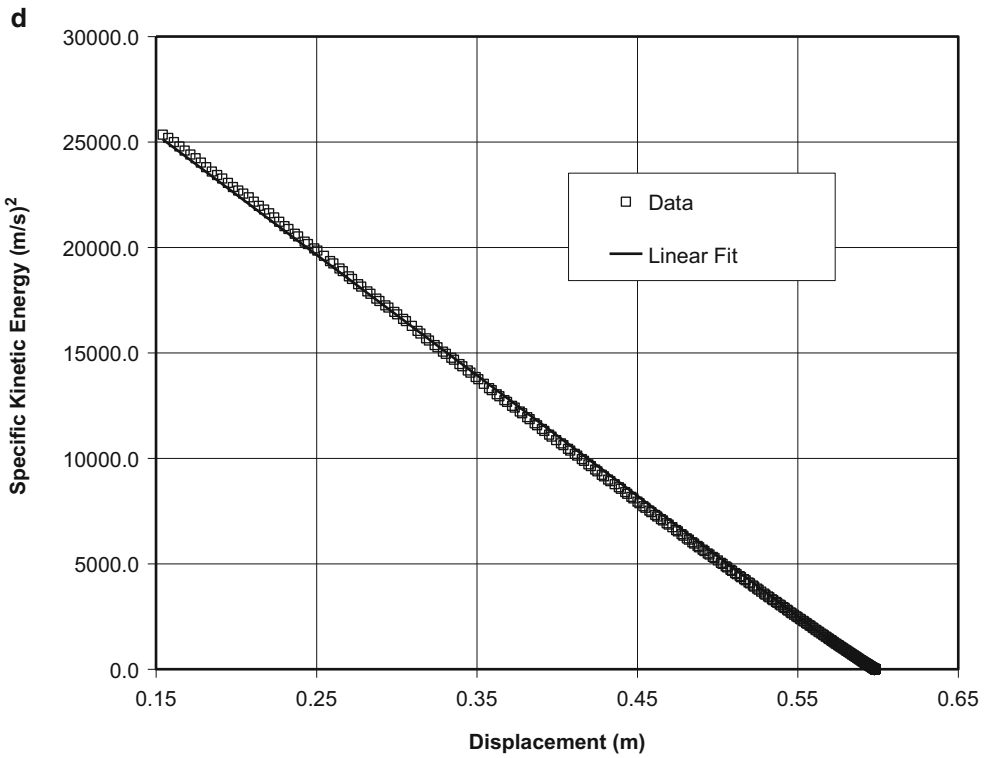

Fig. 31.6 (continued)

31.5 Data and Model Comparisons for $\sigma_{cf} = 39$ MPa

Figures 31.9a–c, 31.10a–c, 31.11a–c, and 31.12a–c show deceleration-time, deceleration-displacement, and specific kinetic energy-displacement for $V_s = 238$, 276, 314, and 456 m/s. Again, this is a complex problem and the deceleration data contains structural and component responses not included in the models. The deceleration-time data and model predictions

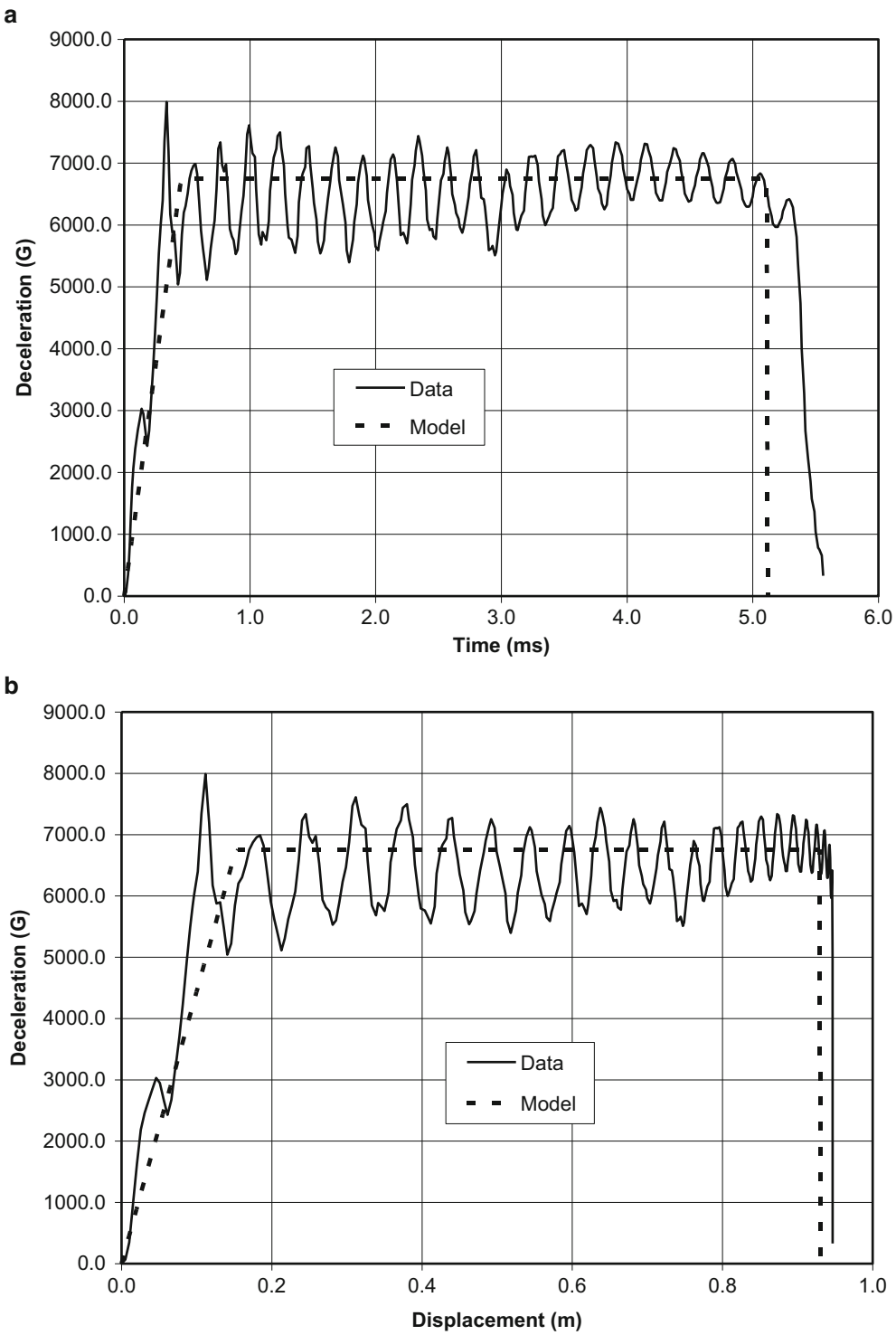

Fig. 31.7 Data and model comparisons for SNL-00-05/3 with $\sigma_{cf} = 23$ MPa and $V_s = 337$ m/s. (**a**) Deceleration-time, (**b**) deceleration-displacement, (**c**) specific kinetic energy-displacement, and (**d**) linear fit to specific kinetic energy-displacement in tunnel region

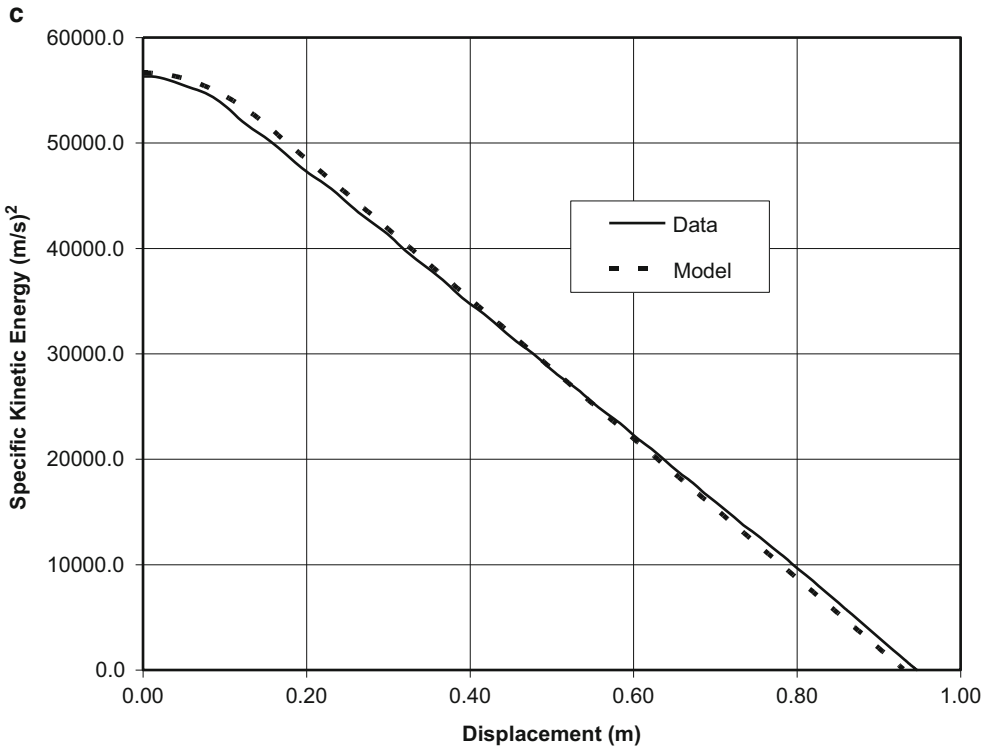

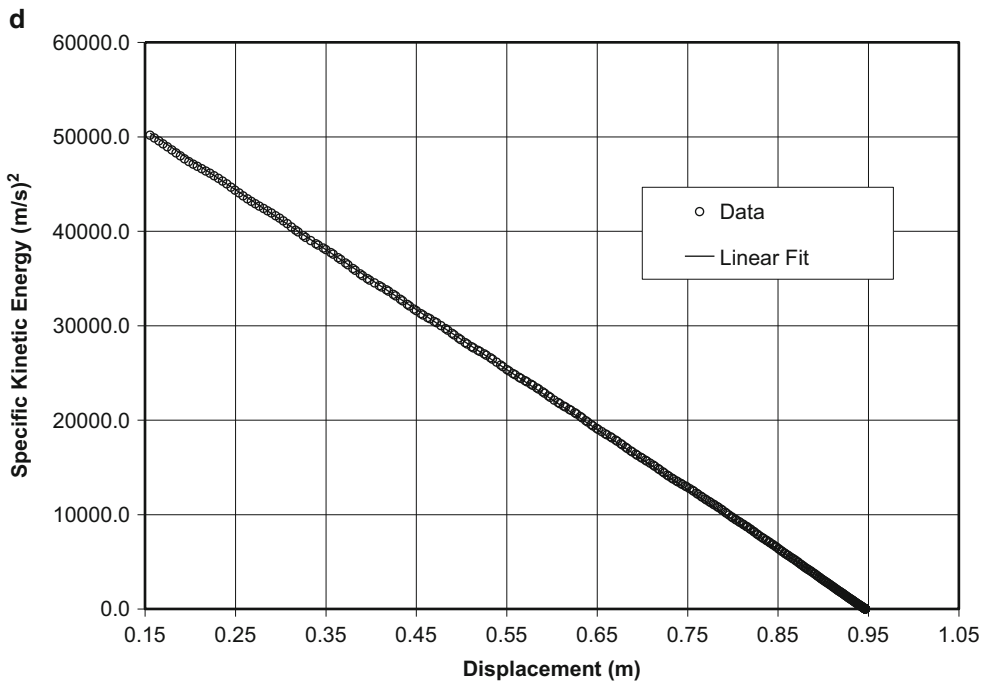

Fig. 31.7 (continued)

are in good agreement for the first half of the time event. After that, the data decay below the model predictions. By contrast, the deceleration-displacement data and model predictions are in reasonable good agreement for the entire event. In addition, Figs. 31.9c, 31.10c, 31.11c, and 31.12c show that the specific kinetic energy-displacement slopes predicted from the model are in good agreement with the data.

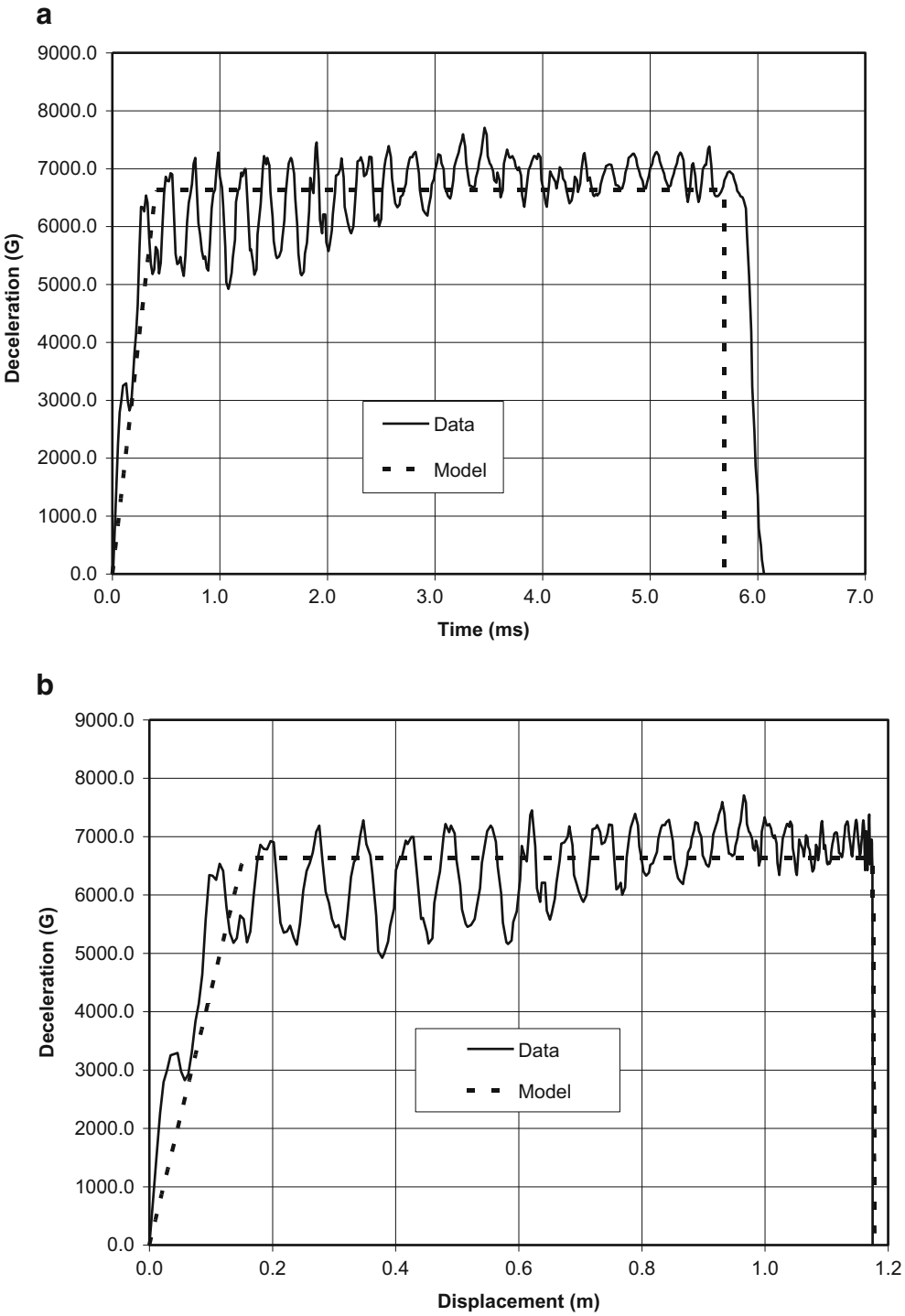

Fig. 31.8 Data and model comparisons for SNL-00-04/4 with $\sigma_{cf} = 23$ MPa and $V_s = 379$ m/s. (**a**) Deceleration-time, (**b**) deceleration-displacement, and (**c**) specific kinetic energy-displacement, and (**d**) linear fit to specific kinetic energy-displacement in tunnel region

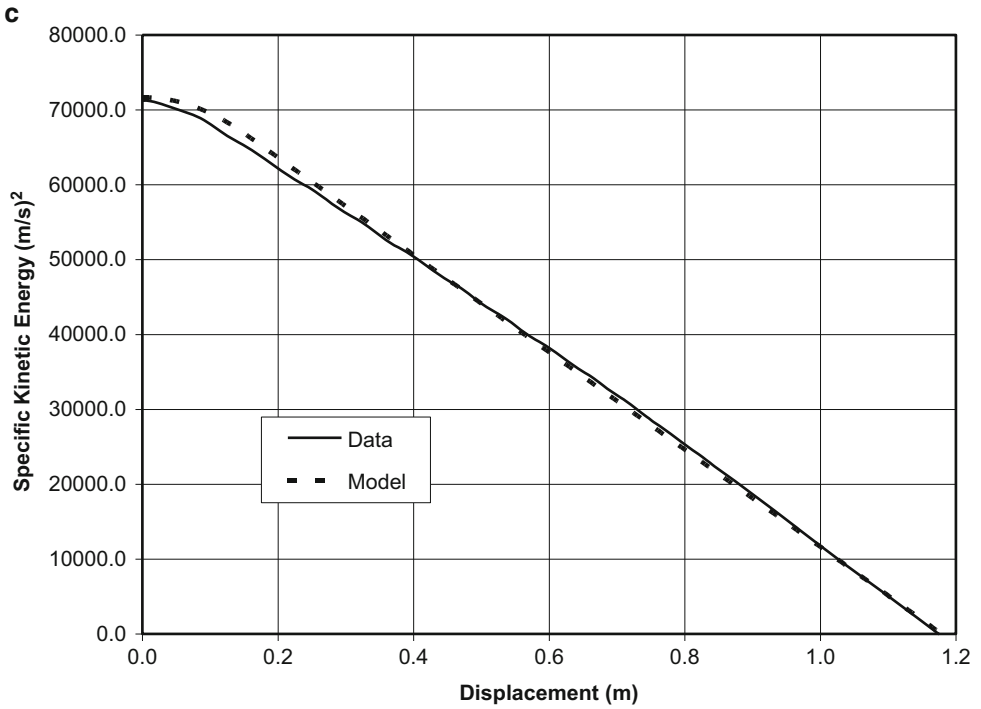

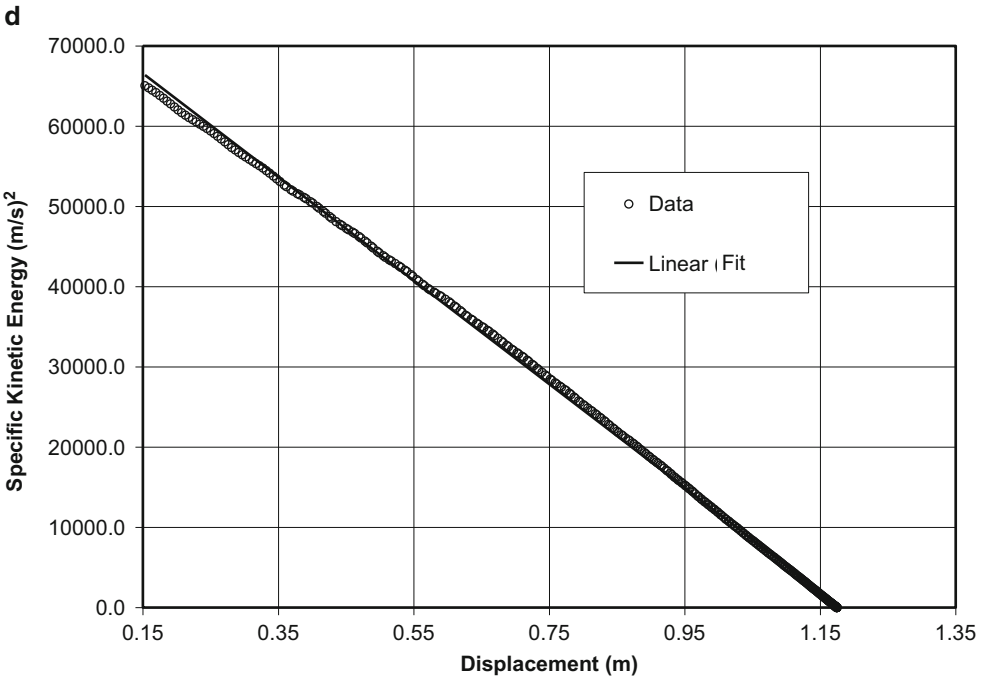

Fig. 31.8 (continued)

Table 31.5 Penetration results in the tunnel region for $\sigma_{cf} = 23$ MPa (3.3 ksi)

Shot and projectile number	Projectile mass (kg)	Striking velocity (m/s)	Method 1 R (MPa)	Method 1 deceleration (G)	Method 2 R (MPa)	Method 2 deceleration (G)
SNL-00-06/2	13.0	139	169	6050	169	6029
SNL-00-03/1	13.0	200	166	5942	157	5628
SNL-00-02/2	13.1	250	166	5896	164	5834
SNL-00-05/3	13.1	337	190	6749	182	6477
SNL-00-04/4	13.1	379	187	6642	185	6587

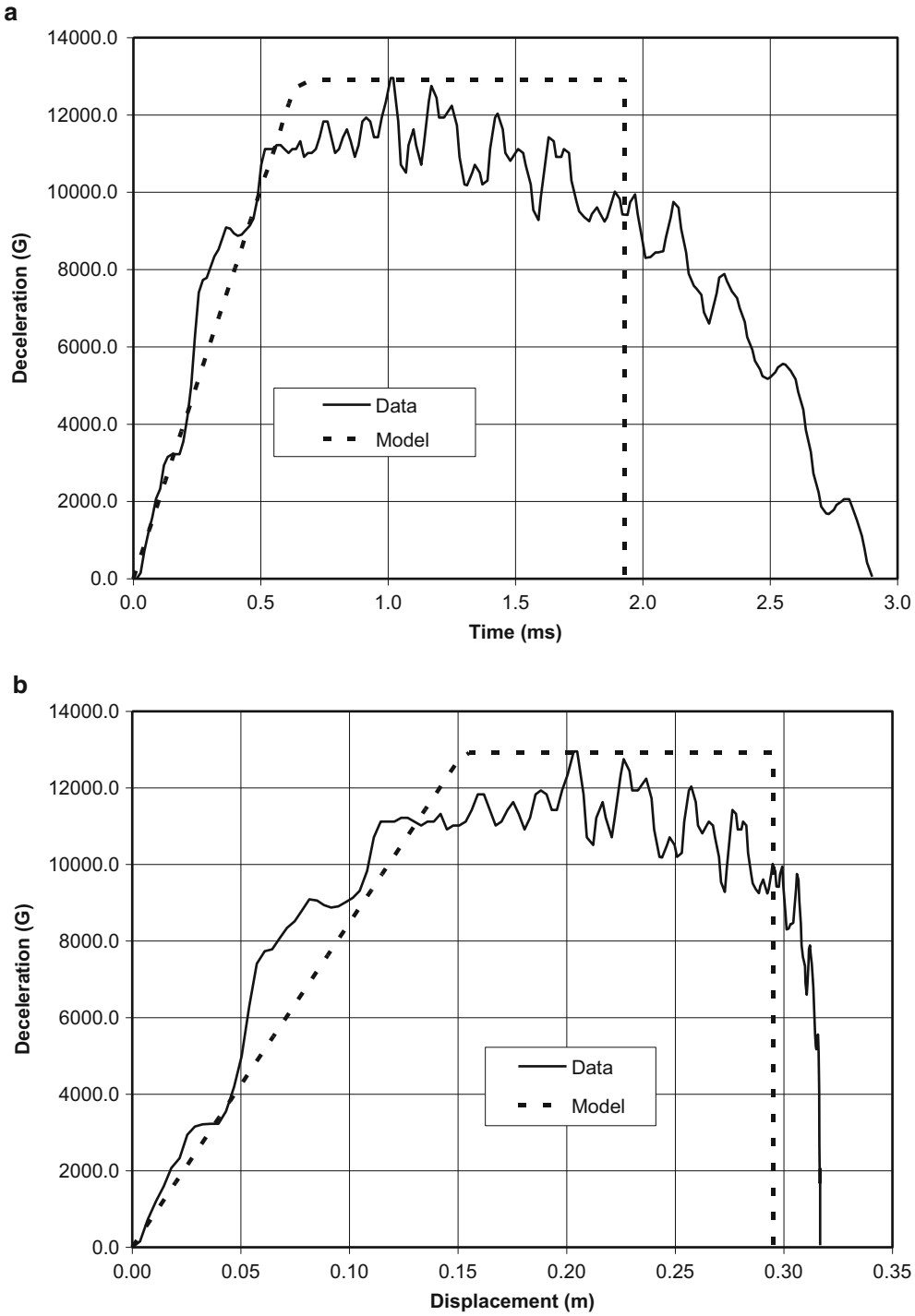

Fig. 31.9 Data and model comparisons for SNL-00-11/3 with $\sigma_{cf} = 39$ MPa and $V_s = 238$ m/s. (**a**) Deceleration-time, (**b**) deceleration-displacement, (**c**) specific kinetic energy-displacement, and (**d**) linear fit to specific kinetic energy-displacement in tunnel region

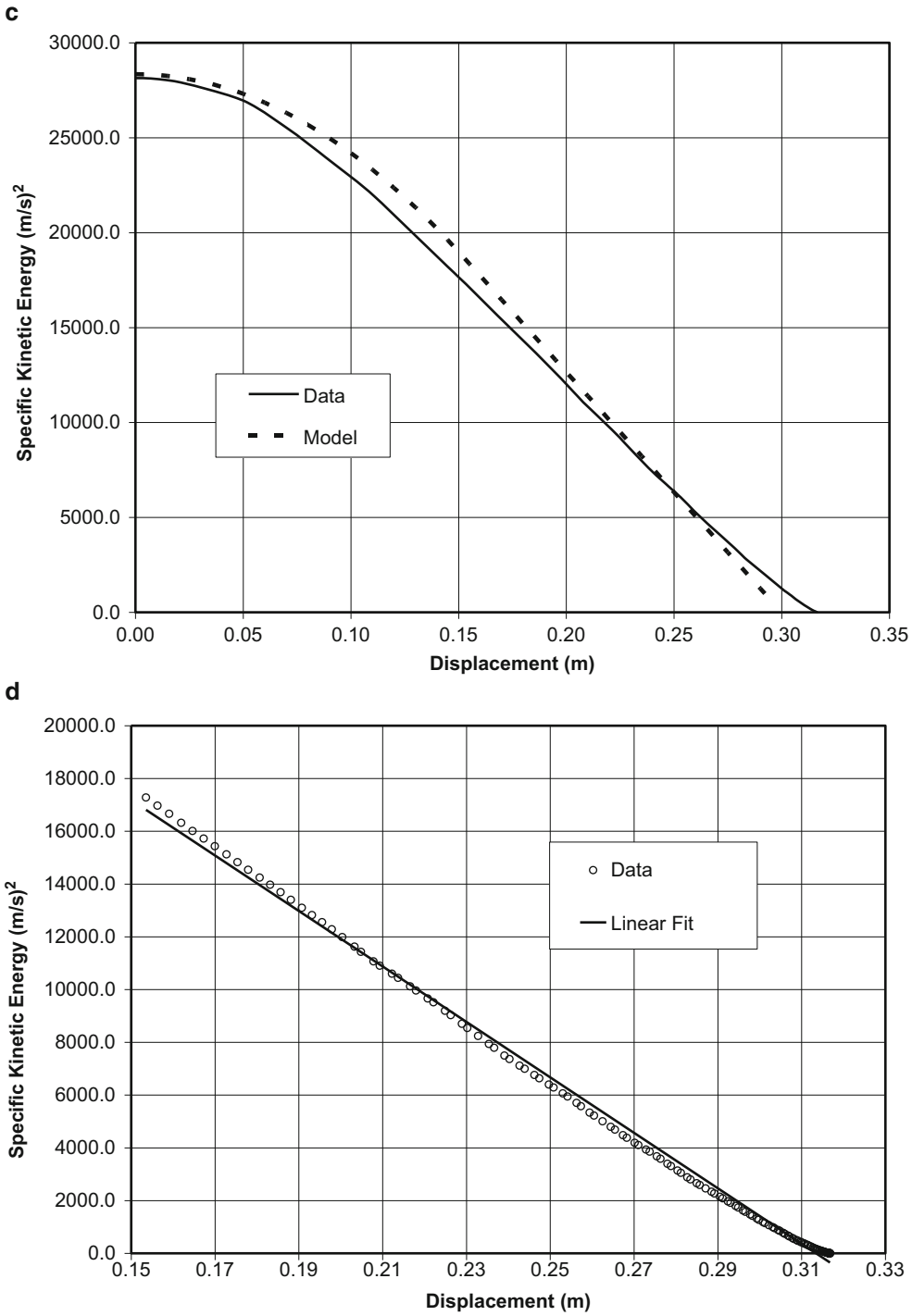

Fig. 31.9 (continued)

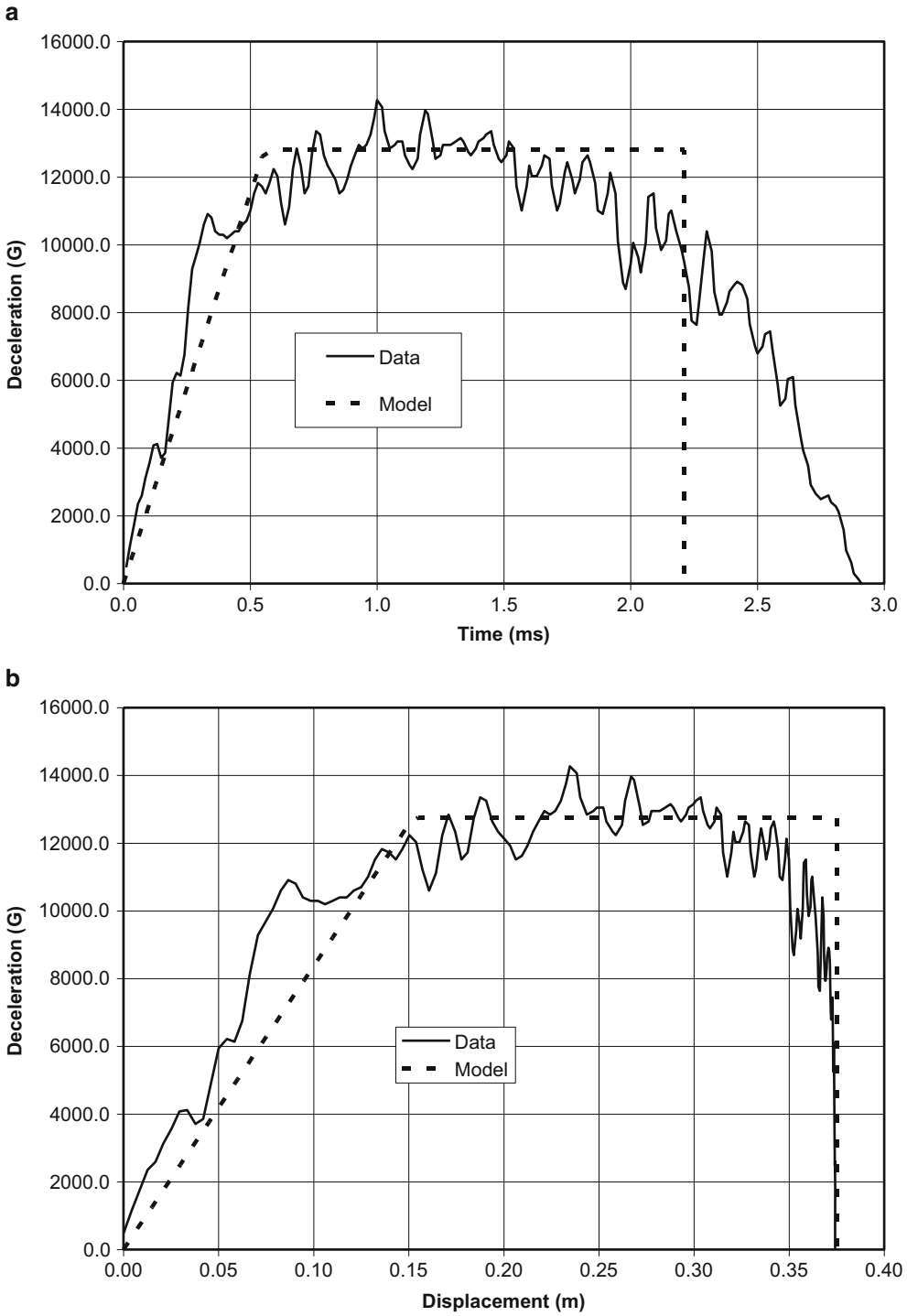

Fig. 31.10 Data and model comparisons for SNL-00-12/4 with $\sigma_{cf} = 39$ MPa and Vs = 276. (**a**) Deceleration-time, (**b**) deceleration-displacement, (**c**) specific kinetic energy-displacement, and (**d**) linear fit to specific kinetic energy-displacement in tunnel region

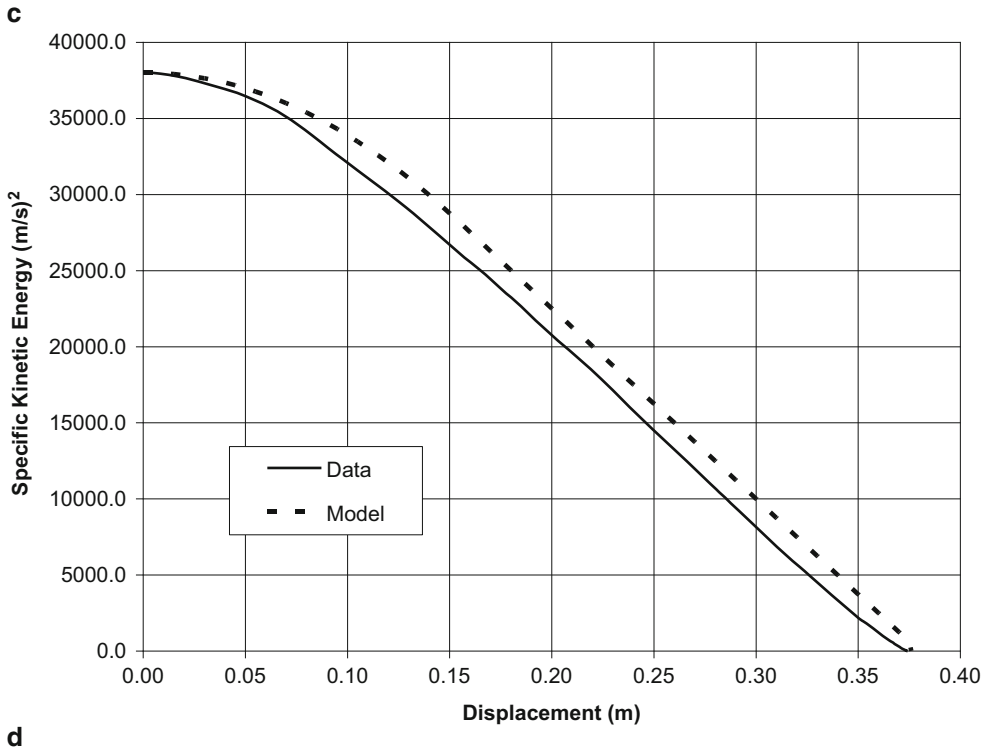

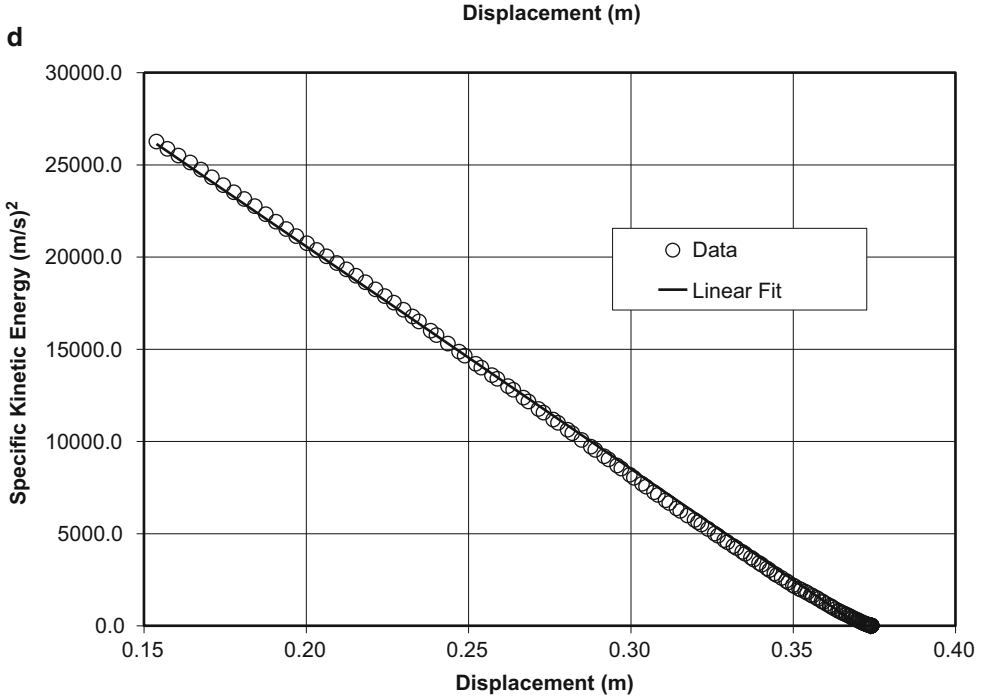

Fig. 31.10 (continued)

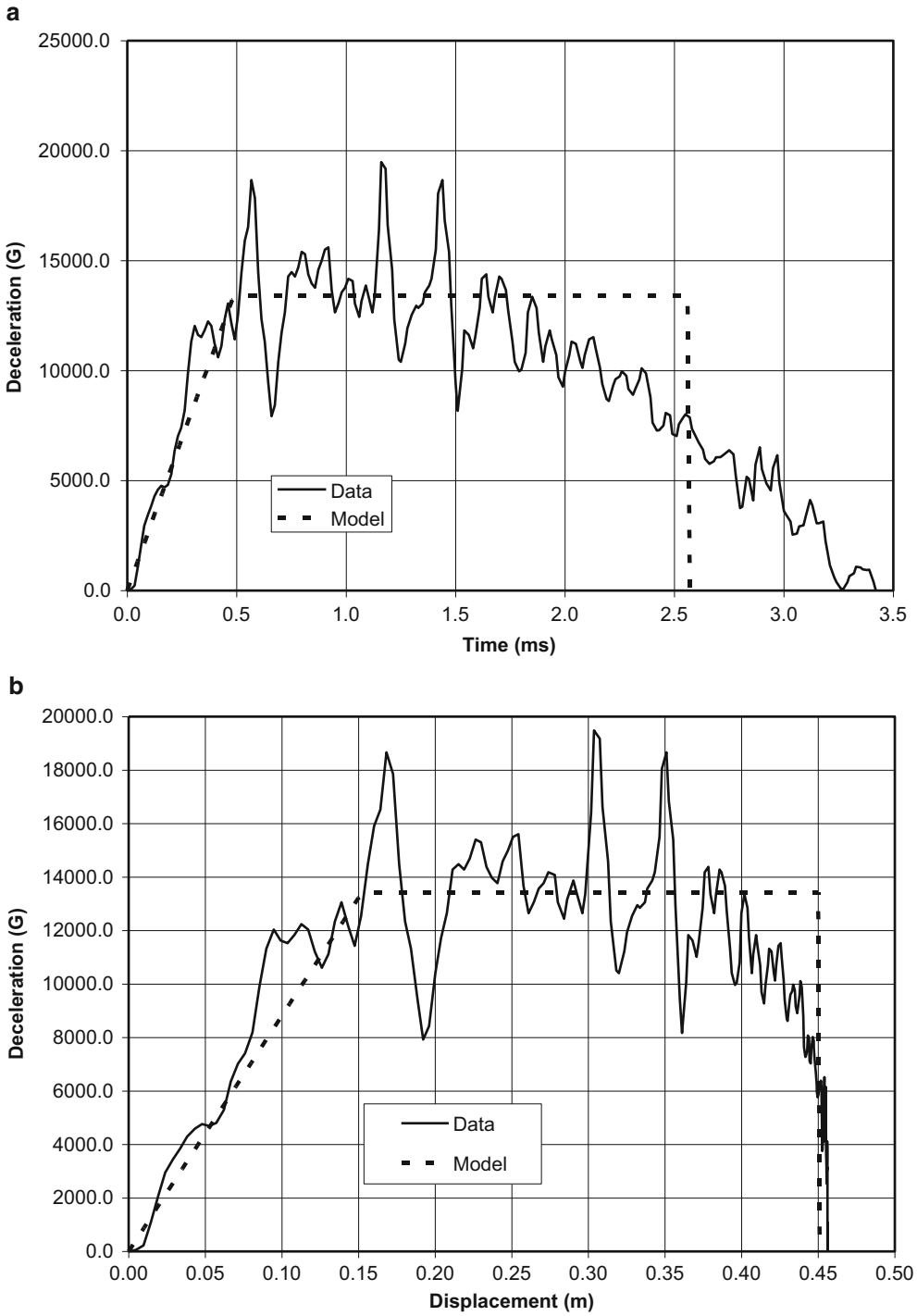

Fig. 31.11 Data and model comparisons for SNL-00-09/1 with $\sigma_{cf} = 39$ MPa and $V_s = 314$ m/s. (**a**) Deceleration-time, (**b**) deceleration-displacement, (**c**) specific kinetic energy-displacement, and (**d**) linear fit to specific kinetic energy-displacement in tunnel region

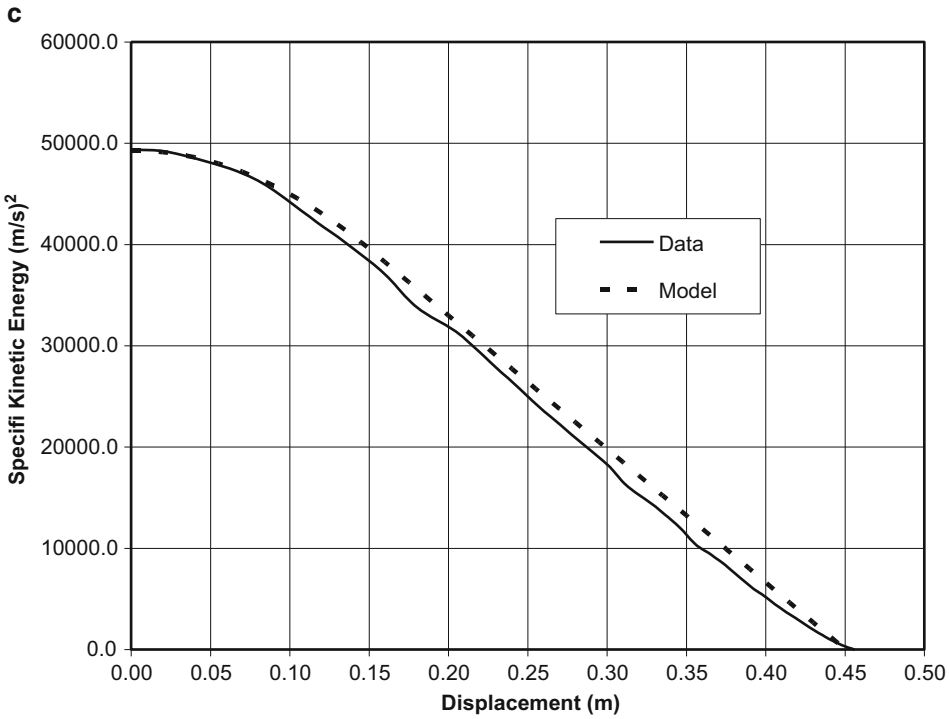

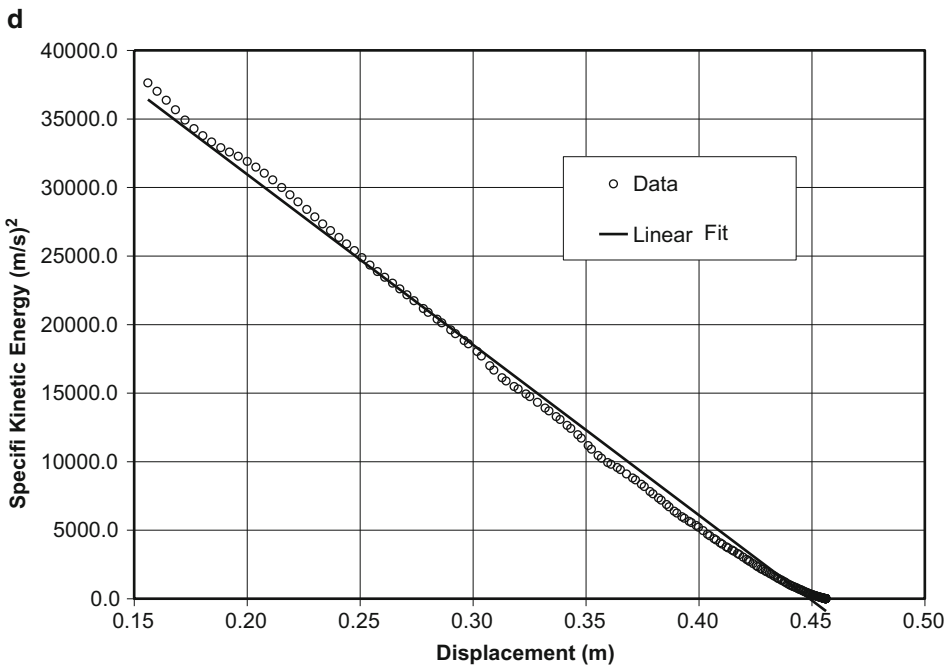

Fig. 31.11 (continued)

Figures 31.9d, 31.10d, 31.11d, and 31.12d show plots of specific kinetic energy versus displacement data in the tunnel region and least squares, linear data fits. The slopes of the linear fits are the projectiles accelerations in the tunnel region. Table 31.6 presents values of R and the constant decelerations in the tunnel region. In Table 31.6, Method 1 uses penetration depth data, and Method 2 uses the slope of the specific kinetic energy versus displacement data. Results from both methods are in close agreement.

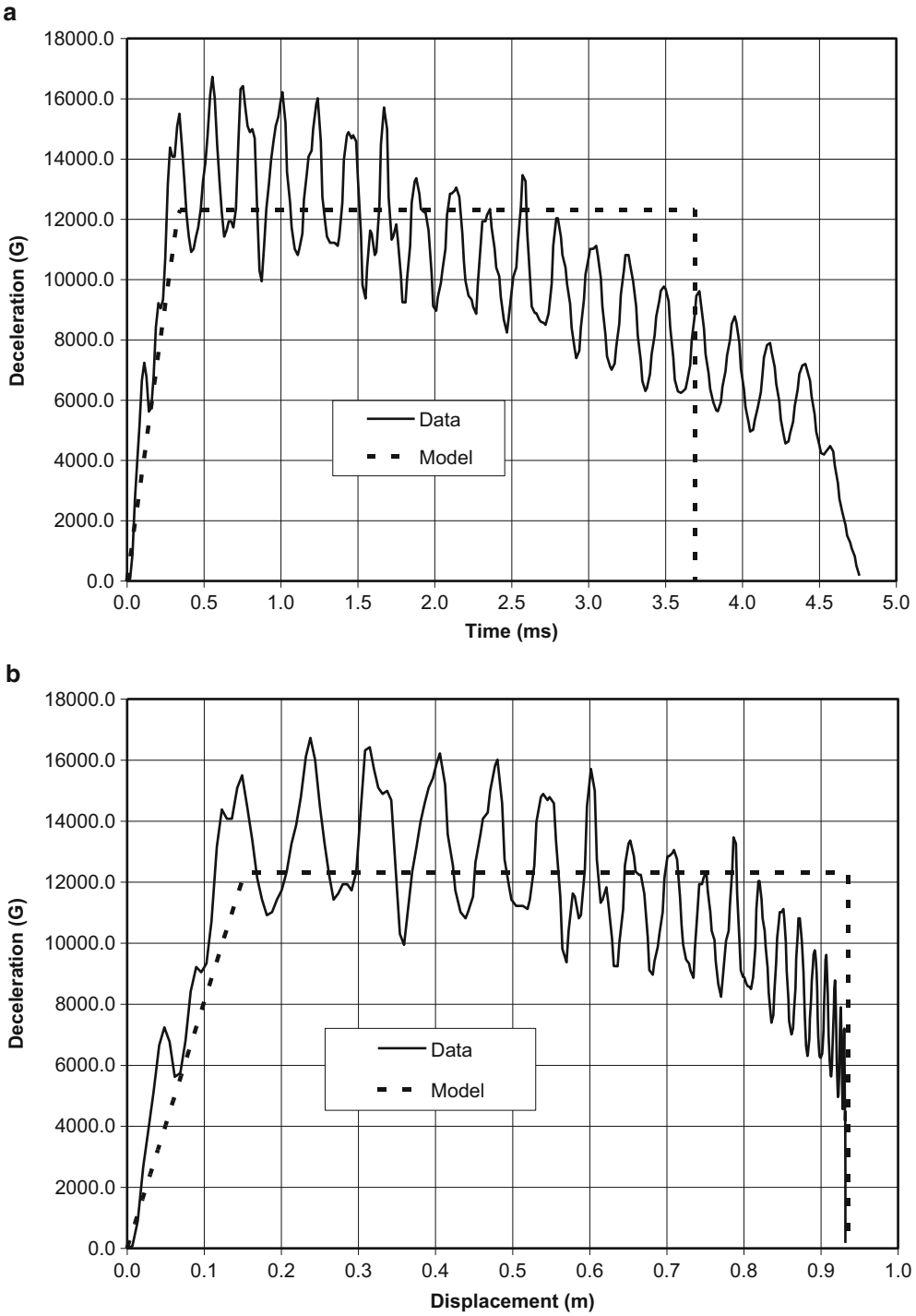

Fig. 31.12 Data and model comparisons for SNL-00-14/5 with $\sigma_{cf} = 39$ MPa and Vs = 456 m/s. (**a**) Deceleration-time, (**b**) deceleration-displacement, and (**c**) specific kinetic energy-displacement, and (**d**) linear fit to specific kinetic energy-displacement in tunnel region

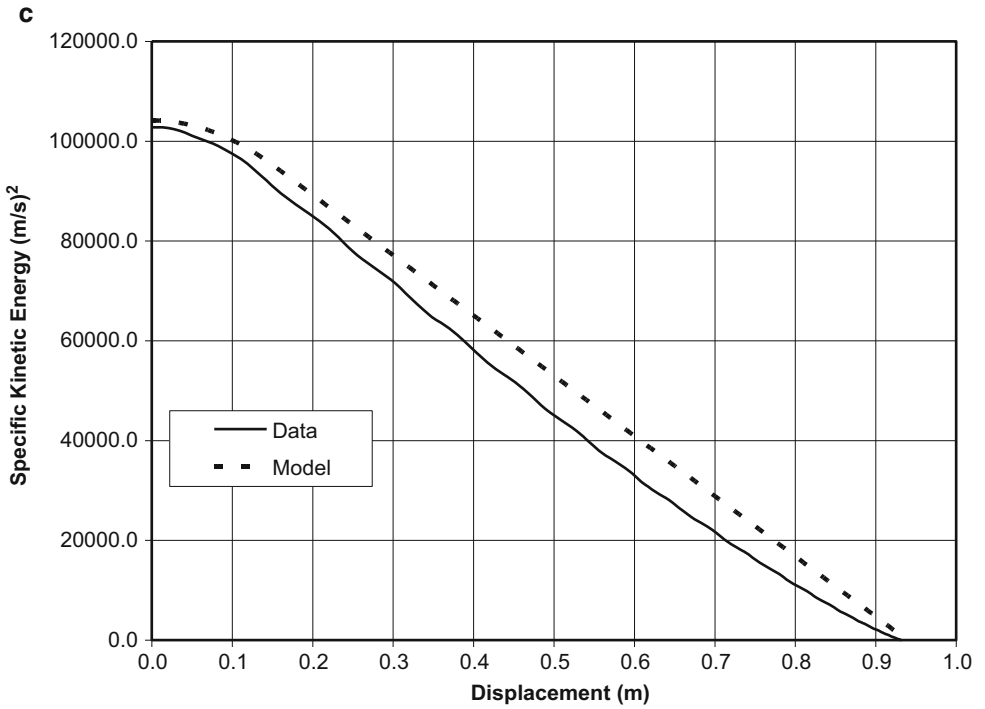

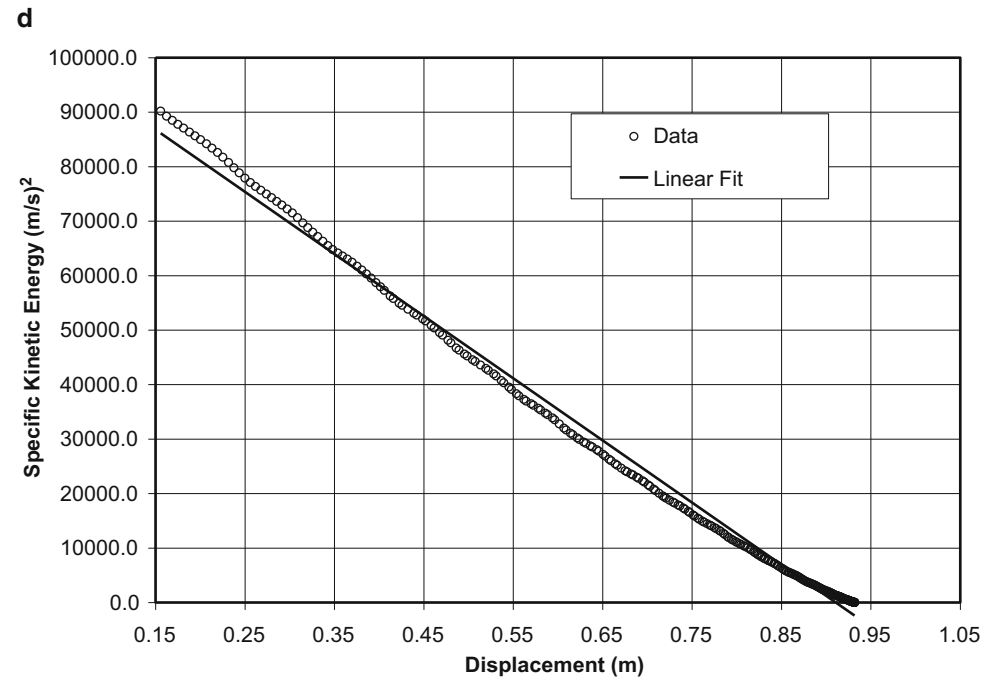

Fig. 31.12 (continued)

Table 31.6 Penetration results in the tunnel region for $\sigma_{cf} = 39$ MPa (5.7 ksi)

Shot and projectile number	Projectile mass (kg)	Striking velocity (m/s)	Method 1 R (MPa)	Method 1 deceleration (G)	Method 2 R (MPa)	Method 2 deceleration (G)
SNL-00-11/3	12.9	238	359	12,949	297	10,729
SNL-00-12/4	12.9	276	354	12,769	341	12,296
SNL-00-09/1	12.9	314	373	13,454	352	12,688
SNL-00-14/5	13.0	456	343	12,277	325	11,640

31.6 Summary

We re-examined data from two sets of penetration experiments [1] that measured deceleration during penetration into concrete targets with compressive strengths of 23 and 39 MPa. The 76.2-mm-diameter, 3 caliber-radius-head (CRH), 13 kg projectiles were machined from 4,340 Rc 45 steel and contained a single-channel acceleration data recorder. For this study, we plotted deceleration versus displacement data and showed that this response could be closely approximated by a linear rise entry region with a depth of two projectile diameters followed by a tunnel region with constant deceleration until the projectile came to rest. With these observations and a new empirical model, we predict accurately the deceleration-displacement response. In addition, we plotted specific kinetic energy versus displacement data and showed a nearly constant slope in the tunnel region. This slope corresponds to the magnitude of the nearly constant deceleration in the tunnel region. Our new empirical model predicts accurately this constant deceleration. Thus, we predict the maximum, constant deceleration in the tunnel region with two different methods. Predictions from both methods are in close agreement.

Acknowledgement This work was supported by contract DTRA02-03-D-0002 to Applied Research Associates.

References

1. Forrestal MJ, Frew DJ, Hickerson JP, Rohwer TA (2003) Penetration of concrete targets with deceleration-time measurements. Int J Impact Eng 28:479–497
2. Frew DJ, Forrestal MJ, Cargile JD (2006) The effect of concrete target diameter on projectile deceleration and penetration depth. Int J Impact Eng 32:1584–1594
3. Li QM, Reid SR, Wen HM, Telford AR (2005) Local impact effects of hard missiles on concrete targets. Int J Impact Eng 32:224–284
4. Li QM, Chen XW (2003) Dimensionless formulas for penetration depth of concrete target impacted by a non-deformable projectile. Int J Impact Eng 28:93–116
5. Rosenberg Z, Dekel E (2010) The deep penetration of concrete targets by rigid rods-revisited. Int J Prot Struct 1:125–144
6. Chen XW, Li QM, Zhang FJ, He LL (2010) Investigation of the structural failure of penetration projectiles. Int J Prot Struct 1:41–65
7. Forrestal MJ, Warren TL (2008) Penetration equations for ogive-nose rods into aluminum targets. Int J Impact Eng 35:727–730
8. Rohwer TA (1999) Miniature single channel memory-based high-Gacceleration recorder (MilliPen). Report no. SAND99-1392C, Albuquerque, Sandia National Laboratories, p 87185
9. Forrestal MJ, Togami TC, Baker WE, Frew DJ (2003) Performance evaluation of accelerometers used for penetration experiments. Exp Mech 43:90–96
10. Foster JT, Frew DJ, Forrestal MJ, Nishida EE, Chen W (2012) Shock testing accelerometers with a Hopkinson pressure bar. Int J Impact Eng 46:56–61

Chapter 32
Dynamic Fracture and Impact Energy Absorption Characteristics of PMMA-PU Transparent Interpenetrating Polymer Networks (IPNs)

K.C. Jajam, H.V. Tippur, S.A. Bird, and M.L. Auad

Abstract In this work, transparent Interpenetrating Polymer Networks (IPNs) were synthesized using poly(methyl methacrylate) (PMMA) as the stiff phase and polyurethane (PU) as the tough phase. Several IPNs with varying PMMA:PU ratios in the range of 90:10 to 70:30 were formulated. Dynamic fracture tests on IPNs were conducted using a long-bar impactor setup in conjunction with digital image correlation method and high-speed photography. Low-velocity impact studies of IPNs were also performed using falling weight drop-tower impact apparatus. Dynamic fracture and low-velocity impact experiments show that an optimum range of PMMA:PU ratio in the IPNs can produce enhanced dynamic crack initiation fracture toughness and impact energy absorption capability when compared to PMMA. Macro scale damage features revealed distinct failure modes as a result of low-velocity impacts.

Keywords Dynamic fracture • Energy absorption • Fracture toughness • Impact behavior • Interpenetrating polymer networks (IPNs) • Transparent polymers

32.1 Introduction

Transparent, fracture-impact resistant polymers are in demand for use in aerospace, armor, automotive, high-speed trains, offshore, and in many electronics applications. Interpenetrating polymer networks (IPNs) are relatively a new class of potential materials for these areas. IPNs are molecular composites where one polymer is synthesized and/or crosslinked in the immediate presence of the other(s) [1]. An example of IPN could be one that combines a thermoplastic polymer with a thermoset where each phase contributes its inherent characteristics to the composite. Thermoplastics offer good ductility but have lower elastic modulus and glass transition temperature (T_g), while thermosets are generally more brittle but stiffer, stronger and offer higher T_g. The concept behind IPNs is to combine the best features of both polymers in order to engineer a new material with optimum stiffness, strength and toughness while preserving the much needed optical transparency intact. Using this approach, the authors [2, 3] have recently synthesized transparent IPNs with poly(methyl methacrylate) (PMMA) and polyurethane (PU) as constituents.

Following the historic works of Ayslworth and Edison [4, 5], and Millar [6], a great deal of research has been conducted on IPNs in the last few decades [7–10]. Although numerous studies have been reported on IPNs, most have resulted in opaque or translucent networks and very limited work exists from the perspective of transparent IPNs for potential use in civilian and military applications. Also, note that much of the published research to date on IPNs has focused on synthesis, morphology and chemistry aspects, and relatively very few works describe mechanical performance [11–14]. Further,

K.C. Jajam • H.V. Tippur (✉)
Department of Mechanical Engineering, Auburn University, Auburn, AL 36849, USA
e-mail: jajamkc@auburn.edu; tippuhv@auburn.edu

S.A. Bird • M.L. Auad
Department of Polymer and Fiber Engineering, Auburn University, Auburn, AL 36849, USA

B. Song et al. (eds.), *Dynamic Behavior of Materials, Volume 1: Proceedings of the 2013 Annual Conference on Experimental and Applied Mechanics*, Conference Proceedings of the Society for Experimental Mechanics Series,
DOI 10.1007/978-3-319-00771-7_32,

they do not address mechanics of fracture under dynamic loading conditions as well as lack in impact energy absorption behavior. These gaps need to be bridged if IPNs are to find applications in aforementioned areas where stress-wave loading dominates. In view of this, the authors [15] have recently performed tensile, fracture and energy absorption studies on transparent PMMA-PU IPNs. This paper presents some of the major observations of their experimental investigation on transparent IPNs.

32.2 IPNs Synthesis and Specimen Fabrication

The reagents used for the PMMA system were: methyl methacrylate (MMA, 99 %, ACROS Organics), trimethylolpropane trimethacrylate (TRIM, Sigma-Aldrich) and 2,2′-Azobisisobutyronitrile (AIBN, 98 %, Sigma-Aldrich), and the reagents used for the PU system were: poly(tetramethylene ether)glycol (PTMG), 2-Ethyl-2-(hydroxymethyl)-1,3-propanediol (TRIOL, 98 %, ACROS Organics), 1,6 diisocyanatohexane (DCH, 99 + %, ACROS Organics) and dibutyltin dilaurate (DBTDL, 98 %, Pfaltz and Bauer, Inc.). The five different compositions (PMMA:PU ratio) of IPNs were prepared, namely 90:10, 85:15, 80:20, 75:25, and 70:30. Initially, a homogeneous mixture was prepared by dissolving the stoichiometric amounts of PTMG, TRIOL and DCH in the MMA monomer and cross-linker TRIM. Next, the free-radical initiator, AIBN was dissolved and finally the calculated amount of DBTDL catalyst was added. After thorough mixing, the mixture was poured into a closed mold made of Teflon. Care was exercised to avoid evaporation of PMMA from the mixture by sealing the mold. The mold containing the PMMA-PU mixture was kept in an oven at 60 °C for 24 h followed by further curing at 80 °C for another 24 h. After curing, the mold was left in the oven at room temperature for another 12 h for complete cooling of the casting. Note that slow cooling from 80 °C to room temperature in the oven prevents warpage of the cured sheets and minimizes residual stresses. Additional details regarding IPN synthesis, network morphology, transparency measurement, thermal and mechanical characterization aspects are available in a recent publication by the authors [3].

The plate specimens of dimensions 60 × 30 × 4.5 mm were fabricated for dynamic fracture experiments. A 6 mm edge notch was first cut into the samples using a diamond impregnated wafer blade. The notch tip was then sharpened using a razor blade in order to have a naturally sharp crack tip to achieve a consistent crack initiation followed by a steady growth [16]. Note that the dynamic fracture tests were conducted using the method of 2D digital image correlation (DIC) to quantify crack tip deformations and hence, the fracture parameters. Therefore, a random speckle pattern was created on the specimen surface by spraying a fine mist of black and white paints successively. Figure 32.1 depicts the specimen geometry with crack tip coordinate system and loading configuration for dynamic fracture experiments. The region in the dotted box represents 28 × 28 mm^2 region-of-interest. For low-velocity impact energy absorption tests, the specimens were fabricated as circular discs of diameter 110 mm and thickness 6 mm.

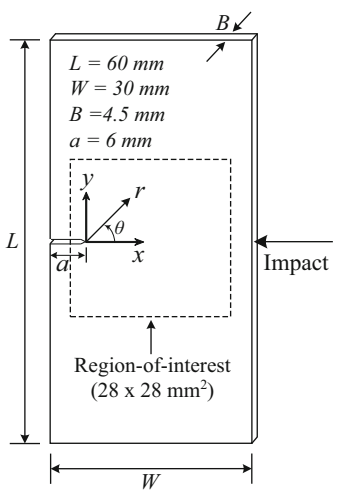

Fig. 32.1 Specimen geometry for dynamic fracture experiments

32.3 Experimental Setup and Testing Procedure

32.3.1 Dynamic Fracture Tests

The dynamic fracture tests were conducted by subjecting IPNs to symmetric 1-point loading and monitoring deformations using 2D DIC technique and high-speed photography. The schematic of the experimental setup used in this study is shown in Fig. 32.2. The setup consists of a long-bar impactor to deliver load to the specimens dynamically and a Cordin-550 high-speed camera for recording the fracture event in real-time. The high-speed camera is capable of recording images on 32 individual 1,000 × 1,000 pixels resolution CCD sensor array positioned circumferentially around a five-facet mirror which reflects and sweeps light over theses sensors (see Ref. [16] for optical details). As shown in Fig. 32.2, the camera was focused on a 28 × 28 mm^2 region-of-interest in the crack tip vicinity. Prior to impacting the specimen, a set of 32 reference (undeformed set) images were recorded at a chosen framing rate. While keeping all camera settings the same, the striker was launched. When the striker impacted the long-bar, it generated a compressive stress wave that propagated the length of the bar before imparting a transient load to the specimen edge. The compressive stress waves then entered the specimen, reflected back as tensile waves and loaded the crack-tip. When the striker contacted the long-bar, an electrical circuit was closed to activate the camera with a user-specified time delay to trigger the two high energy flash lamps. This delay provided sufficient time for the compressive stress wave to travel the length of the long-bar to the specimen crack-tip as well as enough time for the flash lamps to ramp up to their full intensity levels to provide uniform illumination. The second set of 32 images (deformed set) was captured during the specimen failure. In order to capture the entire fracture event, a framing rate

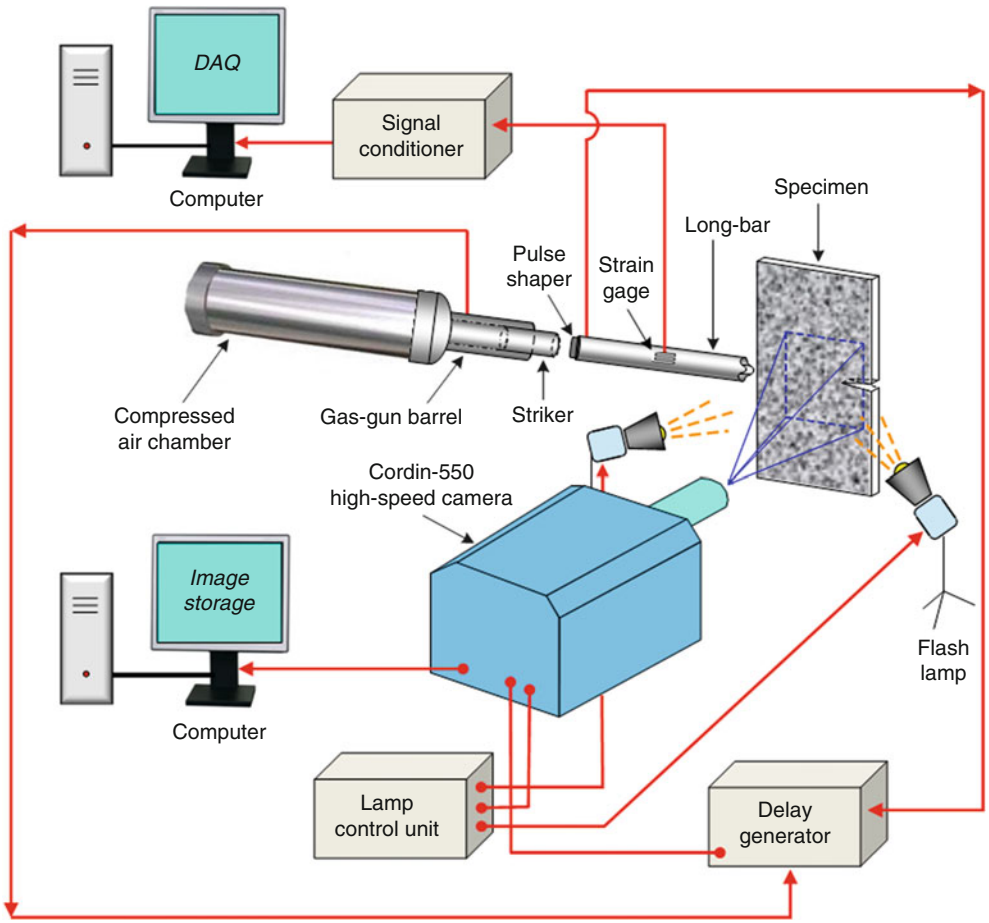

Fig. 32.2 Schematic of dynamic fracture experimental setup

Fig. 32.3 Experimental setup for low-velocity impact tests: (**a**) Dynatup 9250HV drop tower. (**b**) Close-up view of the impactor and specimen support fixture

ranging from 250,000 to 300,000 frames per second was used. A total of 32 images were present in each undeformed and deformed sets. The corresponding images recorded by each sensor were paired and correlated to get crack-opening and crack-sliding displacement fields.

32.3.2 Low-Velocity Impact Tests

In order to quantify energy absorption characteristics of IPNs, low-velocity impact tests were carried out in accordance with ASTM D5628-96 test method [17]. The IPNs were subjected to impact tests using a drop-tower (Instron Dynatup 9250HV) shown in Fig. 32.3a. The drop-tower is equipped with Impulse data acquisition software for recording load history, impact velocity and impact energy absorbed by the specimens. The machine is also fitted with a velocity detector to measure the velocity of the falling tup just before it strikes the specimen. The drop-tower has an instrumented tup (hemispherical head, 12.7 mm diameter) with a load cell capacity of 22.2 kN to record the transient response of the specimens. The specimen support fixture (developed in-house) at the bottom of the drop-tower facilitates circular clamp condition with a clear aperture of 76.2 mm in diameter. The close-up view of the striker head and the fixture are shown in Fig. 32.3b. The impact tests were performed at a fixed energy level (E) of 60 J with a constant drop-mass (m) of 4.85 kg, drop-height (h) 1.27 m, and impact velocity (v_{impact}) 5 m/s. These parameters were established after performing a series of benchmark experiments in order to avoid multiple rebounds and fail the specimens in a single drop/impact. Prior to testing, the load cell was calibrated. The specimen was securely clamped into the specimen support fixture. Using the jog keys and fine position thumbwheel on the drop-tower control panel, the drop-weight cross-head assembly was moved down until the striker head contacted the specimen. The bottom edge of the velocity detector was aligned with the bottom edge of the flag, and at this point the current position of the drop-weight was set to zero height. Next, the drop-weight cross-head assembly was raised to a desired height, and released to impact the specimen. The transient load and energy absorbed by the specimens during the entire impact event were recorded by the Impulse data acquisition software.

32.4 Results and Discussion

32.4.1 Dynamic Fracture Response

The 2D DIC method was used to carry out dynamic fracture tests. From each experiment 64 images were available, 32 from the undeformed set, and 32 from the deformed set, each having a resolution of 1,000 × 1,000 pixels. In this work, a sub-image size of 26 × 26 pixels was chosen for correlation and displacements fields were obtained as a 37 × 37 matrix of data points for each image pair. Subsequently, full-field in-plane displacement contours with 10 μm per contour interval were generated. Further details regarding speckle correlation methodology and image analysis can be found in Refs. [18, 19].

A few representative speckle images of 28 × 28 mm^2 region-of-interest immediately after crack initiation with corresponding crack-opening (along the *y*-axis) and crack-sliding (along the *x*-axis) displacement contours for PMMA, 85:15 and 75:25 IPNs are presented in Fig. 32.4. The crack tip is located at the tip of the arrow in each speckle image.

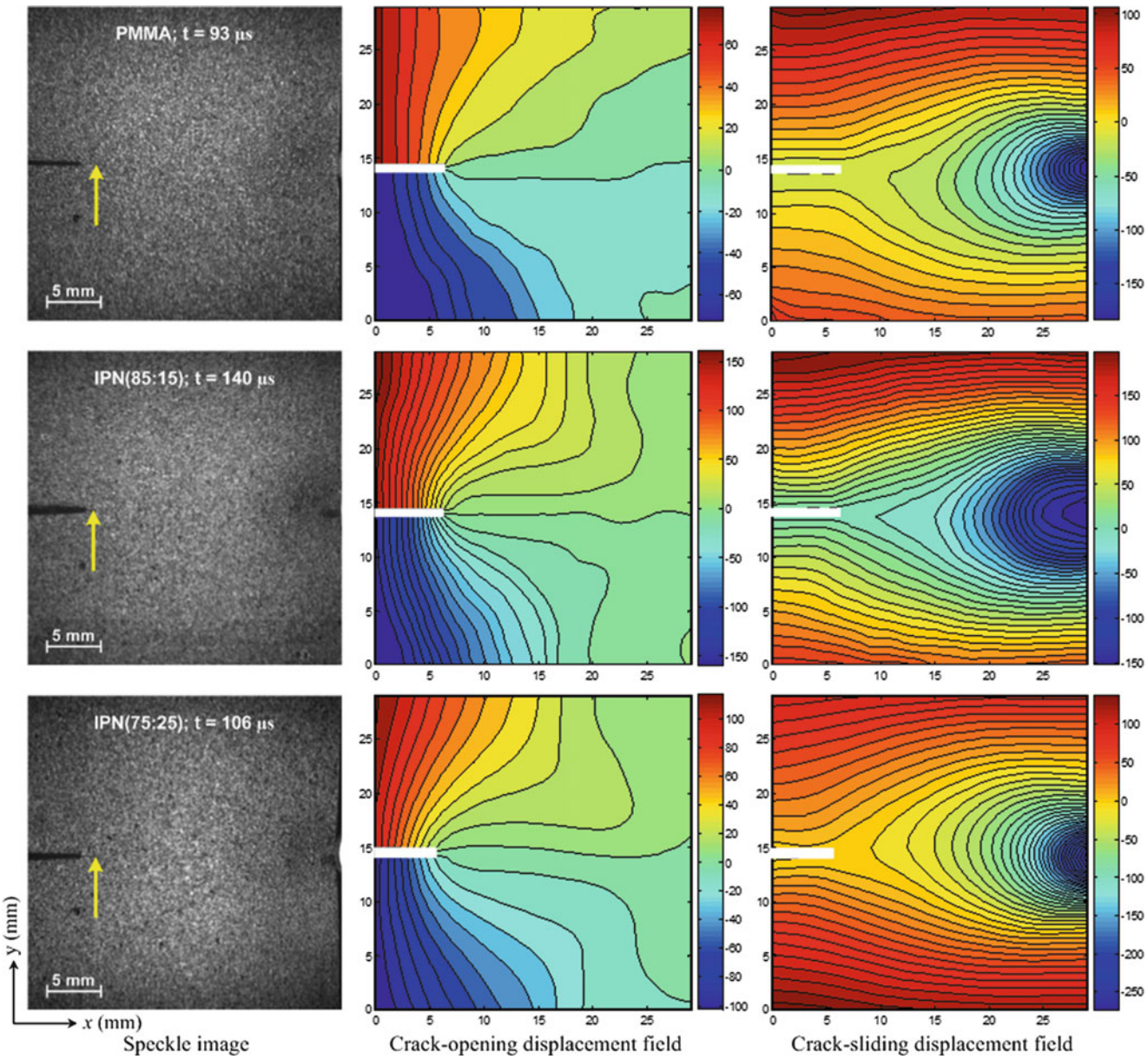

Fig. 32.4 Measured displacement fields corresponding to selected speckle images. The *arrow* in speckle images indicates crack tip position at a given time instant (t). *Color-bars* represent displacement in μm. Contours are plotted at an increment of 10 μm (color figure in online)

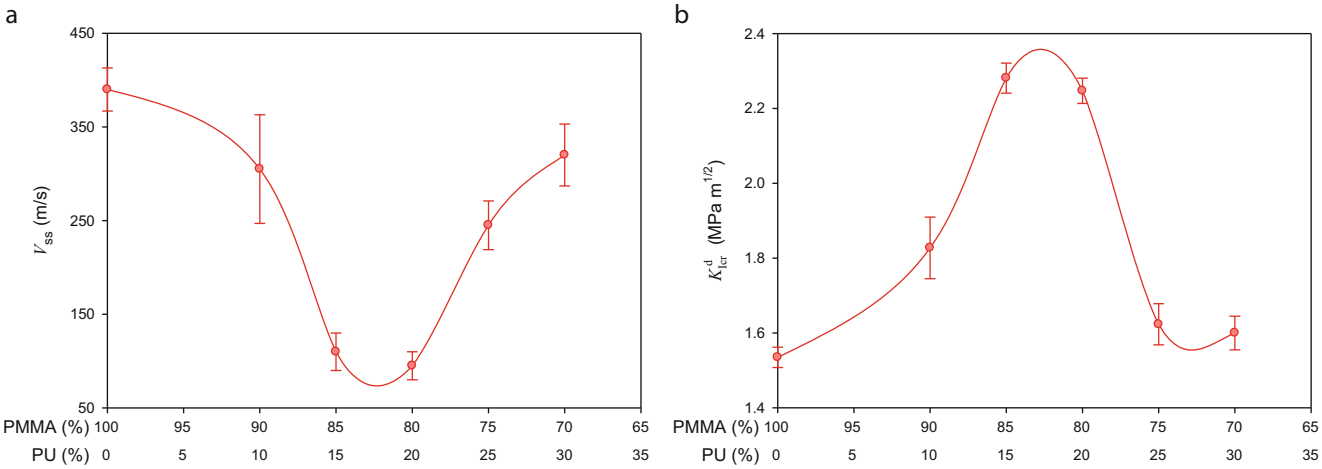

Fig. 32.5 (**a**) Variation of steady state crack velocity (V_{ss}) as a function of IPN composition. (**b**) Variation of mode-I dynamic crack initiation SIF (K^{d}_{Icr}) as a function of IPN composition. (*Solid line*: best fit of data)

The crack-opening and crack-sliding displacement fields show that contour lines and magnitude of displacement (in μm shown by color-bars) are nearly symmetric relative to the crack, consistent with mode-I fracture behavior. By comparing the color bars of the crack-opening displacement fields, it can be seen that the displacement range is higher in IPNs than the one for PMMA with larger deformations in the case of 85:15 IPN. The crack-sliding displacement contours show a set of isolines emerging from right-hand side of the contour plots due to impact loading on the edge of the specimen ahead of the initial crack tip.

In order to evaluate crack velocity, each speckle image from the deformed set was digitized to locate the current position of the crack tip and subsequently the crack velocity was estimated from the crack length history [20]. The variation of steady state crack velocity (V_{ss}) (average values in the time window after rapid acceleration) as a function of IPN composition is depicted in Fig. 32.5a. Each data point represents an average of 3–4 experiments and the error bar corresponds to their standard deviation. From Fig. 32.5a it can be seen that the steady state crack velocity for PMMA is the highest (~375 m/s) among all the specimens tested. On the contrary, IPN samples with PMMA:PU ratio of 85:15 and 80:20 show the least crack speeds (~100 m/s) among all the compositions. The variation of V_{ss} also indicates that further increase or decrease in PU content results in an increase in the steady state crack velocity.

The mode-I dynamic stress intensity factors (SIF) were evaluated using an over-deterministic least-squares analysis of crack-opening displacement fields near the tip of a dynamically loaded stationary crack and for a steadily growing crack according to the methodology described in Ref. [19]. The variation of dynamic mode-I crack initiation SIF (K^{d}_{Icr}) as a function of IPN composition is shown in Fig. 32.5b. It can be seen that the 85:15 and 80:20 IPNs show the highest values of mode-I dynamic crack initiation SIF indicating optimum IPN compositions among all cases for which the dynamic crack initiation toughness is the maximum. Figure 32.5a, b further show that there exists an inverse relationship between steady state crack velocity and mode-I dynamic crack initiation toughness of IPNs at different PMMA:PU ratios.

32.4.2 Impact Energy Absorption

The impact energy absorbed by various IPNs as a function of time is shown in Fig. 32.6. A linear region is evident for all specimens followed by deviations from linearity after which the curves attain a plateau in each case. It should be noted that in the initial stage of impact loading the energy absorption in the specimens is mainly through elastic deformation. Beyond this regime, the specimen absorbs energy through plastic deformation and various other damage mechanisms. In Fig. 32.6, it can be seen that energy absorption rates decrease with increasing PU content. It can be noted that, the 90:10, 85:15 and 80:20 IPNs show nearly equal slopes. Further, the duration of energy absorption for elastic deformation is longer in IPN cases (4–5 ms) than for PMMA (0.75 ms). From Fig. 32.6, it worth noting that IPNs show tremendous impact energy absorption capabilities when compared to neat PMMA. Quantitatively, the energy absorbed by IPNs is 3–4 times that of PMMA.

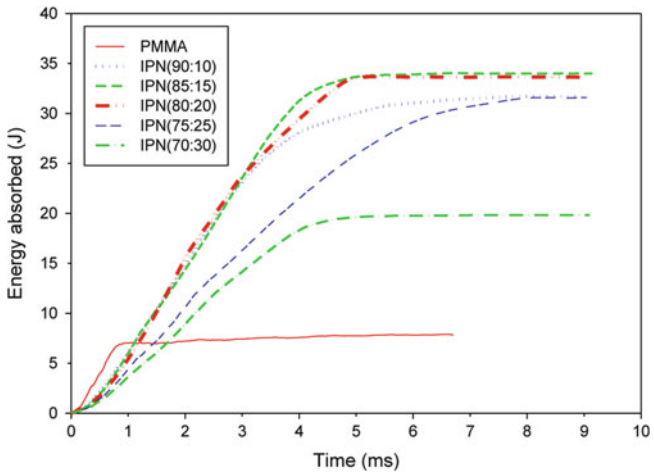

Fig. 32.6 Energy absorbed versus time response from low-velocity impact tests

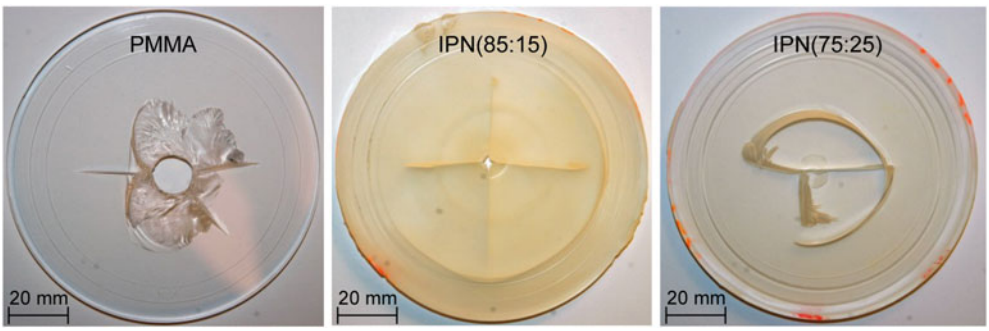

Fig. 32.7 Selected photographs of front surfaces of samples subjected to low-velocity drop-weight impact tests

The energy absorbed is a measure of the toughness of a material which is further defined as an optimum combination of strength and ductility [21]. Also note that among all IPN compositions, the 85:15 and 80:20 cases exhibit the highest damage tolerance and energy absorption capabilities under identical impact conditions.

The photographs of a few selected specimens depicting macro scale damage features of the front surfaces are shown in Fig. 32.7. In all the failed specimens through-the-thickness cracks emanate from the impact point. However, the number of cracks, their length and growth behaviors differ from each other. PMMA being a brittle material compared to the IPNs, fails catastrophically, evidenced by a circular opening due to the complete penetration of the indenter. The main failure mode in this case is spallation around the circular opening followed by the growth of radial cracks. In the case of 85:15 IPN, the tup created a small rupture and generated four radial cracks from the impact point. These through-the-thickness cracks made four quadrants on both front and back surfaces of the specimen, propagated ~90° apart relative to each other, and terminated by forming a shear-craze at the terminal points. Interestingly, the length of the cracks in 85:15 IPN is the longest among all the cases shown here. In case of 75:25 IPN, only three radial cracks are visible confined by a tri-quadrant crack joining the failed petals. The crack lengths in PMMA and 75:25 IPN are shorter than the 85:15 IPN. It should be noted that the through-the-thickness cracking and shear-crazing are dominant failure modes in the case of IPNs.

32.5 Conclusions

The transparent IPNs based on PMMA-PU networks were synthesized with varying PMMA:PU ratios ranging from 90:10 to 70:30. Dynamic fracture tests on IPNs were performed using a long-bar impact loading apparatus in conjunction with 2D DIC method and high-speed photography. Low-velocity impact studies of IPNs were conducted using a drop-tower.

Dynamic fracture tests indicated lower steady state crack velocities in IPNs relative to PMMA with the slowest crack growth in 85:15 and 80:20 IPNs. The dynamic crack initiation toughness enhancement was the highest for 85:15 and 80:20 IPNs. The low-velocity impact response demonstrated higher energy absorption capability of IPNs relative to PMMA with highest energy absorbed by 85:15 and 80:20 IPNs. The overall synergism in crack growth resistance and impact energy absorption ability of IPNs was observed for an optimum range of PMMA:PU ratio.

Acknowledgements The authors gratefully acknowledge the support for this research through a grant HDTRA1-09-1-0023 from the Defense Threat Reduction Agency.

References

1. Sperling LH (1981) Interpenetrating polymer networks and related materials. Plenum, New York
2. Jajam KC, Bird SA, Auad ML, Tippur HV (2011) Development and characterization of a PU-PMMA *transparent* interpenetrating polymer networks (*t*-IPNs). Dyn Behav Mater 1:117–121. doi:10.1007/978-1-4614-0216-9_16
3. Bird SA, Clary D, Jajam KC, Tippur HV, Auad ML (2012) Synthesis and characterization of high performance, transparent interpenetrating polymer networks with polyurethane and poly(methyl methacrylate). Polym Eng Sci. doi:10.1002/pen.23305
4. Vasile C, Kulshreshtha AK (2003) Handbook of polymer blends and composites, 3A. Rapra Technology, Shawsbury
5. Lipatov YS, Alekseeva TT (2007) Phase-separated interpenetrating polymer networks. Springer, Berlin
6. Millar JR (1960) Interpenetrating polymer networks. Styrene-divinylbenzene copolymers with two and three interpenetrating networks, and their sulphonates. J Chem Soc 1311–13117
7. Frisch KC, Klempner D (1990) Advances in interpenetrating polymer networks. Technomic Publishing, Lancaster
8. Gupta N, Srivastava AK (1994) Interpenetrating polymer networks: a review on synthesis and properties. Polym Int 35(2):109–118
9. Suthar B, Xiao HX, Klempner D, Frisch KC (1996) A review of kinetic studies on the formation of interpenetrating polymer networks. Polym Adv Technol 7(4):221–233
10. Sperling LH, Mishra V (1996) The current status of interpenetrating polymer networks. Polym Adv Technol 7(4):197–208
11. Chou YC, Lee LJ (1995) Mechanical properties of polyurethane-unsaturated polyester interpenetrating polymer networks. Polym Eng Sci 35(12):976–988
12. Chakrabarty D, Das B, Roy S (1998) Epoxy resin–poly(ethyl methacrylate) interpenetrating polymer networks: morphology, mechanical, and thermal properties. J Appl Polym Sci 67(6):1051–1059
13. Harismendy I, Del Río M, Marieta C, Gavalda J, Mondragon I (2001) Dicyanate ester–polyetherimide semi-interpenetrating polymer networks. II. Effects of morphology on the fracture toughness and mechanical properties. J Appl Polym Sci 80(14):2759–2767
14. Chen S, Wang Q, Wang T (2011) Hydroxy-terminated liquid nitrile rubber modified castor oil based polyurethane/epoxy IPN composites: damping, thermal and mechanical properties. Polym Test 30(7):726–731
15. Jajam KC, Bird SA, Auad ML, Tippur HV (2013) Tensile, fracture and impact behavior of transparent interpenetrating polymer networks with polyurethane-poly(methyl methacrylate). Polym Test 32:889–900
16. Jajam KC, Tippur HV (2011) An experimental investigation of dynamic crack growth past a stiff inclusion. Eng Fract Mech 78(6):1289–1305
17. ASTM, D5628-96 (1996) Standard test method for impact resistance of flat, rigid plastic specimens by means of a falling dart (tup or falling mass). Annual Book of ASTM Standards, pp 242–251
18. Kirugulige MS, Tippur HV, Denney TS (2007) Measurement of transient deformations using digital image correlation method and high-speed photography: application to dynamic fracture. Appl Opt 46(22):5083–5096
19. Jajam KC, Tippur HV (2012) Quasi-static and dynamic fracture behavior of particulate polymer composites: a study of nano- vs. micro-size filler and loading-rate effects. Compos Part B Eng 43(8):3467–3481
20. Jajam KC, Tippur HV (2012) Role of inclusion stiffness and interfacial strength on dynamic matrix crack growth: an experimental study. Int J Solid Struct 49(9):1127–1146
21. Ritchie RO (2011) The conflicts between strength and toughness. Nat Mater 10(11):817–822

Chapter 33
Estimating Statistically-Distributed Grain-Scale Material Properties from Bulk-Scale Experiments

William L. Cooper

Abstract This research effort studies the use of an inverse optimization method to extract statistically-distributed grain/meso-scale material property parameters (e.g. Weibull shape parameter used to express the grains' fracture strength) from spatially-integrated Kolsky (Split Hopkinson) Pressure Bar data. The compaction of particulate material samples is simulated with specified grain-scale material properties to create standard axial stress-engineering strain plots. These data plots are then analyzed to determine the statistically-distributed grain/meso-scale fracture strength properties. An iterative optimization approach is used to converge upon the most-likely material property parameters for comparison with initial simulation values. General stress–strain trends are illustrated as a function of meso-scale properties like variability in particle size and fracture strength and the strengthening effect of crushed nearest-neighbor grains. Sample inverse analyses are shown.

Keywords Grain-scale • Granular • Inverse method • Kolsky • Materials • Meso-scale • optimization • Particulate • Properties • Split Hopkinson pressure bar • Uncertainty

33.1 Introduction

Although historically particulate/granular materials (PMs) have been treated as continuum materials with great success in civil engineering applications, etc., recent publications have begun to investigate the influence of grain-scale properties upon bulk-scale behaviors. Tordesillas et al. [1, 2] numerically investigated the role of inter-particle friction, packing density and degree of polydispersity in PMs and the emergent role of short, structural force chains and chain networks. Cooper [3] theoretically investigated the permissible lengths of curved force chains with interfacial friction and introduced the concept of communication chains. Communications chains are formed by chains of grains in contact and permit vectored communications between remote points via static chains or dynamically via Solitary Waves; which Yang and Daraio experimentally investigated along curved communication chains [4]. Andrade et al. has extended the 2-D chain concepts into the numerical simulation of sheared 3-D ensembles, obtaining the local dilatancy and friction directly from computed tomography and demonstrating the ability to predict the onset of shear bands in large ensembles [5]. The ability to use both X-ray and neutrons to measure in-situ the tomography and averaged grain-scale strains [6–8] means that simulations no longer have to use representative ensembles. In some cases (e.g. small-scale triaxial experiments) the actual location, shape, orientation and lattice strains of all grains in an experiment can be measured.

Coupling the actual ensemble deformation with the simulated contact mechanics can allow the direct extraction of local friction coefficients, contact laws, grain rotation, dilation, etc. Classically the friction and contact law are measured independently for pairs of grains [9]. However, the ability to simultaneously measure and simulate in-situ grain-scale behaviors allows the grain-sale properties to be accurately determined in-situ, revealing conditional dependencies, etc. The basic idea is that optimization techniques can be used to identify the most-likely friction coefficient, etc. that would give rise to the observed behavior. One key to determining grain/meso-scale material properties is to employ a high-fidelity mechanics model such that the inferred properties are meaningful. Another key is to be able to understand that such

W.L. Cooper (✉)
Air Force Research Laboratory, 101 W. Eglin Blvd Suite 135, Eglin AFB, FL 32542, USA
e-mail: william.cooper@colorado.edu

B. Song et al. (eds.), *Dynamic Behavior of Materials, Volume 1: Proceedings of the 2013 Annual Conference on Experimental and Applied Mechanics*, Conference Proceedings of the Society for Experimental Mechanics Series,
DOI 10.1007/978-3-319-00771-7_33,

properties are statistically-distributed for PMs, and must be properly handled. How precisely can statistically-distributed grain/meso-scale parameters be determined? What concerns ought one to have as such an analysis is performed? The key is to understand how the data is distributed (Gaussian, Weibull, etc.) to minimize the number of state parameters required to express the data.

Given the potential trend towards the use of coupled experiments and simulations to determine grain/meso-scale parameters, a thought experiment is proposed to simulate the compaction of a 1-D chain of grains and then to estimate the statistically-distributed grain fracture strength distribution based upon the bulk-scale stress–strain plot.

33.2 Discussion

Particulate or granular materials are utilized in a wide array of applications. From a deterministic engineering perspective, these materials are most easily employed in applications that do not cause crushing. Engineering applications become more problematic when some degree of material crushing occurs in the system. Luo et al. [10] compacted quartz sand in a Kolsky Bar apparatus using a rigid confinement sleeve to hold the sand sample in place. Multiple compaction experiments were performed at densities between as-poured and fully mechanically-compacted densities. Higher initial densities were associated with stiffer mechanical responses. For each initial density a statistically-distribution family of stress–strain curves resulted about the mean curve. The curves exhibit unique local oscillations in stress as a function of strain; apparently due to the cyclic process of compaction, grain fracture/comminution, and strain to re-load the particulate material. The upshot is that the compaction characteristics of particulate materials must be expressed statistically.

A major reason for the stress–strain curve statistical variability is that the grain fracture strengths are Weibull-distributed at any particular grain size and the nominal fracture strength (i.e. the strength at which 37 % of the grains survive) generally decreases with particle size for non-engineered particles. The Weibull shape parameter varies from ~5 for natural materials (with a variety of intrinsic flaws) up to ~10 for engineered materials (whose flaws have generally been standardized by some aspect of the production process) [11–14].

In the present analysis, the mechanical compaction of a single straight row of spherical grains (1,000 grains, ϕ 1 mm) by a linearly-ramped force (0–52.5 N) is simulated. At elastic stresses the Hertzian response is employed (Young's Modulus: 73 GPa, Poisson's Ratio: 0.17). The grains' fracture strengths are Weibull-distributed (nominal fracture strength: 35 N, shape parameter: 5 scale parameter: 1). The grains are assumed to each have a density of 2.2 g/cm^3 before they fracture. Post-fracture they have the same density, but fill the void between adjacent grains inside a hexagonal column volume with width equal to the grains' diameter. The intermediate compaction process is not considered. Experimental experience shows that crushed sand or glass beads in the false noses on the front of high-speed projectiles are composed of both comminuted and whole grains [15]. Based upon this observation a heuristic rule is employed to account for adjacent comminuted grains. If one (or two) adjacent grain are fractured then the fracture strength is increased by a factor of 2 (or 4).

This simulation approach was selected because of its simplicity. It has only one statistically-distributed parameter (grain fracture strength) so the connection between the statistical grain-scale and bulk-scale data will be readily visible. Later an optimization algorithm is used to determine the most-likely Weibull shape parameter for each compaction curve. The same compaction mechanics are assumed in each case so in fact the Weibull shape parameter error is calculated as opposed to its uncertainty. The difference is that the optimization algorithm is not aware of the initial simulation parameter values and has to estimate them solely from the stress–strain curve. The value of such an approach is that it could be used to estimate grain/meso-scale data from the ubiquitous stress–strain plots measured for many different particulate materials (assuming that the compaction physics are truly representative).

Figure 33.1 shows typical probability and cumulative density functions for 100,000 grains (solid lines) and 1,000 grains (dashed line). The smaller ensemble follows the better-developed statistics of the larger ensemble, but has frequent excursions. In practice a new 1,000-grain Weibull distribution was calculated for each compaction simulation.

Figure 33.2 shows a typical compaction curve along with the fraction of grains crushed. The elastic regime is visible on the far left-hand side of the plot, evidenced by the lack of crushed grains. Thereafter the percentage of crushed grains varies linearly with the engineering strain, reaching a maximum of 45 %. This is to be expected as grain crushing is the major compaction mechanism. Figure 33.3 illustrates the bulk-scale effect of the Weibull-distributed grain fracture strengths. Ten (10) stress–strain curves are shown for different Weibull distributions. Simply allowing the grain fracture strengths to vary, causes the stress–strain curve to expand into a family with local oscillations similar to those shown in [10].

Figure 33.4 illustrates how the stress–strain curve depends upon the various simulation parameters. The three horizontal curves are produced when the grain fracture strengths are set equal as shown. The entire chain of grains collapses as the grain fracture strength is reached. Note that the nominal grain fracture strength in the Weibull distribution corresponds with 37 %

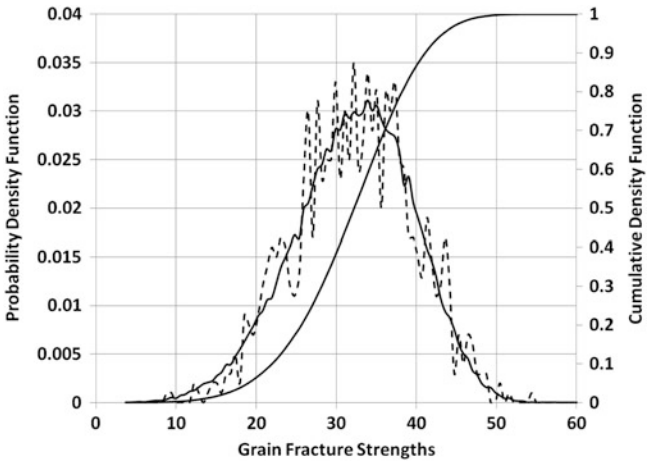

Fig. 33.1 Weibull-distributed grain fracture strengths. *Solid lines*: 100,000 grain ensemble, *Dashed line*: representative 1,000 grain ensemble

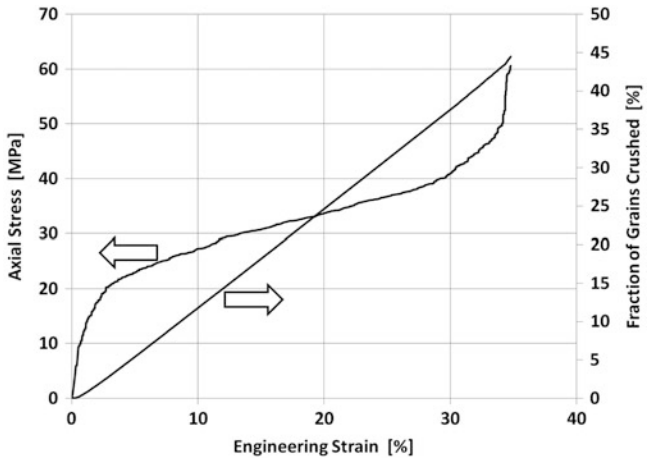

Fig. 33.2 Typical compaction stress-stain plot with fraction of grains crushed

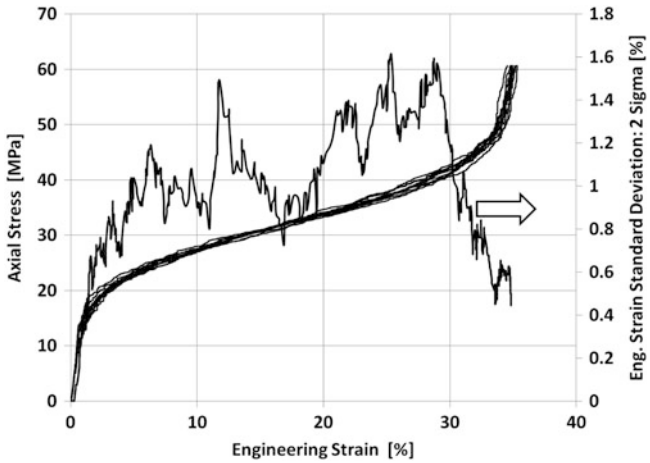

Fig. 33.3 Family of 10 typical stress–strain curves with 2-σ confidence interval

grain survivability. This occurs far to the right in the figure at an engineering strain of ~28 %. More pertinent to the present analysis, increasing the Weibull shape parameter decreases the minimum stress–strain slope (which occurs near the middle of the strain spectrum shown). Recall that "natural" materials tend to have a low shape parameter around 5 and engineered particulate materials tend to have a higher shape parameter around 10. Thus, typical engineering improvements in the materials tend to reduce the width of the Weibull distribution and decrease the minimum slope. This can be problematic

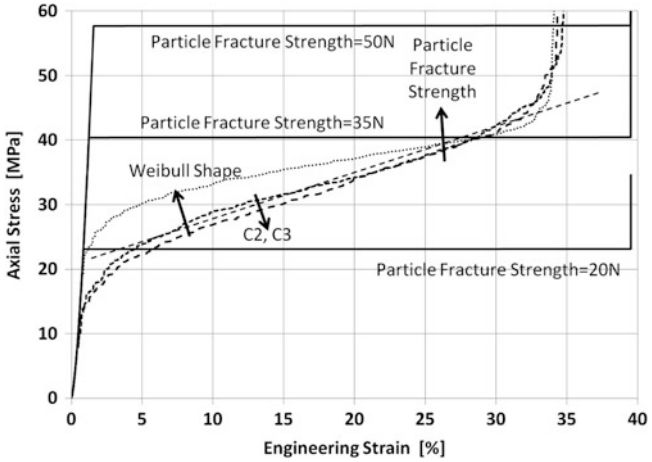

Fig. 33.4 Stress–strain curve trends as function of simulation parameters

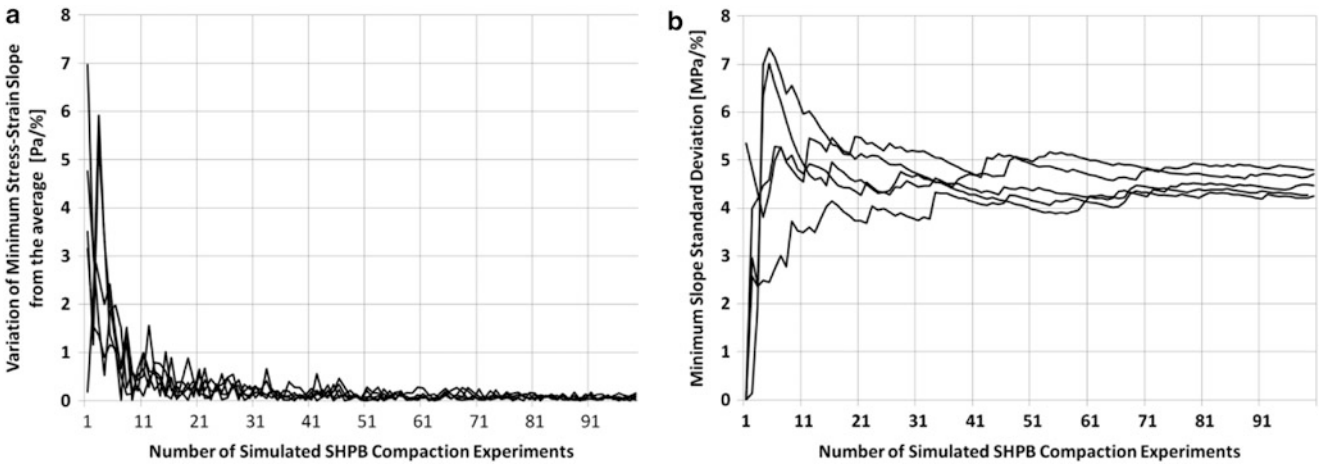

Fig. 33.5 Minimum slope behaviors: (**a**) variation from the mean, (**b**) standard deviation

because it makes the engineering strain less deterministic as a function of axial stress during the compaction (with a reduced minimum slope and statistically-distributed stress–strain curves). The larger the shape parameter, the larger the possible spectrum of engineering strains for a particular stress and the less deterministic behavior. Thus, if well-prescribed compaction behavior is critical then lower Weibull shape parameters may offer some advantage. Finally, the parameters $C2 = 2$ and $C3 = 4$ are the grain fracture strength multiplication factors when one or two (respectively) adjacent grains are already fractured. Increasing these is similar to decreasing the shape parameter and broadening the Weibull distribution.

In general, the Weibull shape parameter is correlated with the minimum stress–strain slope. The minimum slope decreases as the shape parameter increases. However, this relationship is not deterministic. The simulation code broke up the strain spectrum (~0–35 %) into 20 segments, calculated the average stress–strain slope for each, and selected the minimum value. The minimum slope is a statistically-distributed parameter as shown in Fig. 33.5; which shows minimum slope results for five collections of 100 simulations. In Fig. 33.5a the minimum slope values are averaged as each successive simulation is completed. The first-order moment of the minimum slope variation – the difference (absolute value) between the current minimum slope and the average min slope – is minimized after ~30 simulations. This confirms the classical Student T Test small sample theory result. The averaged second-order moment – standard deviation – is shown in Fig. 33.5b. Its behavior is more interesting. It does not converge until ~70 simulations are complete; and even then it does not converge to the same value. Theoretically, these values will converge after enough realizations are considered. However, the differences between the averaged standard deviations indicate differences in the statistical variations in the minimum

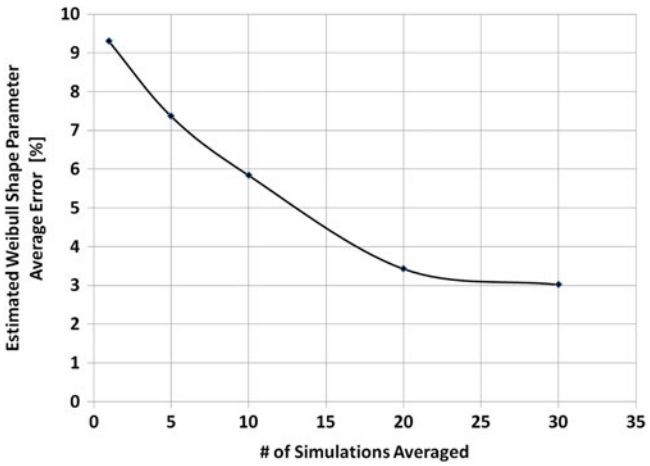

Fig. 33.6 Weibull shape parameter estimation error versus the # of simulations

slope and will affect the robustness of the inverse technique used to infer the Weibull shape parameter from the minimum stress–strain slope. Figure 33.5b also calls into question how many grains are required to obtain bulk-scale data, especially in the presence of emergent effects like shear planes that involve only a fraction of the total grains in the ensemble.

The inverse technique employed the same simulated compaction code described above. Thus, the actual and assumed mechanics are identical. The only difference is that the elastic and fracture parameters are prescribed in the original simulation and inferred via the inverse method. Based upon the fact that the first and second-order moments do not converge until 30–70 realizations are averaged, it is expected that some number of simulations must be averaged to minimize the error between the prescribed and estimated Weibull shape parameters. In practice the elastic parameters are estimated first, then the Weibull shape parameter, and then the nominal fracture strength. The first and last are straight-forward so the estimation of the Weibull shape parameter is focused upon here.

In the inverse method a single compaction simulation is performed with a prescribed Weibull shape parameter. Then ensembles of 1, 5, 10, 20, and 30 simulations are performed with trial shape parameter values. The MATLAB optimization function "fminbnd" is used to iteratively improve the trial value by minimizing the shape parameter objective function (the difference between the minimum slope [based upon the prescribed shape parameter] and the average minimum slope [based upon the trial shape parameter]). The trial values are bounded ≥ 3, ≤ 13. Some delay in the convergence is caused by the statistical nature of the relationship between the minimum slope and the shape parameter. Figure 33.6 shows that increasing the number of averaged simulations reduces the first-order error moment, asymptoting with an error of ~3 %.

33.3 Conclusion

Given a suitably-robust representation of the compaction mechanics, it is possible to use an inverse method to estimate statistically-distributed grain/meso-scale material property parameters from bulk-scale experimental data, e.g. Kolsky or Split Hopkinson Pressure Bar data. The keys are to: have access to bulk-scale experimental data, understand the statistical nature of the property variations so a minimum number of state parameters are required to express the variation, have a robust description of the mechanics, and understand the association between grain/meso-scale parameters and bulk-scale parameters. In this simple case the only statistically-distributed grain-scale parameter was the Weibull shape parameter and it is shown that increasing the number of averaged "trial" simulations leads to reasonably rapid convergence with 20 averaged simulations per trial value. Note that the goal is not to estimate the statistically-distributed data, but rather the parameters which describe it. This dramatically reduces the number of state parameters required to describe the data and increases the rate of convergence. In theory, following the same approach while increasing the number of statistically-distributed parameters simply expands the number of optimization objective functions. The problem should remain tractable and with a suitably robust understanding of the mechanics, it ought to be possible to extract statistically-distributed grain/meso-scale parameters from bulk-scale experimental data.

Acknowledgements We acknowledge the support of the Air Force Office of Scientific Research (Dr. David Stargel) and the Air Force Research Laboratory.

References

1. Peters JF, Muthuswamy M, Wibowo J, Tordesillas A (2005) Characterization of force chains in granular material. Phys Rev E 72:041307. doi:10.1103/PhysRevE.72.041307
2. Muthuswamy M, Tordesillas A (2006) How do interparticle contact friction, packing density and degree of polydispersity affect force propagation in particulate assemblies? J Stat Mech Theory Exp. doi:10.1088/1742-5468/2006/09/P09003
3. Cooper WL (2011) Communication of stresses by chains of grains in high-speed particulate media impacts. In: Proceedings of the SEM XI international congress and exposure on experimental and applied mechanics, Uncasville, 13–17 June 2011
4. Yang J, Daraio C (2012) Frequency- and amplitude-dependent transmission of stress waves in curved one-dimensional granular crystals composed of diatomic particles. Exp Mech. doi:10.1007/s11340-012-9652-y
5. Andrade JE, Avila CF, Hall SA, Lenoir N, Viggiani G (2011) Multiscale modeling and characterization of granular matter: from grain kinematics to continuum mechanics. J Mech Phys Solid 59:237–250. doi:10.1016/j.jmps.2010.10.009
6. Alramahi BA, Khalid AA (2006) Applications of computed tomography (CT) to characterize the internal structure of geomaterials: limitations and challenges. In: Proceedings of the geoShanghai conference – site and geomaterial characterization, vol 149, Geotechnical Special Publication, pp 88–95
7. Hasan A, Khalid A (2012) Three dimensional fabric evolution of sheared sand. Granul Matter 14(4):469–482
8. Penumadu D, Dutta AK, Luo Xin, Thomas KG (2008) Nano and neutron science applications for geomechanics. In: 12th international conference on computer methods and advances in geomechanica, vol 3, Goa, 1–6 Oct 2008, pp 2138–2149
9. Cole DM, Peters JF (2007) A physically based approach to granular media mechanics: grain-scale experiments, initial results and implications to numerical modeling. Granul Matter 9(5):309–321. doi:10.1007/s10035-007-0046-2
10. Luo H, Lu H, Cooper WL, Komanduri R (2011) Effect of mass density on the compressive behavior of dry sand under confinement at high strain rates. Exp Mech 51:1499–1510. (http://dx.doi.org/10.1007/s11340-011-9475-2)
11. McDowell GR, Bolton MD (1998) On the micromechanics of crushable aggregates. Geotechnique 48(5):667–679
12. Lee DM (1992) The angles of friction of granular fills. Ph.D. dissertation, University of Cambridge
13. Weibull W (1951) A statistical distribution function of wide applicability. J Appl Mech 18:293–297
14. Marketos G, Bolton MD (2007) Quantifying the extent of crushing in granular materials: a probability-based predictive method. J Mech Phys Solid 55:2142–2156
15. Cooper WL (2011) Shear stress measurements during high-speed impacts with sand and glass beads. In: Proceedings of the 17th APS SCCM conference, Chicago, IL, USA, 26 Jun–1 July 2011

Chapter 34
Spall Behavior of Cast Iron with Varying Microstructures

Gifford W. Plume IV and Carl-Ernst Rousseau

Abstract The spall strength of five cast irons with varying microstructures have been investigated with the use of plate impact experiments conducted in a vacuum. A single stage gas gun was utilized to drive projectiles to velocities between 100 and 300 m/s, resulting in low to moderate shock loading of the cast iron samples. Measurement of the stress histories were made with the use of commercial manganin stress gauges that were imbedded between the back face of the cast iron specimen and a low impedance backing of polycarbonate. Spall strength values were calculated utilizing the measured peak stress and pullback stress signals captured in the stress history. Strength values were found to vary between 0.44 and 1.6 GPa respectively as a function of the damage evolution from initiation of micro-cracks to complete spall fracture. Post mortem analysis of spalled samples has shown the graphite phase to be the primary factor influencing the failure process. SEM micrographs indicate that initial failure occurs due to the debonding of graphite from the metal matrix. It has been noted that subsequent coalescence of initiated cracks into a complete fracture plane is correlated to both the microstructural components of the metal matrix and relative spacing of the graphite phase.

Keywords Cast Iron • Dynamic fracture • Microstructure • Spall Strength • Spallation

34.1 Introduction

Spallation is a dynamic material failure mode that occurs when tensile stresses are generated by the interaction of two decompression waves. The failure mechanism of spallation has been widely investigated since it was first identified by Hopkinson in 1914. In recent years experimental techniques such as high velocity plate impacts [1, 2], explosive drives [3, 4], and laser ablation [5, 6] have frequently been employed to induce spallation. Records of the wave profiles created by these dynamic events are usually taken in the form of free surface particle velocities [7, 8] or stress histories [9, 10]. From these temporal records, the spallation event is typically quantified in terms of the material's spall strength. As the name suggests, spall strength defines a material's ability to resist spallation, which in turn is a measure of a material's high-rate tensile strength. Thus, the present study focuses solely on this phenomenon as it applies to cast irons of varying microstructure. A background detailing the phenomenology of the failure mode is presented. This is followed by specifics of the experimental process used in the present case, and a discussion of the results obtained.

34.2 Theoretical Considerations

Dynamic fracture, commonly referred to as spalling, is a failure mechanism that involves the interaction of release waves within a sample which create a critical tensile state that invokes failure. For visualization of this process, refer to Fig. 34.1, in which a time-distance plot (a), stress-particle velocity plot (b), and transmitted stress profile (c) are depicted for the case of

G.W. Plume IV (✉) • C.-E. Rousseau
University of Rhode Island, 92 Upper College Rd., 203 Wales Hall, Kingston, RI 02881, USA
e-mail: giffer500@yahoo.com; rousseau@egr.uri.edu

B. Song et al. (eds.), *Dynamic Behavior of Materials, Volume 1: Proceedings of the 2013 Annual Conference on Experimental and Applied Mechanics*, Conference Proceedings of the Society for Experimental Mechanics Series,
DOI 10.1007/978-3-319-00771-7_34,

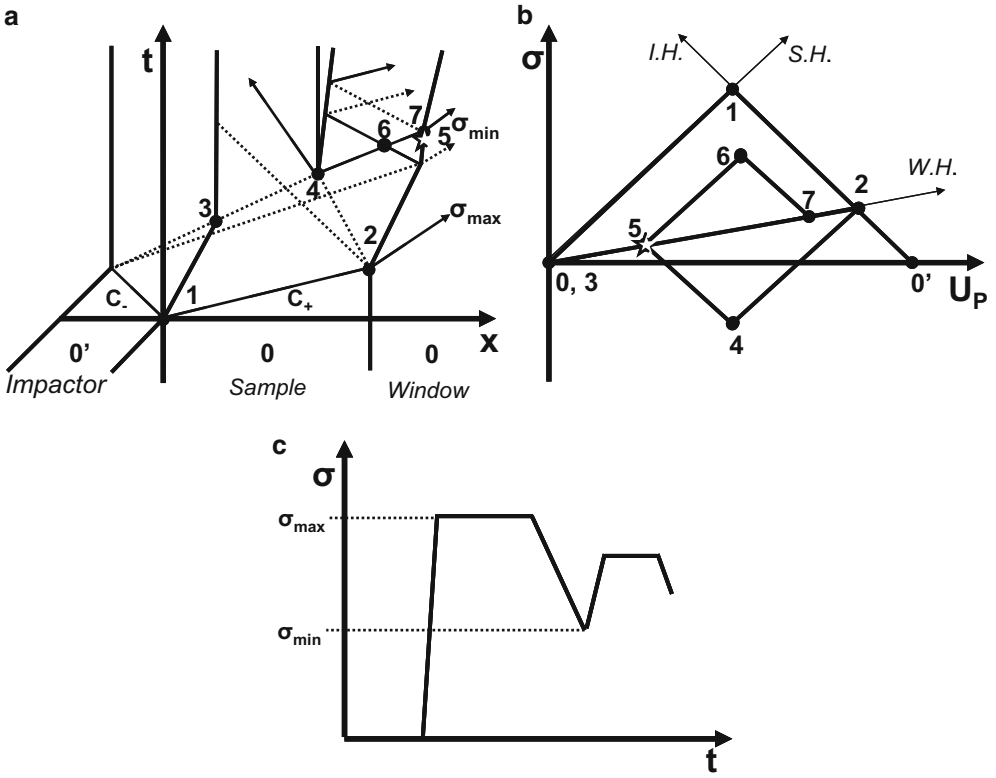

Fig. 34.1 Decomposition of a spall experiment; (**a**) time-distance diagram; (**b**) stress-particle velocity plot; (**c**) stress transmitted to the window

a symmetrical impact of a flyer plate on a sample backed by a low impedance window through which stress transmissions can be measured. In the current case, symmetrical signifies that the contact surface and material of the impactor are the same as the sample.

At the point of impact, compressive waves are generated in the C− and C+ directions respectively in the impactor and sample resulting in state 1 on the stress-particle velocity plane. When the forward moving compressive pulse arrives at the low impedance window, the assumption of continuity at the interface between the sample and window can only be achieved through intersection of their respective Hugoniots in the σ–u_p plane. This assumption requires a C− tensile release wave of magnitude (σ_1–σ_2) to be generated in the sample and a C+ compressive wave of magnitude σ_2 to be generated in the window, resulting in state 2. This compressive transmission to the window is associated with σ_{max} in the stress record found in Fig. 34.1c. Meanwhile the initial C− compressive wave in the impactor reflects off the free surface as a decompression wave traveling in the C+ direction. Its transmission into the sample completely brings the impactor to state 3. Within the sample the C+ and C− release waves interact creating some critical tension signified by state 4. State 4 is observed at the sample window interface as state 5 through a C+ tensile release of the window from state 2 to 5, and a C− compressive reloading of the sample from state 4 to 5. Once this critical tension is achieved, a spall plane is initiated. The near-instantaneous release of tension from the generation of the spall plane causes a compressive pulse to propagate back to the sample-window interface, reloading the window from state 5 associated with σ_{min} in the stress profile found in Fig. 34.1c. The drop in stress from states 2 to 5 associated with σ_{max} and σ_{min} in the stress profile is often termed the pullback signal.

Looking at the Fig. 34.1 it should be noted that state 5 is depicted with a star. The choice of this star is to differentiate it from the other states due to the fact that the characteristic related to state 5 on the time-distance diagram is not depicted. Rarefaction waves are idealized as an infinite number of weak shocks that progressively unload a material from a compressed state. Obviously it would be impossible to draw an infinite number of characteristics representative of the rarefaction wave, however, the divergence of the unloading front is depicted by the region encompassed within the two dotted characteristics that serve to represent the rarefaction fan. It should therefore be noted that state 5, marked with a star, is representative of the final portion of the rarefaction fan that reached the target-window interface before the reloading by the C+ compressive front. The reloading associated with the C+ compression characteristic adjacent to state 5 in the time-distance diagram causes the subsequent second plateau realized at the stress gauge, and can be visualized by following the sample Hugoniot through states 6 and 7 depicted in the stress-particle velocity plot.

It should be noted when referring to Fig. 34.1 that all experimental methods involved in measuring the dynamic tension of a sample associated with state 4 are indirect. This is an apparent factor when one considers the impossibility of introducing a sensor into a sample without inherently influencing its resistance to tensile stress. In light of this, the dynamic tension which represents a material's spall strength is indirectly determined from temporal records of either the stress or particle velocity which are respectively measured at either the interface between the sample's back face and a low impedance window or the sample's free surface. For the case that the sample is backed by a low impedance window the acoustic approach facilitates the determination of the dynamic tension associated with state 4 from the measured stresses at states 2 and 5 in the form:

$$\sigma_{sp} = \frac{1}{2}\sigma_{\min}\left(1 + \frac{Z_s}{Z_w}\right) + \frac{1}{2}\sigma_{\max}\left(1 - \frac{Z_s}{Z_w}\right) \tag{34.1}$$

where σ_{max} is the magnitude of the initial compressive wave (state 2), σ_{min} is the magnitude of the minimum pullback signal (state 5), and the subscript sp is amended in place of state 4 to indicate the calculation of spall strength. The specimen (Z_s) and window (Z_w) impedances can be calculated by the product of their respective initial densities and appropriate wave speeds. Special care must be exercised when calculating these impedances in regards to choosing the appropriate wave speed. If the material response preceding spall is elastic, a longitudinal elastic velocity should be used. On the other hand, if the response is hydrodynamic, a bulk wave speed must be used. It has been widely recognized that when elastic waves are important to the analysis of a hydrodynamic event an equivalent wave speed can be utilized. This equivalent wave speed, proposed by Romanchenko and Stepanov, is the harmonic mean of the longitudinal and bulk wave speeds [9].

34.3 Materials Studied

Five separate cast irons were studied which included four gray cast irons denoted A-D and one ductile cast iron which are representative of typical castings produced in industrial foundries. In order to facilitate calculation of the spall strengths from the experimental records densities were determined along with longitudinal and shear wave speed measurements obtained with the use of ultrasonic transducers employed in a pulse echo mode. The bulk wave speeds were calculated through the well known relationship between the measured longitudinal and shear wave speeds. Table 34.1 contains a summary of these properties for the cast irons tested and the polycarbonate window utilized.

The microstructure of the cast irons studied was investigated with use of a reflection light optical microscope. In accordance to ASTM standard A247 [11], the cast irons were characterized based on their graphite morphology. The graphite found in cast irons A, B, and C can all be classified as Type VII A2. Cast Iron D is classified as a bimodal distribution of graphite types VII A4 and VII D8. The ductile cast iron is classified as Type I with an average of 200 nodules per square millimeter of size class 5. After identification of the graphite phase, the components of the metal matrix of the respective castings were revealed with the use of 4 % nital chemical etching. Castings A and C contained a mixed distribution of pearlite and free ferrite. Casting B and D were almost entirely pearlitic where coarser inter-laminar spacing was observed for casting B. The ductile cast iron contained the typical bull's eye structure where graphite nodules are surrounded by free ferrite in a matrix of pearlite

Table 34.1 Densities and wave speeds of the materials studied

Material	ρ_o (kg/m^3)	c_o (m/sec)	c_s (m/sec)	c_b (m/sec)	c_e (m/sec)
Cast iron A	7,090	4,190	2,510	3,030	3,520
Cast iron B	7,130	4,690	2,600	3,600	4,080
Cast iron C	7,070	4,550	2,520	3,500	3,960
Cast iron D	7,690	4,670	2,650	3,530	4,020
Ductile cast iron	6,970	5,590	3,090	4,300	4,860
Polycarbonate	1,178	2,260	910	2,000	2,120

34.4 Experimental Design

Plate impact experiments were conducted in a vacuum chamber evacuated to 10 Torr with the use of a 50 mm bore single stage helium driven gas gun. The impactors and tested specimens were 45 mm in diameter, and respectively 5 and 10 mm thick. For all experiments, a 20 mm thick polycarbonate backing window was used. PVC sabots were used to carry the impactors down the 2 m long gun barrel while specimens were supported, awaiting impact, by means of small PVC rings which were temporarily bonded to a metal sample holder. In order to help attain better impact planarity, sabots were designed so as to impact the specimen before they fully exited the barrel of the gun. Flyer velocities were captured by means of two laser detectors positioned 12.7 and 38.1 mm from the specimen's front face. Velocity was inferred from the time between interruptions and the distance between the two detectors. 50 Ω manganin stress gauges were embedded between the back surfaces of the test samples and 20 mm thick polycarbonate backing windows with the use of Buehler Epo-Thin Epoxy. A digital oscilloscope was used to capture the output signal of the stress gauge power supply and the laser detectors.

Impacted specimens were captured for post mortem analysis utilizing a soft recovery technique by means of clay bricks coupled with a shock absorbing catch box. Recovered specimens were cut through the thickness in order to expose the spall plane for analysis. Cut specimens were ground and polished to a 1 μm finish for clearer viewing under scanning electron and optical microscopes.

34.5 Results and Discussion

Four separate experiments were conducted covering an impact velocity range of 100–300 m/s for each respective casting. Results from these experiments suggested a strong correlation between the magnitudes of the calculated spall strengths and the damage level initiated. Upper end values of spall strength were found for cases where complete spall fracture occurred, where minor damage levels associated with incomplete fracture produced the lower range. A summary of the resulting spall strengths determined for each respective casting can be found in Fig. 34.2. The shaded regions within this figure indicate experiments where the test samples exhibited complete spall fracture and therefore were not able to be imaged as described in the previous section.

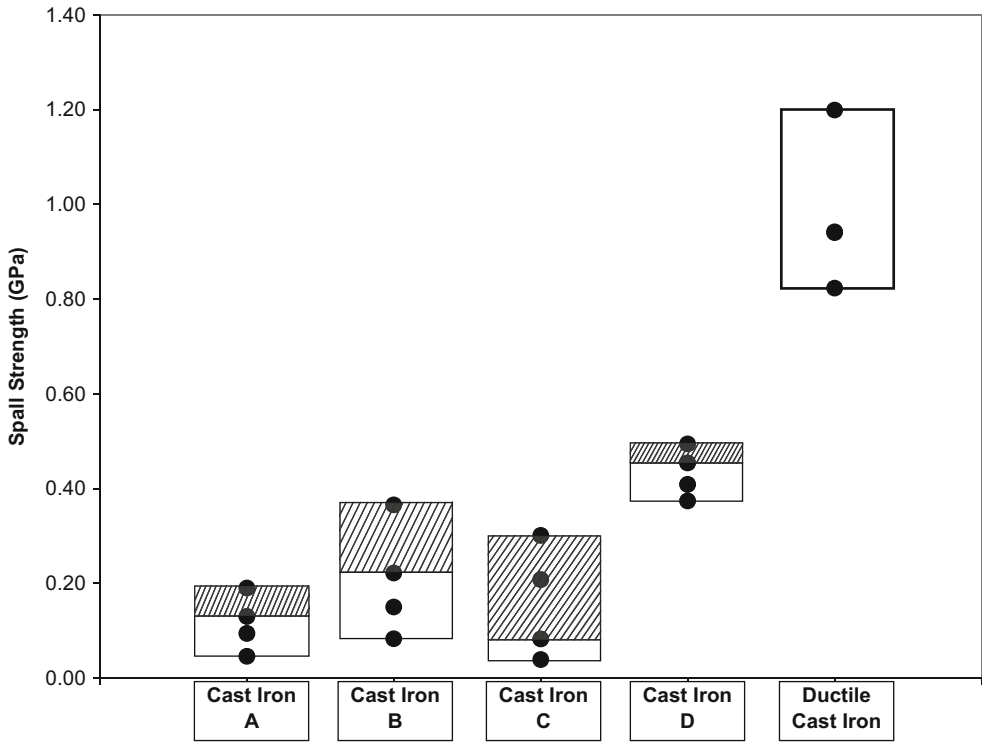

Fig. 34.2 Summary of spall strengths for the five castings studied

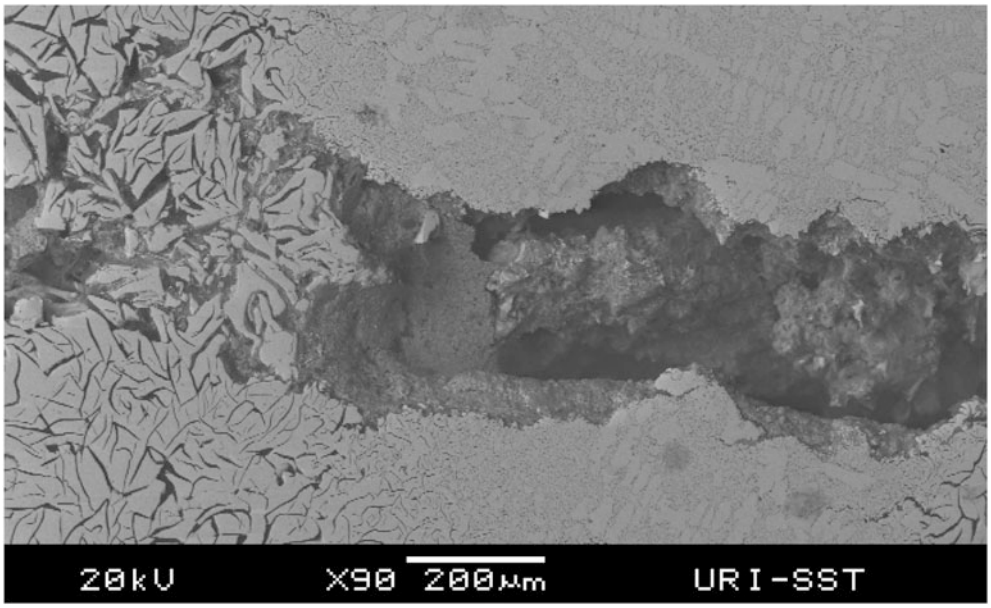

Fig. 34.3 Backscattered image of spall plane in cast iron D from test at 190 m/s taken at 90X

SEM and optical micrographs of recovered samples demonstrated that the initiation of failure is strongly linked to the debonding of graphite from the metal matrix. In cases where graphite existed in the form of coarse flakes, spall plains exhibited large initiated cracks along graphite-matrix interfaces, as noted in the micrographs of the recovered samples from experiments on castings A-C. The relative length of the graphite within each respective casting demonstrated a link to the spall strengths determined, where castings A-C tested with much lower values than casting D which was composed of smaller graphite flakes. In agreement with this observation, the small surface area shared by the graphite nodules and metal matrix in the ductile cast iron resulted in much higher strength values for this material than found for the gray cast irons. The subsequent coalescence of the initiated microcracks required propagation into the metal matrix to form a completed fracture plane. The small range of strengths exhibited by cast iron D indicates that this process can be completed with minimal additional energy in cases where the spacing between graphite flakes is relatively small. This observation is further supported by considering a SEM micrograph of a recovered sample from casting D impacted at 190 m/s found in Fig. 34.3. Within this micrograph graphite of type VII A4 and VII D8 can be noted respectively on the left and right. In the case of the coarse distribution of graphite, the material partially retained its integrity, however, a large spall plane can be noted in the case of the fine distribution. A pearlitic metal matrix is noted to provide an increase in tensile strength through the final stages of spall fracture as indicated by the higher strengths found for casting B in comparison to castings A and C. This observation is in agreement with quasi-static testing of cast irons in literature where it is commonly noted that free ferrite can significantly reduce a castings tensile strength.

34.6 Conclusions

Results from this investigation suggest a strong correlation between the magnitudes of calculated spall strengths and the damage level initiated where an increased amount of energy is required to generate completed fracture planes. The morphology of graphite within cast irons has been shown to strongly affect the material's spall strength. Initiation of spallation is linked to the debonding of graphite from the metal matrix. The subsequent coalescence of initiated cracks into a complete fracture plane is correlated to both the microstructural components of the metal matrix and comparative spacing of the graphite phase. In cases where graphite spacing is relatively small, this process can be completed with minimal additional energy. A metal matrix of pearlite has been linked to increased tensile strength in castings, helping to prevent the coalescence of initiated cracks in the formation of complete spall fracture planes.

References

1. Chen X et al (2006) Spall behavior of aluminum with varying microstructures. Jo App Phys 99:023528
2. Hayun S et al (2010) The high-strain-rate dynamic response of boron carbide-based composites: the effect of microstructure. Acta Mater 58:1721–1731
3. Rybakov AP (2000) Spall in non-one-dimensional shock waves. Int J Impact Eng 24:1041–1082
4. Rybakov AP (2001) Experimental study of spall-fracture zone. Int J Solid Struct 38:5453–5464
5. Wayne L et al (2010) Statistics of weak grain boundaries for spall damage in polycrystalline copper. Scripta Mater 63:1065–1068
6. Pedrazas NA (2012) Effects of microstructure and composition on spall fracture in aluminum. Mater Sci Eng 536:117–123
7. Paris V, Frage N, Dariel MP, Zaretsky E (2010) The spall strength of silicon carbide and boron carbide ceramics processed by spark plasma sintering. Int J Impact Eng 37:1092–1099
8. Yuan F et al (2007) Spall strength of glass fiber reinforced polymer composites. Int J Solid Struct 44:7731–7747
9. Romanchenko VI, Stapanov GV (1981) Dependance of critical stresses on the loading time parameters during spall in copper, aluminum, and steel. J App Mech Tech Phys 21(4):555–561
10. Rosenberg Z et al (1983) Spall studies of differently treated 2024A1 specimens. J Appl Phys 54(5):2147–2152
11. ASTM Standard A247 (2010) Standard test method for evaluating the microstructure of graphite in iron castings, vol 03.03. ASTM International, West Conshohocken, pp 205–214. doi:10.1520/E0247-10

Chapter 35
A Scaling Law for APM2 Bullets and Aluminum Armor

M.J. Forrestal, T.L. Warren, and T. Børvik

Abstract We developed a scaling law to predict the ballistic-limit velocities for 7.62 mm APM2 bullets that perforate armor plates. Data from 5083-H116, 5083-H131, 6061-T651, 6082-T651, and 7075-T651 aluminum armor plates with thicknesses between 20 and 60 mm show that the ballistic limit velocities are proportional to the square root of the product of plate thickness and strength term. The strength term is derived from a cylindrical cavity-expansion analysis that requires large-strain compression data.

Keywords Aluminum armor plates • APM2 bullet • Cylindrical cavity-expansion • Large-strain compression data • Scaling law

35.1 Introduction

We conducted several recent studies to better understand the mechanisms and dominant parameters for 7.62 mm APM2 bullets that perforate aluminum armor plates. As shown in Fig. 35.1, the 7.62-mm-diameter, 10.7 g, APM2 bullet consists of a brass jacket, lead filler, and a 5.25 g, ogive-nose, hard steel core. In [1–3], we conducted experiments with the 10.7 g APM2 bullets and the 5.25 g, ogive-nose, hard steel cores. A comparison of these data showed that the hard steel core dominated the perforation process. In addition, our cylindrical, cavity-expansion, perforation model [1] predictions were in good agreement with the ballistic data for the steel core projectiles. This cavity-expansion model that predicts the ballistic-limit velocity consists of a strength term and a target inertial term [1]. We show in [1–3] that the strength term dominates the perforation process. Because the hard steel core of the APM2 bullet and the strength term in our model dominates, we presented a scaling law or empirical Eq. 35.2 that predicted the ballistic-limit velocity for the 5083-H116 [1] and 7075-T651 [2] aluminum plates. This scaling law shows that the measured ballistic-limit velocities are proportional to the square root of the product of the plate thickness and a target strength term derived from a cylindrical, cavity-expansion model that requires large-strain compression data. Since we proposed this scaling law [2], we have conducted more experiments on 6082-T651 aluminum plates. In addition, we received two more data sets from Gooch and Burkins for 6061-T651 [4] and 5083-H131 [5] aluminum plates. So we now compare our scaling law for the ballistic-limit velocities from five aluminum alloys with plate thickness between 20 and 60 mm.

M.J. Forrestal (✉)
Forrestal Consulting, 3029 Tanglewood Park W, Fort Worth, TX 76109, USA
e-mail: mjforrestal@gmail.com

T.L. Warren, Ph.D.
Warren Consulting, 3804 Shenandoah Pl, NE, Albuquerque, NM 87111, USA
e-mail: tlwarre@msn.com

T. Børvik
Structural Impact Laboratory (SIMLab), Centre for Research-based Innovation (CRI), Department of Structural Engineering, Norwegian University of Science and Technology, Trondheim NO-7491, Norway
e-mail: tore.borvik@ntnu.no

B. Song et al. (eds.), *Dynamic Behavior of Materials, Volume 1: Proceedings of the 2013 Annual Conference on Experimental and Applied Mechanics*, Conference Proceedings of the Society for Experimental Mechanics Series,
DOI 10.1007/978-3-319-00771-7_35,

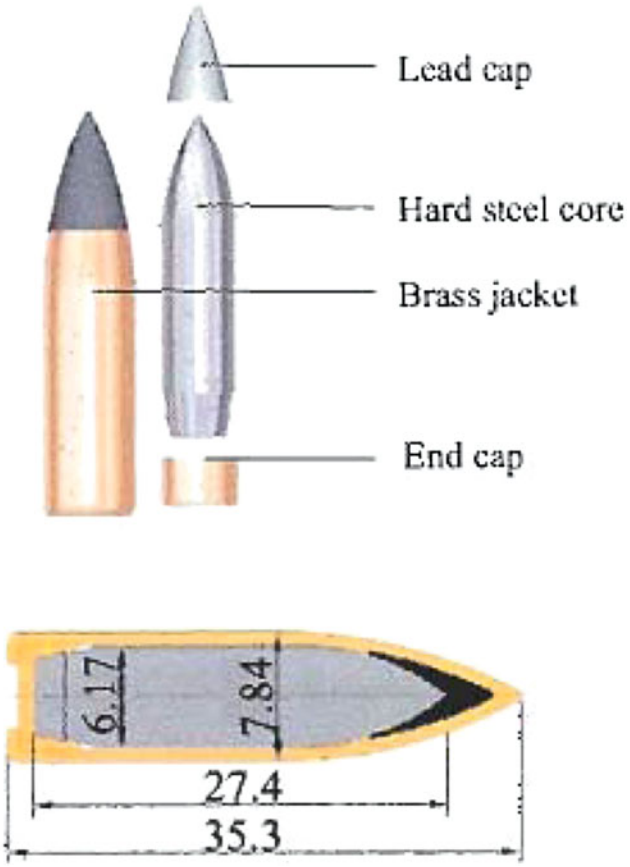

Fig. 35.1 Geometry and dimensions of the 7.62 mm APM2 bullet (in mm)

35.2 Bullet and Aluminum Target Plates

Figure 35.1 shows the dimensions and the parts that make up the APM2 bullet. The 7.62 mm-diameter, 10.7 g, APM2 bullet consists of a brass jacket, an end cap, lead filler, and a 5.25 g, ogive-nose, hard steel core. The steel core has density $\rho_p = 7850$ kg/m^3, hardness Rc 63, ψ = CRH = 3.0 (caliber radius-head), nose length $l = 10.2$ mm, and shank length $L = 16.8$ mm.

For input to our cavity-expansion perforation model, we obtained large-strain, uniaxial compression data [1, 6, 7]. These data were curve-fit with

$$\sigma = \begin{cases} E\varepsilon, & \sigma < Y \\ Y\left(\dfrac{E\varepsilon}{Y}\right)^n, & \sigma^3 \geq Y. \end{cases} \tag{35.1a, b}$$

where σ is the true stress, ε is the true strain, E is the Young's modulus, Y is the yield stress, and n is the strain-hardening exponent. Table 35.1 presents the material parameters and references to the large-strain, compression experiments.

35.2.1 Scaling Law

Reference [1] presents an equation for the ballistic-limit velocity V_{bl} for the hard steel core. If we neglect the small contribution from radial target inertia, we can write the scaling law for the 7.62 mm APM2 bullet as

$$V_{bl} = K[\sigma_s h]^{1/2}, \tag{35.2}$$

Table 35.1 Material parameters

Material	E (GPa)	v	Y (MPa)	n	σ_s (GPa)	References
5083-H116	71	0.33	240	0.108	1.12	[1]
5083-H131	70	0.33	276	0.084	1.18	[8]
6061-T651	69	0.33	262	0.085	1.13	[9]
6082-T651	68	0.33	265	0.055	1.06	[3]
7075-T651	71	0.33	520	0.060	1.85	[10]

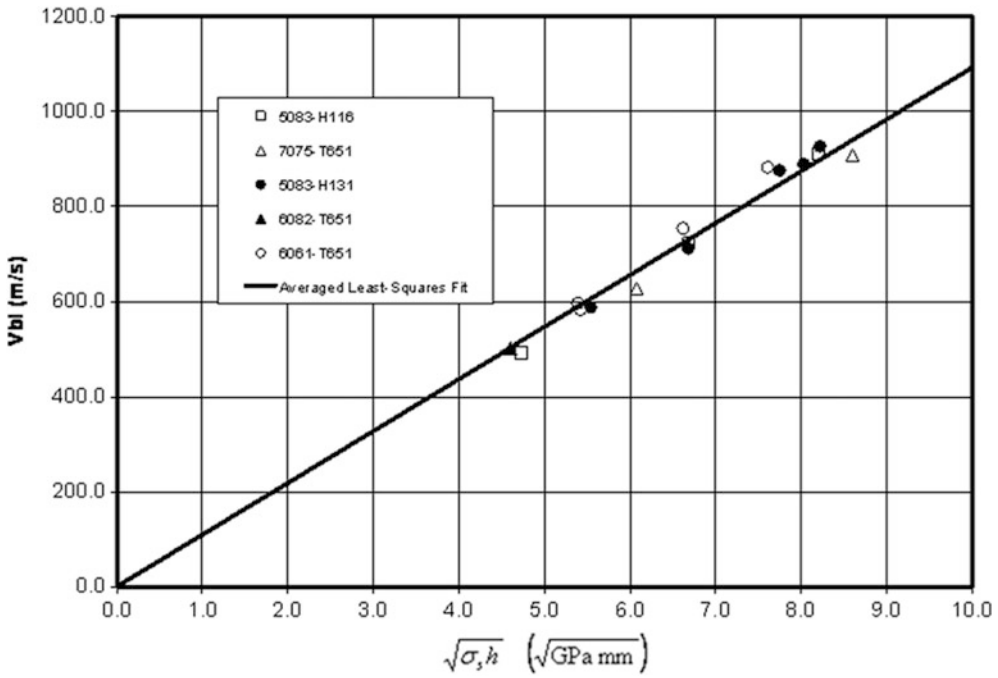

Fig. 35.2 Scaling law and data for the 7.62 mm APM2 bullet and aluminum armor plates

where

$$\sigma_s = \frac{Y}{\sqrt{3}}\left\{1 + \left[\frac{E}{\sqrt{3}Y}\right]^n \int_0^b \frac{(-\ln x)^n}{1-x}\,dx\right\},\ b = 1 - \gamma^2 \tag{35.3a}$$

$$\gamma^2 = \frac{2(1+v)Y}{\sqrt{3}E} \tag{35.3b}$$

Reference [11] gives a procedure to evaluate the integral, and values of σ_s for each aluminum alloy are recorded in Table 35.1.

Figure 35.2 shows the ballistic-limit velocity data recorded in Table 35.2 and a linear, least squares fit with the averaged value of $K = 109.3(\mathrm{m/s})(\mathrm{GPa\ mm})^{-1/2}$ from each of the data sets.

35.3 Discussion

We present a scaling law to predict the ballistic-limit velocity for 7.62 mm APM2 bullets that perforate aluminum armor plates. Data from five aluminum alloy plates show that the ballistic-limit velocities are proportional to the square root of the product of plate thickness and a target strength term. The strength term is derived from a cylindrical, cavity-expansion analysis that requires large-strain compression data.

Table 35.2 Ballistic-limit velocities

Material	h (mm)	V_{bl}(m/s)	References
5083-H116	20.0	492	[1]
5083-H116	40.0	722	[1]
5083-H116	60.0	912	[1]
5083-H131	26.0	588	[5]
5083-H131	37.8	712	[5]
5083-H131	50.9	876	[5]
5083-H131	54.7	890	[5]
5083-H131	57.2	927	[5]
6061-T651	25.7	596	[4]
6061-T651	26.0	583	[4]
6061-T651	38.8	754	[4]
6061-T651	51.2	883	[4]
6082-T651	20.0	501	[3]
7075-T651	20.0	628	[2]
7075-T651	40.0	909	[2]

References

1. Borvik T, Forrestal MJ, Warren TL (2010) Perforation of 5083-H116 aluminum armor plates with ogive-nose rods and 7.62 mm APM2 bullets. Exp Mech 50:969–978
2. Forrestal MJ, Borvik T, Warren TL (2010) Perforation of 7075-T651 aluminum armor plates with 7.62 mm APM2 bullets. Exp Mech 50:1245–1251
3. Forrestal MJ, Borvik T, Warren TL, Chen W (2013) Perforation of 6082-T651 aluminum plates with 7.62 mm APM2 bullets at normal and oblique impacts, Submitted Exp Mech
4. Gooch WA, Burkins MS, Squillacioti RJ (2007) Ballistic testing of commercial aluminum alloys and alternative processing techniques to increase the availability of aluminum armor. In: Proceedings of the 23rd international symposium on ballistics, Spain, pp 981–988
5. Gooch WA (2009) Some 0.30-cal APM2 firing data on 5083-H131. E-mail communication to MJ Forrestal, 9 June 2009
6. Kawahara WA (1990) Effects of specimen design in large-strain compression. Exp Tech 14:58–60
7. Lovato ML, Stout MG (1992) Compression testing techniques to determine the stress/strain behavior of metals subject to finite deformation. Metall Trans A 23A:935–951
8. Forrestal MJ, Luk VK, Brar NS (1990) Perforation of aluminum armor plates with conical-nose projectiles. Mech Mater 10:97–105
9. Piekutowski AJ, Forrestal MJ, Poormon KL, Warren TL (1996) Perforation of aluminum plates with ogive-nose steel rods at normal and oblique impacts. Int J Impact Eng 18:877–887
10. Forrestal MJ, Luk VK, Rosenberg Z, Brar NS (1992) Penetration of 7075-T651 aluminum targets with ogival-nose rods. Int J Solid Struct 29:1729–1736
11. Forrestal MJ, Romero LA (2007) Comment on “Perforation of aluminum plates with ogive-nose steel rods at normal and oblique impacts”. Int J Impact Eng 34:1962–1964

Chapter 36
A Novel Torsional Kolsky Bar for Testing Materials at Constant-Shear-Strain Rates

Jason R. York, John T. Foster, Erik E. Nishida, and Bo Song

Abstract Kolsky bars, also known as split-Hopkinson bars, have been widely used in the dynamic characterization of engineering materials for over 50 years. Kolsky bars can be made to test materials in compression, tension, or torsion, and until recently, have been generally employed in the testing of high-impedance ductile materials to collect rate-dependent stress-strain data during large-strain inelastic flow. The advancement of "pulse-shaping" techniques in the last decade has allowed Kolsky bars to be utilized for testing low-impedance and brittle materials as well. Pulse-shaping is a processes of tailoring the dynamic loading during a test, with consideration given to the material being tested, in order ensure that the sample achieves a state of dynamic stress equilibrium and constant strain-rate if desired. The most common design of torsional Kolsky bars currently in widespread use offer no way to incorporate pulse-shaping. This limits their use mostly to high-impedance, large-strain applications. A novel torsional Kolsky bar design is presented in this work, which allows for straightforward pulse-shaping, similar to the method employed in compression testing, that can be used to test brittle and low-impedance materials as well as to design experiments that ensure the sample is undergoing a constant-shear-strain-rate deformation. Details of the design as well as some preliminary data demonstrating the pulse shaping capabilities collected during tests are presented.

Keywords Kolsky bar • Split-Hopkinson bar • Torsion • Constant-strain-rate • Shear strain

36.1 Introduction

A typical Kolsky bar apparatus [1, 2] is shown in Fig. 36.1, the experimental technique associated with this apparatus uses the elastic response of incident and transmission bars interfaced with a test specimen to characterize its material properties at varying strain-rates. To initiate the experiment a stress wave is applied to one end of the incident bar typically by striking the bar with a projectile fired from a gas gun. As the stress wave interacts with and propagates through the specimen, due to mechanical impedance differences between the sample and bars, a portion of the wave is reflected back through the incident bar, and the remaining pulse is transferred to the transmission bar. From the measured incident, reflected, and transmitted strain histories γ_I, γ_R, and γ_T, the material response can be derived [2]. Material characterization in shear loading can be conducted by modifying the method such that the incident and transmission waves are torsional stress/strain waves. This is typically carried out via a *stored energy* technique, whereby the incident bar is, at once, clamped near the center and a torque is hydraulically applied to the end of the bar, imposing a shear strain in one-half of the bar. The clamp is designed such that it

J.R. York • J.T. Foster (✉)
Mechanical Engineering Department, The University of Texas at San Antonio, One UTSA Circle, San Antonio, TX 78249, USA
e-mail: john.foster@utsa.edu

E.E. Nishida
Terminal Ballistics Technology Department, Sandia National Laboratories, Albuquerque, NM 87185, USA

B. Song
Experimental Solid Mechanics Department, Sandia National Laboratories, Albuquerque, NM 87185, USA

B. Song et al. (eds.), *Dynamic Behavior of Materials, Volume 1: Proceedings of the 2013 Annual Conference on Experimental and Applied Mechanics*, Conference Proceedings of the Society for Experimental Mechanics Series,
DOI 10.1007/978-3-319-00771-7_36,

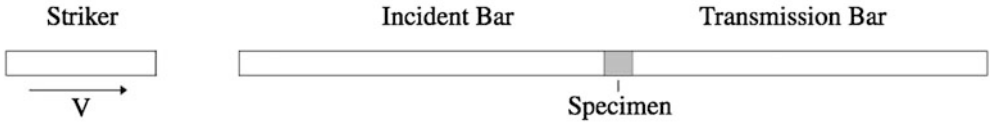

Fig. 36.1 Schematic of a typical Kolsky bar apparatus

can be instantaneously released and the wave then propagates to the sample at the gage-section. When this method is used, the following equations (adapted from those developed by Kolsky) provide the shear-strain and shear-stress histories when dynamic stress-equilibrium is achieved in the specimen

$$\dot{\gamma}_S(t) = \frac{2c_s D_S}{l_S D_b}\gamma_R(t), \tag{36.1a}$$

$$\gamma_S(t) = \frac{2c_s D_S}{l_S D_b}\int_0^t \gamma_R(t)\mathrm{d}t, \tag{36.1b}$$

$$\tau_S(t) = \frac{G_b D_b^3}{8(D_S^2 t_S + t_S^3)}\gamma_T(t), \tag{36.1c}$$

where D, G represent diameter and shear modulus, respectively. t_S and l_S represent thickness and length of the specimen's gage section, while c_s describes shear wave speed. The subscripts S and b indicate specimen and bar properties, respectively. These equations assume a annular thin-wall test specimen. The stored energy technique has the advantage of propagating non-dispersive stress waves; however, the disadvantage of this technique is an inability to control the rate-of-loading of the sample. This can be important when testing materials that, for example, strain harden. In order to impose a constant strain-rate deformation on a material sample that strain hardens, the rate-of-loading must be increased during the portion of loading where the material begins to show an increase in strength. Techniques to achieve this controlled loading have been developed for use in traditional compressive-type Kolsky bar tests and are termed *pulse-shaping*. Pulse-shaping can also be important in the testing of brittle and low-impedance materials. It is the objective of this research to modify the torsional Kolsky bar apparatus such that pulse-shaping techniques can be utilized, thereby increasing the accuracy in which one can report high-shear-strain-rate material properties and widening the range of application materials to include brittle and low-impedance materials.

36.2 Experimental Setup

In tensile and compression Kolsky bar applications, pulse-shaping techniques have emerged as a method of expanding test capabilities by manipulating the input stress wave to fit the test requirements of various materials. There are a several methods of pulse-shaping, such as deformable strikers, dummy specimens, and sacrificial disks. However, wave modification is achieved in each method by a designated plastic deformation occurring before the wave reaches the specimen's gage section. An inexpensive and easily repeatable method of pulse-shaping is the sacrificial disk technique, where a simple disk composed of a material weaker than the striker and impacted bar, is affixed to their interface. During impact, the interfaces of the pulse-shaping disk move at two distinct velocities. As the striker impacts the disk, it is plastically deformed, altering the velocities and resulting pulse. By modifying the material and geometric properties of the disk, various pulse profiles may be created.

Figure 36.2 displays the arrangement and components of the modified torsional Kolsky bar system. For this apparatus, the load is applied to a pulse-shaping bar similarly to an incident bar in compression testing. This bar is mated with a loading lever, interfaced orthogonally with the system's incident bar. In this way, the loading modification that has been well-developed for compression testing may be utilized in torsional testing. Measurements have been made to ensure that bending waves are not present at the sample gage-section.

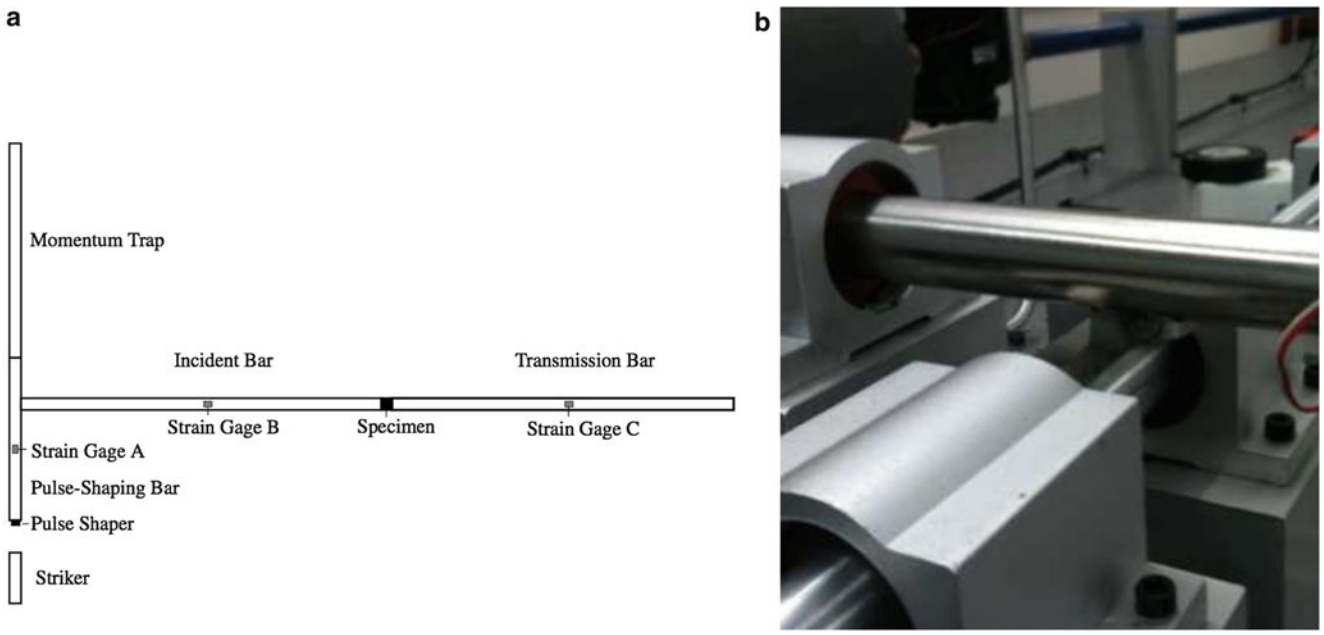

Fig. 36.2 Modified torsional Koslky bar. (**a**) Schematic. (**b**) Photo of interface region

36.3 Experimental Results

This section displays a selection of experimental data resulting from both standard and pulse-shaped loading, at a impact velocity of 10.7 m s-1. In both cases, the specimen was composed of 7075-T6 aluminum. Figure 36.3 shows a clear increase rise time and attenuation of the stress wave profile, displaying the ability to modify incident pulses in a torsional apparatus. Depending of the parameters of the chosen pulse-shaper, the resulting incident pulse may be modified to exhibit an assortment of varied profiles. In this particular test, no attempt was made to tune the pulse such that a constant-strain-rate is achieved in the sample, however, it should be noted that this is possible. In Fig. 36.4, some of the benefits of pulse-shaping are displayed. Although aluminum is a ductile material, the slower increase in loading rate allows the specimen to attain stress equilibrium very early with respect-to-strain, thus an accurate estimate of the materials shear modulus can be obtained, this is typically not the case in a traditional Kolsky bar test. This early equilibrium would prove even more beneficial if testing brittle materials that often fail before obtaining equilibrium, providing no useful data. Figure 36.5 displays the resulting stress-strain curve conducted at a maximum strain rate of approximately 500 s-1. The resulting shear modulus of 26.4 GPa is in agreement with the documented value of 26.9 GPa. The value also yields near the quasi-static shear strength of 331 MPa.

36.4 Summary

The results presented in this work describe a novel torsional Kolsky bar apparatus implementing a pulse-shaping procedure similar to those used in compression Kolsky bars. The resulting data demonstrates the ability to modify applied loading, displaying the potential of the system to improve test validity by providing a more constant strain-rate and equilibrium in the test specimen. These techniques may be further implemented to expand testing to a greater variety of materials and conditions. Although, it was successfully demonstrated that the incident pulse in the system may be modified, improvements to the loading interface must be made to take full advantage of system.

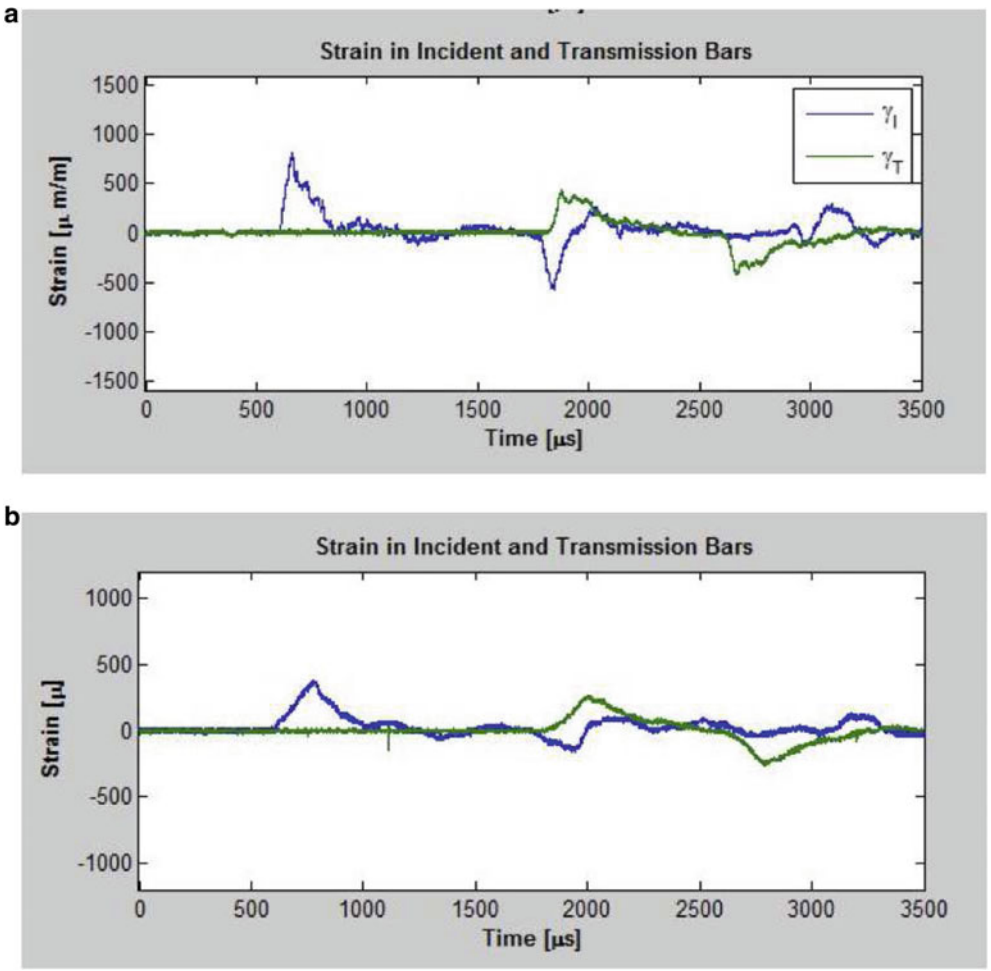

Fig. 36.3 Comparison of response with and without pulse-shaper. (**a**) Incident, reflected, and transmitted waves with no pulse-shaper. (**b**) Incident, reflected, and transmitted waves with pulse-shaper

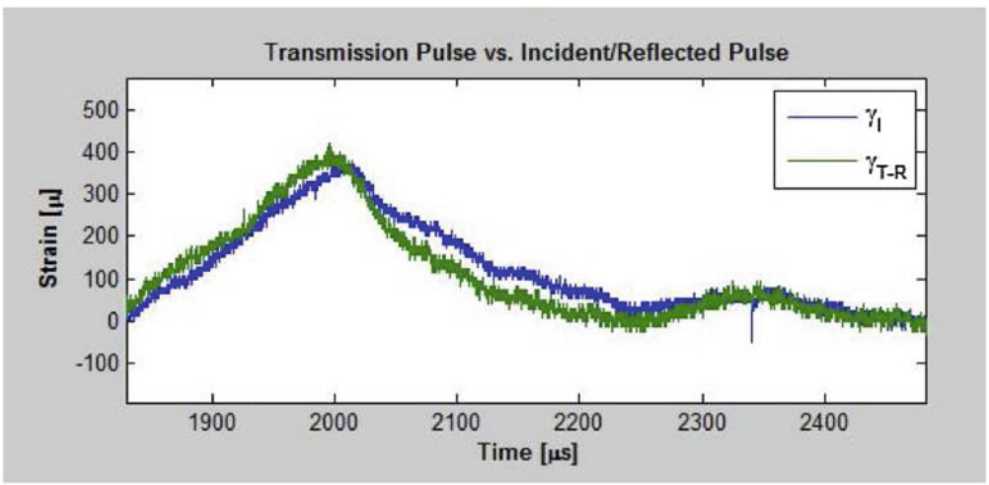

Fig. 36.4 Equilibrium verification

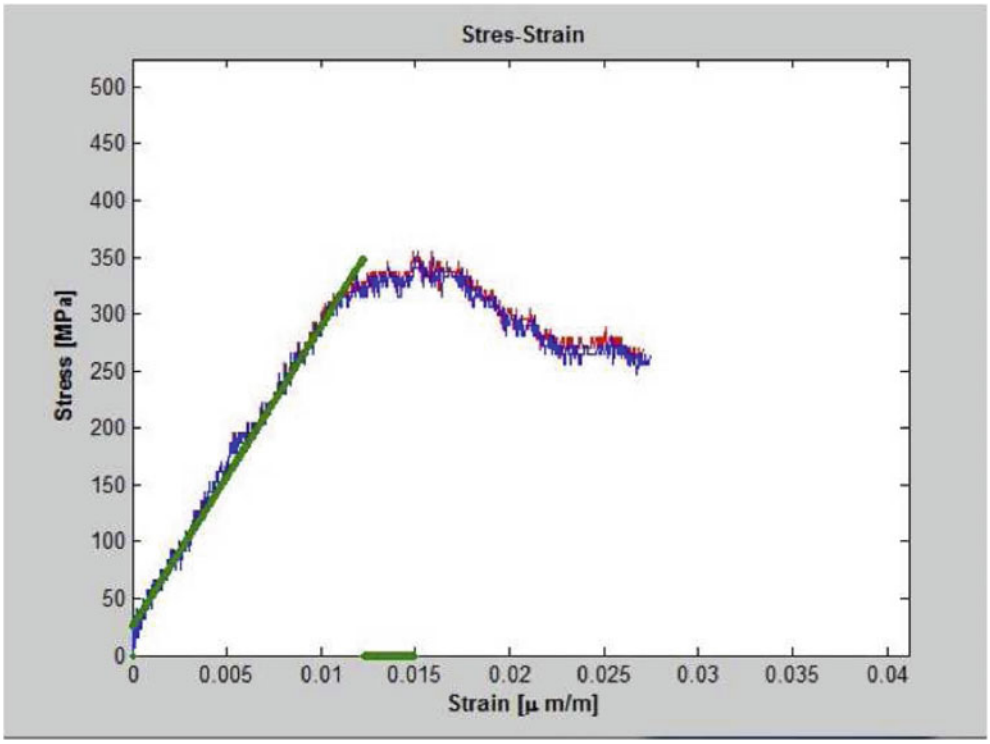

Fig. 36.5 Material stress-strain curve

Acknowledgements This work was partially supported by Sandia National Laboratories. Sandia is a multiprogram laboratory operated by Sandia Corporation, a Lockeed Martin Company, for the United States Department of Energy under Contract DE-AC04–l94AL85000.

References

1. Kolsky H (1949) An investigation of the mechanical properties of materials at very high rates of loading. Proc Phys Soc B 62(11):676–700
2. Chen W, Song B (2010) Split Hopkinson (Kolsky) bar: design, testing and applications. Springer, New York

Chapter 37
A New Method for Dynamic Fracture Toughness Determination Using Torsion Hopkinson Pressure Bar

Addis Kidane and Jy-An John Wang

Abstract A new approach is proposed to determine the dynamic fracture toughness of engineering materials. Although there are well established standard techniques to determine the quasi-static fracture toughness of engineering material, there is still a need for developing experimental techniques to determine the dynamic fracture toughness of materials. Usually an extended quasi-static method is used to determine the dynamic fracture of materials. In most cases, a three point bend specimen is tested using a modified split Hopkinson pressure bar apparatus and a quasi-static relation is used to extract the dynamic fracture parameters by assuming the inertia effect is small and negligible. The technique can only works up to a certain low loading rate where the inertia effect is small and negligible, however it fail to satisfy the main assumption at higher strain rate, where the inertia effect is large. In this paper we propose a new methodology which combines an experimental study, where a spiral notch sample loaded under pure torsion, and numerical simulation of the sample. A torsional Hopkinson pressure bar is used to generate the pure torsion load on the spiral specimen. This method exceptionally avoids the inertia effects, which is a major problem in the conventional dynamic three-point bending experiment.

Keywords Fracture intensity factor • Dynamic fracture • Spiral notched-grove sample • Torsional loading • Hopkinson bar

37.1 Introduction

Fracture mechanics is a well-established subject and today there are different standard experimental methods that can be used to determine the fracture behavior of most engineering materials. These techniques however, have limitation associated with sample size and geometry requirements. There are some other fracture problems that are not straightforward using the available standard methods, and still need further investigation, for examples, evaluating thin film interface fracture toughness. A size requirement to get a valid fracture results is also another drawbacks from the current standard fracture toughness experimental methods, especially in the cases for materials doesn't have enough volume to make the required sample size.

A new experimental technique, Spiral Notch Torsion Fracture Toughness Test (SNTT), has been proposed recently as alternative approach to measure the fracture toughness of engineering materials [1–3]. In this method, a cylindrical specimen with a spiral notch line at 45° pitch will be subjected to pure torsion loading [1–3]. For brittle materials neither fatigue crack nor deep notch is required, just a shallow spiral notch is enough to initiate the mode I fracture, and hence potentially reduce the sample size requirement. The torque force and the associated twist angle will be measured experimentally. The fracture toughness (K_{IC}) can be obtained from the SENT experiment in conjunction

A. Kidane (✉)
Department of Mechanical Engineering, University of South Carolina, Columbia, SC 29208, USA
e-mail: kidanea@cec.sc.edu

J.-A.J. Wang
Mechanical Properties and Mechanics Group, Oak Ridge National Laboratory, Oak Ridge, TN 37831-6069, USA
e-mail: wangja@ornl.gov

B. Song et al. (eds.), *Dynamic Behavior of Materials, Volume 1: Proceedings of the 2013 Annual Conference on Experimental and Applied Mechanics*, Conference Proceedings of the Society for Experimental Mechanics Series,
DOI 10.1007/978-3-319-00771-7_37,

with a three-dimensional finite-element simulation. The technique has been already demonstrated by using different materials, such as ceramics, metals, polymer and concerts [1–4]. The technique is promising to investigate fracture behavior of materials used in pressure vessel, piping structural components and weldments and other unconventional materials.

On the other hand, there is still a demand in finding a standard method to determine the dynamic fracture toughness of engineering materials. Usually, a modified split Hopkinson pressure bar (MSHPB) apparatus is used to investigate the dynamic fracture initiation toughness of materials. The principle of modified MSHPB is similar to general SHPB experiment, except in the case of MSHPB only incident and striker bar are required [5, 6]. In MSHPB experiment, a three point bend single edge specimen will be sandwich between the incident bar and supporting frame. The striker bar, made of the same material used for the incident bar, will be projected towards the incident bar by the help of compressed air and generate a well-defined loading pulse that propagates towards the specimen. Once the compressive stress wave reach the specimen, some of the wave will propagate to the specimen and some of the wave reflected back to the incident bar. Using a strain gage bonded in the incident bar, both the incident and reflected waves can be recorded. Using one dimensional wave theory the force acted on the sample can be calculated as [5, 6]

$$F(t) = (\varepsilon_i(t) + \varepsilon_r(t))EA$$

Where F is the force, ε_i and ε_r are the incident and reflected strain respectively, E is the Young's modulus, and A is the cross sectional area of the bar.

Now, the fracture intensity factor can be calculated using quasi-static equation, [5, 6]

$$K_I(t) = \frac{F(t)}{B\sqrt{W}} F\left(\frac{a}{W}\right)$$

where K_I is the stress intensity factor, B and W are the specimen thickness and width respectively, a the initial crack length and f(a/W) is the geometric factor.

The above equation can be used to calculate the fracture intensity factor if the time of fracture is sufficiently long enough to neglect the inertia effect. To satisfy this condition and to avoid the transient effect, in most cases the experiment has to be conducted at lower speed [8]. This limits the application of the method described above, in the case of only lower strain rate loading. In order to study the dynamic fracture toughness of material at medium and higher loading rate, a better approach is essential. Here we are presenting a technique that can be used to study the dynamic fracture toughness of materials, without the influence of inertia effect.

37.2 Experimental

The proposed experiment is based on the spiral notch sample loaded under pure torsion as proposed by Wang [1–4] for quasi-static fracture. The cylindrical specimen that has spiral notch grove around the specimen at a 45° pitch angle will undergo pure torsion loading. Near the crack front a compression and tension stress fields will be generated on the concentric cylinder of the sample. The tension load, perpendicular to the grooved line, will be responsible to creating a mode I crack opening fields. In the case of dynamic loading, since the loading, torsion, the will be no inertia force associated, which makes the method promising.

37.2.1 Material and Specimen Geometry

In this experiment a polycarbonate specimen is machined from cylindrical bar as shown in the figure. A v-notched spiral group with 45° pitch angle was machined on the surface of the specimen. The diameter of the cylinder and the gage length are 0.5 and 1 in. respectively, and the depth of the grove is 0.1 in. Since polycarbonate is relatively brittle material, the deep notch was not required to create the opening mode fracture; however it was made to be consistent with other materials under investigation. It should be mentioned that, if the material is ductile, either a deep notch or fatigue pre-crack is required. The head of the sample is made hexagonal to easily attaché the sample with the tow bars. As can be seen in the figure, a plane-strain condition is achieved on every plane normal to the spiral groove, which makes the SNTT unique compared with conventional methods (Fig. 37.1) [1].

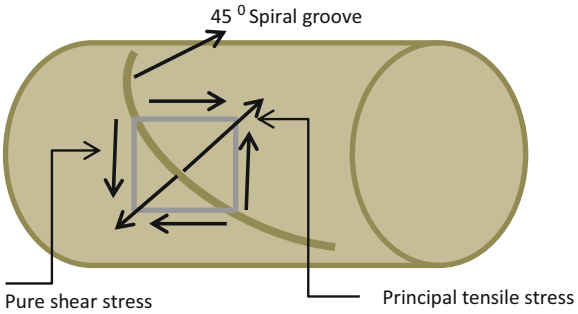

Fig. 37.1 Typical SNTT specimen geometry and configuration

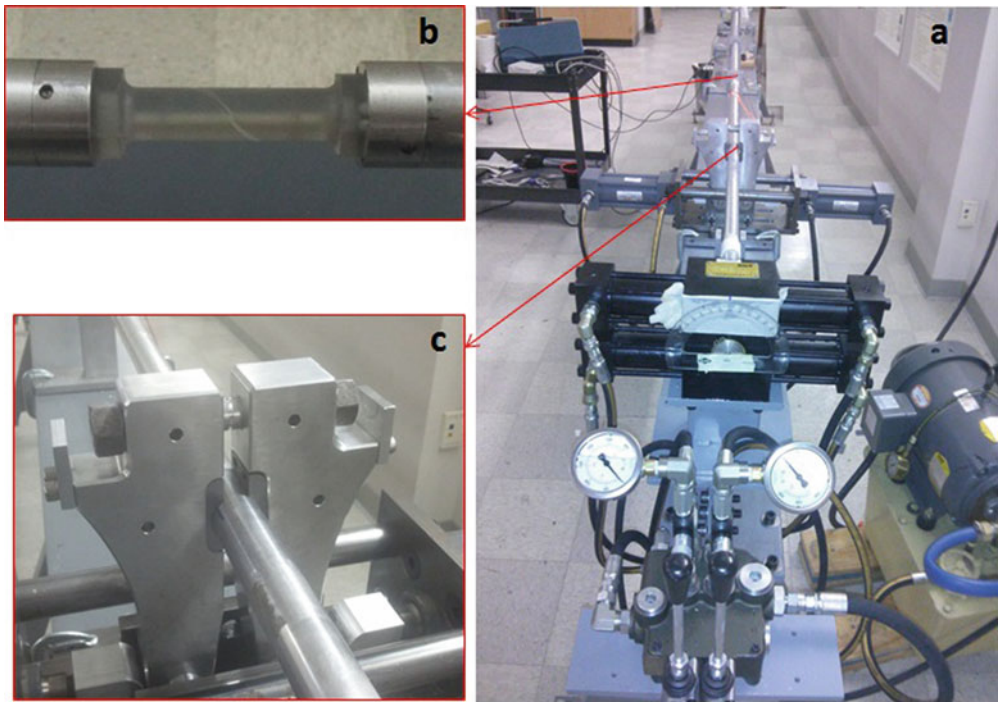

Fig. 37.2 Experimental set up; (**a**) torsion Hopkinson bar (**b**) spiral notch specimen (**c**) clamping mechanism

37.2.2 Experimental Setup

The dynamic experiment is similar to the experiential procedure explained in quasi-static experiment, except the loading mechanism. A detail experimental procedure that are followed for testing SNTT samples under quasi-static loading can be found in reference [1–3]. In the case of dynamic experiment, the SNTT specimen is sandwich between the incident and the transmitter bar of the Torsional Hokinson bar shown in the Fig. 37.2. Torsional Hokinson bar is an experimental technique generally used to study the dynamic shear properties of materials [7]. It works in the same principle as that of usual Hopkinson pressure bar except the loading orientation. The experimental analysis is based on one dimensional wave theory. Detail information, how it works and the theory behind can be obtained in the literature [3, 4], and only brief information is given for brevity. The main parts of the THB apparatus are two elastic bars (incident and transmitter), a clamp with a sudden releasing mechanism, and a mechanism to create toque in the incident bar. During the experiment, the specimen is attached between the two bars. Attaching the sample is sometimes challenging and in this experiment, a hexagon socket joint is used.

To create the dynamic torsional load on the sample, first half part of the incident bar will be held stationary using the clamp mechanism located between the sample and the torque. The position of the clamp determines the duration of the stress pulses and affects the strain on the sample. Then, by rotating the end on the incident bar using the torque mechanism,

torque will be stored in the incident bar between the clamp and the torque mechanism. Finally by suddenly releasing the clamp, the stored toque will be allowed to propagate towards the specimen. Once the shear stress wave reach the sample, some of the wave transmitted to the output bar through the sample and the rest of the wave reflects back to the input bar. The strain associated to these waves can be recorded using the strain gage bonded on the bars. Finally using one dimensional wave theory, the torque and force on both side of the sample can be calculated. The equilibrium of the stress state can be verified by comparing the two forces calculated at the interface of the two sides of the specimen.

37.3 Results and Discussion

Due to unavailability of closed form solution, the fracture parameter is extracted from 3D finite element simulation based on minimum strain energy density criterion. According to the strain energy density criterion, the crack growth occurs when the strain energy density reach a critical value and propagates in the direction of minimum strain energy density [8]. The three-dimensional strain energy density (S) can be written as Eq. 37.1.

$$S = a_{11}K_I^2 + 2a_{12}K_IK_{II} + a_{22}K_{II}^2 + a_{33}K_{III}^2 \tag{37.1}$$

Where K_I, K_{II} and K_{III} are mode-I, mode-II and mode-III stress intensity factor respectively and a_{11}, a_{22} and a_{33} are constants that can be determined from material property and geometry factors.

The stress intensity factor K_I, K_{II} and K_{III} are evaluated from the crack tip opening displacements (CTODs) of a singular prismatic element around the crack front as shown in Fig. 37.3. Typical FEM model is shown in Fig. 37.4, the detail information of the analysis can be obtained elsewhere [1–3].

The fracture starts from the notched surface and propagates towards the center along the spiral notch direction which results in a mode I fracture. Typical fracture surfaces of SNTT samples subjected to pure torsion are shown in the figure. As shown in the figure the crack propagates towards the root of the cylinder insuring a mode I fracture failure (Fig. 37.5) [9].

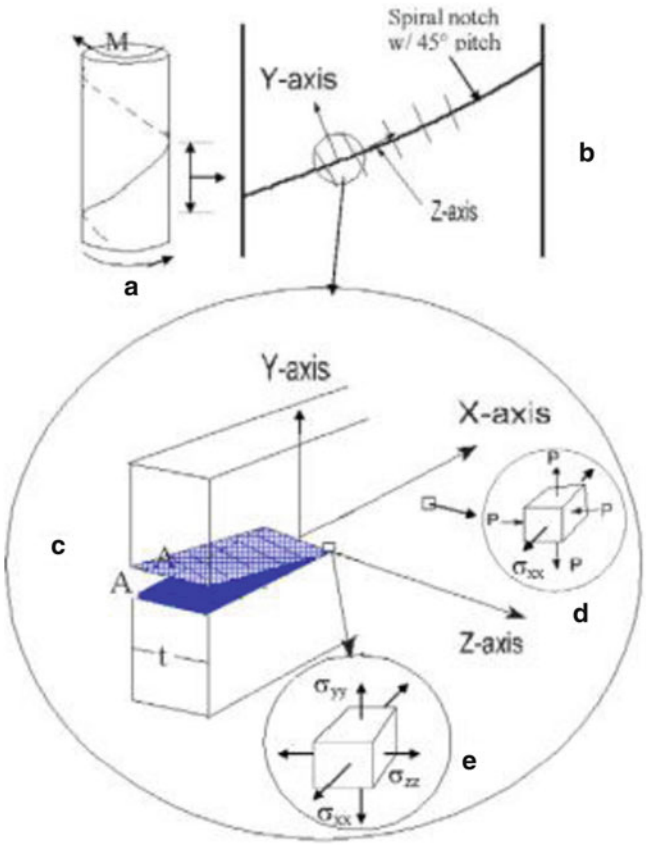

Fig. 37.3 Stress fields in the torsion bar [4]

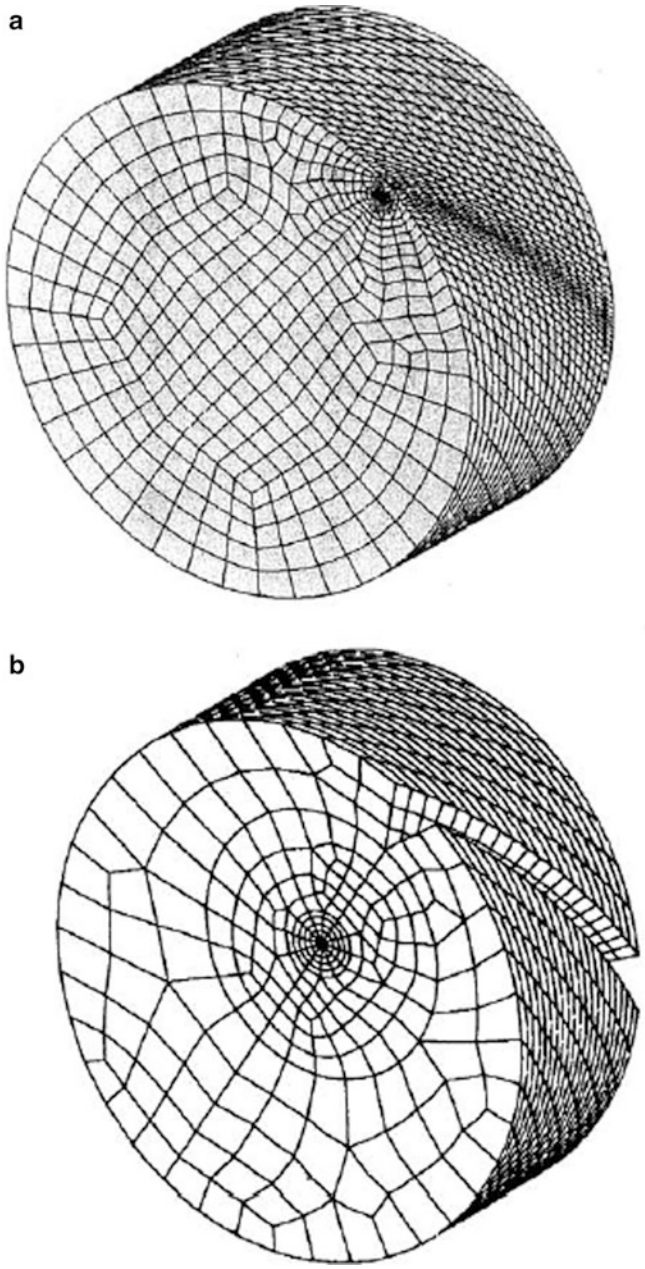

Fig. 37.4 Typical SNTT FEM Models: (**a**) shallow crack; and (**b**) deep fatigue pre-crack [4]

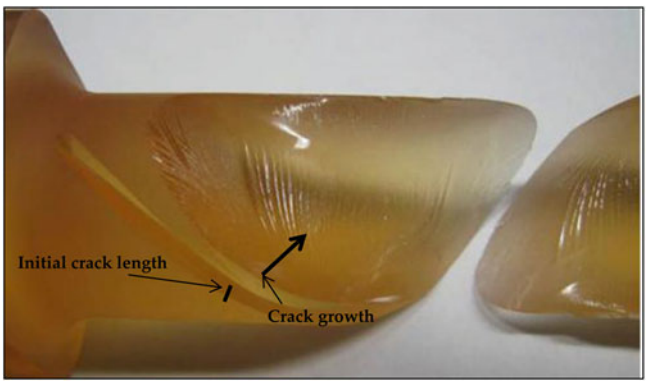

Fig. 37.5 Typical fracture surface of polymer SNTT sample

37.4 Summary

We propose a new methodology which combines an experimental study, where a spiral notch sample loaded under pure torsion, and numerical simulation of the sample to determine the dynamic fracture of engineering materials. A torsional Hopkinson pressure bar is used to generate the pure torsion load on the spiral specimen. This method exceptionally avoids the inertia effects, which is a major problem in the conventional dynamic three-point bending experiment. This is a first attempts to using Torsion Hokinson bar to investigate dynamic fracture for engineering materials. It has a potential to overcome most of the limitations that are exist in conventional experimental techniques and can be introduces a new approach to determine the dynamic fracture toughness of unconventional materials.

References

1. Wang J-AJ, Wright IG, Lance MJ, Liu KC (2006) A new approach for evaluating thin film interface fracture toughness. Mater Sci Eng A 426:332–345
2. Wang JA, Liu KC (2004) A new approach to evaluate fracture toughness of structural materials. J Press Vessel Technol Trans ASME 126:534–540
3. Wang J-A, Liu K, Naus D (2010) A new test method for determining the fracture toughness of concrete materials. Cem Concrete Res 40:497–499
4. Wang J-AJ, Liu KC (2008) An innovative technique for evaluating fracture toughness of graphite materials. J Nucl Mater 381:177–184
5. Rubio L, Fernandez-Saez J, Navarro C (2003) Determination of dynamic fracture-initiation toughness using three-point bending tests in a modified Hopkinson pressure bar. Exp Mech 43(4):379–386
6. Kidane A, Shukla A (2010) Quasi-static and dynamic fracture initiation toughness of Ti/TiB layered functionally graded material under thermo-mechanical loading. Eng Fract Mech 77:479–491
7. Naik NK, Kidane AA, Kavala VR, Ch V (2007) Interlaminar shear properties of polymer matrix composites: strain rate effect. Mech Mater 39:1043–1052
8. Sih GC (1974) Strain energy density factor applied to mixed mode crack problem. Int J Fract 10:305–321
9. Tan T, Ren F, Wang J-A, Lara-Curzio E, Agastra P, Mandell J, Bertelsen MD, LaFrance CM (2013) Investigating fracture behavior of polymer and polymeric composite materials using spiral notch torsion test. Eng Fract Mech 111:109–128

Chapter 38
Characterization of Sheet Metals in Shear over a Wide Range of Strain Rates

Kevin A. Gardner, Jeremy D. Seidt, Matti Isakov, and Amos Gilat

Abstract A new specimen geometry, based on ASTM B831, for characterization of sheet metals in shear is introduced. The specimen can be tested in both quasi-static and dynamic tests using a load frame and a tensile split-Hopkinson bar (SHB) apparatus, respectively. Specimens with this new geometry and spool-shaped torsion specimens were fabricated from the same 0.5″ rolled 2024-T351 aluminum plate. Static and dynamic tests at strain rates up to 2,000 1/s on both samples were conducted using an axial-torsional servo-hydraulic load frame, a tension SHB, and a torsion SHB. Three-dimensional digital image correlation was used to directly measure deformation of the surface of the sample's gage section in both static and dynamic tests. Stress–strain curves obtained from tests with both types of specimens agree, indicating that the new sample geometry is suitable for the characterization of ductile sheet metals in shear.

38.1 Introduction

Many products, such as automobiles and aircraft are comprised of sheet metal. As commercial numerical codes have matured, engineers are using them more and more to optimize designs. For example, automotive engineers run numerical simulations of crash events involving their vehicles to identify components that are likely to fail and potentially injure the occupants. During these events, the components are subjected to complex stress states. In order to have confidence in simulation results, the material models that describe the deformation and failure behavior of these components must be based on and calibrated with experimental data. It is important to determine the shear response of these materials, since effective stress vs. equivalent plastic strain curves from tension and shear tests do not always coincide [1, 2]. In addition, material failure is known to be stress state dependent [3–5], therefore, it is necessary to know the equivalent strain at failure under shear loading conditions.

The shear response of ductile metals is typically determined by conducting torsion tests on thin walled tube samples. Torsion test specimens are spool shaped with a thin walled tube gage section in the middle and flanges on either side that are used to attach the specimen to the test apparatus. While these samples are easily fabricated from round stock or thicker plates, it is impossible to fabricate this geometry from thin sheet metals. ASTM B831 [6] describes a sample geometry that is used to test thin aluminum products in simple shear, see Fig. 38.1. Researchers have previously applied this test method to thin ferritic stainless steel sheet metal and found the results unsatisfactory [7]. The specimens, fabricated following the guidelines in ASTM B831 exhibited large deformation in the area outside the intended gage section as indicated by Fig. 38.2a. In order to prevent this deformation, the thickness was reduced in the area of interest (the center of the test specimen) to limit deformation to within the gage section as illustrated in Fig. 38.2b.

While this test method is intended for use on thin sheets, it is important to compare results from this technique to results from methods previously established. Therefore, both simple shear and torsion test specimens were fabricated from the same 0.5 in thick 2024-T351 rolled aluminum plate. Initially, the sample geometry shown in Fig. 38.2b was fabricated

K.A. Gardner (✉) • J.D. Seidt • A. Gilat
Department of Mechanical and Aerospace Engineering, The Ohio State University, Scott Laboratory, 201 W 19th Ave, Columbus, OH 43210, USA
e-mail: gardner.796@osu.edu

M. Isakov
Department of Materials Science, Tampere University of Technology, Scott Laboratory, 201 W 19th Ave, Columbus, OH 43210, USA

B. Song et al. (eds.), *Dynamic Behavior of Materials, Volume 1: Proceedings of the 2013 Annual Conference on Experimental and Applied Mechanics*, Conference Proceedings of the Society for Experimental Mechanics Series,
DOI 10.1007/978-3-319-00771-7_38,

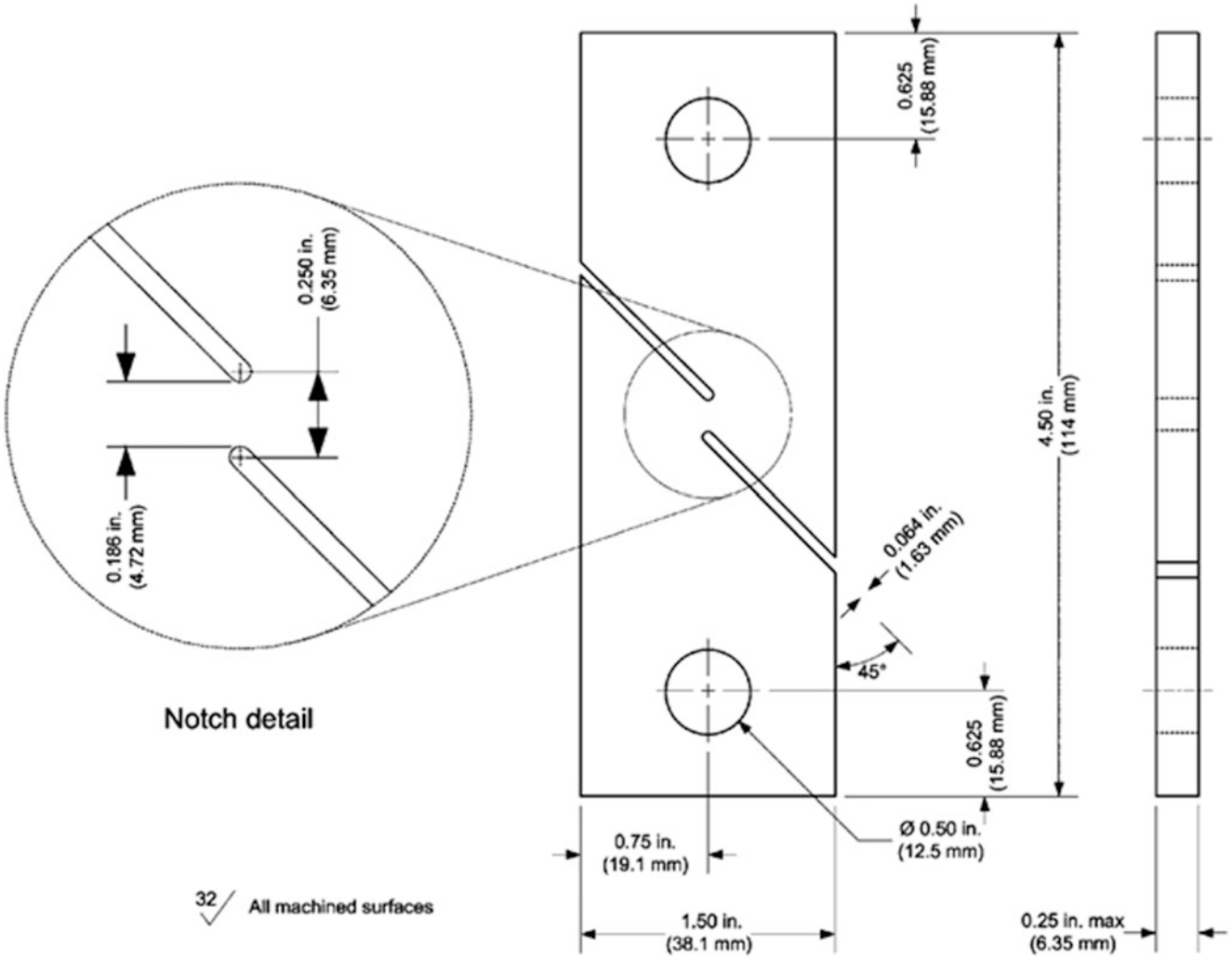

Fig. 38.1 Sample geometry outlined in ASTM B831 for testing of thin aluminum alloys [1]

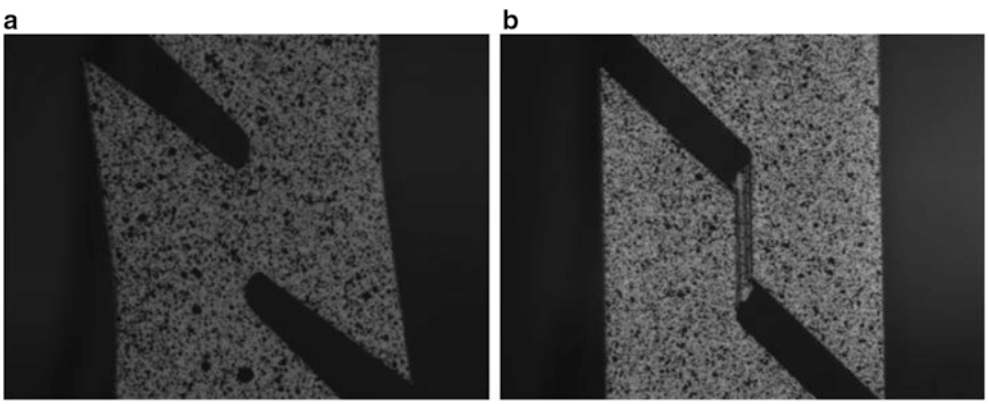

Fig. 38.2 Deformation of sample before and after applying thickness reduction to the gage section [2]

from the plate. Tests were performed at low strain rates with an axial-torsional servo-hydraulic load frame and at high strain rates with a tensile split-Hopkinson bar. Test data was satisfactory at low strain rates, however, high strain rate data was unsatisfactory due to the long duration required to achieve force equilibrium in the specimen. This is due to the fact that the sample geometry was too long (because of the 45° cutouts). To address this shortcoming, a new, simpler geometry is

introduced for characterizing thin, ductile sheet metals in shear. The new specimens were fabricated from the 2024-T351 plate and tested over a shear strain rate range of 0.01–2,000 s^{-1}. Data from these experiments are compared to data from torsion experiments at similar strain rates.

38.2 Experimental

The test specimens, shown in Fig. 38.3, were fabricated from a 0.5 in thick 2024-T351 rolled aluminum plate. Figure 38.3a shows the thin-walled tube torsion specimen. The torsion specimen has a wall thickness of 0.015 in., an inside diameter of 0.511 in. and a gage length of 0.1 in.. The flanges at either end of the specimen are used to attach the specimen to the test apparatus. The new simple shear specimen is shown in Fig. 38.3b. The sample is similar to the design used by Isakov et al. [7], however, the gage section is constructed through cuts made 90° to the loading direction opposed to 45° cuts. This significantly reduces the overall length of the specimen reducing the duration required to reach force equilibrium in dynamic tests. The gage section of the specimen is 0.220 in. long, 0.040 in. thick and 0.040 in. wide. 0.020 in. deep slots are milled from either side of an initially 0.080 in. thickness to concentrate the deformation in the gage section.

The sample geometries are tested at both low and high strain rates. Low strain rate tests (0.01 s^{-1}) were performed using an axial-torsional servo-hydraulic load frame. The samples were affixed to the load frame using hydraulic wedge grips as illustrated by Fig. 38.4a. High strain rate tests (2,000 s^{-1}) were performed using both a tensile split-Hopkinson bar apparatus [8] and a torsion split-Hopkinson bar apparatus [9]. The samples were glued to the tension and torsion bars as illustrated by Figs. 38.4b, c, respectively.

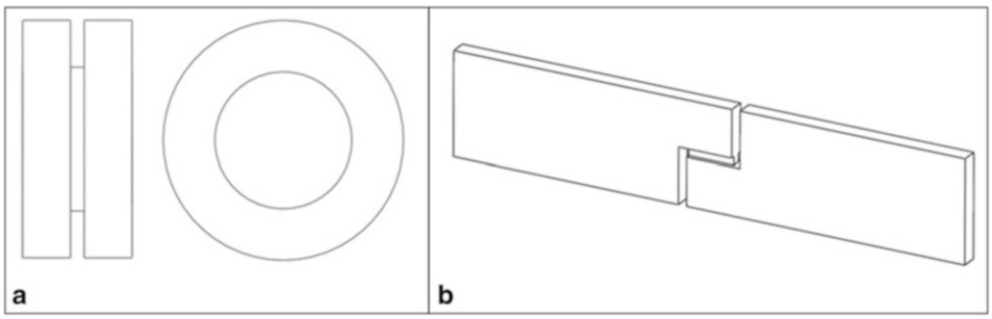

Fig. 38.3 Specimen geometries used in this study: (**a**) thin walled tube torsion specimen, (**b**) new simple shear specimen design

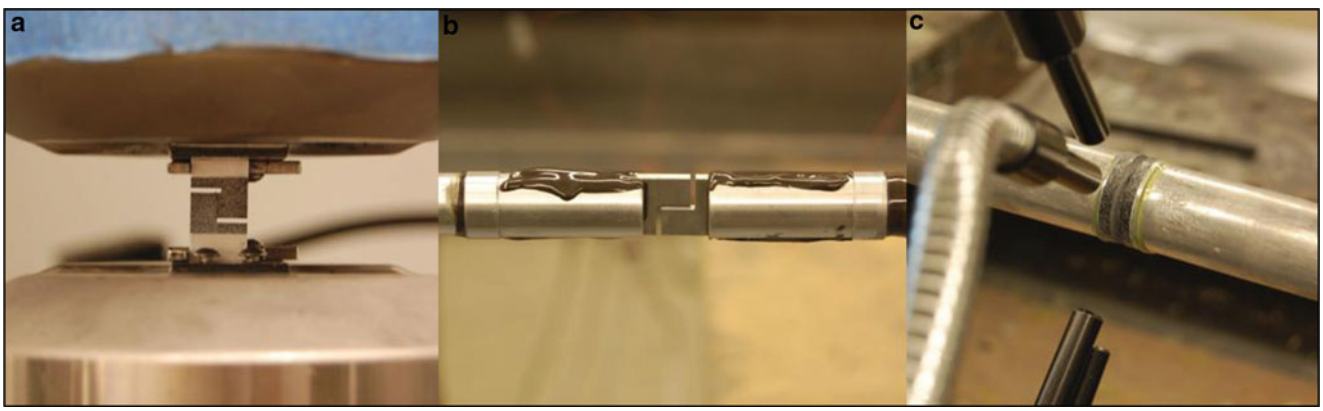

Fig. 38.4 Specimen attachment methodologies: (**a**) simple shear sample mounted in hydraulic wedge grips for low rate testing, (**b**) simple shear sample epoxied to a tensile SHB, (**c**) spool sample epoxied to a torsion SHB apparatus

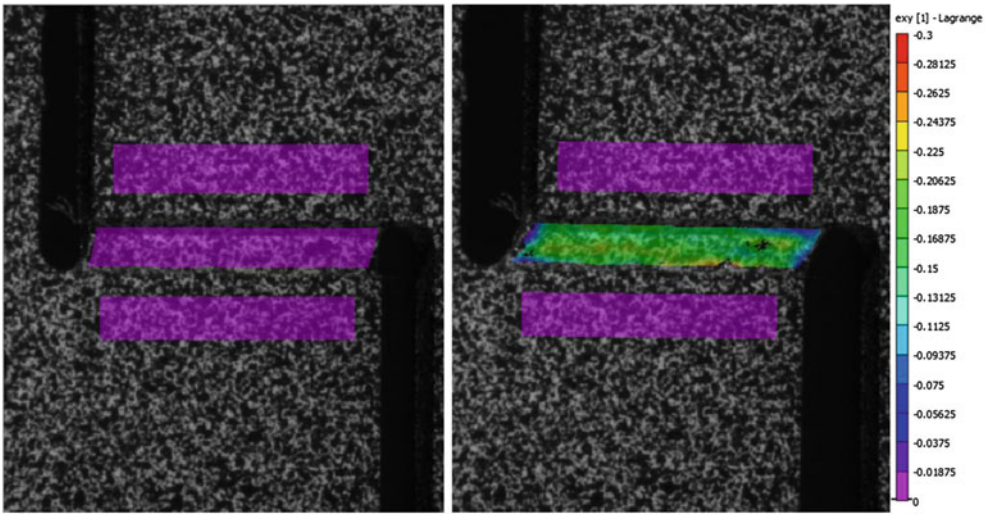

Fig. 38.5 Shear strain contours on the surface of the simple shear test specimen: *left*: un-deformed, *right*: deformed

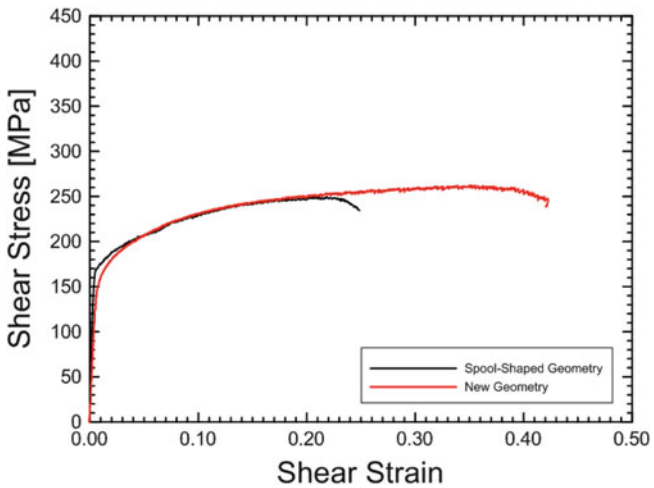

Fig. 38.6 Comparison of shear stress–strain curves obtained from torsion and simple shear tests

Three-dimensional digital image correlation was used during all tests to directly measure strain on the surface of the sample. Low rate strain data was captured using a pair of Point Grey Gras-20S4M-C cameras arranged in a stereo array operating at five frames per second. Similarly, high strain rate data was captured using two Photron Fastcam SA1.1 cameras operating at 100,000 frames per second. Correlated Solutions Vic 3D software was then used to calculate the strains on the surface of the sample during the tests. This setup allows full field shear strain to be determined on the surface of the samples as illustrated in Fig. 38.5. The left image in Fig. 38.5 shows the sample prior to deformation while the right image shows the deformed sample.

Shear stress vs. shear strain curves from simple shear and torsion tests, both conducted at a shear strain rate of roughly 2,000 s^{-1}, are compared in Fig. 38.6. The curves agree up to shear strains of about 22 %, indicating that the new simple shear sample design is adequate to characterize sheet metals in shear. At 22 % shear strain the torsion specimen fails. The simple shear specimen continues to deform until it fails at roughly 40 %. The discrepancy between the failure strains is the subject of an ongoing investigation, however, an initial theory suggests that the torsion sample fails prematurely due to a stress concentration at the sharp edge where the tube specimen meets the flange.

38.3 Summary and Conclusions

A new simple shear sample geometry, based on ASTM B831, is introduced for shear characterization of thin sheet metals. Simple shear and torsion specimens were fabricated from the same 0.5 in 2024-T351 rolled aluminum plate and tested at strain rates ranging from 0.01 to 2,000 s^{-1} to validate the new sample geometry. Tests were performed using an axial-torsional servo hydraulic frame, a tensile split-Hopkinson bar and a torsion split-Hopkinson bar. Digital image correlation was used to measure strain data directly on the surface of the sample for all tests. A comparison of stress strain curves from torsion and simple shear tests shows a strong agreement between curves up to 22 % shear strain indicating that the new sample geometry is suitable to determine the shear response of thin, ductile sheet metals.

Acknowledgements Support for this study was received from the Federal Aviation Administration. Thanks are due to Don Altobelli, Bill Emmerling, and Chip Queitzsch of the FAA.

References

1. Seidt JD, Gilat A (2008) Characterization of 2024-T351 aluminum for dynamic loading applications. In: Proceedings of the SEM international congress and exhibition of experimental and applied mechanics, Orlando
2. Hammer JT, Yatnalkar RS, Seidt JD, Gilat A (2012) Plastic deformation of Ti-6Al-4V plate over a wide range of loading conditions. In: Proceedings of the SEM annual conference on experimental and applied mechanics, Costa Mesa
3. Mackenzie AC, Hancock JW, Brown DK (1977) On the influence of state of stress on ductile failure initiation in high strength steels. Eng Fract Mech 9:167–188
4. Johnson GR, Cook WH (1985) Fracture characteristics of three metals subjected to various strains, strain rates, temperatures and pressures. Eng Fract Mech 21:31–48
5. Bau Y, Wierzbicki T (2004) On fracture locus in the equivalent strain and stress triaxiality space. Int J of Mech Sci 46:81–98
6. ASTM Standard B831 (2005) Standard test method for shear testing of thin aluminum alloy products. ASTM International, West Conshohocken. www.astm.org
7. Isakov M, Seidt J, Östman K, Gilat A, Kuokkala VT (2011) Characterization of a ferritic stainless sheet steel in simple shear and uniaxial tension at different strain rates. In: Proceedings of the ASME 2011 international mechanical engineering congress & exposition, Denver
8. Staab GH, Gilat A (1991) A direct-tension split Hopkinson bar for high strain-rate testing. Exp Mech 31:232–235
9. Gilat A (2000) Torsional Kolsky bar testing, mechanical testing, vol 8, ASM handbook. ASM International, Materials Park

Chapter 39
Material Identification of Blast Loaded Aluminum Plates Through Inverse Modeling

K. Spranghers, D. Lecompte, H. Sol, and J. Vantomme

Abstract This paper deals with full-field measurements of aluminum plates under free air blast loading conditions. A stereoscopic high-speed camera system is used to capture the plate response with an inter frame rate of 6,000 fps. The transient deformation fields are calculated using a three-dimensional digital image correlation technique. The deformation fields are compared by data computed with an explicit finite element method. A good agreement has been found between both experimental and numerical data. Furthermore, a mixed experimental-numerical method is proposed to determine the elasto-plastic material parameters during a free air blast event. The method is solely validated using a virtual experiment.

Keywords 3D digital image correlation • High-speed cameras • Blast loading • Elasto-plastic behavior • Aluminum plates

39.1 Introduction

Analysis of the structural dynamic response caused by an explosion is complex due to the high velocity impact, the transient nature of the deformation and the interactions between the structure and the pressure wave. Much research effort has been focused on the dynamic response of the structural components subjected to blast loading [1–4]. Some of this research has been concentrated on the response of circular and rectangular plates to impulsive loading [5–9]. In these studies, large plastic deformations are obtained and the loading impulse is experimentally determined and compared to analytical and numerical calculations.

To predict the dynamic response of structural components subjected to blast loading one must have the knowledge of the material behavior during these dynamic loading conditions. The main objective of this research is to develop a mixed numerical-experimental system to identify the material parameters of plates subjected to blast loading.

This paper deals with full-field measurements of aluminum plates under free air blast loading conditions. Forty grams of explosive material C4 is detonated at a stand-off-distance of 250 mm and two synchronized high-speed cameras in a stereoscopic setup are used to capture the plate response with an inter frame rate of 6,000 fps. The transient deformation fields are calculated using a three-dimensional digital image correlation technique.

Furthermore, the identified deformation fields are compared by data computed with an explicit finite element method. The Johnson-Cook material model is used to simulate the plastic behavior of the aluminum plates.

Finally, a mixed experimental-numerical method is proposed to determine the elasto-plastic material parameters during a free air blast event. The general philosophy is to compare the results of the experimental observation with numerical simulated data. Tuning of the parameters until the numerical observations match the experimental observations leads to the identification of the unknown material parameters. Hence, the identification of the material behavior is based on a mixed numerical-experimental method, i.e. an inverse method. This inverse approach is solely validated using a virtual experiment.

K. Spranghers (✉) • H. Sol
Department of Mechanics of Materials and Constructions, Vrije Universiteit Brussel (VUB), Pleinlaan 2, Brussels B-1050, Belgium
e-mail: Ken.Spranghers@vub.ac.be

D. Lecompte • J. Vantomme
Civil and Materials Engineering Department, Royal Military Academy (RMA), Av. De la Renaissance 30, Brussels B-1000, Belgium

B. Song et al. (eds.), *Dynamic Behavior of Materials, Volume 1: Proceedings of the 2013 Annual Conference on Experimental and Applied Mechanics*, Conference Proceedings of the Society for Experimental Mechanics Series,
DOI 10.1007/978-3-319-00771-7_39,

Fig. 39.1 Experimental setup

39.2 Experimental Setup

As described by the authors in [10], all experiments are performed in the test bunker of the Laboratory of Analysis of Explosion Effects (LAEE) of the Royal Military Academy (RMA) (see Fig. 39.1). The setup consists of a steel frame (mounting plate, 1,000 mm× 1,000 mm × 15 mm) with a square captivity of 300 mm by 300 mm in the center. The specimen, a thin aluminum plate (type EN AW-1050A) of 400 mm by 400 mm with a thickness of 3 mm, is connected to the steel frame. The connection is established by using a bolts connection with a steel clamp in order to achieve a perfect fixed connection. The explosive material, 40 g of C4, is positioned behind the test plate with a stand-off-distance of 250 mm from the center point in order to obtain a spherical airburst wave.

Two similar Photon© Fastcam Ultima APX-i2 high-speed digital cameras are mounted in a stereo configuration to record synchronized images during the free air blast event. The full-field transient deformations of a thin aluminum plate are obtained using a 3D digital image correlation technique [11]. More details on the stereo calibration, camera system settings, preparation of the specimens and the correlation technique are available in [10, 12]. As soon as the explosion initiates, synchronized stereo images at a frame rate of 6,000 fps are acquired during sheet deformation. During the experiments the plate behavior is observed with a field of view of 500 mm × 500 mm and an image size of 512 × 512 pixels.

39.3 Numerical Setup

39.3.1 Blast Loading

In this paper the explicit finite elemenT program LS-Dyna is used to predict the blast loading response of a clamped aluminum plate. In LS-Dyna, blast simulations can be performed using an empirical method developed by Kingery and Bulmash [13] where air blast parameters from spherical airbursts and from hemispherical surface bursts are predicted by equations. These equations are widely accepted as engineering predictions for determining free-field pressures and loads on structures. The Kingery-Bulmash equations have been automated in the computer program ConWep [14]. Curve-fitting

techniques are used to represent the data with high-order polynomial equations, assuming an exponential decay of the pressure with time. A functional form such as the Friedlander equation can model the typical pressure history in the vicinity of a free-air explosion:

$$P(t) = P_{\max}\left(1 - \frac{t}{t_+}\right)e^{\left(-\frac{at}{t_+}\right)} \tag{39.1}$$

where t_+ is the positive phase duration and the parameter a is called the waveform number and depends on P_{max} (incident pressure or over pressure). Blast pressures in free air, or incident pressures, are seldom of interest. Moreover, the focus of attention is the interaction of these pressures with structures and the subsequent response of the structure itself. Mush like an acoustic wave, when a blast wave encounters a structure the sudden decrease in velocity of the shock wave and particle velocities behind the shock gives rise to an increase in pressure, i.e. the reflected pressure. Due to the large compressibility of air, the reflected pressure is typically much more than doubled, $P_{ref} = C_R\, P_{inc}$ with $2 \leq C_R \leq 8$. The reflected pressure wave has a similar form as the incident pressure wave and can also be modeled by the Friedlander equation (Eq. 39.1) but with a different decay rate (waveform number).

In the idealized case of ConWep there is no decay coefficient and the pressure wave is considered as a special triangular impulse because the structure is considered to be rigid and its surface infinite. ConWep is implemented in a LS Dyna algorithm for blast loads by Randers-Pehrson and Bannister and takes into account the decay coefficient that also updates the pressure history based on changes in the geometry [15, 16]. The objective of this algorithm is to produce an appropriate pressure history given an equivalent TNT explosive weight. The quantities to be determined by the algorithm are: P_{inc} the peak incident pressure; P_{ref} the peak reflected pressure; t_a the time of arrival of the shock wave; t_+ the positive phase duration; and a, b the exponential decay factors for incident and reflected waves, respectively. The input values that need to be chosen are: the amount of explosive charge; R the range from charge location to the centroid of the loaded surface; and $cos\theta$ the cosine of the incident angle, angle between surface normal and range unit vector. The parameters that need to be defined by the user are the TNT-equivalent mass of the explosive and the position of the center of the explosion in space, which defines the stand-off-distance.

39.3.2 Material Model

The Johnson-Cook material model is employed to estimate the effects of strain hardening, strain rate hardening and thermal softening. The flow stress is expressed as:

$$\sigma_y = (A + B\varepsilon_p^n)\left(1 + C\,\ln\frac{\dot{\varepsilon}_p}{\dot{\varepsilon}_0}\right)\left(1 - \left(\frac{T - T_{room}}{T_{melt} - T_{room}}\right)^m\right) \tag{39.2}$$

where A, B, C, n, m are Johnson-Cook material parameters and ε_p the effective plastic strain, $\dot{\varepsilon}_p$ the effective plastic strain rate, $\dot{\varepsilon}_0 = 0.001\ \mathrm{s}^{-1}$ the reference strain rate, T the material's temperature, T_{room} the room temperature, and T_{melt} the material's melting temperature. The Johnson-Cook model parameters for aluminum EN AW-1050A are $A = 110$ MPa, $B = 150$ MPa, $C = 0.014$, $n = 0.360$ and $m = 1.0$ [17].

39.3.3 Finite Element Model

The numerical model is shown in Fig. 39.2. It consists of an aluminum plate (red, 400 mm × 400 mm), a steel mounting frame (blue, 1,000 mm × 1,000 mm) and a steel clamping frame (green, 400 mm × 400 mm, thickness of 50 mm) with respectively 1,600, 9,100 and 700 quadrilateral square Lagrangian shell elements (Belytschko-Lin-Tsay shell elements [16]). Every element has a size of 10 mm × 10 mm and a thickness of 3, 15 and 10 mm respectively for the aluminum plate, the steel mount and the steel clamp. Hinged boundary conditions and a tied contact algorithm between the three parts are applied.

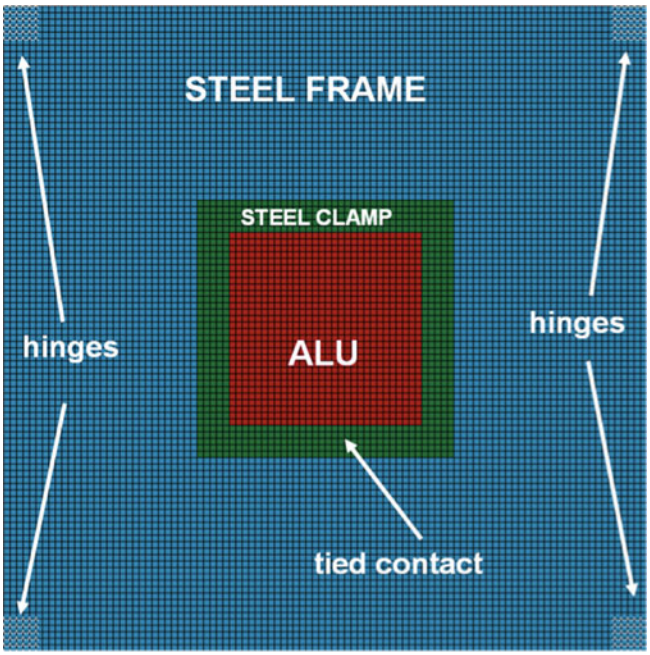

Fig. 39.2 Finite element model (color figure in online)

39.4 Comparison Results

Three identical blast load tests of 40 g C4 with a stand-off-distance of 250 mm are performed as explained in Section "Experimental set up". The comparison of the plate's center point resultant displacements between the experiments and the numerical simulation is shown in Fig. 39.3. The calculated displacement curves follow the experimental displacement curves having a maximum plastic deformation in the first peak, followed by elastic deformations and damping. In the numerical calculations no damping is used. The differences between the three experiments are not negligible (maximum 15 %) although they are reasonable.

Figures 39.4 and 39.5 provide the comparison of the plate surface displacement fields during the explosion at different time steps (from 0.17 to 1.00 ms). The major component is the out-of-plane displacement. Notice the shape of the deformation, which is approximating a rectangular shape in the first 0.5 ms and evolves into a sinusoidal shape after 0.67 ms. After detonation, the pressure wave travels through the air and arrives at the clamped plate, creating a transient distributed load. Initially at 0.17 ms, the reflected pressures are maximum but highly localized at the plate's center point. After 0.17 ms, the reflected pressures decrease rapidly in amplitude (exponential decay) but expand over the whole plate's surface. When the plate is fully loaded over its surface, e.g. at time 0.21 ms, the maximum pressures occur at the plate's boundaries and not in the middle as one would intuitively expect. Detailed pressures profiles are available in [10]. At 0.33 ms, the reflected pressures are reduced to the ambient pressure. The blast impulse hence imparts momentum to the aluminum plate during a very short loading period, from 0 to 0.33 ms. This momentum is large enough to continuously deform the plate after termination of the loading from the shock wave. During the blast impulse all points are forced to move out-of-plane, while points close the boundaries are blocked, resulting in an initial rectangular shape of deformation. When the pressures from the blast load have vanished (i.e. the plate is unloaded), the plate continuous to deform. At 0.33 ms every particle of the plate has a given velocity. From this moment on the plate is starting to act as a free vibration system with initial velocities. Only the inertia forces of the plate's mass cause the plate to deform further. This explains why the rectangular shape of deformation evolves towards a sinusoidal shape, just as the first bending modal mode shape of the plate.

From Figs. 39.3, 39.4 and 39.5 it's clear that the numerical simulation is in a good agreement with the experimental obtained results, providing both a sufficient prediction of the deformation history and distribution along the plate's surface.

39.5 Inverse Modeling

In order to numerically simulate mechanical behavior of materials with sufficient accuracy and computational efficiency, it is necessary to develop appropriate constitutive models. All such models contain a number of material parameters which are to be determined from some kind of experiments with material specimens. Inverse methods are increasingly applied for

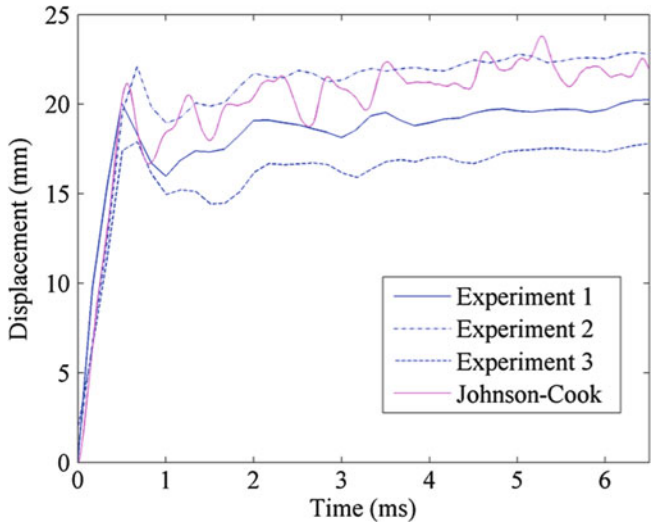

Fig. 39.3 Resultant displacement history

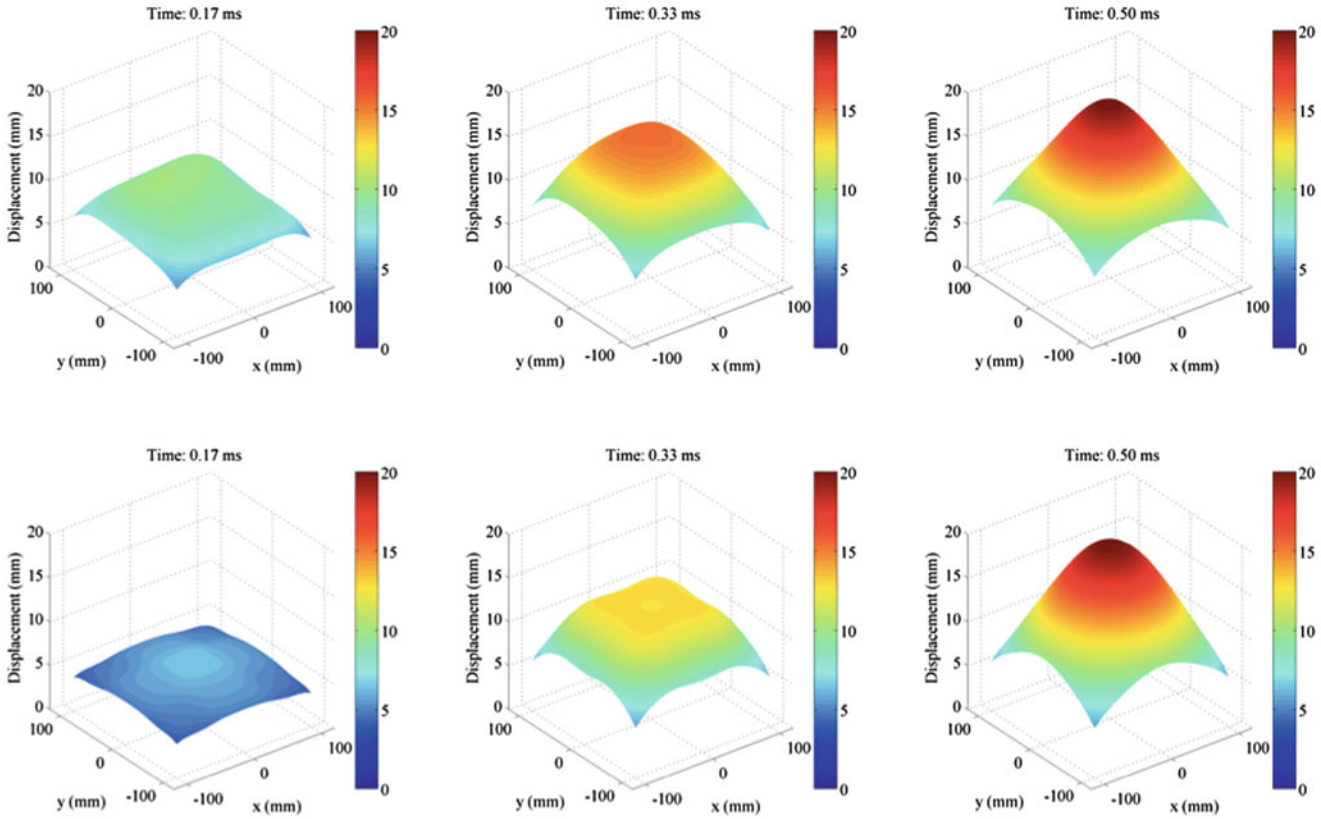

Fig. 39.4 Comparison resultant displacement fields from 0.17 to 0.5 ms (Experimental data: 1st row; numerical data: 2nd row)

the identification of unknown parameters in numerical models. The general idea is to compare the results of an experimental observation with simulated data. Tuning of the parameters until the numerical observations match the experimental observations leads to the identification of the parameters.

Optimization problems are concerned with the minimization (or maximization) of cost functions for which the input data is given by the desired responses of the system. Inverse problems on the other hand make use of measured responses, which are unavoidably corrupted by measurement noise. This implies that it can only be tried to approximate those measured responses as good as possible by a selected model of the system. This objective is often attained by minimizing the sum of

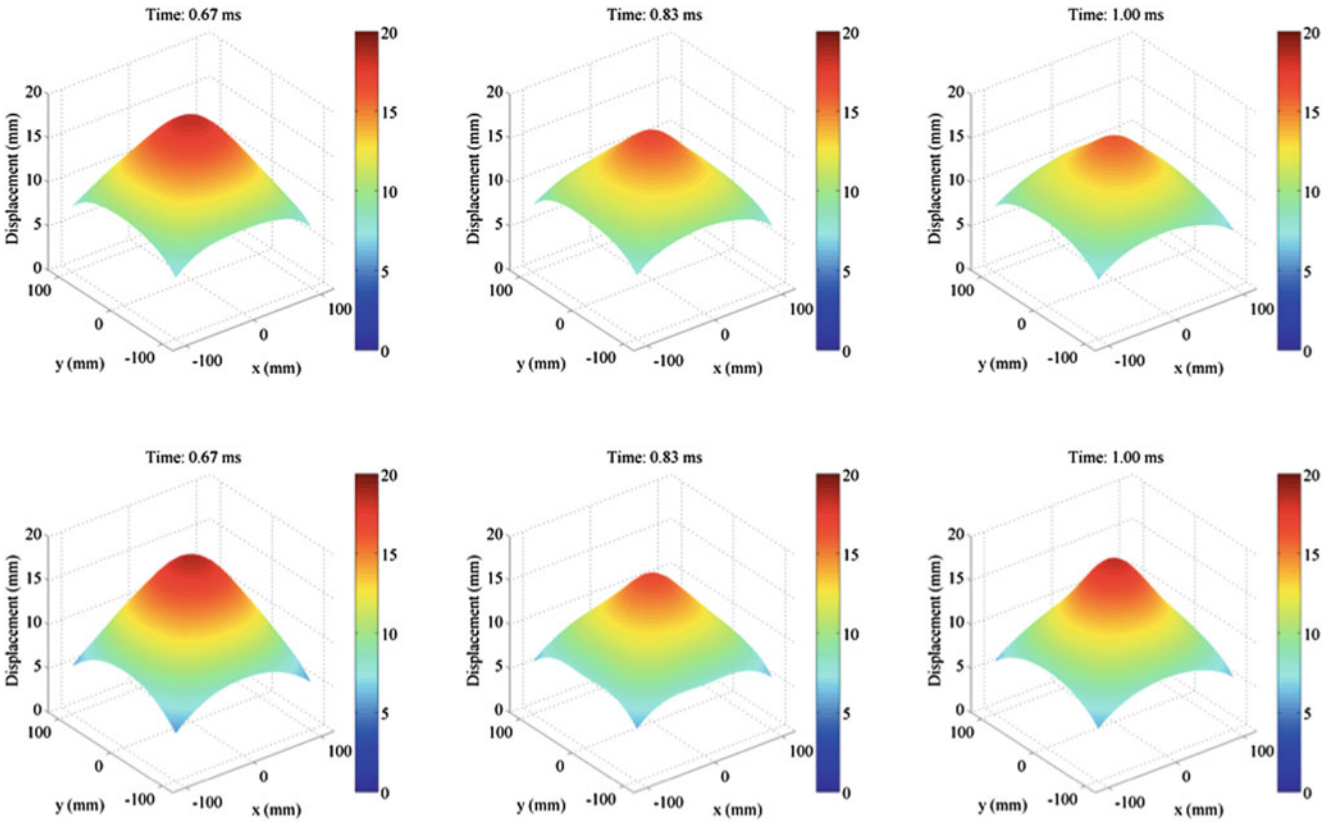

Fig. 39.5 Comparison resultant displacement fields from 0.6 7 to 1.0 ms (Experimental data: 1st row; numerical data: 2nd row)

squared differences between the calculated and measured responses, i.e. by considering a least squares cost function. The latter approach is frequently used in various engineering domains and numerous articles can be found in literature [18], dealing with the minimization of least squares cost functions.

In this paper a Levenberg-Marquardt algorithm (i.e. a gradient-based optimization technique) is applied to minimize the non-linear least squares problem. The ordinary least squares norm is used. The objective function can then be formulated as follows:

$$f(x) = \frac{1}{2}\sum_{i=1}^{n}\left(r_i^{\exp} - r_i^{num}(x)\right)^2 \tag{39.3}$$

where i is the index representing the number of positions in which a response is measured, r_{exp} is the column vector of the n measured responses and $r_{num}(x)$ the column vector of the solution to the direct problem using a given set of m optimization variables $x = (x_1,\ldots,x_m)$. The convergence criterion is based on the step size tolerance, which relates to the size of the last step, meaning the size of the change in location where the objective function was evaluated. For the results presented in this paper the tolerance set on 0.1 %. The sensitivities are calculated as forward finite differences:

$$S_{x_1} = \frac{r_{num}(x_1 + dx_1, x_i) - r_{num}(x_1, x_i)}{dx_1} \tag{39.4}$$

with S_{x1} is the sensitivity column of parameter x_1 , dx_1 the finite difference of parameter x_1 and $r_{num}(x)$ the response of the solution to the direct problem using a given set of parameters. The sizes of the finite differences are investigated by evaluating the conditioning number of the sensitivity matrix. This number should be as close as possible to 1 to obtain a fast and stable convergence. More details on this method can be found in [18].

The in-plane strains ε_{xx} and ε_{yy} in the area of interest are representing the measured responses. As presented in Fig. 39.3, plasticity in occurring in the beginning of the response. Therefore, only experimental data between 0 ms and 1 ms are taking

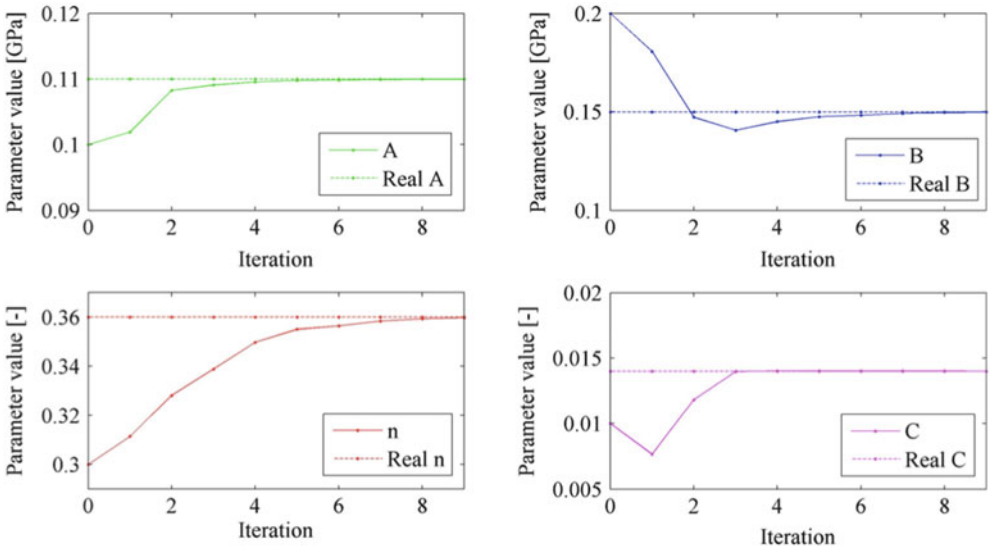

Fig. 39.6 Material parameter identification using a virtual experiment (*solid line*: parameter value, *dashed line*: 'real' value)

into account during optimization. To validate the algorithm, a virtual experiment is used to represent the experimentally obtained responses. As benchmark, the following set of Johnson-Cook parameters is used: $A = 110$ MPa, $B = 150$ MPa, $C = 0.014$, $n = 0.360$ and $m = 1.0$.

During optimization four material parameter are identified starting with initial parameter values $A = 100$ MPa, $B = 200$ MPa, $C = 0.010$ and $n = 0.300$. These four parameters describe the effect of strain and strain rate hardening. Numerical simulations showed that in this case thermal effects are negligible. Therefore, effects of thermal softening are not included in the optimization.

Figure 39.6 illustrates the convergence path of the four elasto-plastic material parameters. The plots show that convergence for all parameters is obtained after nine iterations. For each step in the iterative process, five successive FE-simulations are necessary: one simulation with the current set of parameters and an additional simulation for every unknown parameter to calculate the sensitivities. Accordingly, a total of 45 simulations are needed to attain convergence for all parameters.

39.6 Conclusions

Results show that a free air blast load induces a highly localized, rapid material response and that a 3D high-speed DIC system is a powerful tool that is capable of accurately measuring surface displacement and deformation data at high rates. Using a well-known relationship, the material response is simulated with the finite element method, which gives comparable results with the experimental data from the 3D-DIC.

Furthermore, a free air blast load makes it possible to load a plate specimen at different strain rates in different zones. This makes the test suitable for future material identification using inverse methods, which profit from heterogeneous displacement and strain fields. A mixed experimental-numerical method is proposed to determine the elasto-plastic material parameters during a free air blast event. This method is validated using a virtual experiment.

References

1. Bulson PS (1997) Explosive loading of engineering structures: a history of research and review of recent developments. E&FN SPON, London, p 236
2. Yandzio E, Gough M (1999) Protection of buildings against explosions. Steel Construction Institute, Ascot, p 110
3. Bangash MYH, Bangash T (2006) Explosion-resistant buildings: design, analysis, and case studies. Springer, New York, p 784
4. Jones N (1989) Structural impact. Cambridge University Press, Cambridge, UK, p 575
5. Teeling-Smith RG, Nurick GN (1991) The deformation and tearing of thin circular plates subjected to impulsive loads. Int J Impact Eng 11:77–91
6. Nurick GN, Shave GC (1996) The deformation and tearing of thin square plates subjected to impulsive loads - an experimental study. Int J Impact Eng 18–1:99–116
7. Olson MD, Nurick GN, Fagnan JR (1993) Deformation and rupture of blast loaded square plates - predictions and experiments. Int J Impact Eng 13–2:279–291
8. Neuberger A, Peles S, Rittel D (2007) Scaling the response of circular plates subjected to large and close-range spherical explosions. Part I: Air-blast loading. Int J Impact Eng 34:859–873
9. Neuberger A, Peles S, Rittel D (2007) Scaling the response of circular plates subjected to large and close-range spherical explosions. Part II: Buried charges. Int J Impact Eng 34:874–882
10. Spranghers K, Vasilakos I, Lecompte D, Sol H, Vantomme J (2012) Full-field deformation measurements of aluminum plates under free air blast loading. Exp Mech 52:1371–1384. doi:10.1007/s11340-012-9593-5
11. Sutton MA, Orteu J-J, Schreier HW (2009) Image correlation of shape, motion and deformation measurements: basic concepts, theory and applications. Springer, New York, p 321
12. Tiwari V, Sutton MA, McNeill SR, Xu S, Deng X, Fourney WL, Bretall D (2009) Application of 3D image correlation for full-field transient plate deformation measurements during blast loading. Int J Impact Eng 36:862–874
13. Kingery CN, Bulmash G (1984) Airblast parameters from TNT spherical air burst and hemispherical surface burst. Report ARBL-TR-02555, U.S. Army Ballistic Research Laboratory, USA
14. U.S. Department of the Army (1986) Fundamentals of protective design for conventional weapons, Department of the Army Technical Manual, USA
15. Randers-Pehrson G, Bannister KA (1997) Airblast loading model for DYNA2D and DYNA3D. Report ARBL-TR-1310, U.S. Army Ballistic Research Laboratory, USA
16. Livermore Software technology Corporation (1999) LS-DYNA user's manual: nonlinear dynamic analysis of structures (Version 950), USA, p. 1024
17. Christoulis DK, Guetta S, Guipont V, Jeandin M (2011) The influence of the substrate on the deposition of cold-sprayed titanium: an experimental and numerical study. J Therm Spray Technol 20(3):523–533
18. Lecompte D (2007) Elastic and elasto-plastic material parameter identification by inverse modeling of static tests using digital image correlation. Vrije Universiteit Brussel, Belgium, p 269

Chapter 40
Implosion of a Tube Within a Closed Tube: Experiments and Computational Simulations

Sachin Gupta, James M. LeBlanc, and Arun Shukla

Abstract A comprehensive series of experiments were conducted to study the mechanics of an implosion of a tube occurring within a closed tube. The outer tube has an inner diameter of 0.178 m (7″), a length of 1.82 m (72″), and a maximum hydrostatic pressure of 10.3 MPa (1,500 psi). The implodable volumes consist of aluminum 6061-T6 cylindrical tubing and were placed concentrically within the outer tube and equidistant from the two ends. The effect of the length to diameter (L/d) ratio on the mechanics of the implosion was investigated by varying the outer diameter of the implodable volume while holding the length constant, 0.304 mm (12″). The L/d ratios of 3, 4, 6, and 8 were utilized. The wall thicknesses of the tubes were chosen so as to obtain approximately constant collapse initiation pressures in all of the experiments. The pressure histories generated by the implosion event were captured by dynamic pressure transducers mounted on the inner surface of the outer tube. Computational models of the implosion experiments are currently being developed using the Dynamic System Mechanics Analysis Simulation (DYSMAS) software package. The computational results will be provided in the presentation.

Keywords Implosion • Buckling • Collapse shape • Pressure vessel • Cavitation

40.1 Introduction

The objective of this study was to investigate the mechanics of an implosion of cylindrical tubes occurring within a closed outer tube. A cylindrical pressure vessel designed to a 10.3 MPa (1,500 psi) hydrostatic working pressure was used as the outer tube in which aluminum 6061-T6 implodable volumes were collapsed. The pressure waves generated during the implosion experiments were captured by dynamic pressure transducers mounted on the inner wall of the outer tube.

Recently there has been an increased interest in the pressure waves generated from the implosion of volumes, particularly when the implodable volume is located near an adjacent structure. When a volume is submerged in the high pressure water environment, the pressure differential can cause structure instability. The loss of structure stability results into the collapse of the structure and during this collapse process, a certain amount of energy is released into the surrounding fluid. This energy is generally equal to the product of critical (collapse) pressure and internal volume of the air inside (P_cV). This released energy produces pressure waves in the surrounding environment that can potentially damage the nearby structures. An example of this effect is Super-Kamiokande experiment, where approximately 6,000 photomultiplier tubes were imploded in a chain reaction [1, 2]. In this accident, the implosion of one of the tubes generated pressure waves, which triggered the implosion process in the other tubes.

S. Gupta (✉) • A. Shukla
Dynamics Photomechanics Laboratory, Department of Mechanical, Industrial and Systems Engineering,
University of Rhode Island, Kingston, RI 02881, USA
e-mail: gupsac@gmail.com

J.M. LeBlanc
Naval Undersea Warfare Center (Division Newport), Newport, RI 02841, USA

B. Song et al. (eds.), *Dynamic Behavior of Materials, Volume 1: Proceedings of the 2013 Annual Conference on Experimental and Applied Mechanics*, Conference Proceedings of the Society for Experimental Mechanics Series,
DOI 10.1007/978-3-319-00771-7_40,

There have been some studies reported in the literature involving the pressure waves generated during the implosion process. Turner [3] conducted experiments with thin-wall glass spheres to determine the influence of failure mechanisms on pressure waves. He concluded that the computational model of an underwater implosion event must include the structure that separates the low pressure air from the high pressure water. If the structure is neglected, the model will over predict the peak pressure. Later, Turner and Ambrico [4] conducted near-field pressure wave measurements from an imploding cylinder and used a fluid–structure interaction finite-element methodology to predict the dynamic pressure history and the collapse mechanics during implosion. Ikeda [5] studied the implosion of aluminum cylindrical shell structures in a high-pressure water environment. It was reported that the pressure time history at a certain distance scales well with time and pressure scales from cavitation bubble collapse theory. Ikeda [6] also studied the explosion induced implosion of cylindrical shell structures in high-pressure environments. It was found in the study that the implosion is induced by two mechanisms: the shockwave generated by the explosion and the jet formed during the explosion-bubble collapse. There is limited literature available itself on the implosion of structures in free-field and, to the best of the authors' knowledge, no studies have been reported on the collapse of a tube within a closed environment. This study will investigate the implosion of a tube occurring within a confining tube (a closed environment). Unlike the free-field implosion experiments where the hydrostatic pressure is maintained in the surrounding environment during the collapse process, these experiments were conducted with implodable volumes inside a constant volume of pressurized water.

40.2 Specimen Details

Implodable volumes used in this study were made out of aluminum 6061-T6 cylindrical tubing. After cutting to the desired length of the tube, the ends of the implodable volume were sealed on both ends using caps. End-caps were made out of same material, aluminum 6061-T6, and circumferential o-rings were used to ensure proper sealing at the ends. Table 40.1 shows a layout of experiments conducted during this study. The length of the four implodables was held constant (304.8 mm) and the diameters were increased from 38.1 mm (1.5″) to 101.6 mm (4.0″). The wall thickness was also increased along with the diameter to keep the critical collapse pressure approximately constant. A three-spoke fixture was utilized to hold the implodable volumes concentrically within the outer tube. A schematic of the fixture with the specimen is shown in Fig. 40.1.

Table 40.1 Layout of the experiments

Geometry no.	Wall thickness	Outer diameter	L/D ratio	Collapse pressure MPa (psi)
1	0.89 mm (0.035″)	38.1 mm (1.5″)	8	325 psi
2	1.24 mm (0.049″)	50.8 mm (2.0″)	6	515 psi
3	1.65 mm (0.065″)	76.2 mm (3.0″)	4	510 psi
4	1.65 mm (0.065″)	101.6 mm (4.0″)	3	370 psi

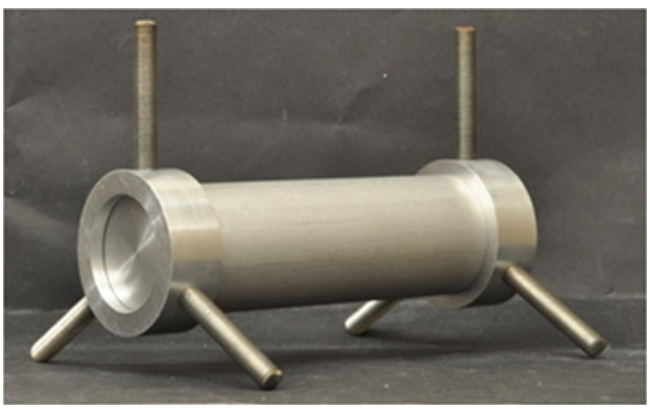

Fig. 40.1 Three-spoke fixture for implodable volume

40.3 Experimental Setup

40.3.1 Outer Tube

A pressure vessel facility with a maximum allowable hydrostatic pressure of 10.3 MPa (1,500 psi) was fabricated for performing tube-in-tube experiments. A schematic diagram of the pressure vessel can be seen in Fig. 40.2. The pressure vessel (outer tube) has an inner diameter of 0.178 m (7.0″), outer diameter of 0.215 m (8.5″) and a length of 1.82 m (72″). The material chosen for the outer tube was SA 106 grade-B carbon steel, which satisfies ASME pressure vessel code. The vessel was mounted horizontally on an I-beam section as shown in Fig. 40.2.

The outer tube contains eight dynamic pressure transducers to capture the pressure histories during the implosion event. These pressure transducers were flush-mounted to the inner wall of the pressure vessel to capture the pressure histories without disturbing wave propagation inside water. Six pressure transducers were placed on the wall of the vessel with 0.304 m (12″) interspacing and two transducers were placed on the end caps. Two static pressure transducers (electronic and dial gage) were also placed on the end caps of the vessel to monitor the hydrostatic pressure inside the vessel during experiments.

40.3.2 Vessel Pressurization

After placing the implodable volumes at the desired location (axially centered and concentric), the vessel was closed and pressurized by an electric hydrostatic test pump. The pressurization rate was kept relatively slow (~1 MPa/min) in order to minimize the dynamic pressurization effects. As the implosion of the specimen occurs, a small noise is generated along with a rapid pressure drop in the hydrostatic pressure inside vessel. At this point, the data acquisition system was triggered, which stored the data 10 s before the trigger point.

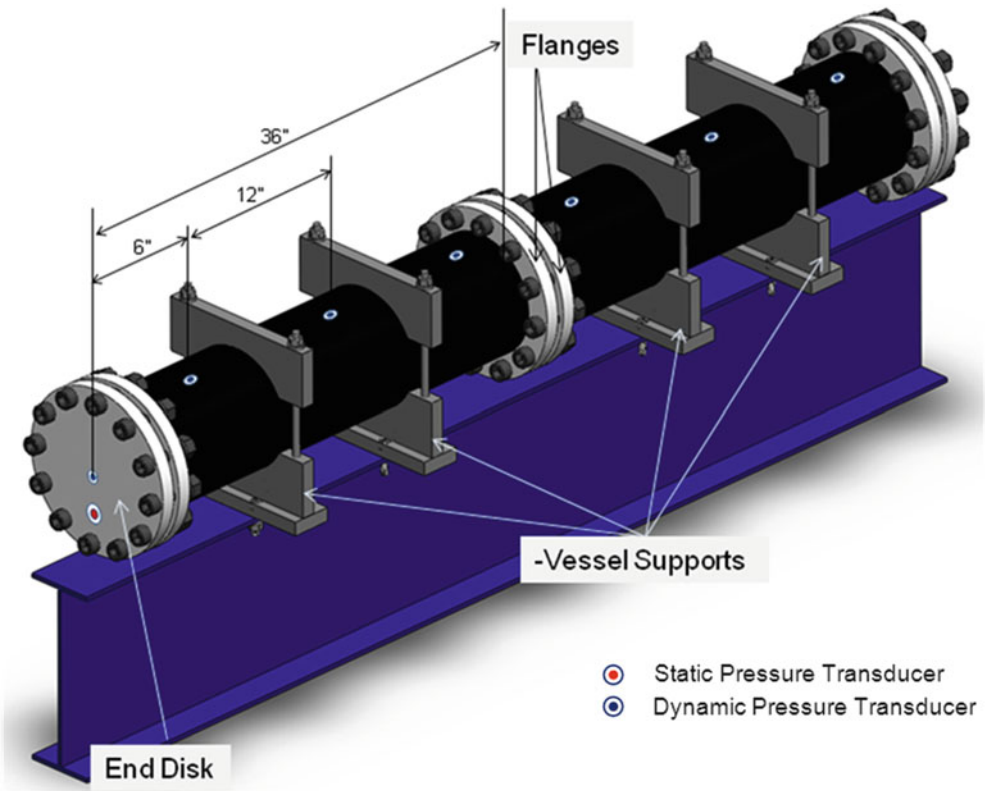

Fig. 40.2 Implosion tube-in-tube experimental setup

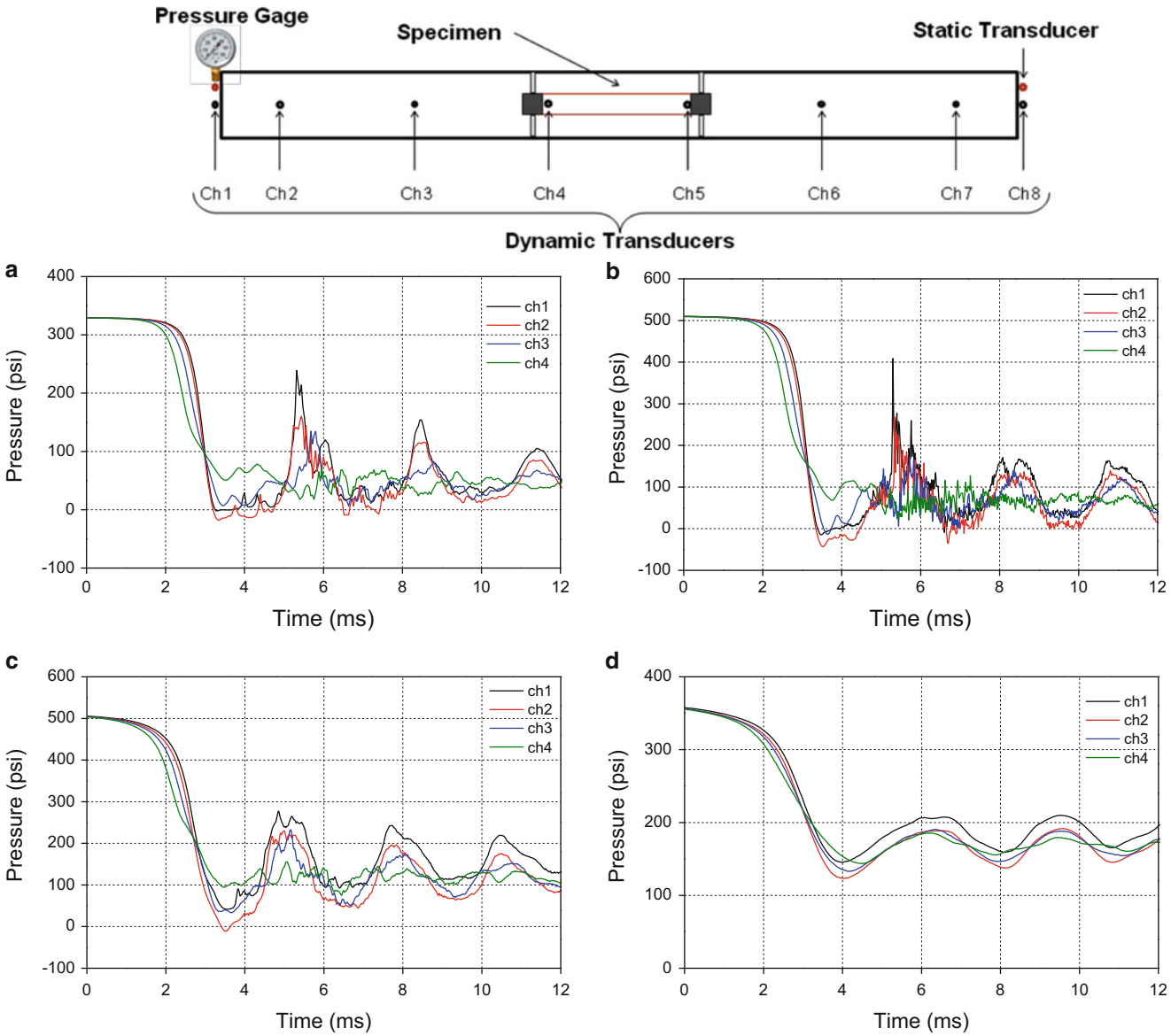

Fig. 40.3 Pressure histories for different geometries. (**a**) 38.1 mm OD (**b**) 50.8mm OD (**c**) 76.2 mm OD (**d**) 101.6 mm OD

40.3.3 Experimental Results

The pressure histories generated during the collapse are shown in Fig. 40.3. The qualitative behavior of the dynamic pressure histories observed in all the geometries is very similar. The full pressure history consists of three significant regions: I) Decrease in the pressure caused by inward motion of the walls of the cylinders corresponding to the onset of the collapse. II) A flat region of zero pressure, as the specimen continues to collapse inwards. III) A positive pressure peak resulting from the walls of the implodable volume coming to rest and the energy of the inward flow of water being converted into a pressure wave. This transformation of kinetic energy results in the generation of a pressure wave in the surrounding, which then travels in the outer tube causing high pressure peaks at the end disks.

In the case of implodable volume with 38.1 mm and 50.8 mm outer diameter (OD), all the regions can be clearly seen in Fig. 40.3a, b. The pressure in region I dropped to almost zero or even negative pressure at the ch1, which indicated the possibility of cavitation around the end-caps. Region II was observed to be approximately 2 ms for 38.1 mm OD specimen and 1 ms for 50.8 mm OD specimen. Followed by region II, a pressure peak of 1.65 MPa (240 psi) and 2.87 MPa (410 psi) was observed for 38.1 mm OD and 50.8 mm OD respectively. After this point, the pressure history generated was oscillatory in nature with decaying magnitude and the time period was found to be 3.1 ms for 38.1 mm OD and 2.8 ms for 50.8 mm OD.

For the case of 76.2 mm OD and 101.6 mm OD, the pressure profiles observed had a small deviation from the other two geometries (see Fig. 40.3c, d). The pressure drops to approximately 0–0.7 MPa (0–100 psi) in region I for 76.2 mm OD, but region II was absent in this case. The pressure switched to region III, which showed a time period of approximately 2.7 ms. For 101.6 mm OD, the pressure drop in region I was relatively small and the lowest pressure observed in this case was 0.85 MPa (125 psi). Similar to 76.2 mm OD, it didn't exhibit region II and very low amplitude pressure waves were seen later in the pressure history.

References

1. http://www-sk.icrr.u-tokyo.ac.jp/cause-committee/1st/report-nov22e.pdf
2. Diwan M, Dolph J, Ling J, Russo T, Sharma R, Sexton K, Simos N, Stewart J, Tanaka H, Arnold D, Tabor P, Turner S (2012) Underwater implosions of large format photo-multiplier tubes. Nucl Instrum Methods Phys Res Sect A Accel Spectrom Detect Assoc Equip 670:61–67, doi:http://dx.doi.org/10.1016/j.nima.2011.12.033
3. Turner SE (2007) Underwater implosion of glass spheres. J Acoust Soc Am 121(2):844–852
4. Turner SE, Ambrico JM (2012) Underwater implosion of cylindrical metal tubes. J Appl Mech 80(1):011013–011013. doi:10.1115/1.4006944
5. Ikeda CM, Wilkerling J, Duncan JH (2009) An experimental investigation of the implosion of cylindrical shell structures. Paper presented at the 62nd annual meeting of the APS division of fluid dynamics Minneapolis, Minnesota, 23 Nov
6. Ikeda CM (2012) Fluid–structure interactions: implosions of shell structures and wave impact on a flat plate. University of Maryland, College Park

Chapter 41
Testing Techniques for Shock Accelerometers below 10,000 g

Waterloo Tsutsui, Nithin Raghunathan, Weinong Chen, and Dimitrios Peroulis

Abstract Research in the fields of impact science and penetration mechanics is often focused on the acceleration of projectiles during launch and penetration. In recent studies, various researchers have started using the Hopkinson bar to evaluate the performance of shock accelerometers for 10,000–100,000 g (1 g = 9.81 m/s^2) accelerations. However, very little work has focused on shock environments below 10,000 g using the Hopkinson bar setup, although it has been reported that there may exist the peak amplitudes of sub 10,000 g acceleration during the penetration of concrete targets. Consequently, the presence of these acceleration levels in projectile penetration yields a definite need to create well-controlled accelerations below 10,000 g in a laboratory setting. In this study, two types of experimental techniques were investigated for accelerometer performance evaluation. The first was to modify the Hopkinson bar setup to test shock accelerometers with special attention to the acceleration level below 10,000 g. The second was to investigate a drop tower tester for the evaluation of shock accelerometers below 1,000 g.

Keywords Hopkinson bar • Drop tower tester • Shock testing • Accelerometer performance evaluation • MEMS impact experiment

41.1 Introduction

This is a report of novel testing techniques on shock accelerometers below 10,000 g (1 g = 9.81 m/s^2). The major milestone, since the first experimental research of the stress wave conducted by Herbert Hopkinson [1] and Bertram Hopkinson [2], was the establishment of the split-Hopkinson (Kolsky) bar testing technique by John Kolsky [3, 4]. The split-Hopkinson bar is widely regarded as the major experimental technique to understand the dynamic behavior of materials. One of the earliest cases of modified Hopkinson bar used for the accelerometer experiment was documented by Robert Sill [5]. Since then, various researchers have proposed the use of the modified Hopkinson bar techniques to perform experiment on the shock accelerometers for ballistic impacts [6–12]. At Purdue University, the investigation for the accelerometer testing techniques was conducted to verify the performance of the microcantilever-based microelectromechanical system (MEMS) g-switch accelerometers developed by Raghunathan et al. [13]. During the course of research, the need for the experimental techniques for the acceleration below 10,000 g became apparent. As a result, experimental techniques below 10,000 g were investigated.

W. Tsutsui (✉)
School of Aeronautics and Astronautics, Purdue University, West Lafayette, IN 47907, USA
e-mail: wtsutsui@purdue.edu

N. Raghunathan • D. Peroulis
School of Electrical and Computer Engineering, Purdue University, West Lafayette, IN 47907, USA
e-mail: nithin@purdue.edu; dperouli@purdue.edu

W. Chen (✉)
School of Aeronautics and Astronautics, Purdue University, West Lafayette, IN 47907, USA

School of Materials Engineering, Purdue University, West Lafayette, IN 47907, USA
e-mail: wchen@purdue.edu

B. Song et al. (eds.), *Dynamic Behavior of Materials, Volume 1: Proceedings of the 2013 Annual Conference on Experimental and Applied Mechanics*, Conference Proceedings of the Society for Experimental Mechanics Series,
DOI 10.1007/978-3-319-00771-7_41,

The first approach was to analyze the use of the existing Hopkinson bar setup, which is normally designed for high-g (above 10,000 g), for the low-g (below 10,000 g) application. This first approach is explained under "Dynamic experiments with the Hopkinson bar." The second approach was to use the drop tower tester to create acceleration below 1,000 g. Various researchers have investigated the drop tower tester for the analysis of the electromechanical device in general [14–18], whereas others investigated the use of drop tower specifically for the MEMS [19–21]. The second approach involved with the use of the drop tower tester is explained under "Dynamic experiments with the drop tower tester."

41.2 Dynamic Experiments with the Hopkinson Bar

The experimental setup for the modified Hopkinson bar is shown in Fig. 41.1. The material of the striker was steel with 19.05 mm diameter and 280 mm length. In addition to the steel striker, a synthetic polymer (polyamides, Nylon 6/6) with 19.05 mm diameter and 350 mm length was used during the research under low gas gun pressure. The incident bar is aluminum with 19.05 mm diameter and 3,657.6 mm length.

For the disc-flyer (Fig. 41.2), its mechanical impedance must be larger than the impedance of the incident bar according to Togami, Baker, and Forrestal [7]; therefore, tungsten was chosen as the material for the disk-flyer. The outside diameter (OD) of the disk-flyer is the same as the striker and incident bar, which is 19.05 mm. The length of both solid and hollow tungsten flyers (Fig. 41.3) is 19.05 mm. The solid tungsten disc-flyer (Fig. 41.3 left) has the accelerometer mounting holes on the non-incident-bar side of the disc. Four mounting holes will accommodate the maximum of two commercially-available accelerometers, specifically, Endevco 7270-series accelerometers and PCB 3991-series accelerometers. The Endevco 7270–60 K accelerometer was used during the experiment.

The hollow tungsten disc-flyer (Fig. 41.3 right) has both solid and hollow sections in the longitudinal direction. The hollow section has the 19.05 mm OD and inner diameter (ID) of 17.04 mm. The ID part has the longitudinal depth of 11.00 mm on the non-incident bar side. The rest of the part, which is 8.05 mm in longitudinal direction, is solid. The pocket with the depth of 11.0 mm accommodates the microcantilever-based MEMS g-switch accelerometer developed at Purdue University [13]. More specifically, the MEMS g-switch was placed inside the pocket and filled with Stycast 1090 SI epoxy to reduce unstable vibrations. To enable the use of the commercially-available accelerometers in addition to the

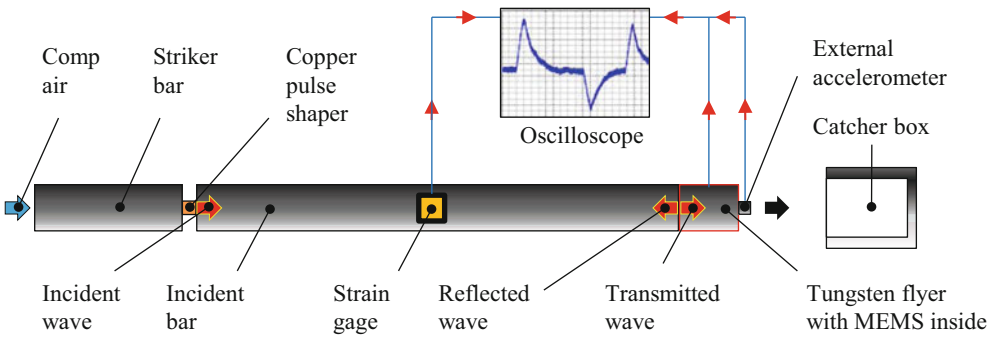

Fig. 41.1 Modified Hopkinson bar

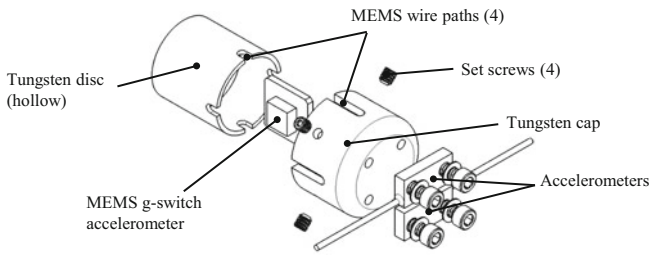

Fig. 41.2 Isometric exploded view of tungsten flyer

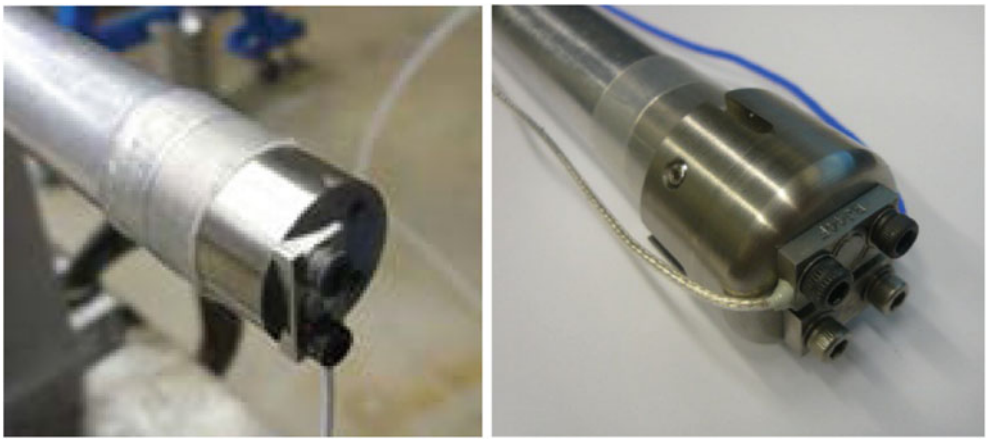

Fig. 41.3 Tungsten flyers

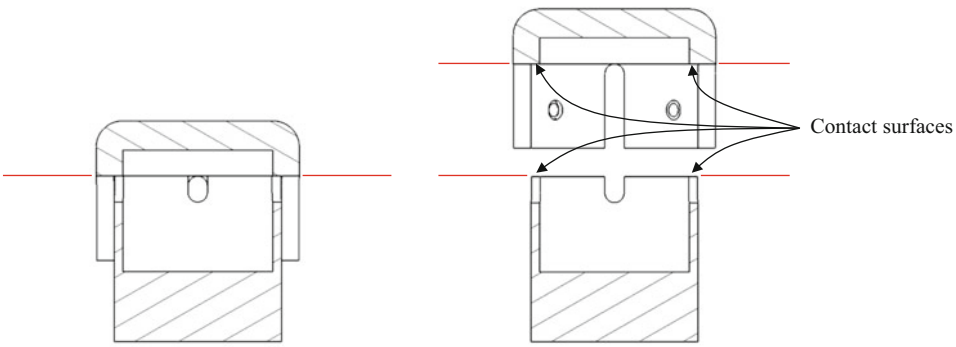

Fig. 41.4 Section views of tungsten flyer: Assembled (*left*) and exploded (*right*)

Purdue-developed MEMS g-switch accelerometer, the tungsten cap (Fig. 41.2) was designed and machined. This cap has the OD of 23.09 mm and length of 16.05 mm. It has the 3 mm radius on the outside surface that touches the bottom of the external accelerometers. This radius prevents the wire damage during the impact event. Although the tungsten cap is held onto the hollow tungsten cap radially by four set screws, the force during the impact experiment is transmitted normally from the hollow tungsten disc to the tungsten cap as shown in the section views in Fig. 41.4.

The experiment was conducted in the following sequence. First, the Endevco 7270–60 K accelerometer was mounted to the tungsten cap. Then, the high-g accelerations above 10,000 g were applied. These high-g accelerations are normally associated with the Hopkinson bar experiment. Then, the theoretical acceleration values were calculated from strain gage signal output. The calculation procedures for the theoretical acceleration based on the strain gage signal were discussed by Togami et al. [7], Forrestal et al. [9], and Foster et al. [11]. The theoretical acceleration values based on the strain gage signals were then compared against the acceleration signal from the Endevco 7270–60 K to make sure that experimental acceleration values conform to the theoretical values.

Next, the Endevco 7270–60 K accelerometer was removed from the cap and mounted to the solid tungsten disc for the experiment in acceleration below 10,000 g. The intention was to have less mass of the tungsten flyer, so that the low acceleration based on the low gas gun pressure could still separate the flyer from the incident bar. From here on, all the acceleration values were based on the theoretically calculated values from the strain gage. The gas gun pressure was reduced gradually until the striker does not come out from the gas gun barrel to reach the incident bar. During the process, it was observed that the steel striker does not move easily under low pressure from the gas gun. As a countermeasure, the polyamide (Nylon 6/6) striker was used, which moved much more easily inside the gas gun barrel at the low gas gun pressure. Finally, the acceleration values from the strain gage were plotted against the gas gun pressure to understand the limitation and characteristic of the low-g acceleration experiment using the Hopkinson bar.

41.3 Dynamic Experiments with the Drop Tower Tester

Instron Dynatup 9250 HV drop tower tester was used in the experiment (Fig. 41.5 right). The bottom portion of the drop mass carriage was modified to accommodate both the Endevco 7270-series accelerometers and MEMS g-switch accelerometers developed at Purdue University (Fig. 41.5 left). The different levels of acceleration values were obtained by dropping the mass from various heights. The drop height was accurately controlled by the Instron controller. The height is independent variable in this experiment. That is, the height in the drop tower tester has the equivalent role of the gas gun pressure in the Hopkinson bar.

Figures 41.6 and 41.7 show "Before" and "After" the impact event with the drop tower tester. During the impact, the bottom part of the carriage makes a contact with the two stoppers, which are mounted directly onto the base plate. As shown in Fig. 41.8, three different stopper materials were examined: Medium urethane, hard urethane, and aluminum alloy 2024. The medium urethane and hard urethane stoppers were commercially available replacement hammer faces manufactured by LIXIE. In the drop tower experiment, the Endevco 7270–2 K was used, whereas 7270–60 K was used in the Hopkinson bar

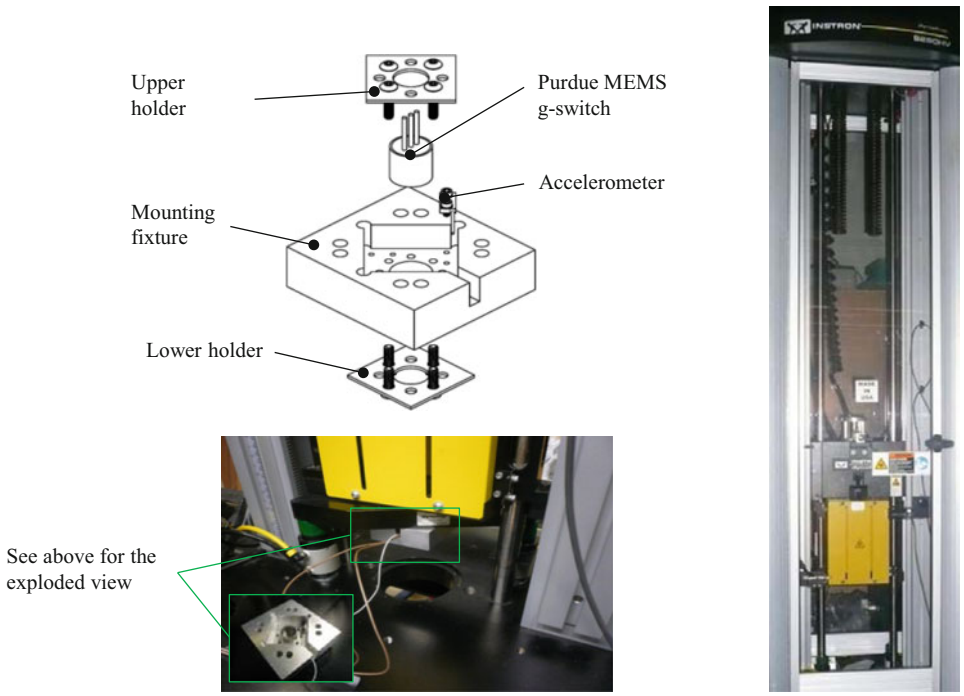

Fig. 41.5 Drop tower tester overview

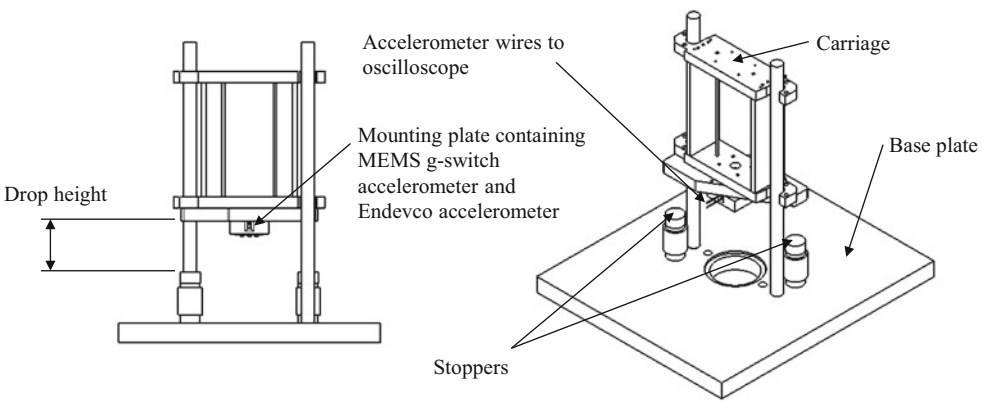

Fig. 41.6 Before drop – Front and isometric views of drop tower tester

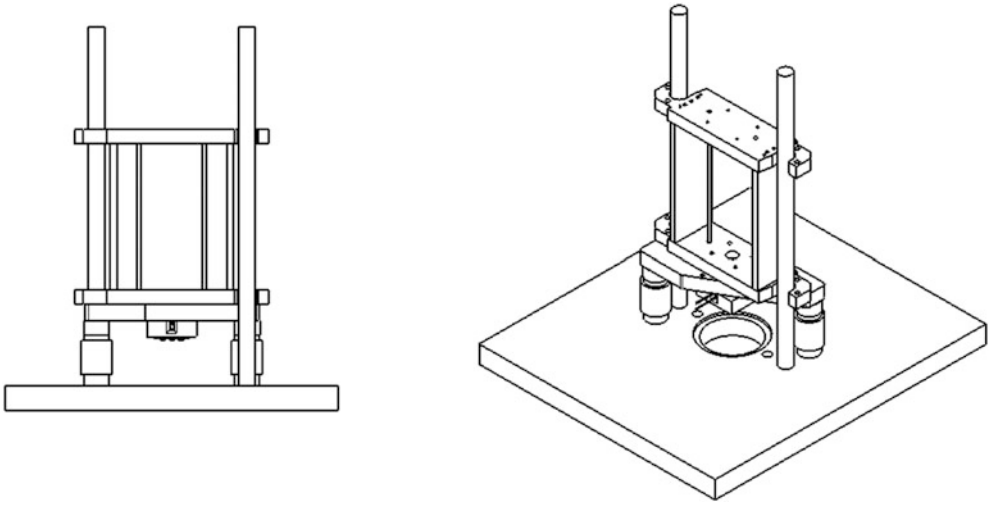

Fig. 41.7 After drop – Front and isometric views of drop tower tester

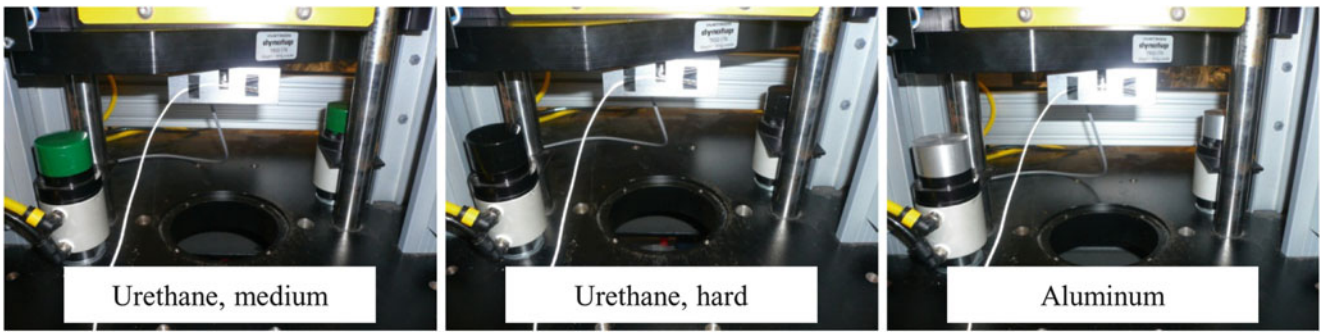

Fig. 41.8 Three different stoppers

experiment. The rated acceleration values for 7270–2 K and 7270–60 K are 2,000 and 60,000 g, respectively. The reason for the use of 7270–2 K was that the expected acceleration in the drop tower tester was much lower in the order of 10 g to several hundred g, rather than the higher acceleration observed during the Hopkinson bar experiment.

41.4 Results and Discussion

Figure 41.9 shows one of the Hopkinson bar experiment results comparing theoretical acceleration profile based on the strain gage signal to the experimentally obtained acceleration profile based on the Endevco accelerometer signal. In this particular case, the gas gun pressure of 40 psi (2.758 bar) was used to obtain the result. It is clear from Fig. 41.9 that the experimentally obtained acceleration profile conforms to the theoretical acceleration profile calculated based on the strain gage signal. In addition to the 40 psi (2.758 bar) gas gun pressure, various other gas gun pressure values, such as 48 psi (3.309 bar) and 53 psi (3.654 bar), were used to conduct the experiment. The trend was the same that all experimentally-obtained acceleration profiles conformed to the theoretically-calculated acceleration profiles similar to Fig. 41.9. With this result in hand, it was concluded that the acceleration profiles based on the Endevco accelerometer is the accurate representation of the acceleration-time history experienced by the MEMS device inside the tungsten flyer.

Figure 41.10 shows the final results of the Hopkinson bar experiment. Although the Hopkinson bar could be used to create the acceleration below 10,000 g, the experimental error becomes larger, especially in the case of steel striker in the very low gas gun pressure. For instance, at 5 psi (0.345 bar) and 10 psi (0.689 bar), the acceleration observed was approximately 3,000 g. However, at 15 psi (1.034 bar) and 20 psi (1.379 bar), the acceleration was about 9,000 g. That is, there was the

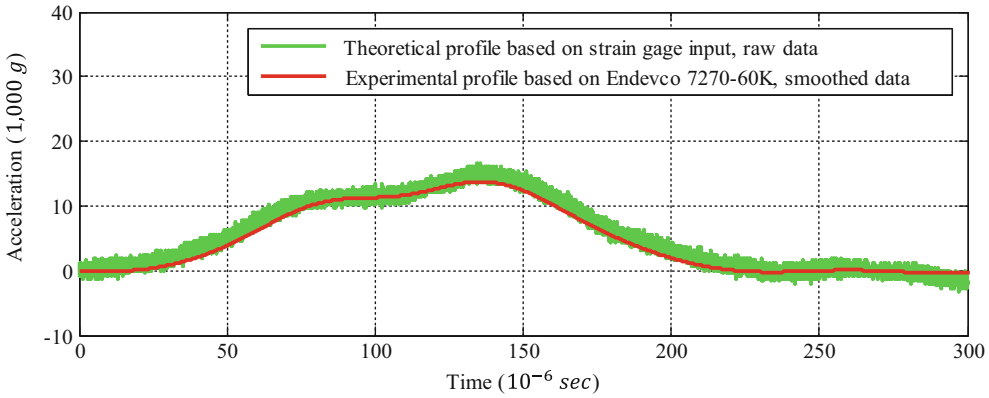

Fig. 41.9 Hopkinson bar: Theoretical acceleration profile based on strain gage signal vs. experimental profile based on Endevco 7270–60 K accelerometer

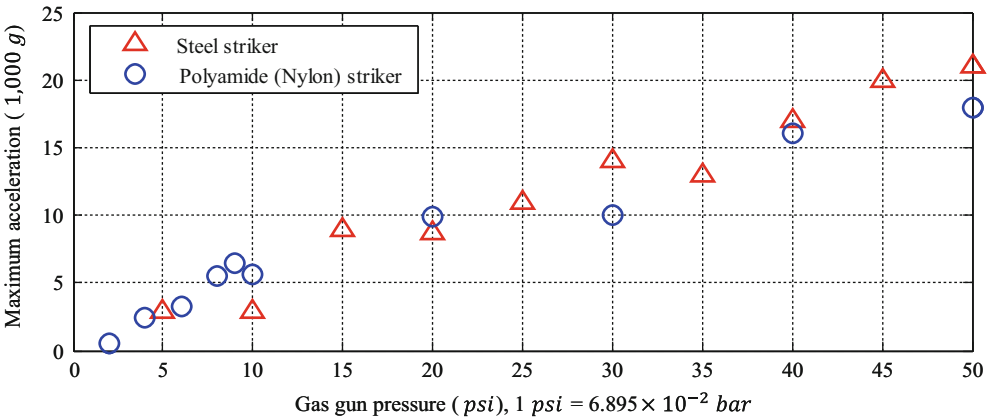

Fig. 41.10 Hopkinson bar: Experimental result

sudden jump of 6,000 g within the mere 5 psi (0.345 bar) difference in the gas gun pressure. In the polyamide (Nylon) striker, it was possible to use the gas gun pressure much lower than those used for the steel striker, which was based on the observation that the polyamide striker moves much more smoothly under the lower pressure than the steel striker due to the difference in weight. However, even the polyamide striker has the similar tendency. For instance, changing the gas gun pressure from 10 psi (0.689 bar) to 20 psi (1.379 bar) made the difference of about 5,000 g, whereas changing the gas gun pressure from 20 psi (1.379 bar) to 30 psi (2.068 bar) did not make any difference in the acceleration of tungsten flyer at the end of the incident bar.

In the Hopkinson bar experiment above, it was demonstrated that the experimental values from the Endevco accelerometer was the accurate representation of the theoretical acceleration values. This became the important information for the experiment in the drop tower tester because there was no strain gage that could be used to calculate the theoretical acceleration values in the drop tower tester. In the drop tower tester, the acceleration values were obtained directly from the Endevco 7270–2 K accelerometer. Figure 41.11 shows the typical acceleration profile obtained from the drop tower tester using the medium urethane stoppers. Since Endevco 7270–2 K was undamped accelerometer, the experimental result needed to be smoothed. Both the raw and smoothed results are shown in Fig. 41.11. The smoothed data shows the maximum acceleration of 100 g. The acceleration profile from Endevco 7270–2 K was combined with the output from the MEMS g-switch accelerometer. Figure 41.11 demonstrates that this particular MEMS g-switch accelerometer was triggered at about 75 g.

In the case of the aluminum stoppers, there was a possibility that the impact event caused certain vibration frequency that excited the resonance of undamped Endevco accelerometer. Figure 41.12 shows the acceleration signal from 10 cm drop using the aluminum stoppers. The raw signal shows the acceleration of more than 10,000 g, whereas the Endevco accelerometer being used was only rated up to 2,000 g. To cope with this situation, one potential approach is to use the damped accelerometer in order to minimize the effect of the resonance frequency upon impact.

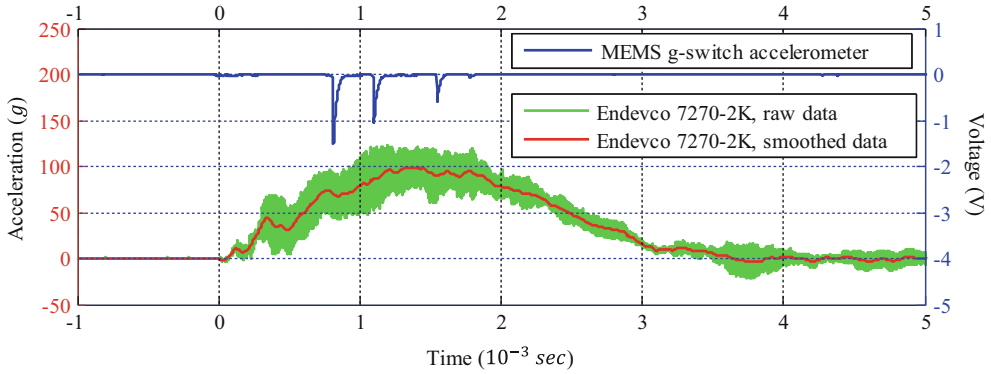

Fig. 41.11 Drop tower: MEMS g-switch triggered at 75 g

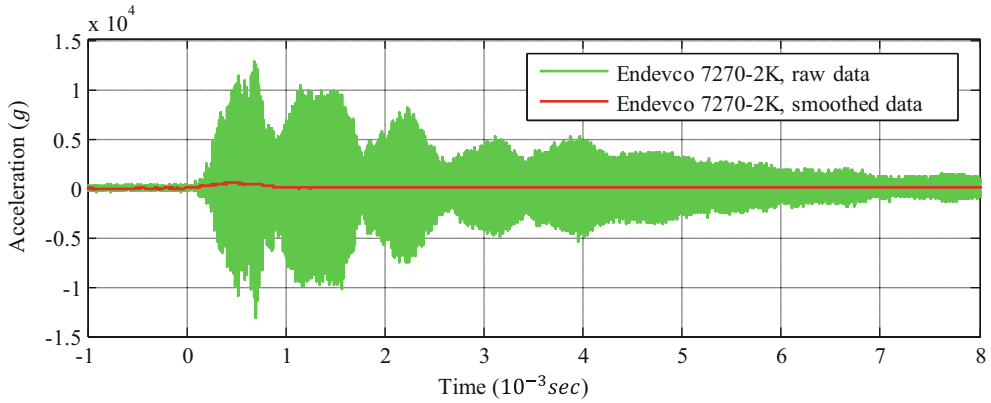

Fig. 41.12 Drop tower: Aluminum stopper, potentially exciting the resonant frequency of the undamped Endevco 7270–2 K accelerometer

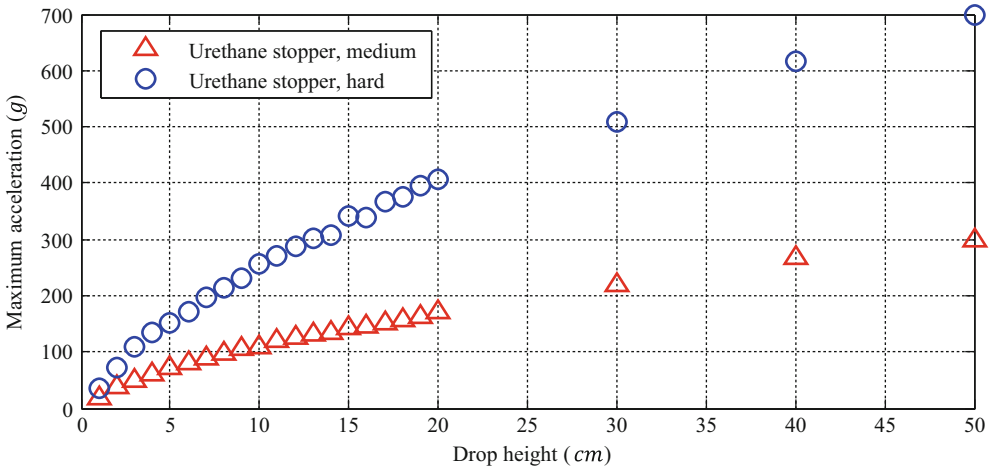

Fig. 41.13 Drop tower: Maximum acceleration versus drop height

Figure 41.13 shows the experimental results of the drop tower tester. Due to the above-mentioned reason, the experimental results for the aluminum stoppers have been excluded. The drop tower tester with the urethane stoppers created the repeatable and accurate accelerations in the controlled fashion. Unlike the Hopkinson bar experiment, small changes in the independent variable, i.e., drop height, made small and predictable changes in the resultant acceleration.

41.5 Conclusion

In order to verify the functionality of the MEMS g-switch accelerometer developed by Raghunathan et al. [13], the experimental technique for the acceleration below 10,000 g was investigated via two methods. The first method was the use of the Hopkinson bar setup. Based on the experimental result, the Hopkinson bar setup is not suitable for acceleration below 10,000 g because the Hopkinson bar setup did not result in the repeatable and accurate acceleration in the controlled fashion. The second approach was the use of drop tower tester. The drop tower tester resulted in the accurate acceleration in the controlled fashion because small change in the independent variable resulted in the predictable change in the resultant acceleration. However, the acceleration only reached about 700 g in the existing setup with the drop height of 50 cm. In order to increase the maximum acceleration values, the aluminum stoppers were used in the experiment. However due to the potential issues with the mechanical vibration resonance of Endevco accelerometer being excited during the impact event, it was not possible to observe the legitimate acceleration values above 700 g. In order to seek the solution to the situation, the future study should incorporate the use of the damped accelerometer to minimize the effect of the resonant frequency.

References

1. Hopkinson J (1872) On the rupture of an iron wire by a blow. Original papers by the late John Hopkinson, edited by Bertram Hopkinson, Cambridge University Press, pp 316–320, 1901. Originally published in proceedings of the Manchester Literary and Philosophical Society, XI, pp 40–45
2. Hopkinson B (1913–1914) The effects of the detonation of gun-cotton. The scientific papers of Bertram Hopkinson, collected and arranged by Sir J. Alfred Ewing and Sir Joseph Larmor, Cambridge University Press, pp 461–474, 1921. Originally published in proceedings of North-East Coast Institution of Engineers and Shipbuilders, XXX
3. Kolsky H (1949) An investigation of the mechanical properties of materials at very high rates of loading. Proc R Soc Lond B 62:676–700
4. Kolsky H (1963) Stress waves in solids. Dover, New York
5. Sill R (1984) Testing techniques involved with the development of high shock acceleration sensors. Endevco technical paper, TP284. San Juan Capistrano
6. Ueda K, Umeda A (1993) Characterization of shock accelerometers using Davies bar and strain gages. Exp Mech 33(3):228–233
7. Togami T, Baker W, Forrestal M (1996) A split Hopkinson bar technique to evaluate the performance of accelerometers. J Appl Mech 63(2):353–356
8. Togami T, Bateman V, Brown F (1997) Evaluation of a Hopkinson bar fly-away technique for high amplitude shock accelerometer calibration. In: Conference: 68, shock and vibration symposium, Baltimore
9. Forrestal M, Togami T, Baker W, Frew D (2003) Performance evaluation of accelerometers used for penetration experiments. Exp Mech 43(1):90–96
10. Frew D, Duong H (2009) A modified Hopkinson pressure bar experiment to evaluate a damped piezoresistive MEMS accelerometer. In: SEM proceedings, Albuquerque, New Mexico, USA, pp 1896–1903
11. Foster J, Frew D, Forrestal M, Nishida E, Chen W (2012) Shock testing accelerometers with a Hopkinson pressure bar. Int J Impact Eng 46:56–61
12. Chen W, Song B (2011) Split Hopkinson (Kolsky) bar. Springer, New York, pp 334–344
13. Raghunathan N, Nishida E, Fruehling A, Chen W, Peroulis D (2010) Arrays of silicon cantilevers for detecting high-g rapidly varying acceleration profiles. In: IEEE Sensors, Kona, Hawaii, USA, pp 1203–1206
14. Endevco (2009) Acceleration levels of dropped objects. Technical report, TP321. San Juan Capistrano
15. Tee T, Luan J, Pek E, Lim C, Zhong Z (2004) Novel numerical and experimental analysis of dynamic responses under board level drop test. In: 5th international conference on thermal and mechanical simulation and experiments in micro-electronics and micro-systems, EuroSim E2004, Brussels, Belgium, pp 133–140
16. Douglas S, Al-Bassyiouni M, Dasgupta A (2010) Simulation of drop testing at extremely high accelerations. 11th international conference on thermal, mechanical, and multiphysics simulation and experiments in micro-electronics and micro-systems, EuroSimE2010, Bordeaux, France, pp 1–7
17. Wong E (2005) Dynamics of board-level drop impact. J Elect Pack 127:200–207
18. Wong E, Mai Y (2006) New insights into board level drop impact. Microelectron Reliab 46:930–938
19. Li G, Shemansky F (2000) Drop test and analysis on micro-machined structures. Sensor Actuator 85:280–286
20. Seo S, Oh S, Han S (2011) Virtual drop test methodology for a MEMS-based sensor. Electron Mater Lett 7(2):109–113
21. Yang C, Zhang B, Chen D, Lin L (2010) Drop-shock dynamic analysis of MEMS/package system. In: 23rd international conference on micro electro mechanical systems (MEMS), IEEE, Hong Kong, China, pp 520–523

Chapter 42
ONR MURI Project on Soil Blast Modeling and Simulation

Richard Regueiro, Ronald Pak, John McCartney, Stein Sture, Beichuan Yan, Zheng Duan, Jenna Svoboda, WoongJu Mun, Oleg Vasilyev, Nurlybek Kasimov, Eric Brown-Dymkoski, Curt Hansen, Shaofan Li, Bo Ren, Khalid Alshibli, Andrew Druckrey, Hongbing Lu, Huiyang Luo, Rebecca Brannon, Carlos Bonifasi-Lista, Asghar Yarahmadi, Emad Ghodrati, and James Colovos

Abstract Current computational modeling methods for simulating blast and ejecta in soils resulting from the detonation of buried explosives rely heavily on continuum approaches such as Arbitrary Lagrangian-Eulerian (ALE) and pure Eulerian shock-physics techniques. These methods approximate the soil as a Lagrangian solid continuum when deforming (but not flowing) or an Eulerian non-Newtonian fluid continuum when deforming and flowing at high strain rates. These two extremes do not properly account for the transition from solid to fluid-like behavior and vice versa in soil, nor properly address advection of internal state variables and fabric tensors in the Eulerian approaches. To address these deficiencies on the modeling side, we are developing a multiscale multiphase hybrid Lagrangian particle-continuum computational approach, in conjunction with coordinated laboratory experiments for parameter calibration and model validation. This paper provides an overview of the research approach and current progress for this Office of Naval Research (ONR) Multidisciplinary University Research Initiative (MURI) project.

Keywords Soil blast • Constitutive modeling • Multiscale computational modeling • Buried soil explosive geotechnical centrifuge experiments • X-ray computed tomography • Quasi-static to high strain rate experimental soil mechanics

42.1 Introduction

The problem of simulating the detonation, ensuing blast wave and ejecta from buried explosives in natural soils remains unsolved because of the wide variability (and uncertainty) in field conditions, ranging from soil type (cohesive versus cohesionless), density, moisture content (partially saturated versus saturated), height of water table, infiltration due to rainfall or snowmelt, presence of roots and/or thick grasses, etc. These conditions will vary depending on whether the explosive is an improvised explosive device (IED) buried in a roadside soil (Fig. 42.1), or a network of landmines placed across a beach. Worst case scenarios of field conditions could be tested and simulated for the combat theater of interest, and proper armoring technologies deployed on vehicles to withstand those conditions, tailoring the armoring for a specific theater.

R. Regueiro (✉) • R. Pak • J. McCartney • S. Sture • B. Yan • Z. Duan • J. Svoboda • W. Mun
Department of Civil, Environmental, and Architectural Engineering, University of Colorado, Boulder, 428 UCB, Boulder, CO 80309, USA
e-mail: richard.regueiro@colorado.edu

O. Vasilyev • N. Kasimov • E. Brown-Dymkoski • C. Hansen
Department of Mechanical Engineering, University of Colorado Boulder, 428 UCB, Boulder, CO 80309, USA

S. Li • B. Ren
Department of Civil and Environmental Engineering, University of California, Berkeley, 783 Davis Hall, Berkeley, CA 94720-1710, USA

K. Alshibli • A. Druckrey
Department of Civil and Environmental Engineering, University of Tennessee, 73A Perkins Hall, Knoxville, TN 37996-2010, USA

H. Lu • H. Luo
Department of Mechanical Engineering, University of Texas, Dallas, 800 West Campbell Rd, Mailstop: EC-38, Richardson, TX 75080-03021, USA

R. Brannon • C. Bonifasi-Lista • A. Yarahmadi • E. Ghodrati • J. Colovos
Department of Mechanical Engineering, University of Utah, 50 South Central Campus Drive, Rm 2202, Salt Lake City, UT 84112-9208, USA

B. Song et al. (eds.), *Dynamic Behavior of Materials, Volume 1: Proceedings of the 2013 Annual Conference on Experimental and Applied Mechanics*, Conference Proceedings of the Society for Experimental Mechanics Series, DOI 10.1007/978-3-319-00771-7_42,

Fig. 42.1 Sequence of images from IED in Iraq hitting U.S. military convoy, demonstrating soil ejecta under asphalt pavement video.google.com

To address this problem, a research program is currently in place with the following main features: (i) integrated experimental mechanics and multiscale computational modeling; (ii) concurrent multiscale approach to simulating soil ejecta (i.e., open-window on pore-grain-scale representation of explosive region where ejecta forms, but with proper boundary conditions (BCs)); and (iii) hierarchical multiscale continuum constitutive modeling at high strain rates, pressures, and large deformations implemented in a multiphasic Lagrangian particle approach for shock wave and soil ejecta prediction. The overall research objective is to numerically predict (a) the propagation of blast waves in soil (accounting for physics at grain-to-application-blast length-and-time-scales); (b) explosive device fragment interaction with soil; and (c) the triphasic soil deformation, fracture, fragmentation and ejecta resulting from the detonation of a buried explosive device in various soil types (cohesive and cohesionless soils, dry to partially saturated and fully saturated) and in-situ material variations.

Soil is generally a triphasic porous medium, composed of a compressible solid (soil skeleton), liquid (usually water), and gas (usually air). For the solid and liquid constituents, a Lagrangian multiscale particle-continuum computational approach naturally provides the transition from solid-like to fluid-like material state upon blast loading, but keeping within a Lagrangian computational framework. The gas (i.e., air) constituent can most efficiently be modeled as a background Eulerian grid accounting for varying air temperature, pressure, humidity, etc., during blast wave propagation. The multiscale Lagrangian approach also more accurately resolves the interfacial mechanics between explosive fragments and soil ejecta resulting from the buried explosive device and ultimately impacting vehicles that need to be protected from such blasts. The main approach is to use a Lagrangian material particle description of the deforming/flowing biphasic (solid and liquid) soil around the initiation of buried explosion and fragmentation (Fig. 42.2), and around fragments as they eject through the soil along with the interacting soil masses. The finite element mesh would need to be adaptively converted to a 'particle' representation of the soil ahead of the blast wave and fragment path (Fig. 42.2), or a 'particle' representation is maintained in the path of the fragments and ejecta. In this particle region, sand grains are represented by discrete elements (DE) that can fracture under grain crushing, and cohesive soil clay matrix (providing cohesion between grains) is modeled using a meshfree 'particle' method with ability to fracture and fragment cohesive soil. The pore liquid can be incorporated directly into the variational meshfree particle formulation as a continuum mixture approximation, unless the soil is purely cohesionless (e.g., a sand) and modeled using DEs, whereby the pore liquid is modeled using another particle method like Smoothed Particle Hydrodynamics (SPH). The soil that behaves more solid-like outside the crater region will be modeled using a Lagrangian multiphase continuum constitutive model appropriate for large strains within a finite element framework, as a higher-order generalized continuum (triphasic micromorphic continuum) to properly account for large deformations and wave propagation (no artificial numerical wave reflections) at the transition from particle region to continuum FE region (Fig. 42.2). Farther away from the blast, the micromorphic continuum finite element model will transition to a viscoelastic dynamic boundary element method (BEM) formulation that allows the waves to propagate to

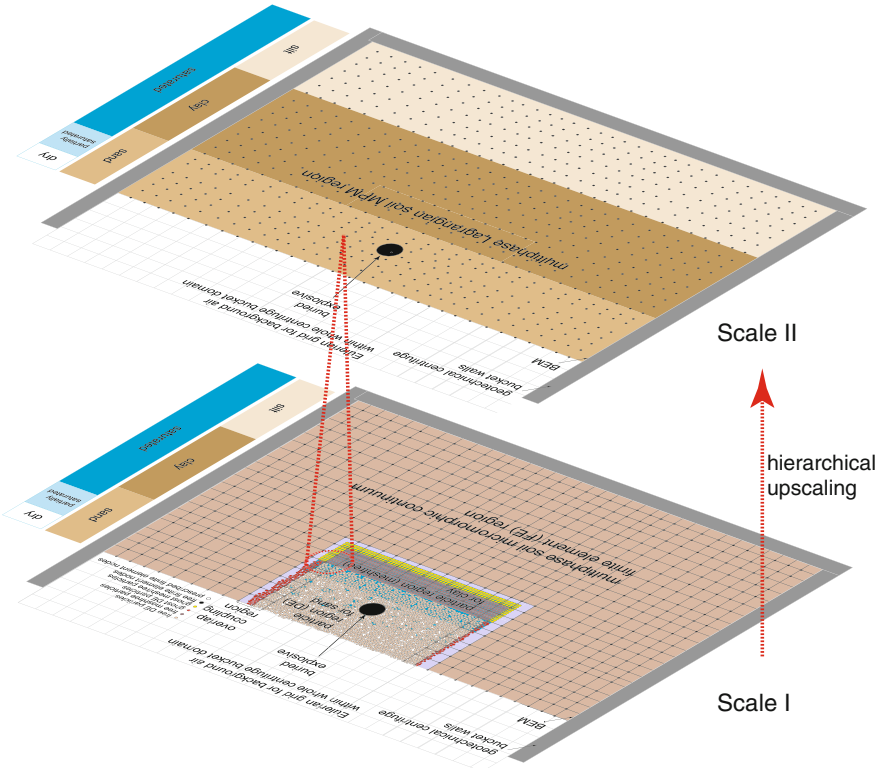

Fig. 42.2 2D illustrations (cross-sections through center of buried explosive) of 3D simulation setups for geotechnical centrifuge validation experiments (Fig. 42.7). Scale I: pore-grain-scale numerical modeling of soil with clay, silt/sand grains, and pore air and water. Scale II: hierarchical continuum constitutive model informed from Scale I; high-strain-rate, large deformation Uintah Material Point Method (MPM) implementation, and triphasic continuum formulation and implementation

infinity without wave reflection (or to represent boundary damping material used in the physical geotechnical centrifuge experiments) as well as other in-situ features such as layering and boulders.

To provide a physical validation of the hybrid coupled Discrete Element Method (DEM) – SPH – Reproducing Kernel Particle Method (RKPM) – Finite Element Method (FEM) – BEM – Computational Fluid Dynamics (CFD) multiscale modeling at Scale I and hierarchical continuum model at Scale II, scaled geotechnical centrifuge experiments (Fig. 42.7) are being conducted to obtain a high-fidelity, repeatable database on all key kinematic and kinetic aspects of the soil, water and air, including those of the ejecta, when subjected to buried explosive loading.

42.2 Technical Updates

42.2.1 High Strain Rate Split Hopkinson Pressure Bar (SHPB) Experiments on Boulder Clay and Mason Sand (Luo, Lu)

Dynamic compressive behavior of dry, partially saturated (as-received), and fully saturated Mason sand and Boulder clay under confinement was characterized using a long split Hopkinson pressure bar (SHPB). A sand sample is enclosed in a hardened steel tube with both ends capped by tungsten carbide rods which match the same mechanical impedance of the steel incident/transmission bars. This assembly is tapped to consolidate the sand grains to reach a desired mass density. For moist sand/clay, grease was used to fill the gap between the tungsten carbide rod and steel tube at each end to seal the ends to prevent the moisture to leak from the gap. For moist sand/clay, shaking assists water to distribute around the sand/clay grains. A moist specimen was kept for 2 days to allow even distribution of moisture. The actual moisture content was determined by weighing the assembly. A strain gage was attached on the external surface of the confining steel sleeve, to

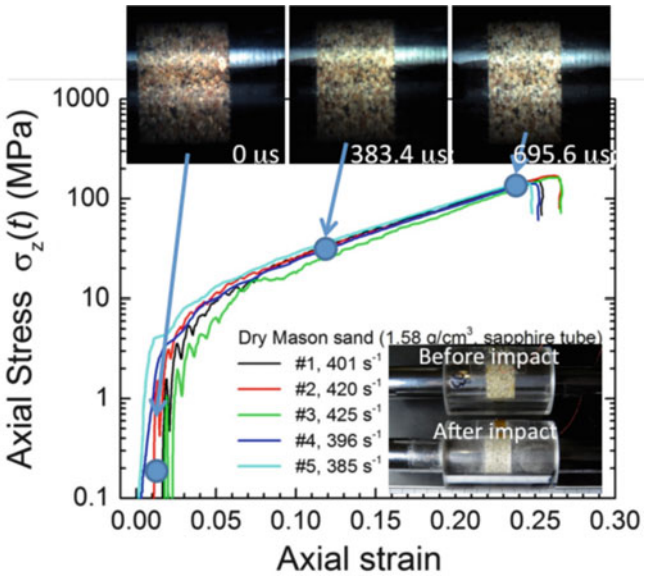

Fig. 42.3 Axial stress-axial strain curves of a dry Mason sand under confinement by a sapphire tube. Images acquired at frame rate 70 k fps show the sand deformation

measure the circumferential strain to allow calculation of the radial stress. This arrangement allows characterization of dynamic response to characterize the volumetric and deviatoric behavior. The void ratio as a function of pressure is determined at high strain rates. A copper disk was used as the pulse shaper. In this experiment, a striker bar of 2.13 m long was used. The incident bar was 8.74 m long, and the transmission bar was 8.74 m long. The stress-strain relationship under constrained impact, the specific energy absorption, and the compressibility of sand/clay were determined. To visually investigate the sand deformation, a transparent sapphire tube was used to confine the sand sample. A Cordin 550-62 high-speed camera was used to acquire the images (Fig. 42.3), which were analyzed using the digital image correlation (DIC) technique. The constitutive behavior is currently being analyzed by the University of Utah team to determine an appropriate constitutive model for these stress paths, and these data will also be used to calibrate the mesoscale computational modeling framework when it is capable of simulating in parallel computation so many sand grains, and clay matrix (when the Boulder clay and Mason sand are mixed in the future).

42.2.2 Quasi-static and Intermediate Strain Rate Triaxial Compression Experiments on Boulder Clay and Mason Sand (Svoboda, Mun, McCartney)

An important part of the project focuses on characterization of the properties of soils under high strain rates and high pressures that may be encountered during buried explosion events. The testing on rate effects focuses on the interpretation of results from axisymmetric triaxial compression tests on clay and sand specimens under saturated and unsaturated conditions with different rates of loading. Relevant results from these tests include the undrained shear strength, stiffness and pore water pressure generation. It is well established that faster loading rates lead to an increase in the undrained shear strength at a rate of approximately 10 % per log cycle of the time to failure. However, these studies did not thoroughly evaluate the influence of rate on shear-induced pore water pressure generation. Times to failure (defined as a failure strain of 20 %) range from 2 h for conventional loading rates to 0.1 s. Slow loading rates were applied in a typical triaxial compression test while faster loading rates were applied in a hydraulic press, both under displacement-controlled conditions. The results from this study indicate that substantial negative pore water pressures can be generated during rapid loading for sands, while positive pore water pressures can be generated for clays, as shown in Fig. 42.4. Unsaturated clays with suction values up to 100 kPa (degrees of saturation greater than 85 %) evaluated in constant water content tests have greater undrained shear strengths than saturated clays for a given loading rate, as expected, but the rate of increase in shear strength with loading rate is lower for unsaturated clays. This is attributed to the lower hydraulic conductivity of the unsaturated clay, as well as collapse of air voids during rapid loading. Overall, this study extends the body of knowledge on the influence of loading rates on clays under different initial conditions.

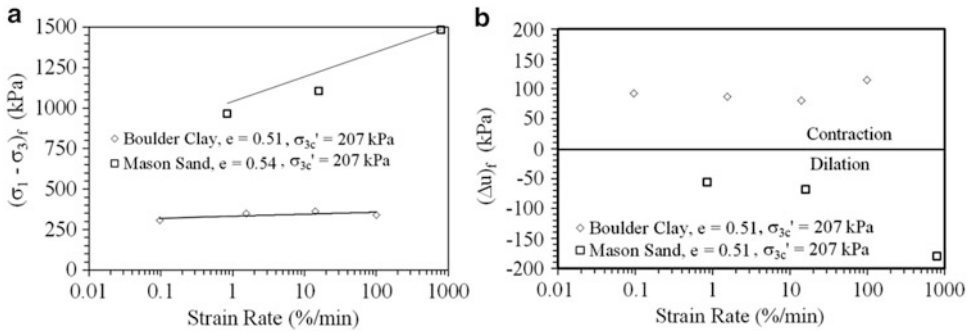

Fig. 42.4 Values at shear failure defined by the stress path tangency failure criterion: (**a**) Principal stress difference for Boulder clay and Mason sand; (**b**) Pore water pressure change for Boulder clay and Mason sand

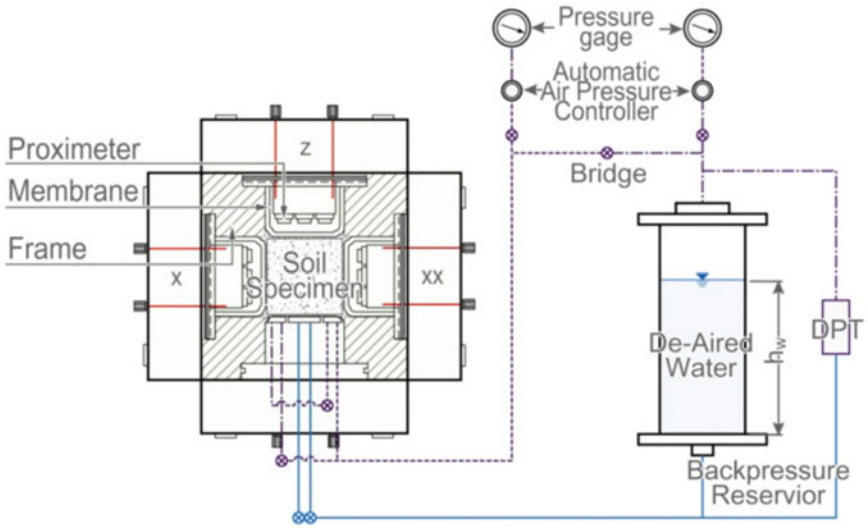

Fig. 42.5 Schematic of the pore-air/water pressure control/monitoring system for cubical cell

The investigation of high pressure effects in compression tests includes a series of tests to characterize the compression behavior of unsaturated compacted clay under higher stresses (up to 35 and 200 MPa). The role of suction on the preconsolidation stress and the slope of the compression curve are being investigated through a series of small diameter oedometer tests and larger-scale true-triaxial (cubical cell) tests on compacted specimens of the same clay under investigation in the rate effects study. A picture of the high pressure true triaxial cell with suction control is shown in Fig. 42.5. The behavior of unsaturated, compacted clay under net mean stresses up to 35 MPa in the oedometer and 200 MPa in the cubical cell have been investigated. These stress ranges are not only suitable for evaluation of the increase in the preconsolidation stress with increasing suction, but are also suitable for evaluation of the point at which the compression curves for different suction values converge and the compacted soil becomes a two-phase material. The curves for different suctions converge at the point where the air voids are compressed. Compression tests are being performed using both constant suction (drained air and water) and constant water content (undrained water, drained air) conditions. Different constitutive relationships for the compression behavior of unsaturated soils available in the literature are being investigated to represent these results, and will be correlated with the constitutive modeling at the University of Utah for this project.

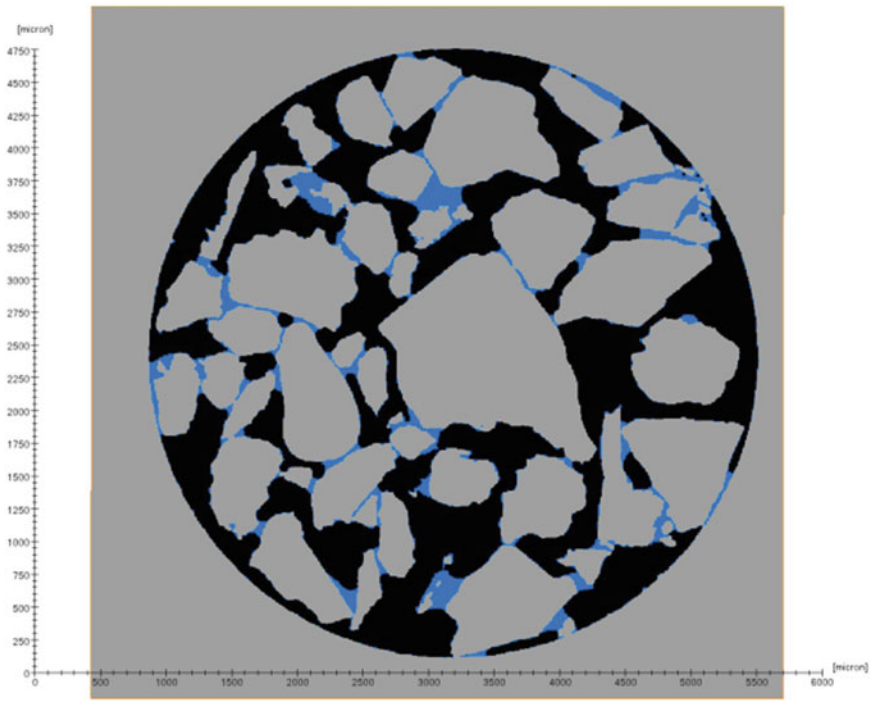

Fig. 42.6 Slice through a specimen of Mason sand showing water (*dark gray*), air (*black*), and particles (*gray*). Tube inner diameter = 4.5 mm

42.2.3 Synchrotron X-Ray Computed Tomography (CT) of Dry, Saturated, and Partially Saturated Mason Sand (Druckrey, Alshibli)

The research team at the University of Tennessee is conducting 3D characterization of the properties of Boulder clay and Mason sand soils at the micro-scale (grain-scale, for sand) using CT to measure the following properties: (1) Morphology of sand particles: samples of Mason sand were placed inside capillary tubes and were scanned using the CT technique for various moisture contents (Fig. 42.6). Particle shape and sphericity were quantified based on particle surface area, volume, longest, intermediate and shortest axes of particles. The geometry of air and water constituents in the voids are also quantified (Fig. 42.6). Such measurements can be used to generate DEM particles with interstitial air and water geometries. (2) Particle-to-particle interaction of sheared sand: in situ CT scans of a sand triaxial specimen were acquired for dry and partially saturated specimens to monitor particle interaction and particle-water interaction during shearing. The results of the analysis will be used to calibrate the mesoscale computational models for partially saturated condition. (3) Investigate the fabric of clay samples at meso-scale level: small samples of tested triaxial specimens will be scanned with the objective to quantify density variation within the sample. The CT technique will also be used to characterize the soil microstructure before and after the buried explosive soil geotechnical centrifuge experiments.

42.2.4 Geotechnical Centrifuge Experiments with Buried Soil Explosives (Hansen, Pak)

To provide a sound physical basis for an in-depth investigation of the buried soil blast problem, an experimental program using the geotechnical centrifuge modeling approach (e.g., Davies [1994], Pak and Guzina [1995], Pak and Soudkhah [2011]) is part of the project. The latest technology for capturing various kinematic and kinetic quantities involved in the high-rate soil dynamics problem, including high-g shock sensors, particle motion tracking, and high-speed cameras with three-dimensional digital image correlations are being tested and deployed in the experiments. Blasts of different intensity are being simulated using both explosive and non-explosive means. Some preliminary results for small-scale blasts using shock-tube type devices and explosives at normal gravity ("1g") in a soil model experiment are shown in Fig. 42.8, illustrating the appeal of both methods.

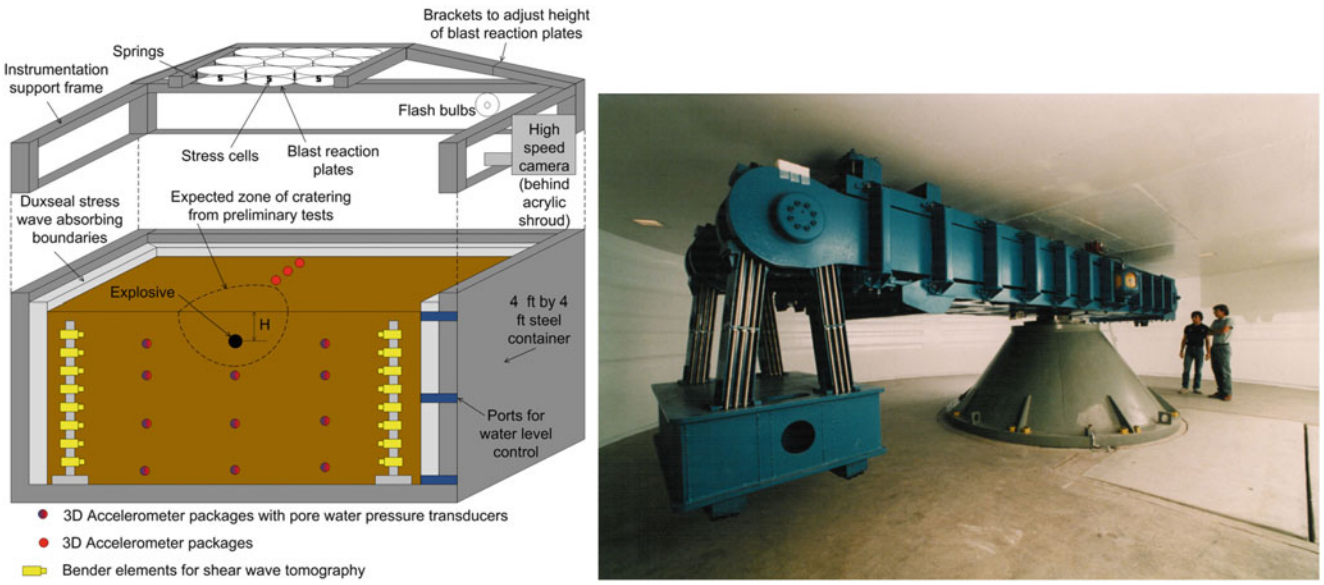

Fig. 42.7 (*Left*) Centrifuge testing setup and instrumentation plan. (*Right*) 400 g-ton geotechnical centrifuge at the University of Colorado Boulder

Fig. 42.8 (*Left*) Mason sand ejecta during shock-tube loaded experiment at 1g. (*Right*) Ejecta and crater formation during high explosive test in Mason sand at 1g

42.2.5 Constitutive Modeling and MPM Simulations for Buried Soil Blasts at Scale II (Bonifasi-Lista, Yarahmadi, Ghodrati, Colovos, Brannon)

The computational solid mechanics (CSM) group at the University of Utah is in charge of developing a high-strain-rate large-deformation continuum constitutive model for soils and implementing it in the material point method (MPM) with explosive loading in the Uintah open source software developed at the University of Utah (Scale II, Fig. 42.2). The MPM is a particle-grid method suitable for solving large deformations in which the constitutive model is history dependent and therefore intolerant to advection errors Sulsky et al. [1994]. The MPM has the advantages of both Eulerian and Lagrangian formulations. The soil constitutive model framework must support cohesive and cohesionless soils at various moisture contents. The macroscale model must be able to capture the influence of the microstructure (hierarchical upscaling between Scale I and Scale II, Fig. 42.2). It also has to be simple enough to be tractable in engineering simulations at large scales. Scaled geotechnical centrifuge tests are conducted to obtain kinematic and kinetic information of soil and subsequent ejecta when subject to buried explosive loading (Figs. 42.7, 42.8). Commonly used scaling laws are strain rate insensitive and hence require validation for soil blast simulations where high strain rate constitutive models are used. We present a simulation of blast loading in the geotechnical centrifuge experiment in Fig. 42.9. The goal of this work is to discern constitutive features essential for predicting results consistent with current scaling laws. A secondary goal is to assess the importance of Coriolis body forces in comparison to centrifugal forces. Preliminary studies of gas expansion in MPM using the recently developed Convected Particle Domain Interpolation (CPDI) integrator (Sadeghirad et al. [2011]) and integrators

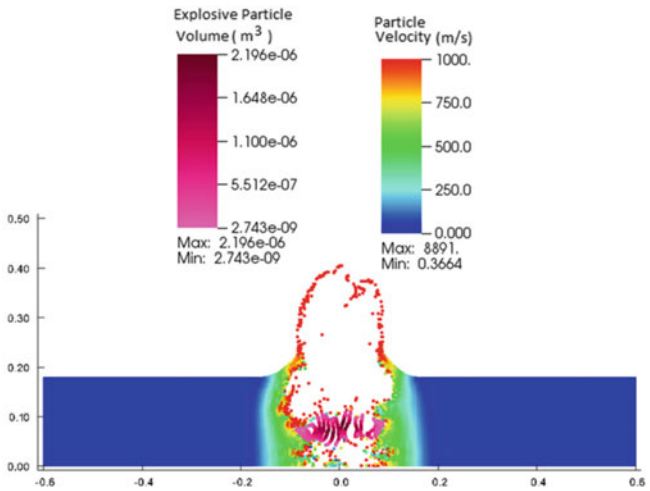

Fig. 42.9 Unlike the 1-g case, this 30-g centrifuge simulation produces two cavities (above and below the *pink-colored* explosive), and it has a visible asymmetry from Coriolis effects (color figure online)

based on the Generalized Interpolation Material Point (GIMP) method, show that the update of the deformation gradients are inconsistent with the update of the position of particles. Two sources of error are identified and analyzed. The first one involves the implementation of boundary tractions. Second, large and rapidly changing velocity gradients, common in blast simulations, appear to introduce numerical discrepancies in the kinematics updates. We will present a new method, called Multi-Point Query (MPQ) to ensure better consistency between updates of the deformation gradient and updates of particle locations.

42.2.6 RKPM/SPH Representation of Clay Fracture and Fragmentation at Scale I (Ren, Li)

A coupled RKPM (e.g., Danielson et al. [2000], Li and Liu [2004]) – SPH (e.g., Lu et al. [2005], Wang et al. [2005], and Bui et al. [2007]) formulation is being developed to simulate blast-induced clay matrix fracture and fragmentation at Scale I, and eventual coupling between clay matrix and sand grains at Scale I. The clay continuum is represented by RKPM zones, while the potential fracture planes are seeded by an SPH network. At the interface between RKPM and SPH, the SPH particles interact both with RKPM and SPH particles, thus bonding the RKPM clay continuum regions together. The SPH method updates the connectivities at every time step, allow the clay regions to separate into fragments. Using this RKPM-SPH coupling methodology for fracture and fragmentation of the clay matrix at Scale I, a cavity expansion simulation is conducted with result shown in Fig. 42.10.

42.2.7 Interaction of Soil Fragments and Background Air via Coupled Computational Fluid Dynamics (CFD) at Scale I (Brown-Dymkoski, Kasimov, Vasilyev)

In order to model flows around obstacles of complex geometries, such as compressible air or explosive gas around soil fragments, several approaches can are used. These methods can be separated into two major groups: body-fitted mesh and immersed boundary methods. The former uses conformal grids with nodes coincident to the surface of an obstacle, while the latter employs forcing upon the constitutive equations to impose appropriate boundary conditions. While body-fitted grids allow for exact boundary conditions to be imposed along the surface, grid meshing and re-meshing can be quite expensive and typically preclude the use of rectilinear grids. Moving and deforming obstacles are particularly problematic as they

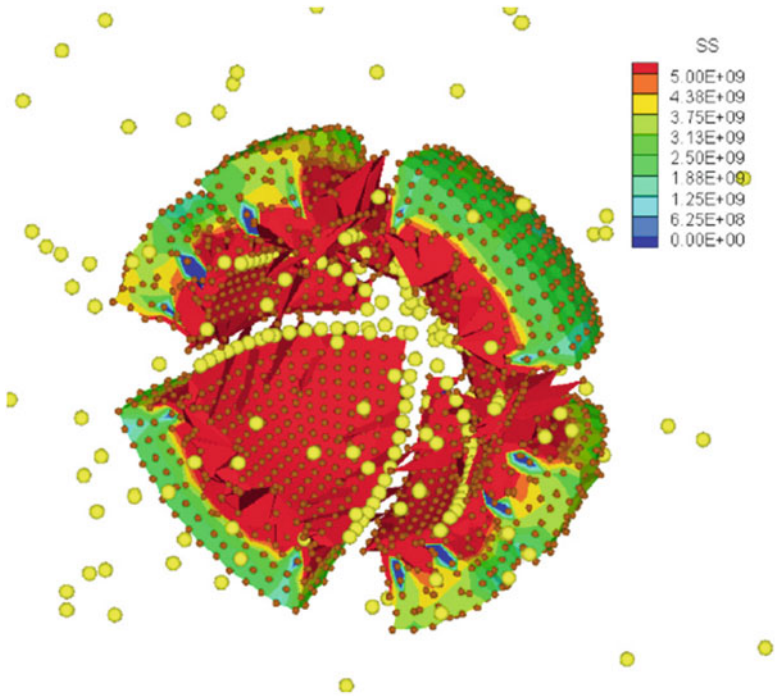

Fig. 42.10 Coupled RKPM-SPH blast simulation showing fracture and fragmentation along SPH layers. Contour values are von Mises stress

necessitate grid adaptation at every time step. Immersed boundary methods avoid the cost and complications of body meshing by introducing the effects of obstacles upon the governing equations themselves. Solid body effects, thus embedded within the flow itself, obviate the rigors of positioning nodes upon a surface. Immersed boundary forcing can be applied either to the continuous or discretized equations. While applying discretized forcing allows for a high level of control based upon the numerical accuracy and conservative properties of the discretization method, this approach lacks generality and flexibility across solvers (Mittal and Iaccarino [2005]). Volume penalization, on the other hand, imposes the effects of solid bodies by introducing forcing terms on the continuous equations and the resulting evolutionary equations are discretized and solved in the normal manner. One such method is the Brinkman Penalization Method (Angot et al. [1999]), which was originally developed for solid, isothermal obstacles in incompressible flows. A principal strength of Brinkman penalization is that error can be rigorously controlled a priori, with the solution converging to the exact in a predictable fashion (Feireisl et al. [2011], Kevlahan and Ghidaglia [2001]).

Brinkman Penalization Methods (Angot et al. [1999], Liu and Vasilyev [2007]), where solid obstacles are modeled as porous media with aporosity approaching zero, have been developed for incompressible andcompressible, viscous and inviscid flows. Until now, the main weakness of volume penalization approaches was the inability to model general boundary conditions, since they were limited to Dirichlet and homogeneous Neumann boundary conditions (Bae and Moon [2012], Kadoch et al. [2012]). This limitation precluded the use of Brinkman penalization for problems involving heat flux or shock reflection. In this work, a novel Characteristic-Based Volume Penalization (CBVP)approach is presented that builds upon Brinkman penalization but adds the flexibility of general boundary conditions. The premise of this new method is to use Brinkman-style forcing for Dirichlet type boundary conditions, while introducing linear convective terms to impose Neumann or Robin type conditions. Large coefficients on the penalization terms ensure that penalization acts on time scales much faster than the ones imposed by the physics. These penalization parameters allow for rigorous error control for each boundary condition type.

Characteristic-Based Volume Penalization (CBVP)

Application of boundary conditions is achieved by introducing additional terms within a penalized region representative of the solid obstacle. This CBVP method can be used to impose BCs for both integrated and non-integrated variables by appropriately combining the CBVP terms for each of the BCs. In this way, penalization can be easily formulated for a wide

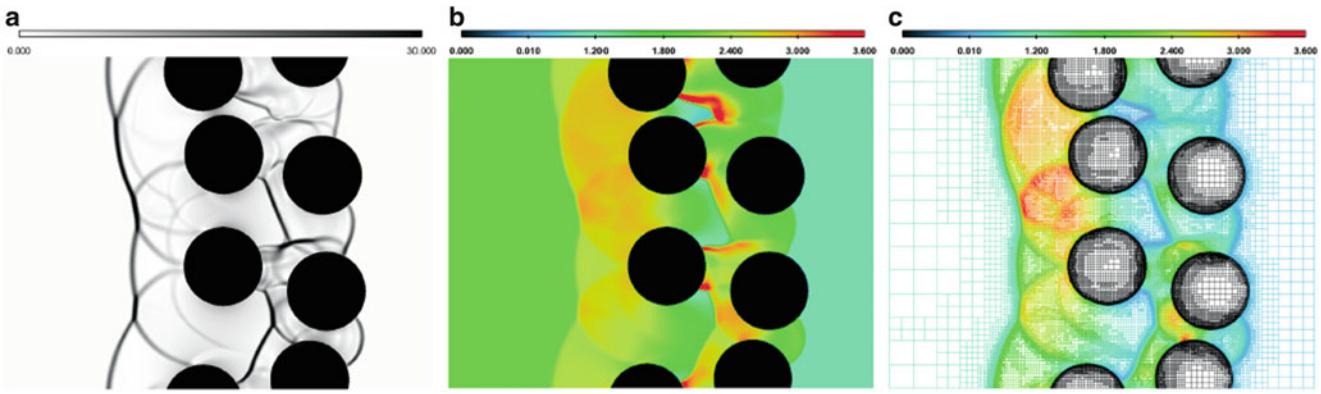

Fig. 42.11 Shock propagation through randomly packed cylinder array using CBVP method: (**a**) Schlieren image of the density field, (**b**) temperature field, and (**c**) computational mesh shaded by pressure field. Effective (non-adaptive) resolution is 1,153 × 896 grid points

variety of flow constitutive equations and BCs. Support of obstacle geometry for CBVP terms requires the definition of a spatial masking function to define the interior and exterior of an obstacle, as well as an additional definition of the normal within the obstacle. An example of a CBVP solution of the shock propagation through a randomly packed stationary cylinder array using Adaptive Wavelet Collocation Method (Vasilyev [2003]) is shown in Fig. 42.11. It should be noted that the CBVP method is applicable both for stationary or moving/deformable obstacles by appropriately modifying the forcing terms. This work is ongoing.

42.2.8 Hybrid OpenMP/MPI Parallel Code Framework for Discrete Element Method (DEM) at Scale I (Yan, Regueiro)

In support of the development of a new hybrid coupled DEM – SPH – RKPM – FEM – BEM – CFD multiscale modeling capability for soils at Scale I, a hybrid OpenMP/MPI parallel code framework is being developed, first for the DEM component of the multiscale model at Scale I. The parallelization starts from spatial domain decomposition and follows Foster's 4-step design methodology (partitioning, communication, agglomeration and mapping). A link-block algorithm is proposed for spatial partitioning and neighbor search (Fig. 42.12). The code is parallelized with message-passing interface (MPI) in distributed-memory mode, such that adjacent spatial blocks communicate through boundary cells; each block can in turn run in parallel with multiple threads in shared-memory (OpenMP) mode. It is expected that the hybrid parallel computing model adapts and scales well on Symmetrical Multiprocessing (SMP) clusters for maximum performance. We manage to minimize communication overhead, maintain adaptive spatial compute grids, keep load balance between compute nodes, handle particle migrations across computed nodes, and clear redundant contact information from adjacent processes, etc. Performance analysis of this parallel code such as speedup, efficiency, scalability is being evaluated based on computations carried out on SMP clusters (see Fig. 42.13).

42.2.9 Overlap Discrete Element (DE) and Micropolar Continuum Finite Element (FE) Coupling at Scale I (Duan, Regueiro)

The multiscale modeling at Scale I requires that we minimize the mesoscale modeling region around the explosive, ejecta, and cratering region in order to minimize computational effort. This requires applying proper BCs on the mesoscale modeling region, which entails overlap coupling of a micromorphic continuum FE implementation and the DE-SPH-RKPM-CFD mesoscale region as shown in more detail in Fig. 42.14 (left-top). We first start with a quasi-static overlap coupling problem between a 1D string of DE elastic particles and a 1D micropolar beam FE shown in Fig. 42.14 (Regueiro and Yan [2013]). Results are shown in Fig. 42.14, illustrating the complexity associated with the coupling between translational and rotational degrees of freedom for the DE model, that must be accommodated by the FE micropolar/micromorphic continuum model.

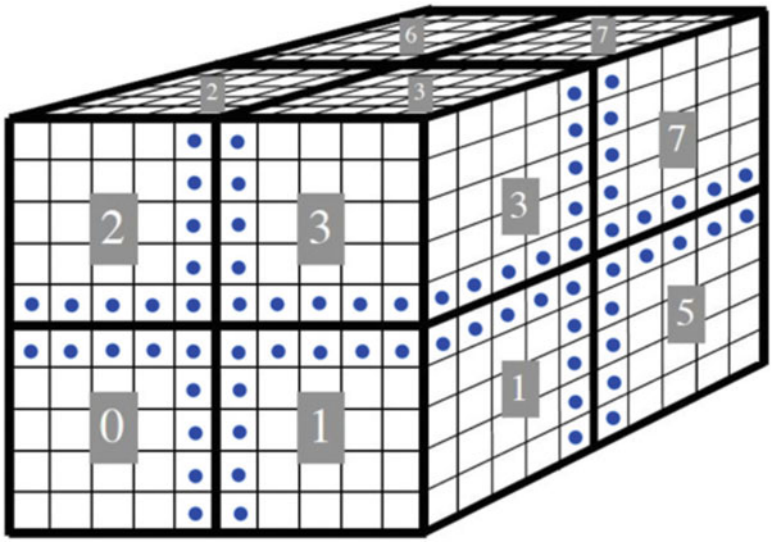

Fig. 42.12 The concept of link-block algorithm for DEM spatial partitioning and neighbor search

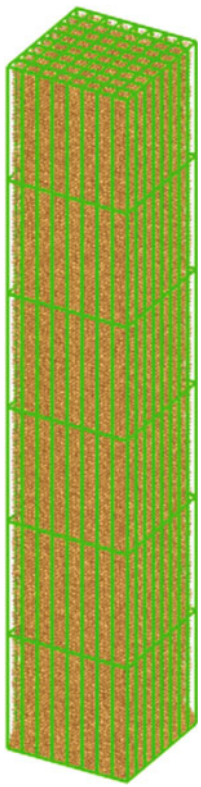

Fig. 42.13 $8 \times 8 \times 6 = 384$ grids for DE gravity deposition computation of 160,000 ellipsoidal particles

Most atomistic-continuum coupling methods ignore the rotational dofs, and thus the coupling is simpler to achieve for those methods. We are extending the overlap coupling to dynamics, micromorphic continuum FE, and eventually DE-SPH-RKPM-CFD for the mesoscale to which to overlap couple a triphasic micromorphic continuum FE.

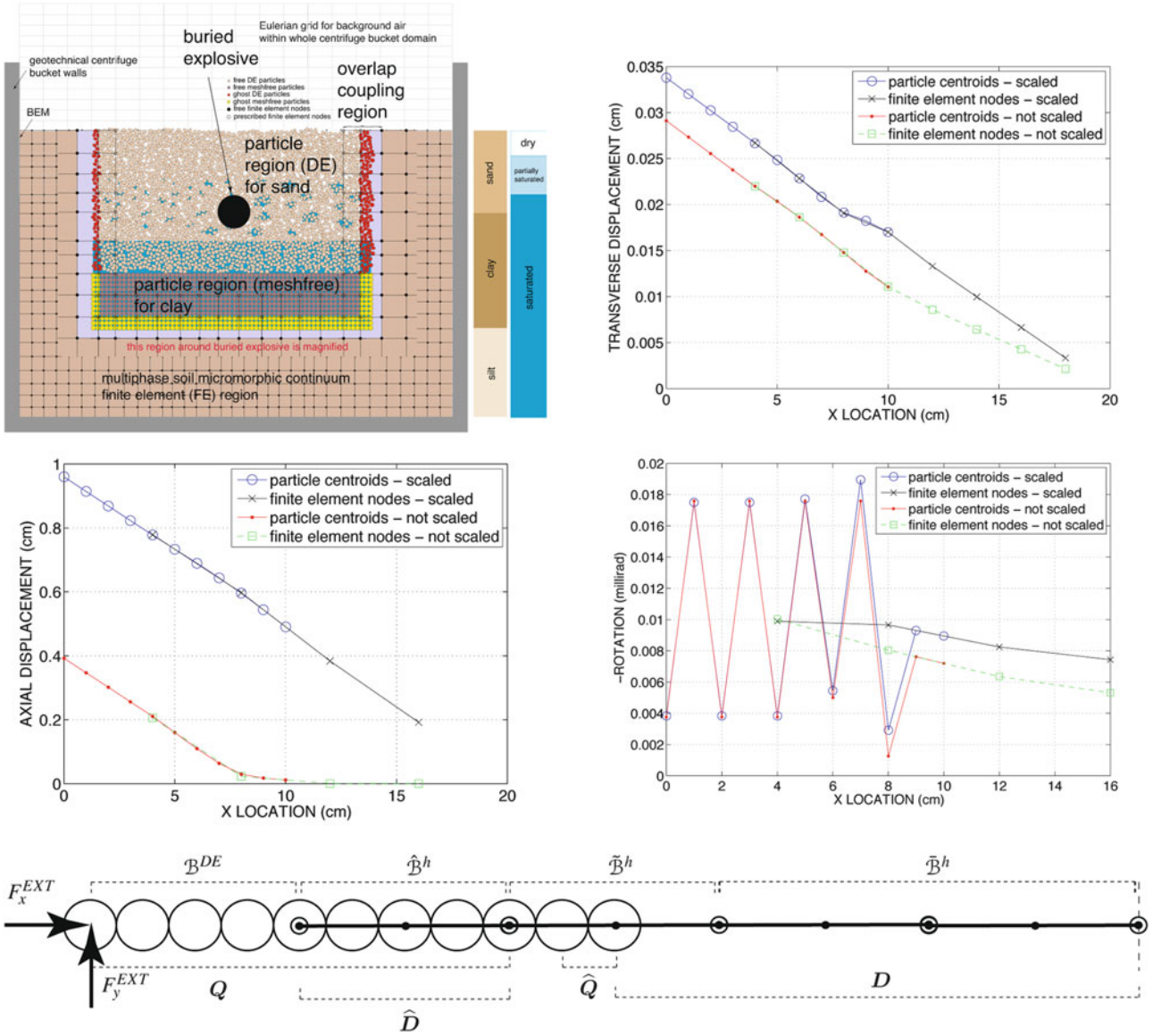

Fig. 42.14 (*Left-top*) Scale I (zoom in of explosive region): concurrent computational multiscale, multiphase failure mechanics of soil under buried explosive loading. (*Bottom*) Overlap coupling between 1D string of 11 DEs, and 4 micropolar FEs. (*Left-middle and right*) Axial displacement, transverse displacement, and rotational degrees of freedom showing scaled and not-scaled energy in the overlap region. The transverse displacement is coupled to the rotational dofs, thus there is a jog in the transition, as the rotational dofs from the DE and FE are significantly different (an artifact of the 1D DE string example, expected to reduce for 2D and 3D overlap coupling implementations)

42.3 Conclusion

We presented a brief overview and technical update of our ONR MURI project on soil blast modeling and simulation. Remaining work includes obtaining repeatable experimental data for homogeneous soils (Boulder clay and Mason sand), inhomogeneous soils (mix of Boulder clay and Mason sand), and layered soils in the geotechnical centrifuge buried explosive experiments, development and testing of Scale I coupled DE-SPH-RKPM-FEM-BEM-CFD code against small scale experimental results, hierarchical coupling between Scale I (mesoscale, or grain-scale, of soil) and Scale II (macroscale continuum modeling) and further modification of Scale II modeling based on upscaling and macroscale experimental data, Synchrotron X-ray CT characterization of mesoscale structure of soil in centrifuge tests (before and after explosive loading),

and combining all features of the project to simulate with some predictive capability the buried soil explosive geotechnical centrifuge experiments. Technology transfer to Department of Defense (DoD) researchers is already ongoing, and further interaction is welcome.

Acknowledgements Funding for this research was provided by Office of Naval Research (ONR) grant N00014-11-1-0691. This funding is gratefully acknowledged.

References

1. Angot P, Bruneau C-H, Fabrie P (1999) A penalization method to take into account obstacles in viscous flows. Numerische Mathematik 81:497–520
2. Bae Y, Moon YJ (2012) On the use of Brinkman penalization method for computation of acoustic scattering from complex boundaries. Comput Fluids 55:48–56
3. Bui HH, Fukagawa R, Sako K, Ohno S (2007) Lagrangian meshfree particles method (SPH) for large deformation and failure flows of geomaterial using elastic-plastic soil constitutive model. Int J Numer Anal Methods Géoméch 32(12):1537–1570
4. Danielson KT, Hao S, Liu W-K, Uras A, Li S (2000) Parallel computation of meshless methods for explicit dynamic analysis. Int J Numer Methods Eng 47:1323–1341
5. Davies MCR (1994) Dynamic soil-structure interaction resulting from blast loading. In: Leung et al (eds) Proceedings of the centrifuge 94, Balkema, pp 319–324
6. Feireisl E, Neustupa J, Stebel S (2011) Convergence of a Brinkman-type penalization for compressible fluid flows. J Differ Equ 250:596–606
7. Kadoch B, Kolomenskiy D, Angot P, Schneider K (2012) A volume penalization method for incompressible flows and scalar advection-diffusion with moving obstacles. J Comput Phys 231(12):4365–4383
8. Kevlahan NK-R, Ghidaglia J-M (2001) Computation of turbulent flow past an array of cylinders using a spectral method with Brinkman penalization. Eur J Mech B Fluids 20(3):333–350
9. Li S, Liu W-K (2004) Meshfree particle methods, 1st edn. Springer, Berlin
10. Liu Q, Vasilyev OV (2007) Brinkman penalization method for compressible flows in complex geometries. J Comput Phys 227(2):946–966
11. Lu Y, Wang ZQ, Chong K (2005) A comparative study of buried structure in soil subjected to blast load using 2D and 3D numerical simulations. Soil Dyn Earthq Eng 25(4):275–288
12. Mittal R, Iaccarino G (2005) Immersed boundary methods. Annu Rev Fluid Mech 37:239–261
13. Pak RYS, Guzina BB (1995) Dynamic characterization of vertically-loaded foundations on granular soils. J Geotech Eng 121(3):274–286
14. Pak RYS, Soudkhah M (2011) On experimental synthesis of seismic horizontal free-field motion of soil in finite-domain simulations with absorbing boundary. Soil Dyn Earthq Eng 31(11):1529–1539
15. Regueiro RA, Yan B (2013) Computational homogenization and partial overlap coupling between micropolar elastic continuum finite elements and elastic spherical discrete elements in one dimension. In: Li S, Gao X-L (eds) Handbook of micromechanics and nanomechanics, vol 1. Pan Stanford, Singapore, pp 1–45
16. Sadeghirad A, Brannon RM, Burghardt J (2011) A convected particle domain interpolation technique to extend applicability of the material point method for problems involving massive deformations. Int J Numer Methods Eng 86(12):1435–1456
17. Sulsky D, Chen A, Schreyer HL (1994) A particle method for history-dependent materials. Comput Methods Appl Mech Eng 118:179–196
18. Vasilyev OV (2003) Solving multi-dimensional evolotion problems with localized structures using second generation wavelets. Int J Comput Fluid Dyn (Special issue on High-resolut methods in Comput Fluid Dyn) 17(2):151–168
19. Wang ZQ, Lu Y, Hao H, Chong K (2005) A full coupled numerical analysis approach for buried structures subjected to subsurface blast. Comput Struct 83(4–5):339–356

Chapter 43
Dynamic Behavior of Saturated Soil Under Buried Explosive Loading

A. Yarahmadi and R. Brannon

Abstract Soil failure under buried explosives detonation and evolution of pore water and air pressures, as well as temperature and deformation increments, are investigated by a set of coupled multiphysics balance equations implemented via Material Point Method (MPM) in Uintah (open-source massively parallel codes). Fluid–structure and fluid–solid interactions are simulated by coupling MPM to a finite-volume, cell-centered, multi-material compressible CFD formulation (Implicit, Continuous fluid, Eulerian: ICE) including the transformation of the High-Explosive (HE) solid into highly pressurized gaseous products. Blast waves in the soil are simulated by Jones-Wilkins-Lee (JWL++) detonation model of HE material. The dynamic compacting of partially saturated soil or sediment in the neighborhood of a concentrated explosive source is studied via implementing a plastic gas continuum model. This approach also includes modeling of detonation waves transition from the high pressure plastic gas zone to the moderate pressure elastic–plastic zone. In addition to the governing equations for wave propagation (originated with the explosion), the non-linear coupled macroscopic momentum/mass balance for both the solid matrix and the fluid phase in a saturated porous medium are solved numerically in low-moderate pressure zone.

Keywords Explosive loading • Soil • MPM • Multiphase • Detonation

43.1 Introduction

The conventional computational methods in shock-physics that have been used for simulation of soil failure under buried explosive loading do not take account of all the physical phenomena such as solid to fluid-like behavior transition in soil and advection or rezoning errors in internal state variables (ISVs) calculation (Brannon et al. [1], Farnsworth and Robinson [2]). The alternative approach is implementing a numerical particle-grid method such as Material Point Method (MPM) (Sulsky et al. [3, 4]), which is more appropriate for solving large deformations in geomaterials and complex geometries. Moreover, the computational cost of the MPM is reasonable and it has the advantages of Eulerian formulation owing to the usage of background grid.

The soil failure under blast loading is simulated in this study by the coupled multiphysics balance equations implemented via MPM in Uintah (open-source massively parallel codes including MPM). First, the blast detonation for high explosives with MPMICE in Uintah is validated with an experimental approach and then a geotechnical centrifuge model for blast in soil is simulated by MPMICE with some modification to take account of the Coriolis body force effect. Furthermore, the conventional scaling laws for buried explosives are compared with Uintah outcome and a kinematics analysis is performed to assess the significance of the rotation of principal directions of stretch in large deformation of soil particles. Finally, temperature evolution and pore collapse in a soil element under uniaxial loading with high temperature are investigated.

A. Yarahmadi (✉) • R. Brannon
Department of Mechanical Engineering, University of Utah, Salt Lake City, UT, USA
e-mail: a.yarahmadi@utah.edu

B. Song et al. (eds.), *Dynamic Behavior of Materials, Volume 1: Proceedings of the 2013 Annual Conference on Experimental and Applied Mechanics*, Conference Proceedings of the Society for Experimental Mechanics Series,
DOI 10.1007/978-3-319-00771-7_43,

43.2 Qualitative Validation of Detonation Simulation and MPMICE in Uintah

In Uintah, blast waves can result from Jones-Wilkins-Lee (JWL) detonation or deflagration of high-explosive (HE) material, with mechanical or thermal initiation. The solid HE transfers into highly pressurized gaseous products which occupy the solid explosive regions after explosion. Fluid–structure interactions are supported in Uintah with MPMICE, i.e. a coupling finite-volume, cell-centered, multi-material compressible CFD formulation (Implicit, Continuous fluid, Eulerian: ICE from Kashiwa and Rauenzahn [5]) with MPM for the solid. Uintah detonation modeling with MPMICE has been observed and verified through considering a 2-D explosion and shock-wave simulation in a flyer-plate impact experiment (Fig. 43.1). The run distances to detonation for several input shock pressures were obtained and then the data was plotted on log-log axes (called Pop Plot from Ramsey and Popolato [6]). This plot demonstrates the relative shock sensitivities and the lengths needed for shock to detonation transition (SDT). Over the moderate range of the shock initiation pressure (a range from 2.5 to 20 GPa for HE), linear fits precisely designate Pop Plot data (Souers et al. [7]), and as we observed in Fig. 43.1, Uintah output shows the correct behavior (Fig. 43.2).

43.3 Geotechnical Centrifuge Modeling and Assessment of Scaling Laws for Buried Explosives

A geotechnical centrifuge imposes an augmented gravitational acceleration to physical models in order to produce equal self-weight stresses in both the model and prototype (known as one to one stress scaling) and provides some useful benchmarks for verification of computational models. If we scale down the length *(L)* of the model and scale up the gravity *(g)* simultaneously with a given scaling factor *(N)* and assuming that the same mass density of soil (ρ) is equal in both the model and prototype (Kutter [8])

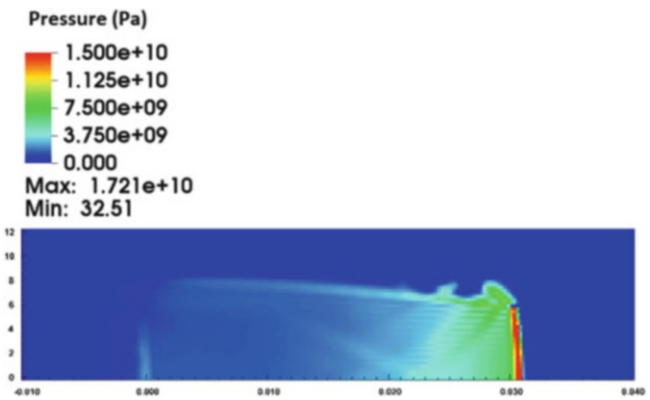

Fig. 43.1 Pressure contour for shock front wave

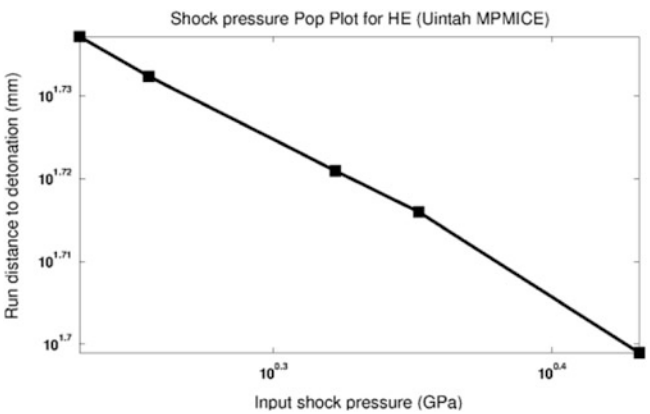

Fig. 43.2 Pop Plot from Uintah output

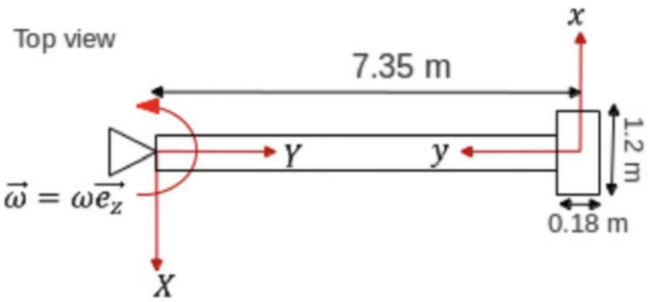

Fig. 43.3 Schematic of the simulated centrifuge and bucket

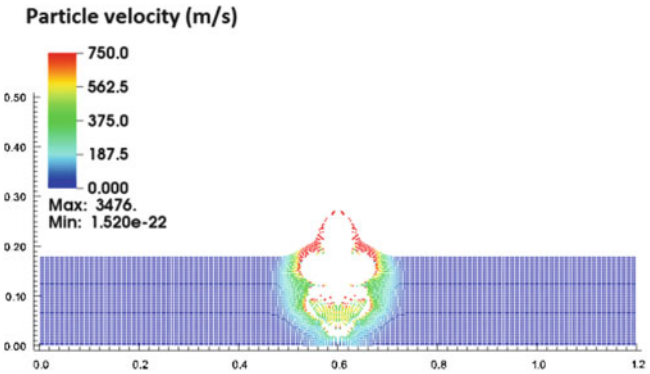

Fig. 43.4 Particle velocity (bucket simulation)

$$\sigma^* = F^* \Big/ (L^*)^2 = m^* a^* \Big/ (L^*)^2 = \rho^* (L^*)^3 a^* \Big/ (L^*)^2 = \rho^* L^* a^* = 1(1/N)N = 1 \tag{43.1}$$

where the asterisk indicates the scaled quantity (magnitude of the quantity in the model to that in the prototype).

The schematic of the simulated centrifuge and bucket is demonstrated in Fig. 43.3. Figure 43.4 depicts the buried explosive simulation which is performed for the increased acceleration of 20 g ($N = 20$). The failure criterion is Mohr-Coulomb with a tensile cutoff failure surface. As Fig. 43.4 illustrates, the region at the bottom of the explosive cavity opens a transient secondary void (which is not observed in 1 g simulation) due to the imposed inertial (centrifuge) body force. If we add the Coriolis force to the body force term, the total effective body force on the bucket is

$$\mathbf{b} = \mathbf{g} + (\omega \times \omega \times \mathbf{r} - \mathbf{2}\omega \times \mathbf{V}) \tag{43.2}$$

where ω, **V** and **r** are the centrifuge angular velocity, particle velocity and particle location with respect to the center of rotation, respectively.

We define a new parameter, Coriolis importance factor, η, as

$$\eta = |\mathbf{V}|/(|\mathbf{V}| + |r\omega|/2) \tag{43.3}$$

which is fundamentally the ratio of the Coriolis force to the total body force and hence it varies between 0 and 1. The magnitudes of Coriolis importance factor (Fig. 43.5) are high (especially near the explosive source) indicating that Coriolis effect is significant in the centrifuge test modeling.

Figure 43.6 depicts the bucket simulation with implementing both centrifugal and Coriolis forces in the MPMICE code. The asymmetry (particles inclination to the right) is specifically due to the Coriolis force. We can also observe the huge dilation of the explosive particles (located mostly in the middle of the bucket) through the illustrated particles volume in Fig. 43.6.

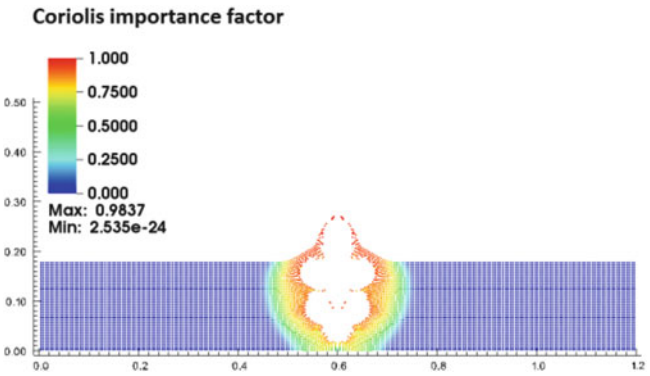

Fig. 43.5 Coriolis importance factor (bucket simulation)

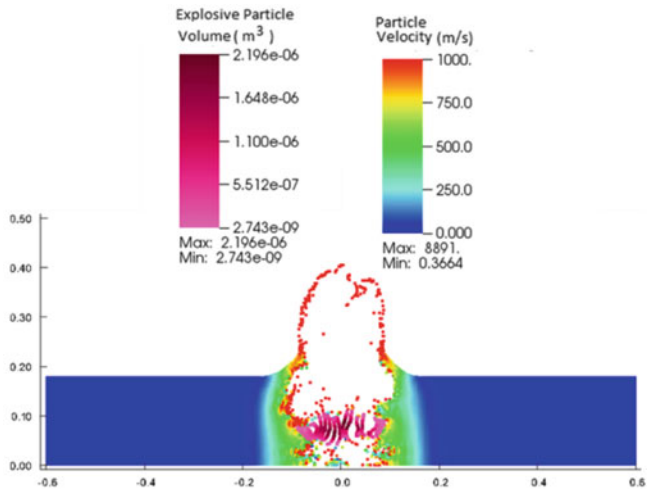

Fig. 43.6 Asymmetry in the centrifuge test modeling due to Coriolis body force

The conventional scaling laws for buried explosives are based on dimensional analysis through groups of dimensionless parameters (Bridgman [9]) or curve-fitting of experimental data (Cooper [10]). To assess the accuracy of the scaling laws, we performed the bucket simulation for a larger scale ($N = L_2/L_1 = 2 \rightarrow g_2/g_1 = 1/2$) and compared the Uintah output with one of the most common scaling laws for spherical explosive charges known as one-third power-law (Bridgman [9], Cooper [10], Chabai [11])

$$\frac{d_1}{d_2} = \frac{r_1}{r_2} = \left(\frac{\rho_2}{\rho_1}\right)^{1/3} \left(\frac{W_1}{W_2}\right)^{1/3} \tag{43.4}$$

where d is the depth of burst, r is the crater radius, W is the explosive charge weight and ρ is the mass density of the soil. The simulation is 2-D, the media are the same, and the predicted crater radius for small and large simulations are 0.08 and 0.15 m, respectively; thus

$$\begin{cases} \rho_1 = \rho_2 \\ W_1/W_2 = (r_{W1}/r_{W2})^2 = (0.04/0.08)^2 = 0.25 \rightarrow (W_1/W_2)^{(1/3)} \approx 0.63 \\ r_1 = 0.08m,\ r_2 = 0.15m \rightarrow (r_1/r_2) = 0.08/0.15 \approx 0.53 \end{cases} \rightarrow \text{Relative error} = \frac{0.63 - 0.53}{0.53} = 19\%$$

The large relative error of 19 % implies uncertainty in the empirical scaling law (as also noted by Chabai [11]) and/or missing physics in the model (e.g., no rate dependence as yet), which undermines reliability of the predictions for the types and quantities of explosives of interest. This result implies the need for further investigation.

43.4 Kinematics Analysis

Large stretch is certainly essential for this simulation, but the rotation of stretch direction should be investigated more thoroughly. The presented graphs in Figs. 43.7 and 43.8 are the plots of *Z*-norm which is defined as

$$\|\bar{\mathbf{Z}}\| = \|\overline{\mathbf{D}}\,\overline{\mathbf{V}} - \overline{\mathbf{V}}\,\overline{\mathbf{D}}\| / \|\bar{\mathbf{D}}\| \tag{43.5}$$

where $\boldsymbol{D}$ is the symmetric part of velocity gradient, $\boldsymbol{V}$ is the spatial stretch tensor from polar decomposition and the bar implies the unrotated tensor. *Z*-norm is considered as a measure of rotation of the stretch principal directions. Figure 43.7 demonstrates the *Z*-norm for a particle at the surface of the bucket and at the closest point to the symmetry axis and Fig. 43.8 shows the same parameter for simple shear. Compared to simple shear (which produces larger *Z*-norms at the same stretch ratios), the bucket simulation shows relatively small values of rotation of the stretch principal directions. Therefore, we can conclude that since the principal directions of stretch do not rotate significantly, the Kroner decomposition of deformation gradient (to elastic and plastic parts) is not crucial for this simulation.

43.5 Pore Collapse and Temperature Evolution in a Soil Element

Since the time scale for an explosive event is very small, we can assume that buried explosion is an adiabatic process. Accordingly the primary source of entropy generation is mechanical dissipation which is taken to be bounded by the plastic work rate given by (Brannon [12])

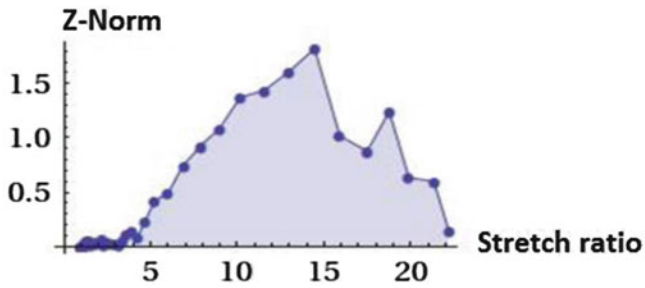

Fig. 43.7 Plot of *Z*-norm for the bucket simulation

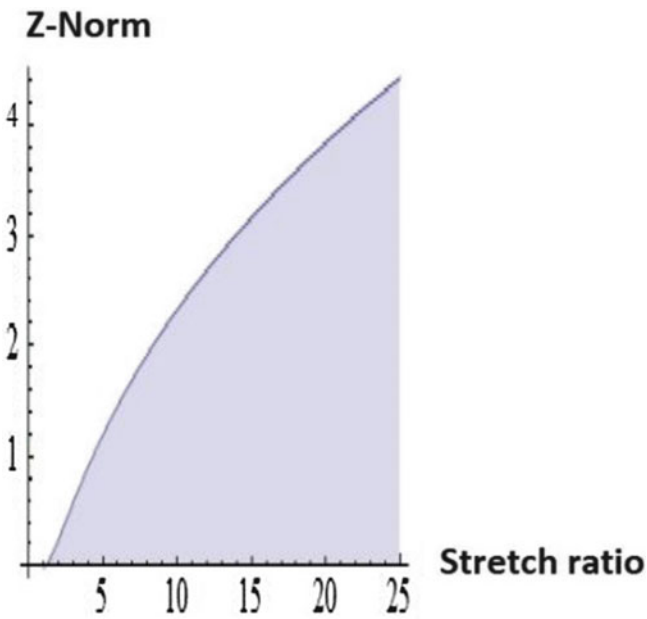

Fig. 43.8 Plot of the *Z*-norm for simple shear

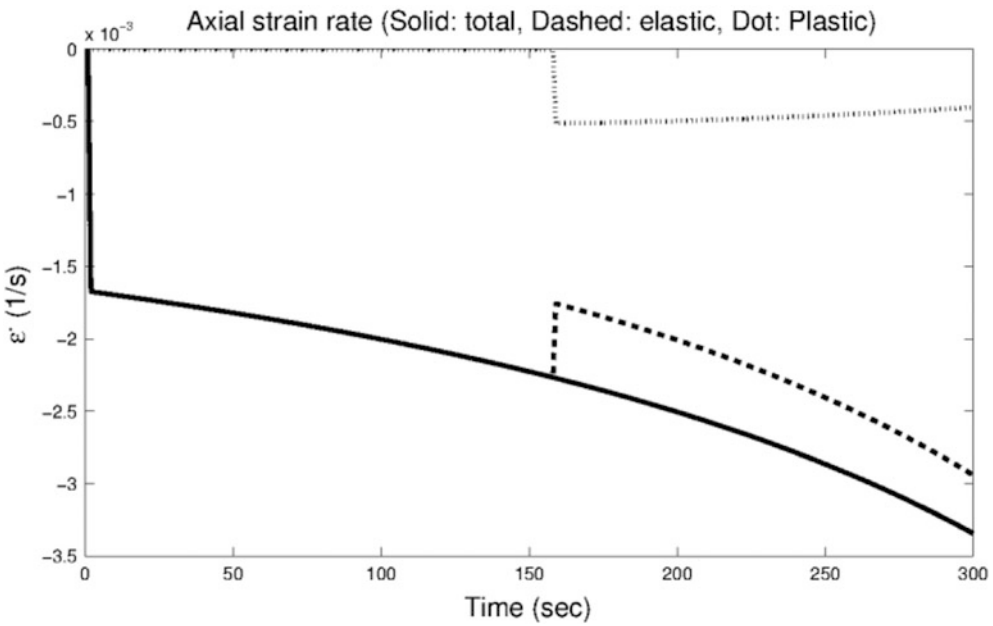

Fig. 43.9 Total, elastic and plastic strain rate in a soil element under uniaxial loading (compression)

$$T\dot{s} = \frac{1}{\rho}\sigma : \dot{\varepsilon}^{\mathbf{p}} \tag{43.6}$$

where s is entropy, T is temperature, and $\dot{\varepsilon}^{\mathbf{p}}$ is the plastic strain rate (the dot denotes the material time-rate of the variable). Furthermore, neglecting plastic volume change of the solid phase (*cf.* Brannon [12]), the porosity evolution $(\dot{\phi})$ is

$$\dot{\phi} = (1-\phi)tr\dot{\varepsilon}^{\mathbf{p}} \tag{43.7}$$

A single element test for soil under compressive uniaxial strain loading with high temperature (common in shock physics) is performed based on a generalized plasticity algorithm with elastic–plastic decomposition of the total strain rate (explained in detail in Brannon et al. [13] and Fuller et al. [14]) and an upper-bound yield function for porous media (Gurson [15]). Figure 43.9 shows the strain rates in the element and Figs. 43.10 and 43.11 depict temperature and porosity evolution (pore collapse) for initial temperature and porosity of 3,000 K and 0.4, respectively. As Fig. 43.10 illustrates, temperature slightly increases in both elastic and plastic phases due to negative strain rate and dissipation (dominant terms in this simulation).

43.6 Conclusion

The JWL detonation simulation via the implemented MPMICE in Uintah demonstrated very satisfactory consistency with the "Pop Plot" experimental trends observed relating shock pressure and distance to detonation. This methodology was used to simulate a dynamic geotechnical centrifuge test for buried explosive. The results implied that the Coriolis body force effect could be significant owing to the high particle velocities, the common scaling laws for buried explosives do not predict the explosion parameters accurately and the rotation of principal directions of stretch is not large enough in large deformation of soil particles under blast loading to merit implementation of a Kroner decomposition of deformation. Finally, the temperature evolution and pore collapse in a soil element under uniaxial loading with initial high temperature were demonstrated.

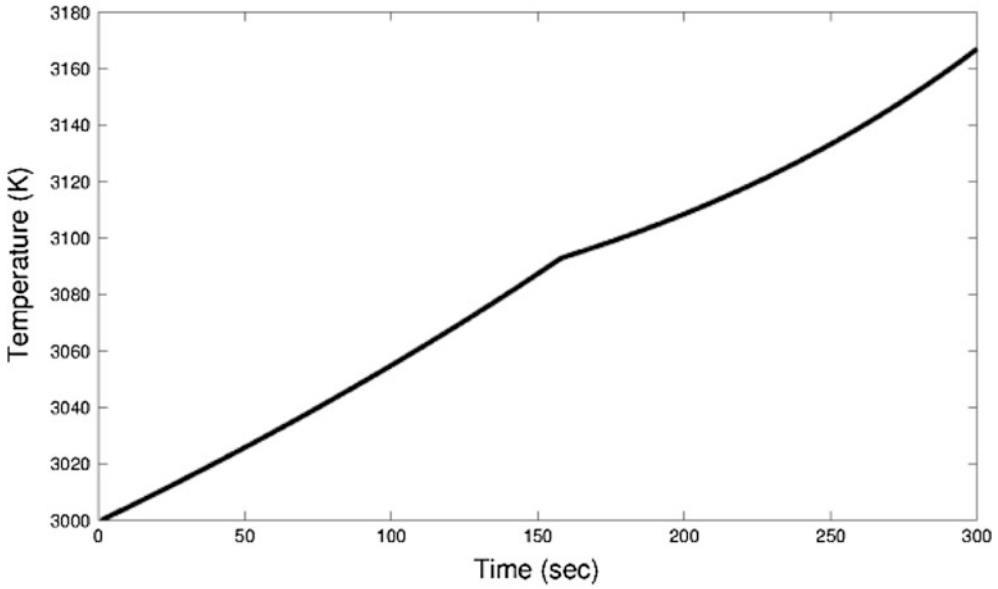

Fig. 43.10 Temperature evolution in a soil element under uniaxial loading (compression)

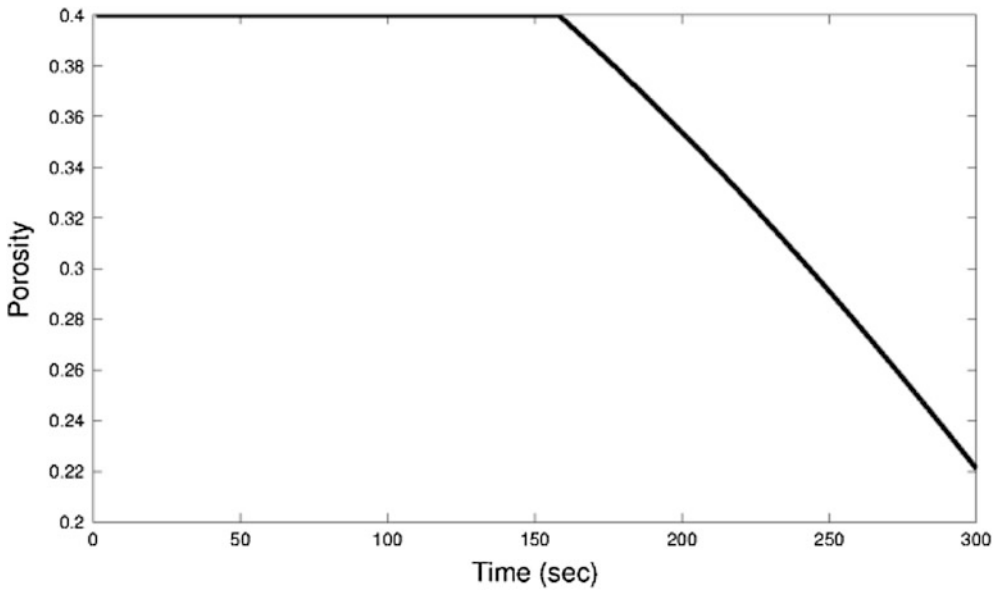

Fig. 43.11 Porosity evolution in a soil element under uniaxial loading (compression)

References

1. Brannon RM, Wells JM, Strack OE (2007) Validating theories for brittle damage. Metall Mater Trans A 38:2861–2868
2. Farnsworth GV, Robinson AC (2003) Improved kinematic options in ALEGRA. Sandia National Laboratories, SAND2003-4510
3. Sulsky D, Chen A, Schreyer HL (1994) A particle method for history-dependent materials. Comput Meth Appl Mech Eng 118:179–196
4. Sulsky D, Zhou SJ, Schreyer HL (1995) Application of a particle-in-cell method to solid mechanics. Comput Phys Commun 87:236–252
5. Kashiwa BA, Rauenzahn RM (1994) A cell-centered ICE method for multiphase flow simulations. Los Alamos National Laboratory, LA-UR-93-3922
6. Ramsey JB, Popolato A (1965) Office of Naval Research, ACR-126. In: Proceedings of fourth symposium on detonation, White Oak
7. Souers PC, Anderson S, Mercer J, McGuire E, Vitello P (2000) JWL++: a simple reactive flow code package for detonation. Propell Explos Pyrot 25(2):54–58

8. Kutter BL (1992) Dynamic centrifuge modeling of geotechnical structures, Transportation research record 1336. National Research Council, Washington, DC, pp 24–30
9. Bridgman PW (1949) Dimensional analysis. Yale university Press, New Haven
10. Cooper PW (2007) Scaling and explosives engineering applications. Sandia National Laboratories, Apr 2007
11. Chabai AJ (1965) On scaling dimensions of craters produced by buried explosives. J Geophys Res 70(20):5075–5098
12. Brannon RM (2007) Elements of phenomenological plasticity: geometrical insight, computational algorithms, and applications in shock physics. In: Shock wave science and technology reference library: solids I, vol 2. Springer, New York, pp 189–274
13. Brannon RM, Fossum AF, Strack OE (2012) KAYENTA: theory and user's guide, Sandia report, SAND2009-2282
14. Fuller TJ, Brannon RM, Strack OE, Bishop JE (2010) Initial inclusion of thermodynamic considerations in Kayenta, Sandia report, SAND2010-4687
15. Gurson AL (1977) Continuum theory of ductile rupture by void nucleation and growth. Part I: yield criteria and flow rules for porous ductile media. J Eng Mater Technol Trans ASME 99:2–15

Chapter 44
Sand Penetration: A Near Nose Investigation of a Sand Penetration Event

John Borg, Andrew Van Vooren, Harold Sandusky, and Joshua Felts

Abstract This paper presents experimental and computational results relative to a long-rod penetrating dry granular sand at velocities near 100 m/s. The objective of this work is to develop a fundamental understanding of the formation and transmission of dynamic force chains, and the motion and fracture of the individual sand grains as the projectile passes. This is accomplished by several very different experiments including: characterization of the elastic properties of sand, fracture characteristics of individual sand grains and launching a projectile along a view window, backed by sand, in order to directly view and photograph the projectile/sand interactions. Within the sand system, a two-wave structure was observed, composed of a compaction wave (bow shock) that detaches from the dart and moves through the sand at a wave speed near 100 m/s and a damage wave, which remains near the leading edge of the dart. The compaction wave removes porosity and the damage wave fractures grains in the region near the projectile nose. Grain fracture is not observed at dart speeds below 35 m/s.

Keywords Sand penetration • Longitudinal and shear sound speed in sand • Elastic properties of sand • Fracture strength

44.1 Introduction

The penetration dynamics of a projectile launched into a heterogeneous target have long been of interest and remain an active research area. Experimental investigations have demonstrated that the penetration behavior of a projectile can vary against differing heterogeneous materials such as soil [1–4], sand [5–19], concrete [20–23], as well as laminated and/or composite materials. Soil, specifically loose dry sand, has demonstrated a wide range of behaviors when subjected to shock and impact loading. Grain fracture, pore collapse and the formation of force chains are some of the important phenomena which govern the sand behavior at the small scale, complicate the dynamic target-projectile interactions moving up in scale, and are suspected to contribute to differing degrees of penetration performance at the largest scales. The objective of this work is to explore the formation of force chains, and to observe and quantify the fracture of individual sand grains when subjected to a penetration event. This is accomplished with a novel experimental technique that uses an optically accessible target tank in order to directly observe the projectile-target interactions.

Impact and penetration of loose dry materials, such as sand, have been modeled utilizing a variety of empirical, analytic and numeric techniques. Simple analytic hydrodynamic approximations have successfully been used to predict the bulk behavior of a wide variety of projectile-target configurations, including materials with porosity [24, 25]. Often the performance of a penetration event is based on bulk postmortem metrics such as depth of penetration, projectile erosion, shot-line deviations, crater formation and excavation. Often the depth of penetration is compared to the hydrodynamic limit, defined as the ratio of penetration depth to projectile length and is proportional to the square root of the ratio of the projectile and target densities, P/L~ $\sqrt{\rho_p/\rho_{00}}$, [26, 27]. For the projectile and sand targets investigated here, the measured P/L ratio is

J. Borg (✉) • A. Van Vooren
Department of Mechanical Engineering, Marquette University, Milwaukee, WI 53233, USA
e-mail: john.borg@mu.edu

H. Sandusky • J. Felts
Indian Head Division, Naval Surface Warfare Center, 101 Strauss Ave, Indian Head, MD 20640, USA

B. Song et al. (eds.), *Dynamic Behavior of Materials, Volume 1: Proceedings of the 2013 Annual Conference on Experimental and Applied Mechanics*, Conference Proceedings of the Society for Experimental Mechanics Series,
DOI 10.1007/978-3-319-00771-7_44,

larger than 5, whereas the square root of the density ratio is near 2. Thus this estimate does not accurately characterize the depth of penetration. Charters and Summers suggested estimates of penetration can be made by equating the kinetic energy of the projectile to the target resistances times an assumed excavated volume [28]. The volume estimated can either be a hemisphere, as originally assumed by Charters and Summers, or a cone, where the diameter of the cone is equal to the penetration depth; both are presented in Eq. 44.1.

$$P = \left(\frac{81}{4\pi}\frac{\rho_p}{\rho_t}\frac{KE}{St}\right)_{Hemi}^{1/3} = \left(\frac{162}{\pi}\frac{\rho_p}{\rho_t}\frac{KE}{St}\right)_{Cone}^{1/3} \tag{44.1}$$

The target resistance, St, is assumed to be the flow stress and therefore an expression for the depth of penetration can be obtained. In addition, we propose a simple analytic solution based on a simple force balance and the resistance due to individual grain fracture. Reviews of empirical and approximate methods can be found in Zukas, et al. [29] and Orphal [30].

44.2 Experimental Setup and Results

The Ottawa sand used in these experiments consisted of 99 % pure quartz (2.65 g/cm^3), had rounded grains and were rather light transparent; thus they appeared clear. The sand had an average grain diameter between 0.45 and 0.55 mm, and an average bulk density of 1.56 g/cm^3. Three sets of complementing experiments were conducted and are reported in this work: (1) pulse send-receive for longitudinal and shear sound speed measurements in wet and dry sand, (2) single grain static fracture tests and (3) gas gun dynamic penetration experiments. The following reviews each in turn.

44.2.1 Pulse Send and Receive Sound Measurements

The longitudinal and shear sound speeds of both dry and wet bulk Ottawa sand were measured with an Olympus high voltage (900 V) impulse ultrasonic pulse-receiver unit (model 5058PR). Several standard materials such as PMMA, Aluminum and water, were tested in order to insure the system measurements were consistent with published results. In order to calculate the velocity, the pulse transient time was measured for a given sample thickness. The transient time was measured as the rising edge wave arrival time rather than the group velocity arrival time. For the longitudinal measurements, dry sand samples ranged in thickness from 1.4 to 3.2 cm were as the thickness of wet sand samples was near 2.4 cm.

The longitudinal and shear wave speeds for sand are presented in Fig. 44.1b; the error bars represent the range of values obtained through repeated tests of different sand samples. We interpret the variation in measurements to be a reflection of the variation in sand ensemble arrangements. The average longitudinal speed for dry sand (zero percent water by volume) is near

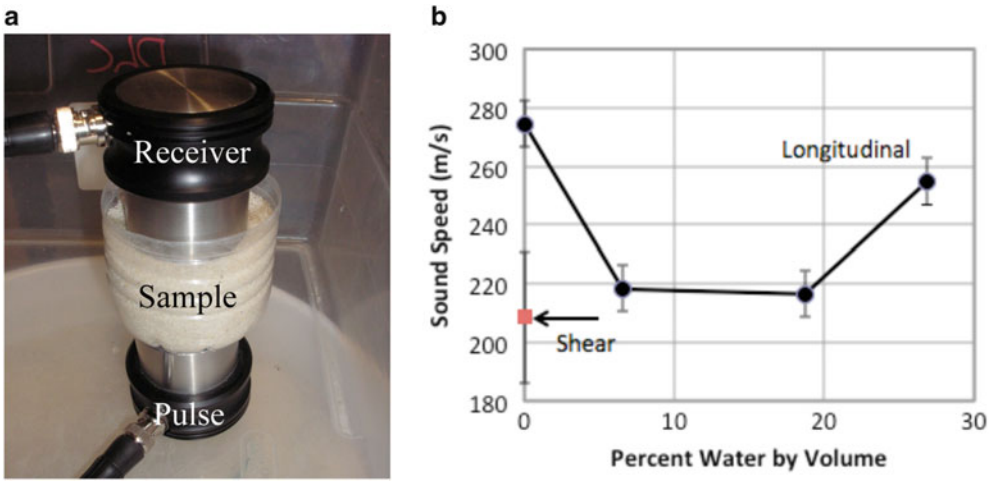

Fig. 44.1 Pulse-receiver setup and results for longitudinal and shear sound speed measurements (**a**) Olympus pulse-receiver unit with sand sample, (**b**) Longitudinal and shear sound speed measurements

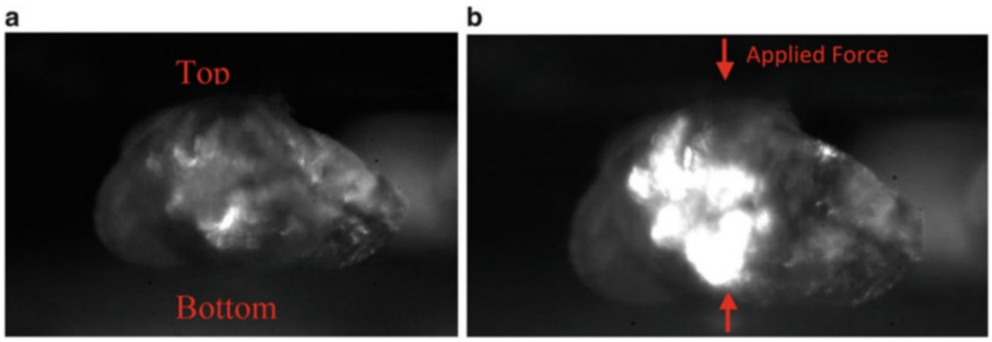

Fig. 44.2 Frames showing the progression of a grain from (**a**) intact to (**b**) fractured with increased reflectivity. The height of the grain is 0.486 mm

274 m/s; Liu and Nagle reported averages near 280 m/s [31]. The shock velocity-particle velocity Hugoniot intercept for dry sand was measured in plane strain experiments to be 243 m/s [32]. If we used the group transient time the average longitudinal wave speed would be nearer to 100 m/s. The longitudinal sound speed is reduced when water is added, possibly due to a reduction in grain-on-grain friction which would retard force chain transmissions. The longitudinal sound speed is rather constant over a wide range of moisture contents. As the moisture nears the volume fraction of sand (28 %), the sand becomes completely water saturated. The longitudinal sound speed for saturated sand increases relative to partially saturated sand, but does not recover to longitudinal sound speed of dry sand.

The average shear sound speed of dry sand was measured to be near 208 m/s, with a much larger variation between independent measurements for given grain arrangements, as indicated by the large vertical error bars. With the longitudinal and shear wave speeds we can calculate the elastic properties for dry sand. The average Poisson's ratio was 0.13 but varied from 0 to near 0.15 and the average elastic modulus was 120 MPa and bulk modulus of 36 MPa. The bulk sound speed of sand is 153 m/s, which is far below most shock velocity-particle velocity Hugoniot intercepts for sand [32].

44.2.2 Single Grain Static Fracture Experiments

This set of experiments was composed of two parts; the first was focused on observing the phenomenon wherein grains of sand would increase in reflectivity when experiencing an external force, and determining whether or not this increase was reversible once the force was removed and the second part of this experiment was aimed at gathering data on the stress/strain relationship for single grains of sand.

In the first experiment, a single grain of sand was placed in between two metal plates, and a force (i.e. pressure) was quasi-statically increased until the grain began to fracture and then eventually was completely crushed. This process was filmed with the Photron high speed camera, and a 1 kW Halogen light. The lighting was placed behind the camera so that all the light collected was reflected from the sand. This process of fracturing and crushing a grain was repeated 25 times. It was observed that the grains form crack faces which propagate throughout the grain, and this face is responsible for the increased reflectivity. Figure 44.2 shows the frame before (a) and the frame after (b) a crack face has formed (1 thousandth of a second apart); note the increase in reflectivity. Nearly identical phenomena has been observed in more controlled tests of pure quartz samples in a split Hopkinson bar configuration [33].

Although the grain has increased in reflectance it has not visibly failed, it has only been damaged. The grain remains intact until further strain causes it to accrue further damage and eventually catastrophically fail. In addition we appreciate that some fracture surfaces must form in an orientation such that light does not reflect back to the camera. Given the grain morphology, the planarity of the fracture surface and the angle of the light to the camera, it is unclear what percentage of the fracture surfaces can be detected using this method. If we correlate an increase in reflected light to damage and fracture, it is likely that more damage and fracture has occurred than is evident by an increase in reflectivity. However, on average, a strong correlation can be made.

In order to make certain that this phenomenon was not the result of a force or strain dependent luminescence this experiment was repeated in low light conditions. When this was done the camera did not measure any light; thus it was concluded that the increase in measured light is due to reflectance and not luminescence. Although it cannot be conclusively determined that the grain does not luminesce, such low levels of illumination (if present) are not detectable by our cameras.

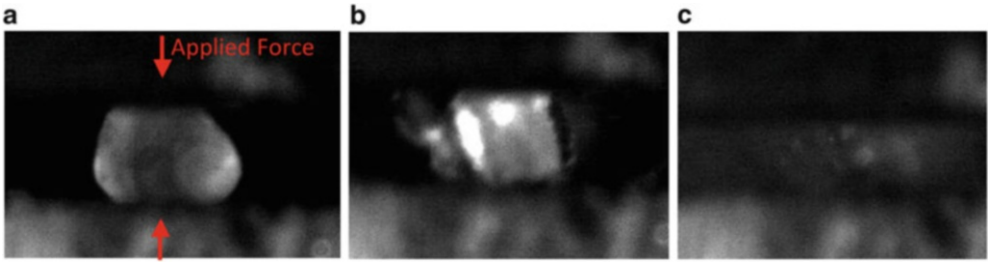

Fig. 44.3 Frames showing the progression of a grain from (**a**) intact to (**b**) fractured with fragments to (**c**) catastrophically fractured

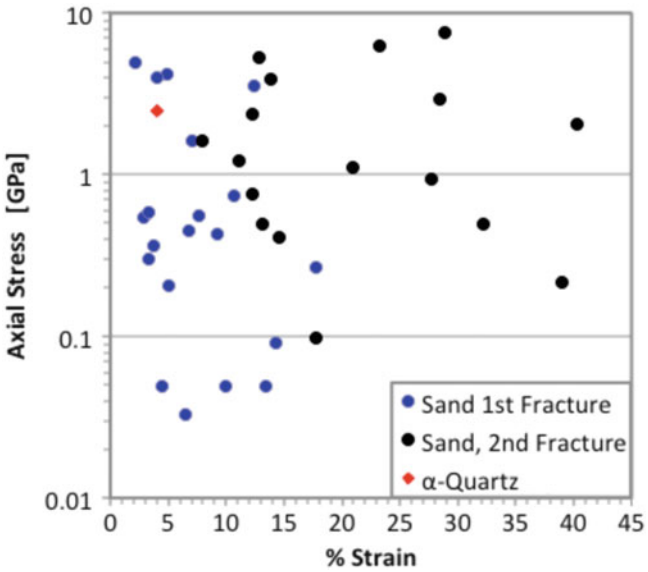

Fig. 44.4 Plot of "stress versus strain" for a single grain of sand and a Hopkinson bar data point for pure quartz [33]

When a video of a grain fracture event is viewed, the grain progresses from intact, then multiple fracture events occur, and eventually the grain fails catastrophically, Fig. 44.3. Typically shards of the grain spall before the grain catastrophically fails. For each different fracture a different amount of force (i.e. work) would be required to cause additional fracture surfaces to be created. This information shaped the direction in which the following grain fracture experiments were carried out.

In the second group of quasi-static experiments, a single grain was crushed using a force transducer on the top platen and a flat metal fixture on the bottom. A video of the grain being crushed was taken while collecting data from the force transducer. The camera and force transducer were synchronized. After the experiment was completed the video results were analyzed. The initial height of the grain was measured in pixels and was used as the base height since no force had yet been applied to the grain. This frame was also used to calculate the approximate cross-sectional area by assuming that the width and depth were equal. Then the frame before the first time the grain fractured was found, and once again the height of the grain in pixels was measured. The time that this frame occurred was used to find the corresponding force from the oscilloscope data. This was then repeated for the last fracture before the grain was completely crushed. These two data points were recorded as the first and second fractures respectively. This was repeated 20 times, and the results are presented in Fig. 44.4. In addition, the individual stress strain result obtained from controlled Hopkinson bar experiments on α-quartz is presented in Fig. 44.4 [33]. It is interesting to note that the results obtained in this work are within the range of the Hopkinson bar result.

These results are not intended to be a true stress–strain relationship. Given the morphology and composition of individual grains, the pre-damage and loading direction, these results represent a statistical envelope of axial loads in which one might expect grains to fracture. These results may be useful in giving an approximate average stress/strain that a single grain will undergo before catastrophically fracturing, which can be used in modelling the dart penetration experiment.

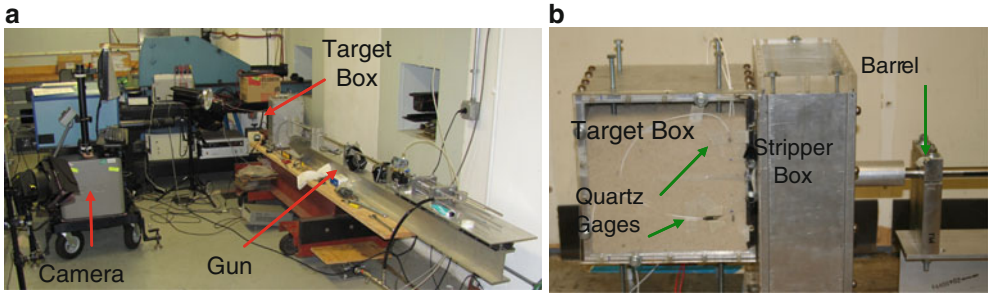

Fig. 44.5 Experiment setup of the (**a**) the gun and camera setup and (**b**) the target box

44.2.3 Gas Gun Experiments

Figure 44.5a presents a photograph of the test setup, showing the orientation of the horizontally mounted air driven gas gun, the target box and the high-speed camera. Figure 44.5b presents a photograph of the gun barrel, stripper box and target tank. Experiments were conducted such that the 1.27 cm diameter air gun launches a long rod projectile at approximately 100 m/s into a 35 cm (shot direction) $\times$ 25 cm $\times$ 18 cm tank filled with Ottawa sand.

The objective was to gain visual access to the semi-infinite target and produce two-dimensional planar photographs of the penetration event. Thus the target tank was constructed from optically accessible 1.0 cm thick polycarbonate (i.e. bullet proof glass) and the gun barrel was aligned to the tank such that the projectile remained in near contact with the polycarbonate view window for the first portion of the penetration event. A similar technique was used in the exploration of low speed impacts and impact crater formation due to small charge explosives [34, 35]. The aluminum projectiles (i.e. darts) used in these experiments were 10.16 cm long and 0.635 cm diameter with a flat nose and were launched with a full-bore 5 cm long nylon sabot. After exiting the barrel, the dart free flies through the stripper box which acts as a blast chamber. The dart enters a tapered section that guides it into the target box and along the view window. The dart penetrates a make-switch, which triggers the camera and oscilloscopes, just before entering the target box. The sabot is separated from dart in the stripper box by impacting a stripper plate once the dart is nearly 1 cm into the sand. The sabot is caught and held such that no blast air is allowed to enter the target tank. Two quartz PCB Piezotronics 208C01 pressure gauges were buried in the sand to measure the passing stress wave.

The penetration event was photographed using a Photron RS and/or a Cordin 550 camera. The Photron camera was used to visualize nearly the entire sand box field of view (FOV) of 26 cm $\times$ 22 cm with frame rates near 12,000 frames per second and a resolution of 512 $\times$ 432. The Cordin camera was configured to take 64 images at a resolution of 1,024 $\times$ 1,024 pixels with a FOV of 2.7 cm $\times$ 2.7 cm at an acquisition rate near 120,000 frames per second.

An aspect of these experiments that becomes important when viewing the results is the orientation of the camera and lighting. The cameras were placed approximately 36 cm from, and right angles to, the target window. Lighting was accomplished with two halogen lights placed approximately 72 cm from the target view window, behind the camera and slightly off angle in order to avoid bright spots in the camera FOV. Thus all the light collected by the camera was reflected from the sand grains. This is an important aspect of the photographic record where the light measured by the camera increases due to an increase in reflected light from fractured sand grains.

In the initial experiments a two-wave structure was observed propagating through the sand that was composed of a compaction wave (or bow shock) and a damage wave. The compaction wave detaches from the projectile and propagates through the sand at an average velocity near 100 m/s. The compaction wave's initial velocity was approximately 20 % greater than the projectile velocity, and decays as it traverses the target tank. The compaction wave removes porosity through the translation and rearrangement of grains and results in the formation of force chains.

The damage wave fractures grains in the region near the nose of the projectile. Evidence of this two-wave structure can be seen in Fig. 44.6, where the dart travels from right to left. The compaction wave is best identified by viewing a series of images (i.e. watching a movie) thus it has been highlighted here for clarity. The dart appears as a blur in the center-right of the Fig. 44.6b, c. Given the relatively low framing rate of these imagines the compaction wave and force chains appear as streaks. The damage wave appears as a brighter conical region near the nose of the projectile. Later, experiments were done to confirm that the fracture cone around the dart resulted from an increase in reflectivity from the increased surface area of the fractured grains. This will be discussed in greater detail below. From these initial experiments it was determined that the fracture cone was visible at launch velocities above 35 m/s, which means that at velocities above 35 m/s sand grain fracture is an important mechanism in the penetration event.

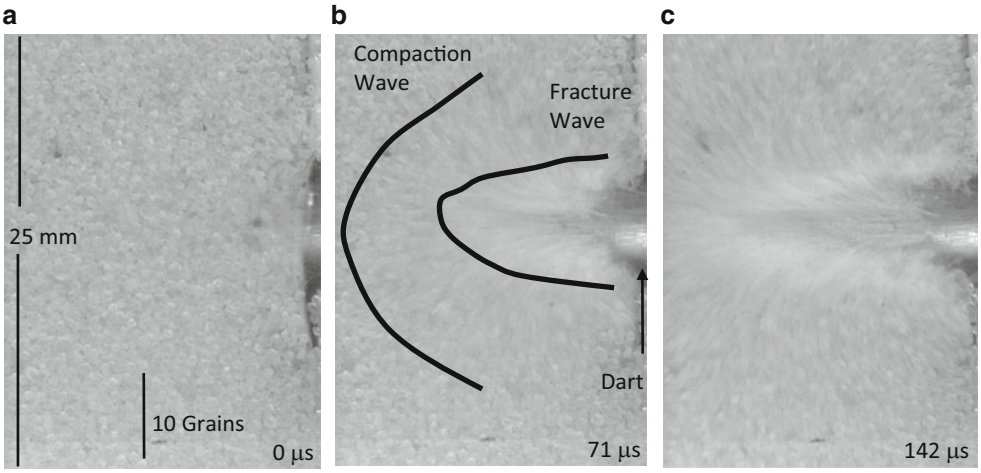

Fig. 44.6 Three frames 71 μs apart, showing the progression of the two-wave structure: compaction and fracture. Dart is moving right to left 100 m/s

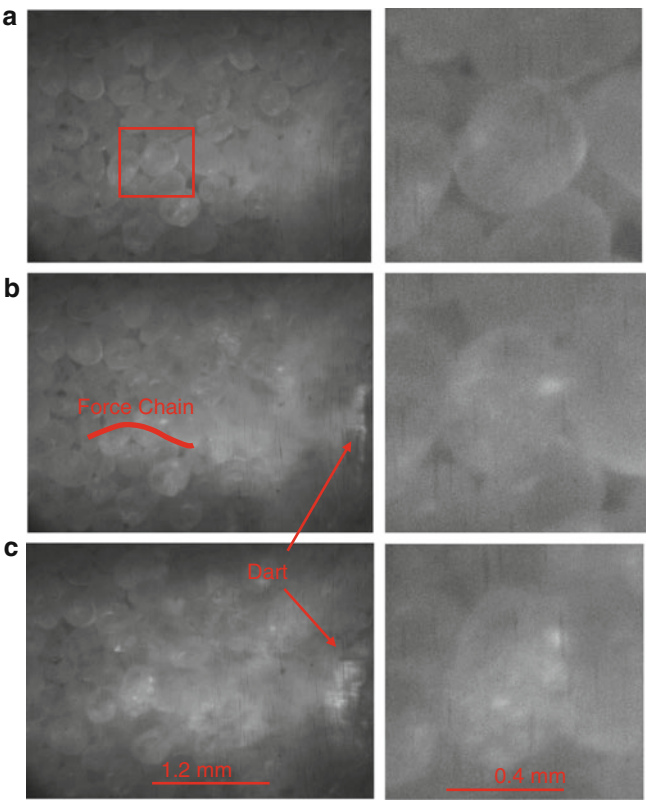

Fig. 44.7 Frames showing the progression from free grain to stress bridge formation to grain fracture. The right column presents an individual grain, highlighted in red in frame (**a**) of the left column, undergoing a dynamic fracture event. The time between frames (**a**) to (**c**) is approximately 80 μs

In order to further investigate the fracture cone region, high magnification and high framing rate images were obtained with a 1 megapixel Cordin 550 camera. This camera was used to obtain images at 175,000 frames per second. With this higher magnification individual grains can be tracked and the formation of force chains and fracture can be observed. Figure 44.7 presents a series of photographs in which the dart is traveling from right to left with an initial velocity near 100 m/s. These images illustrate individual grains being pushed together and rearranging, until coming into closer contact

with other grains and forming the force chains. Grains within these force chains increase in reflected light and subsequently fracture. An individual grain involved in this process is highlighted in Fig. 44.7a with a square and a magnified view of this grain as it forms a force chain and fractures is presented in the right column. This grain is initially ahead of the fracture wave in Fig. 44.7a. It becomes involved in a 3–5 grain force chain in Fig. 44.7b and there appears within the grain a brighter spot, i.e. an increase in reflectance. We believe this to be a result of grain damage, i.e. an increase in fracture surfaces within the grain, which results in greater reflectivity. Finally the grain catastrophically fractures and shatters into many smaller shards in Fig. 44.7c. There are multiple bright spots that emanate from the fractured shards. Note the total translation of the grain is quite small. It has fractured near the same location from which it started. Also note that to the right of the fractured grain there appears a rather diffuse, bright cloud, where it is difficult to distinguish individual grains. This is a collection of fracture grains, the fracture wave, and is the source of the "white trail" left behind by sand penetration which has been observed by others [6, 19].

Based on viewing multiple video records, it appears that for impact velocities near 100 m/s the force chains are on average 5–10 grains long. At any given frame of the video, approximately 75 % of the grains will be involved within a force chain. Thus one fourth of the grains in the FOV are free floating and not involved in a force chain. It is also important to note that there is very little grain rotation in front of the dart, grains are generally pushed in the direction in which the projectile is traveling. Finally, not all grains are involved in a force chain fracture. Only one grain needs to fracture to release the stress within the chain; the remaining grains are then free to be taken up by new force chains. With these experiments, the FOV is such that only grains directly in front of the projectile are viewed. In future testing we plan to move the FOV to view the shear regions to the side of the dart.

44.3 Numerical Calculations

A simple model consisting of a force balance can be constructed by considering only axial stress, Y, acting on the nose of the dart,

$$d^2x/dt^2 = \beta YA/m \tag{44.2}$$

$$x(t) = \mathrm{v}_0 t + \beta YAt^2/2m \tag{44.3}$$

where m and A is the mass and frontal area of the dart respectively. The stress acting on the dart is taken to represent only grain fracture, as presented in Fig. 44.4, where the average axial fracture stress is near 0.5 GPa. This equation can be integrated to give Eq. 44.3, where v_0 is the initial velocity of the dart. Since the dart surface area is in contact with individual grains and since not all grains fracture, included is a factor β, which is less than one and which reduces the total force acting on the nose. Beta was selected to be the solid volume fraction of the sand, 0.55, times the fraction of grains observed to fracture, 0.1, which results in a β factor of 0.055. Figure 44.8 presents the analytic solution, Eqs. 44.2 and 44.3, along with Eq. 44.1, the Charters and Summers relation, as compared to the experimental data. The simple analytic solution predicts the early time dart penetration where grain fracture dominates the forces acting on the nose of the dart. As the dart velocity

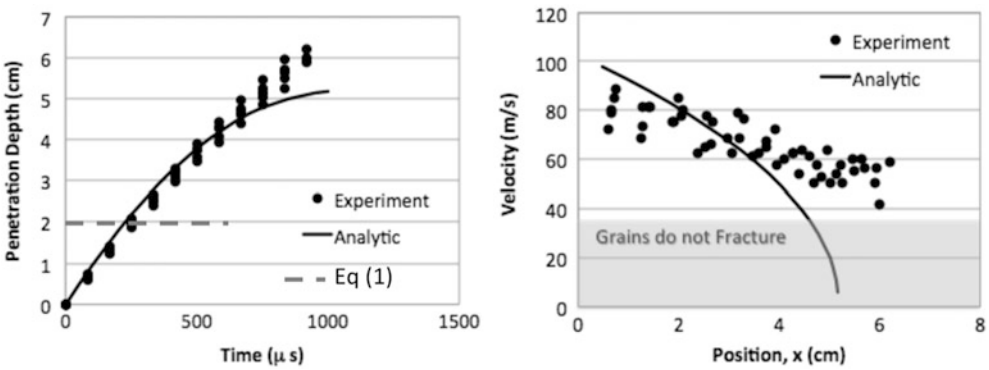

Fig. 44.8 Comparison of experimental and analytic penetration behavior. Below a threshold velocity near 35 m/s grains do not fracture

drops, and grain fracture is no longer observed, the analytic solution under predicts the dart penetration depth. Thus we conclude that other, lower magnitude forces, such as excavation and friction dominate the flow. The Charters and Summers relation predicts a total penetration depth of 2 cm, which is quite low compared to our data.

44.4 Conclusions

This work demonstrates a fundamental mechanism in the penetration of granular materials, namely the formation of force chains and dynamic fracture. Although this process has been observed in static experiments and demonstrated numerically, these are the first experiments (that we are aware of) that dynamically capture this phenomena experimentally. Grain fracture was not observed at velocities below 35 m/s but instead grains are displaced as the dart progresses through the sand. A quasi-static experiment was used to estimate the fracture strength of individual sand grains, the results of which were used to construct an analytic solution for the penetration event. This analytic solution under predicts the depth of penetration when grain fracture is no longer observed. The elastic properties of sand were measured however there is much scatter in the data which will be investigated further in the future.

Acknowledgements This work was funded by the Defense Threat Reduction Agency (DTRA) under contract HDTRA1-09-0045. We would like to thank Drs. Richard Lewis and Su Peiris for serving as program managers.

References

1. Byers RK, Chabai AJ, Walsh RT (1975) Predictions of projectile penetration phenomena and comparison with experiments in a soil medium. Sandia National Laboratories report, Albuquerque, NM, USA, 75–0174
2. Bernard RS, Creighton DC (1979) Projectile penetration in soil and rock: analysis for non-normal impact. US Army Engineer Waterways Experiment Station, technical report SL-79-15, Vicksburg, MS, USA
3. Richmond PW (1980) Influence of nose shape and L/D ratio on projectile penetration in frozen soil. US Army Cold Regions Research and Engineering Laboratory, special report 80–17
4. Forrestal MJ, Luk VK (1992) Penetration into soil targets. Int J Impact Eng 12:427–444
5. Allen WA, Mayfield EB, Morrison HL (1957) Dynamics of a projectile penetrating sand. J Appl Phys 28(3):370–376
6. Allen WA, Mayfield EB, Morrison HL (1957) Dynamics of a projectile penetrating sand Part II. J Appl Phys 28(11):1331–1335
7. Wang WL (1969) Experimental study of projectile penetration in Ottawa sand at low velocities. J Spacecraft Rockets 6(4):497–498
8. Savvateev AF, Budin AV, Kolikov VA, Rutberg PG (2001) High-speed penetration into sand. Int J Impact Eng 26(1):675–681
9. Houa M, Penga Z, Liua R, Wua Y, Tiana Y, Lua K, Chan CK (2005) Projectile impact and penetration in loose granular bed. Sci Technol Adv Mater 6:855–859
10. Bless SJ, Berry TD, Pedersen B, Lawhorn W (2009) Sand penetration by high-speed projectiles. In: Shock proceedings from the shock compression of condensed matter-2009, Nashville
11. Boguslavskii Y, Drabkin S, Salman A (1996) Analysis of vertical projectile penetration in granular soils. J Phys D: Appl Phys 29:905–916
12. Collins AL, Addiss JW, Walley SM, Promratana K, Bobaru F, Proud WG, Williamson DM (2011) The effect of rod nose shape on the internal flow fields during the ballistic penetration of sand. Int J Impact Eng 38:951–963
13. Collins JA, Sierakowski RL (1976) Studies on the penetration Of Eglin sand. AFRL report AFATL-TR-76-122
14. Forrestal MJ, Longcope DB, Lee LM (1983) Analytical and experimental studies on penetration into geological targets. In: Proceeding of the interaction of non-nuclear munitions with structures. Report AD-A132-115, US Air Force Academy, Colorado, pp 23–26, May 1983
15. Savvateevetal AE (2001) High-speed penetration into sand. Int J Impact Eng 26:675–681
16. Stone GW (1994) Projectile penetration into representative targets Sandia report 1490 UC-704 Oct 1994
17. Taylor T, Fragaszy RJ, Carlton LH, ASCE Members (1991) Projectile penetration in granular soils. J Geotech Eng-ASCE 117:4
18. Wang WL (1969) Experimental study of projectile penetration in Ottawa sand at low velocities. Engineering notes, p 497, Apr 1969
19. Watanabe K, Tanaka K, Iwane K, Fukuma S, Takayama K, Kobayashi H (2011) Sand behavior induced by high-speed penetration of projectile. AFOSR report, AOARD-094011, Tokyo, Feb 2011
20. Yankelevsky DZ (1997) Local response of concrete slabs to low velocity missile impact. Int J Impact Eng 19(4):331–343
21. Corbett GG, Reid SR, Johnson W (1996) Impact loading of plates and shells by free-flying projectiles: a review. Int J Impact Eng 18:141–230
22. Forrestal MJ, Altman BS, Cargille JD, Hanchack SJ (1994) An empirical equation for penetration depth of ogive-nose projectiles into concrete targets. Int J Impact Eng 15(4):395–405
23. Gran JK, Frew DJ (1997) In-target radial stress measurements from penetration experiments into concrete by ogive-nose steel projectiles. Int J Impact Eng 19(8):715–726
24. Tate A (1967) A theory for the deceleration of long rods after impact. J Mech Phys Solids 15:387–399
25. Grove B (2006) Theoretical considerations on the penetration of powdered metal jets. Int J Impact Eng 33:316–325
26. Evans WM, Pack DC (1951) Penetration by high-velocity ('Munroe') jets: II. Proc Phys Soc B 64:303
27. Tate A (1986) Long rod penetration models Part II. Extensions to the hydrodynamic theory of penetration. Int J Mech Sci 28(9):599–612

28. Charters AC, Summers JL (1959) Comments on the phenomena of high-speed impact. NOLR1238. U.S. Naval Ordance Lab, White Oak, pp 200–221
29. Zukas JA, Nicholas T, Swift HF, Greszczuk LB, Curran DR (1992) Impact dynamics. Kriger Publishing Company, Malabar
30. Orphal DL (2006) Explosions and impacts. Int J Impact Eng 33:496–545
31. Liu C, Nagel S (1993) Sound in a granular material: disorder and nonlinearity. Phys Rev B 48(21):15646–15650
32. Brown JL, Vogler TJ, Grady DE, Reinhart WD, Chhabildas LC, Thornhill TF (2007) Dynamic compaction of sand, shock compression of condensed matter. In 15th APS topical conference on shock compression of condensed matter, vol 52, no. 8, Sunday–Friday, June 24–29, 2007; Kohala Coast, Hawaii
33. Kimberley J, Ramesh KT, Barnouin OS (2010) Visualization of the failure of quartz under quasi-static and dynamic compression. J Geophy R 115:B08207
34. Houa M, Penga Z, Wua R, Liua Y, Tiana Y, Lua K, Chanb CK (2005) Projectile impact and penetration in loose granular bed. Sci Technol Adv Mater 6:855–859
35. Piekutowski A (1980) Formation of bowl-shaped craters. In: Proceedings of 11th lunar planetary science conference, Houston, TX, USA, pp 2129–2144

Chapter 45
Poncelet Coefficients of Granular Media

Stephan Bless, Bobby Peden, Ivan Guzman, Mehdi Omidvar, and Magued Iskander

Abstract We have developed a new technique for precise measurement of deceleration of projectiles in sand. It uses a PDV to observe the back of a sphere. Impacts were conducted up to 300 m/s, and trajectories were observed for more than 10 projectile diameters. The precise measurements allow us to calculate Poncelet parameters for spheres in dry and saturated sand and fused quartz. We find that the coefficients needed to describe the data change at about 100 m/s, and Poncelet values that give accurate estimates of deceleration will usually fail to predict ultimate penetration depth. For comparing materials, we find sand is harder to penetrate than fused quartz. Dense materials are harder to penetrate than less dense materials. Dry materials are harder to penetrate than saturated materials.

Keywords Granular materials • Sand • PDV • Poncelet

45.1 Introduction

Travel of projectiles through sand has been a topic of interest to military and civil engineers for centuries. The high strain rate properties and penetration mechanics of sand have been extensively reviewed in two recent papers [1, 2]. Modern experimental work in this field is often dated from the studies of Allen [3], who measured penetration and penetration rates for hollow rods. More recent studies have done much to reveal the phenomenology of sand penetration (e.g. [4–7]).

Understanding projectile penetration in sand proceeds through the development of mesoscale models The greatest promise lies in numerical models based on evolving concepts for granular flow, including force chain evolution [8], particle crushing [9], and development and evolution of heterogeneities (e.g. [8, 10]). Evaluation of models will require precision data for the deceleration of projectiles during penetration, since (by Newton's third law of motion) the stress on the projectile is also the stress on the sand at the projectile interface. Concurrent with mesoscale modeling, considerable engineering progress can also be made using continuum-level phenomenological models, of which generally take the form of Eq. 45.1.

$$F = M\frac{dV}{dt} = -AC\rho V^2 - BV - AR \tag{45.1}$$

Here F is the force on the projectile, M and V are the mass and velocity of the projectile, ρ is the density of the penetrated medium, and A is the projectile frontal area. Here the velocity squared term is usually assumed to represent inertia. It depends on velocity squared because of an argument that also dates back to Newton: in order to advance into a medium at a velocity V, the penetrator must move material aside at a velocity proportional to V. The coefficient C plays a role similar

S. Bless (✉) • I. Guzman • M. Omidvar • M. Iskander
New York University Polytechnic Institute, New York, USA
e-mail: sbless@poly.edu

B. Peden
Department of Engineering Mechanics, University of Texas at Austin, Austin, USA

B. Song et al. (eds.), *Dynamic Behavior of Materials, Volume 1: Proceedings of the 2013 Annual Conference on Experimental and Applied Mechanics*, Conference Proceedings of the Society for Experimental Mechanics Series,
DOI 10.1007/978-3-319-00771-7_45,

to a drag coefficient, CD, and it expresses the role of nose shape. Note however, that in conventional aerodynamics, the area times velocity squared is multiplied by 0.5 CD, so for similar flow behavior, C = CD/2. The R term is usually considered to be a static strength term, proportional to the yield strength of the material. Dimensional arguments imply that the middle term is due to viscous effects. Equation 45.1 written without the viscous term (B = 0) is known as the Poncelet Equation.

Experimentalists need to provide data that can discriminate between models. As is the case in many other applications of penetration mechanics, measurement of depth of penetration (DOP) does not provide an adequate basis for model calibration or verification. The reason is that the there are several different types of forces that act on projectiles. Even in the simple Poncelet model with the interpretation given above, these include inertia which dominates at high velocity (but which, by itself, never brings a projectile to rest) and the strength, which dominates at low velocity.

Distinguishing between models can only be accomplished through measurements of deceleration. Data for deceleration at a range of velocities can be used to evaluate the terms in Eq. 45.1 Unfortunately, since deceleration is the second derivative of displacement, it is quite difficult to obtain time-resolved deceleration data from displacement measurements, such as are obtained with a high speed camera. What is needed is a way to directly measure deceleration or velocity. Direct measurement of deceleration is possible using a VISAR [11]. However, using a VISAR for measurement of deep penetration into a granular material probably presents insurmountable difficulties associated with limited depth of field and sensitivity to amplitude fluctuations. We have used direct measurement of velocity. This is made possible by application of the newly-developed PDV instrument (e.g. [12–14]).

45.2 Experimental Techniques

Projectiles used in this study were steel ball bearings launched with a compressed gas gun. For the PDV experiments, the diameter was 14 mm. Targets for the experiments are at least 150 mm × 150 mm. We have separately published details of the PDV techniques, gun designs, and sample preparation [14].

In dry materials the PDV was able to follow the motion of the spherical projectile until almost rest. An example of a PDV spectrogram is shown in Fig. 45.1 for a shot into dry sand at 300 m/s. The color indicates the spectral intensity for a given wavelength, and the narrow red line indicates there is very little uncertainty. There is an initial ringing in the velocity which is probably due to elastic waves in the projectile. Beyond that, the velocity history is remarkably smooth. There appears to be an abrupt change in decay characteristic at about 75 m/s.

For shots into saturated material, the PDV's view of the projectile was apparently cut off by ejecta, and good data were only obtained for about half of the penetration. For example, Fig. 45.2 shows velocity data for dense oil-saturated quartz.

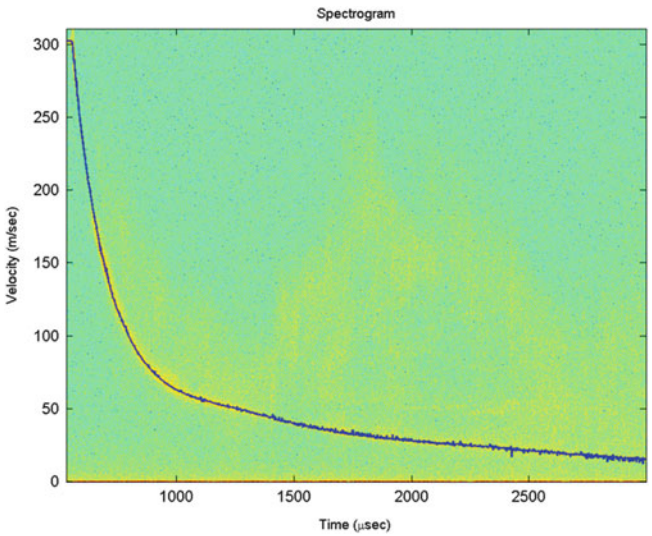

Fig. 45.1 Velocity history of a 14-mm sphere penetrating sand (shot 1421) (color figure in online)

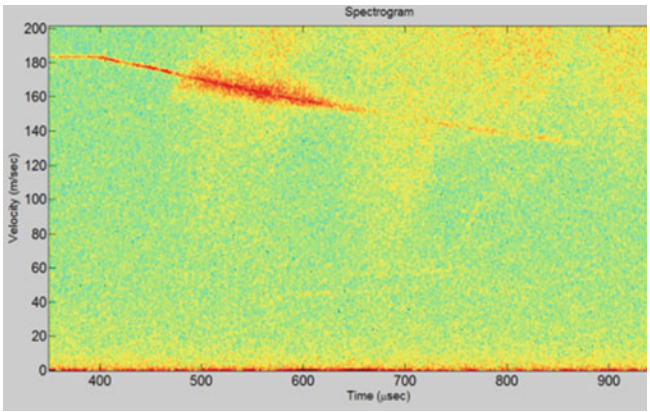

Fig. 45.2 Velocity history of a 14-mm sphere penetrating oil-saturated quartz (shot 1436)

Table 45.1 Conditions tested with the PDV that returned good data

Shot ID	Velocity (m/s)	Target	Density (g/cm^3)
1411	306	Quartz/oil	1.52
1413	303	Quartz/oil	1.52
1414	283	Quartz/oil	1.52
1436	183	Quartz/oil	1.52
1437	166	Quartz/oil	1.52
1429	300	Dense packed quartz	1.30
1430	303	Loose packed quartz	1.19
1420	299	Dense packed sand	1.82
1421	302	Dense packed sand	1.82
1426	270	Dense packed sand	1.82
1427	306	Loose packed sand	1.59
1428	299	Loose packed sand	1.59
1415	304	Water/sand loose	1.99
1418	302	Water/sand loose	1.99
1426	299	Water/sand dense	2.12
1424	303	Water/sand loose	2.12
1425	304	Water/sand loose	2.12

45.3 Experiments

Tests using the PDV were conducted on dry crushed quartz glass and oil-saturated quartz glass, as well as dry sand and water-saturated sand. The sand targets were prepared at two different densities. Table 45.1 is a matrix for the PDV tests that returned good data.

In addition, two DOP (depth of penetration tests) tests were conducted on saturated quartz at 190 m/s. The penetration was 266 and 274 mm.

45.4 Experimental Results

It can be seen from Figs. 45.1 and 45.2 that the velocity decay as a function of time is approximately exponential, down to about 80–100 m/s. This is what is predicted from Eq. 45.1 when the first term dominates, e.g. a simple drag law with the retarding force proportional to V^2. Below 80 m/s, their is a large reduction in slope of the V, t line.

Figure 45.3 is a comparison of all the PDV experimental results for impacts at about 300 m/s, grouped by target medium, and plotted as velocity vs penetration depth. The initial slope is almost linear with a slight positive curvature. According to the Poncelet equation, as the R term begins to dominate, the curvature will become negative, and the V, x curve will intersect the $V = 0$ axis at a perpendicular angle. It can be seen that for conditions that were repeated, the velocity decay curves are remarkably similar.

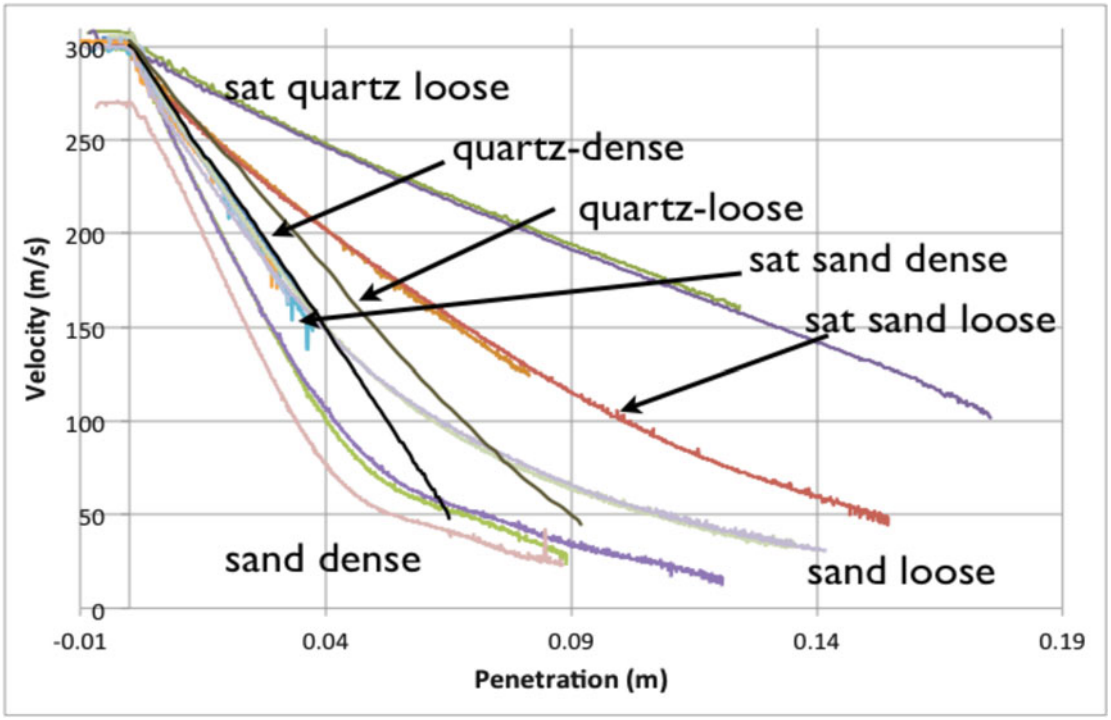

Fig. 45.3 Comparisons of velocity decay in different materials

There is a definite ranking of the stopping power of the different media. Sand was harder to penetrate than fused quartz. Dense materials were harder to penetrate than less dense materials. Dry materials were harder to penetrate than saturated materials.

45.5 Poncelet Parameters

Initial insight into Poncelet parameters can be obtained from DOP data. When the Poncelet equation is solved for final penetration, and assuming spherical projectiles of diameter d, the result is

$$P = \frac{\rho_p d}{3\rho C} \ln\left[\frac{\rho C V_0^2}{R} + 1\right] \tag{45.2}$$

For a given material, the penetration of a sphere (normalized by diameter) would scale as the ratio of penetrator to target density. The DOP data presented above can be combined with data from [15], which includes 10-mm diameter spheres striking quartz oil targets. Three different density quartz/oil targets were used, loose (1.56–1.58 g/cm^3, similar to our material), medium dense (1.60–1.63 g/cm^3) and dense (1.67 g/cm^3). The projectiles were aluminum, steel, or tungsten carbide. A correction from the low density in [15] to the density used here was made by computing the change of p/d with density, then the change in that ratio with velocity, then extrapolating to the velocity in our DOP test. (The correction was 9 %.) It is indeed the case, as shown in Fig. 45.4 the penetration generally scales as projectile density. However, there is more scatter for the low density material.

Poncelet parameters C and R can be obtained by curve fitting the PVD data. Only data above 100 m/s were used because it was clear that for all materials except dry fused quartz, below that velocity a lower value of C was required. The values of R were adjusted to within about 0.5 MPa and C within 0.05 to maximize the fit between the impact velocity and 100 m/s. Fits were judged by the RMS deviation from the data.

Figure 45.5 shows illustrative data for dense and loose dry sand. For loose sand, the best rms fit for $300 > V > 100$ m/s was obtained with $R = 0$ and $C = 0.79$. Other shots in dry loose sand resulted in almost identical values. However, although the data for dense sand the RMS fit was substantially better with $R = 17$ MPa and $C = 0.75$; this was true for each of the

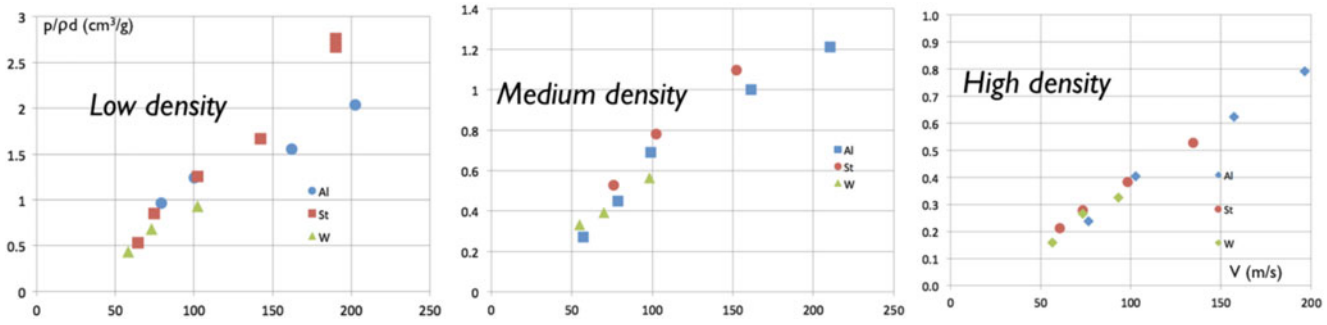

Fig. 45.4 Comparison of penetration depth of various spherical projectiles in quartz-oil of three different densities (Data from this paper plus [15])

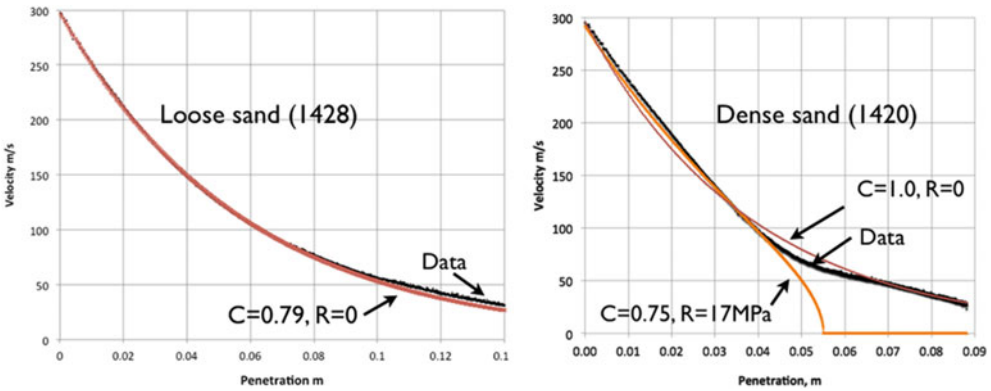

Fig. 45.5 Representative data for loose and dense dry sand compared with Poncelet best fits

shots into dry dense sand. In both cases, the best Poncelet fit for $V > 100$ m/s is clearly inadequate for lower velocities. Figure 45.5 also shows the fit for shot 1420 with $R = 0$. Although it is clearly not as good for $V > 100$ m/s as with $R = 17$ MPa, it follows the entire deceleration remarkably well. Of course, $R = 0$ predicts inifinite penetration, so eventually this Poncelet fit must diverge considerably from the actual penetration path. The other shots in dense dry sand when fit with $R = 0$ had C up to 1.2 with a mean of 1.06. The $R = 0$ solution fits whole data set better, even though it is less accurate for $V > 100$ m/s.

The Poncelet fit for dry granulated fused quartz is shown in Fig. 45.6. Again the data above 100 m/s are fit very well with the two parameter Poncelet model. However, for the fused quartz, the strength parameter, R, is far from zero. For the loose material, $R = 18.5$ MPa, $C = 0.5$; for the less dense material, $R = 25$ MPa, $C = 0.55$. Also, it is again true that the single set of Poncelet parameters does a very inadequate job of describing the final penetration depth.

The Poncelet fits for representative water saturated sand and oil saturated quartz shots are shown in Fig. 45.7. For dense water saturated sand, there was a gap in the data. There were three shots that gave virtually identical velocity decay, but only to about 170 m/s, at which point the signal was lost. In shot 1419 the signal recovered at 40 m/s. The Poncelet fit to the velocity data for $V > 150$ m/s were $C = 0.5$ $R = 10$ MPa. However, these values predict a velocity of 6 m/s at the time when the actual velocity was observed to be 40 m/s. Thus, this result is consistent with the others – fitting Poncelet parameters at $V > 100$ m/s does not produce a good estimate of the final penetration depth. Moreover, for the loose wet sand, even above 100 m/s, there is no resolvable strength; $R = 0$. However, the best-fit Poncelet curves ($C = 0.4$) dips above and below the data.

Both of the quartz-oil shots at 300 m/s impact velocity were very well fit by the Poncelet curves; they also had no strength ($R = 0$) and $C = 0.27$. However, the two other shots at below 200 m/s were best fit with $C = 0.21$ and 0.25 and $R = 0.6$ MPa. This trend suggests that the Poncelet parameters may evolve during penetration, with C decreasing and R increasing. Unfortunately, there were not enough data to adequately evaluate this hypothesis.

Table 45.2 summarizes the data for Poncelet coefficients for velocities exceeding 100 m/s. Systematically, as materials are saturated, the drag parameters drops and the strength drops.

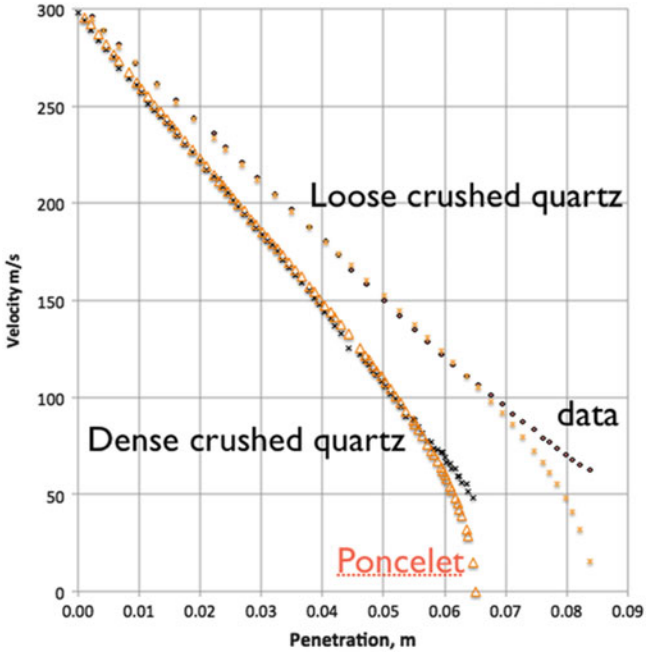

Fig. 45.6 Data for dry crushed quartz glass, compared to Poncelet model

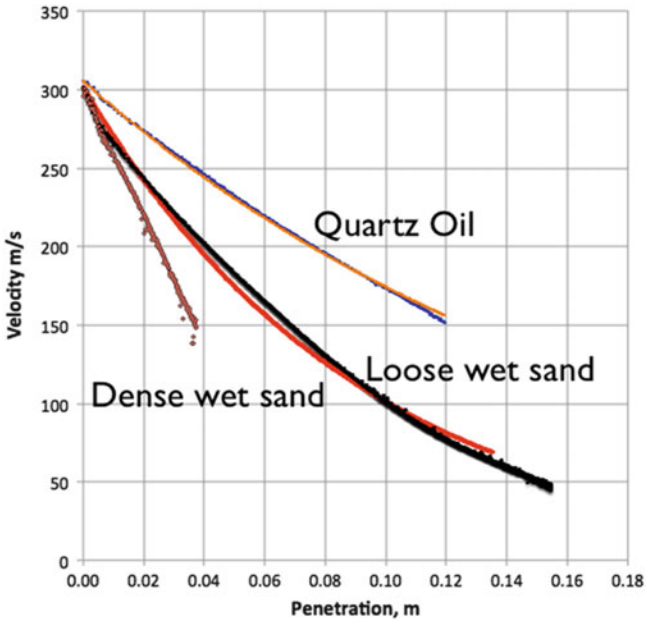

Fig. 45.7 Data (*black lines*) and Poncelet fits for saturated materials

Table 45.2 Summary of Poncelet coefficients from fitting deceleration data from 300 to 100 m/s

Material	Density	C	R(MPa)
Crushed quartz glass	1.30	0.52	22
Oil saturated quartz glass	1.52	0.21–0.26	0
Loose sand	1.59	0.79–0.81	0
Water saturated loose sand	1.99	0.4	0
Dry dense sand	1.82	0.75	17
Water saturated dense sand	2.12	0.5	10

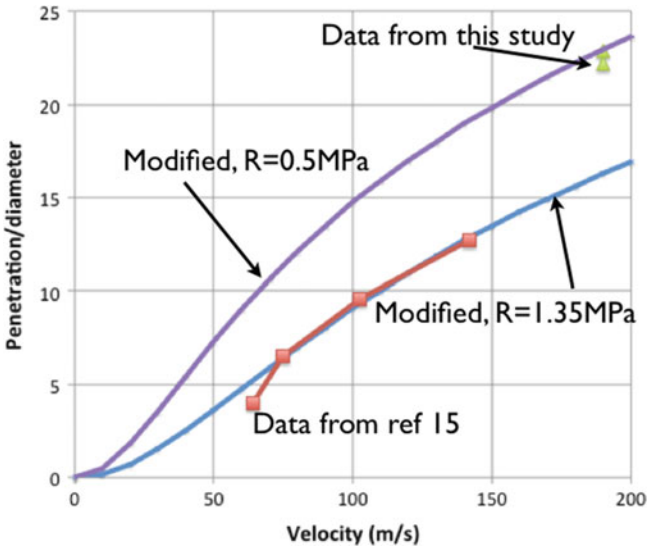

Fig. 45.8 Modifications of R value in Poncelet fit for quartz/oil to match DOP data. C = 0.25

The PDV data suggest that much penetration takes place at low velocity. This was also noted in [7] for rods penetrating sand. There is an overlap in impact velocity for the PDV experiments in quartz oil at V < 200 m/s and the DOP data obtained here as well as that reported in [15], with which we can compare Poncelet curves derived from PDV measurements with actual penetration depth. Equation 45.2 is used to compute penetration. Very small changes in R (which scarcely affect the fit to the dynamic data) can account for the final penetration depths. However, a single value of R cannot match all of the data. This is shown in Fig. 45.8. Quartz-oil in [15] was slightly denser than the sand used in this study, and a modest dependence of R on density might account for the results shown in Fig. 45.8.

45.6 Discussion

For granular materials, it is usually found that the shear strength, Y, is proportional to the pressure, P, which can be expressed as $Y = \alpha P$. If we approximate $P = \rho V^2/2$, and add this term to C, then we get

$$C = C_i + \alpha/2. \tag{45.3}$$

where C_i is the drag coefficient due purely to inertial forces. A value of $\alpha = 1.26$ is given by [16]. The inertial drag for high Reynolds number is about 0.2. Together, we get the approximation C = 0.8. This in excellent agreement with the measured value for dry sand for V > 100 m/s.

For a liquid saturated medium, one would expect α near zero, and the value of the drag coefficient would be similar to that of the liquid. This is the case for oil. For water, C is about twice the value expected from the effect of water alone.

For all of the sand materials tested there is a bifurcation in behavior at about 100 m/s. The Poncelet penetration equation can be used to fit deceleration data above that speed with very good precision, but those values will not give a useful estimate of the final penetration. The reason is that the deceleration history is only weakly sensitive to the R parameter; DOP on the other hand is very sensitive to R. For quartz materials, the situation is less severe; values of Poncelet coefficients that are compatible with the high speed deceleration data can give adequate depth of penetration predictions.

Acknowledgements The experiments were carried out at the Institute for Advanced Technology at the University of Texas at Austin (now closed). The authors are grateful for the help of IATs technical staff in conducting the experiments. This work was sponsored by the Defense Threat Reduction Agency under grant HDTRA1-10-1-0049

References

1. Omidvar M, Iskander M, Bless S (2012) Stress–strain behavior of sand at high strain rates. Int J Impact Eng 49:192–213
2. Omidvar M, Iskander M, Bless S (2013) Projectile penetration into sand. Submitted to Int J Impact Eng
3. Allen WA, Mayfield EB, Morrison HL (1957) Dynamics of a projectile penetrating sand. J Appl Phys 28:370–376

4. Borg JP, Morrissey M, Perich C, Vogler T, Chhabildas L (2013) In situ velocity and stress characterization of a projectile penetrating a sand target: experimental measurements and continuum simulations. Int J Impact Eng 51:23–35
5. Flis WJ, Jann D, Shan L (2008) Supersonic penetration by wedges and cones into dry sand. In: Proceedings of 14th International symposium ballistics, Quebec City, Canada, pp 22–26 Sept 2008
6. Savvateev AF, Budin AV, Kolikov VA, Rutberg PG (2001) High-speed penetration into sand. Int J Impact Eng 26:675–681
7. Bless SJ, Cooper W, Watanabe K (2011) Penetration of rigid rods into sand. In: International symposium on ballistics, Maimi, Sept 12–15 2011
8. Kondic L, Fang X, Losert W, O'Hern CS, Behringer RP (2012) Microstructure evolution during impact on granular matter. Phys Rev E. 85:011305-1-17
9. Cooper WL (2011) Communication of stresses by chains of grains in high speed particulate media impacts. Dynamic behavior of materials. In: Proceedings of Soc for Exp Mech, Series 99, Uncasville, CT, USA, vol 1, pp 99–107
10. Gimbert F, Amitrano D, Weiss J, Combe G (2012) From quasi-static to dense flow regime in compression frictional granular media, arXiv 12081930
11. Barker LM, Hollenbach RE (1970) Shock-wave studies of PMMA, fused Silica, and sapphire. J Appl Phys 41:4208–4226
12. Strand OT, Goosman D, Martinez C, Whitworth C (2006) Compact for high speed velocimetry using heterodyne techniques. Rev Sci Inst 77:83108
13. Levinson S, Satapathy S (2009) High-resolution projectile velocity and acceleration measurement using photonic doppler velocimetry. In: Proceedings of 16th American Physical Society topical conference shock compression of condensed matter, Nashville, TN, USA, 28 June–3 July 2009
14. Peden R, Omidvar M, Bless S, Iskander M (2013) Photonic-doppler-velocimetry for study of rapid penetration into sand. Submitted to Geotech Test J
15. Guzman I, Iskander M (2013) Geotechnical properties of sucrose-saturated fused quartz for use in physical modeling. To appear in Geotech Test J
16. Laine L, Sandvik LA (2001) Derivation of mechanical properties for sand. In: Proceedings of 4th Asia-Pacific conference on shock and impact loads on structures, Singapore, Nov 2001 pp 361–368

Chapter 46
Effect of Moisture on the Compressive Behavior of Dense Eglin Sand Under Confinement at High Strain Rates

Huiyang Luo, William L. Cooper, and Hongbing Lu

Abstract Dynamic compressive behavior of moist Eglin sand (Quikrete #1961 sand quarried in Pensacola, FL) under confinement was characterized using a long split Hopkinson pressure bar (SHPB). Moist sand grains were confined inside a hollow cylinder of hardened steel and capped by cemented tungsten carbide (WC) cylindrical rods with the same mechanical impedance as steel bars. A high-vacuum grease was used to seal the gaps to prevent leaking of moisture from the cavity. A given mass of water was added into dry sand. This assembly was subjected to repeated manual shaking to consolidate sand to attain the given bulk mass densities, and allow the water to be evenly-distributed around the sand grains. After 2 days of setting, the sand assembly is then sandwiched between incident and transmission bars on SHPB for dynamic compression under high strain rate. Sand specimens of five moisture contents in weight ratios of 0 %, 4.2 %, 8.2 %, 12.4 % and 16.5 %, were characterized to determine the volumetric and deviatoric behavior at high strain rates, and the moisture effect was discussed. The stresses-strain relationship and the compressibility of sand were determined as a function of sand moisture.

Keywords Modified Split Hopkinson pressure bar (SHPB) • Moisture • Dynamic compaction of sand • Confinement • Hydrostatic pressure

46.1 Introduction

Sand has many engineering applications such as for use as a construction material widely used in civil engineering structures and highways, and a raw material for fabrication of glass and silicon. Sand is often used to provide ballistic protection for military structures. Understanding the mechanical behavior of sand is also important to investigate the interaction of blast wave induced by improvised explosive devices with military vehicles and personnel, as well as earthquakes and landslides. Numerous researches on the behavior of sand for geological and civil engineering applications focus primarily on the mechanical behavior at low stress levels and under quasi-static loading conditions [1–4]. Its mechanical behavior under relatively high stresses and high strain rates has not been well understood, due to the limitations at that time in dynamic characterization of sand using conventional split Hopkinson pressure bar (SHPB).

The mechanical behavior of geomaterials has been characterized at high strain rates on sand and soil with moisture [5], dry soft soil [6], dry clayey/silty soil [7], and dry sand [8], etc. Pulse shaping techniques, developed in recent years for SHPB, can facilitate in establishing dynamic equilibrium and constant strain rate conditions necessary in a valid dynamic compression test [9]. For the dynamic behavior of sand, a modified SHPB with pulse shaping technique has been used to characterize the behavior of sand confined in a steel sleeve to determine the effects of moisture content [10], strain rate and confinement [11]. Recently, Luo et al., successfully developed a technique to prepare sand samples with consistent mass densities for dynamic compression on SHPB [12], combined with pulse shaper and strain gage attached on the outer surface of confining cylinder tube. Further, with the use of this technique, the effects of particle size of dense sand was determined on

H. Luo • H. Lu (✉)
Department of Mechanical Engineering, The University of Texas at Dallas, Richardson, TX 75080, USA
e-mail: hongbing.lu@utdallas.edu

W.L. Cooper
Air Force Research Laboratory, Eglin Air Force Base, Eglin, FL 32542, USA

B. Song et al. (eds.), *Dynamic Behavior of Materials, Volume 1: Proceedings of the 2013 Annual Conference on Experimental and Applied Mechanics*, Conference Proceedings of the Society for Experimental Mechanics Series,
DOI 10.1007/978-3-319-00771-7_46,

the compressive behavior under high strain rates [13]. The same dry Eglin sand was also investigated under triaxial loading through active hydraulic-pressure confinement up to 100 MPa pressure on SHPB at high strain-rates [14]. Stress–strain behavior of sand was also recently reviewed at high strain rates [15]. The stress–strain curve at high strain-rate was necessary input for constitutive modeling simulation subjected to blast [16]. We report the results on the compressive behavior of assorted sand with different moisture contents under stiff confinement provided by a hollow steel cylinder (12.7 mm inner diameter and 19.3 mm outer diameter) on a modified long SHPB, to determine the dependence of dynamic mechanical behavior of the sand on the moistures.

46.2 Experimental

In this investigation, a 11 m long modified SHPB was used with a pulse shaping technique to apply dynamic compression over relatively long loading time (up to ~1.5 ms) and to reach relatively high compressive strains [17, 18]. The SHPB, as shown schematically in Fig. 46.1a, consists of a solid stainless steel bars (7.5 m long for the incident bar and 3.66 m long for the transmission bar) with an outer diameter of 19 mm and a strain data acquisition system. Instead of sand having grain in directly contact with bar ends, tungsten carbide cylindrical rods, was inserted between sand grains and bars ends, to prevent sand grain indentation into bar ends. To allow preparation of sand samples with consistent mass densities, we employed an assembly to prepare a sand specimen, and then directly used it in the SHPB apparatus for dynamic compression.

The assembly consists of two cemented WC rods with a diameter of 12.7 mm and a hollow high carbon steel cylinder. The WC rods have a mechanical impedance that matches well with both the incident and transmission stainless steel bars with a diameter of 19 mm [19, 20]. Sand grains were first poured into the hollow steel cylinder with one end closed by a WC rod. A schematic diagram of sand assembly is shown in Fig. 46.1b. The total mass of the assembly, including sand, is less than 200 g, so that it can be easily shaken manually to consolidate the sand sample to attain maximum initial mass densities. 2.0000 g of sand was added into the hollow steel tube capped with one WC rod, monitored by weighting with a high-resolution digital balance (Denver Instrument APX-200, 0.1 mg resolution, 200 g capacity). For the dry sand specimen, sand grains were confined inside a hollow cylinder of hardened steel and capped by WC cylindrical rods. High-vacuum grease was used to seal the gaps between WC rods and the steel tube. For moist sand specimen, a given mass of water was added into dry sand by weighting the WC rod on sand specimen. By shaking the assembly (more than 30 min), sand samples with maximum initial mass densities can be prepared, through monitoring the length of the enclosed sand sample by measuring the total length of the sand assembly with a caliper. The repeated manual shaking also allows the water to be evenly-distributed around the sand grains. After 2 days, it was weighted again, and was then sandwiched between incident and transmission bars on SHPB for dynamic compression under high strain rates. Sand specimens of five moisture contents in weight ratios of 0 %, 4.2 %, 8.2 %, 12.4 % and 16.5 %, were characterized to determine the dynamic behavior at high strain rates.

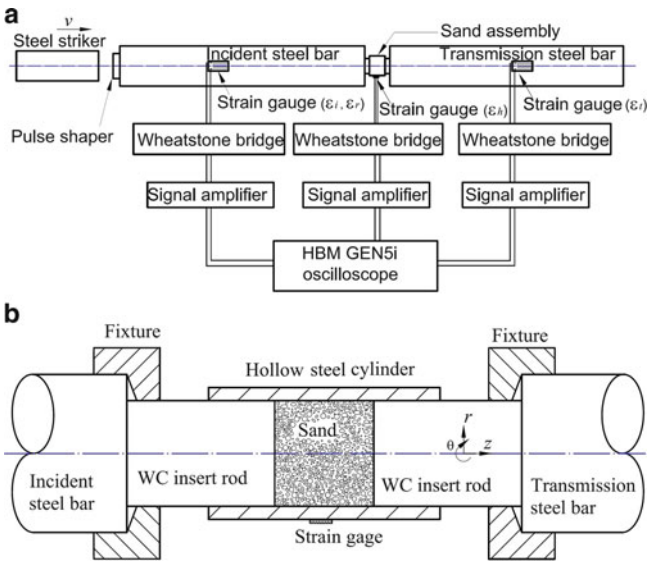

Fig. 46.1 Schematic SHPB setup for testing confined sand. (**a**) SHPB diagram; (**b**) Test section for sand assembly

A strain gage was attached on the external surface of the confining steel sleeve [8, 12, 13]. The lateral deformation of the sand sample was measured by the strain gage, and the radial/circumferential stresses were determined. This arrangement allows characterization of dynamic response for the volumetric and deviatoric behavior of sand. Further analysis yields the void ratio – pressure relationship at high strain rates. In each experiment, the sand assembly was sandwiched between incident and transmission bars on SHPB. Compressive loading was applied on the sand specimen through WC rods in direct contact with the sand sample. The as-received assorted sand filled in the hollow cylinder assembly had a dense mass density of 1.75 g/cm^3. A sand specimen had length/diameter ratio of 0.715. All assorted sand specimens had the same length to diameter ratios, while the moisture contents are varied from 0 % to 16.5 % w/w. In each moist specimen, dry sand mass densities are all at 1.75 g/cm^3 in spite of water contents. When the length of sand specimen reached a stable value of 9.07 mm during shaking, the mass density reached the maximum value for the given moist sand.

A copper disk was used as pulse shaper in the SHPB experiments by placing it on the impact surface of the incident bar. A 1.22 m long steel striker, with the same diameter as that of both the incident and transmission bars, launched by compressed air in a gas gun, impacts the pulse shaper and generates a desired compressive wave traveling in the incident bar to induce a nearly constant strain rate in the sand sample. A Nicolet Sigma-30 digital oscilloscope (12-bit resolution, 10 Ms/s sampling rate) was used to acquire strain signals through Wheatstone bridges and a Vishay 2310A signal conditioning amplifier (125 kHz frequency response) connected to the strain gages. In a valid SHPB experiment in which a specimen is loaded by equal forces from both ends, the compressive stress in the specimen (the axial stress σ_z) was determined from transmission signals $\varepsilon_t(t)$, and the axial strain rate and strain history were calculated from reflected signals $\varepsilon_r(t)$ [21].

For a cylindrical specimen confined by a hollow cylinder within the elastic range [22, 23], the confining radial and circumferential pressures, as well as circumferential strain on a sample were determined. The hardened steel hollow cylinder (4,340 harden steel) was used in this work, to prevent sand particle from indenting into the inner surface of steel cylinder. In this study, we used the confinement method developed by Ravi-Chandar et al. under quasi-static compression of polymer, for dynamic compression of sand on SHPB to characterize the hydrostatic and deviatoric behavior of sand at high strain rates. With the known axial, confining stress and strain histories, the hydrostatic pressure (isotropic stress, or mean stress) $\sigma_m(t)$ and the volumetric deformation $\varepsilon_m(t)$, are determined. The maximum shear stress $\tau_e(t)$ is applied on any plane inclined at 45° angle with respect to the longitudinal direction (the z-axis), and the maximum shear strains $\gamma_e(t)$ could be calculated [12, 13]. With the known values of hydrostatic and shear stresses, the hydrostatic and deviatoric behavior of sand under multi-axial stress state can be determined at high strain rates. In this investigation all tests were conducted at room temperature (~23 °C) and near 26 % relative humidity environment. Under each testing condition, eight samples were tested to evaluate reproducibility of experimental results, and the average values are reported.

46.3 Results

All as-received dry sand used in this work was silica based fine grain Quikrete #1961 sand quarried in Pensacola, FL, washed and kiln-dried by Eglin Air Force Base. It may be noted that Eglin sand has been characterized by the Air Force Research Laboratory at Eglin Air Force Base extensively and is currently widely used by researchers in the U.S. and Europe [14]. The sand grains are irregular and identified to be comprised primarily of alpha-quartz crystals. The particle size distributions of the as-received sand has the d_{60} value as 0.408 mm, and the effective grain size d_{10} as 0.175 mm; and the uniformity U (defined as d_{60}/d_{10}) of 2.33. After SHPB experiments on 1.75 g/cm^3 unsorting sand, the crushed sand samples were sorted and the particle size distributions were determined [12]. The average values for d_{60}, d_{10} and U of the compacted sand are determined as 0.225, 0.033, and 6.82, respectively, indicating a large size variation for the crushed sand [12]. The initial dry dense mass densities were all achieved as 1.75 g/cm^3, after adding water, the actual sand bulk densities have changed to 1.82, 1.89, 1.97 and 2.04 g/cm^3, for the corresponding moisture contents 4.2 %, 8.2 %, 12.4 % and 16.5 %, respectively.

Typical recorded input and output signals from strain gages attached to the bars, and hoop signal from strain gages mounted on the confinement sleeve in circumferential surface in a SHPB test, are similar to our previous results on assorted sand [12]. In the dynamic compaction testing of sand using SHPB apparatus, dynamic equilibrium state is established when the stresses applied on both ends of the specimen are equal. To examine the dynamic equilibrium condition, the front stress and the back stress on the specimen are calculated following the 1-wave, and 2-wave methods [21]. The dynamic equilibrium and strain rate history is also similar to our previous results [12]. In a valid SHPB experiment, the incident, transmitted, and reflected signals are processed further to determine the stress and strain histories at high strain rates.

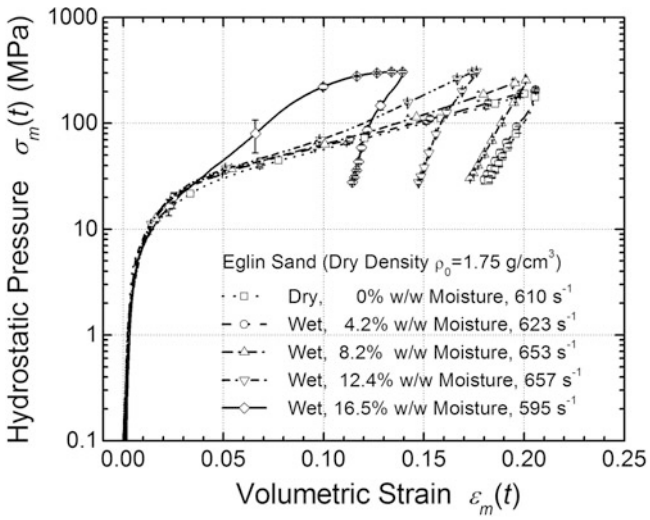

Fig. 46.2 Results of hydrostatic pressure –volumetric strain of moist assorted sands

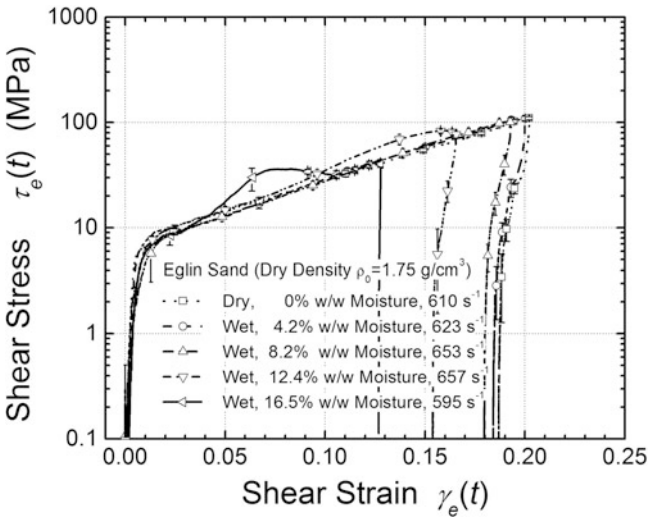

Fig. 46.3 Results of shear stress –shear strain of moist assorted sands

An Eglin sand specimen is comprised of sand grains primarily in the range of 0.1–1 mm with irregular shape. Different sand grains are randomly stacked together, giving large variation in sand packing, including variation in end contact conditions with WC rods, from one sample to another, potentially leading to large variation in data. When assorted sand was consolidated through shaking to reach a maximum density of 1.75 g/cm^3, all the fine sand grains were allowed to move and rotate to fill the cavities between large sand grains, giving much lower porosity variation from sample to sample in packing configuration than the case with the loose sand. The experimental results tend to be more consistent than loose sand samples.

46.3.1 Volumetric and Deviatoric Behavior

Since the initial mass density has significant effects on the mechanical behavior of assorted dry sand [12], the actual density of moist sand also has some effects on the stress–strain curves. For moist sand under confinement, the hydrostatic pressure – volumetric strain, and shear stress – shear strain curves under confinement are plotted at high strain rates in the neighborhood of 600 s^{-1}, as shown in Figs. 46.2 and 46.3, respectively. In Figs. 46.2 and 46.3, the stress components are plotted in logarithmic scale while the strain is plotted in linear scale. In these semi-logarithmic plots, the volumetric and deviatoric stresses follow approximately a two-segment linear relationship with the strain. The first linear segment occurs within the initial 4 MPa hydrostatic pressure in Fig. 46.2, and 2 MPa shear stress in Fig. 46.3, respectively, most likely due to elastic deformation of sand grains. It can be referred to as sand grain-level elastic behavior, similar to the situation under

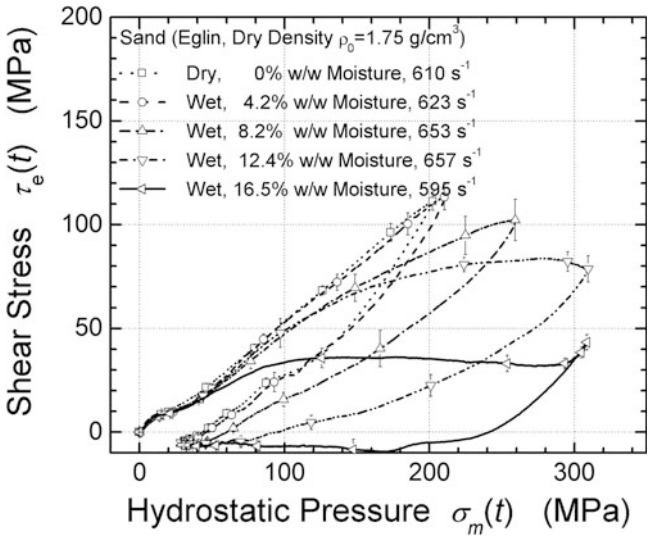

Fig. 46.4 Shear stress-hydrostatic pressure of moist assorted sands on SHPB

quasi-static compression [24]. They all behave similarly in this segment in spite of moisture contents, indicating that moisture has negligible effect at initial 1 % ~ 2 % small strain. The second linear segment on a semi-logarithmic scale occurs at compressive stress larger than stress (12 MPa for hydrostatic pressure in Fig. 46.2 and 8 MPa for shear stress in Fig. 46.3). At stress between 4–12 MPa for hydrostatic pressure (Fig. 46.2), and 2–8 MPa for shear stress (Fig. 46.3), there is a gradual transition region between the two linear segments in the semi-logarithmic scale, respectively. The behavior shows mass density compaction at the transition of the two linear segments. They all behave very close in this transition region in spite of moisture contents at 2 % ~ 4 % small strains. The difference becomes significant at strains larger than 5 % strain for the second linear segment. It is perhaps associated with sand grain compaction through grain crushing, rearrangement of crushed fragments. The smaller fragments fill the gaps between large sand grains to provide resistance for compression. The behavior in this region depends highly on moisture contents. At higher mass density, the sand grains are closely packed. Hence, they provide higher resistance for gain rearrangement, and consequent crushing becomes dominant. Moisture provides lubrication at the contact points between sand grains. However, when the sand is compacted to dense and the void among sand grain becomes smaller, the water will carry loads.

For dry sand and 4.2 % w/w moist sand, the volumetric and deviatoric behavior is very close, indicating that at low moisture content, the effect is negligible. When the moisture contents increase to 8.2 % w/w, the volumetric behavior become slightly stiffer than that at lower moist content (0 % and 4.2 % w/w), and deviatoric behavior, however, is nearly identical. When the moisture content increases to 12.4 % w/w, the volumetric behavior is stiffer than that at lower moist content (0 %, 4.2 % and 8.2 % w/w), and deviatoric behavior becomes slightly stiffer. When the moisture content increases to the highest level used in this paper, 16.5 % w/w, the volumetric behavior shows significantly stiffer than that at lower moist contents, and the deviatoric behavior shows firstly suddenly shift upward (stiffer) at 5 % ~ 8 % shear strain, then drops down (softener) to curve following that of the lower moist sand. This trend is different from the trend in the stress – strain curves with different initial density for dry sand, which shift evenly upwards. The unloading curve shows a steep reduction in stress. Similar behaviors were found for deviatoric response (Fig. 46.3). The next should be investigated the shear stress-hydrostatic pressure relationship with effects of moisture contents.

46.3.2 Shear Stress-Hydrostatic Pressure Relationship

For the constitutive behavior of geotechnical materials, the Drucker-Prager models and Mohr-Coulomb model are widely used at quasi-static condition [25–28]. In these models, shear stress is often plotted as a function of hydrostatic pressure to describe multi-axial failure behavior of brittle materials, such as rocks, ceramics and sand/soil. In this study, shear stress and hydrostatic pressure histories are determined under the 1D confined compression on SHPB. These are used to investigate the effect of moisture on the shear stress-hydrostatic pressure relationship.

Figure 46.4 shows the shear stress – hydrostatic pressure relationship during both loading and unloading stages for five moist sands up to maximum axial stress of 295 ~ 414 MPa. During the loading stage, shear stress exhibits a linear

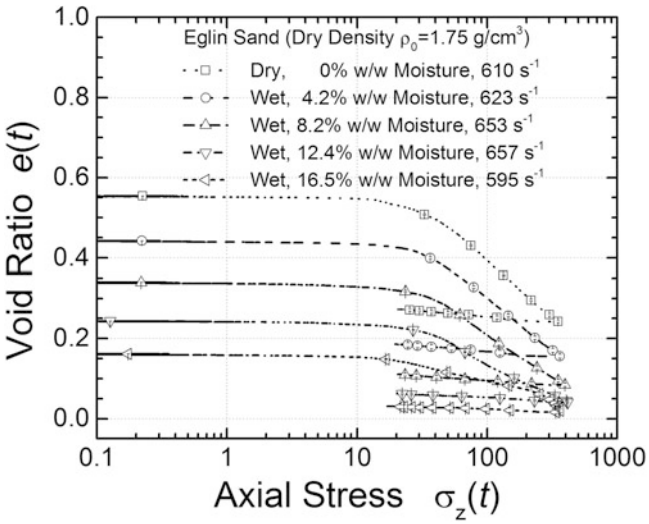

Fig. 46.5 e – log p curves of moist assorted sands on SHPB

relationship with the hydrostatic pressure for dry sand. The unloading path does not follow the loading path, giving rise to a hysteresis hoop which represents the energy dissipation of sand due primarily to sand fracture during compression. For the five moist sands, the initial curves are close to each other (within the experimental deviation) below 20 MPa hydrostatic pressure, which is below preconsolidation at strain at 2 % ~ 5 % since sand grains did not fail or break; instead they just rearrange themselves by slip and rotation. It indicates that the relationship in this range is not sensitive to moisture at lower pressure. In general, the failure surface of sand such as shear stress-hydrostatic pressure relationship is a complex function of time (or strain rate), stress, density, moisture contents and sand morphology, etc. [29]. With increasing moisture, shear stress decreases gradually with hydrostatic pressure, showing softening-like behavior as the water served as lubrication, and also carry loads due to incompressibility. Beyond preconsolidation, the sand grains begin to fracture by crushing to form tiny fragments and powder. The curves show a significant difference; they are sensitive on moisture contents. The sand continues to fail until void disappears and most sand grains are completely compacted, and the final compacted sand powder under confinement theoretically should behave as monolithic sand rock. It should be noted that, the highest moisture content at 16.5 % w/w shows a shear yielding-like platen from hydrostatic pressure 100–300 MPa range, then the curve becomes higher rapidly. We next investigate the void ratio as a function of pressure under moist condition.

46.3.3 Compressibility of Sorted Sands

We investigate the compressibility in terms of e-log p curve. To evaluate the compressibility of sand we adapt the approach often used in soil mechanics, in which the void ratio e is plotted as a function of axial pressure p, (σ_z, instead of the hydrostatic pressure σ_m), to give e-log p curve. This description makes it consistent with the term used in soil mechanics [1, 2] under quasi-static loading conditions. It may be noted that results on the e-log p relationship of sand at high strain rates was sparse except several references [12, 13]. The measurements of both radial and circumferential stresses and strains in the sand sample in this work made it possible to report the relationship.

In Fig. 46.5, two linear segments appear in the e-log p curve, representing a power law relationship between e and p, similar to what was observed under quasi-static loading conditions [1–4]. Three important parameters of soil mechanics [30, 31], namely, the pre-consolidation pressure p_c, representing the effective vertical stress to cause the destructuration of natural sand and the transitional pressure between the two linear segments, and the compression index C_c, representing the magnitude of the slope in the linear segments of the e-log p curve after pre-consolidation, and swell index C_S, defined as the slope at unloading stage to describe the expansion occurring upon unloading, were to be determined. The three parameters p_c, C_c and C_S are summarized in Table 46.1, also listed are the initial void ratio and the maximum axial stress σ_z.

With water added, the initial void ratio decreases with increasing moisture content since the total volume and the volume occupied by sand grains were kept unchanged. The saturation is defined as the ratio of water volume to the total void volume (water and air). It is noted that, the fully saturated state cannot be achieved. In this work, 80 % of saturation has been realized, even under 30 min shaking and 48 h of setting. The e-log p curve during unloading also follows a linear

Table 46.1 Parameters of compressibility of moist Eglin sand

Moisture (w/w)	Saturation	p_c (MPa)	C_c	C_S	e_0	Max σ_z (MPa)
0	0 %	29.1	0.289	0.0299	0.554	351
4.2	20 %	28.3	0.265	0.0287	0.442	361
8.2	40 %	27.9	0.229	0.0266	0.340	295
12.1	60 %	26.4	0.188	0.0144	0.244	414
16.5	80 %	18.4	0.0739	0.0121	0.161	367

relationship, indicating that e follows a power law relationship with p during unloading, as described by swell index C_S. At these high strain rates, with the increase of moisture content, both the pre-consolidation pressure and compression index decrease. The unloading shows slightly different behavior, swell index C_S decreases with the increase of moisture content.

46.4 Discussion

The stress–strain behavior of partially saturated sand under high-statin rate depends strongly on the confinement pressure, initial mass density and the degree of saturation [15]. The moisture gives rise of, the behavior is initially softened, then becomes stiffer with increasing moisture level [10], at loose Eglin sand with density of 1.52 g/cm^3. Under shock loading, both loose and dense sand are crushed [32]. Liquefaction was observed at intermediate strain rate earlier [33]. The resistance to projectile penetration in saturated sand was also found to decrease, as compared to dry sand [34]. However, in our case, the dry and moist sands are dense with mass density of 1.75 g/cm^3, and the lock-up phenomenon [10] did not happen. Water is incompressible, much stiffer than compressible air. If the compressive strains on SHPB are not sufficient to drive out the air voids or compressed, the stress–strain response will exhibit similar behavior. Therefore, partially saturated sand (4.2 % w/w, 8.2 % w/w, even 12.4 % w/w) does not have much higher stiffness than dry sand, and the stiffness increases slightly with the decrease of the degree of saturation. At higher level of saturation, the void is smaller and the water fills the pores.

46.5 Conclusion

The dynamic compressive behavior of moist Eglin sand under stiff confinement was investigated using a modified long split Hopkinson pressure bar (SHPB) at high strain rates (~600 s^{-1}) up to 414 MPa compressive stress, using a sand specimen assembly with WC inserts inside a steel tube. The assembly allows shaking to consolidate sand to prepare sand samples with dense initial mass densities. Sand samples of assorted sand with five moisture contents were compressed on SHPB at high strain rates. A strain gage was attached on the external surface of the confining steel sleeve to measure the circumferential strain, to determine both the bulk and the deviatoric responses. The curves of hydrostatic pressure-volumetric strain, shear stress-shear strain of sand under 3D stress state are determined up to 21 % compressive strain and up to 414 MPa axial compressive stresses at high strain rates. Moisture shows significant effects on volumetric and deviatoric behavior at higher moisture contents. At lower moisture contents, moisture does not have significant effect on the shear stress-hydrostatic pressure relationship. At 16.5 % w/w moisture content, shear stress-hydrostatic pressure relation shows softening and yield-like behavior. The e-log p curves, representing the sand compressibility as a function of moisture content, were compared and model parameters were determined. Significant moisture effects have been identified at the highest moisture content. These results can be analyzed further for constitutive modeling and for mesoscale simulations to understand the dynamics of moist sand under high pressure and high rate deformation.

Acknowledgements We acknowledge the support of ONR Multidisciplinary University Research Initiative program (MURI) BAA 10–026.

References

1. Yamamuro JA, Bopp PA, Lade PV (1996) One-dimensional compression of sands at high pressure. J Geotech Eng 122:147–154
2. Russell AR, Khalili N (2004) A bounding surface plasticity model for sands exhibiting particle crushing. Can Geotech J 41:1179–1192
3. Vallejos J (2008) Hydrostatic compression model for sandy soils. Can Geotech J 45:1169–1179

4. Graham J, Alfaro M, Ferris G (2004) Compression and strength of dense sand at high pressure and elevated temperatures. Can Geotech J 41:1206–1212
5. Charlie WA, Ross CA, Pierce SJ (1990) Split-Hopkinson pressure bar testing of unsaturated sand. Geotech Test J 13:291–300
6. Bragov AM, Grushevsky GM, Lomunov AK (1996) Use of the Kolsky method for confined tests of soft soils. Exp Mech 36:237–242
7. Felice CW, Gaffney ES, Brown JA, Olsen JM (1987) Dynamic high stress experiments on soil. Geotech Test J 10:192–202
8. Bragov AM, Lomunov AK, Sergeichev IV, Tsembelis K, Proud WG (2008) Determination of physicomechanical properties of soft soils from medium to high strain rates. Int J Impact Eng 35:967–976
9. Frew DJ, Forrestal MJ, Chen W (2002) Pulse shaping techniques for testing brittle materials with a split Hopkinson pressure bar. Exp Mech 42:93–106
10. Martin BE, Chen W, Song B, Akers SA (2009) Moisture effects on the high strain-rate behavior of sand. Mech Mater 41:786–798
11. Song B, Chen W, Luk V (2009) Impact compressive response of dry sand. Mech Mater 41:777–785
12. Luo H, Lu H, Cooper WL, Komanduri R (2011) Effect of mass density on the compressive behavior of dry sand under confinement at high strain rates. Exp Mech 51:1499–1510
13. Lu H, Luo H, Cooper WL, Komanduri R (2013) Effect of particle size on the compressive behavior of dry sand under confinement at high strain rates. Conf Proc SEM Dyn Behav Mater 1:523–530
14. Martin BE, Kabir E, Chen W (2013) Undrained high-pressure and high strain-rate response of dry sand under triaxial loading. Int J Impact Eng 54:51–63
15. Omidvar M, Iskander M, Bless S (2012) Stress–strain behavior of sand at high strain rates. Int J Impact Eng 49:192–213
16. Higgins W, Chakraborty T, Basu D (2012) A high strain-rate constitutive model for sand and its application in finite-element analysis of tunnels subjected to blast. Int J Numer Anal Meth Geomech. doi:10.1002/nag.2153
17. Luo H, Lu H, Leventis N (2006) The compressive behavior of isocyanate-crosslinked silica aerogel at high strain rates. Mech Time-Depend Mater 10:83–111
18. Luo H, Churu G, Fabrizio EF, Schnobrich J, Hobbs A, Dass A, Mulik S, Zhang Y, Grady BP, Capecelatro A, Sotiriou-Leventis S, Lu H, Leventis N (2008) Synthesis and characterization of the physical, chemical and mechanical properties of isocyanate-crosslinked vanadia aerogels. J Sol–gel Sci Technol 48:113–134
19. Chen W, Luo H (2003) Dynamic compressive testing of intact and damaged ceramics. Ceram Eng Sci Proc 24:411–416
20. Chen W, Luo H (2004) Dynamic compressive responses of intact and damaged ceramics from a single split Hopkinson pressure bar experiment. Exp Mech 44:295–299
21. Gray GT III (2000) Classic split-Hopkinson pressure bar testing. In: Mechanical testing and evaluation metals handbook, vol 8. American Society for Metals, Materials Park, pp 462–476
22. Ravi-Chandar K, Ma Z (2000) Inelastic deformation in polymers under multiaxial compression. Mech Time-Depend Mater 4:333–357
23. Knauss WG, Emri I, Lu H (2008) Mechanics of polymers: viscoelasticity. In: Sharpe WN, Sharpe WN (eds) Handbook of experimental solid mechanics. Springer, New York, pp 49–95
24. Hagerty MM, Hite DR, Ullrich CR, Hagerty DJ (1993) One-dimensional high-pressure compression of granular material. J Geotech Eng-Trans ASCE 119:1–18
25. Resende L, Martin JB (1985) Formulation of Drucker-Prager cap model. J Eng Mech 111:855–881
26. Drucker DC, Gibson RE, Henkel DJ (1957) Soil mechanics and work-hardening theories of plasticity. Trans ASCE 122:338–346
27. Chen WF, Mizuno E (1990) Nonlinear analysis in soil mechanics: theory and implementation. Elsevier, New York
28. Sandler IS, DiMaggio FL, Baladi GY (1967) Generalized cap model for geological materials. J Geotech Eng 102:683–699
29. Cooper WL, Breaux BA (2010) Grain fracture in rapid particulate media deformation and a particulate media research roadmap from the PMEE workshops. Int J Fract 162:137–150
30. Lambe TW, Whitman RV (1969) Soil mechanics, 3rd edn. Wiley, New York
31. Terzaghi K, Peck RB, Mesri G (1996) Soil mechanics in engineering practice. Wiley, New York
32. Veyera GE, Charlie WA, Hubert ME (2002) One-dimensional shock-induced pore pressure response in saturated carbonate sand. Geotech Test J 25:277–288
33. Whitman RV, Healy KA (1962) Shear strength of sands during rapid loadings. J Soil Mech Found ASCE 88:99–132
34. Savvateev AF, Budin AV, Kolikov VA, Rutberg PG (2001) High-speed penetration into sand. Int J Impact Eng 26:675–681

Chapter 47
Shearing Rate Effects on Dense Sand and Compacted Clay

Jenna S. Svoboda and John S. McCartney

Abstract This paper reports the findings of a series of triaxial compression tests performed on saturated specimens of compacted clay and dense sand at axial strain rates ranging from 0.01 %/min to 800 %/min. The purpose of these tests is to provide a baseline for the shear strength of near surface soils during buried explosions, and to evaluate the transition from conventional quasi-static experimental soil mechanics to faster rate testing. The behavior of the saturated clay and sand specimens under undrained loading is examined in detail using pore water pressure measurements at the boundary, which permits evaluation of the impact of the rate of loading on the effective stress paths during shearing.

Keywords Axisymmetric triaxial testing • Soil shear strength • Strain rate • Blast loading • Experimental soil mechanics

47.1 Introduction

The impact of high axial compression rates on the shear strength of soils has been a topic of interest for many years. This information is important to understand and simulate dynamic loading of soils in events such as explosions and earthquakes, as well as in rapid construction loading. Thus, a thorough understanding of the behavior of soil subject to high strain rates is an important factor. However, the effects of high strain rates on the shear strength and excess pore water pressure of compacted clay and dense sand under saturated conditions have not been thoroughly investigated in terms of effective stress. The effect of loading rate was investigated in this study by performing consolidated undrained (CU) triaxial tests on two soils under the same effective confining stress. The specimens were sheared using conventional axial strain rates depending on the rate of consolidation (0.01–0.1 %/min), as well as under axial strain rates up to 800 %/min.

47.2 Background

It has been well established in several classic studies that the shear strength of remolded clays is dependent upon the axial strain rate during axisymmetric triaxial compression testing (Casagrande and Shannon [1], Richardson and Whitman [2]; Olson and Parola [3]; Lefebvre and LeBoeuf [4]; Zhu and Yin [5]). Specifically, the shear strength of clay at failure increases with increasing strain rate. The average rate of increase for soil under normally consolidated stress state is 10 % per log cycle of the time to failure, where failure is often defined as 15 % axial strain. Casagrande and Shannon [1] were the first to observe an increase in shear strength at higher strain rates. Richardson and Whitman [2] expanded this research by incorporating pore water pressure measurements at the boundaries of the specimens. They verified the hypothesis that the increase in shear strength with increasing strain rate was due to a lower magnitude of pore water pressure at failure. Lefebvre and LeBoeuf [4] investigated the effects of changing the initial stress state by conducting tests on both intact overconsolidated samples and remolded normally consolidated specimens of the same clay. Zhu and Yin [5] looked at changes in soil behavior with

J.S. Svoboda • J.S. McCartney (✉)
Department of Civil, Environmental and Architectural Engineering, University of Colorado Boulder, UCB 428, Boulder, CO 80309, USA
e-mail: john.mccartney@colorado.edu

B. Song et al. (eds.), *Dynamic Behavior of Materials, Volume 1: Proceedings of the 2013 Annual Conference on Experimental and Applied Mechanics*, Conference Proceedings of the Society for Experimental Mechanics Series, DOI 10.1007/978-3-319-00771-7_47,

increasing strain rate as the over consolidation ratio changed. Olson and Parola [3] were one of the only researchers who investigated the behavior of compacted clay soils. However, they only considered the effect of strain rate on shear strength when varying the initial compaction water content, and did not consider saturated conditions. They were not able to monitor generation of excess pore water pressure during shearing. Accordingly, the impact of the excess pore water pressures on the behavior of saturated compacted clays subject to increased strain rates have not yet been thoroughly addressed in the literature.

Most of the classic papers on the impact of axial strain rate on the shear strength of sands focused on dry conditions, and it is not until recent years that saturated conditions have been considered. The shear strength response of sands subject to increased loading rates is quite variable depending upon the saturation conditions as well as the density of the test material. Casagrande and Shannon [1] and Dayal and Allen [6] looked at the effect of strain rate on the shear strength of dry sands. Both studies observed that the shear strength of dry sands is relatively insensitive to the axial strain rate (or penetration rate). Yamamuro and Abrantes [7] investigated the effect of strain rate on saturated medium dense sand under drained triaxial compression, and observed that the shear strength of the sand increased by nearly 50 % from a strain rate of 0.0024–1764 %/s. Whitman [8] evaluated the shear strength of loose saturated sand, and observed an increase in shear strength of up to 200 % due to decreases in excess pore water pressure. This indicates that the faster shearing rates lead to dilation. Shearing of loose sands under slow axial strain rates typically leads to contraction and positive pore water pressure, which means that a transition in behavior of saturated sand behavior occurs with faster loading rates. The mechanisms of this transition are discussed in detail by Omidvar et al. [9]. Despite the previous studies on saturated loose and medium dense sands, the shear strength behavior and excess pore water pressure generation of saturated dense sands during high strain rate triaxial compression tests has not been fully investigated in the literature and is a focal point of this paper.

47.3 Materials

Two natural soils, a sand and clay obtained from the region around Boulder, Colorado were chosen as test materials for this study. The clay was obtained from a stockpile of soil from a construction site on the University of Colorado Boulder campus, and is referred to as Boulder clay. The clay was processed after collection to remove all particles greater than the #10 sieve, which provided a more homogeneous and consistent material for experimental testing. The sand was purchased from a quarry in Longmont, Colorado (Colorado Materials), and is referred to as Mason sand.

Soil classification tests were performed on Mason sand to measure the grain size distribution (ASTM D422 [10]), specific gravity (ASTM D854 [11]), maximum dry density, and minimum dry density. Relevant grain size distribution parameters (D_{10}, D_{30}, D_{50}, C_u, C_z) and are listed in Table 47.1. The sand has negligible fines content. Based on the grain size distribution curve, Mason sand is classified as poorly graded sand (SP) according to the Unified Soil Classification System (USCS). The specific gravity G_s was measured to be 2.62. The minimum void ratio of 0.50 corresponds to a maximum dry density of 1.74 kg/m^3, while the maximum void ratio of 0.78 corresponds to minimum dry density of 1.47 kg/m^3. Soil classification tests were also performed on Boulder clay to measure the grain size distribution (ASTM D422 [10]), Atterberg limits (ASTM D4318 [12]), specific gravity (ASTM D854 [11]), standard Proctor compaction curve (ASTM D698 [13]), and compression curve and consolidation characteristics (ASTM D2435 [14]). Relevant grain size distribution parameters (D_{10}, D_{30}, D_{50}, percent fines) and soil index properties (liquid limit LL and plasticity index PI) are listed in Table 47.1. Boulder clay is classified as a low plasticity clay (CL) according to the Unified Soil Classification System (USCS). The specific

Table 47.1 Index properties of Mason sand and Boulder clay

Mason sand			Boulder clay		
Property	Value	Units	Property	Value	Units
D_{10}	0.20	mm	D_{10}	$<1.7 \times 10^{-4}$	mm
D_{30}	0.44	mm	D_{30}	<0.001	mm
D_{60}	0.90	mm	D_{50}	0.001	mm
C_u	4.5	–	% Fines	100	%
C_z	1.1	–	LL	43	–
G_s	2.62	–	PI	22	–
e_{min}	0.50	–	G_s	2.70	–
ρ_{max}	1.74	kg/m^3	γ_{d_max}	17.5	kN/m^3
e_{max}	0.78	–	w_{opt}	18	%
ρ_{min}	1.47	kg/m^3			

gravity G_s was measured to be 2.70. From the standard Proctor compaction test, an optimal water content of 18 % corresponds to the maximum dry unit weight of 17.5 kN/m^3. An oedometer test was performed on a specimen of Boulder clay compacted to at optimal conditions then soaked in the oedometer to reach as close to saturated conditions as possible. The results from the test indicate that the clay has an apparent preconsolidation stress of 300 kPa, a compression index c_c of 0.23, and a recompression index c_r of 0.041.

47.4 Conventional Triaxial Testing

Five consolidated undrained (CU) triaxial tests were conducted in accordance to ASTM D4764 [15] to determine the effective shear strength parameters of Boulder clay. Similarly, a series of four consolidated undrained (CU) triaxial compression tests were performed on Mason sand using the same testing standard. Each clay specimen was compacted using a mechanical press in a cylindrical mold having a height of 71.1 mm and a diameter of 35.6 mm. To ensure uniformity throughout the sample, each specimen was compacted using five lifts of equal mass. This method of compaction is referred to as "static compaction". The target dry unit weight and water content for each specimen were 17 kN/m^3 (target void ratio of 0.51) and 17.5 % respectively. These values correspond to 0.6 % of the maximum standard Proctor dry density and 10 % dry of the standard Proctor optimum water content, respectively. After the specimen was prepared and the cell was assembled, the specimen was placed under a vacuum of 80 kPa and the cell filled with water. The dense sand specimen was prepared by placing the bottom platen of the triaxial cell on a shaking table, and pouring sand into the latex membrane fitted on the inside of a split mold. The dense sand samples were prepared using a mechanical vibrator, and the sand was vibrated in three lifts within the split mold until reaching a target void ratio of 0.54. The relative density corresponding to this target void ratio can be calculated as follows:

$$I_D = \frac{(e_{\max} - e)}{(e_{\max} - e_{\min})} \tag{47.1}$$

A value of I_D of 0.88 corresponds to the target void ratio, indicating that the sand is dense. After vibration, the top cap was then placed on the sand specimen, the membrane was attached, and the specimen was placed under a vacuum of 80 kPa.

The saturation procedures for both soil types were similar. After specimen preparation and filling of the triaxial cell with water, the unsaturated specimens were permitted to de-air under vacuum for at least 1 h. A seating cell pressure of 20 kPa was then applied to the cell water. Next, de-aired water was permitted to flush through the specimen from the bottom while vacuum was maintained on the top. After water was observed to exit from the top of the specimen, the water vapor was flushed from the top of the specimen and the sample was placed under backpressure. Specifically, the cell pressure and the pressure applied to the water within the specimen were increased in stages until reaching a measured value of Skempton's B parameter of 0.9, or when the B parameter remained constant with additional increases in backpressure. In most tests, a cell pressure of 483 kPa and a backpressure of 276 kPa were applied at the end of saturation.

After saturation of each specimen, a specific effective stress was applied and consolidation was permitted to occur until the volume change inferred from the cell water level and backpressure water levels reached equilibrium. Upon completion of consolidation, the specimens of Boulder clay were sheared to an axial strain of 15 % in 150 min (an axial strain rate of 0.0686 mm/min), and the specimens of Mason sand were sheared to an axial strain of 15 % in 20 min (an axial strain rate of 1.28 mm/min). These times to failure (and corresponding shearing rates) were defined using the value of t_{50} for the soil specimens calculated from the consolidation data (ASTM D2435 [1]). For all Mason sand tests, the load was applied using a hydraulic press. The load for the Boulder clay was applied using an electrically driven motor for slower tests and the hydraulic press for higher rates. All sand and clay tests were run under strain-controlled conditions. During shearing, the variables measured include the pore water pressure at the bottom of the specimen, the axial load, and the axial displacement. From this data, the shear strength (in terms of principal stress difference), principal stress ratio, and excess pore water pressure were calculated. The shear strength as a function of axial strain is shown in Fig. 47.1a for Mason sand and in Fig. 47.1b for Boulder clay, the principal stress ratio as a function of axial strain is shown in Fig. 47.2a for Mason sand and Fig. 47.2b for Boulder clay, and the excess pore water pressure as a function of axial strain is shown in Fig. 47.3a for Mason sand and Fig. 47.3b for Boulder clay.

In each of the tests, shear failure of the specimen was defined as the point where the maximum value of internal friction is mobilized, which is referred to as the stress path tangency failure criterion. In a consolidated undrained triaxial compression test, the point where the maximum friction is mobilized occurs at the maximum value of the principal stress ratio, σ_1'/σ_3'. Examination of a Mohr circle at failure indicates that the principal stress ratio is directly proportional to the friction angle

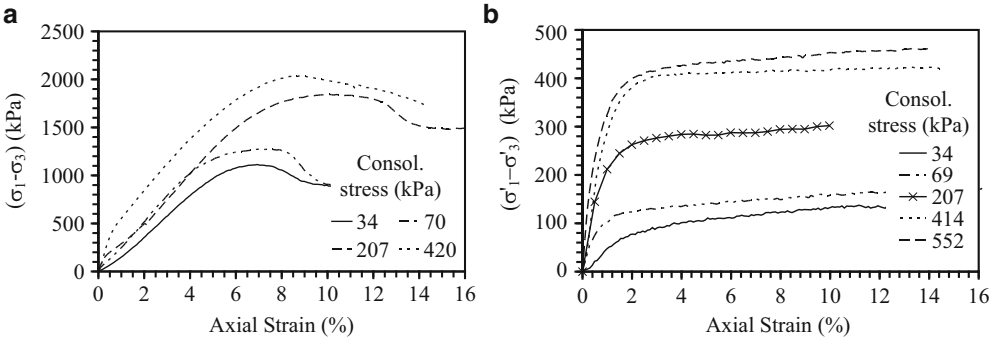

Fig. 47.1 Principal stress difference versus axial strain for conventional loading rate: (**a**) Mason sand; (**b**) Boulder clay

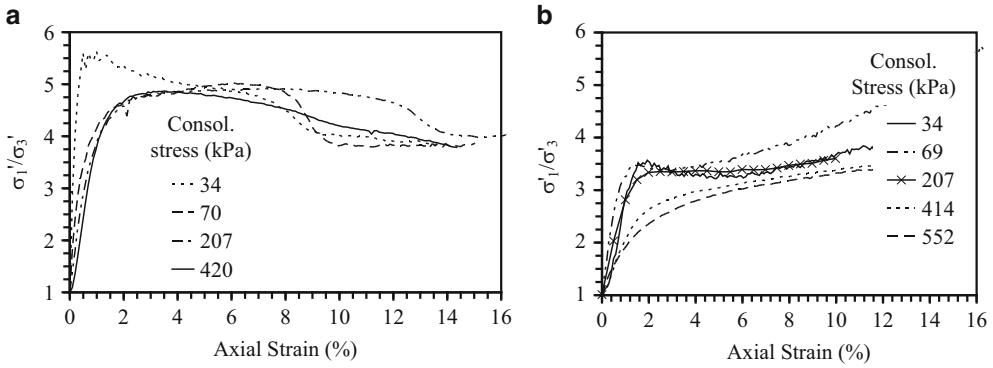

Fig. 47.2 Principal stress ratio versus axial strain under conventional loading rate: (**a**) Mason sand; (**b**) Boulder clay

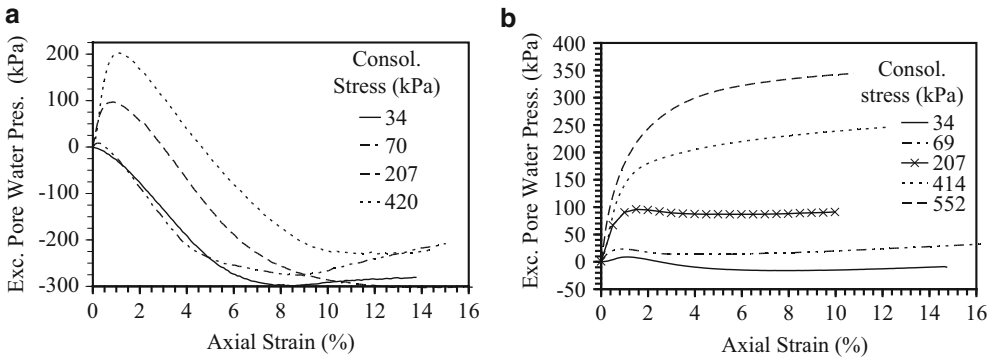

Fig. 47.3 Excess pore water pressure versus axial strain for conventional loading rates: (**a**) Mason sand; (**b**) Boulder clay

$[\sigma_1'/\sigma_3' = \tan^2(45 + \phi'/2)]$. The points of failure defined using the stress path tangency failure criterion in a modified Mohr-Coulomb stress space (triaxial stress space: effective confining stress versus principal stress difference) for specimens consolidated to different initial effective consolidation stresses are shown in Fig. 47.4a for Mason sand and Fig. 47.4b for Boulder clay. The failure envelopes in triaxial stress space can be defined by fitting a line through the failure points. The angles of inclination of the lines shown in the modified Mohr-Coulomb diagrams in Fig. 47.4 correspond to the tangents of the transformed friction angle, α, while the y-intercepts correspond to the transformed apparent cohesion values, d. The following equations were used to convert the modified Mohr-Coulomb parameters of the failure envelope to the conventional Mohr-Coulomb failure envelop parameters, as follows:

$$\phi' = \sin^{-1}\left(\frac{\tan(\alpha)}{2 + \tan(\alpha)}\right) \tag{47.2}$$

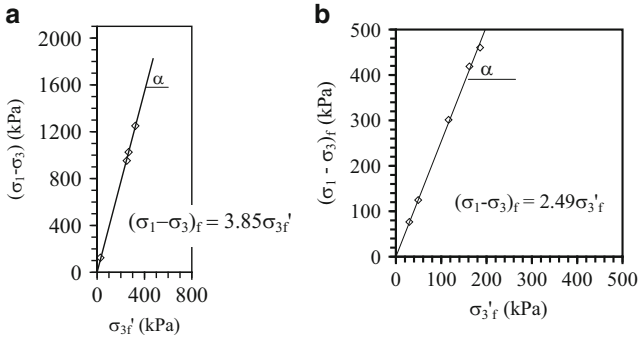

Fig. 47.4 Failure envelopes defined using the stress path tangency failure criterion: (**a**) Mason sand; (**b**) Boulder clay

Table 47.2 Modified and conventional Mohr-Coulomb failure envelope parameters for Mason sand and Boulder clay

Mason sand			Boulder clay		
Parameter	Value	Units	Parameter	Value	Units
α	75.3	°	α	68.5	°
d	0.0	kPa	d	0.0	kPa
ϕ'	41.0	°	ϕ'	34.0	°
c'	0.0	kPa	c'	0.0	kPa

$$c' = \frac{d[1 - \sin(\phi')]}{2\cos(\phi')} \tag{47.3}$$

where ϕ' is the effective friction angle and c' is the apparent cohesion. The values of α and d calculated from the data in Fig. 47.4 as well as the Mohr-Coulomb parameters calculated using Eqs. 47.2 and 47.3 are summarized in Table 47.2.

47.5 Rate Effects

To investigate the effects of strain rate on the shear strength of Boulder clay and Mason sand, additional consolidated undrained triaxial tests were preformed at increased loading rates. Tests were performed on Boulder clay at three different axial strain rates: 0.1 %/min, 1.5 %/min and 16 %/min and four tests were preformed on Mason sand at different axial strain rates: 0.9 %/min, 1.5 %/min, 16%/min and 215 %/min. Each specimen was prepared and saturated using the same procedures discussed in the previous section for conventional consolidated undrained triaxial tests. All specimens were sheared until reaching an axial strain of 15 %, so the shearing rates correspond to times to failure of 150, 10, and 1 min for Boulder clay and times to failure of 20, 10, 1 and 0.1 min for Mason sand. Similar to the standard tests, the variables measured during shearing include the excess pore water pressure at the bottom of the specimen, axial load, and axial displacement. The variation of shear strength (in terms of the principal stress difference), principal stress ratio and excess pore water pressure with axial strain for the Mason sand are shown in Figs. 47.5a, 47.6a, and 47.7a, respectively, while those for Boulder clay are shown in Figs. 47.5b, 47.6b, and 47.7b, respectively. The shear strength at failure was defined using stress path tangency criterion, and the points of failure are indicated in Figs. 47.5 through 47.7 with hollow squares.

47.6 Analysis

The shear strength (principal stress difference) at failure defined by the stress path tangency failure criterion for both soils is plotted versus logarithm of strain rate in Fig. 47.8a. The shear strength of Mason sand during undrained shearing increases linearly at approximately 30 % per log cycle of time to failure. Compared to the results from previous studies (Yamamuro and Abrantes [7]; Whitman [8]), it appears that the increase of shear strength with strain rate of saturated dense sand is not as pronounced for dense sand as it is for medium dense and loose sand. The shear strength for Boulder clay increases log-linearly with increasing strain rate. The percent increase in shear strength for the Boulder clay is approximately 9 % per log

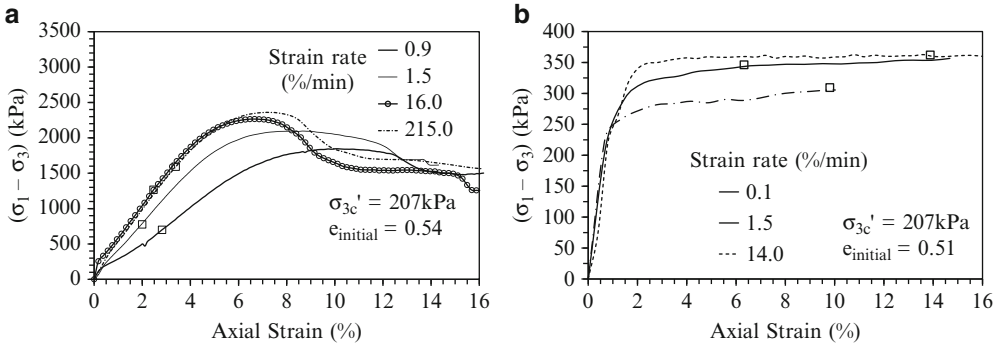

Fig. 47.5 Principal stress difference with axial strain for different times to failure: (**a**) Mason sand; (**b**) Boulder clay

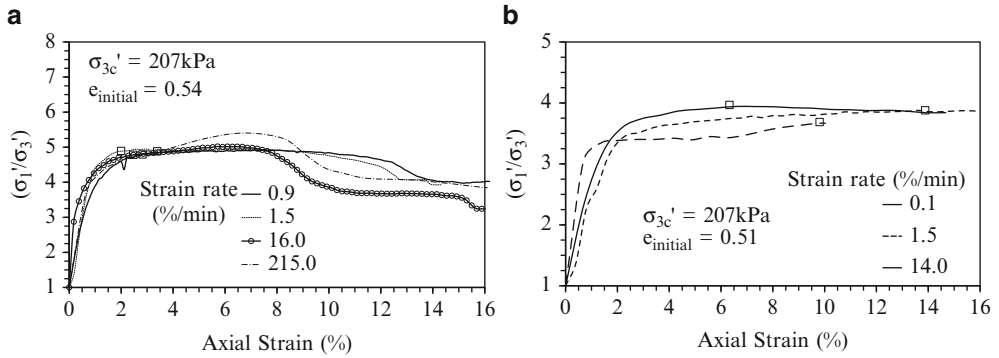

Fig. 47.6 Principal stress ratio with axial strain for different times to failure: (**a**) Mason sand; (**b**) Boulder clay

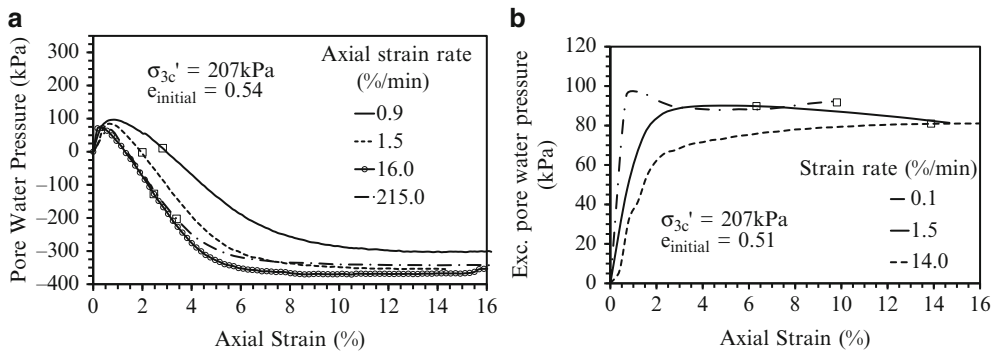

Fig. 47.7 Excess pore water pressure with axial strain for different times to failure: (**a**) Mason sand; (**b**) Boulder clay

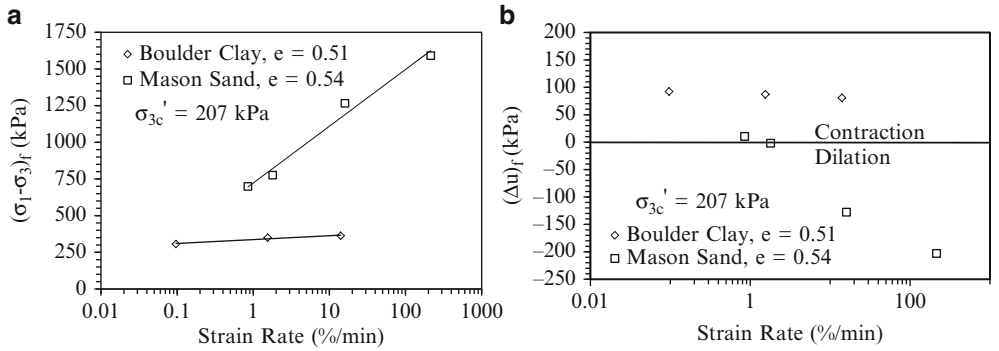

Fig. 47.8 Impact of strain rates on Mason sand and Boulder clay: (**a**) Shear strength; (**b**) Excess pore water pressure

cycle of time to failure. This rate of increase in shear strength is consistent with previous studies conducted on normally consolidated, remolded clays by Casagrande and Shannon [1], Richardson and Whitman [2] and Lefebvre and LeBoeuf [4].

The values of excess pore water pressure at the point of failure defined by the stress path tangency failure criterion for both soils under different rates of shearing are shown in Fig. 47.8b. The Mason sand data indicates a negative excess pore water pressure that decreases with increasing strain rate. This suggests that the increase in shear strength of the Mason sand is due to increasing amounts of dilation. The excess pore water pressure at failure for Boulder clay is positive, and decreases with increasing axial strain rate. This observation is consistent with studies conducted by Richardson and Whitman [2] and Lefebvre and Leboef [4]. Both studies found that for normally consolidated, remolded clay the shear strength increased with increasing strain rate, and this strength increase was accompanied by a decrease in pore water pressure. Thus, it is believed that the increase in shear strength of the Boulder clay with increasing strain rate is due to an increase in effective stress caused by the decrease in pore water pressure.

47.7 Conclusion

The results presented in this study emphasize the importance of monitoring the pore water pressure response during triaxial compression tests on soils under high rates of strain. Both sands and clays were observed to have an increase in shear strength with increasing axial strain rates, although the rate of increase in the shear strength of sand was greater due to the negative excess pore water pressure induced by dilation during shearing.

Acknowledgements Funding for this research was provided by Office of Naval Research (ONR) grant N00014-11-1-0691. This funding is gratefully acknowledged.

References

1. Casagrande A, Shannon WL (1948) Stress-deformation and strength characteristics of soils under dynamic loads. In: Proceedings of 2nd ICSMFE, Rotterdam, Netherlands, vol V, pp 29–34
2. Richardson AM, Whitman RV (1963) Effect of strain-rate upon undrained shear resistance of a saturated remolded fat clay. Geotechnique 13(4):310–324
3. Olson RE, Parola JF (1967) Dynamic shearing properties of compacted clay. In: Proceedings of international symposium on wave propagation and dynamic properties of earth materials, University of New Mexico, Albuquerque, New Mexico, pp 173–182
4. Lefebvre G, LeBoeuf D (1987) Rate effects and cyclic loading of sensitive clays. J Geotech Eng 113:476–489
5. Zhu J, Yin J (2000) Strain-rate-dependent stress strain behavior of overconsolidated Hong Kong marine clay. Can Geotech J 37:1272–1282
6. Dayal U, Allen JH (1975) The effect of penetration rate on the strength of remolded clay and sand samples. Can Geotech J 12(3):336–348
7. Yamamuro JA, Abrantes AE (2003) Behavior of medium sand under very high strain rates. In: Proceedings 1st Japan-US workshop on testing, modeling and simulation, ASCE Geotechnical Special Publication, Boston, Massachusetts, no. 143, pp 61–70
8. Whitman RV (1970) The response of soils to dynamic loading. Report no. 26. U.S. Army Corps of Engineers. Waterways Experiment Station
9. Omidvar M, Iskander M, Bless S (2012) Stress–strain behavior of sand at high strain rates. Int J Impact Eng 49:192–213
10. ASTM D422 (2007) Standard test method for particle-size analysis of soils. ASTM Int, West Conshohocken
11. ASTM D854 (2002) Standard test method for specific gravity of soil solid by water pycnometer. ASTM Int, West Conshohocken
12. ASTM D4318 (2000) Standard test method liquid limit, plastic limit and plasticity index of soil. ASTM Int, West Conshohocken
13. ASTM D698 (2003) Standard test method for laboratory compaction characteristics of using standard effort. ASTM Int, West Conshohocken
14. ASTM D2435 (2004) Standard test methods for one dimensional consolidation properties of soil using incremental loading. ASTM Int, West Conshohocken
15. ASTM D4764 (2002) Standard test method for consolidated undrained triaxial compression test for cohesive soils. ASTM Int, West Conshohocken

Chapter 48
High-Energy Diffraction Microscopy Characterization of Spall Damage

John F. Bingert, Robert M. Suter, Jonathan Lind, Shiu Fai Li, Reeju Pokharel, and Carl P. Trujillo

Abstract The emerging characterization technique of high-energy diffraction microscopy (HEDM) was used to investigate ductile dynamic damage evolution in a Cu polycrystal. Experimental efforts were undertaken with the goal of elucidating correlations between microstructural features with preferred damage nucleation sites and the progression of damage at the localization stage. HEDM was used to microstructurally map the initial volume of a 1.2 mm-diameter Cu sample. HEDM in the near-field mode collects diffraction information from high-energy synchrotron radiation to non-destructively probe microstructure and orientation in three dimensions in volumes approaching the bulk scale. The Cu sample was subsequently planar shock-loaded in a plate-on-plate geometry and soft-recovered, using an assembly specially developed for sub-size samples. The ex situ shocked sample was then re-characterized by HEDM, providing data on the location of incipient spall voids with respect to the local microstructural neighborhood. In addition, diffraction quality and misorientation gradient data provide qualitative measures of the spatial distribution of stored work and indicate regions of plastic localization. This provides the potential for unprecedented insight as to the relative preference of spall nucleation sites and correlations between microstructure, damage, and plastic flow.

Keywords High-energy diffraction microscopy • Damage • 3D characterization • Spall • Synchrotron radiation

48.1 Introduction

Material damage initiation, and its evolution to eventual failure, is controlled by its relationship with the microstructure within which it occurs. However, the mechanisms by which microstructure affects damage are not thoroughly understood due to the stochastic nature of most damage processes, along with the complexity and variability of material structures. This understanding is required to attain a physically-based predictive model of damage and subsequent failure. The difficulty of correlating microstructural features with damage is especially true for dynamic processes.

A common challenge in this regard is that the relationship between damage processes and the microstructure occurs in a 3-dimensional (3D) frame. Although some of the structure–property relationships can be elucidated by stereological analysis of 2-dimensional sections, a complete description requires quantitative visualization of the surrounding neighborhood and its interaction with the damage front. This can be understood by considering the challenge of identifying damage initiation sites from a sample in the ex situ state. For a destructively prepared 2D section, the damage site itself has generally obliterated the region that initially constituted the initiation site. In addition, other clues as to the nature of the damage process are inaccessible since they reside out of the observation plane.

J.F. Bingert (✉) • C.P. Trujillo
Los Alamos National Laboratory, P.O. Box 1663, Los Alamos, NM 87545, USA
e-mail: bingert@lanl.gov

R.M. Suter • J. Lind • R. Pokharel
Carnegie Mellon University, 5000 Forbes Avenue, Pittsburgh, PA 15213, USA

S.F. Li
Lawrence Livermore National Laboratory, 7000 East Avenue, Livermore, CA 94550, USA

B. Song et al. (eds.), *Dynamic Behavior of Materials, Volume 1: Proceedings of the 2013 Annual Conference on Experimental and Applied Mechanics*, Conference Proceedings of the Society for Experimental Mechanics Series,
DOI 10.1007/978-3-319-00771-7_48,

The research described here involved the 3D characterization of ductile dynamic damage, referred to as spall [1], in a copper polycrystalline sample. A previous effort to investigate spall through 3D characterization used serial sectioning of a *post mortem* tantalum sample to probe the relationship between incipient spall voids and their microstructural neighborhood [2]. Through 3D interrogation several features of the damage region could be identified, such as the development of a 3D plastic zone network between seemingly isolated spherical voids. This was surmised to be a precursor to the development of a spall failure plane. However, these data left many questions unanswered, such as the nature of the true initiation site, the local structure with respect to the embryonic stages of the damage process, and characterization of the entire damage region rather than a metallographic subset.

In order to overcome these shortcomings, an approach leveraging the penetrating features of synchrotron-generated high-energy x-rays was recommended. The development of 3D X-ray diffraction (3DXRD) based techniques at synchrotron sources has opened a frontier of research involving 3D non-destructive characterization of materials [3, 4]. In particular, orientation mapping through high-energy diffraction microscopy (HEDM) [4] is particularly suited to identify microstructural neighborhoods corresponding to damage features. An optimal approach would be an in situ diagnostic capability that permits direct observation of dynamic damage evolution. Although 3DXRD techniques have been used to observe plastic deformation and damage in uninterrupted and interrupted in situ tests associated with quasi-static deformation [5–7], the combination of spatial and temporal resolution required for dynamic diffraction imaging of metals is well beyond current synchrotron sources. Nascent techniques are being developed at the Advanced Photon Source (APS) at Argonne National Laboratory (ANL) to directly interrogate dynamic processes [8–10], and these promise to bring remarkable insight. However, the spatially resolved diffraction necessary to reconstruct microstructures is currently unattainable. Therefore, the subject research was intended to exploit currently available synchrotron capabilities. Specifically, an experiment was designed to pre-characterize a bulk specimen, perform ex situ dynamic deformation, then to non-destructively recharacterize the same sample.

48.2 Materials and Experimental Method

An incipient spall sample was prepared from a plate of 99.997 % pure polycrystalline Cu (C101) in the as-received ½-hard condition. Copper was chosen as a representative face-centered cubic metal that exhibits a low nucleation threshold to spall, so that subsequent impact testing resulted in a reasonable probability of developing incipient spall voids. In addition, the relatively low Z-number made it amenable to X-ray penetration of a significant volume, as opposed to the previously characterized tantalum material. A section of the plate was machined, then annealed in vacuum at 450 °C for 30 min in order to obtain a strain-free initial state with a sufficiently coarse grain size to enable subsequent resolution of grain-scale microstructural features. An electron backscatter diffraction (EBSD)-generated 2D crystal direction map from a representative section of the annealed sample is shown in Fig. 48.1. The mean grain size, defined by the general high-angle boundary network, was 30 μm. Inclusion of the recrystallization twin boundaries in the measurement resulted in a calculated mean grain size of 14 μm. The distribution of grain size was very wide, with some grains on the order of 100–200 μm.

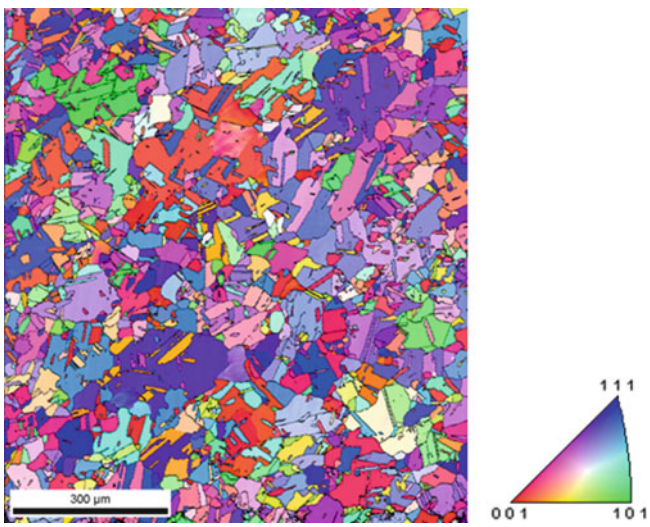

Fig. 48.1 EBSD crystal direction map of rolling direction-normal section from recrystallized Cu

Fig. 48.2 Schematic of cylindrical HEDM sample indicating pre-shocked measured region. Dimensions in mm (color figure in online)

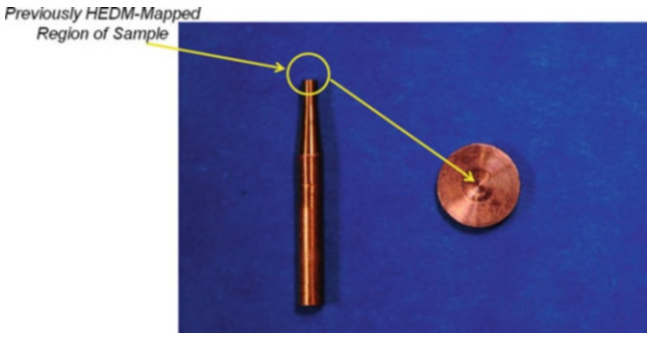

Fig. 48.3 Photograph of mini-spall target assembly consisting of pre-characterized sample surrounded by two momentum trap rings, along with original HEDM sample

The fabricated sample configuration for HEDM measurement at the APS is shown schematically in Fig. 48.2. The yellow-highlighted region in the 1.2 mm-diameter cylindrical sample represents the location of the volume subsequently 3D characterized at APS. This region was referenced to the end of the sample to provide registration for sectioning of the shock sample.

HEDM was performed at the APS 1-ID beamline. Diffraction data were collected on 170 non-destructive 2D slices through the entire diameter of the sample with 4 μm spacing between slices. It was important to pre-characterize a comparatively significant volume (~0.7 mm^2) in order to provide adequate material to enable near-bulk shock loading. Following HEDM characterization, the mapped volume was micro-machined from the sample, with a small buffer length of non-measured material on either end resulting in a machined length of 0.725 mm.

A novel method was developed to enable shock loading of such a relatively diminutive sample. The 'mini-spall' sample design needed to address several requirements; provide plate-on-plate impact, radial momentum trapping, and soft-capture capability. A 7.6 mm-diameter gas-driven Taylor gun was modified to use in place of a traditional gas gun typically used for plate impact experiments on larger targets. Several trials on sub-size samples were performed to develop an adequate design to strip the sample from its momentum traps after impact, and also to calibrate the impact velocity to produce incipient spall voids within the sample. Figure 48.3 shows a photograph of the final target assembly configuration prior to shock impact, consisting of the sample embedded within two radial momentum traps of the same Cu material, along with the HEDM sample from which it was machined.

The target assembly was impacted at 300 ms^{-1} by an assembly consisting of a pusher machined from MZ-24 syntactic foam (Engineered Syntactic Systems, Attleboro, MA) and a 0.36 mm-thick Cu flyer plate that contacted the target. The flyer plate was designed to be half the thickness of the target sample in order to induce maximum negative pressure, and therefore potential shock damage, along the mid-plane of the sample. The chronological progression of the shock experiment, recovered sample, and HEDM sample are depicted in Fig. 48.4. This new HEDM sample was subsequently recharacterized at APS.

48.3 Results and Discussion

Indexing of the HEDM-generated diffraction patterns through a forward-modeling technique [4] elicits information on the spatial position, crystallographic orientation, and relative confidence of the indexing. Figure 48.5 shows a representative layer of the microstructure as measured by HEDM from the pre-shocked sample. This orientation map is generated by assigning colors indexed to crystallographic orientation space, while misorientation boundaries greater than 15° are outlined.

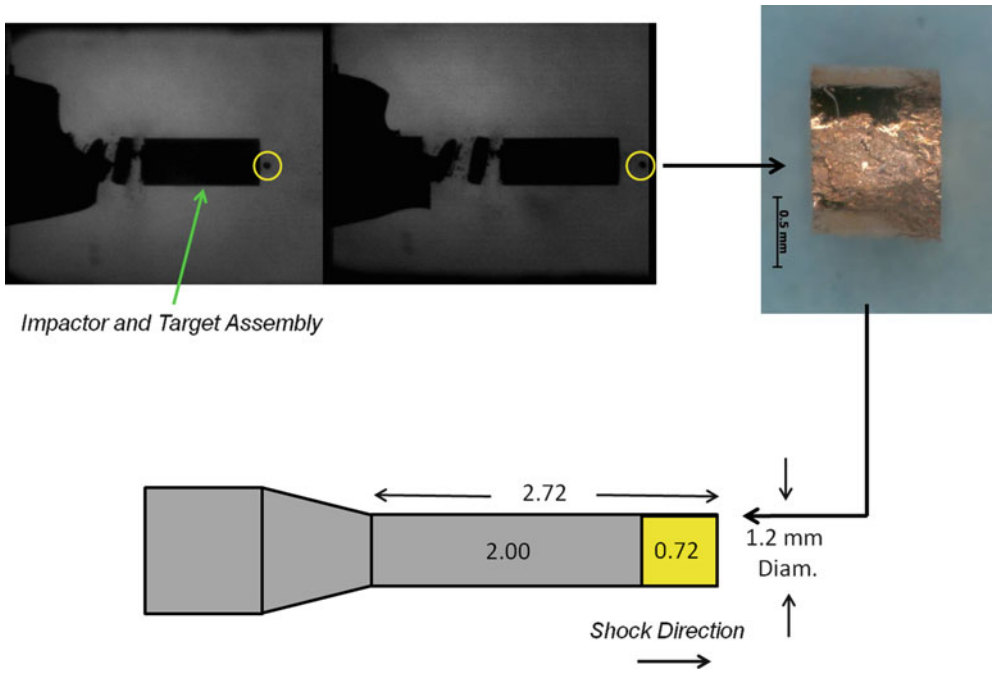

Fig. 48.4 High-rate camera images from the shock experiment show the release of the sample (*circled*) from the target assembly after impact. A photograph of the recovered sample and a schematic showing the placement of the shocked sample in the new HEDM sample are also shown

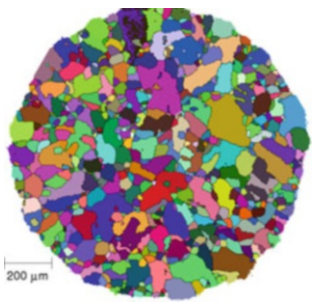

Fig. 48.5 Orientation map from one of 170 HEDM-measured layers of the pre-shocked Cu sample (color figure in online)

The complete reconstruction of the pre-shocked sample was performed on the measured 170 layers. Figure 48.6 shows two perspectives of the 3D reconstruction, with the colors again representing different orientations. This volume incorporated on the order of 10^4 individual grains, and provided a near-bulk polycrystalline assemblage for subsequent shock loading.

In addition to identifying individual grains based on misorientation, several other microstructural parameters can be derived from HEDM data, quantified, and mapped. Four different representations from the same layer of HEDM data are shown in Fig. 48.7. The crystal direction map provides information on directions of individual grains with respect to a chosen reference frame (normal direction in this case), referenced to the colored inverse pole figure. The index confidence map is a relative measure of the quality of the diffraction pattern generated at each voxel. For the recrystallized microstructure considered in the pre-shocked condition, higher confidence is correlated with the interiors of larger grains, while the grain boundary regions show lower confidence. For deformed material, index confidence may be a proxy to identify spatial gradients in plastic work. The kernel misorientation map displays the local orientation gradient within a user-defined region. Regions with high kernel misorientation may represent 'hot spots' of damage nucleation in deformed material. Finally, different grain boundary types can be displayed by a grain boundary map. In the case of Fig. 48.7d, the map shows coincident site lattice (CSL) boundaries in the Cu, which are derived from the recrystallization twin network. All of these representations can be generated in 3D and thus provide insight as to the complete network of grain boundaries, grain edges (triple points in 2D), and their relationship to misorientation gradients, voids, cracks, and any other features of interest.

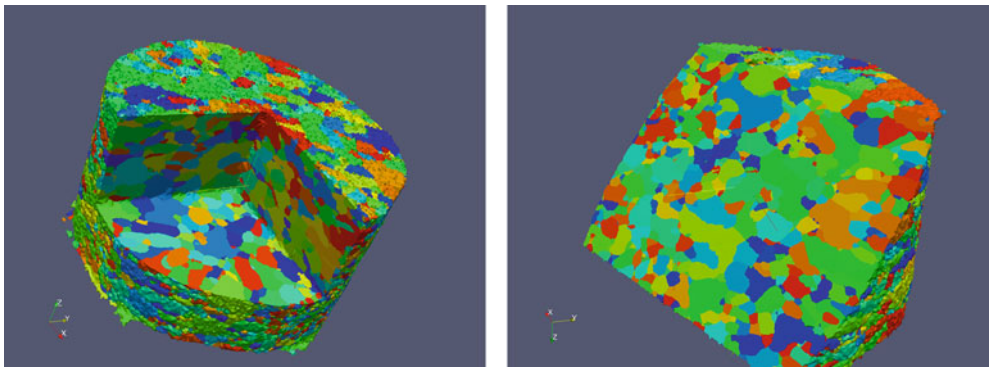

Fig. 48.6 3D reconstruction of the 170 HEDM layers from the pre-shocked Cu sample (color figure in online)

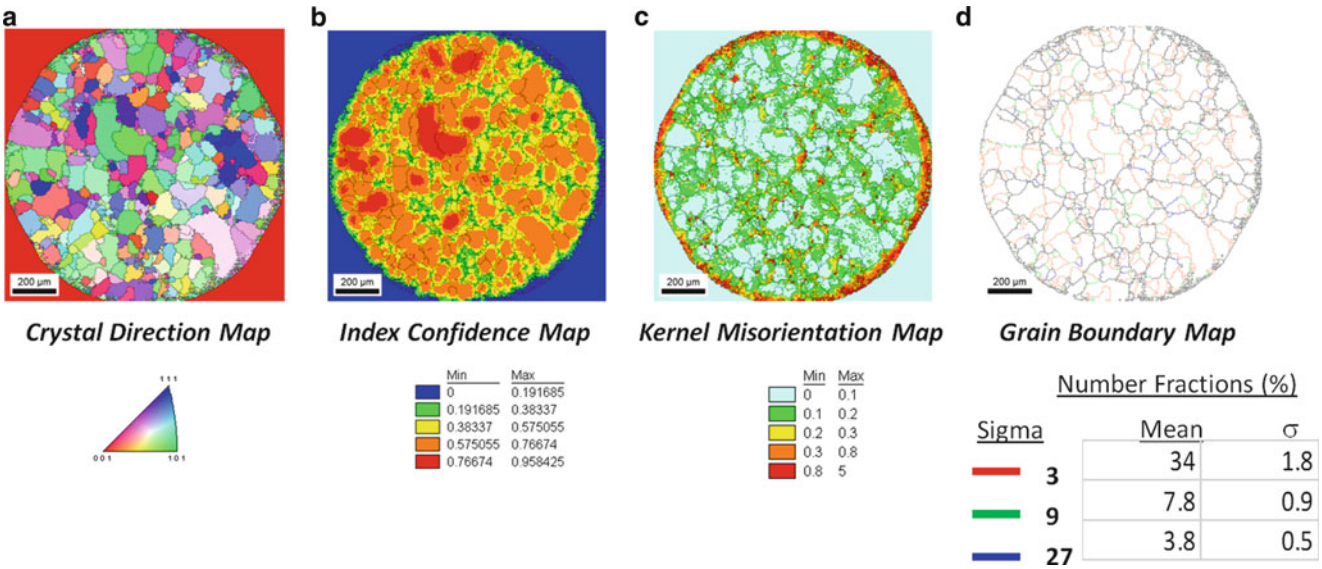

Fig. 48.7 Several microstructural representations derived from the HEDM data of the pre-shocked Cu sample (color figure in online)

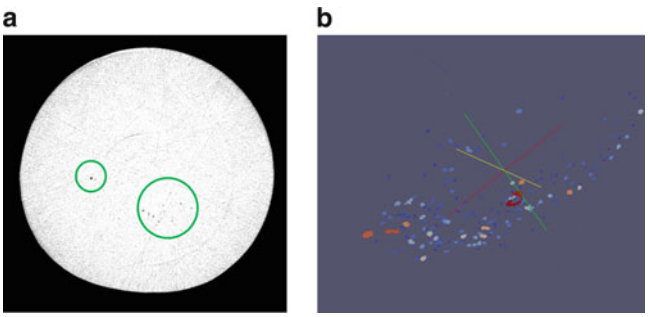

Fig. 48.8 Tomographic representations from the post-shock Cu sample; (**a**) 2D section with regions of incipient spall circled, (**b**) 3D distribution of segmented voids

Following the ex situ shock impact experiment, tomographic characterization was performed at APS prior to HEDM interrogation. Tomography results (Fig. 48.8) reveal that a void network associated with shock-induced incipient spallation has evolved across the sample's mid-plane. The 3D segmentation indicates that voids were heterogeneously distributed across the mid-plane, and were captured in their small (less than the average grain size), incipient state. This is encouraging

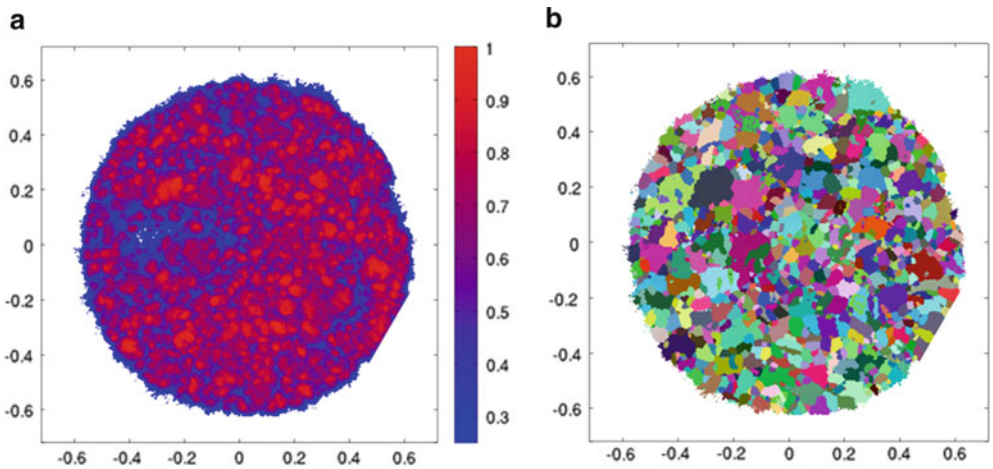

Fig. 48.9 2D maps from post-shocked Cu; (**a**) index confidence, (**b**) orientation

for further analysis, as it suggests that the neighborhood surrounding the initiation site should be preserved. However, in order to explore the relationship between damage and microstructure the shock-affected structure must be indexed.

For the post-shock sample, 130 layers spaced 4 μm apart were collected, representing 520 μm of the total 720 μm axial sample length. These measured sections captured the damaged mid-plane region. Diffraction patterns for deformed material are not as tractable to standard solution modeling as strain-free structures. Techniques to permit indexing of HEDM diffraction data from deformed microstructures are currently evolving [11]. This can be challenging due to non-ideal diffraction patterns related to dislocation-generated peak broadening and potential peak shifts from residual strain in the deformed sample. A new peak ID method utilizing a Laplacian coupled with a Gaussian filter for noise reduction was required for the shocked Cu. Figure 48.9 shows confidence and orientation maps for a successfully indexed layer. The confidence map indicates regions (blue) of increased stored work that may be associated with strain localization surrounding a void. The orientation map shows that the improved indexing routine can provide solutions for non-ideal diffraction from a deformed sample. Completion of this analysis will allow spatial information of voids from tomography with the associated HEDM microstructural data, and finally registration with the pre-shock HEDM data.

48.4 Summary

HEDM data was non-destructively collected on a significant volume of polycrystalline Cu in both the pre- and post-shock state. A novel ‘mini-spall’ experimental procedure was developed in order to generate shock-driven incipient spall in a 1.2 mm-diameter sample amenable to 3D synchrotron interrogation. These results provide for unprecedented insight between microstructure and damage evolution in an unperturbed near-bulk system. Complete indexing of the shocked structure, followed by registration of coordinates between the initial and shocked states, will generate a comprehensive 3D catalog of void initiation sites, the microstructure correlated with these sites, and any plastic gradients evolved between the voids. This database will be especially valuable for the continued development and validation of microstructure-sensitive damage models.

Acknowledgments The authors would like to thank several individuals for their assistance: C.M. Hefferan (CMU) for HEDM measurements at APS, R. Randolph (LANL) for micro-machining, M.F. Lopez (LANL) for heat treating, G.T. Gray III (LANL) for providing material, M. Tucker (LANL) for APS assistance, and D. Martinez (LANL) for experimentation. U. Lienert (ANL) provided invaluable technical assistance at APS. The authors gratefully acknowledge the support of the Joint DoD/DOE Munitions Program and the National Nuclear Security Administration’s Science Campaign 2. In addition, the LANL LDRD Program and associated collaborations with E.K. Cerreta and C.A. Bronkhorst were instrumental in securing APS beam time. Use of the Advanced Photon Source was supported by the U.S. DOE/BES under Contract No. DE-AC02-06CH11357. Los Alamos National Laboratory is operated by Los Alamos National Security, LLC, for the National Nuclear Security Administration of the U.S. Department of Energy under contract DE-AC52-06NA25396.

References

1. Meyers MA, Aimone CT (1983) Dynamic fracture (spalling) of metals. Prog Mater Sci 28:1–96
2. Bingert JF, Henrie BL, Worthington D (2007) Three-dimensional characterization of incipiently spalled tantalum. Met Mater Trans A 38:1712–1721
3. Suter RM, Hefferan C, Li SF, Hennessy D, Xiao C, Lienert U, Tieman B (2008) Probing microstructure dynamics with X-ray diffraction microscopy. J Eng Mater Technol 130, 021007
4. Lienert U, Li SF, Hefferan CM, Lind J, Suter RM, Bernier JV, Barton NR, Brandes MC, Mills MJ, Miller MP, Jakobsen B, Pantleon W (2011) High-energy diffraction microscopy at the advanced photon source. JOM 63:70–77
5. Ludwig W, King A, Herbig M, Reishig P, Marrow J, Babout L, Lauridsen EM, Proudhon H, Buffiere JY (2010) Characterization of polycrystalline materials using synchrotron X-ray imaging and diffraction techniques. JOM 62:22–28
6. Herbig M, King A, Reischig P, Proudhon H, Lauridsen EM, Marrow J, Buffiere JY, Ludwig W (2011) 3-D growth of a short fatigue crack within a polycrystalline microstructure studied using combined diffraction and phase-contrast X-ray tomography. Acta Mater 59:590–601
7. Pokharel R, Li SF, Lind J, Hefferan CM, Lienert U, Lebensohn RA, Suter RM, Rollett AD (2012) Quantifying damage accumulation using state-of-the-art FFT method. Mater Sci Forum 702–703:515–518
8. Jensen BJ, Luo SN, Hooks DE, Fezzaa K, Ramos KJ, Yeager JD, Kwiatkowski K, Shimada T, Dattelbaum DM (2012) Ultrafast, high-resolution, phase contrast imaging of impact response with synchrotron radiation. AIP Adv 2, 012170
9. Luo SN, Jensen BJ, Hooks DE, Fezzaa K, Ramos KJ, Yeager JD, Kwiatkowski K, Shimada T (2012) Gas gun shock experiments with single-pulse x-ray phase contrast imaging and diffraction at the advanced photon source. Rev Sci Instrum 83, 073903
10. Jensen BJ, Owens CT, Ramos KJ, Yeager JD, Saavedra RA, Iverson AJ, Luo SN, Fezzaa K, Hooks DE (2013) Impact system for ultrafast synchrotron experiments. Rev Sci Instrum 84, 013904
11. Li SF, Lind J, Hefferan CM, Pokharel R, Lienert U, Rollett AD, Suter RM (2012) Three-dimensional plastic response in polycrystalline copper via near-field high-energy X-ray diffraction microscopy. J Appl Cryst 45:1098–1108

Chapter 49
Quantitative Visualization of High-Rate Material Response with Dynamic Proton Radiography

E.N. Brown, R.T. Olson, G.T. Gray III, W.T. Buttler, D.M. Oro, M.B. Zellner, D.P. Dandekar, N.S.P. King, K.K. Kwiatkowski, F.G. Mariam, M. Marr-Lyon, F.E. Merrill, C. Morris, D. Tupa, A. Saunders, and W. Vogan

Abstract Proton Radiography or pRad was invented at Los Alamos National laboratory employing a very high-energy proton beam to acquire up to 37 images of dynamic experiments often driven by high explosives (HE). The high energy of the beam from the Los Alamos Neutron Science Center's 800-mega-electron-volt (MeV) proton linear accelerator (LINAC) provides penetrating power sufficient to resolve fine details (~65 μm resolution) in materials and structures under extreme conditions that are difficult to discern with other techniques. Three experiments utilizing pRAD to quantitative visualize the dynamic response of materials are presented. High strain-rate (10^7 s^{-1}) strength measurements are performed by visualizing a Rayleigh-Taylor unstable interface driven by HE products with pRAD tied to material pedigree, processing and phase changes. High-explosive driven ejecta experiments probing the Richtmyer-Meshkov instability in metals employ pRAD's ability to visualize the nuances of unstable spike growth with complementary diagnostics. Experiments impacting and penetrating glass probe the anomalous material response and Equation-of-State under a complex three-dimensional loading using both pRAD's ability to visualize and determine material density. In all three experiments proton radiography provides temporal and spatial visualization of dynamic material deformation and the ability to make in situ measurement of material state.

Keywords Quantitative visualization • Proton radiography • High strain-rate strength • Richtmyer-Meshkov instability • Penetration

49.1 Introduction

The proton radiography (pRad) facility at the Los Alamos Neutron Science Center (LANSCE) (see [1–5], Fig. 49.1) provides a unique capability using a proton beam and magnetic lens imaging system to study complex material response under extreme loading conditions. The 800 MeV protons penetrate through dense objects (up to 60 g/cm^2 areal density) with outstanding spatial (65 μm) and temporal resolution (exposure duration of ~150 ns and minimum inter frame spacing as fast as 250 ns, although longer inter frame times are often chosen based on experimental requirements) for up to 37 images (21 with the highest spatial resolution). As protons interact through the strong nuclear force and the electromagnetic force, quantitative visualization by pRad (Fig. 49.2) allows for simultaneous imaging and determination of material properties [1].

E.N. Brown (✉) • R.T. Olson • W.T. Buttler • D.M. Oro • N.S.P. King • K.K. Kwiatkowski • F.E. Merrill
Los Alamos National Laboratory, P-23, Mail Stop H803, Los Alamos, NM 87545, USA
e-mail: en_brown@lanl.gov

G.T. Gray III
Los Alamos National Laboratory, MST-8, Mail Stop G755, Los Alamos, NM 87545, USA

M.B. Zellner • D.P. Dandekar
U.S. Army Research Laboratory, RDRL-WMP-D, Aberdeen, MD 21005, USA

F.G. Mariam • C. Morris • D. Tupa • A. Saunders
Los Alamos National Laboratory, P-25, Mail Stop E549, Los Alamos, NM 87545, USA

M. Marr-Lyon • W. Vogan
Los Alamos National Laboratory, WX-3, Mail Stop H846, Los Alamos, NM 87545, USA

B. Song et al. (eds.), *Dynamic Behavior of Materials, Volume 1: Proceedings of the 2013 Annual Conference on Experimental and Applied Mechanics*, Conference Proceedings of the Society for Experimental Mechanics Series,
DOI 10.1007/978-3-319-00771-7_49,

Fig. 49.1 LANSCE experimental areas [4]. For scale, the LINAC measures almost 1 km in length

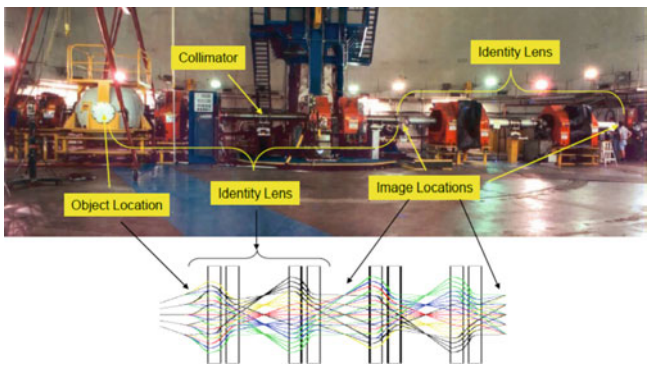

Fig. 49.2 800 MeV pRad facility at LANSCE [4]

In contrast with x-radiography, its positively charged proton beam can be manipulated with electromagnetic lenses to eliminate parallax effects in the object plane by forming a plane wave proton pulse, much like an optical lens manipulating photon beams. Moreover, pRad images through high explosive (HE) products that obscure high speed optical imaging. Advances in magnetic lens designs significantly mitigate blur in the image plane from protons energy lose passing through dense objects in interaction plane [5].

Proton Radiography provides unique insights in to dynamic experiment and understanding of the fundamental behavior of materials. It has been used to diagnose more than 300 dynamic experiments. It has significantly advanced our understanding of the response of materials under extreme loading and the detonation physics of HE. High explosive induced spall and damage in metals are complex phenomena with relevance to many areas of materials science for which pRad is a useful quantitative tool, as outlined in work by Holtkamp et al. [6]. Quantitative, direct density measurements to better than 1 % accuracy have been made in shock-compression experiments using the plate-impact technique with proton radiography providing unprecedented data for the development of robust equations of state [7, 8]. Oró et al. [9] utilized pRad to study the transport of tungsten particles ejected into a gas from a shocked interface. Ferm et al. [10] employed transmission radiographs from pRad to map out the undetonated regions of insensitive explosive PBX 9502 to better understand corner turning of the detonation front. Aslam et al. [11] similarly used the ability of pRad to image the detonation of PBX 9502 to study the effects of confinement. Smilowitz et al. [12, 13] observed the mass flow and density changes in the ideal explosive PBX 9501 over the final seconds prior to the thermal explosion. Adding new dynamic loading capability, the Precision High Energy-density Liner Implosion eXperiment (PHELIX) has been commissioned as a pulsed power platform to perform magnetically driven hydrodynamics experiments at pRad [14]. While the unique capabilities of pRad make for an unparalleled tool for the study of very rapid events, it also can be applied as an in-situ diagnostic for longer time scale phenomenon such as monitoring of alloy melt fluid flow and solidification [15].

The current work highlights three experiments where proton radiography provides temporal and spatial visualization of dynamic material deformation and the ability to make in situ measurement of material state. High strain-rate (10^7 s^{-1}) strength measurements are performed by visualizing a Rayleigh-Taylor unstable interface driven by HE products with pRAD tied to material pedigree, processing and phase changes. High-explosive driven ejecta experiments probing the Richtmyer-Meshkov instability in metals employ pRAD's ability to visualize the nuances of unstable spike growth with commentary diagnostics. Experiments impacting and penetrating glass probe the anomalous material response and Equation-of-State under a complex three-dimensional loading using both pRAD's ability to visualize and determine material density.

49.2 Utilization of LANL's Proton Radiography Facility to Study High Strain Rate Material Strength

Numerous industrial, engineering, and defense applications rely on the ability to predict the plastic deformation of metals using large-scale hydrodynamic simulations. These simulations utilize embedded constitutive models [16–20] describing the continuum-level strength of the material. The strength model parameters are primarily obtained through the fitting of stress–strain curves obtained from quasi-static load frames and Hopkinson bar experiments. As such, both the strength models and the simulations that rely on them are most accurate throughout the range of conditions where these experimental techniques are well suited to yield data: strains <100 % and strain-rates $<10^4\ s^{-1}$. These conditions span the range of interest for most industrial and engineering applications, but often defense applications such as explosive loading and high-velocity impact reach conditions with strains of several 100 % at strain rates between $10^5\ s^{-1}$ and $10^8\ s^{-1}$. The validity of strength models at these more extreme conditions is currently being assessed using experiments that generate and measure strength-inhibited Rayleigh-Taylor (RT) instability growth in metals.

The measurement of RT instability growth in solid metals has been extensively used to assess dynamic material strength using pulsed power, lasers, and HE as the accelerating mechanism. Recently, a series of such experiments building on the techniques originally developed by Barnes et al. [21] have been conducted at the Los Alamos Neutron Science Center (LANSCE). The experimental technique utilizes the by-products from a HE plane wave lens to shocklessly accelerate a sample with a sinusoidal perturbation imposed on one surface, illustrated in Fig. 49.3.

The Proton Radiography (pRad) facility at LANSCE is used to measure the growth rate of the unstable perturbations as a function of time. Measurements acquired during each experiment typically result in 20–40 pRad radiographs with a temporal spacing of 350–500 ns and a spatial resolution of ~100 μm. A representative proton radiography data set is shown below in which an annealed copper sample was perturbed with an initial sinusoidal perturbation 2.0 mm in wavelength and 55 μm in amplitude, shown in Fig. 49.4. The HE by-products reached the perturbed surface of the sample and began to accelerate it 6.9 μs after the experiment was initiated.

Analysis of each proton radiograph yields the peak-to-trough perturbation amplitude at each image acquisition time. The perturbation amplitude as a function of time is compared to the perturbation growth rate predicted using different strength models in hydrodynamic simulations. Variation of sample material, acceleration, and the initial perturbation amplitude allows us to assess the predictive accuracy of strength models under these high strain and strain-rate conditions. This technique has recently been applied to the phase (bcc-hcp (α-ε)) dependent strength of iron [22].

49.3 Utilization of LANL's Proton Radiography Facility to Study Ejecta

In one type of dynamic experiment, the pRad tool has been used to develop physics based ejecta models for shock-loaded metals [23]. These physics and engineering models are being developed and implemented in hydrodynamics codes to better understand the dynamics of material failure of shock-loaded materials as the shockwaves reach and reflect from the metal-vacuum interface of shock-loaded materials. The basic geometry from this work, and the concepts and 2 pRad images are seen in Fig. 49.5. This figure presents a snapshot of unstable Richtmyer-Meshkov (RM) growth of solid and liquid metals in vacuum [23]. The metals were HE loaded by detonation of a 76 mm diameter plane wave lens used to initiate other explosives such as a TNT or PBX 9501 booster. The TNT type explosives were used to drive a shockwave into Sn, causing the Sn to liquefy and the surface perturbations to unstably grow. The PBX 9501 was used to shock OFHC Cu. In the Sn case the goal was to validate the applicability of RM physics to ejecta formation from roughened surfaces as the shockwaves

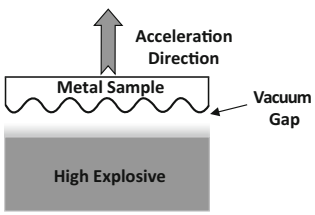

Fig. 49.3 Schematic of a strength-inhibited RT instability growth in metals being driven with HE

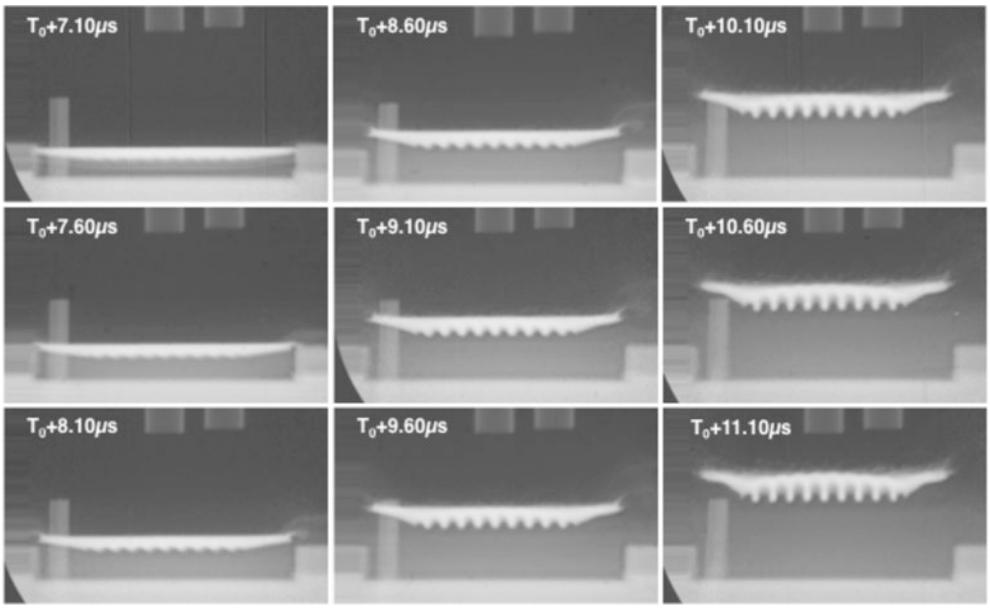

Fig. 49.4 Movie of strength-inhibited Rayleigh-Taylor (*RT*) instability growth in solid metals. Time increases from the *top left* image to the *bottom right* image

interact with the surface perturbations or scratches, and in the Cu case we were evaluating the utility of RM physics to evaluate material strength at high strains and strain rates.

Considering Fig. 49.5 in more detail, to the left is the notional geometry typically used in RM-physics experiments at pRad. For example, we encase the 76 mm diameter HE lens in acetal plastic to confine the explosion and maintain detonation pressures. The HE lens then initiates the HE booster (TNT or PBX 9501) that drives a shockwave into the target assembly. As illustrated in the center panel, the target has small sinusoidal perturbations on it that are characterized by wavelength, l, and amplitude, *h*. As the mostly planar shockwaves arrives at the interface it first releases to zero pressure at the perturbation minima and then reflects back into the metal as a rarefaction wave. A brief time later the shockwave releases to zero pressure at the perturbation maxima, also reflecting back into the metal as a rarefaction wave. Under these conditions, the stresses produced by the shockwave interacting with the perturbations cause the perturbation minima to compress, invert, and then grow in tension as RM instabilities (spikes) into vacuum. Because the compressed RM spikes grow quickly relative to the initial perturbation maxima, the initial maxima invert and form bubbles that unstably grow into the metal causing metal to flow into the spikes to support the spike growth. In this picture, bubbles and spikes refer to peak penetration depths on the opposite sides of the free-surface, which is nominally defined as the plane through the inflections of the initial two-dimensional sinusoidal surface perturbations. Importantly, the shocked free-surface will have a particle velocity caused by the impulse that is related to the strength of the impulse. The bubbles grow in a negative sense into the metal (Sn or Cu) relative to the free surface, and the spikes grow in a positive sense relative to the free surface. Thus there are three velocities that are important: the bubble, the free-surface, and the spike velocities. These physics are notionally illustrated in the center panel. The final panel shows 1 snapshot of each the Sn and Cu from two pRad experiments. These target assemblies had wavenumber amplitude products of $kh \in \{3/4, 1/8, 3/8, 3/2\}$ from the top in Fig. 49.5. Clearly evident are bubble and spike dynamics for the *kh* products in the Sn and Cu. The images to the right in Fig. 49.5 were acquired 7.7 μs after the shockwave reached the Sn/Cu interface. The shockwave pressures for the two geometries were 210 kbar (21 GPa) for the Sn, and 360 kbar (36 GPa) for the Cu. The free-surface and spike velocities can be estimated from the image time (7.7 μs), and the distance the surface and spikes have traveled. Full documentation of these experiments is in [23].

The goal of the Sn work was an ejecta model based on RM physics. That model is represented by Eqs. 2.1–2.9 in [23]. The Cu data evaluated an idea developed by Piriz et al. in [24]. In that work they postulated that the growth and arrest of surface perturbations in shocked metals that were solid on shock and release could be used to estimate material strength. In applying their ideas we estimate the material strength of Cu from the $kh = 3/8$ perturbation region of Cu to be about 0.5 GPa [23]. The idea is to look at perturbations that invert, grow, and then arrest. It is seen that for $kh = \{3/1, 3/2\}$ that the instabilities grow without bound, like the liquefied Sn. In this case they have formed ejecta. When the growth begins and then arrests the velocimetry contains information about material strength. We are currently exploring these types of Cu data further with simulations and strength models, such as PTW [25], and hope to report on that work soon.

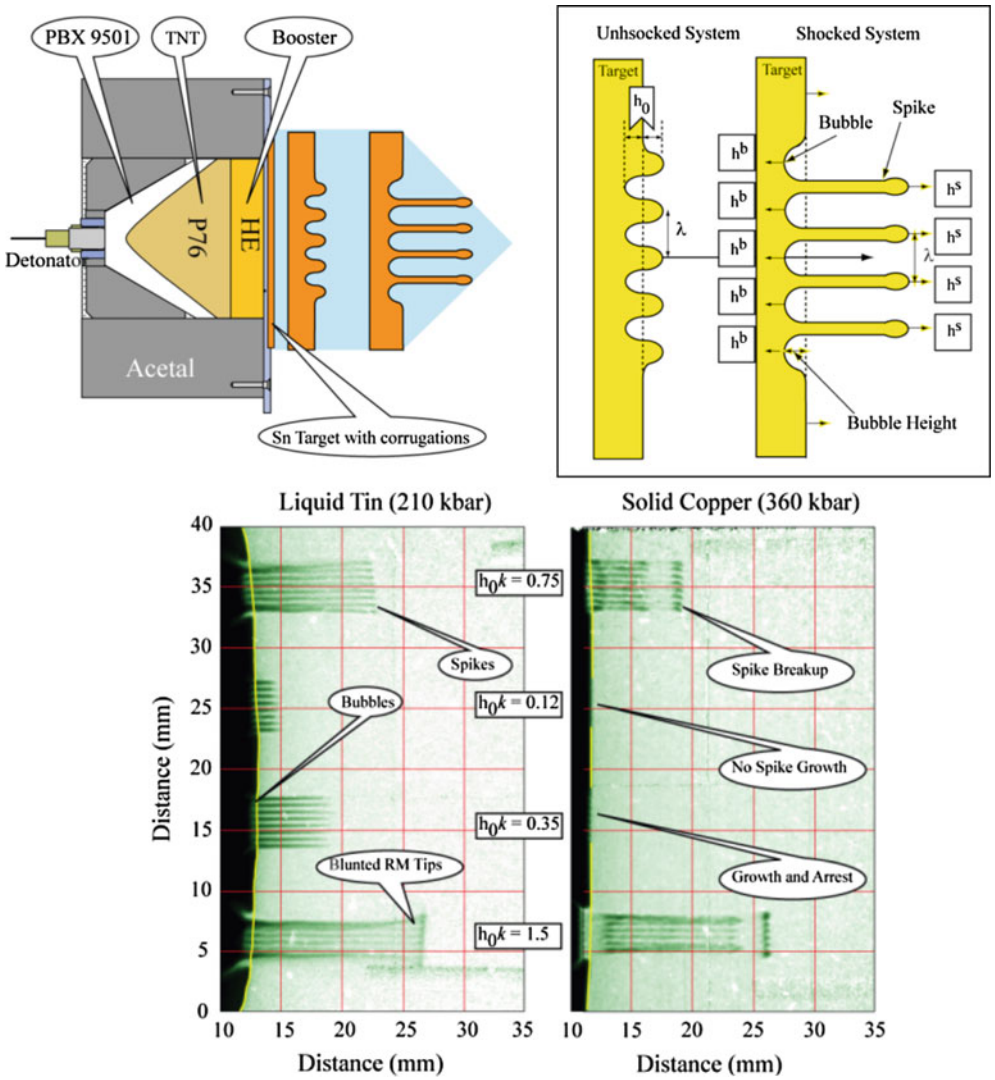

Fig. 49.5 The left figure approximates our typical experimental geometry, in which an HE booster is initiated with a 76 mm diameter HE lens. The sample surface has sinusoidal perturbations defined by their wavelength (λ) and amplitude (h), as shown in the middle figure. The pRad proton beam is aligned along the perturbations to image the unstable Richtmyer-Meshkov flows, as shown in the pRad images to the extreme right. The perturbations are characterized by the wavenumber ($k = 2\pi/\lambda$) amplitude products (kh), and the growth rates are higher for larger kh

49.4 Utilization of LANL's Proton Radiography Facility to Study Penetration Dynamics

Recently U.S. Army Research Laboratory (ARL) scientists began utilizing the Los Alamos National Laboratory (LANL) proton radiography (PRad) facility to simultaneously study compression of a material and associated penetration dynamics at extreme pressures. The study consisted of observing a metallic jet penetrating a cylinder of armor material at LANL's PRad facility. The goal of this study was to gather, high resolution, time-sequenced information essential for understanding how a current armor material's physical mechanisms enhance penetration resistance during jet interactions. Figure 49.6 shows a time-sequential series of radiographs acquired just after the metallic jet impacted a target from one experiment.

In this experiment, radiographs provided information about the jet penetration rate, jet erosion dynamics, target material deformation and the penetration cavity evolution. The relatively long mean free path of 800 MeV protons, combined with a 120 mm × 120 mm imaging window, allowed material density measurements with sufficient contrast in targets where geometry provided some level of inertial confinement. Using static radiographs, the density of nominal material was measured to within 4 % of the absolute material density. Because of the PRad technique's unique capability to measure absolute material density at numerous times, ARL scientists were able to study the evolution of the 3-dimensional

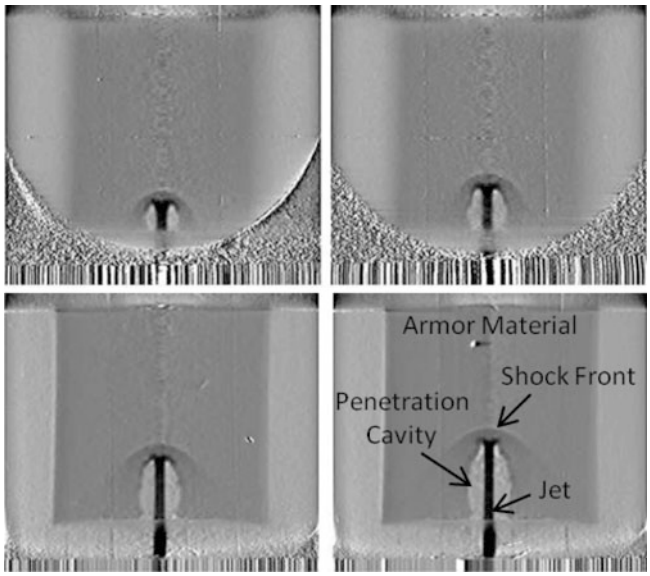

Fig. 49.6 Movie of a metallic jet penetrating into a cylindrically shaped armor material. Time increases from the *top left* image to the *bottom right* image

compression front (often referred to as a Mach cone) from impact, throughout its development, to its relatively steady state structure. This relatively steady state structure becomes established after ~5 μs of penetration for the material studied. Density measurements made within the steady state region directly ahead of the jet revealed the highest densities. In this region, the measured value of the density is found to be significantly different from both density measurements made quasistatically using diamond anvil cells (DAC), and dynamically from uniaxial compression plate impact experiments at similar pressures. Absolute material density measurements from proton radiography during the penetration event indicated that, when probed dynamically with a jet, the armor material specimen compressed only to ~70 % of the density which would be expected when applying material equation of state derived from quasistatic DAC and plate impact experiment measurements. Since theories of penetration mechanics are contingent on the penetrating medium's compressibility, deformation response, and ultimate density, a clear understanding of the in situ material response (i.e. the observed discrepancy in density) is important for designing armor with a high penetration resistance.

49.5 Conclusions

The Proton Radiography or pRad facility at Los Alamos National Laboratory is a robust tool for the quantitative visualization of material response at length-scales from the meso-scale to the continuum under high-rate loading. It is applicable to a wide range of experiments including strength inhibited RT growth, RMI in solids, and penetration as presented here, as well as a much broader range of experiments including material damage, shock physics, and HE detonation physics. Quantitative visualization by pRad allows for simultaneous imaging and determination of material properties.

Acknowledgements Los Alamos National Laboratory is operated by LANS, LLC, for the NNSA of the US Department of Energy under contract DE-AC52-06NA25396. M.B. Zellner and D.P. Dandekar wish to acknowledge collaborations with R. Becker, D. Kleponis, P. Patel, J. Runyeon, and T. Bjerke at ARL.

References

1. Gavron A, Morris CL, Ziock HJ, Zombro JD (1996) Proton radiography, Los Alamos national laboratory report LA-UR-96-420
2. Lisowski PW, Schoenberg KF (2006) The Los Alamos Neutron Science Center. Nucl Instrum Methods Phys Res A 562:910
3. Mariam FG, Merrill FE, Espinoza CJ, Heidemann JA, Hollander BJ, Kwiatkowski KK, Lopez JD, Lopez RP, Marr-Lyon M, McNeil WV, Morley DJ, Morris C, Murray MM, Nedrow P, Perry JO, Saunders A, Tainter AM, Trouw FR, Tupa D (2012) Proton radiography: its uses and resolution scaling. In: Grim GP, Barber HB (eds) Penetrating radiation systems and applications XIII. Proceedings of SPIE – the international society for optical engineering, vol 8509, 850904. doi: 10.1117/12.930569

4. Merrill FE (2008) and the pRad collaboration Proton Radiography Primer. http://lansce.lanl.gov/pRad/docs/pRad_Primer2.pdf
5. Merrill FE, Campos E, Espinoza C, Hogan G, Hollander B, Lopez J, Mariam FG, Morley D, Morris CL, Murray M, Saunders A, Schwartz C, Thompson TN (2011) Magnifying lens for 800 MeV proton radiography. Rev Sci Instrum 82:103709
6. Holtkamp DB, Clark DA, Ferm EN, Gallegos RA, Hammon D, Hemsing WF, Hogan GE, Holmes VH, King NSP, Liljestrand R, Lopez RP, Merrill FE, Morris CL, Morley KB, Murray MM, Pazuchanics PD, Prestridge KP, Quintana JP, Saunders A, Schafer T, Shinas MA, Stacy HL (2004) A survey of high explosive-induced damage and spall in selected metals using proton radiography. In: Furnish MD, Gupta YM, Forbes JW (eds) Shock compression of condensed matter – 2003: proceedings of the conference of the American physical society topical group on shock compression of condensed matter. AIP conference proceedings, vol 706, p 477. doi:http://dx.doi.org/10.1063/1.1780281
7. Schwartz CL, Hogan GE, Kwiatkowski K, Rigg PA, Rightley PM, Mariam FG, Marr-Lyon M, Merrill FE, Morris CL, Saunders A, Tupa D (2007) New capabilities of 800 MeV proton radiography at Los Alamos. In: Elert M, Furnish MD, Chau R, Holmes N, Nguyen J (eds) .Shock compression of condensed matter – 2007: proceedings of the conference of the American physical society topical group on shock compression of condensed matter. AIP conference proceedings, vol 955, p 1135. doi:http://dx.doi.org/10.1063/1.2832918
8. Rigg PA, Schwartz CL, Hixson RS, Hogan GE, Kwiatkowski KK, Mariam FG, Marr-Lyon M, Merrill FE, Morris CL, Rightly P, Saunders A, Tupa D (2008) Proton radiography and accurate density measurements: a window into shock wave processes. Phys Rev B 77:220101(R)
9. Oró DM, Hammerberg JE, Buttler WT, Mariam FG, Morris C, Rousculp C, Stone JB (2012) A class of ejecta transport test problems. In: Elert ML, Buttler WT, Borg JP, Jordan JL, Vogler TJ (eds) Shock compression of condensed matter – 2011: proceedings of the conference of the American physical society topical group on shock compression of condensed matter. AIP conference proceedings, vol 1426, p 1351. doi: 10.1063/1.3686531
10. Ferm EN, Morris CL, Quintana JP, Pazuchanic P, Stacy H, Zumbro JD, Hogan G, King N (eds) Proton radiography examination of unburned regions in PBX 9502 corner turning experiments. In: Furnish MD, Thadhani NN, Horie Y (eds) Shock compression of condensed matter – 2001: 12th APS topical conference. AIP conference proceedings, vol 620, p 966. doi:http://dx.doi.org/10.1063/1.1483699
11. Aslam TD, Scott I, Jackson SI, John S, Morris JS (2009) Proton radiography of PBX 9502 detonation shock dynamics confinement sandwich test. In: Elert ML, Buttler WT, Furnish MD, Anderson WW, Proud WG (eds) Shock compression of condensed matter 2009: proceedings of the American physical society topical group on shock compression of condensed matter. AIP conference proceedings, vol 1195, p 241. doi:http://dx.doi.org/10.1063/1.3295113
12. Smilowitz L, Henson BF, Romero JJ, Asay BW, Schwartz CL, Saunders A, Merrill FE, Morris CL, Kwiatkowski K, Hogan G, Nedrow P, Murray MM, Thompson TN, McNeil W, Rightley P, Marr-Lyon M (2008) Direct observation of the phenomenology of a solid thermal explosion using time-resolved proton radiography. Phys Rev Lett 100:228301
13. Smilowitz L, Henson BF, Romero JJ, Asay BW, Saunders A, Merrill FE, Morris CL, Kwiatkowski K, Grim G, Mariam F, Schwartz CL, Hogan G, Nedrow P, Murray MM, Thompson TN, Espinoza C, Lewis D, Bainbridge J, McNeil W, Rightley P, Marr-Lyon M (2012) The evolution of solid density within a thermal explosion. I. Proton radiography of pre-ignition expansion, material motion, and chemical decomposition. J Appl Phys 111:103515
14. Rousculp CL, Reass WA, Oro DM, Turchi PJ, Hollander BJ, Griego JR, Reinovsky RE (2011) The phelix pulsed power project: bringing portable magnetic drive to world class radiography. In: IEEE pulsed power conference, p 1067. doi 10.1109/PPC.2011.6191644
15. Clarke A, Imhoff S, Gibbs P, Cooley J, Morris C, Merrill F, Hollander B, Mariam F, Ott T, Barker M, Tucker T, Lee W-K, Fezzaa K, Deriy A, Patterson B, Clarke K, Montalvo J, Field R, Thoma D, Smith J, Teter D (2013) Proton radiography peers into metal solidification. Scient Reports 3:2020. doi:10.1038/srep02020
16. Steinberg DJ, Cochran SG, Guinan MW (1980) A constitutive model for metals applicable at high-strain rate. J Appl Phys 51:1498
17. Johnson GR, Cook WH (1983) A constitutive model and data for metals subjected to large strains, high strain rates and high temperatures. In: The proceedings of the 7th international symposium on ballistics, The Hague, Apr 1983
18. Preston DL, Tonks DL, Wallace DC (2003) Model of plastic deformation for extreme loading conditions. J Appl Phys 39:211
19. Zerilli FJ, Armstrong RW (1987) Dislocation-mechanics-based constitutive relations for material dynamics calculations. J Appl Phys 61:1816
20. Follansbee PS, Kocks UF (1988) A constitutive description of the deformation of copper based on the use of the mechanical threshold stress as an internal state variable. Acta Metall 36:81
21. Barnes JF, Blewett PJ, McQueen RG, Meyer KA, Venable D (1974) Taylor instability in solids. J Appl Phys 45:727
22. Belof JL, Cavallo RM, Olson RT, King RS, Gray GT III, Holtkamp DB, Chen S-R, Rudd RE, Barton NR, Arsenlis A, Remington BA, Park H-S, Prisbrey ST, Vitello PA, Bazan G, Mikaelian KO, Comley AJ, Maddox BR, May MJ (2012) Rayleigh-Taylor strength experiments of the pressure-induced $\alpha \rightarrow \varepsilon \rightarrow \alpha'$ phase transition in iron. In: Elert ML, Buttler WT, Borg JP, Jordan JL, Vogler TJ (eds) Shock compression of condensed matter – 2011: proceedings of the conference of the American Physical Society topical group on shock compression of condensed matter. AIP conference proceedings, vol 1426, p 1521. doi:10.1063/1.3686572
23. Buttler WT, Oro DM, Preston DL, Mikaelian KO, Cherne FJ, Hixson RS, Mariam FG, Morris C, Stone JB, Terrones G, Tupa D (2012) Unstable Richtmyer-Meshkov growth of solid and liquid metals in vacuum. J Fluid Mech 703:60–84
24. Piriz AR, Lopez-Cela JJ, Tahir NA, Hoffmann DHH (2008) Richtmyer-Meshkov instability in elastic–plastic media. Phys Rev E 78:056401
25. Preston DL, Tonks DL, Wallace DC (2003) Model of plastic deformations for extreme loading conditions. J Appl Phys 93:211–220

Chapter 50
Investigation of Dynamic Material Cracking with In Situ Synchrotron-Based Measurements

K.J. Ramos, B.J. Jensen, J.D. Yeager, C.A. Bolme, A.J. Iverson, C.A. Carlson, and K. Fezzaa

Abstract The development of time-resolved techniques that provide in situ spatially resolved measurements of the dynamic response of materials is a long-standing scientific need. Traditional methods use continuum measurements to infer the microstructure response of materials subjected to high strain rate loading; whereas advances in synchrotron capabilities and diagnostics provide unique opportunities to interrogate materials in situ. Recently we have implemented and performed experiments on a gas-gun system using single X-ray bunch phase contrast imaging (PCI) at the Advanced Photon Source to examine shock-induced phenomena. PCI is especially well suited for observing interfaces, something for which common shock physics and impact diagnostics are not. Here we present an overview of the capability and results from PCI investigations of in situ damage, including cracking and spall.

Keywords Synchrotron PCI • X-ray imaging • Dynamic cracking • Spall

50.1 Introduction

In uniaxial compression and tension experiments, traditional velocimetry diagnostics are used to detect dynamically created interfaces associated with material damage by observing wave interactions with free surfaces [1–3]. Interpretation of these wave interactions becomes increasingly more difficult when the interfaces are sufficiently heterogeneous and oblique to the shock front [4–6]. Optical imaging techniques can assist with interpretation but cannot resolve the initiation, propagation, and coalescence of cracking and spall in situ [7]. For these reason, new diagnostics are needed that can provide time and spatially resolved, in situ measurements of the dynamic response of materials. The ability to examine such processes is useful for understanding damage and failure processes in structural and armor materials [1, 2] and making direct measurements of material parameters, such as plane strain fracture toughness, under dynamic loading [8].

Phase contrast imaging (PCI) has shown promise for studying the dynamics of transient phenomena. One particularly compelling demonstration compared laser-lighted shadowgraphs with ultrafast synchrotron PCI to resolve the structure of high-speed liquid jets and sprays [9]. The jets and sprays appeared optically opaque in the shadowgraphs whereas PCI revealed fine features of the inner structure. The 472 ns 'superbunch' of the hybrid singlet mode was sufficient for imaging the low-velocity 20–70 m/s jets with 30 μm resolution associated with blur because of material motion. Recently, we have extended the application of PCI to examine the impact response of materials. Impact experiments involve particle and shock velocities up to 10 km/s. To minimize the effect of motion-blur on the image resolution and measurement after unloading

K.J. Ramos (✉) • B.J. Jensen • J.D. Yeager • C.A. Bolme
Los Alamos National Laboratory, PO BOX 1663, Los Alamos, NM 87545, USA
e-mail: kramos@lanl.gov

A.J. Iverson • C.A. Carlson
National Security Technologies, 182 East Gate Drive, Los Alamos, NM 87544, USA

K. Fezzaa
Advanced Photon Source, Argonne National Laboratory, 9700 South Cass Avenue, Argonne, IL 60439, USA

B. Song et al. (eds.), *Dynamic Behavior of Materials, Volume 1: Proceedings of the 2013 Annual Conference on Experimental and Applied Mechanics*, Conference Proceedings of the Society for Experimental Mechanics Series,
DOI 10.1007/978-3-319-00771-7_50,

from uniaxial strain, shorter exposures times are required (sub-nanosecond). This presents challenges with the total photon flux available from a single X-ray bunch, detection capabilities, and synchronization of the impact event with detectors and the X-ray bunch.

Towards this goal, we developed the IMPact System for Ultrafast Synchrotron Experiments (IMPULSE) located at the Advanced Photon Source (APS) [10]. IMPULSE consists of a mobile, single-stage gas gun with X-ray ports on the target chamber, degrees of freedom for target alignment with the beam, and a diagnostic system designed for synchronizing timing during synchrotron experiments [11]. Following an initial detector study that demonstrated the ability to image microstructure features in solids on sub-μs time scales using intensified charge-coupled detectors (ICCD) [12], the IMPULSE system was inserted into and synchronized with the X-ray beam at Sector 32 of the APS [10]. PCI images with 2–6 μm spatial resolution were successfully obtained using a single 80 ps duration X-ray pulse (FWHM) available every 153 ns in the standard mode of operation for the storage ring [13]. Synchronization was further improved by an order of magnitude to increase image intensity and eliminate photo bleaching of the scintillators [11]. With these improvements and approximately 5X more sensitive detectors, the capability to obtain multiple PCI images per experiment at 153 ns spacing was achieved by optically splitting the scintillator light to multiple ICCDs [14]. The frames were increased from one to four frames per experiment over several experimental series that required the development of a robust detector system using motorized positioning to optimize the spatial resolution on all cameras simultaneously [13, 14]. Here we report our progress using the IMPULSE capability to resolve the initiation, propagation, and coalescence of cracking. We compare our original experiments with our current four-frame capability (2–3 μm spatial resolution) to demonstrate important considerations in both diagnostic setup and experimental configuration. We also discuss ongoing efforts to quantitatively interpret the PCI images that are now available.

50.2 Experiments

PCI experiments were conducted at the APS Sector 32 beamline using the standard mode that provides 80 ps duration (FWHM) x-ray pulses every 153.3 ns [15]. The undulator gap was set to 30 mm and the sample-to-scintillator distances were between 220 and 320 mm. For this gap, the majority of the intensity was located in the first harmonic centered around 12.75 keV with a bandwidth of 0.74 keV FWHM and the peak radiance was about 3.85×10^{13} photons/s/0.1 % bandwidth. More detailed specifications of the beamline design are provided by Shen et al. [16]. Figure 50.1 illustrates the PCI experimental configuration within the X-ray hutch. This arrangement has been described in detail elsewhere [11, 13]. Briefly described, a series of slow and fast shutters are used to bracket the impact event typically within 15–30 ms of X-ray exposure. The beam is transmitted through X-ray transparent windows and interacts with the sample during impact. The X-rays are converted into visible light by the LuAG:Ce ($Lu_3Al_5O_{12}$:Ce) scintillator and directed towards Princeton Instruments PI-MAX ICCD optical cameras by a turning mirror. PI-MAX I and custom PI-MAX II cameras were used in this work and the effect on data will be detailed elsewhere [14]. A microscope objective is used to attain the desired magnification and the light is split and relayed to multiple ICCD cameras. The irradiance at Sector 32 and efficiency of the detection system is currently sufficient for obtaining PCI images at a minimum I/I_0 ratio of approximately 0.25 which enables investigation of materials with the thicknesses illustrated in Fig. 50.2. Figure 50.3 illustrates the impact experiment

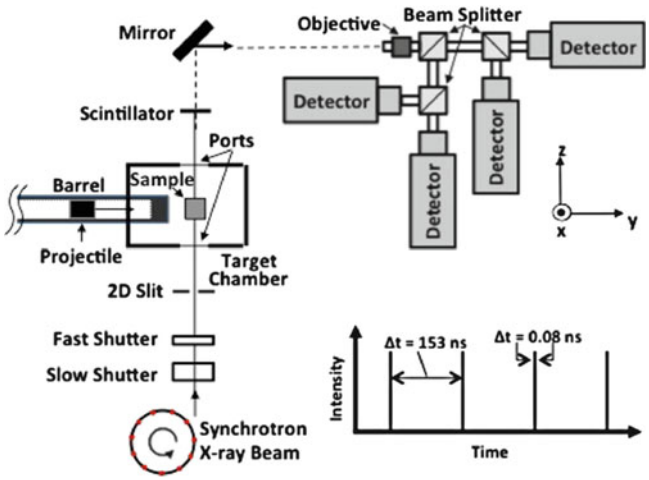

Fig. 50.1 Arrangement for gas-gun driven experiments using PCI at APS Sector 32

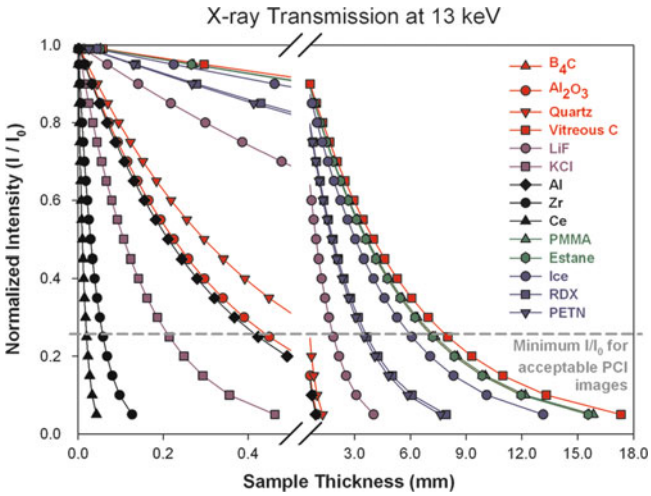

Fig. 50.2 I/I_0 ratios as a function of thickness for obtaining acceptable PCI image at APS Sector 32 using the current detection system (color figure in online)

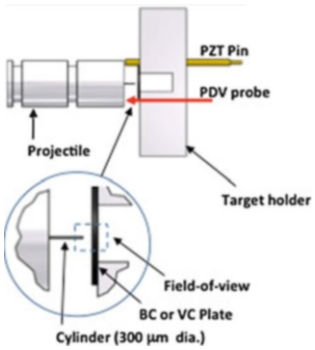

Fig. 50.3 Illustration of the impact experiment used to study crack nucleation and propagation

Table 50.1 Summary of experiments

Experiment configuration			Projectile velocity		Image times after
Cylinder Impactor	Target	Thickness along beam (mm)	(mm/µs)	Impact pressure[a] (GPa)	impact (µs)
Steel	PMMA	8	0.367	1.22	1.00
Steel	B_4C	8	0.616	8.8	1.40
Steel	VC	8	0.655	3.67	0.39
Cu	VC/soda lime glass/VC	1/0.5/1	0.685	4.17	1.30
Cu	VC	8	0.809	4.53	0.45/0.60/0.75/1.05

[a]Impact pressures were calculated by impedance matching using Hugoniots for the impactor and target materials and projectile velocities

used to study crack nucleation and propagation. It consisted of 300 µm diameter by 1 mm long cylinders striking plates of various materials as summarized in Table 50.1. The signal from a lead-zirconate-titanate (PZT) impact pin triggers a delay pulse generator (Stanford Research Systems DG535), which in turn triggers the ICCDs, and photon Doppler velocimetry (PDV) to record data at desired times after impact.

50.3 Results

The PCI results from three initial experiments are shown in Fig. 50.4. These images show stainless steel needles impacting Poly(methyl methacrylate) (PMMA), vitreous carbon (VC), and boron carbide (B_4C) plates. In Fig. 50.4a, the steel needle cleanly penetrates the PMMA with little observed deformation. For the B_4C and VC experiments (Fig. 50.4b, c), significant deformation of both the needles and the plates was observed with cracking visible in both plate materials. Note the layers,

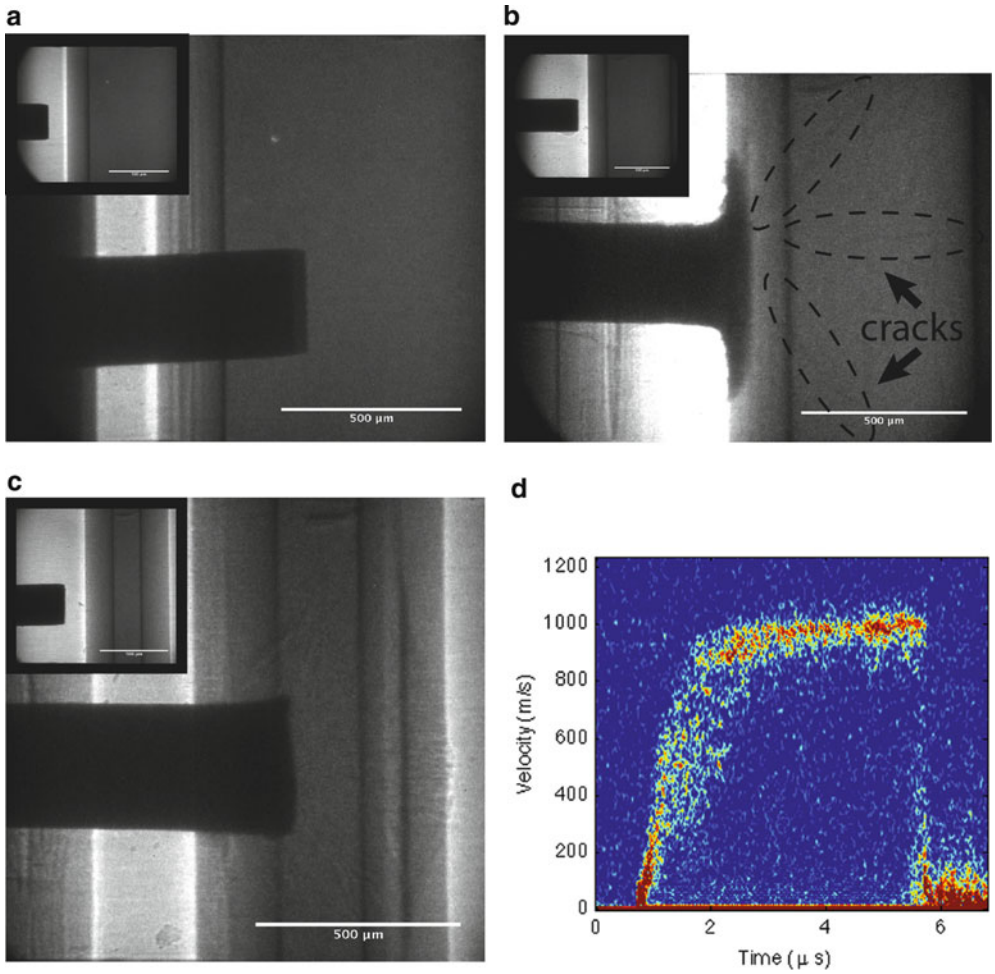

Fig. 50.4 PCI images of stainless steel needles impacting (**a**) PMMA, (**b**) B_4C, and (**c**) VC with static pre-shot images inset and (**d**) PDV data from the rear surface for VC (color figure in online)

visible in the plate before impact, are artifacts caused by misalignment of the plate with the X-ray beam. The width of the layers represents the obtuse cross-section. The extra vertical line visible in the VC experiment was a result of spall and fragmentation caused by release of the initial shock wave from the rear free surface. The PDV velocity history in Fig. 50.4d, obtained at this surface exhibited ramp compression, characteristic of VC [17], and a diffuse velocity region during which the ramp released from the rear surface, causing spall and fragmentation. To study denser materials with greater X-ray absorption, we explored an impedance matching sample configuration, which consisted of a 0.5 mm thick piece of soda lime (SL) glass sandwiched between two pieces of 1 mm VC. The X-ray beam penetrated through the two VC and glass layers as depicted in Fig. 50.5a. These VC layers were used to lessen the effect of lateral release waves on the observed deformation. The PCI images shown in Fig. 50.5b illustrate a Cu cylinder impacting the center SL glass plate. Significant deformation of the Cu and cracking in the SL glass were observed.

These initial results were promising and clearly pointed to areas for further improvement. As summarized in the introduction, a series of improvements to synchronization and the detection system were undertaken to use the available photons at Sector 32 more efficiently [11, 13, 14]. Following these improvements, the initial experiments were revisited to demonstrate their effects on the resolution of crack nucleation, propagation, and coalescence. Four frames of PCI images recorded the impact of a Cu cylinder onto a VC plate (Fig. 50.6). Cracks were observed to nucleate after impact and propagate to the rear surface where they coalesced in the spall area that developed following release of the compression wave from the rear surface. The resolution of the cracks was significantly improved compared to the initial results and sufficient for conducting detailed in situ crack investigations. A 7.5X objective was used for these images (1.42 µm/pixel) and the resolution was estimated to be 2–3 µm after using an Air Force resolution target to resolve the 4.39 µm/line pair.

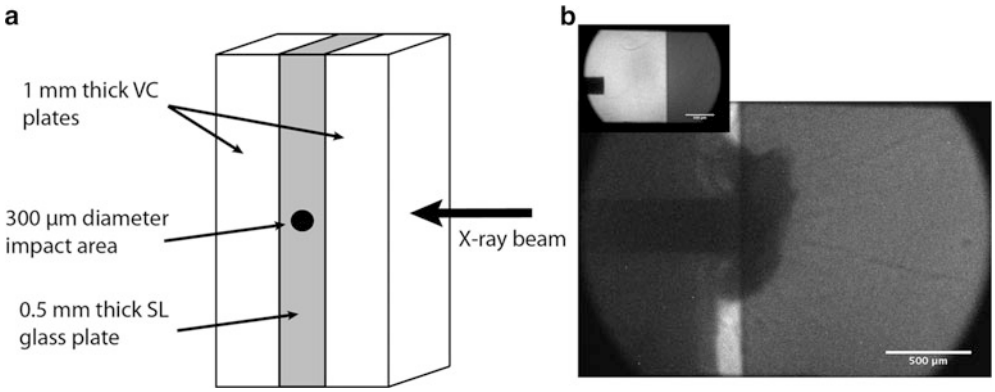

Fig. 50.5 (**a**) Schematic of the sandwich target configuration and (**b**) PCI image of a machined Cu cylinder impacting soda lime glass with static pre-shot image inset

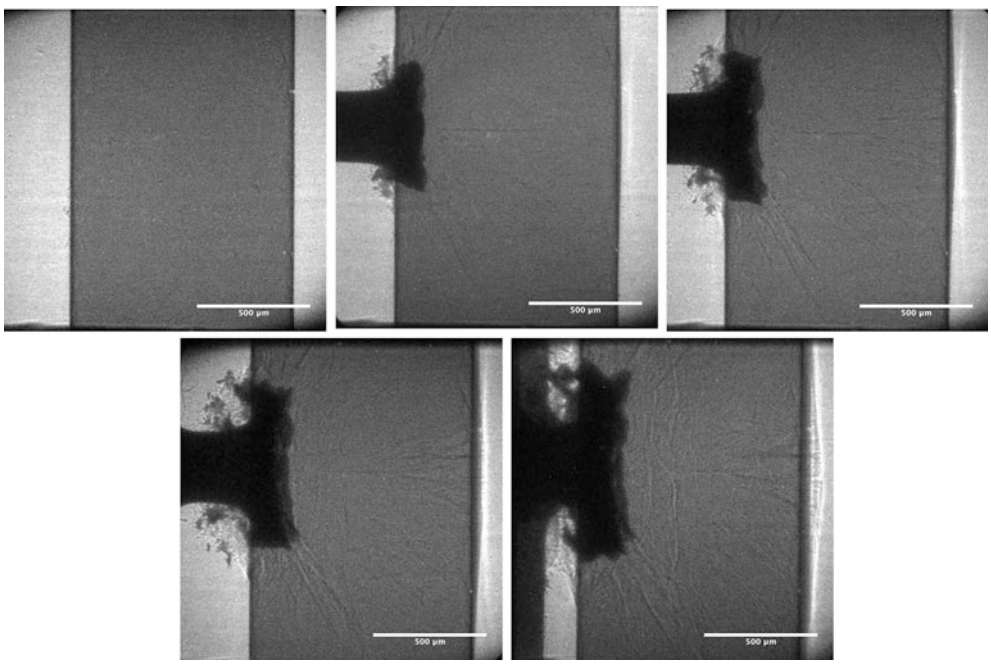

Fig. 50.6 PCI images of a machined Cu cylinder impacting vitreous carbon

50.4 Discussion

Crack nucleation, propagation, and coalescence can be seen using the IMPULSE capability. The four frame diagnostic setup, which uses four PI-MAX II ICCDs, provides sufficient spatial resolution to see an abundance of cracks within the brittle VC target. However, quantitative interpretation of the images and applying the method to less X-ray transparent materials remains challenging. Stock et al. confronted similar challenges while applying PCI to the investigation of fatigue cracks in Al and comparing with X-ray absorption microtomography [18]. They demonstrated that PCI was superior for resolving cracks through edge enhancement. The difficulty in quantitative interpretation arose from the two-dimensional projection of cracks in PCI images which was overcome using stereographic techniques for three-dimensional mapping [19]. This method is not

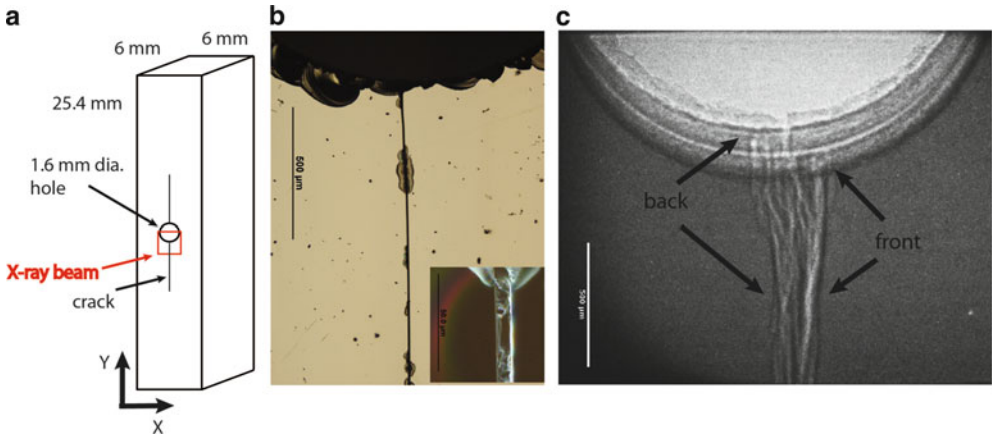

Fig. 50.7 (**a**) Schematic of the CT sample configuration along with (**b**) bright field optical image (*dark field inset*) and (**c**) PCI image of the crack (color figure in online)

currently feasible on the gas gun system because it would require multiple X-ray beams and longer exposure times to achieve sufficient signal-to-noise through relatively thick, X-ray opaque materials. Overcoming these limitations requires well-posed crack configurations to simplify data interpretation and the use of higher energy X-rays available at other beam lines.

Quantitative interpretation of cracking during cylinder impact is difficult because of two-dimensional projection. A cone of cracks formed and propagated towards the rear surface and was projected and overlapped in the PCI image. Therefore we fabricated a VC specimen that contained a single crack generated using compact tension (CT) to explore and illustrate the effects of the two-dimensional projection in a simpler configuration. The configuration of the CT sample is depicted in Fig. 50.7 (a) along with optical (b) and PCI images (c) of the crack. The crack is 8 μm wide at the surface as observed with optical microscopy and was imaged with the 5X objective for PCI. The image size scale was 2.14 μm/pixel and was sufficient to resolve the 6.21 μm/line pair on an Air Force resolution chart. Therefore, the PCI in Fig. 50.7c has a resolution of approximately 3–4 μm. The crack was resolved by PCI and appeared bigger because of misalignment with the beam. The crack and CT hole were misaligned with the beam by 2° and 2–4° rotation about the x and y-axis, respectively. The misalignment is beneficial for interpretation. The origin of the crack at the hole is clearly visible at the front and back surfaces of the 6 mm thick VC. In this alignment the crack appears to be approximately 80 μm thick in PCI, which is ten times bigger than the size of the crack at the surface using optical microscopy. Without knowing the sample contains a single crack, it would appear in PCI that there were two cracks or a single 200 μm thick crack with significant internal structure. These interpretation challenges illustrates why it is important to choose better-posed geometries than the cylindrical impact to study dynamic cracking with PCI. Prakash and Clifton have used a suitable configuration for studying crack propagation under conditions of plain strain during dynamic, planar-loading [8]. A spall configuration was used to create plane strain from the interaction of release waves at the precise location of a fatigue crack propagated and arrested halfway into a shock-loading specimen. In future work, we will directly observe the crack tip in similar configurations with PCI.

To broaden the application of PCI, the ability to image through denser materials is needed. In Fig. 50.2, the normalized X-ray intensity is plotted versus thickness for a variety of materials that can be studied with the X-ray energies and detection system used at APS Sector 32. This capability is sufficient for studying low density, low atomic number materials such as plastics like PMMA and Estane, glasses like VC, ceramics like B_4C, and molecular materials like water ice and explosives with thicknesses ranging from 4 to 8 mm. These thicknesses are sufficient for maintaining uniaxial strain within the central region of the sample during impact loading experiments. To image samples that are more opaque to X-rays, we designed an experimental configuration that used a thin SL glass sample (0.5 mm thick) sandwiched between two X-ray transparent VC plates (each 1 mm thick). These two plates were used to maintain the stress within the sample to provide sufficient time to perform the experiment prior to arrival of the edge release waves. In Fig. 50.5b, PCI results were presented for this configuration where cracks were successfully observed through the stack. Further work is needed to understand the loading conditions achieved (P,T states, etc.) using this configuration. Alternatively, imaging through larger monolithic samples requires higher energy X-rays that can penetrate through greater thicknesses for a wider range of materials. This is shown in Figure 50.8 where I/I_0 ratios are plotted as a function of thickness for a range of materials. It is evident that 50–100 keV is sufficient for imaging through a wider range of materials, including metals such as titanium, iron, copper, zirconium, and cerium. Detector feasibility tests are planned for the higher energy X-rays available at APS Sector 1.

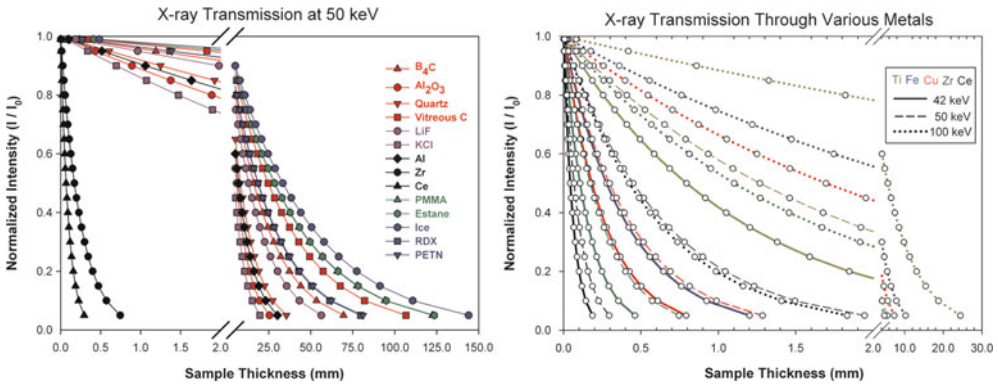

Fig. 50.8 I/I_0 ratios as a function of thickness for a range of materials at higher X-ray energies (color figure in online)

50.5 Conclusion

Single X-ray bunch phase contrast imaging coupled with the IMPULSE system located at Sector 32 of the APS was used to examine crack nucleation, propagation, and coalescence in various materials including vitreous carbon, boron carbide, PMMA, and soda lime glass. Images with 2–3 μm resolution were obtained and showed cracking within the samples as a function of time. Two experimental configurations were used to obtain such data and each highlighted the practical difficulties associated with the measurements. This demonstrated the need for well-defined and systematic series of experiments to examine single crack behavior. Further effort is needed to provide quantitative interpretation of cracking and to extend PCI to denser, less X-ray transparent materials such as metals.

Acknowledgements The authors wish to thank C. Owens and T. Pierce for assistance with sample preparation and gun operation, S.N. Luo, K. Kwiatkowski, and T. Shimada for their contributions to the initial PCI detection system, C. Liu and C.M. Cady for the CT sample, and A. Deriy (ANL) for diagnostic expertise at APS Sector 32-ID. This work was supported by the U.S. Department of Energy through LANL's MaRIE, Science Campaigns, and LDRD Program and National Security Technologies (NSTec) Shock Wave Related Diagnostics Program. Yeager was supported by an Agnew National Security Postdoctoral Fellowship. Los Alamos National Laboratory, an affirmative action equal opportunity employer, is operated by Los Alamos National Security, LLC, for the National Nuclear Security Administration of the U.S. Department of Energy under contract DE-AC52-06NA25396. Use of the Advanced Photon Source, an Office of Science User Facility operated for the U.S. Department of Energy (DOE) Office of Science by Argonne National Laboratory, was supported by the U.S. DOE under Contract No. DE-AC02-06CH11357.

References

1. Meyers MA, Aimone CT (1983) Dynamic fracture (spalling) of metals. Prog Mater Sci 28:1–96
2. Curran DR, Seaman L (1987) Dynamic failure of solids. Phys Rep 147(5):253–388
3. Kanel GI (2001) Distortion of the wave profiles in an elastoplastic body upon spalling. J Appl Mech Tech Phys 42(2):358–362
4. Kanel GI, Bogatch AA, Razorenov SV, Chen Z (2002) Transformation of shock compression pulses in glass due to the failure wave phenomena. J Appl Phys 92(9):5045–5052
5. Kanel GI, Razorenov SV, Utkin AV, He H, Jing F, Jin X (1998) Influence of the load conditions on the failure wave in glasses. High Press Res 16:27–44
6. Kanel GI, Zaretsky EB, Rajendran AM, Razorenov SV, Savinykh AS, Paris V (2009) Search for conditions of compressive fracture of hard brittle ceramics at impact loading. Int J Plast 25:649–670
7. Field JE, Walley SM, Proud WG, Goldrein HT, Siviour CR (2004) Review of experimental techniques for high rate deformation and shock studies. Int J Impact Eng 30:725–775
8. Prakash V, Clifton J (1990) Experimental and analytical investigation of dynamic fracture under conditions of plane strain. In: Ernst HA, Saxena A, McDowell DL (eds) Fracture mechanics: twenty-second symposium, ASTM International, Atlanta, pp 412–444
9. Wang Y, Liu X, IM K, Lee W, Wang J, Fezzaa K, Hung DLS, Winkelman JR (2008) Ultrafast X-ray study of dense-liquid-jet flow dynamics using structure-tracking velocimetry. Nat phys 4:305–309
10. Jensen BJ, Luo SN, Hooks DE, Fezzaa K, Ramos KJ, Yeager JD, Kwiatkowski K, Shimada T, Dattelbaum DM (2012) Ultrafast, high resolution, phase contrast imaging of impact response with synchrotron radiation. AIP Adv 2(1):012170–012176
11. Jensen BJ, Owens CT, Ramos KJ, Yeager JD, Saavedra RA, Iverson AJ, Luo SN, Fezzaa K, Hooks DE (2013) Impact system for ultrafast synchrotron experiments. Rev Sci Instrum 84(1):013904–013905

12. Yeager JD, Luo SN, Jensen BJ, Fezzaa K, Montgomery DS, Hooks DE (2012) High-speed synchrotron X-ray phase contrast imaging for analysis of low-Z composite microstructure. Compos Part A Appl Sci Manufact 43(6):885–892
13. Luo SN, Jensen BJ, Hooks DE, Fezzaa K, Ramos KJ, Yeager JD, Kwiatkowski K, Shimada T (2012) Gas gun shock experiments with single-pulse x-ray phase contrast imaging and diffraction at the Advanced Photon Source. Rev Sci Instrum 83(7):073903
14. Iverson AJ, Carlson C, Young J, Curtis, A, Jensen BJ, Ramos KJ, Yeager JD, Montgomery D, Fezzaa K (2013) X-ray diffraction and multi-frame phase contrast imaging diagnostics for IMPULSE at the Advanced Photon Source. Shock Compression of Condensed Matter 2013: Proceeding of the American Physical Society Topical Group on Shock Compression of Condensed Matter
15. Sajaev VV (2013) Storage ring operation modes. http://aps.anl.gov/Facility/Storage_Ring_Parameters/node5.html%3E. Accessed 20 Mar 2013
16. Shen Q, Lee W-K, Fezzaa K, Chu YS, De Carlo F, Jemian P, Ilavsky J, Erdmann M, Long GG (2007) Dedicated fullfield X-ray imaging beamline at advanced photon source. Nucl Instrum Methods Phys Res Sect A Accel Spectrom Detect Assoc Equip 582(1):77–79
17. Wu C, Gupta YM (2002) ISP report: the shock response of vitreous carbon, Institute for Shock Physics
18. Stock SR, Ignatiev K, Davis GR, Elliot JC, Fezzaa K, Lee W-K (2002) Fatigue cracks in aluminum samples studied with x-ray phase contrast imaging and with absorption microtomography. Adv X-Ray Anal 45:123–127
19. Ignatiev K, Lee W-K, Fezzaa K, Davis GR, Elliot JC, Stock SR (2003) Three-dimensional mapping of fatigue crack position via a novel x-ray phase contrast approach. Adv X-Ray Anal 46:314–319

Chapter 51
Impact Bend Tests Using Hopkinson Pressure Bars

R.A. Govender, G.S. Langdon, and G.N. Nurick

Abstract Bend tests under impact loading have traditionally been conducted using drop weight testers. However, the force readings from drop weight testers suffer from increasing oscillation (due to load frame vibration and stress wave excitation) as the impact velocity is increased. Different configurations of Hopkinson Pressure Bars (HPB) were adapted to conduct bend tests at impact rates have been presented in the literature. HPB are a well understood tool for measuring impact forces and velocities, but are limited by the duration of the impact event which may be measured. Thus prior HPB based bend test rigs have been limited to very short duration tests, and hence to materials with small deflections to failure. Some of the HPB bend test rigs have struggled with capturing well resolved force measurements, particularly for less rigid specimens. This paper presents a novel configuration of a HPB based bend test that results in vastly improved resolution of force measurements and increases the permissible specimen deflection by an order of magnitude greater than presented in past literature. Some results are presented for tests on Glass Fibre Reinforced Polypropylene (Twintex).

Keywords High strain rate testing • Hopkinson pressure bar • Flexural tests • Fibre reinforced polymers • Failure

51.1 Introduction

Impact loading of structures often involves a substantial bending component. As modern products are increasingly expected to perform after significant impact events, it is necessary to perform impact bending tests with increasing fidelity of measurements. The typical impact bend test has been performed using drop weight testers, instrumented with load cells. However, the measurements from these load cells often display oscillations, which can obscure critical data and increase in magnitude as the impact velocity is increased. The oscillations are due to the excitation of stress waves within the specimen and load frame and associated vibrations [1]. The impact velocity achievable with a drop weight tester is also limited by the available height.

Hopkinson Pressure Bars (HPB), which are a more appropriate means of measuring impact forces and velocities, have been adapted to bend test configurations. The simplest of these uses an input HPB to both impact a simply supported specimen and measure the specimen response, as shown in Fig. 51.1. This arrangement has been applied to both conventional flexural specimens, e.g. [2, 3] and notched fracture specimens, e.g. [4–6]. These studies have focussed on relatively stiff specimens with small deflections to failure ($\approx \leq 1$ mm). The deflection limitation is due to the limiting duration and loading velocity associated with a given HPB. The inherent duration limit of HPB is due to the requirement for no overlap of the incident (ε_I) and reflected (ε_R) strain waves and is determined by the physical length of the HPB and its wave speed. The loading velocity is limited by the requirement for the waves in the HPB to remain below the elastic limit of the bar material.

The force measurement in this arrangement is taken from the sum of the incident and reflected waves, shifted from the strain gauge to the bar-specimen interface:

$$F(t) = A_{bar}E_{bar}(\varepsilon'_I(t) + \varepsilon'_R(t)) \tag{51.1}$$

R.A. Govender (✉) • G.S. Langdon • G.N. Nurick
Blast, Impact and Survivability Research Unit, Department of Mechanical Engineering, University of Cape Town, Private Bag X3, Rondesbosch, 7701 Cape Town, South Africa
e-mail: reuben.govender@uct.ac.za

B. Song et al. (eds.), *Dynamic Behavior of Materials, Volume 1: Proceedings of the 2013 Annual Conference on Experimental and Applied Mechanics*, Conference Proceedings of the Society for Experimental Mechanics Series,
DOI 10.1007/978-3-319-00771-7_51,

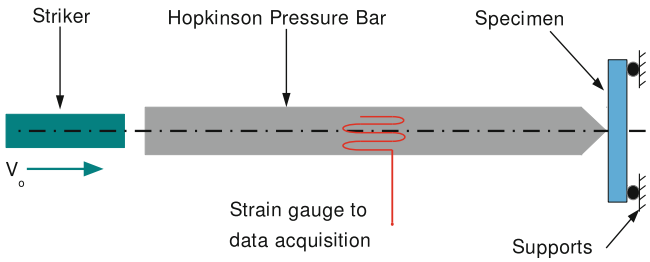

Fig. 51.1 Impact bend test using single input HPB

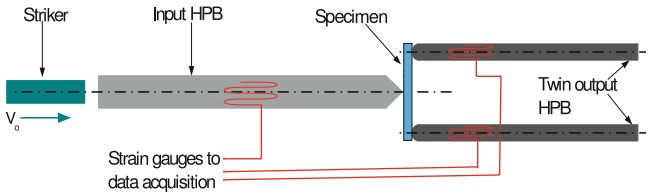

Fig. 51.2 SHPB used for bend tests with twin output bars

As these waves are opposite in sign (compressive incident wave and tensile reflected wave), the force exerted on the specimen is proportional to the difference in magnitude of the two. If this arrangement is used to test a relatively flexible specimen, the reflected wave is very close in magnitude to the incident wave due to the impedance mismatch between bar and specimen. The strain gauge data acquisition has to be set to capture the maximum magnitude of the incident wave, which results in very poor resolution of small differences between the incident and reflected waves, as noted in [5]. Hence this arrangement is not well suited to testing relatively flexible specimens.

Other bend test arrangements have used a Split HPB (SHPB) layout, with both an input and transmission bar. The better examples of this arrangement have used twin output HPB [7–9], as shown in Fig. 51.2, to avoid a test fixture with a large mass between the specimen and output bar.

Results reported in [7] showed almost no force was transmitted to the output bars, thus rendering the output bars of little use to force measurement. This was due to the output bars being used as the outer supports: the specimens tested in [7] were brittle ceramic, and failure occurred before the event could be transmitted from the central loading point to the outer supports by flexural and shear waves. Thus none of impact bend test arrangements in the literature seem suitable for testing flexible specimens and capturing well resolved force measurements. This investigation presents a novel arrangement of a HPB based impact bend test, which provides improved force resolution and superior deflection capacity.

51.2 Experimental Details

The new HPB Impact Bend test apparatus is shown in Fig. 51.3 and is explained with the aid of a schematic in Fig. 51.4. The specimen is supported at the two outer points on an impacter. The impacter is accelerated to the desired velocity using a pusher bar in a gas gun barrel. The pusher bar is arrested by a stopper, secured a predetermined distance from the barrel. The impacter, which runs on axial bearings, then continues at a constant velocity until the specimen impacts centrally against a HPB. The HPB is used to measure both the force and velocity at the central impact point of the specimen, while the position of the impacter is measured using a Reflective Object Sensor (ROS). A second stopper, which is omitted from both Figs. 51.3 and 51.4 for clarity, is used to arrest the impacter and specimen.

This arrangement provides all the necessary boundary conditions and measurements for an impact bend test, while having several advantages over previous arrangements for testing flexible specimens. The impacter supports the specimen at the outer points, where one is not interested in the force measurement. Thus it is only necessary to measure the displacement or position of the impacter, which is achieved using a non-contact Reflective Object Sensor (ROS). As this is a non-contact measurement, it does not suffer from vibrations as LVDT or other contact instruments do. The gas gun used to accelerate the impacter is easily capable of attaining impact velocities of approximately 15 m/s in a run up of less than 200 mm. The output bar is only used to measure force and velocity at the central impact point. In HPB arrangements as shown in Fig. 51.1, the input HPB parameters (bar material, diameter, length) must be chosen based on the loading requirements (impact velocity and energy) which often leads to compromises for the force measurement. In this case the bar material and diameter may be chosen specifically to suit the force measurement, improving resolution significantly. As the HPB is used as an output bar,

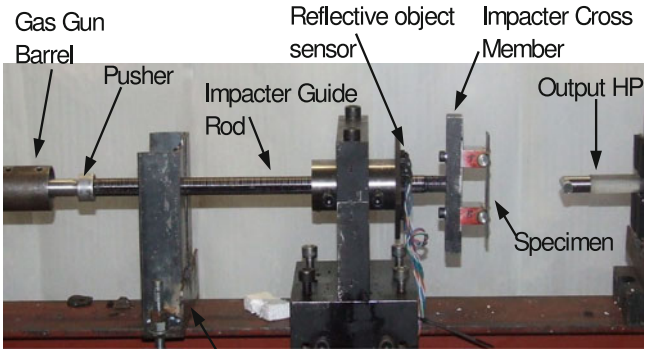

Fig. 51.3 HPB impact bend test apparatus

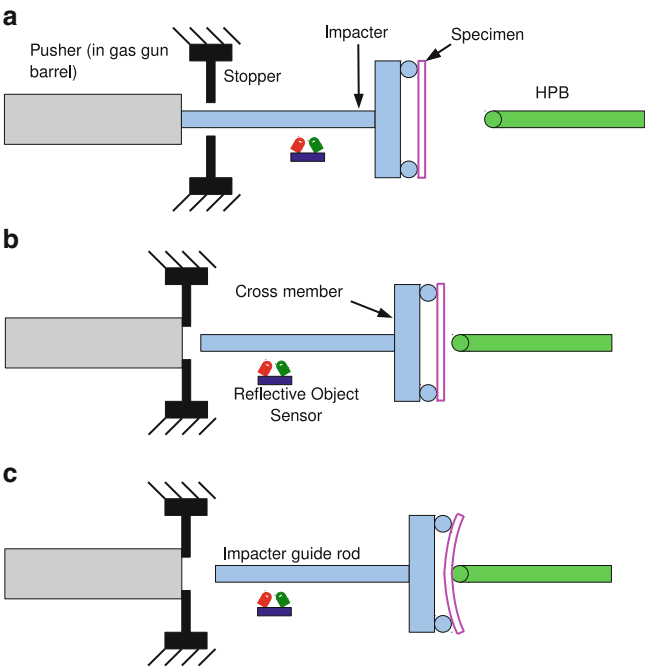

Fig. 51.4 Schematic explaining HPB impact bend test apparatus. (**a**) Pusher and impacter being accelerated by gas gun toward HPB. (**b**) Pusher arrested by stopper; impacter travelling at constant velocity towards HPB. (**c**) Specimen impacts centrally against HPB; inertia of impacter keeps outer supports moving, causing specimen to deform; force measured by HPB

the strain gauge may be mounted much closer to the impact end (as opposed to mid length on an input bar), which permits a longer duration of measurement for the same length of bar. This arrangement was designed for very flexible specimens, where the expected forces were in the range of a few hundred to a few thousand Newtons. At these low forces, one would either have to use a very small diameter metal bar (which is not necessarily practical) or resort to semiconductor strain gauges in order to obtain an acceptable signal to noise ratio for the strain gauge measurements. Using a polymeric bar, such as polycarbonate, results in much higher strains for the same force due to its lower elastic modulus ($E_y \approx 2.5$ Gpa). Polymeric HPB have a further advantage, as their inherently low wave speed ($C_o \approx 1{,}450$ m/s) increases the permitted measurement duration by a factor of almost three when compared to metallic HPB ($C_o \approx 5{,}100$ m/s). In this case, the polycarbonate output bar has a diameter of 16.7 mm and is 2,000 mm long, which permits a measurement duration of approximately 2.4 ms. Coupled with the increased impacter velocities, this permits experiments where the specimen deflection is approximately 10 mm, which is almost an order of magnitude greater than published in [2–9]. As polymeric HPB exhibit visco-elastic behaviour, the calibration of the bar and data processing of the signals is more complicated than for a metallic bar. However, if one has already implemented dispersion correction for a metallic HPB, then the visco-elastic correction simply requires the addition of correction for the attenuation effects. The details of data processing from a

polymeric HPB may be found in [10, 11]. The specimen supports on the impacter are adjustable up to a span of 100 mm. The specimen proportions stated in ASTM D790 were used, which specifies a 16:1 support span:specimen thickness ratio. The experiments in this paper are based on nominally 4 mm thick specimens and a support span of 64 mm. Both the strain gauge output on the HPB and the output of the ROS are captured on the same data acquisition system, at a sampling rate of 10 MSa/s at 16 bit resolution. The position of the impacter is measured directly using the ROS and is denoted x_{Imp}. Accounting for the velocity of the HPB tip, the specimen deflection δ_{Spec} is calculated from:

$$\delta_{Spec}(t) = x_{Imp}(t) - \int_0^t C_o \varepsilon_T(\tau) d\tau \tag{51.2}$$

The force measured by the output HPB F_{Out} is obtained from:

$$F_{out}(t) = A_{bar} E_{bar} \varepsilon'_T(t) \tag{51.3}$$

$\varepsilon'_T(t)$ denotes the transmitted strain captured on the output bar, shifted to the bar-specimen interface using the visco-elastic wave correction detailed in [11]. As the force measured by the HPB includes that necessary to decelerate the impacter, the force exterted on the specimen F_{Spec} is given by:

$$F_{Spec}(t) = F_{Out}(t) - m_{Imp} \frac{d^2 x_{Imp}}{dt^2} \tag{51.4}$$

m_{Imp} is the mass of the impacter, which was 1.0 kg.

The specimens used in this investigation were woven Glass Fibre Reinforced Polypropylene (GFPP), commercially sold as Twintex. GFPP panels were prepared to a nominal thickness of 4 mm. Specimens of width 25 mm and length 100 mm were cut from the panels using abrasive waterjet cutting. High speed video was captured using a Photron APX-RS camera, at a rate of 22,500 frames per second. The image resolution was 384 × 256 pixels at this rate.

51.3 Results and Discussion

All tests in this series were conducted at a nominal impact velocity of 8 m/s. An example of the raw analogue signals captured during a typical test is shown in Fig. 51.5. Impact occurred at 5.9 ms, with peak force at 7.3 ms. This peak force was confirmed to coincide with failure using high speed video, which showed a similar lapse of 1.4 ms between impact and failure. Frames from the high speed video are shown in Fig. 51.6. The specimen failure is clearly marked by the transition from a smooth parabolic profile in (a) to a sharp V profile in (b).

The specimen failed well within the 2.4 ms duration limit of this arrangement. The HPB strain gauge and ROS output voltages are processed to force and displacement respectively, which may then be plotted together as shown in Fig. 51.7. The early oscillation appears to be a feature of the test arrangement as it appears in all seven tests in this series, which are shown in Fig. 51.8. After the initial large oscillation, the specimen responds in an approximately linear manner as one would expect for GFPP, before exhibiting a well defined failure associated with fibre failure at the outer surface. Further analysis of the flexural strength and rate sensitivity is intended for future publications.

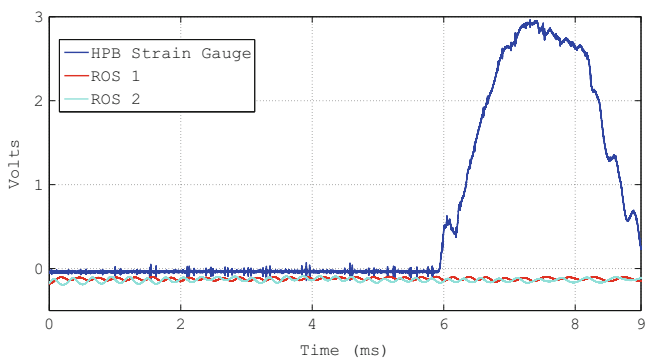

Fig. 51.5 Typical raw signals from HPB impact bend test

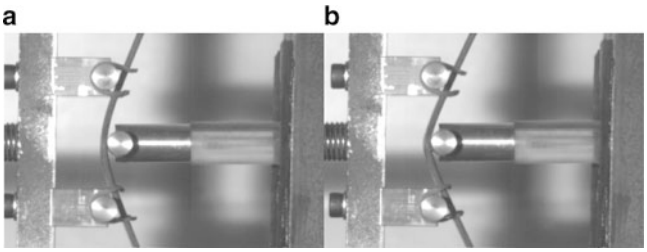

Fig. 51.6 Frames from high speed video showing specimen prior to and after failure

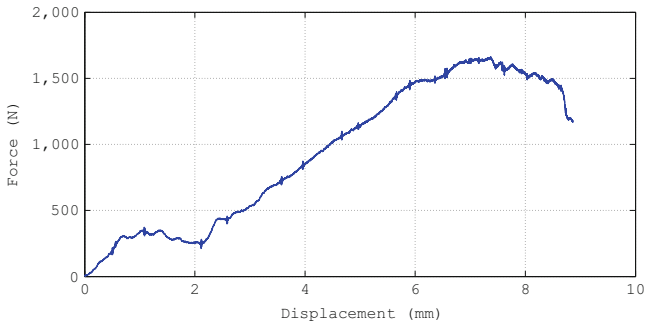

Fig. 51.7 Force displacement plot from HPB impact bend test

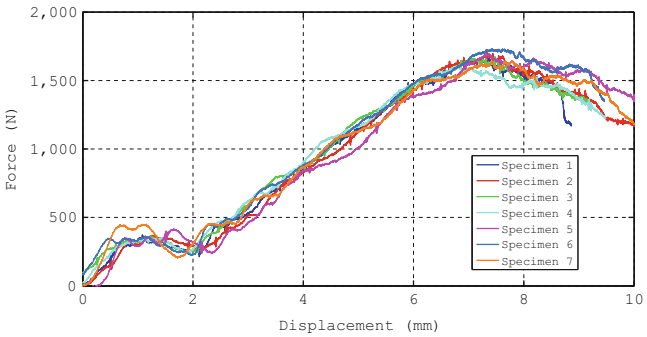

Fig. 51.8 Force displacement plot from HPB impact bend test

The early oscillation evident in all tests had a half period (peak to trough) varying from 0.09 to 0.11 ms. This did not correspond directly to any of the flexural modes of either the specimen or the impacter cross member. These oscillations may not be attributed to through thickness stress waves in the specimen nor the aluminium head of the HPB, which have wave transit times of the order of a few microseconds. The time taken for a axial stress wave to transit the impacter is 0.137 ms, making it unlikely these are the sole cause of the oscillations. Preliminary finite element analysis of the experiment does show similar oscillations after impact, suggesting that these oscillations are due to coupling of several vibration modes of the specimen and impacter.

51.4 Summary

A novel arrangement of a HPB Impact Bend Test apparatus was presented, which permits testing of very flexible specimens with deflections of the order of 10 mm. The resolution and duration of force measurement were significantly improved. The duration limit of this arrangement is due to the length of the HPB, which was the longest polycarbonate bar locally available. There is potential for longer durations by sourcing longer bars – the current support bed will easily accomodate a 5 m long bar. As there is no fixture between the specimen and HPB, the force measurement is direct and is easily corrected for the

inertia of the impacter. The force measurements do show some early oscillations, but these decay in sufficient time so that the forces associated with failure are not obscured. Further investigation of these oscillations is planned to improve the apparatus. Tests conducted on GFPP specimens showed consistent response, with acceptable scatter of the failure force.

References

1. Field JE, Walley SM, Proud WG, Goldrein HT, Siviour CR (2004) Review of experimental techniques for high rate deformation and shock studies. Int J Impact Eng 30:725–775
2. Park SW, Zhou M, Veazie DR (2000) Time-resolved impact response and damage of fiber reinforced composite laminates. J Compos Mater 34:879–904
3. Hallett SR (2000) Three-point beam impact tests on T300/914 carbon fibre composites. Compos Sci Technol 60:115–124
4. Ruiz C, Mines RAW (1985) The Hopkinson pressure bar: an alternative to the instrumented pendulum for Charpy tests. Int J Fract 29:101–109
5. Bacon C, Farm J, Lataillade JL (1994) Dynamic fracture toughness determined from load point displacement. Exp Mech 34:217–223
6. Rubio L, Fernandez-Saez J, Navarro C (2003) Determination of dynamic fracture initiation toughness using three point bending testing in a modified HPB. Exp Mech 43:379–386
7. Delvare F, Hanus JL, Bailly P (2010) A non-equilibrium approach to processing Hopkinson bar bending test data: application to quasi-brittle materials. Int J Impact Eng 37:1170–1179
8. Yokoyama T, Kishida K (1989) A novel impact three point bend test method for determining dynamic fracture initiation toughness. Exp Mech 29:188–194
9. Rubio-Gonzalez C, Gallardo-Gonzalez JA, Mesmacque G, Sanchez-Santana U (2008) Dynamic fracture toughness of pre-fatigued materials. Int J Fatigue 30:1056–1064
10. Bacon C (1998) An experimental method for considering dispersion and attenuation in a viscoelastic Hopkinson bar. Exp Mech 38:242–249
11. Curry R, Cloete T, Govender R (2012) Implementation of viscoelastic hopkinson bars. In: Hiermaier S (ed) DYMAT 2012 – 10th international conference on the mechanical and physical behaviour of materials under dynamic loading, Freiburg

Chapter 52
A Methodology for In-Situ FIB/SEM Tension Testing of Metals

J.P. Ligda, Q. Wei, W.N. Sharpe, and B.E. Schuster

Abstract We report on recent investigations into the mechanical properties of metallic micro-specimens deformed in tension and compression. We will focus on investigations using a custom test apparatus for in-situ focused ion beam and scanning electron microscope (FIB/SEM) mechanical testing. Our system utilizes a 3-axis piezoelectric positioning system that enables precise alignment of the micro-specimens within a tensile grip. Loads are applied using a high-resolution linear actuator with a reported resolution of ~1 nm and measured with a strain gage based S-beam load cell. The load cells have a capacity of 10 or 100 g with a resolution of ~0.01 g. Specimen load/stress and crosshead displacements are measured using a customized data acquisition program, while the specimen strain is calculated from SEM micrographs using an open source digital image correlation script developed by Eberl and coworkers for MATLAB©. This system was used to investigate response of coarse grained and nanocrystalline tantalum micro-pillars with minimum dimensions smaller than 10 μm.

Keywords In-situ • SEM • Microtension • Tantalum • Nanocrystalline

52.1 Introduction

There is an increasing prevalence of literature reports on mechanical testing of materials that have dimensions in the micron and nanometer scale [1–3]. While most of these reports focus on compressive behavior, shifting toward tensile testing will allow for more effective ductility, elastic modulus, and strength measurements [4–7]. This is advantageous for ultra-fine grained (UFG) and nanocrystalline (NC) metals where the processing techniques either do not yield large volumes or leave materials with residual porosity [8, 9]. Specifically, high pressure torsion (HPT) processing yields disk samples with a 12 mm diameter and 1.5 mm thickness that also contain a grain size gradient with respect to radial position [9]. The small specimen sizes can overcome these processing downfalls by performing site-specific mechanical tests. However, the reduced dimensions of the tensile specimens also means that proper testing requires an in-situ scanning electron microscope (SEM) testing stage coupled with digital image correlation (DIC) for strain measurement [4, 10, 11]. This report presents the results of microtension testing of a Tantalum foil and includes specimen fabrication, testing, and SEM imaging for DIC strain matching. The goal is to determine the proper testing parameters that yield accurate Elastic modulus values.

J.P. Ligda (✉)
Nanoscale Science Program, University of North Carolina at Charlotte, Charlotte, NC 28223, USA

Army Research Laboratory, Weapons and Materials Research Directorate, Aberdeen Proving Ground, MD 21005, USA
e-mail: jonathan.p.ligda.ctr@mail.mil

Q. Wei
Mechanical Engineering Department, University of North Carolina at Charlotte, Charlotte, NC 28223, USA

W.N. Sharpe
Mechanical Engineering Department, Johns Hopkins University, Baltimore, MD 21218, USA

B.E. Schuster (✉)
Army Research Laboratory, Weapons and Materials Research Directorate, Aberdeen Proving Ground, MD 21005, USA
e-mail: brian.e.schuster.civ@mail.mil

B. Song et al. (eds.), *Dynamic Behavior of Materials, Volume 1: Proceedings of the 2013 Annual Conference on Experimental and Applied Mechanics*, Conference Proceedings of the Society for Experimental Mechanics Series,
DOI 10.1007/978-3-319-00771-7_52,

52.2 Specimen Fabrication

Thin foils, 15 μm thick, of coarse grain Ta were used to characterize the in-situ SEM stage, sample design, and testing parameters. To achieve the micron scale dimensions, an FEI Nova Nanolab 600 focused ion beam (FIB) microscope was used to mill the "dog-bone" tensile geometry. There are three main steps in fabricating a tensile specimen, two thinning steps and a final milling of the "dog-bone" geometry. The first thinning is a rough, fast milling at 30 kV/21 nA, followed by a second, finer thinning at 30 kV/2.7 nA. After the thinning was completed, a plate with the desired gauge thickness is left, like that shown in Fig. 52.1. Once this plate is at the desired thickness, it is positioned in plane-view with respect to the ion beam. Milling the final tensile specimen was done by using bitmaps of the "dog-bone" pattern at 30 kV/2.7 nA. For this work the gauge width/thickness was kept constant at 8.0 μm in order to determine a specimen geometry that reliably produced deformation and failure inside the gauge section. Examples of the attempted tensile geometries are shown in Fig. 52.2a–c. There was a thicker grip portion on the free end between Fig. 52.2a, b, while Fig. 52.2c has the addition of a slight curvature to the gauge section. In order to measure strain accurately, Pt markers were deposited in the gauge section. Deposition of 1.0 μm thick Pt markers was done using the electron beam to minimize damage to the specimen surface at 10 kV/8.4 nA. The marker geometry was either lines or circles where the sizes varied from 500 to 100 nm.

52.3 Experimental Procedure

These micrometer size specimens are too small for conventional or even millimeter scale tensile testing stages. Instead, an in-situ SEM testing stage was designed and built to be used inside the FIB chamber. A diagram of this stage is shown in Fig. 52.3, it consists of an aluminum frame, sample positioning piezoelectric motors, high resolution linear actuator, and a load cell. Three individual attocube© motors control sample positioning in the x, y, and z directions, the x-axis has a maximum travel distance of 5.0 mm and step size of 50 nm, while the y- and z-axis only have a 2.0 mm maximum travel and 25 nm step size. The linear actuator is a high resolution nanopositioning piezoelectric motor from PI© with 38 μm of total travel and a resolution of 1.0 nm. A Futek© S-beam strain gauge based load cell is attached to the linear actuator and has a maximum load capacity of 100 g and resolution of 0.1 g. These three components make up the bulk of the in-situ set-up

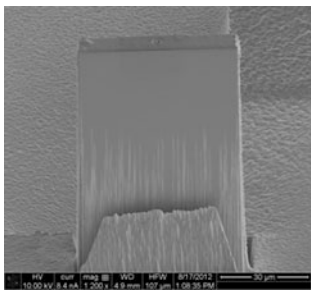

Fig. 52.1 Plate with the desired gauge thickness

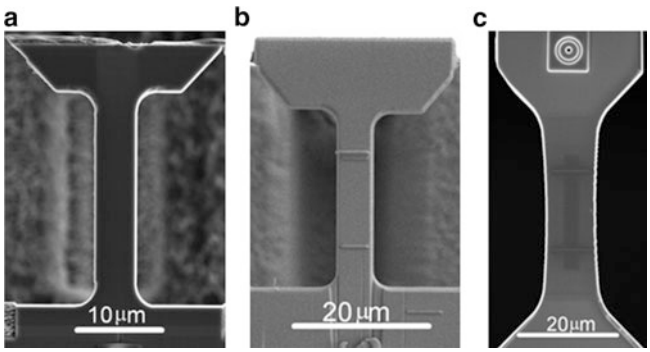

Fig. 52.2 Examples of the attempted tensile geometries

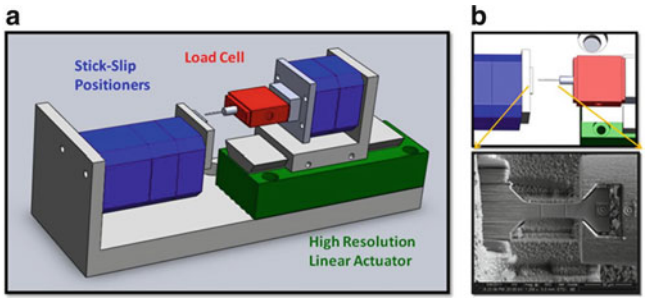

Fig. 52.3 SEM testing stage

but in order to grip the specimen during the test, a tungsten needle was attached to the load cell, a schematic of which is shown in the top image of Fig. 52.3b. At the end of this needle a grip is milled through the entire thickness using the FIB, Fig. 52.3b bottom. This grip must be made specific to the tensile specimens, and specifically it must be wide enough to allow the free end of the specimen to pass through and the angled portion must match the angled section on the specimen.

Testing begins by positioning the free end of the specimen in the grip using the attocubes©. Using the x-axis, the specimen was moved into contact inside the grip until the initial preload (L) is $0.5 \leq L \leq 1.0$ g. Once the specimen is loaded in the grip the actuator is controlled through a LabView program that allows the user to define the total number of data points, time of test in seconds, and actuator starting position and ending position. Number of points and time of test should be enough so that the step size over the total travel of the actuator is 1.0 nm/s. During testing the LabView program records and outputs the load (grams), actuator position (μm), and time (sec).

A MATLAB© based DIC program is used calculate the strain from sequential SEM images of the Pt markers in the gauge section [12]. For accurate strain calculation there must be a high contrast between the Pt markers and the tensile specimen material. Proper contrast is achieved by altering electron beam imaging conditions such as the accelerating voltage, beam current, detector type, dwell time, and resolution. Accelerating voltage and beam current were kept at either 5.0 kV/0.40 nA or 2.0 kV/81 pA. At these beam conditions both the Everhart-Thornley (ETD) and Through- the-Lens (TLD) detectors were used for imaging since they also affect the final images. Resolutions of 1,024 × 884, 2,098 × 1,768, and 4,096 × 3,900 were used to determine which allows for the most effective analysis during digital image correlation (DIC). The dwell time must be set at a level that allows for decent signal acquisition by the detector but keeps the total imaging time short, this has been set at 3.0 or 10 μs.

52.4 Results and Discussion

Three different specimen designs were used to determine which would reliably fail in the gauge section. The main difference between these designs is the stabilization on the free end and amount of curvature in the gauge section. For the first design, which had no stabilization or curvature, the free end bent while in the grip. Adding a thicker section to the free end of the specimen, while still maintaining a straight gauge section, did not work either as the specimen broke at the grip-specimen contact region, Fig. 52.4a. Taking guidance from the design used for metallic glasses, a 200 μm radius of curvature was added to the gauge section. Figure 52.4b shows a failed specimen with the addition of this curvature, showing failure in the gauge section between the Pt markers. This final design was used for multiple tests on the Ta foil and a Pd-based metallic glass and all failed in the gauge section.

Accurately testing these tensile specimens requires reliably measuring the load and calculating the strain. Since the load measurements are made using the Futek© load cell, it is not difficult to calculate the stress values. Obtaining the strain values is more difficult, as the tracking of Pt gauge markers must be done using DIC post-test. Effective DIC tracking is dependent on high quality SEM images, which start with the Pt marker dimensions and the e-beam imaging parameters. Best DIC tracking is achieved when the contrast between the tensile specimen material and markers is high, so the goal for the images is to have high intensity at the Pt markers and low intensity elsewhere. The SEM micrographs in Fig. 52.5 show the effects of different marker dimensions. Figure 52.5a shows an image of 500 nm wide rectangles under imaging conditions of 2.0 kV/210 pA. While there appears to be two bright vertical strips at the marker positions, the line profile during DIC showed multiple peaks. Measuring the actual marker width gives 800 nm, this is too wide to effectively run the DIC. Decreasing the rectangle width to 200 nm and imaging at 2.0 kV/210 pA and 5 kV/0.40 nA, Fig. 52.5b and c respectively, shows high

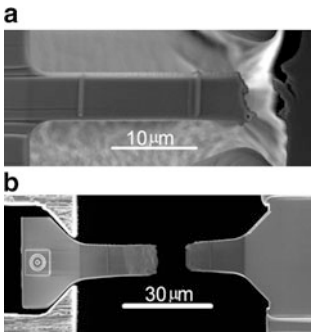

Fig. 52.4 Specimen showing failure at the grip-specimen contact region (**a**) and failure in the gauge section between the Pt markers (**b**)

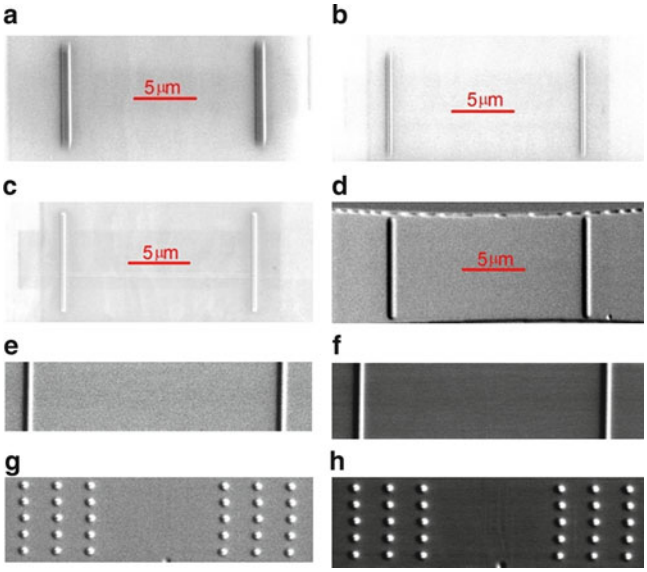

Fig. 52.5 SEM micrographs showing the effects of different marker dimensions

brightness values over the whole image, resulting in ineffective matching during DIC. However, it was noticed that the contrast/brightness would change once contact between the tensile specimen and grip was made at the start of testing. Using the previously defined marker dimensions, a specimen was put under a small amount of pre-load (~0.5 g) and imaged at 5 kV/0.40 nA, shown in Fig. 52.5d. This image shows a greatly improved contrast between the marker and specimen, but attempts to run the DIC matching had sporadic success. The actual width of these markers is 400 nm, still too wide, but reducing this dimension and imaging at 5 kV does improve the matching. To determine if continuing to reduce the marker width improves the performance, Pt lines were used. The patterning software does not define a width for the line feature but observations give a thickness of ~400 nm, surprisingly close to that of the 200 nm defined patterns. Figure 52.5e and f show images of line Pt markers taken at 5 kV/0.40 nA and 10 kV/8.4 nA respectively. These line markers under either beam condition are effectively and accurately matched in each image. This improvement in matching, despite have similar dimensions to the previous markers, is attributed to the beam scanning during deposition. The beam follows a serpentine pattern during deposition of a rectangular pattern, but for a line pattern the beam only moves along one direction. The serpentine scan results in two lines for each marker that show up as separate peaks during the DIC while the line scan creates only a single line. The final images, Fig. 52.5g, h, show 100 nm diameter circle markers at 5 kV/0.40 nA and 10 kV/8.4 nA respectively. As a note, all images were taken using the Everhart-Thornley (ETD) detector to take advantage of the "shadowing" effect . This microscope does have a Through-the-Lens detector (TLD), but the DIC did not work properly for images taken using this detector.

Other factors influencing the image quality and DIC matching are image resolution and magnification as they both affect the physical distance represented by each pixel. True stress vs. true strain plots for tests where the resolution is 1,024 $\times$ 884 and magnification at 3,500 were first calculated to be negative and the scatter between successive strain points is 0.002. A small number of pixels spanned the width of the markers for this test, meaning the physical area represented by each

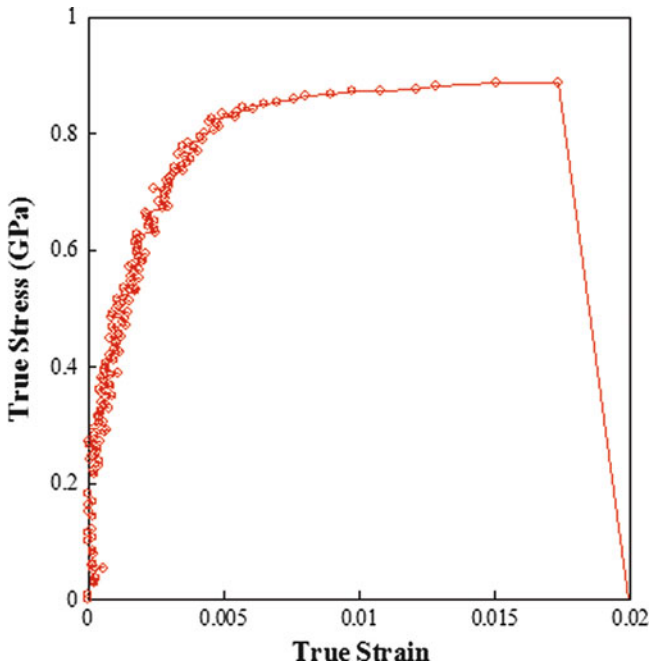

Fig. 52.6 True stress vs. strain, resolution 1024 × 884

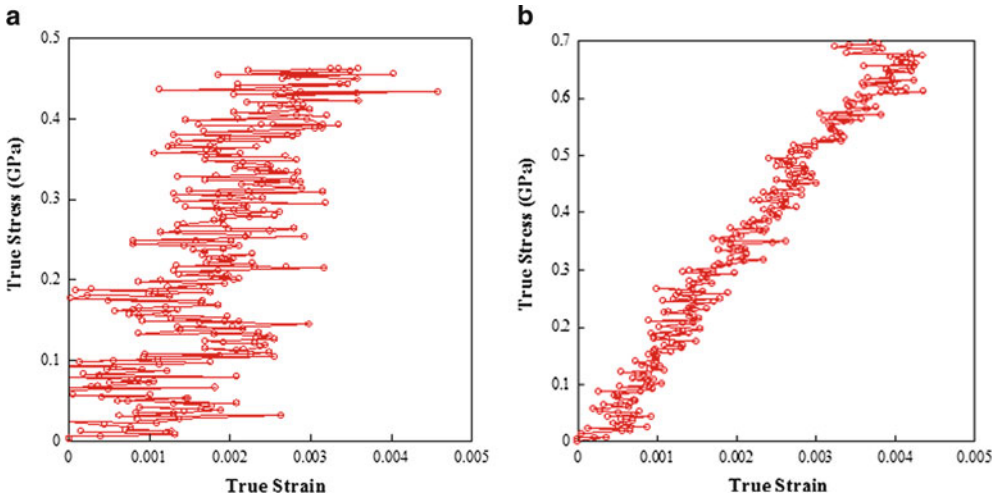

Fig. 52.7 Comparison of 1024 × 884 resolution (**a**) and 2048 × 1768 resolution (**b**)

pixel was large. This means the scatter here is most likely due to shifts in the individual pixel representing the peak intensity during the DIC line profile scan. Increasing the magnification to 5,000 increases the number of pixels that span the marker, decreasing the physical distance each one represents. The true stress versus strain plot, Fig. 52.6, shows that increasing the magnification greatly improves the strain matching. Unfortunately, this is the limit to the magnification level, any higher and the markers will no longer be in the field of view. Therefore, to further improve the strain matching the image resolution must be changed.

A higher resolution also means a smaller portion of the specimen is represented in each pixel, which results in a more accurate DIC strain matching. It should now be noted that the scan dwell time must be long enough to get a decent signal to noise ratio during scanning, and is usually set to 3.0 or 10 µs. For these dwell times, imaging at a higher resolution means an increase in the total time to take an image, making it more likely to miss critical plastic events during testing. Figure 52.7a

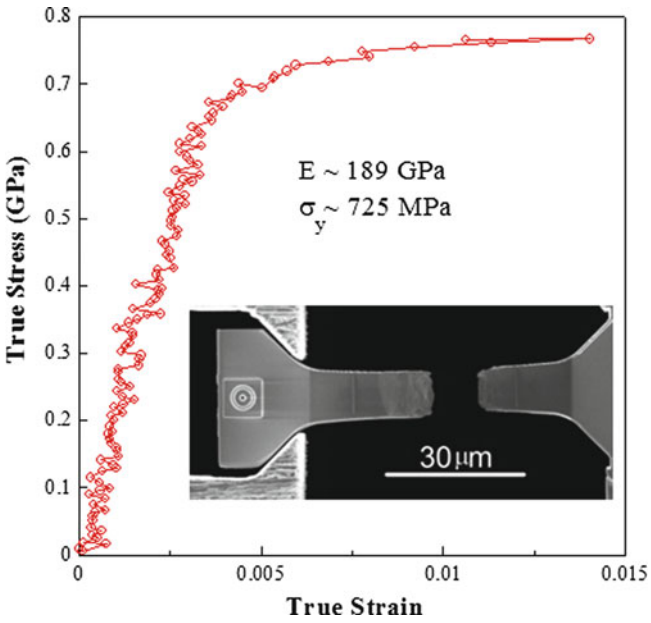

Fig. 52.8 True stress vs. strain plot and inset SEM image

shows a true stress vs. strain plot for a specimen that was tested with the same imaging parameters as Fig. 52.6. Unlike the previous test, this plot shows scattering in the strain data, suggesting these parameters are not optimum. For the next test, the magnification is kept at 5,000 but the resolution is increased to 2,048 × 1,768, giving the plot shown in Fig. 52.7b. This increase in resolution greatly improved the quality of the strain data, as there is less scatter in the data and the elastic modulus is measured as 170 GPa, close to the accepted modulus of 186 GPa for bulk tantalum [13]. Increasing the resolution to the next allowable level, 4,096 × 3,986, presents a few technical difficulties. The first is that at this resolution the time to acquire an image is 2 min, mostly due to the excess scanned area that is not part of the gauge section. It would be advantageous to be able to control the aspect ratio of the scan as at a magnification of 5,000× a majority of the image area still consists of open space or specimen regions that are not the gauge section. The second problem is that the automatic image capture software on the microscope does not function at this resolution setting.

To overcome these two problems, a third party imaging software from 4Pi was used to acquire high resolution SEM images with a reduced scan area that only includes the tensile gauge section. Using this new image capture software, a specimen was tested using the following parameters. The specimen design was the type defined previously, where the free end was stabilized, the gauge section had a 200 μm radius of curvature, and lines were used for the Pt markers. Imaging was done with the electron beam settings at 5 kV/0.40 nA, magnification at 5,000 and the resolution set to 4,096 × 1,024. The true stress vs. strain plot and inset SEM image, Fig. 52.8, shows a well-defined elastic regime and a transition to a plastic regime following yielding. In this plot the elastic modulus is measured as 189 GPa. Also from this plot, the yield stress is determined to be 725 MPa with ~1.0 % tensile elongation. The accurate determination of the elastic modulus confirms that these are the optimum conditions for accurate tensile testing.

The parameters determined from the tests on the Ta foil were then used to for microtensile tests on UFG/NC Ta disk processed by HPT. As was mentioned previously, the HPT processed disks are only 12 mm in diameter and the grain size depends on the radial position (X), grain size should be larger near the center (X = 1.0 mm) and smaller at the disk edge (X = 6.0 mm) [14, 15]. Utilizing microscale specimen sizes, tension testing is done at multiple radial positions to ensure each specimen has a homogeneous grain size [9]. This allows the observed mechanical properties to be related back to underlying microstructures [9]. Figure 52.9a, b shows true stress vs. strain plots and inset SEM micrographs for two UFG/NC Ta specimens fabricated at radial positions on the disk, X = 4.0 and 5.9 mm respectively. The specimen at X = 4.0 mm shows 4.0 % tensile ductility and a slight neck forming in the gauge section. However, the specimen at X = 5.9 mm shows that there is a transition in the deformation mode to formation of shear bands. The only way such a transition could have been observed is with the use of the microscale testing techniques developed in this report.

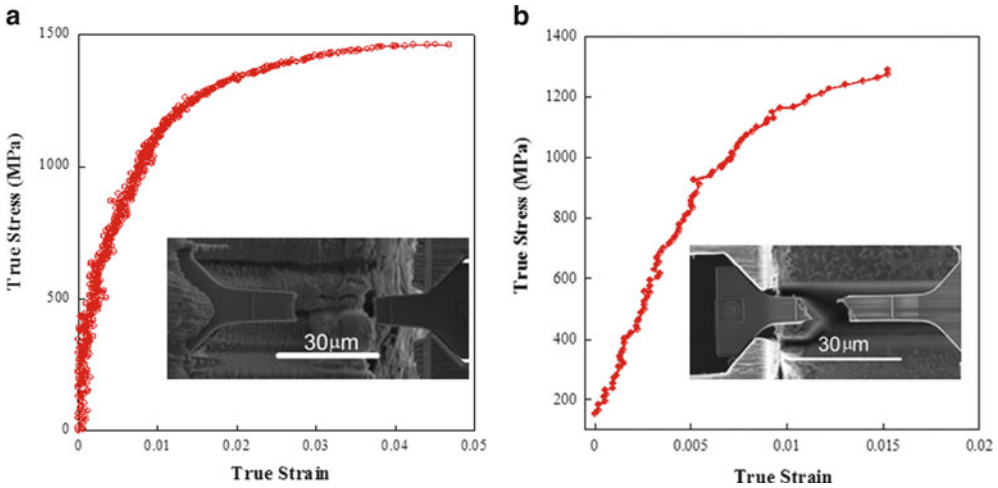

Fig. 52.9 True stress vs. strain plots and inset SEM micrographs for two UFG/NC Ta specimens fabricated at radial positions on the disk, X = 4.0(**a**) and 5.9 (**b**) mm

52.5 Conclusion

An in-situ SEM microtension stage was designed and a testing methodology was developed for specimens with dimensions on the order of tens of microns. Using coarse grain Ta thin foils, proper specimen geometry was determined to ensure the highest stress concentration occurs in the middle of the gauge section. Imaging parameters in the SEM were also determined to achieve a high contrast between the Pt gauge markers and specimen material which allowed for accurate strain measurements. This testing methodology was successfully implemented for UGF/NC Ta, where an influence in the grain size on the deformation mode was observed.

References

1. Uchic MD, Shade PA, Dimiduk DM (2009) Plasticity of micrometer-scale single crystals in compression. Annu Rev Mater Res 39:361–386
2. Greer JR, De Hosson JTM (2011) Plasticity in small-sized metallic systems: intrinsic versus extrinsic size effect. Prog Mater Sci 56:654–724
3. Uchic MD, Dimiduk DM, Florando JN, Nix WD (2004) Sample dimensions influence strength and crystal plasticity. Science 305:986–989
4. Gianola DS, Eberl C (2009) Micro- and nanoscale tensile testing of materials. J Miner Met Mater Soc 61(3):24–35
5. Sharpe WN, Yuan B, Edwards RL (1997) A new technique for measuring the mechanical properties of thin films. J Microelectromech S 6(3):193–199
6. Kiener D, Grosinger W, Dehm G, Pippan R (2008) A further step toward an understanding of size-dependent crystal plasticity: In situ tension experiments of miniaturized single-crystal copper samples. Acta Mater 56:580–592
7. Kim JY, Jang D, Greer JR (2010) Tensile and compressive behavior of tungsten, molybdenum, tantalum, and niobium at the nanoscale. Acta Mater 58:2355–2363
8. Schuster BE, Ligda JP, Pan ZL, Wei Q (2011) Nanocrystalline refractory metals for extreme condition applications. JOM 63(12):27–31
9. Ligda JP, Schuster BE, Wei Q (2012) Transition in the deformation mode of nanocrystalline tantalum processed by high pressure torsion. Scr Mater 67:253–256
10. Sharpe WN, Pulskamp J, Gianola DS, Eberl C, Polcawich RG, Thompson RJ (2007) Strain measurements of silicon dioxide microspecimens by digital imaging processing. Exp Mech 47(5):649–658
11. Gianola DS, Sedlmayr A, Monig R, Volkert CA, Major RC, Cyrankowski E, Asif SAS, Warren OL, Kraft O (2011) In situ nanomechanical testing in focused ion beam and scanning electron microscopes. Rev Sci Instrum 82:6
12. Eberl C, Gianola DS, Bundschuh S (2010) Digital image correlation and tracking. Mathworks
13. MatWeb. Available www.matweb.com
14. Valiev RZ, Ivanisenko YV, Rauch EF, Baudelet B (1996) Structure and deformation behavior of Armco iron subjected to severe plastic deformation. Acta Mater 44(12):4705–4712
15. Zhilyaev AP, Langdon TG (2008) Using high-pressure torsion for metal processing: fundamentals and applications. Prog Mater Sci 53:893–979

Chapter 53
Characterization of Damage Evolution in Ti_2AlC and Ti_3SiC_2 Under Compressive Loading

R. Bhattacharya and N.C. Goulbourne

Abstract Ti_2AlC and Ti_3SiC_2 are representative members of MAX phase materials, which are thermodynamically stable ternary compounds. These materials are known to exhibit a unique combination of properties typical of ceramics (high elastic stiffness) and metals (high ductility). They are known to be stable at high temperatures and exhibit damping behavior characterized by hysteresis under cyclic loading. In this work, damage initiation and evolution under high strain-rates in MAX phases is studied using Split Hopkinson Pressure Bar (SHPB) technique coupled with in-situ high speed imaging. Traditionally the constitutive response under high strain rates is deduced from the experimental data (from strain gages) using standard wave analysis techniques. Since this technique does not involve a methodology to predict crack initiation in the material, the result is an overestimation of strain values. This is particularly crucial for determining material response of *newer* class of materials like MAX phases, which have not been widely characterized under high strain-rates. The coupling of the experimental set-up with in-situ imaging facilitates subsequent analysis of experimental results by Digital Image Correlation (DIC). The combination of strain field images with the strain histories are used to determine the point and values of strains at which damage initiated in the specimen. In this way, a direct relationship of the stress-time response with the strain field and damage evolution during the test is obtained. For strain rates of up to 4500 s^{-1}, strain values of ~5 % were observed before macroscopic cracks develop. From analysis of images, mixed mode (combination of mode I and mode II) crack formation and propagation are observed. The results from this analysis establish the synergy and necessity of using in-situ imaging (and DIC) with the SHPB technique for characterizing nano-layered ternary ceramics.

Keywords Damage evolution • DIC • MAX phase materials • SHPB • High strain-rate

53.1 Introduction

$M_{n+1}AX_n$ phase materials are nano-layered ternary solids where M is an early transition metal, A is an A-group element and X is Carbon (C) or Nitrogen (N). The value of n typically varies from 1 to 3 [1, 2]. Ti_2AlC and Ti_3SiC_2 are two representative members of the 2-1-1 and 3-1-2 type MAX phase materials. These materials exhibit a unique combination of properties of typical ceramics and metals, which makes them highly suitable for applications involving dynamic loading conditions (e.g. hypersonic jets). Previous work by the authors has dealt with establishing correct experimental protocols and strain-rate dependent constitutive response of Ti_2AlC under dynamic loading [3]. In this paper we report some of the key features and mechanisms by which damage propagates in MAX phases under high strain-rates using Digital Image Correlation (DIC).

Damage evolution in typical ceramics such as SiC [4], Al_2O_3 [5], AlN [6, 7] under compressive and tensile loading have been reported in the literature. Under compressive loading the principal features underlying the damage evolution involve multiple cracks originating from microflaws whereas tensile damage is induced by single dominant crack [5, 8]. Shih et al. [4] reported that a combination of mechanisms were responsible for damage evolution in SiC which includes role of

R. Bhattacharya (✉)
Department of Materials Science and Engineering, The University of Michigan, 2006 FXB Building, 1320 Beal Avenue, Ann Arbor, MI 48109, USA
e-mail: ribh@umich.edu

N.C. Goulbourne
Department of Aerospace Engineering, The University of Michigan, 2006 FXB Building, 1320 Beal Avenue, Ann Arbor, MI 48109, USA

B. Song et al. (eds.), *Dynamic Behavior of Materials, Volume 1: Proceedings of the 2013 Annual Conference on Experimental and Applied Mechanics*, Conference Proceedings of the Society for Experimental Mechanics Series,
DOI 10.1007/978-3-319-00771-7_53,

imperfections and second phase inclusions as potential damage initiation sites, elastic anisotropy and grain orientations, dislocation pile-ups, etc. It was also reported that under high strain-rate deformations, fracture in unconfined specimens is associated with some plastic deformation. In conventional ceramics such as SiC, formation of deformation twins is the mechanism responsible for plasticity. It should be noted that for MAX phase materials, the c/a ratio in the hexagonal crystal structure is ~4–6 and hence only limited slip (basal) and no twinning is possible. Therefore, a combination of mechanisms such as kink band formations, buckling of nano-laminates are key mechanisms by which these solids deform [3, 9]. Riou et al. [10], Paliwal and Ramesh [11] reported the use of high-speed imaging to visualize the damage evolution under impact type loading conditions in SiC and AlON. The use of this advanced technique facilitated measurement of crack velocity, densities as well as visualization of damage zone formations. Here we combine this technique with strain field evolution obtained from DIC to anticipate locations and nature of crack paths. The high strain-rate uniaxial compression loading was achieved using the well-known Split Hopkinson Pressure Bar (SHPB) technique [12, 13].

For the experimental studies reported here, 2D DIC has been used to calculate strain from images obtained using a Photron® SA5 high speed camera, operated at 100,000–150,000 frames per second (fps). The specimen is therefore assumed to be nominally planar and assumed to deform only in the original object plane. It must be noted that this non-contact method to calculate strain fields is prone to errors due to image distortion and de-correlations arising from experimental vibrations, lens aberrations and misalignments, etc. Moreover correlation errors are possible for situations where curved surfaces are analyzed using 2D DIC [14]. For the results presented here, ARAMIS® (by Trillion systems) is used to perform the calculations. The strain calculation algorithm is based on minimization of a correlation function given by [15–17]:

$$C\ (\Phi) = 1 - \frac{\int_D (f(xi) - \bar{f})(g(\Phi(xi) - \bar{g})dx}{\sqrt{\int_D (f(xi) - \bar{f})^2 dx}\sqrt{\int_D (g(\Phi(xi)) - \bar{g})^2 dx}}, \tag{53.1}$$

where $\bar{f} = \int f(x)dx$, and the integrals indicate integration over the domain D (subset size). The mechanical transformation $\Phi(\mathrm{x})$ between the reference image grey level $f(x)$ and the deformed image grey level $g(x)$ is approximated using an interpolation (or shape) function. Minimization of the correlation function allows calculation of the parameters of the shape function. For most strain calculations, a linear interpolation is used. However, the calculation of displacements using a spline interpolation can also be selected. Strains in the x and y directions are then calculated by numerically differentiating the displacement fields, resulting in the following tensor:

$$\epsilon = \begin{bmatrix} \dfrac{\partial u}{\partial x} & \dfrac{1}{2}\left(\dfrac{\partial u}{\partial y} + \dfrac{\partial v}{\partial x}\right) \\ \dfrac{1}{2}\left(\dfrac{\partial u}{\partial y} + \dfrac{\partial v}{\partial x}\right) & \dfrac{\partial v}{\partial y} \end{bmatrix}, \tag{53.2}$$

where u and v are displacements the in x and y directions respectively. It must be noted that once a crack initiates, strain calculations based on Eq. 53.2 are not strictly valid and the displacement gradient tensor (Eq. 53.3) must be used to clearly observe the gradients in the field. In ARAMIS®, displacement gradients cannot be viewed explicitly and hence the strain tensor will be used to depict the fields involving cracks although the strains are *apparent or artificial* because rigid body motions are not accounted for.

$$\nabla u = \begin{bmatrix} \dfrac{\partial u}{\partial x} & \dfrac{\partial u}{\partial y} \\ \dfrac{\partial v}{\partial x} & \dfrac{\partial v}{\partial y} \end{bmatrix} \tag{53.3}$$

This paper is organized into three broad sections. Section 53.2 outlines the experimental methodologies. The results from the experiments are reported in Sect. 53.3, with Sect. 53.3.1 reporting the damage evolution of Ti_2AlC and Ti_3SiC_2 under high strain rate loading. The microstructural analysis of the specimens before and after deformation is reported in Sect. 53.3.2 and a discussion of the results is presented in Sect. 53.4. Section 53.5 summarizes the conclusions from the analysis with possible scope and direction of future work.

53.2 Experimental Methodologies

The experimental steps along with a description of the set-up and apparatus used are outlined in this section. The first sub-section describes the material processing and characterization techniques with description of sample sizes used for testing. In Sect. 53.2.2, the mechanical testing procedure with a brief description and schematic of the set-up is shown.

53.2.1 Material Preparation

The materials used for the experiments are polycrystalline Ti_2AlC and Ti_3SiC_2 received from Texas A&M University. The samples are processed from powders using a pressureless sintering process and Spark Plasma Sintering (SPS) (for details regarding the synthesis see [18]). Cylindrical discs were machined for high strain-rate testing using Electro Discharge Machining (EDM) to ensure smooth and flat parallel surfaces. Based on experimental protocols developed by the authors, a Length (L) : Diameter (D) ratio of 0.25–0.5 with a diameter ratio ($D_{Specimen}$: D_{bar}) of 0.5–0.75 is used for all the tests reported here. Specimen geometry and size effects were crucial in ensuring the dynamic equilibrium condition, as pointed out earlier [3]. For subsequent DIC analysis, machined specimen surfaces are speckled (See Fig. 53.1b). Two samples are used for each testing condition. For microstructural characterizations (presented in Sect. 53.3.2) of as-processed specimens, samples were polished to mirror finish and etched in a $HF:HNO_3:H_2O$ solution mixed in the ratio 1:1:1.

53.2.2 Mechanical Testing

High strain-rate loading of MAX phase samples are performed using a SHPB technique. Figure 53.1 shows a schematic of the SHPB set-up (Fig. 53.1a) and image of a speckled specimen (Fig. 53.1b) captured at a given frame rate during experiments. A detailed description of the set-up coupled with in-situ imaging and data analysis method (2-wave analysis) has been reported earlier [3, 12, 13]. For the tests reported here, the striker bar velocities ranged from ~14–30 m/s. Specific details regarding the properties and dimensions of the bar material are presented in Tables 53.1, and 53.2, respectively.

The two different experimental set-ups (Table 53.2) are made of same material but have different dimensions of the bar. The specimen sizes are adjusted accordingly depending on the set-up used. For tests reported here, set-up I is used for Ti_2AlC and set-up II is used for Ti_3SiC_2 specimens.

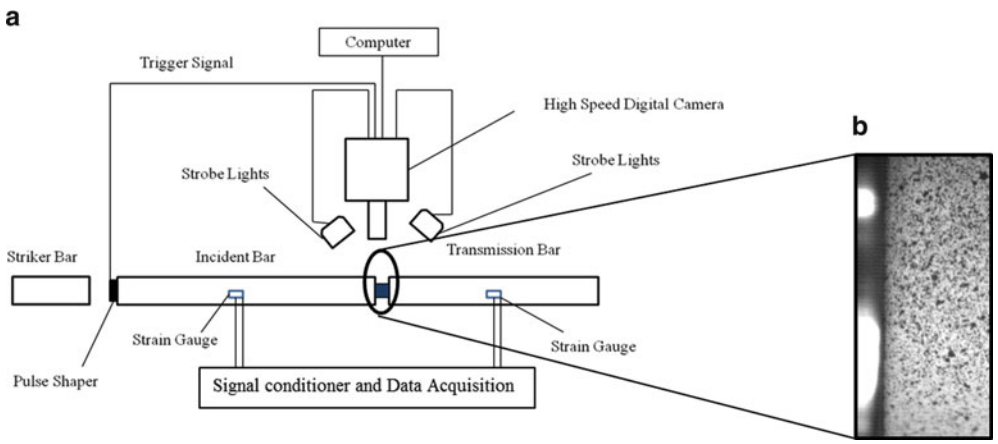

Fig. 53.1 (**a**) Schematic of Split Hopkinson Pressure bar (SHPB) experimental set-up showing a high speed camera, (**b**) Image of speckled specimen captured at a frame rate of 131,250 fps using Photron® SA5 camera and 200 mm lens (camera resolution: 128 × 272)

Table 53.1 Properties of the bar material used for data analysis

Material	440C Stainless steel
Young's Modulus	220 GPa
Ultimate Tensile Strength	1,965 MPa
Density	7,620 kg/m^3

Table 53.2 Dimensions of the experimental set-ups

	Incident bar length (m)	Transmission bar length (m)	Striker bar length (mm)	Diameter of the bars (mm)
Set-up I	1.83	1.22	305	12.7
Set-up II	2.43	1.77	700	38.1

53.3 Experimental Results

53.3.1 Damage Evolution in Ti_2AlC and Ti_3SiC_2

In this work, we obtained strain-rates in the range 2,500–4,500 s^{-1} for Ti_2AlC and 1,500–2,500 s^{-1} for Ti_3SiC_2. Compressive loading of the samples under high strain-rates resulted in significant strain followed by crack formations and subsequent crushing after attainment of dynamic equilibrium. The results from this analysis showed that the material response is strain-rate dependent. The inferred nature of the data analysis technique (two wave analysis) often leads to an overestimation in the calculated strain. For accurate determination of strains, strain was also calculated using DIC. Figures 53.2a–d show a comparison between the strain histories calculated using DIC and conventional strain gages. The error bars indicate the range of values (maximum and minimum) within which the mean strain varies over the entire specimen surface. It is observed that cracks start forming at strains ~2–5 % whereas the wave analysis technique predicts much higher values of strains (~25 %). Hence truncation of the data from wave analysis is done to obtain constitutive response (Fig. 53.4). Figures 53.2c, d show the truncated strain value and different regimes in the strain calculation by DIC in Ti_2AlC and Ti_3SiC_2 respectively. For regime 1, the strains are calculated before any macroscopic visible crack is formed and these represent the real strains in the material. In this regime, the error (or residual) between the strain gage measurements and DIC calculations of strain are of the order of ~2 %. Regime 2 is the damage evolution stage of the test when splitting of cracked surfaces has already begun. This regime is terminated by complete fragmentation of the specimens. It must be noted that the strains reported in this regime are not real strains but apparent or artificial strains (See Sect. 53.1).

Figure 53.3 shows the stress (σ_{xx}) versus time relationship for a Ti_2AlC specimen tested at ~3,000 s^{-1} combined with ε_{yy} strain fields obtained from DIC analysis. The compressive load is applied to the cylindrical specimen in the axial direction, as shown in the schematic. Since the specimen is unconfined, the deformation is accompanied by tensile strains in the longitudinal direction. It is observed that the material undergoes some amount of inelastic deformation possibly due to kink band formations which is initiated by buckling of nano-laminates (point (b)) before reaching the peak stress value (point (f)). It is observed that prior to damage the strain field has a heterogeneous character and the DIC calculations are able to anticipate the formation of cracks (indicated by a red band of large strain at point (d)) a few frames before the crack is actually observed in the high speed images (point (e)). At (e) the first cracked surfaces formed start splitting and opening. Subsequently as the stress increases, multiple cracks open – this leads to softening and eventually crushing (point (f)). At some strain-rates the sample obtained after loading is flattened into a flat disc with some radial cracks distributed along the circumference. For the specimen shown in Fig. 53.3, the cracks are observed parallel to the loading axis, which indicated an opening or mode I type of fracture.

A shear type fracture with cracks oriented at a certain angle to the loading axis is observed in some specimens, as shown in Fig. 53.4. The deformation map shown here relates the axial and longitudinal strain fields corresponding to different points on the constitutive response for Ti_2AlC tested at ~3,500 s^{-1}. The stress–strain response shows non-linear elastic and "yielding" type behavior before attainment of peak stress. It is believed that the elastic-inelastic transition (around point (b) in Fig. 53.3) corresponding to the yielding type behavior is due to onset of kink band formations in the nano-layered structure. This particular feature opposes the damage propagation and delays complete crushing of the specimen. The kink band formations are associated with movement of dislocations from a buckled state of nano-layers and subsequent alignment in the form of dislocation walls, which eventually form boundaries of the kink band. Although kink bands strengthen the

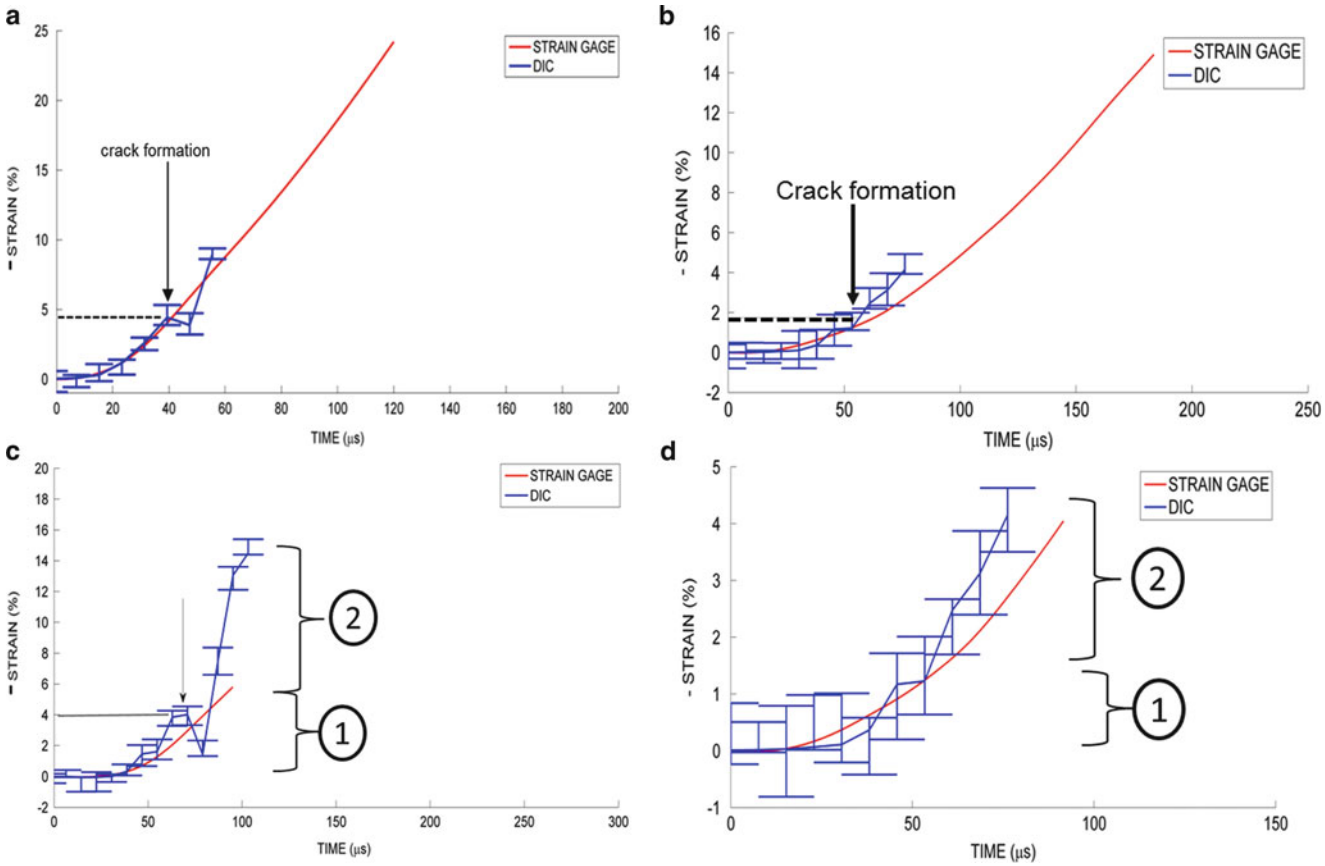

Fig. 53.2 Axial Strain (ε_{xx}) histories showing overestimation of strains by wave analysis technique and comparison with DIC strain calculation for (**a**) Ti_2AlC and (**b**) Ti_3SiC_2. Proper truncation of data and real strain-damage regimes are shown in (**c**) for Ti_2AlC and (**d**) for Ti_3SiC_2

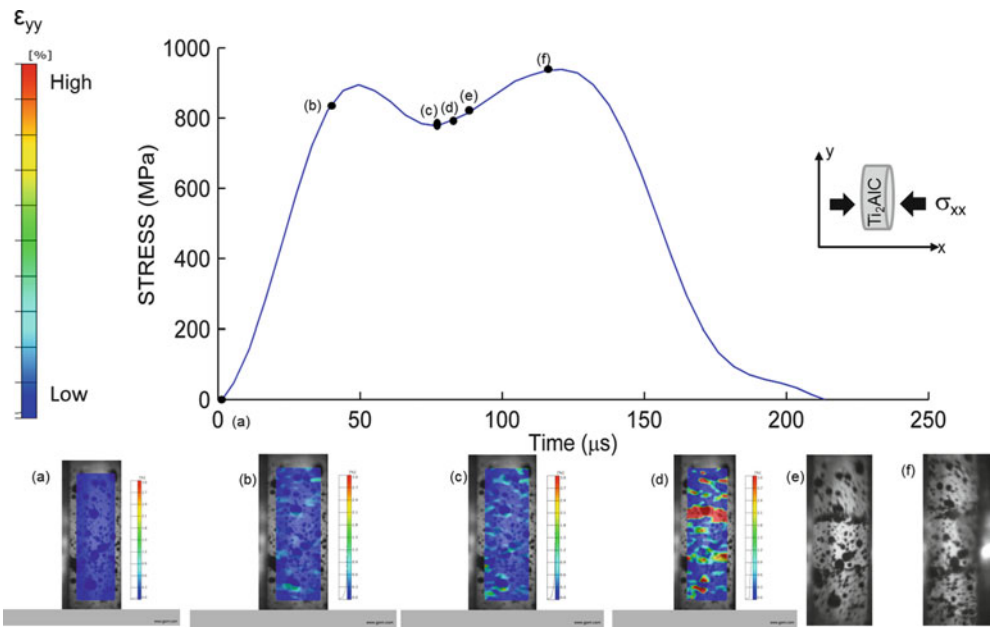

Fig. 53.3 Stress versus time behavior (*top*). (*Bottom*) Strain fields and damage evolution for a Ti_2AlC specimen tested at a strain rate of ~3,000 s^{-1} showing the locations and stresses at which cracks initiate and propagate. Points (**a**)–(**f**) on the stress-time curve correspond to the images below

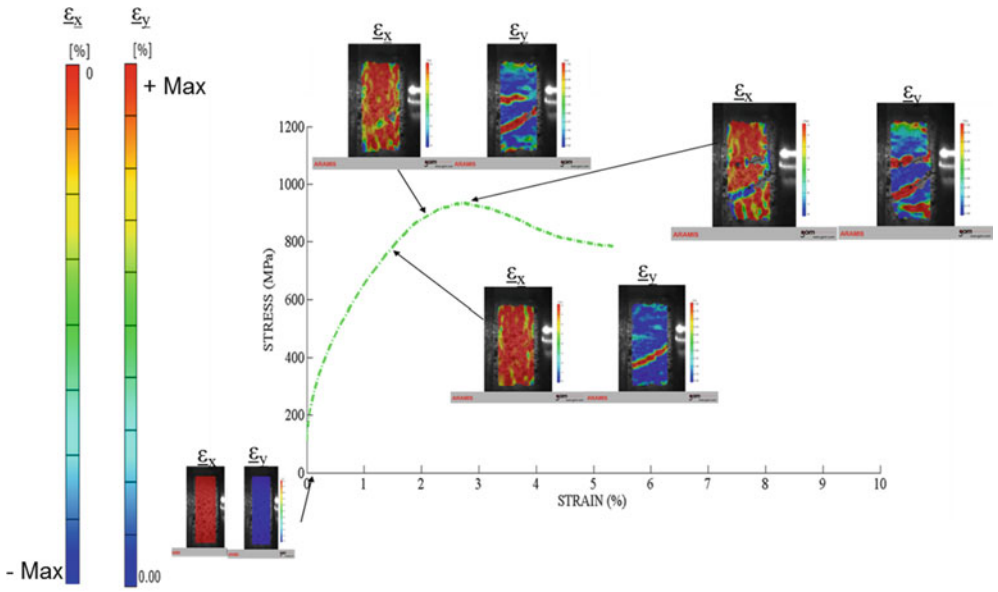

Fig. 53.4 Deformation map showing the stress–strain response combined with the strain field evolution maps obtained from DIC analysis showing strains in axial (ε_{xx}) and lateral (ε_{yy}) directions. The crack formation paths indicate mixed mode (mode I and mode II) type fracture

solid, they are often accompanied by delaminations which may soften the material. It should be noted that the term yielding to describe the elastic-inelastic transition is not completely accurate in the classical sense because it doesn't have a direct correlation to slip systems. A more generalized terminology is Inelastic Deformation Stress (IDS), as pointed out by Barsoum [1, 2]. In this paper the terms are used interchangeably. In the non-linear regime, the strains have a heterogeneous character. The longitudinal strain fields reveal bands of high strain region oriented at a certain angle and parallel to the axis corresponding to subsequent crack formation at those locations. From this figure (Fig. 53.4), it is inferred that both opening and shear type mechanisms are operative in Ti_2AlC under high strain-rate deformation.

Figure 53.5 shows the stress versus time behavior for a Ti_3SiC_2 sample tested at ~2,500 s^{-1}. It is observed that the initial response along with elastic-inelastic transition (point (b)) is similar to Ti_2AlC after which the specimen deforms inelastically (due to kink band formations). However, in this case several jumps in the stress values after the transition point are noticed. This is possibly due to internal damage mechanisms prior to complete fracture. The rise in the stress (for example, between (c) and (d)) could be attributed to localized hardening caused by kink band formations in the nano-layered microstructure. A subsequent drop in the stress ((e)–(f)) then would indicate mechanisms like delaminations, grain cracking and pullouts, growth and possible coalescence of microcracks from initially present microflaws eventually leading to complete fragmentation ((h)-end point on the curve). For comparison, a well-known material (Al-6061 alloy) was tested at strain rate ~4,000 s^{-1}, as shown in Fig. 53.6. The ductile metal deformed homogenously to strains of up to 15 % without any signs of internal or external damage or crack formation, as opposed to Ti_2AlC or Ti_3SiC_2. It is observed that a constant stress state is obtained in the specimen for a longer time (compared to MAX phase materials). The rough appearance of the plateau region is due to experimental noise induced by vibration of loading frame, etc. and not indicative of any particular material property or deformation mechanism.

53.3.2 Microstructural Features

In this section, microstructural features of the specimens under as-processed and fractured condition (post high strain-rate loading) are presented. Figure 53.7a shows the microstructure of Ti_2AlC after etching. The grain sizes vary in the range ~20–90 μm and have a plate-like character. The white bright particles observed in the micrograph are second phase TiC particles. Figures 53.7b–d show micrographs of specimens post-fracture. A coexistence of fibrous (ductile) and cleaved regions (marked F and C respectively) is observed, which suggests that there is a coexistence of brittle and ductile modes of fracture (quasiductile type behavior). Figure 53.7d shows a kink banded region of the nano-laminates. Extensive kink band formation is the major deformation mechanism which causes strengthening and prevents fracture. Furthermore,

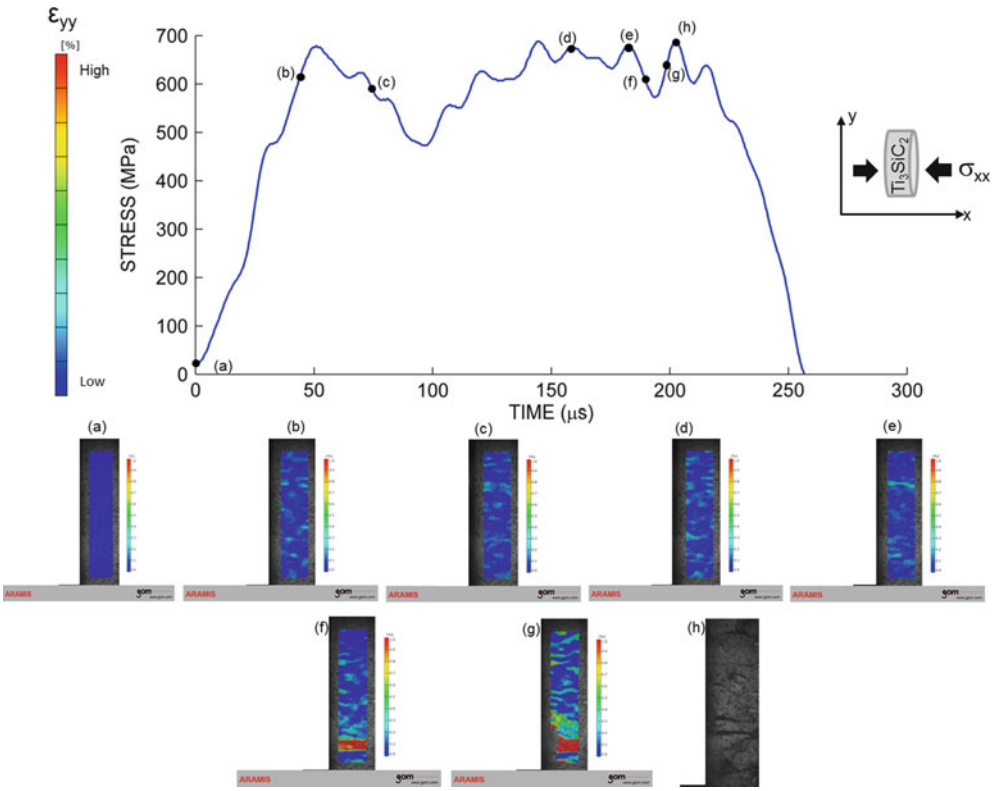

Fig. 53.5 Stress-time behavior, longitudinal strain fields and damage evolution for a Ti_3SiC_2 specimen tested at a strain rate of ~2,500 s^{-1} showing the locations and stresses at which cracks initiate and propagate. Points (**a**–**h**) on the stress-time curve correspond to the images below

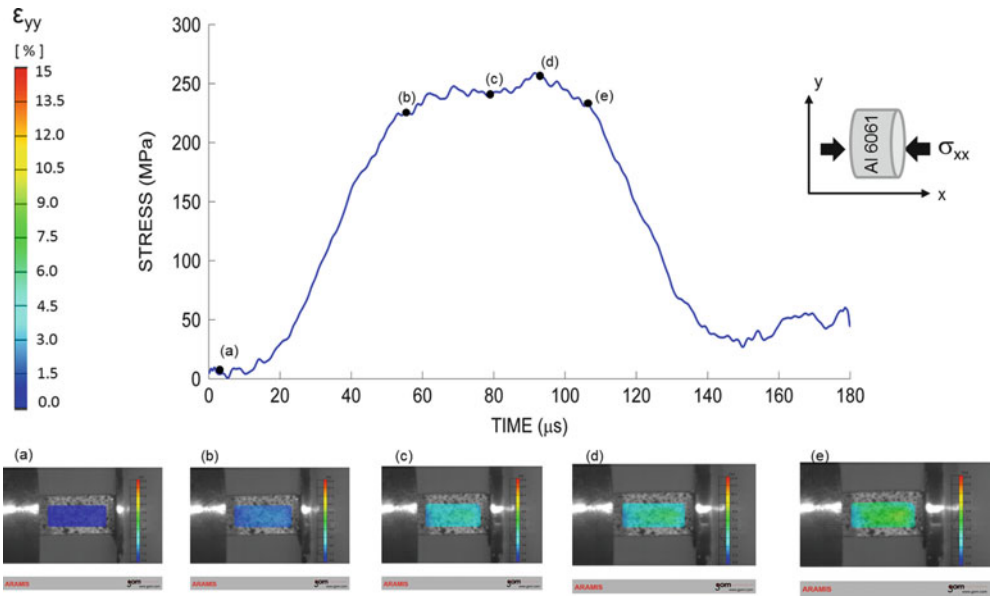

Fig. 53.6 Stress-time behavior, longitudinal strain fields for Al-6061 specimen tested at a strain rate of ~4,000 s^{-1} showing the homogenous nature of the strain fields. Points (**a**–**e**) on the stress-time curve correspond to the images below

delaminations around kink bands, buckled grains, transgranular and intergranular fractures are also observed. It is understood that second phase particles, grain boundaries and microflaws inherent in the as-processed specimens are regions where the propensity of damage is high. However, a significant amount of energy from applied stress goes into buckling and kinking of nano-laminates which are the major deformation mechanisms thereby preventing or delaying formation of cracks.

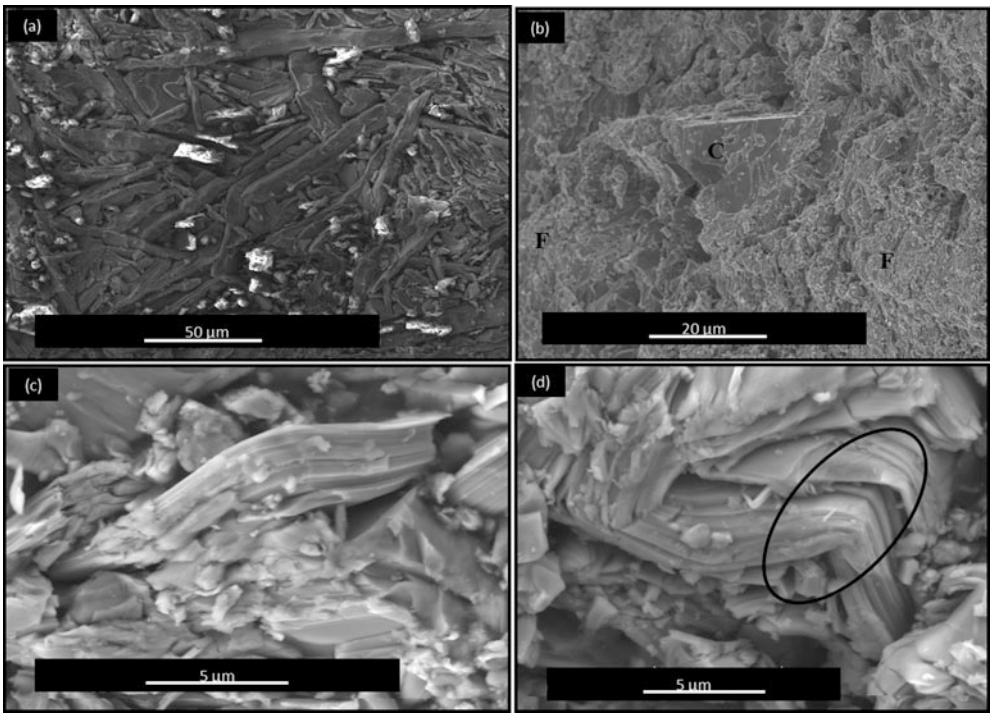

Fig. 53.7 Microstructural features of Ti_2AlC under as processed conditions showing (**a**) grain structure, (**b**) co-existence of cleavage planes and fibrous (ductile) regions in the fractured specimen indicating *quasiductile* response, (**c**) buckled nano-laminates, and (**d**) kink bands and delaminations of nano-laminates

53.4 Discussion

The strain fields and damage evolution mechanisms for high strain-rate response (2,000–3,500 s^{-1}) in Ti_2AlC and Ti_3SiC_2 are analyzed in this study. The specimens are loaded in compression at high strain-rates using SHPB coupled with in-situ high speed imaging. Subsequent analysis using DIC revealed the crack formation paths and strains at which cracks were visible. This analysis is crucial in delineating the accurate response for MAX phase materials by avoiding the overestimation of strain by conventional strain gage-wave analysis method (Sect. 53.3.1). The strain field evolution showed a heterogeneous nature which is attributed to the agglomeration of microflaws distributed in the specimen. These microflaws are induced during processing and act as localized damage initiation sites. Moreover there is a distribution of second phase TiC particles (Fig. 53.7a) which are stiffer than Ti_2AlC thereby leading to a variation in local strains. This inhomogeneity in the microstructure contributes to the inhomogeneities in strain fields and internal damage mechanisms in these materials ultimately leading to its fracture. Previous work has shown that fragmentation of the specimen into relatively smaller pieces post-deformation is due to a cumulative effect of internal damage mechanisms [6, 11]. Ravichandran and Subhash [6] modeled damage evolution in AlN on the principle that tension cracks (wing cracks) are nucleated at tips of compressive microcracks even under overall compression. This process is strain rate dependent and there exists a critical strain rate depending on the material properties such as shear wave speed, length of the specimen, modulus and yield strength. Performing the calculations for Ti_2AlC and Ti_3SiC_2 shows that the value of critical strain rate is 800–1,000 s^{-1}. For the tests reported here, the strain-rates are much higher than the critical value range and it is believed that a mechanism similar to this is operative.

The macroscopic crack propagation along with internal damage is the driving forces for fracture. The macroscopic crack formations show a combination of axial splitting (mode I) and shear type fracture (mode II), as pointed out in Sect. 53.3. However these materials undergo irreversible rearrangements such as kink band formations which mitigate fracture up to a certain value of stress (peak stress). These features are the source of observed ductility in MAX phase materials. For conventional ceramics with hexagonal crystal structures (such as SiC), it has been reported that twinning is a dominant mechanism contributing to damage tolerance and plasticity. However due to the crystal structure parameters in ternary MAX phase ceramics, these deformation modes are not possible (See Sect. 53.1). The nano-layers present in the microstructure

initially buckle under applied load and then gradually evolve into an irreversible kink band, the boundaries of which are defined by dislocations aligned on basal planes of the hexagonal crystal structure. This leads to strengthening which prevents propagation of internal damage. Microstructural characterizations show that a combination of competing mechanisms such as laminate buckling and kinking, delaminations around kink bands, cleavage fracture, transgranular and intergranular cracking are responsible for damage evolution thereby causing a *pseudoductile* behavior even under high strain-rates.

53.5 Conclusions

Ti_2AlC and Ti_3SiC_2 are representative members of MAX phase ternary ceramics, which are characterized by a distinct nano-layered structure. High strain-rate damage evolution mechanisms in these materials were studied experimentally by in-situ high speed imaging and DIC analysis. The importance of DIC analysis in conjunction with the standard wave analysis technique for obtaining accurate material response is shown by comparing DIC strain calculations with the strain gage measurements and truncating data accurately before formation of cracks. The results from the analysis suggest that damage in these materials propagate by a combination of competing mechanisms like microcrack growth and coalescence from internal flaws, grain cracking, delaminations, buckling and kink band formations of nano-layers. The competitions between the ductile and brittle modes lead to significant ductility with an elasto-plastic type deformation before fracture at high strain-rates (~3,500 s^{-1}). Analysis of the macroscopic crack formations reveal that a combination of mode I (opening) and mode II (shear) type that lead to ultimate fracture.

Acknowledgements This work was supported by AFOSR under MURI (FA 9550-09-1-0686) and the authors would like to thank the program manager, Dr. David Stargel. The authors would like to thank Dr. M Radovic and Dr. I Karaman (TAMU) for providing the Ti_2AlC samples which have been used in this work. The authors also acknowledge Prof. Anthony M Waas and Dr. Mark Pankow for use of the SHPB lab set up and fruitful discussions on the experimental techniques

References

1. Barsoum MW, El-Raghy T, Radovic M (2000) Ti_3SiC_2: a Layered Machinable Ductile Carbide. Interceram 49(4):226–233
2. Barsoum MW, Radovic M (2011) Elastic and mechanical properties of the MAX phases. Annu Rev Mater Res 41:9.1–9.33
3. Bhattacharya R, Goulbourne N (2012) Deformation mechanisms in $M_{n+1}AX_n$ phase ternary ceramics at High Strain Rates. In: Proceedings of SEM XII international congress and exposition on experimental and applied mechanics, Costa Mesa, 11–14 June 2012
4. Shih CJ, Meyers MA, Nesterenko VF, Chen SJ (2000) Damage evolution in dynamic deformation of silicon carbide. Acta Mater 48:2399–2420
5. Lankford J (2000) Temperature-strain rate dependence of compressive strength and damage mechanisms in aluminium oxide. J Mater Sci 16:1567–1578
6. Ravichandran G, Subhash G (1995) A micromechanical model for high strain rate behavior of ceramics. Int J Solids Struct 32(17):2627–2646
7. Subhash G, Ravichandran G (1998) Mechanical behavior of a hot pressed aluminum nitride under uniaxial compression. J Mater Sci 33:1933–1939
8. Courtney TH (2005) Mechanical behavior of materials. Waveland Press, Long Grove. ISBN 155664256
9. Lo WT, Jeng CA, Huang JL, Lu HH, Lii DF (2008) Investigation of ballistic impact properties and fracture mechanisms of Ti_3SiC_2 ternary ceramics. J Alloys Compd 455:413–419
10. Riou P, Denoual C, Cottenot CE (1998) Visualization of the damage evolution in impact silicon carbide ceramics. Int J Impact Eng 21(4):225–235
11. Paliwal B, Ramesh KT (2006) Direct observation of the dynamic compressive failure of a transparent polycrystalline ceramic (AlON). J Am Ceram Soc 89(7):2128–2133
12. Chen WW, Song B (2011) Split Hopkinson (Kolsky) bar: design, testing and applications. Springer, New York. ISBN 9781441979810
13. Gama BA, Lopatnikov SL, Gillespie JW Jr (2004) Hopkinson bar experimental technique: a critical review. Appl Mech Rev 57(4):223–250
14. Sutton MA, Orteu JJ, Schreier HW (2009) Image correlation for shape, motion and deformation measurements: basic concepts, theory and applications. Springer, New York. ISBN 978-0-387-78746-6
15. ARAMIS software manual (2007) (http://www.gom.com/3d-software/aramis-software.html)
16. Fazzini M, Mistou S, Dalverny O, Robert L (2010) Study of image characteristics on digital image correlation error assessment. Opt Lasers Eng 48:335–339
17. Zhang H, Huang G, Song H, Kang Y (2012) Experimental investigation of deformation and failure mechanisms in rock under indentation by digital image correlation. Eng Fract Mech 96:667–675
18. Hu L, Benitez R, Basu S, Karaman I, Radovic M (2012) Processing and characterization of porous Ti_2AlC with controlled porosity and pore size. Acta Mater 60(18):6266–6277

Chapter 54
Viscoelastic Behaviour of Maturating Green Poplar Wood

Guillaume Pot, Evelyne Toussaint, Catherine Coutand, and Jean-Benoît Le Cam

Abstract Trees can modify the orientation of their trunk and branches by asymmetrical production of reaction wood. Even though biomechanical models that simulate gravitropic movements are proposed in the literature, recent studies show that they cannot fit the righting-up movement of young, fast growing poplar trees at the intra annual scale. This discrepancy could be explained by the fact that cell maturation is not considered in these models. Another important point is that the knowledge of viscoelastic properties of green wood is poorly studied in the literature, while some biomechanical models show that viscoelasticity of wood can be an important parameter in the tree gravitropic response. These models only provide qualitative results and the viscoelastic properties of wood have to be characterized. The goal of this work is to study the evolution of viscoelastic properties of green wood during maturation. The effects of viscoelasticity corresponding to mechanical solicitation (stress or strain) can be studied by creep or relaxation tests. For the wood of standing tree, internal stresses are due to the maturation and growth of the tree. These constraints can thus act as mechanical stresses and cause deformation of green wood specimens. The effect of these internal stresses on specimens taken from the trunk is first studied in the present work. In the second part of the paper, a study of creep bending of clamped-free wooden boards cut within the last growth ring is presented.

Keywords Green wood • Viscoelasticity • Maturation • Burgers' model • Internal maturation stresses

54.1 Introduction

Gravitropic movements of trees allow them to control their posture by maintaining and modifying the orientation of their trunk and branches. These movements are ensured thanks to asymmetrical differentiation of reaction wood also called tension wood (TW) in most deciduous species and that is produced on one side of the axis [1]. Wood which is localized on the other side of the axis is called opposite wood (OW). The difference of internal stresses between the two sides of the axis enables the movements of the trunk. Wood cells are created at the periphery of the trunk between wood and bark [2], and during the maturation, wood cells tend to shrink in the longitudinal direction. These maturation strains are locked by the cells created earlier which are already stiffer. Consequently, internal maturation stresses are produced.

Several models that enable the internal maturation stresses to be determined can be found in the literature [3, 4]. More particularly, Dlouhà et al. [5] and Coutand et al. [6] have shown that viscoelasticity can increase the righting-up efficiency of trees. In order to determine quantitatively the effect of such behaviour of wood in the gravitropic process, experimental studies must be performed. Because wood contains a large amount of water and thus cells moisture content is above fiber

G. Pot • E. Toussaint (✉)
Clermont Université, Université Blaise Pascal, Institut Pascal, BP 10448, F-63000 Clermont-Ferrand, France

CNRS, UMR 6602, Institut Pascal, F-63171 Aubiere, France
e-mail: evelyne.toussaint@univ-bpclermont.fr

C. Coutand
Université Blaise Pascal, UMR 547 PIAF, INRA, Clermont Université, 63100 Clermont-Ferrand, France

J.-B. Le Cam
Université de Rennes 1, LARMAUR – ERL CNRS 6274, Campus de Beaulieu, Bât. 10B, 35042 Rennes Cedex, France

B. Song et al. (eds.), *Dynamic Behavior of Materials, Volume 1: Proceedings of the 2013 Annual Conference on Experimental and Applied Mechanics*, Conference Proceedings of the Society for Experimental Mechanics Series,
DOI 10.1007/978-3-319-00771-7_54,

saturation point, most of the studies that deal with wood viscoelastic properties focus on mechano-sorptive behavior [7]. In the frame of the modeling of tree gravitropism, the viscoelastic properties of green wood, i.e. wood above fiber saturation point are necessary. Only few studies are dedicated to the experimental characterization of the viscoelastic behaviour of green wood (see Dlouhà et al. [8], Kojima and Yamamoto [9] for instance). None of them has studied the viscoelastic behaviour of TW, or the effect of maturation on viscoelastic properties.

The aim of the present work is to characterize the viscoelastic properties of green poplar wood in order to enhance the prediction of biomechanical models of the gravitropic process. The effect of the maturation process on viscoelasticity is also discussed. An experimental methodology is proposed in order to eliminate the effect of internal maturation stresses in the time-dependent behaviour of wood samples. The materials and methods used are first described. Then, results are presented and discussed.

54.2 Materials and Methods

54.2.1 Experimental Set-up

Seven two-years-old hybrid poplars (*Populus deltoides* x *Populus nigra*, cv I4551) planted in individual 60 L containers were tilted at about 35° from the vertical at the beginning of the third year of growth. Consequently, TW was produced on the upper-side of the tilted axis (see Fig. 54.1a). The diameter growth rate in the basal part of the tree (lower than 20 cm from ground) was calculated using weekly trunk diameter measurements. It was about 0.16 ± 0.03 mm/day. One tree was felled approximately each week during 2 months. Thus, a felling time after tilting can be defined. A piece of the trunk of 8 cm in length was taken from the basal part of each felled tree. A board 6 mm in width in the tangential direction was cut using a band saw (see Fig. 54.1a). Then, after the bark was manually removed, approximately 1.3 mm thick slats were cut using a razorblade (see Fig. 54.1b). Cutting with a razorblade induces no loss of material, so the complete sequence of slats represents the last intra-ring radial variation of wood. Slats were set in water in plastic containers once they were cut in order to keep wood above fiber saturation point. They were left at room temperature (about 20 °C). These slats were directly used for curvature measurements and creep tests.

54.2.2 Determination of Wood Cells Age

Wood cells age was determined under the assumption of a constant growth rate on both sides of the trunk. For that purpose, the eccentricity δ of the trunk and the radial position of each slat were measured. Then, by plotting δ versus the difference between the radius of the tree at a given time r and the radius at the beginning of the growing season r_0, an eccentricity coefficient K_d equal to 0.4 was determined. Finally, thanks to experimental values, growth rates of upper side G_{tw} and of lower side G_{ow} were about $G_{tw} = 0.12$ mm/day and $G_{ow} = 0.050$ mm/day. Finally, this method enables properties to be represented according to the wood cells age, therefore to different maturation times.

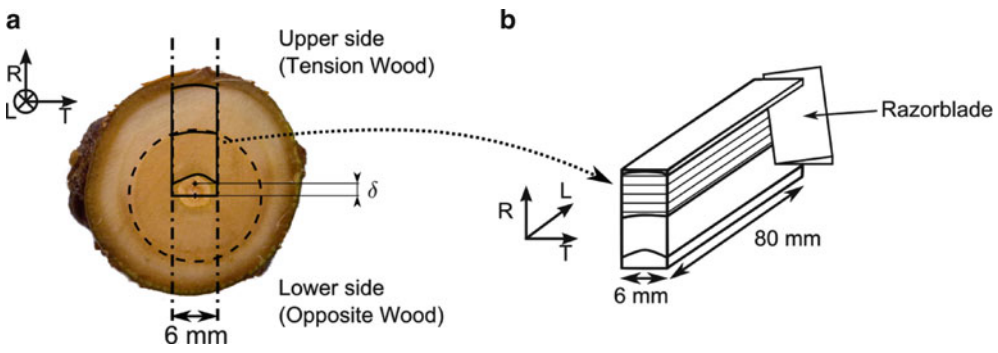

Fig. 54.1 Preparation of the samples. (**a**) Image of a cross-section of the trunk (**b**) drawing of the half board

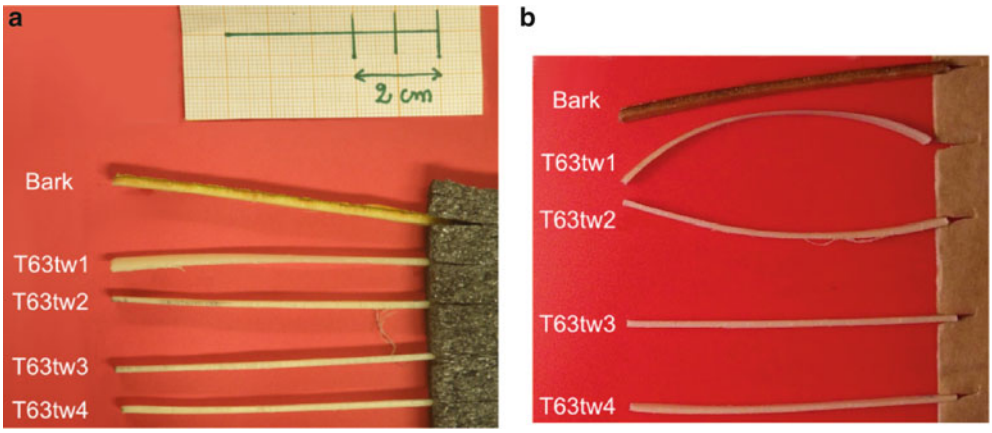

Fig. 54.2 TW samples of tree T63 in the longitudinal-radial plane: (**a**) 5 min after cutting, (**b**) 1 week after cutting

54.2.3 Autonomous Curvature Measurements

In the tree, internal maturation stresses exists in the three directions but are the highest in the longitudinal direction [2]. Sawing operations allow to release these stresses. Moreover, within the thickness of each slat, maturation of wood cells induces a gradient of properties. Finally, when slats are sawed, a curvature in the longitudinal-radial plane can occur.

Curvatures of hydrated slats were experimentally determined using full field measurements. For that purpose, high definition images (3648×2736 pixels^2) of the samples were first recorded immediately after cutting. Then, images were regularly taken for 8 weeks (see Fig. 54.2). The autonomous curvature of some samples increased with time. The shape of each slat was fitted by a circle using the least squares method with a MATLAB routine [10]. Curvature was defined as positive when center of curvature was on the side towards the center of the trunk, and defined as negative otherwise. The coefficient of correlation was above 0.95 for all the samples. Finally, a curvature radius was attributed to each image of each sample during slat autonomous deformation.

54.2.4 Creep Tests

After internal maturation stresses of the previous samples were fully relaxed, bending creep test were performed in a water saturated media (see Fig. 54.3). The samples were anchored at one end by clamping them over a length of 22 mm between two aluminium plates maintained by a screw. Weights were suspended from the free end of the samples; thus a constant load was applied. The samples of trees T49 and T63 (that is trees felled after 49 and 63 days respectively) were tested just after autonomous curvature measurements.

Deflection of the samples was measured thanks to two vertical reference points chosen in scales submerged into the aquarium and located in the same plane as the samples (see Fig. 54.3). Deflection was calculated as the vertical difference between unloaded state and loaded state. The spatial resolution was about 0.1 mm. The samples tested present different maturating states, and consequently different stiffnesses. The applied load was calculated for each slat, using experimental preliminary results obtained on three-point bending tests [11] and a theoretical initial deflection of 3 mm. As a first approximation, the compliance J(t) was calculated using the following equation

$$J(t) = \frac{3Iv(t)}{PL^3} \tag{54.1}$$

where I is the second moment of area, v(t) is the deflection which depends on time, P is the applied load and L is the free sample length which mean value was 54 ± 1 mm.

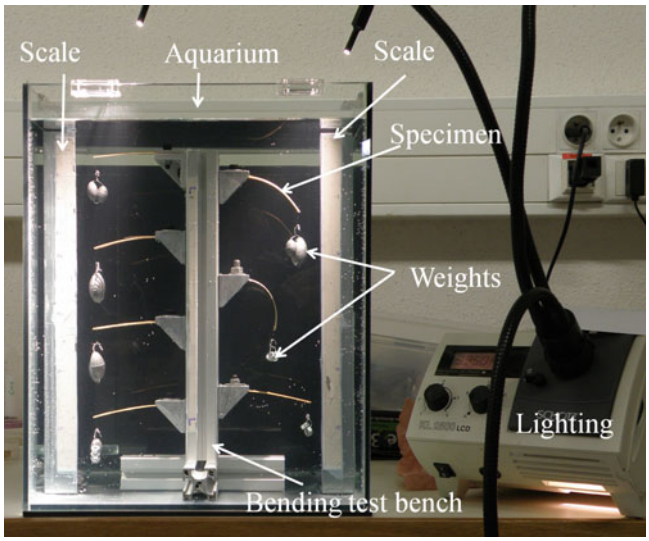

Fig. 54.3 Experimental set-up for creep tests

54.3 Results and Discussion

54.3.1 Behaviour of Small Slats Under Internal Maturation Stresses

Figure 54.4 shows the representative temporal evolution of the autonomous curvature of samples cut from the same tree and subjected to their internal maturation stresses. Initial curvature is closed to zero. Autonomous curvature increases significantly in absolute value for TW samples close to the cambium (see for example samples number 1 and 2). Neither the other TW sample in the inner part of the ring nor OW samples display curvature.

Autonomous curvatures are principally due to a gradient of internal maturation stresses from the external side to the internal side of the slat. This stress gradient produces a bending moment that induces an autonomous curvature if the samples are thin enough to flex. Since green wood is a viscoelastic material, the curvature changes with time as creep occurs. At the same time, stresses progressively relax. TW samples close to the cambium present a positive curvature while second TW samples present a negative curvature. In the literature, tree internal maturation stresses are calculated under the assumption of instantaneous maturation and elastic behaviour of wood [2–4]. The result is an internal maturation stress logarithmic curve that exhibits a radial gradient of stresses in the trunk. It is represented by a dashed line in Fig. 54.5.

Since it is monotonous, this stress profile cannot explain the different autonomous curvature directions between first and second TW samples. Actually, if we consider that cells close to the cambium are not totally mature, then there is a positive gradient of stresses while the cells are maturating. Furthermore, the maturation of peripheral cells induces compression of the inner cells, therefore the stress gradient becomes negative for this inner cells (similarly to the instantaneous maturation models of the literature). Figure 54.5 shows such a supposed stress profile. This stress profile can explain the difference in sign of autonomous curvature of the slats.

54.3.2 Creep Tests Results

Creep curves of tree T63 are presented in Fig. 54.6. Both TW and OW creep curves first present an exponential part, then reach an oblique asymptote. This behaviour can be modeled by Burgers' model. The creep function of this model is given by the following function:

$$J(t) = \frac{1}{E_0} + \frac{t}{\eta_\infty} + \frac{1}{E_1}(1 - e^{-t/\tau}) \tag{54.2}$$

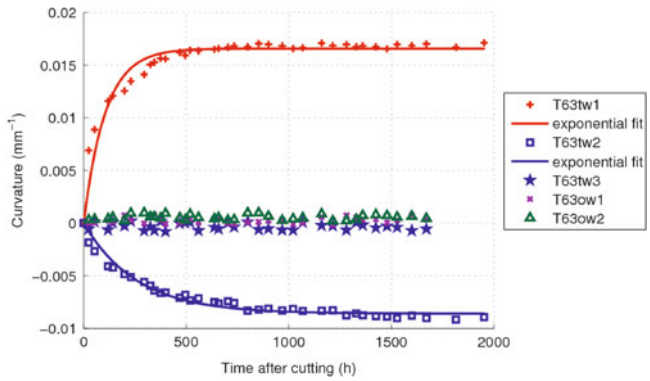

Fig. 54.4 Typical results in terms of temporal evolution of samples' autonomous curvature (tree T63)

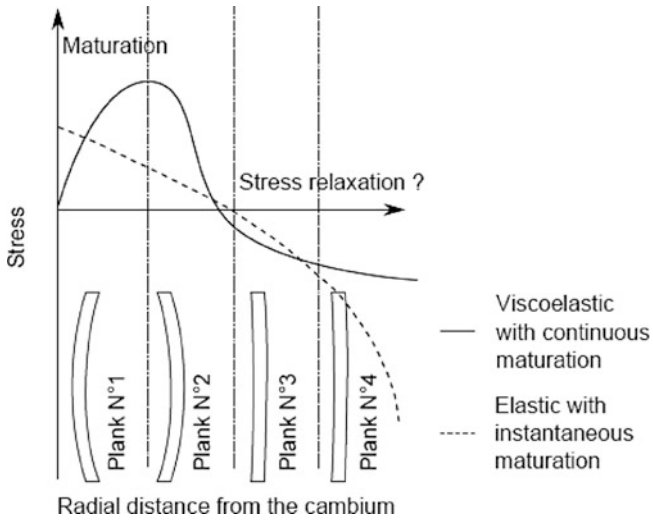

Fig. 54.5 Diagram of probable internal maturation stress profile on TW side

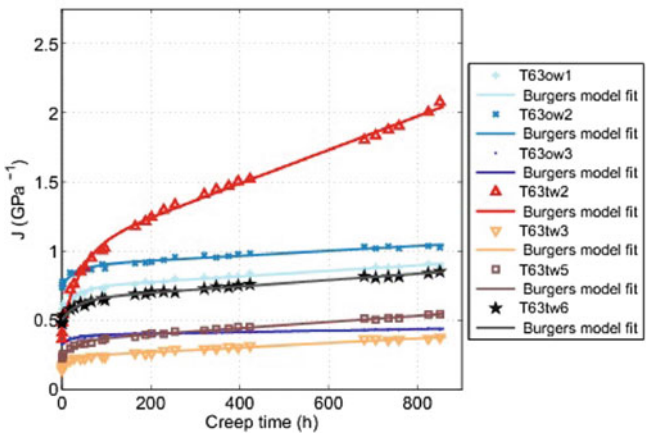

Fig. 54.6 Compliance according to creep time for tree T63

where E_0 is the elastic modulus, η_∞ is the linear viscosity of the dashpot in series, E_1 is the spring modulus in parallel and $\tau = \frac{\eta_1}{E_1}$ is the relaxation time.

A numerical fit of the creep curves enables us to obtain the four viscoelastic parameters of Burgers' model. Under the assumption of a constant maturation process in terms of viscoelastic properties during the vegetative season, these results correspond to the evolution of the viscoelastic properties of green poplar wood according to maturation time (Fig. 54.7).

The variations with wood cells age of viscoelastic parameters appear very similar between OW and TW samples. This would seem to show that viscoelastic behaviour does not depend on the type of wood considered. The higher the maturation

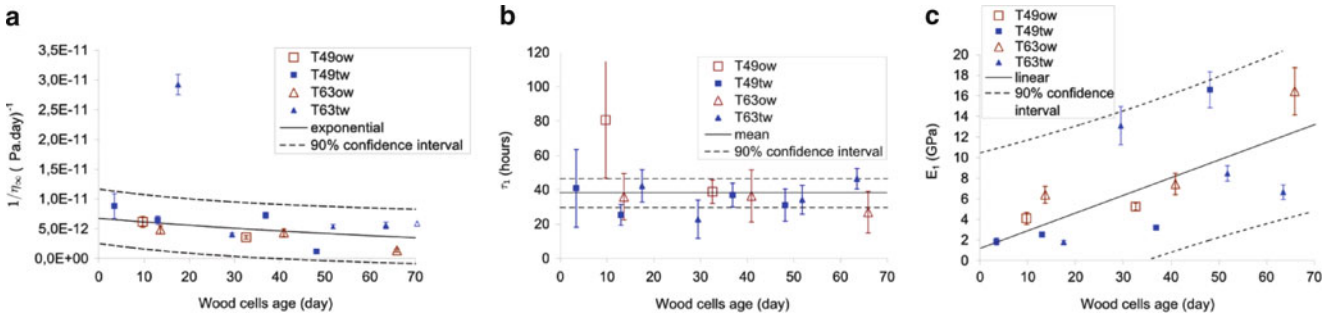

Fig. 54.7 Burgers' model parameters versus wood cell age for two different trees and both OW and TW

of wood, the higher E1 and η_∞. So wood tends to lose its viscoelastic behaviour with maturation. τ is quasi constant and its mean value is 38 $\pm$ 8 h. Finally, the results present quite high variability that can be attributed to wood itself. They cannot be compared to any data in literature since no study dealing with poplar green wood viscoelasticity exists. Despite of their variability, these results allow us to obtain reasonable value of the viscoelastic parameters of green poplar wood.

54.4 Conclusion

In this study, the viscoelastic behaviour of small slats of green poplar wood has been studied. Samples were first subjected to their own, internal maturation stresses. Only the two first TW slats in the outer part of the trunk curve with time. These results can be explained by internal maturation stress relaxation. After autonomous curvature of the samples stopped and thus stresses were fully relaxed, creep test were performed on the same specimens. Creep curves of each samples have been fitted using a Burgers' rheological model and its viscoelastic parameters were determined according to the mean wood cells age of each sample. Green wood shows a tendency to lose its viscoelastic behaviour with maturation. The results of this experimental study provide information on the viscoelasticity of green wood that can be useful for other works dealing with green wood. In particular, the viscoelastic parameters obtained will be used in a biomechanical model such as Coutand et al. model's [6] in order to simulate gravitropic reaction with experimental values of viscoelastic parameters.

References

1. Scurfield G (1973) Reaction wood: its structure, function. Science 179:647–655
2. Fournier M, Chanson B, Thibaut B, Guitard D (1991) Mechanics of standing trees: modelling a growing structure submitted to continuous and fluctuating loads. 2. Tridimensional analysis of maturation stresses. Case of standard hardwood. Ann For Sci 48:527–546
3. Kubler H (1959) Studies on growth stresses in trees. 1. The origin of growth stresses and the stresses in transverse direction. Holz als Roh Werkstoff 17:1–9
4. Archer RR, Byrnes FE (1974) On the distribution of tree growth stresses. Part I: An anisotropic plane strain theory. Wood Sci Technol 8:184–196
5. Dlouhà J, Alméras T, Clair B et al (2008) Biomechanical performances of trees in the phase of active reorientation. Acta Univ Agric Silv Mendel Brun 56:39–44
6. Coutand C, Mathias J-D, Jeronimidis G, Destrebecq J-F (2011) TWIG: a model to simulate the gravitropic response of a tree axis in the frame of elasticity and viscoelasticity, at intra-annual time scale. J Theor Biol 273:115–129
7. Bowyer JL, Shmulsky R, Haygreen JG (2007) Forest products and wood science: an introduction, 5th Rev edn. Iowa State University Press, Ames
8. Dlouha J, Clair B, Arnould O et al (2009) On the time-temperature equivalency in green wood: characterisation of viscoelastic properties in longitudinal direction. Holzforschung 63:327–333
9. Kojima Y, Yamamoto H (2004) Effect of microfibril angle on the longitudinal tensile creep behavior of wood. J Wood Sci 50:301–306
10. Gilat A (2004) MATLAB: an introduction with applications, 2nd edn. Wiley, Hoboken
11. Pot G (2012) Mechanical characterization of green wood during maturation process and modeling of gravitropic reaction of young poplar. Thesis of Blaise Pascal University

Chapter 55
Permeability and Microcracking of Geomaterials Subjected to Dynamic Loads

Wen Chen, Christian La Borderie, Olivier Maurel, Thierry Reess, Gilles Pijaudier-Cabot, and Franck Rey Betbeder

Abstract When subjected to dynamic loads, the mechanic properties like damage, permeability and strength of cohesive materials such as concrete, rocks or ceramics are greatly influenced by loading rate. Furthermore, quasi-brittle geomaterials exhibit a microcracking more distributed under dynamic loads compared to the one generated by static loads. This article focuses on the influence of dynamic loads on the permeability and damage of cohesive cementitious materials. The practical objective is to develop a technique aimed at inducing a distributed state of microcracking in rocks instead of localized fracture to stimulate the production of tight gas reservoirs, a potential alternative to hydraulic fracturing. The dynamic loads are compressive shock waves generated in water by Pulsed Arc Electrohydraulic Discharges (PAED). The experiments were carried out on small hollow cylinder specimens under different vertical and radial confinements. Shock waves are generated in the centre of the specimen and propagate in water and into the solid. The specimen is damaged by the pressure waves and its permeability increases with the evolution of damage. Here both concrete specimens and rock specimens were tested. X-ray scans and microtomography have been used to analyze the evolution of the microstructure of representative specimens qualitatively. At the meantime, the simulation was carried out by the finite element codes Europlexus and Cast3M. An anisotropic damage model is devised which takes account of the loading rate effect and the crack closure effect. The coupling between the anisotropic damage and permeability has been realised. A good correlation has been observed between the experimental and the numerical results.

Keywords Concrete • Sandstone • Shock waves • Microstructure • Damage • Fracture • Permeability

55.1 Introduction

The mechanical behaviour like of cohesive materials such as concrete and rocks depends quite strongly on the rate of loading [1]. When subjected to dynamic loads, the strength increases with the loading rate. In addition, quasi-brittle geomaterials exhibit a microcracking more distributed under dynamic loads compared to the one generated by static loads [2, 3]. The evolution of microstructure under mechanical loads can be characterized by the variation of permeability and the variation of stiffness, material damage. In the past years, a great achievement has been obtained in the studies of the relationship between the evolution of microstructure of quasi-brittle materials, the permeability and damage under static

W. Chen (✉)
Laboratoire d'étude des microstructures et de mécanique des matériaux, Université de Lorraine, Nancy, France
e-mail: wen.chen@univ-lorraine.fr

C. La Borderie • O. Maurel • T. Reess
Laboratoire des sciences de l'ingénieur appliquées à la mécanique et au génie électrique, Université de Pau et des Pays de l'Adour, Pau, France

G. Pijaudier-Cabot
Laboratoire des fluides complexes et leurs reservoirs, Université de Pau et des pays de l'Adour, Pau, France

F.R. Betbeder
Total, CSTJF, Pau, France

B. Song et al. (eds.), *Dynamic Behavior of Materials, Volume 1: Proceedings of the 2013 Annual Conference on Experimental and Applied Mechanics*, Conference Proceedings of the Society for Experimental Mechanics Series,
DOI 10.1007/978-3-319-00771-7_55,

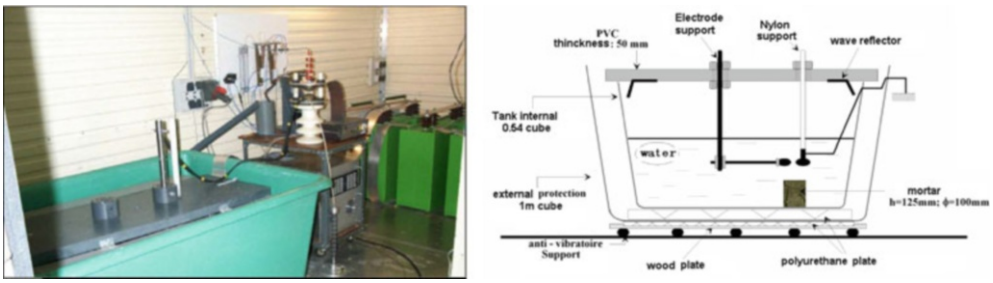

Fig. 55.1 Photograph and experimental set-up for PAED on mortar samples

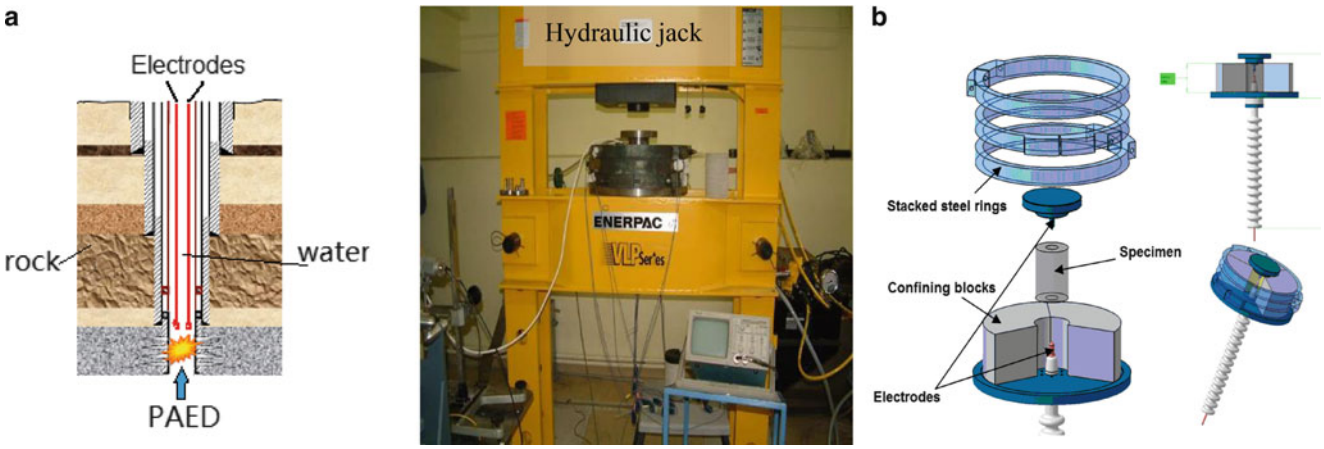

Fig. 55.2 (**a**) Generation of the dynamic loads by a shock wave induced by PAED, (**b**) Overall view of the test set-up

loads [4, 5]. Otherwise in dynamic domain, the effect of loading rate on the microstructure and damage, relative to the material permeability remains, however, to be investigated. The purpose of this paper is to focus on a specific type of dynamic loads and to discuss the correlation between the evolution of microstructure, the material damage and permeability of cohesive materials.

The present study is part of a global research program which has been carried in collaboration with TOTAL SA. This research program is aimed at developing of an alternative stimulation technique to hydraulic fracturing in the petrolic domain. Geological reservoirs contain gas generally stored in very fine occluded pores in low permeable rocks (0.1 mD) at certain depths. The conventional oil and gas stimulation technique, hydraulic fracturing, generates few large localized cracks in the periphery of the well in order to increase the permeability of rocks and enhance oil or gas production [6]. Unfortunately, this technique dose not ameliorate the interconnection of the occluded pores over a large area. Hence the production remains modest. Furthermore, hydraulic fracturing uses the chemical additions to stabilise crack opening and enhance the production of gas. Those chemical additions may diffuse to the aquifer and induce the damage to environment. Since 2011 May, hydraulic fracturing for oil and gas production has been forbidden in France.

The developed stimulation technique uses dynamic loads to generate distributed micro cracks and increase the permeability of rocks [7]. The dynamic load is a compression underwater shock wave generated by Pulsed Arc Electrohydraulic Discharges (PAED) [8]. The shock wave is propagated in water and transmitted to the sandstone in the wall of the oil well. The shock waves fragment the occluded pores and generate distributed damage around a borehole, which induce a augmentation of permeability of rocks [7] (Fig. 55.2a).

In order to investigate the feasibility of the developed stimulation technique, a preliminary experimental program has been carried out to observe the effect of compression pressure waves induced by PAED on permeability intrinsic to mortar specimens [9]. The wave is generated into water and then transmitted to the specimen (diameter 100 mm, height 125 mm), which is immersed. The photograph and schema of set-up is plotted by Fig. 55.1. The pressure wave amplitude was controlled by the variation of the injected electrical energy and by the distance between the electrodes and the surface of the

specimen. It is observed that the permeability of mortar specimens increase both with the amplitude of the pressure wave and of number of repeated shocks.

After that, a more realistic experimental program has been executed in laboratory. Hollow concrete and sandstone cylinder specimens have been tested to mimic the configuration of an oil well. The specimens were subjected three levels of combined lateral and vertical loads which represent the states of stress underground at depths of 0, 1,550 and 2,250 m. The confinement plays a important role in the experimental study. Subjected to tri-axial loads, the strength of rocks is much higher than that which is measured under unique axial loads. Hence in situ condition, the effectiveness of the electrical fracturing may be decreased by initial compression stresses due to the gravity. The shock waves were generated by two electrodes which were placed in side of the hollow cylinder (external diameter 125 mm, internal diameter 50 mm, height 180 mm) which is filled with water. Three experimental parameters have been studied: the electrical injected energy, the number of shocks applied to the specimen and the confinement levels. Both mortar specimens and sandstone specimens have been tested. The mechanic properties of mortar specimens such as permeability, strength and microstructure are close to tight rocks. Experiments were carried out first on mortar specimens first because that the properties of mortar are less dispersed than those of sandstone generally, making it easier to highlight basic phenomena with less scattering of experimental data. For each specimen, the radial permeability to nitrogen was tested before and after the application of electrical shocks. X-ray scans have been also employed to characterized the evolution of the microstructure of representative specimens subjected to dynamic loads. Similar results have been obtained as in preliminary experimental program, the intrinsic permeability of the specimens increased both with the electrical energy which was involved in the PAED and the number of repeated shocks. Furthermore, the experimental data proves that the same increases of permeability may be obtained by injecting a relatively large quantity of electrical energy or a much smaller quantity of electrical energy if loads are repeated [10].

At the means time, a numerical model has been developed to address a numerical description to the experimental data and then to simulate the electrical fracturing in oil well in real size [11]. The whole electrical fracturing process, the generation of the shock waves due to PAED and the propagation of the shock waves in water and then in the solid phase, has been simulated with the finite-element computer code EUROPLEXUS and CAST3M. The generation and propagation of shocks waves in water due to PAED has been simulated by a diphasic model (liquid water and vapour) [12, 13]. A 3D new constitutive model for concrete (and possible rocks) is devised, which describes anisotropic damage and cracking, takes account of the loading rate effect, the crack closure effect and the conservation of fracturing energy related to element size. An anisotropic method has been proposed to calculate the permeability based on the anisotropic damage [14]. Numerical results were compared with experimental data and consistent correlation agreements have been obtained.

55.2 Experimental Program

55.2.1 Experimental Set-up and Material Properties of Specimens

The experimental set-up is plotted in Fig. 55.2b. Two electrodes are placed inside the hollow cylindrical specimens (external diameter 125 mm, internal diameter 50 mm, height 180 mm), which is filled with water. A 2,000 kN hydraulic jack has been used to apply the vertical confinement. And the lateral confinement pressure is applied by three stacked steel rings (600 mm diameter, 60 mm height and 30 mm thick) tightened with a beam wrench. Three confining blocks made of ultra high performance concrete reinforced with metallic fibres are placed between the specimen and steel rings in order to absorb the shock wave and to homogenize the radial pressure on the external face of the specimen. Three levels of combined confinement have been used which correspond the states of stress underground at depths of 0, 1,550 and 2,250 m. The detail of the vertical and lateral stresses are presented in Table 55.1.

In the experimental program, mortar specimens were tested first whose mechanic properties like permeability, strength and microstructure are close to sandstone. The mortar specimens were made with a maximal grain size of 2 mm and a water cement ratio of 0.6. The mortar specimens were the same size as rock specimens which were cored from sandstone blocks. The average mechanical properties of the specimens of the two materials are detailed in Table 55.2.

Radial permeability experiment has been carried out by injecting an inert gas (nitrogen) into the cylindrical borehole of the specimens under ambient conditions (20 °C). The schema of the permeability cell is illustrated in Fig. 55.3b. The specimens were tested both before and after PAED process. A Mass Flow Meter (MFM) has been used to measure the equivalent volumetric gas flow rate. Based on the injected flow rate Q_i [m^3/s] and the inner and outer pressures, the apparent permeability K_a [m^2] is obtained by using Darcy's law and the mass balance equation. Then the intrinsic permeability K_v [m^2] is calculated by extrapolating the apparent gas permeability K_a due to the Klinkenberg relationship.

Table 55.1 Vertical and lateral stresses of mortar

	Vertical loads (MPa)	Lateral stresses (MPa)	Simulated deepness (m)
Low confinement	2	2	0
Medium confinement	19.5	9.1	1,500
High confinement	40	25	2,250

Table 55.2 Average mechanical properties of mortar and sandstone

	f_c (MPa)	f_t (MPa)	E (MPa)	K_v (m^2)
Mortar	19.6	4.9	17,300	1.10^{-17}
Moliere sandstone	49	6.35	19,000	1.10^{-17} to 2.10^{-16}

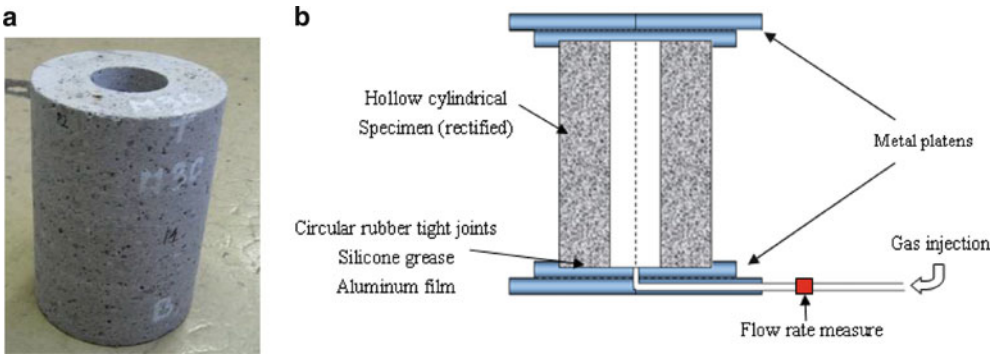

Fig. 55.3 (**a**) Test specimen, (**b**) Schematic representation of the permeability cell

55.3 Experimental Results

55.3.1 Influence of Injected Electrical Energy on Permeability

In order to observe the effect of the quantity of the injected energy and of the number of shock waves to the permeability of the specimens, two sequences of tests have been executed : sequence "one shock" and sequence "multi-shock". In the sequence one shock, only a single shock has been applied to the mortar specimens with a variable injected energy under confinement. The three confinement levels have been considered. The evolution of permeability with the quantity of injected energy subjected to high and low confinement are presented in Fig. 55.4. Three zones distinct have been observed in the curves permeability-injected energy. For example in the case of low confinement, no significant variation in permeability is observed when the injected energy is below 190 J. If the injected energy varies from 190 to 300 J, permeability increases almost linearly in a semi-log plot. Above 300 J, the intrinsic permeability remains constant at about 10^{-15} m^2. Because the specimens are so damaged that macro cracks are generated. The permeability is beyond the measurable range of the present apparatus. Hence the damage threshold to the injected energy, where the permeability begins increase significantly, is 190 J. Under medium and high confinement, the same trend of evolution of permeability with injected energy is observed. The damage threshold to injected energy are 500 and 5.11 kJ for the series of test under medium and high confinement respectively. The experimental data proves the effect of confinement to measured permeability as expected. Higher the level of combined confinement, lower the permeability measured for the same injected energy. The ratio between permeability measured under medium confinement and low confinement is approximately equal to one order of magnitude. The ratio between permeability measured under high confinement and low confinement is approximately equal to 20.

Sandstone specimens have been tested also in the sequence "one shock". Only high confinement has been considered. The same evolution of permeability with injected energy is observed with the damage threshold 4.2 kJ (Fig. 55.5). For the reason that the rock specimens are not as homogenous as mortar specimens, more disturbance is observed in the experimental data with sandstone specimens.

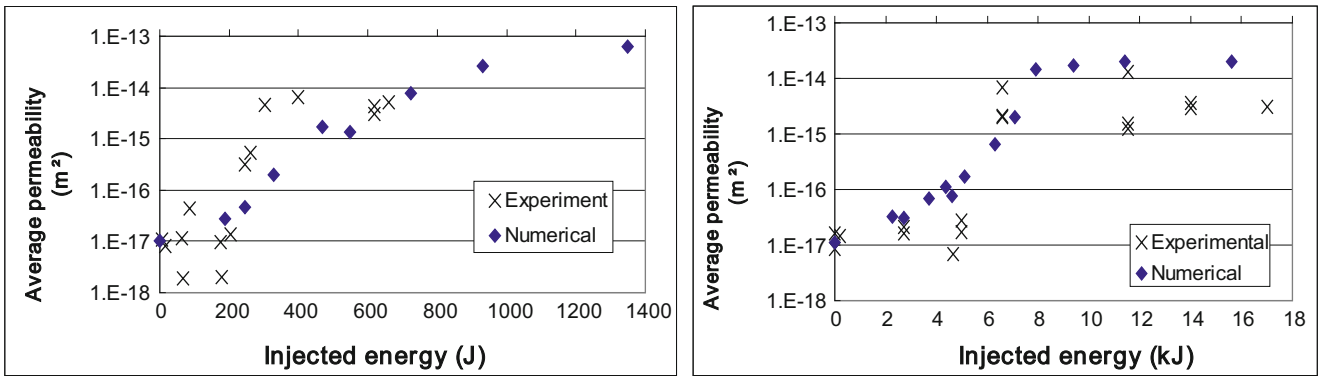

Fig. 55.4 Comparison of the experimental and the numerical average permeability under low confinement (*left*) and high confinement (*right*)

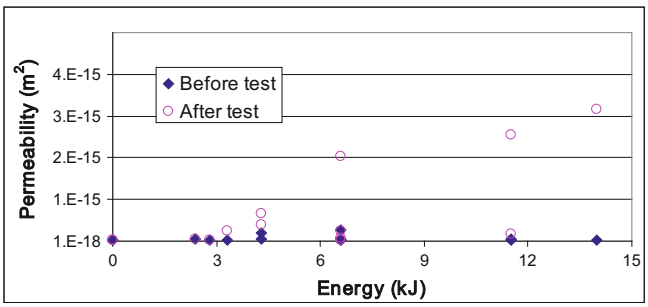

Fig. 55.5 Evolution of the permeability of rock specimens with injected energy before and after test

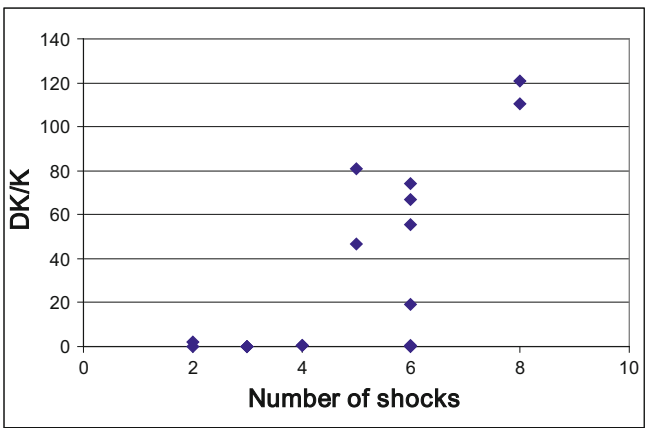

Fig. 55.6 Evolution of the permeability of mortar (*left*) and tight (*right*) specimens with the number of shocks

55.3.2 Influence of Number of Shocks on Permeability

In the sequence "multi-shock", repeated loads have been applied to both mortar and rock specimens. Only high confinement is considered. The injected energy pour each load was constant, 2.7 kJ for the mortar specimens and 2.2 kJ for the rock specimens respectively. The variations of the intrinsic permeability of mortar and rock specimens with the number of shocks are illustrated in Fig. 55.6. K_0 is the initial permeability and ΔK is the increment of permeability after electrical fracturing. The Fig. 55.6 illustrates the effect of number of shocks (3, 6 and 9 shocks) to the permeability of mortar specimens. The permeability increases almost linearly with the number of shocks in a semi-log plot. The repeated shocks , varied from 2 to 8,

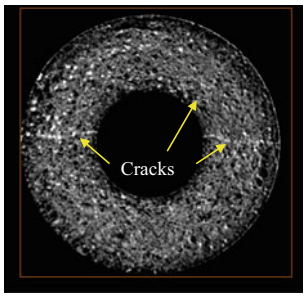

Fig. 55.7 Cross-section after CT scanning of mortar specimen

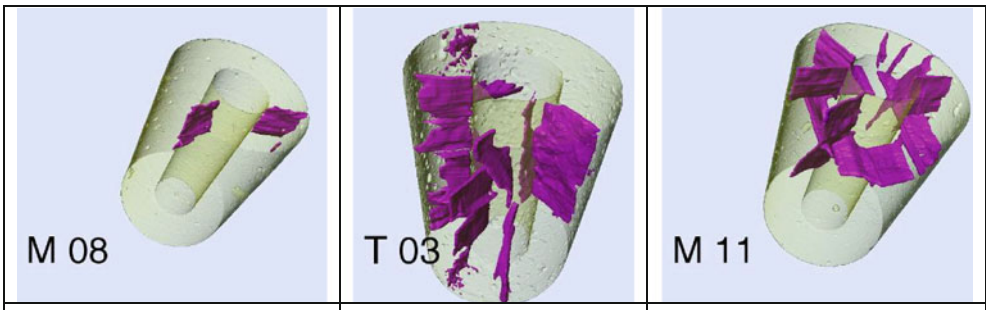

E_b = 200 J	E_b = 6.6 kJ	E_b = 17 kJ
K_y = 1.48 10^{-17} m^2	K_y = 2.1 10^{-15} m^2	K_y = 3. 10^{-15} m^2
S_{crack} = 63 cm^2	S_{crack} = 439 cm^2	S_{crack} = 351 cm^2

Fig. 55.8 Three dimension tomography scans after one shock with injected electrical energy ranging from 200 J (*left*) to 17 kJ (*right*)

have been applied to on rock specimens. The Fig. 55.6 also shows the variation of the ratio between the increment of permeability and initial permeability with the number of shocks. If the number of shocks is below four, no significant augmentation of permeability is observed. Above four shocks, the relative variation of permeability increases almost linearly with number of shocks in semi-log plot. Hence, the same trend of evolution of permeability with the number of shocks has been obtained for both mortar and rock specimens after four shocks. The permeability increases span over a range of almost two orders of magnitude which is above the scattering of data.

55.3.3 Evolution of the Microstructure Illustrated by X-ray Scans

X-ray tomography has been employed to analyse qualitatively the evolution of microstructure subjected to dynamic loads. Both mortar and rock specimens have been scanned before and after shocks. Figure 55.7 presents an example of a cross-section after CT scanning of the mortar specimen after electrical fracturing. The density of material is linearly denoted by the level of grey. So the white zones related to the pores and cracks with density close to zero. The darkest zones represent the virgin material with density close to 2.5 kg/dm^3.

3D-scans are illustrated in Figs. 55.8 and 55.9. Scans have been subtracted to each other in order to observe the evolution of cracking before and after shocks. The resolution of the CT scan is approximately 0.25 mm. Taking the difference between the two scans provides an increase of resolution of about 0.02 mm. Hence, only the cracks with the opening above 0.02 mm can be observed by CT scan. The dark zones in these photos represent the visible cracks. The correlation between the qualitative results of the image analysis, the amount of crack surface and permeability of mortar specimens has been analysed. The total amount of crack surface S_{crack} has been used to characterize the cracking pattern. The Fig. 55.8 presents the influence of injected energy on the generation of cracks. A single shock has been applied to the specimens with a variable quantity of injected energy under high confinement. When the injected energy is above the damaging threshold, both the permeability and the crack surface increase quickly with injected energy. For specimens T03 and M11, the permeability is within the same order of magnitude ($2.1 \cdot 10^{-15}$ and $3.0 \cdot 10^{-15}$ m^2 respectively) and the crack surface is also within the same

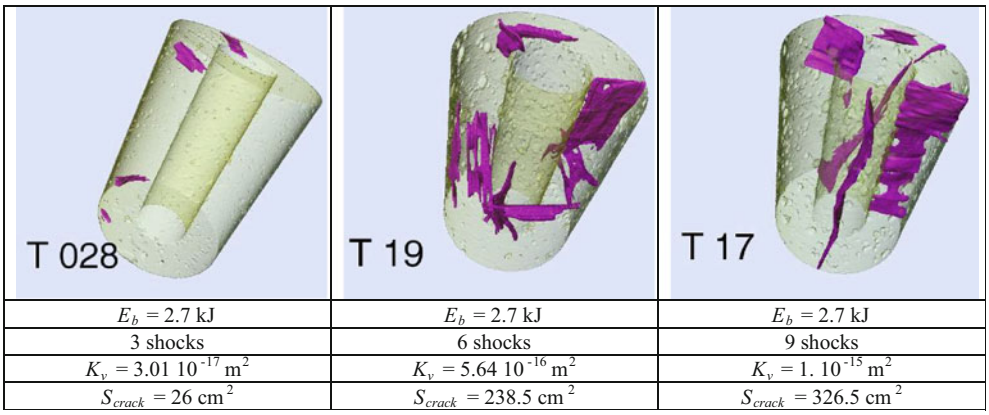

E_b = 2.7 kJ	E_b = 2.7 kJ	E_b = 2.7 kJ
3 shocks	6 shocks	9 shocks
K_y = 3.01 10^{-17} m^2	K_y = 5.64 10^{-16} m^2	K_y = 1. 10^{-15} m^2
S_{crack} = 26 cm^2	S_{crack} = 238.5 cm^2	S_{crack} = 326.5 cm^2

Fig. 55.9 Three dimension tomography scans after one shock (*left*), three shocks (*middle*) and nine shocks (*right*) with injected electrical energy of 2.7 kJ for each shock

range (439 and 351 cm^2 respectively). The Fig. 55.9 illustrate the effect of the number of repeated shocks with constant injected energy to the permeability of mortar specimen under high confinement. The permeability and the crack surface augment quickly with the number of shocks. Based on the image analysis of the two sequences of experiment, diffuse cracks have been observed during electrical fracturing, which is what is expected from dynamic loads.

55.4 Numerical Simulation

The entire electrical fracturing process is described numerically with three models: fluid and solid finite element meshes with the FSA algorithm for the interface between the two, a diphasic model for water, and the 3D anisotropic model for mortar and rocks. Adapting a continuum anisotropic damage model according to Desmorat [15], the new constitutive model describes anisotropic cracking and damage, the crack closure effect, strain rate effects [16] and the variation of fracture energy with mesh element size. In addition, a permeability tensor is derived from the damage tensor, and the mechanical model is coupled with a mass transport model [17], i.e. a simple Darcy like description of fluid flow in damaged concrete.

The hollow specimen tested by Chen et al. [7] is analysed using the model developed in the previous section. The Finite Element mesh used is given in Fig. 55.10. A quarter of specimen was simulated using symmetry conditions in order to reduce computation time. An example of numerical results is presented at Figs. 55.11 and 55.4. The Fig. 55.11 plots the map of damage and flow into the specimen loaded with two shock waves of energy 188 and 1.35 kJ. The flow increases locally at the damaged zone. The experimental and numerical permeability versus shock wave energy curves are illustrated in Fig. 55.4. A good correlation is observed between the experimental and numerical results.

55.5 Conclusions

This paper aimed at investigating a technique to increase the intrinsic permeability of tight rocks nearby a borehole with dynamic loads. The dynamic load is generated by a shock wave induced by Pulsed Arc Electrohydraulic Discharges (PAED) in water. Laboratory experiments on mortar and rocks subjected to a static load system representative of underground conditions have been presented. Tests with single shocks and variable energy levels show there are thresholds of injected energy wave above which damage and increase of permeability are observed. This threshold increases with the confinement stress on the specimen. Results from repeated shock tests show that the permeability increases with the number of shocks, even if a moderate electrical energy corresponding to the threshold observed in single shock tests under high confinement has been used. An accumulation of damage as a function of the number of shocks is observed. X-ray tomography has been used to visualize the evolution of cracking with permeability. X-Ray tomography shows that the amount of crack surface induced by the dynamic loads increases both with injected electrical energy and the number of shocks. X-Ray tomography shows also that many cracks develop in the course of the experiments. Rather diffuse cracking occurs, which is what is expected from dynamic loads.

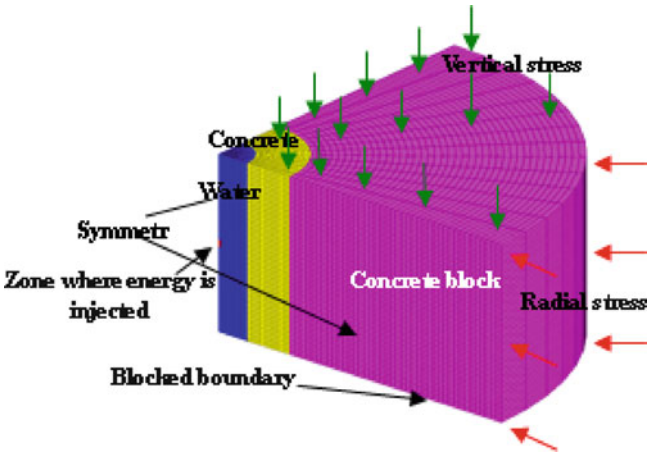

Fig. 55.10 Finite element mesh of the simulation

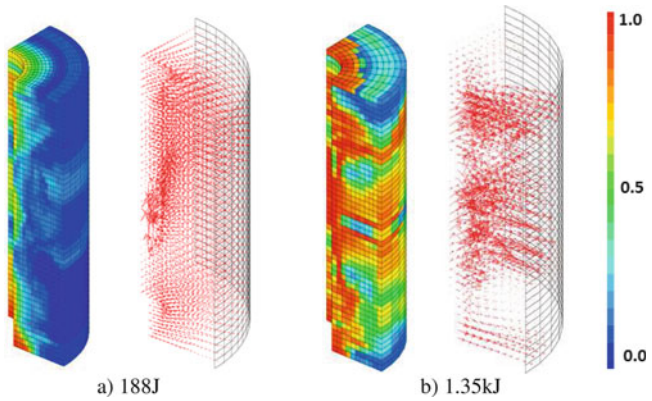

Fig. 55.11 Evolution of damage and flux vector with different injected energy under low confinement

At the means time, a visco-elastic anisotropic damage model is proposed for concrete and rocks [18]. This model deals with the micro-defects closure effect and the variation of fracture energy with mesh element size. The damage state is represented by a single second-order damage tensor available both in traction and compression. By taking advantage of this anisotropic description of damage, anisotropic permeability has been calculated. A good agreement is observed between experimental and numerical permeability.

Acknowledgments The authors wants to acknowledge the Total company and the Aquitaine council for their support.

References

1. Abrams DA (1917) Effect of rate of application load on the compressive strength of concrete. In: Proceedings, ASTM 17, Part 2, pp 146–165
2. Denoual C, Hild F (2002) Dynamic fragmentation of brittle solids: a multi-scale model. Eur J Mech A/Solids 21:105–120
3. Cao J, Chung DDL (2001) Defect dynamics and damage of concrete under repeated compression, studied by electrical resistance measurement. Cement Concr Res 31:1639–1642
4. Choinska M, Khelidj A, Chatzigeorgiou G, Pijaudier-Cabot G (2007) Effects and interactions of temperature and stress-level related damage on permeability of concrete. Cement Concr Res 37:79–88
5. Jason L, Pijaudier-Cabot G, Ghavamian S, Huerta A (2007) Hydraulic behaviour of a representative structural volume for containment buildings. Nucl Eng Des 237:1259–1274
6. Zhang GQ, Chen M (2010) Dynamic fracture propagation in hydraulic re-fracturing. J Petrol Sci Eng 70:266–272
7. Chen W, Maurel O, Reess T, Matallah M, De Ferron A, La Borderie C, Pijaudier-Cabot G, Rey-Bethbeder F, Jacques A (2012) Experimental study on an alternative stimulation technique for tight gas reservoirs based on dynamic shock waves generated by Pulsed Arc Electrohydraulic Discharges. J Petrol Sci Eng 88–89:67–74

8. Touya G, Reess T, Pécastaing L, Gibert A, Domens P (2006) Development of subsonic electrical discharges in water and measurements of the associated pressure waves. J Phys Appl Phys 39:5236–5244
9. Maurel O, Reess T, Matallah M, De Ferron A, Chen W, La Borderie C, Pijaudier-Cabot G, Jacques A, Rey-Bethbeder F (2010) Electrohydraulic shock wave generation as a means to increase intrinsic permeability of mortar. Cement Concr Res 40:1631–1638
10. Chen W (2010) Fracturation électrique des géomatériaux – Etude de l'endommagement et de la perméabilité. Ph.D. Dissertation (in French), Université de Pau et des Pays de l'Adour
11. Laborderie C, Chen W, Pijaudier-Cabot G (2011) Projet tight gas reservoirs, couplages fissuration -endommagement – perméabilité pour la fracturation par arc électrique. Rapport final simulations numériques
12. Lepareux M (1994) Programme PLEXUS matériau eau modèle homogène équilibre. Rapport DMT 94/398
13. Chen W, Maurel O, Reess T, Matallah M, De Ferron A, La Borderie C, Pijaudier-Cabot G, Rey-Bethbeder F, Jacques A (2011) Experimental and numerical study of shock wave propagation in water generated by Pulsed Arc Electrohydraulic Discharges. Int J Heat Mass Trans, submitted
14. Chen W, La Borderie C, Maurel O, Pijaudier-Cabot G (2011) Modelling of damage and permeability of concrete and rocks subjected to dynamic loads. In: Proceedings of MAMERN'11, Saidia, Marocco, pp 284–288
15. Desmorat R, Gatuingt F, Ragueneau F (2007) Nonlocal anisotropic damage model and related computational aspects for quasi-brittle materials. Eng Fract Mech 74:1539–1560
16. Dubé J-F, Pijaudier-Cabot G, La Borderie C (1996) A rate dependant damage model for concrete in dynamics. J Eng Mech ASCE 122 (10):939–947
17. Chatzigeorgiou G, Picandet V, Khelidj A, Pijaudier-Cabot G (2005) Coupling between progressive damage and permeability of concrete: analysis with a discrete model. Int J Numer Anal Meths Geomech 29:1005–1018
18. Chen W, Maurel O, Reess T, Matallah M, De Ferron A, La Borderie C, Pijaudier-Cabot G, Jacques A, Rey-Bethbeder F (2011) Modelling of anisotropic behavior of concrete materials under dynamic loads. Eur J Environ Civ Eng 15(5/2011):727–742

Chapter 56
Vibration Analysis and Design of a Monumental Stair

Mehdi Setareh

Abstract Walking or running up and down a stair may result in vibrations that can be annoying to people. In extreme cases the large movements of a stair may promote the feeling that the structure is not safe. In recent years, a trend has appeared in architecture to design monumental stairs with slender structural components and few supports. This has resulted in structures with low natural frequencies and effective mass, which may become susceptible to large levels of vibrations. This paper presents a brief overview of the past research on the issues related to the vibration serviceability of staircases. In addition, it provides the details of the structural analysis and design of a monumental stair located in an art museum. A computer model for the vibration analysis and various design modifications was created. Since the design to resist the static loads resulted in low natural frequencies, it was believed that the structure is susceptible to large vibrations. Several modifications to the original design of the structure were made, which included the exclusion and inclusion of the non-structural elements; addition of steel risers; introduction of steel plates, vertical and diagonal members between the top and bottom chords of the stringers; and changing the boundary conditions. The main objective was to increase the natural frequencies of the structure such that human movements could not excite the main modes of vibration and, therefore, the stair response will remain within the acceptable range. The vibration response when people walked at normal speed, briskly, and running down the stair were analytically estimated. These results showed that the stair movements were within the acceptable range when individuals descended the stair at the normal pace. Based on the review of the existing literature, vibration serviceability of staircases require further research to provide guidelines for designers to more accurately predict and evaluate their dynamic performance when subjected to human movements.

Keywords Staircase • Vibration serviceability • Human vibrations • Vibration analysis • FE modeling

56.1 Background

Large movements of staircases may result in the annoyance and/or discomfort of the users. In extreme cases, they may also cause safety concerns for the building occupants. In recent years, renowned architects such a Frank Gehry, Zaha Hadid, etc. have designed slender, light and flexible monumental stairs, which have resulted in vibration serviceability issues which required the special attention by structural engineers ([1–8]).

The first research study on the stair vibration serviceability due to human movements was conducted by [9]. He reported that when 15 people descended a stair at the speed of 2 steps/s, the maximum applied force was about four times their body weights, and increased to 12 when they jumped on the stair. Only the peak force amplitude was found in this study without measuring the input forcing functions. Reference [10] measured the average applied dynamic force from a single footfall on a stair. They found that descending at a normal rate generates forces up to twice the body weight, and running down three steps at a time results in forces up to five times the body weight.

M. Setareh (✉)
School of Architecture and Design, Virginia Tech, Blacksburg, VA 24060, USA
e-mail: setareh@vt.edu

B. Song et al. (eds.), *Dynamic Behavior of Materials, Volume 1: Proceedings of the 2013 Annual Conference on Experimental and Applied Mechanics*, Conference Proceedings of the Society for Experimental Mechanics Series,
DOI 10.1007/978-3-319-00771-7_56,

The applied human dynamic force on floors, stairs, etc., $F(t)$, is defined in terms of Fourier Series as:

$$F(t) = G[1 + \sum_{i=1}^{n} \alpha_i \sin(2\pi i f_p t + \phi_i)] \tag{56.1}$$

where G is the weight of person, α_i is the dynamic load factor (DLF) or Fourier coefficient for the *i-th* harmonic, f_p is the step frequency, t is the time variable, and ϕ_i is the phase angle associated with the *i-th* harmonic.

References [11, 12] recorded the forcing functions on stairs, and studied the effects of group loading, in addition to acceptable vibration levels for stairs. They also found that individuals can descend a stair at speeds up to 4.5 steps/s. References [11, 12] concluded that, in general, the DLF for the first harmonic, α_1, is larger when people ascend a stair than when they descend it; however, the opposite is true for the higher harmonics. They also stated that the natural frequency was not affected by the presence of 27 people on a stair; however the damping increased from 2.2% (for the empty stair) to 6% (with people). They indicated that due to the fixed geometry of stair (tread and riser size), people tend to move at close speeds on crowded stairs, which results in group effects. They mentioned that they measured the vibration response of a stair when an individual and a group of 27 people ascended and descended (without providing any details). References [11, 12] mentioned that when people move slowly on stairs, the group effect is negligible. Using a Monte Carlo analysis, they found that the modal force for a group of 27 people can be up to three time that of an individual (enhancement factor = 3). They attributed the low limit of stair response from the group to the increase in damping due to the presence of people. It should be noted that they did not directly measure the enhancement factor.

References [11, 12] noted the lack of guidance on the acceptable stair vibration limits in the literature and defined a non-dimensional factor, R, representing the multiplier to the base perception acceleration based on the British Standard [13]. They recommended R = 32 for the light-use stairs (e.g., in offices), R = 24 for heavy use stairs (e.g., in public buildings), and R = 64 for very lightly-used stairs and for cases where large groups of people may use the stairs at the same time, based on the vibrations resulted from one person ascending/descending the stair. The basis and origin of these recommendations are unknown and there is no evidence in the literature as how the authors obtained the values.

References [14, 15] studied the differences between the loads from people on floors and stairs. They noted that the most comfortable step frequency for ascent was near 2 steps/s (when walking) and close to 3.3 steps/s (when running). For descents, the comfortable paces were below 2.3 steps/s (walk) and above 3.3 steps/s (run). They reported that, similar to the ascending results, the subjects felt natural descending footfall rates were 2.0 steps/s and 3.3 steps/s. References [14, 15] measured the first four harmonic DLFs for people walking on a floor and a stair. They reported much larger second harmonic DLF for descents compared to ascents, in particular for high footfall rates. Also, the first harmonic DLF of fast descents (measured at 4.3 steps/s) was much larger than for normal walk descents (1.85 steps/s). They noted no major differences between the DLFs of higher harmonics for descents and ascents; however, they found forces up to three times the body weight for fast descents and about twice the body weight for slow descents. For fast ascents, the measured forces were up to 2.5 times the subjects' body weights. Reference [14] concluded that: (1) the second harmonic DLF of fast descent was about three times that of ascent; (2) the first harmonic DLF for ascent or descent force on a stair was about 2.5 time that of walking on a flat floor; and (3) the second harmonic DLF for stair ascent/descent forces was about six time that of walking on flat floors. They also recommended that any staircase having a natural frequency of less than 10 Hz may be dynamically responsive to the applied footfall forces, which may result in unacceptable vibrations.

Reference [16] conducted comprehensive experimental studies to measure a person's applied forces on a stair, in addition to estimating the group loads using the Monte Carlo analysis technique. Upon the completion of a number of ascending/descending tests by individuals on a limited size laboratory stair, he found that the most important factor affecting the DLF values of various harmonics was the step frequency. From the tests involving 25 individuals ascending/descending a laboratory stair, he found the most comfortable footfall rate for ascent was about 2 steps/s (walking) and 3.3 steps/s (running). The maximum possible ascent rate was measured at 4.5 steps/s. Reference [16] noted that even though the general shape of forcing functions applied by individuals ascending or descending a stair did not vary with the stair pitch, their amplitudes changed. He reported that descending with speeds up to 4 steps/s were comfortable for everyone who participated in the experiments. This was not consistent with the previous findings of the same researcher. He also reported that comparing the applied forces with those on flat floors, the magnitude of forces on stairs were larger and higher footfall rates were also possible. References [15, 16] repeated their previous recommendation regarding staircases to be designed for a minimum natural frequency of 10 Hz to prevent annoying vibrations. Using the Monte Carlo analysis, [16] studied the effects of a group of people ascending/descending a stair, and computed the enhancement factor as the ratio between the first harmonic DLF from a group of people moving on a stair to that of an individual. He computed the most likely enhancement factors to be 2.2, 2.8, and 3.8 for 9, 18, and 27 people, respectively, which were relatively consistent with 1.8, 2.2, and 3.1 reported by [12].

Using the results of the force measurements from people moving on a laboratory stair, [16] computed the DLFs for up to four harmonics. For the ascents, the results of his studies can be summarized as (ranges are reported as the mean ±2 standard deviation): (1) for the first harmonic, the average DLF at 2.0 steps/s (walk) was about 0.4, and at 3.3 steps/s (run) was close to 1.0; (2) for the second harmonic, he reported a DLF variation of up to 0.22 and a mean of 0.13 at 4 steps/s (walk) and 0.07 at 7 Hz (run); (3) for the third harmonic, the DLF ranged up to 0.11 with a mean of 0.06; and (4) for the fourth harmonic, the DLF varied up to 0.07 with a mean value of 0.03. From the measured descent forces, [16] concluded that: (1) for the first harmonic, the average DLF at 2.0 steps/s (walk) was about 0.5 and at 3.5 steps/s (run) was approximately 0.8; (2) the range for the second harmonic DLF was 0.03–0.33 with a mean of 0.20; (3) for the third harmonic, the DLF range was up to 0.16 with a mean of 0.09; and (4) the fourth harmonic DLF ranged up to 0.13 with a mean of 0.06. Reference [16] found that the second harmonic DLF of ascents were larger for stairs with higher pitch. From the reported measured DLF values, it was observed that even though the first harmonic DLF's generally increase with an increase in the footfall rate, the opposite is the case for the higher harmonics. Reference [16] also found that the first harmonic of ascent force on the stair was larger than for descent; however, the second harmonic DLF for very fast descent (greater than 4 steps/s) was about three times greater than for ascent.

Reference [17] studied the serviceability performance of steel and reinforced concrete stairs using six mockups. All stairs had very high natural frequencies and were not susceptible to large vibrations from human movements. Based on the results of their tests, [17] concluded that, in general, cast-in-place concrete stairs performed better in terms of vibration serviceability than their steel counterparts. They also found that the normal walking speed on stairs was about 1.8 steps/s. This is not consistent with the observations of [12], and [16]. They also reported very large damping ratios (5–7%) for the tested stairs, which may have been due to the fact that the mockup stairs had very high natural frequencies and the collected vibration data was contaminated with large amount of noise. Reference [17] noted that the tread finish had a major influence on the computed r.m.s. of the measured acceleration when people ascended or descended the stairs. They also reported that the vibrations were larger when people ascended the stairs that when they descended, which is not consistent with the other reported studies.

Reference [2] conducted vibration measurements and computer modeling of a slender steel stair. They measured the natural frequency and damping ratio of the structure using an impulse hammer ($f_1 = 7.3$ Hz and $\xi_1 = 1.1\%$). They used the recommendations of [12] as related to the levels of stair vibrations acceptable to humans, which were in r.m.s. values and converted to the equivalent peak accelerations. They also modified the DLF values suggested by [16] for a 25% probability of exceedance, and a damping ratio of 1% and used of a 0.35 adjustment factor to consider imperfect resonances, and repeated the recommendations of [11] and [12] to increase the response by a factor of 3.0 to estimate the stair vibrations from a group. Reference [2] made all their recommendations based only on the study of a single staircase.

There have been several publications on the design of monumental stairs using Finite Elements Analysis method. Reference [1] discussed the design and vibration analysis of a stair using the SAP2000 structural analysis program, while [3] conducted a study of a 39 ft long steel stair. They use tuned mass dampers (TMD) to correct possible excessive vibrations of the stair. Reference [4] presented the details of two monumental stairs for an art gallery in Toronto, Canada. They used SAP2000 for the structural analysis and concluded that one of the stairs was susceptible to excessive vibrations, for which they installed a TMD in the landing area.

Reference [5] provided the details of a stair located in a store in Las Vegas, Nevada. They also used SAP2000 to model the structural and non-structural components of the stair. Reference [6] conducted the analysis of a stair located at a Canadian University using the SAP2000 and subjected it to walking loads recommended in the design guides. They reduced the computed steady-state using an adjustment factor, $R = 0.70$, to consider the imperfect resonance response of the stair. The authors found that the vibration acceptability criteria of different design guides are not consistent and concluded that more research to better define the forcing function and damping values for stairs are needed.

Reference [7] discussed the vibration testing and Finite Element Analysis of a steel stair with excessive vibrations due to human movements located at a British University. They used the shell elements to model the main structure of the stair, and beam elements to represent the handrail bars in the ABAQUS structural analysis software. They also conducted an operational modal analysis of the stair when subjected to ambient excitations. Using the recorded decay curves, they measured a damping ratio variation of 0.4–0.6%, depending on the vibration amplitude. They also conducted a Finite Element model updating analysis using the FEMtools software. From the comparison of the results, they validated the importance of the handrail on the computed response using the ABAQUS. Reference [18] studied the differences between the right versus the left foot loading in terms of DLF of different harmonics, and step frequency when a person ascends or descends a stair. They also studied the effects of stair geometry on step frequency and DLFs. They found that the slowest step frequencies were in the 0.8–1.9 steps/s range when one ascends two steps at a time, and that two step descents were not possible. They also concluded that the normal walk step frequency range was 1.5–2.5 steps/s for one step at a time ascents, and 1.6–3.6 steps/s for descents, which were not consistent with the findings of [16]. They also reported that the first

harmonic DLF for descents are larger than ascents at the same step frequency, which is also not consistent with the conclusions made by [11, 12, 16].

Reference [8] conducted the only study on the effects of people on the dynamic properties of a stair using measured vibration responses. They used a mass-spring-damper modal model to represent the human dynamic action on a stair. They measured the natural frequencies and damping ratios for the first two modes of the stair when it was empty as: $f_1 = 4.7$ Hz, $\xi_1 = 0.4\%$, and $f_2 = 8.8$ Hz, $\xi_2 = 0.3\%$. They noted that the presence of 20 people doubled the first mode damping ratio, and 40 people raised it by about five times, to 2.1%. The measured damping ratios from this study were not consistent with the inconclusive recommendations of [2, 11, 12, 19].

56.2 Description of the Monumental Staircase

The steel structure monumental staircase is located at a museum in Michigan. This paper presents the analysis and design of the stair, which connects the first and second levels of the building. The original static design of the support structure consisted of HSS 12 × 3 × 5/16 for the top and bottom chords and HSS 3 × 3 × 5/16 at 1.22 m (4 ft) on-center forming a Vierendeel truss for each stair stringer. Cross-bracings L 3 × 3 × 1/4 connected the bottom chords of the two stringers throughout the length of the stair. The total depth (end to end) of the chords in the landing area was 0.94 m (37 in.). To provide better vibration performance, the overall depth of the stringers was raised by 159 mm (6.25 in.) to 1.10 m (43.5 in.). The upper chord of stringers included 70 mm (2.75 in.) plywood covering weighing 287 Pa (6 psf); metal studs at 406 mm (16 in.) on-center, 192 Pa (4 psf); handrails, 335 Pa (7 psf), resulting in a total superimposed dead load of 321 N/m (22 lb/ft). The lower stinger's superimposed dead load was estimated at 263 N/m (18 lb/ft). The treads were made of 51 mm (2 in.) wood flooring, 383 Pa (8 psf); 19 mm (0.75 in.) thick plywood sheathing, 144 Pa (3 psf); and 6.4 mm (0.25 in.) thick steel plate, 479 Pa (10 psf).

56.3 Structural Analysis and Design Modifications

A computer model of the stair was created using the SAP2000 structural analysis program. Several different cases and assumptions to modify the stair design in an attempt to increase the natural frequency and reduce the vibration response were considered. Here, a few representative cases will be presented:

Case 1: Neglected the stiffness of the risers, landing steel plate, and the non-structural elements of the guard rails along the stringers; however, the masses of all components were considered.

Case 2: Treads, made of 6.4 mm (0.25 in.) thick steel plates, were included using frame elements. Also, 6.4 mm (0.25 in.) thick steel plate for the landing area was represented in the model by shell elements. The masses of all components were considered.

Case 3: Treads and risers, made of 6.4 mm (0.25 in.) thick steel plates, were included in the model. The folded plate behavior of the steel plate was modeled as uniform-thick orthotropic shell elements in the SAP2000 computer software. The 6.4 mm (0.25 in.) thick steel plate in the landing area was modeled using shell elements; however, the stiffness of the non-structural guardrails along the stringers was neglected. The masses of all components were included.

Case 4: In an effort to increase the natural frequencies of the stair, a 6.4 mm (0.25 in.) thick steel plate was added between the stringers lower and upper chords. The plate was assumed to be welded to the chords and to the verticals of the Vierendeel truss.

Case 5: To reduce the costs of the construction, the steel plate placed between the top and bottom chords of the stringers was limited to the first two web panels from each ends, and the plywood sheathing was eliminated to reduce mass and, therefore, increase the natural frequencies. In lieu of steel plates, HSS 5 × 3 × 5/16 were added as diagonal members in all the truss panels (except the locations with steel plates). The cross-bracing members were also eliminated since they did not have any effects on the dynamic performance of the stair. A total superimposed dead load of 263 N/m (18 lb/ft) per stringer (excluding the metal railings) was assumed.

The stair stringers were supported only at their two ends, where they were connected to the concrete floor slabs. For each of the above cases, these supports were assumed as pinned or fixed. Table 56.1 shows the first two mode natural frequencies for each case with the pinned or fixed end conditions.

Table 56.1 Natural frequencies for different cases

	f_1 (Hz)		f_2 (Hz)	
Case	Pinned	Fixed	Pinned	Fixed
1	5.7	6.8	10.4	11.7
2	6.1	7.4	11.5	13.0
3	6.6	8.2	12.3	14.1
4	8.6	9.7	15.9	17.5
5	8.2	9.15	16.8	18.4

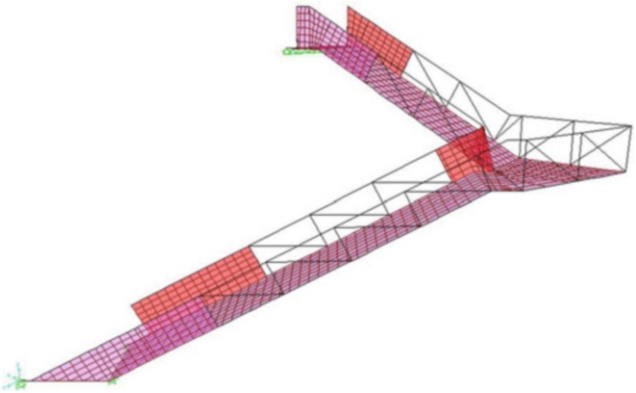

Fig. 56.1 Structural model of the staircase

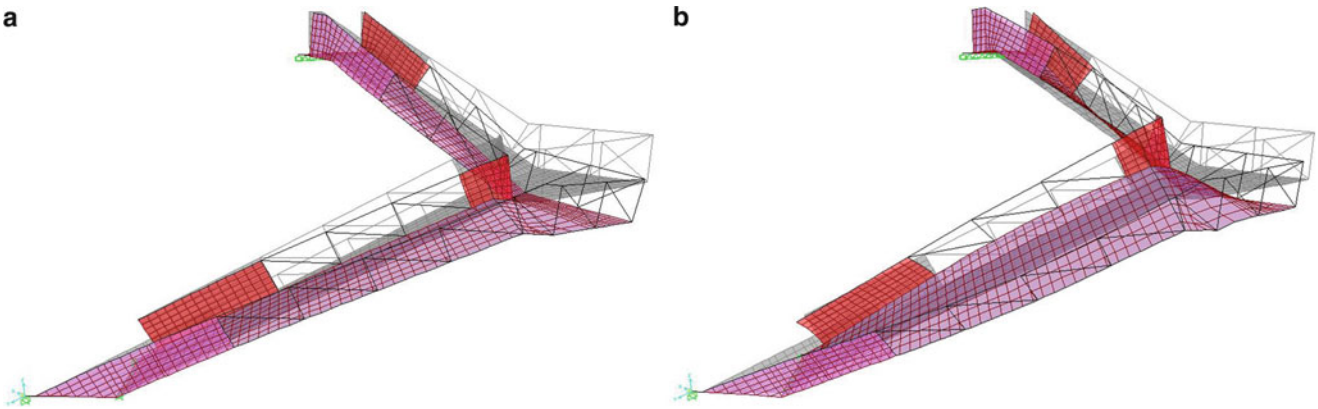

Fig. 56.2 Staircase mode shapes, (**a**) mode 1 ($f_1 = 9.15$ Hz), (**b**) mode 2 ($f_2 = 18.4$ Hz)

Case 5, with fixed end supports, was used for the final design of the stair. Figure 56.1 shows the three-dimensional computer model of the structure, and Fig. 56.2 is the first two modes of vibration.

Since the natural frequency for the second mode of vibration is above 10 Hz, there is a very remote possibility that this mode can be excited due to human movements on the stair. However, the third and fourth sub-harmonics of the first mode natural frequency, at 3.05 Hz, and 2.29 Hz, are within the range of human running and walking excitation on a stair, respectively. As indicated in the previous section, the reported modal damping ratios for stairs vary significantly (from 0.4% to 6%). Here, a value of 1% was assumed for all modes of vibrations. A unit vertical force was applied at the center of the landing and the steady-state responses at the outer corner of the landing, which are expected to have the largest response in the entire structure in the vertical (Z-axis) and horizontal (Y-axis only) directions, were computed, and shown in Fig. 56.3a, b as the frequency responses functions (FRF). Note that only the larger lateral response (Y-axis) is shown here.

Considering one person walking or running down the stair, a complete steady-state response may not be achieved. Therefore, the walking and running forcing functions for 2.0 steps/s (normal walk), 2.29 steps/s (fast walk), and 3.05 steps/s (run) were found. Based on the recommendation of [16], the DLF values for the first three sub-harmonics of walk forcing

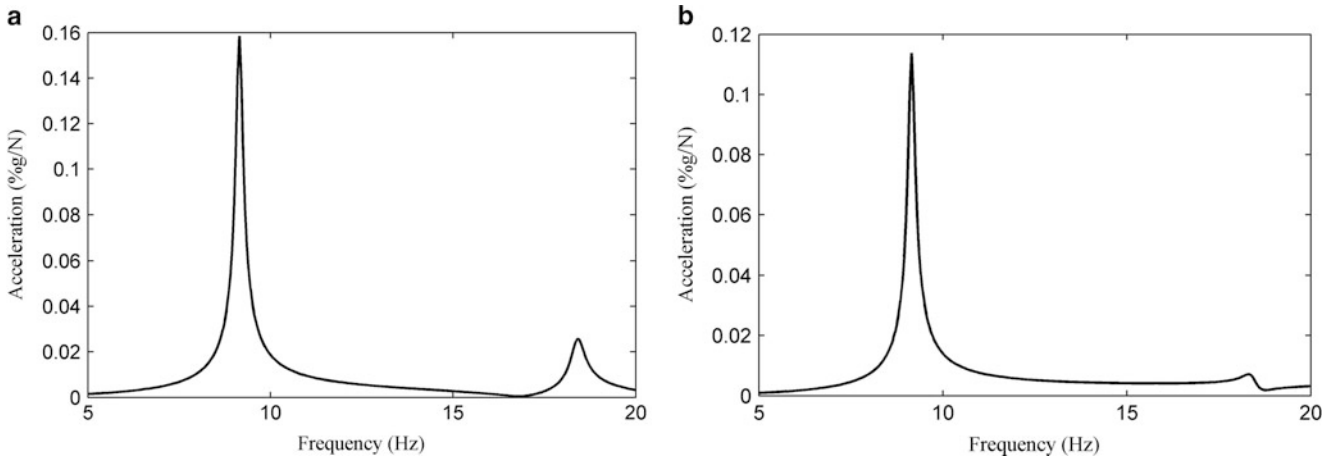

Fig. 56.3 Frequency response function of the outer corner of landing for load at the center of landing area, (**a**) vertical (Z) direction, (**b**) lateral (Y) direction

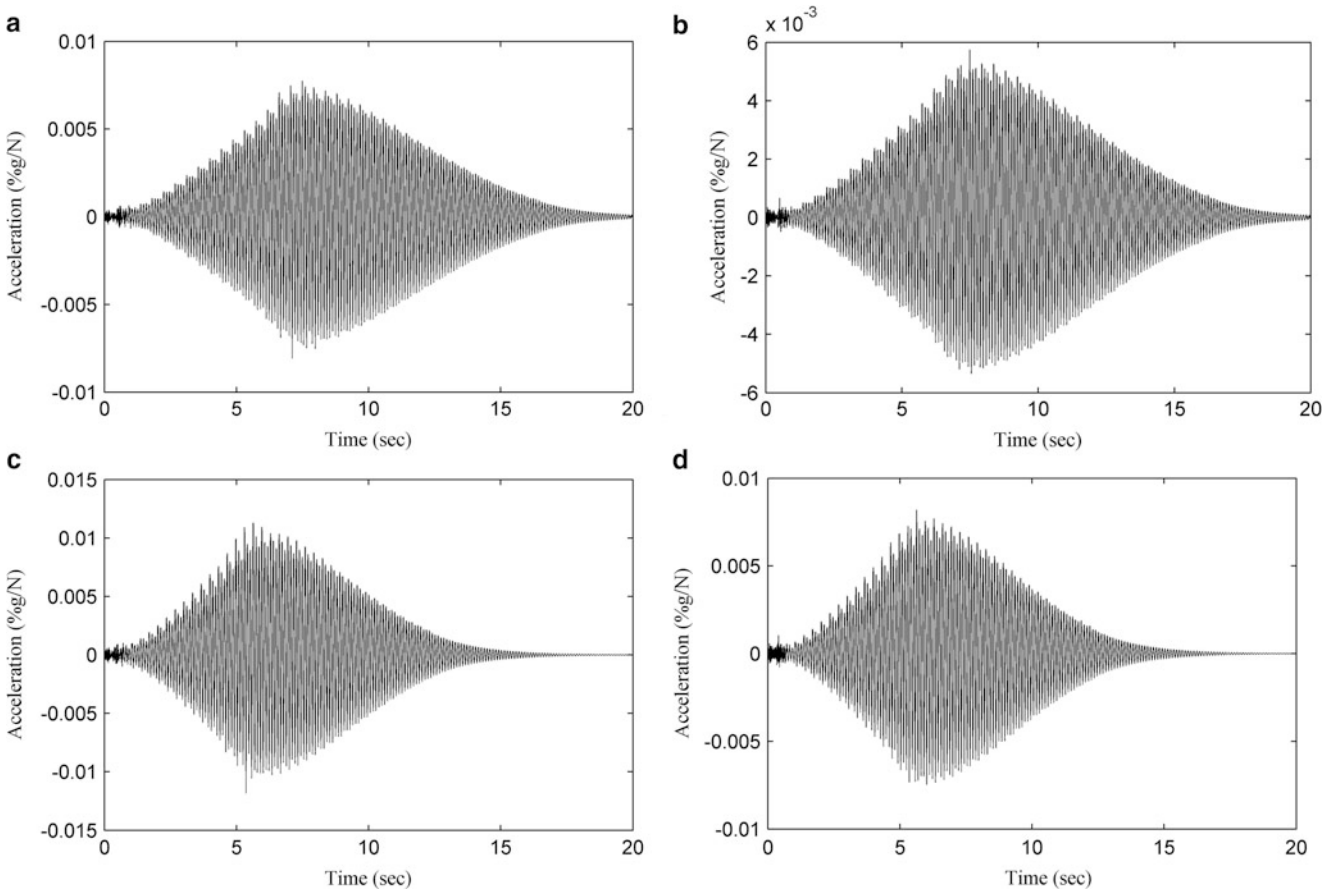

Fig. 56.4 Time history response of the outer corner of landing in the vertical (Z) and lateral (Y) directions when person descends at different speeds (G = 1 N), (**a**) vertical (Z) response (Fast Walk @ 2.29 steps/s), (**b**) lateral (Y) response (Fast Walk @ 2.29 steps/s), (**c**) vertical (Z) response (Run @ 3.05 steps/s), (**d**) lateral (Y) response (Run @ 3.05 steps/s)

functions, see Eq. 56.1, ($\alpha_1 = 0.5$, $\alpha_2 = 0.2$, $\alpha_3 = 0.09$, $\alpha_4 = 0.06$) were used. For the forcing function representing the person running on the stair, the DLF values used were $\alpha_1 = 0.8$, $\alpha_2 = 0.2$, $\alpha_3 = 0.09$, and $\alpha_4 = 0.06$. Considering a normalized person's weight of unity (G = 1 in Eq. 56.1), Fig. 56.4 shows the time history response of the outer corner of the landing when the person descends the stair at different speeds: (1) one-fourth harmonic of the first mode resonance

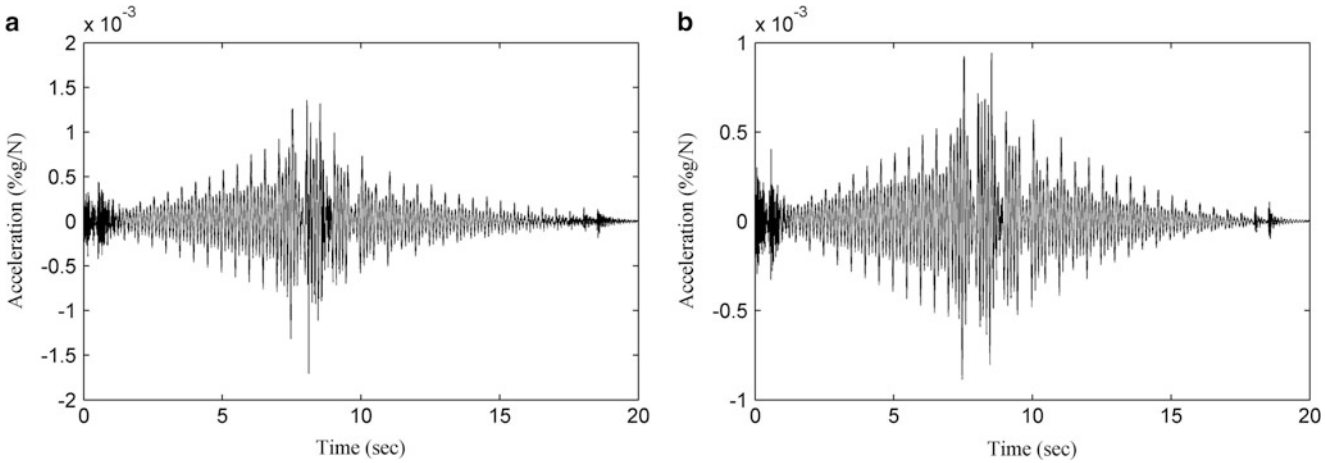

Fig. 56.5 Time history response of the outer corner of landing in the vertical (Z) and lateral (Y) directions when person descends at 2 steps/s (G = 1 N), (**a**) vertical (Z) response, (**b**) lateral (Y) response

frequency (2.29 steps/s) representing the person walking briskly down the stair, and (2) one-third harmonic of the first mode resonance frequency (3.05 steps/s) representing the individual running down the stair.

Using the results given in Figs. 56.3 and 56.4 the adjustment factors to consider the incomplete resonances during the one-fourth harmonic walk and one-third harmonic run are computed. The peak vertical (Z-direction) response from person walking down the stair (Fig. 56.4a) is 0.008%g/N (0.0356%g/lb). The peak value at the first mode resonance (Fig. 56.3a) is 0.1585%g/N (0.705%g/lb), and after adjusting this for the on-fourth harmonic DLF is $0.1585 \times 0.06 = 0.0095$%g/N. Therefore, the adjustment factor is 0.0080/0.0095 = 0.84. Calculating the same using the square-root-of-sum-of-squares (SRSS) for the X and Y directions, results in an adjustment factor of 0.84. Repeating the same calculation for running at 3.05 steps/s results in adjustment factors of 0.83 for the vertical and 0.80 for the lateral directions. Therefore, it seems that the computed adjustment factors in this study are closer to the values used by [6], i.e., R = 0.70; and the recommendation by [2] is unconservative. However, two points should be noted here: (1) the adjustment factor depends on the total length and geometry of the stair; and (2) the results presented here are based on computer analysis and can be different if the field measured vibration responses are used.

From the results shown in Fig. 56.4, the maximum vibration responses for the vertical and lateral (SRSS of the X and Y components) for the brisk walk at 2.29 steps/s and run at 3.05 steps/s for a unit applied load are:

Brisk Walk-Vertical = 0.0080%g/N (0.0356%g/lb)
Brisk Walk-Lateral = 0.0057%g/N (0.0254%g/lb)
Run-Vertical = 0.012%g/N (0.0526%g/lb)
Run-Lateral = 0.0082%g/N (0.0363%g/lb)

Considering the average weight of an individual as 75 kg (165 lb), the computed peak vibrations will be:

Brisk Walk-Vertical $= 0.008 \times 75 \times 9.81 = 0.059$ g
Brisk Walk-Lateral = 0.042 g
Run-Vertical = 0.087 g
Run-Lateral = 0.060 g

As indicated in the Introduction section, [11, 12] recommended an R value of 24 for public buildings. Considering the excitation at 9.15 Hz (first mode resonance frequency), the acceptable r.m.s. acceleration limit based on [13] for the vertical direction is 0.0058 m/s^2 and for lateral direction is 0.017 m/s^2. Converting these values to their equivalent peak in gravitation acceleration, the acceptable peak accelerations considering R = 24 are: vertical direction = 0.02 g, and lateral direction = 0.059 g.

From the comparison of the above maximum responses and the allowable values, it can concluded that the stair is not acceptable in the vertical direction if one walks or runs down the stair at one-fourth or one-third sub-harmonics of the first mode resonance frequency. The vibrations are; however, acceptable in the lateral direction. It is expected that the majority of people descending or ascending a stair in a museum at the normal walking speed of about 2 steps/s. Therefore, the vibration response of the outer corner of the landing in the vertical and lateral directions when one descends at 2 steps/s were computed and illustrated in Fig. 56.5. The peak value for the vertical direction is 0.0017%g/N (0.0076%g/lb) and 0.0011%g/N

(0.0049%g/lb) for the lateral direction (based on SRSS of the X and Y components). These result in terms of the peak accelerations for a 75 kg (165 lb) person are 0.012 g for the vertical direction and 0.008 g for the lateral direction. The acceptable limits based on the lowest values of the perception curves from [13], considering R = 24, for the vertical direction is 0.017 g and for the lateral directions is 0.012 g. This means that the stair vibrations are within the acceptable range if people walk at a normal pace.

As indicated before, based on studies of [11, 12, 16] when a group of people run fast down a stair, vibrations up to three times those resulted by an individual can be expected. Even though, [11, 12] recommend R = 64 for such cases, it is clear that the resulting vibrations of the stair used in this study will be more than the acceptable limits. Such situations are not expected in the environment considered here, except when an emergency may arise. It is assumed that people will be able to tolerate higher levels of vibrations during such rare occasions.

56.4 Summary and Conclusions

This paper presented a brief overview of the available literature on the vibration serviceability problems in staircases due to human movements. Based on this review, vibration serviceability of staircases require further research to provide guidelines for designers to more accurately predict and evaluate their dynamic performance when subjected to human movements.

A slender monumental stair was studied and modifications to its structure were made to make it less susceptible to excessive vibration. Based on the results of the computer analysis presented here, the vibrations will be within the acceptable range as long as the individuals walk over the stair at or below the normal speed range. The structure may be susceptible to unacceptable vibrations if people ascend or descend the stair rapidly.

References

1. Arbitrio V (2009) Longchamp stair optimization and vibration study. Structure, Feb, pp 10–13
2. Davis B, Murray TM (2009) Slender monumental stair vibration serviceability. J Archit Eng ASCE 15(4):111–121
3. Huntington DJ, Mooney JW (2011) How to keep monumental stairs from vibrating. In: Proceedings of the structures congress 2011, ASCE, Las Vegas, Nevada, United States, pp 2572–2584
4. Howes C, Gordon E (2011) The spiral stairs at the art gallery of Ontario. In: Proceedings of the structures congress 2011, ASCE, Las Vegas, Nevada, United States, pp 2594–2604
5. Howes C, Krynski M, Kordt S (2011) The feature stair at Louis Vuitton in crystals at city center. In: Proceedings of the structures congress 2011, ASCE, Las Vegas, Nevada, United States, pp 2585–2593
6. Eid R, Seica M, Stevenson D, Howe B (2011) Staircase vibrations due to human activity. In: Proceedings of the structures congress 2011, ASCE, Las Vegas, Nevada, United States, pp 2562–2571
7. Belver AV, Zivanovic S, Dang HV, Istrate M, Iban AL (2012) Modal testing and FE model updating of a lively staircase structure. In: Topics in modal analysis I, vol 5, Proceedings of the society for experimental mechanics conference, series 30, Jacksonville, FL, USA, pp 547–557
8. Cappellini A, Manzoni S, Vanali M (2012) Experimental and numerical studies of the people effects on a structure modal parameters. In: Topics on the dynamics of civil structures, vol 1, Proceedings of the society for experimental mechanics conference, series 26, Jacksonville, FL, USA, pp 17–25
9. Nilsson L (1976) Impact produced by human motion, Swedish Council for Building Research, report no D13: Part 1
10. Alcock NJ, Lander LE (1987) Vibration of staircases. Undergraduate project thesis, University of Bristol, UK
11. Bishop NWM, Willford M, Pumphrey R (1993) Multi-person excitation of modern slender staircases. Engineering for Crowd Safety, Elsevier Science, Amsterdam, pp 399–408
12. Bishop NWM, Willford M, Pumphrey R (1995) Human induced loading of flexible staircases. Safety Sci 18:261–276
13. BS 6472 (1984) Evaluation of human exposure to vibration in buildings (1 Hz to 80 Hz). International Organization for Standardization, Geneva
14. Kerr SC, Bishop NWM (1997) Human induced loading of flexible staircases. In: Topping BHV, Leeming MB (eds) Innovation in civil and structural engineering. Civil-Comp Press, Edinburgh, pp 311–317
15. Kerr SC, Bishop NWM (2001) Human induced loading on flexible staircases. Eng Struct 23:37–45
16. Kerr SC (1998) Human induced loading on staircases. Ph.D. thesis, Mechanical Engineering Department, University of London, London
17. Kim SB, Lee YH, Scanlon A, Kim H, Hong K (2008) Experimental assessment of vibration serviceability of stair systems. J Construct Steel Res 64:253–259
18. Kasperski M, Czwikla B (2012) A Refined Model for Human Induced Loads on Stairs. In: Topics on the dynamics of civil structures, vol 1, Proceedings of the society for experimental mechanics conference, series 26, Jacksonville, FL, USA, pp 27–39
19. Smith AL, Hicks SJ, Devine PJ (2009) Design of floors for vibration: a new approach. The Steel Construction Institute, Ascot/Berkshire

Chapter 57
Improvement of Safety Engineering Design in Rotating Structures by Detection of Resonance Frequency Signals

Hisham A.H. Al-Khazali and Mohamad R. Askari

Abstract Rotor Dynamics is the study of dynamics and stability of rotating machinery, and it plays an important role in improving the safety and performance of the systems that it is a part of. Rotating machinery is seen in several applications in our daily life. These include machine tools, power stations, turbo-machinery, aircraft jets, automobiles, and marine propulsion, among others.

As the rotational velocity of any rotating object increases, its level of vibration often passes through a maximum at what is called a critical speed (Resonance). This is commonly excited by unbalance of the rotating structure. If the amplitude of vibration at these critical speeds is excessive, catastrophic failure can occur.

Engineers who design large rotors are challenged to design safe rotating machinery using physical prototypes and tests alone.

In this study we detect resonance frequency in rotor machines with high speeds by using experimental technique used thus far is called Modal Testing, this technique has been used to obtain the Model and Dynamic response properties of structures. Finite Element (FE) models using the eigen analysis capability were used to simulate the vibration and the results were compared with experimental data. The aim of this research using measuring devices to detect resonance frequency in rotor machines in early stage this is used to identify the operational behaviour of any safety-critical failure condition or fault condition or human error that could lead to a hazard and potential mishap influence requirements to drive control strategies and safety attributes in the form of safety design features or safety devices to prevent, eliminate and control (mitigation) safety risk that could help the designers to have better understanding of rotor performance at the system design stage.

Keywords Resonance • FRF • Rotor machines • Modal testing • Safety design

57.1 Introduction

Safety-engineers take an early design of a system, analyze it to find what faults can occur, and then propose safety requirements in design specifications up front and changes to existing systems to make the system safer. In an early design stage, often a fail-safe system can be made acceptably safe with a few sensors and some software to read them.

Reliability assessment and risk analysis of rotating machine rotors in various overload and malfunction situations present challenge to engineers and operators. Design and safety assessment of rotating machines shall be involved complete simulations of all possible overload, malfunction and accident scenarios [1]. Otherwise it may end up with equipment that is not safe over the full operating ranges. Rotor large deformation can be result of overloading, over-speed, resonance, whirling, accident, component failure, surge, stall, off design operation, etc. and may lead to stress exceeding the safe limit [2, 3], failure of machine component, machine explosion and equipment coming apart. Each scenario can cause serious damages and injuries. For reliability and safety assessment of all possible scenarios of rotating machine malfunction, it is

H.A.H. Al-Khazali (✉)
Faculty of Science, Engineering and Computing, School of Mechanical and Automotive Engineering, Kingston University, London, UK
e-mail: k0903888@kingston.ac.uk

M.R. Askari
Faculty of Science, Engineering and Computing, School of Aerospace and Aircraft Engineering, Kingston University, London, UK
e-mail: M.Askari@kingston.ac.uk

B. Song et al. (eds.), *Dynamic Behavior of Materials, Volume 1: Proceedings of the 2013 Annual Conference on Experimental and Applied Mechanics*, Conference Proceedings of the Society for Experimental Mechanics Series,
DOI 10.1007/978-3-319-00771-7_57,

necessary to develop an analytical method to obtain details of forces, stress and strain values for rotor under large deformation [1, 4].

Every object depending on its mass and stiffness when excited vibrates at its natural frequency. Watches, musical instruments, microwave ovens, mobile phones and many other devices in our day-to-day life make use of this phenomenon. However, there is an undesirable side to these vibrations that can lead to the failure of structures and components. This failure mode, resonance failures, is equally applicable to large structures and small machine parts alike. Not only bridges, towers and skyscrapers, but also blades, bearings, piping and fasteners can fail due to resonance. Air and gas vapour columns can also resonate at their natural frequencies, in the same way that percussion instruments work, and this can lead to failures [5–7].

Design of high speed rotor systems involve working out suitable rotor geometry, selection of bearings, placement of bearings, rotor dynamic analysis, critical speed estimation, unbalance and bow responses, damper design and stability studies. Development of such rotor systems present several challenges right from precision manufacturing, rotor assembly, dynamic balancing followed by extensive experimentation [8–10].

The modal model (natural frequencies, mode shapes and modal damping) of a complete machine based on the in-situ experimental modal tests is one possible modelling approach, Irretier [6].

All objects in the universe resonate at their natural frequency when excited. This can cause catastrophic failures in structures, machines, and components [11]. The increase in amplitude of oscillation of an electric or mechanical system exposed to a periodic force whose frequency is equal or very close to the natural un-damped frequency of the system [8, 11].

57.1.1 Analysis Techniques

Analysis techniques can be split into two categories: qualitative and quantitative methods. Both approaches share the goal of finding causal dependencies between a hazard on system level and failures of individual components. Qualitative approaches focus on the question “What must go wrong, such that a system hazard may occur?”, while quantitative methods aim at providing estimations about probabilities, rates and/or severity of consequences [2, 5].

57.1.2 Applications

- Rotating machinery diagnostics.
- Analysis of noise and vibration problems related to rotational forces, e.g., in automotive and aircraft engines, transmissions, gearboxes, compressors, pumps, turbines, electric motors.
- Order analysis [3, 9].

57.2 Method

57.2.1 Test Procedure

Basically, the rotor consisted of a shaft with a nominal diameter of 10 mm, with an overall length of 610 mm. Two plain bearings, RK4 Rotor kit made by Bently Nevada (the advanced power systems energy services company), are used to extract the necessary information for diagnostic of rotating machinery, such as turbines and compressor [4, 8]. Shaker test or (an electromagnetic shaker), see Fig. 57.1a, also known as an electro dynamic shaker (consist of a magnet, moving block and a coil in the magnet) or Hammer test, see Fig. 57.1b [5]. To find the modes of vibration of a machine or structure, The rig installed with two accelerometers (model 333B32 or 339A32, sensitivity 97.2 and 98.6 mV/g) in Y and Z direction [12], it was attached to the test structure with creating a computer when taking readings in file that was dimensions and introducing it with the data within the program (Smart Office) [8, 12, 13].

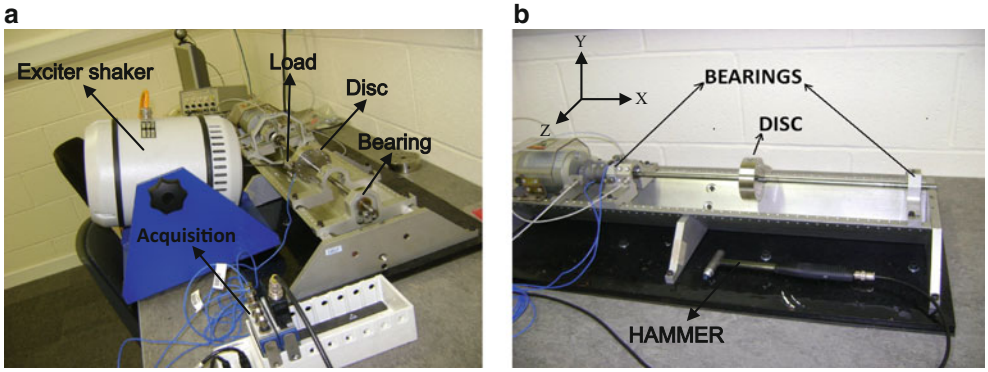

Fig. 57.1 Experimental setup for the modal testing. (**a**) Shaker excited shaft. (**b**) Hammer excited shaft

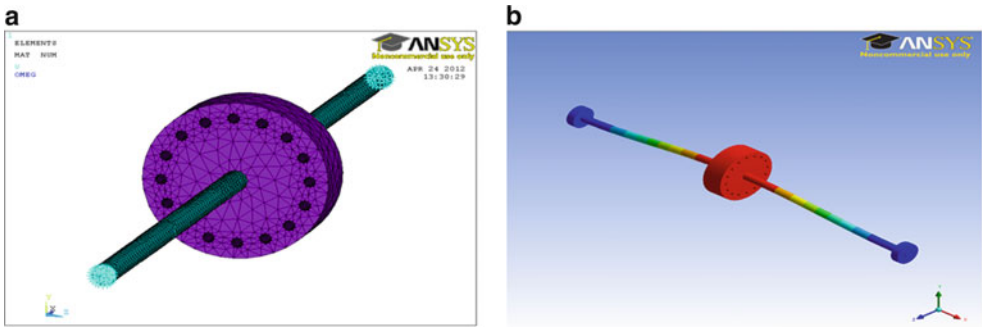

Fig. 57.2 Finite element simulations, first mode shape for one disc with two bearings. (**a**) Show node mesh. (**b**) Natural frequency 29.95 Hz

57.2.2 Equation of Motion

57.2.2.1 Definition of Frequency Response Functions (FRFs)

The general equation of motion for a rotating and supporting structure are given by [7, 9, 14]:

$$[M]\{\ddot{q}(t)\} + [(C]\{\dot{q}(t)\} + [K]\{q(t)\} = \{F(t)\} \tag{57.1}$$

$$H_{jk}(\omega) = \sum_{r=1}^{n} \frac{\phi_{jr}\,\phi_{kr}}{M_r\left[\omega_r^2 - \omega^2 + 2\,i\,\omega\,\xi_r\,\omega_r\right]} \tag{57.2}$$

$$\vec{FRF\ matrix} = \begin{bmatrix} \vec{H}_{11,\vec{r}} & & & \\ \vec{H}_{21,\vec{r}} & \vec{H}_{22,\vec{r}} & & \\ \vec{H}_{31,\vec{r}} & \vec{H}_{32,\vec{r}} & \vec{H}_{33,\vec{r}} & \\ \vec{H}_{41,\vec{r}} & \vec{H}_{42,\vec{r}} & \vec{H}_{43,\vec{r}} & \vec{H}_{44,\vec{r}} \end{bmatrix} \tag{57.3}$$

57.2.3 Validation Study

Simulation of a model in FE for validate; include rotor system one disc with multi degree of freedom (Y and Z directions) has been used to demonstrate the above capability, see Fig. 57.2. A program has been written in ANSYS12. The Finite Element (FE) method used in ANSYS Parametric Design Language (APDL), offers an attractive approach to modelling a rotor dynamic system.

57.3 Results (Tables and Figures)

From Fig. 57.3 we can see the value of natural frequency is 29.95 Hz, obtained from ANSYS figure is good agreement when comparison with the natural frequency value obtained from experimental is 29.79 Hz as shown in Fig. 57.4 for the first mode shape. These comparison values data are tabulated in Table 57.1.

The values of natural frequency obtained by using shaker test shown in Fig. 57.5a (displacement versus time) is in agreement with the values obtained from the simulation in Fig. 57.5b, and for different mode (time domine) as shown in Fig. 57.6.

57.3.1 Vibration Analysis Software in Experimental Method

The orbit analysis post-processing wizard (Fig. 57.7):

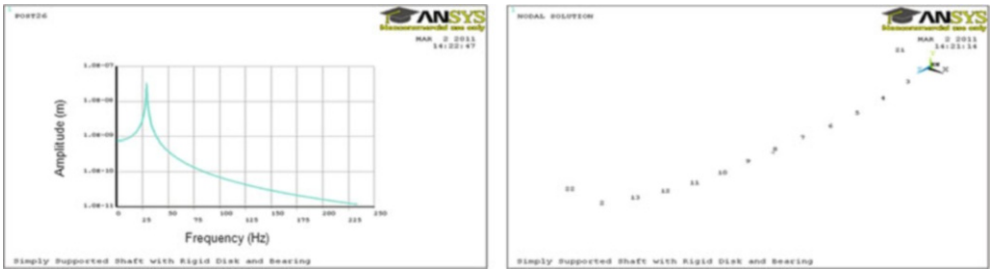

Fig. 57.3 Frequency Response Function (FRF) for the 1st mode shape. ANSYS figure

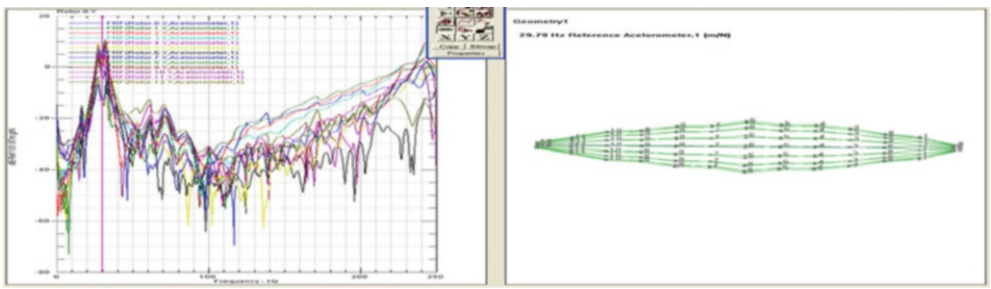

Fig. 57.4 Stationary load in the middle for one disc configuration, FRF versus frequency (Hz), first mode shape, natural frequency 29.79 Hz, range (0–500) Hz

Table 57.1 Comparison between natural frequency (Hz), outcomes from experiment and ANSYS for one disc configuration

Mode shape	ω_n, ANSYS, (Hz)	ω_n, Experiment, (Hz)	Error %
1	29.95	29.79	0.497

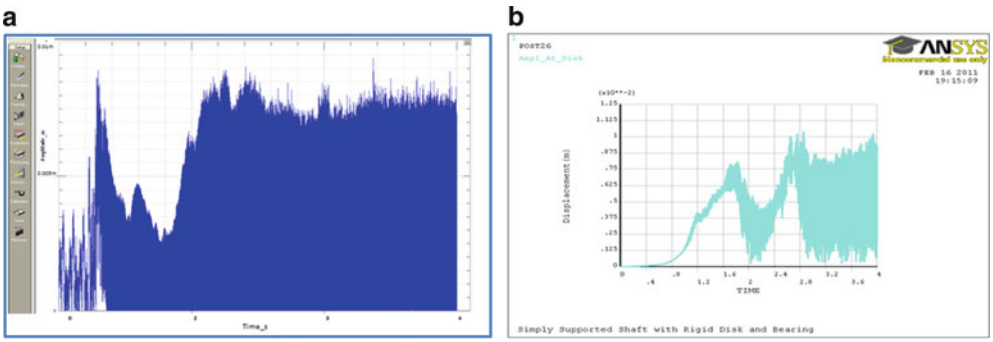

Fig. 57.5 Amplitude versus time, (time domine). (**a**) Experimental, (b) Computational

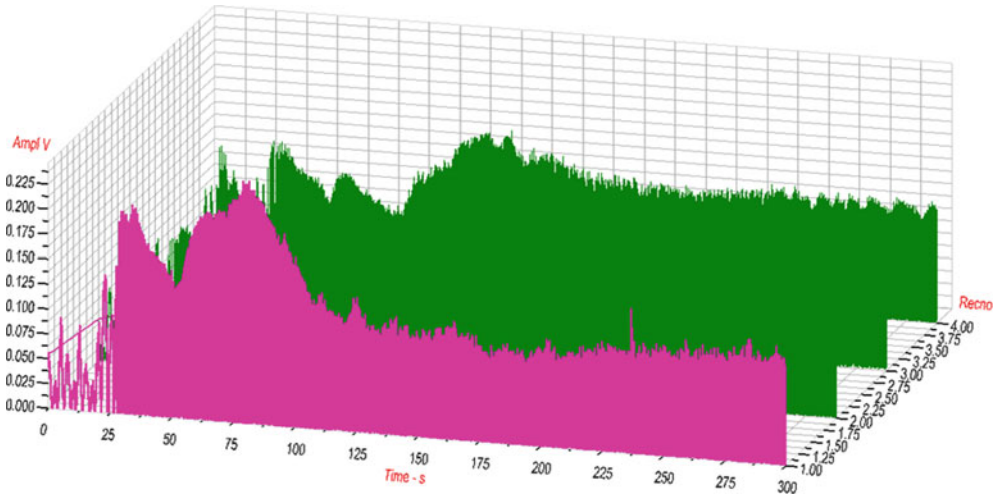

Fig. 57.6 Amplitude versus time, for different mode (time domine)

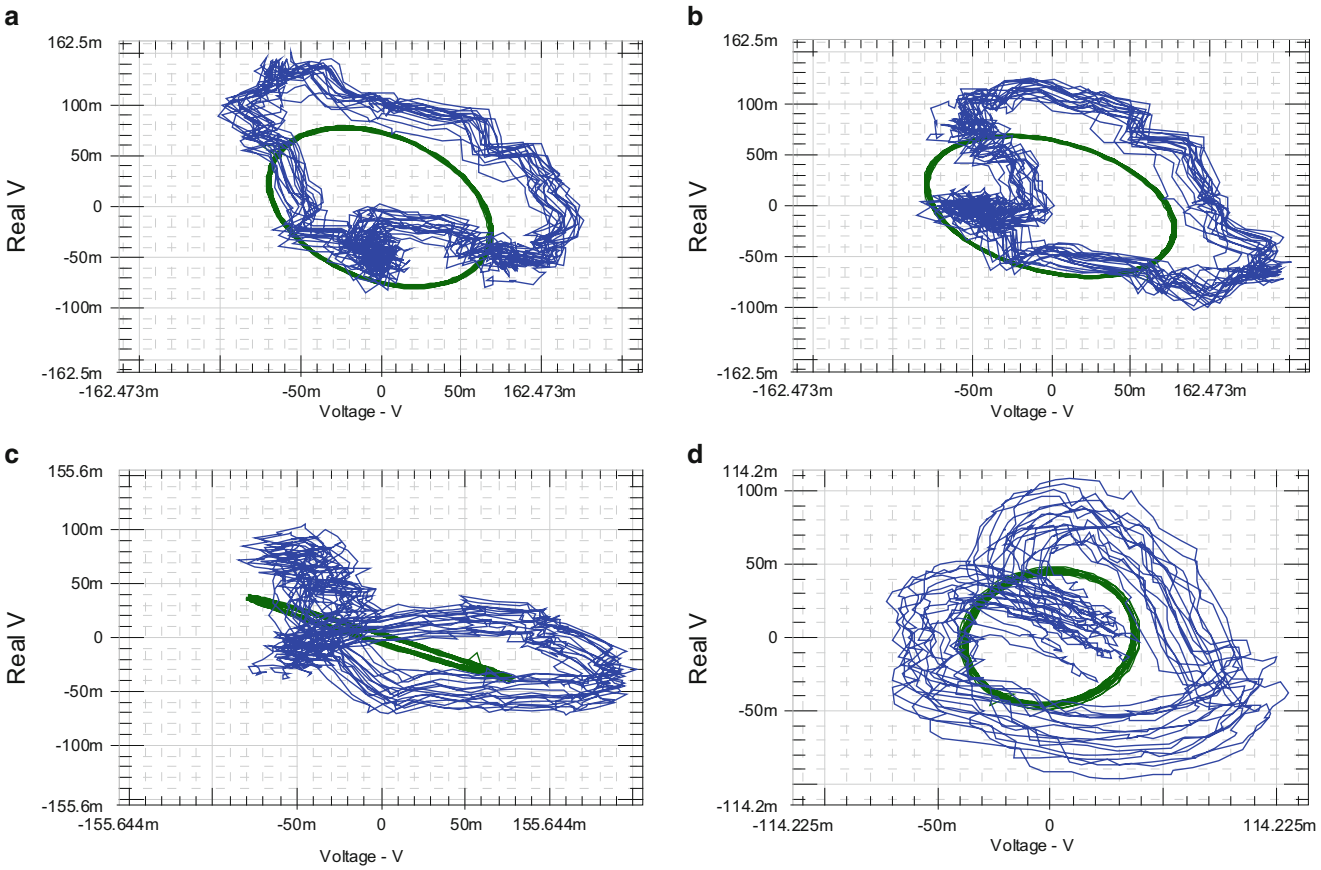

Fig. 57.7 Experimental orbits analysis fundamentals behaviour of the rotor at the different measured planes in first critical speed

57.3.2 The Shock Capture Module

The shock capture module [15] provides shock capture, data validation and reporting as shown in Fig. 57.8. It allows to use a library of standard test limit overlays, capture data from any number of channels, including triax's, filter the data, automatically adjust overlays for best fit.

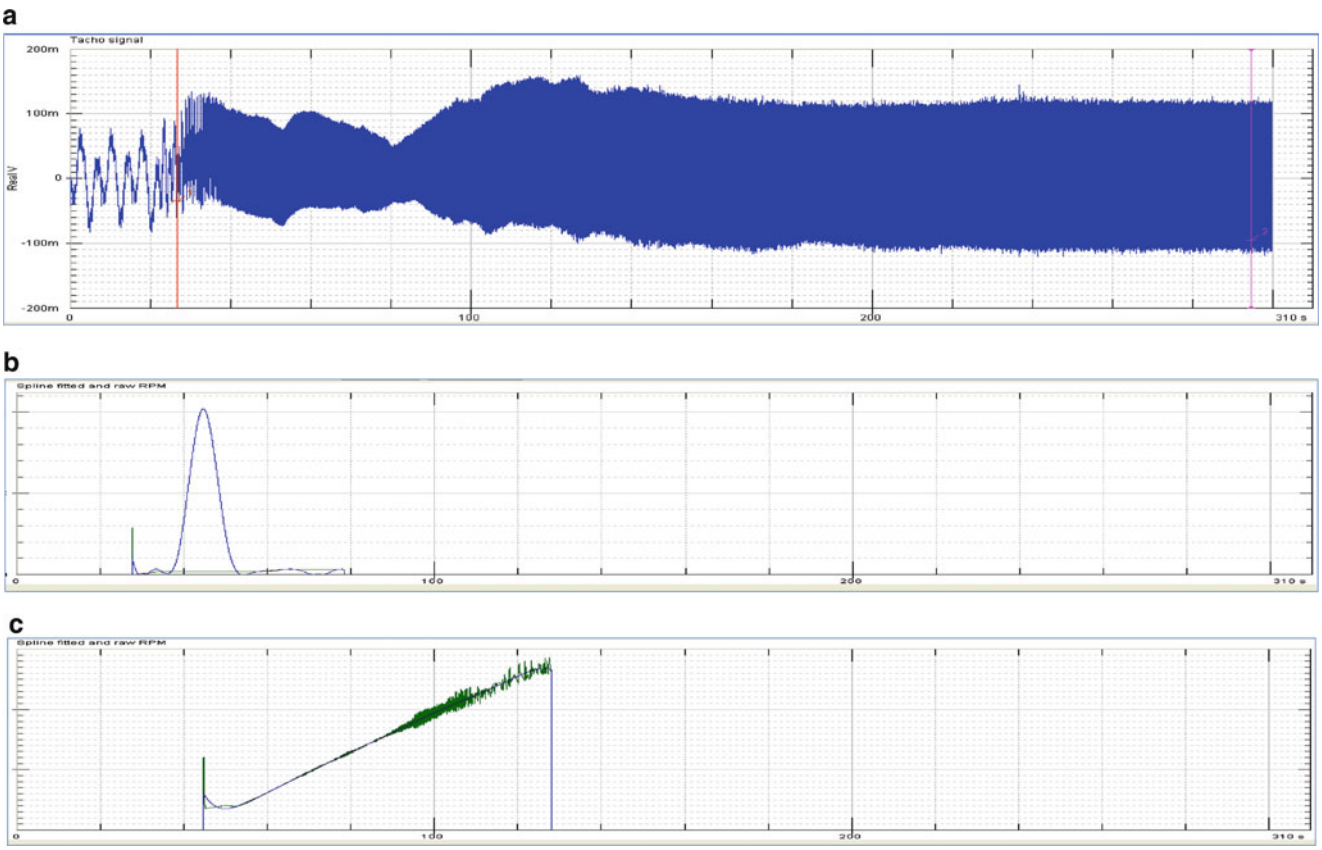

Fig. 57.8 Shock capture module. (**a**) Tacho signal. (**b**) Before use filter. (**c**) Improved or decay shock capture after used window filter

The software is then used in analysis of multiple machine vibration parameters to assess operating performance. Maintenance personnel then use the data to determine if unscheduled maintenance is necessary or if shutdown is required.

57.3.3 Reaction Forces in the Left and Right Bearings

With further simulation we find the relationship between the reaction forces with respect to time. The excitation frequency and amplitude are different with different rotational speeds. The Fig. 57.9a–d shows the variation of reaction forces in the right and left bearings at different speeds of rotation, from the figure the right bearing carry the maximum reaction force.

57.4 Discussions and Conclusions

The amplitude of forced vibration can become very large when a frequency component of the excitation source approaches one of the natural frequency of the system particularly fundamental on such as condition is referred to as resonance this is potential causing failure in both machine and structure**,** so for this reason is very important for designer safety have a mean of determine describe of structure is can be described by in either time domain or frequency domain. In physics, resonance is the tendency of a system (usually a linear system) to oscillate at large amplitude at some frequencies than at others. These are known as the system's resonant frequencies (or resonance frequencies), see Figs. 57.3, 57.4, and 57.5. At these frequencies, even small periodic driving forces can produce large amplitude oscillations. Resonances occur when a system is able to store and easily transfer energy between two or more different storage modes (such as kinetic energy and potential energy in the

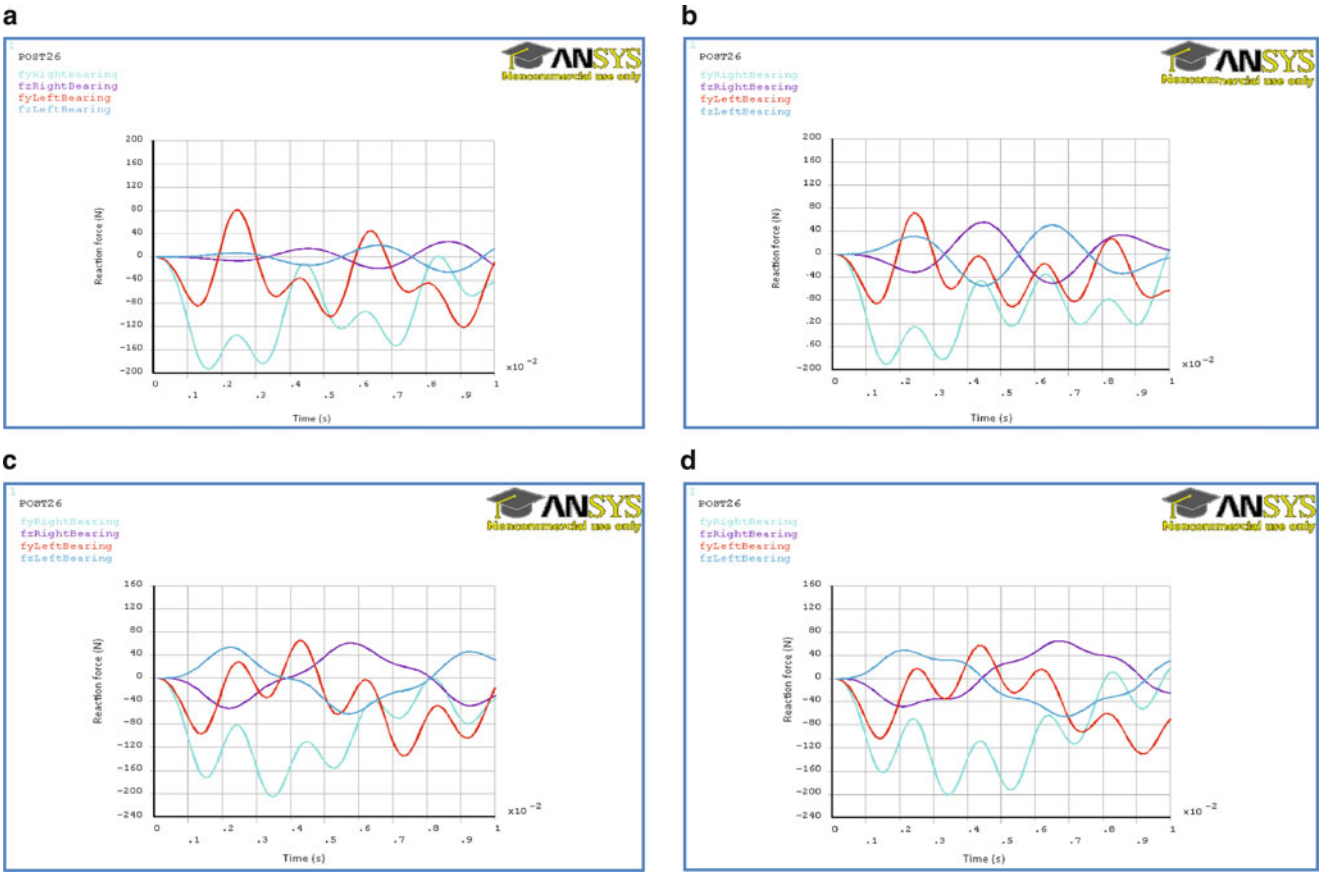

Fig. 57.9 Variation of bearings reaction force versus time at different speeds of rotation, one disc in the middle. (**a**) Reaction force (Fy and Fz) at 1,000 rpm. (**b**) Reaction force (Fy and Fz) at 3,000 rpm. (**c**) Reaction force (Fy and Fz) at 6,000 rpm. (**d**) Reaction force (Fy and Fz) at 10,000 rpm

case of a pendulum). However, there are some losses from cycle to cycle, called damping. When damping is small, the resonant frequency is approximately equal to a natural frequency of the system, which is a frequency of unforced vibrations.

From this study conclude the vibration analysis software can be used effectively to analyze new products, or to evaluate the vibration that occurs in rotating machinery, see Fig. 57.7. Using vibration analysis software for assessing machinery vibration is a cost-effective method to minimize down time and maximize equipment utilization knowledgement, we can conclude the vibration analysis software is an essential tool for analyzing and evaluating the mechanical vibration that occurs in rotating machinery and demonstration accurate diagnosis of machine vibration conditions, including bearing vibration simplifies the task and increases the speed of collecting vibration monitoring data. Vibration analysis software can be used effectively to analyze new products, or to evaluate the vibration that occurs in rotating machinery. Finite element analysis software allows engineers to optimize new product designs by predicting the vibration scenarios that would occur during operation.

The benefit in safety design for machinery safety was implement tailor-made concepts with our in-depth design optimise results through structured processes work in compliance with relevant regulations including the machinery directive and international standards and it is envisaged that the approach is not limited to the condition monitoring and predictive failure but could help the designers to have better understanding of rotor performance at the system design stage.

The results obtained from the experimental and numerical analysis by using ANSYS12 are used to find the relationships between the cyclic reaction bearing forces, see Fig. 57.9. The performance of reaction bearing forces in the right and left bearings with different speeds is shown in Fig. 57.9a–d, it is found that with increase in speed of rotation, the reaction forces increase for both right and left bearings. The figure also show the maximum reaction force in Y direction for the bearings, the rotor transient effect disappears after a few second while the reaction in Z direction increases slowly in both bearings until it reaches maximum value as the speed increases, the results show the right bearing carry maximum reaction force in the beginning, which is a good indication of lubrication level for a particular bearing to increase its life time.

Acknowledgments This project has been realized with great help, and kind collaboration of Kingston University London in UK for technical support, also the Iraqi Ministry of Higher Education and Iraqi Cultural Attaché in London for financial support.

References

1. Muszynska A (1995) Vibrational diagnostics of rotating machinery malfunctions. Int J Rotat Mach 1(3–4):237–266, USA
2. Hutin C (2000) Modal analysis is using appropriated excitation techniques. J Sound Vib 34(10):18–25
3. Genta G (2005) Dynamics of rotating systems. Springer, New York
4. http://www.mpihome.com/
5. Al-Khazali HAH, Askari MR (2012) The experimental analysis of vibration monitoring in system rotor dynamic with validate results using simulation data. In: International Scholarly Research Network (ISRN mechanical engineering), vol 2012, Hindawi Publishing Corporation USA, pp 1–17. doi:10.5402/2012/981010, ISSN: 2090–5130 (Online)
6. Irretier HD (2002) History and development of frequency domain methods in experimental modal analysis. Journal De Physique 12 (11):91–100
7. Hillary B, Ewins DJ (1984) The use of strain gauge in forces determination and frequency response function measurements. In: Proceedings, IMAC, vol 2, Orlando, FL, USA
8. Al-Khazali HAH, Askari MR (2012) Determination and simulation of modal parameter on revolving machines using vibration analysis, paper no. #216. In: Del Grosso AE, Basso P (eds) Smart structures, proceedings of the 5th European conference on structural control – EACS 2012, University of Genoa and University DI PAVIA, Erredi Grafiche Editoriali S.n.c. Genova, Held at 18–20 June, Genoa, pp 1–10, ISBN 978-88-95023-13-7
9. Rao JS (2007) Rotor dynamics, Revised 3rd edn. New Age International
10. Karimulla S, Gupta RK, Gouthaman G (2009) Design and development of high speed spin test facility. Adv Vib Eng 8(2):183–191
11. Chiang LH, Russell EL, Braatz RD (2001) Fault detection and diagnosis in industrial systems. Springer-velar, Berlin
12. Walter PL (1999) Accelerometer selection for and application to modal analysis. In: Proceedings of the 17th international modal analysis conference, Kissimmee, pp 566
13. Rangwala RS (2005) Turbo-machinery dynamics design and operation. McGraw-Hill, New York
14. Srivastava SC, Verma AK, Chavda PH, Wankhede AK, Gouthaman G (2002) An experimental study of flexible rotor to suppress resonance using resonance jumping technique by stiffness switching with active magnetic bearings. In: International conference on vibration engineering and technology on machinery (VETOMAC-2), New Delhi, India
15. Allemang RJ, Brown DL (1995) Experimental modal analysis. In: Harris CM (ed) Shock and vibration handbook, 4th edn. McGraw-Hill, New York, Chapter 21

Dr. Hisham A. H. Al-Khazali. He has PhD Student in Kingston University London, SEM member, Society for Experimental Mechanics. Inc., in USA, and SAI member, The Science and Information Organization in USA. He was born in 28 Aug 1973 Baghdad/Iraq. He received his B.Sc. (Eng.), in Mechanical Engineering 1996, University of Technology, Baghdad. MSc in Applied Mechanics, University of Technology, Baghdad 2000.

Dr. Hisham A.H. Al-Khazali

Dr. Mohamad R. Askari, BSc (Eng), MSc, PhD, CEng, MIMechE, MRAeS. He is Principal Lecturer, Blended Learning Coordinator, member teaching staff in Kingston University London. His Teaching Area: Applied Mechanics, Aerospace Dynamics, Dynamics and Control, Structural and Flight Dynamics, Engineering Design, Software Engineering to BEng Mechanical and Aerospace second and final years. He is Year Tutor for BEng, Mechanical Engineering Course and School Safety Advisor.

Dr. Mohamad R. Askari

Chapter 58
Dynamic Compressive Response of Unsaturated Clay Under Confinements

Y.Q. Ding, W.H. Tang, X. Xu, and X.W. Ran

Abstract The dynamic compression properties of unsaturated clay under confinements were investigated with a split-Hopkinson pressure bar. Clay specimen was placed inside an aluminum alloy confinement tube. The clay specimen had a dry density of 1.70 g/cm^3 with moisture contents varied from 0 % to 15 % by weight. A controlled loading pulse allowed the specimen to acquire stress equilibrium and a constant strain rate of 1,600 ~ 1,700 s^{-1}. The confinement pressure was determined through measurement of circumferential strain. The experiment results indicate that the addition of water acts to lubricate the clay particles thus reducing friction between the particles and offering less resistance to compression. But adding more water will up to a point where the voids is nearly fully compressed and displaced by water, making it difficult for clay particles to displace into the interstitial gaps, and then increasing the degree of saturation gradually increases stiffness.

Keywords Unsaturated clay • Moisture content • Dynamic compression • SHPB • Confinement

58.1 Introduction

Soils are the widely used foundation material in civil and defense constructions, and are categorized as gravel, sand, silt, or clay, depending on the predominant particle size involved. Recently, the increasing interest in studying dynamic properties of soils is the need to solve a number of problems that require quantitative evaluation of behavior of such media under intensive dynamic loading such as strong seismic motions, blast wave propagation or impacts and so on. As a three-phase material consisting of solid particles, water, and air, the dynamic mechanical behavior of soils is largely dependent on the size of its solid particles, voids and moisture content.

Martin [1] studied the effects of moisture content on the high strain-rate mechanical properties of fine grain sand at a constant strain-rate of about 400 s^{-1} with a split-Hopkinson pressure bar. The sand specimen confined in a hardened steel tube, had a dry density of 1.50 g/cm^3 with moisture contents varied from 3 % to 20 % by weight. The experimental results indicate that partially saturated sand is more compressible than dry sand with the softest behavior observed at 7 % moisture content. Arlery [2] conducted the planar shock experiments performed with gas and powder guns on dry, 53 % and 87 % water-saturated by volume (the moisture contents is 0 %, 10.3 %, and 17.1 % respectively by weight) sand specimens in the pressure range of 1–10 GPa, and the experimental results show significant differences in dynamic behavior of the material according to water content. For a given compression, water incorporation increases shock velocity and pressure in the material.

In this work, the dynamic compression experiments on unsaturated clay specimen under confinements with different moisture content varied from 0 % to 15 % by weight were conducted by a split-Hopkinson pressure bar test system.

Y.Q. Ding (✉) • W.H. Tang • X. Xu • X.W. Ran
Institute of Engineering Physics, College of Science, National University of Defense Technology, Changsha 410073, China
e-mail: yqding_nudt@163.com

B. Song et al. (eds.), *Dynamic Behavior of Materials, Volume 1: Proceedings of the 2013 Annual Conference on Experimental and Applied Mechanics*, Conference Proceedings of the Society for Experimental Mechanics Series,
DOI 10.1007/978-3-319-00771-7_58,

58.2 Experimental Procedures

58.2.1 Specimen Preparation

The material investigated in this study is silica based fine grain clay. The particle size distribution of the clay particles were measured by the densimeter method and are shown in Table 58.1, the solid particle density ρ_{s0} was measured to 2.74 g/cm^3. The dynamic compressive response of the unsaturated clay was investigated in this study at various moisture contents ranging from 0 % to 15 % by weight with all specimens having a dry density of 1.70 g/cm^3. All specimens were in an undrained condition, where water or air is not allowed to escape. The specimens were confined using a 2,024 aluminum alloy tube with an outer diameter of 28 mm, inner diameter of 20 mm and length of 14 mm to achieve high confinement levels and to replicate a uniaxial strain condition.

Before the specimen preparation, the clay was dried in the dry oven. A piece of impervious film is placed on top of the scale, and 4.27 g of dry clay weighed. The appropriate weight water (e.g., 0.17 g for 4 % moisture) is slowly released from the syringe into the dry clay until the measured weight of scale is equal to 4.44 g and evenly distributed uniformly. Then, the mixed clay is poured into the aluminum alloy tube and tapped lightly to even the top surface shown in Fig. 58.1. The inner surface of the tube was smeared the lubricant oil to reduce the friction between the tube and the clay. The inside height of the two steel pistons is 3 mm. The upper steel piston is then placed on top of the clay and slightly pressed by using the hydraulic jack to ensure the interface between the piston and partially saturated clay is flat. The assembled specimen is shown in Fig. 58.2. The size of the specimen is ϕ 20 $\times$ 8 mm, and the initial physical properties of the five moisture contents clay specimens were listed in Table 58.2.

58.2.2 Modified SHPB

In this investigation, a modified SHPB was used with a pulse shaping technique to apply dynamic compression. The SHPB apparatus, as shown in Fig. 58.3, consisted of a solid LC4 aluminum alloy bars (Young's modulus E_0 is 72 GPa, density ρ is 2.78 g/cm^3, and wave speed c_0 is 5,184 m/s). The striker bar is 500 mm long, the incident bar is 2,000 mm long, and the transmission bar is 1,000 mm long, all with an outer diameter of 20 mm. An eraser pulse shaper putted on the interface where the striker bar impacts the incident bar, and a specimen sandwiched between the incident and transmission bars. Compressed air released using a fast acting valve launches the striker bar into the incident bar creating a compressive wave that travels down the incident bar towards the specimen. Since the impedance of the clay specimen is less than that of the bars, part of the compressive wave propagates through the specimen to the transmission bar and part is reflected back into the incident bar as

Table 58.1 Particle size distribution in the clay specimen

Particle dimension (mm)	>0.075	0.075 ~ 0.005	<0.005
Proportion (%)	0	71.4	28.6

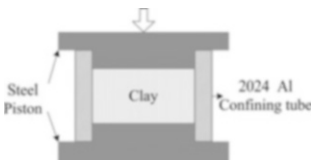

Fig. 58.1 Schematic of the specimen preparation steps for SHPB experiments

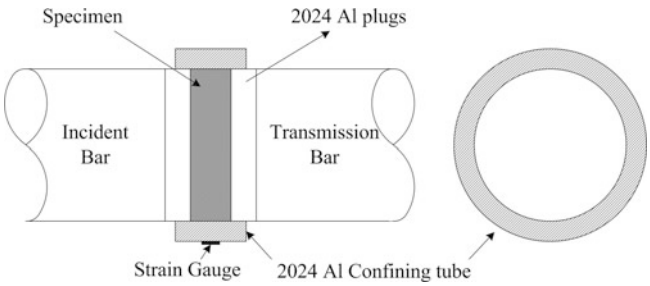

Fig. 58.2 Schematic of the test section of the clay assembly on SHPB apparatus

Table 58.2 The initial physical properties of the clay specimen

Initial moisture content w (%)	0.0	4.0	8.0	12.0	15.0
Initial saturation S_r (%)	0.0	18.0	35.9	53.9	67.4
Initial mass density ρ_0 (g/cm^3)	1.70	1.77	1.84	1.90	1.96
The mass of specimen (g)	4.27	4.44	4.61	4.78	4.91
The mass of water (g)	0.0	0.17	0.34	0.51	0.64

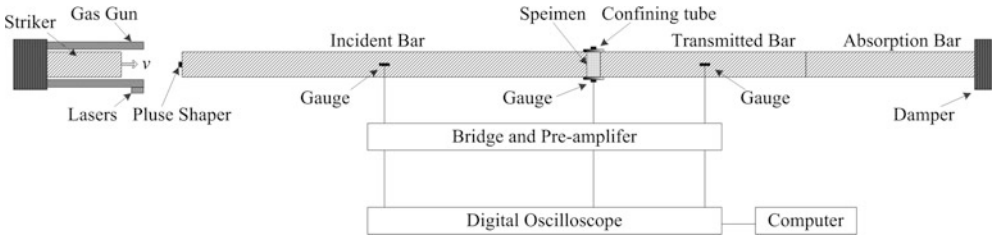

Fig. 58.3 Schematic of SHPB apparatus used for dynamic compaction of unsaturated clay

a tensile wave. The incident stress wave contains no high-frequency components, enabling it to propagate along the bar without dispersion and then deforming the specimen uniformly. The nearly non-dispersive waves measured at strain gage locations on the bar surfaces away from the specimen can be used to determine the specimen response. Strain gages mounted on the incident bar measure the incident, ε_i, and reflected, ε_r, strains and gages mounted on the transmission bar measure the transmitted strain, ε_t. Each set of strain gages are connected to form a Wheatstone bridge excited by a constant power supply. Finally, the signals are conditioned by KD 6009 pre-amplifier and recorded with the DPO 4104 high speed digital oscilloscope.

The front and back stress of the specimen σ_1, σ_2 is given by the following equations.

$$\sigma_1 = \frac{A_0}{A_s} E(\varepsilon_i + \varepsilon_r) \tag{58.1}$$

$$\sigma_2 = \frac{A_0}{A_s} E(\varepsilon_t) \tag{58.2}$$

where A_0 is the bar cross section area and A_s is the specimen cross section area respectively.

The two relations above allow direct verification of stress equilibrium by comparing σ_1 and σ_2 obtained from experiments. If a state of dynamic stress equilibrium exists, where the stresses on both sides of the specimen are equal, then specimen axial stress σ_{zz}, strain-rate $\dot{\varepsilon}_{zz}$, and axial strain ε_{zz} can then be derived using the strain signals measured from the bar surface by the following equations.

$$\sigma_{zz} = \frac{A_s}{A_0} E_0 \varepsilon_t \tag{58.3}$$

$$\dot{\varepsilon}_{zz} = \frac{2c_0}{l_s} \varepsilon_r \tag{58.4}$$

$$\varepsilon_{zz} = \frac{2c_0}{l_s} \int_0^t \varepsilon_r(\tau) d\tau \tag{58.5}$$

where l_s is the initial length of the specimen.

The strain gage was attached on the out surface of the tube, as shown in Fig. 58.3. In the experimental process, the specimen was under the axial compression loading, but the radial expand is restricted by the tube. By using the thick-walled cylinder theory, the circumferential strain of the out surface of the tube, the pressure p_1 of inner face of the tube and the radial displacement U_r are obtained by the following equations.

$$p_1 = \frac{R_2^2 - R_1^2}{2R_1^2} E_j \varepsilon_j \tag{58.6}$$

$$U_r = \frac{R_1 \varepsilon_j}{2}\left[(1-\upsilon_j)+(1+\upsilon_j)\frac{R_2^2}{R_1^2}\right] \tag{58.7}$$

where R_1 and R_2 is the inner and outer radius of the tube, E_j is the Young's modulus of the tube material, υ_j is the poisson ratio of the tube material. The confinement stress σ_{rr} and the radial strain ε_{rr} are obtained can obtained by the interface equilibrium using the following equations.

$$\sigma_{rr} = \sigma_{\theta\theta} = p_1 = \frac{R_2^2 - R_1^2}{2R_1^2} E_j \varepsilon_j \tag{58.8}$$

$$\varepsilon_{rr} = \varepsilon_{\theta\theta} = \frac{\varepsilon_j}{2}\left[(1-\upsilon_j)+(1+\upsilon_j)\frac{R_2^2}{R_1^2}\right] \tag{58.9}$$

The calculation results indicate that the radial strain ε_{rr} can be neglected compared to the axial strain ε_{zz}. Then, the hydro pressure p, volume strain ε_v, shear stress τ and shear strain γ_e are obtained by the following equations.

$$p = \frac{1}{3}(\sigma_{zz} + 2\sigma_{rr}) \quad \text{and} \quad \varepsilon_v = \varepsilon_{zz} + 2\varepsilon_{rr} \approx \varepsilon_{zz} \tag{58.10}$$

$$\tau = \frac{1}{2}(\sigma_{zz} - \sigma_{rr}) \quad \text{and} \quad \gamma_e = \varepsilon_{zz} - \varepsilon_{rr} \approx \varepsilon_{zz} \tag{58.11}$$

58.3 Experimental Results and Discussion

58.3.1 Dynamic Equilibrium and Repeatability of SHPB Data

Typical recorded signals from strain gages attached to the bars, together with the circumferential strain signal measured by the strain gage attached to the outer surface of the confining hollow aluminum alloy tube in a SHPB test are plotted in Fig. 58.4. The 'input' designates the signal acquired from the incident bar, the 'output' designates the signal acquired from the transmission bar, while the 'hoop strain' designates the signal acquired from the confining tube. The loading duration is about 200 μs. To examine the dynamic equilibrium condition, the front stress and the back stress on the specimen are calculated following the Eqs. 58.1 and 58.2. The stress at the front face (the end of specimen in contact with the incident bar) and back face (the end of specimen in contact with the transmission bar) with time are shown in Fig. 58.5 for the examination

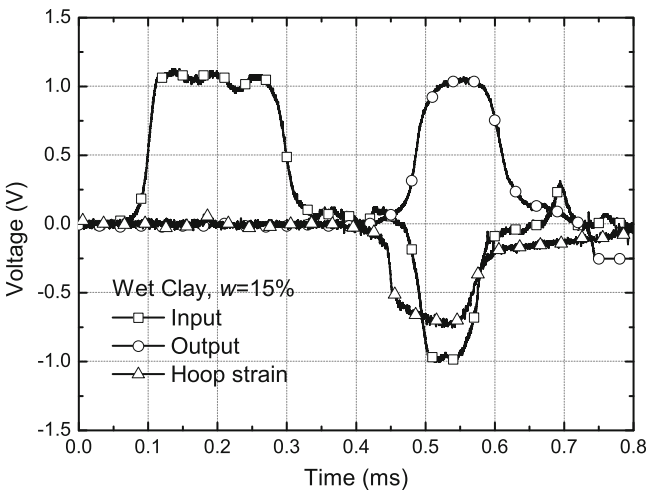

Fig. 58.4 Typical oscilloscope recordings of input, output, and hoop strain (wet clay with an initial moisture content of 15 %)

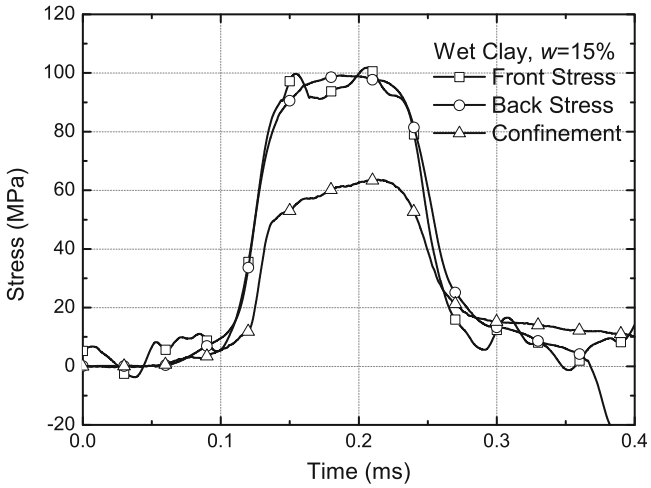

Fig. 58.5 Typical dynamic stress equilibrium check and confinement pressure (wet clay with an initial moisture content of 15 %)

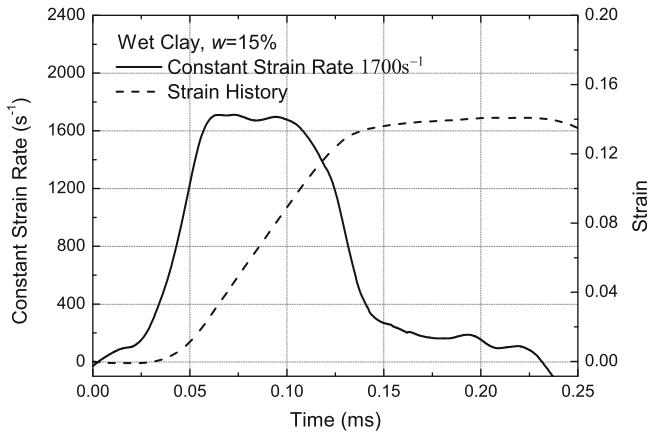

Fig. 58.6 Strain rate and strain history (wet clay with an initial moisture content of 15 %)

of dynamic stress equilibrium, as well as confining pressure histories. Comparing to the stress on the back face, the stress curve at the front face shows light oscillations, which may due to the frictional effects of the solid grains in the clay specimen. The front stress was very close to the back stress during loading after 100 μs loading time, indicating that the dynamic equilibrium condition has nearly been established and the specimen was uniformly loaded.

Figure 58.6 shows the strain rate and strain histories of wet clay specimen with 15 % moisture content by weight. The nearly flat phase in strain rate history indicates that a constant strain rate has been nearly achieved with 60 and 100 μs. The data reported as results near the average strain rate calculated within 60 and 100 μs. The strain rate decreases gradually after 100 μs. The strain as a function of time is shown in Fig. 58.6. In a valid SHPB experiment, the incident, transmitted, and reflected signals are processed further to determine the stress–strain relationship at high strain rates.

In the present work, the experimental repeatability and reliability was examined at first. The resulting axial stress-axial strain curves are compared under the same testing condition. The compressive stress–strain curves of wet clay specimen of 4 % moisture content are shown in Fig. 58.7 with good reproducibility. Under each set of testing conditions, 4–6 experiments were conducted, and the average results are reported.

58.3.2 Effect of the Moisture Content

In this work, the unsaturated specimen consists of a clay skeleton and pores filled with air and water in an undrained state. The specimen was placed in the aluminum alloy confinement which preferentially allows axial strain to occur, since radial stress generated by the aluminum alloy confinement will constrict lateral expansion. For uniaxial strain conditions the

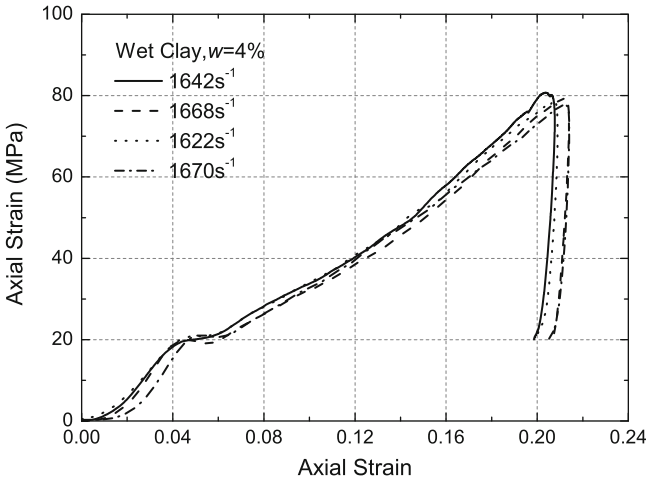

Fig. 58.7 Reproducibility of axial stress-axial strain of wet clay with initial moisture content of 4 %

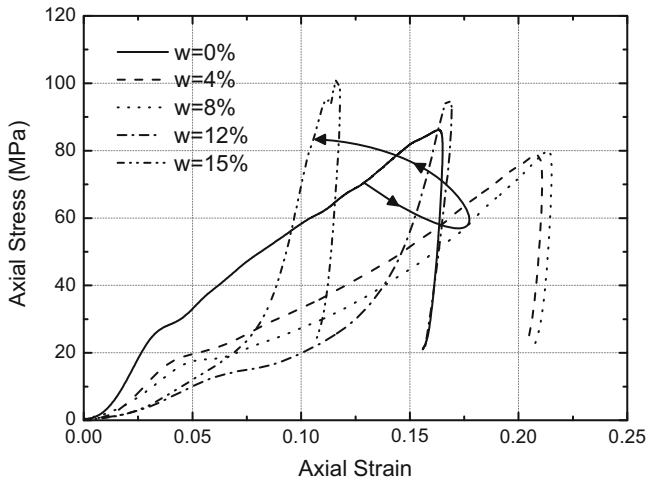

Fig. 58.8 Results of axial stress–strain of clays with different moisture content

volume fraction of air voids in the specimen is directly related to the percent strain required to remove the air voids. When the percent strain is equal to the maximum percent volume of air, it can be assumed that the specimen is fully saturated.

For unsaturated clay specimen under confinement, the axial stress-axial strain curves, hydrostatic pressure- volumetric strain curves, and shear stress-shear strain curves determined at high strain rates (1,600 $\sim$ 1,700 s^{-1}) were plotted in Figs. 58.8, 58.9, and 58.10, respectively. Similarly to the experimental data of moistured sand reported by Martin [1] and the review wrote by Omidvar [3], under dynamic loading the response of unsaturated clay may be dominated by air or water depending on the moisture content. Water is much stiffer than air. If the strains produced by the dynamic loading are not sufficient to displace all the air voids, the stress–strain response will not exhibit a lock-up response, as indicated in Fig. 58.8 (moisture content of 4 % and 8 %). Under such loading conditions unsaturated clay is more compliant compared to dry clay and the stiffness degrades with increasing moisture content. At high moisture contents the voids may become saturated under dynamic loading and the response will be essentially governed by the water in the pores as shown in Fig. 58.8 (moisture content of 12 % and 15 %).

The initial softening response at lower moisture contents is due to the possible explanations as discussed by Martin [1] and Omidvar [3]. The addition of water acts to lubricate the clay particles thus reducing friction and offering less resistance to compression. In the initial stage of compression progress, the friction between the solid grains is the main mechanism to resist the deformation. Because of the lubrication of the existed water in clay specimen, the shear resistance of clay specimen decreased with moisture content increased. The slide of the grains and the collapse of the pore space, together with the rearrangement of the grains are the main mechanism.

Introducing more water will further ease compression, up to a point where the air within voids is nearly fully displaced by water, making it difficult for clay particles to displace into the interstitial gaps. The gap between the grains is become too

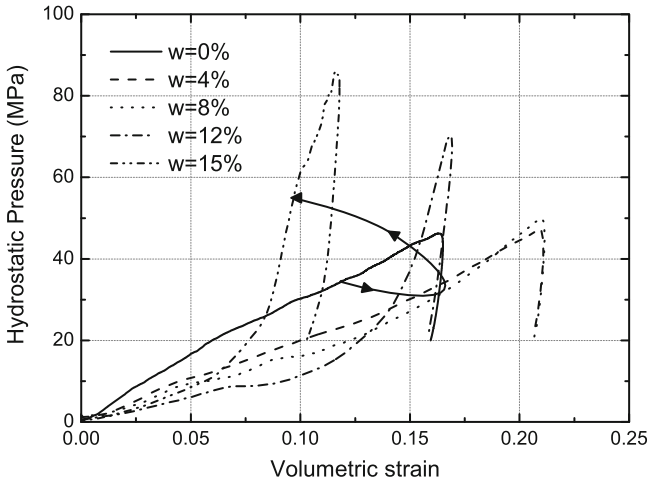

Fig. 58.9 Results of hydrostatic pressure versus volumetric strain of clays with different moisture content

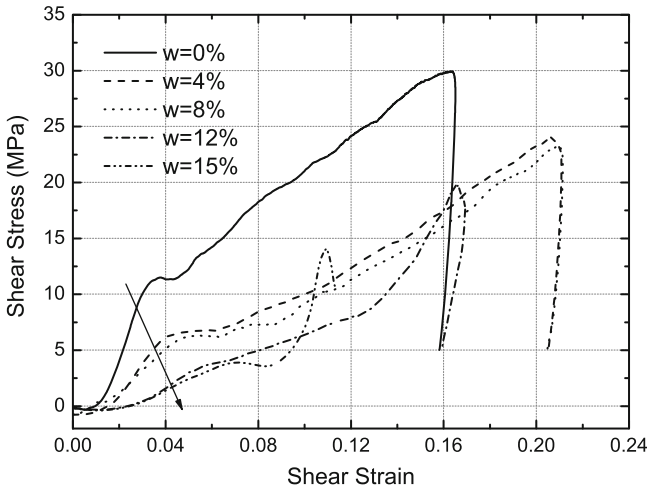

Fig. 58.10 Results of shear stress versus shear strain of clays with different moisture content

small, and then the specimen approach to saturated condition, due to the rapid loading, the water in the pore has no time to escape. The water begins to undertake the loading together with the solid. From this point on, increasing the degree of saturation gradually increases stiffness. The initial response is due to lessened shear resistance due to reduction of contact stresses, while the later response results from elimination of free volume.

58.3.3 Energy Absorption of Unsaturated Clay

The energy absorption capability for unsaturated clay specimens under confined compression is estimated according to Luo [4] in this work. The energy absorption density is calculated in term of the area enclosed by the stress–strain curve. The specific energy absorption is then calculated in terms of the energy absorption density divided by the initial mass density. The specific energy absorptions under axial, volumetric and deviatoric deformations under these situations are calculated from Figs. 58.8, 58.9, and 58.10, respectively, under the maximum axial stress and strain attained in experiments. The specific energy absorption values of unsaturated clay specimens due to axial, volumetric and deviatoric deformations are listed in Table 58.3. The relationship curves of volumetric and deviatoric energy absorption ratio and moisture content are plotted in Fig. 58.11. It can be found that the moisture content has significant influence on the energy absorption capability of unsaturated clay. The specific axial energy absorption and the deviatoric energy absorption ratio are decreased, while the volumetric energy absorption ratio is increased by the increased moisture content in the clay specimens. Since the water cannot undertake the deviatoric stress leading to the shearing resistance of wet clay specimen is descending with the ascending moisture content. But the comparatively incompressibility of the water make the volumetric energy absorption

Table 58.3 Energy absorption and compressibility of clay on SHPB

Initial moisture content (%)	0	4	8	12	15
Maximum mass density (g/cm^3)	2.03	2.23	2.33	2.29	2.21
Maximum saturation (%)	0	39.6	81.7	96.0	96.8
Maximum axial stress (MPa)	86.1	78.7	79.8	94.9	100.8
Maximum axial strain (%)	16.3	20.8	21.3	16.7	11.6
Specific axial energy absorption (J/g)	4.3	4.1	3.7	1.6	1.2
Specific volumetric energy absorption (J/g)	2.1	2.3	2.0	1.0	0.9
Specific deviatoric energy absorption (J/g)	1.6	1.2	1.1	0.4	0.1

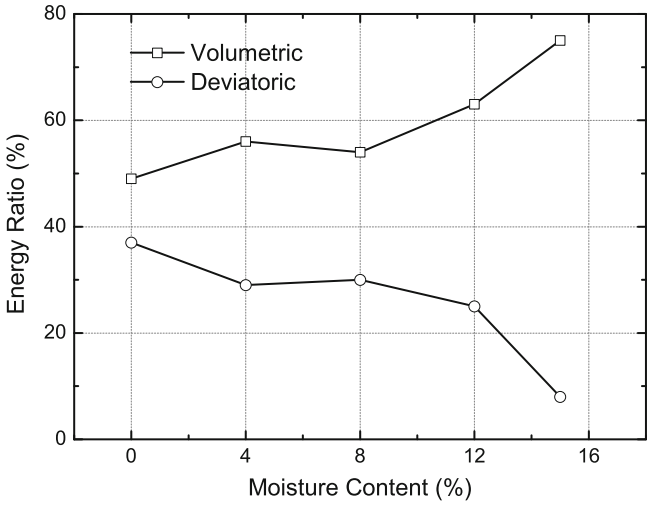

Fig. 58.11 Results of energy ratio versus moisture content

ratio increased by the increased moisture content in wet clay specimens. Furthermore, comparing to the experimental data reported in Luo [4], the axial energy absorption capability of the dry clay (4.3 J/g of the initial density is equal to 1.70 g/cm^3) is found lower than the dry sand (15.2 J/g of initial density is equal to 1.69 g/cm^3).

58.4 Conclusions

The dynamic compressive behavior of unsaturated clay under stiff confinement using aluminum alloy cylinder tube was investigated using a modified split Hopkinson pressure bar (SHPB) at high strain rates (1,600 $\sim$ 1,700 s^{-1}) up to 100 MPa compressive stress. A clay specimen preparation assembly was developed. The assembly allows consolidating clay to prepare clay specimens with given initial moisture contents. Clay specimens of five initial moisture contents (0 %, 4 %, 8 %, 12 %, and 15 % by weight) were compressed at high strain rates. A strain gage was attached on the external surface of the confining aluminum alloy sleeve to measure the circumferential strain, to determine both the bulk and the deviatoric responses. Significant moisture content effects and the highly repeatable SHPB data have been identified. The curves of axial stress-axial strain, hydrostatic pressure-volumetric strain, shear stress-shear strain of clay are determined up to 21.3 % compressive strain and up to 100 MPa axial compressive stress at high strain rates. The specific energy absorption of clay specimens with different moisture contents under volumetric and deviatoric deformations were obtained in the present paper.

Acknowledgements This work was supported by the Natural Science Foundation of China (NSFC) through Grant No. 11002162.

References

1. Martin BE, Chen W, Song B et al (2009) Moisture effects on the high strain-rate behavior of sand. Mech Mater 41(6):786–798
2. Arlery M, Gardou M, Fleureau J et al (2010) Dynamic behaviour of dry and water-saturated sand under planar shock conditions. Int J Impact Eng 37(1):1–10
3. Omidvar M, Iskander M, Bless S (2012) Stress–strain behavior of sand at high strain rates. Int J Impact Eng 49:192–213
4. Luo H, Lu H, Cooper W et al (2011) Effect of mass density on the compressive behavior of dry sand under confinement at high strain rates. Exp Mech 5(9):1–12

Chapter 59
Dynamic Tensile Testing of Based and Welded Automotive Steel

J.G. Qin, Y.L. Lin, F.Y. Lu, R. Chen, and M.Z. Liang

Abstract Strength and ductility data at high strain rates (~1,200 s^{-1}) for UTS800, UTS700 automotive steel and their electron beam welded (EBW) were obtained using a split Hopkinson tensile bar apparatus. The stress–strain curves of the materials were obtained, tensile strength, elongation, reduction in area, and energy dissipated were acquired. From the experimental results, based UTS800 shows higher flow stress but lower fracture elongation than based UTS700. When comparing welded materials to the corresponding based materials, the flow stress presents little different but the fracture elongation displays distinct decreased. Digital image correlation was used together with high-speed photography to study the strain localisation in the tensile specimens. By using digital image correlation, the in-plane strain field and local fracture strain of the specimen were obtained.

Keywords Automotive steel • Dynamic tensile behaviour • Split Hopkinson tensile bar • Digital image correlation

59.1 Introduction

High strength steels are extensively used in the transportation industry to improve crashworthiness, increase safety and reduce weight of the automobiles [1–5]. The knowledge of the dynamic stress–strain curve and crashworthiness parameters of such advanced high strength steels is necessary for the effective design of automobile components. So it is important to investigate the mechanical behaviour of automotive steels under dynamic loading.

In practice, applications frequently require the welding of various components to reduce the cost and difficulty of the machining process. However, rapid heating and cooling and filler material fusion into the weld metal often lead to inhomogeneous metallurgical and mechanical conditions in the welded joints, even if the filler metal is the same as the based metal [6]. The thermal effects associated with the welding process usually cause the failure of a structure at its welded joints [7]. Consequently, it is very necessary to obtain the welding characteristics of high strength steels and compare with the based materials.

The most widely used method for high strain rate testing in the range of strain rates from 10^2 s^{-1} to 10^4 s^{-1} is the Split Hopkinson bar method [8] due to its relative simplicity and robustness. In order to obtain more meaningful measurements of strain in specimen, a robust full-field measurement method is required. Digital image correlation (DIC) has become popular for full-field measurements in problems related to solid mechanics [9]. The advantage of this method is its simplicity and that it sometimes avoids difficult interpretations of interferometric fringes [10].

In this paper, high strength steels UTS800, UTS700 and their electron beam welded (EBW) were tested under dynamic tensile loading using the split Hopkinson tensile bar apparatus. From the obtained stress–strain curves, the important mechanic characteristic parameters of materials were compared and discussed. The DIC technique combining high-speed photography was used in a representative test for welded UTS700 (~1,270 s^{-1}) to obtain the full field strain and local strain information of specimen during tensile loading.

J.G. Qin (✉) • Y.L. Lin • F.Y. Lu • R. Chen • M.Z. Liang
College of Science, National University of Defense Technology, Changsha, Hunan 410073, People's Republic of China
e-mail: jg_qin@yahoo.cn

B. Song et al. (eds.), *Dynamic Behavior of Materials, Volume 1: Proceedings of the 2013 Annual Conference on Experimental and Applied Mechanics*, Conference Proceedings of the Society for Experimental Mechanics Series,
DOI 10.1007/978-3-319-00771-7_59,

59.2 Experimental Procedures

The commercially available high strength sheet automotive steels UTS800 and UTS700 are examined in this study. Table 59.1 lists the chemical composition of these materials. Autogenously full penetration bead-on-plate electron beam weldments are made on coupons by electron beam welding (EBW), which would provide high quality weld joint because of high vacuum environment. The welding process was performed with an electron beam welding machine. So there are four types of samples to be investigated: based UTS800, based UTS700, welded UTS800 and welded UTS700.

The specimen, with dumbbell-shaped flat, 1.8 mm thickness, is illustrated in Fig. 59.1 for dynamic tensile deformation. A refractory inorganic adhesive is used to connect dynamic specimen with incident/transmitted bars, as shown in Fig. 59.2. The thickness of each adhesive layer is 0.10 mm. A split Hopkinson tensile bar (SHTB) apparatus is used to characterize the dynamic properties of the investigated material (Fig. 59.3). It mainly consists of two aluminium bars with a diameter of 20 mm, i.e. the input and the output bar (measuring 3.3 and 1.8 m in length, respectively) between which a specimen of the test material is attached. A striker made of a hollow tube that is accelerated towards the anvil of the input bar produces an incident tensile wave in the input bar which travels towards the specimen, where it interacts with this specimen and is partly reflected back into the input bar. The other part, the transmitted wave, travels along the output bar. The strain histories of the different waves (incident, reflected and transmitted wave, respectively denoted as $\varepsilon_i(t)$, $\varepsilon_r(t)$, $\varepsilon_t(t)$), are recorded by means of strain gauges mounted on both bars. By adjusting the impact speed of the striker the strain rate can be varied.

According to the one-dimensional wave theory and the assumption of a uniaxial and homogeneous stress and strain in the specimen, the stress, strain and strain rate in the specimen can be written as follows [8]:

$$\sigma(t) = \frac{E_b A_b}{A_s} \varepsilon_t(t) \tag{59.1}$$

Table 59.1 Chemical composition of the investigated steels (in weight percent)

	C	Si	Mn	P	S	Fe
UTS800	0.15	0.33	1.46	0.016	0.012	Balanced
UTS700	0.17	0.2	0.42	0.023	0.027	Balanced

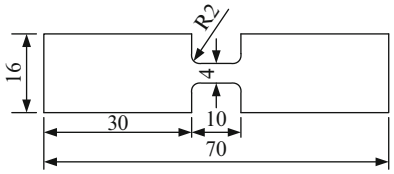

Fig. 59.1 Specimen geometry for tensile impact tests

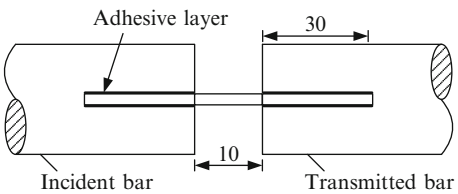

Fig. 59.2 Connection of specimen to bars

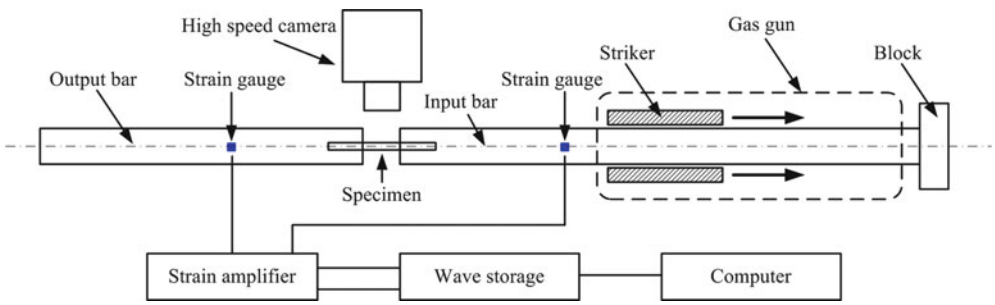

Fig. 59.3 Schematic representation of a SHTB setup

$$\varepsilon(t) = \frac{U_{ob} - U_{ib}}{L_s} = -\frac{2C_b}{L_s}\int_0^t \varepsilon_r(\tau)d\tau \tag{59.2}$$

$$\dot{\varepsilon}(t) = \frac{V_{ob} - V_{ib}}{L_s} = -\frac{2C_b}{L_s}\varepsilon_r(t) \tag{59.3}$$

Where A_s and L_s are the cross-sectional area and the length of the testing region of the specimen. C_b is the one-dimensional elastic stress wave velocity in the input/output bar material, A_b the cross-section area and E_b Young's modulus of the input/output bar, U_{ib} and U_{ob} the displacements of the specimen/input bar interface and the specimen/output bar interface and V_{ib} and V_{ob} are the corresponding interface velocities.

DIC is used to assess the full field strain in the dynamic tensile specimen. Therefore, a fine speckle pattern is sprayed randomly on the specimen surface. Images with a resolution of 704 × 208 pixels and a frame rate of 37,500 fps are recorded with a Photron FASTCAMSA-1 high speed camera.

59.3 Results and Discussion

Several specimens of each material are tested. Figure 59.4 is the true stress–true strain curves of based UTS800 and based UTS700 steels. Figures 59.5 and 59.6 show the true stress–true strain curves of welded UTS800 and welded UTS700 steels, respectively. From these Figures, it is seen that the results of tests are very repeatable.

In Fig. 59.7, Stress–strain curves of all four investigated steels are compared together. It is seen in Fig. 59.7, the stress–strain curves of based UTS800 almost overlap the ones of welded UTS800, except there is a little scatter at the end of the curves. This means the dynamic mechanical behaviour of welded UTS800 is nearly the same as the based UTS800. On the other hand, the stress–strain curves of based UTS700 intersect the ones of welded UTS700, this causes the flow stress of welded UTS700 is higher in small strain (<~17 %) but lower in large strain (>~17 %) than based UTS700. When comparing to UTS700, flow stress of UTS800 is higher both in based and welded materials. The fracture strains of welded UTS800 and welded UTS700 are scattered, this indicates that the scattered fracture strain have been caused by the uncertainty of welded process, because this scatter is not pronounced in based UTS800 and based UTS700. Especially noteworthy is the yield properties of materials have also been affected by the process of welded, the clear yield peak, observed at the onset of plastic deformation in the based materials, disappears or weakens in the welded materials with the bake hardening treatment during the process of welded, this phenomenon was also been found in TRIP steel by Slycken et al. [11].

To avoid the stress oscillations in initial plastic range, the stress corresponding to 4 % offset strain, $\sigma_{0.04}$, is used to evaluate the yield property of materials. Figure 59.8 shows the tensile strength σ_b and $\sigma_{0.04}$ of all four investigated steels. It is

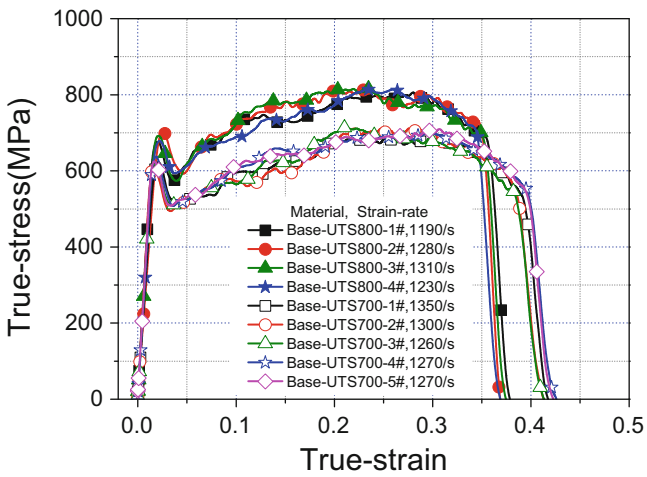

Fig. 59.4 Stress–strain curves of based UTS800 and based UTS700 steels

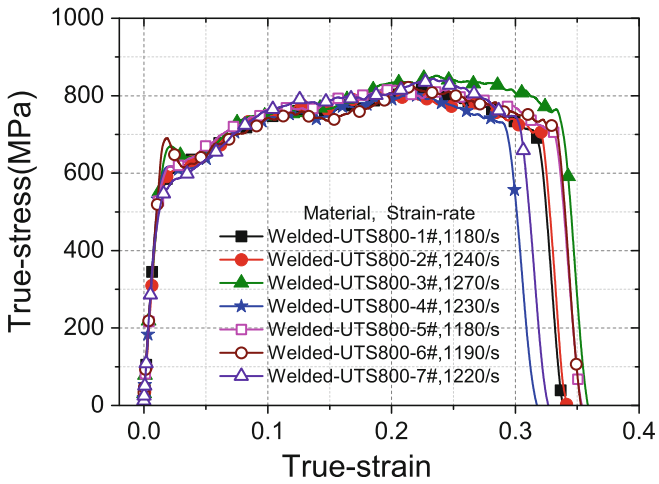

Fig. 59.5 Stress–strain curves of welded UTS800 steel

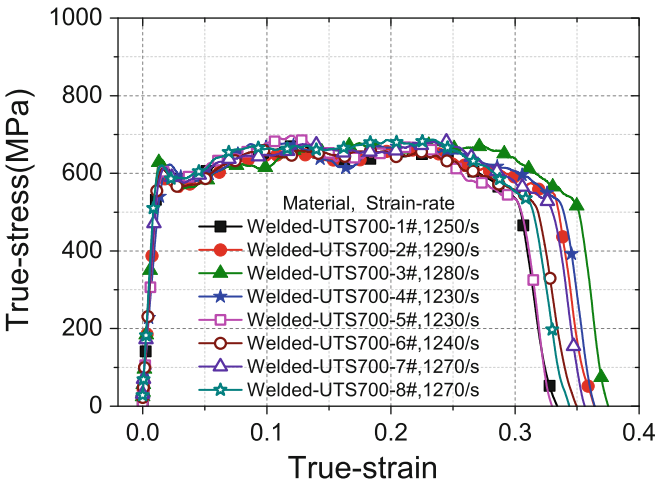

Fig. 59.6 Stress–strain curves of welded UTS700 steel

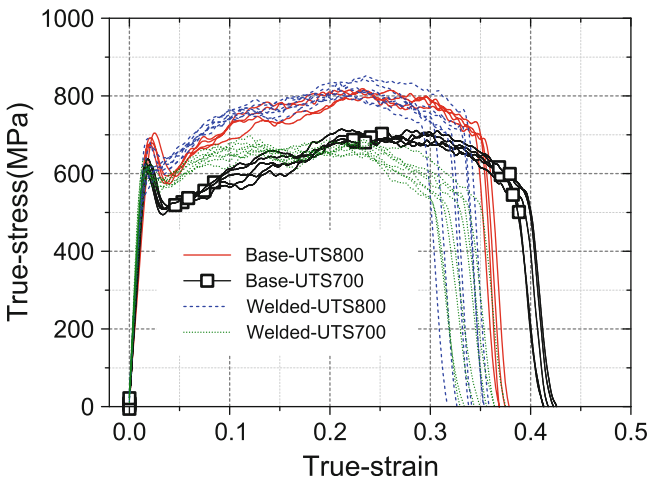

Fig. 59.7 Stress–strain curves of all four investigated steels

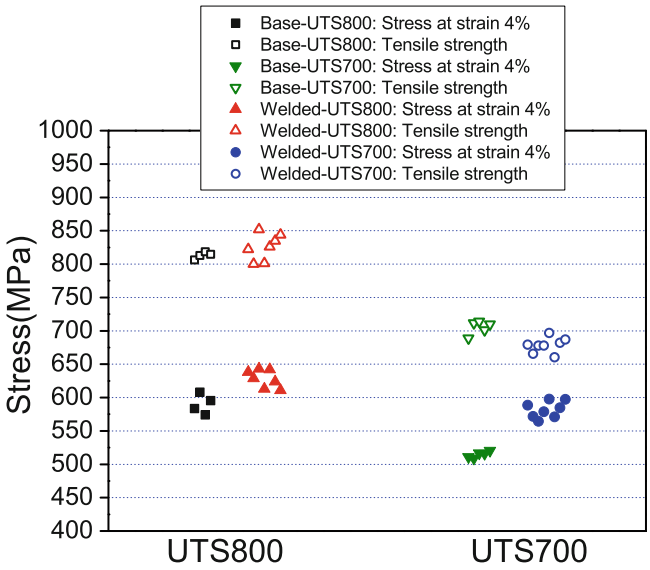

Fig. 59.8 Comparison of strength property of all four investigated steels

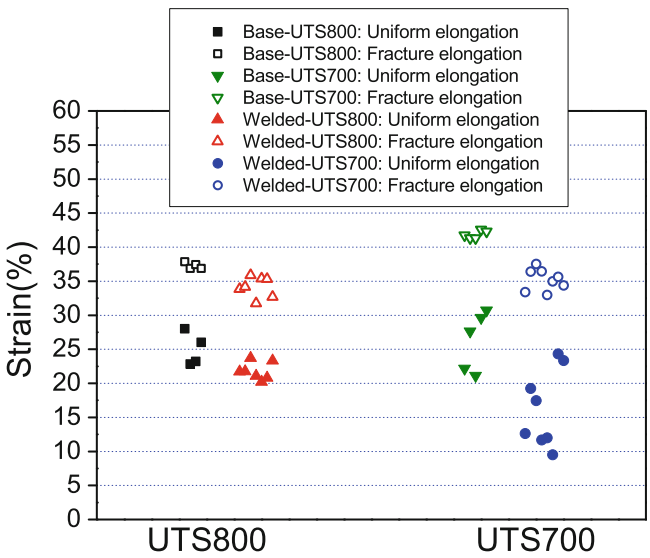

Fig. 59.9 Comparison of elongation property of all four investigated steels

seen in Fig. 59.8, the average of $\sigma_{0.04}$ and σ_b for welded UTS800 are 628.6 and 825.6 Mpa, which are 6.5 % and 1.5 % higher than based UTS800, respectively. The average of $\sigma_{0.04}$ and σ_b for welded UTS700 are 581.9 and 678.6 Mpa, which are 13.1 % higher but 1.5 % lower than based UTS700, respectively. This conclusion can be derived from the stress–strain curves of based UTS700 intersect the ones of welded UTS700. When comparing to UTS700, for both based and welded materials, $\sigma_{0.04}$ and σ_b of UTS800 are higher. The increment of σ_b is larger than that of $\sigma_{0.04}$, this means the strain-hardening rate of UTS800 is larger than UTS700. Consideration from the behaviour of strength, UTS800 is more excellent than UTS700 because of higher strength and good stability for welding.

Figure 59.9 shows the uniform elongation and fracture elongation of all four investigated steels. As seen in Fig. 59.9, for both UTS800 and UTS700, the uniform elongation and fracture elongation of welded materials are lower than based materials. For example, the fracture elongation of welded UTS800 and welded UTS700 are 0.341 and 0.352, which are 8.4 % and 15.9 % lower than based UTS800 and based UTS700, respectively. Especially noteworthy is quite some scatter in the uniform elongation of both based and welded UTS700, this is due to the stress–strain curve is flat near maximum stress, as seen in Fig. 59.7. When comparing UTS800 to UTS700, the fracture elongation of based UTS700 is 12.3 % higher than

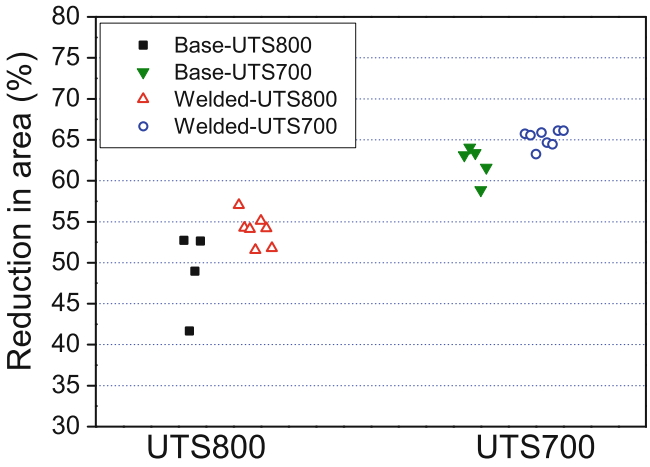

Fig. 59.10 Comparison of reduction in area of all four investigated steels

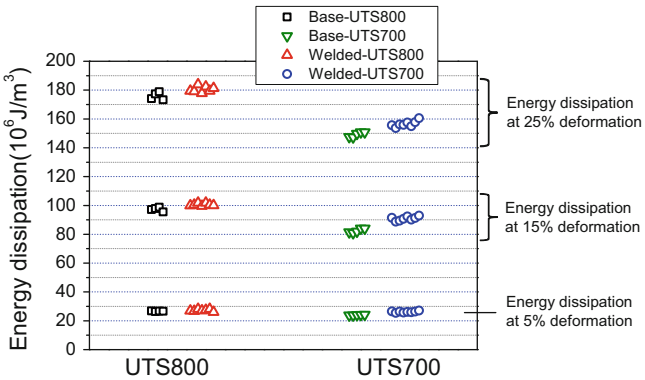

Fig. 59.11 Comparison of energy dissipation of all four investigated steels

based UTS800, but fracture elongation of welded UTS700 exhibits minor difference from welded UTS800, only 3.1 % higher. These can be concluded that, although there are pronounced differences of fracture elongation between based UTS800 and based UTS700, the fracture elongations of welded UTS800 and welded UTS700 show little different after being effected by the process of welding.

Another frequently used parameter to evaluate the ductility of material is reduction in area, *A*%. In Fig. 59.10, the *A*% of all four investigated steels is represented, from this figure, it is clear that the *A*% of based and welded UTS700 are higher than based and welded UTS800, for example, *A*% of based and welded UTS700 are 0.622 and 0.652, which are 27.0 % and 20.8 % higher than based and welded UTS800, respectively. On the other hand, *A*% of welded materials are higher than based materials, 10.2 % for UTS800 and 4.9 % for UTS700.

When comparing dynamic result to static tensile test, since test specimens of different geometry and different measuring techniques are usually used, the comparisons of the uniform elongation and fracture elongation are trivial. But once the cross-section areas of gauge sections are same between the dynamic and static specimen geometries, this condition is frequently achieved in many researches, the reduction in area, *A*%, could be as an important parameter to make a comparison of material ductility between dynamic and static loadings.

Usually high strength steel performs low ductile. Different parameters can be used to evaluate the crash resistance performance of steels. The energy absorbed equaled the area value under true stress vs. true strain curve by the material gives valuable information. In Fig. 59.11, the comparison of energy dissipated by all four investigated steels at 5 %, 15 %, and 25 % strain is given. It is clear that, at all three strains, the same conclusion is: energy dissipated by welded UTS800 is the highest, followed by based UTS800, and then welded UTS700, value by based UTS700 is the lowest. For the same material, energy dissipated by welded steel is a little higher than based steel. Both based and welded materials, the differences of energy dissipated between UTS800 and UTS700 are more pronounced at larger strain. For example, energies dissipated by based and welded UTS800 are 175.9 and 180.5 MJ/m^3, which are 17.8 % and 15.3 % higher than based and welded UTS700, respectively. Consideration from the behaviour of energy absorbed, UTS800 is more excellent than UTS700 whether welded or not.

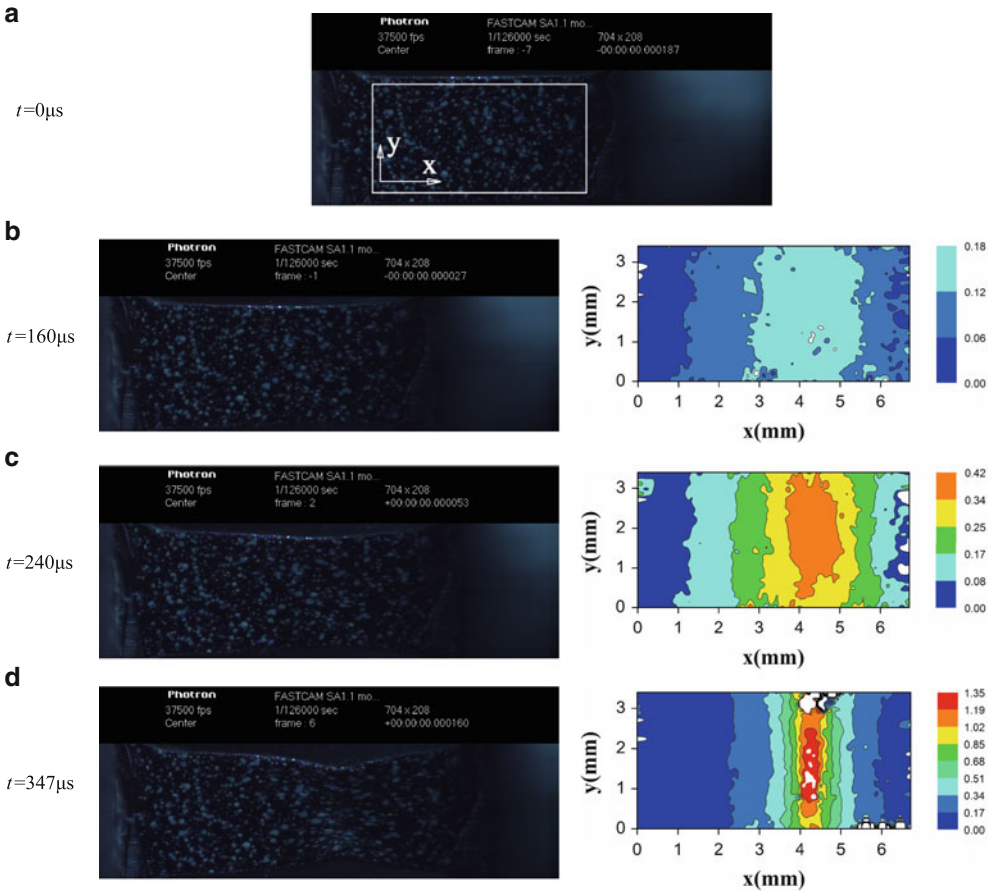

Fig. 59.12 Sequence of images of specimen deformation and corresponding strain distribution of X-direction at three stages

The DIC technique is used in a representative test for welded UTS700 (~1,270 s^{-1}) to obtain the full field strain of specimen during tensile loading. Figure 59.12 shows the high-speed sequence obtained for experiment and the strain distribution of X-direction calculated from DIC. Figure 59.12a is the reference image and the rectangle in the image is the region of interest. The specimen begins to be loaded at 0 μs, and is under the uniform elongate state at 160 μs, the middle gauge section of specimen is necking at 240 μs, and the specimen begins fracture at 347 μs. At 160 μs, Fig. 59.12b shows the high-speed image deformed uniformly and the strain of gauge section center is about 0.12–0.18. At 240 μs, the Fig. 59.12c shows pronounced necking in the high-speed image and the strain of middle part of the region is obviously larger than the two side parts, reaches about 0.34–0.42. At 347 μs, Fig. 59.12d shows that the necking of specimen is much more serious, and the fracture begins in the middle of the specimen, the strain distribution shows that the local fracture strain of this material reaches about 1.35, this parameter can be used as an important material parameter in numerical simulation.

59.4 Conclusion

Dynamic tensile behaviour of based and welded automotive steel, UTS800 and UTS700 are presented in this article. Split Hopkinson tensile bar tests are performed to obtain the stress–strain curves at higher strain rates. The tensile strength, elongation, reduction in area, and energy dissipated of all four investigated steels are compared. Results show that UTS800 presents more excellent strength and crash energy absorption potential than UTS700. Based UTS700 exhibits a little excellent deformability than based UTS800, but welded UTS700 displays nearly no differences with welded UTS800. Considered from the shapes of the stress–strain curves, UTS800 exhibits more excellent stability after being welded than UTS700.

In order to capture the inception and development of strain localization of specimen during dynamic loading, high-speed photography is used. A full-field measuring system based on digital image correlation is successfully applied to track the displacement and strain field from initial plasticity to fracture, and thus provided some substantial information concerning the localisation and hence the inception of ductile failure. By using these techniques, the local fracture strain of material, the important parameter which often be used in numerical simulation, could be obtained.

Acknowledgements This work was financially supported by the Natural Science Foundation of China (Grant Nos. 11172328, 11202232 and 11132012), and the foundation of National University of Defense Technology (Grant No. JC-11-02-17).

References

1. Khan AS, Baig M, Choi SH, Yang HS, Sun X (2012) Quasi-static and dynamic responses of advanced high strength steels: experiments and modeling. Int J Plast 30–31:1–17
2. Van Slycken J, Verleysen P, Degrieck J, Bouquerel J, De Cooman BC (2007) The effect of silicon, aluminium and phosphor on the dynamic behavior and phenomenological modelling of multiphase TRIP steels. Met Mater Int 13(2):93–101
3. Curtze S, Kuokkala VT, Hokka M, Peura P (2009) Deformation behavior of TRIP and DP steels in tension at different temperatures over a wide range of strain rates. Mater Sci Eng A 507(1–2):124–131
4. Huh H, Kim SB, Song JH, Lim JH (2008) Dynamic tensile characteristics of TRIP-type and DP-type steel sheets for an auto-body. Int J Mech Sci 50(5):918–931
5. Winkler S, Thompson A, Salisbury C, Worswick M, Van Riemsdijk I, Mayer R (2008) Strain rate and temperature effects on the formability and damage of advanced high-strength steels. Metall Mater Trans A 39(6):1350–1358
6. Tang W, Shi YW (1995) Influence of strength matching and crack depth on fracture toughness of welded joints. Eng Fract Mech 51(4):649–659
7. Lee DG, Jang KC, Kuk JM, Kim IS (2004) Fatigue properties of inertia dissimilar friction-welded stainless steels. J Mater Process Technol 155-156:1402–1407
8. Kolsky H (1949) An investigation of the mechanical properties of materials at very high rates of loading. Proc Phys Soc B 62:676–700
9. Sutton M, McNeill S, Helm J, Chao Y (2000) Advances in two-dimensional and three-dimensional computer vision. Photomechanics 77:323–372
10. Hung PC, Voloshin A (2003) In-plane strain measurement by digital image correlation. J Braz Soc Mech Sci Eng 25(3):215–221
11. Van Slycken J, Verleysen P, Degrieck J, Samek L, De Cooman B (2006) High-strain-rate behavior of low-alloy multiphase aluminum-and silicon-based transformation-induced plasticity steels. Metall Mater Trans A 37(5):1527–1539